

Studying the influence of close companions on late stellar evolution



Kumulative Habilitationsschrift
der Mathematisch-Naturwissenschaftlichen Fakultät
der Universität Potsdam

vorgelegt von

Veronika Katharina Schaffenroth

aus
Sulzbach-Rosenberg

Contents

1	Introduction	1
2	Stellar evolution and interactions	3
2.1	Single star evolution of low-mass stars	3
2.2	Stellar interactions in binary systems	5
2.2.1	Mass transfer	5
2.2.2	Irradiation	10
2.2.3	Synchronization	10
2.2.4	Orbital period variations	12
2.3	Evolved stars	13
2.3.1	Hot subdwarf stars	13
2.3.2	(Pre-) extremely low mass white dwarfs	17
2.3.3	Binary central stars of planetary nebulae	19
2.3.4	(Hot) white dwarfs	20
3	Analysis methods	21
3.1	Finding close binaries	21
3.1.1	Color selection	21
3.1.2	Light curves	23
3.1.3	Photometric surveys	25
3.2	Analysis of primary star	31
3.2.1	Spectral analysis	31
3.2.2	Spectral energy distribution	31
3.3	Close binary analysis	35
3.3.1	Radial velocity curve	35
3.3.2	Light curve analysis	36
3.3.3	Absolute parameters	36
3.3.4	Eclipse timing	37
4	Discussion and Summary	39
5	Appended papers	43
5.1	Hot subdwarfs in close binaries	43
5.2	Hot subdwarf binaries with M dwarf or brown dwarf companions	44
5.3	Hot subdwarf binaries with white dwarf companions	45
5.4	(Pre-) White dwarfs with close companions	45
	Bibliography	301
	Acknowledgements	304

1 Introduction

Stars are the most fundamental constituents of galaxies. The age, distribution, and composition of the stars in a galaxy can be used to derive the history and evolution of the host galaxy. The stars are responsible for synthesizing and distributing heavier elements. The understanding of the host stars is essential to decode the characteristics of planetary systems. This means that studying the formation, evolution, and death of stars is a central field of astrophysics.

Most stars are not born alone but are found to have one or several companions. In a significant fraction of those systems the companions will interact with each other during their lifetime and so influence each other significantly. This can lead to substantial changes in the evolution of stars in close binary systems and cannot be neglected, if we want to understand stellar evolution. There are different kinds of interactions, which are observed. Tidal interactions can influence the stellar rotation velocity. Strong irradiation can alter the structure of the companions and is vital also for the understanding of close-in planets such as Hot Jupiters. Magnetic interactions can change the orbital period of the binary systems.

The most important interaction is mass transfer from one star to the other. Depending on the initial separation of the system this can happen in different evolutionary phases. The mass ratio of both stars in the binary system is determining, if the mass transfer is stable or not. Binary systems with two stars of similar mass can experience stable mass transfer when they are close enough. Thereby mass is transferred from one star to the other changing both stellar masses. The companion accreting the matter is spun-up and so rejuvenated. In systems where the stars have significantly different masses the mass transfer is expected to happen on a dynamical timescale and the rate of mass transfer will be so high that a common envelope around both stars is formed. Friction in the envelope leads to a rapid shrinking of the orbit on the timescale of a few thousands of days and is difficult to observe. The observation of many evolved systems with orbital separations smaller than the radius of a red giant shows that such a phase must exist. During the spiral-in, energy and angular momentum is transferred to the envelope and can lead to its ejection, when the transferred energy is sufficient to unbind it.

Common-envelope evolution is crucial to understand many exciting systems, which are observed in our universe. It is essential for the formation of stellar-mass gravitational merger sources, as it can bring compact-object binaries close enough together so that gravitational waves can lead to a merger within a Hubble time. This phase is also vital for the understanding of progenitor systems of supernovae type Ia, which are used as standard candles to derive distances to far galaxies. With their help the existence of cosmological dark energy could be inferred. Supernovae type Ia are thought to be produced by the explosion of carbon-oxygen white dwarfs exceeding their upper mass limit, the Chandrasekhar mass. The most likely progenitor systems are still under debate.

The common envelope phase is one of the most significant and least-constrained processes in stellar binary evolution and one of the most important unsolved problems in the understanding of stellar evolution. As it is a short-lived phase, direct observations are very unlikely and a statistically significant sample of systems after this phase is necessary to gain insight into it. For the physical understanding of this process (magneto-) hydrodynamical simulations have to be performed. A large enough sample of post-common envelope systems with observed masses,

radii and orbital separations can provide the parameter range that has to be explained by the simulations.

In this thesis I make a significant contribution to the investigation of binary systems after the common envelope phase by newly discovering a large sample post-common envelope systems and also significantly increasing the number of systems with derived parameters. This sample is a first step to acquire a statistically significant sample for a better understanding of this crucial but not yet understood phase. Moreover, I also present the detailed analysis of several kinds of interesting close binary systems studying different aspects of these systems, as the influence of tidal forces, the effect of mass transfer and orbital period changes among other things.

In the following I will give a short introduction to the current state of knowledge regarding stellar evolution of single stars and the influence of close companions on this evolution. Moreover, I give a short introduction into the different kinds of close binary systems we studied. I also give a short summary of the methods used to investigate those systems. Subsequently to the appended papers I will discuss the results and give a short summary.

2 Stellar evolution and interactions

For the understanding of the evolution of binary stars, we must first understand the evolution of single stars and can then try to understand how this evolution is changed in close binaries.

2.1 Single star evolution of low-mass stars

Stars change their structure and composition and hence their properties significantly during their lifetime. All stars are formed by the collapse of clouds of gas called molecular clouds. As soon as they ignite the hydrogen in their core, they are found on the main sequence (MS, Fig. 2.1). They stay there most of their lifetime fusing the hydrogen in the stellar core to helium. The evolution of a star depends mainly on its initial mass. Massive stars are found to be significantly brighter than less massive stars and therefore burn their 'fuel' much faster. They live only a few million years in contrast to low-mass stars, which live for billions of years. The structure of low-mass stars ($M \lesssim 2.5 M_{\odot}$) shows fundamental differences compared to intermediate-mass ($2.5 M_{\odot} \gtrsim M \gtrsim 8 M_{\odot}$) and high-mass stars ($M \gtrsim 8 M_{\odot}$). Low-mass stars have relatively low temperatures in their envelopes so that the hydrogen is not fully ionized. Higher energy photons from the interior of the star are easily absorbed by the neutral hydrogen atoms and hence energy is transported dominantly by convection. These large scale movements cause mixing in the envelope. More massive stars fuse hydrogen in their core via the highly temperature dependent CNO cycle (low-mass stars operate via the less temperature sensitive pp-chains) leading to a temperature gradient too strong for radiative transport. From this follows that low-mass stars have radiative cores and convective envelopes, but more massive stars have convective cores and radiative envelopes instead. This has a significant impact on the further evolution.

The evolution of a low-mass star in the Hertzsprung-Russell diagram (HRD) is shown in Fig. 2.1. In the following I will briefly summarize the evolution of a low-mass star, as described for example in Kippenhahn et al. (2013), or Pols (2011). As we have seen, the core in low-mass stars is radiative. This means that mixing in the core is not possible and hydrogen is consumed starting in the center. During the time on the main sequence the star evolves towards higher luminosities and radii. After the hydrogen in the center is exhausted a smooth transition to shell burning takes place. Due to this shell burning the core keeps growing in mass and starts to contract. The star is moving away from the main sequence onto the subgiant branch, where the envelope starts to expand and cools down slowly. Due to the high density in the core, the electron gas becomes degenerate at some point and a isothermal, stable He core is formed. As the He core is getting more and more massive due to shell-burning, the core keeps contracting. The envelope is expanding quickly and cooling down due to the energy produced from the burning shell. The star is moving up the red giant branch (RGB). The envelope becomes fully convective reaching layers where H-burning took place previously transporting processed material to the surface. In this phase the outer layers of the star are less bound and a stellar wind can remove part of the envelope.

At the tip of the red giant branch the core of the star has reached the critical temperature

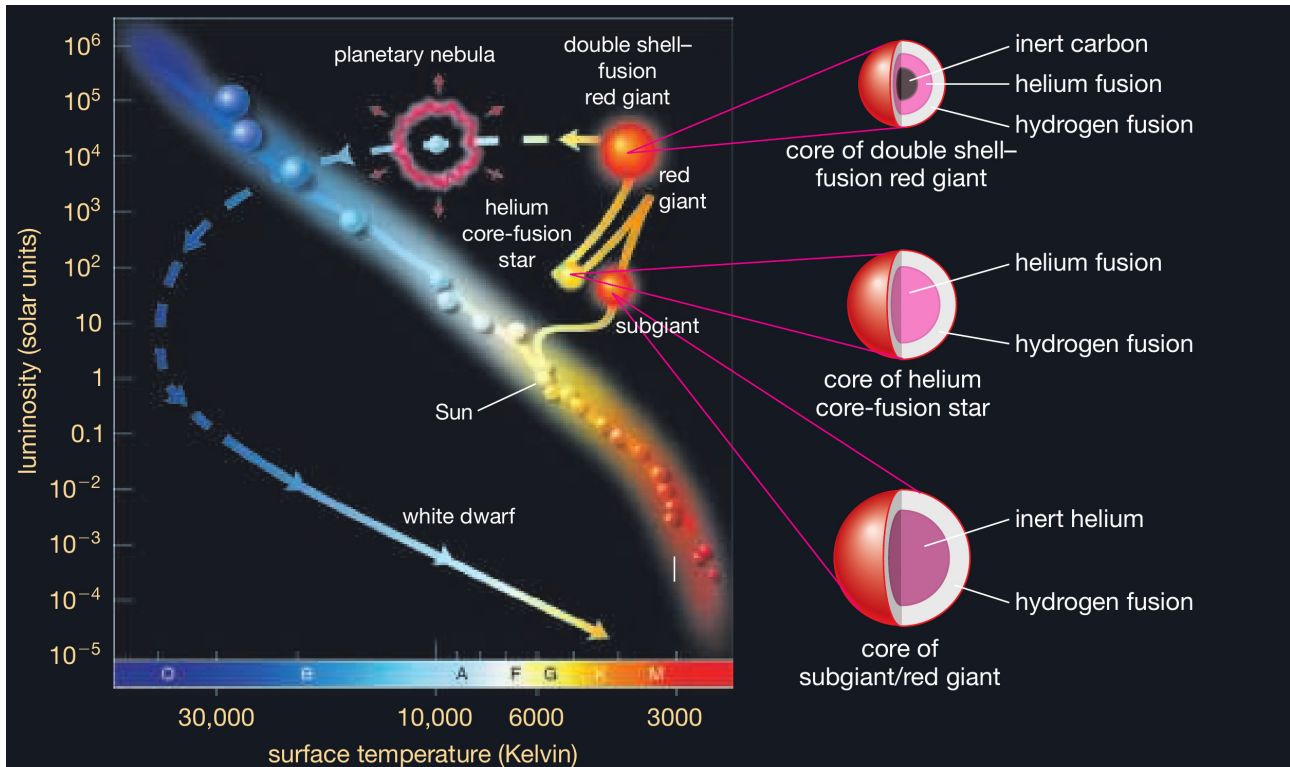


Figure 2.1: The life track of our Sun from its main-sequence stage to the white dwarf stage. The core structure is shown at key stages (Bennett 2018).

($\sim 10^8$ K) and the necessary mass to ignite He. This core ignition mass ($M_{\text{core}} \sim 0.47 M_{\odot}$) is independent of the stellar mass and is also called the canonical mass for helium-burning. Energy losses via neutrinos lead to cooling in the center and so helium is ignited in a shell around the center first. Helium is fused to carbon (and later to oxygen) via the triple-alpha process, which is highly temperature dependent. This means that the nuclear energy released heats up the core quickly, but as the gas is degenerate, it cannot expand. This leads to a runaway process, which is explosively burning the helium, called the helium flash. As the temperature keeps rising, the degeneracy in the core is lifted at some point, the core can expand again and stable He-core burning sets in. During this phase of stable He-core burning (and stable H-shell burning) the stars occupy a region of constant luminosity, the horizontal branch (HB). Different amounts of mass-loss on the RGB will lead to horizontal branch stars with envelopes of different thickness. The thinner the hydrogen envelope the hotter the star will appear. This leads to the observed morphology of the horizontal branch. Key factors to explain the different mass-loss on the RGB are metallicity, helium abundance and age. Young, metal-rich horizontal branch stars will cluster in the Red clump, close to the red giant branch. Metal-poor, old stars are found from the red horizontal branch to the blue horizontal branch with spectral types from K to A. Even more to the blue the extreme horizontal branch can be found, which will be discussed in more detail later. More massive stars of intermediate mass do not experience a helium flash, but are starting to quietly fuse He in the core, as soon as the conditions are fulfilled.

After the central He is exhausted, the CO core contracts and He-shell burning sets in. The star reaches the asymptotic giant branch (AGB), where the outer layers quickly expand again. After the fuel of the He-shell is exhausted, a phase of double (H and He) shell-burning begins, which leads to thermal pulses caused by He-shell flashes. This leads to strong mass loss, which sheds the outer layers of the AGB star. When the mass of the H-rich envelope becomes very small, the envelope shrinks and the star leaves the AGB towards higher temperatures.

When it exceeds an effective temperature $T_{\text{eff}} > 30\,000$ K, the star develops a weak wind and the strong UV radiation ionizes the circumstellar envelope, which was lost on the AGB. The circumstellar material starts radiating in recombination lines and appears then as a planetary nebula. When nuclear fusion no longer provides any energy, the core cools, contracts and becomes fully degenerate. This is the final stage of stellar evolution of low- and intermediate-mass stars and such objects are called white dwarfs (WD).

2.2 Stellar interactions in binary systems

So far we have seen, how low-mass stars are evolving. The evolution of single stars depends mainly on the initial mass. Other less important parameters that affect stellar evolution are the metallicity, magnetic fields and rotational velocity of the star. Rotation is especially important for more massive stars from spectral type A to O, as they tend to be fast rotators on the main sequence (Palacios 2013). Rotation may change the shape of the stars, their lifetimes, surface parameters and abundances. Also the metallicity has an impact on the overall stellar properties and modifies the size, the internal structure, and the lifetime of a star (Bolmont et al. 2017). The origin and effect of magnetic fields on stellar evolution is less clear.

However, many stars are found not to be single, but have one or several companions. For stars of $\sim 1 M_{\odot}$ about half are found in binary or multiple systems (see Offner et al. 2022, for a review). About 15% of those systems are so close together that they will interact during their lifetime. This will change their masses, rotation and other properties significantly. In the rest of the systems both stars do not influence each other but evolve effectively like single stars. The question now is, what kind of interactions do we find in systems with small enough separation and what is their impact on stellar evolution?

2.2.1 Mass transfer

The most important interaction is mass transfer from one star to the other. For the understanding of mass transfer the concept of the Roche lobe is important. Around each star of a pair of stars orbiting each other the Roche lobe is the region where matter is still gravitationally bound to the star. As soon as one star grows larger than its Roche lobe, mass will be lost from the donor star and some or all of the mass will be accreted onto the secondary star (gainer) and mass transfer occurs. The size of the Roche lobe can be approximated by a very useful formula for the Roche lobe R_L derived by Eggleton (1983), which is accurate to better than $\sim 1\%$ in all cases:

$$\frac{R_L}{a} \approx \frac{0.49q^{2/3}}{0.6q^{2/3} + \ln(1 + q^{1/3})}. \quad (2.1)$$

From this formula we can easily see that the size of the Roche lobe decreases, if the orbital separation, which is linked to the orbital period via Kepler's third law, is shrinking. Hence, mass transfer will occur, when the two stars are getting close enough together and/or one star increases its size significantly.

Depending on the evolutionary phase, when the mass transfer is happening, historically mass transfer is grouped into three different cases:

- Case A: The initial orbital period is short enough (a few days) for a star to fill its Roche lobe during the expansion on the main sequence, when the star is still burning H in the core.

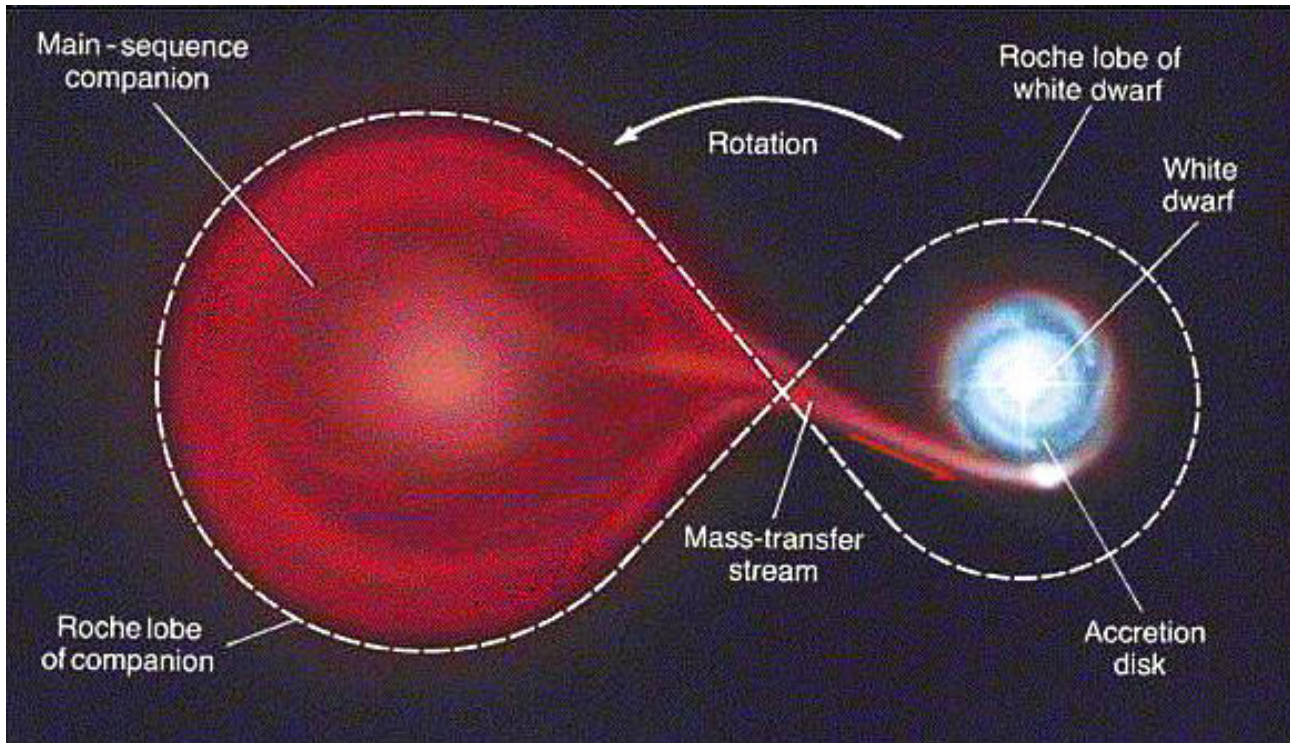


Figure 2.2: Illustration of the Roche-lobe overflow of a main-sequence donor onto a white dwarf (<https://chandra.harvard.edu/edu/formal/snr/images/dwarf.jpg>)

- Case B: The initial orbital period is of the order of several days to several 100 d, so that the star will fill its Roche lobe on the red giant branch in the H-shell burning phase.
- Case C: The initial orbital period exceeds several hundred days so that no mass transfer takes place on the RGB, but only later on the AGB after core helium exhaustion.

A nice introduction to close binaries and their interactions can be found in Hilditch (2001) from the observational point of view and Eggleton (2006) from the theoretical point of view. Based on those two books I will give a short review on the properties of mass transfer in binary stars.

We distinguish between two cases of mass transfer: conservative and non-conservative mass transfer (depending on whether angular momentum and mass is conserved in the stellar system or gets lost). In order to derive conditions for stable mass transfer let us first assume that the mass transfer is conservative. We have already seen that for mass transfer to happen the donor has to fill the Roche lobe. As the Roche lobe depends on the mass ratio (see eq. 2.1), which is changing when mass is transferred, the size of the Roche lobe will change during the mass transfer. Using mass and angular momentum conservation we can calculate how the Roche lobe changes during the mass transfer:

$$\frac{\dot{R}_{L,d}}{R_{L,d}} = \frac{-2\dot{m}_d}{m_d} \left(\frac{5}{6} - \frac{m_d}{m_g} \right), \quad (2.2)$$

where $R_{L,d}$ is the Roche lobe of the donor star, $\dot{R}_{L,d}$ its change, m_d and m_g are the masses of the donor and gainer star, and \dot{m}_d the mass transfer rate. This means that for a critical mass ratio $q_{\text{crit}} = \frac{m_d}{m_g} < 5/6$ the Roche lobe will keep expanding and the mass transfer will be stable. In such a stable mass transfer phase, a stream of material will be formed, which will flow onto the companion via the inner Lagrangian point L_1 , where the gravitational and centrifugal

forces counteract each other. Usually an accretion disk around the companion is formed, as the material still has angular momentum. Such a process is called Roche-lobe overflow (RLOF, see Fig. 2.2 for an illustration).

We have seen that there exists a critical mass ratio for mass transfer to be stable. In reality it is a bit more complicated to calculate this critical mass ratio, as it also has to be taken into account how the donor and gainer stars radii react to the mass loss/gain. This also depends a lot on the behavior of the envelope (radiative/convective). A typical critical mass ratio for a red giant transferring mass to a main sequence companion is $q_{\text{crit}} = \frac{m_d}{m_g} < 1.2 - 1.5$.

The transfer of mass also has an impact on the orbit of the binary. If the donor star is more massive than the gainer, the orbit will shrink. However, if the mass gainer is more massive, the orbit will expand and mass transfer will be interrupted. So in this case the constant loss of angular momentum from the system is required for continuing stable mass transfer (e.g. accreting white dwarfs with K or M donors: cataclysmic variables, CVs).

There are several reasons for a mass transfer to be non-conservative:

- mass loss
 - stellar wind
 - unstable mass transfer
- angular momentum loss
 - gravitational waves
 - magnetic braking
 - tidal friction.

When the mass donor is significantly more massive than the gainer, the Roche lobe is shrinking and the donor star will be stripped fast. Matter is filling the binary orbit and a common envelope (CE) around both stars is formed. A review about the current knowledge of the common envelope phase can be found in Ivanova et al. (2013) and Ivanova et al. (2020). Here I will give a short summary.

The common envelope phase can be broken down into several phases.

- I Loss of corotation: a stable binary with a circular orbit and a donor star with the rotation synchronized to the orbital period is transformed to a spiraling-in binary due to the unstable mass transfer and friction in the envelope.
- II Plunge-in: rapid spiral-in during which orbital energy is deposited into the envelope and drives its expansion. This may lead to dynamical ejection of the envelope or merger of both stars.
- III Self-regulating spiral-in: envelope may expand enough so that spiral-in slows down, self-regulating state can be formed, in which frictional luminosity released by the spiral-in is radiated away.
- IV Termination of the self-regulating phase: self-regulated spiral-in ends with the ejection of the envelope or when the secondary or the core of the primary overfills its Roche lobe.
- V Post-CE evolution: final properties not set until some time after envelope ejection, circumstellar matter or stellar winds can change eccentricity or widen the system, or also lead to mergers in the most extreme case.

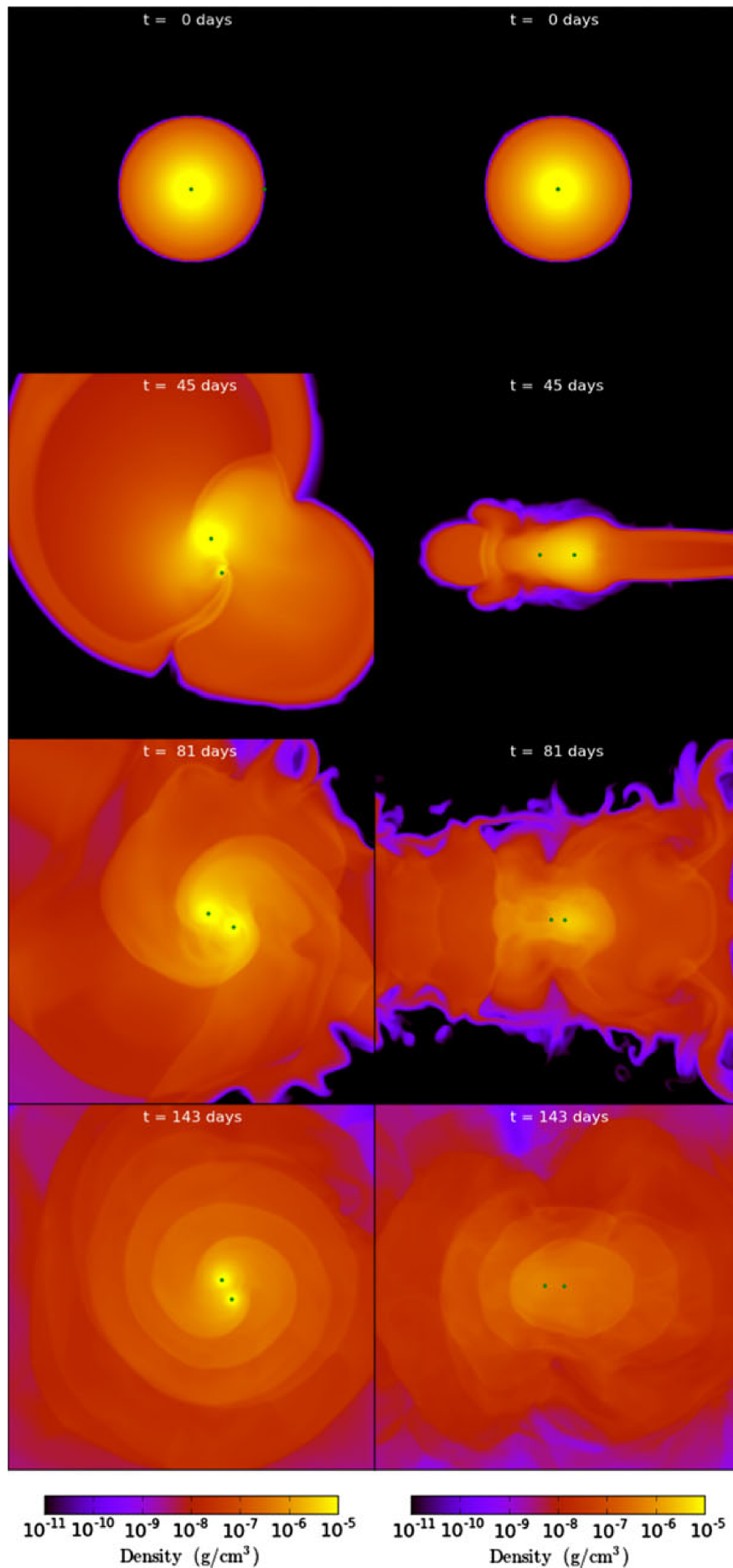


Figure 2.3: Hydrodynamical simulation of a common envelope event with a $0.88 M_{\odot}$ giant and a $0.6 M_{\odot}$ MS star, likely leading to the formation of a close binary (Ivanova et al. 2013).

To predict the fate of a common envelope phase the energy budgets are calculated. To eject the envelope enough orbital energy ΔE_{orb} has to be deposited into the envelope to exceed the binding energy E_{bind}

$$E_{\text{bind}} = \Delta E_{\text{orb}} = E_{\text{orb,i}} - E_{\text{orb,f}} = -\frac{Gm_1m_2}{2a_i} + \frac{Gm_{1,c}m_2}{2a_f}. \quad (2.3)$$

Hereby, the change in orbital energy can be calculated from the initial and final orbital separations of the binary a_i and a_f before and after the common envelope phase, as well as the mass of the companion m_2 , the initial mass of the primary m_1 , and the core mass of the primary $m_{1,c}$.

Not all of the orbital energy can be used to drive the envelope ejection. Hence, the common-envelope efficiency α_{CE} is introduced, which represents the fraction of the available orbital energy. The binding energy of the star also depends on the structure of the envelope. This is considered by a second parameter λ :

$$E_{\text{bind}} = \frac{m_1m_{1,\text{env}}}{\lambda R_1} = \alpha_{\text{CE}} \left(-\frac{Gm_1m_2}{2a_i} + \frac{Gm_{1,c}m_2}{2a_f} \right). \quad (2.4)$$

This formula can be used to parameterize the common envelope phase in population synthesis studies. However, to understand the physical processes simulations have to be performed. Due to the large range of timescales multiple simulation codes have to be used to study common envelope evolution. The initial model for the donor star is generated using a 1D stellar evolution code. This 1D model has to be mapped onto a 3D grid, so that a (magneto-) hydrodynamical simulation of the plunge-in phase can be carried out (see Fig. 2.3 for an example). This can result in discretization errors. To restore hydrostatic equilibrium the mapped stellar model is relaxed in isolation. Afterwards a compact companion is placed inside the Roche lobe and then the evolution is followed until the ejection of the envelope. An earlier start of the simulation close to the onset of the Roche-lobe overflow would be desirable, but is not possible, as the computational costs are too high. Such simulations have shown that additional energy sources have to be invoked to explain the ejection of the envelope (see e.g. [5]). Several energy sources were proposed:

- thermal energy: energy of the matter compared to a zero-energy state, includes internal kinetic energy of the matter and energy stored in radiation,
- recombination energy: during the envelope ejection can plasma recombine and some atoms will form molecules, which releases binding energy; calculated by the ionization and dissociation potentials for each ion and atom present,
- tidal heating: not an energy source, but a transfer mechanism, taking energy out of the binary orbit and stellar spin. The tidal heating time scale seems to be longer than dynamical spiral-in,
- nuclear energy: nuclear fusion, stream of hydrogen-rich material can reach H-burning shell and lead to a explosive CE ejection,
- accretion energy: luminosity of accretion onto the secondary.

The contribution of these additional energy sources is still under debate. Soker et al. (2018) have argued that the recombination energy is radiated away during the common envelope evolution, and hence does not play a significant role in the ejection of the envelope. Moreover, the simulations still have problems to explain the observed parameters of post-common envelope systems (see [5]).

We have seen that, if both stars are close enough together they can start mass-transfer. This changes significantly the stellar masses of both stars. As discussed in the previous section the mass of the star and its envelope determines decisively the future evolution of a star. This will also be discussed in a lot more detail in the next section. In the case of Roche-lobe overflow the donor star will lose part up to most of the envelope. The gainer star on the other hand will grow in mass and size, and will be spun-up by the mass transfer. Therefore it will appear younger after the mass transfer, which means it gets rejuvenated (see [4]).

In the case of the common envelope phase the primary star will lose (almost) the complete envelope, which makes further phases of shell-burning impossible and changes the future evolution significantly (more details in the next section). The influence of the common envelope phase on the companion is not really understood yet. The orbital period in such a system shrinks by several orders of magnitude allowing future episodes of mass transfer (see [1] and [3]).

2.2.2 Irradiation

In very close binaries consisting of a compact hot primary star and a cool, low-mass companion of similar or even larger size a very distinct effect is visible, called the reflection or irradiation effect. In such short-period binaries we expect the companion to rotate synchronously with the orbital period due to tidal interactions, as the companion has low mass and a convective envelope (more details in the next section). The strong UV irradiation heats up the side of the companion facing the primary star to temperatures of about 10 000 to 20 000 K (Vučković et al. 2016; Kiss et al. 2000). Due to the high temperature contrast between the heated and unheated side of the companion, the contribution of the companion to the total flux of the system is varying with the orbital phase. In the light curve this can be seen as a quasi-sinusoidal variation with the orbital phase. This is illustrated in Fig. 2.4. The irradiation of the companion by the primary star also has a significant effect on the structure of the envelope, especially its temperature structure (Vučković et al. 2016). As the unheated side of the companion is much cooler than the primary star, the primary star outshines the companion and no absorption lines of the companion can be found in the spectrum. However, in some cases narrow emission lines originating from the heated side of the companion have been observed (e.g., Vučković et al. 2016). Those emission lines can be used to constrain the reflection effect and derive the radial velocity of the companion. The reflection effect is also observed in close-in planets, such as Hot Jupiters, with significantly smaller amplitudes. The irradiation has a strong impact on the planet causing evaporation, inflation, or day-to-night side flows. More details about the irradiation effect and the properties of systems showing this effect can be found in Chapter 2.3.1 and 3.1.2, as well as [1]-[3] and [6]-[9].

2.2.3 Synchronization

Also tidal interactions become important in very close binaries. The gravitational forces in a binary system can cause a deformation of the stellar shape. The companion is not spherical any more but shows tidal bulges. If those tidal bulges are not on a line connecting the centers of both stars but have a certain tidal lag, gravitational attraction will cause a torque on the

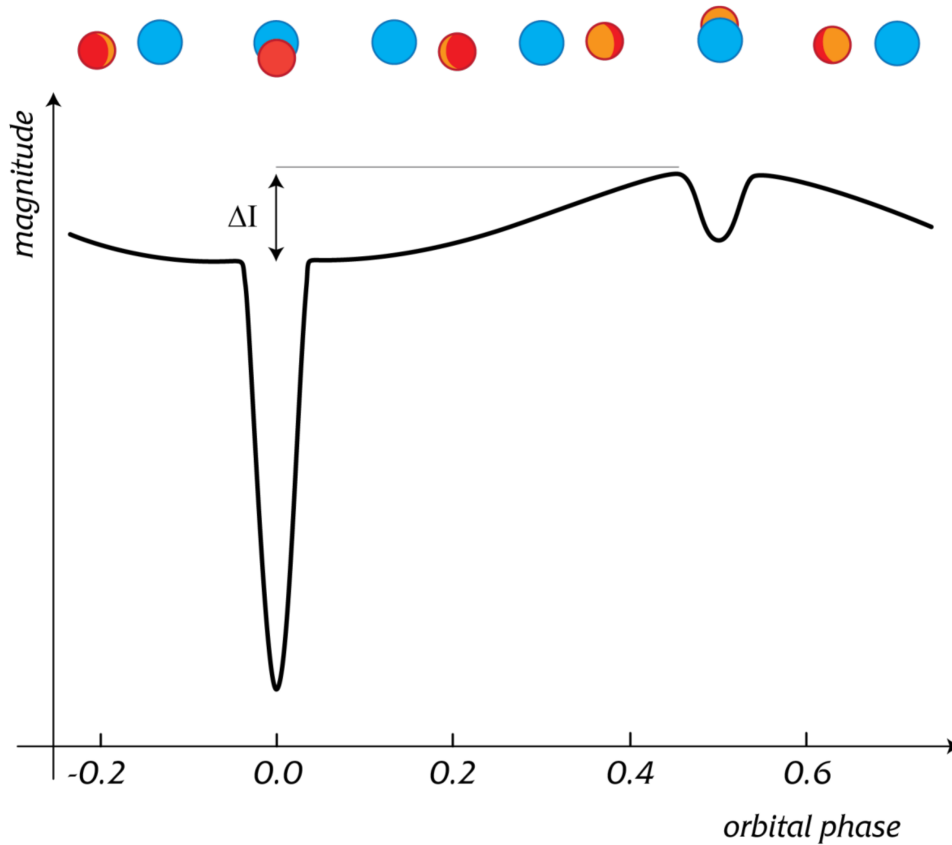


Figure 2.4: Illustration of the reflection or irradiation effect in close binaries with a hot compact binary and a cool low-mass companion (adopted from Daniela Bartková, <https://www.astro.sk/iau100/bezovec/wp-content/uploads/2021/09/13-Bartkova-The-reflection-effect-in-binary-systems.pdf>). Additionally also a primary and secondary eclipse are visible.

bulges, which is forcing the stellar rotation rates to get synchronized to the orbital period. The synchronization mechanism depends on the structure of the envelope. A summary of the different theories is given in Preece et al. (2018). In convective regions the movement of material over large distances causes a natural turbulent viscosity. This viscosity provides a drag causing the required lag.

For stars with convective cores and radiative envelopes the theories have been more controversial. There are two competing theoretical prescriptions for tidal dissipation in such stars predicting significantly different timescales. Tassoul & Tassoul (1992) suggested that large-scale meridional flows very efficiently synchronize a star. However, the physical validity of Tassoul’s mechanism is under debate. Zahn (1977) proposed that the periodic tidal potential induced by the companion excites g-mode pulsations in the core, which are damped at the radiative boundary. The timescale for synchronization depends on the mass and radius of the star, the mass ratio of the binary and the orbital separation of the binary. This mechanism was shown to be too inefficient to describe the observed level of synchronization of some early-type main-sequence spectroscopic binaries. However, this description does not consider the effect of convective dissipation in the stellar core. Preece et al. (2018) redid this calculation for a special case of post-common envelope binaries, which will be discussed in the next section, predicting that in none of those binaries the rotational period of the primary should be synchronized to the orbital period.

This shows that a close companion can not only influence the primary star via mass transfer

but also change its rotational velocity by tidal interactions. The mechanism and hence the timescale to achieve synchronization is still under debate. Synchronization is also discussed further in [6] and [2].

2.2.4 Orbital period variations

In post-common envelope binaries orbital period changes became interesting, as such changes have been found in most studied systems. Those changes can indicate one or several additional companions orbiting around the binary system. In several post-common envelope binaries circumbinary planetary companions have been claimed causing the observed period changes on timescales of years. Continuing observations cannot confirm those planetary systems in most cases, leaving doubt that planetary companions can indeed explain the observed period changes.

In very close binaries, where the main sequence companion has a magnetic field, this magnetic field will also have a significant impact on the orbital period of the system. Such magnetic fields are induced in stars with convective envelopes by the dynamo effect. There are two different proposed mechanisms, which work in this kind of binaries. Bours et al. (2016) give a good introduction to those two effects. Very well studied is magnetic braking, which works not only in binaries, but also in single stars. The main sequence star emits a stellar wind that flows away from the star and is forced by the magnetic field to corotate with the star up to the Alfvén radius, where the magnetic energy density is equal to the kinetic energy density. At this radius the matter decouples from the magnetic field and takes away angular momentum, which decreases the rotation rate of a single star. In a close binary the low-mass companion will rotate synchronously with the orbital period. Hence, the angular momentum, which is carried away by the stellar wind, leads to a loss of orbital angular momentum causing a period decrease. In fully convective stars, as very low mass M dwarfs (dM) or brown dwarfs (BD) with masses less than $0.35 M_{\odot}$, this mechanism is predicted to be very inefficient (e.g., Schreiber et al. 2010). Magnetic braking is very important to explain e.g., stable mass transfer in CVs.

Applegate (1992) proposed another effect, which is now called Applegate mechanism. The author suggested that a main-sequence companion in a close binary may experience magnetic cycles. During this cycles angular momentum is redistributed between the core and the outer layers of the star by torques induced by the differential rotation and turbulent motion in the convective regions. This causes the star to deform, which changes its gravitational quadrupole moment and with it the orbital period on quasi-periodic time-scales same as the magnetic activity cycles. Bours et al. (2016) measured the period changes in 67 different WD+dM/K systems and showed that period changes are much more prominent in binaries with companions of spectral type M6 or earlier than in binaries with late dM or BD companions giving an observational hint that the Applegate mechanism might indeed be important in binaries with companions of early M or K type companions. The effect might be able to explain the observed period changes showing that a third body in the system might not be necessary. Therefore, the period changes could be used to investigate magnetic activity cycles of active stars in close binary systems.

In [6] we investigated the period variations in an sdB+BD system. In such a system magnetic effects are not expected.

2.3 Evolved stars

So far we discussed the kind of interactions, that can be observed in close binary systems showing the influence of the close companion on the evolution of the primary star and vice versa. In the following I will give a short introduction to the different kinds of evolved stars, which I investigate in this thesis.

2.3.1 Hot subdwarf stars

Hot subdwarf stars of spectral type O and B (sdO/B) are quite rare and unusual objects, but perfectly suited targets for our goals, as will be shown in the following. A comprehensive review on those objects has been given in Heber (2009, 2016). I will give here a short summary of the most important properties of those stars.

In a HRD they are found between the main sequence and the white dwarf sequence (see Fig. 2.5). They represent several stages of the late evolution of low-mass stars. The classification of hot subdwarf stars is based on spectroscopy. An sdB, which is the most frequent subtype, has colors similar to a B type MS star, but with Balmer lines, which are abnormally broad due to a higher surface gravity. This also makes them easily recognizable, as they show Balmer lines only up to $n \approx 12$. Most but not all of the sdBs show additional weak He I lines in the spectrum. The sdO stars can be divided into H strong- and He-strong (He-sdO). They show He II lines and in He-sdOs the Balmer lines can be completely absent. Hot subdwarfs showing He I and weak He II lines are also called sdOB stars.

Subdwarf O stars include a rich mixture of different kinds of stars, e.g. post-RGB, post-HB, and post-AGB stars. Central stars of planetary nebulae (CSPN), showing only absorption lines are often termed subdwarf O stars as well. The luminosities of sdO stars are spanning two orders of magnitude and can be subdivided into luminous and compact sdOs.

Most of the B-type subdwarfs were identified as helium burning stars of about half a solar mass on the Extreme Horizontal Branch (EHB). Due to the extremely thin hydrogen envelope ($M_{\text{env}} < 0.01 M_{\odot}$) that they retain they are not able to sustain hydrogen shell burning in contrast to normal horizontal branch stars. They are stripped cores of red giants, which lost most of the envelope at the tip of the RGB and which managed to ignite helium. Normal single star evolution cannot explain the huge mass loss necessary to strip the envelope on the RGB.

About 1/3 of the sdB stars show composite spectra, which means that not only spectral lines of the sdB, but also of a F/G/K-type companion are visible. Those systems were found to have periods of several hundred days (Vos et al. 2019). The other 2/3 of the sdB stars are single-lined. Several RV surveys have been carried out to look for unseen companions showing that at least half of them are found in close binaries with periods of about one hour to 30 days, which corresponds to an orbital separation of less than one solar radius to tens of solar radii. As sdB stars evolve from red giant stars, which were much larger in size than the present-day orbital separation, those binaries must have evolved through a previous common envelope phase. The unseen companion is in most cases either a white dwarf or an M-type main sequence star.

Binary population synthesis has identified several possible channels explaining the formation of hot subdwarfs in close binaries (an illustration of some of the channels is shown in Fig. 2.6):

- Stable RLOF channel: the red giant loses its entire envelope during a phase of stable RLOF to become an sdB star in a long-period binary with a main-sequence companion. The mass ratio of the progenitor system ($q = \frac{m_{\text{donor}}}{m_{\text{gainer}}}$) is required to be below 1.2 – 1.5. Models predict periods up to 1200 days close to what is observed (see Chen et al. 2013).

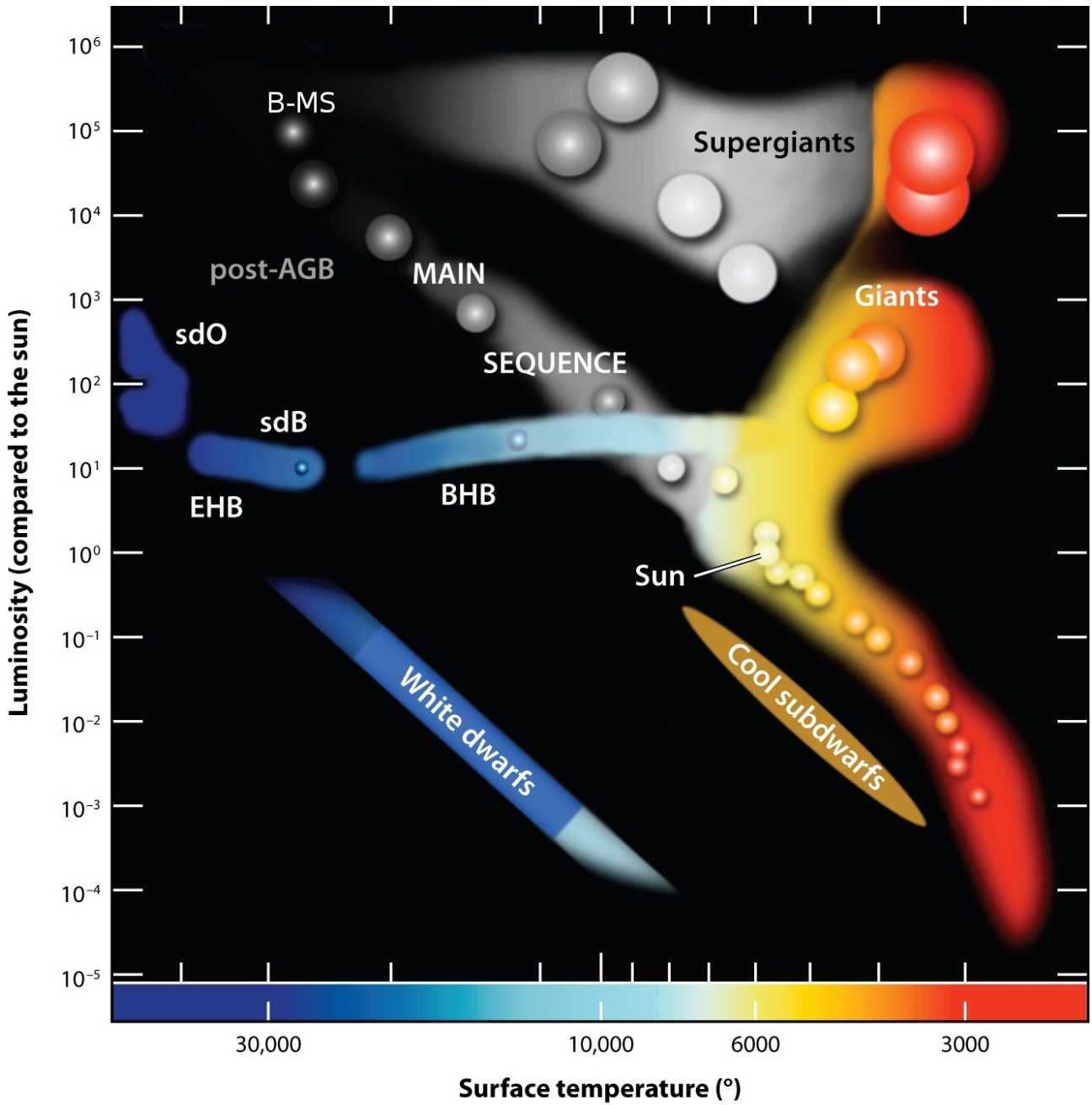


Figure 2.5: HRD highlighting the position of hot subdwarf (sdB and sdO) stars together on the extreme horizontal branch (EHB) located below the hot end of the main sequence but above the white dwarf cooling sequence, from Heber (2009).

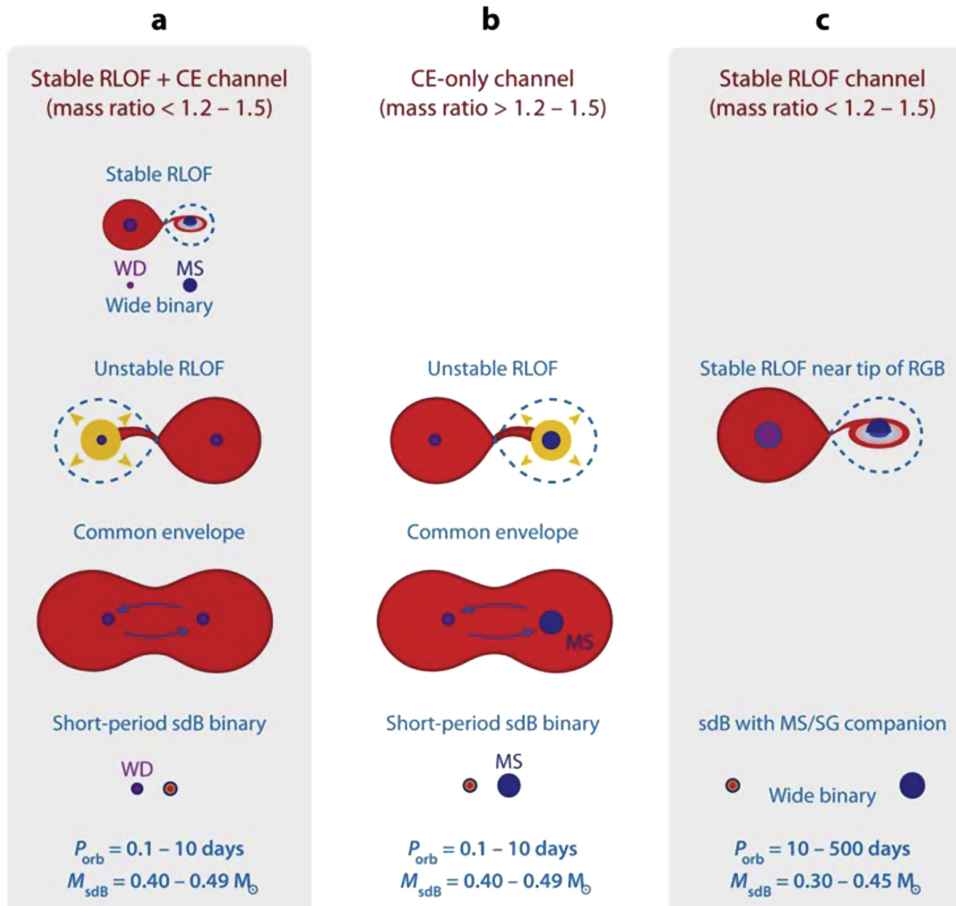


Figure 2.6: Some formation channels of sdB stars in close binaries, from Heber (2016).

- Stable RLOF + CE channel: after an RLOF phase, a common envelope phase can occur when the companion fills its Roche lobe on the RGB. The more massive star has already evolved to a WD and so a close binary of a WD and an sdB with a period of $\sim 0.1 - 10$ days is formed.
- CE channel: if the mass ratio is above $1.2 - 1.5$, the mass transfer will be unstable and a CE will be formed leaving behind an sdB with a very low-mass main sequence companion with a predicted period of 0.1 to 10 days.
- Be+sdO systems: some Be stars were spun up through mass transfer in a close binary system, leaving the former mass donor star as a hot, stripped-down object. Such hot subdwarf stars were predicted to form, when the mass donor begins mass transfer during its shell-hydrogen burning phase. Several such system have been identified using far-UV data (Wang et al. 2021).

For the common envelope channel it has been predicted that not only stellar companions, but also substellar companions might be responsible for the stripping of the envelope. The discovery of several sdB+BD systems (Geier et al. 2011b; Schaffenroth et al. 2014, 2015, [6]) shows that this is indeed possible. The fate of the substellar object is still an open question. This will be discussed in more details in the attached papers and the discussion.

Another open question is the formation of the about 1/3 apparently single sdBs. RV studies with high resolution spectra have shown that those exist. There have also been several channels proposed to create such objects:

- substellar companions might have been responsible for the mass loss but got evaporated or merged with the core during the common envelope phase.
- helium white dwarf mergers: during the earlier binary evolution most of the H envelope of both stars was ejected forming a tight He WD binary. The less massive and, hence, larger white dwarf fills its Roche lobe, mass is transferred to a disk around the more massive one, which can be accreted. If the mass of the two merged white dwarfs exceeds the canonical mass required for He burning, a helium burning core is formed. The post-merger evolutionary tracks agree with the atmospheric parameters of he-rich hot subdwarf stars.
- merger of a He WD with a low-mass, hydrogen burning star: creates a star with helium core and a thick hydrogen envelope that evolves into an sdB star in a few Gyr.
- He mixing on the RGB: a higher He abundance in the envelope increases the luminosity at the tip of the RGB causing stronger mass loss. More likely in globular clusters.
- hot-flasher scenario: with sufficient mass loss on the RGB the star can depart from the RGB and experience a helium core flash while it is already descending the white dwarf cooling track. Depending on the evolutionary phase where the helium flash occurs H-rich or He-rich subdwarfs can be formed.

We have seen that different channels to form hot subdwarfs are proposed. Binary population synthesis predicts different mass distributions, period distributions, and companion distributions from those different channels (see Fig. 2.7 and Han et al. 2002, 2003). Therefore, those parameters are very important to get a better understanding of the formation of hot subdwarf stars. Eclipsing binaries and pulsating hot subdwarfs can be used to derive the masses of the hot subdwarf (see Fig. 2.7 for a comparison of the theoretical mass distribution for different formation channels with the observed mass distribution). About 1/3 of all hot subdwarfs are in post common-envelope systems either with low-mass stellar or substellar companions, or with white dwarf companions. Hence, short-period subdwarf binaries are key objects to understand this important phase.

Hot subdwarfs with close, massive white dwarf companions are of interest for cosmology, as they are candidates for progenitors of type Ia supernovae (SN Ia). SN Ia are crucial for the cosmic distance ladder used to determine the expansion of the universe. The origin of SN Ia is believed to be the thermonuclear explosion of a white dwarf reaching a mass close to the Chandrasekhar limit of $1.4 M_{\odot}$. This can happen either by the merger of two compact objects (double degenerate channel) or by accretion from another star (single degenerate channel). Hot subdwarfs with close, massive white dwarf companions can be progenitors for both channels, if the total mass of the binary system is close to $1.4 M_{\odot}$. The hot subdwarf can either start transferring mass to the WD companion still during the hot subdwarf phase or it evolves to a CO WD and can merge with the companion eventually. Confirmed progenitor systems of SN Ia are extremely rare so far. These close binary systems are also of interest as gravitational wave sources, in particular as verification sources for the upcoming Laser Interferometer Space Antenna (LISA).

Hot subdwarfs with cool, low-mass companions on the other hand are interesting, because they show a reflection effect, which is also observed in planetary systems with Hot Jupiters, for example. However, sdBs with cool, low-mass companions are much better suited to study the reflection effect, as it is about 500 times stronger than in Hot Jupiter systems. Moreover, such sdB binaries can be used to study the impact of a common envelope phase on low-mass stellar and substellar companions. As the subdwarf and the dM or BD are of similar size and

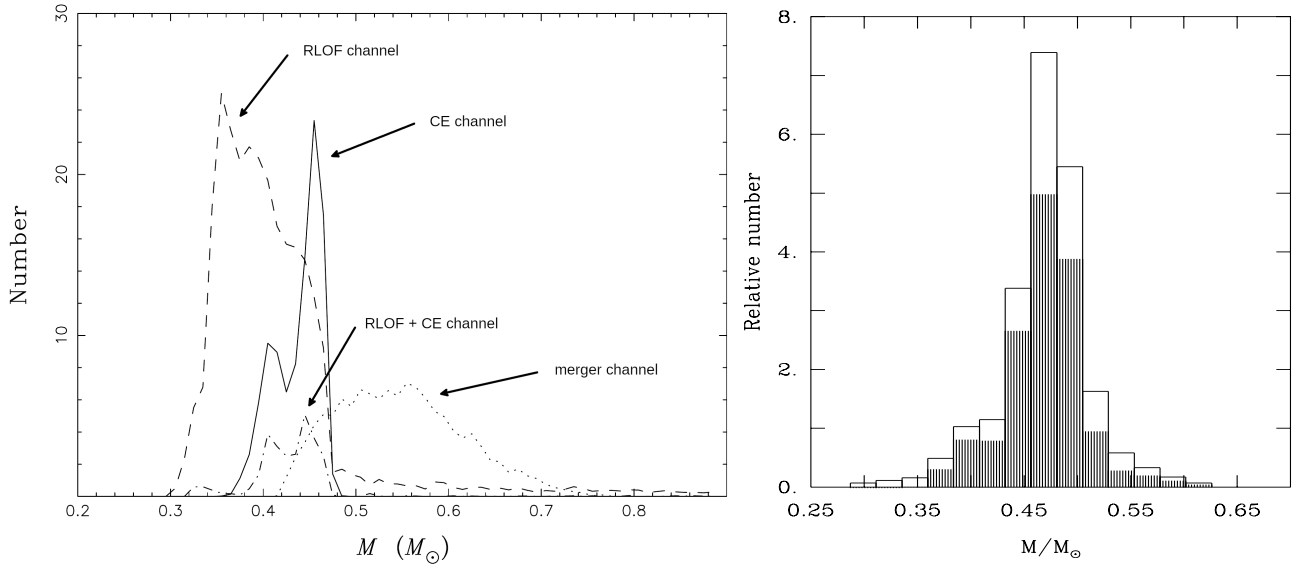


Figure 2.7: Theoretical and observed mass distributions of hot subdwarf stars. On the left panel the mass distributions predicted by Han et al. (2003) for different formation channel are shown. On the right panel the observed mass distributions derived by asteroseismology (dark area) and eclipsing binaries (Fontaine et al. 2012) are shown.

the orbital separation is of the order of one solar radius, such systems have a high probability to be eclipsing. Such objects are called HW Virginis systems (HW Virs) after the prototype. Eclipsing binary stars are very important to derive stellar masses and radii. So far only 20 of the known H Vir systems with periods between 0.07 and 0.25 d have been analyzed.

Subdwarf B stars have a lifetime of about 100-150 Mio years burning He on the EHB. During the post-EHB evolution they undergo a phase of He-shell burning, where they are found in the sdO regime. The lifetime is supposed to be about 1/10 of the lifetime on the EHB. As no hydrogen envelope is left they evolve directly towards the WD cooling sequence avoiding the AGB (see Fig. 2.8). Hot subdwarf binary populations are studied in [1]-[4] and the analysis of individual close sdB binary systems with BD/dM or WD companions are analysed in [6]-[12].

2.3.2 (Pre-) extremely low mass white dwarfs

In order to form a hot subdwarf through mass transfer in close binaries the mass transfer has to happen close to the tip of the RGB, as the core mass must be close to the mass required for He-burning when the red giant fills its Roche lobe. Hence also binaries should exist, which result from the stripping of the envelope of a red giant star before helium burning ignites. Such objects are close relatives to sdB stars, and were also discussed in Heber (2016). As they never burn He, the remnant will be a He-WD. The evolutionary timescale of a single star to evolve into a He-WD exceeds the age of the universe by far. Hence, they must have been formed by binary interactions. About 10% of the white dwarfs have masses below $0.5 M_{\odot}$. However, not all of them have to be He-WDs, as intermediate mass RGB stars may ignite He in non-degenerate conditions at core masses down to $0.33 M_{\odot}$ and so CO-WDs with masses down to this limit can exist. About 30% of the low mass white dwarfs (LMWD, 0.3 to $0.5 M_{\odot}$) are apparently single similar to sdB stars.

In Fig. 2.8 we can see the evolution of stripped objects with different core masses. As discussed in the last section, sdBs are found on the EHB and evolve after the helium in the core is exhausted via the sdO regime towards the white dwarf cooling track. Progenitors of

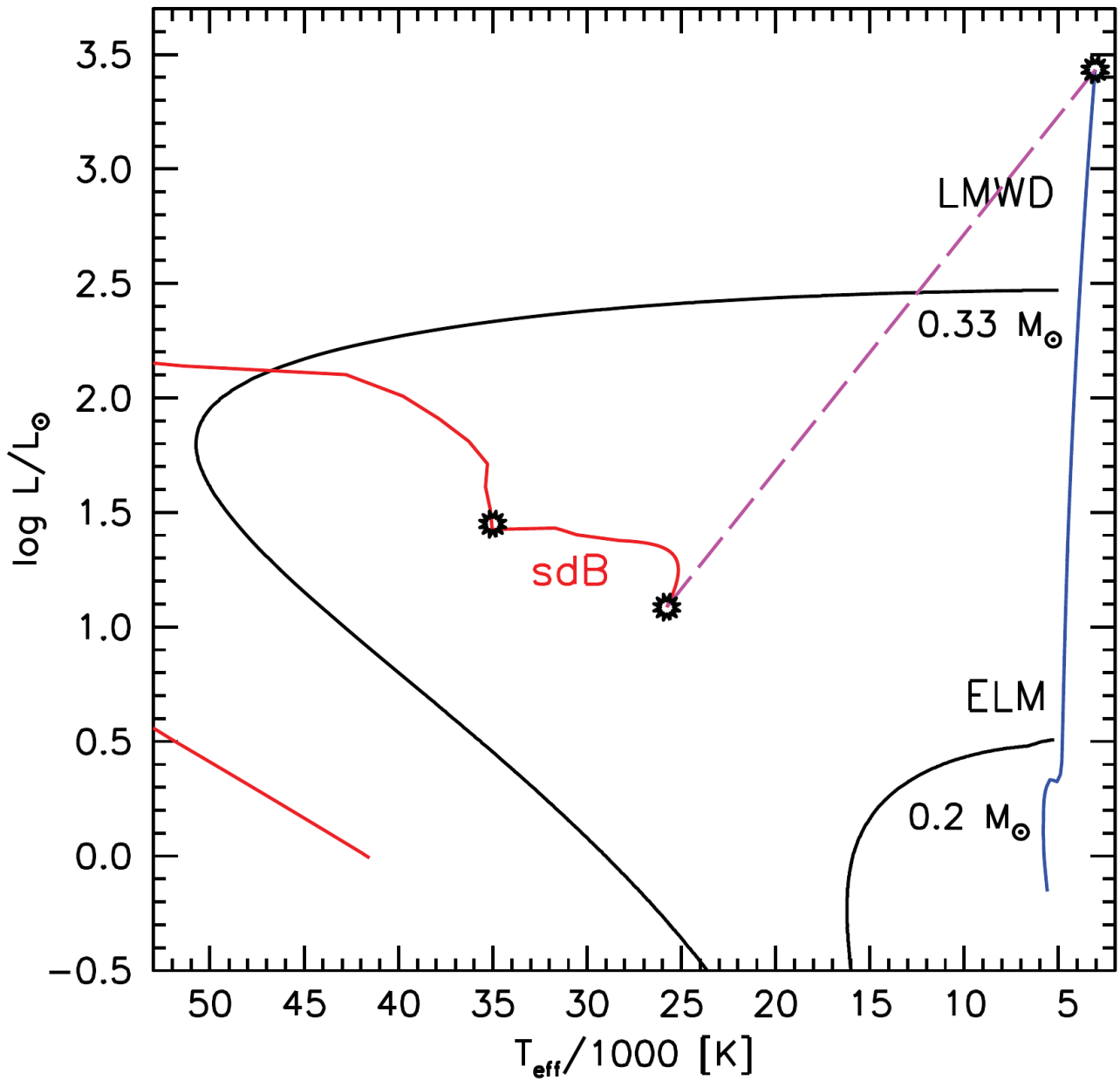


Figure 2.8: Sketch of the evolution of an $1 M_{\odot}$ star (blue) in the HRD, stripped at a core mass of $0.47 M_{\odot}$ in red (sdB) and a core mass of $0.2 M_{\odot}$ (extremely low mass white dwarf, ELM) and $0.33 M_{\odot}$ (low mass white dwarf, LMWD) in black (Heber 2016).

extremely low mass white dwarfs (ELM) with masses between 0.15 to 0.3 M_{\odot} (and LMWD from low-mass stars) terminate the RGB early, when the envelope is stripped, and evolve through the region of the hot subdwarf stars towards the white dwarf cooling track. Such objects have been termed pre-He WDs, post-RGB stars, proto-helium white dwarfs, or pre-ELM. As pre-ELM are passing through the same region in the HRD, where sdBs are found, it is not possible to distinguish easily between a core-helium burning object and a pre-ELM from the position in the HRD or the spectra alone. This can only be done with a mass determination of the sdB. The lifetime of a pre-ELM depends heavily on the mass ($t > 100$ Myr for $M < 0.25 M_{\odot}$). The majority of the ELM are found in binaries with orbital periods shorter than one day and companions, which are white dwarfs as well. As the orbital periods are so short many systems are expected to start mass transfer within a Hubble time. The nature of this mass transfer depends on the mass ratio, as we have seen before. One confirmed pre-ELM is investigated in [16].

2.3.3 Binary central stars of planetary nebulae

As stated before, the planetary nebula (PNe) phase is a short stage in the late evolution of low-mass and intermediate-mass stars, when they get hot enough to ionize their ejected envelope before they enter the WD cooling track. PNe enrich the interstellar medium with processed material and are hence important for the galactic evolution and probes of nucleosynthesis processes. They have a wide range of morphologies. Less than 20% are spherically symmetric, the rest has elliptical, bipolar or butterfly-shaped geometries (Decin et al. 2020). On the other hand the wind of $\sim 80\%$ of the AGB stars is spherical symmetric. There are different hypotheses to explain this various shapes including rapidly spinning or strongly magnetic single stars. The favored hypothesis at the moment is close binaries being surrounded by a common gaseous envelope. A good review about binary central stars of planetary nebula was given by Boffin & Jones (2019) and Jones (2020). Here I will give a summary of the most important facts.

The fraction of PNe found to host a post-common-envelope central star system is at least 12–21%, significantly higher than the number of low- or intermediate-mass stars that are expected to evolve through a CE phase, which might indicate that PNe are more easily formed via a CE. 20% of the post-CE CSPN show photometric variability due to tidal deformations called ellipsoidal modulation or deformation. All those system consist of two (pre-) white dwarfs (double-degenerate systems, DD). The amplitude of the ellipsoidal deformation decreases rapidly with orbital separation (see also next section). So more DD systems have been detected through their radial velocity variability. The formation of those systems most likely involve a first phase of stable mass transfer, followed by a second CE phase when the secondary fills its Roche lobe. Due to their short periods such systems are predicted to eventually merge and are hence interesting as SN Ia progenitors, if the sum of their masses exceeds the Chandrasekhar limit.

About 45% of the about 150 known binary CSPN are showing a reflection effect in their lightcurves (see <http://www.drdjones.net/bCSPN/>). They have periods of 0.1 up to ten or even more days and are consisting of a hot (pre-) WD and a cool main sequence companion. 19 of those systems additionally show eclipses in the light curves.

Not all of the CSPNs are found to be post-AGB stars. If the two stars experience stable RLOF on the RGB, this phase can be terminated and the He core will evolve towards higher temperatures at near-constant luminosity evolving into a post RGB-PNe. Such post-RGB stars have lower luminosities than their cousins, the post-AGB stars, as well as lower masses. If the mass ratio was large enough a common envelope phase can occur instead perhaps leading to the formation of a post-RGB PN with a He-WD or sdB primary, as e.g. suggested for EGB5

by (Geier et al. 2011a). In [14] we reinvestigated a very interesting binary CSPN.

2.3.4 (Hot) white dwarfs

White dwarfs are the final stage of evolution of 97% of all stars. Therefore, they allow to study the stellar evolution of their progenitors and the age structure and star formation history of our galaxy. When shell burning stops completely the core starts to cool and becomes fully degenerate. The rest of its evolution it cools down emitting radiation and neutrinos. Recently observational evidence has been found that some white dwarfs can maintain hydrogen shell burning in a thick hydrogen shell delaying their cooling (Chen et al. 2021).

White dwarfs are classified by their spectra depending on their surface composition and temperature. Due to gravitational settling hydrogen will float on top resulting in a hydrogen-rich DA WD. Helium-rich WDs are either called DO ($45\,000\text{ K} < T_{\text{eff}} < 120\,000\text{ K}$, He II lines), DB ($12\,000\text{ K} < T_{\text{eff}} < 45\,000\text{ K}$, He I lines) or DC ($T_{\text{eff}} < 12\,000\text{ K}$, no lines). Both classes show also different subclasses: DQ (additional carbon lines) or DZ (accreted metal lines) WDs. A third class of white dwarfs with temperatures between $75\,000$ to $200\,000\text{ K}$ are the PG1159 stars. They are extremely hot and luminous degenerate objects with spectra dominated by He II and highly excited carbon and oxygen lines (see Sion 2011, for a summary).

For the hottest WDs ($100\,000\text{ K} < T_{\text{eff}} < 250\,000\text{ K}$) H-deficient WDs outnumber H-rich WDs by a factor of five, whereas at cooler temperatures it is the opposite (Bédard et al. 2020). This fact is not understood yet, but might indicate mixing of H and He or different evolutionary timescales of H-rich and H-deficient WDs. Amongst the hottest white dwarfs a significant fraction of about 10% of these objects show spectral lines of ultra-highly excited (UHE) metals, e.g. C VIII, N VII. This so-called UHE phenomenon is one of the least understood effects observed in hot WDs, as it requires temperatures of the order of 10^6 K (more details can be found in [13]). Many of the UHE WDs also show photometric variations, which could shed some light on this open question. One possibility causing this variations could be binarity.

As white dwarfs are the end point of stellar evolution, a significant fraction of them is found in binaries, same as their progenitor systems. Such systems are important to understand the final fate of binary stars. Wide binaries are important to understand the initial-final-mass relation, which is a key parameter to test stellar evolution theory. A large sample of post-common envelope systems with white dwarf primaries have been found, but only few white dwarfs with FGK type companions have been found so far by detecting a UV excess (Parsons et al. 2023). Those systems can be post-common envelope systems or RLOF systems with longer periods. In the latter case the stable mass transfer can lead to a spun-up of the companions causing strong chromospheric activity and spots. This leads to sinusoidal light variations with the rotational period of the companion due to the spots and H α emission and CaII H and K emission-line cores from the chromospheric activity. With a detail analysis of such a rare and interesting target the fundamental parameters can be derived and the previous and future evolution can be constrained (see [15]).

3 Analysis methods

3.1 Finding close binaries

So far mostly individual objects have been analyzed adding among the hot subdwarf binaries, but also hot white dwarfs and CSPNs. This adds up to a few tens of systems with known parameters for each type of system. In order to shed more light on the formation and stellar evolution of our systems, we need to go from individual objects to whole populations in order to reach a statistically significant sample. This requires a systematic search for evolved, close binary stars.

3.1.1 Color selection

The targets we are looking for are hot (and therefore blue), faint objects. To select them we need to have information about their colors and absolute magnitudes. This is either provided by photometric surveys, if they observe in different filters (see next section), or e.g. the *Gaia* spacecraft, which was launched on 19.12.2013. *Gaia* measures parallaxes, proper motions, spectral energy distributions (3300 – 10500 Å), and high resolution spectra (8450 – 8720 Å) of about one billion stars. From this data distances, colors and absolute magnitudes can be derived among other parameters. This can be used to systematically find candidates for hot subdwarfs, CSPNs and hot white dwarfs.

In Fig. 3.1 the selection of hot subluminescent star candidates by Culpan et al. (2022) is shown. This is an updated version of the first catalog published by Geier et al. (2019). They used the *Gaia* EDR3 color-magnitude diagram (CMD) to select candidates. To determine the region, where the hot subluminescent stars are found, they looked first at the position of the known hot subdwarfs ($2 \text{ mag} < G_{\text{abs}} < 7 \text{ mag}$, $G_{\text{BP}} - G_{\text{RP}} < 0.7 \text{ mag}$). This information was used to construct a catalog of hot subluminescent star candidates, as shown in Fig. 3.1. They limit themselves to targets with parallax errors better than 20%. As the astrometry of *Gaia* is less accurate in crowded fields, they considered only targets, which do not have close neighbors of similar magnitude within 5". For the rest of the targets a stricter parallax error limit of 10% was applied. For the targets with less accurate parallaxes, the proper motion was used as a criterion. Targets, which are closer, will have a larger motion on the sky on average, which means that the proper motions at a certain brightness can be used as a proxy for the distance. The authors used the reduced proper motion H_G , which is defined as

$$H_G = G + 5 \log_{10}(\mu) + 5, \quad (3.1)$$

with G the unfiltered *Gaia* magnitude and $\mu = \sqrt{\mu_{\text{ra}}^2 + \mu_{\text{dec}}^2}$ the proper motion. In Fig. 3.1 the criterion to remove the main sequence and cool white dwarfs for the parallax and reduced proper motions selection are shown together with the distribution of the targets on the sky. *Gaia* also provides errors on the G magnitude resulting from several single measurements. An excess in the flux error compared to the error a typical target at a certain G magnitude indicates photometric variability and can be used to select targets, which show most likely light

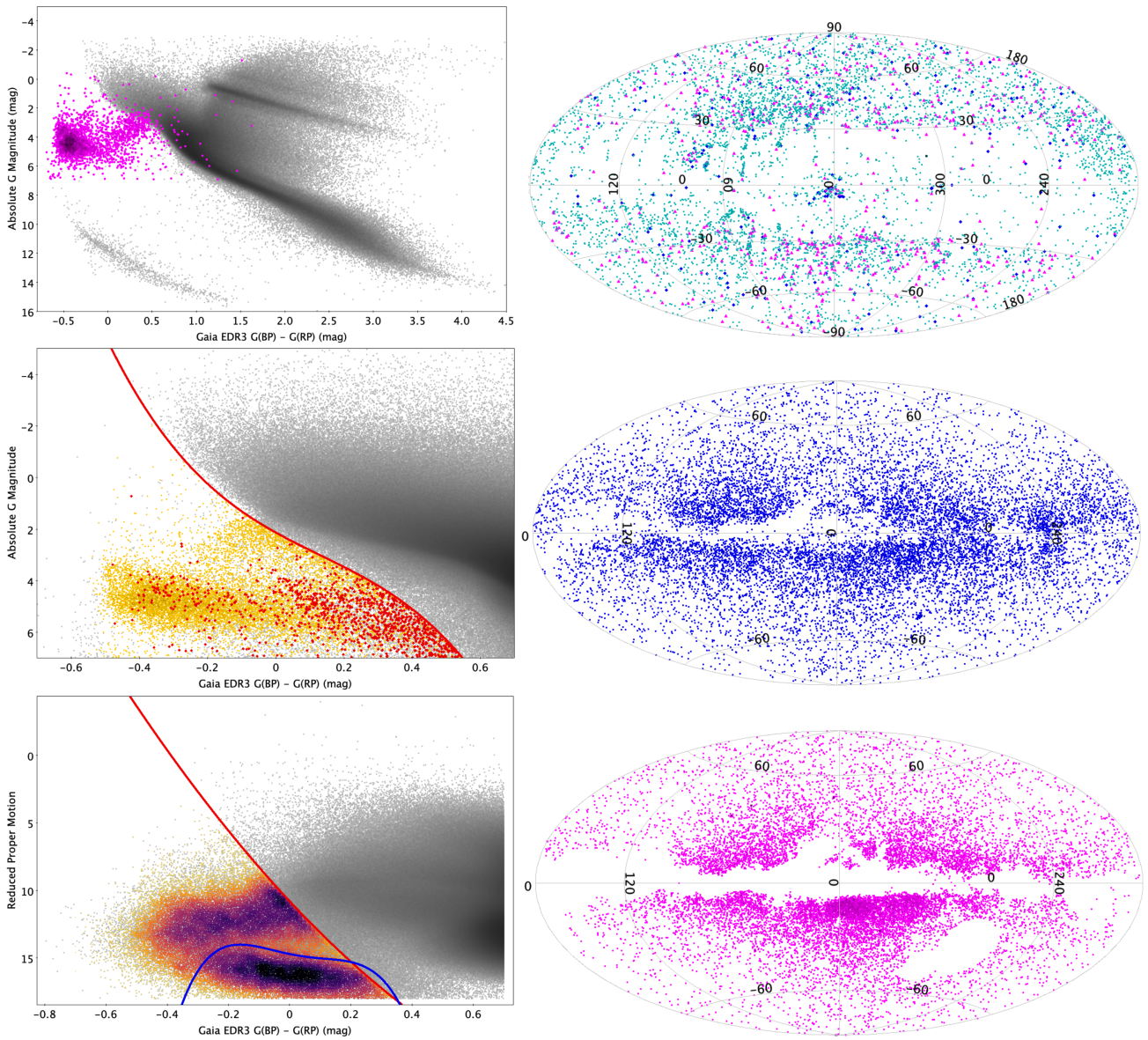


Figure 3.1: Comparison of the position of the known hot subdwarfs (top panel) and the hot subluminal star candidates from the parallax selection (middle panel) and from the proper motion selection (lower panel) in the color-magnitude diagram (CMD) and on the sky (Culpan et al. 2022). The different symbols in the right upper panel represent single hot subdwarfs (cyan squares), wide binary systems (magenta triangles), and close binary systems (blue diamonds). In the middle panel the variable star candidates are shown with the red diamonds. The red line shows the cutoff used to remove the main sequence, the blue line the cutoff used to remove white dwarfs.

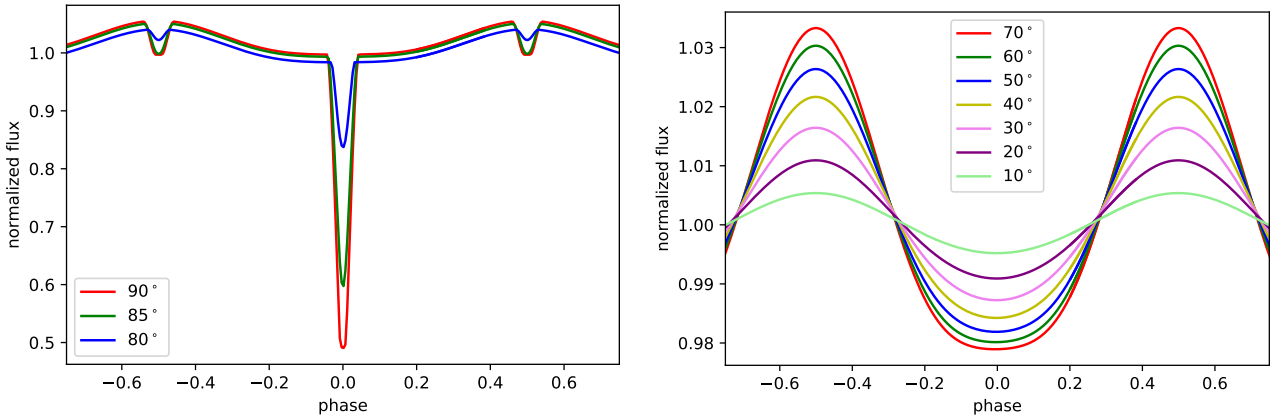


Figure 3.2: Synthetic light curves of a typical reflection effect system with a hot subdwarf primary and a cool, low-mass main sequence companion with different inclinations calculated with LCURVE.

variations. However, not all systems with known light variations show an excess in the flux error.

3.1.2 Light curves

The *Gaia* hot subluminous star candidate catalog provides us with 61 585 mostly hot subdwarf candidates, but also some CSPN, and hot white dwarf candidates. The question now is how to find close binaries among all those targets. A significant number of the close binaries shows light variations, as mentioned before. We can use those light variations for the selection of new close binary systems. In the following I will give more details on the light variations, which are observed.

Reflection effect As we have seen before, close binaries with a hot compact primary and a cool, low-mass companion, will show a reflection effect. The amplitude A of the reflection depends on the flux difference between the hot and cool side compared to the total luminosity of the binary. We can use the black body approximation ($B_\lambda(T) = \frac{2hc^2/\lambda^5}{e^{hc/\lambda kT} - 1}$) to demonstrate the main dependencies

$$A(\lambda) = \frac{F_{2,\text{hot}}(\lambda) - F_{2,\text{cool}}(\lambda)}{F_1(\lambda) + F_{2,\text{cool}}(\lambda)} = \frac{B_\lambda(T_{2,\text{hot}} = T_{2,\text{cool}} \cdot [1 + \alpha(\frac{T_1}{T_{2,\text{cool}}})^4(\frac{R_1}{a})^2]^{1/4})R_2^2 - B_\lambda(T_{2,\text{cool}})R_2^2}{B_\lambda(T_1)R_1^2 + \underbrace{B_\lambda(T_{2,\text{cool}})R_2^2}_{\ll B_\lambda(T_1)R_1^2}}. \quad (3.2)$$

Hereby, α is the fraction of the irradiating flux F_1 of the primary star, which is used to heat up one side of the companion, $F_{2,\text{hot};\text{cool}}$ the flux of the irradiated or not irradiated side of the companion, a the orbital separation and T_1 and $T_{2,\text{hot};\text{cool}}$ the temperature of the primary and secondary star, (irradiated or not irradiated side) respectively, and $R_{1,2}$ the radius of the primary and the secondary star. We can see that the amplitude mainly depends on the temperature and size of both stars as well as the orbital separation of the binary and that it is wavelength dependent, as the observed flux is different for different wavelengths.

In Fig. 3.2 we can see how the light curve of a typical reflection effect system looks like. The shape of the reflection effect depends on the inclination of the binary system, as this impacts

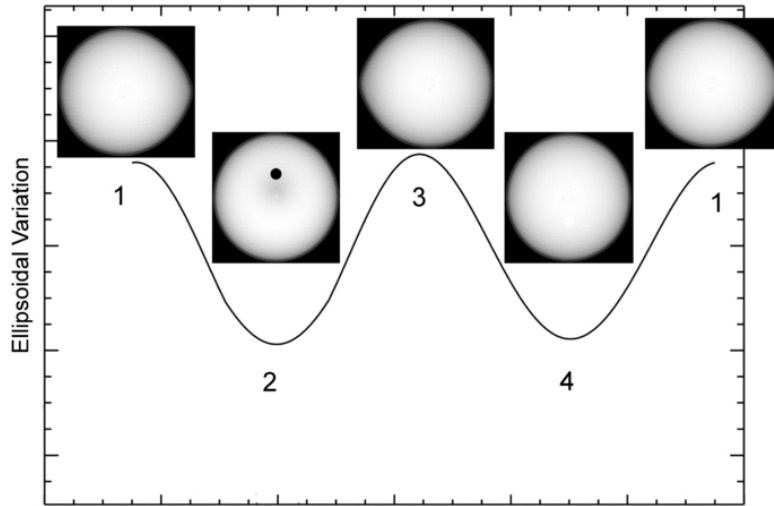


Figure 3.3: Illustration of the phases of ellipsoidal variation (Jackson et al. 2012).

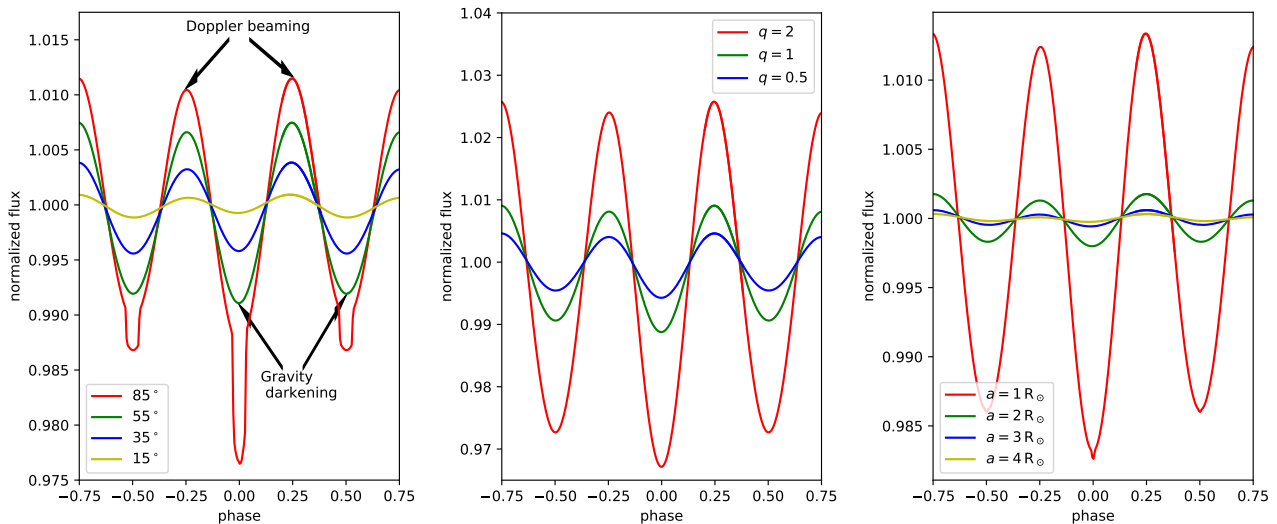


Figure 3.4: Synthetic light curves of a typical ellipsoidal system with a hot subdwarf primary and a white dwarf companion with different inclinations, mass ratios and orbital separations calculated with LCURVE.

the visible area of the hot side of the companion. For high inclinations we will see additionally primary and secondary eclipses. Even when the eclipses are not visible anymore, we can still see the reflection effect. With smaller inclinations the shape of the reflection effect is getting more and more sinusoidal. This effect is also discussed in detail in [2], where we analyzed a large sample of reflection effect systems.

Ellipsoidal deformation For the reflection effect to be visible we need a companion of similar or larger size than the primary star otherwise the amplitude will be very small. This means in the case that the companion is compact, e.g. a white dwarf with a size similar to Earth, this effect will not be visible. However, if the orbital separation is small enough, tidal influences will become important. The primary star will begin to deviate from its spherical shape and get ellipsoidal. This results in a quasi-sinusoidal variation in flux with twice the orbital period, as is illustrated in Fig. 3.3. The amplitude of this variation correlates strongly with the inclination, mass ratio, and orbital separations (see Fig. 3.4). This means that systems with short periods,

large mass ratios and high inclinations will be much easier to find.

There are two effects visible in the light curves of ellipsoidal systems, which cause a deviation from the sinusoidal shape. One is caused by the large radial velocities of the hot subdwarf with a few 100 km/s. Objects moving at great speed are not emitting the light spherically symmetric anymore, but preferentially in the direction of its movement. Therefore, the flux we observe is lower, when the star moves away from us than when it approaches the observer. This results in a difference in the height of the two maxima. In some longer-period systems of a few hours to days period, this so-called Doppler beaming can still be detected even when ellipsoidal deformation is not visible anymore, if the S/N and the projected radial velocity are high enough.

The second effect, which is visible in the two minima, is caused by gravity darkening. As the star is ellipsoidal, its radius is varying and thus also does the surface gravity. In regions of lower surface gravity lower pressure and temperature is necessary to reach hydrostatic equilibrium. Therefore, regions with larger radii will be cooler and thus fainter. As can be seen in Fig. 3.3, the star will be distorted towards the inner Lagrangian point. This results in a deeper minimum when we see the side pointing towards the companion. A very nice example of an sdB+WD system showing ellipsoidal deformation is discussed in [11].

3.1.3 Photometric surveys

As we have seen, close binaries can be detected by their light variations. This means new systems can be found by obtaining and looking through the light curves of the hot subluminescent star candidates. As we have about 63 000 candidates, it would take a while to obtain light curves for each target. Luckily several photometric surveys exist, which are taking light curves of many different stars. We can just crossmatch our catalog with this photometric surveys or use our own color cuts and download the light curves of our selected targets. In this work we use several different photometric surveys, both ground-based and space-based.

Optical Gravitational Lensing Experiment The Optical Gravitational Lensing Experiment (OGLE) project started in 1992 with the 1-m Swope telescope at the Las Campanas observatory in Chile. The main goal was searching for dark matter using the microlensing phenomenon. Due to limited observation time they were only observing a small area of the sky in the direction of the Galactic bulge. This was only the pilot project and in 1995 they started building a dedicated telescope at Las Campanas, the 1.3-m Warsaw telescope. With this telescope they could observe additional fields towards the Magellanic clouds and the Galactic center increasing the number of monitored targets from two million to a few tens of millions. In 2001 they upgraded the CCD camera to an eight detector mosaic camera with 2048×4096 pixel and the difference imaging technique was implemented into the data reduction pipeline allowing mmag accuracy photometry even in very crowded fields. In 2010 they started the fourth phase of the project with another upgrade to a 32 CCDs mosaic camera with in total 262.5 Mpixel and a 1.5 deg^2 field of view monitoring now over a billion sources regularly (see Udalski et al. 2015, for a detailed description).

Gravitational microlensing is still an important science driver. However, they have also been searching for all kinds of variable stars, such as e.g. eclipsing binaries, pulsating stars or planetary transits providing large statistical samples for the first time. OGLE-IV is observing several fields on the sky towards the densest stellar fields (see Fig. 3.5) in two different filters (V and I, see Fig. 3.6). Interstellar extinction plays a very important role in those regions. The cadence of the observations is depending on the field from one observation every 19 minutes up to one observation every few days, giving a few hundreds to thousands of data points per target in I and less in V. The limiting magnitude is varying from field to field with a range of

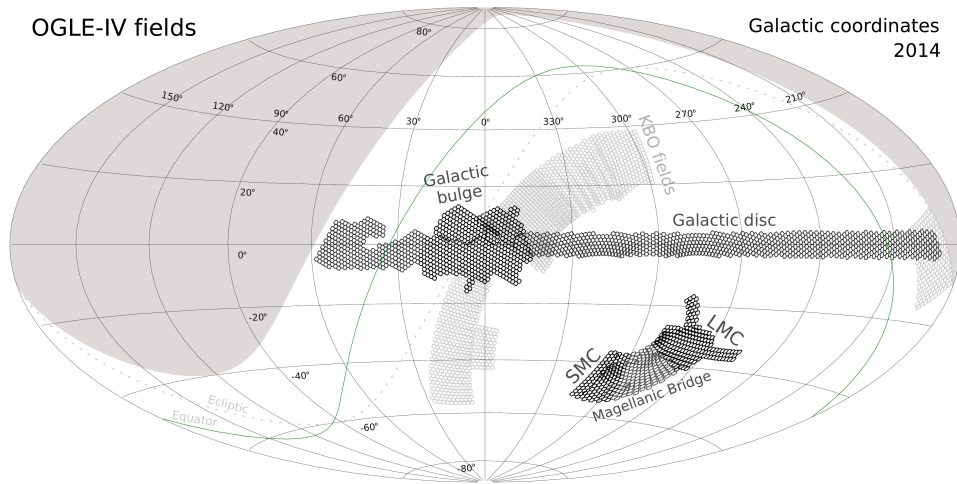


Figure 3.5: OGLE-IV sky coverage in Galactic coordinates (Udalski et al. 2015).

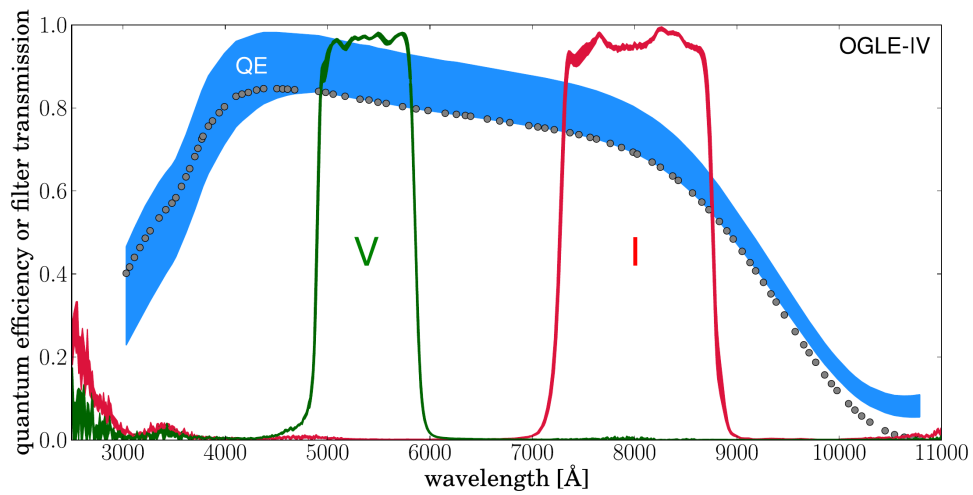


Figure 3.6: Pass-bands of the OGLE-IV filters and quantum efficiency (QE) of the OGLE-IV CCDs (Udalski et al. 2015).

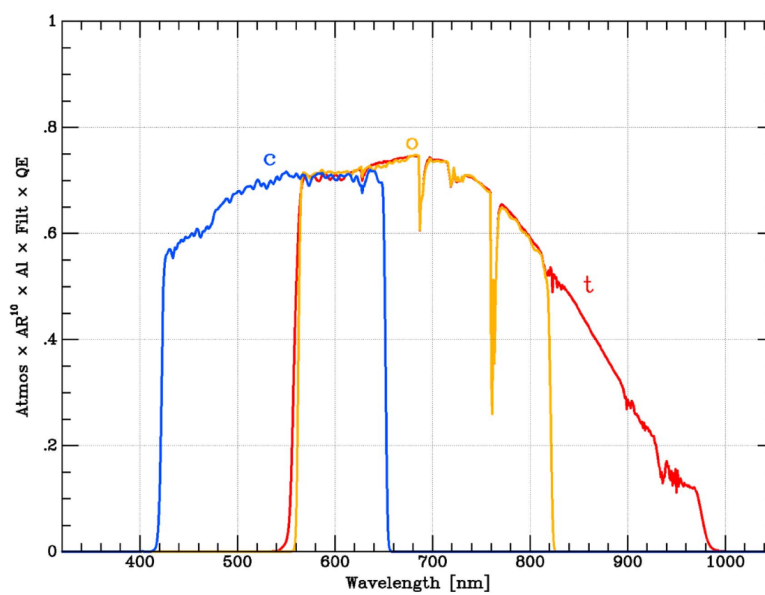


Figure 3.7: Total throughput of the ATLAS primary *c* (blue), *o* (orange) and *t* (red) filters (Tonry et al. 2018).

$10 < I < 19$ mag in the Galactic disk fields and $12 - 13 < I < 21 - 22$ mag in the Galactic bulge and Magellanic cloud fields being complete to $I \approx 18 - 19$ mag in the most crowded fields. The OGLE team does not provide all observed light curves, but only data, which has been extensively checked and classified. Due to COVID-19 they stopped operations for 2.4 years but continued observing in August 2022. The current status of the OGLE project and all the published data can be obtained at <http://ogle.astrouw.edu.pl>. As OGLE is observing in very crowded fields, where the accuracy of the *Gaia* astrometry is significantly worse, the hot subluminous star catalog cannot be used, but color and orbital period cuts have to be applied to the OGLE targets using the magnitudes of the OGLE I and V light curves.

Asteroid Terrestrial-impact Last Alert System The Asteroid Terrestrial-impact Last Alert System (ATLAS) is a large photometric survey imaging the entire sky every night and able to process the data in real time. The main goals of this project are finding potentially hazardous asteroids but also tracking variables and discovering transients, such as e.g. supernovae or gamma-ray bursts. ATLAS started operations in 2015/2017 with two independent units on two different Hawai'ian islands. In late 2021 two additional sites in South Africa and Chile went online allowing for 24 hours continuous observations. All sites consist of a 0.5m telescope with a 10kx10k CCD camera, a field of view of $5.4^\circ \times 5.4^\circ$, and a pixel scale of $1.86''$. With the two units in Hawaii they cover the entire accessible sky with a cadence of two days with four exposures (over a 1 hr interval). They observe in the *c* band in dark time and in the *o* band (see Fig. 3.7) in bright time with an exposure time of 30 s giving a 5σ limiting magnitude of 19.5 mag (see Tonry et al. 2018, for a detailed description). A first catalog of variable stars based on analyzing the light curves of 142 million stars was published by Heinze et al. (2018) identifying 4.7 million candidate variables. The light curves can be obtained via MAST CasJobs (<http://mastweb.stsci.edu/mcasjobs/home.aspx>). Light curves of any target observed by ATLAS with any telescope can be requested at <https://fallingstar-data.com/forcedphot/>, which are then constructed using difference imaging on the server.

The K2 mission The *Kepler* spacecraft was launched in 2009. Its prime objective was to find Earth-like planets in the habitable zone of Sun-like stars. Therefore, it monitored about 150 000 stars in the Cygnus-Lyra region for a little bit more than four years consecutively. *Kepler* was in an Earth-trailing heliocentric orbit and hosted a 0.95-m aperture Schmidt telescope. The *Kepler* photometer consisted of 21 CCD modules covering in total a field of view of 116 deg^2 and a pixel scale of $3.98''$. The wavelength coverage of the *Kepler* filter from about 400 to 900 nm is shown in Fig. 3.8.

After two reaction wheels stopped working in May 2013 the original *Kepler* mission could not be continued, as the spacecraft could not kept stable enough to continue observing the dedicated field. After one year a new concept for spacecraft operations was developed, the *K2* mission. It was an entirely community driven mission. All targets were proposed through the guest observer program. The original *Kepler* mission was mainly observing Sun-like stars and only very few hot stars, but the *K2* mission covered a wide range of astrophysical topics including variable and pulsating stars, as well as transients.

Using the radiation pressure of the Sun they managed to keep the spacecraft stable on one field for 80 days. In total the *K2* mission observed 20 different fields during its lifetime of another 4 years. As soon as the fuel was exhausted, operations had to be terminated, when the spacecraft could not be kept stable anymore. Due to jitter of the spacecraft the quality of the light curves degraded compared to the original *Kepler* mission, but was still excellent (see Fig. 3.9). Science observations were taken in two different timing settings: long (30 min) or

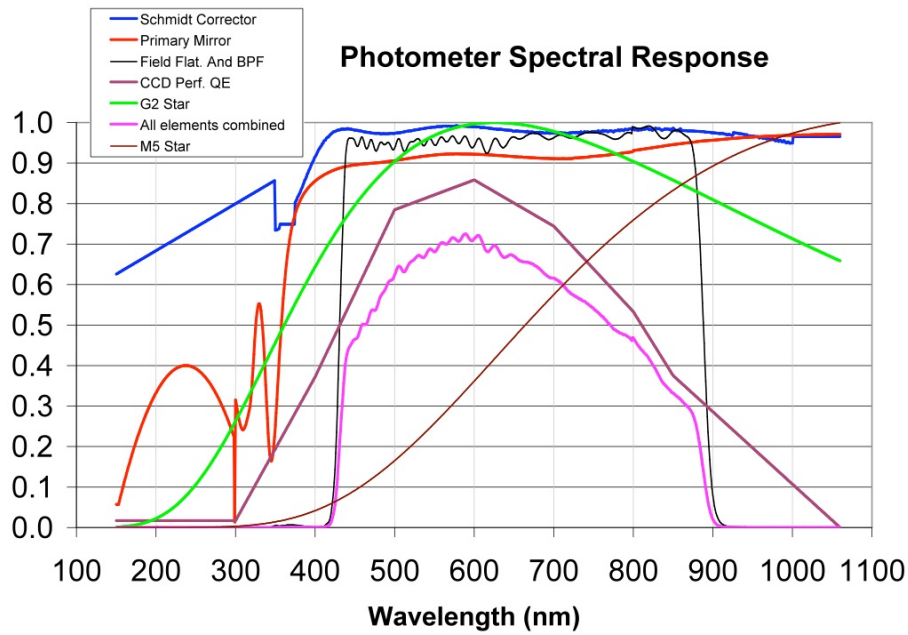


Figure 3.8: *Kepler* Instrument Response function (<https://keplergo.github.io/KeplerScienceWebsite/the-kepler-space-telescope.html>).

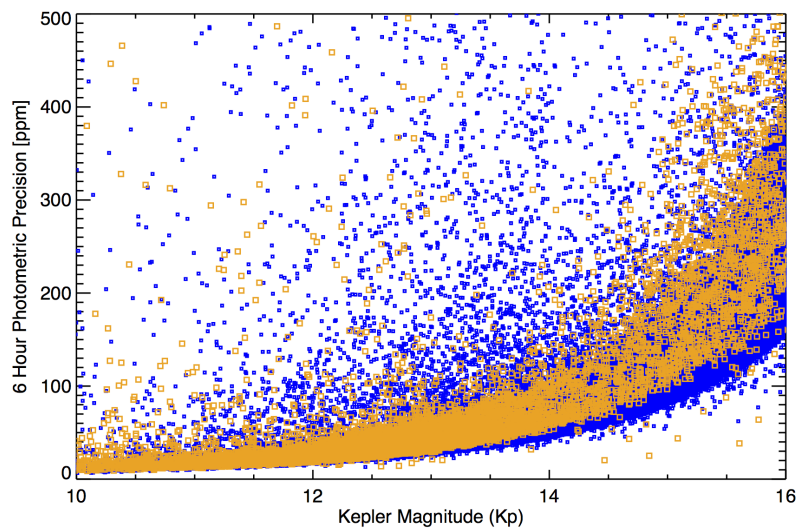


Figure 3.9: Combined differential photometric precision of a 6 hour observation with *Kepler* (blue) and *K2* (orange) (<https://keplergo.github.io/KeplerScienceWebsite/the-kepler-space-telescope.html>).

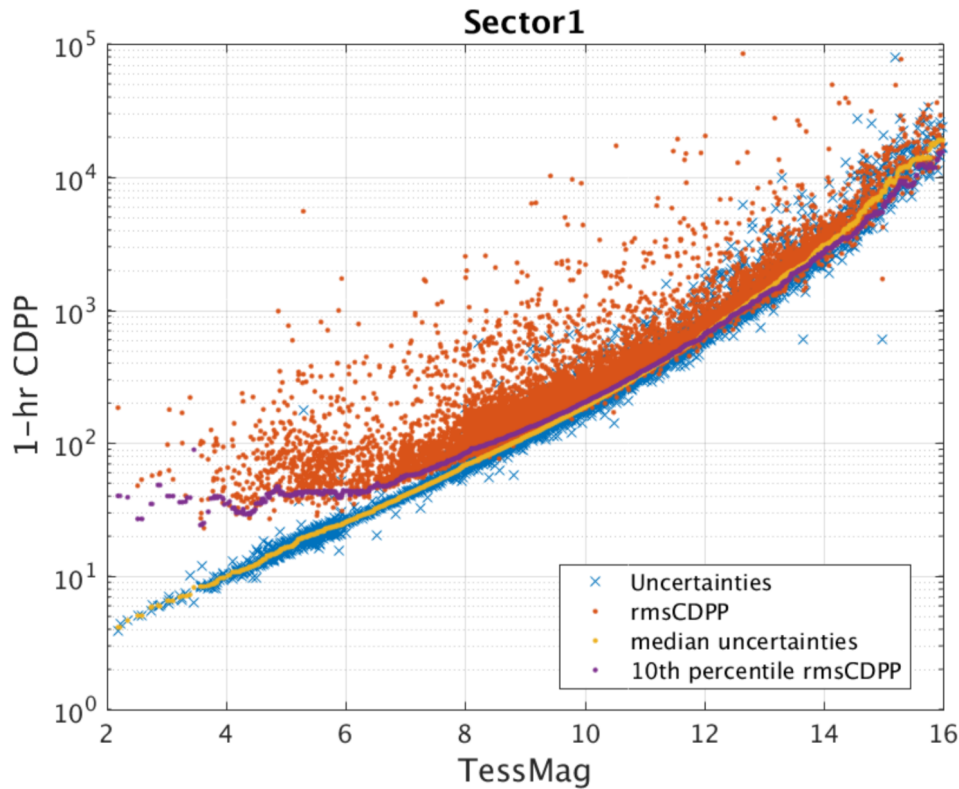


Figure 3.12: Combined differential photometric precision of a 1 hour observation with *TESS* (<https://heasarc.gsfc.nasa.gov/docs/tess/observing-technical.html>).

and extracting light curves from the full frame images. In this work we used the python package `LIGHTKURVE` (<https://docs.lightkurve.org/>).

The primary mission was followed by a first extended mission of about two years involving also an extensive guest investigator program, where targets could be proposed by the community. In this mission 10 min full frame images were created instead of 30 min and additional to the 2 min cadence also 20 s cadence data for an even smaller number of targets were downloaded. Since October 2022 *TESS* is in its second extended mission, which is mainly community based with another large guest investigator program. As in the first extended mission selected targets are observed in 2 min or 20 s cadence. As the data transfer rate could be increased due to an additional data link, full-frame images can be provided every 200 s, which will allow to derive light curves with 200 s cadence for 80% of the sky with space-based quality (see Fig. 3.12).

From the light curves of our targets we can derive periods by using a Lomb Scargle periodogram (see Fig. 3.13 for an example). This algorithm is perfect for detecting periodic signals especially in unevenly sampled data (see VanderPlas 2018, for a detailed description of the algorithm and its properties). Phase-folding to the highest peak in the periodogram and binning allows us to inspect the light curve shapes, which then can be used to identify and classify close binaries by eye, as described in the previous sections (more details how those surveys are used for the target selection can also be found in [1] and [3]).

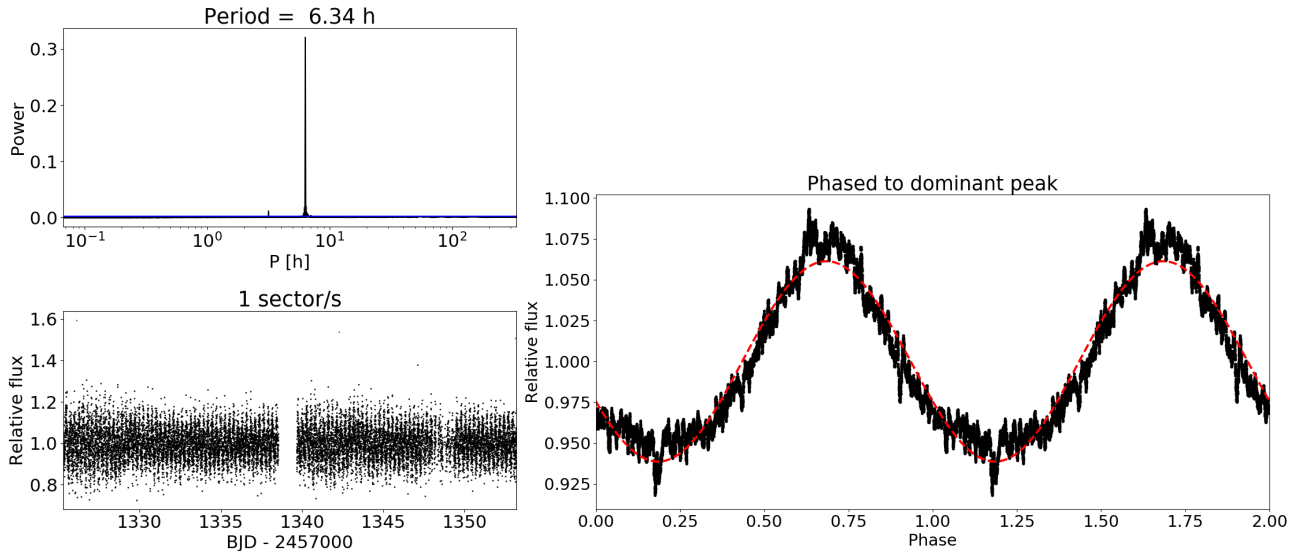


Figure 3.13: Periodogram, light curve, and phase-folded light curve of an example target observed by *TESS* (adopted from Pelisoli, priv. com.)

3.2 Analysis of primary star

In order to derive the parameters of our targets a detailed analysis has to be done. As the hot subdwarf is much brighter than the unseen companion and therefore dominating the spectra, we analyze it first using spectra and the spectral energy distribution. In the following I briefly summarize our different analysis methods.

3.2.1 Spectral analysis

For the spectral analysis pre-calculated grids of synthetic spectra are fitted to the spectral lines simultaneously using a χ^2 minimization in order to derive the effective temperature T_{eff} , the surface gravity $\log g$ and the helium abundance $\log y$ (see Fig. 3.14 for an example). In spectra with sufficient resolution ($R \gtrsim 5000 - 10000$) and high signal-to-noise we can also determine the projected rotational velocity and abundances of other elements as e.g. C, N, O, Mg, Si, Fe, ... The synthetic spectra were calculated using a hybrid LTE/NLTE approach, which was extensively tested for B-type stars (e.g. Nieva & Przybilla 2007). It is based on three different codes. Line-blanketed, plane-parallel model atmospheres are computed in LTE with a mean abundance pattern for sdBs taken from Naslim et al. (2013) (scalable for different metallicities) using ATLAS (Kurucz 1996). The occupation number densities are then derived in NLTE for hydrogen, helium, and for selected metals using DETAIL (Giddings 1981; Butler & Giddings 1985). In the last step the synthetic spectrum is then calculated with SURFACE (Giddings 1981; Butler & Giddings 1985) using the previously calculated population numbers and detailed line profiles (see also [6] for more details on the spectral analysis).

3.2.2 Spectral energy distribution

Obtaining high resolution, high S/N spectra costs a lot of observing time. Luckily, crucial information about the primary star (and in some cases about the secondary as well) can also be derived by constructing a spectral energy distribution (SED) of the star from single epoch photometric observations in the UV, optical and infrared. Those measurements are provided

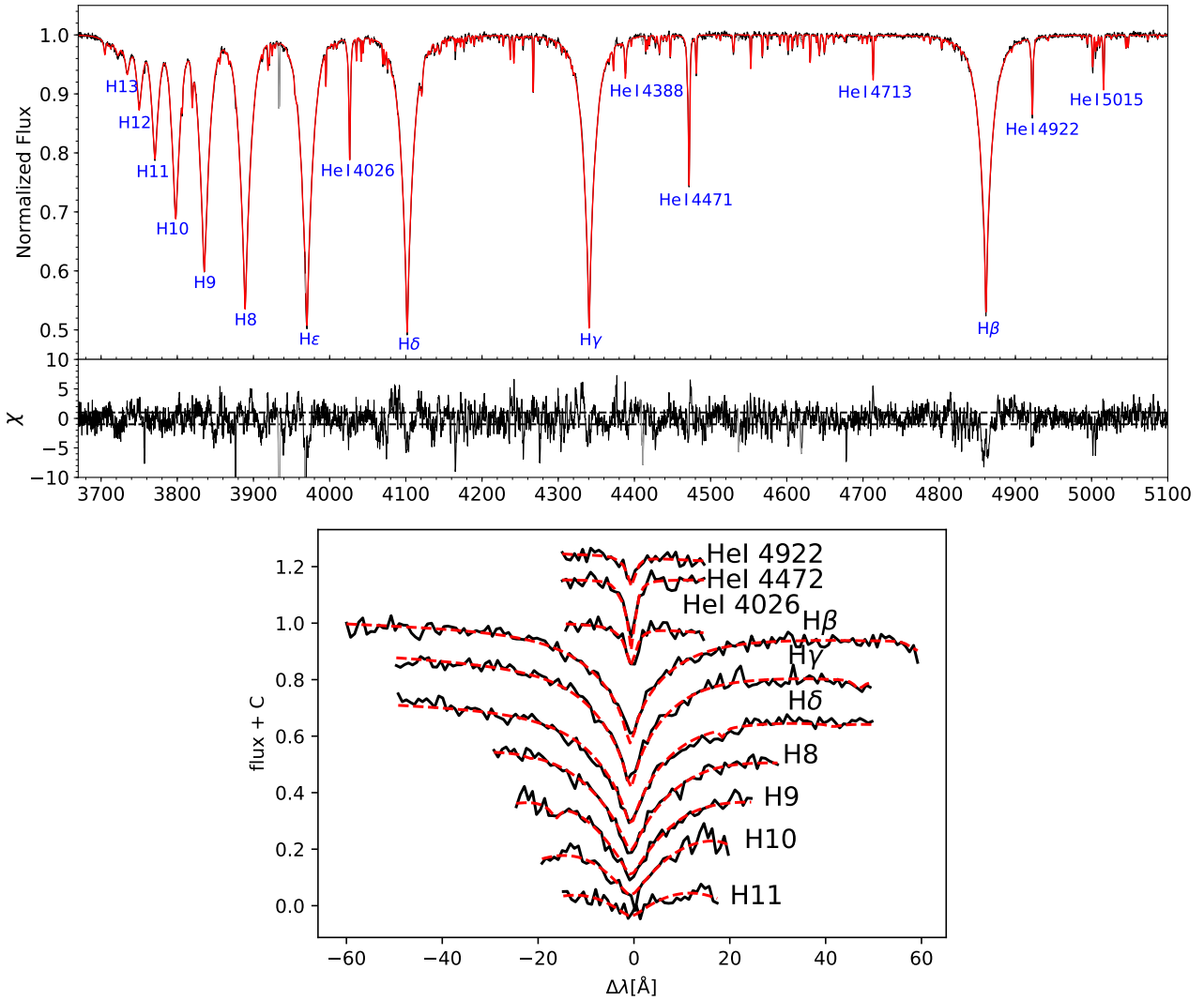


Figure 3.14: Spectral fit of two sdBs with high resolution spectra (taken from [6]) and low resolution spectra (taken from [2]).

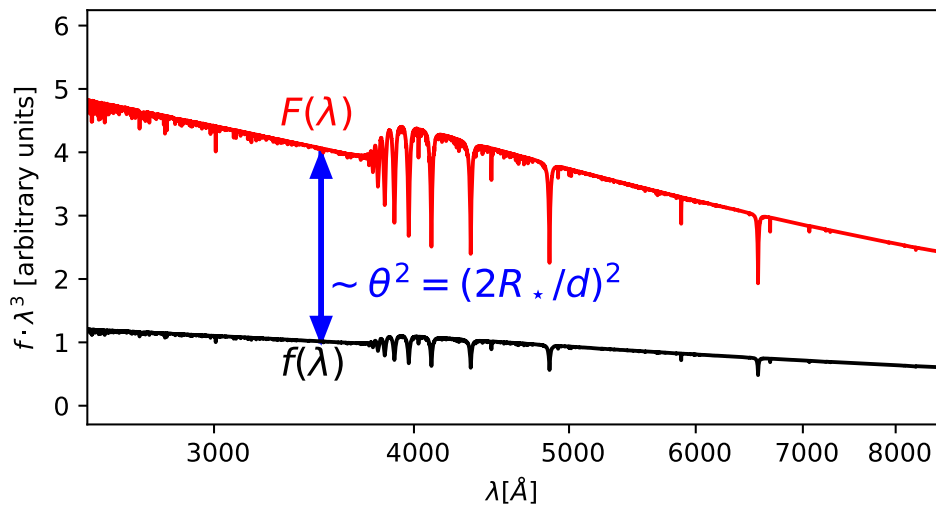


Figure 3.15: Deriving the angular diameter or rather the stellar radius by scaling the model flux at the stellar surface $F(\lambda)$ to fit the flux $f(\lambda)$ observed at the detector.

by different photometric surveys. The SEDs can be used e.g. to determine the effective temperature of a star, to identify an infrared excess caused by the presence of a cool companion or to derive interstellar extinction. A detailed description of the method was given by Heber et al. (2018).

For the construction of the observational SED we use all in the literature available photometric measurements. Additionally, UV magnitudes are derived from spectra observed with the International Ultraviolet Explorer (IUE) when available by using three box filters covering the spectral ranges 1300–1800 Å, 2000–2500 Å, and 2500–3000 Å.

Using the same grid of model atmospheres as for the spectral analysis (see Sect. 3.2) we can construct synthetic SEDs and synthetic colors. The magnitude of a photometric passband is defined as

$$\text{mag}_x = -2.5 \log \left(\frac{\int_0^\infty r_x(\lambda) f(\lambda) d\lambda}{\int_0^\infty r_x(\lambda) f^{\text{ref}}(\lambda) d\lambda} \right) + \text{mag}_x^{\text{ref}}, \quad (3.3)$$

where $r_x(\lambda)$ is the response function of the filter and $f(\lambda)$ the flux at the detector. This flux can be calculated by the model flux at the stellar surface $F(\lambda)$ and the angular diameter of the star $\theta = 2R_\star/d$ (with R_\star the radius of the star and d the distance to the star), as demonstrated in Fig. 3.15:

$$f(\lambda) = \theta^2 F(\lambda)/4. \quad (3.4)$$

To set the zero point of the filter to a predefined magnitude $\text{mag}_x^{\text{ref}}$ the flux f^{ref} of a reference star is necessary (usually Vega). Interstellar extinction is considered by multiplying the synthetic flux with a reddening factor $10^{-0.4A(\lambda)}$. Thereby $A(\lambda)$, the extinction at wavelength λ , is a function of the color excess $E(B - V)$ and the extinction parameter $R_V = A(V)/E(B - V)$ (3.1 for the Milky Way). Fig 3.16 shows the effect of reddening on the SED.

In the case that not only a hot primary but also a cool companion is visible as an excess in the infrared, a combined SED needs to be generated from the spectra of the two components (see Fig. 3.17 for an example) together with an additional parameter, the surface ratio $S = \frac{A_c}{A} = \frac{\Theta_c^2}{\theta^2}$. From this surface ratio the angular diameter of the companion Θ_c can be calculated.

For the analysis of the SEDs χ^2 minimization is used to find the global best-fit in the multi-parameter space for a composite fit of a hot primary and a cool companion c with the following parameter, as discussed:

- angular diameter θ
- surface ratio $S = (\theta_c/\theta)^2$
- effective temperatures $T_{\text{eff}}, T_{\text{eff},c}$
- surface gravities $\log g, \log g_c$
- helium abundance $\log(n(\text{He})/n(\text{all}))$
- metallicity $z, [\text{Fe}/\text{H}]$
- interstellar reddening parameter $E(B - V)$ or $E(44 - 55)$.

The shape of the SED is most sensitive to interstellar extinction (see Fig. 3.16), as well as changes in effective temperature (see Fig. 3.18). Furthermore, the angular diameter can be derived by the SED fit, as shown in Fig. 3.15. All other parameters have only a minor effect. As $\log g$ cannot be derived by the fitting of the SED, it is preferable to determine it from

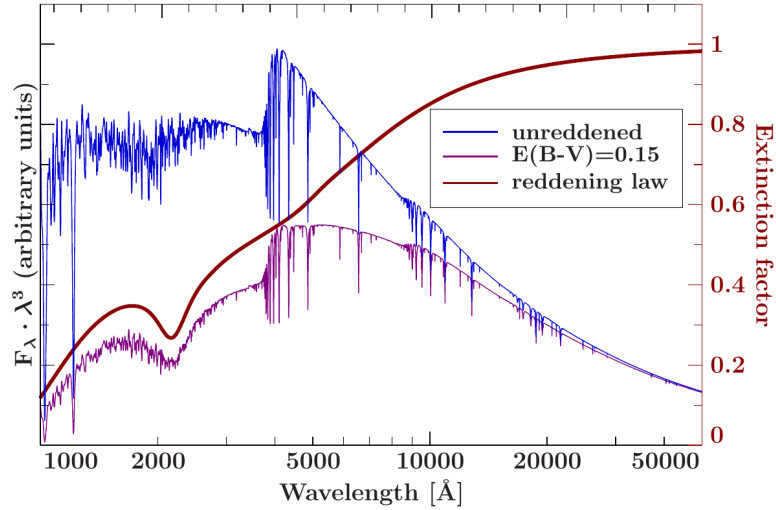


Figure 3.16: The impact of interstellar reddening on SEDs (Heber et al. 2018).

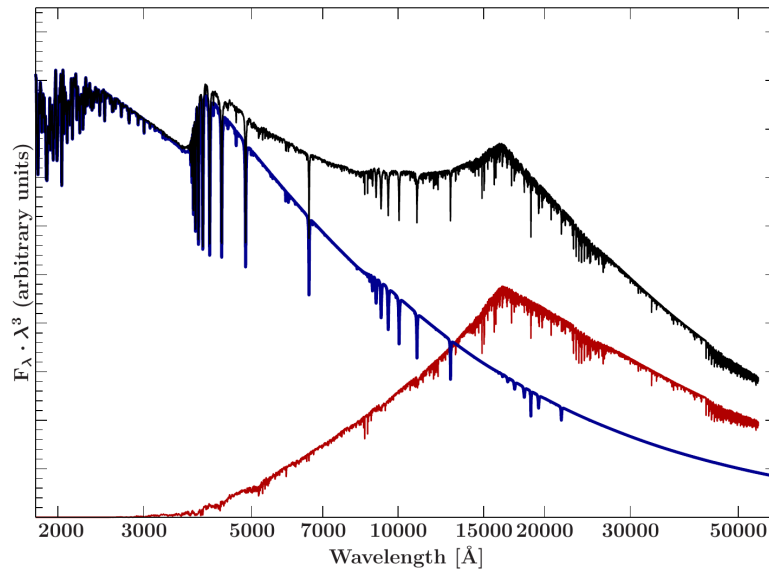


Figure 3.17: Synthetic SED for a composite-spectrum sdB binary (Heber et al. 2018).

spectral fitting. We can then also calculate fundamental parameters (mass, radius, luminosity) of the stars, when the distance d of the star is known e.g. from the Gaia parallax ϖ .

- radius $R = \theta/2\varpi$
- mass $M = gR^2/G$
- luminosity $L/L_{\odot} = (R/R_{\odot})^2(T_{\text{eff}}/T_{\text{eff},\odot})^4$
- radius of the companion $R_c = \sqrt{S}\theta/2\varpi$
- mass of the companion $M_c = g_c R_c^2/G$
- luminosity of the companion $L_c/L_{\odot} = (R_c/R_{\odot})^2(T_{\text{eff},c}/T_{\text{eff},\odot})^4$.

More details on the SED analysis are also given in [1] and [6].

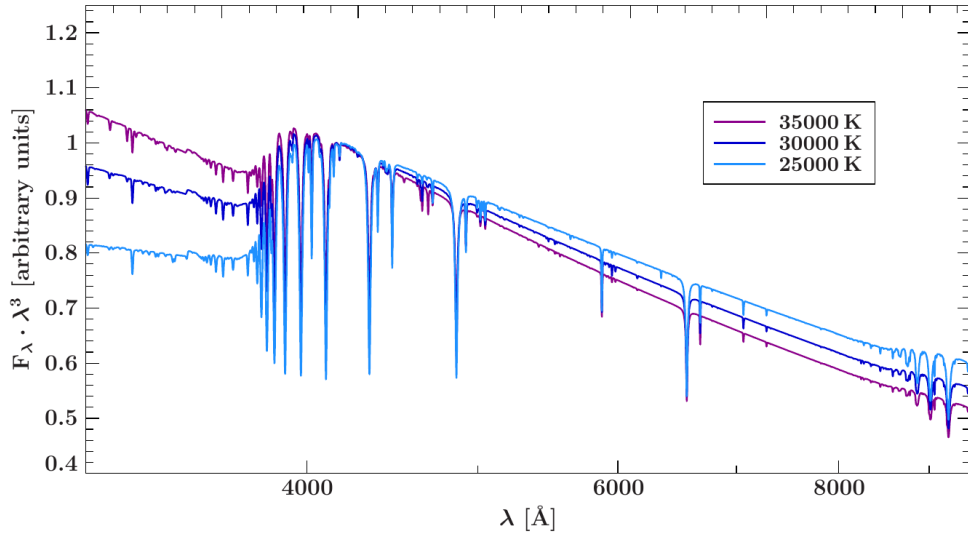


Figure 3.18: The impact of effective temperature on the SED (Schaffenroth 2016).

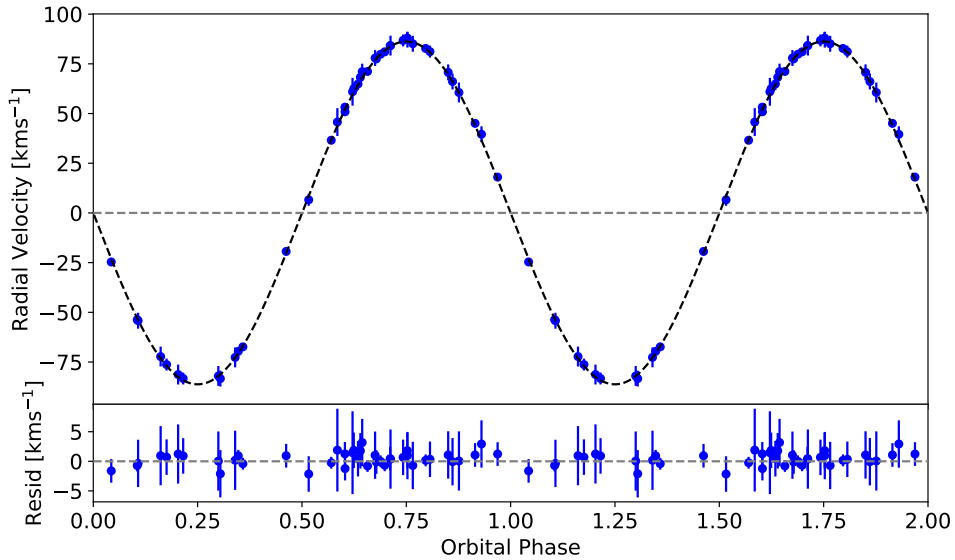


Figure 3.19: RV curve of the sdB+dM system EC01578-1743 (taken from [2]).

3.3 Close binary analysis

As discussed before, many close binaries show light variations. Both stars orbit each other, which additionally leads to measurable radial velocity variations. A combination of photometric and spectroscopic analysis together with the analysis of the primary, as shown in the previous section, enables us to characterize the system.

3.3.1 Radial velocity curve

In a binary with a circular orbit the radial velocity (RV) of both stars will change sinusoidally with the orbital period as they orbit around their common center-of-mass. Due to the Doppler effect we can measure radial velocities by the shift of the spectral lines. In this work two different methods are used to derive the RVs. On the one hand we fit Gaussians and Lorentzians to the hydrogen and helium lines and on the other hand we use cross-correlation, if the wavelength coverage of the spectrum is large enough. To the RV measurements a sine function with the

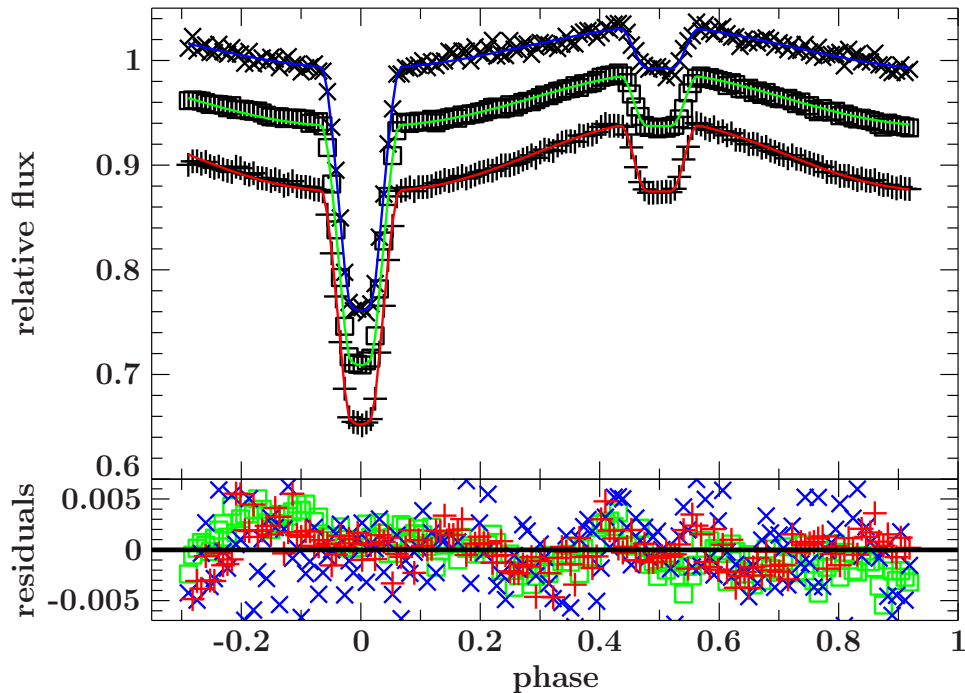


Figure 3.20: Fitted light curve of the sdB+BD system J0820 (taken from [6]).

orbital period derived by the light curve was fitted in order to measure the semi-amplitude of the radial velocity curve. An example can be seen in Fig. 3.19.

3.3.2 Light curve analysis

To model the light curve two different codes are used: LCURVE (Copperwheat et al. 2010) and MORO (Drechsel et al. 1995). Both codes are based on the widely used Roche model. The stars are subdivided into small elements and the flux of the system at a given orbital phase is then calculated by the sum of the flux of the visible elements. Both codes consider effects like irradiation, limb darkening and gravity darkening. MORO also considers the change of the shape of a star by radiation pressure, whereas LCURVE is designed only for detached binaries but also includes Doppler beaming, gravitational lensing, spots and accretion disks, as it was developed for cataclysmic variables. To derive the best-fitting parameters with uncertainties Markov Chain Monte Carlo (MCMC) computations are performed for LCURVE. More details about the light curve analysis are described in [6]. The result of an analysis using LCURVE is shown in Fig. 3.20 in an example fit. From the light curve the inclination as well as relative radii in units of the separation are derived. The analysis of those light curves is also discussed in more details in [2] and [6].

3.3.3 Absolute parameters

To derive the absolute parameters, we combine the results from the light curve analysis (P , i , R_1/a , R_2/a) to the results of the RV curve (K_1) fitting either under the assumption of a canonical mass for the primary or by deriving the mass with the SED analysis. In most cases the luminosity of the primary is much higher than the one of the companion, so that we have only single-lined binaries. Therefore, the mass of the companion is given by the mass

function:

$$f(m) = \frac{M_2^3 \sin^3 i}{(M_1 + M_2)^2} = \frac{PK_1^3}{2\pi G}. \quad (3.5)$$

The orbital separation a is then given by

$$a = \frac{P}{2\pi} \frac{K_1}{\sin(i)} (1/q + 1), \quad (3.6)$$

and we can derive the absolute radii with the help of the relative radii derived from the light curve (see also [2] and [6]-[11]).

3.3.4 Eclipse timing

Orbital period variations of eclipsing binaries can be derived by measuring the times of the primary eclipses. The time between two consecutive eclipses is given by the orbital period. If we do not have a consecutive light curve but observations spread over a longer time span, it is not so easy to measure the orbital period changes directly. A powerful tool is here the so-called $O - C$ diagram. A nice introduction is given in Lutz (2011). $O - C$ stands for "observed-minus-calculated". To calculate the eclipse times a constant period is assumed. This means that the time of the primary eclipse after E cycles is expected at:

$$C = T_0 + PE, \quad (3.7)$$

where T_0 is the time of the first primary eclipse and P is the orbital period. If the period is not constant, the eclipse time that we observe will deviate and can be approximated by a Taylor series:

$$O = T_0 + \frac{dT}{dE}E + \frac{1}{2} \frac{d^2T}{dE^2}E^2 + \dots, \quad (3.8)$$

thereby $\frac{dT}{dE}$ is given by the period. So we can calculate the deviation of the calculated from the observed eclipse time:

$$O - C = \frac{1}{2} P \dot{P} E^2. \quad (3.9)$$

This shows that a linearly changing period will result in a parabola in the O-C diagram. A circumbinary third body in the system introduces a periodic oscillation of the binary around the barycenter of the triple system. If the orbit is circular, this will result in a sinusoidal variation in the O-C diagram with the orbital period of the third body P'

$$O - C = \frac{M_2}{M_1 + M_2} \frac{a' \sin i'}{c} \sin \frac{2\pi}{P'} t. \quad (3.10)$$

As we can see, the semi-amplitude of this $O - C$ variation depends on the mass of the companion M_2 , the combined mass of the binary M_1 , the separation between the companion and the binaries barycenter a' and the orbital inclination i' . To derive the eclipse times different methods can be used. In [6] LCURVE is used to derive the eclipse times by fitting the light curve with a synthetic model.

4 Discussion and Summary

In this thesis I contribute to the discovery and observation of close binaries with focus on post-common envelope binaries. Binary systems, where both components are close enough and the masses are quite different, experience a phase of unstable mass transfer, called common envelope phase. This phase is very important for a multitude of different systems but poorly understood. As the timescales are very short (on the order of only a few years), it is very difficult to observe this phase directly. We have to rely on the observation and analysis of systems after this phase for a better understanding.

In Kruckow et al. (2021) a catalogue of 839 potential post-common envelope binaries was compiled. Thereby 185 systems were classified as sdO/B with either compact companions, such as white dwarfs, neutron stars or black holes, or low-mass main sequence or substellar companions. Most of these systems are investigated in [1]. Moreover, 123 are double white dwarfs and the majority of 316 systems are white dwarfs with main sequence companions from spectral type M to A or BDs. For another 170 systems with WD primaries the companion type is unknown. The sample of close white dwarf binaries is quite inhomogeneous, as it originates from a multitude of progenitor systems including post-RGB and post-AGB systems of different masses. More than half of the WDs with MS companions is also currently transferring mass and so already changed significantly after the common envelope phase. Therefore, it is not straightforward to derive the system parameters before and after the common envelope phase, which is essential to gain insights into the common envelope phase.

Subdwarf B stars on the other hand have had a very similar evolution, where a red giant with an initial mass around one solar mass was stripped at the tip of the red giant branch. One third of all sdB stars are found in post-common envelope systems. In [1] we investigate the sample of known hot subdwarfs in close binaries and are able to get the first unbiased period distribution of the sdB+dM/BD systems. Moreover, the nature of the companion for 75% of all the known systems could be derived by analysing the light curves provided by *TESS*. We are finding 1/3 of the sdBs with dM/BD companions and 2/3 with WD companions. This is a large progress compared to Kupfer et al. (2015), where the authors could constrain the companion type only in 80 systems. Especially, for longer period systems a much clearer picture emerges, showing that the period distribution of the sdB+dM/BD systems is much narrower than the one of the sdB+WD systems. Moreover, we could also show for the first time that there is a significant difference between the mass distribution of sdBs with dM/BD companions and with WD companions showing that they might come from different populations. The sdB+WD systems are expected to have had a previous Roche lobe overflow phase, so this result is not surprising. By phase-folding and inspecting the light curves of hot subdwarf candidates observed with *TESS* we also discovered 82 new reflection effect systems and 23 sdB+WD showing light variations.

The analysis of the light curves is presented in [2]. A new analysis method was developed, which allowed to derive absolute parameters for the sdB and the companions even for system showing no eclipses but only the reflection effect. This was possible due to the excellent quality of the *TESS* light curves. In this way we could derive the parameters for 20 irradiation effect systems and also analyzed 10 systems showing ellipsoidal modulation expanding the studied

parameter range to longer orbital periods and a wider companion mass range. This new method also increases the sample of systems for which absolute parameters can be derived significantly.

Of special interest are eclipsing post-common envelope binaries, as they allow a much more accurate determination of the absolute parameters. Only 20 eclipsing sdB binaries with cool low-mass companions (HW Vir systems) were known. Therefore, we started a project looking for more such systems. This project is called EREBOS (Eclipsing Reflection Effect Systems from Optical surveys). We are looking in all available photometric surveys to find more HW Vir candidates. An introduction to the project is given in [3]. In this way we could increase the number of known HW Vir systems to 200. For the future we plan to achieve a statistically significant sample by studying those newly discovered systems.

Additionally to investigating the population of sdBs in close binaries, we studied several interesting close binaries with hot subdwarf primaries and dM/BD or WD companions doubling the number of systems with derived parameters. The detailed analysis of individual close sdB binaries with dM/BD or WD companions are provided in [2] and [6]-[12]. We could increase the parameter range in orbital period and companion mass of studied post-common envelope systems with hot subdwarf primaries significantly. Such detailed analysis of single systems will be very important in the future for the understanding of larger samples of systems. A paper to constrain the common envelope phase using those parameters is in planning (Vos et al. in prep). This has been done previously by Ge et al. (2022) using the old sample by Kupfer et al. (2015) considering only minimum masses. For white dwarf binaries this was done in Zorotovic et al. (2010) and Zorotovic & Schreiber (2022).

For the prototype sdB+BD system (J0820, see [6]) we did a very detailed analysis with data we collected over more than 10 years. We were able to constrain the system much better using all different analysis methods discussed in the introduction. On the basis of this system we could also study synchronization in close binaries with radiative atmospheres showing that the observations do not agree with predictions by theory (Preece et al. 2018). Moreover, we detected a decay of the orbital period much larger than what is expected by gravitational waves. We suggested for the first time that this observed orbital period change might come from the change in angular momentum caused by the ongoing synchronization in this system. Other than that no larger scale period variations are observed in this system, as is the case in almost all other close sdB binaries, which were studied. Those orbital period changes were explained by a third circumbinary planetary companion. Bours et al. (2016) suggested that this might come from magnetic interactions with the M dwarf companion instead. The fact that only the studied sdB+dM show period variations on longer time scales, but not the sdB+BD system J0820 and the sdOB+BD system AA Dor, affirms this theory.

For the physical understanding of the common envelope phase hydrodynamical simulations have to be performed. This has been done using different codes (see Ivanova et al. 2020, for a summary). In [5] we used AREPO (Springel 2010), which was originally developed for cosmological simulations but was adopted by Ohlmann et al. (2016) for common envelope simulations. In a test case of a $1 M_{\odot}$ star we used this code to investigate the minimum mass of a companion to create enough turbulence to eject the envelope. The result that brown dwarfs with masses down to $0.05 M_{\odot}$ are able to eject the envelope fits very well to our discovery of several sdB+BD systems. The comparison to the observations, however, shows that the separation, which is predicted by the simulation is about one order of magnitude too large. The increasing sample of sdB+BD/dM systems with different periods and companion masses will be essential to improving the simulations.

Post-common envelope systems are also found with (hot) WD or CSPN primaries. Studying such objects is also interesting for the understanding of the common envelope phase as they cover a larger parameter space and so also the common envelope efficiency of more massive

objects can be studied to investigate the effect of the primary mass on the common envelope phase. We reinvestigated one such system in [14] showing that the previous determination of the masses was incorrect, which has a large impact on the previous and future evolution of the system. We checked that the system is not a progenitor system for a SNIa as previously suggested.

Also many hot WDs show interesting characteristics. About 10% of these objects show spectral lines of ultra-highly excited (UHE) metals. Additionally many of the UHE WDs also show photometric variations. The cause of those light variations is still an open question. In [13] we investigated several such systems showing that it is unlikely that the light variations are caused by binarity.

A previous Roche lobe overflow phase can also be responsible for the formation of hot subdwarfs. 23 systems with solved orbits are known (Vos et al. 2019) and more systems have been identified by their composite spectra or SEDs. With the help of the rotational variability *TESS* light curves we could show in [4] that almost all companions are spun-up most likely due to the previous accretion phase. This is observational evidence that the companions are indeed responsible for the mass loss in (almost) all cases and that (almost) all sdBs were formed due to binary interactions.

WDs can also be found in post-RLOF systems, where the companion is spun-up and therefore showing stronger activity. Such systems are important as they can be used to understand how binary interactions alter the intrinsic properties of the stars. We discovered and analyzed one more of those important systems in [15].

In the next years, we will have to deal with large amounts of data, coming from different photometric and spectroscopic surveys, such as the Legacy Survey of Space and Time (LSST) at the Vera Rubin observatory, *PLATO*, and *4MOST*. They will be discovering many new systems. For the understanding of those large samples, we need detailed analyses of individual systems, which are of special interest. This will be very helpful to develop methods, which can be used in to derive parameters of large samples of post-common envelope stars. For achieving this goal this thesis is an important step, as it is dealing with large amounts of data, selecting interesting targets, as well as studying individual systems in detail.

5 Appended papers

5.1 Hot subdwarfs in close binaries

- [1] **Hot subdwarfs in close binaries observed from space I: orbital, atmospheric, and absolute parameters and the nature of their companions: Schaffenroth, V. ; Pelisoli, I. ; Barlow, B. N. ; Geier, S. ; Kupfer, T. 2022, A&A 666A, 182**

I was leading the paper and contributed to the search of light variations and classification of these. Thereby I was supported by IP and BB. Moreover, I performed the analysis of the sample in order to classify the nature of the primary and secondary stars as well as deriving the mass and period distributions. SG and TK supported the paper with useful discussions and suggestions.

- [2] **Hot subdwarfs in close binaries observed from space II: analysis of the light curves: Schaffenroth, V. ; Barlow, B. N.; Pelisoli, I. ; Geier, S. ; Kupfer, T. 2023, A&A 673, A90**

I was leading the paper and performed the analysis of the investigated systems as well as their interpretation. BB was supporting the paper with the observation of additional data and the derivation of radial velocity curves. IP was contributing to the classification of the systems and with useful suggestions to the analysis. SG and TK supported the paper with useful discussions and suggestions.

- [3] **The EREBOS project: Investigating the effect of substellar and low-mass stellar companions on late stellar evolution. Survey, target selection, and atmospheric parameters: Schaffenroth, V.; Barlow, B. N.; Geier, S.; Vučković, M.; Kilkeny, D.; Wolz, M.; Kupfer, T.; Heber, U.; Drechsel, H.; Kimeswenger, S.; Marsh, T.; Wolf, M.; Pelisoli, I.; Freudenthal, J.; Dreizler, S.; Kreuzer, S.; Ziegerer, E. 2019, A&A, 630, A80**

I was leading the paper and performed the search for new systems as well as their analysis and the interpretation of the results. The rest of the authors contributed with observing data for the project. Moreover they added to the discussion of the results.

- [4] **Alone but not lonely: Observational evidence that binary interaction is always required to form hot subdwarf stars: Pelisoli, Ingrid; Vos, Joris; Geier, Stephan; Schaffenroth, Veronika; Baran, Andrzej S. 2020, A&A, 642, A180**

I added to the interpretation and discussion of the results, as SG and AB. IP and JV performed the target selection, analysis and interpretation of the results.

- [5] **Formation of sdB-stars via common envelope ejection by substellar companions:** Kramer, M.; Schneider, F. R. N.; Ohlmann, S. T.; Geier, S.; **Schaffenroth, V.**; Pakmor, R.; Röpke, F. K. 2020, *A&A*, 642, A97

The simulations were performed by MK, SO, RP and FP. I contributed to the discussion of the results and the comparison with observations together with SG.

5.2 Hot subdwarf binaries with M dwarf or brown dwarf companions

- [6] **A quantitative in-depth analysis of the prototype sdB+BD system SDSS J08205+0008 revisited in the Gaia era:** **Schaffenroth, V.**; Casewell, S. L.; Schneider, D.; Kilkenny, D.; Geier, S.; Heber, U.; Irrgang, A.; Przybilla, N.; Marsh, T. R.; Littlefair, S. P.; Dhillon, V. S. 2021, *MNRAS*, 501, 3847

I was leading the paper and performed the light curve analysis. Moreover, I also did the analysis of the eclipse timing as well as the investigation of the causes of the period decrease. SC supported the paper by obtaining additional data and searching for signs of a companion. DS performed the spectral analysis. SG derived the RV curve. UH, AI and NP contributed to the spectral analysis. TM, SL and VD provided some of the photometric data. DK derived the eclipse timings.

- [7] **Multi-filter Time Series Observations of Eleven Blue Short Period ATLAS Variable Stars:** Koen; C. **Schaffenroth, V.**; Kniazev, A. 2023, *AJ*, 165, 142

CK performed the target selection, obtained the photometric data and contributed to the analysis of the pulsating systems. I performed the light curve analysis of the reflection effect systems.

- [8] **Eclipsing Binaries Found by the EREBOS Project: Gaia DR2 6097540197980557440-a Deeply Eclipsing sdB+dM System:** Corcoran, Kyle A.; Barlow, Brad N.; **Schaffenroth, Veronika**; Heber, Uli; Walser, Stephen; Irrgang, Andreas, 2021, *ApJ*, 918, 28

CK, BB, and SW obtained the data and performed the analysis of the radial velocity curve. I performed the light curve analysis and the analysis of the spectral energy distribution, as well as the interpretation of the results. UH and IA performed the analysis of the spectra.

- [9] **EPIC 216747137: a new HW Vir eclipsing binary with a massive sdOB primary and a low-mass M-dwarf companion:** Silvotti, R.; **Schaffenroth, V.**; Heber, U.; Østensen, R. H.; Telting, J. H.; Vos, J.; Kilkenny, D.; Mancini, L.; Ciceri, S.; Irrgang, A.; Drechsel, H. 2021, *MNRAS*, 500, 2461

RS discovered the target and lead the analysis and discussion of the results. I performed the light curve analysis and contributed to the discussion of the results. UH performed the spectral analysis and the SED fit with support by IA. RO, JV, and JT obtained the spectral follow-up and derived the RV curve. DK obtained the photometric follow-up.

5.3 Hot subdwarf binaries with white dwarf companions

- [10] **Pulse Timing Discovery of a Three-Day Companion to the Hot Subdwarf BPM 36430:** B. A. Smith; B. N. Barlow; B. Rosenthal, J. J. Hermes; **V. Schaffenroth** 2022, *ApJ*, 939, 57

BS, BB, BR, JH obtained the data and performed the analysis of the light curve. I did the analysis of the spectral energy distribution and contributed to the discussion of the results.

- [11] **A hot subdwarf-white dwarf super-Chandrasekhar candidate supernova Ia progenitor:** Pelisoli, Ingrid; Neunteufel, P.; Geier, S.; Kupfer, T.; Heber, U. ; Irrgang, A.; Schneider, D.; Bastian, A. ; van Roestel, J. ; **Schaffenroth, V.** ; Barlow, B. N. 2021, *Nature Astronomy*, 5, 1052

IP carried out the radial velocity measurements and fitting and the light curve fitting, and led the writing of the manuscript. PN calculated the evolution of the system. SG and UH performed the spectral fitting. TK did the spectroscopic reduction and cross-checked the light curve fitting. DS and UH performed the SED fitting. AI wrote the SED fitting tool and calculated the spectral models used for SED and spectral fitting. AB calculated the Galactic orbit of the system. JvR. performed the spectroscopic observations and contributed to the light curve fit. BNB and me contributed to the analysis of the light curve. All authors reviewed the manuscript.

- [12] **New X-ray observations of the hot subdwarf binary HD 49798/RX J0648.0-4418:** Mereghetti, S.; Pintore, F.; Rauch, T.; La Palombara, N.; Esposito, P.; Geier, S.; Pelisoli, I.; Rigoselli, M.; **Schaffenroth, V.**; Tiengo, A., 2021, *MNRAS*, 504, 920

SM and FP obtained the data and performed the analysis. TR calculated the synthetic spectra used. GS, IP, and VS added to the discussion and inspired the project.

5.4 (Pre-) White dwarfs with close companions

- [13] **Mysterious, variable, and extremely hot: White dwarfs showing ultra-high excitation lines. I. Photometric variability:** Reindl, Nicole; **Schaffenroth, Veronika**; Filiz, Semih; Geier, Stephan; Pelisoli, Ingrid; Kepler, Souza Oliveira 2020, *A&A*, 2021, 647, A184

NR lead the paper, performed the target selection and the period analysis of the light curves. I performed the light curve analysis and added to the discussion. The rest of the authors contributed by providing data for the paper.

- [14] **An in-depth reanalysis of the alleged type Ia supernova progenitor Henize 2-428:** Reindl, N.; **Schaffenroth, V.**; Miller Bertolami, M. M.; Geier, S.; Finch, N. L.; Barstow, M. A.; Casewell, S. L.; Taubenberger, S. 2020, *A&A*, 638, A93

NR lead the paper, performed the spectral analysis and derived the RV curve. I performed the light curve analysis. MMB developed the evolutionary scenario. SG, NF, MB, SC contributed to the observation and analysis of the spectra.

- [15] **An extremely hot white dwarf with a rapidly rotating K-type subgiant companion: UCAC2 46706450:** Werner, Klaus; Reindl, Nicole; Löbbling, Lisa; Pelisoli, Ingrid; **Schaffenroth, Veronika**; Rebassa-Mansergas, Alberto; Irawati, Puji; Ren, Juanjuan 2020, **A&A**, 642, A228


KW and NR performed the analysis of the system. LL, IP and I contributed to the observation of the light curve and the discussion. ARM , PI, and JR obtained spectroscopy.

- [16] **Quantitative spectral analysis of the sdB star HD 188112: A helium-core white dwarf progenitor** Latour, M.; Heber, U.; Irrgang, A.; **Schaffenroth, V.**; Geier, S.; Hillebrandt, W.; Röpke, F. K.; Taubenberger, S.; Kromer, M.; Fink, M. 2016, **A&A**, 585, A115

ML, UH and IA performed the spectral analysis. I provided the line lists for the calculation of the synthetic spectra.

Hot subdwarfs in close binaries observed from space

I. Orbital, atmospheric, and absolute parameters, and the nature of their companions

V. Schaffenroth¹, I. Pelisoli^{2,1}, B. N. Barlow³, S. Geier¹, and T. Kupfer⁴

¹ Institute for Physics and Astronomy, University of Potsdam, Karl-Liebknecht-Str. 24/25, 14476 Potsdam, Germany
e-mail: schaffenroth@astro.physik.uni-potsdam.de

² Department of Physics, University of Warwick, Gibet Hill Road, Coventry CV4 7AL, UK

³ Department of Physics and Astronomy, High Point University, High Point, NC 27268, USA

⁴ Department of Physics and Astronomy, Texas Tech University, PO Box 41051, Lubbock, TX 79409, USA

Received 8 June 2022 / Accepted 3 July 2022

ABSTRACT

Context. About a third of the hot subdwarfs of spectral type B (sdBs), which are mostly core-helium-burning objects on the extreme horizontal branch, are found in close binaries with cool, low-mass stellar, substellar, or white dwarf companions. They can show light variations due to different phenomena.

Aims. Many hot subdwarfs now have space-based light curves with a high signal-to-noise ratio available. We used light curves from the Transiting Exoplanet Survey Satellite and the K2 space mission to look for more sdB binaries. Their light curves can be used to study the hot subdwarf primaries and their companions, and obtained orbital, atmospheric, and absolute parameters for those systems, when combined with other analysis methods.

Methods. By classifying the light variations and combining these with the fit of the spectral energy distribution, the distance derived by the parallaxes obtained by *Gaia*, and the atmospheric parameters, mainly from the literature, we could derive the nature of the primaries and secondaries in 122 (75%) of the known sdB binaries and 82 newly found reflection effect systems. We derived absolute masses, radii, and luminosities for a total of 39 hot subdwarfs with cool, low-mass companions, as well 29 known and newly found sdBs with white dwarf companions.

Results. The mass distribution of hot subdwarfs with cool, low-mass stellar and substellar companions, differs from those with white dwarf companions, implying they come from different populations. By comparing the period and minimum companion mass distributions, we find that the reflection effect systems all have M dwarf or brown dwarf companions, and that there seem to be several different populations of hot subdwarfs with white dwarf binaries – one with white dwarf minimum masses around $0.4 M_{\odot}$, one with longer periods and minimum companion masses up to $0.6 M_{\odot}$, and at the shortest period, another with white dwarf minimum masses around $0.8 M_{\odot}$. We also derive the first orbital period distribution for hot subdwarfs with cool, low-mass stellar or substellar systems selected from light variations instead of radial velocity variations. It shows a narrower period distribution, from 1.5 h to 35 h, compared to the distribution of hot subdwarfs with white dwarfs, which ranges from 1 h to 30 days. These period distributions can be used to constrain the previous common-envelope phase.

Key words. binaries: close – subdwarfs – white dwarfs – stars: late-type – stars: horizontal-branch – stars: fundamental parameters

1. Introduction

Hot subdwarfs of spectral type O and B (sdO/Bs) are a mixture of different kinds of evolved stars located at or close to the bluest end of the horizontal branch, referred to as the extreme horizontal branch (EHB). Subdwarf O stars consist of many different objects, including post-red giant branch and post-asymptotic giant branch stars. Most sdBs, on the other hand, which are mostly found on the EHB, are core-helium-burning objects with very thin envelopes and masses close to the core-helium-flash mass of $0.47 M_{\odot}$ – for sdBs coming from low-mass star progenitors. A higher mass range of 0.35 – $0.65 M_{\odot}$ is possible for sdBs originating from more massive stars. A small fraction of sdBs are composed of extremely low-mass pre-white dwarfs (pre-ELM WDs), which can cross the EHB on their way to the WD cooling track (Heber 2009, 2016). Significant mass loss on the red giant branch (RGB) is necessary to form sdO/Bs, and Han et al. (2002, 2003) proposed different binary evolution channels to form such

objects. Stable mass transfer leads to a composite sdB system with a K to F type companion and orbital periods of a few hundred days (Vos et al. 2018). They are double-lined binaries in the visible range, showing spectral features from both the sdB and the cool companion. In the case of a larger mass ratio – above 1.2–1.5 – the mass-transfer is unstable and results in a common-envelope phase. The outcome of this poorly understood phase (Ivanova et al. 2013) is an sdB with a cool, low-mass companion, with a period of 0.05 days to around one day (Schaffenroth et al. 2019). Finally, after a stable mass transfer phase has passed, unstable mass transfer can commence once the sdB's companion evolves into a red giant, leading to a short-period binary with a WD companion. Core-helium-burning sdBs will evolve to sdOBs or sdOs after He-exhaustion in the core, before contracting onto the WD cooling track.

Most sdB binaries exhibit different kinds of variability in their light curves. Pelisoli et al. (2020) found that many of the composite sdB binaries show small amplitude variations in their

light curves, with periods of 0.5 days to a few days, due to spots on the companions. Subdwarf B stars with WD companions can show ellipsoidal deformation and even Doppler beaming in their light curves when the orbit is close enough and the WD massive enough (Kupfer et al. 2022, 2020a,b, 2017a). Systems with cool, low-mass companions show unique light curve variations that result from the extreme temperature difference and small separation distance between the two stars (as small as $0.5\text{--}1 R_{\odot}$). The UV-bright hot subdwarf irradiates the side of the cool companion facing it, and this leads to hot and cold sides of the companion since they are tidally locked. The irradiated face rotating in and out of view produces a quasi-sinusoidal flux variation called the reflection effect that exhibits broad minima and sharper maxima. In systems with inclination angles $\geq 60\text{--}65^{\circ}$, eclipses can be observed given the right combination of stellar sizes and orbital separation. Such eclipsing sdB binaries are called HW Vir systems (e.g., Menzies et al. 1986; Schafferoth et al. 2019, 2021). Finally, some hot subdwarfs show variability due to short-period pulsations on the order of minutes (for sdO/Bs with $T_{\text{eff}} > 30\,000\text{ K}$) and long-period (for sdO/Bs with $T_{\text{eff}} < 30\,000\text{ K}$), low-amplitude pulsations on the order of hours (see Lynas-Gray 2021; Kupfer et al. 2019, for a summary). Some targets in binaries can even show variability due to both pulsations and binary effects (e.g., Vučković et al. 2007).

Geier et al. (2019) published a catalog of 39 800 hot subluminescent star candidates with $G < 19\text{ mag}$ based on *Gaia* DR2 (Gaia Collaboration 2018) colors, parallaxes, and proper motions, and several ground-based, multiband photometry surveys. They expect the majority of the candidates to be hot sdO or sdBs, followed by blue horizontal branch stars, hot post-AGB stars, and central stars of planetary nebulae (PN). The main purpose of their catalog is to serve as a target list for current and future large-scale photometric and spectroscopic surveys.

One of those surveys is the Transiting Exoplanet Survey Satellite (TESS) mission (Ricker et al. 2015), which is observing over 90% of the northern and southern sky in different sectors. Each sector has a field of view of $24^{\circ} \times 90^{\circ}$ and is observed for 27 consecutive days, with a short break halfway through for data downlinking. The full frame images are downloaded every 30 min (and since sector 28, every 10 min), providing light curves of all stars in the field of view of 30 min (10 min) cadence. A number of preselected stars are downloaded every 2 min (since sector 28, some also with 20 s cadence). As members of the TESS Asteroseismic Consortium (TASC) Working Group (WG) 8 on compact pulsators, with the subgroup WG8.4 on binaries, we were able to provide input target lists, including bright hot subdwarfs from the hot subluminescent star candidate catalog (Geier et al. 2019), as well as with Guest Investigator programs G022141, G03221, and G04091 (PI: Brad Barlow). The majority of these targets were submitted because they were either known variable hot subdwarfs or strong candidates for variability based on their anomalous *Gaia* flux errors and other metrics (Barlow et al. 2022). This provides us with a few thousand space-quality light curves of hot subdwarf stars, including the few tens of light curves already obtained from K2 (Howell et al. 2014) from different successful proposals. Consequently, we possess for the first time an expansive, high signal-to-noise ratio (S/N) data set of hot subdwarf light curves. Sahoo et al. (2020) and Baran et al. (2021a) used the 30 min cadence TESS light curves of observed targets from the hot subluminescent star candidate catalog (Geier et al. 2019) to search for light variations of hot subdwarf candidates and found several sdB+dM/BD candidates.

In this paper we present our search for hot subdwarfs with cool, low-mass companions, showing the reflection effect and hot subdwarfs with white dwarf companions exhibiting ellipsoidal deformation and/or beaming, as well as a characterization of these systems. In Sect. 2 we give more details about our target selection and our search for light variations. In Sect. 3 we present our characterization of the primary star using the parallaxes and proper motions provided by *Gaia*, as well as the fit of the spectral energy distribution allowing us to get a mass distribution for the sdB in close binaries. In Sect. 4 we show the distribution of the orbital parameters (period, semiamplitude of the radial velocity, RV, curve) of our targets and compare the different populations. In Sect. 5 we conclude and provide a short summary of our results.

2. Target selection and search for light variations

To look for reflection effect systems in the TESS light curves, we searched TESS sectors 1–36 for variability in all stars brighter than $G < 16\text{ mag}$ from the *Gaia* DR2 catalog of hot subluminescent stars (Geier et al. 2019), as well as the catalog of spectroscopically confirmed hot subdwarf stars (in total 2883 targets with 2 min cadence light curves and 353 targets with 20 s cadence light curves) (Geier 2020). We used the light curves made available by the TESS Science Processing Operations Center (SPOC) through the Barbara A. Mikulski Archive for Space Telescopes MAST¹, using the PDCSAP flux, which corrects the simple aperture photometry (SAP) by removing instrumental trends, as well as contributions to the aperture expected to come from neighboring stars other than the target of interest, given a pre-search data conditioning (PDC). This is essential for TESS, as the pixel size is almost 21 arcsec. Through the CROWDSAP parameter, the pipeline also provides an estimate of how much of the flux in the aperture belongs to the target. To avoid possible zero-point inconsistencies between different sectors, we divided the flux by the mean flux in each sector for each star.

We used the Python package Astropy (Astropy Collaboration 2013, 2018) to calculate the Lomb-Scargle periodogram (Lomb 1976; Scargle 1982) of all light curves up to the Nyquist frequency, oversampling by a factor of ten. Light curves were then phase-folded to the period corresponding to the strongest peak, or twice this period for ellipsoidal systems, which have first harmonic peaks stronger than the fundamental orbital frequency. Our custom script that downloads the light curves and generates diagnostic plots with the periodogram and phase-folded light curves is publicly available². We visually inspected the diagnostic plots for all targets to confirm any variability and selected all objects showing a reflection effect (with and without eclipses), as well as stars showing ellipsoidal deformation. All targets with confirmed light variations can be found in Table A.4.

Additionally, we inspected the TESS or K2 light curves of all hot subdwarfs with orbits characterized by RV measurements (Kupfer et al. 2015, and references in Table A.4). All light curves were downloaded, phase-folded to the orbital period, and binned using the Python package LIGHTKURVE (Lightkurve Collaboration 2018)³. We computed the periodogram around the orbital period to search for any small peaks resulting from weak reflection or ellipsoidal deformation signals. For targets without any variations, we phase-folded the light curve to the orbital period derived by time-resolved spectroscopy

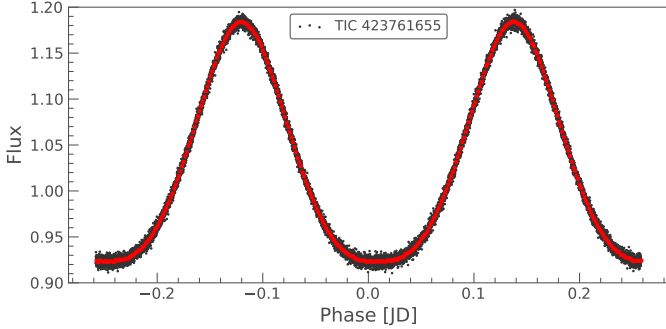
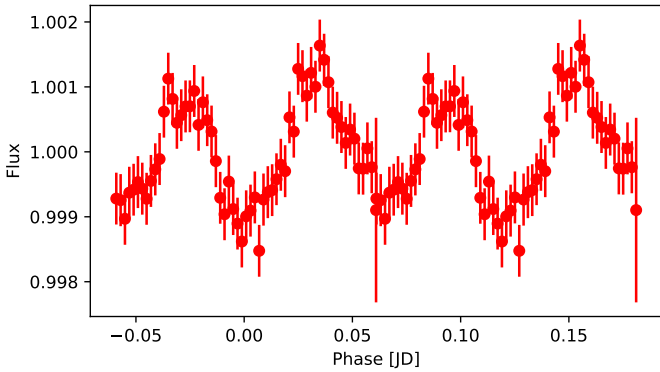
¹ <https://mast.stsci.edu/>

² <https://github.com/ipelisolli/TESS-LS>

³ <https://docs.lightkurve.org>

Table 1. Result of our light curve search.

Type	Number (analyzed)
New reflection effect systems	82 (0)
Reflection effect systems with solved orbits	20 (17)
HW Vir systems	35 (0)
HW Vir system with solved orbits	17 (17)
Ellipsoidal deformation	19 (11)
Doppler beaming	16 (1)


Fig. 1. Example TESS light curve of a reflection effect system (EC01578–1743). The light curve is shown phase-folded to the orbital period (black points) and is also binned (red points).

Fig. 2. Example TESS light curve of an ellipsoidal system (PG 1043+760) additionally showing Doppler beaming. The light curve is shown phase-folded to the orbital period and is binned.

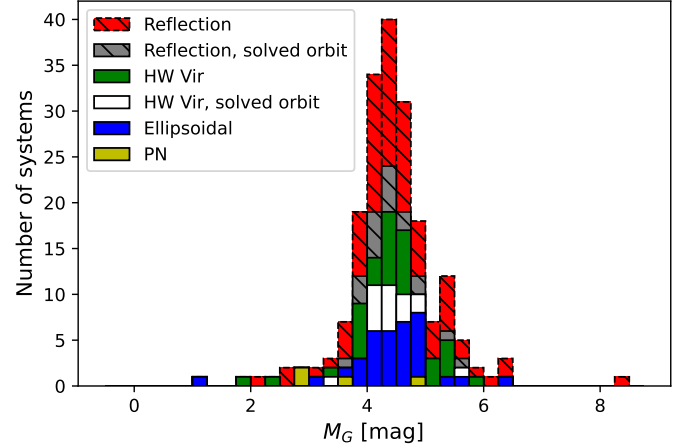
and determined the signal-to-noise ratio. The results of our search are shown in Tables 1, A.3, and A.4. Example TESS light curves of a reflection effect system, as well as an ellipsoidal system showing also Doppler beaming, can be found in Figs. 1 and 2. The complete set of light curves, along with full details regarding our modeling and analysis methods, will be presented in an additional paper (Paper II, Schaffenroth et al., in prep.).

3. Characterizing the primary star

3.1. Absolute magnitude and reduced proper motion

3.1.1. Method

Both hot subdwarf and hot WD binaries containing cool, low-mass companions can show a reflection effect (Schaffenroth et al. 2019), as can some sDOs that are central stars of planetary nebulae (CSPN). In order to determine the true nature of the primary star, we used the colors, parallaxes,


Fig. 3. *Gaia* absolute magnitude M_G of all our targets, divided into different groups according to the different light curve variations they show, as shown in the legend.

and proper motion from *Gaia* EDR3 (Gaia Collaboration 2021), as was done in Schaffenroth et al. (2019) for newly discovered HW Vir systems. Using the *Gaia* G magnitude together with the parallax, we could determine the absolute magnitude of our targets using the distance modulus ($G - M_G = 5 \log_{10} d - 5$). We ensured that all of our targets except one (which we identified as a potential triple system) had a small uncertainty in their parallax ($\lesssim 10\%$) and a renormalized unit weight error (RUWE) below 1.4 (e.g., Penoyre et al. 2022). A higher RUWE indicates potential problems with the parallax.

Another way to confirm our target selection is to determine the reduced proper motions $H_G = G + 5(\log \mu + 1)$. Stars that are farther away should show less transverse velocity on average than those that are closer, and the reduced proper motion is, therefore, a proxy for the distance; closer objects should have larger reduced proper motions. Typically, hot subdwarfs show reduced proper motions between 5 and 14 mag (e.g., Schaffenroth et al. 2019).

3.1.2. Results

The results are found in Table A.4. Inspecting the absolute magnitude M_G distribution of all our targets (Fig. 3), we see that it peaks around $M_G = 4.5$, as expected for hot subdwarf stars (Geier 2020). We only have one target with $M_G > 7$ mag, which is most likely a WD primary. We also have some targets with $M_G < 3$ mag, which are known CSPNs, or pre-ELM WDs. Our reduced proper motion distribution shown in Fig. 4 also confirms that our targets are most likely hot subdwarf stars.

Since hot subdwarfs are of spectral type O and B, they have temperatures between 25 000 and 50 000 K and blue colors. Their luminosities are lower than the luminosities of main sequence stars and higher than the luminosities of hot white dwarfs. To check where we find our targets in the color-magnitude diagram, we plot a $G_{BP} - G_{RP}$ versus M_G diagram (see Fig. 5). Both the absolute magnitude and $G_{BP} - G_{RP}$ color were corrected for interstellar extinction using 3D maps (Lallement et al. 2014; Capitanio et al. 2017). Our targets are located at $-0.5 < G_{BP} - G_{RP} < 0.3$, with most of the targets clustering at $G_{BP} - G_{RP} < -0.25$. There is a slight trend that targets with $G_{BP} - G_{RP} > -0.25$ seem to have smaller M_G . As all of those targets show a high extinction, this trend can most likely be

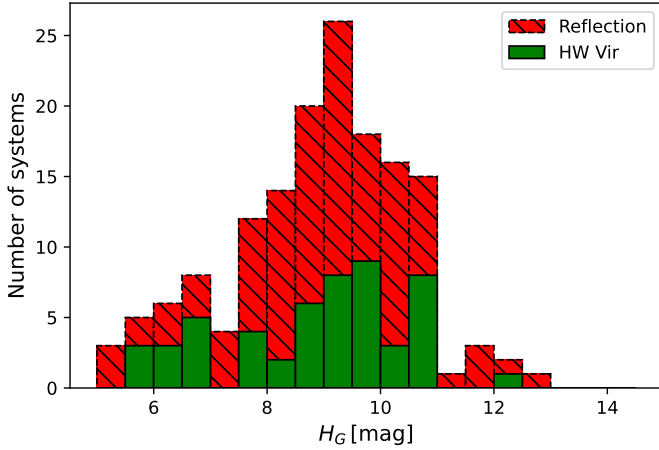


Fig. 4. Reduced proper motion of all our reflection effect systems (eclipsing and non-eclipsing).

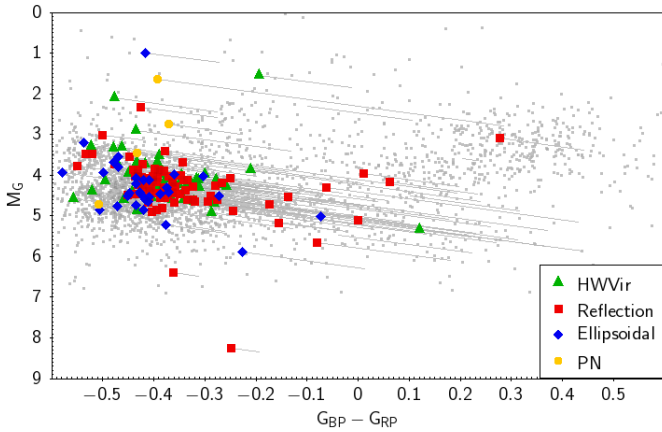


Fig. 5. $G_{BP}-G_{RP}$ vs. M_G diagram. The targets are again grouped according to their light variations. All targets have been corrected for interstellar extinction using Stilism⁴. The correction is shown with the gray lines. In comparison, the known sdO/Bs taken from Geier (2020) are shown with the gray data points.

explained by insufficient correction of the interstellar extinction. The distribution of our targets on the sky (Fig. 6) shows that most of the targets with high extinction are found close to the galactic plane, up to $\pm 20^\circ$ away. The comparison with the known sdO/Bs from Geier (2020) shows quite a good agreement. One target is found with $G_{BP}-G_{RP} = 0.3$ at an absolute magnitude $M_G = 3$, consistent with known composite sdB stars. Only a few of our targets are found at $G_{BP}-G_{RP} < -0.45$, which is probably due to the fact that most of them are cooler core-helium-burning sdB stars rather than evolved sdO stars. The comparison of the position of all our targets grouped together by the observed light variations (Fig. 7) shows that all different target types seem to be equally distributed on the sky.

3.2. Spectral energy distribution

3.2.1. Method

To confirm a candidate's status as a hot subdwarf, we need to derive the effective temperature T_{eff} and surface gravity $\log g$. The best way to determine atmospheric parameters is to observe

⁴ <https://stilism.obspm.fr/>

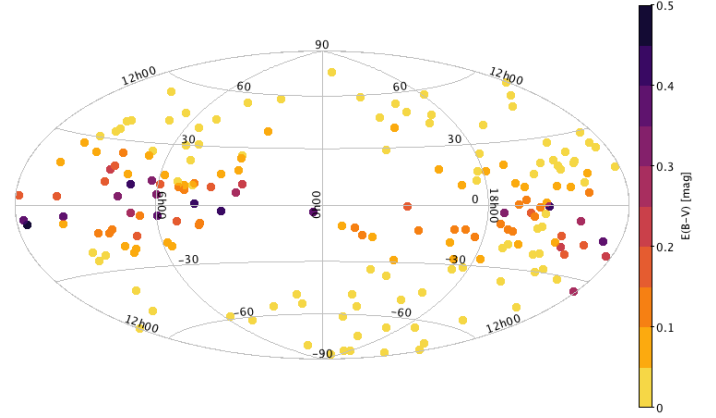


Fig. 6. Position of our targets on the sky (in galactic coordinates). The color coding is given by the color excess $E(B - V)$.

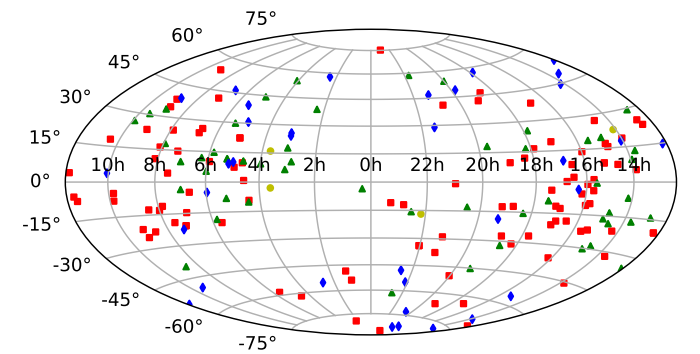


Fig. 7. Comparison of the position of our targets on the sky (in galactic coordinates). The green triangles mark HW Virs, the red squares mark the reflection effect systems, the blue diamonds mark the ellipsoidal systems, and the yellow circles mark the CSPNs.

and model the target's spectrum. However, it is also possible to determine T_{eff} , as well as the radius and the luminosity, by fitting the spectral energy distribution (SED) with synthetic spectra and combining this with the distance from the *Gaia* parallax (see Heber et al. 2018; Irrgang et al. 2021, for more details on this method). The shape of the SED gives us T_{eff} , as well as the interstellar reddening. Also, by comparing the observed and synthetic flux, $f(\lambda)$ and $F(\lambda)$, respectively, we can derive the angular diameter $\theta = 0.5 \sqrt{\frac{f(\lambda)}{F(\lambda)}}$, which can be used to derive the radius $R = \theta/(2\varpi)$ and the luminosity $L/L_\odot = (R/R_\odot)^2 (T_{\text{eff}}/T_{\text{eff},\odot})^4$ by using the *Gaia* parallax ϖ and parallax offset. Using the $\log g$ determined by the spectral fitting, and the radius determined by the SED and *Gaia* distance, we can also derive the mass of the hot subdwarf $M = gR^2/G$ for the hot subdwarf binaries with known atmospheric parameters.

3.2.2. Results

One example SED fit is shown in Fig. 8. Unfortunately, the SED fitting is not straightforward for the reflection effect systems since our targets show light variations, and the photometry we used from the literature was taken at a random phase.

In light of the above, we tested our method on reflection effect and ellipsoidal systems with known atmospheric parameters and sufficient photometric data (see Table A.1 for the results). The comparison between effective temperatures determined by a spectral fitting and a spectral energy distribution

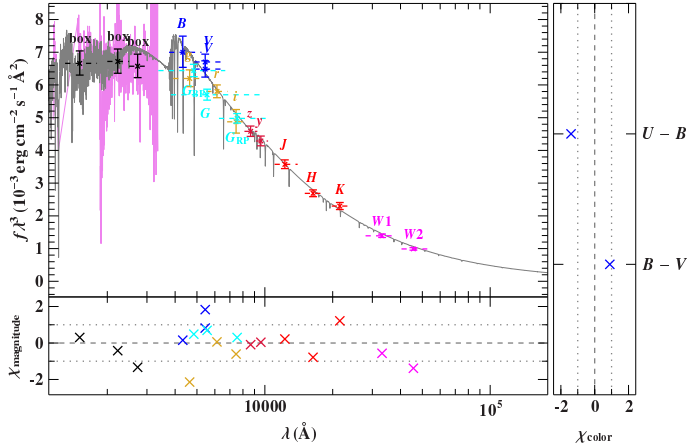


Fig. 8. Example of an SED fit (for the sdB+WD system PG 1519+640).

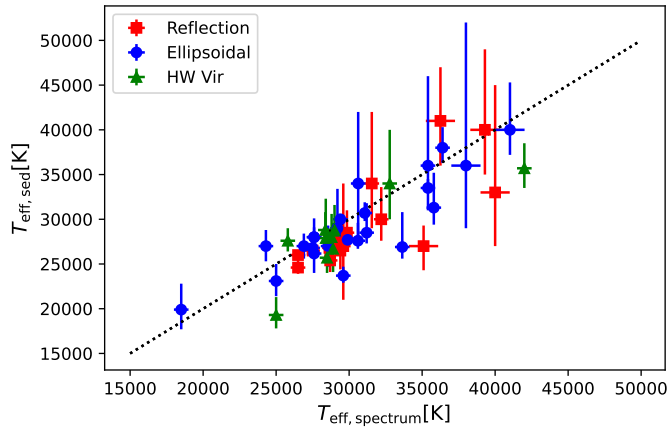


Fig. 9. Comparison of the effective temperature determined by spectral fitting and spectral energy distribution fitting. Blue circles mark systems showing ellipsoidal deformation, green triangles mark HW Vir systems and red squares mark reflection effect systems.

fitting (Fig. 9) shows that for systems with $T_{\text{eff}} \lesssim 32\,000$ K, the fitting of the SED can determine the T_{eff} very well if we neglect infrared photometry, since the contribution of the companion gets larger there. Ultraviolet (UV; International Ultraviolet Explorer, IUE, or Galaxy Evolution Explorer, GALEX, far-UV, FUV, or near-UV, NUV, and Sloan Digital Sky Survey, SDSS, u' photometry are essential for disentangling the effect of T_{eff} and interstellar reddening on the SED by covering the Balmer jump, so we exclude all targets without sufficient UV photometry from the SED fitting. For hotter systems, we see a larger scatter. For $T_{\text{eff}} > 42\,000$ K the Balmer jump is not visible anymore, and so the temperature can no longer be derived without constraining the interstellar reddening. There is also a slight tendency that the SED fitting derives smaller temperatures than the spectral fitting.

Using the derived luminosities, we construct a Hertzsprung-Russell diagram (HRD) for reflection effect and ellipsoidal systems with spectroscopic parameters for the first time. This is shown in Fig. 10. The sdBs on the EHB with temperatures below $33\,000$ K are found at similar luminosities between 15 and $40 L_{\odot}$. At larger temperatures, the luminosity increases with the temperature, but also a larger scatter is visible resulting from larger differences in the radii. Németh et al. (2012) showed that the He abundances and the difference in He abundance increases with the temperature. The larger scatter of the radii, and hence

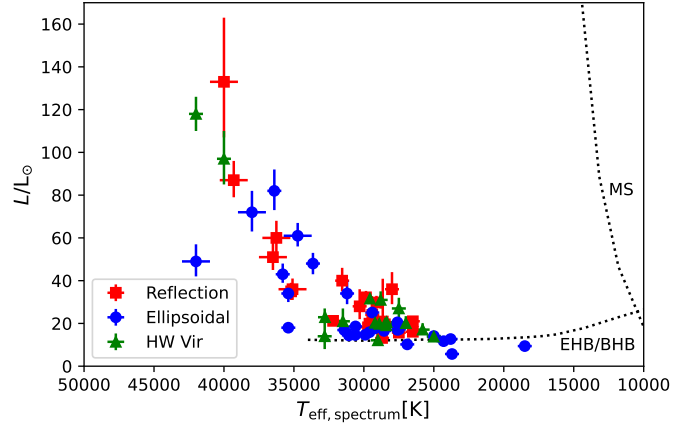


Fig. 10. Hertzsprung-Russell diagram of our targets with known atmospheric parameters. Blue circles mark systems showing ellipsoidal deformation, green triangles mark HW Vir systems, and red squares mark reflection effect systems. The dotted lines mark the zero-age main sequence or EHB/BHB.

the luminosity at larger temperatures, may be related to those He abundance differences.

With the spectroscopic $\log g$ and the radius from the SED fitting, we were able to derive the mass distribution of reflection effect, HW Vir and ellipsoidal systems. A similar approach was used in Krzesinski & Balona (2022), which derived the mass distribution of pulsating hot subdwarf candidates with spectroscopic parameters to be a broad peak, with the maximum at $0.45 M_{\odot}$. However, they state that their analysis might not be reliable or useful for deriving masses of single systems.

Our results are shown in Figs. 11–13, and Table A.1. For the HW Vir systems, we derived a mass of $0.46^{+0.08}_{-0.12} M_{\odot}$ using a skewed normal distribution. As the typical mass error is about $0.05 M_{\odot}$, this suggests an intrinsically broader peak. The non-eclipsing reflection effect systems seem to have a broader peak, with more higher-mass sdBs. As the only difference compared to the HW Vir systems is that they have no eclipses, we would not expect any difference. Determining atmospheric parameters from reflection effect systems has to be done with caution, as the contribution of the companion to the total flux changes with the orbital phase causing the reflection effect. So the atmospheric parameters have to be determined at or close to phase zero, when only the cool side of the companion is visible, or at the secondary eclipse, when the companion is occulted by the sdB in an eclipsing system. Most of the atmospheric parameters of the reflection effect systems have been determined from a single spectrum or co-added spectra at different orbital phases, causing systematic shifts to higher temperatures and a higher $\log g$. This influences the determination of the radius and results in a shifted mass. The HW Vir systems have been studied much more carefully, and so their determined atmospheric parameters are much more reliable.

The masses of the sdBs with white dwarf companions show a distribution with a similar width but a peak shifted to lower masses at $0.38^{+0.12}_{-0.08} M_{\odot}$. The distribution also seems to be slightly asymmetric, extending to higher masses. The cumulative distribution shows the shift in mass more clearly, and shows that it is indeed significant.

The samples were taken from the literature and are not complete, but are suffering from selection effects, which are not easy to determine. However, in the *Gaia* color-magnitude diagram (Fig. 5) and the sky distribution (Fig. 7), we can see that

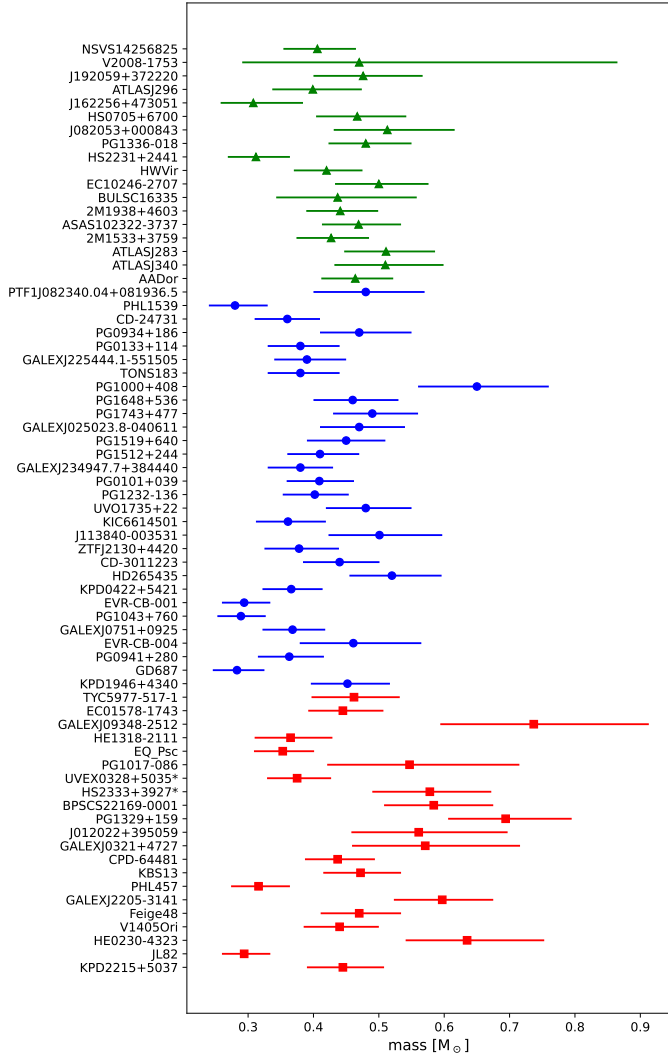


Fig. 11. Masses determined by combining the spectroscopic analysis with the fit of the SED and the *Gaia* parallaxes. Blue symbols mark systems showing ellipsoidal deformation, green symbols mark HW Vir systems, and red symbols mark reflection effect systems.

sdB+WD and the sdB+dM populations are overlapping well. The sdBs in the systems of both populations have been identified the same way by color selection. Hence, we expect that the selection effects should be similar for both populations and that they are comparable nevertheless.

The sdB+WD systems have been found preferably by RV variations in contrast to the HW Vir systems, as the sdB+WD systems show much smaller light variations. Both samples included only systems at the short period end of their period distribution (see Table A.4). A larger sample over a larger period range for both populations will be necessary to confirm our findings, and also to find or exclude differences in the sdB mass in systems with different orbital periods.

By fitting the SED and combining this with the *Gaia* parallax, we can also constrain the atmospheric parameters of our reflection effect candidates, which do not have spectroscopic parameters, by fitting the SED and assuming a canonical mass for the sdB. From the radius that we derive, we can constrain the $\log g$ in this way and constrain the atmospheric parameters for 44 targets with sufficient UV photometry. The results can be found in Table A.2. The atmospheric parameters are compared

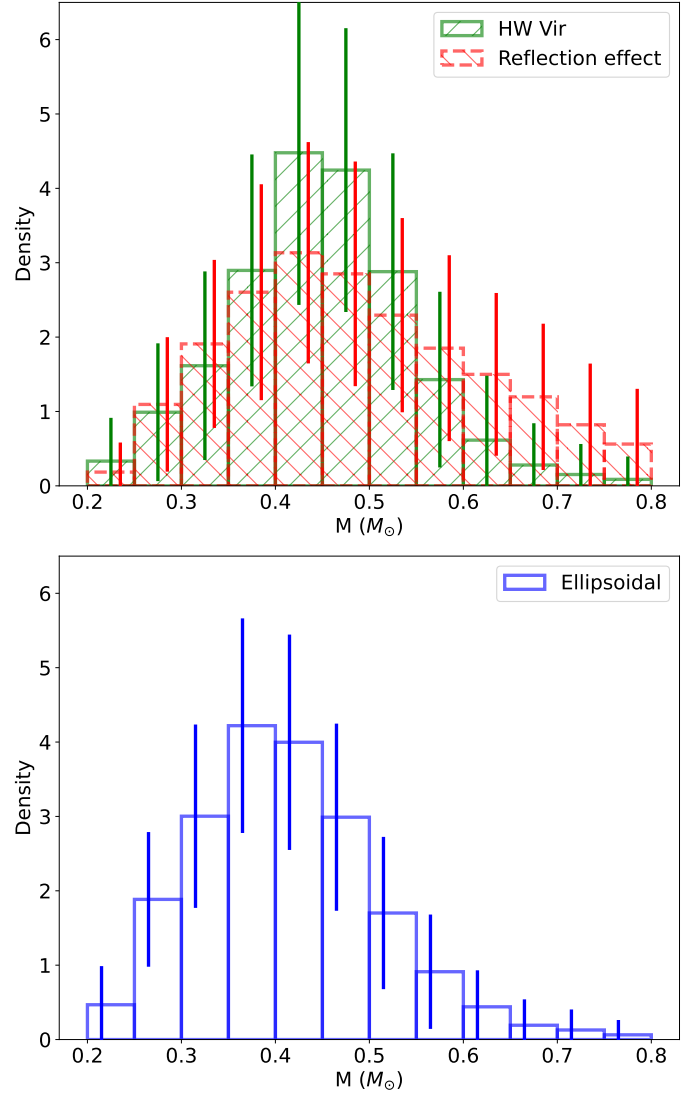


Fig. 12. Histogram of the masses determined by combining the spectroscopic analysis with the fit of the SED and the *Gaia* parallaxes.

to the solved systems in the $T_{\text{eff}}-\log g$ diagram (Fig. 14). This shows that our reflection effect candidate systems are mostly found on the EHB. Some of the candidates are on post-EHB tracks, which means the He in the core was exhausted and they are evolving away from the EHB. Only one candidate was found above the EHB, which could be a lower-mass pre-He WD.

4. The period distribution from light variations found by TESS

4.1. The selection effects of TESS

In order to judge the completeness of our reflection effect sample, we simulated the expected amplitude of the reflection effect for a typical sdB+dM system with different orbital periods and compared this to the noise level of the TESS satellite for stars of different brightness (see Fig. 15). This was done by checking the noise level in the light curves of different sdB stars of the same brightness that did not show any variations in the light curve. For a 15 mag system, the detection limit is about 0.3%. As expected, the amplitude of the variations decreases with lower inclination. But even with a low inclination of only 10° , we would expect

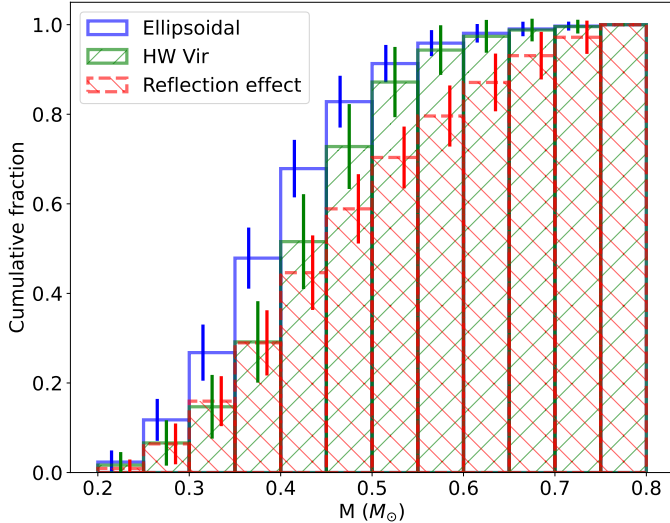


Fig. 13. Cumulative distribution of the masses determined by combining the spectroscopic analysis with the fit of the SED and the *Gaia* parallaxes.

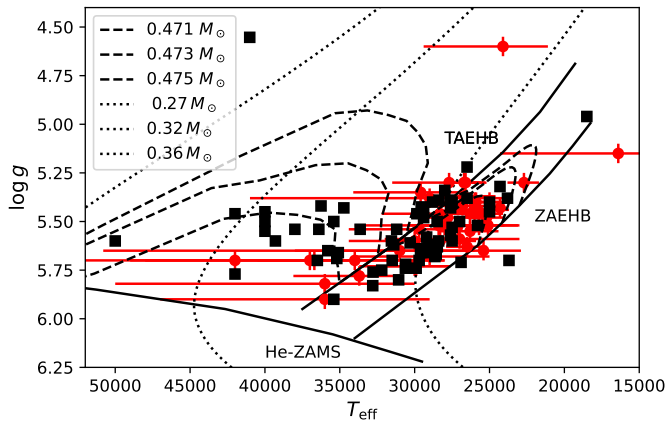


Fig. 14. T_{eff} – $\log g$ diagram of the sdB binaries with spectroscopic parameters (black squares) compared to the reflection effect candidates (red diamonds). The solid black lines mark the zero-age extreme horizontal branch (ZAEHB), the terminal-age extreme horizontal branch (TAEHB), and the He main sequence (He ZAMS). The dashed lines are evolutionary tracks by Dorman et al. (1993) for sdB masses of 0.471, 0.473, and 0.475 M_{\odot} . The dotted lines are tracks for extremely low-mass white dwarfs of a mass of 0.27, 0.32, and 0.36 M_{\odot} by Althaus et al. (2013).

to detect the reflection effect for a system brighter than 15 mag with TESS up to two days, for higher inclinations of about 40° and up to about 6 days, and in inclinations of more than 60° up to 8 days. Since the reflection effect becomes more sinusoidal at low inclinations, it is quite hard to distinguish it from other variations like pulsations or spots. Consequently, we will probably find low-inclination reflection effects only for the systems in which the period is already known from the RV curve. But the inclination should correlate with the period, and so this should not influence the period distribution we derive.

Another selection effect could come from TESS having such large pixels (21 arcsec per pixel). If another star of comparable or higher brightness is close to the star, the light curve can become contaminated. TESS tries to correct for this additional flux through its reported PDCSAP flux, and it uses the CROWD-SAP keyword in the header to quantify the contamination level.

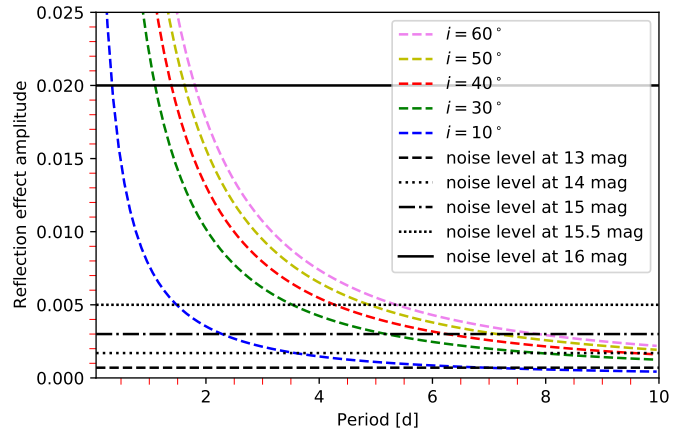


Fig. 15. Amplitude of the reflection effect of a typical sdB+dM system for different periods and inclinations. The black lines mark the TESS noise level for stars of different brightness.

This correction can overestimate or underestimate the flux, and so the amplitude is not entirely reliable when a bright star is so close and it contributes significantly to the flux in the target pixel. This means that we might miss some reflection effect systems when unrelated stars are too close, but overall this correction seems to be quite good (a few percent difference; see Paper II for more details) and there is no reason why this should influence the period distribution of the detected systems.

As the amplitude of the ellipsoidal modulation is much smaller, as can be seen in Fig. 2, this is very different for sdB+WD systems because we will only find the systems with the closest periods and/or highest-mass companions in our light variation search, if the period is not known by RV variations, for example.

4.2. Period distribution of the reflection effect systems

Taking all of this into account, we will never acquire a complete sample of reflection effect binaries from light curves alone, and the situation is even worse for the ellipsoidal systems. We do expect to find most reflection systems with higher inclinations observed by TESS up to periods around 7 days, as they can be identified from their light curve shapes with ease. Figure 16 presents our observed orbital period distribution for sdBs with cool, low-mass companions. To ensure we do not see any difference with the brightness, we also checked the distributions of reflection effect systems of different brightness with a two-sample Kolmogorov–Smirnov test, but we could not find any significant differences. The period distribution shows that the reflection effect systems without eclipses tend to be found at periods longer than the eclipsing systems. This is expected as the eclipse probability decreases quickly with increasing separation distance and period. The period distribution shows a broad peak from 2 to 8 h and falls off quickly on either end. There are very few systems with periods shorter than 2 h, and none are below 1.2 h. Above 8 h, the distribution falls off quickly, and only a handful of systems are found beyond 20 h. Despite our ability to detect systems with periods up to several days, the longest-period system we found has a period of 35 h. Since we do not find any longer-period systems, they either do not exist, or they are incredibly rare. As TESS continues to observe more and more reflection effect systems, increasing the sample size, hopefully this question can be answered.

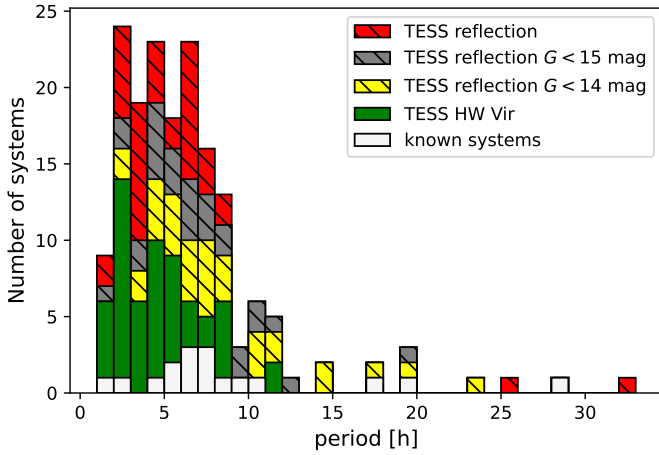


Fig. 16. Period distribution of the reflection effect systems with and without eclipses observed by TESS. The known reflection effect systems are marked in white, the eclipsing reflection effect systems are marked in red, and the reflection effect systems without eclipses are marked in yellow, green, and gray, for systems with $G < 13$ mag, $G < 14$ mag, and all other systems, respectively.

5. The companions of the close sdB binaries with solved RV curves

5.1. The nature of the companion

As we have seen, the reflection effect generates a flux variation that is detectable at periods up to several days. The light variation from ellipsoidal deformation or Doppler beaming, however, is much weaker on average (below 0.1–0.2%) at periods up to about one day, and is not detectable at longer periods. We can use these facts to differentiate between cool, low-mass companions and white dwarf companions (more details and the analysis of those systems is shown in Paper II) for the systems with periods known from RV variations.

We phased the available light curves of all hot subdwarfs with solved orbits. 135 of the 165 systems have *Kepler* or TESS light curves, and of those, 40 show a reflection effect and 33 show ellipsoidal deformation or Doppler beaming, indicating that they have a white dwarf companion (see Paper II for more details). The rest do not show significant variations at the orbital period. We derived the S/N for all light curves not exhibiting any variations. The results can be found in Table A.3.

To constrain the nature of the companion, we used the amplitude estimates at a given period and inclination shown in Fig. 15. Under the assumption that all orbital plane orientations are equally probable, the probability of the inclination being lower than 10° is only $1 - \cos 10^\circ = 1.5\%$ (Gray 2005). Therefore, we classify as sdB+WD systems all sdB binaries with light curves having a S/N smaller than the amplitude expected for a reflection effect system observed at an inclination angle $< 10^\circ$ (probability $> 98.5\%$).

Moreover, for companion masses larger than $0.45 M_\odot$, we would expect to see an infrared excess in the SED, if the companion was a main sequence companion. Therefore, we also classify all sdB binaries with minimum companion masses $> 0.45 M_\odot$ as sdB+WD systems. The minimum companion masses can be derived by the mass function:

$$f(M_1, M_2) = \frac{M_2^3 \sin^3 i}{(M_1 + M_2)^2} = \frac{PK_1^3}{2\pi G}, \quad (1)$$

assuming a mass of $0.47 M_\odot$ for the sdB and an inclination of 90° . We were unable to constrain the nature of the companion in this way for only 12 of our systems, as the noise in their light curves was too large and the minimum companion mass was too small. In total, this gives us 83 sdB+WD systems and allows us to constrain the nature of 75% of all close sdB binaries with solved orbits.

Most of the sdB binaries with solved orbits have been detected by RV variations, a method biased toward shorter periods, higher companion masses, and higher inclinations. Only very few of these were found by light variations. In this sample, about one-third of the sdB binaries have M dwarf or brown dwarf companions, and two-thirds have white dwarf companions.

5.2. The period distributions

The updated period distributions of the dM/BD and WD companions and their differences are also interesting, as shown in Fig. 17. We already discussed the distribution of the reflection effect and HW Vir systems showing periods from 2 h to about 1 day. The systems with WD companions, on the other hand, show a broad distribution from just about one hour to 27 days. On top of this broad distribution, we find two distinct peaks at around one day and around 5–10 days. The companion is still undefined only for a small number of systems. Most of them have periods longer than one day, agreeing well with the distribution of the WD companions, so it is likely they are also sdB+WD systems.

5.3. The minimum companion masses

To get a clearer picture of the masses of the close companions to hot subdwarf stars, we updated the plot of RV semiamplitude versus orbital period for all known sdB binaries (as shown in Kupfer et al. 2015) with spectroscopic solutions, and with TESS or Kepler light curves (Fig. 18). We also plot the minimum companion mass distribution in Fig. 19.

Our new sample adds many more systems with companion mass constraints to this plot. As we have seen, it is possible to constrain the minimum mass of the companion from the RV semiamplitude of the sdB and the orbital period, when assuming a mass for the sdB. This is given by the black lines for different periods. For a random distribution of system angles, the probability of having a system with an inclination $> 60^\circ$ is the same as for an inclination of $< 60^\circ$, and so about half of the companions should have masses of only up to 20% higher than the minimum companion mass.

We find that systems with cool, low-mass companions cluster around the hydrogen-burning limit with masses up to $0.25 M_\odot$ with one exception. The white dwarf companions to sdB stars have higher minimum masses, and it looks like there are three different populations. At the shortest periods, from approximately one to about three hours, a small group of WD companions with minimum companion masses around 0.7 to $0.8 M_\odot$ are found. Most of the WD companions are found in binaries with longer periods. Up to a period of about 4 days, they seem to have significantly lower minimum companion masses with a mass ratio close to one (around $0.4 M_\odot$, when assuming an sdB mass of $0.4 M_\odot$). Systems with periods belonging to the second peak in the period distribution, around 5–10 days, show some indication of slightly higher minimum companion masses above $0.4 M_\odot$ and up to $0.6 M_\odot$.

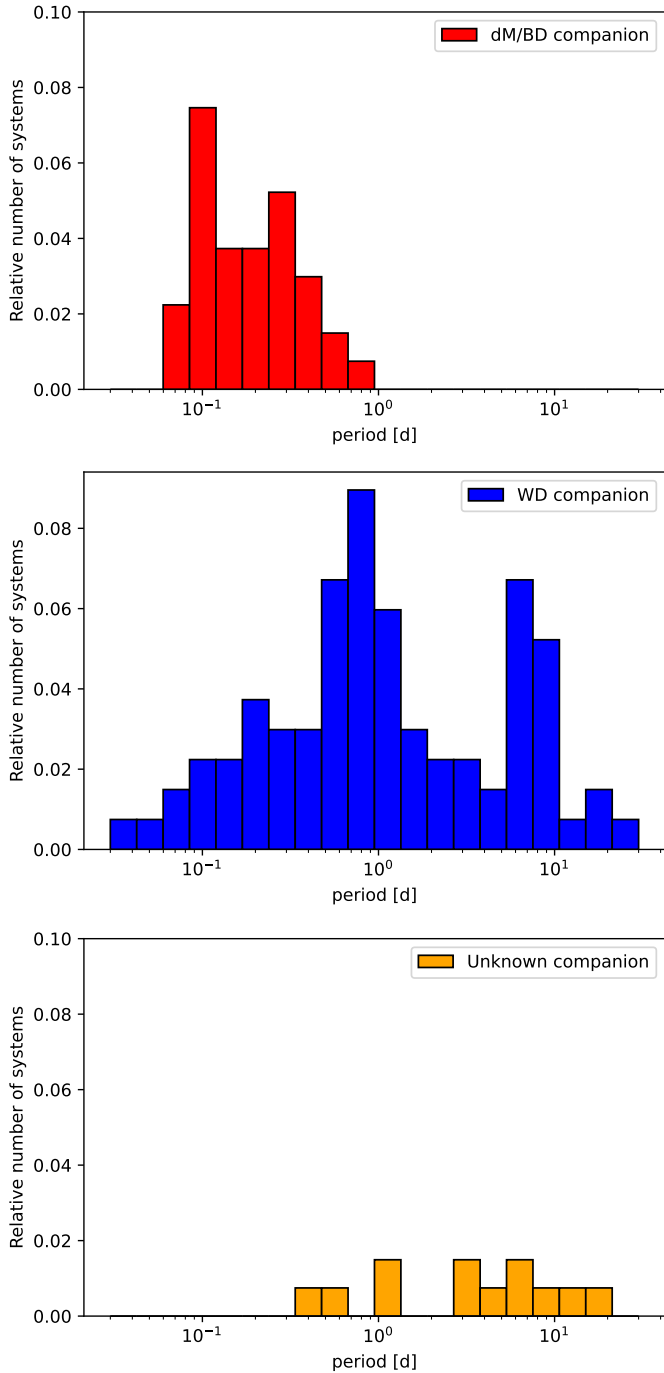


Fig. 17. Period distribution of the hot subdwarf binaries with solved orbits, with dM/BD companions in the *top panel*, with WD companions in the *middle panel*, and with unknown companions in the *lower panel*.

6. Discussion and conclusions

Our light variation search increases the number of known reflection effect systems from 19 to 104 systems. Moreover, we detected 23 new sdB+WD systems showing tiny variations with amplitudes below $\sim 0.1\%$, due to Doppler beaming or ellipsoidal deformation in their light curves.

The characterization of the reflection effect systems in our sample shows that all, except one, have hot subdwarf primaries. The one exception was a system with a white dwarf primary. Similar results were found in other surveys, such as EREBOS (Schaffenroth et al. 2019). The detection of a white dwarf pri-

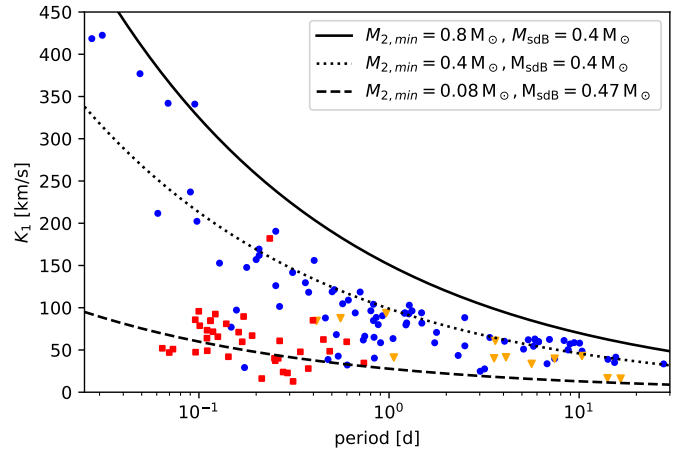


Fig. 18. RV semiamplitudes of all known short-period sdB binaries with spectroscopic solutions and with TESS or Kepler light curves plotted against their orbital periods (red squares: dM/BD companions; blue circles: WD companions; yellow diamonds: unknown type). The lines mark a certain minimum companion mass derived from the binary mass function (assuming 0.47 or $0.4 M_{\odot}$ for the sdBs).

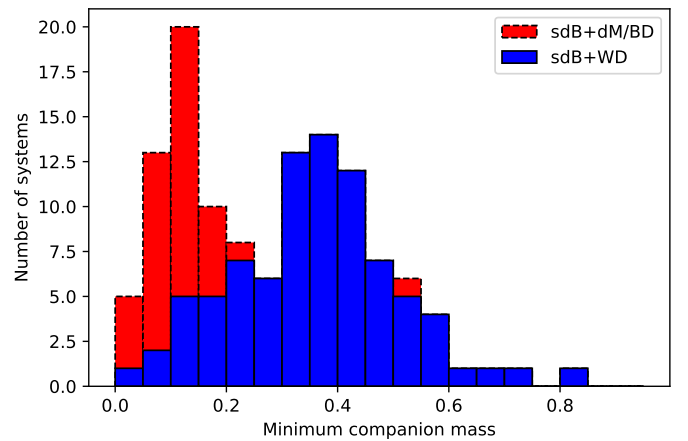


Fig. 19. Minimum companion mass distribution of all known short-period sdB binaries with spectroscopic solutions and with TESS or K2 light curves (assuming $0.47 M_{\odot}$ for an sdB with a dM/BD companion, or $0.4 M_{\odot}$ for an sdB with a WD companion).

mary is not a complete surprise, since we selected targets from the *Gaia* DR2 catalog of hot subluminal stars, which does have some overlap with the white dwarf catalog. Nonetheless, most of the primaries in our systems should be sdO/B stars. The reflection effect is only visible in hot white dwarfs, which are much rarer. Moreover, white dwarfs are much fainter than hot subdwarf stars. And since sdBs are mainly formed by binary evolution, the binarity rate of sdBs is much higher than that of WDs. That is why reflection effect systems with hot subdwarf primaries will dominate all surveys for reflection effect systems.

To check the mass determination of the sdB using the SED and the *Gaia* parallaxes, we compared the masses derived by this method with the masses derived by the light curve analysis of several ellipsoidal systems. This is shown in Table 2. The masses derived by the two different methods agree very well within the errors for all systems, thereby showing the validity of our spectrophotometric *Gaia* distance method.

The comparison of the mass distributions of the sdB+dM and the sdB+WD (Fig. 12) shows that they differ significantly.

Table 2. Masses of the solved sdB+WD systems derived by light curve analysis and SED fitting.

Target	$M_{\text{sdb,SED}}$ [M_{\odot}]	$M_{\text{sdb,lc}}$ [M_{\odot}]	References
KPD1946+4340	$0.452^{+0.065}_{-0.056}$	$0.47^{+0.03}_{-0.03}$	Bloemen et al. (2011)
CD-3011223	$0.44^{+0.061}_{-0.056}$	$0.47^{+0.03}_{-0.03}$	Geier et al. (2013)
PTF1J0823+0819	$0.48^{+0.09}_{-0.08}$	$0.45^{+0.09}_{-0.07}$	Kupfer et al. (2017a)
EVR-CB-001	$0.294^{+0.04}_{-0.034}$	$0.21^{+0.05}_{-0.05}$	Ratzloff et al. (2019)
EVR-CB-004	$0.461^{+0.104}_{-0.082}$	$0.52^{+0.04}_{-0.04}$	Ratzloff et al. (2020a)
ZTFJ2130+4420	$0.378^{+0.061}_{-0.053}$	$0.337^{+0.015}_{-0.015}$	Kupfer et al. (2020b)
HD265435	$0.59^{+0.17}_{-0.14}$	$0.64^{+0.10}_{-0.09}$	Pelisolì et al. (2021)

The mass distribution of sdBs with WD companions is shifted to lower masses compared to sdBs with dM/BD companions. This implies that sdBs with dM/BD companions come from a different population than sdBs with WD companions. The sdB+dM systems show a peak around the canonical mass for He-burning, and a few systems at higher and lower mass, as predicted by binary population synthesis models (Han et al. 2002, 2003). Those non-canonical systems can originate from young, higher-mass systems igniting He in the core under non-degenerate conditions, or they can be pre-He WDs not massive enough for He-burning that are passing through the sdB region in the HRD. The sdB+WDs, on the other hand, show many more low-mass systems. The sdB binaries with massive companions are observed toward the Galactic plane, where younger stars are found. This indicates that those systems are preferably formed in younger populations than the sdB+dM stars. The other sdB+WD systems seem to be equally distributed on the sky (see Fig. 7).

The observation of space-based light curves with a high S/N , covering a time span of at least 27 days and up to several months of so many sdBs, gave us, for the first time, a large sample of reflection effect binaries. Since they were selected mainly from the *Gaia* hot subdwarf catalog and had no prior RV measurements, this gives us the first period distribution of sdB+dM systems selected only by light variations. The orbital period distribution of post-common-envelope binaries is mainly dependent on the criterion for the ejection of the common envelope (Han et al. 2002), and so this distribution can be used to constrain the common-envelope phase when combined with the companion mass distribution, as done in Ge et al. (2022), for the sample of hot subdwarf binaries from Kupfer et al. (2015), or comparing it to a modeled sdB binary sample using binary population synthesis.

Aided by high-quality TESS light curves, we were able to constrain the nature of the companion in 75% of the sdB binaries with solved orbits and compare them. As seen in Fig. 17, the period distribution of the sdB+dM systems is concentrated in a much smaller period range compared to the sdB+WD systems, which are found over a wide range of periods, from 0.03 to 30 days. The distribution of the minimum companion masses found at a certain orbital period (Fig. 18) shows that the companions in the reflection effect systems have minimum masses typical for BD/dM systems ($0.05\text{--}0.2 M_{\odot}$). There is no visible change with the orbital period. For the sdB+WD systems this is different. There seem to be two distinct groups of companion masses. At the shortest periods, below 0.1 d, WD companions with high minimum masses around $0.8 M_{\odot}$ are found, which could be CO- or ONe-WDs. At longer periods, the WD companions seem to have significantly lower minimum masses, with masses around $0.4 M_{\odot}$. Many of those could be He-WD com-

panions. At the longest periods, the masses seem to be slightly higher, indicating a third population of low-mass CO-WD companions. This could suggest that sdB+WD systems at the shortest periods come from a different population, with higher-mass progenitors having higher-mass companions than the longer period sdB+WD systems, which is consistent with predictions by binary population synthesis (Han et al. 2002, 2003).

The high S/N light curves allowed us to derive parameters for a large number of sdB+dM/BD and sdB+WD systems. Details of this light curve modeling and the analysis are discussed in a separate paper (Paper II).

As TESS continues to observe, the number of high-quality reflection effect and sdB+WD light curves will continue to grow. This will further increase our sample size and improve constraints on the mass and period distributions. Future spectroscopic and photometric surveys such as 4MOST, BlackGem, and *Vera Rubin* Observatory will also increase our sample size and our knowledge about these systems.

Acknowledgements. This research made use of Lightkurve, a Python package for Kepler and TESS data analysis (Lightkurve Collaboration 2018). This paper includes data collected by the TESS mission, which are publicly available from the Mikulski Archive for Space Telescopes (MAST). Funding for the TESS mission is provided by NASA's Science Mission Directorate. V.S. and S.G. acknowledge funding from the German Academic Exchange Service (DAAD PPP USA 57444366) for this project and would like to thank the host institution Texas Tech University for the hospitality. V.S. was funded by the Deutsche Forschungsgemeinschaft under grant GE2506/9-1. I.P. was partially funded by the Deutsche Forschungsgemeinschaft under grant GE2506/12-1 and by the UK's Science and Technology Facilities Council (STFC), grant ST/T000406/1. T.K. acknowledges support from the National Science Foundation through grant AST #2107982, from NASA through grant 80NSSC22K0338 and from STScI through grant HST-GO-16659.002-A. B.N.B. was supported by the National Science Foundation grant AST-1812874. We thank Uli Heber for comments on the manuscript. We thank Andreas Irrgang for the development of the SED fitting tool and making it available to us.

References

- Afşar, M., & Ibanoglu, C. 2008, *MNRAS*, 391, 802
- Althaus, L. G., Miller Bertolami, M. M., & Corsico, A. H. 2013, *A&A*, 557, A19
- Astropy Collaboration (Robitaille, T. P., et al.) 2013, *A&A*, 558, A33
- Astropy Collaboration (Price-Whelan, A. M., et al.) 2018, *AJ*, 156, 123
- Baran, A. S., Sahoo, S. K., Sanjayan, S., & Ostrowski, J. 2021a, *MNRAS*, 503, 3828
- Baran, A. S., Østensen, R. H., Heber, U., et al. 2021b, *MNRAS*, 503, 2157
- Barlow, B. N., Kilkenny, D., Drechsel, H., et al. 2013, *MNRAS*, 430, 22
- Barlow, B. N., Corcoran, K. A., Parker, I. M., et al. 2022, *ApJ*, 928, 20
- Bell, K. J., Kosakowski, A., Kilic, M., et al. 2019, *Res. Notes Am. Astron. Soc.*, 3, 81
- Bloemen, S., Marsh, T. R., Østensen, R. H., et al. 2011, *MNRAS*, 410, 1787
- Brown, W. R., Beers, T. C., Wilhelm, R., et al. 2008, *AJ*, 135, 564
- Capitaino, L., Lallemand, R., Vergely, J. L., Elyajouri, M., & Monreal-Ibero, A. 2017, *A&A*, 606, A65
- Chen, A., O'Donoghue, D., Stobie, R. S., et al. 1995, *MNRAS*, 275, 100
- Copperwheat, C. M., Morales-Rueda, L., Marsh, T. R., Maxted, P. F. L., & Heber, U. 2011, *MNRAS*, 415, 1381
- Dorman, B., Rood, R. T., & O'Connell, R. W. 1993, *ApJ*, 419, 596
- Drechsel, H., Heber, U., Napiwotzki, R., et al. 2001, *A&A*, 379, 893
- Drilling, J. S. 1985, *ApJ*, 294, L107
- Edelmann, H., Heber, U., Hagen, H. J., et al. 2003, *A&A*, 400, 939
- Edelmann, H., Heber, U., Altmann, M., Karl, C., & Lisker, T. 2005, *A&A*, 442, 1023
- For, B. Q., Green, E. M., Fontaine, G., et al. 2010, *ApJ*, 708, 253
- Gaia Collaboration (Brown, A. G. A., et al.) 2018, *A&A*, 616, A1
- Gaia Collaboration (Brown, A. G. A., et al.) 2021, *A&A*, 649, A1
- Ge, H., Tout, C. A., Chen, X., et al. 2022, *ApJ*, 933, 137
- Geier, S. 2020, *A&A*, 635, A193
- Geier, S., Heber, U., Kupfer, T., & Napiwotzki, R. 2010, *A&A*, 515, A37
- Geier, S., Hirsch, H., Tillich, A., et al. 2011a, *A&A*, 530, A28
- Geier, S., Napiwotzki, R., Heber, U., & Nelemans, G. 2011b, *A&A*, 528, L16
- Geier, S., Marsh, T. R., Wang, B., et al. 2013, *A&A*, 554, A54

- Geier, S., Østensen, R. H., Heber, U., et al. 2014, *A&A*, **562**, A95
- Geier, S., Østensen, R. H., Nemeth, P., et al. 2017, *A&A*, **600**, A50
- Geier, S., Raddi, R., Gentile Fusillo, N. P., & Marsh, T. R. 2019, *A&A*, **621**, A38
- Gray, D. F. 2005, *The Observation and Analysis of Stellar Photospheres* (Cambridge: Cambridge University Press)
- Han, Z., Podsiadlowski, P., Maxted, P. F. L., Marsh, T. R., & Ivanova, N. 2002, *MNRAS*, **336**, 449
- Han, Z., Podsiadlowski, P., Maxted, P. F. L., & Marsh, T. R. 2003, *MNRAS*, **341**, 669
- Heber, U. 2009, *ARA&A*, **47**, 211
- Heber, U. 2016, *PASP*, **128**, 082001
- Heber, U., Drechsel, H., Østensen, R., et al. 2004, *A&A*, **420**, 251
- Heber, U., Irrgang, A., & Schaffenroth, J. 2018, *Open Astron.*, **27**, 35
- Hillwig, T. C., Frew, D. J., Reindl, N., et al. 2017, *AJ*, **153**, 24
- Howell, S. B., Sobeck, C., Haas, M., et al. 2014, *PASP*, **126**, 398
- Irrgang, A., Geier, S., Heber, U., et al. 2021, *A&A*, **650**, A102
- Ivanova, N., Justham, S., Chen, X., et al. 2013, *A&ARv*, **21**, 59
- Koen, C. S., & Ramsay, G. 2014, *MNRAS*, **442**, L61
- Kawka, A., Vennes, S., Németh, P., Kraus, M., & Kubát, J. 2010, *MNRAS*, **408**, 992
- Kawka, A., Vennes, S., O’Toole, S., et al. 2015, *MNRAS*, **450**, 3514
- Kilkenny, D., & Stone, L. E. 1988, *MNRAS*, **234**, 1011
- Kilkenny, D., Koen, C., & Worters, H. 2010, *MNRAS*, **404**, 376
- Kilkenny, D., O’Donoghue, D., Worters, H. L., et al. 2015, *MNRAS*, **453**, 1879
- Kilkenny, D., Worters, H. L., O’Donoghue, D., et al. 2016, *MNRAS*, **459**, 4343
- Koen, C. 2009, *MNRAS*, **395**, 979
- Koen, C., O’Donoghue, D., Kilkenny, D., Stobie, R. S., & Saffer, R. A. 1999, *MNRAS*, **306**, 213
- Krzyszinski, J., & Balona, L. A. 2022, *A&A*, **663**, A45
- Kupfer, T., Geier, S., Heber, U., et al. 2015, *A&A*, **576**, A44
- Kupfer, T., van Roestel, J., Brooks, J., et al. 2017a, *ApJ*, **835**, 131
- Kupfer, T., Ramsay, G., van Roestel, J., et al. 2017b, *ApJ*, **851**, 28
- Kupfer, T., Bauer, E. B., Burdge, K. B., et al. 2019, *ApJ*, **878**, L35
- Kupfer, T., Bauer, E. B., Burdge, K. B., et al. 2020a, *ApJ*, **898**, L25
- Kupfer, T., Bauer, E. B., Marsh, T. R., et al. 2020b, *ApJ*, **891**, 45
- Kupfer, T., Bauer, E. B., van Roestel, J., et al. 2022, *ApJ*, **925**, L12
- Lallement, R., Vergely, J.-L., Valette, B., et al. 2014, *A&A*, **561**, A91
- Lamontagne, R., Demers, S., Wesemael, F., Fontaine, G., & Irwin, M. J. 2000, *AJ*, **119**, 241
- Latour, M., Fontaine, G., & Green, E. 2014, in 6th Meeting on Hot Subdwarf Stars and Related Objects, eds. V. van Grootel, E. Green, G. Fontaine, & S. Charpinet, *ASP Conf. Ser.*, **481**, 91
- Lei, Z., Zhao, J., Németh, P., & Zhao, G. 2018, *ApJ*, **868**, 70
- Lightkurve Collaboration (Cardoso, J. V. d. M., et al.) 2018, *Astrophysics Source Code Library* [record ascl:1812.013]
- Lomb, N. R. 1976, *Ap&SS*, **39**, 447
- Lynas-Gray, A. E. 2021, *Front. Astron. Space Sci.*, **8**, 19
- Maxted, P. F. L., Heber, U., Marsh, T. R., & North, R. C. 2001, *MNRAS*, **326**, 1391
- Menzies, J. W., & Marang, F. 1986, in *Instrumentation and Research Programmes for Small Telescopes*, eds. J. B. Hearnshaw, & P. L. Cottrell, *IAU Symp.*, **118**, 305
- Mickaelian, A. M. 2008, *AJ*, **136**, 946
- Möller, L. 2021, Master’s Thesis, University of Erlangen-Nürnberg
- Morales-Rueda, L., Maxted, P. F. L., Marsh, T. R., Kilkenny, D., & O’Donoghue, D. 2005, in 14th European Workshop on White Dwarfs, eds. D. Koester, & S. Moehler, *ASP Conf. Ser.*, **334**, 333
- Németh, P., Kawka, A., & Vennes, S. 2012, *MNRAS*, **427**, 2180
- O’Donoghue, D., Kilkenny, D., Koen, C., et al. 2013, *MNRAS*, **431**, 240
- Orosz, J. A., & Wade, R. A. 1999, *MNRAS*, **310**, 773
- Østensen, R. H., Oreiro, R., Solheim, J. E., et al. 2010a, *A&A*, **513**, A6
- Østensen, R. H., Green, E. M., Bloemen, S., et al. 2010b, *MNRAS*, **408**, L51
- Østensen, R. H., Geier, S., Schaffenroth, V., et al. 2013, *A&A*, **559**, A35
- Pawar, T. 2020, Ph.D. Thesis, University of Potsdam
- Pelisolì, I., Vos, J., Geier, S., Schaffenroth, V., & Baran, A. S. 2020, *A&A*, **642**, A180
- Pelisolì, I., Neunteufel, P., Geier, S., et al. 2021, *Nat. Astron.*, **5**, 1052
- Penoyre, Z., Belokurov, V., & Evans, N. W. 2022, *MNRAS*, **513**, 2437
- Pribulla, T., Dimitrov, D., Kjurkchieva, D., et al. 2013, *Inf. Bull. Var. Stars*, **6067**, 1
- Ratzloff, J. K., Barlow, B. N., Kupfer, T., et al. 2019, *ApJ*, **883**, 51
- Ratzloff, J. K., Kupfer, T., Barlow, B. N., et al. 2020a, *ApJ*, **902**, 92
- Ratzloff, J. K., Barlow, B. N., Németh, P., et al. 2020b, *ApJ*, **890**, 126
- Reed, M. D., Kawaler, S. D., Zola, S., et al. 2004, *MNRAS*, **348**, 1164
- Reed, M. D., Yeager, M., Vos, J., et al. 2020, *MNRAS*, **492**, 5202
- Ricker, G. R., Winn, J. N., Vanderspek, R., et al. 2015, *J. Astron. Telesc. Instrum. Syst.*, **1**, 014003
- Rodríguez-López, C., Ulla, A., & Garrido, R. 2007, *MNRAS*, **379**, 1123
- Sahoo, S. K., Baran, A. S., Sanjayan, S., & Ostrowski, J. 2020, *MNRAS*, **499**, 5508
- Scargle, J. D. 1982, *ApJ*, **263**, 835
- Schaffenroth, V., Geier, S., Drechsel, H., et al. 2013, *A&A*, **553**, A18
- Schaffenroth, V., Classen, L., Nagel, K., et al. 2014a, *A&A*, **570**, A70
- Schaffenroth, V., Geier, S., Heber, U., et al. 2014b, *A&A*, **564**, A98
- Schaffenroth, V., Geier, S., Heber, U., et al. 2018, *A&A*, **614**, A77
- Schaffenroth, V., Barlow, B. N., Geier, S., et al. 2019, *A&A*, **630**, A80
- Schaffenroth, V., Casewell, S. L., Schneider, D., et al. 2021, *MNRAS*, **501**, 3847
- Schindewolf, M., Levitan, D., Heber, U., et al. 2015, *A&A*, **580**, A117
- Silvotti, R., Østensen, R. H., Bloemen, S., et al. 2012, *MNRAS*, **424**, 1752
- Vos, J., Németh, P., Vučković, M., Østensen, R., & Parsons, S. 2018, *MNRAS*, **473**, 693
- Vučković, M., Aerts, C., Østensen, R., et al. 2007, *A&A*, **471**, 605
- Vučković, M., Østensen, R. H., Aerts, C., et al. 2009, *A&A*, **505**, 239
- Vučković, M., Bloemen, S., & Østensen, R. 2014, in 6th Meeting on Hot Subdwarf Stars and Related Objects, eds. V. van Grootel, E. Green, G. Fontaine, & S. Charpinet, *ASP Conf. Ser.*, **481**, 259
- Vučković, M., Østensen, R. H., Németh, P., Bloemen, S., & Pápics, P. I. 2016, *A&A*, **586**, A146

Appendix A: Parameters of the close sdB binaries in TESS

Table A.1. Atmospheric and absolute parameters of the sdB binaries with spectroscopic parameters, and with space-based light curves determined by spectroscopy and a spectral energy distribution fitting, together with the *Gaia* parallax.

target	$T_{\text{eff,spec}}$ [K]	$\log g_{\text{spec}}$ [cgs]	$T_{\text{eff,sed}}$ [K]	M_{sed} [M_{\odot}]	L_{sed} [L_{\odot}]	R_{sed} [R_{\odot}]
Reflection effect systems						
KPD2215+5037	29600 ± 1000	5.64 ± 0.10	27000 ⁺⁷⁰⁰⁰ ₋₆₀₀₀	0.445 ^{+0.063} _{-0.055}	19.9 ^{+1.9} _{-1.7}	0.170 ^{+0.005} _{-0.005}
JL82	26500 ± 500	5.22 ± 0.1	26000 ⁺⁵⁰⁰ ₋₆₀₀	0.294 ^{+0.04} _{-0.034}	21 ^{+1.9} _{-2.0}	0.222 ^{+0.006} _{-0.006}
HE0230-4323	31552 ± 500	5.60 ± 0.07	34000 ⁺⁸⁰⁰⁰ ₋₅₀₀₀	0.635 ^{+0.118} _{-0.094}	40 ⁺⁶ ₋₅	0.211 ^{+0.014} _{-0.012}
V1405Ori	35100 ± 800	5.66 ± 0.11	27000 ⁺²³⁰⁰ ₋₂₇₀₀	0.44 ^{+0.06} _{-0.055}	36 ⁺⁵ ₋₅	0.166 ^{+0.006} _{-0.006}
Feige48	29850 ± 500	5.46 ± 0.05	28500 ⁺²⁵⁰⁰ ₋₁₈₀₀	0.47 ^{+0.064} _{-0.059}	32.2 ⁺³ _{-2.8}	0.213 ^{+0.007} _{-0.007}
GALEXJ2205-3141	28150 ± 500	5.68 ± 0.10	26800 ⁺¹¹⁰⁰ ₋₁₀₀₀	0.597 ^{+0.078} _{-0.074}	20.9 ⁺²⁰ _{-1.8}	0.186 ^{+0.005} _{-0.005}
PHL457	26500 ± 1100	5.38 ± 0.12	24600 ⁺¹²⁰⁰ ₋₇₀₀	0.316 ^{+0.048} _{-0.042}	16.1 ^{+1.9} _{-1.8}	0.191 ^{+0.008} _{-0.008}
KBS13	29700 ± 500	5.70 ± 0.05	-	0.472 ^{+0.062} _{-0.057}	18.2 ^{+1.6} _{-1.5}	0.162 ^{+0.004} _{-0.004}
CPD-64481	27500 ± 500	5.60 ± 0.05	26500 ⁺¹²⁰⁰ ₋₅₀₀	0.437 ^{+0.057} _{-0.050}	15.7 ^{+1.3} _{-1.3}	0.1748 ^{+0.0032} _{-0.0030}
GALEXJ0321+4727	27990 ± 400	5.34 ± 0.07	-	0.571 ^{+0.145} _{-0.112}	36 ⁺⁸ ₋₇	0.219 ^{+0.005} _{-0.004}
J012022+395059	29400 ± 500	5.48 ± 0.05	26500 ⁺²¹⁰⁰ ₋₂₁₀₀	0.561 ^{+0.136} _{-0.103}	24 ⁺⁶ ₋₄	0.194 ^{+0.019} _{-0.016}
PG1329+159	29100 ± 900	5.62 ± 0.10	27400 ⁺¹¹⁰⁰ ₋₁₀₀₀	0.694 ^{+0.101} _{-0.088}	29.8 ^{+3.1} _{-2.9}	0.215 ^{+0.008} _{-0.008}
BPSCS22169-0001	39300 ± 500	5.600 ± 0.05	40000 ⁺⁹⁰⁰⁰ ₋₅₀₀₀	0.584 ^{+0.091} _{-0.076}	87 ⁺⁹ ₋₈	0.202 ^{+0.009} _{-0.008}
HS2333+3927	36500 ± 1000	5.70 ± 0.10	-	0.578 ^{+0.094} _{-0.088}	51 ⁺⁷ ₋₆	0.177 ^{+0.011} _{-0.010}
UVEX0328+5035	28500 ± (500)	5.500 ± (0.05)	-	0.375 ^{+0.052} _{-0.046}	19.6 ^{+1.9} _{-1.8}	0.182 ^{+0.006} _{-0.006}
PG1017-086	30300 ± 500	5.61 ± 0.10	-	0.547 ^{+0.168} _{-0.126}	28 ⁺⁸ ₋₆	0.196 ^{+0.025} _{-0.021}
EQ Psc	28700 ± 500	5.63 ± 0.05	25400 ⁺¹³⁰⁰ ₋₁₃₀₀	0.353 ^{+0.048} _{-0.044}	13.2 ^{+1.3} _{-1.2}	0.151 ^{+0.005} _{-0.005}
HE1318-2111	36300 ± 1000	5.42 ± 0.1	41000 ⁺⁶⁰⁰⁰ ₋₅₀₀₀	0.365 ^{+0.064} _{-0.055}	60 ⁺⁸ ₋₈	0.196 ^{+0.012} _{-0.011}
GALEXJ09348-2512 ^a	40800 ± 500	5.55 ± 0.05	33000 ⁺¹²⁰⁰⁰ ₋₆₀₀₀	0.737 ^{+0.176} _{-0.143}	133 ⁺³⁰ ₋₂₆	0.241 ^{+0.023} _{-0.020}
EC01578-1743 ^a	32200 ± 500	5.75 ± 0.05	30000 ⁺³⁶⁰⁰ ₋₂₄₀₀	0.445 ^{+0.062} _{-0.053}	21.2 ^{+1.9} _{-1.7}	0.148 ^{+0.005} _{-0.004}
TYC5977-517-1 ^a	35200 ± 500	5.69 ± 0.05	-	0.462 ^{+0.07} _{-0.065}	35 ⁺⁴ ₋₄	0.162 ^{+0.08} _{-0.007}
HW Vir systems						
AADor	42000 ± 1000	5.460 ± 0.05	35700 ⁺²⁸⁰⁰ ₋₂₂₀₀	0.464 ^{+0.058} _{-0.052}	118 ⁺⁸ ₋₈	0.206 ^{+0.005} _{-0.005}
ATLASJ340	40000 ± 1000	5.450 ± 0.05	-	0.510 ^{+0.098} _{-0.078}	116 ⁺¹⁶ ₋₁₄	0.225 ^{+0.014} _{-0.013}
ATLASJ283	50000 ± 1000	5.600 ± 0.05	-	0.511 ^{+0.075} _{-0.064}	201 ⁺¹⁷ ₋₁₆	0.189 ^{+0.008} _{-0.007}
2M1533+3759	29200 ± 500	5.58 ± 0.05	-	0.427 ^{+0.058} _{-0.053}	20.3 ^{+2.0} _{-1.8}	0.176 ^{+0.006} _{-0.005}
ASAS102322-3737	28400 ± 500	5.600 ± 0.05	27900 ⁺⁴⁴⁰⁰ ₋₂₈₀₀	0.469 ^{+0.065} _{-0.056}	19.1 ^{+1.9} _{-1.6}	0.181 ^{+0.006} _{-0.005}
2M1938+4603	29600 ± 500	5.43 ± 0.05	-	0.441 ^{+0.058} _{-0.052}	31.6 ^{+2.7} _{-2.5}	0.213 ^{+0.006} _{-0.005}
BULSC16335	31500 ± 500	5.70 ± 0.05	-	0.437 ^{+0.121} _{-0.094}	21 ⁺⁶ ₋₅	0.156 ^{+0.018} _{-0.016}
EC10246-2707	28900 ± 500	5.64 ± 0.05	26700 ⁺²⁹⁰⁰ ₋₂₆₀₀	0.500 ^{+0.076} _{-0.067}	19.8 ^{+2.3} _{-2.0}	0.178 ^{+0.008} _{-0.007}
HWVir	28500 ± 500	5.63 ± 0.05	25700 ⁺¹⁹⁰⁰ ₋₁₇₀₀	0.42 ^{+0.055} _{-0.050}	19.9 ^{+1.9} _{-1.7}	0.190 ^{+0.005} _{-0.005}
HS2231+2441	28400 ± 500	5.39 ± 0.05	28800 ⁺²⁰⁰⁰ ₋₁₅₀₀	0.312 ^{+0.052} _{-0.043}	20.6 ^{+2.6} _{-2.3}	0.189 ^{+0.010} _{-0.009}
PG1336-018	32800 ± 500	5.76 ± 0.05	34000 ⁺⁶⁰⁰⁰ ₋₄₀₀₀	0.480 ^{+0.070} _{-0.057}	22.9 ^{+2.3} _{-2.0}	0.153 ^{+0.005} _{-0.005}
J082053+000843	25800 ± 300	5.52 ± 0.04	27600 ⁺¹⁴⁰⁰ ₋₁₂₀₀	0.513 ^{+0.103} _{-0.082}	17.1 ^{+3.0} _{-2.5}	0.208 ^{+0.017} _{-0.015}
HS0705+6700	28800 ± 900	5.40 ± 0.10	28000 ⁺²⁶⁰⁰ ₋₂₂₀₀	0.467 ^{+0.075} _{-0.063}	31 ⁺⁴ ₋₄	0.225 ^{+0.011} _{-0.010}
J162256+473051	29000 ± 600	5.65 ± 0.06	28800 ⁺²⁸⁰⁰ ₋₂₀₀₀	0.308 ^{+0.076} _{-0.05}	12.1 ^{+2.7} _{-2.0}	0.139 ^{+0.014} _{-0.011}
ATLASJ296	25000 ± 500	5.45 ± 0.05	19300 ⁺²⁰⁰⁰ ₋₁₅₀₀	0.399 ^{+0.075} _{-0.062}	13.8 ^{+2.2} _{-1.9}	0.199 ^{+0.013} _{-0.012}
J192059+372220	27500 ± 1000	5.40 ± 0.10	-	0.476 ^{+0.091} _{-0.076}	27 ⁺⁵ ₋₄	0.230 ^{+0.016} _{-0.014}
V2008-1753	32800 ± 250	5.83 ± 0.04	-	0.47 ^{+0.395} _{-0.179}	14 ⁺¹³ ₋₆	0.124 ^{+0.042} _{-0.026}
NSVS14256825	40000 ± 500	5.50 ± 0.05	-	0.406 ^{+0.059} _{-0.052}	82 ⁺⁷ ₋₈	0.189 ^{+0.007} _{-0.007}

Table A.1. continued.

target	$T_{\text{eff,spec}}$ [K]	$\log g_{\text{spec}}$ [cgs]	$T_{\text{eff,sed}}$ [K]	M_{sed} [M_{\odot}]	L_{sed} [L_{\odot}]	R_{sed} [R_{\odot}]
Ellipsoidal and beaming systems						
KPD1946+4340	34200±500	5.43±0.10	-	0.452 ^{+0.065} _{-0.056}	61 ⁺⁶ ₋₅	0.216 ^{+0.008} _{-0.007}
GD687	24300±500	5.32±0.07	27000 ⁺¹⁸⁰⁰ ₋₁₇₀₀	0.283 ^{+0.042} _{-0.037}	11.7 ^{+1.5} _{-1.3}	0.194 ^{+0.008} _{-0.008}
PG0941+280	29400±500	5.43±0.05	30000 ⁺²⁷⁰ ₋₂₀₀₀	0.363 ^{+0.053} _{-0.048}	25.1 ^{+2.7} _{-2.5}	0.194 ^{+0.008} _{-0.007}
EVR-CB-004	41000±200	4.55±0.03	40000 ⁺⁵³⁰⁰ ₋₂₈₀₀	0.461 ^{+0.104} _{-0.082}	910 ⁺¹⁹⁰ ₋₁₆₀	0.60 ^{+0.06} _{-0.05}
GALEXJ0751+0925	30620±400	5.74±0.10	34000 ⁺⁸⁰⁰⁰ ₋₆₀₀₀	0.368 ^{+0.05} _{-0.046}	14.6 ^{+1.4} _{-1.3}	0.136 ^{+0.005} _{-0.004}
PG1043+760	27600±800	5.39±0.10	28000 ⁺²¹⁰⁰ ₋₄₀₀₀	0.289 ^{+0.038} _{-0.036}	17 ^{+1.6} _{-1.6}	0.180 ^{+0.005} _{-0.005}
EVR-CB-001	18500±500	4.96±0.04	19900 ⁺²⁹⁰⁰ ₋₂₂₀₀	0.294 ^{+0.04} _{-0.034}	9.4 ^{+1.2} _{-1.1}	0.300 ^{+0.007} _{-0.007}
KPD0422+5421	25000±1500	5.40±0.10	23100 ⁺¹⁹⁰⁰ ₋₁₇₀₀	0.366 ^{+0.048} _{-0.044}	14.1 ^{+1.4} _{-1.3}	0.201 ^{+0.005} _{-0.005}
HD265435	34300 ±400	5.62±0.10	26900 ⁺³⁹⁰⁰ ₋₁₃₀₀	0.59 ^{+0.17} _{-0.14}	51 ⁺⁵ ₋₅	0.203 ^{+0.007} _{-0.007}
CD-3011223	29200±400	5.66±0.05	29000 ⁺⁴⁴⁰⁰ ₋₂₇₀₀	0.44 ^{+0.061} _{-0.056}	17.7 ^{+1.7} _{-1.6}	0.164 ^{+0.005} _{-0.005}
ZTFJ2130+4420	42000±300	5.77±0.05	-	0.378 ^{+0.061} _{-0.053}	49 ⁺⁸ ₋₇	0.134 ^{+0.007} _{-0.007}
J113840-003531	31200±600	5.54±0.09	28500 ⁺³³⁰⁰ ₋₁₂₀₀	0.501 ^{+0.096} _{-0.078}	34 ⁺⁶ ₋₅	0.201 ^{+0.013} _{-0.013}
KIC6614501	23700±500	5.70±0.10	-	0.361 ^{+0.058} _{-0.049}	5.7 ^{+0.8} _{-0.7}	0.142 ^{+0.007} _{-0.007}
UVO1735+22	38000±500	5.54±0.05	36000 ⁺¹⁶⁰⁰⁰ ₋₇₀₀₀	0.48 ^{+0.07} _{-0.061}	72 ⁺¹⁰ ₋₉	0.197 ^{+0.008} _{-0.008}
PG1232-136	26900±500	5.71±0.05	27000 ⁺¹⁴⁰⁰ ₋₁₄₀₀	0.402 ^{+0.052} _{-0.049}	10.2 ^{+1.0} _{-0.9}	0.148 ^{+0.004} _{-0.004}
PG0101+039	27500±500	5.53±0.07	26800 ⁺⁶⁰⁰ ₋₇₀₀	0.409 ^{+0.053} _{-0.050}	17.2 ^{+1.6} _{-1.5}	0.183 ^{+0.005} _{-0.005}
GALEXJ234947.7+384440	23800±350	5.380±0.06	-+-	0.38 ^{+0.05} _{-0.05}	12.7 ^{+1.2} _{-1.2}	0.210 ^{+0.004} _{-0.004}
PG1512+244	29900±900	5.74±0.09	27700 ⁺¹³⁰⁰ ₋₁₂₀₀	0.41 ^{+0.06} _{-0.05}	14.7 ^{+1.3} _{-1.2}	0.143 ^{+0.004} _{-0.004}
PG1519+640	30600±500±	5.72±0.05	27600 ⁺²⁰⁰⁰ ₋₉₀₀	0.45 ^{+0.06} _{-0.06}	18.6 ^{+1.6} _{-1.5}	0.154 ^{+0.004} _{-0.004}
GALEXJ025023.8-040611	28300±500	5.67±0.10	27000 ⁺²³⁰⁰ ₋₂₃₀₀	0.47 ^{+0.07} _{-0.06}	16.5 ^{+1.7} _{-1.5}	0.166 ^{+0.006} _{-0.006}
PG1743+477	27600±800	5.57±0.10	28000 ⁺¹¹⁰⁰ ₋₁₅₀₀	0.49 ^{+0.07} _{-0.06}	19.3 ^{+1.8} _{-1.7}	0.193 ^{+0.005} _{-0.005}
PG1648+536	31400±(500)	5.62±(0.05)	-+-	0.46 ^{+0.07} _{-0.06}	16.9 ^{+2.4} _{-2.2}	0.176 ^{+0.005} _{-0.005}
PG1000+408	36400±900	5.540±0.10	38000 ⁺²³⁰⁰ ₋₁₇₀₀	0.65 ^{+0.11} _{-0.09}	82 ⁺¹⁰ ₋₉	0.229 ^{+0.011} _{-0.011}
TONS183	27600±0.05	5.43±0.05	26170 ⁺²⁷⁰ ₋₂₅₀	0.38 ^{+0.06} _{-0.05}	20.5 ^{+2.1} _{-1.9}	0.198 ^{+0.007} _{-0.007}
GALEXJ225444.1-551505	31070±300	5.80±0.05	30700 ⁺¹²⁰⁰ ₋₉₀₀	0.39 ^{+0.06} _{-0.05}	14.4 ^{+1.2} _{-1.1}	0.131 ^{+0.0029} _{-0.0025}
PG0133+114	29600±900	5.66±0.10	23700 ⁺¹⁰⁰⁰ ₋₈₀₀	0.38 ^{+0.06} _{-0.05}	15.9 ^{+1.7} _{-1.5}	0.152 ^{+0.006} _{-0.005}
PG0934+186	35800±200	5.65±0.02	31300 ⁺³⁹⁰⁰ ₋₁₉₀₀	0.47 ^{+0.08} _{-0.06}	43 ⁺⁵ ₋₄	0.171 ^{+0.007} _{-0.007}
CD-24731	35400±500	5.90±0.05	33500 ⁺¹⁰⁰⁰ ₋₅₀₀	0.36 ^{+0.05} _{-0.05}	18 ^{+1.3} _{-1.2}	0.1128 ^{+0.0022} _{-0.0021}
PHL1539	35400±500	5.500±0.05	36000 ⁺¹⁰⁰⁰⁰ ₋₅₀₀₀	0.28 ^{+0.05} _{-0.04}	34 ⁺⁴ ₋₄	0.156 ^{+0.007} _{-0.007}
PTF1J082340.04+081936.5	27000±500	5.50±0.05	26400 ⁺¹²⁰⁰ ₋₁₂₀₀	0.48 ^{+0.09} _{-0.08}	20.1 ^{+3.3} _{-2.6}	0.205 ^{+0.013} _{-0.012}

Notes. Spectroscopic parameters can be found in Kupfer et al. (2015) and references therein, as well as references in Table A.4^a paper II.

Table A.2. Atmospheric parameters, luminosities, and radii of the reflection effect candidates without known atmospheric parameters determined by using the SED fitting together with the *Gaia* parallax.

target	$T_{\text{eff, sed}}$ [K]	$\log g_{\text{sed, canonical}}$ [cgs]	L_{sed} [L_{\odot}]	R_{sed} [R_{\odot}]
2M0748+3042	33700 ⁺⁴⁴⁰⁰ ₋₂₉₀₀	5.78	21 ⁺¹⁴ ₋₉	0.150 ^{+0.012} _{-0.015}
HE0505-3833	26500 ⁺¹⁴⁰⁰ ₋₁₃₀₀	5.63	13.2 ^{+3.1} _{-2.6}	0.175 ^{+0.008} _{-0.007}
MCT0049-3059	24300 ⁺⁷⁰⁰ ₋₅₀₀	5.43	15.3 ^{+2.2} _{-1.8}	0.221 ^{+0.010} _{-0.010}
TYC4542-482-1	16400 ⁺⁷⁹⁰⁰ ₋₂₄₀₀	5.15	8.7 ^{+2.6} _{-0.165}	0.305 ^{+0.028} _{-0.052}
EC21390-2930	29000 ⁺¹²⁰⁰⁰ ₋₅₀₀₀	5.38	17 ⁺⁴⁷ ₋₁₄	0.241 ^{+0.026} _{-0.049}
2MASSJ18424506+6956202	37000 ⁺¹²⁰⁰⁰ ₋₉₀₀₀	5.7	17 ⁺⁶⁷ ₋₁₇	0.169 ^{+0.032} _{-0.030}
GALEXJ06206-5705	31000 ⁺⁷⁰⁰⁰ ₋₅₀₀₀	5.65	16.7 ^{+20.3} _{-9.75}	0.176 ^{+0.017} _{-0.024}
2MASSJ06125523+5750507	27000 ⁺⁵⁰⁰⁰ ₋₄₀₀₀	5.59	10.3 ^{+13.1} _{-6.0}	0.185 ^{+0.026} _{-0.023}
EC01578-1743	30000 ⁺³⁷⁰⁰ ₋₂₄₀₀	5.73	14.9 ^{+8.6} _{-5.2}	0.158 ^{+0.009} _{-0.013}
KUV04421+1416	25700 ⁺²²⁰⁰ ₋₂₆₀₀	5.52	14 ⁺⁶ ₋₆	0.196 ^{+0.013} _{-0.011}
GALEXJ01077-6707	25200 ⁺¹²⁰⁰ ₋₁₂₀₀	5.48	15.3 ^{+3.3} _{-2.8}	0.208 ^{+0.008} _{-0.007}
GAIADR2 2333936291513550336	26300 ⁺²⁰⁰⁰ ₋₁₉₀₀	5.55	15 ⁺⁹ ₋₆	0.107 ^{+0.03} _{-0.025}
GAIADR2 3573130082641947392	25700 ⁺¹⁰⁰⁰ ₋₁₀₀₀	5.45	18.2 ^{+3.5} _{-2.8}	0.218 ^{+0.01} _{-0.01}
GAIADR2 6366169442902410368	25000 ⁺¹³⁰⁰ ₋₁₄₀₀	5.4	18 ⁺⁵ ₋₄	0.231 ^{+0.011} _{-0.011}
GAIADR2 6724092123091015552	29600 ⁺⁴⁵⁰⁰ ₋₂₈₀₀	5.35	33 ⁺²⁵ ₋₁₅	0.248 ^{+0.016} _{-0.025}
GAIADR2-2911497105202950400	27100 ⁺²⁷⁰⁰ ₋₂₂₀₀	5.52	17 ⁺⁹ ₋₆	0.2 ^{+0.016} _{-0.016}
GAIADR2-3040772322279673472	26700 ⁺¹²⁰⁰ ₋₁₁₀₀	5.3	29 ⁺⁷ ₋₆	0.256 ^{+0.013} _{-0.013}
GAIADR2-5434436383219257472	28300 ⁺³⁹⁰⁰ ₋₂₅₀₀	5.46	22 ⁺¹⁵ ₋₉	0.217 ^{+0.015} _{-0.02}
GaiaDR2-3040772322279673472	26600 ⁺¹⁴⁰⁰ ₋₁₃₀₀	5.30	28 ⁺⁸ ₋₆	0.256 ^{+0.014} _{-0.013}
GaiaDR2-2909497952544966272	29000 ⁺⁵⁰⁰⁰ ₋₄₀₀₀	5.68	13 ⁺¹³ ₋₇	0.17 ^{+0.014} _{-0.021}
GAIADR2 5416091856344970880	28300 ⁺³⁶⁰⁰ ₋₂₄₀₀	5.6	16 ⁺¹¹ ₋₇	0.184 ^{+0.016} _{-0.017}
GAIADR2 5576826952945841408	25800 ⁺²²⁰⁰ ₋₂₁₀₀	5.44	17 ⁺⁹ ₋₆	0.219 ^{+0.019} _{-0.017}
CRTSJ064417.6-464020	26800 ⁺³¹⁰⁰ ₋₂₄₀₀	5.42	20 ⁺¹² ₋₈	0.225 ^{+0.018} _{-0.018}
GAIADR2 5647303827227273088	42000 ⁺¹⁴⁰⁰⁰ ₋₅₀₀₀	5.7	60 ⁺¹⁰⁰ ₋₄₀	0.165 ^{+0.028} _{-0.023}
GAIADR2 5296462581763471104	36000 ⁺¹⁴⁰⁰⁰ ₋₆₀₀₀	5.82	16 ⁺⁴⁰ ₋₁₃	0.146 ^{+0.018} _{-0.027}
2MASSJ08412266+0630294	36700 ⁺³⁸⁰⁰ ₋₂₉₀₀	5.7	37 ⁺²¹ ₋₁₂	0.162 ^{+0.014} _{-0.013}
SDSSJ075314.03+111240.1	27800 ⁺²⁴⁰⁰ ₋₂₁₀₀	5.48	22 ⁺¹² ₋₈	0.212 ^{+0.026} _{-0.023}
GAIADR2 3083335826137398400	36000 ⁺¹¹⁰⁰⁰ ₋₇₀₀₀	5.9	15 ⁺³⁵ ₋₁₂	0.13 ^{+0.027} _{-0.023}
SDSSJ044246.86-071654.4	22700 ⁺¹¹⁰⁰ ₋₁₀₀₀	5.3	15.6 ^{+3.5} _{-2.9}	0.259 ^{+0.013} _{-0.012}
EC02406-6908	25100 ⁺²⁰⁰⁰ ₋₂₁₀₀	5.52	13 ⁺⁶ ₋₄	0.197 ^{+0.012} _{-0.011}
GALEXJ14019-7513	34000 ⁺¹⁴⁰⁰⁰ ₋₆₀₀₀	5.7	15 ⁺³⁹ ₋₁₂	0.16 ^{+0.017} _{-0.03}
HE0516-2311	25900 ⁺¹⁴⁰⁰ ₋₁₅₀₀	5.4	21 ⁺⁷ ₋₆	0.229 ^{+0.024} _{-0.021}
EC23068-4801	29900 ⁺³²⁰⁰ ₋₂₂₀₀	5.73	15 ⁺⁹ ₋₅	0.157 ^{+0.014} _{-0.013}
GAIADR2-6652952415078798208	24100 ⁺⁵³⁰⁰ ₋₃₀₀₀	4.6	48 ⁺⁶⁰ ₋₂₉	0.48 ^{+0.06} _{-0.06}
CRTS-J120928.2-435809	26000 ⁺²⁶⁰⁰ ₋₂₃₀₀	5.4	19 ⁺¹¹ ₋₇	0.228 ^{+0.021} _{-0.02}
GAIADR2-2943004023214007424	26300 ⁺²⁴⁰⁰ ₋₂₂₀₀	5.46	18 ⁺⁹ ₋₆	0.214 ^{+0.086} _{-0.076}
GAIADR2-5289914135324381696	30000 ⁺⁴⁴⁰⁰ ₋₂₈₀₀	5.6	20 ⁺¹⁶ ₋₉	0.183 ^{+0.026} _{-0.022}
PG1628+181	26000 ⁺¹⁵⁰⁰ ₋₁₄₀₀	5.45	18 ⁺⁶ ₋₅	0.216 ^{+0.015} _{-0.014}
J306.3118+58.8522	25400 ⁺²⁵⁴⁰⁰ ₋₂₅₀₀	5.65	10 ⁺⁹ ₋₅	0.176 ^{+0.041} _{-0.03}
GaiaDR2-2993468995592753920	29700 ⁺⁴⁷⁰⁰ ₋₂₉₀₀	5.54	22 ⁺¹⁹ ₋₁₀	0.198 ^{+0.023} _{-0.022}
J084.4719-00.8239	28400 ⁺²¹⁰⁰ ₋₁₆₀₀	5.52	21 ⁺⁸ ₋₅	0.2 ^{+0.013} _{-0.012}
J129.0542-08.0399	26700 ⁺²⁴⁰⁰ ₋₂₁₀₀	5.37	23 ⁺¹³ ₋₈	0.237 ^{+0.031} _{-0.025}
GaiaDR2-2969438206889996160	27700 ⁺³⁸⁰⁰ ₋₂₅₀₀	5.3	29 ⁺²¹ ₋₁₂	0.262 ^{+0.019} _{-0.024}
J089.3714-14.1662	28000 ⁺⁶⁰⁰⁰ ₋₄₀₀₀	5.52	16 ⁺¹⁸ ₋₉	0.203 ^{+0.019} _{-0.025}

Table A.3. Classification of *TESS* targets with no variations.

target	period	K_1	$M_{2,\min}(M_{\text{sdB}} = 0.47 M_{\odot})$	$M_{2,\min}(M_{\text{sdB}} = 0.4 M_{\odot})$	signal-to-noise
White dwarf companions (M dwarf excluded)					
KPD1930+2752	0.0950933	341	0.90	0.85	ell
J083006+475150	0.1478000000	77.00	0.14	0.12	1%
GALEXJ0805-1058	0.1737030000	29.20	0.05	0.04	0.04%
J165404+303701	0.2535700000	126.10	0.32	0.29	0.4%
HE0532-4503	0.2656000000	101.50	0.25	0.22	0.4%
KUV16256+4034	0.4776000000	38.70	0.10	0.09	0.02%
GALEXJ0507+0348	0.5281270000	68.20	0.20	0.18	0.2%
PG1247+554	0.60274	32.20	0.09	0.08	0.01%
PG1248+164	0.7323200000	61.80	0.20	0.18	0.5%
PG0849+319	0.7450700000	66.30	0.22	0.20	0.5%
PG1230+052	0.8371770000	40.40	0.13	0.11	0.1%
PG1116+301	0.8562100000	88.50	0.34	0.32	0.4%
PG0918+029	0.8767900000	80.00	0.30	0.28	0.1%
EC12408-1427	0.9024300000	58.60	0.20	0.19	0.05%
PG2331+038	1.2049640000	93.50	0.44	0.40	0.5%
HE1047-0436	1.2132500000	94.00	0.44	0.41	0.5%
HE2150-0238	1.3210000000	96.30	0.48	0.44	0.3%
PG1403+316	1.7384600000	58.50	0.27	0.25	0.7%
V1093Her	1.7773200000	70.80	0.35	0.33	0.3%
CPD-201123	2.3098	43.50	0.21	0.19	0.05%
TON245	2.5010000000	88.30	0.58	0.54	0.5%
PG1253+284	3.01634	24.80	0.12	0.11	0.01%
PG0958-073	3.1809500000	27.60	0.14	0.12	0.7%
KIC10553698	3.3870000000	64.80	0.42	0.39	lc
J183249+630910	5.4000000000	62.10	0.50	0.46	0.5%
HE1115-0631	5.8700000000	61.90	0.52	0.48	1%
PG0907+123	6.1163600000	59.80	0.51	0.47	0.2%
PG1032+406	6.7791000000	33.70	0.24	0.22	0.1%
Feige108	8.7465100000	50.20	0.46	0.43	0.5%
KIC11558725	10.0545000000	58.10	0.63	0.58	lc
KIC7668647	14.1742000000	38.90	0.40	0.37	lc
LB1516	10.3598000000	48.600	0.48	0.44	0.2%
PG1619+522	15.3578000000	35.20	0.36	0.33	0.1%
White dwarf companions (minimum mass, ^a Kupfer et al. (2015))					
J082332+113641	0.2070700000	169.40	0.44	0.41	3%
J172624+274419 ^a	0.5019800000	118.90	0.41	0.37	5%
KPD2040+3955	1.4828600000	94.00	0.49	0.45	3%
J002323-002953 ^a	1.4876000000	81.80	0.40	0.37	2%
GALEXJ0812+1601 ^a	5.1000000000	51.00	0.37	0.34	1%
PG1244+113 ^a	5.7521100000	54.40	0.43	0.39	1%
J095238+625818 ^a	6.9800000000	62.50	0.58	0.54	1%
PG0940+068	8.3300000000	61.20	0.62	0.57	0.3%
Feige108 ^a	8.7465100000	50.20	0.46	0.43	1%
EC20260-4757	8.9520000000	57.10	0.57	0.53	0.5%
PG1110+294 ^a	9.4152000000	58.70	0.61	0.57	1%
PG0919+273 ^a	15.5830000000	41.50	0.47	0.43	1%
PG0850+170	27.8150000000	33.50	0.45	0.42	0.1%
Undefined companions					
J095101+034757	0.4159000000	84.40	0.23	0.21	1.5%
HE1059-2735	0.5556240000	87.70	0.28	0.26	1%
J150829+494050	0.9671640000	93.60	0.39	0.36	1%
J113241-063652	1.0600000000	41.10	0.14	0.13	1.5%
KPD0025+5402	3.5711000000	40.20	0.23	0.21	3%
PB7352	3.6216600000	60.80	0.40	0.37	2%
TONS135	4.1228000000	41.40	0.25	0.23	0.5%
PG0839+399	5.6222000000	33.60	0.22	0.20	1%
J032138+053840	7.4327	39.70	0.31	0.28	0.3%
PG1558-007	10.3495000000	42.80	0.40	0.37	0.75%
CS1246	14.1050000000	16.60	0.13	0.12	3%
EGB5	16.5320000000	16.10	0.14	0.13	0.3%

Table A.4. All confirmed systems with light variations.

TIC number	name	alternative name	RA [deg]	DEC [deg]	classification	G [mag]	$B_p - R_p$ [mag]	parallax [mas]	distance [kpc]	G_{abs} [mag]	reduced pm	period [h]	reference ^d
reflection effect systems													
4491131	2M0748+3042	Ton287	117.233	30.713	sdB	14.046156	-0.347797	1.334	0.750	4.672	10.473	5.53	Németh et al. (2012)
14081239	HE0505-3833	HE0505-3833a	76.745	-38.488	sdB	14.145108	-0.362259	1.228	0.815	4.591	8.454	7.73	O'Donoghue et al. (2013)
	28762714	FB50145+363	27.171	36.564	sd	15.462710	-0.194446	3.786	0.264	8.354	12.404	3.03	Mickaëlian (2008)
66398320	MCT0049-3059	PHL867	12.907	-30.716	sdB	14.340959	-0.392432	0.907	1.102	4.130	10.141	5.83	Lamontagne et al. (2000)
67423472	2M0156+4003	"	29.005	40.056	sdBVp	11.430020	-0.347691	3.438	0.291	4.111	8.833	4.65	Geier et al. (2019)
103871878	2MASSJ2002943+3137190	"	300.123	31.622	sd	15.480430	0.090571	1.324	4.871	4.871	10.932	6.74	Geier et al. (2019)
122889490	2MASSJ18330407+4637053	"	278.267	46.618	sd	15.698741	-0.312881	1.433	0.698	6.481	11.739	1.7	Geier et al. (2019)
137608661	2M0943+7831	TYC4544-2658-1	145.973	78.528	sdBV+dM	11.111541	-0.416957	3.899	0.256	4.066	8.485	7.21	Østensen et al. (2010a)
138025887	2MASS05545291+7745425	"	88.72	77.762	sdB	15.808988	-0.406666	0.816	1.226	5.367	7.348	4.06	Geier et al. (2019)
142785398	TYC4542-482-1	TYC4542-482-1	154.505	75.224	sd	12.597594	-0.237924	2.139	0.467	4.249	8.021	4.68	Schaffner et al. (2019)
162128750	2MASSJ22035140+3002560	"	330.964	30.049	sd	13.595135	-0.286156	1.417	0.706	4.353	9.129	5.92	Brown et al. (2008)
173295499	2MASSJ23063044+4418488	FB82.304+440	346.627	-44.314	sd	14.289134	-0.127421	1.606	0.623	5.318	10.536	4.22	Geier et al. (2019)
189585096	GALEXJ09348-251248	GALEXJ09348-251248	143.701	-25.213	sdB	13.044951	-0.422069	1.047	0.955	3.145	9.094	3.43	Mickaëlian (2008)
207085743	JL251	JL251	23.053	-49.561	sDO	14.297598	-0.350369	0.950	1.053	4.186	9.246	10.17	Németh et al. (2012)
209393544	EC21390-2930	TYC6952-17-1	325.487	-29.275	sdB+F	12.802671	-0.350422	1.677	0.596	3.926	10.106	10.1	Rodríguez-López et al. (2007)
229751806	2MASSJ18424506+6956202	HS1843+6953	280.688	69.939	sdB	15.237090	-0.344561	0.619	1.616	4.194	8.622	8.08	Kilkenny et al. (2016)
240946701	2MASSJ01335301+5005132	"	18.471	50.087	sd	14.954076	-0.093790	1.021	0.979	5.000	7.641	7.44	Edelmann et al. (2003)
258826647	HS1909+7004	HS1909+7004	287.227	70.159	sdB	15.478670	-0.279844	0.416	2.403	3.575	8.362	8.49	Geier et al. (2019)
259257018	2MASSJ000231.3+425310	CRTSJ000231.3+425310	0.63	42.886	sd	14.322986	-0.226666	0.926	1.080	4.156	6.193	3.74	Østensen et al. (2010a)
260369118	GALEXJ06206-5705	"	95.161	-57.094	sDOB	14.669856	-0.341110	0.869	1.151	4.365	8.955	6.01	Geier et al. (2019)
270491267	2M1529+7011	2MASSJ15292631+701154370	232.36	70.198	sd	12.444365	-0.359034	1.981	0.505	3.929	9.543	4.79	Mickaëlian (2008)
279373920	TYC4470-864-1	TYC4470-864-1	324.573	72.186	sd	11.331290	-0.289723	1.460	0.685	2.152	5.231	11.24	Geier et al. (2019)
312220636	2MASS05534886+3256017	2MASS05534886+3256017	88.454	32.934	sdB	14.134800	-0.068189	1.460	0.685	4.956	8.035	8.48	Lei et al. (2018)
322550178	2MASSJ06125523+5750507	"	93.23	57.848	sd	15.785784	-0.236645	0.609	1.641	4.710	8.712	3.09	Geier et al. (2019)
333419799	2MASSJ23354250+3944269	HS2333+3927	353.927	39.741	sdB+dM	14.565003	-0.288353	0.848	1.179	4.207	7.031	4.12	Heber et al. (2004)
409649971	GALEXJ175340.57-500741.80	"	268.419	-50.128	sdB+FTV	12.893204	0.441393	1.249	0.801	3.375	8.460	2.18	Németh et al. (2012)
423761655	EC01578-1743	GD1068	30.055	-17.479	sdB	12.023732	-0.364106	3.510	0.285	4.750	10.262	6.19	Kilkenny et al. (2016)
436579904	KUV04421+1416	KUV04421+1416	71.237	14.364	sdBVp	14.948787	0.367522	1.441	0.694	5.742	9.106	9.54	paper II
466277784	GALEXJ20228-6525	"	305.713	-65.423	sdB	13.283801	-0.328036	1.662	0.602	4.387	9.105	14.37	Koen et al. (1999)
52078744	GALEXJ01077-6707	"	16.941	-67.128	sdB	13.915939	-0.254942	1.397	0.716	4.642	10.325	23.67	O'Donoghue et al. (2013)
1672501769	GAIA DR2 5266468802206471296	"	97.502	-71.894	sd	14.247365	-0.242032	1.089	0.919	4.432	8.590	3.83	Kilkenny et al. (2016)
268722844	GAIA DR2 2208678999172871424	"	347.643	65.009	sd	14.590969	0.117362	1.366	0.732	5.268	9.915	4.89	Geier et al. (2019)
274949927	WISEJ003429.0+733329	"	8.621	73.558	sd	14.594332	0.087897	1.293	0.773	5.153	8.538	7.01	Geier et al. (2019)
202125132	LAMOSTJ001655.344+511349.7	"	4.230	51.230	sd	16.327900	-0.195572	0.468	2.136	4.680	10.442	6.50	Geier et al. (2019)
122889490	GAIA DR2 2118607522015143936	"	278.267	46.618	sd	15.698741	-0.312881	1.433	0.698	6.481	11.739	1.70	Geier et al. (2019)
360026652	J194649.77+395937.3	GAIA DR2 2073337845177375488	296.708	39.994	sd	14.381372	-0.156038	0.836	1.196	3.993	10.387	10.83	Geier et al. (2019)
96951246	J074.5735+30.3930	GAIA DR2 156955941997427456	74.574	30.593	sd	15.701506	0.311461	0.951	1.052	5.592	10.930	3.82	Geier et al. (2019)
202836039	GAIA DR2 391484413605892096	"	8.422	49.670	sd	16.094654	-0.179298	0.511	1.958	4.635	8.911	6.74	Geier et al. (2019)
367014246	J077.5424+30.1127	GAIA DR2 156174219292702624	77.542	30.113	sd	15.741088	0.230632	0.869	1.150	5.437	7.727	2.75	Geier et al. (2019)
295895179	J004.2697+53.7150	GAIA DR2 2184734315978100096	304.270	53.715	sd	16.325329	0.030304	0.635	1.574	5.340	9.917	5.11	Geier et al. (2019)
5051080	TYC5977-517-1	"	109.919	-21.889	sdB	12.131400	-0.357847	2.822	0.354	4.384	9.293	3.45	Geier et al. (2019)
12379252	GAIA DR2 2333936291513550336	TonS138	001.290	-26.530	sdB	15.990884	-0.372682	0.461	2.168	4.311	7.843	6.36	Sahoo et al. (2020)
386644511	GAIA DR2 3573130082641947392	PG1145-135	177.050	-13.772	sd	14.255842	-0.338502	0.986	1.014	4.225	9.982	12.57	Sahoo et al. (2020)
265124418	GAIA DR2 6366169442902410368	JL24	293.905	-76.804	sdB	15.260036	0.011702	0.798	1.253	4.771	10.978	5.02	Sahoo et al. (2020)
86141703	GAIA DR2 6724092123091015552	"	271.718	-43.559	sd	13.453639	-0.198243	1.300	0.769	4.023	10.064	4.28	Sahoo et al. (2020)

Table A.4. continued.

TIC number	name	alternative name	RA [deg]	DEC [deg]	classification	G [mag]	$B_p - R_p$ [mag]	parallax [mas]	distance [kpc]	G_{abs} [mag]	reduced pm	period [h]	reference ^a
37004041	GAIA DR2 2911497105202950400	"	0901.499	-25.198	sd	15.138751	-0.341063	0.674	1.483	4.283	8.304	6.80	Sahoo et al. (2020)
63113578	GAIA DR2 2921050693020996864	"	104.606	-25.415	sd	11.487005	0.229303	2.693	0.371	3.638	5.793	11.65	Sahoo et al. (2020)
32302937	GAIA DR2 3040772322279673472	"	117.391	-09.096	sd	14.247949	-0.293413	0.849	1.177	3.893	7.644	6.28	Sahoo et al. (2020)
73238638	GAIA DR2 3083216116810048768	J08032076-0039394	120.837	-00.661	sd	15.307982	-0.394972	0.471	2.121	3.675	7.652	3.30	Sahoo et al. (2020)
170310610	GAIA DR2 5434436383219257472	"	151.133	-35.062	sd	14.031923	-0.268618	1.100	0.909	4.239	9.303	19.51	Sahoo et al. (2020)
775878600	GAIA DR2 5561999385810491264	"	102.726	-44.265	sd	15.300258	-0.260799	1.035	0.966	5.375	12.533	4.24	Sahoo et al. (2020)
1036707862	GAIA DR2 5878535306051735424	"	218.251	-61.355	sd	15.063677	0.222188	1.478	0.676	5.912	9.258	7.26	Sahoo et al. (2020)
4161582	GAIA DR2 88025005422941440	LAMOST J073756.25+311646.5	114.484	+31.280	sdB	13.553999	-0.257770	1.289	0.776	4.105	10.202	6.18	Baran et al. (2021a)
406417817	GAIA DR2 1831343410431617920	"	308.210	+24.1193	sd	14.702023	-0.069664	0.885	1.129	4.438	10.087	4.82	Baran et al. (2021a)
397552904	GAIA DR2 2303705631625361024	"	316.637	+85.090	sd	12.870154	0.105246	0.902	1.109	2.646	5.258	10.09	Baran et al. (2021a)
609725827	GAIA DR2 264551735705888384	"	004.155	+78.922	sd	16.536114	-0.166992	0.384	2.603	4.458	9.264	2.56	Baran et al. (2021a)
32302937	GAIA DR2 3040772322279673472	"	117.391	-09.096	sd	14.247949	-0.293413	0.849	1.177	3.893	7.644	6.28	Geier et al. (2019)
37118148	GAIA DR2 2909497952544966272	"	090.666	-28.769	sd	14.271790	-0.261527	1.161	0.861	4.596	8.979	6.42	Geier et al. (2019)
65145461	GAIA DR2 30618984417753216	"	112.588	-02.108	sd	15.541340	-0.244382	0.614	1.629	4.482	6.559	2.79	Geier et al. (2019)
83081722	GAIA DR2 5526271511387514880	"	125.329	-43.615	sd	16.373169	0.431673	0.570	1.753	5.154	5.948	3.98	Geier et al. (2019)
102332341	GAIA DR2 5416091856344970880	"	154.574	-42.595	sd	15.532931	-0.21985	0.659	1.517	4.628	11.581	2.51	Geier et al. (2019)
108121382	GAIA DR2 5611820525418596608	"	111.946	-28.733	sd	16.240723	-0.030918	0.438	2.281	4.450	8.879	4.96	Geier et al. (2019)
123027362	GAIA DR2 5511191365810066176	"	113.398	-44.101	sd	15.921090	0.197431	0.470	2.125	4.284	8.431	3.40	Geier et al. (2019)
146117756	GAIA DR2 5546533513520296192	"	123.417	-33.947	sd	13.890878	-0.204649	1.398	0.715	4.618	10.701	2.52	Geier et al. (2019)
148044670	GAIA DR2 5576826952945841408	"	100.2231	-38.416	sd	15.530023	-0.306595	0.544	1.837	4.209	9.772	7.44	Geier et al. (2019)
154909544	GAIA DR2 5596751409325049856	"	122.670	-29.364	sd	15.046183	-0.206454	0.764	1.309	4.461	9.405	3.05	Geier et al. (2019)
170100070	CRS J064417.6-464020	"	101.074	-46.672	sd	15.329434	-0.272529	0.605	1.652	4.239	8.497	7.60	Geier et al. (2019)
270809851	GAIA DR2 3153962921190111744	"	105.150	+06.940	sd	15.968775	-0.162899	0.628	1.593	4.958	9.033	3.16	Geier et al. (2019)
283497784	GAIA DR2 56473038272723088	"	128.373	-26.167	sd	16.046017	-0.367107	0.376	2.663	3.919	9.716	2.87	Geier et al. (2019)
356837752	GAIA DR2 5296462581763471104	"	135.468	-65.037	sd	16.200062	-0.106041	0.576	1.735	5.004	10.256	6.34	Geier et al. (2019)
332831934	GAIA DR2 30105159958663287424	"	084.560	+10.765	sd	16.415363	0.181255	0.864	1.157	6.099	9.875	25.1	Geier et al. (2019)
366656123	2MASS J08412266+0630294	"	130.344	+06.508	sd	14.809977	-0.375967	0.758	1.319	4.209	7.325	8.08	Geier et al. (2019)
371016851	GAIA DR2 524348268698229376	"	146.604	-69.641	sd	14.370837	0.233464	1.042	0.960	4.460	9.811	5.8	Geier et al. (2019)
415143942	GAIA DR2 561570808498439488	"	114.650	-23.896	sd	15.152763	-0.150249	0.719	1.391	4.436	7.943	2.67	Geier et al. (2019)
415224879	GAIA DR2 5716391812157166336	"	114.693	-19.528	sd	13.484192	-0.405651	1.100	0.909	3.692	6.267	5.16	Geier et al. (2019)
405300501	GAIA DR2 5709912046530451840	"	128.513	-16.288	sd	15.327970	-0.064170	0.732	1.366	4.651	8.282	32.95	Geier et al. (2019)
468928859	SDSS J075314.03+11240.1	"	118.308	+11.211	sd	15.587963	-0.346142	0.479	2.088	3.990	8.708	6.39	Geier et al. (2019)
803870626	GAIA DR2 3083335826137398400	"	122.435	-00.564	sdB	16.227335	-0.399355	0.469	2.130	4.585	8.549	6.35	Geier et al. (2019)
56124677	SDSS J044246.86-071654.4	"	070.695	-07.282	sd	14.565370	-0.196526	0.875	1.143	4.274	9.502	2.46	Geier et al. (2019)
59896227	GAIA DR2 5560591014496851584	"	110.464	-41.986	sdB	15.900676	0.316098	0.622	1.608	4.870	6.454	4.98	Geier et al. (2019)
63202939	GAIA DR2 5610452114472366208	"	104.854	-27.972	sdB	15.189713	0.059291	0.771	1.297	4.626	10.357	3.09	Geier et al. (2019)
430960919	KPD 2215+5037	"	334.337	50.883	sdB	13.727200	-0.220415	1.588	0.630	4.732	9.051	7.39	Kilkenny & Stone (1988)
352480413	EC 21313-7301	JL82	324.01	-72.81	sdBV+dM	12.341767	-0.340793	2.273	0.440	4.125	9.306	17.6	Koen (2009)
142200764	HE0230-4323	HE0230-4323	38.228	-43.174	sdBVp	13.720080	-0.331779	1.151	0.869	4.026	8.575	10.81	Kilkenny et al. (2010)
436579904	V1405Or	KUV04421+1416	071.237	+14.364	sdBV+dM	14.948787	-0.367522	1.441	0.694	5.742	9.106	9.55	Reed et al. (2020)
138618727	Feige48	GAIA DR2 859683853719128192	176.810	61.259	sdBV	13.412467	-0.401045	1.264	0.791	3.921	10.566	8.25	Reed et al. (2004)
229050493	GALEX J222058-3141	TYC7489-686-1	331.466	-31.685	sdB	12.333248	-0.353193	2.585	0.387	4.395	9.138	8.2	Latour et al. (2014)
K2 246023959	PHL 457	"	349.852	-08.877	sdB+dM	12.919305	-0.386751	1.927	0.519	4.344	9.102	7.51	Németh et al. (2012)
137306463	KBS13	KIC1868650	291.539	+37.336	sdB+dM	13.594062	-0.304792	1.717	0.582	4.768	8.399	7.02	Schaffenroth et al. (2014a)
14959862	CPD-64481	CPD-64481	86.997	-64.384	sdB+dM	11.266701	-0.419136	4.396	0.228	4.482	8.601	6.65	Schaffenroth et al. (2014a)
384992041	GALEX J032139.63+472718.83	C1Mc lotte 20488	50.415	47.455	sdB+dM	11.561150	-0.112490	3.800	0.263	4.460	10.426	6.39	Schaffenroth et al. (2014a)
186484490	J012022+395059	'FBSO117+396'	020.096	+39.850	sdBV+dM	15.391892	-0.358782	0.569	1.757	4.168	6.978	6.048	Németh et al. (2012)
95526898	PG1329+159	Feige81	202.973	15.688	sdB+dM	13.485176	-0.396293	1.236	0.809	3.945	10.733	5.99	Østensen et al. (2013)
279494178	BPS CS 22169-0001	"	059.097	-15.155	sdB	12.833820	-0.401266	1.443	0.693	3.630	5.134	5.99	Maxted et al. (2001)
333419799	2MASS J23354250+3944269	HS2333+3927	353.927	39.741	sdB	14.565003	-0.288353	0.848	1.179	4.207	7.031	4.12	Schaffenroth et al. (2014a)
458785169	UVEX J032855.25+503529.8529.8	Lam30	52.23	50.592	sdB+dM	14.152331	0.127456	1.712	0.584	5.320	8.415	2.64	Heber et al. (2004)
466277784	EC20182-6534	GALEX J202228-6525	305.714	-65.422	sdB	13.283801	-0.328036	1.662	0.602	4.387	9.105	14.37	Kupfer et al. (2015)

Table A.4. continued.

TIC number	name	alternative name	RA [deg]	DEC [deg]	classification	G [mag]	$B_p - R_p$ [mag]	parallax [mas]	distance [kpc]	G_{abs} [mag]	reduced pm	period [h]	reference ^d
FFI	PG1017-086	"	155.060	-08.896	sdB	14.379933	-0.383316	0.883	1.133	4.109	9.283	1.75	Kupfer et al. (2015)
K2 246387816	EQ Psc	"	353.644	-01.327	sdB	13.017534	-0.331545	2.383	0.420	4.903	11.006	19.22	Jeffery & Ramsay (2014)
6116091	GAIA DR2 6196248648201755904	HE1318-2111	200.315	-21.455	sDO	14.678945	-0.305944	0.706	1.416	3.923	7.862	11.71	Sahoo et al. (2020)
428683815	EC11575-1845	"	180.023	-19.034	sDO	13.086413	-0.263646	2.138	0.468	4.737	8.654	7.87	Chen et al. (1995)
HW Vir systems													
165797593	2M0808+3202	CRTSJ080826.6+320230	122.111	32.042	sd	13.780928	-0.322651	1.205	0.830	4.185	8.976	8.87	Scharifnoth et al. (2019)
259864042	EC02406-6908	EC02406-6908	40.325	-68.924	sdB	14.648366	-0.354427	0.933	1.072	4.497	9.071	11.04	Kilkenny et al. (2015)
271164763	KIC09472174	TYC3556-3568-1	294.636	46.066	sdBYg+dM	12.114145	-0.344645	2.441	0.410	4.052	6.288	3.02	Baran et al. (2021b)
365213081	2MASSJ20463817+5147357	KPD2045++5136	311.659	51.793	sdB	15.228562	0.177142	0.931	1.074	5.074	9.859	2.15	Øksens et al. (2010b)
396004353	GALEXJ14019-7513	EVR-CB-0003	210.481	-75.226	sdB	13.511192	-0.239632	1.767	0.566	4.747	10.33	3.16	Kilkenny & Stone (1988)
408187719	HE0516-2311	HE0516-2311	79.529	-23.146	sdB	15.890226	-0.355661	0.416	2.403	3.987	9.193	2.19	Scharifnoth et al. (2019)
139266474	EC23068-4801	"	347.431	-47.758	sdB	15.363094	-0.387761	0.695	1.439	4.573	10.971	6.34	Scharifnoth et al. (2019)
345449417	HS0349+0700	HZ5	57.93	7.157	sdB	14.395279	-0.094592	1.405	0.712	5.133	9.385	1.57	Kilkenny et al. (2016)
4996778	GAIA DR2 4508520908288492672	"	277.816	13.755	sd	15.155028	-0.136569	0.567	1.765	3.921	5.807	4.74	Edelmann et al. (2003)
281048821	J286.6485+28.1219	"	286.6485	+28.1219	sd	15.643991	-0.121305	0.637	1.570	4.665	10.302	2.69	Geier et al. (2019)
1957912171	J316.0059+34.6100	"	316.0059	+34.6100	sd	17.398054	-0.131012	0.160	6.262	3.415	9.913	2.64	Scharifnoth et al. (2019)
322390461	GAIA DR2 2219505890166498048	"	326.736	66.26855	sd	16.205957	0.371214	0.680	1.471	5.367	10.871	4.84	Scharifnoth et al. (2019)
441613385	VSX075328.9+722424	"	118.370	72.407	sdB	16.480227	-0.210146	0.376	2.662	4.354	9.295	5.085	Baran et al. (2021b)
2003333263	J331.6658+32.7267	"	331.6666	+32.727	sd	16.921835	-0.149397	0.304	3.287	4.338	9.566	5.29	Pribulla et al. (2013)
944066506	J309.1155+22.8396	"	309.116	23.840	sd	16.967440	-0.073616	0.412	2.425	5.044	10.633	8.63	Scharifnoth et al. (2019)
76760933	GAIA DR2 6652952415078798208	"	270.707	55.550	sd	13.832330	-0.275429	0.529	1.890	2.450	8.786	8.67	Sahoo et al. (2020)
258379678	CRTS J120928.2-435809	"	182.368	-43.969	sd	15.336974	-0.197598	0.621	1.611	4.301	10.951	4.17	Sahoo et al. (2020)
33743252	GAIA DR2 2943004023214007424	"	093.197	-17.675	sd	13.994193	-0.240567	1.198	0.835	4.387	7.755	11.73	Sahoo et al. (2020)
42566802	J096.6239+02.8462	"	096.624	-02.846	sdB	16.009615	0.038681	0.535	1.868	4.653	5.848	4.77	Scharifnoth et al. (2019)
308541002	GAIA DR2 5289914135324381696	"	121.206	-61.559	sd	16.539120	-0.122172	0.420	2.379	4.657	12.216	5.20	Sahoo et al. (2020)
818308005	GAIA DR2 5518740367833012224	"	120.006	-47.274	sd	17.446575	-0.012293	0.076	13.141	1.853	10.763	4.92	Sahoo et al. (2020)
356085716	PG 1628+181	"	306.312	+18.022	sdB	15.729773	-0.270555	0.628	1.591	4.364	9.654	7.43	Baran et al. (2021a)
459182998	GAIA DR2 1131845039229607680	"	137.582	+78.173	sd	16.141058	-0.402	2.487	2.487	4.163	9.755	5.63	Baran et al. (2021a)
1400704733	GAIA DR2 141171518648285056	"	268.790	+54.158	sd	16.99810	-0.351522	0.292	3.419	4.330	10.760	8.73	Baran et al. (2021a)
1979105817	J306.3118+58.8522	"	306.312	+58.852	sd	17.534945	-0.132929	0.385	2.599	5.461	7.687	4.93	Scharifnoth et al. (2019)
2051607908	GAIA DR2 2283172389416472320	"	350.260	+80.125	sd	17.622341	-0.023394	0.355	2.817	5.373	10.345	8.84	Baran et al. (2021a)
1684897611	GAIA DR2 452743855589780352	"	272.241	+19.402	sd	17.549710	-0.284513	0.191	5.249	3.949	10.911	7.90	Baran et al. (2021a)
34264736	GAIA DR2 2993468995592753920	"	094.761	-14.287	sd	15.907853	-0.074766	0.527	1.896	4.518	7.839	4.22	Geier et al. (2019)
11197405	J084.4719+00.8239	"	084.472	-00.824	sdB	15.181983	-0.070962	0.803	1.245	4.706	6.987	1.81	Scharifnoth et al. (2019)
51431668	J129.0542+08.0399	"	129.054	-08.040	sdB	15.280132	-0.367052	0.507	1.972	3.805	8.659	3.13	Scharifnoth et al. (2019)
139397815	GAIA DR2 2969438206889996160	"	079.949	-19.282	sdB	13.594079	-0.349399	1.077	0.929	3.754	6.130	6.59	Geier et al. (2019)
139785230	J112.2726+18.6176	"	112.273	-18.618	sd	15.912261	-0.507	1.972	4.438	9.927	2.25	Scharifnoth et al. (2019)	
264749962	J109.7402+07.6536	"	109.740	+07.653	sd	15.216421	-0.404513	0.525	1.906	3.816	5.843	2.03	Scharifnoth et al. (2019)
311271081	J080.5805+10.6719	"	080.581	+10.672	sd	14.472228	0.258853	1.450	0.690	5.278	8.708	1.48	Scharifnoth et al. (2019)
317804295	J089.3714+14.1662	"	089.371	-14.166	sd	15.924339	-0.439569	0.977	1.023	5.874	8gAL.278	4.10	Scharifnoth et al. (2019)
425064757	AA Dor	"	082.918	-69.884	sdOB	11.009821	-0.478417	2.838	0.352	3.365	9.687	6.27	Vučković et al. (2016)
2046417955	GAIA DR2 20032421230122936	ATLASJ340	340.213	54.631	sdB	14.979544	0.011270	0.701	1.427	4.208	6.789	5.66	Scharifnoth et al. (2019)
FFI	ATLASJ283	J283.03168923859	283.03168923859	+14.76306734163	sdB	14.992987	0.239105	0.852	1.174	4.645	10.888	5.66	Scharifnoth et al. (2019)
148785530	2M1533+3759	FBS1531+381	233.456	37.991	sdB+dM	12.941533	-0.383593	1.905	0.525	4.340	9.108	3.88	Pawar (2020)
73764693	ASAS 102322-3737	TYC7709-376-1	155.841	-37.617	sdB+dM	11.692036	-0.352816	3.543	0.282	4.439	9.625	3.34	For et al. (2010)
271164763	2M1938+4603	KIC9472174	294.63591839353	+46.06640687693	sdB+dM	12.114145	-0.344645	2.441	0.410	4.052	6.288	3.02	Scharifnoth et al. (2013)
k2-e09	OGLE-BUL-SC16335	OGLE-BLG-ECL-163	272.45013125844	-26.69705718192	sdB+dM	16.544252	0.269485	0.668	1.496	5.670	6.869	2.93	Øksens et al. (2010b)
193092806	EC10246-2707	EC10246-2707	156.736	-27.383	sdB+dM	14.437633	-0.328232	1.018	0.982	4.477	8.714	2.84	Barlow et al. (2013)

Table A.4. continued.

TIC number	name	alternative name	RA [deg]	DEC [deg]	classification	G [mag]	$B_p - R_p$ [mag]	parallax [mas]	distance [kpc]	G _{abs} [mag]	reduced pm	period [h]	reference ^a
K2 228755638	HWVir	"	191.08436809847	-08.67141649181	sdB+dM	10.590079	-0.558919	5.773	0.173	4.397	6.892	2.76	Vučković et al. (2014)
175402069	PG1336.018	NYVir	204.701	-2.03	sdBVp+dM	13.366823	-0.401715	1.680	0.595	4.493	9.023	2.42	Vučković et al. (2009)
611402948	1018.4128+22.9608	PTF1011339.09+225739.1	111.232	+12.9608	sd	16.610086	-0.386513	0.422	2.369	4.737	8.927	5.60	Schaffenroth et al. (2019)
FFI	PTF1J0724+1253	"	111.232	+12.883	sdB	17.818432	-0.477533	0.240	4.167	4.719	9.503	2.40	Schindewolf et al. (2015)
99641129	H50705+6700	V*V470Cam	107.675	66.929	sdB+dM	14.616244	-0.360858	0.789	1.267	4.103	9.054	2.30	Drechsel et al. (2001)
455206965	108205+0008843.4	"	125.223	0.145	sdB+BD	15.158632	-0.351009	0.657	1.523	4.245	6.969	2.31	Schaffenroth et al. (2021)
19355713	PG1621+476	J162256+473051	245.736	47.514	sdB+BD	16.218710	-0.403603	0.551	1.814	4.926	9.412	1.68	Schaffenroth et al. (2014b)
467187065	2MASSJ19444284+5449426	ATLAS1296	296.179	54.829	sdB	15.750846	-0.233982	0.644	1.552	4.797	7.874	1.54	Schaffenroth et al. (2019)
FFI	J192059+372220	SDSSJ192059.78+372220.0	290.24904856394	+37.37221528999	sdB	15.761664	-0.141020	0.498	2.007	4.249	8.415	4.05	Schaffenroth et al. (2018)
272717401	KPD1946+4340	"	296.9287	+43.7924	Ellipsoidal + beaming systems	14.223958	-0.278768	0.852	1.174	3.876	7.482	9.69	Bloemen et al. (2011)
67598107	GD687	"	017.578	-34.000	sdOB	14.074328	-0.376294	1.205	0.830	4.479	9.878	9.06	Geier et al. (2010)
233635622	PG0941+280	"	145.977	+27.783	sdB	13.196795	-0.403038	1.532	0.653	4.122	11.372	7.46	Geier et al. (2014)
1973623	EVRCB-004	"	133.302	-28.768	sdB	13.107076	-0.271864	0.422	2.367	1.236	5.097	6.08	Ratzloff et al. (2020a)
320417198	GALEXJ0751+0925	GALEXJ075147.0+092526	117.946	+09.424	sdB	14.064508	-0.382053	1.478	0.677	4.913	9.188	4.28	Németh et al. (2012)
142491300	PG1043+760	"	161.771	+75.740	sdB	13.701308	-0.328960	1.446	0.692	4.502	4.811	2.88	Kawka et al. (2015)
FFI	EVRCB-001	"	132.065	-74.322	sdB	12.566651	-0.155235	2.207	0.453	4.286	10.072	2.34	Ratzloff et al. (2019)
8773989	KPD0422+5421	"	066.529	+54.471	sdB	14.626647	0.220573	1.507	0.663	5.518	9.625	2.16	Orosz & Wade (1999)
68495594	HD265435	"	103.351	+33.059	sdB	12.087978	-0.425845	2.167	0.462	3.767	6.204	1.65	Peisoff et al. (2021)
107548305	CD-3011223	"	212.817	-30.884	sdB	12.296151	-0.387547	2.820	0.355	4.547	6.922	1.18	Geier et al. (2013)
240326669	ZTF12130+4420	UCAC4 672-097665	322.736	+44.346	sdB	15.438982	-0.044588	0.764	1.309	4.854	6.422	0.66	Kupfer et al. (2020b)
FFI	OW10741+2948	"	115.275	-29.803	sdB	19.932531	0.013504	0.188	5.328	6.300	12.251	0.74	Kupfer et al. (2017b)
279342801	EC02200-2338	"	035.583	-23.416	sdB	11.988973	-0.404593	3.108	0.322	4.452	9.598	19.25	Kawka et al. (2015)
80427831	EC00404-4429	"	010.702	-44.224	sdB	13.637740	-0.396522	1.527	0.655	4.556	10.650	3.08	Kawka et al. (2015)
K2 201424163	J113840-003531	"	174.669	-00.592	sdB	14.423926	-0.435413	0.773	1.294	3.864	11.552	4.98	Geier et al. (2011a)
kp1r006614501	KIC6614501	"	294.208	42.0288	sdB	15.935427	-0.258789	0.792	1.262	5.430	6.052	3.78	Silvotti et al. (2012)
386703105	PG1232-136	"	188.828	-13.919	sdB	13.229093	-0.368810	2.214	0.452	4.955	11.597	8.76	Edelmann et al. (2005)
349534378	UV01735+22	"	264.360	+22.149	sdB	11.801611	-0.452375	2.281	0.438	3.592	8.495	30.67	Edelmann et al. (2005)
K2 212410755	EC13332-1424	"	203.973	-14.670	sdB	13.365768	-0.361939	1.580	0.633	4.359	9.698	19.87	Kupfer et al. (2015)
363766470	HS1741+2133	[CW83]1735+22	265.829	+21.5438	sdB	13.992819	-0.264079	1.070	0.935	4.139	9.354	4.78	Edelmann et al. (2003)
455755305	GALEXJ234947.7+384440	"	357.449	+38.745	sdB	11.715421	-0.189247	3.872	0.258	4.655	3.698	10.38	Kawka et al. (2010)
229664008	PG1512+244	"	228.635	+24.178	sdB	13.176018	-0.364226	2.170	0.461	4.858	11.138	30.48	Morales-Rueda et al. (2005)
137840206	EC22202-1834	"	335.742	-18.320	sdB	13.790620	-0.370770	1.195	0.837	4.177	10.120	16.92	Copperwheat et al. (2011)
229805551	EC21556-5552	"	329.753	-55.634	sdB	13.103904	-0.394528	2.022	0.495	4.632	6.748	20.89	Copperwheat et al. (2011)
202491630	PG1519+640	"	204.130	+63.869	sdB	12.379927	-0.423141	2.734	0.366	4.564	10.382	12.97	Copperwheat et al. (2011)
10932480	GALEXJ025023.8-040611	"	042.600	-04.104	sdB	13.002628	-0.386107	2.025	0.494	4.535	10.632	15.92	Németh et al. (2012)
193600962	PG1743+477	"	266.110	+47.696	sdB	13.734726	-0.386953	1.293	0.773	4.293	9.162	12.03	Morales-Rueda et al. (2005)
274385041	PG1648+536	"	252.499	+53.525	sdB	14.009392	-0.338769	1.172	0.853	4.354	10.726	13.02	Copperwheat et al. (2011)
9376301	PG1000+408	"	150.976	+40.572	sdB	13.249913	-0.309614	0.999	1.001	3.248	6.990	26.76	Copperwheat et al. (2011)
66493797	TONS183	"	015.323	-33.713	sdB	12.581187	-0.410837	2.048	0.488	4.138	8.605	19.87	Geier et al. (2011a)
220488137	GALEXJ225444.1-551505	"	343.686	-55.252	sdB	12.141099	-0.453845	3.384	0.296	4.788	9.584	29.25	Kawka et al. (2015)
346894954	PG0133+114	"	024.109	+11.659	sdB	12.275509	-0.344523	3.153	0.317	4.769	9.905	29.70	Morales-Rueda et al. (2005)
91986289	PG0934+186	"	144.318	+18.420	sdB	13.075914	-0.458850	1.538	0.650	4.010	9.247	97.73	Copperwheat et al. (2011)
33490778	CD-24731	"	025.952	-24.086	sdB	11.684070	-0.494827	4.334	0.231	4.869	11.611	138.74	Geier et al. (2011a)
142875987	PHL1539	"	051.643	-31.062	sdB	14.022624	-0.479381	1.076	0.930	4.181	10.142	60.11	Bell et al. (2019)
342025025	ULISge	"	295.543	+17.0873	sdO	14.974704	0.284213	0.365	2.739	2.787	9.539	11.16	Afşar & İbanoglu (2008)
423311936	V4771Yf	"	277.827	+26.937	sdO	14.957651	-0.229764	0.404	2.474	2.991	6.469	11.32	Afşar & İbanoglu (2008)
FFI	HaT7	PN HaT7	268.539	-60.833	sdO	14.829035	-0.306667	0.587	1.704	3.672	10.279	7.73	Hillwig et al. (2017)
334382552	EGB5	"	122.803	+10.955	sdO	13.775318	-0.472623	1.593	0.628	4.787	10.030	396.77	Geier et al. (2011b)
120596335	CD-486027	"	163.669	-48.785	sdO	12.135967	-0.276526	1.226	0.816	2.579	8.616	8.57	Drilling (1985)

Central stars of planetary nebula

Notes. ^a light variation analysis an/or atmospheric parameters or spectral classification.

Hot subdwarfs in close binaries observed from space II: Analyses of the light variations

V. Schaffenroth¹, B. N. Barlow², I. Pelisoli^{3,1}, S. Geier¹, and T. Kupfer⁴

¹ Institute for Physics and Astronomy, University of Potsdam, Karl-Liebknecht-Str. 24/25, 14476 Potsdam, Germany
e-mail: schaffenroth@astro.physik.uni-potsdam.de

² Department of Physics and Astronomy, High Point University, High Point, NC 27268, USA

³ Department of Physics, University of Warwick, Gibet Hill Road, Coventry CV4 7AL, UK

⁴ Department of Physics and Astronomy, Texas Tech University, PO Box 41051, Lubbock, TX 79409, USA

Received 08 August 2022; accepted 24 February 2023

ABSTRACT

Context. Hot subdwarfs in close binaries with either M dwarf, brown dwarf, or white dwarf companions show unique light variations. In hot subdwarf binaries with M dwarf or brown dwarf companions, we can observe the so-called reflection effect, while in hot subdwarfs with close white dwarf companions, we find ellipsoidal modulation and/or Doppler beaming.

Aims. Analyses of these light variations can be used to derive the mass and radius of the companion and determine its nature. Thereby, we can assume the most probable sdB mass and the radius of the sdB derived by the fit of the spectral energy distribution and the *Gaia* parallax.

Methods. In the high signal-to-noise space-based light curves from the Transiting Exoplanet Survey Satellite and the *K2* space mission, several reflection effect binaries and ellipsoidal modulation binaries have been observed with much better quality than with ground-based observations. The high quality of the light curves allowed us to analyze a large sample of sdB binaries with M dwarf or white dwarf companions using *LCURVE*.

Results. For the first time, we can constrain the absolute parameters of 19 companions of reflection effect systems, covering periods from 2.5 to 19 hours and with companion masses from the hydrogen-burning limit to early M dwarfs. Moreover, we were able to determine the mass of eight white dwarf companion to hot subdwarf binaries showing ellipsoidal modulations, covering the as-yet unexplored period range of 7 to 19 hours. The derived masses of the white dwarf companions show that all but two of the white dwarf companions are most likely helium-core white dwarfs. Combining our results with previously measured rotation velocities allowed us to derive the rotation period of seven sdBs in short-period binaries. In four of those systems, the rotation period of the sdB agrees with a tidally locked orbit, whereas in the other three systems, the sdB rotates significantly more slowly.

Key words. binaries (including multiple): close; Stars: variables: general; subdwarfs; Stars: horizontal-branch; white dwarfs; Stars: low-mass; Stars: late-type; Stars: fundamental parameters, Techniques: radial velocities

1. Introduction

Hot subdwarfs of spectral type O and B (sdO/B) are stars with temperatures from $\sim 25000 - 60000$ K and luminosities, placing them between main sequence stars and white dwarfs. Most of the sdBs are found on the extreme horizontal branch (EHB). Their formation processes are still unclear, but most of the sdBs are believed to be core-He burning objects that lost most of their envelope on the tip of the red giant branch (RGB). The H-rich sdOs are believed to be the progeny of the sdBs after the helium in the core is exhausted showing He-shell burning. Their evolution is much faster and thus they are considered to be rarer than the sdB (Heber 2009, 2016).

Pelisoli et al. (2020) suggested that the formation of typical sdBs requires binary interaction. Indeed, one-third of the sdBs is found in sdB+F/G/K type main sequence companions with periods of several hundred days (Vos et al. 2013, 2018). Another third of the sdBs is found in close binaries with low-mass main sequence stars of spectral type M close to the hydrogen burning limit or even brown dwarf companions (dM/BD) or white dwarf (WD) (Maxted et al. 2002; Kupfer et al. 2015; Schaffenroth et al. 2019) with periods of less than 1 hour to 27 days. Such short periods can only be explained by a previous common en-

velope phase Han et al. (2002, 2003). The remaining sdBs are apparently single.

The nature of the companions in many of these close sdB binaries can easily be identified by their characteristic light variations using high signal-to-noise (S/N) light curves. Close binaries with dM/BD companion show a significant quasi-sinusoidal variation over each orbit with an amplitude from a few percent up to $\sim 20\%$ (see Fig. D.1). The strength of this variation, called the reflection or irradiation effect, increases from blue to red wavelengths. It results from a large temperature difference between the sdB primary and the cooler companion, but a similar or even larger size of the secondary compared to the sdB. Due to the high irradiating flux from the sdB, one side of the companion is heated up from temperatures originally around 3000 K to temperatures from 10 000 – 20 000 K (Vučković et al. 2008; Kiss et al. 2000). Consequently, the contribution of the companion to the total system flux significantly increases when the hot side is visible. As those systems have small separations from ~ 0.5 to a few solar radii (e.g., Schaffenroth et al. 2014b, 2015, 2021), a significant percentage of them also show eclipses. These are referred to as HW Vir binaries (after the prototype system). Both the shape and strength of the reflection effect depend strongly

on the orbital inclination (Schaffenroth et al. 2014a) and so light curves with sufficient S/N can be used to constrain system parameters, even without eclipses.

Since white dwarfs are much smaller than M dwarfs or brown dwarfs, the reflection effect cannot be observed in sdB+WD systems. However, a close WD companion can cause an ellipsoidal deformation of the hot subdwarf, which leads to a quasi-sinusoidal variation with half the orbital period. The amplitude of this ellipsoidal modulation can be up to almost 10% in the most extreme cases (e.g., Maxted et al. 2000; Bloemen et al. 2011). Due to gravity darkening, the depths of the two minima are usually different, and lower flux is observed when the side of the hot subdwarf facing the companion is visible. As the orbital velocities are quite high, Doppler beaming from the hot subdwarf is also observed, resulting in more flux when it is approaching Earth than when it moves away (e.g., Geier et al. 2013; Telting et al. 2014; Kupfer et al. 2017a,b, 2022; Pelisoli et al. 2021). The amplitude is strongly scaled with the separation and the companion mass, while longer period systems (of less than a few hours) have ellipsoidal modulation amplitudes below 0.5% and can only be found in space-based light curves. This fact can also be used to distinguish between WD and dM/BD companions, when high S/N light curves are available, as the amplitude of the reflection effect is much higher and would be visible up to several days in the *TESS* light curves (see Schaffenroth et al. 2022, hereafter, Paper I). Hence, a dM/BD companion can be excluded, if no variations can be detected.

In Paper I, we used this method to determine the nature of the companion for 75% of the known close hot subdwarf binaries. Moreover, we performed a search for more sdB binaries that show a reflection effect, ellipsoidal modulation, or Doppler beaming using light curves provided by the *TESS* (Transiting Exoplanet Survey Satellite) (Ricker et al. 2015) and *K2* (Howell et al. 2014) missions. In total, we found 85 new reflection effect systems (including also systems found by Baran et al. 2021; Sahoo et al. 2020; Barlow et al. 2022), 8 new ellipsoidal systems, and 16 systems showing Doppler beaming in the light curve, in addition to the 17 reflection effect and 11 ellipsoidal systems already known.

In this paper, we present the analysis of 19 sdB+dM/BD systems showing a reflection effect and 25 sdB+WD systems showing ellipsoidal modulation or Doppler beaming. In Sect. 2, we discuss the target selection and data sources. In Sect. 3, we discuss the analysis of the sdB binaries with cool, low mass companions. In Sect. 4, we discuss the analysis of the sdB with white dwarf companions. In Sect. 5, we give a short summary and a discussion of the results.

2. Target selection and data sources

We selected all sdB binaries with radial velocity curves published in the literature, which were observed by *TESS* or *K2* and show light variations indicating a hot subdwarf binary. In the case of sdB+dM systems, we only focused on the non-eclipsing systems. Moreover, we also included three bright sdB binaries for which we could obtain spectroscopic follow-up. All light curves were downloaded, phase-folded to the orbital period determined by a periodogram around the orbital period known from radial velocity (RV) variations, and binned using the Python package LIGHTKURVE (Lightkurve Collaboration et al. 2018)¹.

¹ <https://docs.lightkurve.org>

3. Cool, low mass companions to sdB stars

3.1. Method

The presence of a reflection effect indicates a cool, low-mass companion of similar size in close orbit with the hot subdwarf. Without eclipses, it is difficult to determine the inclination of the system, as the amplitude is degenerate in inclination and size of the companion (Schaffenroth et al. 2014a). In that paper, the authors also showed that the shape of the reflection effect changes with inclination, suggesting that it might be possible for high-quality light curves to provide tight constraints on the inclination angle even without eclipses. The same was also shown by Østensen et al. (2013). With the space-based light curves available from *TESS* and *K2*, this is now possible for the first time. With the light curves from the original Kepler mission, it was not possible, as only very few hot subdwarfs were observed and amongst them, only one reflection effect system showed eclipses. We analyzed all reflection effect systems with solved RV curve atmospheric parameters derived from spectroscopy and space-based light curves (19 systems in total).

For the analysis of the light curves, we used LCURVE (see Copperwheat et al. 2010, for more details) as described in Schaffenroth et al. (2021). As we did not see any eclipses, the mass ratio and the radii were not well constrained from the light curve alone. To obtain an appropriate solution, we had to make some initial assumptions.

All studied reflection effect systems are single-lined binaries. Therefore, the mass ratio cannot be determined with time-resolved spectroscopy. The sdB mass was derived by the fitting of the spectral energy distribution (SED) and combining this with the *Gaia* parallax in Paper I. However, within the framework of this paper, we see that the masses for the reflection effect systems have to be taken with caution, as the mass distribution of the HW Vir systems shows discrepancies with the distribution of the reflection effect systems. Therefore, we use the assumption of the canonical He-flash mass of $0.47 M_{\odot}$ for the sdB for this analysis and is the most likely mass of a sdB in a sdB+dM binary (Paper I, Han et al. 2002, 2003; Fontaine et al. 2012).

With this assumption and the inclination determined from the light curve analysis (which is not dependent on the mass ratio but sensitive to the light curve shape; see also Barlow et al. in prep, hereafter, Paper III), it is possible to get the mass ratio together with the separation of the system from the mass function determined by the radial velocity curve (see Table 1 for the parameters of the analyzed reflection effect systems). The effective temperature is fixed to the value derived from spectral fitting (see Paper I for a summary of all atmospheric parameters). As the contribution of the dark side of the companion to the flux is negligible, the temperature of the companion cannot be constrained and is hence fixed to a typical value for an M dwarf of 3000 K. Changes in the temperature of the companion therefore have a negligible effect on the other derived parameters. The SED fitting in combination with the *Gaia* parallax (see Paper I) provides the radius of the sdB, R_1 , and with the derived separation, a , we can set the relative radius of the sdB ($r_1 = R_1/a$), which is then used as parameter in the light curve fitting.

For simplicity, the absorption factor, which is the percentage of the flux of the sdB used to heat up the irradiated companion side using a blackbody approximation, is fixed to 1. The gravitational and limb darkening coefficients were fixed according to the tables of Claret et al. (2020b). We adopted their values closest to the atmospheric parameters for the *TESS* filter. Only the inclination and the radius of the companion were varied; all other parameters are fixed as explained above.

We performed Markov chain Monte Carlo (MCMC) computations using `emcee` (Foreman-Mackey et al. 2013) to derive the distribution of the inclination and radius of the companion and to determine the uncertainties of both parameters. We tried to vary also the radius of the sdB using a Gaussian prior. Due to the residuals in the light curves (discussed later in this paper; also, see Fig. D.1), this did not work. So, we fixed the radius of the sdB, neglecting its uncertainty. As a result, the uncertainties in i and r_2 will be underestimated. We performed several tests to quantify this by also varying the sdB radius. The uncertainty in r_2 and i doubled in our test. As the uncertainty of the separation is dominating the overall uncertainty, the increase in the uncertainty of the companion's radius can be neglected. However, doubling the uncertainty in the inclination results in 50% larger error bars in the mass ratio and companion mass and radius in our test. These results also depend on the quality of the light curve and the inclination. In the future this uncertainty will be included, when the mass of the sdB is constrained as well by the SED fit, as soon as reliable atmospheric parameters are available.

In Fig. 1, we give an example of the MCMC results. There is some degeneracy between the orbital inclination and the radius of the companion visible, but the χ^2 distribution is symmetric around the minimum, representing the best solution. Some sdBs show short-period pulsations on the order of minutes (for sdO/B with $T_{\text{eff}} > 30000$ K) and long-period pulsations of low-amplitude (for sdO/B with $T_{\text{eff}} < 30000$ K) on the order of hours (see Lynas-Gray 2021; Kupfer et al. 2019, for a summary). In some sdB binaries, we thus see a superposition of the pulsation and the binary signal, which complicates the analysis. The phasing and binning of the light curves smoothed out the pulsations present in some of the systems, however, the noise was still increased compared to the non-pulsating systems, leading to larger errors for the parameters compared to other systems with similar magnitudes. The pre-whitening of the pulsation frequencies could improve this, especially for longer period pulsations. However, a characterization of these pulsations is beyond the scope of this paper.

Due to the large pixel size, the *TESS* light curves must be treated with care, especially if bright, unresolved stars fell on the same pixel. The PDCSAP flux provided in the Science Processing Operations Center (SPOC) light curves can be used to correct for this additional flux. However, this correction is not always perfect and can lead to the amplitude of the variation being over- or underestimated. For some targets, a different amplitude in different sectors can be observed. The comparison with published light curves in other filters was used to choose the light curve with the correct amplitude. As we have discussed, the shape of the light curve is determined by the inclination. The amplitude on the other side is determined by the temperature of the primary and the orbital separation derived by time-resolved spectroscopy, as well as the radius of the companion. An overestimated amplitude would therefore result in an overestimated radius for the companion. We checked the field of view for *TESS* and the CROWDSAP parameter for all our targets. With the exception of HS2333+3927 and TYC5977-517-1, the CROWDSAP parameter was close to 1, showing that no stars are blending into the target pixel and, hence, no correction of the amplitude of the variation by the *TESS* team was necessary.

3.2. Results of the light curve analysis

To investigate the blending effect on the results further, we had a closer look at the *TESS* light curve of HS2333+3927.

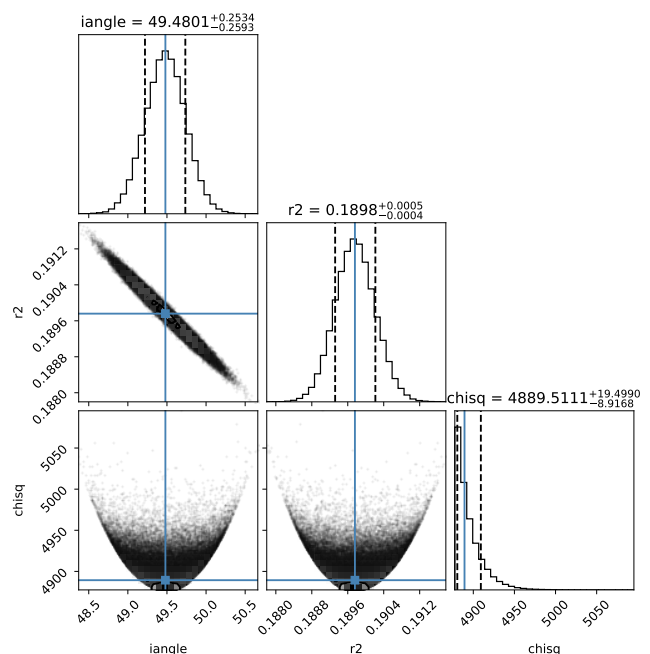


Fig. 1: Corner plot of the MCMC calculations of EC 01578-1743 showing the distribution of the orbital inclination (i angle), the radius of the companion (r_2), and the χ^2 ($chisq$).

TESS observed this system in two different sectors (sector 16/17; CROWDSAP=0.78/0.75). The amplitude in the first sector is about 10% larger. We chose the light curve from the second sector, as the amplitude of the reflection effect of the first sector (50%) is much larger than the amplitude expected for the *TESS* filter compared to the observations by Heber et al. (2004) in B (20%), V (25%), and R (30%). This indicates that the light curve of the first sector seems to be overcorrected. The analysis of the *TESS* light curve from sector 17 (see Fig. D.1o) can confirm the results of Heber et al. (2004), showing that the correction can be trusted in this case, as we suspected.

To check the influence of an amplitude too large, we also fit the light curve from sector 16. We get the same inclination but a radius of $0.47 \pm 0.02 R_{\odot}$, which is 17% larger than the companion radius determined by the light curve of the other sector. As expected, the higher amplitude does not affect the determination of the inclination but will lead to a higher companion radius. Fortunately this affects only two of our targets, as discussed before. A more detailed discussion on the other object is given in Sect. 3.3.1.

When investigating the residuals of our highest S/N light-curve fits (see Fig. D.1), we can see a recurring pattern that grows in strength with increasing inclination. For example, the residuals for GALEX J0321+4727 and EC 01578-1743 show that the fit overestimates the flux right at the moment the reflection effect peaks, but immediately underestimates the flux on either side of the peak. The inability of the LCURVE models to fit the reflection effect shape precisely in this region reveals the limitations of the reflection effect model and the way it handles irradiation. The models improve with smaller sdB radii, suggesting that the illumination of the side of the companion facing the hot subdwarf is not homogeneous. This effect is very small (on the order of 0.25-0.5%) compared to the amplitude of the reflection effect (5-20%). Hence, we do not expect that this will have a substantial impact on the results.

Table 1: Orbital parameters of the solved reflection effect systems with space-based light curves from time-resolved spectroscopy and the analysis of the light curve. The objects are ordered according to their inclination.

target	P_{RV} [d]	γ [km s ⁻¹]	K_1 [km s ⁻¹]	$P_{lc,TESS/Kepler}^*$ [d]
BPSCS22169-0001 ^d	0.214	-	16.2 ± 0.5	0.216895
PHL457 ^d	0.3128 ± 0.0007	-	12.8 ± 0.08	0.313012
KBS13 ^d	0.2923 ± 0.0004	7.53 ± 0.08	22.82 ± 0.23	0.292365
Feige48 ^e	0.343608 ± 0.0000005	-47.9 ± 0.1	28.0 ± 0.2	0.343608
GALEXJ2205-3141 ^c	0.341543 ± 0.000008	-19.4 ± 1.7	47.8 ± 2.2	0.341552
GALEXJ09348-2512 ^a	0.1429032 ± 0.0000011	50.6 ± 2.1	37 ± 4	0.142903
EQ Psc ^b	0.800880 ± 0.000097	25.9 ± 1.3	34.9 ± 1.6	0.800970
PG1329+159 ^d	0.249699 ± 0.0000002	-22.0 ± 1.2	40.2 ± 1.1	0.249696
CPD-64481 ^d	0.277263 ± 0.000005	94.1 ± 0.3	23.9 ± 0.05	0.277264
JL82 ^d	0.73710 ± 0.00005	-1.6 ± 0.8	34.6 ± 1.0	0.733799
TYC5977-517-1 ^a	0.14387147 ± 0.0000025	-	87 ± 2	0.143871
GALEXJ0321+4727 ^c	0.265856 ± 0.000003	69.6 ± 2.2	60.8 ± 4.5	0.265857
SDSSJ012022+395059 ^d	0.252013 ± 0.000013	-47.3 ± 1.3	37.3 ± 2.8	0.251975
UVEX0328+5035 ^d	0.11017 ± 0.00011	44.9 ± 0.7	64.0 ± 1.5	0.110163
HS2333+3927 ^d	0.1718023000 ± 0.0000009	-31.40 ± 2.1	89.60 ± 3.2	0.171801
V1405Ori ^d	0.398	-33.6 ± 5.5	85.1 ± 8.6	0.398005
HE1318-2111 ^d	0.487502 ± 0.0000001	48.9 ± 0.7	48.5 ± 1.2	0.487424
EC01578-1743 ^a	0.2581015 ± 0.0000025	-23.19 ± 0.4	86.5 ± 0.5	0.258104
HE0230-4323 ^d	0.45152 ± 0.00002	16.6 ± 1.0	62.4 ± 1.6	0.450029

^a this paper ^b Baran et al. (2019) ^c Németh et al. (2012); Kawka et al. (2015) ^d Kupfer et al. (2015, and references therein) ^e Latour et al. (2014) * typical error 0.0001 d

Table 2: Inclination, separation, and mass ratio of the analyzed reflection effect systems, together with the calculated mass and radius of the companion.

target	i [°]	q	a [R _⊙]	M_2 [M _⊙]	R_2 [R _⊙]	P_{rot} [d]
BPSCS22169-1	7.7 ± 1.1	0.492 ± 0.132	1.35 ± 0.30	0.231 ± 0.062	0.309 ± 0.072	0.16 ± 0.04
PHL457	9.3 ± 1.6	0.416 ± 0.085	1.69 ± 0.37	0.196 ± 0.040	0.157 ± 0.035	-
KBS13	10.1 ± 0.4	0.552 ± 0.038	1.040 ± 0.063	0.260 ± 0.018	0.284 ± 0.020	-
Feige48	16.3 ± 1.4	0.495 ± 0.089	1.83 ± 0.30	0.232 ± 0.042	0.266 ± 0.044	0.36 ± 0.07
GALEXJ2205-3141	17.3 ± 2.6	1.12 ± 0.21	2.05 ± 0.36	0.527 ± 0.100	0.419 ± 0.075	-
GALEXJ09348-2512	24.0 ± 3.0	0.351 ± 0.099	0.99 ± 0.26	0.165 ± 0.046	0.175 ± 0.048	-
EQPsc	25.4 ± 0.5	0.724 ± 0.073	3.07 ± 0.24	0.222 ± 0.019	0.181 ± 0.014	-
PG1329+159	31.8 ± 2.1	0.356 ± 0.037	1.44 ± 0.15	0.167 ± 0.018	0.199 ± 0.021	0.64 ± 0.07
CPD-64481	34.3 ± 2.2	0.187 ± 0.012	1.473 ± 0.12	0.088 ± 0.006	0.118 ± 0.010	1.22 ± 0.30
JL82	34.6 ± 1.1	0.511 ± 0.043	3.06 ± 0.22	0.240 ± 0.020	0.249 ± 0.018	0.61 ± 0.07
TYC5977-517-1	35.0 ± 0.25	0.678 ± 0.026	1.07 ± 0.034	0.319 ± 0.012	0.380 ± 0.013	-
GALEXJ0321+4727	38.6 ± 0.9	0.495 ± 0.060	1.55 ± 0.17	0.233 ± 0.028	0.298 ± 0.033	-
SDSSJ012022+395059	39.9 ± 7.0	0.343 ± 0.070	1.44 ± 0.36	0.16 ± 0.033	0.242 ± 0.063	-
UVEX0328+5035	41.4 ± 0.5	0.341 ± 0.012	0.83 ± 0.03	0.160 ± 0.006	0.250 ± 0.010	-
HS2333+3927	42.8 ± 0.5	0.609 ± 0.017	1.18 ± 0.05	0.388 ± 0.017	0.401 ± 0.017	-
V1405Ori	43.0 ± 0.9	0.829 ± 0.141	2.17 ± 0.30	0.390 ± 0.066	0.341 ± 0.047	-
HE1318-2111	48.5 ± 1.7	0.335 ± 0.018	2.23 ± 0.11	0.158 ± 0.008	0.277 ± 0.014	-
EC01578-1743	49.5 ± 0.25	0.591 ± 0.009	1.548 ± 0.013	0.278 ± 0.004	0.294 ± 0.003	-
HE0230-4323	52.6 ± 1.5	0.470 ± 0.027	2.18 ± 0.11	0.221 ± 0.013	0.309 ± 0.016	-

Tables 1 and 2 offer a summary of all derived parameters. The period derived from the RV curve and the light curve agree very well in most cases. As the *TESS* is covering at least 27 d continuously, the period from the light curve is more trustworthy and the error on the period from the RV curve taken from the literature might be underestimated in some cases. All companions are likely M dwarf companions, with masses from 0.088 to 0.5 M_⊙. For five systems with published rotational velocities, we were also able to derive the rotational period by combining the velocity with the inclination and radius derived in Paper I

($P_{rot} = \frac{2\pi R \sin i}{v_{rot} \sin i}$). We find that the sdB is rotating significantly (with more than three sigma) slower than the orbital period in three systems. More details on the individual systems can be found in the appendix in Sect. A. In the subsections that follow, we introduce and discuss the newly discovered reflection effect systems.

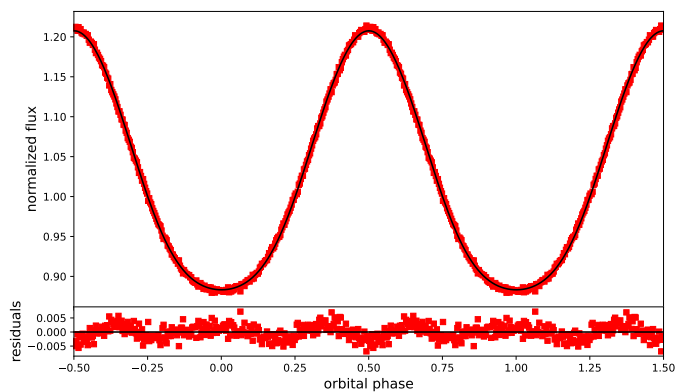


Fig. 2: Phased *TESS* light curve of TYC5977-517-1 (given by the red squares) together with the best-fit model given by the black line. Lower panel shows the residuals.

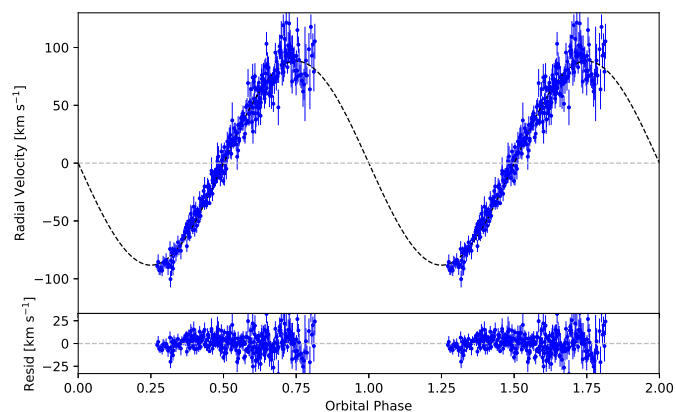


Fig. 3: Radial velocity curve of TYC5977-517-1 phased to the orbital period. Black line is the best-fit model. Blue dots display the data, including the uncertainties.

3.3. Newly discovered reflection effect systems

3.3.1. TYC5977-517-1

TYC5977-517-1 was identified as a hot subdwarf candidate in the *Gaia* catalogue of hot subluminal star candidates (Geier et al. 2019). It was also reported to be an eclipsing contact binary candidate in the ATLAS survey (Heinze et al. 2018). By inspecting the *TESS* light curve (see Fig. 2) we discovered that it is not, in fact, an eclipsing binary but, instead, a reflection effect binary with a period of 0.14387147 d. We obtained time-series spectroscopy with the Goodman spectrograph on the SOAR telescope over three consecutive nights in June 2019, taking 67, 120, and 113 spectra each night. Each spectrum had an integration time of 30 s and each series had a cycle time of ≈ 42 s. Since the target was setting for the season and only visible for the first 1.25 hr, we could only follow it for one-third of its orbit each night. Unfortunately, its nearly integer-value orbital frequency ($6.95 d^{-1}$) meant our starting observing phase did not drift much night to night and, in total, our spectra only cover just over half of the orbit. Nonetheless, we successfully derived the RV curve ($K_1 = 87 \pm 2 \text{ km s}^{-1}$, see Fig. 3 and Table C.1). This was possible due to fact that the orbital period could be determined by photometry. To derive the atmospheric parameters, we fit the hydrogen and helium lines of this spectrum with synthetic spectra calculated by a hybrid local thermodynamic equilibrium

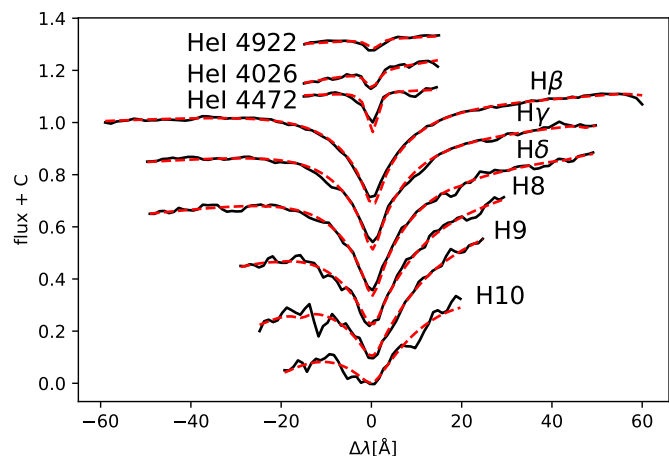


Fig. 4: Spectral line fit of hydrogen and He lines of the SOAR spectrum of TYC5977-517-1. The best fit is shown as the dashed red line. Black line displays the data.

librium (LTE)/non-LTE (NLTE) model atmospheric approach, as described in Schaffenroth et al. (2021) using SPAS (Hirsch 2009). We obtained $T_{\text{eff}} = 35200 \pm 500 \text{ K}$, $\log g = 5.69 \pm 0.05$, $\log y = -2.02 \pm 0.05$ (the spectral line fit is shown in Fig. 4).

TESS observed the system in sectors 7, 33, and 34 (CROWD-SAP=0.49/0.37/0.34). A significantly higher reflection effect amplitude was observed in the first sector compared to the other two sectors, which were similar, so we excluded the light curve observed in the first sector, as it is probably overcorrected (as discussed in the previous section). The best fit results in a companion mass of $0.319 \pm 0.012 M_{\odot}$ and a radius of $0.380 \pm 0.010 R_{\odot}$.

3.3.2. EC01578-1743

EC01578-1743 was found to be a sdB by the Edinburgh-Cape Blue Object (EC) Survey (Kilkenny et al. 2016). This system was identified as a reflection effect system in the Evryscope survey (Ratzloff et al. 2020a). Inspecting the *TESS* light curves, we also found this system to have a strong reflection effect with an amplitude of 20% and period of 0.258104 d. Its shape indicated a higher inclination angle, but no eclipses are visible in the data.

In order to derive the radial velocity curve, we obtained high-resolution spectra using the CHIRON echelle spectrometer on the CTIO 1.5-m telescope (Tokovinin et al. 2013). Observations were taken at sporadic intervals from December 2017 to September 2018 (in total 39 single spectra) and cover the full range of orbital phases (see Fig. 5 and Table C.2). A 2.7" fiber was used to cover the wavelength range 4400–8800 Å with a spectral resolution of $R \approx 28000$. Extracted and wavelength-calibrated spectra were delivered by a pipeline running at Georgia State University (Brewer et al. 2014). In order to measure the radial velocities we used cross-correlation with the IRAF task FXCOR. To fit the radial velocity curve we used the Python package RADVEL (Fulton et al. 2018)² getting a semi-amplitude of the radial velocity curve of $K_1 = 86.5 \pm 0.5 \text{ km s}^{-1}$ (see Fig. 5). To derive the atmospheric parameters we additionally took one spectrum with SOAR/Goodman. The analysis was done the same way as for TYC5977-517-1 and resulted in $T_{\text{eff}} = 32000 \pm 500 \text{ K}$, $\log g = 5.75 \pm 0.06$, $\log y = -2.0 \pm 0.1$ (the spectral-line fit is shown in Fig. 6). The best fit of the light curve (see Fig. 7) was

² <https://radvel.readthedocs.io/>

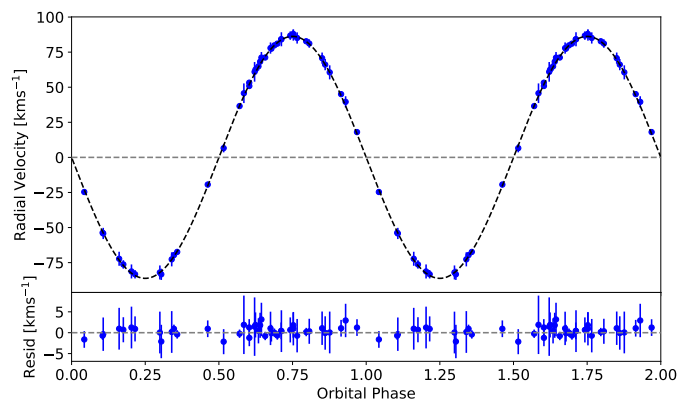


Fig. 5: Radial velocity curve of EC01578-1743 phased to the orbital period. The black line is the best fit model, the blue dots are the data including uncertainties.

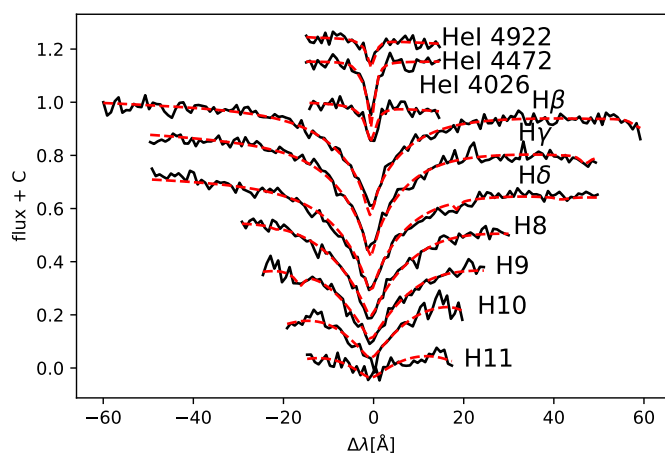


Fig. 6: Spectral line fit of hydrogen and He lines of the SOAR spectrum of EC01578-1743. The best fit is shown in the dashed red line, the black line shows the data.

found for an inclination of $49.5^\circ \pm 0.25^\circ$. From this we can constrain the mass and radius of the companion to $0.278 \pm 0.004 M_\odot$ and $0.294 \pm 0.0025 R_\odot$.

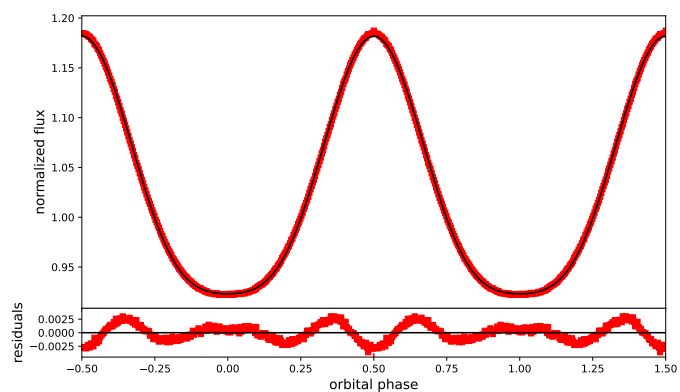


Fig. 7: Phased *TESS* light curve of EC 01578-1743 (given by the red squares) together with the best-fit model given by the black line. The lower panel shows the residuals.

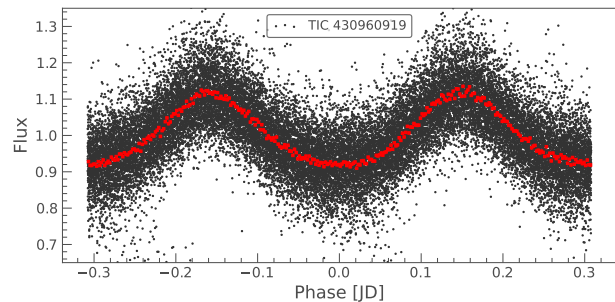


Fig. 8: *TESS* light curve of KPD2215+5037 phase-folded to the dominant peak in the periodogram determined by the light curve.

3.3.3. KPD2215+5037

KPD2215+5037 was identified as a subdwarf by [Downes \(1986\)](#) in the Kitt Peak-Downes Survey for Galactic Plane Ultraviolet-Excess Objects. A survey for RV variable hot subdwarfs by [Copperwheat et al. \(2011\)](#) found it to be varying with a period of 0.809146 d. The *TESS* light curve shows a variation at 0.3078784 d with the typical shape of a reflection effect (Fig. 8). An additional sinusoidal variation at 6.5 d is visible. However, this signal probably originates from a known red, long-period variable 25 arcsec away. To confirm that the 0.3 d signal is coming from our target, we also extracted the light curve from the *TESS* fullframe images (FFI) from the single pixel, which should not be influenced by the brighter target. We confirm the 0.3 d signal most likely comes from our target and that the longer-period variation does not. This was also confirmed using the Python package *TESS-LOCALIZE*³ ([Higgins & Bell 2022](#)). To confirm the light curve period, additional time-resolved spectroscopy and photometry should be undertaken in the future.

3.3.4. GALEX J1753-5007 – A triple system?

GALEX J1753-5007 (GALEX J175340.5-500741) was discovered in the GALEX survey and classified as a sdB with an F7V companion due to an infrared SED excess by [Németh et al. \(2012\)](#). Furthermore, [Kawka et al. \(2015\)](#) carried out spectroscopic follow-up of this target confirming it to be RV variable and, hence, in a close binary system. As they could not find any variation with an upper limit of 20 mmag in the ASAS light curve, these authors suggested that the companion is a WD. We can confirm from fitting the SED the same way as described in [Heber et al. \(2018\)](#); [Irrgang et al. \(2021\)](#) and Paper I (see Fig. 9) that it is a sdB with an F type companion ($T_{\text{eff},2} = 6000^{+400}_{-250}$ K).

The *TESS* light curve (Fig. 10) shows clearly a reflection effect with an amplitude of about 6% with a period of 0.0907405 d. As the *TESS* filter is much redder than the ASAS filter, the amplitude in *TESS* is expected to be significantly higher. That could explain why the ASAS light curve did not show any variation. For an sdB + FV star, such a short period is not possible as the F star would be larger than the orbital separation. So it is most likely that an inner binary with a cool, low-mass companion is being orbited by an F star in a wide orbit and this is actually a triple system. Only very few confirmed sdBs in triple systems are known (see e.g. [Pelisoli et al. 2020](#)). The astrometric orbits,

³ <https://github.com/Higgins00/TESS-Localize>

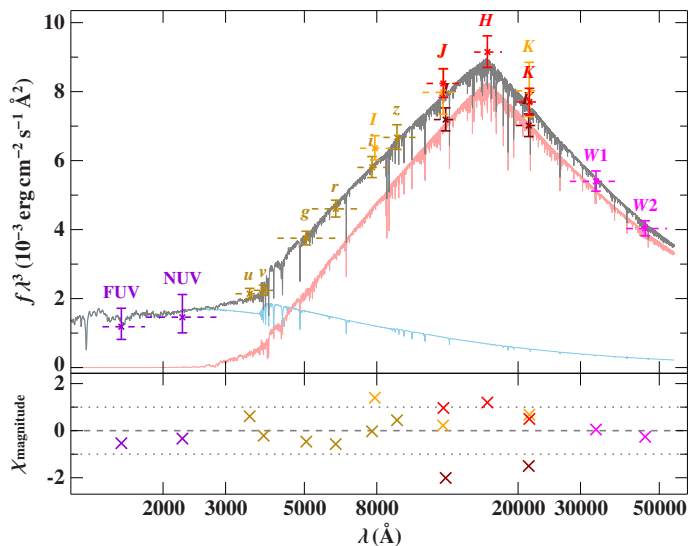


Fig. 9: Spectral energy distribution of GALEX J1753-5007 showing a sdB with an F7V companion.

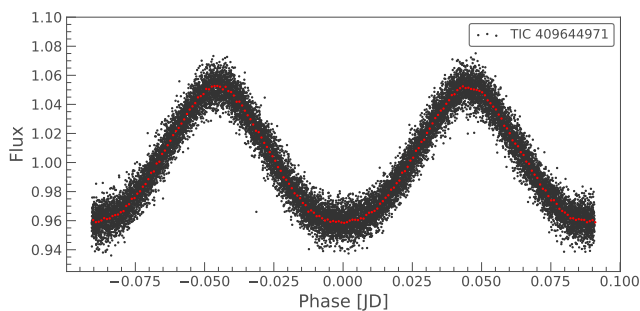


Fig. 10: TESS light curve of GALEX J1753-5007 phase-folded to the dominant peak in the periodogram determined by the light curve.

which will be released by *Gaia* eventually, could confirm this. The large RUWE of 31.846 already indicates that a single-star solution is not a good fit, suggesting a non-negligible astrometric wobble that could be caused by a longer period companion.

4. Hot subdwarfs with white dwarf companions showing ellipsoidal deformation and/or beaming in their light curves

4.1. Method

While searching for light variations of the hot subdwarf binaries with known orbital periods, we detected several targets showing small variations with half of the orbital period and uneven minima/maxima. The most probable explanation for these variations is ellipsoidal deformation of the hot subdwarf due to a nearby white dwarf companion. We also found several systems showing tiny variations ($\sim 0.01\% - 0.1\%$) with the orbital period that are most likely due to Doppler beaming of the hot subdwarf, also indicative of a nearby white dwarf companion. No ellipsoidal deformation was retrieved in these cases because the separation of the components is too large (more details in the next subsection). Most of these variations would not have been found without pre-

vious knowledge of the orbital period since their periodogram peaks are barely visible above the noise.

To confirm the ellipsoidal deformation and/or beaming in the light curves, we fit them using *LCURVE* as we did for the reflection effect systems. We assumed the mass and radius of the sdB as determined by the SED fitting and *Gaia* parallax (see Paper I) and used the RV semi-amplitude to derive the orbital separation from the mass function, and the atmospheric parameters from the spectral analysis to constrain as many parameters as possible. For the limb-darkening, gravity darkening, and beaming coefficients, we used the values closest to the atmospheric parameters of the hot subdwarf from the tables of Claret et al. (2020a,b) for the *TESS* and *Kepler* filters.

Similarly to the analysis of the reflection effect systems as shown in Sect. 3, we performed an MCMC varying the inclination as well as the mass ratio and the radius of the sdB using a prior to include the uncertainties of both parameters.

4.2. Results of the light curve analysis

All light curves can be found in Fig. D.2, along with their best-fitting models, which agree well with the data. For the systems showing ellipsoidal modulation and Doppler beaming, we were able to derive inclinations and, hence, also the mass of the companion. The results are summarized in Table 3. All but two companions are more likely He WDs rather than CO WDs. We were also able to derive the rotational velocity of the sdB in two systems the same way as for the sdB+dM systems. In one system, the sdB seems to rotate a bit slower than the orbital rotations, which has implications on the light curve. More details can be found in Sect. B.7.

The systems showing only Doppler boosting are not sensitive to the mass or inclination, as shown in Sect. 4.3.1, so we only overplotted the synthetic light curve calculated using the sdB radius and mass, as well as the mass ratio and orbital separation derived by the RV semi-amplitude and orbital period from the light curve to show that the variation can indeed be explained by beaming (Fig. D.2 i-x). In total, we were able to detect Doppler beaming in 16 sdB binaries with periods ranging from 9 hours to 5. days. In the next sections we discuss two newly confirmed sdB+WD systems, and in appendix B, we provide more details on some of the individual sdB+WD systems.

4.3. Newly confirmed sdB+WD systems

4.3.1. PG 1232-136

PG 1232-136 was found to be a sdB star in the Palomar-Green survey (Green et al. 1986). Spectroscopic follow-up by Edelmann et al. (2005) revealed that it is in a close binary system with 0.3630 d period and a quite large RV amplitude ($129.60 \pm 0.4 \text{ km s}^{-1}$). Geier et al. (2010b) constrained the rotational velocity of the sdB to $v_{\text{rot}} \sin i < 5 \text{ km s}^{-1}$. Assuming synchronization, they derived a minimum mass of the companion of $6 M_{\odot}$. As the companion is not visible in the spectrum, they assumed it to be a black hole candidate.

The *TESS* light curve showed a tiny variation with an amplitude of only about 0.2% amplitude with the orbital period derived by the RV curve, suggesting a reflection effect. The light curve analysis showed that the variation could be explained by a reflection effect with the size and mass of a He-WD companion. Phasing the RV curve and the light curve to the same ephemeris, however, showed that the variation is not a reflection effect but most likely Doppler beaming resulting from the high velocity of

Table 3: Period, RV curve parameters, inclination, mass ratio, separation, and companion mass of the analyzed ellipsoidal systems, together with the minimum companion mass. The objects are ordered following their orbital period.

target	P_{RV} [d]	γ [km/s]	K_1 [km/s]	i [$^\circ$]	q	a [R_\odot]	M_2 [M_\odot]	$M_{2,\min}^*$ [M_\odot]	P_{rot} [d]
PG1043+760 ^a	0.1201506	24.80	63.60	15 \pm 0.6	1.65 \pm 0.11	0.94 \pm 0.04	0.48 \pm 0.08	0.09	-
GALEXJ075147.0+092526 ^b	0.178319	15.50	147.70	74 \pm 10	0.85 ^{+0.09} _{-0.04}	1.19 \pm 0.08	0.31 ^{+0.07} _{-0.03}	0.31	-
HS1741+213 ^a	0.2	-	157	47 \pm 11	1.45 ^{+0.65} _{-0.3}	1.4 \pm 0.3	0.58 ^{+0.15} _{-0.08}	0.36	-
PG1136-003 ^a	0.207536	23.30	162.00	75 \pm 11	0.90 ^{+0.10} _{-0.04}	1.4 \pm 0.1	0.45 ^{+0.08} _{-0.04}	0.38	-
GD687 ^a	0.37765 ^a	32.30	118.30	58 \pm 8	1.23 ^{+0.24} _{-0.14}	1.9 \pm 0.2	0.35 ^{+0.09} _{-0.06}	0.32	0.39 \pm 0.05
GALEXJ234947.7+384440 ^a	0.462516	2.00	87.90	70 \pm 10	0.64 ^{+0.08} _{-0.04}	2.2 \pm 0.2	0.26 ^{+0.04} _{-0.04}	0.24	-
PG0101+039 ^a	0.569899	7.30	104.70	89.4 \pm 0.6	0.8174 ^{+0.0001} _{-0.0001}	2.53 \pm 0.01	0.34 ^{+0.04} _{-0.04}	0.33	0.85 \pm 0.09
EC13332-1424 ^a	0.82794	-53.20	104.10	82 \pm 2	1.0 ^{+0.1} _{-0.1}	3.4 \pm 0.2	0.40 ^{+0.06} _{-0.06}	0.39	-
PG1232-136 ^a	0.363	4.10	129.60	-	-	-	-	0.36	-
PG1743+477 ^a	0.515561	-65.80	121.40	-	-	-	-	0.39	-
PG1519+640 ^a	0.54029143	0.10	42.70	-	-	-	-	0.10	-
GALEXJ025023.8-040611 ^b	0.6641	0.00	93.90	-	-	-	-	0.30	-
PG1648+536 ^a	0.6109107	-69.90	109.00	-	-	-	-	0.36	-
EC22202-1834 ^a	0.70471	-5.50	118.60	-	-	-	-	0.44	-
EC02200-2338 ^a	0.8022	20.70	96.4	-	-	-	-	0.35	-
TONS183 ^a	0.8277	50.50	84.80	-	-	-	-	0.29	-
EC21556-5552 ^a	0.834	31.40	65.00	-	-	-	-	0.21	-
PG1000+408 ^a	1.049343	56.60	63.50	-	-	-	-	0.22	-
GALEXJ225444.1-551505 ^b	1.22702	4.20	79.70	-	-	-	-	0.32	-
PG0133+114 ^a	1.23787	-0.30	82.00	-	-	-	-	0.34	-
PG1512+244 ^a	1.26978	-2.90	92.70	-	-	-	-	0.41	-
UVO1735+22 ^a	1.278	20.60	103.00	-	-	-	-	0.48	-
PG0934+186 ^a	4.051	7.70	60.30	-	-	-	-	0.38	-
CD-24731 ^a	5.85	20.00	63.00	-	-	-	-	0.50	-

^a Kupfer et al. (2015, and references therein)

^b Kawka et al. (2015)

* under the assumption: $M_{\text{sdB}} = 0.4 M_\odot$

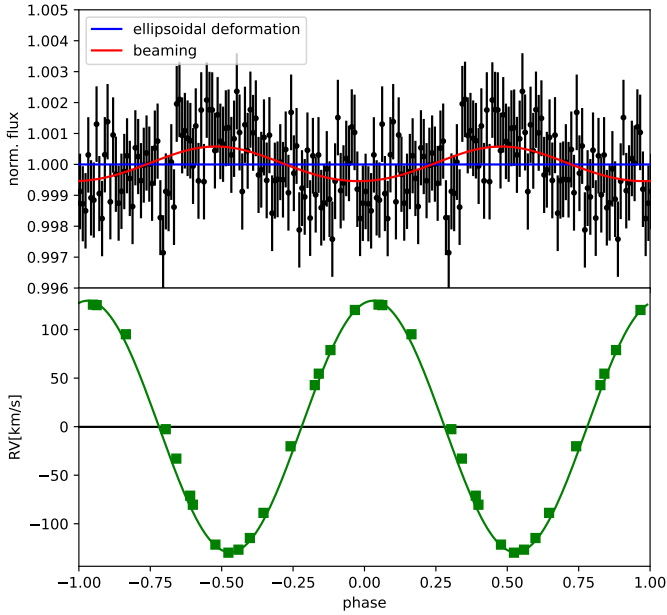


Fig. 11: Phased *TESS* light curve and RV curve of PG 1232-136. Upper panel shows the *TESS* light curve phased with the period determined from the *TESS* light curve. Lower panel shows the RV curve measured by Edlmann et al. (2005) phased with the same period.

the sdB, as the light variation is aligned with the RV variation and we observe the highest flux when the sdB is moving towards

us (see Fig. 11). To check if this can help us constrain the nature of the companion, we calculated several light curve models with different inclinations. Unfortunately, even at lower inclinations (i.e., higher companion masses), we would not expect to detect the ellipsoidal deformation of the sdB (see Fig. 11). Hence, we observe only the beaming of the sdB, which varies with the radial velocity curve and, thus, the light curve does not provide any additional information; however, if we had detected the same signal in an unknown sdB binary, we would have been able to predict the amplitude of the RV curve. This also means that it is not possible to constrain the mass of the companion, as we cannot constrain the inclination.

4.3.2. KPD 0629-0016

KPD 0629-0016 was first discovered to be a slowly pulsating sdB star by Koen (2007). The observation of the sdB by the CoRoT (COncvection, ROTation, and planetary Transits) satellite (Baglin et al. 2006) opened up a new era in sdB asteroseismology leading to the detection of a large number of g-mode pulsations (Charpinet et al. 2010). This rich spectrum could be used to derive the structural and core parameters of the sdB (Van Grootel et al. 2010). An additional binary signal could not be found in the CoRoT data; however, as a lot of binary systems have orbital periods in the same range as the g-mode pulsations, it is not easy to find them in the light curve. We took spectroscopic follow-up of this sdB to search for RV variations in three runs with the EMMI and EFOSC2 spectrograph mounted at the ESO/NTT telescope in Chile (080.D-0685(A), 082.D-0649(A), 092.D-0040(A), PI: S. Geier). More details on the observations and the RV determination can be found in Geier et al. (2014). The RV curve

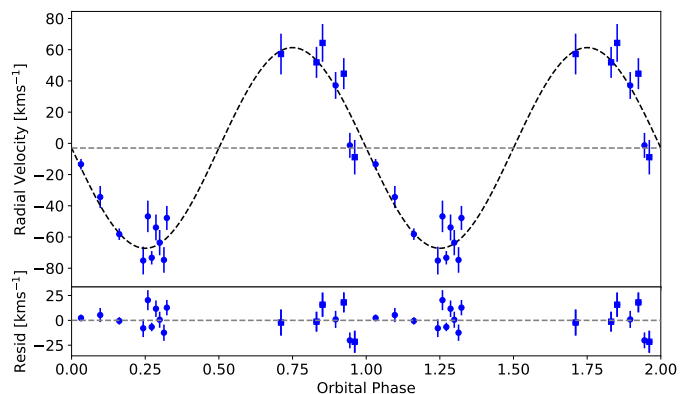


Fig. 12: RV curve of KPD 0629-0016 phased to the most probable orbital period with the best-fitting RV model curve shown with the black sinusoidal curve. Data observed with the EMMI spectrograph are shown with the blue circles and the EFOSC2 data are shown with the blue squares. Lower panel shows the residuals.

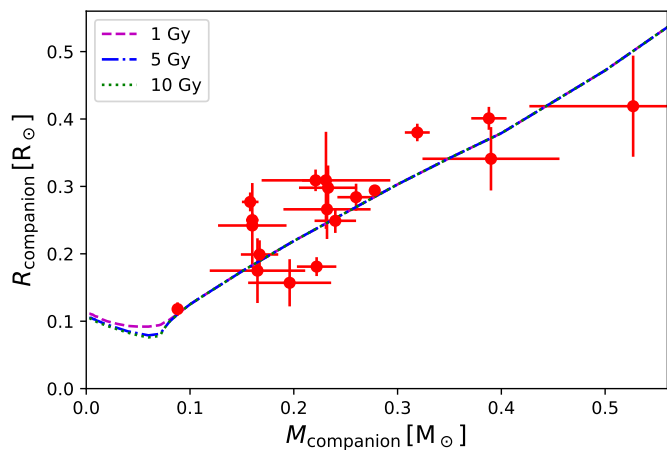


Fig. 13: Mass-radius relation of the companions in the analyzed reflection effect systems compared to theoretical calculations for an age from 1 to 10 Gy by Baraffe et al. (2015).

phased to the most probable orbital period (0.8754 ± 0.0001 d) can be found in Fig. 12 and it results in a semi-amplitude of $K_1 = 64.4 \pm 3.4$ km/s, from which a minimum mass of $0.22 M_\odot$ can be derived for the companion. As in the CoRoT light curve no period near the orbital period could be detected, an M dwarf companion can most likely be excluded and the companion must be a WD. The system was also observed by *TESS* in sector 6 and 33. The analysis of the light curve also shows no detectable period close to the orbital period with an upper limit of 1.0% confirming that the companion is most likely a WD, but the quality of the light curve is not high enough to detect light variations.

5. Discussion and summary

For the first time we analyze a larger sample of reflection effect systems and derive the masses and radii of the companion under the assumption of a canonical mass sdB, which is the most likely mass as shown by the mass distribution of the sdBs in HW Vir systems (see Paper I), as well as the radius of the sdB derived by the fit of the SED and the Gaia parallax (Paper I).

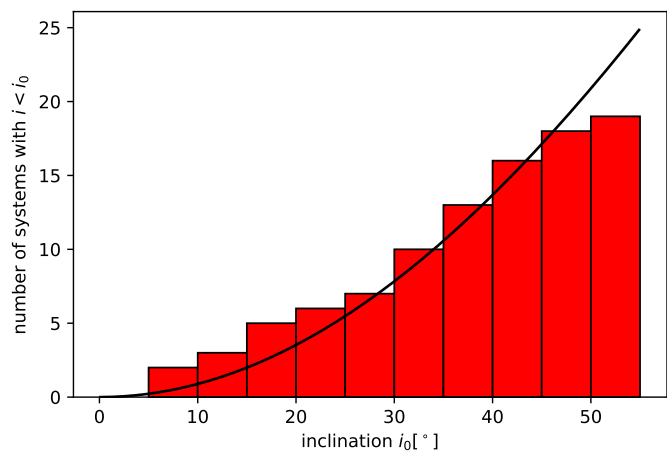


Fig. 14: Inclination distribution of the analyzed reflection effect systems. Black line shows the number of systems we expect to find when we assume that the orientation of a sdB binary is uniformly distributed. Due to the projection effect, it is much more likely to find binary systems at high rather than low inclinations.

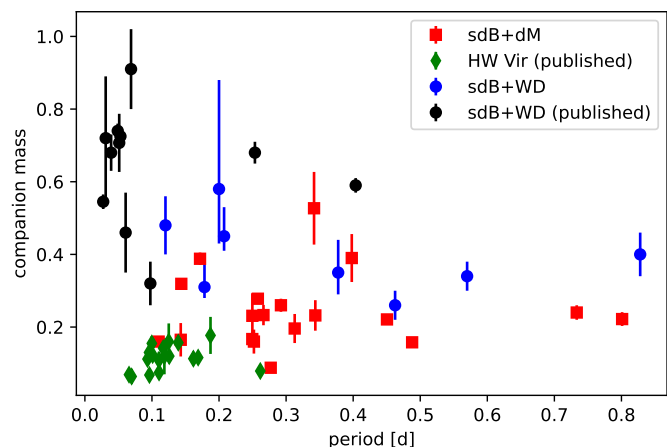


Fig. 15: Period vs. companion mass for the reflection effect systems (sdB+dM, with red squares) and the ellipsoidal modulation systems (sdB+WD, with blue circles). For comparison, we show the parameters of the published reflection effect systems (see Schaffenroth et al. 2018, and references therein) as well as the published sdB+WD systems: KPD1946+4340 (Bloemen et al. 2011); CD-3011223 (Geier et al. 2013); PTF1J0823+0819 (Kupfer et al. 2017b); OWJ074106.0–294811.0 (Kupfer et al. 2017a); EVR-CB-001 (Ratzloff et al. 2019); EVR-CB-004 (Ratzloff et al. 2020b); HD265435 (Pelisoli et al. 2021); ZTFJ2130+4420 (Kupfer et al. 2020b); ZTFJ2055+4651 (Kupfer et al. 2020a); PTF1J223857.11+743015.1 (Kupfer et al. 2022); and OWJ081530.8-342123.5 (Ramsay et al. 2022)

To check the validity of our method, we also compared the mass and radius we derived for the companion to theoretical mass-radius relations by Baraffe et al. (2015). This is shown in Fig. 13. There is some scatter, which was also found in other investigations (e.g., Parsons et al. 2018), but most of the companions agree well with the theoretical predictions. This shows that our assumption of the canonical mass is not so far off and our method works quite well. A change in the assumed mass of the sdB will lead to a systematic shift of the companion mass.

In the future, the sdB mass should be constrained using the SED fit and *Gaia* parallax, after a careful determination of the atmospheric parameters at phase 0. This will allow for the determination of reliable companion masses and radii as well as reliable error bars, since the companion is much fainter and the contribution of the dark side to the spectrum is negligible.

The orientations of sdB binaries in space should be uniformly distributed. Thus, higher inclinations are more likely to be seen than low inclinations, due to the projection effect. The probability of a system to have an inclination lower than a certain value of i_0 can easily be calculated by $P_{i < i_0} = 1 - \cos i_0^2$ (Gray 2005). We can use this to estimate how many systems we expect to find below a certain inclination and compare this to the inclination distribution we measure. This comparison is shown in Fig. 14. As we are only including non-eclipsing systems, we did not find any systems with inclinations higher than $\sim 55^\circ$. Moreover, most of the analyzed systems are systems which have been found before in different ways and are not homogeneously selected. At the highest inclinations, the measured distribution starts to deviate from expectation. It appears as though we are finding too few systems at high inclinations; this is perhaps because we are starting to see (tiny) eclipses at these inclinations. Nevertheless, despite the inhomogeneous target selection, we still managed to obtain a good agreement, showing that systematic effects seem to play a minor role and we can indeed derive inclinations from the reflection effect systems.

Our sample of reflection effect systems includes sdBs with companions covering the entire mass range of dM stars from the hydrogen burning limit to early M dwarfs with masses around $0.4 M_\odot$, also for a large segment of the period range from 0.1 to 0.8 d. For the previously found reflection effect systems with brown dwarf candidates (KBS13, BPS CS 22169-1, PHL457, CPD-64 481), we have shown that most of them just have low inclinations and so, the companions are M dwarfs instead. This means so far still no BDs around sdBs in longer periods have been confirmed and the BDs in sdB binaries are still preferentially found at close periods below 0.1 d (Schaffenroth et al. 2019).

We also found 24 sdB+WD systems showing tiny variations with amplitudes below $\sim 0.1\%$ due to Doppler beaming or ellipsoidal deformation. A fitting of the light curves allowed us to derive the masses of the WD companion for 8 systems. We derived masses for the companions from 0.25 to $0.6 M_\odot$ with orbital periods of these systems from 0.132 to 0.83 d.

There were 16 longer period systems showing only Doppler beaming and so no additional information could be derived from the light curve in this case, as the semi-amplitude of the RV curve K_1 was derived before. We could show that the variation could indeed be explained by Doppler beaming by overplotting a model calculated using the sdB radius and the K_1 . Finding more Doppler beaming in systems without solved orbits would allow us to derive the period and the K_1 without spectroscopy.

To compare our sample to the sample of published sdB+dM/BD and sdB+WD systems, we also plotted the period-companion mass diagram (see Fig. 15). It is evident that the sample known so far only covers a very small parameter range. For sdB+dM/BD systems, only those with short orbital periods and low companion masses have been studied. The same has been true for the sdB+WD systems, for which those with the shortest periods and highest-mass companions have been studied preferentially. Our new sample covers a much larger orbital period and companion mass range than before.

For the sdB+WD systems we can see that the highest companion masses are found at the shorter periods below 0.2 d,

where we have two WD companions which are more likely to be CO WDs. The rest of the companions have masses below $0.45 M_\odot$ and are most likely He WDs. If they evolved from higher mass stars with $2 - 3 M_\odot$, WDs with masses $> 0.33 M_\odot$ could also be CO WDs, in principle, but such objects are expected to be much more rare. This sample of studied post-common envelope systems over a large parameter range is ideal to constrain the common envelope phase, as done for instance, in Ge et al. (2022). A large sample of post-common envelope binaries with known masses of both primary star and companion, as well as orbital separations and orbital periods is necessary for such studies. This is beyond the scope of this paper, but we are already preparing a paper to use this sample to constrain sdB formation by a common envelope phase (Vos et al. in prep.). Moreover, it is important to compare such a sample to the parameters predicted by hydrodynamical simulations, as done in Kramer et al. (2020), who simulated a red giant of $1 M_\odot$ being stripped by a substellar companion in a common envelope phase evolving to an sdB.

Using the previously measured projected rotational velocity of some of the sdBs and the radius of the sdB derived by the SED, together with the *Gaia* parallax as well as the determined inclination, we could also measure the rotation period for sdBs with dM as well as WD companions. We find that in three systems (with orbital periods from 0.25 to 0.56 d) out of seven, the sdB is rotating significantly slower than the orbital period. On the other hand, systems with even longer periods of 0.7 d seem to be (almost) synchronized. This agrees well with the findings of Silvotti et al. (2022) and Schaffenroth et al. (2021), stating that both synchronized and non-synchronized systems are found on the EHB, suggesting that synchronization is taking place on the EHB. Theoretical synchronization theories (Preece et al. 2018) predict that none of the sdBs in close binary systems are expected to be synchronized and, thus, the observations cannot be explained by theory at present.

The high S/N of the *TESS* light curves allowed us to almost double the sample of studied sdB+dM/BD and sdB+WD systems. Additional sectors of *TESS* data are already available and the future photometric surveys, such as those planned by the Vera Rubin observatory or *PLATO* as the successor of *TESS*, will allow us to obtain a statistically significant sample of post-common envelope systems with hot subdwarf primaries.

Acknowledgements. This research made use of Lightkurve, a Python package for Kepler and *TESS* data analysis (Lightkurve Collaboration et al. 2018). Based on observations collected at the European Organisation for Astronomical Research in the Southern Hemisphere under ESO programme(s) 080.D-0685(A), 082.D-0649(A), 092.D-0040(A). This paper includes data collected by the *TESS* mission, which are publicly available from the Mikulski Archive for Space Telescopes (MAST). Funding for the *TESS* mission is provided by NASA's Science Mission directorate. VS and SG acknowledge funding from the German Academic Exchange Service (DAAD PPP USA 57444366) for this project and would like to thank the host institution Texas Tech University for the hospitality. VS was funded by the Deutsche Forschungsgemeinschaft under grant GE2506/9-1. IP was partially funded by the Deutsche Forschungsgemeinschaft under grant GE2506/12-1 and by the UK's Science and Technology Facilities Council (STFC), grant ST/T000406/1. IP acknowledges support from the UK's Science and Technology Facilities Council (STFC), grant ST/T000406/1. BNB was supported by the National Science Foundation grant AST-1812874 and by NASA through grant 80NSSC21K0364. TK acknowledges support from the National Science Foundation through grant AST #2107982, from NASA through grant 80NSSC22K0338 and from STScI through grant HST-GO-16659.002-A. We thank Uli Heber for comments on the manuscript and Lars Möller for sharing his radial velocity measurements with us. We thank Andreas Irrgang for the development of the SED fitting tool and making it available to us. We thank Alfred Tillich for observing some of the spectra used in this paper. We thank Stephen Walser for helping with some of the SOAR and Chiron observations used in this paper.

References

- Baglin, A., Auvergne, M., Boissard, L., et al. 2006, in 36th COSPAR Scientific Assembly, Vol. 36, 3749
- Baraffe, I., Homeier, D., Allard, F., & Chabrier, G. 2015, *A&A*, 577, A42
- Baran, A. S., Sahoo, S. K., Sanjayan, S., & Ostrowski, J. 2021, *MNRAS*
- Baran, A. S., Telting, J. H., Jeffery, C. S., et al. 2019, *MNRAS*, 489, 1556
- Barlow, B. N., Corcoran, K. A., Parker, I. M., et al. 2022, *ApJ*, 928, 20
- Berger, J. & Fringant, A. M. 1980, *A&A*, 85, 367
- Blanchette, J. P., Chayer, P., Wesemael, F., et al. 2008, *ApJ*, 678, 1329
- Bloemen, S., Marsh, T. R., Østensen, R. H., et al. 2011, *MNRAS*, 410, 1787
- Brewer, J. M., Giguere, M., & Fischer, D. A. 2014, *PASP*, 126, 48
- Charpinet, S., Green, E. M., Baglin, A., et al. 2010, *A&A*, 516, L6
- Christlieb, N., Wisotzki, L., Reimers, D., et al. 2001, *A&A*, 366, 898
- Claret, A., Cukanovaite, E., Burdge, K., et al. 2020a, *A&A*, 641, A157
- Claret, A., Cukanovaite, E., Burdge, K., et al. 2020b, *A&A*, 634, A93
- Copperwheat, C. M., Marsh, T. R., Dhillon, V. S., et al. 2010, *MNRAS*, 402, 1824
- Copperwheat, C. M., Morales-Rueda, L., Marsh, T. R., Maxted, P. F. L., & Heber, U. 2011, *MNRAS*, 415, 1381
- Downes, R. A. 1986, *ApJS*, 61, 569
- Dreizler, S., Schuh, S. L., Deetjen, J. L., Edelmann, H., & Heber, U. 2002, *A&A*, 386, 249
- Edelmann, H., Heber, U., Altmann, M., Karl, C., & Lisker, T. 2005, *A&A*, 442, 1023
- Edelmann, H., Heber, U., Hagen, H. J., et al. 2003, *A&A*, 400, 939
- Feige, J. 1958, *ApJ*, 128, 267
- Fontaine, G., Brassard, P., Charpinet, S., et al. 2012, *A&A*, 539, A12
- For, B. Q., Edelmann, H., Green, E. M., et al. 2008, in *Astronomical Society of the Pacific Conference Series*, Vol. 392, *Hot Subdwarf Stars and Related Objects*, ed. U. Heber, C. S. Jeffery, & R. Napiwotzki, 203
- Foreman-Mackey, D., Hogg, D. W., Lang, D., & Goodman, J. 2013, *PASP*, 125, 306
- Fulton, B. J., Petigura, E. A., Blunt, S., & Sinukoff, E. 2018, *PASP*, 130, 044504
- Ge, H., Tout, C. A., Chen, X., et al. 2022, *arXiv e-prints*, arXiv:2205.14256
- Geier, S., Classen, L., Brünner, P., et al. 2012, in *Astronomical Society of the Pacific Conference Series*, Vol. 452, *Fifth Meeting on Hot Subdwarf Stars and Related Objects*, ed. D. Kilkeny, C. S. Jeffery, & C. Koen, 153
- Geier, S., Heber, U., Kupfer, T., & Napiwotzki, R. 2010a, *A&A*, 515, A37
- Geier, S., Heber, U., Podsiadlowski, P., et al. 2010b, *A&A*, 519, A25
- Geier, S., Hirsch, H., Tillich, A., et al. 2011a, *A&A*, 530, A28
- Geier, S., Marsh, T. R., Wang, B., et al. 2013, *A&A*, 554, A54
- Geier, S., Maxted, P. F. L., Napiwotzki, R., et al. 2011b, *A&A*, 526, A39+
- Geier, S., Nesslinger, S., Heber, U., et al. 2008, *A&A*, 477, L13
- Geier, S., Østensen, R. H., Heber, U., et al. 2014, *A&A*, 562, A95
- Geier, S., Raddi, R., Gentile Fusillo, N. P., & Marsh, T. R. 2019, *A&A*, 621, A38
- Gray, D. F. 2005, *The Observation and Analysis of Stellar Photospheres*
- Green, E. M., Fontaine, G., Reed, M. D., et al. 2003, *ApJ*, 583, L31
- Green, R. F., Schmidt, M., & Liebert, J. 1986, *ApJS*, 61, 305
- Guseinov, O. K., Novruzova, K. I., & Rustamov, I. S. 1983, *Ap&SS*, 96, 1
- Han, Z., Podsiadlowski, P., Maxted, P. F. L., & Marsh, T. R. 2003, *MNRAS*, 341, 669
- Han, Z., Podsiadlowski, P., Maxted, P. F. L., Marsh, T. R., & Ivanova, N. 2002, *MNRAS*, 336, 449
- Heber, U. 2009, *ARA&A*, 47, 211
- Heber, U. 2016, *PASP*, 128, 082001
- Heber, U., Drechsel, H., Østensen, R., et al. 2004, *A&A*, 420, 251
- Heber, U., Irrgang, A., & Schaffenroth, J. 2018, *Open Astronomy*, 27, 35
- Heinze, A. N., Tonry, J. L., Denneau, L., et al. 2018, *AJ*, 156, 241
- Higgins, M. E. & Bell, K. J. 2022, *arXiv e-prints*, arXiv:2204.06020
- Hirsch, H. 2009, Phd thesis, Friedrich Alexander Universität Erlangen Nürnberg
- Howell, S. B., Sobek, C., Haas, M., et al. 2014, *PASP*, 126, 398
- Irrgang, A., Geier, S., Heber, U., et al. 2021, *A&A*, 650, A102
- Jeffery, C. S. & Ramsay, G. 2014, *MNRAS*, 442, L61
- Kawka, A., Vennes, S., Németh, P., Kraus, M., & Kubát, J. 2010, *MNRAS*, 408, 992
- Kawka, A., Vennes, S., O'Toole, S., et al. 2015, *MNRAS*, 450, 3514
- Kilkenny, D., Koen, C., O'Donoghue, D., & Stobie, R. S. 1997, *MNRAS*, 285, 640
- Kilkenny, D., Luvhimbi, E., O'Donoghue, D., et al. 1995, *MNRAS*, 276, 906
- Kilkenny, D., Worters, H. L., O'Donoghue, D., et al. 2016, *MNRAS*, 459, 4343
- Kiss, L. L., Csák, B., Szatmáry, K., Fűrész, G., & Sziládi, K. 2000, *A&A*, 364, 199
- Koen, C. 2007, *MNRAS*, 377, 1275
- Koen, C. 2009, *MNRAS*, 395, 979
- Koen, C. 2019, *MNRAS*, 490, 1283
- Koen, C., O'Donoghue, D., Kilkenny, D., Stobie, R. S., & Saffer, R. A. 1999, *MNRAS*, 306, 213
- Koen, C., O'Donoghue, D., Pollacco, D. L., & Nitta, A. 1998, *MNRAS*, 300, 1105
- Kramer, M., Schneider, F. R. N., Ohlmann, S. T., et al. 2020, *A&A*, 642, A97
- Kupfer, T., Bauer, E. B., Burdge, K. B., et al. 2019, *ApJ*, 878, L35
- Kupfer, T., Bauer, E. B., Burdge, K. B., et al. 2020a, *ApJ*, 898, L25
- Kupfer, T., Bauer, E. B., Marsh, T. R., et al. 2020b, *ApJ*, 891, 45
- Kupfer, T., Bauer, E. B., van Roestel, J., et al. 2022, *ApJ*, 925, L12
- Kupfer, T., Geier, S., Heber, U., et al. 2015, *A&A*, 576, A44
- Kupfer, T., Geier, S., McLeod, A., et al. 2014, in *Astronomical Society of the Pacific Conference Series*, Vol. 481, *6th Meeting on Hot Subdwarf Stars and Related Objects*, ed. V. van Grootel, E. Green, G. Fontaine, & S. Charpinet, 293
- Kupfer, T., Ramsay, G., van Roestel, J., et al. 2017a, *ApJ*, 851, 28
- Kupfer, T., van Roestel, J., Brooks, J., et al. 2017b, *ApJ*, 835, 131
- Latour, M., Fontaine, G., & Green, E. 2014, in *Astronomical Society of the Pacific Conference Series*, Vol. 481, *6th Meeting on Hot Subdwarf Stars and Related Objects*, ed. V. van Grootel, E. Green, G. Fontaine, & S. Charpinet, 91
- Lightkurve Collaboration, Cardoso, J. V. d. M., Hedges, C., et al. 2018, *Lightkurve: Kepler and TESS time series analysis in Python*, *Astrophysics Source Code Library*
- Lisker, T., Heber, U., Napiwotzki, R., et al. 2005, *A&A*, 430, 223
- Lynas-Gray, A. E. 2021, *Frontiers in Astronomy and Space Sciences*, 8, 19
- Maxted, P. F. L., Heber, U., Marsh, T. R., & North, R. C. 2001, *MNRAS*, 326, 1391
- Maxted, P. F. L., Marsh, T. R., Heber, U., et al. 2002, *MNRAS*, 333, 231
- Maxted, P. F. L., Marsh, T. R., & North, R. C. 2000, *MNRAS*, 317, L41
- Maxted, P. F. L., Morales-Rueda, L., & Marsh, T. R. 2004, *Ap&SS*, 291, 307
- Möller, L. 2021, *Elemental abundances of sdB-Stars as benchmark for diffusion models*
- Morales-Rueda, L., Maxted, P. F. L., Marsh, T. R., North, R. C., & Heber, U. 2003, *MNRAS*, 338, 752
- Napiwotzki, R., Yungelson, L., Nelemans, G., et al. 2004, in *Astronomical Society of the Pacific Conference Series*, Vol. 318, *Spectroscopically and Spatially Resolving the Components of the Close Binary Stars*, ed. R. W. Hilditch, H. Hensberge, & K. Pavlovski, 402–410
- Németh, P., Kawka, A., & Vennes, S. 2012, *MNRAS*, 427, 2180
- Østensen, R. H., Geier, S., Schaffenroth, V., et al. 2013, *A&A*, 559, A35
- O'Toole, S. J., Heber, U., & Benjamin, R. A. 2004, *A&A*, 422, 1053
- Parsons, S. G., Gänsicke, B. T., Marsh, T. R., et al. 2018, *MNRAS*, 481, 1083
- Pelisoli, I., Neunteufel, P., Geier, S., et al. 2021, *Nature Astronomy*, 5, 1052
- Pelisoli, I., Vos, J., Geier, S., Schaffenroth, V., & Baran, A. S. 2020, *A&A*, 642, A180
- Pojmanski, G. 1997, *Acta Astron.*, 47, 467
- Preece, H. P., Tout, C. A., & Jeffery, C. S. 2018, *MNRAS*, 481, 715
- Ramsay, G., Woudt, P. A., Kupfer, T., et al. 2022, *MNRAS*, 513, 2215
- Randall, S. K., Matthews, J. M., Fontaine, G., et al. 2005, *ApJ*, 633, 460
- Ratzloff, J. K., Barlow, B. N., Kupfer, T., et al. 2019, *ApJ*, 883, 51
- Ratzloff, J. K., Barlow, B. N., Németh, P., et al. 2020a, *ApJ*, 890, 126
- Ratzloff, J. K., Kupfer, T., Barlow, B. N., et al. 2020b, *ApJ*, 902, 92
- Reed, M. D., Terndrup, D. M., Østensen, R., et al. 2010, *Ap&SS*, 329, 83
- Ricker, G. R., Winn, J. N., Vanderspek, R., et al. 2015, *Journal of Astronomical Telescopes, Instruments, and Systems*, 1, 014003
- Sahoo, S. K., Baran, A. S., Sanjayan, S., & Ostrowski, J. 2020, *MNRAS*, 499, 5508
- Schaffenroth, V., Barlow, B. N., Drechsel, H., & Dunlap, B. H. 2015, *Astronomy and Astrophysics*, 576, A123
- Schaffenroth, V., Barlow, B. N., Geier, S., et al. 2019, *A&A*, 630, A80
- Schaffenroth, V., Casewell, S. L., Schneider, D., et al. 2021, *MNRAS*, 501, 3847
- Schaffenroth, V., Classen, L., Nagel, K., et al. 2014a, *Astronomy and Astrophysics*, 570, A70
- Schaffenroth, V., Geier, S., Heber, U., et al. 2018, *Astronomy and Astrophysics*, 614, A77
- Schaffenroth, V., Geier, S., Heber, U., et al. 2014b, *Astronomy and Astrophysics*, 564, A98
- Schaffenroth, V., Pelisoli, I., Barlow, B. N., Geier, S., & Kupfer, T. 2022, *A&A*, 666, A182
- Silvotti, R., Németh, P., Telting, J. H., et al. 2022, *MNRAS*, 511, 2201
- Telting, J. H., Baran, A. S., Németh, P., et al. 2014, *A&A*, 570, A129
- Tokovinin, A., Fischer, D. A., Bonati, M., et al. 2013, *PASP*, 125, 1336
- Van Grootel, V., Charpinet, S., Fontaine, G., & Brassard, P. 2008, *A&A*, 483, 875
- Van Grootel, V., Charpinet, S., Fontaine, G., Green, E. M., & Brassard, P. 2010, *A&A*, 524, A63
- Verbeek, K., de Groot, E., Groot, P. J., et al. 2012, *MNRAS*, 420, 1115
- Vos, J., Németh, P., Vučković, M., Østensen, R., & Parsons, S. 2018, *MNRAS*, 473, 693
- Vos, J., Østensen, R. H., Németh, P., et al. 2013, *A&A*, 559, A54
- Vučković, M., Østensen, R., Bloemen, S., Decoster, I., & Aerts, C. 2008, in *Astronomical Society of the Pacific Conference Series*, Vol. 392, *Hot Subdwarf Stars and Related Objects*, ed. U. Heber, C. S. Jeffery, & R. Napiwotzki, 199
- Wegner, G. & McMahan, R. K. 1985, *AJ*, 90, 1511

Appendix A: Known reflection effect systems

Appendix A.1: BPS CS 22169-1

BPS CS 22169-0001 was discovered to be a sdB binary with very small RV amplitude by [Edelmann et al. \(2005\)](#). [Geier et al. \(2012\)](#) reported a tiny reflection effect with a period of 0.214 d. The minimum mass of the companion is only $0.026 M_{\odot}$. [Geier et al. \(2010b\)](#) also derived the rotational velocity of the sdB and calculated a companion mass of $0.19 M_{\odot}$ assuming tidal synchronization. However, in recent years, this assumption has been questioned ([Schaffenroth et al. 2021](#); [Preece et al. 2018](#)) and this would require a low inclination, which is quite unlikely.

The analysis of the *TESS* light curve (Fig. D.1a) results in an inclination of $7.6^{\circ} \pm 1.0^{\circ}$ resulting in a mass and radius of the companion of $0.23 \pm 0.03 M_{\odot}$ and $0.31 \pm 0.05 R_{\odot}$, demonstrating that it is indeed an M dwarf companion rather than a brown dwarf. With the radius of the sdB from the SED fit together with the determined inclination and the projected rotational velocity measured by [Geier et al. \(2010b\)](#) it is possible to derive the rotational velocity ($P_{\text{rot}} = 0.16 \pm 0.04$ d). This shows that the sdB rotation is almost tidally locked to the orbit.

Appendix A.2: PHL 457

PHL 457 was also discovered to be a close sdB binary with small RV amplitude by [Edelmann et al. \(2005\)](#). Light variations caused by long-period pulsations were found by [Blanchette et al. \(2008\)](#). [Schaffenroth et al. \(2014a\)](#) observed a small reflection effect in PHL 457 with a period of 0.3128 d and confirmed a small RV amplitude of only $K_1 = 12.8 \pm 0.08 \text{ km s}^{-1}$. This results in a minimum mass of $0.027 M_{\odot}$ for the companion, making it a brown dwarf if the inclination exceeds 21° . The likelihood of this being the case is 94%.

PHL 457 was observed in *K2* and *TESS*. [Baran et al. \(2019\)](#) analyzed the pulsations of PHL 457 and detected short- and long-period pulsations from 4.5 min to 1.8 hours. Our analysis of the *K2* light curve (Fig. D.1b) results in an inclination of $9.3^{\circ} \pm 1.6^{\circ}$, which translates to a companion mass and radius of $0.19 \pm 0.04 M_{\odot}$ and $0.16 \pm 0.04 R_{\odot}$. Hence, the companion is determined to be a low-mass M dwarf instead of a brown dwarf.

Appendix A.3: KBS 13

This sdB binary systems was found to show a reflection effect with a period of 0.2923 d by [For et al. \(2008\)](#). They derived a semi-amplitude of the radial velocity curve of $K_1 = 22.82 \pm 0.23 \text{ km s}^{-1}$. Using the mass function, a canonical mass for the sdB and the period from the *K2* and *TESS* light curves ($P = 0.292365$ d), we derive a minimum mass of only $0.045 M_{\odot}$, which is well below the limit for hydrogen burning.

From analysis of the *TESS* light curve (Fig. D.1c), we could derive an inclination of the system of $10.1^{\circ} \pm 0.4^{\circ}$, which gives us a mass for the companion of $0.260 \pm 0.008 M_{\odot}$ and a radius of $0.284 \pm 0.015 R_{\odot}$. Thus, the companion is an M dwarf and not a brown dwarf.

Appendix A.4: Feige 48

Feige 48 was identified to be a sdB star by [Green et al. \(1986\)](#). [Koen et al. \(1998\)](#) observed this target and found that it is one of the coolest sdBs showing short-period pulsations. [O'Toole et al. \(2004\)](#) analyzed UV spectra of Feige 48 proving that it is a close binary with a period of 0.376 d and a RV semi-amplitude of

$K_1 = 28 \pm 0.2 \text{ km s}^{-1}$. Assuming that the sdB rotation is tidally locked to the orbit, they derived a mass of $0.46 M_{\odot}$ for the companion and claimed it is most likely a white dwarf as they did not detect a reflection effect. [Van Grootel et al. \(2008\)](#) corroborated this by performing an asteroseismic analysis with the best model being for an object having a solid-body rotation with the orbital period. [Geier et al. \(2010b\)](#) re-measured the rotational velocity and derived a slightly higher $v \sin i = 8.5 \pm 1.5 \text{ km/s}$. A follow-up analysis of this system with time-resolved spectroscopy and photometry by [Latour et al. \(2014\)](#) found a shorter orbital period of only 0.3438 d and a reflection effect with the same period; therefore, they claimed that the companion is an M dwarf instead of a white dwarf.

The *TESS* light curve confirms the reflection effect (see Fig. D.1d). We were able to fit it and could so derive the inclination ($i = 16.3^{\circ} \pm 1.4^{\circ}$) and the mass and radius of the companion ($M_{\text{comp}} = 0.232 \pm 0.020 M_{\odot}$, $R_{\text{comp}} = 0.266 \pm 0.033 R_{\odot}$), confirming the M dwarf nature of the companion. Using the inclination, the radius of the sdB and projected rotational velocity by [Geier et al. \(2010b\)](#) we can calculate the rotational period of the sdB ($P_{\text{rot}} = 0.36 \pm 0.07$ d), showing that the rotation is most likely synchronized to the orbital period.

Appendix A.5: GALEX J2205-3141

[Németh et al. \(2012\)](#) identified GALEX J2205-3141 (GALEX J220551.8-314105) to be a sdB star from spectroscopic follow-up from the hot subdwarf candidates identified in the Galaxy Evolution Explorer (GALEX)/Guide star catalog (GSC) survey by an UV excess. Photometric and spectroscopic follow-ups carried out by [Kawka et al. \(2015\)](#) showed that the sdB is in a close binary system with an M dwarf companion with a period of 0.341543 d, as it shows a RV variation of $K_1 = 47.8 \pm 2.2 \text{ km/s}$ and a 4% amplitude reflection effect.

The *TESS* light curve also shows this reflection effect (see Fig. D.1e). From the best fit, we could derive an inclination of $17.3^{\circ} \pm 2.6^{\circ}$, giving a companion mass and radius of $0.53 \pm 0.10 M_{\odot}$ and $0.42 \pm 0.08 R_{\odot}$, which means the companion is an early M dwarf. This would be the highest mass companion found so far. At a mass this high it should be possible to detect spectral line contamination from the companion in the sdB spectrum. The radius of the companion is a bit smaller than expected for such an object, so the mass might be overestimated. The SED fitting (see Paper I) indicates that the mass of the sdB is not canonical but higher. More spectroscopic follow-up is necessary to determine the $\log g$ around phase 0, when the contribution of the companion is smallest, to better constrain the companion.

Appendix A.6: GALEX J09348-2512

GALEX J09348-2512 (GALEX J093448.2-251248) was found to be an sdB star by [Németh et al. \(2012\)](#). When searching for short-period variables in the ATLAS survey, [Koen \(2019\)](#) discovered light variations with a period of 0.143 d and an amplitude of 0.05 mag, indicating the presence of reflected light from the companion. The analysis suggested a companion mass close to $0.1 M_{\odot}$ but was lacking spectroscopic confirmation.

[Möller \(2021\)](#) analyzed archival spectra of this system and confirmed it to be a sdB binary ($T_{\text{eff}} = 40800 \pm 1000 \text{ K}$, $\log g = 5.55 \pm 0.10$) with a RV semi-amplitude of $K_1 = 37 \pm 4 \text{ km s}^{-1}$. The minimum companion mass can be calculated to $0.06 M_{\odot}$, which is below the hydrogen burning limit.

This system was also observed by *TESS*, which confirmed it to be a reflection effect system with a period of 0.142903 d. The analysis of the *TESS* light curve (Fig. D.1f) resulted in an inclination $i = 24.0^\circ \pm 3.0^\circ$ and a mass and radius of the companion of $0.165 \pm 0.022 M_\odot$ and $0.175 \pm 0.035 R_\odot$, showing that it is a low-mass M dwarf companion. The mass of the sdB derived by the SED method and *Gaia* parallax (see Paper I) is $0.737^{+0.176}_{-0.143} M_\odot$, namely, it is higher than the canonical sdB mass. However, the radius from the SED agrees with the radius derived by the light curve assuming a canonical mass for the sdB, while no consistent solution could be found using the mass derived by SED and parallax. This suggests that the determination of the mass with this method relying mainly on the $\log g$ determination from the co-added spectrum is not reliable because of contamination by light from the companion. This further demonstrates why we prefer the assumption of the canonical mass for the sdB for now.

Appendix A.7: EQ Psc

EQ Psc (PB 5450) was identified as a sdB star by Berger & Fringant (1980). Green et al. (2003) discovered long-period pulsations. From the *K2* light curve, Jeffery & Ramsay (2014) found that it not only shows several pulsation periods, but also a reflection effect with a period of 0.801 d. Baran et al. (2019) re-analyzed the photometry after combining it with additional time-resolved data. They found RV variations ($34.9 \pm 1.6 \text{ km s}^{-1}$) with the same period and confirmed the primary to be a sdB star.

The best fit of *TESS* the light curve (see Fig. D.1g) was found for an orbital inclination of $i = 25.4^\circ \pm 1.5^\circ$, giving us a mass and radius of the companion of $0.222 \pm 0.019 M_\odot$ and $0.181 \pm 0.014 R_\odot$. The radius of the companion is significantly smaller as expected by theoretical calculations (see Fig. 13). The SED and together with the parallax preferred a sdB mass of $0.35 M_\odot$, which results in a mass and radius of the companion of $0.253 \pm 0.012 M_\odot$ and $0.179 \pm 0.014 R_\odot$, which agrees better. Its mass is below the minimum mass for core helium burning, which could indicate that the hot subdwarf originates from a intermediate-mass progenitor or is a pre-He WD.

Appendix A.8: PG 1329+159

PG 1329+159 was discovered to be a sdB star by the Palomar Green (PG) survey (Green et al. 1986). In a survey to search for close sdB binaries, Morales-Rueda et al. (2003) found it to be RV variable with a period of 0.249699 d. Using follow-up photometry Maxted et al. (2004) found this system to also show a reflection effect indicating it to be a sdB+dM system.

The analysis of the *TESS* light curve (Fig. D.1h) gave an inclination of $i = 37.8^\circ \pm 2.1^\circ$, resulting in a mass and radius of the companion of $0.167 \pm 0.008 M_\odot$ and $0.199 \pm 0.016 R_\odot$. Geier et al. (2010b) also measured the rotational velocity of the sdB. Combining this result with sdB radius and inclination, we derived a rotational period of $P_{\text{rot}} = 0.64 \pm 0.07$ d. This means that rotation period is significantly higher than the orbital period.

Appendix A.9: CPD-64 481

CPD-64 481 is another close sdB binary with small RV amplitude discovered by Edelmann et al. (2005). Schaffenroth et al. (2014a) found a small reflection effect in its light curve with a period of 0.277263 d. In this case, the minimum companion mass was found to be $0.048 M_\odot$ making it another brown dwarf candidate.

CPD-64 481 was observed by *TESS* in 26 different sectors. From the analysis of the light curve (see Fig. D.1i), we could derive an inclination of $i = 34.3^\circ \pm 2.2^\circ$, resulting in a mass and radius for the companion of $0.088 \pm 0.006 M_\odot$ and $0.118 \pm 0.035 R_\odot$, showing that the companion is probably a low-mass M dwarf very close to the hydrogen-burning limit. Using the projected rotational velocity by Geier et al. (2010b) the rotation period is derived to be $P_{\text{rot}} = 1.22 \pm 0.30$ d. In this case, the sdB is thus shown to be rotating significantly more slowly than in a synchronized case.

Appendix A.10: JL 82

JL 82 was identified as a sdB star by the EC survey (Kilkenny et al. 1995). RV measurements from Edelmann et al. (2005) confirmed it to be a close sdB binary with a period of 0.737 d and a minimum companion mass of $0.1 M_\odot$. Koen (2009) showed that this star shows a reflection effect as well as long-period pulsations with periods between 1 and 4 hours.

The *TESS* light curve (Fig. D.1j) also shows this reflection effect. The best fit results in an inclination of the system to $29.1^\circ \pm 1.1^\circ$, which constrains the companion mass and radius to $0.240 \pm 0.009 M_\odot$ and $0.249 \pm 0.013 R_\odot$. With the radius of the sdB from the SED fit together with the inclination and the projected rotational velocity measured by Geier et al. (2010b) we can derive the rotational velocity ($P_{\text{rot}} = 0.61 \pm 0.07$ d). This shows that the sdB rotation is probably tidally locked to the orbit.

Appendix A.11: GALEX J0321+4727

Kawka et al. (2010) found GALEX J0321+4727 (GALEX J032139.8+472716) to be a close sdB binary with a period of 0.26584 d and $K_1 = 59.8 \pm 4.5 \text{ km s}^{-1}$, showing a reflection effect of about 6%.

The *TESS* light curve shows this reflection effect with a larger amplitude, as expected at longer wavelengths (Fig. D.1l). From the analysis of the light curve we derived an inclination of $38.6^\circ \pm 0.9^\circ$, which gives a companion mass and radius of $0.233 \pm 0.013 M_\odot$ and $0.298 \pm 0.026 R_\odot$.

Appendix A.12: SDSS J012022+395059

SDSS J012022+395059 (FBS 0117+396) was found to be a sdB star by Geier et al. (2011b). As this target showed quite a large radial velocity shift in a short time, it was flagged as a high-priority target for follow-up. Østensen et al. (2013) showed that this star exhibits a reflection effect and short-period pulsations. Additionally they also obtained spectroscopy showing it is indeed a close binary system with a period of 0.252013 d. The analysis of the *TESS* light curve (Fig. D.1m) resulted in an inclination of $i = 40^\circ \pm 7^\circ$, giving a companion mass and radius of $0.161 \pm 0.033 M_\odot$ and $0.241 \pm 0.062 R_\odot$.

Appendix A.13: UVEX 0328+5035

Verbeek et al. (2012) identified UVEX 0328+5035 (UVEX J032855.25+503529.8) as a single-lined sdB in the UV-Excess Survey of the Northern Galactic Plane (UVEX) survey. Kupfer et al. (2014) obtained spectroscopic and photometric follow-up observations and found it to be in a close binary with a period of 0.11017 d and a reflection effect amplitude of about 25%. The *TESS* light curve (Fig. D.1n) gives an inclination of $41.4^\circ \pm 0.6^\circ$

and a mass and radius of the companion of $0.160 \pm 0.003 M_{\odot}$ and $0.160 \pm 0.012 R_{\odot}$.

Appendix A.14: HS 2333+3927

This target was selected as a hot subdwarf candidate from the Hamburg-Schmidt (HS) Survey and confirmed as an sdB by [Edelmann et al. \(2003\)](#), who also identified it to be RV variable from two spectra. [Heber et al. \(2004\)](#) carried out photometric and spectroscopic follow-up observations of this target, confirming it to be a close reflection effect binary with a period of 0.1718023 d and RV semi-amplitude of $K_1 = 89.6 \text{ km s}^{-1}$. For the companion they derived a mass of $0.24 - 0.32 M_{\odot}$.

In their analysis, they found that the radius of the sdB is too small compared to the spectroscopic one. Even using a higher or lower mass for the sdB cannot solve this issue. It also does not agree with the radius determined by the SED (see Paper I), which agrees well with the spectroscopic $\log g$, when assuming a canonical mass. No model could be found for the correct radius of the sdB, as the size of the companion would have to be larger than its Roche lobe to match the amplitude of the reflection effect. By increasing the 'absorb' factor to absorb=2, we can solve this issue. This has also been found for other systems (e.g., [Schaffenroth et al. 2014b](#)). One possible explanation for this is that we are using a blackbody instead of a synthetic spectrum for modelling the reflection effect. This underestimates the flux of the sdB in the UV, and HS 2333+3927 is relatively hot and so a lot of the stellar flux is emitted in the UV.

We get an inclination of $42.8^{\circ} \pm 0.5^{\circ}$ and a mass and radius of the companion of $0.286 \pm 0.008 M_{\odot}$ and $0.40 \pm 0.02 R_{\odot}$ with this assumption. The companion is hence an early M dwarf. To solve this issue, the spectral analysis should be re-done with the newest generation of model spectra to see whether the problem can be solved, as a higher temperature of the sdB would also result in a higher reflection effect amplitude.

Appendix A.15: V1405 Ori

KUV 0442+1416, also called V1405 Ori, was identified as an sdO or sdB by [Wegner & McMahan \(1985\)](#). [Koen et al. \(1999\)](#) demonstrated an absence of He II lines, making it a sdB star. Additionally, they detected short-period pulsations and reddening in this target, which could either come from interstellar reddening or from a cool companion. [Reed et al. \(2010\)](#) later discovered a reflection effect with an amplitude of about 20%. They also found RV variations with a period of 0.398 d and a semi-amplitude of $K_1 = 85.1 \pm 8.6 \text{ km s}^{-1}$, which results in a minimum companion mass of $0.25 M_{\odot}$, making it an early M type companion.

The *TESS* light curve confirms the observation of the reflection effect (Fig. D.1p). From the analysis, we find an inclination of $43^{\circ} \pm 0.9^{\circ}$ as well as a mass and radius of the companion of $0.390 \pm 0.031 M_{\odot}$ and $0.341 \pm 0.038 R_{\odot}$, making it an early type M dwarf, as expected.

Appendix A.16: HE 0230-4323

HE 0230-4323 was found to be a sdB star by [Lisker et al. \(2005\)](#) and confirmed to be in a close binary system by [Edelmann et al. \(2005\)](#) with a period of 0.4515 d. [Koen \(2007\)](#) found it to show a reflection effect as well as low-amplitude pulsations with periods between 24 to 45 min in the light curve.

The *TESS* light curve (Fig. D.1s) confirms this reflection effect. The best fit constrains the inclination of the system to $52.6^{\circ} \pm 1.5^{\circ}$, which constrains the companion mass and radius to $0.209 \pm 0.006 M_{\odot}$ and $0.307 \pm 0.012 R_{\odot}$.

Appendix A.17: HE 1318-2111

HE 1318-2111 was discovered to be a sdB star in the EC survey ([Kilkenny et al. 1997](#)). [Christlieb et al. \(2001\)](#) rediscovered it in the Hamburg/ESO objective-prism (HE) survey. In the ESO Supernovae type Ia Progenitor survey (SPY) [Napiwotzki et al. \(2004\)](#) took spectroscopic follow-up of several sdO/B stars and discovered that HE 1318-2111 was in a close binary system with a period of 0.487 d. In the *TESS* light curves, we discovered that it also shows a reflection effect. At the same time [Sahoo et al. \(2020\)](#) also found the reflection effect in the light curves of sdB candidates from [Geier et al. \(2019\)](#) derived by the *TESS* full-frame images. From the light curve, we derived an orbital inclination of $i = 56.5^{\circ} \pm 1.7^{\circ}$, giving us a mass and radius of the companion of $0.158 \pm 0.006 M_{\odot}$ and $0.277 \pm 0.015 R_{\odot}$.

Appendix B: The sdB+WD systems

Appendix B.1: PG 1043+760

PG 1043+760 was identified to be a hot subdwarf in the PG survey ([Green et al. 1986](#)). [Maxted et al. \(2001\)](#) discovered it to be in a close binary with a period of 0.12 d. They could not detect any light variations and claimed therefore that the companion must be a low-mass He WD.

The light curve of PG 1043+760 (see Fig. D.2c) observed by *TESS* shows ellipsoidal modulation and beaming with an amplitude of only 0.2%. From a modeling of the light curve, we derived a very low inclination of only $15^{\circ} \pm 0.6^{\circ}$ and a mass ratio of 1.65 ± 0.11 , which results in a companion mass of $0.48 \pm 0.08 M_{\odot}$ and, hence, the companion could be a CO WD or a He WD orbiting a sdB with a mass of $0.289_{-0.036}^{+0.038} M_{\odot}$.

Appendix B.2: GALEX J0751+0925

GALEX J0751+0925 (GALEX J075147.0+092526) was found to be a sdB by [Németh et al. \(2012\)](#). Furthermore, [Kawka et al. \(2015\)](#) carried out spectroscopic follow-up of this star and discovered that it is in a close binary with a period of 0.178319 d. They also checked the light curve of the system taken by the All Sky Automated survey (ASAS, [Pojmanski 1997](#)) but could not see any variation with an upper limit of 44 mmag. So they concluded that the unseen companion is most likely a WD.

The *TESS* light curve of this system (see Fig. D.2b) varies with half of the orbital period most likely due to ellipsoidal deformation confirming that the companion is indeed a WD. Our analysis results in an inclination of $i = 74 \pm 10^{\circ}$ and a mass ratio of $0.85_{-0.04}^{+0.09}$, making the companion a He WD with a mass of $0.31+0.07_{-0.03} M_{\odot}$.

Appendix B.3: HS1741+2133

HS 1741+2133 was identified as a sdB by [Edelmann et al. \(2003\)](#). [Kupfer et al. \(2014\)](#) observed this system further and found it to be a close sdB binary with a period of 0.2 d and a semi-amplitude of $K_1 = 157 \text{ km/s}$, giving a minimum companion mass of $0.39 M_{\odot}$. As no photometric variability with an upper limit of 6 mmag was found by [Dreizler et al. \(2002\)](#), they concluded that the companion must be a WD.

HS1741+2133 was only observed on the full-frame images in sector 26 with an exposure time of 1426 sec resulting in 12 data points per orbital period. Phase-folding it to the orbital period showed an ellipsoidal deformation (Fig. D.2d). From the light curve, we obtained an inclination of $47^\circ \pm 11^\circ$ resulting in a companion mass of $0.58^{+0.3}_{-0.15} M_\odot$. Thus, the companion is most likely a CO WD. To exclude smearing effects, the analysis should be repeated using a higher cadence light curve.

Appendix B.4: PG 1136-003

PG 1136-003 was also found to be a sdB by Green et al. (1986). Spectroscopic follow-up by Geier et al. (2011a) showed a large RV shift over a period of one day and made it a high priority target. Geier et al. (2011b) showed that it is a close binary with a period of 0.207536 d. The companion has a minimum mass of $0.42 M_\odot$ and is most likely a WD.

The 30 min *K2* light curve of PG 1136-003 (see Fig. D.2e) clearly shows ellipsoidal modulation as well as beaming due to a massive compact companion confirming that it is most likely a WD companion. As the cadence of the light curve is 10% of the orbital period, smearing will be quite important and the amplitude of the ellipsoidal modulation will be underestimated. Thus, a photometric follow-up has to be obtained for an analysis of the system. Fortunately, the system was also observed in *TESS* with a 2 min cadence. The analysis of this light curve resulted in an inclination of $75^\circ \pm 11^\circ$, as well as a mass ratio of $0.90^{+0.10}_{-0.04}$, corresponding to a companion mass of $0.45^{+0.08}_{-0.05} M_\odot$. With this mass, the companion could be a He WD or a low-mass CO WD orbiting a sdB star with $0.501^{+0.096}_{-0.078} M_\odot$.

Appendix B.5: GD 687

GD 687 was classified first as a WD by Guseinov et al. (1983). Lisker et al. (2005) revised that classification and determined the star to be a sdB instead. Geier et al. (2010a) discovered that it is RV variable with a period of 0.37765 d. Using the assumption of a tidally locked rotation, they derived a mass of $0.7 \pm 0.2 M_\odot$ for the companion, which would mean it is very likely a CO WD.

The system was also observed by *TESS*, and the phased light curve (Fig. D.2a) shows a sinusoidal variation with a period of half of the orbital period, which is most likely due to ellipsoidal deformation. From the fit of the light curve we get an inclination of $58^\circ \pm 8^\circ$ with a mass ratio of $1.23^{+0.24}_{-0.14}$, which constrains the white dwarf companion to a He WD with a mass of $0.35^{+0.09}_{-0.06} M_\odot$, as the mass of the sdB is only $0.283^{+0.042}_{-0.037} M_\odot$. This means that the sdB is more likely a pre-He WD instead of a helium-core burning object. Using the rotational velocity by Geier et al. (2010a), as well as the inclination and sdB radius, we derived a rotational period of $P_{\text{rot}} = 0.39 \pm 0.05$ d, agreeing with a tidally locked rotation of the sdB.

Appendix B.6: GALEX J234947.7+384440

GALEX J234947.7+384440 was identified as an RV variable sdB by Kawka et al. (2010). Based on the lack of photometric variability, these authors suggested that the companion is most likely a WD with a minimum mass of $0.24 M_\odot$. The *TESS* light curve (Fig. D.2h) clearly shows two peaks over one orbital period, indicating Doppler beaming and ellipsoidal modulation. We obtained a good solution for an inclination of $70^\circ \pm 10^\circ$. This corresponds to a He WD companion with a mass of only $0.26 \pm 0.04 M_\odot$.

Appendix B.7: PG0101+039

PG0101+039 (Feige 11) was classified as A0p star by Feige (1958). Later this classification was revised in the PG survey (Green et al. 1986) and the star identified as sdB star. Maxted et al. (2001) showed that the sdB is in a close binary with period of 0.567 d orbited by a white dwarf companion. Green et al. (2003) discovered that the sdB also shows low-amplitude long-period pulsations. Randall et al. (2005) analyzed the ~ 400 h long light curve of PG0101+039 observed with the MOST satellite and found that in addition to several pulsation modes, a long-period variation is also visible with half the orbital period and likely originates from ellipsoidal deformation of the sdB. Geier et al. (2008) investigated this system further by trying to model the ellipsoidal deformation by determining the inclination by measuring the rotational velocity of the sdB and assuming synchronization. They found that the amplitude of the variation is of the order of what is expected from ellipsoidal deformation, but the period was not sufficiently well determined to match the light variations with the RV variations.

PG0101+039 was also observed by the *K2* mission. The light curve phased to the orbital period is shown in Fig. D.2g. The main variation seems not to be half of the orbital phase, but instead, the light curve seems to vary with the full orbital period and is dominated by beaming. However, there is a second, much smaller peak at half of the orbit showing a tiny ellipsoidal deformation. From the light curve, we get a good solution for a very high inclination close to $89.4^\circ \pm 0.06^\circ$, resulting in a mass ratio of $0.8174^{+0.0001}_{-0.0001}$, corresponding to a He WD companion with $0.34 \pm 0.04 M_\odot$. Using the rotational velocity measured by Geier et al. (2008) we derived a rotational period of $P_{\text{rot}} = 0.85 \pm 0.09$ d, which means that the sdB rotation is not tidally locked, but the sdB is rotating slower. The light curve model does not agree perfectly, but some residuals remain, which probably come from the effect of the tidal bulge lacking behind, as the sdB rotates more slowly than the orbital period. A more detailed analysis that factors in this aspect is beyond the scope of this paper, but ought to be performed in the future.

Appendix B.8: EC 13332-1424

EC 13332-1424 was classified as a sdB in the EC survey (Kilkenny et al. 1997). Spectroscopic follow-up by Copperwheat et al. (2011) showed that the sdB is in a close binary system with a period of 0.82794 d with a semi-amplitude of the RV curve of $104.1 \pm 3.0 \text{ km s}^{-1}$. Using this result we can calculate a minimum mass of the companion of $0.43 M_\odot$, so it is most likely a white dwarf.

EC 13332-1424 was observed in the *K2* mission and in the light curve a clear periodic signal with the orbital period is visible (see Fig. D.2f). There is one dominating peak visible, which is most likely resulting from Doppler beaming as in PG 1232-136. Moreover, there is a smaller variation apparent most likely due to a tiny ellipsoidal deformation. From the light curve, we can constrain the inclination to $i = 82^\circ \pm 2^\circ$ resulting in a He-WD companion with a mass of $0.4 \pm 0.06 M_\odot$ assuming the most probable mass of an sdB with a WD companion ($0.4 M_\odot$, see Paper I).

Appendix C: Radial velocity measurements

Table C.1: RV measurements of TYC5977-517-1

BMJD	RV [km/s]	RV error [km/s]
58641.48626	60.1	11.8
58641.48675	56.6	4.1
58641.48724	51.3	12.4
58641.48772	23.8	12.4
58641.48821	39.3	6.3
58641.48870	49.4	6.2
58641.48919	36.3	17.6
58641.48968	39.4	7.5
58641.49017	27.0	8.1
58641.49065	50.5	17.2
58641.49163	57.3	15.5
58641.49212	41.8	8.6
58641.49261	47.8	10.2
58641.49310	89.3	10.3
58641.49359	71.9	10.1
58641.49408	68.9	9.3
58641.49456	45.7	11.2
58641.49505	54.9	8.8
58641.49554	44.0	11.1
58641.49603	54.3	8.4
58641.49652	37.4	7.0
58641.49701	56.1	10.1
58641.49750	81.7	8.3
58641.49799	60.3	11.6
58641.49847	66.9	11.6
58641.49896	34.3	15.4
58641.49945	82.8	7.1
58641.49994	80.7	3.6
58641.50043	95.2	13.7
58641.50092	68.1	15.0
58641.50140	105.4	9.2
58641.50189	73.0	12.6
58641.50238	81.9	12.8
58641.50287	107.6	16.4
58641.50336	79.6	9.2
58641.50385	88.0	11.4
58641.50434	106.8	15.5
58641.50483	86.7	14.6
58641.50531	73.9	22.4
58641.50580	56.6	10.4
58641.50629	73.4	9.3
58641.50678	77.8	9.2
58641.50727	65.9	8.3
58641.50776	59.1	14.5
58641.50824	66.1	11.8
58641.50873	61.4	5.3
58641.50922	75.3	9.9
58641.50971	62.1	9.0
58641.51020	62.8	11.7
58641.51069	57.2	7.3
58641.51118	48.0	13.3
58641.51167	54.1	13.6
58641.51215	63.2	40.9
58641.51264	74.8	14.4
58641.51313	61.8	7.7
58641.51411	84.6	14.0
58641.51460	49.9	17.3
58641.51509	103.9	10.8
58641.51557	78.9	10.9
58641.51606	88.8	9.4
58641.51655	65.1	17.0
58641.51704	91.4	15.1
58642.45281	-94.3	7.2
58642.45330	-83.9	7.6
58642.45378	-71.1	4.8
58642.45427	-79.5	5.5
58642.45476	-72.0	3.8

Table C.1: RV measurements of TYC5977-517-1 (continued)

BMJD	RV [km/s]	RV error [km/s]
58642.46040	-53.7	7.2
58642.46089	-65.7	5.2
58642.46138	-53.9	7.0
58642.46187	-54.8	5.7
58642.46236	-49.7	7.9
58642.46284	-37.8	7.8
58642.46333	-41.7	10.3
58642.46382	-51.8	3.4
58642.46431	-31.6	9.0
58642.46480	-51.6	5.9
58642.46529	-37.2	9.8
58642.46578	-48.2	6.1
58642.46627	-37.7	5.2
58642.46675	-44.2	4.1
58642.46724	-24.4	6.2
58642.46773	-30.6	6.0
58642.46822	-25.9	4.6
58642.46871	-26.3	4.6
58642.46920	-18.1	4.0
58642.46969	-14.1	8.1
58642.47018	-27.4	4.7
58642.47066	-21.5	2.1
58642.47115	-14.3	7.4
58642.47164	-12.6	4.3
58642.47213	-28.6	1.5
58642.47262	-19.0	3.4
58642.47311	-0.5	11.6
58642.47360	-20.5	6.4
58642.47409	-9.8	6.9
58642.47457	-8.9	5.7
58642.47506	-10.3	3.4
58642.47555	0.7	11.5
58642.47604	7.5	16.4
58642.47653	11.8	9.0
58642.47702	-2.4	5.7
58642.47751	-6.8	7.1
58642.47800	-0.0	9.8
58642.47848	-0.8	5.7
58642.47897	-9.4	3.3
58642.47946	-2.8	10.7
58642.47995	3.5	7.5
58642.48044	1.1	9.1
58642.48093	14.3	9.1
58642.48142	21.9	6.9
58642.48190	28.4	8.3
58642.48239	23.7	13.5
58642.48288	14.2	5.0
58642.48337	43.0	15.5
58642.48386	26.9	6.2
58642.48435	36.2	4.8
58642.48484	33.9	7.1
58642.48533	22.4	5.5
58642.48581	11.6	11.3
58642.48630	17.0	6.4
58642.48679	27.1	6.4
58642.48728	39.2	7.3
58642.48777	44.9	4.8
58642.48826	46.1	5.8
58642.48875	43.1	8.9
58642.48924	28.3	3.9
58642.48972	31.5	8.6
58642.49021	54.6	6.2
58642.49070	56.2	6.1
58642.49119	75.2	12.2
58642.49168	49.2	10.9
58642.49217	55.6	16.0
58642.49266	70.0	6.2

Table C.1: RV measurements of TYC5977-517-1 (continued)

BMJD	RV [km/s]	RV error [km/s]
58642.49315	49.8	14.1
58642.49363	33.3	10.4
58642.49412	61.7	4.7
58642.49461	81.1	11.4
58642.49510	43.7	6.4
58642.49559	54.8	5.2
58642.49608	49.0	5.7
58642.49657	53.7	7.0
58642.49705	62.3	7.8
58642.49754	58.5	4.2
58642.49803	82.1	9.6
58642.49852	72.3	6.6
58642.49901	73.6	7.0
58642.49950	65.5	8.3
58642.49999	83.4	13.7
58642.50048	71.0	5.7
58642.50096	76.7	7.1
58642.50145	66.0	3.1
58642.50194	80.2	8.7
58642.50243	77.3	6.5
58642.50292	79.4	3.1
58642.50341	78.8	6.0
58642.50390	83.3	6.3
58642.50439	86.1	6.2
58642.50487	79.1	3.3
58642.50536	93.7	6.8
58642.50585	81.1	3.1
58642.50634	84.0	8.7
58642.50683	107.0	10.3
58642.50732	103.8	8.0
58642.50781	91.0	8.8
58642.50830	93.8	3.5
58642.50879	84.8	8.3
58642.50927	113.5	11.0
58642.50976	98.8	9.6
58642.51025	98.6	6.5
58642.51074	89.0	5.6
58642.51123	100.5	7.9
58642.51172	107.0	11.2
58642.51221	100.8	9.6
58642.51269	97.7	4.6
58642.51318	104.3	12.3
58642.51367	98.6	4.6
58642.51416	94.6	5.2
58642.51465	78.4	5.5
58642.51514	99.0	4.6
58642.51563	121.1	11.1
58642.51612	108.5	7.1
58643.45344	-82.9	3.1
58643.45393	-79.4	6.5
58643.45442	-86.6	4.0
58643.45491	-86.1	4.7
58643.45539	-84.8	4.3
58643.45588	-86.8	4.9
58643.45637	-80.1	6.0
58643.45686	-79.5	4.3
58643.45735	-80.9	4.3
58643.45784	-77.7	5.9
58643.45833	-80.6	4.3
58643.45882	-83.9	6.9
58643.45931	-81.9	3.6
58643.45979	-68.2	6.8
58643.46028	-78.2	4.8
58643.46077	-71.3	5.3
58643.46126	-85.2	5.8
58643.46175	-68.6	6.1

Table C.1: RV measurements of TYC5977-517-1 (continued)

BMJD	RV [km/s]	RV error [km/s]
58643.46224	-69.0	5.5
58643.46273	-72.0	7.0
58643.46322	-69.7	5.3
58643.46370	-62.5	5.8
58643.46419	-69.5	4.1
58643.46468	-65.6	5.3
58643.46517	-69.8	7.4
58643.46566	-60.0	4.9
58643.46615	-59.1	3.4
58643.46664	-56.7	5.9
58643.46713	-53.7	5.1
58643.46761	-49.7	4.4
58643.46810	-46.7	3.5
58643.46859	-52.2	6.0
58643.46908	-44.1	5.3
58643.46957	-57.8	3.6
58643.47006	-47.2	3.7
58643.47054	-44.8	5.9
58643.47103	-46.1	5.2
58643.47152	-43.2	6.8
58643.47201	-36.2	3.9
58643.47250	-37.0	6.2
58643.47299	-38.1	4.7
58643.47348	-34.1	2.8
58643.47397	-38.8	2.8
58643.47446	-36.2	6.3
58643.47494	-39.6	3.7
58643.47543	-30.8	3.6
58643.47592	-28.5	4.0
58643.47641	-23.5	4.0
58643.47690	-30.3	4.0
58643.47739	-29.4	2.2
58643.47788	-28.2	5.6
58643.47836	-28.2	3.7
58643.47885	-15.3	5.4
58643.47934	-22.5	5.1
58643.47983	-17.1	4.0
58643.48032	-3.2	7.3
58643.48081	-8.8	7.1
58643.48130	-13.9	3.0
58643.48179	-1.5	3.2
58643.48227	-5.0	4.7
58643.48276	-1.2	5.5
58643.48325	-4.5	6.6
58643.48374	-2.0	6.1
58643.48423	4.8	3.3
58643.48472	2.6	7.5
58643.48521	16.1	7.0
58643.48570	8.9	5.4
58643.48619	11.1	6.5
58643.48667	20.0	3.9
58643.48716	13.1	4.6
58643.48765	15.0	5.9
58643.48814	24.8	8.4
58643.48863	15.2	5.6
58643.48912	22.6	3.8
58643.48961	30.5	8.7
58643.49010	21.3	5.5
58643.49058	26.3	2.8
58643.49107	21.9	3.2
58643.49156	24.2	4.4
58643.49205	28.3	6.9
58643.49254	27.7	3.8
58643.49303	32.2	5.7
58643.49352	39.1	7.6
58643.49401	25.2	2.6
58643.49449	35.8	3.6

Table C.1: RV measurements of TYC5977-517-1 (continued)

BMJD	RV [km/s]	RV error [km/s]
58643.49498	40.9	3.6
58643.49547	38.7	4.5
58643.49596	49.1	6.8
58643.49645	45.8	4.5
58643.49694	45.3	2.3
58643.49743	40.1	3.2
58643.49791	42.9	1.6
58643.49840	41.6	2.3
58643.49889	48.3	7.5
58643.49938	58.9	3.3
58643.49987	56.4	5.4
58643.50036	41.6	6.8
58643.50085	54.2	2.2
58643.50134	49.3	4.1
58643.50182	57.8	4.7
58643.50231	70.1	3.2
58643.50280	59.2	5.4
58643.50329	71.2	2.5
58643.50378	75.6	5.4
58643.50427	70.6	3.1
58643.50476	69.1	4.0
58643.50525	78.9	8.8
58643.50574	68.4	4.0
58643.50622	78.3	2.4
58643.50671	89.7	6.0
58643.50720	75.8	5.7
58643.50769	89.3	3.0
58643.50818	89.3	1.9

Table C.2: RV measurements of EC 01578-1743

BMJD	RV [km/s]	RV error [km/s]
58117.61897	-97.5	1.3
58136.59910	63.0	2.0
58144.57225	31.1	1.7
58149.54667	41.0	1.5
58149.56061	19.9	1.3
58174.50767	25.6	1.4
58176.51123	-90.2	1.8
58329.90219	50.4	1.2
58329.91613	61.4	1.1
58329.93007	67.8	1.0
58332.86085	-75.1	1.2
58332.87480	-92.2	2.8
58332.88874	-105.0	2.4
58344.82524	-39.3	1.3
58344.83918	-14.7	1.4
58344.85313	13.2	1.7
58344.86707	43.0	1.2
58344.88101	58.0	1.2
58345.89400	32.3	1.5
58345.90800	52.1	1.0
58345.92199	64.2	1.0
58345.93598	65.3	0.9
58357.80549	67.1	1.1
58357.81943	60.6	1.3
58357.83338	46.1	1.0
58357.84732	24.7	0.9
58357.86126	-2.4	1.0
58358.80734	44.9	1.1
58358.82128	60.3	1.1
58358.83523	66.9	1.2
58358.84917	62.6	1.0
58358.86311	50.7	1.1
58379.88558	-102.6	3.1
58382.80772	41.2	1.7
58382.82166	57.9	1.5
58383.75839	-106.0	4.3
58383.77257	-87.5	1.7
58384.72334	-44.9	1.3
58384.73941	-72.7	1.4

Table C.3: RV measurements of KPD 0629-0016

BMJD	RV [km/s]	RV error [km/s]	instrument
54476.69426	37.1	8.6	EMMI
54477.61197	-1.3	8.0	EMMI
54477.68846	-13.4	3.4	EMMI
54478.62101	-34.4	7.1	EMMI
54478.67763	-58.2	3.7	EMMI
54478.77402	-73.3	4.3	EMMI
54479.62414	-75.1	8.9	EMMI
54479.63799	-46.8	10.1	EMMI
54479.66199	-53.9	8.3	EMMI
54479.67306	-63.6	8.1	EMMI
54479.68573	-74.7	8.2	EMMI
54479.69438	-47.8	7.7	EMMI
54755.78643225	57.23	13.05	EFOSC2
54756.78528812	64.36	12.14	EFOSC2
56690.53874	51.89	9.95	EFOSC2
56690.61981	44.66	9.95	EFOSC2
56691.52766	-8.88	11.04	EFOSC2

Appendix D: Light curves of the reflection effect and the ellipsoidal and Doppler beaming systems

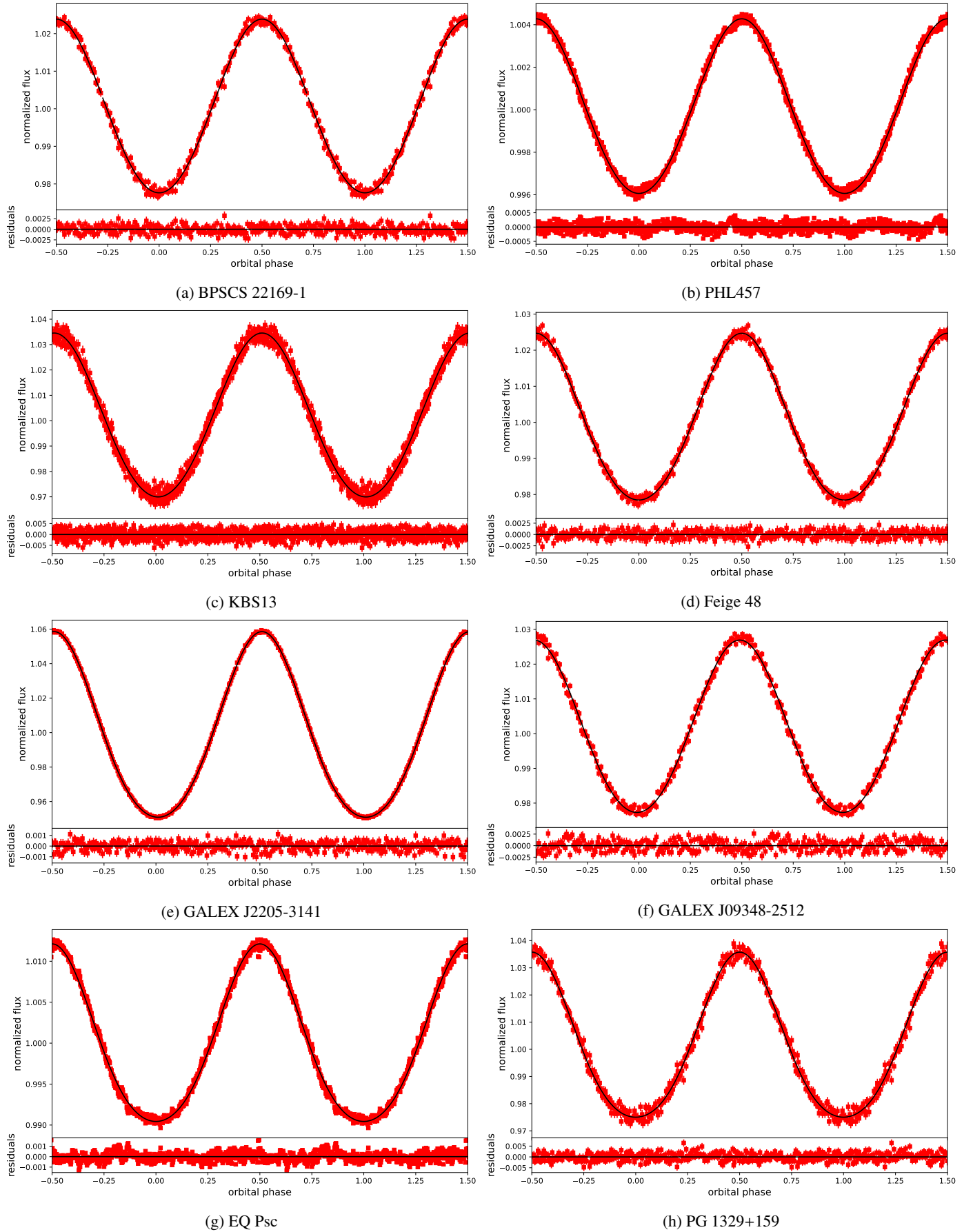


Fig. D.1: Phased light curve (given by the red squares) together with the best-fit model given by the black line. Lower panel shows the residuals.

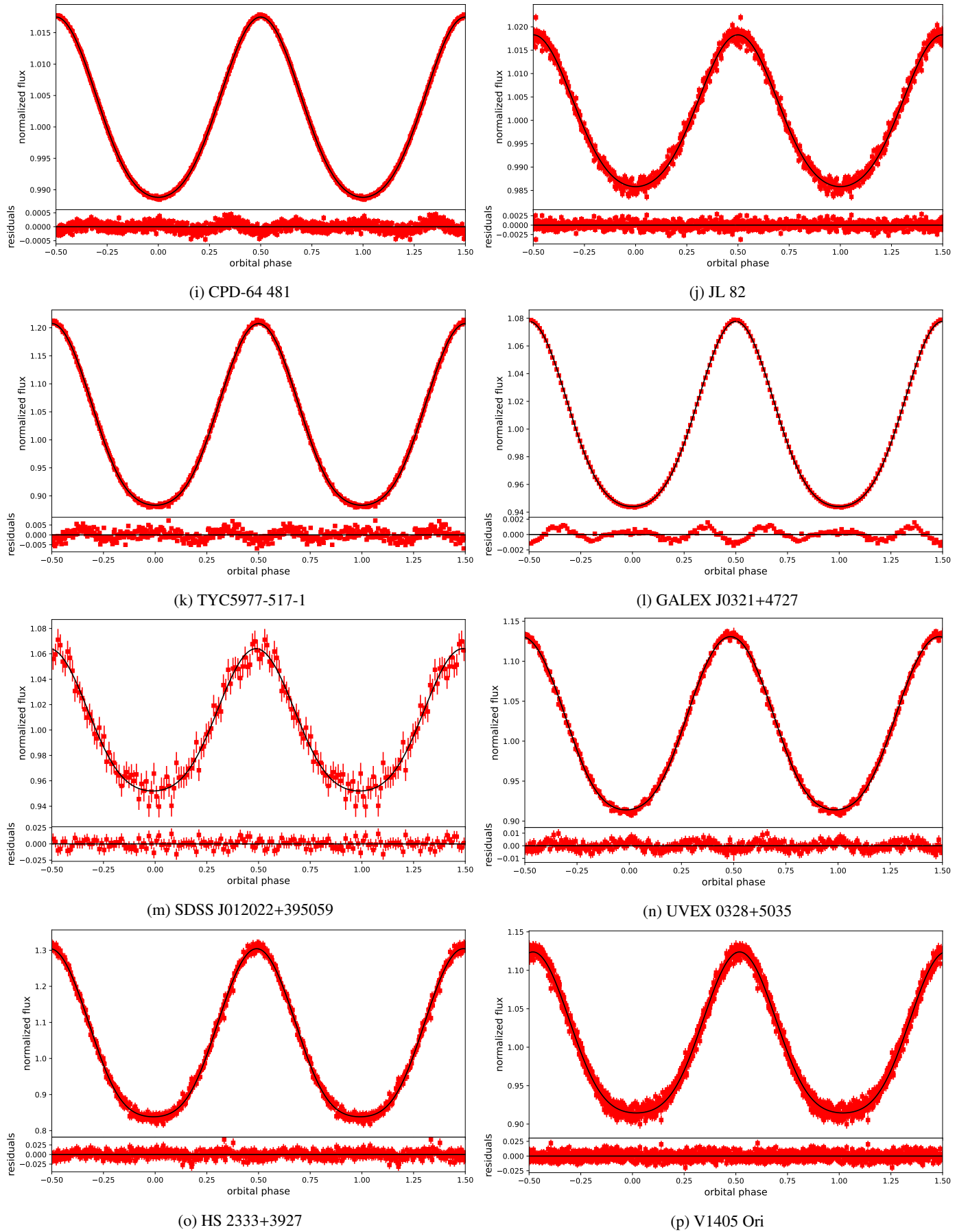


Fig. D.1: Phased light curve (given by the red squares) together with the best-fit model given by the black line. Lower panel shows the residuals (continued).

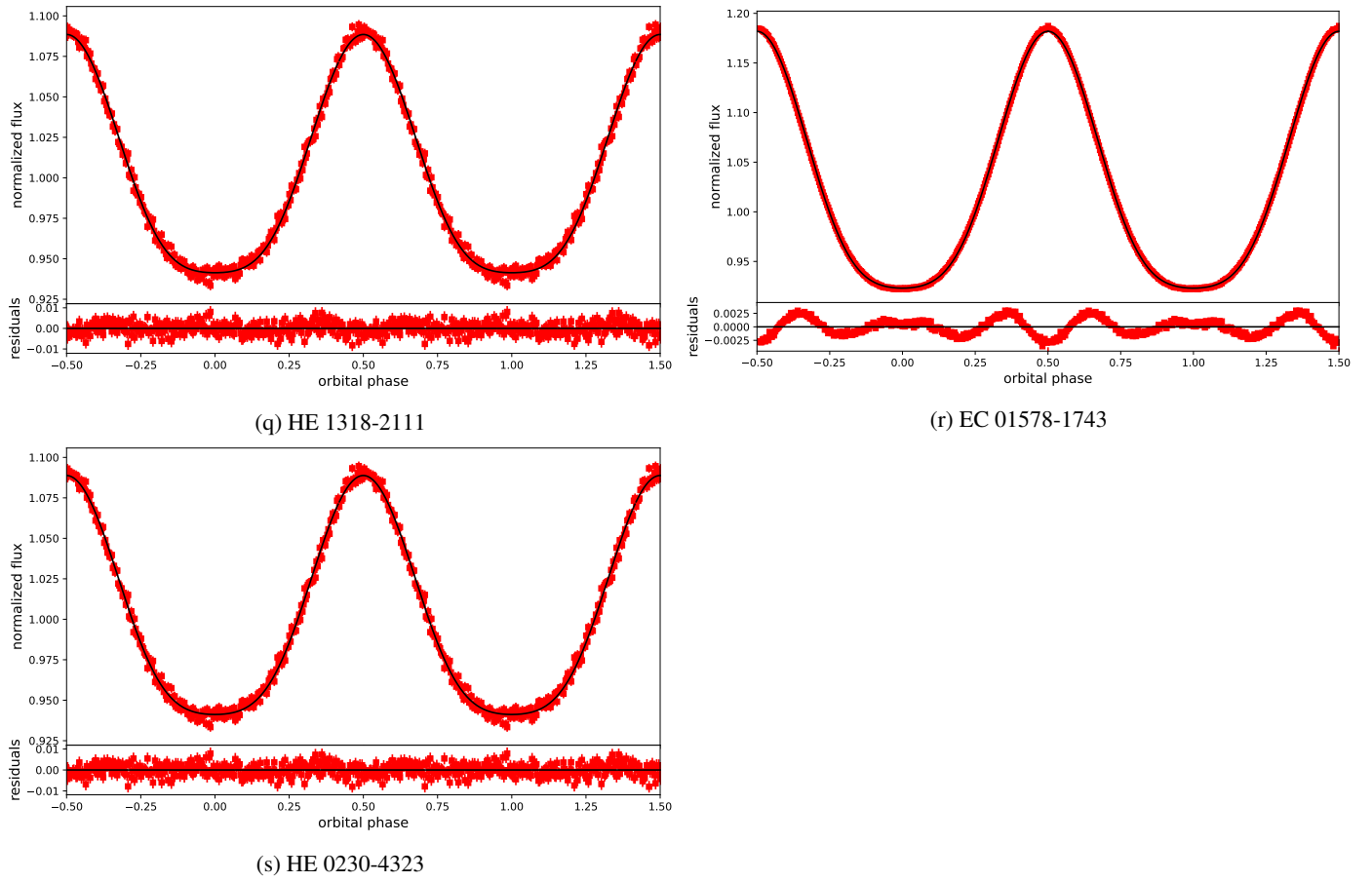


Fig. D.1: Continuation: Phased light curve (given by the red squares) together with the best-fit model given by the black line. Lower panel shows the residuals (continued).

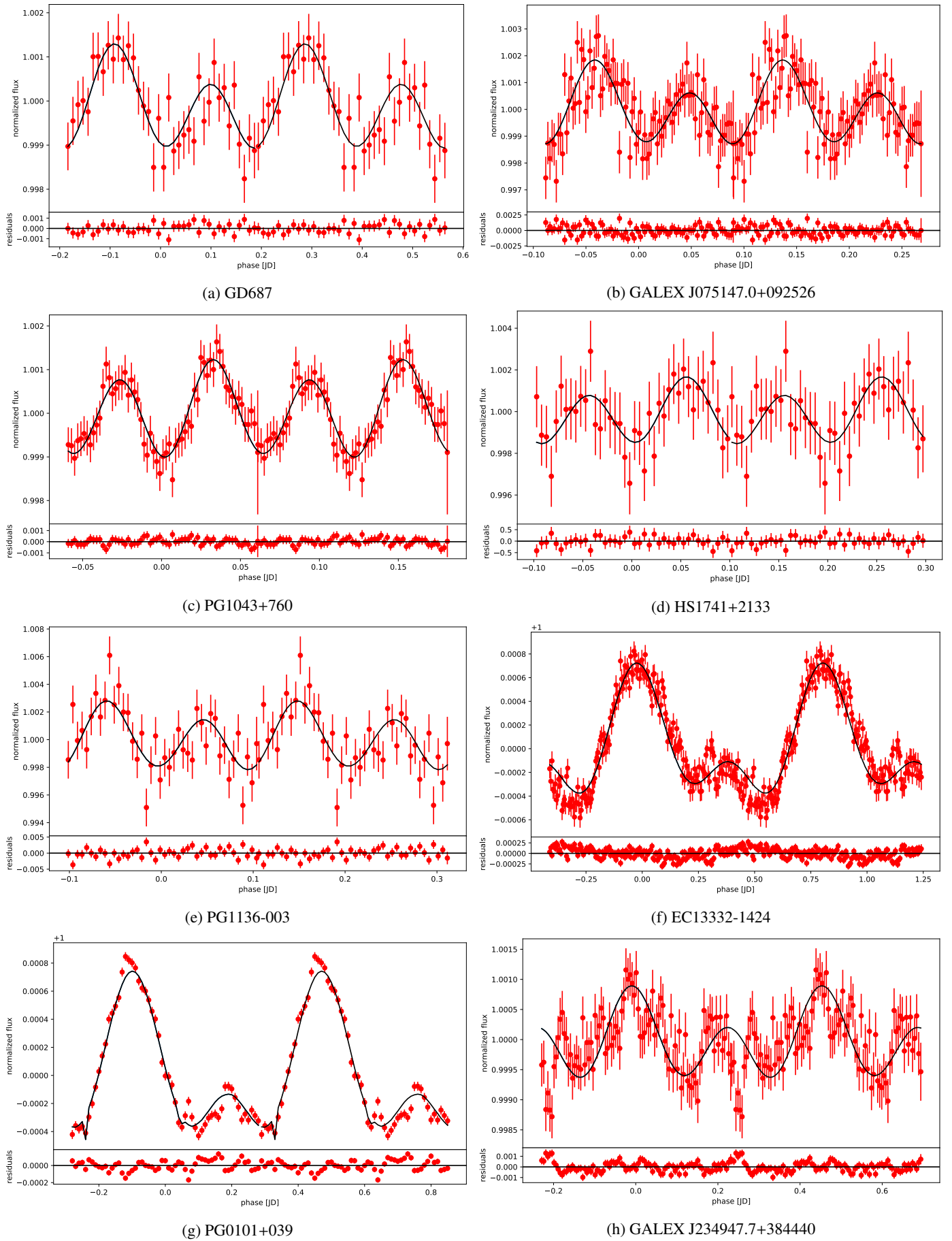


Fig. D.2: Binned light curve of the newly confirmed sdB+WD systems with best model fit shown with the black line and the residuals in the lower panel.

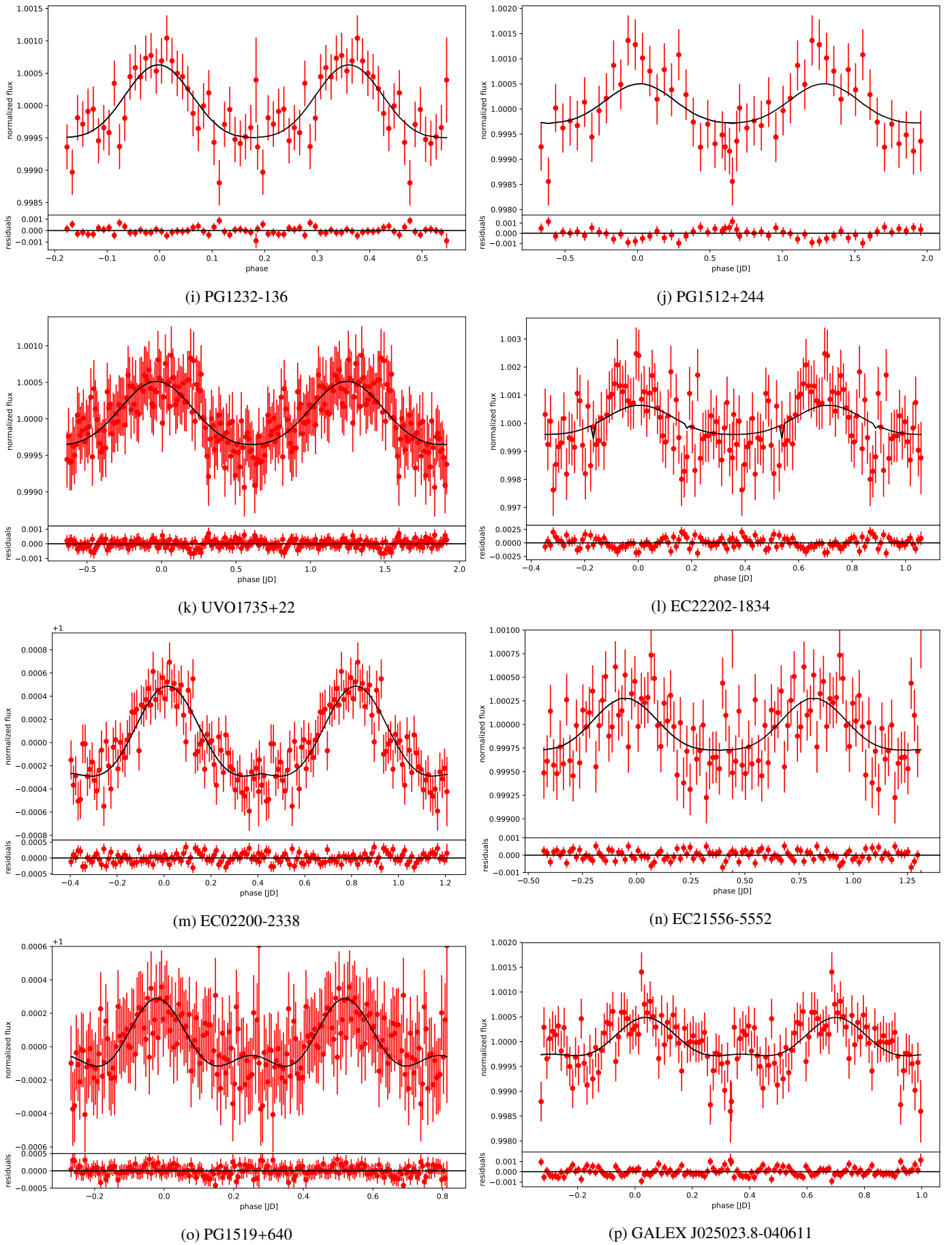


Fig. D.2: Binned light curve of the newly confirmed sdB+WD systems with best model fit shown with the black line and the residuals in the lower panel (continued).

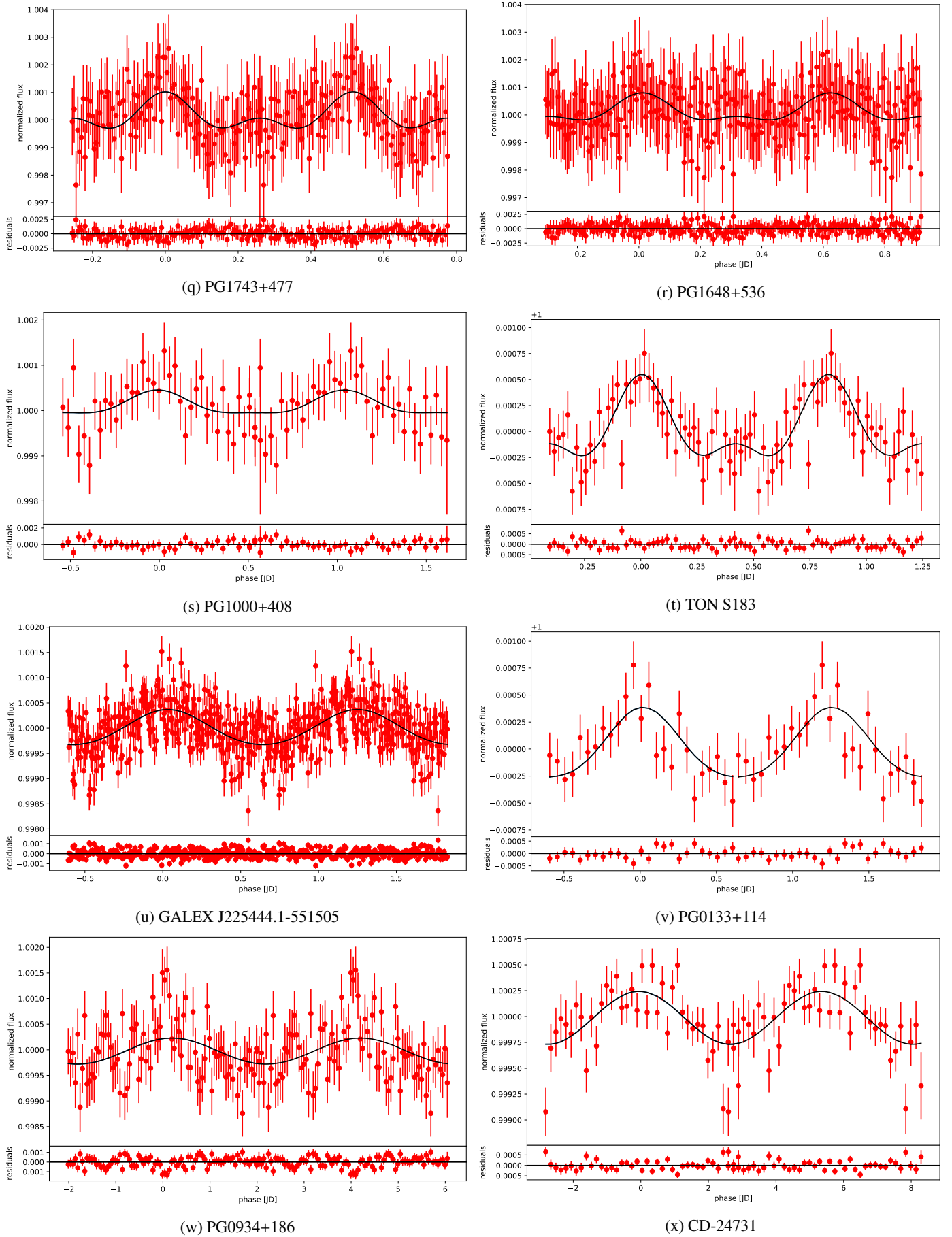


Fig. D.2: Binned light curve of the newly confirmed sdB+WD systems with best model fit shown with the black line and the residuals in the lower panel (continued).

The EREBOS project: Investigating the effect of substellar and low-mass stellar companions on late stellar evolution

Survey, target selection, and atmospheric parameters

V. Schaffenroth¹, B. N. Barlow², S. Geier¹, M. Vučković³, D. Kilkenny⁴, M. Wolz⁵, T. Kupfer⁶, U. Heber⁵, H. Drechsel⁵, S. Kimeswenger^{7,8}, T. Marsh⁹, M. Wolf¹⁰, I. Pelisoli¹, J. Freudenthal¹¹, S. Dreizler¹¹, S. Kreuzer⁵, and E. Ziegerer⁵

¹ Institut für Physik und Astronomie, Universität Potsdam, Haus 28, Karl-Liebknecht-Str. 24/25, 14476 Potsdam-Golm, Germany
e-mail: schaffenroth@astro.physik.uni-potsdam.de

² Department of Physics, High Point University, One University Parkway, High Point, NC 27268, USA

³ Instituto de Física y Astronomía, Facultad de Ciencias, Universidad de Valparaíso, Gran Bretaña 1111, Playa Ancha, Valparaíso 2360102, Chile

⁴ Department of Physics & Astronomy, University of the Western Cape, Private Bag X17, Bellville 7535, South Africa

⁵ Dr. Remeis-Observatory & ECAP, Astronomical Institute, Friedrich-Alexander University Erlangen-Nürnberg, Sternwartstr. 7, 96049 Bamberg, Germany

⁶ Kavli Institute for Theoretical Physics, University of California, Santa Barbara, CA 93106, USA

⁷ Institut für Astro- und Teilchenphysik, Universität Innsbruck, Technikerstrasse 25/8, 6020 Innsbruck, Austria

⁸ Instituto de Astronomía, Universidad Católica del Norte, Av. Angamos 0610, Antofagasta, Chile

⁹ Department of Physics, University of Warwick, Coventry CV4 7AL, UK

¹⁰ Astronomical Institute, Faculty of Mathematics and Physics, Charles University, V Holešovičkách 2, 180 00 Praha 8, Czech Republic

¹¹ Institut für Astrophysik, Georg-August Universität Göttingen, Friedrich-Hund-Platz 1, 37077 Göttingen, Germany

Received 4 June 2019 / Accepted 19 July 2019

ABSTRACT

Eclipsing post-common-envelope binaries are highly important for resolving the poorly understood, very short-lived common-envelope phase of stellar evolution. Most hot subdwarfs (sdO/Bs) are the bare helium-burning cores of red giants that have lost almost all of their hydrogen envelope. This mass loss is often triggered by common-envelope interactions with close stellar or even substellar companions. Cool companions to hot subdwarf stars such as late-type stars and brown dwarfs are detectable from characteristic light-curve variations – reflection effects and often eclipses. In the recently published catalog of eclipsing binaries in the Galactic Bulge and in the Asteroid Terrestrial-impact Last Alert System (ATLAS) survey, we discovered 125 new eclipsing systems showing a reflection effect seen by visual inspection of the light curves and using a machine-learning algorithm, in addition to the 36 systems previously discovered by the Optical Gravitational Lesing Experiment (OGLE) team. The Eclipsing Reflection Effect Binaries from Optical Surveys (EREBOS) project aims at analyzing all newly discovered eclipsing binaries of the HW Vir type (hot subdwarf + close, cool companion) based on a spectroscopic and photometric follow up to derive the mass distribution of the companions, constrain the fraction of substellar companions, and determine the minimum mass needed to strip off the red-giant envelope. To constrain the nature of the primary we derived the absolute magnitude and the reduced proper motion of all our targets with the help of the parallaxes and proper motions measured by the *Gaia* mission and compared those to the *Gaia* white-dwarf candidate catalog. It was possible to derive the nature of a subset of our targets, for which observed spectra are available, by measuring the atmospheric parameter of the primary, confirming that less than 10% of our systems are not sdO/Bs with cool companions but are white dwarfs or central stars of planetary nebula. This large sample of eclipsing hot subdwarfs with cool companions allowed us to derive a significant period distribution for hot subdwarfs with cool companions for the first time showing that the period distribution is much broader than previously thought and is ideally suited to finding the lowest-mass companions to hot subdwarf stars. The comparison with related binary populations shows that the period distribution of HW Vir systems is very similar to WD+dM systems and central stars of planetary nebula with cool companions. In the future, several new photometric surveys will be carried out, which will further increase the sample of this project, providing the potential to test many aspects of common-envelope theory and binary evolution.

Key words. binaries: eclipsing – brown dwarfs – binaries: spectroscopic – binaries: close – subdwarfs – surveys

1. Introduction

Most subluminescent B stars (sdBs) are core helium-burning stars with very thin hydrogen envelopes and masses around $0.5 M_{\odot}$ (Heber 2009, 2017). To form such an object, the hydrogen envelope of the red-giant progenitor must be stripped off almost entirely. Since a high fraction of sdB stars are members of short-

period binaries (Maxted et al. 2001), common envelope ejection triggered by a close stellar companion is generally regarded as the most probable formation channel for many of the sdB stars.

There is however increasing evidence that substellar companions might also have a significant influence on sdB star formation (which is still poorly understood) and it has been proposed that planets and brown dwarfs could be responsible for

the loss of envelope mass in the red-giant phase of sdB progenitors (Soker 1998). As soon as the primary star evolves to become a red giant, close substellar companions must enter a common envelope. Whether those objects are able to eject the envelope and survive, evaporate, or merge with the stellar core depends mostly on their mass. While planets below $10 M_{\text{Jup}}$ might not survive the interactions, companions exceeding this mass might be able to eject the envelope and survive as close companions (Soker 1998).

The best evidence for interactions with substellar companions is provided by the discovery of three close, eclipsing sdB binaries with brown dwarf companions. Photometric and spectroscopic follow-up observations of the sdB binary J162256+473051 revealed that the system is eclipsing with a period of 0.069 d and the companion is probably a brown dwarf with a mass of $0.064 M_{\odot}$ (Schaffenroth et al. 2014a). The short-period system J082053+000843 (0.096 d) is also eclipsing, and the companion has a mass in the range $0.045\text{--}0.067 M_{\odot}$ (Geier et al. 2011). Schaffenroth et al. (2015) discovered another, especially interesting eclipsing hot subdwarf that shows pulsations and has a brown dwarf companion with a mass of $0.069 M_{\odot}$ (V2008-1753, 0.065 d). Additionally, two sdB systems with candidate brown dwarf companions have been detected (periods ~ 0.3 d, Schaffenroth et al. 2014b), but since they do not eclipse, only minimum companion masses – both below the hydrogen-burning limit – can be derived (0.048 and $0.027 M_{\odot}$).

The most successful way to detect eclipsing binaries with cool stellar or substellar companions (HW Vir systems) is by inspecting their light curves, which, in addition to the eclipses, show a characteristic quasi-sinusoidal variation caused by the so-called reflection effect (see Schaffenroth et al. 2018, and references therein). This effect is observed in any close binary system consisting of a hot primary and a cool companion. As the secondaries in these systems are supposed to orbit synchronously, the hemisphere of the cool companion facing the hot primary is constantly irradiated, which leads to an increased flux over the orbital phase as the heated side of the secondary comes into view (see Wilson 1990; Budaj 2011, for a detailed discussion of this effect).

The amplitude of the reflection effect scales with the temperature ratio and the radii of the primary and secondary stars, as well as the inverse orbital separation (Wilson 1990; Budaj 2011). Hence, the reflection effect is strongest when both components of a close binary system have a very small separation, similar radii, and a high temperature difference. In systems consisting of a low-mass main sequence star or brown dwarf and a hot, compact star like a hot subdwarf, these conditions are fulfilled. The same features can be seen in very hot white dwarf binaries with cool companions, such as NN Serpentis (Parsons et al. 2010), or post-AGB stars with cool, main sequence companions, including central stars of planetary nebula (e.g., UU Sge, Afşar & Ibanoglu 2008).

Due to the short periods and similar radii of the components, sdB binaries with low-mass companions also have a high probability of eclipsing. Such systems are of great value because they allow the determination of the masses and radii of both components, as well as their separation, with an accuracy up to a few percent using combined photometric and spectroscopic analyses. The known sample of eclipsing and noneclipsing systems is relatively inhomogeneous, with most having been found in photometric surveys due to their characteristic light curve variations (e.g., Schaffenroth et al. 2013) or from light curves only covering a few hours aimed at searching for pulsations (e.g., Jeffery & Ramsay 2014). These published systems have orbital

periods between 0.069 d and 0.26 d (Schaffenroth et al. 2018, and references therein).

A photometric follow-up of spectroscopically selected targets (Schaffenroth et al. 2018) also allowed us to determine the fraction of substellar companions to sdBs. We derived a value of more than 8% for substellar companions in close orbits around sdBs. Moreover, they seem to be at least as frequent as low-mass stellar companions, as two of the four reflection-effect binaries we discovered are sdBs with substellar companions.

This shows that close substellar companions are able to eject a red-giant envelope and that they are much more frequent than predicted by standard binary-evolution theory. Due to their high fraction of close substellar companions, hot subdwarfs are well suited to the study of interactions between stars and brown dwarfs or giant planets. To understand both the common envelope phase under extreme conditions and the role of close-in planets and brown dwarfs for late stellar evolution, we need to study a large and homogeneously selected sample of eclipsing sdB binaries.

2. Project overview

The increasing number of photometric surveys provides us with a huge source to find more eclipsing hot subdwarf stars. Thirty-six new HW Vir candidates were discovered by the Optical Gravitational Lensing Experiment (OGLE) project (Pietrukowicz et al. 2013; Soszyński et al. 2015), almost tripling the number of such objects known and providing the first large sample of eclipsing sdBs. These systems have been identified by their blue colors, short orbital periods, and characteristic light curves in the *I*-band.

To investigate this unique sample of HW Vir candidates, we conduct the EREBOS (Eclipsing Reflection Effect Binaries from Optical Surveys) project, which aims to measure orbital, atmospheric, and fundamental parameters.

Key questions we want to answer over the course of the EREBOS project include the following: What is the minimum mass of the companion necessary to eject the common envelope? Is there a well-defined minimum mass or a continuum ranging from the most massive brown dwarfs down to hot Jupiter planets? What is the fraction of close substellar companions to sdBs and how does it compare to the possible progenitor systems such as main sequence stars with brown dwarf or hot Jupiter companions? To address these questions and understand both the common envelope phase under extreme conditions and the role of close-in planets and brown dwarfs for late stellar evolution, we need to know the parameters of post-common-envelope systems over as much of the period distribution as possible.

In the following sections we discuss our target selection, try to constrain the nature of the primary star, and present the first results based on orbital parameters from the light curves and atmospheric parameters from the spectra we have taken so far.

3. Target selection

As already described, hot subdwarf binaries with cool, low-mass companions exhibit a unique light-curve shape produced by their strong eclipses and reflection effect. By visual inspection of light curves, the OGLE team identified 36 new HW Vir candidates in their sample (Pietrukowicz et al. 2013; Soszyński et al. 2015). In the course of the OGLE survey, approximately 450 000 new eclipsing binaries have been published to date (Soszyński et al. 2016). More light-curve surveys monitoring billions of stars are

available. As we are searching for systems with a defined set of characteristics, we developed a set of criteria to select a limited number of potential targets for our own visual inspection.

3.1. Light-curve surveys

We used two different surveys to search for light curves with the typical properties that we require.

3.1.1. OGLE project

OGLE is a long-term, large-scale photometric sky survey focused on variability. Its original purpose was the detection of micro-lensing events and it therefore focuses on observing fields with high stellar densities. A detailed description of the fourth phase of the project can be found in Udalski et al. (2015). OGLE-IV is conducted at the Las Campanas Observatory in Chile with a 1.3 m telescope dedicated to the project.

More than a billion sources are regularly monitored in different fields in the Galactic Bulge, the Small and Large Magellanic Clouds, and the Galactic disk. The OGLE-IV camera is equipped with V - and I -band interference filter sets. The OGLE I -band filter very closely resembles the standard Johnson I -band filter; the OGLE-IV V -band filter is similar to the standard Johnson filter but extends slightly less far into the red. Most of the observations are performed in the I filter and the resulting light curves have from several hundred to more than a thousand data points with an integration time of 100 s. The OGLE-IV photometry covers the range of $12 < I < 20.5$ mag (Udalski et al. 2008). The light curves are published in different catalogs together with an ephemeris for each star.

3.1.2. ATLAS project

ATLAS is a high-cadence all-sky survey system designed to find dangerous near-Earth asteroids. ATLAS achieved first light in June 2015 and now consists of two independent units, one on Haleakala (HKO), and one on Mauna Loa (MLO) in the Hawai'ian islands. Details of the project can be found in Tonry et al. (2018). Each telescope is a 0.65 m Schmidt observing in a cyan filter (c , covering 420–650 nm) and an orange filter (o , 560–820 nm). The fisheye camera takes 32 s exposures on a 40 s cadence and ATLAS covers the entire accessible sky with a cadence of 2 days over a magnitude range $0 < m < 20$. As of the end of January 2018, ATLAS had taken about 600 000 exposures resulting in 240 million light curves with more than 100 epochs.

3.2. Color selection and period constraints

Because sdBs are hot and therefore blue, we limited our search to the bluest targets in OGLE. As OGLE observes not only in the I -band but also in the V -band for most targets (more details in Sect. 3.1), we could use the color index $V - I$ for the selection. The Galactic Bulge is a very dense region and has very patchy and substantial reddening. Because of this, we cannot simply apply color cuts characteristic for hot subdwarfs. Instead, we investigated the colors of the HW Vir candidates identified by Pietrukowicz et al. (2013) and Soszyński et al. (2015) and decided to limit our search to targets with $V - I < 1$ (see Fig. 1), as only three systems were found outside these limits. The longest-period HW Vir system previously known is AA Dor with a period of 0.26 d. The longest-period reflection-effect system has a period of 0.8 d (Jeffery & Ramsay 2014).

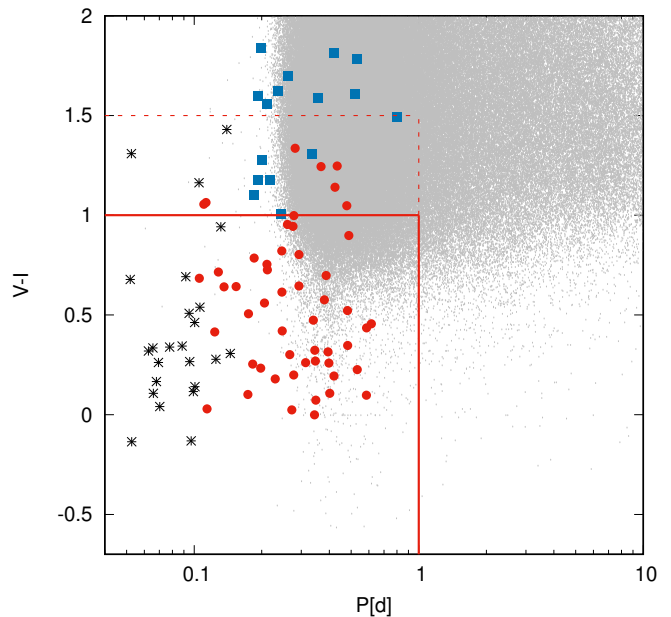


Fig. 1. Period and color selections applied to the eclipsing systems published by the OGLE team (Soszyński et al. 2016). HW Vir systems found by the OGLE team are shown as black stars. Red circles represent those found by visual inspection and blue squares those found by machine learning. It can be seen that we select short-period binaries with the bluest colors.

Consequently, we focused our search on systems with orbital periods less than one day. Later, we also started to extend our search up to $V - I < 1.5$.

Figure 1 shows the color and period selection we applied and the systems we found. These criteria left us with 2200 systems, each of which was phased with the ephemeris provided by the OGLE team. We inspected the light curves of all 2200 systems visually and found 51 new HW Vir candidates with periods between 0.1 and 0.6 d. Most of the other light curves were consistent with contact systems or β Lyrae-type binaries. It is unsurprising that for the shortest periods almost all blue objects are HW Vir system candidates, as blue main sequence stars are much larger and have longer periods.

3.3. Light-curve selection with machine learning

To identify additional systems not covered by the initial color selection we used the light curves of the 87 identified systems as a training set for machine learning.

As this set already includes systems with a large period range, variety of inclinations, and different S/N, it is ideally suited for training. For this we used the support vector machine (SVM) provided by the PYTHON package SKLEARN. We performed a C -Support Vector Classification (SVC) with the default squared exponential (rbf) kernel with a penalty parameter, C , of 10^5 and a Kernel coefficient, γ , of 10^{-2} . All 450 000 eclipsing binaries were phased with the OGLE ephemerides. The SVM was then trained with the previously identified systems and applied to all OGLE light curves.

Using the above procedure, 2613 light curves were selected. These were inspected again visually. In this way, 20 new systems were found, which have redder colors than our initial color selection. For two of these new systems, no observations are available in the V band. Only six out of 87 systems found previously by our color criteria were not detected by the SVM. All of those

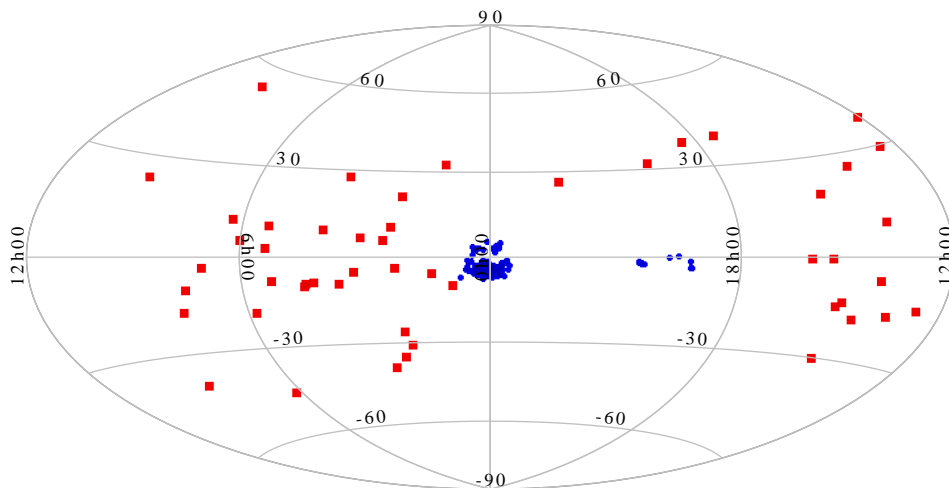


Fig. 2. Distribution of the OGLE targets (blue circles) and the ATLAS targets (red squares) on the sky. The OGLE fields in the Galactic disk and the Galactic Bulge are clearly visible. The ATLAS targets are distributed over the whole sky accessible from the northern hemisphere.

systems have very poor S/N. This means the number of false positives is still relatively high, but we are dealing with a sufficiently small number of systems to investigate them all by eye. In the future we would like to improve this process by creating a sample of synthetic light curves with different inclinations, S/N, and orbital periods.

3.4. Cross-matching the *Gaia* catalog of hot subdwarf stars with ATLAS

Geier et al. (2019) published a catalog of candidate hot subdwarf stars of the complete sky. This catalog was used to search for more HW Vir systems by cross-matching it with ATLAS. With the cross-match, 1600 objects from the *Gaia* hot-subdwarf catalog were found in ATLAS. All of them were again phased after identifying the period with a Lomb-Scargle algorithm (Lomb 1976; Scargle 1982) and were then inspected visually. Fifty additional new HW Vir candidates were found in the ATLAS data, as well as several known systems. The light curves of all systems in our sample can be found in Figs. A.1 and A.2.

Figure 2 shows the Galactic distribution of the new HW Vir candidates. The OGLE and *Gaia* magnitudes of all our targets, along with those of the published HW Vir binaries, can be found in Tables A.1 and A.2. The OGLE targets, shown with blue circles, are found in the Bulge and the Galactic disk fields of OGLE. The ATLAS targets, shown with red squares, are distributed over the complete sky accessible from the Northern hemisphere.

The magnitude distribution of our targets is illustrated in Fig. 3. The OGLE targets peak at a brightness of 19 mag, which is much fainter than any previously known systems and makes the follow-up more difficult. However, we found several brighter systems in the ATLAS survey.

4. Spectral parameters of the EREBOS targets

We can obtain very accurate orbital parameters from the light curves: the orbital period, the inclination of the system, and the relative radii. However, the light curve analysis suffers from degeneracies due to several coupled parameters, and so it is essential to constrain as many of these parameters as possible using time-resolved spectroscopy. For 27 of our targets, we already have spectroscopic follow-up to confirm the nature of the primary star. All our observing runs can be found in Table 1. In the following we give more details of the spectroscopic

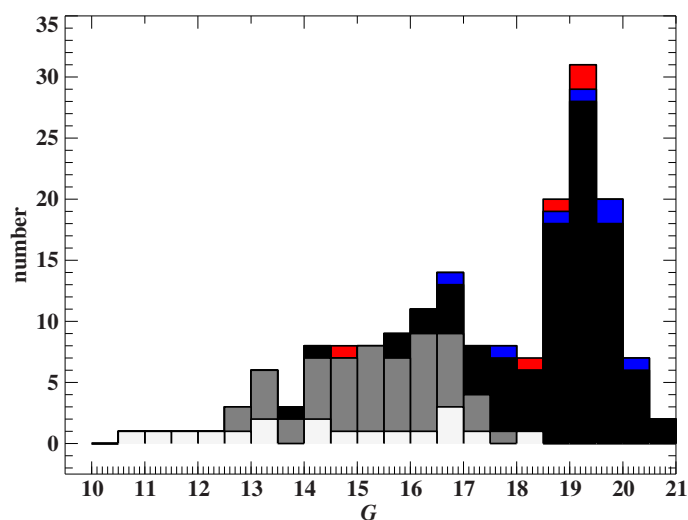


Fig. 3. Magnitude distribution of the published HW Vir systems (white), the ATLAS HW Vir candidates (gray), the OGLE HW Vir candidates (black), the eclipsing systems with candidate white dwarf primaries (blue) and the central stars of planetary nebula (red; more details are given in Sect. 5 and Tables A.1–A.3).

observations and show the first atmospheric parameters derived. Figure 4 shows three examples of our co-added spectra from the ESO-VLT/FORS2 spectrograph.

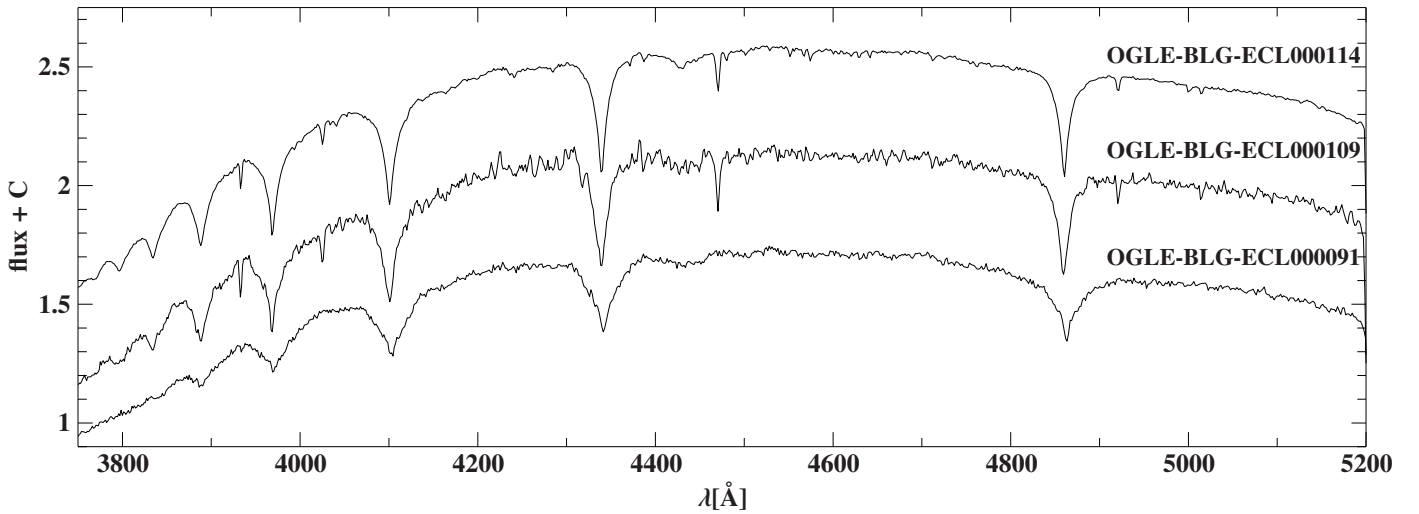
4.1. Spectroscopic observations

4.1.1. ESO-NTT/EFOSC2

For the brighter systems we used the EFOSC2 spectrograph mounted at the 3.58 m ESO/NTT telescope. Nine of our systems have been observed in several runs (092.D-0040(A), 099.D-0217(A), 0101.D-0791(A)). We always took several spectra per star in grism Gr#19 (4441–5114 Å) with a 1'' slit to achieve a resolution of $R \sim 3000$ to derive a radial-velocity curve covering the whole orbit. This grism includes H β as well as HeI 4472 and 4922. Usually, several objects were observed in a repeating sequence but always with exposure times less than 5–10% of the orbital period to avoid orbital smearing. To derive the atmospheric parameters, moreover, one spectrum per star was taken with grism Gr#07 (3270–5240 Å) with resolution $R \sim 500$ –700. This grism covers the Balmer jump.

Table 1. Spectroscopic follow-up observations.

Date	Nights	Run	Telescope and instrument	Observers
09/10 May 2015	2	095.D-0167(A)	ESO-VLT/FORS2	S. Kimeswenger
Oct. 2015–Jun. 2017	12.5	196.D-0214(A-D)	ESO-VLT/FORS2	Service
04/05 Aug. 2016	2	NOAO 2016B-0283	SOAR/Goodman	B. Barlow
30/31 Mar. 2016	2	NOAO 2016A-0259	SOAR/Goodman	B. Barlow
07/08 Jun. 2016	2	NOAO 2016A-0259	SOAR/Goodman	B. Barlow
01–05 Feb. 2014	4	092.D-0040(A)	ESO-NTT/EFOSC2	S. Geier
01–04 Jul. 2017	3	099.D-0217(A)	ESO-NTT/EFOSC2	E. Ziegerer
30 Jul.–02 Aug. 2018	3	0101.D-0791(A)	ESO-NTT/EFOSC2	S. Kreuzer
26 Feb. 2019	1	SO2018B-002	SOAR/Goodman	I. Pelisoli

**Fig. 4.** Three example spectra showing a typical sdB (OGLE-BLG-ECL-000114), a DA white dwarf (OGLE-BLG-ECL-000091), and a pre-He white dwarf (OGLE-BLG-ECL-000109). SdBs and pre-He white dwarfs show very similar spectra and can only be distinguished by deriving the atmospheric parameters.

4.1.2. ESO-VLT/FORS2

Most of the OGLE target periods are quite short and, as we are interested especially in the shortest periods, this limits the exposure times greatly; EFOSC2 is not adequate for observation of those targets. We applied successfully for an ESO large program with ESO-VLT/FORS (196.D-0214(A-D)) for fainter, short-period systems, after a feasibility study in visitor mode (095.D-0167(A)). In our first run on 10 May 2015 we observed one 20-mag object (OGLE-GD-ECL-10384) for a half a night taking 24 spectra using Grism GRIS_600B+22 (330–621 Å, 1'' slit, $R \sim 780$) each with an exposure time of 600 s and covering two full orbits. The ESO large program was executed in service mode over the course of two years. We divided all observations into 1 hour observing blocks (OBs), in which time-resolved spectroscopy of one target was performed per block. As the periods of many of our targets are very short, a significant part of the orbit can be covered in one hour. For these observations we used Grism GRIS_1200B+97 (3660–5110, 1'' slit, $R \sim 1420$). We limited the exposure time to $\sim 5\%$ of the orbital period to prevent orbital smearing. About 6–8 spectra were taken per OB. For each target, several OBs were taken to cover the whole orbit distributed over one semester.

The observation of the Bulge targets and the data analysis turned out to be less straightforward than expected, as we have problems with the enormous crowding in the Bulge field, which complicates photometry as well as spectroscopy. Already, the

identification of the targets was a huge challenge at the beginning, because of the lack of good finding charts in the visual, which lead to misidentification of the target in some cases. Additionally, the ESO-VLT/FORS2 spectrograph was found not to be as stable as expected, because it was not designed for the determination of radial velocities. This complicates the determination of accurate radial velocity curves. Hence, we concentrate only on the determination of the atmospheric parameters for this paper, as more work is needed to derive the radial velocity curves from the FORS2 spectra. The radial velocities of all of our targets will be presented in future papers.

Individual spectra were then co-added after being corrected for radial velocity so that we could use the co-added spectra for atmospheric analyses. Radial velocities were determined with the IRAF¹ task FXCORR for cross-correlation against model spectra and co-added spectra to measure the radial velocity shifts in the Balmer and helium lines.

4.1.3. SOAR/Goodman

We have collected time-resolved spectroscopy of many of the brighter, short-period systems with the Goodman Spectrograph on the 4.1 m SOUTHERN Astrophysical Research (SOAR) telescope (Clemens et al. 2004). Four of our targets have been observed to date with time allocated through the National

¹ Tody (1986).

Table 2. Atmospheric parameters of our observed targets from the ERE-BOS project spectroscopy with statistical errors.

Target name	T_{eff} [10^3 K]	$\log g$ [cgs]	$\log y$
OGLE-BLG-ECL-000114 ^(a) ^(c)	29.2 ± 0.5	5.55 ± 0.07	-2.28 ± 0.10
OGLE-BLG-ECL-000139 ^(c)	29.6 ± 0.5	5.50 ± 0.06	-2.97 ± 0.13
OGLE-BLG-ECL-000103 ^(a)	29.5 ± 0.4	5.70 ± 0.05	-1.75 ± 0.11
OGLE-BLG-ECL-000163 ^(c)	28.0 ± 0.3	5.37 ± 0.04	-1.96 ± 0.10
OGLE-BLG-ECL-000124 ^(a)	26.3 ± 0.7	5.46 ± 0.06	-2.02 ± 0.16
OGLE-BLG-ECL-000010 ^(a)	27.9 ± 0.7	5.32 ± 0.06	-2.59 ± 0.18
OGLE-BLG-ECL-000202 ^(a)	36.3 ± 0.5	5.25 ± 0.09	-3.17 ± 0.12
OGLE-BLG-ECL-000110 ^(a)	23.6 ± 0.5	5.35 ± 0.05	-2.30 ± 0.13
OGLE-BLG-ECL-000109 ^(a)	29.3 ± 0.3	6.05 ± 0.05	-1.96 ± 0.10
OGLE-BLG-ECL-000212 ^(a)	30.1 ± 0.5	5.38 ± 0.07	-2.64 ± 0.11
OGLE-BLG-ECL-000207 ^(a)	24.4 ± 0.4	5.54 ± 0.06	-2.15 ± 0.14
OGLE-BLG-ECL-173411 ^(b)	26.0 ± 0.1	5.28 ± 0.03	-2.48 ± 0.11
OGLE-BLG-ECL-361688 ^(b)	27.2 ± 1.3	5.20 ± 0.08	-2.39 ± 0.02
OGLE-BLG-ECL-416194 ^(b)	35.6 ± 0.9	5.34 ± 0.20	-2.21 ± 0.35
OGLE-BLG-ECL-017842 ^(b)	29.7 ± 0.8	5.81 ± 0.17	-2.65 ± 0.28
OGLE-BLG-ECL-280838 ^(b)	28.3 ± 0.6	5.55 ± 0.08	-2.78 ± 0.25
OGLE-BLG-ECL-412658 ^(b)	36.7 ± 0.8	5.48 ± 0.08	-2.49 ± 0.33
OGLE-GD-ECL-08577 ^(b)	28.4 ± 1.0	5.43 ± 0.15	-2.01 ± 0.27
OGLE-GD-ECL-10834 ^(a)	27.6 ± 0.8	5.64 ± 0.16	-2.54 ± 0.18
OGLE-GD-ECL-11388 ^(b)	29.0 ± 0.3	5.56 ± 0.04	-2.77 ± 0.05
OGLE-GD-ECL-11471 ^(a)	28.4 ± 0.5	5.71 ± 0.10	-2.17 ± 0.08
J282.4644-13.6762 ^(b)	27.5 ± 0.6	5.54 ± 0.07	-2.25 ± 0.21
J351.7186+12.5060 ^(b)	29.0 ± 0.4	5.68 ± 0.08	-1.86 ± 0.14
J315.0724-14.190 ^(b)	30.2 ± 2.0	5.96 ± 0.38	-2.00 ± 0.16
J079.5290-23.1458 ^(b)	30.9 ± 0.7	5.75 ± 0.09	-1.96 ± 0.14
J129.0542-08.0399 ^(c)	31.1 ± 0.3	5.49 ± 0.06	-2.85

Notes. ^(a)ESO-VLT/FORS2. ^(b)ESO-NTT/EFOSC2. ^(c)SOAR/Goodman.

Optical Astronomy Observatory (NOAO Proposal IDs 2016B-0283, 2016A-0259, SO2018B-002). Our standard observing configuration uses a 930 mm^{-1} VPH grating from Syzygy Optics, LLC, in conjunction with a $1.03''$ longslit to achieve a spectral resolution of 2.9 \AA ($R \sim 1500$) over the wavelength range $3600\text{--}5300 \text{ \AA}$. We observed each target using a series of consecutive spectra covering one full orbital period. In order to maximize our duty cycle, the spectral images were binned 2×2 , resulting in a pixel scale of $0.3''$ per binned pixel in the spatial direction and 0.84 \AA per binned pixel in the dispersion direction. We again kept the integration times to less than 5% of the orbital period to avoid phase smearing. We use Gaussian fits to the Balmer lines to determine radial velocities and created a co-added spectrum for atmospheric modeling after individually correcting their velocities.

4.2. Atmospheric parameters

Atmospheric parameters were determined by calculating synthetic spectra using LTE model atmospheres with solar metallicity and metal line blanketing (Heber et al. 2000) and fitting these to the Balmer and helium lines using SPAS (Hirsch 2009). In this way, we determined the atmospheric parameters (effective temperature T_{eff} , surface gravity $\log g$ and helium abundance $\log y$) for 25 systems, which can be found in Table 2. Some example line fits are showed in Fig. 5. The errors given are only statistical errors. As the contribution of the companion to the visible flux varies over the orbital phase due to the reflection effect, apparent variations of the atmospheric parameters are found in some eclipsing sdB binaries with cool companions with high-S/N spectra on the order of 1500 K and 0.1 dex over the whole orbital

phase (Schaffenroth et al. 2014a). This means that in the case of systems with very low statistical error we have to adopt an uncertainty of 750 K in temperature and 0.05 dex in $\log(g)$.

The parameters show that the primaries are mostly typical for HW Vir systems (see Schaffenroth et al. 2018, and references therein). OGLE-BLG-ECL-000091 and J186.9106-30.7203 are the only exceptions, as both clearly look like DA white dwarfs with very broad Balmer lines (see Fig. 4 for an example).

However, it is not only the tracks of He-core burning objects that cross the extreme horizontal branch, but also those of post-RGB objects with masses too low to burn He in the core (see Fig. 6). Both of the above evolve directly into He-WD and are therefore also called pre-He WDs. The lifetime of pre-He WDs crossing the EHB is only one hundredth of the lifetime of a core-He-burning sdB on the EHB. Therefore, we expect them to be much rarer and that most objects on the EHB are hot subdwarfs. This also depends, however, on the birth rate of these systems, which is unknown. This means in most cases that it is not possible to distinguish between sdBs and pre-He WDs from the atmospheric parameters alone.

To compare the atmospheric parameters of our targets to other sdB binaries we plotted the $T_{\text{eff}}\text{--}\log g$ diagram of the reflection-effect systems and other sdB binaries from Kupfer et al. (2015) in Fig. 6. The published HW Vir and reflection-effect systems seem to cluster in a relatively small region of the $T_{\text{eff}}\text{--}\log g$ diagram. Very few are found on the EHB at higher temperatures. Our new systems almost double the number of atmospheric parameter determinations for sdBs with cool, low-mass companions. It appears now that the EHB is well populated with such systems. It is only near the He-main sequence (HeMS) that we still do not find any HW Vir systems. Moreover, we find three systems which have already evolved away from the EHB.

An interesting system is OGLE-BLG-ECL-000109, which lies clearly below the He-main sequence. This means it cannot be a He-core burning object is most probably a post-RGB object with a mass that is too low to burn He in the core. The position of OGLE-BLG-ECL-000109 agrees best with a track for a very low-mass white dwarf with a mass near $0.27 M_{\odot}$ (Althaus et al. 2013). Some HW Vir systems have been found where the analysis could not unambiguously distinguish between a helium-core-burning object on the extreme horizontal branch and a pre-He WD (e.g., J082053+000843 and HS 2231+2441, Geier et al. 2011; Almeida et al. 2017). This is the first HW Vir system lying significantly below the EHB and can only be explained by being a pre-He white dwarf.

5. Constraining the nature of the primary star

We selected our candidates purely based on the shapes of their light curves. To learn about the population of our targets, we need to constrain the nature of the primary star. The easiest way to do this is with spectroscopy and so far we have spectroscopic confirmation for 25 systems with a most likely hot subdwarf primary. Only two of our targets have a white dwarf primary (see Sect. 4.2).

For the rest of our sample, we have not yet obtained spectroscopy. As described in Sect. 2, white dwarfs or post-AGB objects can be possible contaminants in our sample. Of course, such systems are no less interesting, but it is important to have a homogeneous sample from which to draw conclusions.

The ESA *Gaia* Data Release 2 (Gaia Collaboration 2018b) provided us for the first time with tools to constrain the nature of the primary star. All results and *Gaia* parameters for our systems

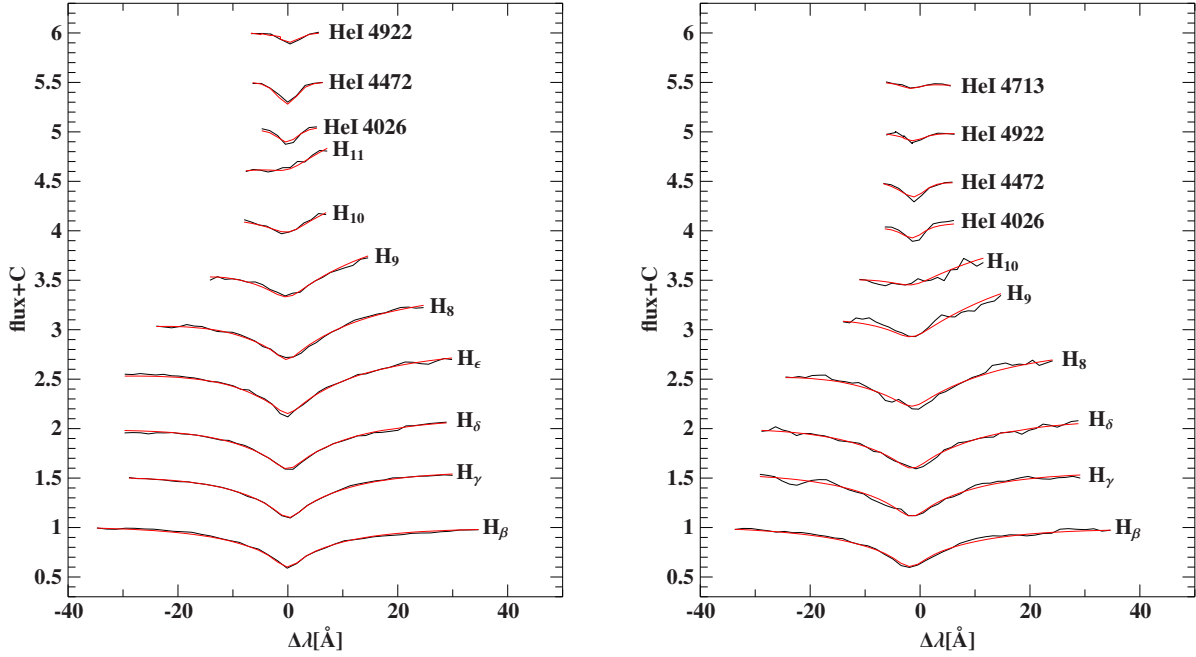


Fig. 5. Example fits of hydrogen and helium lines with model spectra for a typical sdB (OGLE-BLG-ECL-000103, *left panel*), and a pre-He WD star (OGLE-BLF-ECL-000109, *right panel*). The atmospheric parameters of these stars are given in Table 2.

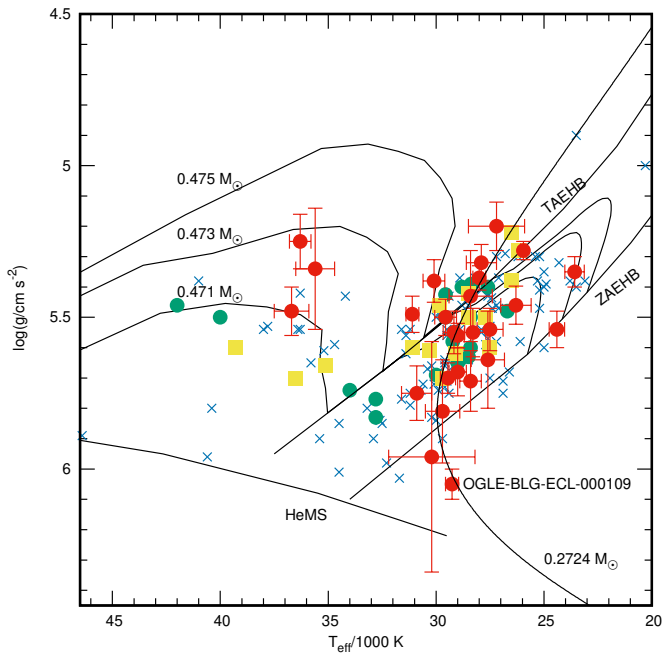


Fig. 6. $T_{\text{eff}} - \log g$ diagram of the HW Virginis systems. The zero-age EHB and ZAEHB, and the terminal-age EHB and TAEHB are superimposed by evolutionary tracks by Dorman et al. (1993) for sdB masses of 0.471, 0.473, and 0.475 M_{\odot} with one track for an extremely low-mass white dwarf of a mass of 0.2724 M_{\odot} by Althaus et al. (2013). The newly found systems are shown as red circles with error bars. The published HW Vir systems are shown as green circles, the reflection effect systems without eclipses as yellow squares. The blue crosses represent other sdB binaries (Kupfer et al. 2015), either with white dwarf or unknown companions.

can be found in Tables A.1, A.2, A.4, and A.5. Parallaxes and proper motions are available for 75 of the 107 OGLE targets and all ATLAS targets have.

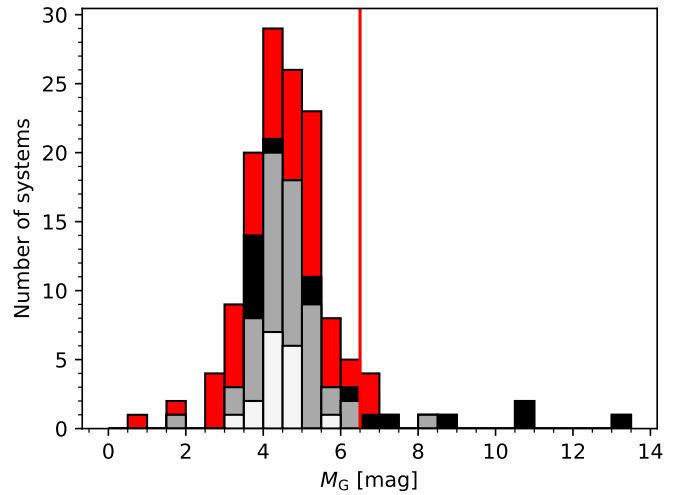


Fig. 7. Distribution of the absolute G magnitude (M_G) of our targets. The published HW Vir stars are shown in white; the ATLAS targets are displayed in gray; and the OGLE targets with parallaxes with errors less than 25% are displayed in black. For the rest of the OGLE targets we used the distances by Bailer-Jones et al. (2018), shown in red. The red line marks $M_G = 6.5$ mag, above which the primary stars are faint enough that they are more likely to be white dwarfs.

5.1. Absolute magnitudes and distances

As seen in Fig. 6 it is not possible to uniquely distinguish sdBs from pre-He WDs from the atmospheric parameters alone. However, the masses and radii of pre-He WDs are expected to be lower, and therefore, the absolute magnitudes are fainter. Hot subdwarf stars have radii around 0.15–0.2 R_{\odot} , comparable to M dwarf stars. White dwarfs have radii that are much smaller – comparable to that of Earth ($\sim 0.01 R_{\odot}$) – and usually have much fainter absolute magnitudes.

In Fig. 7 the distribution of the absolute G magnitude (M_G) is shown. Absolute magnitudes were calculated via the distance

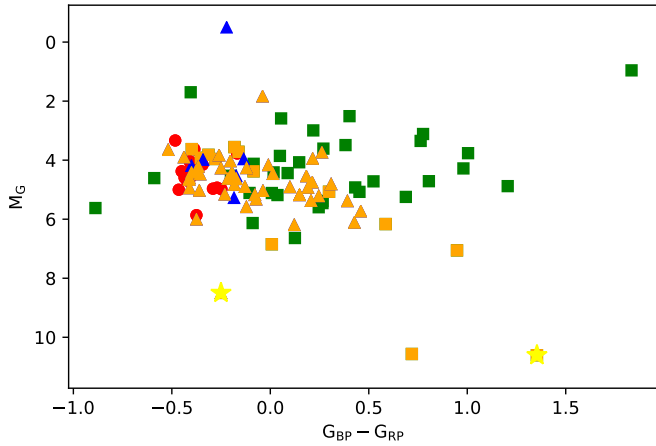


Fig. 8. Color–magnitude diagram of all our targets in *Gaia* colors. Red circles represent the published HW Vir systems for comparison. Squares indicate the OGLE targets and triangles the ATLAS targets. Targets with parallaxes better than 25% are marked in orange. For the green OGLE targets and the blue ATLAS targets we used the distances by Bailer-Jones et al. (2018). The yellow stars mark our confirmed system with a white dwarf primary.

modulus $G - M_G = 5 \log_{10} d - 5 + (A_G)$. We used the distances published by Bailer-Jones et al. (2018). Distances with large parallax errors are mostly based on the length scale model they use, which is unclear for sdBs, and therefore they have to be taken with caution. As all our systems show photometric variability, the uncertainty in G will also be larger than that given in the DR2 *Gaia* catalog. On the other hand, outliers are neglected for the determination of G , and therefore the mean *Gaia* magnitude should give a good estimate of the correct sdB magnitude (Riello et al. 2018).

For targets in the Bulge, the reddening cannot be neglected, and we constrained the reddening $E(B - V)$ by using Stilism² (Lallement et al. 2014), which gives the reddening at certain coordinates depending on the distance. In most cases, we derive only a lower limit for the reddening because the dust maps do not extend far enough ($<1-2$ kpc). To obtain the *Gaia* G -band extinction coefficient A_G we used Eq. (1) from the *Gaia* Collaboration (2018a), which uses G , BP, RP, and $E(B - V)$ as input parameters. For some of the OGLE targets, no BP or RP was given in the *Gaia* data, so we assumed similar colors to those found for the other OGLE targets (see Fig. 8).

When looking at the distribution of absolute G magnitudes of all targets, it is obvious that the different subsamples show the same distribution peaking at $M_G = 4.5$ mag – as expected for sdBs. We checked the absolute magnitudes of the white dwarf candidates from the *Gaia* white dwarf catalog (Gentile Fusillo et al. 2019) and the *Gaia* hot subdwarf catalog (Geier et al. 2019). Most of the objects with $M_G > 6.5$ are classified as white dwarf stars, and therefore a white dwarf primary is more likely. Nine of our objects have absolute magnitudes fainter than 6.5 mag and two of them have been spectroscopically confirmed as white dwarfs. On the other hand, three of them have been confirmed as sdBs. As mentioned before, the reddening we applied is only a lower limit, and therefore the absolute magnitude of the OGLE targets is an upper limit. The temperatures of those three targets is relatively low for sdBs with 24 000–26 000 K. It is also possible that they are pre-He WDs instead of sdBs.

² <https://stilism.obspm.fr/>

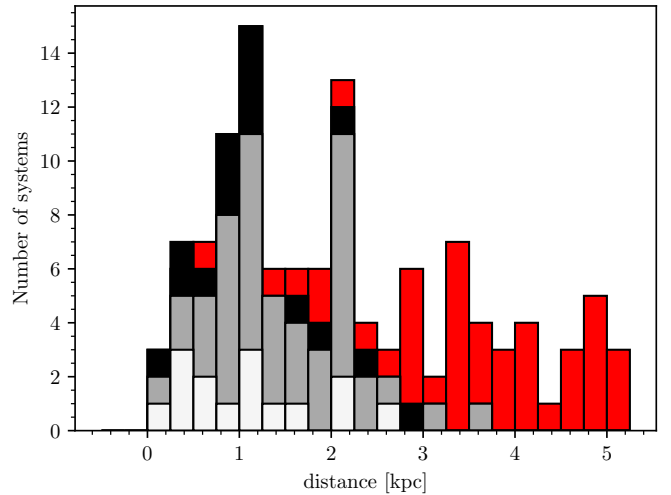


Fig. 9. Distance distribution of our targets. The published HW Vir stars are shown in white, the ATLAS targets are displayed in gray, and the OGLE targets with parallaxes that have errors of less than 25% are displayed in black. For the rest of the OGLE targets, shown in red, we used the distances by Bailer-Jones et al. (2018).

Another criterion is the color of the targets, which we can combine with absolute magnitude in a color magnitude diagram, shown in Fig. 8. The published HW Vir stars (see Tables A.1 and A.4) are concentrated at $BP - RP < 0$. The ATLAS targets show a larger spread, but we neglected reddening for those, which might be important for more distant targets. Due to the high reddening, which can only be poorly constrained in the bulge, the OGLE targets have an even wider distribution in color.

From the *Gaia* parallaxes it is also possible to determine the distances of the objects; this is shown in Fig. 9. The distance distribution agrees nicely with the distribution of the *Gaia* hot subdwarf catalog (Geier et al. 2019). The only difference is that there appear to be anomalously few objects observed at distances between 1.25 kpc and 2 kpc. This bi-modality is mainly seen in the ATLAS targets. As expected from their fainter magnitudes, the OGLE targets are mostly further away (80% have distances >2.5 kpc). All but two targets with distances larger than 3 kpc have large parallax errors and hence uncertain distances.

5.2. Reduced proper motions

As the reddening cannot be constrained perfectly for the more-distant objects, and because they have parallaxes with large errors, the absolute magnitudes of these targets are not reliable. However, to distinguish hot white dwarfs from hot subdwarf stars, reduced proper motions can be used. The reduced proper motion, defined as $H_G = G + 5(\log \mu + 1)$, can be used as a proxy for the distance of an object, since more-distant objects exhibit less movement, on average. Gentile Fusillo et al. (2015) showed that this selection method is well suited to separate hot subdwarfs from white dwarf candidates.

Figure 10 shows the distribution of the reduced proper motions of our targets superimposed with the distribution for white dwarfs taken from the *Gaia* white dwarf catalog (Gentile Fusillo et al. 2019). It is clear that the subdwarfs are found at smaller reduced proper motions. However, there is a region where both distributions overlap and the nature of the primary cannot be determined unambiguously. Combining the selection from the absolute magnitude with the reduced proper

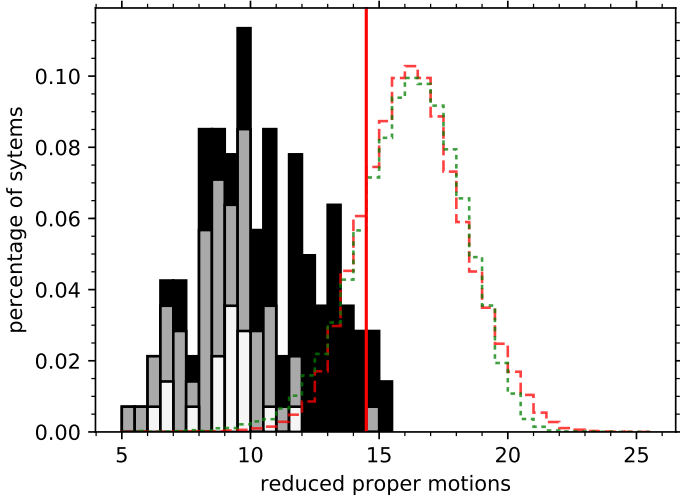


Fig. 10. Normalized distribution of the reduced proper motions of our targets (white are the published HW Vir systems, gray the ATLAS targets, and black the OGLE targets). Superimposed are the reduced proper motions of the objects with a white dwarf probability greater than 90% from the *Gaia* white dwarf catalog (Gentile Fusillo et al. 2019), shown with the red dashed line. The green dotted line shows the subsample of the targets with spectral classification from SDSS spectra. The red line marks our reduced proper motion cut of $H_G < 14.5$; at higher values, targets are less likely to be hot subdwarfs.

motion and the spectroscopically confirmed targets, we decided to define the cut at $H_G < 14.5$. This leaves us with seven objects, which have higher probabilities of being white dwarf binaries with cool, low-mass companions out of 123 objects with *Gaia* parallaxes and proper motions. All white dwarf binary candidates can be found in Tables A.2 and A.5. This means that the white dwarf binaries represent only a very small part of our sample and most targets are indeed hot subdwarf binaries.

This becomes even more clear when we look at the relation between reduced proper motion and apparent G magnitude (Fig. 11). The bulk of white dwarfs is seen at larger reduced proper motions than the sdBs and also at fainter apparent magnitudes. It is not surprising that most white dwarfs are fainter as they have much smaller radii. Only very few white dwarfs are found in the overlapping region. However, they are much more frequent, and so an uncertainty for some OGLE targets remains.

5.3. Binary central stars of planetary nebula

Another class of objects that can have similar light curves to those of HW Vir systems are binary central stars of planetary nebula (bCSPNs) with cool, low-mass companions. For those objects, whether the nebulae are ejected AGB or RGB envelopes, or ejected common envelopes (e.g., Hillwig et al. 2017) is under debate. With our selection criteria we cannot properly distinguish bCSPNs from sdBs. However, bCSPNs have relatively short lifetimes and are therefore much rarer (Miller Bertolami 2016). In our absolute magnitude distribution, we have a few targets which are much brighter than the rest. For the latter, the probability of being a post-AGB binary with an extremely hot primary is higher. OGLE-BLG-ECL-412658 with an absolute magnitude of $1.69^{+0.92}_{-0.98}$ was found to be an sdB star with a temperature of 35 600 K evolving away from the EHB. Two of our targets (J265.3145+29.5881 and OGLE-BLG-ECL-149869) seem to have an absolute magnitude brighter than 1 mag, which is much brighter than one would expect for a hot

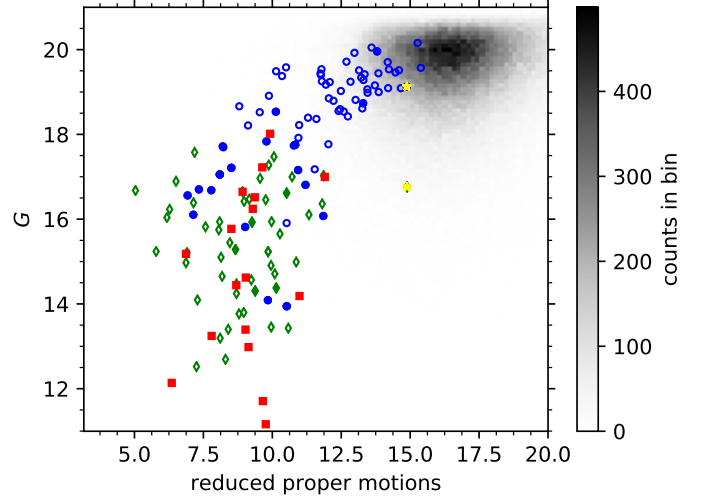


Fig. 11. Relation between reduced proper motion and apparent G magnitude. Filled symbols mark objects with spectral confirmation. Red squares represent the published HW Vir systems, green diamonds the ATLAS targets, and blue circles the OGLE targets. The yellow star marks the confirmed white dwarf binary. Superimposed is the number distribution of objects with a white dwarf probability greater than 90% from the *Gaia* white dwarf catalog (Gentile Fusillo et al. 2019).

subdwarf. However, both have a very small and uncertain parallax. J171.4930–20.1447 on the other hand has an absolute magnitude of 1.66 ± 0.22 with a small parallax error of only 10% and is therefore the best candidate to be a post-AGB object.

Miszalski et al. (2009) performed a survey to find planetary nebulae in the direction of the Galactic Bulge. Four objects from our target list were confirmed as planetary nebulae by these latter authors; these can be found in Tables A.3 and A.6. Another known planetary nebula was found in the cross-match of the *Gaia* hot subdwarf catalog with ATLAS. Currently only 11 eclipsing central stars of planetary nebula showing a reflection effect are known³.

5.4. Nature of the primary star

By combining all criteria, it is safe to say that we have only a small level of contamination by white dwarfs or post-AGB binaries, probably less than 10%. For most of our target sample, an sdB primary star is most likely. This is also supported by the fact that only 2 out of 28 targets were confirmed not to have an sdB primary (see Sect. 4.2).

6. Results

6.1. The period distribution of eclipsing hot subdwarfs with cool companions

With all the newly discovered candidate HW Vir systems presented here, the number of known systems has increased from 20 to 170. The most straightforward parameter to derive from light curves of eclipsing binaries is the orbital period. It can be found in Table A.1. All light curves are displayed in Figs. A.1 and A.2. The period distribution is shown in Fig. 12. The previously known period distribution of the HW Vir systems covered a range of 0.07–0.26 d with a sharp peak around 0.1 d; the

³ <http://www.drdjones.net/bCSPN/>

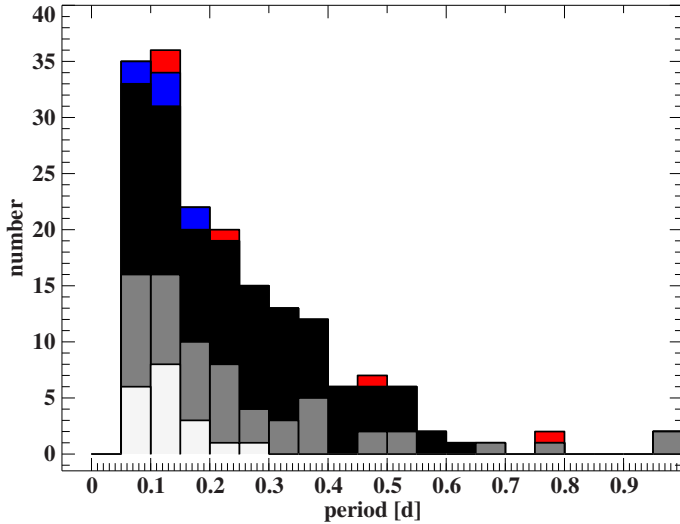


Fig. 12. Period distribution for all our targets. The currently published HW Vir systems are shown in white, with the ATLAS targets in gray, and the OGLE targets in black. In blue we marked those systems which have a higher probability of being white dwarf binaries, in red the central stars of planetary nebula.

distribution of the new systems is much broader, now spanning periods from just 0.05 d to more than one day.

As the eclipsing probability strongly correlates with the period, it is not surprising that most systems are found at periods around 0.1 d – as seen in the smaller sample. The number of systems at shorter periods has increased, but we also find a significant number at longer periods – up to 0.5 d. This population was previously completely unknown, but most of the known systems were found while looking for short-period pulsations with light curves of perhaps only an hour or two, and therefore long-period systems would not necessarily have been detected. Apart from the smaller chance of detecting eclipses, reflection effects will tend to become much smaller as the component separation and period increase.

As we limit ourselves to eclipsing systems, we also tried to constrain the true period distribution. For this we had to correct for the number of systems which are not selected by EREBOS because they do not show eclipses. The probability of eclipses occurring is dependent on the relative radius of both stars and therefore correlates with the orbital separation a , ($p_{\text{ecl}} = \frac{r_1+r_2}{a}$). The separation a can be calculated from the masses and the period ($a = (G \frac{m_1+m_2}{4\pi^2})^{1/3} \cdot P^{2/3}$). We assumed for the eclipsing probability the median masses and radii of the published HW Vir systems (see Schaffenroth et al. 2018). The corrected period distribution can be found in Fig. 13. Up to a period of 0.35 d it appears to be a fairly flat distribution. For longer periods – up to one day – the number of systems drops significantly. Above 0.55 d we found only eight systems. This small number of systems does not allow significant conclusions to be drawn on the number of systems for periods longer than 13 h.

6.2. Selection effects

For interpretation of the period distribution it is important to understand the selection effects that limit the detection of HW Vir systems at certain periods. To detect the shortest-period systems, a short cadence of observation of the light curve is essential. The light curve surveys we used have relatively random cadence. The shortest-period eclipsing system released by the

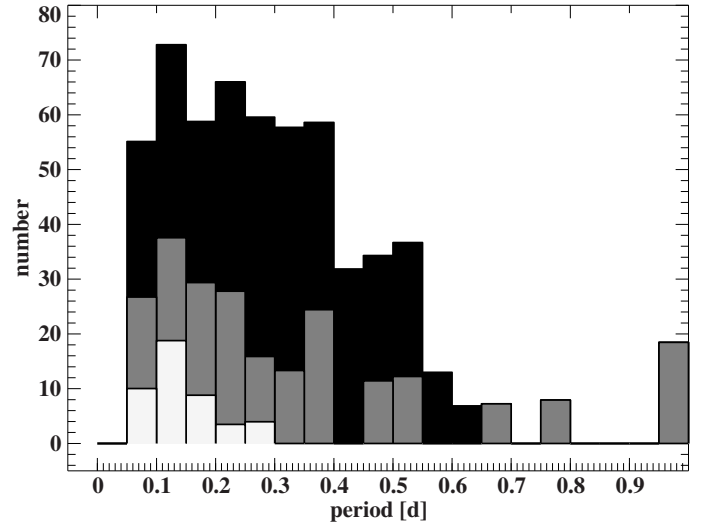


Fig. 13. Period distribution for all our targets corrected for the eclipsing probability. The currently published HW Vir systems are shown in white, the ATLAS targets in gray, and the OGLE targets in black.

OGLE team has a period of 0.052 d and is part of our target sample. The shortest-period system we found in the ATLAS survey has a period of 0.062 d. In OGLE, three systems with significantly shorter periods have been found. We were able to find systems with shorter periods of around 0.05 d when phasing the ATLAS light curves of the sdB candidates from the hot subdwarf *Gaia* catalog (Geier et al. 2019). The question is, why did we not find such short-period systems in ATLAS? One explanation is that they might be very rare. From the OGLE catalog it is hard to say what the minimum period of a HW Vir system is, as there were no shorter-period systems released. To solve the question about the minimum period, we have to wait for photometric surveys observing a large number of systems with a better cadence and more epochs.

The eclipsing probability decreases substantially as the period increases, so it is not surprising that we do not find systems with periods longer than about a day. The eclipsing probability for those systems is less than 10%. The reflection effect also gets weaker with increasing period. We expect to find only systems with an extremely high reflection effect for periods larger than one day assuming the quality of the light curves from the OGLE and ATLAS surveys. Such systems are much rarer than the typical systems (see the light curves of our targets shown in Figs. A.1 and A.2). To find longer-period sdB binaries with cool companions we need a larger sample and have to include the systems showing only the reflection effect, as well as observations with very accurate light curves.

7. Discussion

For population synthesis, the criteria for the ejection of the common envelope are crucially determined by the orbital-period distribution of post-CE binaries (Han et al. 2002). Hence, a period distribution as complete as possible is important for the understanding of those parameters.

7.1. Companion masses and periods of the known reflection-effect binaries

Figure 14 shows the companion masses of the published HW Vir systems (Schaffenroth et al. 2018, and references therein for

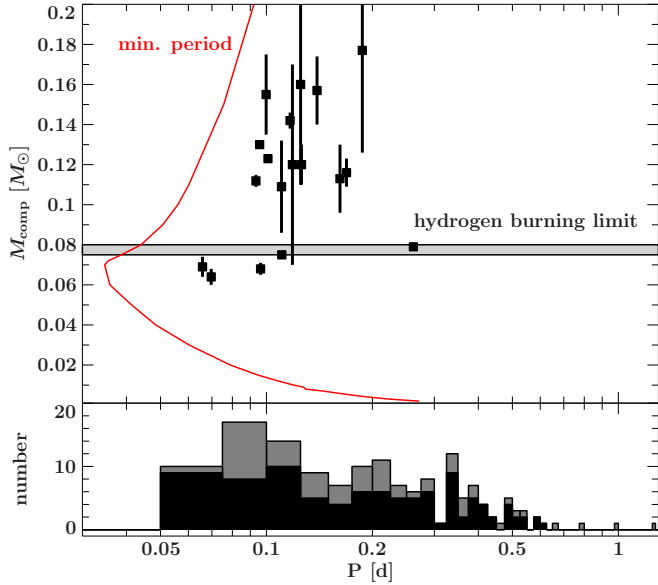


Fig. 14. Period/companion mass diagram of the published HW Vir systems. A summary of the parameters can be found in Schaffenroth et al. (2018) and references therein. The gray area marks the hydrogen-burning limit. Companions with smaller masses are substellar. The solid red line denotes the minimum period at which a companion of a certain mass can exist in orbit around a canonical-mass sdB, assuming the companion cannot exceed its Roche radius. In the lower panel the period distribution of the newly discovered HW Vir systems presented here is shown for comparison (OGLE targets in black and ATLAS targets in gray).

a summary of the orbital parameters) plotted against their orbital periods – there is no obvious correlation between companion mass and period. However, the confirmed substellar companions seem to be found preferentially in the shortest-period systems. The minimum period possible for a system consisting of an sdB and a companion of a certain mass can be calculated by assuming that the radius of the companion cannot exceed its Roche radius. To derive the Roche radius we used the formula by Eggleton (1983), which depends on the mass ratio and separation of the binary. For the radius of the companion we used the mass–radius relation by Baraffe et al. (1998), and for the sdB mass we adopt the canonical value ($\sim 0.47 M_{\odot}$).

The minimum orbital period is reached for an sdB with a cool, low-mass companion in the brown dwarf mass range. When we look at the period distribution of the newly discovered systems, which is shown in Fig. 14 for comparison, we can see that the number of short-period systems below 0.1 d has increased substantially. In particular, in the period range below 0.1 d, where all the currently confirmed brown dwarf companions have been found, we discovered 30 new systems, down to almost the minimal possible period at 0.04 d (see also Nelson et al. 2018).

To find possible Jupiter-mass planets we have to search for longer periods, because these planets get destroyed during the common-envelope phase if they are too close to the star. We estimate that they can only survive at periods longer than 0.2–0.25 d (see Fig. 14). The only eclipsing sdB binary with a cool, low-mass companion known to have such a period was AA Dor. The newly discovered systems increase the range of periods up to more than one day, allowing a search for close Jupiter-mass objects around hot subdwarf stars, which could be responsible for the formation of the sdB. This newly discovered sample provides a unique opportunity to study the

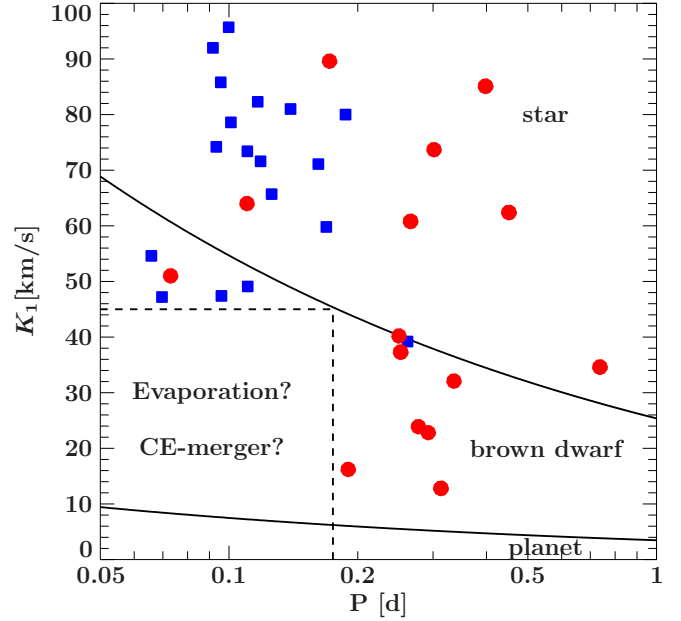


Fig. 15. Updated version of Fig. 4 from Schaffenroth et al. (2014b) adding the HW Vir systems published since then (see Schaffenroth et al. 2018, for a table of the parameters of all published HW Vir systems). Shown are the RV semi-amplitudes of all known sdB binaries with reflection effects and spectroscopic solutions plotted against their orbital periods. Blue squares mark eclipsing sdB binaries of HW Vir type where the companion mass is well constrained and red circles show systems without eclipses, where only lower limits can be derived for the companion masses. The dashed lines mark the regions to the right where the minimum companion masses derived from the binary mass function (assuming $0.47 M_{\odot}$ for the sdBs) exceed $0.01 M_{\odot}$ (lower curve) and $0.08 M_{\odot}$ (upper curve).

parameters of post-common-envelope systems over a large period range.

For non-eclipsing systems, the absolute mass of the companion cannot be determined. Some first tests show, however, that the inclination and radii can be constrained with light curves of space-based quality (Schaffenroth et al., in prep.), which will allow us to constrain the companion masses. Assuming the canonical sdB mass, a minimum mass for all companions can be derived. An overview of the 33 known sdB binaries with reflection effects and known orbital parameters is shown in Fig. 15. Although only minimum masses can be derived for most of the companions, we can use this sample to do some statistics. While most companions are late M-dwarfs with masses close to $\sim 0.1 M_{\odot}$, there is no sharp drop below the hydrogen-burning limit. The fraction of close substellar companions is substantial. An obvious feature in Fig. 15 is the lack of binaries with periods shorter than ~ 0.18 d and $K < 47 \text{ km s}^{-1}$ corresponding to companion masses of less than $\sim 0.06 M_{\odot}$. This feature is not caused by selection effects: the comparable radii of giant planets and stars close to the hydrogen-burning limit means that their eclipse depths would be similar, and their shorter orbital periods would mean the reflection effect should be as strong as or stronger than that of typical HW Vir binaries. An explanation for the lack of objects at short periods could be that the companion triggered the ejection of the envelope, but was destroyed during the common-envelope phase. This could also explain the formation of some of the single sdBs. Our target sample is ideal for studying this region in the diagram more thoroughly, as it significantly increases the number of known systems with periods smaller than 0.15 d.

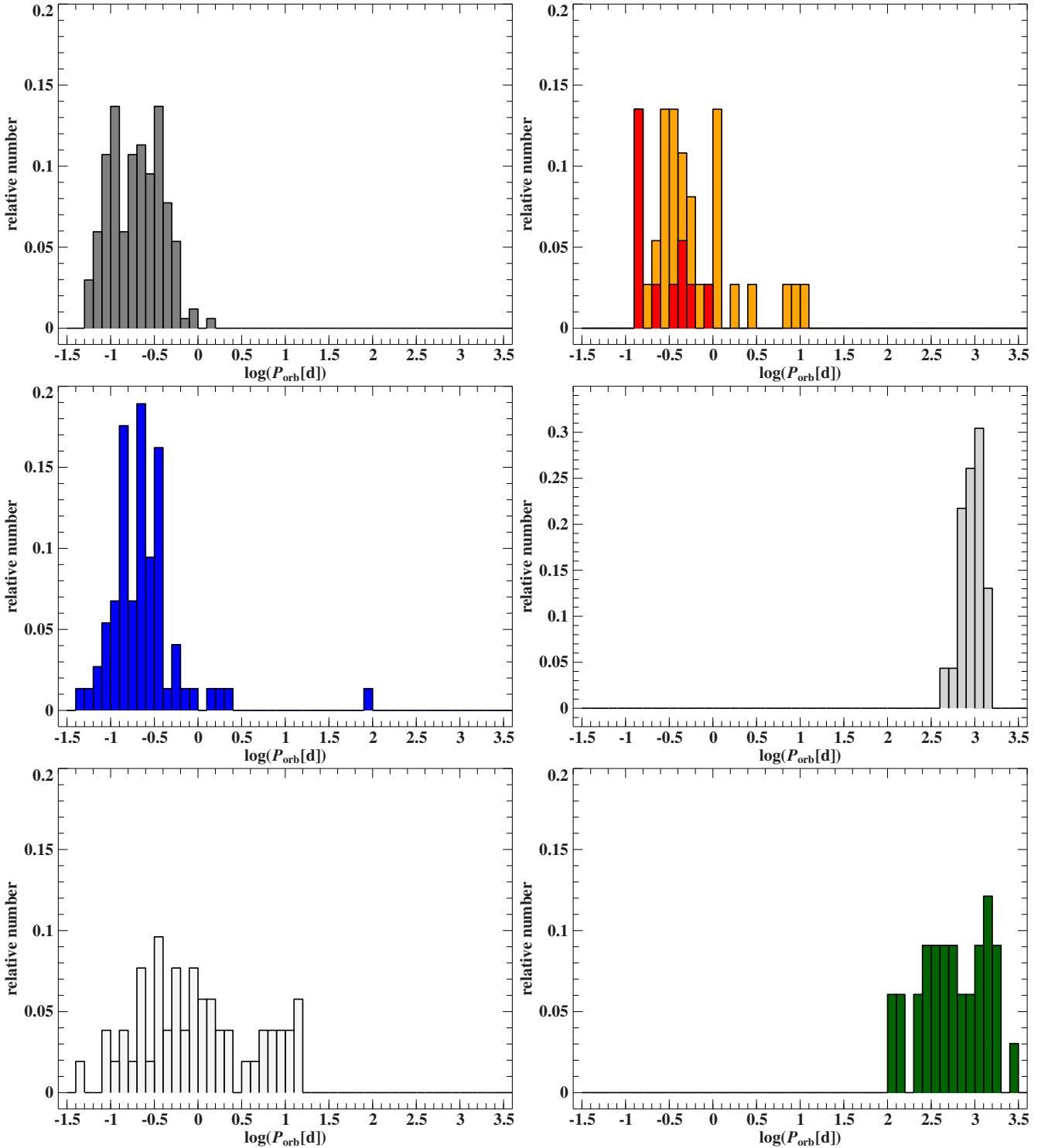


Fig. 16. Period distribution of different kinds of post-common-envelope systems. *Left: top:* all HW Vir systems including the HW Vir candidate systems from this paper (gray); *middle:* known eclipsing WD+dM/BD systems from [Parsons et al. \(2015\)](#) (blue); *bottom:* known sdB+WD systems from [Kupfer et al. \(2015\)](#) (white). *Right: top:* known eclipsing binary central stars of planetary nebula showing a reflection effect (red) and noneclipsing binary central stars of planetary nebula showing a reflection effect (orange³); *middle:* known sdB + main sequence companions from the Roche lobe overflow channel ([Vos et al. 2019](#), light-gray); *bottom:* post-AGB binaries from [Oomen et al. \(2018\)](#), dark green).

7.2. Comparison with related (eclipsing) binary populations

It is also interesting to compare our period distribution with the distribution of other types of post-common envelope systems. This is shown in Fig. 16. The eclipsing WD+dM/BD systems show a very similar distribution. However, the longest-period

systems have periods of 2.3 d. All the systems with periods longer than 0.5 d have WD primaries with masses greater than $0.55 M_{\odot}$ and have to be post-AGB stars. The longest-period system KOI-3278 with a period of 88 d is a post-common envelope system of a CO-WD with a G type companion ([Parsons et al. 2015](#)). It is the longest-period eclipsing post-common-envelope

system known. As the primary is a CO white dwarf it has to be a post-AGB binary. The white dwarf is much smaller than the subdwarf, which means that the eclipsing probability is much smaller for white dwarf binaries. However, they are much more common than hot subdwarf stars.

As already discussed in Kupfer et al. (2015) the period distribution of the known sdB+WD systems resulting from the second common envelope channel is much broader than the period distribution of the reflection-effect systems with a secondary peak at periods of several days.

Another type of post-common-envelope systems are the binary central stars of planetary nebula. As only 11 eclipsing systems are known, we also added systems which only show the reflection effect. The period distribution of the eclipsing bCSPNs with cool companions looks very similar to the distribution of the HW Vir systems. However, systems showing only the reflection effect and no eclipses are found up to periods of several days, almost as long as the sdB+WD systems. The primary can be a very hot WD or sdO and so the amplitude of the reflection effect is relatively large in some but not all cases. The bCSPNs can either be post-RGB or post-AGB systems.

The longest-period post-common-envelope system with an sdB primary has a period of 27.8 d, but the nature of the companion has not yet been determined. For comparison we also added the group of long-period sdB systems with FGK companions showing composite spectra. They are found at periods of a few 100 d which means they were formed through the Roche lobe overflow channel. The shortest period for such sdB binaries is 479 d (Vos et al. 2019). No systems with periods in the range ~28–480 d have been found yet.

Oomen et al. (2018) published a sample of 33 post-AGB binaries. They have periods similar to those of long-period sdB binaries and share other characteristics with this latter group (e.g., significant eccentricities in many systems); population synthesis, on the other hand, predicted periods of a few days for common-envelope systems (Nie et al. 2012). Oomen et al. (2018) claim that post-AGB stars with periods less than 100 d should fill their Roche lobes and therefore evolve into bCSPNs quickly or contain hotter post-AGB primaries. Those should be distinguishable from post-RGB stars quite easily, as they are expected to be much more luminous.

8. Summary and outlook

In the EREBOS project we study a large sample of homogeneously selected HW Vir systems. We investigated two photometric surveys to find more such systems and increased the number of known systems by a factor of almost ten. We plan a photometric and spectroscopic follow-up of as many targets as possible to determine the fundamental stellar (M , R), atmospheric (T_{eff} , $\log g$), and binary parameters (a , P). At the moment we already have spectroscopic follow-up for 28 objects. For several of our systems we took photometric follow-up in several bands (B , V , R), which is essential for modeling the reflection effect.

For 25 of our targets, it has been spectroscopically confirmed that they are indeed systems consisting of a hot subdwarf primary and a cool, low-mass companion; only two targets have a DA primary. Four systems in our sample were confirmed to be central stars of planetary nebula. This means that ~90% of our target sample are most likely to be eclipsing hot subdwarf binaries.

The main goal of EREBOS is to investigate HW Vir systems over the whole range of the period distribution. We hope to improve the understanding of the common-envelope phase by

investigating a large number of post-common-envelope binaries. Moreover, we are especially interested in the influence of the lowest-mass companions – brown dwarfs or massive planets – on stellar evolution. A future goal is an improved physical model of the reflection effect, which we hope to achieve with this huge sample of reflection-effect binaries.

A byproduct that will emerge from our sample is a mass–radius relation for cool, low-mass objects which are highly irradiated by a hot companion. This should shed light on the question of how much such objects are inflated.

The TESS mission, which is observing at the moment, provides 27 d light curves of each field and, for a few bright targets, light curves with a 2 min cadence are transmitted. The full-frame images are transferred every 30 min, allowing us to derive the light curves of all targets. This will give 27 d light curves of space-based quality, allowing us to detect reflection effects with periods of several days and to find the longest-period reflection-effect systems. It will also provide excellent light curves to expand our target sample further. Additionally, several ground-based surveys are providing or will provide excellent light-curve data in several photometric bands, which will find a large number of new HW Vir systems (e.g., ZTF and BlackGEM, of which we are now members).

Acknowledgements. Based on observations collected at the European Organisation for Astronomical Research in the Southern Hemisphere under ESO programme(s) 092.D-0040(A), 095.D-0167(A), 196.D-0214(A-D), 099.D-0217(A), 0101.D-0791(A). Also based on observations obtained at the Southern Astrophysical Research (SOAR) telescope, which is a joint project of the Ministério da Ciência, Tecnologia, Inovações e Comunicações (MCTIC) do Brasil, the US National Optical Astronomy Observatory (NOAO), the University of North Carolina at Chapel Hill (UNC), and Michigan State University (MSU). We would like to thank the Chilean Time Allocation Committee for awarding us time for complementing the EREBOS Project with the proposal CL-2016B-018. Unfortunately, there was an error on our side and the finder chart was wrongly marked so that the data were not used in the analysis presented in this paper. V.S. is supported by the Deutsche Forschungsgemeinschaft (DFG) through grant GE 2506/9-1. BB is supported by the National Science Foundation grant AST-1812874. DK acknowledges financial support from the University of the Western Cape and the National Research Foundation of South Africa. IP acknowledges funding by the Deutsche Forschungsgemeinschaft under grant GE2506/12-1. This work was supported by the National Science Foundation through grant PHY 17-148958. V.S. and S.G. were supported by the DAAD PPP USA for this project. Thereby, we would also like to thank the Kavli Institute for Theoretical Physics, UC Santa Barbara for hosting V.S. and S.G. during the stay funded by DAAD PPP USA, where a large part of the manuscript was written. This research has made use of ISIS functions (ISIScripts) provided by ECAP/Remeis observatory and MIT (<http://www.sternwarte.uni-erlangen.de/isis/>). This work has made use of data from the European Space Agency (ESA) mission *Gaia* (<https://www.cosmos.esa.int/gaia>), processed by the *Gaia* Data Processing and Analysis Consortium (DPAC, <https://www.cosmos.esa.int/web/gaia/dpac/consortium>). Funding for the DPAC has been provided by national institutions, in particular the institutions participating in the *Gaia* Multilateral Agreement.

References

- Afşar, M., & Ibañoğlu, C. 2008, *MNRAS*, **391**, 802
 Almeida, L. A., Daminieli, A., Rodrigues, C. V., Pereira, M. G., & Jablonski, F. 2017, *MNRAS*, **472**, 3093
 Althaus, L. G., Miller Bertolami, M. M., & Córsico, A. H. 2013, *A&A*, **557**, A19
 Bailer-Jones, C. A. L., Rybizki, J., Fournesneau, M., Mantelet, G., & Andrae, R. 2018, *VizieR Online Data Catalog*: I/347
 Baraffe, I., Chabrier, G., Allard, F., & Hauschildt, P. H. 1998, *A&A*, **337**, 403
 Budaj, J. 2011, *AJ*, **141**, 59
 Clemens, J. C., Crain, J. A., & Anderson, R. 2004, in Ground-based Instrumentation for Astronomy, eds. A. F. M. Moorwood, & M. Iye, *Proc. SPIE*, **5492**, 331
 Dorman, B., Rood, R. T., & O’Connell, R. W. 1993, *APJ*, **419**, 596
 Eggleton, P. P. 1983, *ApJ*, **268**, 368
 Gaia Collaboration (Babusiaux, C., et al.) 2018a, *A&A*, **616**, A10

- Gaia Collaboration (Brown, A. G. A., et al.) 2018b, [A&A](#), **616**, A1
- Geier, S., Schaffenroth, V., Drechsel, H., et al. 2011, [ApJ](#), **731**, L22
- Geier, S., Raddi, R., Gentile Fusillo, N. P., & Marsh, T. R. 2019, [A&A](#), **621**, A38
- Gentile Fusillo, N. P., Gänsicke, B. T., & Greiss, S. 2015, [MNRAS](#), **448**, 2260
- Gentile Fusillo, N. P., Tremblay, P.-E., Gänsicke, B. T., et al. 2019, [MNRAS](#), **482**, 4570
- Han, Z., Podsiadlowski, P., Maxted, P. F. L., Marsh, T. R., & Ivanova, N. 2002, [MNRAS](#), **336**, 449
- Heber, U. 2009, [ARA&A](#), **47**, 211
- Heber, U. 2017, in [Stripped Red Giants - Helium Core White Dwarf Progenitors and their sdB Siblings](#) (San Francisco: ASP), ASP Conf. Ser., 509, 85
- Heber, U., Reid, I. N., & Werner, K. 2000, [A&A](#), **363**, 198
- Hillwig, T. C., Frew, D. J., Reindl, N., et al. 2017, [AJ](#), **153**, 24
- Hirsch, H. 2009, Phd Thesis, Friedrich Alexander Universität Erlangen Nürnberg, Germany
- Jeffery, C. S., & Ramsay, G. 2014, [MNRAS](#), **442**, L61
- Kupfer, T., Geier, S., Heber, U., et al. 2015, [A&A](#), **576**, A44
- Lallement, R., Vergely, J.-L., Valette, B., et al. 2014, [A&A](#), **561**, A91
- Lomb, N. R. 1976, [Ap&SS](#), **39**, 447
- Maxted, P. F. L., Heber, U., Marsh, T. R., & North, R. C. 2001, [MNRAS](#), **326**, 1391
- Miller Bertolami, M. M. 2016, [A&A](#), **588**, A25
- Miszalski, B., Acker, A., Moffat, A. F. J., Parker, Q. A., & Udalski, A. 2009, [VizieR Online Data Catalog](#): 349
- Nelson, L., Schwab, J., Ristic, M., & Rappaport, S. 2018, [ApJ](#), **866**, 88
- Nie, J. D., Wood, P. R., & Nicholls, C. P. 2012, [MNRAS](#), **423**, 2764
- Oomen, G.-M., Van Winckel, H., Pols, O., et al. 2018, [A&A](#), **620**, A85
- Parsons, S. G., Marsh, T. R., Copperwheat, C. M., et al. 2010, [MNRAS](#), **402**, 2591
- Parsons, S. G., Agurto-Gangas, C., Gänsicke, B. T., et al. 2015, [MNRAS](#), **449**, 2194
- Pietrukowicz, P., Mróz, P., Soszyński, I., et al. 2013, [Acta Astron.](#), **63**, 115
- Riello, M., De Angeli, F., Evans, D. W., et al. 2018, [A&A](#), **616**, A3
- Scargle, J. D. 1982, [ApJ](#), **263**, 835
- Schaffenroth, V., Geier, S., Drechsel, H., et al. 2013, [A&A](#), **553**, A18
- Schaffenroth, V., Geier, S., Heber, U., et al. 2014a, [A&A](#), **564**, A98
- Schaffenroth, V., Classen, L., Nagel, K., et al. 2014b, [A&A](#), **570**, A70
- Schaffenroth, V., Barlow, B. N., Drechsel, H., & Dunlap, B. H. 2015, [A&A](#), **576**, A123
- Schaffenroth, V., Geier, S., Heber, U., et al. 2018, [A&A](#), **614**, A77
- Soker, N. 1998, [AJ](#), **116**, 1308
- Soszyński, I., Stępień, K., Pilecki, B., et al. 2015, [Acta Astron.](#), **65**, 39
- Soszyński, I., Pawlak, M., Pietrukowicz, P., et al. 2016, [Acta Astron.](#), **66**, 405
- Tody, D. 1986, in [Instrumentation in Astronomy VI](#), ed. D. L. Crawford, [Proc SPIE](#), **627**, 733
- Tonry, J. L., Denneau, L., Heinze, A. N., et al. 2018, [PASP](#), **130**, 064505
- Udalski, A., Pont, F., Naef, D., et al. 2008, [A&A](#), **482**, 299
- Udalski, A., Szymański, M. K., & Szymański, G. 2015, [Acta Astron.](#), **65**, 1
- Vos, J., Vučković, M., Chen, X., et al. 2019, [MNRAS](#), **482**, 4592
- Wilson, R. E. 1990, [ApJ](#), **356**, 613

Appendix A: Light curves, orbital parameters, magnitudes, *Gaia* parallaxes, and proper motions of all our targets

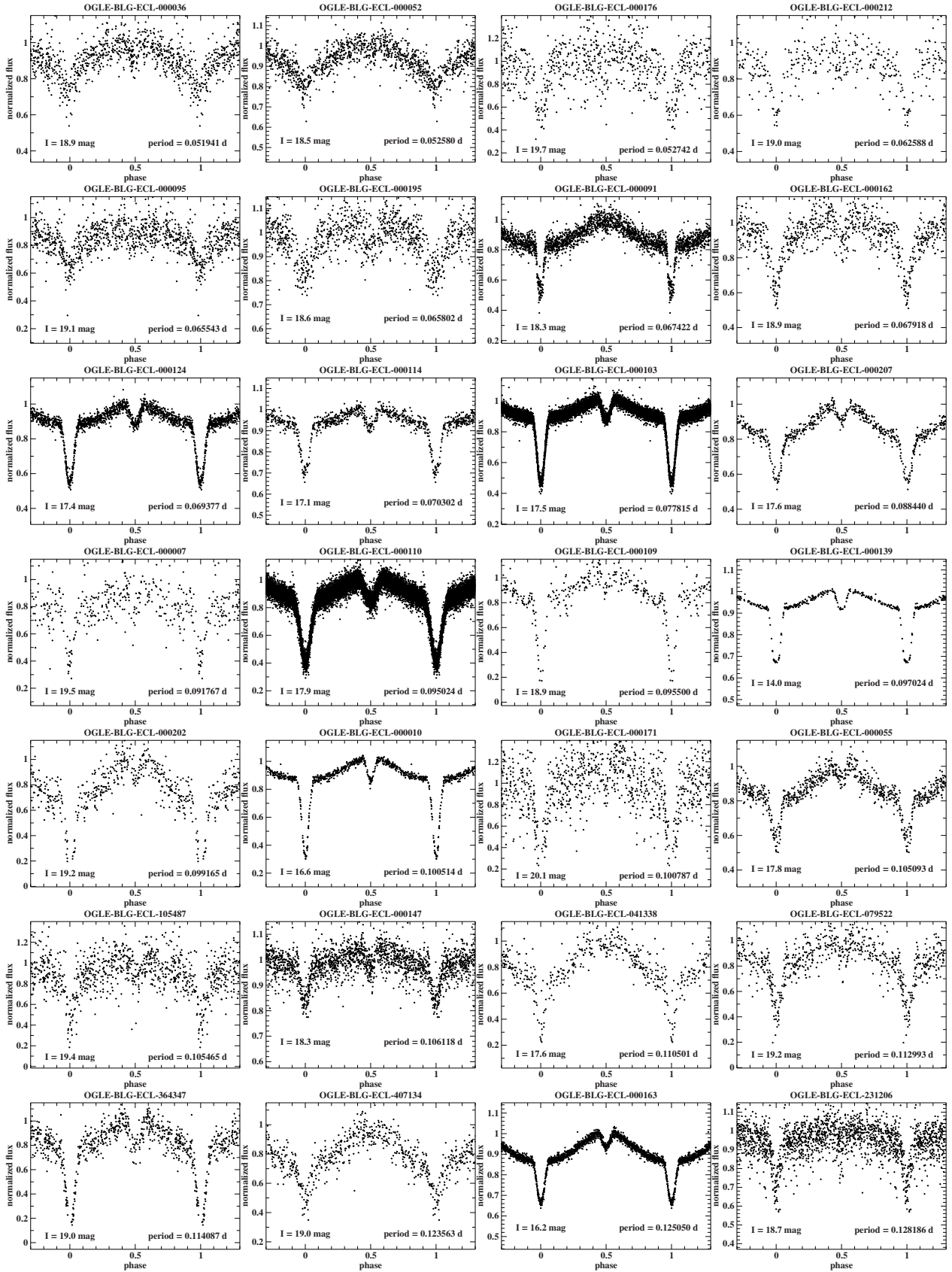


Fig. A.1. Phased light curves of all our HW Vir candidates from the OGLE survey.

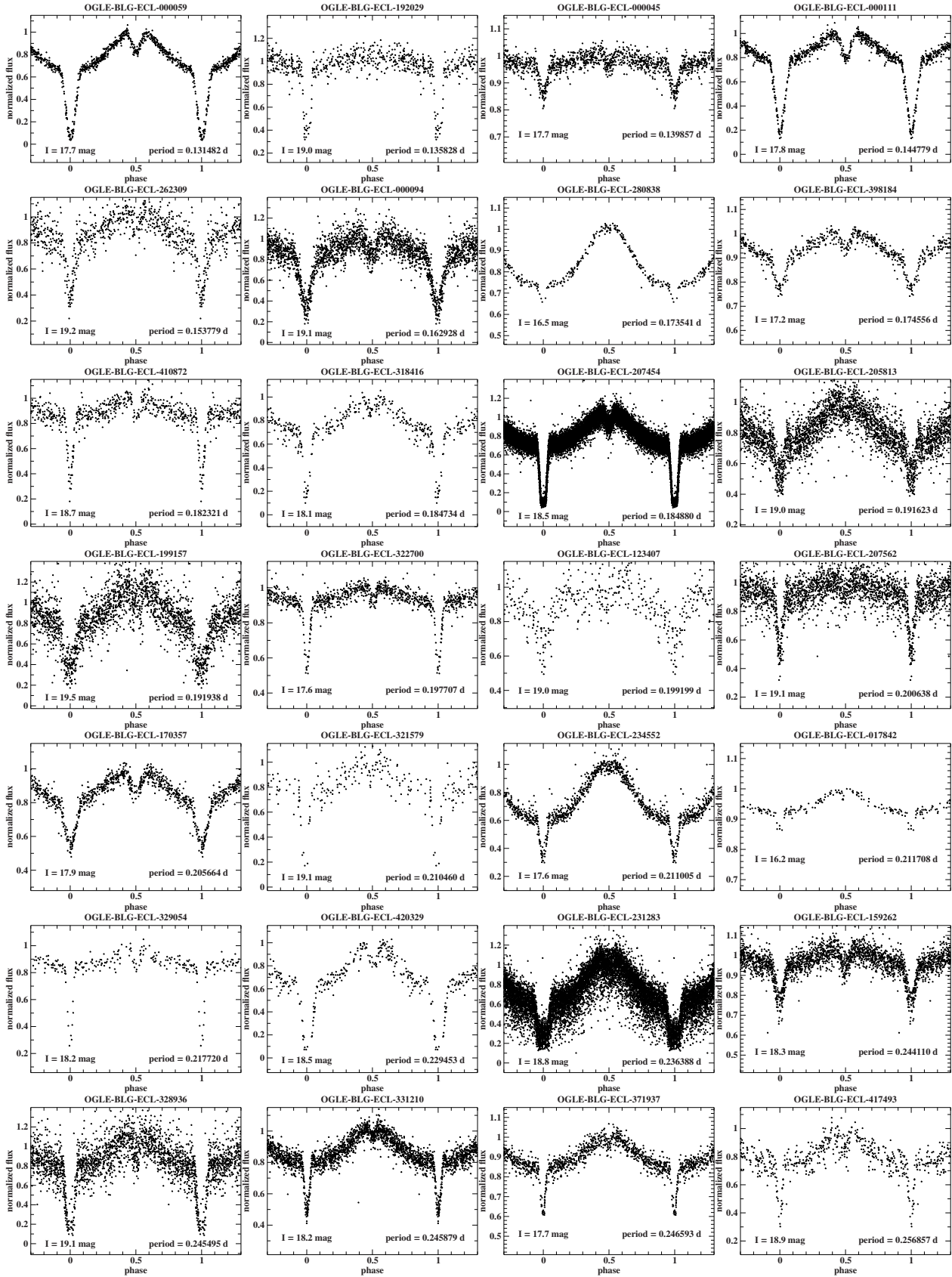


Fig. A.1. continued.

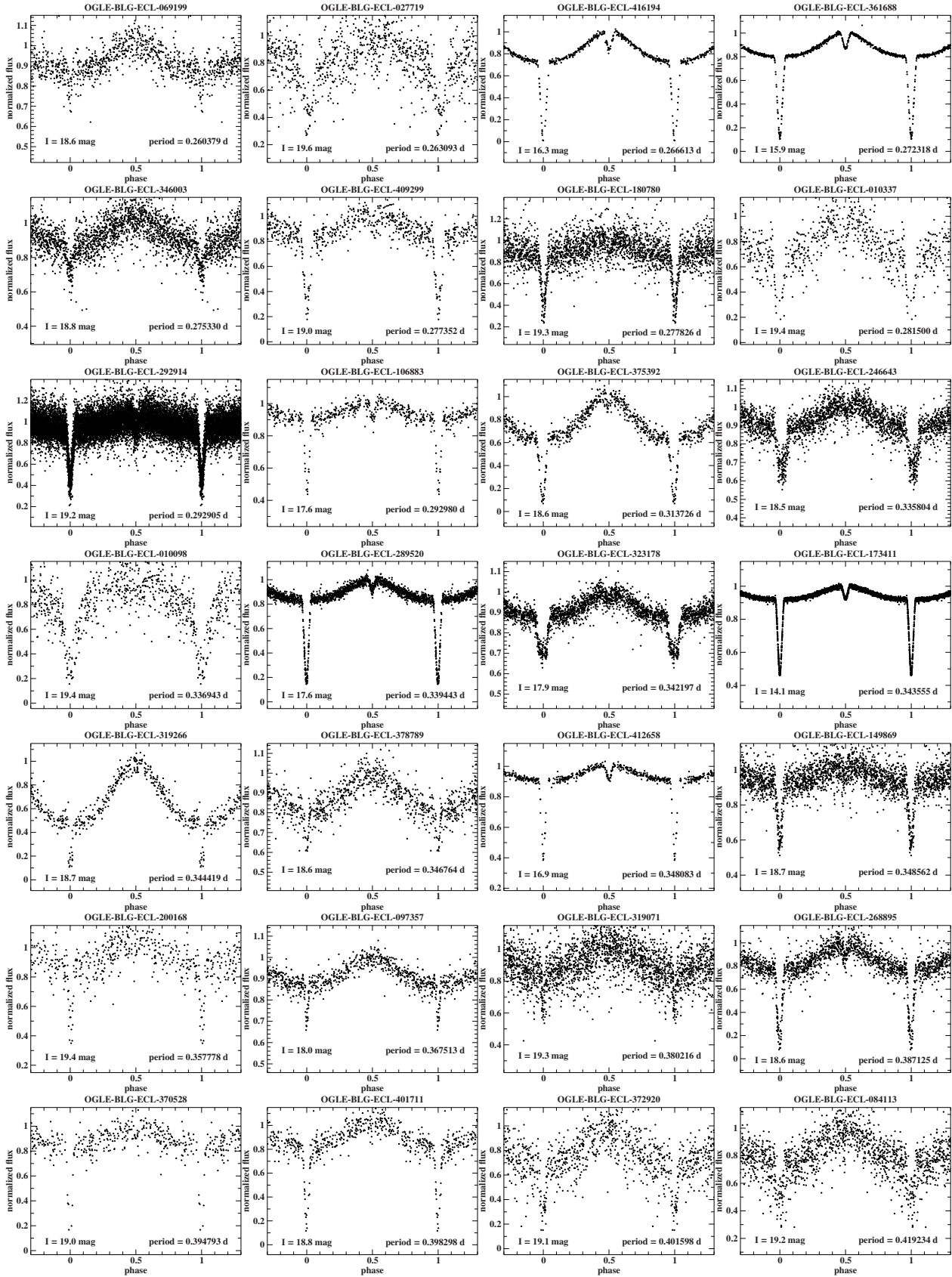


Fig. A.1. continued.

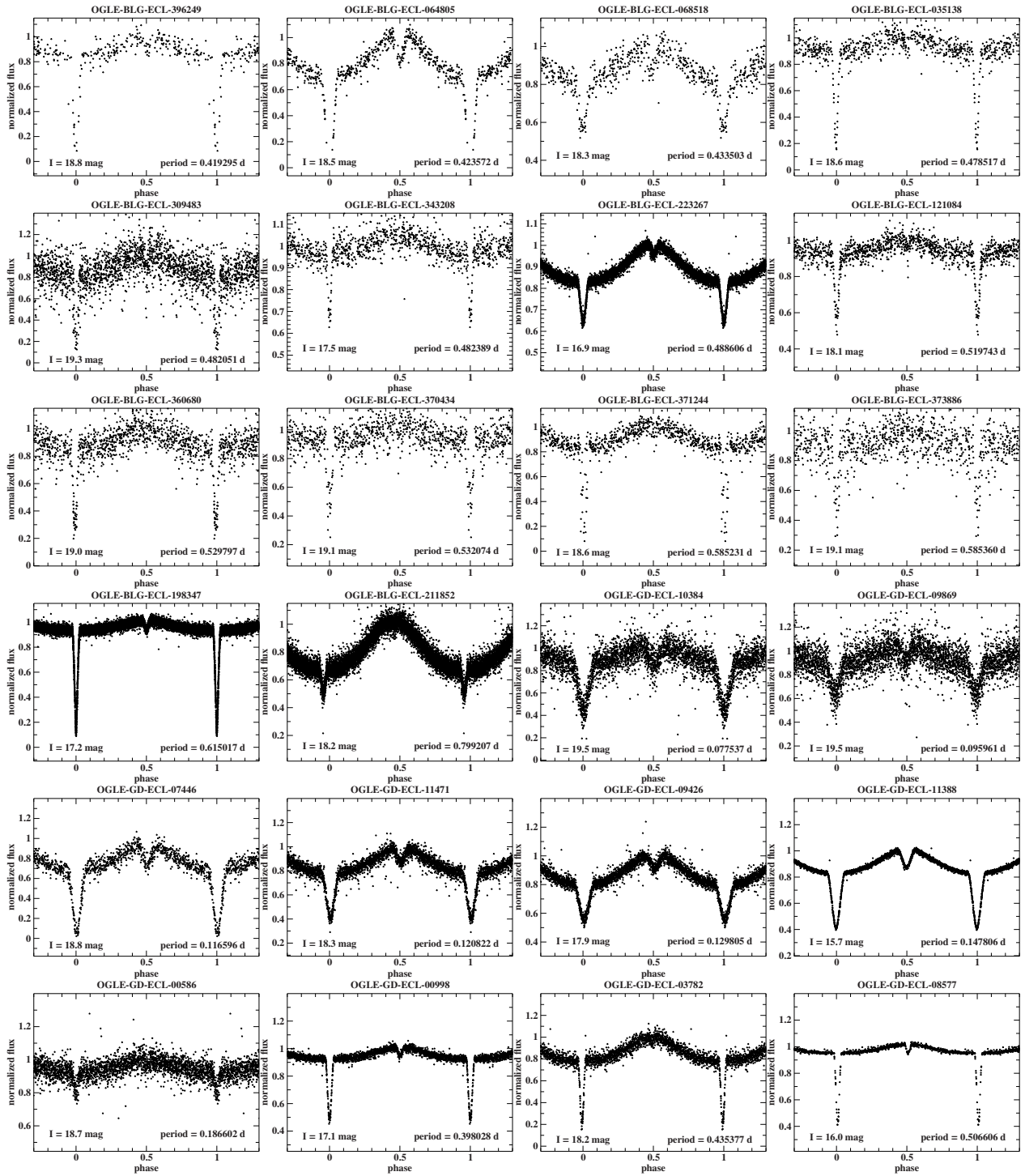


Fig. A.1. continued.

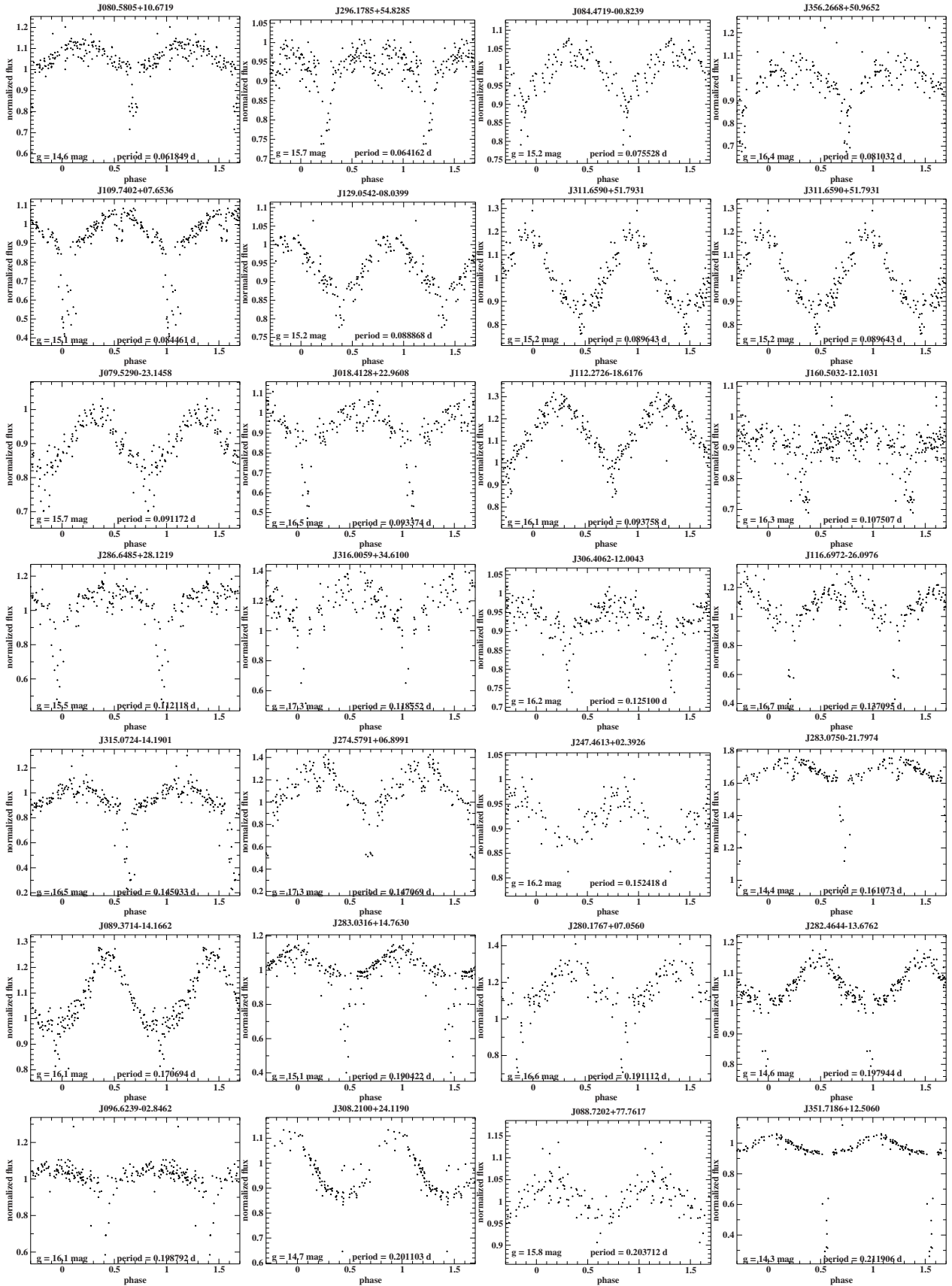


Fig. A.2. Phased light curves of all our HW Vir candidates from the ATLAS survey.

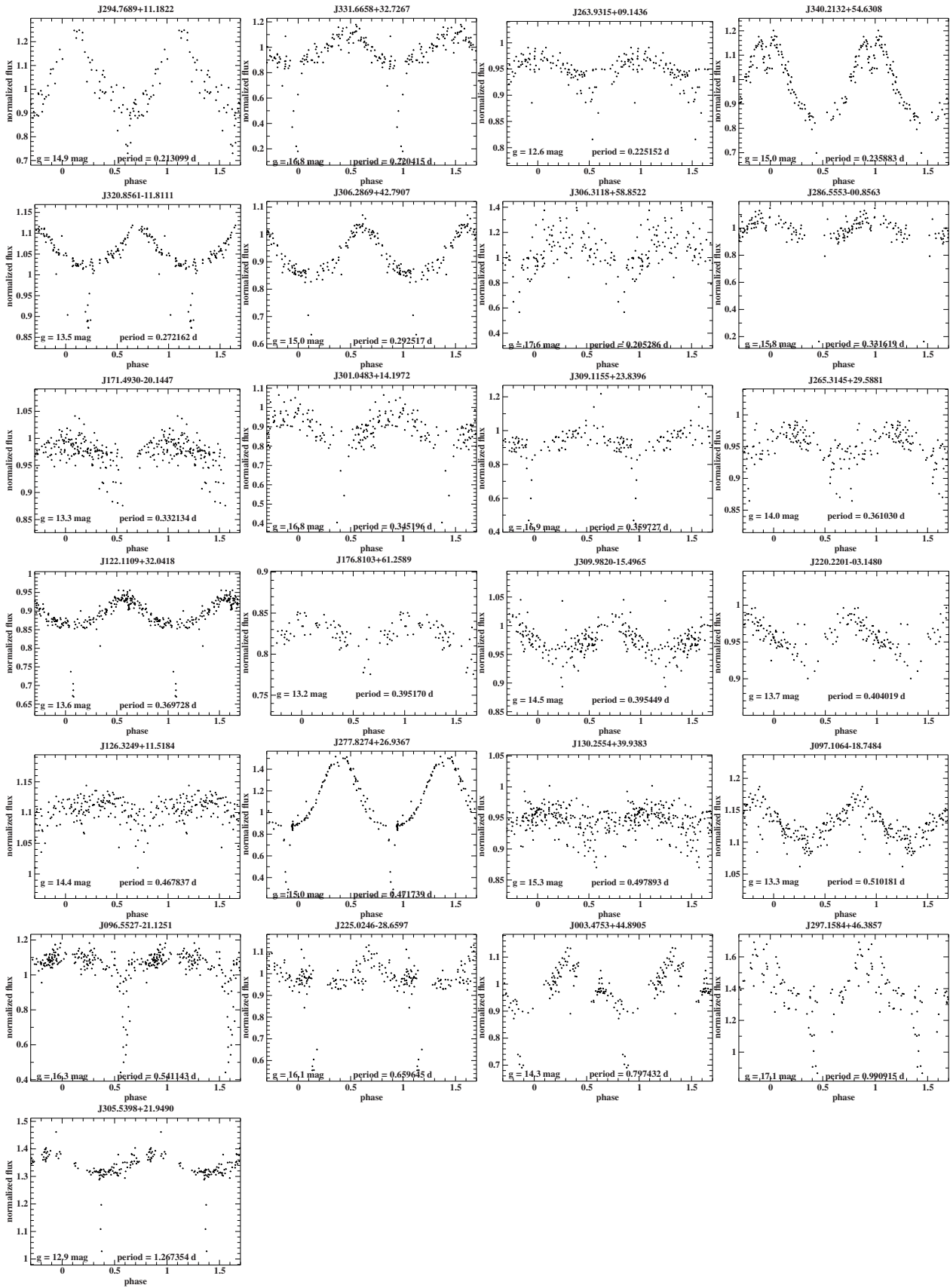


Fig. A.2. continued.

Table A.1. Orbital parameters, *Gaia* and OGLE magnitudes, and coordinates of the HW Vir candidates and published HW Vir systems (objects in bold face were confirmed by deriving the atmospheric parameters).

Target	RA (OGLE) [h]	Dec (OGLE) [°]	RA (<i>Gaia</i>) [h]	RA (<i>Gaia</i>) [°]	<i>I</i> [mag]	<i>V</i> [mag]	<i>G</i> [mag]	ΔG [mag]	G_{BP} [mag]	ΔG_{BP} [mag]	G_{RP} [mag]	ΔG_{RP} [mag]	$G_{BP} - G_{RP}$ [mag]	<i>P</i> d	T_0 HJD-2400000
Discovered by Soszyński et al. (2015)															
OGLE-BLG-ECL-000036	17:41:20.55	-34:34:48.5	17:41:20.5412	-34:34:48.546	18.945	19.623	19.5374	0.0154	—	—	—	—	—	0.05194084	7000.0499
OGLE-BLG-ECL-000052	17:47:43.31	-23:31:22.1	17:47:43.3091	-23:31:22.252	18.499	19.808	19.5879	0.0091	19.5473	0.0777	17.9754	0.0826	1.5719	0.05258043	7000.0167
OGLE-BLG-ECL-000176	18:12:13.63	-33:09:43.7	18:12:13.6385	-33:09:43.583	19.730	19.594	19.7050	0.0133	19.1867	0.1426	19.8247	0.9303	-0.6380	0.05274168	7000.0339
OGLE-BLG-ECL-000212	18:36:22.73	-23:15:45.0	18:36:22.7387	-23:15:45.340	19.006	19.325	19.6910	0.0120	—	—	—	—	—	0.06258789	7000.0820
OGLE-BLG-ECL-000095	17:57:36.65	-33:57:34.0	17:57:36.5306	-33:57:33.810	19.066	19.401	19.4170	0.0084	—	—	—	—	—	0.06554264	7000.0499
OGLE-BLG-ECL-000195	18:16:16.40	-28:10:36.0	18:16:16.3969	-28:10:36.082	18.582	18.689	18.7529	0.0100	—	—	—	—	—	0.06580196	7000.0212
OGLE-BLG-ECL-000162	18:09:33.86	-32:23:44.6	18:09:33.8597	-32:23:44.726	18.891	19.057	19.0726	0.0066	—	—	—	—	—	0.06791815	7000.0119
OGLE-BLG-ECL-000124	18:02:17.95	-32:01:50.0	18:02:17.9411	-32:01:50.008	17.426	17.688	17.7567	0.0042	17.4801	0.0091	16.9374	0.0399	0.5427	0.06937682	7000.0453
OGLE-BLG-ECL-000114	18:00:48.04	-35:38:35.1	18:00:48.0453	-35:38:35.166	17.077	17.118	17.2112	0.0078	16.9399	0.0324	16.6411	0.0258	0.2988	0.07030228	7000.0020
OGLE-BLG-ECL-000103	17:59:27.25	-27:25:56.8	17:59:27.2465	-27:25:56.766	17.468	17.807	17.8347	0.0045	17.8371	0.0391	17.3107	0.0322	0.5265	0.07781521	7000.0597
OGLE-BLG-ECL-000207	18:20:48.29	-24:27:07.0	18:20:48.2906	-24:27:07.033	17.640	17.984	18.1092	0.0136	18.0425	0.0593	17.7270	0.0661	0.3155	0.08843965	7000.0017
OGLE-BLG-ECL-000007	17:18:11.61	-28:59:37.3	17:18:11.6110	-28:59:37.375	19.493	20.185	20.4080	0.0301	—	—	—	—	—	0.09176723	7000.0033
OGLE-BLG-ECL-000110	18:00:23.28	-28:23:42.1	18:00:23.2861	-28:23:42.131	17.948	18.456	18.5350	0.0189	—	—	—	—	—	0.09502377	7000.0263
OGLE-BLG-ECL-000109	18:00:16.41	-36:31:25.3	18:00:16.4124	-36:31:25.368	18.925	19.191	19.2823	0.0161	18.9251	0.0757	18.4102	0.1597	0.5149	0.09550029	7000.0407
OGLE-BLG-ECL-000139	18:04:31.04	-34:19:43.6	18:04:31.0580	-34:19:43.523	14.045	13.914	13.9457	0.0063	13.7603	0.0238	13.9672	0.0417	-0.2069	0.09702380	7000.0100
OGLE-BLG-ECL-000202	18:17:56.68	-28:39:02.9	18:17:56.6657	-28:39:05.732	19.200	19.316	19.1591	0.0073	—	—	—	—	—	0.09916540	7000.0760
OGLE-BLG-ECL-000010	17:27:44.28	-29:46:16.1	17:27:44.2816	-29:46:16.110	16.639	17.101	17.1583	0.0056	17.0577	0.0279	16.1389	0.0489	0.9188	0.10051416	7000.0433
OGLE-BLG-ECL-000171	18:11:14.75	-32:16:27.2	18:11:14.8601	-32:16:28.626	20.078	20.219	19.9110	0.0111	19.2952	0.2139	18.8204	0.0961	0.4748	0.10078663	7000.0580
OGLE-BLG-ECL-000055	17:49:43.09	-22:29:15.4	17:49:43.0914	-22:29:15.339	17.797	18.960	18.7530	0.0099	—	—	—	—	—	0.10509323	7000.0514
OGLE-BLG-ECL-000147	18:05:33.33	-32:10:34.6	18:05:33.3261	-32:10:34.706	18.342	18.881	18.9100	0.0088	—	—	—	—	—	0.10611778	7000.0953
OGLE-BLG-ECL-000163	18:09:48.03	-26:41:49.4	18:09:48.0319	-26:41:49.387	16.245	16.523	16.5603	0.0052	—	—	—	—	—	0.12505021	7000.0859
OGLE-BLG-ECL-000059	17:50:34.10	-34:13:50.2	17:50:34.1006	-34:13:50.304	17.666	18.608	18.6631	0.0149	—	—	—	—	—	0.13148233	7000.0952
OGLE-BLG-ECL-000094	17:57:31.37	-31:25:25.4	17:57:31.4483	-31:25:25.581	19.087	—	19.5113	0.0065	—	—	—	—	—	0.16292828	7000.0356
Discovered by visual inspection															
OGLE-BLG-ECL-105487	17:47:15.77	-22:55:18.5	17:47:15.7101	-22:55:19.629	19.442	20.126	19.6696	0.0128	—	—	—	—	—	0.1054648	7000.0822
OGLE-BLG-ECL-041338	17:36:06.87	-34:37:06.5	17:36:06.8697	-34:37:06.487	17.604	18.659	18.5950	0.0139	—	—	—	—	—	0.11105012	7000.0924
OGLE-BLG-ECL-079522	17:43:38.97	-24:15:31.3	17:43:38.9684	-24:15:31.578	19.205	20.269	20.0601	0.0367	19.5534	0.2860	17.7107	0.0234	1.8427	0.1129930	7000.0799
OGLE-BLG-ECL-364347	18:12:51.10	-31:10:14.1	18:12:51.0838	-31:10:14.221	18.997	19.026	19.2429	0.0209	18.6740	0.0938	18.9633	0.2516	-0.2893	0.1140869	7000.0928
OGLE-BLG-ECL-407134	18:19:07.87	-26:29:30.5	18:19:07.8651	-26:29:30.574	19.041	19.456	19.6110	0.0183	—	—	—	—	—	0.1235625	7000.0914
OGLE-BLG-ECL-231206	17:59:24.29	-33:31:04.0	17:59:24.2811	-33:31:04.130	18.705	19.420	19.5035	0.0082	—	—	—	—	—	0.1281863	7000.0216
OGLE-BLG-ECL-262309	18:02:12.03	-33:22:08.2	18:02:11.9499	-33:22:09.435	19.184	19.826	19.7152	0.0089	—	—	—	—	—	0.1537792	7000.0666
OGLE-BLG-ECL-280838	18:03:54.09	-34:45:39.6	18:03:54.0855	-34:45:39.617	16.497	16.598	16.7027	0.0091	16.4888	0.0286	16.3790	0.0482	0.1099	0.1735412	7000.0052
OGLE-BLG-ECL-398184	18:17:27.43	-23:38:23.7	18:17:27.4271	-23:38:23.746	17.204	17.710	17.7677	0.0068	17.4846	0.0352	16.4825	0.0310	1.0021	0.1745556	7000.0294
OGLE-BLG-ECL-410872	18:19:52.79	-25:42:51.0	18:19:52.7931	-25:42:50.926	18.674	18.928	19.0237	0.0097	18.9291	0.1107	18.1640	0.2186	0.7650	0.1823207	7000.0004
OGLE-BLG-ECL-170357	17:54:10.83	-34:54:46.6	17:54:10.8320	-34:54:46.639	17.922	18.482	18.5383	0.0095	18.3272	0.0758	17.5961	0.0811	0.7311	0.2056641	7000.1561
OGLE-BLG-ECL-234552	17:59:41.59	-27:04:43.7	17:59:41.5851	-27:04:43.646	17.602	18.356	18.5224	0.0201	—	—	—	—	—	0.2110051	7000.0007
OGLE-BLG-ECL-017842	17:28:16.21	-25:18:32.6	17:28:16.2145	-25:18:32.621	16.166	16.892	16.8087	0.0022	17.0810	0.0104	16.2588	0.0192	0.8221	0.2117081	7000.1370
OGLE-BLG-ECL-420329	18:22:11.10	-30:24:58.2	18:22:11.0871	-30:24:58.244	18.531	18.710	19.0404	0.0211	18.2531	0.0666	17.5671	0.0569	0.6860	0.2294529	7000.2201
OGLE-BLG-ECL-328936	18:08:38.73	-25:53:12.1	—	—	19.092	19.913	—	—	—	—	—	—	—	0.2454952	7000.0413
OGLE-BLG-ECL-331210	18:08:54.16	-25:34:01.4	18:08:54.1601	-25:34:01.431	18.157	18.772	18.7924	0.0170	—	—	—	—	—	0.2458786	7000.0320
OGLE-BLG-ECL-371937	18:13:51.29	-26:21:57.7	18:13:51.2878	-26:21:57.809	17.737	18.157	18.2107	0.0082	17.9334	0.0460	17.4454	0.0592	0.4880	0.2465935	7000.0228
OGLE-BLG-ECL-069199	17:41:55.62	-34:11:41.9	17:41:55.6163	-34:11:41.884	18.637	19.591	19.4899	0.0099	—	—	—	—	—	0.2603793	7000.2581

Table A.1. continued.

Target	RA (OGLE) [h]	Dec (OGLE) [°]	RA (Gaia) [h]	RA (Gaia) [°]	<i>I</i> [mag]	<i>V</i> [mag]	<i>G</i> [mag]	ΔG [mag]	G_{BP} [mag]	ΔG_{BP} [mag]	G_{RP} [mag]	ΔG_{RP} [mag]	$G_{BP} - G_{RP}$ [mag]	<i>P</i> d	T_0 HJD-2400000
OGLE-BLG-ECL-416194	18:20:59.03	-23:33:16.5	18:20:59.0333	-23:33:16.495	16.252	16.553	16.6824	0.0072	16.6707	0.0233	16.4027	0.0494	0.2680	0.2666134	7000.2491
OGLE-BLG-ECL-361688	18:12:30.17	-28:51:38.7	18:12:30.1734	-28:51:38.785	15.929	15.953	16.1052	0.0051	15.8646	0.0185	15.7477	0.0281	0.1169	0.2723178	7000.0658
OGLE-BLG-ECL-346003	18:10:35.24	-26:07:21.6	18:10:35.1052	-26:07:17.362	18.803	19.747	19.4353	0.0083	-	-	-	-	-	0.2753299	7000.4769
OGLE-BLG-ECL-409299	18:19:33.79	-23:51:15.9	18:19:33.7948	-23:51:16.091	19.032	19.231	19.3004	0.0272	19.0977	0.3740	17.9132	0.0978	1.1845	0.2773518	7000.2157
OGLE-BLG-ECL-180780	17:55:05.47	-31:14:17.9	17:55:05.4752	-31:14:17.871	19.293	20.291	20.0489	0.0203	-	-	-	-	-	0.2778255	7000.1195
OGLE-BLG-ECL-010337	17:24:10.01	-28:35:35.9	17:24:10.0059	-28:35:35.983	19.367	20.703	20.5854	0.0296	-	-	-	-	-	0.2814997	7000.0028
OGLE-BLG-ECL-292914	18:05:00.13	-28:35:13.6	18:05:00.0830	-28:35:14.571	19.179	19.824	19.2344	0.0188	19.1103	0.6196	-	-	-	0.2929049	7000.2193
OGLE-BLG-ECL-106883	17:47:27.25	-36:29:24.9	17:47:27.2422	-36:29:24.936	17.617	18.420	18.3932	0.0048	18.4827	0.0339	17.1023	0.0016	1.3805	0.2929798	7000.0139
OGLE-BLG-ECL-375392	18:14:18.14	-31:36:26.8	18:14:18.1485	-31:36:26.841	18.640	18.901	19.2339	0.0190	18.4983	0.0872	17.7958	0.0923	0.7026	0.3137258	7000.2870
OGLE-BLG-ECL-010098	17:24:00.01	-29:28:12.5	17:24:00.0578	-29:28:11.761	19.428	-	20.1427	0.0179	-	-	-	-	-	0.3369434	7000.1339
OGLE-BLG-ECL-289520	18:04:41.70	-29:54:00.5	18:04:41.7087	-29:54:00.613	17.581	18.055	18.2194	0.0165	17.8709	0.0553	17.0891	0.0340	0.7818	0.3394434	7000.0543
OGLE-BLG-ECL-173411	17:54:26.36	-28:34:07.0	17:54:26.3522	-28:34:06.883	14.131	14.130	14.0885	0.0018	13.9270	0.0106	14.1119	0.0101	-0.1849	0.3435548	7000.0286
OGLE-BLG-ECL-319266	18:07:36.41	-34:43:28.9	18:07:36.4027	-34:43:28.898	18.674	18.997	19.3762	0.0260	19.0780	0.2175	18.9677	0.2145	0.1103	0.3444195	7000.6715
OGLE-BLG-ECL-378789	18:14:44.69	-28:57:44.2	18:14:44.6916	-28:57:44.258	18.603	18.872	19.0310	0.0161	-	-	-	-	-	0.3467644	7000.0418
OGLE-BLG-ECL-412658	18:20:13.27	-27:47:59.0	18:20:13.2730	-27:47:59.017	16.917	16.990	17.0540	0.0034	16.8286	0.0658	16.8328	0.0400	-0.0042	0.3480831	7000.1221
OGLE-BLG-ECL-097357	17:46:08.35	-21:56:27.6	17:46:08.3420	-21:56:27.582	17.984	19.228	18.9991	0.0062	19.3222	0.0563	17.7589	0.0756	1.5633	0.3675127	7000.0981
OGLE-BLG-ECL-319071	18:07:35.24	-27:31:35.0	18:07:35.5247	-27:31:33.731	19.309	19.885	18.8135	0.0054	18.9003	0.1039	17.6951	0.6661	1.2052	0.3802164	7000.0315
OGLE-BLG-ECL-268895	18:02:48.49	-31:24:54.5	18:02:48.4980	-31:24:54.612	18.645	19.343	19.2940	0.0170	-	-	-	-	-	0.3871253	7000.2090
OGLE-BLG-ECL-370528	18:13:40.19	-32:14:05.7	18:13:40.1892	-32:14:05.783	18.977	19.292	19.4409	0.0098	-	-	-	-	-	0.3947927	7000.2090
OGLE-BLG-ECL-401711	18:18:04.19	-26:43:38.2	18:18:04.2013	-26:43:38.253	18.768	19.027	19.1560	0.0140	18.4584	0.0776	17.5346	0.0325	0.9238	0.3982982	7000.1101
OGLE-BLG-ECL-372920	18:13:58.75	-27:22:37.8	18:13:58.830	-27:22:41.169	19.082	19.189	19.4530	0.0086	-	-	-	-	-	0.4015976	7000.2938
OGLE-BLG-ECL-396249	18:17:08.57	-30:16:59.4	18:17:08.5691	-30:16:59.399	18.773	18.967	19.1734	0.0084	-	-	-	-	-	0.4192946	7000.1723
OGLE-BLG-ECL-064805	17:41:07.28	-36:16:14.2	17:41:07.2855	-36:16:14.073	18.486	19.626	19.5125	0.0137	19.6405	0.0471	18.3523	0.0475	1.2881	0.4235718	7000.2688
OGLE-BLG-ECL-068518	17:41:48.40	-25:38:18.3	17:41:48.4036	-25:38:18.452	18.328	19.575	19.6080	0.0164	-	-	-	-	-	0.4335034	7000.4262
OGLE-BLG-ECL-035138	17:34:38.69	-29:30:27.2	17:34:38.6864	-29:30:27.413	18.613	19.661	19.4035	0.0093	19.2705	0.0955	17.3664	0.0385	1.9041	0.4785170	7000.3017
OGLE-BLG-ECL-309483	18:06:34.70	-28:39:30.6	18:06:34.7055	-28:39:32.198	19.335	19.857	18.7657	0.0063	-	-	-	-	-	0.4820508	7000.4321
OGLE-BLG-ECL-343208	18:10:15.94	-30:11:29.0	18:10:15.9358	-30:11:29.025	17.516	17.863	17.7365	0.0055	17.3498	0.0334	16.2742	0.0319	1.0756	0.4823891	7000.2935
OGLE-BLG-ECL-223267	17:58:42.63	-30:32:30.3	17:58:42.6301	-30:32:30.363	16.911	17.809	17.7154	0.0057	17.9629	0.0399	16.8509	0.0668	1.1120	0.4886060	7000.0614
OGLE-BLG-ECL-370434	18:13:39.47	-29:15:07.6	18:13:39.4723	-29:15:07.698	19.101	19.327	19.3897	0.0111	-	-	-	-	-	0.5320739	7000.2405
OGLE-BLG-ECL-371244	18:13:46.06	-29:20:02.8	18:13:46.0571	-29:20:02.933	18.603	18.701	18.8510	0.0060	18.2166	0.0558	17.8200	0.2896	0.3966	0.5852307	7000.2551
OGLE-BLG-ECL-373886	18:14:06.07	-29:48:54.3	18:14:06.0695	-29:48:52.952	19.089	19.524	18.6124	0.0055	-	-	-	-	-	0.5853605	7000.0558
OGLE-BLG-ECL-198347	17:56:33.97	-29:26:01.2	17:56:33.9734	-29:26:01.333	17.206	17.662	17.6949	0.0061	17.6301	0.0188	16.8119	0.0213	0.8182	0.6150169	7000.3334
OGLE-BLG-ECL-318416	18:07:31.18	-24:01:54.6	18:07:31.1841	-24:01:54.577	18.094	19.196	19.2538	0.0226	-	-	-	-	-	0.1847337	7000.0294
OGLE-BLG-ECL-205813	17:57:12.48	-28:52:25.6	17:57:12.4139	-28:52:24.074	19.040	20.219	19.4436	0.0108	-	-	-	-	-	0.1916233	7000.0378
OGLE-BLG-ECL-199157	17:56:37.97	-31:05:29.7	17:56:37.6202	-31:05:28.262	19.529	21.129	20.0206	0.0121	-	-	-	-	-	0.1919381	7000.0519
OGLE-BLG-ECL-123407	17:49:41.82	-34:11:35.3	17:49:41.9127	-34:11:38.071	19.016	20.853	19.6336	0.0126	-	-	-	-	-	0.1991986	7000.1729
OGLE-BLG-ECL-207562	17:57:21.28	-31:56:36.6	17:57:21.1689	-31:56:36.575	19.096	20.372	19.9740	0.0136	-	-	-	-	-	0.2006380	7000.0581
OGLE-BLG-ECL-321579	18:07:50.93	-22:37:02.2	18:07:50.9363	-22:37:02.244	19.139	20.697	20.3230	0.0143	20.2982	0.4991	19.3387	0.1871	0.9596	0.2104603	7000.1584
OGLE-BLG-ECL-329054	18:08:39.45	-22:51:59.7	18:08:39.4549	-22:51:59.688	18.240	19.415	19.2777	0.0062	19.9306	0.1568	18.5997	0.0884	1.3309	0.2177201	7000.0170
OGLE-BLG-ECL-041045	17:36:02.64	-27:25:44.0	17:36:02.6371	-27:25:43.931	18.481	20.766	19.9243	0.0097	20.2728	0.1044	18.1757	0.0803	2.0970	0.2237511	7000.1412
OGLE-BLG-ECL-231283	17:59:24.75	-28:09:08.8	17:59:24.7791	-28:09:09.640	18.804	20.428	18.8813	0.0130	18.2003	0.1022	16.6024	0.0384	1.5979	0.2363880	7000.2339
OGLE-BLG-ECL-417493	18:21:17.14	-26:45:46.7	18:21:17.1408	-26:45:46.723	18.890	100	19.3402	0.0094	19.0778	0.1806	18.6415	0.2489	0.4363	0.2568567	7000.2398

Discovered by machine-learning

Table A.1. continued.

Target	RA (OGLE) [h]	Dec (OGLE) [°]	RA (Gaia) [h]	RA (Gaia) [°]	I [mag]	V [mag]	G [mag]	ΔG [mag]	G _{BP} [mag]	ΔG _{BP} [mag]	G _{RP} [mag]	ΔG _{RP} [mag]	G _{BP} - G _{RP} [mag]	P d	T ₀ HJD-2400000
OGLE-BLG-ECL-027719	17:32:38.16	-27:50:26.2	17:32:38.2008	-27:50:24.509	19.620	21.317	19.5813	0.0107	-	-	-	-	-	0.2630934	7000.2164
OGLE-BLG-ECL-246643	18:00:46.01	-29:58:15.0	18:00:46.0987	-29:58:10.614	18.455	19.764	19.0641	0.0072	-	-	-	-	-	0.3358044	7000.2823
OGLE-BLG-ECL-323178	18:08:01.17	-26:38:35.1	18:08:01.1779	-26:38:34.930	17.880	100	19.0909	0.0069	18.7340	0.1481	-	-	-	0.3421973	7000.0782
OGLE-BLG-ECL-149869	17:52:29.43	-32:49:16.4	17:52:29.7227	-32:49:15.747	18.693	20.723	15.9081	0.0035	16.9763	0.0164	14.6421	0.0026	2.3342	0.3485623	7000.1851
OGLE-BLG-ECL-200168	17:56:43.01	-22:56:30.3	17:56:43.0116	-22:56:30.294	19.437	21.027	20.7668	0.0237	20.7848	0.3923	18.6832	0.1009	2.1015	0.3577783	7000.3460
OGLE-BLG-ECL-084113	17:44:19.76	-33:32:51.3	17:44:19.6818	-33:32:52.940	19.216	21.031	19.5899	0.0078	-	-	-	-	-	0.4192342	7000.3904
OGLE-BLG-ECL-121084	17:49:23.69	-33:13:36.1	17:49:23.6770	-33:13:36.039	18.080	19.690	19.4170	0.0157	19.2939	0.0689	17.4074	0.0724	1.8865	0.51927431	7000.3441
OGLE-BLG-ECL-360680	18:12:22.62	-26:30:56.6	18:12:22.6006	-26:30:57.120	19.001	20.783	19.7776	0.0168	-	-	-	-	-	0.5297970	7000.0115
Discovered by Pietrukowicz et al. (2013)															
OGLE-GD-ECL-10384	13:27:03.73	-65:11:19.9	13:27:03.7270	-65:11:19.878	19.453	-	19.9579	0.0082	-	-	-	-	-	0.07753698	3836.73261
OGLE-GD-ECL-11471	13:35:14.73	-64:21:10.3	13:35:14.7270	-64:21:10.343	18.293	-	18.7344	0.0049	18.6583	0.0301	18.2105	0.0517	0.4478	0.12082222	3836.83212
OGLE-GD-ECL-09426	13:17:02.49	-65:02:49.6	13:17:02.4923	-65:02:49.653	17.932	-	18.5535	0.0078	18.4271	0.0391	17.6575	0.0436	0.7695	0.12980473	3836.72076
OGLE-GD-ECL-11388	13:34:49.88	-64:08:31.8	13:34:49.8727	-64:08:31.760	15.669	-	15.8160	0.0031	15.7348	0.0134	15.5836	0.0595	0.1512	0.14780615	3836.82903
OGLE-GD-ECL-00586	10:39:25.72	-62:37:44.7	10:39:25.7159	-62:37:44.600	18.668	-	18.9821	0.0036	19.0557	0.0919	18.7389	0.0909	0.3168	0.18660216	4391.60358
OGLE-GD-ECL-00998	10:40:56.64	-63:01:05.4	10:40:56.6278	-63:01:05.412	17.061	-	17.1764	0.0016	17.1308	0.0096	17.0888	0.0139	0.0420	0.3980283	4391.71856
OGLE-GD-ECL-03782	10:51:10.78	-60:52:15.6	10:51:10.7830	-60:52:15.599	18.154	-	18.4242	0.0044	18.0375	0.0447	17.8376	0.0320	0.1999	0.43537749	3965.11231
OGLE-GD-ECL-08577	11:56:24.56	-62:17:42.2	11:56:24.5578	-62:17:42.209	16.026	-	16.0750	0.0014	15.9713	0.0067	16.0600	0.0053	-0.0886	0.50660638	2735.23316
Discovered by cross-match of the sdB candidate catalogue (Ceiter et al. 2019) with the ATLAS survey															
J080.5805+10.6719	-	-	05:22:19.3241	+10:40:18.929	-	-	14.4737	0.0032	14.5147	0.0089	14.2688	0.0121	0.2459	0.061840	-
J296.1785+54.8285	-	-	19:44:42.8539	+54:49:42.887	-	-	15.7794	0.0039	15.6488	0.0086	15.9266	0.0184	-0.2777	0.064162	-
J084.4719-00.8239	-	-	05:37:53.257	-00:49:26.232	-	-	15.2110	0.0061	15.0980	0.0191	15.2268	0.0206	-0.1289	0.075528	-
J356.2668+50.9652	-	-	23:45:04.0480	+50:57:54.737	-	-	16.4713	0.0029	16.3610	0.0155	16.5339	0.0155	-0.1728	0.081032	-
J109.7402+07.6536	-	-	07:18:57.6669	+07:39:13.221	-	-	15.2378	0.0134	14.9908	0.0381	15.5092	0.0605	-0.5185	0.084461	-
J129.0542-08.0399	-	-	08:36:13.0283	-08:02:23.815	-	-	15.2848	0.0037	15.0924	0.0145	15.4925	0.0209	-0.4001	0.088868	-
J311.6590+51.7931	-	-	20:46:38.1684	+51:47:35.595	-	-	15.2337	0.0090	15.2457	0.0254	15.0974	0.0317	0.1483	0.0896	KPD2045+5136
J311.6590+51.7931	-	-	20:46:38.1684	+51:47:35.596	-	-	15.2337	0.0090	15.2457	0.0254	15.0974	0.0317	0.1483	0.0896	KPD2045+5136
J079.5290-23.1458	-	-	05:18:06.9667	-23:08:45.258	-	-	15.9275	0.0050	15.7357	0.0145	16.1465	0.0174	-0.4108	0.0912	HE0516-2311
J018.4128+22.9608	-	-	01:13:39.0902	+22:57:39.072	-	-	16.6468	0.0084	16.4956	0.0389	16.8708	0.0429	-0.3751	0.093374	PTF1 J011339.09+225739.1
J112.2726-18.6176	-	-	07:29:05.4489	-18:37:03.600	-	-	15.9418	0.0066	15.9616	0.0242	15.7786	0.0213	0.1830	0.093758	-
J160.5032-12.1031	-	-	10:42:00.7895	-12:06:11.358	-	-	16.4582	0.0028	16.2701	0.0096	16.6802	0.0269	-0.4102	0.107507	-
J286.6485+28.1219	-	-	19:06:35.6471	+28:07:19.206	-	-	15.6530	0.0037	15.5384	0.0152	15.7333	0.0406	-0.1949	0.112118	-
J316.0059+34.6100	-	-	21:04:01.4226	+34:36:36.289	-	-	17.4740	0.0155	17.3061	0.0402	17.4794	0.0456	-0.1733	0.118552	-
J306.4062-12.0043	-	-	20:25:37.4999	-12:00:15.437	-	-	16.3625	0.0067	16.1781	0.0165	16.5786	0.0230	-0.4005	0.125100	-
J116.6972-26.0976	-	-	07:46:47.3314	-26:05:51.586	-	-	16.6760	0.0073	16.5850	0.0187	16.6633	0.0198	-0.0783	0.137095	-
J315.0724-14.1901	-	-	21:00:17.4007	-14:11:24.592	-	-	16.6154	0.0120	16.3880	0.0249	16.7483	0.0368	-0.3604	0.145033	EC20575-1423
J274.5791+06.8991	-	-	18:18:18.9987	+06:53:56.835	-	-	17.2759	0.0166	17.1661	0.0589	17.3013	0.0675	-0.1351	0.147069	-
J247.4613+02.3926	-	-	16:29:50.7152	+02:23:33.367	-	-	16.3865	0.0024	16.2136	0.0104	16.5552	0.0124	-0.3416	0.152418	-
J283.0750-21.7974	-	-	18:52:17.999	-21:47:50.649	-	-	13.7667	0.0042	13.6419	0.0177	13.8451	0.0263	-0.2032	0.1611	GALEX J18522-2147
J089.37114-14.1662	-	-	05:57:29.1559	-14:09:58.600	-	-	15.9389	0.0113	16.0456	0.0297	15.6187	0.0417	0.4269	0.170694	-
J283.0316+14.763	-	-	18:52:07.6088	+14:45:47.277	-	-	14.9895	0.0059	15.0230	0.0187	14.8099	0.0220	0.2131	0.190422	-
J280.1767+07.0560	-	-	18:40:42.4151	+07:03:21.760	-	-	16.4190	0.0118	16.4178	0.0131	16.2269	0.0467	0.1909	0.191112	J18404240+0703219
J282.4644-13.6762	-	-	18:49:51.4652	-13:40:34.145	-	-	14.3768	0.0066	14.4924	0.0201	14.1010	0.0246	0.3914	0.197944	-
J096.6239-02.8462	-	-	06:26:29.7438	-02:50:46.495	-	-	16.0394	0.0029	15.9877	0.0106	15.9744	0.0070	0.0133	0.198792	-

Table A.1. continued.

Target	RA (OGLE) [h]	Dec (OGLE) [°]	RA (Gaia) [h]	RA (Gaia) [°]	<i>I</i> [mag]	<i>V</i> [mag]	<i>G</i> [mag]	ΔG [mag]	<i>G_{BP}</i> [mag]	ΔG_{BP} [mag]	<i>G_{RP}</i> [mag]	ΔG_{RP} [mag]	<i>G_{BP} - G_{RP}</i> [mag]	<i>P</i> d	<i>T</i> ₀ HJD-2400000
J308.2100+24.1190	-	-	20:32:50.4112	+24:07:08.615	-	-	14.7108	0.0063	14.6140	0.0160	14.7345	0.0239	-0.1206	0.201103	-
J088.7202+77.7617	-	-	05:54:52.8389	+77:45:42.398	-	-	15.8202	0.0023	15.7324	0.0073	15.8045	0.0097	-0.0722	0.203712	-
J351.7186+12.5060	-	-	23:26:52.4591	+12:30:21.885	-	-	14.3078	0.0042	14.1959	0.0116	14.3779	0.0217	-0.1820	0.211906	-
J294.7689+11.1822	-	-	19:39:04.5423	+11:10:56.324	-	-	14.9084	0.0140	14.7724	0.0423	14.9634	0.0479	-0.1910	0.213099	-
J331.6658+32.7267	-	-	22:06:39.8046	+32:43:36.459	-	-	16.9620	0.0106	16.8287	0.0322	17.0130	0.0443	-0.1843	0.220415	-
J263.9315+09.1436	-	-	17:35:43.5538	+09:08:36.942	-	-	12.6920	0.0023	12.5503	0.0113	12.8003	0.0111	-0.2500	0.225152	-
J340.2132+54.6308	-	-	22:40:51.1862	+54:37:50.978	-	-	14.9722	0.0087	14.9222	0.0235	14.9323	0.0332	-0.0101	0.235883	-
J320.8561-11.8111	-	-	21:23:25.4731	-11:48:40.134	-	-	13.4534	0.0028	13.2825	0.0093	13.6389	0.0119	-0.3564	0.272162	-
J306.2869+42.7907	-	-	20:25:08.8665	+42:47:26.757	-	-	15.1000	0.0102	15.0385	0.0316	15.0759	0.0334	-0.0374	0.292517	-
J306.3118+58.8522	-	-	20:25:14.8400	+58:51:08.093	-	-	17.5747	0.0048	17.5646	0.0157	17.4430	0.0158	0.1216	0.292517	-
J286.5553-00.8563	-	-	19:06:13.2906	-00:51:22.654	-	-	15.7495	0.0074	15.7649	0.0162	15.5581	0.0291	0.2067	0.331619	-
J171.4930-20.1447	-	-	11:25:58.3423	-20:08:40.982	-	-	13.3999	0.0003	13.3643	0.0022	13.4037	0.0014	-0.0393	0.332134	-
J301.0483+14.1972	-	-	20:04:11.6037	+14:11:50.179	-	-	16.8928	0.0034	16.7976	0.0101	17.0286	0.0390	-0.2310	0.345196	-
J309.1155+23.8396	-	-	20:36:27.7384	+23:50:22.619	-	-	16.9985	0.0040	16.9078	0.0124	17.0294	0.0159	-0.1216	0.359727	-
J265.3145+29.5881	-	-	17:41:15.4919	+29:35:17.273	-	-	14.0951	0.0005	13.9843	0.0036	14.2061	0.0014	-0.2218	0.361030	-
J122.1109+32.0418	-	-	08:08:26.6123	+32:02:30.424	-	-	13.7978	0.0023	13.6255	0.0139	13.9907	0.0129	-0.3652	0.366728	-
J176.8103+61.2589	-	-	11:47:14.4977	+61:15:31.790	-	-	13.4276	0.0010	13.2351	0.0085	13.6733	0.0046	-0.4382	0.395170	-
J309.9820-15.496	-	-	20:39:55.6936	-15:29:47.498	-	-	14.5672	0.0020	14.3821	0.0085	14.7605	0.0077	-0.3783	0.395449	-
J220.2201-03.1480	-	-	14:40:52.8285	-03:08:52.659	-	-	13.8180	0.0013	13.6667	0.0070	13.9911	0.0060	-0.3244	0.404019	-
J126.3249+11.5184	-	-	08:25:17.9929	+11:31:06.307	-	-	14.6493	0.0008	14.6707	0.0066	14.4555	0.0035	0.2152	0.467837	PG1438-029
J130.2554+39.938	-	-	08:41:01.3143	+39:56:18.127	-	-	15.4462	0.0006	15.2556	0.0093	15.6683	0.0032	-0.4127	0.497893	PG0837+401
J097.1064-18.7484	-	-	06:28:25.5359	-18:44:54.177	-	-	13.1928	0.0015	13.0578	0.0070	13.3178	0.0048	-0.2600	0.510181	-
J096.5527-21.1251	-	-	06:26:12.6481	-21:07:30.695	-	-	16.2325	0.0019	16.3254	0.0065	16.0634	0.0105	0.2620	0.541143	-
J225.0246-28.6597	-	-	15:00:05.9159	-28:39:34.874	-	-	16.1051	0.0018	15.9689	0.0096	16.1840	0.0068	-0.2151	0.659645	v
J003.4753+44.8905	-	-	00:13:54.0948	+44:53:26.005	-	-	14.2447	0.0030	14.2394	0.0105	14.1398	0.0105	0.0996	0.797432	-
J297.1584+46.3857	-	-	19:48:38.0340	+46:23:08.708	-	-	17.0287	0.0104	17.0851	0.0330	16.7764	0.0318	0.3087	0.990915	-
J305.5398+21.9490	-	-	20:22:09.5639	+21:56:56.655	-	-	12.5219	0.0007	12.6790	0.0020	12.2196	0.0023	0.4594	1.267354	-
Published HW Vir systems															
HW-Vir	-	-	12:44:20.2386	-08:40:16.849	-	-	10.6098	0.0058	10.4585	0.0167	10.8655	0.0285	-0.4070	-	-
V2008-1753	-	-	20:08:16.3432	-17:53:10.637	-	-	16.9955	0.0034	16.8229	0.0252	17.0934	0.0228	-0.2705	-	-
NSVS14256825	-	-	20:20:00.4587	+04:37:56.520	-	-	13.2452	0.0043	13.0598	0.0119	13.4457	0.0131	-0.3859	-	-
2M1938+4603	-	-	19:38:32.6124	+46:03:59.139	-	-	12.1376	0.0037	11.9377	0.0114	12.3415	0.0161	-0.4038	-	-
AA-Dor	-	-	05:31:40.3599	-69:53:02.159	-	-	11.1617	0.0074	10.9411	0.0162	11.4239	0.0137	-0.4828	-	-
HS 2231+2441	-	-	22:34:21.4839	+24:56:57.390	-	-	14.1867	0.0030	14.0124	0.0080	14.4216	0.0161	-0.4092	-	-
NSVS7826147	-	-	15:33:49.4443	+37:59:28.094	-	-	12.9817	0.0050	12.7609	0.0142	13.2110	0.0173	-0.4501	-	-
SDSS J1622	-	-	16:22:56.6650	+47:30:51.125	-	-	16.2446	0.0040	16.0495	0.0142	16.4848	0.0140	-0.4353	-	-
SDSS J0820+0008	-	-	08:20:53.5359	+00:08:43.500	-	-	15.1821	0.0020	14.9984	0.0090	15.3867	0.0075	-0.3882	-	-
SDSS J192059	-	-	19:20:59.7745	+37:22:20.020	-	-	15.7712	0.0031	15.6720	0.0107	15.8399	0.0109	-0.1679	-	-
ASAS J102322	-	-	10:23:21.8948	-37:36:59.904	-	-	11.7078	0.0027	11.5076	0.0092	11.9111	0.0115	-0.4036	-	-
EC10246-2707	-	-	10:26:56.4747	-27:22:57.098	-	-	14.4421	0.0035	14.2744	0.0108	14.6434	0.0135	-0.3689	-	-
HS 0705+6700	-	-	07:10:42.0512	+66:55:43.520	-	-	17.2224	0.0053	17.4472	0.0141	14.7911	0.0152	-0.3439	-	-
Konkoly	-	-	06:40:29.1211	+38:56:51.889	-	-	14.6222	0.0102	17.0411	0.0278	17.3322	0.0696	-0.2911	-	-
VSX J075+7224	-	-	07:53:28.8620	+72:24:24.460	-	-	16.5155	0.0097	16.2780	0.0210	16.5262	0.0308	-0.2482	-	-
NY-Vir	-	-	13:38:48.1466	-02:01:49.209	-	-	13.3943	0.0056	13.2055	0.0190	13.6296	0.0240	-0.4240	-	-
PTF1 J0724+1253	-	-	07:24:55.7504	+12:53:00.301	-	-	18.0152	0.0372	17.6089	0.0218	18.0737	0.0908	-0.4648	-	-
PTF1 J0113+2257	-	-	01:13:39.0902	+22:57:39.072	-	-	16.6468	0.0084	16.4956	0.0389	16.8708	0.0429	-0.3751	-	-

Table A.2. Orbital parameters, OGLE and *Gaia* magnitudes, and coordinates of the white dwarf candidates (objects in bold face were confirmed by deriving the atmospheric parameters).

Target	RA (OGLE) [h]	Dec (OGLE) [°]	RA (<i>Gaia</i>) [h]	RA (<i>Gaia</i>) [°]	<i>I</i> [mag]	<i>V</i> [mag]	<i>G</i> [mag]	ΔG [mag]	G_{BP} [mag]	ΔG_{BP} [mag]	G_{RP} [mag]	ΔG_{RP} [mag]	$G_{BP} - G_{RP}$ [mag]	<i>P</i> [d]	T_0 HJD-2400000
OGLE-BLG-ECL-000091 ⁽¹⁾	17:56:38.74	-31:16:28.8	17:56:38.8029	-31:16:28.883	18.254	—	19.1304	0.0109	18.5850	0.0853	17.1033	0.1069	1.4818	0.06742161	7000.0016
OGLE-BLG-ECL-207454 ⁽²⁾	17:57:20.62	-29:33:50.3	17:57:20.3861	-29:33:51.328	18.525	19.310	19.4611	0.0130	—	—	—	—	—	0.1848801	7000.1690
OGLE-BLG-ECL-192029 ⁽²⁾	17:56:01.82	-27:13:24.6	17:56:01.8191	-27:13:24.458	19.022	19.663	19.5699	0.0059	19.8330	0.0504	18.9572	0.1026	0.8758	0.1358285	7000.0366
OGLE-GD-ECL-09869 ⁽⁵⁾	13:24:02.36	-64:41:21.9	13:24:02.3654	-64:41:21.859	19.473	—	20.1570	0.0080	19.9348	0.0772	19.3598	0.1178	0.5750	0.09596148	3836.77432
OGLE-GD-ECL-07446 ⁽⁵⁾	11:31:05.84	-61:04:36.4	11:31:05.8451	-61:04:36.393	18.797	—	19.5351	0.0091	—	—	—	—	—	0.1165955	2735.17078
OGLE-BLG-ECL-322700 ⁽²⁾	18:07:57.92	-31:10:13.9	18:07:57.9143	-31:10:13.922	17.593	17.826	17.9185	0.0151	—	—	—	—	—	0.1977067	7000.1551
J186.9106-30.7203 ⁽⁴⁾	—	—	12:27:38.5954	-30:43:13.116	—	—	16.7608	0.0048	16.6019	0.0136	16.8524	0.0259	-0.2505	0.1235	ECl2250-3026

Notes. ⁽¹⁾Discovered by Soszyński et al. (2015). ⁽²⁾Discovered by visual inspection. ⁽³⁾Discovered by machine-learning. ⁽⁴⁾Discovered by Pietrukowicz et al. (2013). ⁽⁵⁾Discovered by cross-match of the sdB candidate catalog (Geier et al. 2019) with the ATLAS survey.

Table A.3. Orbital parameters, OGLE and *Gaia* magnitudes, and coordinates of central stars of planetary nebula from Miszalski et al. (2009).

Target	Planetary nebula	RA (OGLE) [h]	Dec (OGLE) [°]	RA (<i>Gaia</i>) [h]	RA (<i>Gaia</i>) [°]	<i>I</i> [mag]	<i>V</i> [mag]	<i>G</i> [mag]	ΔG [mag]	G_{BP} [mag]	ΔG_{BP} [mag]	G_{RP} [mag]	ΔG_{RP} [mag]	$G_{BP} - G_{RP}$ [mag]	<i>P</i> [d]	T_0 HJD-2400000
OGLE-BLG-ECL-000045 ⁽¹⁾	Pe 1-9	17:45:36.77	-23:02:26.1	17:45:36.7590	-23:02:26.307	17.736	19.166	18.7573	0.0071	18.4291	0.1355	17.3009	0.0376	1.1283	0.13985716	7000.0072
OGLE-BLG-ECL-000111 ⁽¹⁾	BMP 1800-3408	18:00:26.16	-34:08:02.3	18:00:26.1596	-34:08:02.348	17.825	18.132	18.3643	0.0228	18.0724	0.0605	17.5176	0.0542	0.5548	0.14477890	7000.1238
OGLE-BLG-ECL-159262 ⁽³⁾	H 2-29	17:53:16.82	-32:40:38.5	17:53:16.8248	-32:40:38.464	18.308	19.313	19.0919	0.0084	—	—	—	—	—	0.2441101	7000.2000
OGLE-BLG-ECL-211852 ⁽³⁾	PHR 1757-2824	17:57:42.29	-28:24:07.8	17:57:42.2886	-28:24:07.924	18.194	19.688	19.4525	0.0359	—	—	—	—	—	0.7992066	7000.7602
J27.8274+26.9367 ⁽⁴⁾	PNA6646(N477)Lyrae	—	—	18.31.18.5911	+26.56.12.110	—	—	14.9397	0.0241	14.7389	0.0589	15.0386	0.0702	-0.2997	0.471739	—

Notes. ⁽¹⁾Discovered by Soszyński et al. (2015). ⁽²⁾Discovered by visual inspection. ⁽³⁾Discovered by machine-learning. ⁽⁴⁾Discovered by Pietrukowicz et al. (2013). ⁽⁵⁾Discovered by cross-match of the sdB candidate catalog (Geier et al. 2019) with the ATLAS survey.

Table A.4. *Gaia* parallaxes, proper motions and calculated reduced proper motions, distances, absolute *G* magnitudes, and reddening of the HW Vir candidates and published HW Vir systems.

Target	Parallax [mas]	Proper motion in RA [mas yr ⁻¹]	Proper motion in Dec [mas yr ⁻¹]	M_G [mag]	Reduced proper motion [kpc]	Distance [kpc]	Distance [kpc]	A_G [mag]	$E(B-V)$	Reddening corrected M_G	
OGLE-BLG-ECL-000036	-1.6483 ± 1.0676	2.780 ± 1.490	0.424 ± 1.406	—	11.78 ± 1.24	—	—	4.814 ^{+3.884} _{-2.395}	2.15	0.7	3.97 ^{+1.49} _{-1.28}
OGLE-BLG-ECL-000176	0.5533 ± 0.8016	-3.889 ± 1.854	-6.848 ± 1.823	8.41 ± 3.14	14.18 ± 0.30	1.807 ± 2.618	1.807 ± 2.618	4.391 ^{+4.276} _{-2.541}	0.87	0.25	5.62 ^{+1.87} _{-1.47}
OGLE-BLG-ECL-000095	-1.0688 ± 0.8665	-3.316 ± 1.539	-5.131 ± 1.273	—	13.34 ± 0.37	—	—	5.388 ^{+4.396} _{-2.699}	0.85	0.30	4.90 ^{+1.50} _{-1.29}
OGLE-BLG-ECL-000124	0.6039 ± 0.1953	0.801 ± 0.269	-4.044 ± 0.226	6.66 ± 0.70	10.83 ± 0.48	1.655 ± 0.535	1.655 ± 0.535	1.829 ^{+1.958} _{-0.643}	0.85	0.297	5.59 ^{+0.94} _{-1.58}
OGLE-BLG-ECL-000114	0.3114 ± 0.1447	-0.715 ± 0.281	-1.675 ± 0.233	4.67 ± 1.00	8.513 ± 0.95	3.211 ± 1.492	3.211 ± 1.492	3.319 ^{+2.982} _{-1.214}	0.75	0.25	3.85 ^{+0.98} _{-1.39}
OGLE-BLG-ECL-000103	0.4470 ± 0.1580	-1.184 ± 0.298	-2.154 ± 0.240	6.08 ± 0.76	9.787 ± 0.69	2.237 ± 0.790	2.237 ± 0.790	2.368 ^{+2.016} _{-0.791}	1.84	0.611	4.12 ^{+0.88} _{-1.33}
OGLE-BLG-ECL-000207	0.5080 ± 0.2117	-1.718 ± 0.388	-3.771 ± 0.319	6.63 ± 0.90	11.19 ± 0.44	1.968 ± 0.820	1.968 ± 0.820	2.206 ^{+2.485} _{-1.139}	1.28	0.421	5.11 ^{+1.94} _{-1.34}
OGLE-BLG-ECL-000110	1.0838 ± 0.4635	1.606 ± 0.629	-1.326 ± 0.509	8.70 ± 0.92	10.12 ± 0.65	0.922 ± 0.394	0.922 ± 0.394	1.449 ^{+4.337} _{-0.727}	1.03	0.354	6.69 ^{+3.00} _{-3.00}
OGLE-BLG-ECL-000109	0.3392 ± 0.4224	-1.126 ± 0.827	-6.275 ± 0.718	6.93 ± 2.70	13.30 ± 0.30	2.948 ± 3.671	2.948 ± 3.671	4.183 ^{+4.121} _{-2.237}	0.72	0.25	5.45 ^{+1.66} _{-1.48}
OGLE-BLG-ECL-000139	1.0819 ± 0.0700	-15.532 ± 0.103	-13.644 ± 0.084	4.11 ± 0.14	10.52 ± 0.06	0.924 ± 0.059	0.924 ± 0.059	0.906 ^{+0.062} _{-0.055}	0.34	0.107	3.82 ^{+0.13} _{-0.14}
OGLE-BLG-ECL-000010	0.9459 ± 0.1032	-2.578 ± 0.200	-5.076 ± 0.164	7.03 ± 0.23	10.93 ± 0.33	1.057 ± 0.115	1.057 ± 0.115	1.044 ^{+0.132} _{-0.106}	0.90	0.333	6.16 ^{+0.23} _{-0.25}
OGLE-BLG-ECL-000147	0.5976 ± 0.3561	-0.328 ± 0.672	-1.526 ± 0.593	7.79 ± 1.29	9.876 ± 0.85	1.673 ± 0.997	1.673 ± 0.997	2.942 ^{+4.328} _{-1.605}	0.87	0.3	5.69 ^{+1.71} _{-1.96}

Table A.4. continued.

Target	Parallax mas	Proper motion in RA mas yr ⁻¹	Proper motion in Dec mas yr ⁻¹	M_G mag	Reduced proper motion	Distance kpc	Distance (Bailei-Jones et al. 2018) kpc	A_G	$E(B - V)$	Reddening corrected M_G
OGLE-BLG-ECL-000163	0.8046 ± 0.0988	-0.312 ± 0.177	-1.142 ± 0.147	6.08 ± 0.26	6.926 ± 1.54	1.242 ± 0.152	1.224 ^{+0.180} _{-0.139}	0.95	0.328	5.17 ^{+0.26} _{-0.29}
OGLE-BLG-ECL-000059	0.4753 ± 0.2497	1.045 ± 0.498	0.212 ± 0.396	7.04 ± 1.14	8.802 ± 1.52	2.103 ± 1.105	2.703 ^{+3.658} _{-1.227}	1.18	0.40	5.32 ^{+1.31} _{-1.85}
OGLE-BLG-ECL-000094	-0.7059 ± 0.4071	-2.386 ± 1.070	-4.770 ± 0.946	-	13.14 ± 0.35	-	6.603 ^{+4.547} _{-2.864}	2.47	0.8	2.94 ^{+1.23} _{-1.13}
Discovered by visual inspection										
OGLE-BLG-ECL-041338	0.1501 ± 0.2868	-3.745 ± 0.509	-4.593 ± 0.417	4.47 ± 4.14	12.45 ± 0.28	6.662 ± 12.72	4.244 ^{+3.483} _{-1.912}	2.14	0.7	3.31 ^{+1.30} _{-1.30}
OGLE-BLG-ECL-364347	-0.3769 ± 0.5970	2.011 ± 0.877	-4.831 ± 0.879	-	12.83 ± 0.34	-	5.333 ^{+4.363} _{-2.646}	1.0	0.3	4.60 ^{+1.48} _{-1.29}
OGLE-BLG-ECL-262309	1.1368 ± 0.8114	-3.027 ± 1.163	-2.512 ± 1.013	9.99 ± 1.54	12.68 ± 0.53	0.879 ± 0.627	3.913 ^{+4.271} _{-2.522}	0.72	0.25	6.03 ^{+2.24} _{-1.60}
OGLE-BLG-ECL-280838	1.2217 ± 0.1316	1.334 ± 0.193	-0.116 ± 0.166	7.13 ± 0.23	7.336 ± 0.31	0.818 ± 0.088	0.814 ^{+0.102} _{-0.082}	0.30	0.102	6.84 ^{+0.23} _{-0.25}
OGLE-BLG-ECL-398184	-0.0275 ± 0.2003	-3.171 ± 0.316	-6.386 ± 0.263	-	12.03 ± 0.26	-	5.244 ^{+3.307} _{-1.998}	1.66	0.6	2.50 ^{+1.04} _{-1.06}
OGLE-BLG-ECL-410872	1.3732 ± 0.7829	-0.857 ± 0.833	-4.852 ± 0.780	9.71 ± 1.23	12.48 ± 0.36	0.728 ± 0.415	2.781 ^{+3.613} _{-1.908}	1.42	0.5	5.38 ^{+2.31} _{-1.80}
OGLE-BLG-ECL-170357	0.4048 ± 0.3246	-1.949 ± 0.486	-6.163 ± 0.395	6.57 ± 1.74	12.59 ± 0.30	2.470 ± 1.980	3.605 ^{+4.004} _{-1.916}	0.83	0.3	4.92 ^{+1.57} _{-1.02}
OGLE-BLG-ECL-234552	0.7229 ± 0.3190	0.615 ± 0.898	-1.478 ± 0.634	7.81 ± 0.95	9.544 ± 0.85	1.383 ± 0.610	1.856 ^{+3.403} _{-0.843}	2.02	0.661	5.15 ^{+2.36} _{-1.31}
OGLE-BLG-ECL-017842	0.8732 ± 0.0914	-4.059 ± 0.166	-6.388 ± 0.124	6.51 ± 0.22	11.20 ± 0.23	1.145 ± 0.119	1.126 ^{+0.133} _{-0.109}	1.48	0.524	5.07 ^{+0.22} _{-0.24}
OGLE-BLG-ECL-331210	-0.0771 ± 0.3893	2.207 ± 0.773	-4.313 ± 0.666	-	12.21 ± 0.37	-	4.605 ^{+3.542} _{-2.105}	1.82	0.6	3.65 ^{+1.32} _{-1.23}
OGLE-BLG-ECL-371937	0.3351 ± 0.2232	-0.923 ± 0.366	-1.208 ± 0.298	5.83 ± 1.44	9.120 ± 0.91	2.984 ± 1.987	3.301 ^{+3.331} _{-1.426}	1.18	0.4	4.43 ^{+1.22} _{-1.50}
OGLE-BLG-ECL-069199	-0.5766 ± 0.5746	1.274 ± 1.212	0.438 ± 0.962	-	10.13 ± 2.49	-	5.123 ^{+3.956} _{-2.416}	1.82	0.6	4.12 ^{+1.38} _{-1.23}
OGLE-BLG-ECL-416194	0.4321 ± 0.0803	-1.637 ± 0.153	0.296 ± 0.133	4.86 ± 0.40	7.787 ± 0.38	2.314 ± 0.430	2.224 ^{+0.538} _{-0.366}	1.39	0.45	3.55 ^{+0.39} _{-0.47}
OGLE-BLG-ECL-361688	0.5848 ± 0.0797	-0.947 ± 0.143	-1.298 ± 0.121	4.94 ± 0.29	7.134 ± 0.99	1.709 ± 0.233	1.665 ^{+0.277} _{-0.208}	0.62	0.202	4.37 ^{+0.29} _{-0.33}
OGLE-BLG-ECL-346003	-1.7211 ± 0.6870	-0.339 ± 1.169	-2.881 ± 1.085	-	11.74 ± 0.47	-	5.447 ^{+3.806} _{-2.410}	1.49	0.5	4.26 ^{+1.26} _{-1.15}
OGLE-BLG-ECL-180780	0.2082 ± 1.3760	-1.766 ± 2.594	-4.819 ± 2.134	6.64 ± 14.3	13.60 ± 0.43	4.803 ± 31.74	4.770 ^{+4.477} _{-2.716}	1.49	0.5	5.16 ^{+1.82} _{-1.43}
OGLE-BLG-ECL-106883	0.2078 ± 0.2194	-0.847 ± 0.417	-3.711 ± 0.314	4.98 ± 2.29	11.29 ± 0.51	4.812 ± 5.080	4.213 ^{+3.630} _{-1.833}	0.99	0.4	4.27 ^{+1.24} _{-1.34}
OGLE-BLG-ECL-375392	0.0384 ± 0.5554	-3.511 ± 0.670	-1.206 ± 0.583	2.15 ± 31.4	12.08 ± 0.38	26.04 ± 376.6	4.875 ^{+4.311} _{-2.543}	0.72	0.25	5.07 ^{+1.60} _{-1.37}
OGLE-BLG-ECL-289520	0.1000 ± 0.2081	-2.299 ± 0.389	-2.709 ± 0.326	3.21 ± 4.51	10.97 ± 0.43	10.0 ± 20.81	5.297 ^{+4.115} _{-2.277}	1.11	0.4	3.48 ^{+1.22} _{-1.24}
OGLE-BLG-ECL-173411	1.1658 ± 0.0781	3.388 ± 0.111	-1.3718 ± 0.096	4.42 ± 0.14	9.839 ± 0.14	0.857 ± 0.057	0.842 ^{+0.061} _{-0.053}	0.54	0.168	3.91 ^{+0.14} _{-0.15}
OGLE-BLG-ECL-319266	1.2061 ± 0.7047	1.222 ± 1.134	-0.980 ± 0.970	9.78 ± 1.26	10.35 ± 1.22	0.829 ± 0.484	3.366 ^{+2.313} _{-1.716}	0.61	0.2	6.13 ^{+1.72} _{-1.72}
OGLE-BLG-ECL-412658	0.0275 ± 0.1197	1.338 ± 0.251	-0.905 ± 0.216	-0.7 ± 9.45	8.095 ± 0.63	36.36 ± 158.2	6.530 ^{+3.767} _{-2.266}	1.28	0.4	1.69 ^{+0.92} _{-0.98}
OGLE-BLG-ECL-097357	-0.8233 ± 0.5011	5.920 ± 0.949	-7.261 ± 0.886	-	13.85 ± 0.21	-	5.274 ^{+3.646} _{-2.292}	2.04	0.8	3.34 ^{+1.23} _{-1.14}
OGLE-BLG-ECL-319071	0.2558 ± 0.3518	-3.392 ± 0.612	-6.053 ± 0.494	5.85 ± 2.98	13.01 ± 0.26	3.909 ± 5.376	4.113 ^{+3.857} _{-2.056}	1.03	0.4	4.71 ^{+1.50} _{-1.43}
OGLE-BLG-ECL-370528	-0.2739 ± 0.5421	-4.313 ± 0.850	-6.275 ± 0.776	-	13.84 ± 0.24	-	5.323 ^{+4.353} _{-2.628}	0.72	0.25	5.08 ^{+1.47} _{-1.29}
OGLE-BLG-ECL-401711	-0.2382 ± 0.5974	-7.937 ± 0.905	-1.998 ± 0.709	-	13.72 ± 0.23	-	4.673 ^{+3.854} _{-2.317}	1.09	0.4	4.71 ^{+1.48} _{-1.30}
OGLE-BLG-ECL-396249	0.7458 ± 0.4545	0.077 ± 0.975	-3.582 ± 0.916	8.53 ± 1.32	11.94 ± 0.45	1.340 ± 0.817	2.931 ^{+4.141} _{-1.734}	0.87	0.3	5.96 ^{+1.94} _{-1.91}
OGLE-BLG-ECL-064805	0.5328 ± 0.5693	-3.814 ± 2.051	-9.661 ± 1.553	8.14 ± 2.32	14.59 ± 0.22	1.876 ± 2.005	3.463 ^{+3.583} _{-1.949}	1.57	0.6	5.24 ^{+1.79} _{-1.54}
OGLE-BLG-ECL-035138	-0.0858 ± 0.6721	-2.495 ± 1.306	-1.601 ± 1.072	-	11.76 ± 0.81	-	4.942 ^{+4.346} _{-2.599}	2.17	0.9	3.76 ^{+1.62} _{-1.36}
OGLE-BLG-ECL-343208	-0.0859 ± 0.2725	-0.606 ± 0.508	-4.016 ± 0.400	-	10.77 ± 0.47	-	5.869 ^{+4.258} _{-2.554}	0.78	0.3	3.11 ^{+1.24} _{-1.18}
OGLE-BLG-ECL-223267	0.9587 ± 0.2169	1.192 ± 0.316	0.382 ± 0.252	7.62 ± 0.49	8.202 ± 1.02	1.043 ± 0.235	1.101 ^{+0.525} _{-0.269}	0.45	0.164	7.05 ^{+0.60} _{-0.84}
OGLE-BLG-ECL-371244	-0.4320 ± 0.3190	-3.153 ± 0.535	-3.016 ± 0.444	-	12.05 ± 0.35	-	6.454 ^{+4.284} _{-2.697}	0.73	0.25	4.07 ^{+1.17} _{-1.10}
OGLE-BLG-ECL-373886	-0.3410 ± 0.2982	-3.048 ± 0.512	-7.951 ± 0.433	-	13.26 ± 0.22	-	6.440 ^{+4.304} _{-2.693}	0.73	0.25	3.83 ^{+1.17} _{-1.11}
OGLE-BLG-ECL-198347	0.4145 ± 0.3912	1.238 ± 0.873	0.308 ± 0.691	5.78 ± 2.04	8.223 ± 1.96	2.412 ± 2.276	3.949 ^{+4.445} _{-2.157}	1.72	0.6	2.99 ^{+1.17} _{-1.58}

Table A.4. continued.

Target	Parallax mas	Proper motion in RA mas yr ⁻¹	Proper motion in Dec mas yr ⁻¹	M_G mag	Reduced proper motion	Distance kpc	Distance (Baiter-Jones et al. 2018) kpc	A_G	$E(B - V)$	Reddening corrected M_G
Discovered by machine-learning										
OGLE-BLG-ECL-318416	0.3164 ± 0.4136	0.832 ± 0.742	3.118 ± 0.662	6.75 ± 2.83	11.79 ± 0.79	3.160 ± 4.131	3.399 ^{+3.185} _{-1.689}	3.13	1	3.46 ^{+1.49} _{-1.43}
OGLE-BLG-ECL-417493	0.3945 ± 0.5938	-4.357 ± 1.652	-4.102 ± 1.773	7.32 ± 3.26	13.22 ± 0.45	2.534 ± 3.815	3.923 ^{+3.831} _{-2.174}	1.19	0.4	5.18 ^{+1.75} _{-1.47}
OGLE-BLG-ECL-027719	0.4597 ± 1.5284	1.216 ± 1.761	0.921 ± 1.138	7.89 ± 7.21	10.49 ± 2.77	2.175 ± 7.232	4.650 ^{+4.416} _{-2.682}	3.07	1.25	3.17 ^{+1.86} _{-1.44}
OGLE-BLG-ECL-246643	-0.1021 ± 0.6879	0.606 ± 0.822	-7.505 ± 0.661	-	13.44 ± 0.26	-	4.994 ^{+4.395} _{-2.633}	1.49	0.5	4.08 ^{+1.62} _{-1.37}
OGLE-BLG-ECL-323178	0.4895 ± 0.5022	-8.580 ± 1.215	-9.785 ± 1.045	7.53 ± 2.22	14.66 ± 0.17	2.042 ± 2.095	3.560 ^{+3.698} _{-1.972}	1.49	0.5	4.84 ^{+1.75} _{-1.54}
OGLE-BLG-ECL-149869	-0.8822 ± 0.5073	6.957 ± 1.183	-4.639 ± 0.936	-	10.51 ± 0.28	-	6.166 ^{+4.422} _{-2.769}	1.0	0.5	0.95 ^{+1.29} _{-1.17}
OGLE-BLG-ECL-084113	0.5347 ± 0.5057	-2.733 ± 1.716	-4.204 ± 1.395	7.76 ± 2.05	12.62 ± 0.47	1.870 ± 1.768	3.693 ^{+3.960} _{-2.106}	1.41	0.6	4.87 ^{+1.83} _{-1.58}
Discovered by Pietrukiewicz et al. (2013)										
OGLE-GD-ECL-I0384	0.3950 ± 0.5550	-5.694 ± 1.088	-1.414 ± 0.883	7.94 ± 3.05	13.79 ± 0.39	2.531 ± 3.557	3.305 ^{+3.174} _{-1.750}	1.50	0.5	5.86 ^{+1.63} _{-1.46}
OGLE-GD-ECL-I1471	0.3424 ± 0.2020	-7.850 ± 0.290	-2.237 ± 0.260	6.40 ± 1.28	13.29 ± 0.09	2.920 ± 1.722	2.886 ^{+2.412} _{-1.105}	1.32	0.44	5.11 ^{+1.05} _{-1.01}
OGLE-GD-ECL-09426	0.0072 ± 0.1926	-5.820 ± 0.224	-0.874 ± 0.250	-2.1 ± 58.0	12.40 ± 0.09	138.8 ± 3715.	5.068 ^{+3.195} _{-1.911}	1.42	0.5	3.60 ^{+1.06} _{-1.02}
OGLE-GD-ECL-I1388	0.5684 ± 0.0410	-1.901 ± 0.052	-3.927 ± 0.055	4.58 ± 0.15	9.014 ± 0.44	1.759 ± 0.126	1.681 ^{+0.127} _{-0.111}	0.97	0.313	3.71 ^{+0.15} _{-0.14}
OGLE-GD-ECL-00586	-0.0684 ± 0.2731	-6.921 ± 0.460	3.694 ± 0.449	-	13.45 ± 0.18	-	5.414 ^{+3.860} _{-2.312}	0.90	0.3	4.41 ^{+1.20} _{-1.16}
OGLE-GD-ECL-00998	0.3419 ± 0.0724	-7.063 ± 0.128	2.373 ± 0.120	4.84 ± 0.45	11.53 ± 0.10	2.924 ± 0.619	2.774 ^{+0.801} _{-0.515}	1.00	0.32	3.96 ^{+0.44} _{-0.35}
OGLE-GD-ECL-03782	0.2652 ± 0.1555	-6.738 ± 0.256	2.802 ± 0.234	5.54 ± 1.27	12.74 ± 0.14	3.770 ± 2.210	3.399 ^{+2.429} _{-1.187}	1.24	0.4	4.52 ^{+0.93} _{-1.17}
OGLE-GD-ECL-08577	0.4869 ± 0.0463	-14.264 ± 0.075	-0.781 ± 0.060	4.51 ± 0.20	11.84 ± 0.01	2.053 ± 0.195	1.949 ^{+0.200} _{-0.167}	1.00	0.31	3.62 ^{+0.19} _{-0.21}
Discovered by cross-match of the sdB candidate catalogue (Geier et al. 2019) with the ATLAS survey										
J080.5805+10.6719	1.3803 ± 0.0363	-0.674 ± 0.065	-6.971 ± 0.053	5.17 ± 0.05	8.700 ± 0.30	0.724 ± 0.019	0.710 ^{+0.018} _{-0.017}			
J296.1785+54.8285	0.5856 ± 0.0473	2.227 ± 0.116	-1.361 ± 0.101	4.61 ± 0.17	7.862 ± 0.41	1.707 ± 0.137	1.628 ^{+0.138} _{-0.118}			
J084.4719-00.8239	0.8389 ± 0.0460	-2.039 ± 0.079	-0.774 ± 0.071	4.82 ± 0.11	6.904 ± 0.32	1.192 ± 0.065	1.152 ^{+0.065} _{-0.059}			
J356.2668+50.9652	0.3896 ± 0.0673	-3.380 ± 0.092	-0.715 ± 0.072	4.42 ± 0.37	9.163 ± 0.12	2.566 ± 0.443	2.327 ^{+0.437} _{-0.324}			
J109.7402+07.6536	0.4464 ± 0.0642	-1.273 ± 0.117	-0.191 ± 0.102	3.48 ± 0.31	5.786 ± 0.22	2.240 ± 0.322	2.077 ^{+0.326} _{-0.251}			
J129.0542-08.0399	0.6364 ± 0.0783	-4.740 ± 0.114	-0.145 ± 0.077	4.30 ± 0.26	8.664 ± 0.05	1.571 ± 0.193	1.488 ^{+0.198} _{-0.158}			
J311.6590+51.7931	0.9476 ± 0.0313	3.139 ± 0.062	-7.766 ± 0.055	5.11 ± 0.07	9.848 ± 0.23	1.055 ± 0.034	1.025 ^{+0.034} _{-0.032}			
J311.6590+51.7931	0.9476 ± 0.0313	3.139 ± 0.062	-7.766 ± 0.055	5.11 ± 0.07	9.848 ± 0.23	1.055 ± 0.034	1.025 ^{+0.034} _{-0.032}			
J079.5290-23.1458	0.5047 ± 0.0547	0.225 ± 0.066	4.642 ± 0.081	4.44 ± 0.23	9.263 ± 0.47	1.981 ± 0.214	1.835 ^{+0.205} _{-0.169}			
J018.4128+22.9608	0.6973 ± 0.0949	1.559 ± 0.186	-2.389 ± 0.156	5.86 ± 0.29	8.923 ± 0.60	1.434 ± 0.195	1.342 ^{+0.197} _{-0.154}			
J112.2726-18.6176	0.4980 ± 0.0422	-3.836 ± 0.052	5.124 ± 0.062	4.42 ± 0.18	9.972 ± 0.27	2.008 ± 0.170	1.902 ^{+0.169} _{-0.144}			
J160.5032-12.1031	0.4170 ± 0.1020	-2.816 ± 0.219	-3.608 ± 0.154	4.55 ± 0.53	9.761 ± 0.36	2.398 ± 0.586	2.002 ^{+0.458} _{-0.329}			
J286.6485+28.1219	0.5398 ± 0.0438	-3.205 ± 0.066	-7.776 ± 0.076	4.31 ± 0.17	10.27 ± 0.23	1.852 ± 0.150	1.766 ^{+0.151} _{-0.129}			
J316.0059+34.6100	0.1817 ± 0.0990	-2.780 ± 0.130	-1.760 ± 0.152	3.77 ± 1.18	10.06 ± 0.33	5.503 ± 2.998	3.870 ^{+1.649} _{-1.005}			
J306.4062-12.0043	0.3279 ± 0.1144	-7.108 ± 0.182	-10.029 ± 0.107	3.94 ± 0.75	11.81 ± 0.14	3.049 ± 1.064	2.718 ^{+1.181} _{-0.679}			
J116.6972-26.0976	0.4778 ± 0.0705	-0.258 ± 0.116	0.393 ± 0.108	5.07 ± 0.32	5.037 ± 4.93	2.092 ± 0.308	1.993 ^{+0.347} _{-0.260}			
J315.0724-14.1901	0.4502 ± 0.0836	-5.938 ± 0.129	-1.084 ± 0.091	4.88 ± 0.40	10.51 ± 0.07	2.221 ± 0.412	2.073 ^{+0.455} _{-0.322}			
J274.5791+06.8991	0.1457 ± 0.1127	0.239 ± 0.162	-3.295 ± 0.175	3.09 ± 1.67	9.870 ± 0.62	6.863 ± 5.308	4.593 ^{+2.587} _{-1.453}			
J247.4613+02.3926	0.2961 ± 0.0853	0.026 ± 0.141	1.415 ± 0.093	3.74 ± 0.62	7.140 ± 1.63	3.377 ± 0.972	3.019 ^{+1.070} _{-0.656}			
J283.0750-21.7974	1.1064 ± 0.0564	6.858 ± 0.085	-7.440 ± 0.071	3.98 ± 0.11	8.792 ± 0.15	0.903 ± 0.046	0.884 ^{+0.047} _{-0.045}			
J089.3714-14.1662	1.0591 ± 0.0772	0.747 ± 0.123	-2.586 ± 0.127	6.06 ± 0.15	8.089 ± 0.73	0.944 ± 0.068	0.921 ^{+0.072} _{-0.062}			

Table A.4. continued.

Target	Parallax mas	Proper motion in RA mas yr ⁻¹	Proper motion in Dec mas yr ⁻¹	M_G mag	Reduced proper motion	Distance kpc	Distance (Bailer-Jones et al. 2018) kpc	A_G $E(B-V)$	Reddening corrected M_G
J283.0316+14.763	0.8698 ± 0.0359	-3.058 ± 0.059	-14.661 ± 0.066	4.68 ± 0.08	10.86 ± 0.14	1.149 ± 0.047	1.114 ^{+0.046} _{-0.043}		
J280.1767+07.0560	0.4815 ± 0.0699	0.479 ± 0.123	3.214 ± 0.145	4.83 ± 0.31	8.978 ± 0.69	2.076 ± 0.301	1.984 ^{+0.342} _{-0.256}		
J282.4644-13.6762	1.5653 ± 0.0428	2.661 ± 0.076	-13.978 ± 0.070	5.34 ± 0.05	10.14 ± 0.14	0.638 ± 0.017	0.627 ^{+0.017} _{-0.016}		
J096.6239-02.8462	0.4611 ± 0.0844	0.759 ± 0.118	-0.748 ± 0.129	4.35 ± 0.39	6.177 ± 1.19	2.168 ± 0.396	2.065 ^{+0.477} _{-0.331}		
J308.2100+24.1190	0.7881 ± 0.0347	-9.323 ± 0.052	-7.410 ± 0.050	4.19 ± 0.09	10.09 ± 0.11	1.268 ± 0.055	1.226 ^{+0.054} _{-0.050}		
J088.7202+77.7617	0.7646 ± 0.0887	1.169 ± 0.133	1.918 ± 0.147	5.23 ± 0.25	7.577 ± 0.89	1.307 ± 0.151	1.253 ^{+0.160} _{-0.128}		
J351.7186+12.5060	1.2448 ± 0.0555	8.830 ± 0.114	-5.366 ± 0.058	4.78 ± 0.09	9.378 ± 0.10	0.803 ± 0.035	0.785 ^{+0.035} _{-0.033}		
J294.7689+11.1822	0.8013 ± 0.0578	-1.848 ± 0.087	-10.039 ± 0.073	4.42 ± 0.15	9.953 ± 0.20	1.247 ± 0.090	1.211 ^{+0.093} _{-0.081}		
J331.6658+32.7267	0.4018 ± 0.1109	-2.392 ± 0.141	-2.276 ± 0.216	4.98 ± 0.59	9.555 ± 0.41	2.488 ± 0.686	2.171 ^{+0.648} _{-0.452}		
J263.9315+09.1436	2.0485 ± 0.0633	-8.817 ± 0.119	-9.889 ± 0.101	4.24 ± 0.06	8.302 ± 0.12	0.488 ± 0.015	0.482 ^{+0.015} _{-0.014}		
J340.2132+54.6308	0.6631 ± 0.0393	-1.350 ± 0.060	1.979 ± 0.060	4.08 ± 0.12	6.869 ± 0.77	1.508 ± 0.089	1.447 ^{+0.089} _{-0.079}		
J320.8561-11.8111	1.5770 ± 0.0531	-0.013 ± 0.099	-20.000 ± 0.088	4.44 ± 0.07	9.958 ± 0.10	0.634 ± 0.021	0.623 ^{+0.021} _{-0.020}		
J306.2869+42.7907	0.9446 ± 0.0371	2.159 ± 0.063	-3.432 ± 0.061	4.97 ± 0.08	8.139 ± 0.44	1.058 ± 0.041	1.028 ^{+0.041} _{-0.038}		
J306.3118+58.8522	0.5054 ± 0.0995	-0.750 ± 0.213	-0.366 ± 0.175	6.09 ± 0.42	7.181 ± 0.77	1.978 ± 0.389	1.888 ^{+0.472} _{-0.320}		
J286.5553-00.8563	0.8175 ± 0.0566	-1.677 ± 0.090	-2.360 ± 0.081	5.31 ± 0.15	8.057 ± 0.59	1.223 ± 0.084	1.187 ^{+0.087} _{-0.076}		
J171.4930-20.1447	0.4499 ± 0.0438	-8.461 ± 0.061	-5.345 ± 0.041	1.66 ± 0.21	8.401 ± 0.11	2.222 ± 0.216	2.051 ^{+0.201} _{-0.169}		
J301.0483+14.1972	0.4311 ± 0.0944	0.515 ± 0.135	-0.660 ± 0.097	5.06 ± 0.27	6.506 ± 1.75	2.319 ± 0.507	2.218 ^{+0.662} _{-0.423}		
J309.1155+23.8396	0.4990 ± 0.0912	-3.480 ± 0.130	-4.315 ± 0.127	5.48 ± 0.39	10.71 ± 0.29	2.004 ± 0.366	1.917 ^{+0.444} _{-0.308}		
J265.3145+29.5881	0.0206 ± 0.0330	-2.156 ± 0.055	-3.773 ± 0.059	-4.3 ± 3.47	7.285 ± 0.42	0.843 ± 0.033	8.288 ^{+1.758} _{-1.360}		
J122.1109+32.0418	1.1859 ± 0.0466	-10.565 ± 0.077	2.206 ± 0.056	4.16 ± 0.08	8.963 ± 0.04	0.822 ± 0.026	0.823 ^{+0.033} _{-0.030}		
J176.8103+61.2589	1.2162 ± 0.0394	-25.921 ± 0.064	-7.395 ± 0.062	3.85 ± 0.07	10.58 ± 0.02	0.822 ± 0.026	0.802 ^{+0.026} _{-0.024}		
J309.9820-15.496	0.8922 ± 0.0790	6.778 ± 0.126	-5.284 ± 0.075	4.31 ± 0.19	9.238 ± 0.15	1.120 ± 0.099	1.093 ^{+0.107} _{-0.093}		
J220.2201-03.1480	1.3336 ± 0.0589	6.857 ± 0.127	-39.698 ± 0.089	4.44 ± 0.09	11.84 ± 0.05	0.749 ± 0.033	0.735 ^{+0.033} _{-0.030}		
J126.3249+11.5184	0.6919 ± 0.0501	-5.017 ± 0.085	-0.797 ± 0.053	3.84 ± 0.15	8.178 ± 0.07	1.445 ± 0.104	1.379 ^{+0.103} _{-0.090}		
J130.2554+39.938	0.6579 ± 0.0632	2.820 ± 0.090	-2.846 ± 0.070	4.53 ± 0.20	8.460 ± 0.37	1.519 ± 0.146	1.433 ^{+0.142} _{-0.119}		
J097.1064-18.7484	1.3179 ± 0.0309	4.406 ± 0.062	-8.549 ± 0.060	3.79 ± 0.05	8.108 ± 0.19	0.758 ± 0.017	0.742 ^{+0.017} _{-0.016}		
J096.5527-21.1251	0.2694 ± 0.0531	0.417 ± 0.075	0.931 ± 0.097	3.38 ± 0.42	6.275 ± 2.14	3.711 ± 0.731	3.154 ^{+0.613} _{-0.454}		
J225.0246-28.6597	0.4906 ± 0.1126	-2.628 ± 0.314	-10.769 ± 0.284	4.55 ± 0.49	11.32 ± 0.18	2.038 ± 0.467	1.973 ^{+0.646} _{-0.399}		
J003.4753+44.8905	1.3319 ± 0.0407	-3.707 ± 0.049	-6.840 ± 0.030	4.86 ± 0.06	8.699 ± 0.24	0.750 ± 0.022	0.735 ^{+0.022} _{-0.021}		
J297.1584+46.3857	0.3320 ± 0.0604	-2.657 ± 0.113	-8.867 ± 0.126	4.63 ± 0.39	11.86 ± 0.22	3.012 ± 0.547	2.775 ^{+0.594} _{-0.422}		
J305.5398+21.9490	4.3828 ± 0.2266	-0.028 ± 0.312	-8.819 ± 0.336	5.73 ± 0.11	7.249 ± 0.23	0.228 ± 0.011	0.227 ^{+0.012} _{-0.011}		
HW-Vir	5.7972 ± 0.0849	8.969 ± 0.175	-15.677 ± 0.107	4.42 ± 0.03	6.893 ± 0.10	0.172 ± 0.002	0.171 ^{+0.002} _{-0.002}		
V2008-1753	0.3866 ± 0.1238	-4.219 ± 0.213	8.610 ± 0.121	4.93 ± 0.69	11.90 ± 0.20	2.586 ± 0.828	2.442 ^{+1.145} _{-0.626}		
NSVS14256825	1.1929 ± 0.0599	8.063 ± 0.090	1.133 ± 0.062	3.62 ± 0.10	7.798 ± 0.04	0.838 ± 0.042	0.820 ^{+0.043} _{-0.039}		
2M1938+4603	2.4952 ± 0.0404	5.196 ± 0.077	-4.638 ± 0.077	4.12 ± 0.03	6.352 ± 0.20	0.400 ± 0.006	0.396 ^{+0.006} _{-0.006}		
AA-Dor	2.7188 ± 0.0588	-12.109 ± 0.096	51.071 ± 0.122	3.33 ± 0.04	9.761 ± 0.04	0.367 ± 0.007	0.364 ^{+0.008} _{-0.007}		
HS 2231+2441	0.9331 ± 0.0733	12.467 ± 0.209	-19.217 ± 0.154	4.03 ± 0.17	10.98 ± 0.07	1.071 ± 0.084	1.039 ^{+0.057} _{-0.074}		

Published HW Vir systems

Table A.4. continued.

Target	Parallax mas	Proper motion in RA mas yr ⁻¹	Proper motion in Dec mas yr ⁻¹	M_G mag	Reduced proper motion kpc	Distance kpc	Distance (Bailler-Jones et al. 2018) kpc	A_G	$E(B - V)$ corrected M_G
NSV S7826147	1.9007 ± 0.0476	0.012 ± 0.074	-17.025 ± 0.096	4.37 ± 0.05	9.137 ± 0.12	0.526 ± 0.013	0.518 ^{+0.013} _{-0.012}		
SDSS J1622	0.4672 ± 0.0562	-3.406 ± 0.106	-2.223 ± 0.128	4.59 ± 0.26	9.291 ± 0.27	2.140 ± 0.257	1.974 ^{+0.246} _{-0.199}		
SDSS J0820+0008	0.6609 ± 0.0632	0.567 ± 0.098	-2.100 ± 0.063	4.28 ± 0.20	6.869 ± 0.93	1.513 ± 0.144	1.440 ^{+0.147} _{-0.123}		
SDSS J192059	0.3987 ± 0.0488	-2.150 ± 0.079	-2.809 ± 0.082	3.77 ± 0.26	8.514 ± 0.47	2.508 ± 0.306	2.342 ^{+0.310} _{-0.247}		
ASAS J102322	3.7390 ± 0.0599	-33.259 ± 0.059	-20.126 ± 0.088	4.57 ± 0.03	9.656 ± 0.02	0.267 ± 0.004	0.265 ^{+0.004} _{-0.004}		
EC10246-2707	0.8953 ± 0.0632	-4.571 ± 0.108	-5.413 ± 0.104	4.20 ± 0.15	8.693 ± 0.23	1.116 ± 0.078	1.081 ^{+0.080} _{-0.070}		
HS 0705+6700	0.8056 ± 0.0498	-0.409 ± 0.061	-7.637 ± 0.070	4.15 ± 0.13	9.039 ± 0.28	1.241 ± 0.076	1.195 ^{+0.077} _{-0.068}		
Konkoly	0.3538 ± 0.1004	0.277 ± 0.166	-3.026 ± 0.153	4.96 ± 0.61	9.635 ± 0.67	2.826 ± 0.802	2.368 ^{+0.662} _{-0.448}		
VSX J075+7224	0.4939 ± 0.0881	3.463 ± 0.125	1.338 ± 0.147	4.98 ± 0.38	9.363 ± 0.24	2.024 ± 0.361	1.814 ^{+0.558} _{-0.252}		
NY-Vir	1.8116 ± 0.0632	-6.112 ± 0.127	-11.914 ± 0.093	4.68 ± 0.07	9.028 ± 0.14	0.551 ± 0.019	0.544 ^{+0.018} _{-0.018}		
PTFI J0724+1253	0.2496 ± 0.1612	-1.187 ± 0.371	-2.091 ± 0.371	5.00 ± 1.40	9.920 ± 0.66	4.006 ± 2.587	2.502 ^{+0.997} _{-0.635}		
PTFI J0113+2257	0.6973 ± 0.0949	1.559 ± 0.186	-2.389 ± 0.156	5.86 ± 0.29	8.923 ± 0.60	1.434 ± 0.195	1.342 ^{+0.197} _{-0.154}		

Table A.5. *Gaia* parallaxes, proper motions and calculated reduced proper motions, distances, absolute G magnitudes and reddening of the white dwarf candidates.

Target	Parallax mas	Proper motion in RA mas yr ⁻¹	Proper motion in Dec mas yr ⁻¹	M_G mag	Reduced proper motion kpc	Distance kpc	Distance (Bailler-Jones et al. 2018) kpc	A_G	$E(B - V)$ Reddening corrected M_G
OGLE-BLG-ECL-000091 ⁽¹⁾	2.4371 ± 0.4993	-8.415 ± 0.815	-11.326 ± 0.709	11.0 ± 0.44	14.87 ± 0.13	0.410 ± 0.084	0.441 ^{+0.191} _{-0.101}	0.30	0.128
OGLE-BLG-ECL-207454 ⁽²⁾	6.3403 ± 1.4567	-7.147 ± 1.491	-7.039 ± 1.391	13.4 ± 0.49	14.46 ± 0.26	0.157 ± 0.036	0.177 ^{+5.471} _{-0.171}	0.18	0.065
OGLE-BLG-ECL-192029 ⁽²⁾	2.0833 ± 0.4635	-2.160 ± 1.046	-14.402 ± 0.883	11.1 ± 0.48	15.38 ± 0.14	0.480 ± 0.106	0.522 ^{+0.304} _{-0.139}	0.415	0.157
OGLE-GD-ECL-09869 ⁽⁵⁾	0.6784 ± 0.5749	-10.260 ± 1.476	-2.394 ± 1.111	9.31 ± 1.84	15.27 ± 0.29	1.474 ± 1.249	2.753 ^{+3.088} _{-1.548}	1.32	0.45
OGLE-GD-ECL-07446 ⁽⁵⁾	0.5187 ± 0.3764	-8.549 ± 0.886	1.546 ± 0.637	8.10 ± 1.57	14.22 ± 0.22	1.927 ± 1.398	2.384 ^{+2.505} _{-1.110}	0.80	0.275
OGLE-BLG-ECL-322700 ⁽²⁾	1.5609 ± 0.2189	1.270 ± 0.468	-3.828 ± 0.413	8.88 ± 0.30	10.94 ± 0.46	0.640 ± 0.089	0.651 ^{+0.121} _{-0.088}	0.34	0.12
J186-9106-307203 ⁽⁴⁾	2.2032 ± 0.1113	-39.388 ± 0.216	-15.242 ± 0.124	8.47 ± 0.10	14.88 ± 0.02	0.453 ± 0.022	0.449 ^{+0.024} _{-0.021}		

Notes. ⁽¹⁾Discovered by Soszyński et al. (2015). ⁽²⁾Discovered by visual inspection. ⁽³⁾Discovered by machine-learning. ⁽⁴⁾Discovered by Pietrukowicz et al. (2013). ⁽⁵⁾Discovered by cross-match of the sdB candidate catalogue (Geier et al. 2019) with the ATLAS survey.

Table A.6. *Gaia* parallaxes, proper motions and calculated reduced proper motions, distances, absolute G magnitudes and reddening of central stars of planetary nebula from Miszalski et al. (2009).

Target	Parallax mas	Proper motion in RA mas yr ⁻¹	Proper motion in Dec mas yr ⁻¹	M_G mag	Reduced proper motion kpc	Distance kpc	Distance (Bailler-Jones et al. 2018) kpc	A_G	$E(B - V)$ Reddening corrected M_G
OGLE-BLG-ECL-000111 ⁽¹⁾	-0.6078 ± 0.3030	-1.016 ± 0.451	-4.317 ± 0.403	-	11.59 ± 0.43	-	7.238 ^{+4.519} _{-2.906}	1.48	0.5
OGLE-BLG-ECL-159262 ⁽³⁾	0.8984 ± 0.5485	-6.094 ± 0.961	-8.566 ± 0.739	8.85 ± 1.32	14.20 ± 0.19	1.113 ± 0.679	3.196 ^{+4.243} _{-2.045}	1.49	0.5
J277.8274+26.9367 ⁽⁴⁾	0.3286 ± 0.0440	-1.936 ± 0.052	0.692 ± 0.070	2.52 ± 0.29	6.5 ± 0.39	3.099 ± 0.415	2.768 ^{+0.394} _{-0.310}		

Notes. ⁽¹⁾Discovered by Soszyński et al. (2015). ⁽²⁾Discovered by visual inspection. ⁽³⁾Discovered by machine-learning. ⁽⁴⁾Discovered by Pietrukowicz et al. (2013). ⁽⁵⁾Discovered by cross-match of the sdB candidate catalogue (Geier et al. 2019) with the ATLAS survey.

Alone but not lonely: Observational evidence that binary interaction is always required to form hot subdwarf stars

Ingrid Pelisoli¹, Joris Vos¹, Stephan Geier¹, Veronika Schaffenroth¹, and Andrzej S. Baran²

¹ Institut für Physik und Astronomie, Universität Potsdam, Haus 28, Karl-Liebknecht-Str. 24/25, 14476 Potsdam-Golm, Germany
e-mail: pelisoli@astro.physik.uni-potsdam.de

² ARDASTELLA Research Group, Institute of Physics, Pedagogical University of Krakow, ul. Podchorążych 2, 30-084 Kraków, Poland

Received 22 May 2020 / Accepted 9 August 2020

ABSTRACT

Context. Hot subdwarfs are core-helium burning stars that show lower masses and higher temperatures than canonical horizontal branch stars. They are believed to be formed when a red giant suffers an extreme mass-loss episode. Binary interaction is suggested to be the main formation channel, but the high fraction of apparently single hot subdwarfs (up to 30%) has prompted single star formation scenarios to be proposed.

Aims. We investigate the possibility that hot subdwarfs could form without interaction by studying wide binary systems. If single formation scenarios were possible, there should be hot subdwarfs in wide binaries that have undergone no interaction.

Methods. Angular momentum accretion during interaction is predicted to cause the hot subdwarf companion to spin up to the critical velocity. The effect of this should still be observable given the timescales of the hot subdwarf phase. To study the rotation rates of companions, we have analysed light curves from the Transiting Exoplanet Survey Satellite for all known hot subdwarfs showing composite spectral energy distributions indicating the presence of a main sequence wide binary companion. If formation without interaction were possible, that would also imply the existence of hot subdwarfs in very wide binaries that are not predicted to interact. To identify such systems, we have searched for common proper motion companions with projected orbital distances of up to 0.1 pc to all known spectroscopically confirmed hot subdwarfs using *Gaia* DR2 astrometry.

Results. We find that the companions in composite hot subdwarfs show short rotation periods when compared to field main sequence stars. They display a triangular-shaped distribution with a peak around 2.5 days, similar to what is observed for young open clusters. We also report a shortage of hot subdwarfs with candidate common proper motion companions. We identify only 16 candidates after probing 2938 hot subdwarfs with good astrometry. Out of those, at least six seem to be hierarchical triple systems, in which the hot subdwarf is part of an inner binary.

Conclusions. The observed distribution of rotation rates for the companions in known wide hot subdwarf binaries provides evidence of previous interaction causing spin-up. Additionally, there is a shortage of hot subdwarfs in common proper motion pairs, considering the frequency of such systems among progenitors. These results suggest that binary interaction is always required for the formation of hot subdwarfs.

Key words. subdwarfs – binaries: general – stars: variables: general

1. Introduction

Hot subdwarf stars are underluminous objects that lie in the extreme horizontal branch (EHB, Heber 1986). They have thinner hydrogen envelopes ($M_{\text{env}} < 0.02 M_{\odot}$) than canonical horizontal branch stars, being thus unable to sustain hydrogen shell burning. Because of their thin envelopes, they also appear hotter than their canonical counterparts. They show temperatures $T_{\text{eff}} > 20\,000$ K and surface gravities in the range $4.5 < \log g < 6.5$ (for a complete review of hot subdwarfs, see Heber 2016).

The characterisation of hot subdwarfs is of interest for many fields of astronomy, from extragalactic to stellar astrophysics. In extragalactic astrophysics, they are known to account for a large fraction of the ultraviolet excess observed in early-type galaxies (O’Connell 1999). They contribute to Galactic astrophysics by allowing us to probe the gravitational potential of the Milky Way, and in particular the mass of the dark matter halo (Tillich et al. 2011), because they can be among the fastest stars in the Galaxy (e.g. the hypervelocity star US708 in Geier et al. 2015). They can also show pulsations, being remarkable targets

for asteroseismology and allowing us to place constraints in stellar evolution theory (Charpinet et al. 2009). Hot subdwarfs in close binaries can qualify as type Ia supernova progenitors (e.g. Maxted et al. 2000) and/or verification sources for future space-based gravitational wave detectors such as the Laser Interferometer Space Antenna (LISA, see Kupfer et al. 2018).

Despite their ubiquitous importance in astronomy, their formation remains puzzling. The consensus is that hot subdwarfs are the progeny of low- to intermediate-mass stars that have undergone an episode of enhanced mass-loss at the tip of the red-giant branch (RGB). Binary interaction is the main evoked explanation for such an episode.

Three main binary evolution scenarios have been described in detail by Han et al. (2002, 2003): (i) common envelope evolution, (ii) stable Roche-lobe overflow (RLOF), and (iii) the merger of two He white dwarfs. In scenario (i), the more massive star in the binary would evolve to the RGB and fill its Roche lobe, inefficiently transferring mass to the companion and leading to the formation of a common envelope; this envelope is eventually ejected, leaving an exposed He-burning core in a

close binary (orbital period of up to a few days). If the mass transfer is instead stable (scenario ii), the outer layers of the hot subdwarf progenitor are slowly stripped away by its companion. This channel leads to the formation of hot subdwarfs with main sequence companions in wide binaries (orbital periods of tens to hundreds of days).

Supporting these two channels, a large fraction of hot subdwarfs are found in binaries. About one-third are found in close binaries with periods from hours to a few days, consistent with scenario (i), mostly showing white dwarf or M-type main sequence stars as companions (Maxted et al. 2001; Morales-Rueda et al. 2003; Geier et al. 2011a; Copperwheat et al. 2011), whereas 30–40% show composite-colours and/or spectra indicating the presence of K to F type companions in wide orbits (Stark & Wade 2003). The latter are often referred to as composite hot subdwarfs (Vos et al. 2018a).

It should be noted that the large observed fraction of composite binaries is not necessarily an indication of a previous mass-transfer phase forming the hot subdwarf. Given evolutionary timescales and the age of the Universe, hot subdwarf progenitors descend from main sequence stars of type F or earlier, which have binary fractions $\geq 50\%$ (e.g. Duchêne & Kraus 2013). Therefore, a similar fraction of hot subdwarfs in composite binaries could be expected, even if interaction was not required to form them.

A first attempt to verify whether the visible companions in composite hot subdwarf systems were sufficiently close to support previous interaction was made by Heber et al. (2002), who tried to resolve 19 composite systems with the *Hubble* Space Telescope. Considering the observed separation distribution of progenitors in binary systems, about one third of the observed sample should have been resolved. However, only two systems were resolved, one of which turned out to be a hierarchical triple system with the sdB being part of a close, single-lined binary.

Although this result already indicated a significant deviation of the separation distribution of composite hot subdwarfs from their progenitor systems, the stable RLOF-channel could only be finally proven when the first orbital solutions of composite sdB systems were determined (Deca et al. 2012; Barlow et al. 2012, 2013; Vos et al. 2012, 2013). The derived long periods also required an update of the binary evolution models to be consistent with observations (Chen et al. 2013). A dedicated survey of a small sample of composite systems bright enough to be observed with high-resolution spectrographs showed that a high fraction of systems shows radial velocity variability and, importantly, high values of $v \sin i (> 10 \text{ km s}^{-1})$ for the companions, suggesting a high rate of previous interactions (Vos et al. 2018a).

On the other hand, for a large fraction of hot subdwarfs, of up to 30%, no companions have been found. This fraction is even much higher for the hot subdwarfs found in globular clusters (see Latour et al. 2018, and references therein). In the binary framework, these single objects are mainly explained as the result of the remaining scenario: a merger of two He white dwarfs. In fact a few single hot subdwarfs are found to be fast rotators, supporting this theory (e.g. EC 22081-1916 and SB290 in Geier et al. 2011b, 2013, respectively). However, most of the single hot subdwarfs have been found to be very slow rotators both from analyses of the rotational line broadening (Geier & Heber 2012) and from asteroseismic analyses of space-based light curves (Baran et al. 2009, 2012; Pablo et al. 2012; Reed et al. 2014). In addition, the agreement between model predictions and observations is still poor (Zhang et al. 2009), and the predicted broad mass distribution of systems resulting from mergers seems to be at odds with the observed narrow dis-

tribution (Schneider et al. 2019). Moreover, the companions of helium white dwarfs are found to be mostly canonical to massive white dwarfs (Brown et al. 2020), suggesting a shortage of progenitors for the merger scenario.

Alternative formation scenarios relying on single star evolution have been proposed. D’Cruz et al. (1996) proposed that strong stellar wind mass loss in the RGB phase could place some objects in the EHB. Sweigart (1997) suggested that helium mixing from the hydrogen shell into the envelope, driven by internal rotation, could cause enhanced mass-loss in the RGB. However, if these single evolution scenarios were indeed possible, there must also be hot subdwarfs in wide binaries that have undergone no interaction. In these systems, neither of the components should show any measurable traces of previous interactions, such as increased rotation rates due to transfer of angular momentum observed in the confirmed RLOF systems (Vos et al. 2018a) or pollution due to accreted matter. In particular, given the properties of the progenitor systems (e.g. De Rosa et al. 2014; Moe & Di Stefano 2017; El-Badry & Rix 2019), there must be a significant fraction of very wide, resolved visual binaries observable as common proper motion pairs.

In this work, we investigate the possibility that hot subdwarfs could form without binary interaction by (i) characterising rotation rates for the companions in known composite binaries believed to have formed via the RLOF channel and (ii) searching for common proper motion companions to all spectroscopically confirmed hot subdwarfs. In Sect. 2, we analyse light curves from the Transiting Exoplanet Survey Satellite (TESS) for known hot subdwarfs in composite binaries in search for evidence of mass transfer. Mass transfer causes angular momentum to be gained by the companion stars, which are thus predicted to spin up (e.g. Kippenhahn & Meyer-Hofmeister 1977; Popham & Narayan 1991). In Sect. 3, we perform a search for common proper motion companions to hot subdwarfs with projected orbital distances up to 20 000 AU (≈ 0.1 pc), where no interaction is expected. We present a discussion of our results in Sect. 4, and conclude in Sect. 5.

2. TESS light curves for composite hot subdwarfs

The TESS mission (Ricker et al. 2015) was launched in 2018 to obtain high-precision photometry from space with the goal of finding nearby rocky exoplanets. The nominal two-year mission observed 26 sky sectors, each with a field of $24^\circ \times 90^\circ$, for 27 days. The sectors cover over 90% of the sky, avoiding only a narrow band around the ecliptic already partially explored by the K2 mission (Howell et al. 2014). There is overlap between different sectors, therefore the total coverage can be much larger than 27 days (up to 351 days for stars around both ecliptic poles). TESS obtained images of each sector every 2 s, which were used for guiding. These 2 s images were stacked into 20 s, 2 min, or 30 min cadence images that could be downloaded to the ground. The 20 s cadence postage-stamps were only downloaded for a small number of very bright asteroseismology targets, whereas 2 min postage-stamps were obtained for a large number of objects proposed by the community. Finally, every pixel observed by TESS in the nominal two-year mission was downloaded at 30 min cadence.

Although TESS has been designed as an exoplanet mission, the cadence and high precision are also of particular interest for studying binary stars and intrinsic stellar variability. For evolved compact stars such as hot subdwarfs and also white dwarfs, the TESS Asteroseismic Science Consortium (TASC) Working Group 8 (WG8) has proposed an extensive variability survey

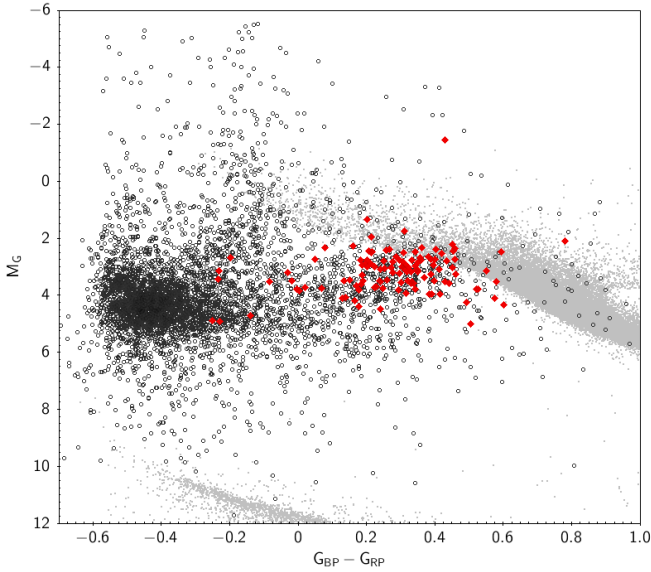


Fig. 1. Colour-magnitude diagram showing all stars from the catalogue of Geier (2020) as dark grey circles. The composite systems analysed in this work are shown as red diamonds. At this point, no quality cuts have been performed in the astrometry, which explains the high spread. Sample C of Lindegren et al. (2018) is shown in light grey to facilitate the location of the main sequence and other evolutionary stages.

including all known evolved compact stars brighter than 16th magnitude. Up to Sector 20, 1125 hot subdwarf and candidates from the catalogues of Geier et al. (2017) and Geier et al. (2019) were observed in 2 min cadence.

The catalogue of spectroscopically confirmed hot subdwarfs from Geier et al. (2017) has recently been updated taking into account input from the *Gaia* data release 2 (DR2, Gaia Collaboration 2018), as well as the latest releases of the Large Sky Area Multi-Object Fibre Spectroscopic Telescope (LAMOST, Zhao et al. 2012). We have crossmatched the updated catalogue (Geier 2020) with the list of observed stars from the TASC WG8. We identified 156 stars classified as composite hot subdwarfs with main sequence companions (sdO/B + MS, + A, + F, + G, + K) observed up to Sector 20. We note that, although cooler companions are predicted, these systems would not be detected as composite because the hot subdwarf completely dominates the light, and therefore M companions are not included in our analysis. Similarly, in systems with earlier-type companions, the hot subdwarf would not be detected in optical observations, therefore such systems are also not included in our sample. We note, however, that mass transfer from hot subdwarfs has been invoked to explain the fast rotation of Be stars (Wang et al. 2018), therefore there is already evidence for mass transfer in binary systems of hot subdwarfs with early-type companions.

To remove objects that might not be real binaries, but rather have been misclassified due to contamination by a nearby star, we excluded objects with another source in *Gaia* DR2 within 5 arcsec, unless they were confirmed radial velocity variables. We also excluded objects classified as close binaries in the literature, since those are formed by the common envelope and not the RLOF channel, as well as objects whose fit to the spectral energy distribution (SED) indicated they were actually single stars. We were then left with 123 composite hot subdwarfs observed with TESS (Fig. 1).

We have searched for variability in the light curves of all 123 composite objects using a Lomb-Scargle periodogram

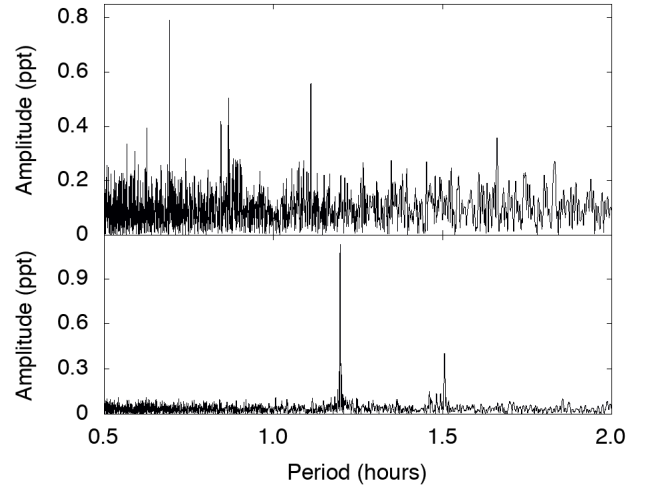


Fig. 2. TIC 71013467 (top) and TIC 158235404 (bottom), two new pulsators that are part of our sample. They show periods in the range of 45 min to 2 h, typical of *g*-mode hot subdwarf pulsators (Green et al. 2003).

(Lomb 1976; Scargle 1982). We have used the light curves made available by the TESS Science Processing Operations Center (SPOC), and specifically the PDCSAP flux, which corrects the simple aperture photometry (SAP) to remove instrumental trends, as well as contributions to the aperture expected to come from neighbouring stars other than the target of interest given a pre-search data conditioning (PDC). This is particularly relevant for TESS because the pixel size is nearly $21''$. The pipeline also provides an estimate of how much of the flux in the aperture belongs to the target systems in the CROWDSAP parameter. To avoid possible zero-point inconsistencies between different sectors, the reported fluxes were divided by the mean flux in each sector for each star. We have also performed sigma-clipping to exclude any measurements more than 5-sigma away from the median value.

Our initial analysis consisted of calculating the periodogram up to the Nyquist frequency, with sampling to give ten points per significant periodogram peak, phase-folding the data to the dominant peak, and inspecting the periodogram and phase-folded light curve to confirm any variability. We have found 90 out of the 123 stars (73%) to show periodic variability. The false-alarm probability (FAP) of the dominant period for objects classified as variable was in most cases $\text{FAP} \leq 10^{-20}$. For two objects, the periodogram is typical of *g*-mode hot subdwarf pulsators (Green et al. 2003), as shown in Fig. 2. Both of these are new discoveries; they are discussed in Appendix A, and the identified periods are listed in Table A.1.

For the remaining objects, the variability cannot be attributed to pulsations of the hot subdwarf star. It instead likely originates in the main sequence companion. One possible scenario is an interplay between stellar activity and rotation, as seen for many *Kepler* (e.g. Reinhold & Gizon 2015) and *K2* objects (e.g. Reinhold & Hekker 2020). The activity causes temperature and therefore brightness changes across the surface of the star, which are seen as periodic variability as the star rotates. To test whether that was the cause of the variability, we have analysed the light curves for these 90 variable objects following the approach of Reinhold & Reiners (2013), as summarised below.

Firstly, a Lomb-Scargle periodogram was calculated up to the Nyquist frequency. We have set the minimal frequency to $2/T$, where T is the time span of the light curve (e.g. $T = 27$ days

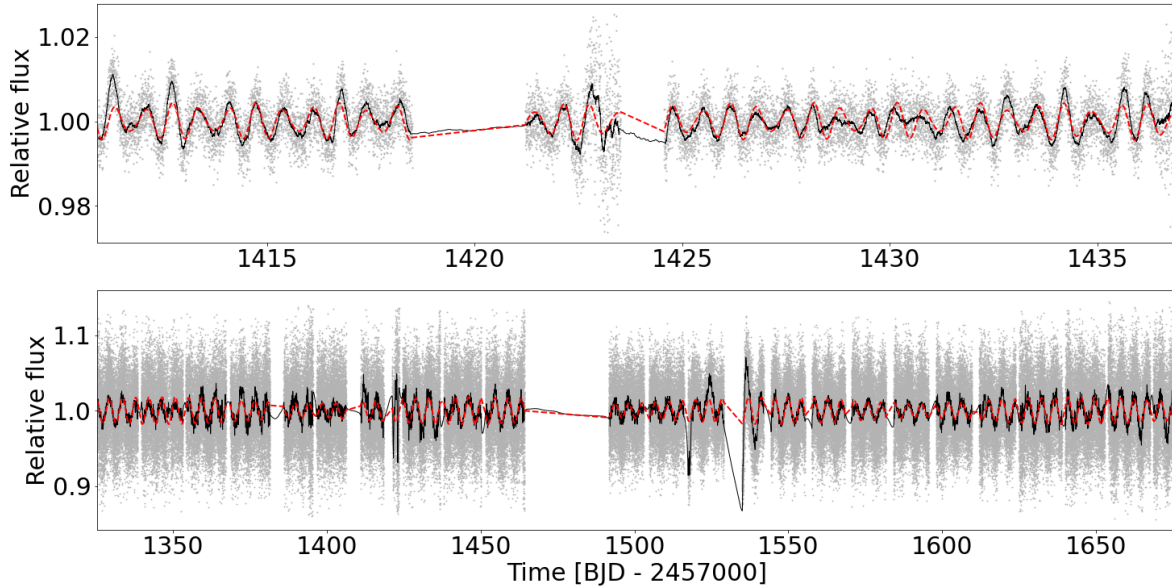


Fig. 3. TIC 12528447 (*top*) and TIC 382518318 (*bottom*), two systems for which the variability has been attributed to rotation of the main sequence companion. The former was observed in only one sector, while the latter is in the TESS continuous viewing zone and has 2 min cadence data for 12 sectors. The grey dots are the TESS data, the black line is a running mean every 50 points, and the dashed red line is the multi-component fit.

for objects observed in only one sector). This assumes that a minimum of two cycles are necessary to detect the variability. As above, we used an oversampling factor of ten to determine the frequency step, that is $\delta f = 1/(10T)$. Once the dominant peak was identified, we have performed pre-whitening to identify a second possible peak. Computing a Lomb-Scargle periodogram is equivalent to fitting a sine wave to the data, hence the pre-whitening consists on simply subtracting the fitted sine wave from the data, and computing the periodogram of the residuals. As we are only interested in the dominant period and not in all observed periods, this process was performed only once.

The main goal of the pre-whitening was to verify that the dominant period was not an alias. In some cases spots can be located on opposite sides of the star, in which case the dominant peak will actually correspond to half the rotation period. Following the prescription of Reinhold & Reiners (2013), we have compared the two periods with largest power in the periodogram and, if the difference between twice the first period and the second period was less than 5%, we selected the longer one, which is more likely the correct period.

For many stars, differential rotation is present, in which case a second dominant peak which is not an alias is detected. To identify this, we checked whether the period P_2 was within 30% of P_1 (which suggests it is consistent with differential rotation, Reinhold & Reiners 2013). Defining $\alpha = |P_2 - P_1|/\max(P_1, P_2)$, we verified if P_2 was such that $\delta f < \alpha < 0.3$, where the lower limit accounts for the frequency resolution of each light curve of $1/(10T)$. If α was within these limits, P_2 was accepted as a second significant period arising from differential rotation, otherwise it was discarded. This step was performed to improve accuracy on P_1 , since the second sine wave with period P_2 can have a significant effect on the light curve. Last, sine parameters for both P_1 and P_2 , when significant, were used as input for a global sine fit, summing both sine waves and allowing for both periods to vary. We show two examples in Fig. 3.

Finally, as our goal is to study a clear sample of rotators, we attempted to remove from the sample objects whose cause of variability is possibly not rotation or whose periods are not well

determined. Systems were flagged by visual inspection when the light curve was not obviously periodic, or when the periods seemed to be only marginally significant. We also compared the number of zero crossings with the prediction for a sine wave. A single sine wave has two zero crossings per period, therefore the observed period is indeed due to rotation we should expect a number of crossings of the order of $N = T \times 2/P_1$. A number of crossings higher than that hints at a different cause for variability, such as stellar pulsations or irregular variations. We estimated the number of zero crossings by smoothing the data using a boxcar average with a width of $5 \times P_1$, followed by an average every ten points to reduce fluctuations due to uncertainty in flux. The number of crossings was not used as a hard-limit, given that more crossings can be shown if, for example, there are spots on opposite sides of the star, or if the rotation pattern exhibits double dips (as seen predominantly for slow rotators, Basri & Nguyen 2018).

We instead further inspected objects showing more than two crossings per period. Many of those had already been flagged as uncertain during our initial inspection. An example is shown in Fig. 4. Other objects not previously flagged showed higher number of crossings mainly because of fluctuations due to the uncertainty in flux. We further flagged as uncertain three objects showing a number of crossings lower than predicted that clustered closely to the two identified pulsators (see Fig. 5). We were then left with 61 composite systems whose variability we interpret as due to rotation, listed in Table 1. The remaining 29 variable objects are listed in Table 2. An interpretation on the origin of their variability is out of the scope of this work. It is quite possible that they are also rotators, but we do not treat them as such so that our sample consists only of stars whose variability can be safely interpreted as due to rotation. Objects not observed to show periodic variability (NOV) are listed in Table 3 with the respective detection limits.

Figure 6 shows, in black, the histogram of the obtained periods for the 61 presumably rotational variables. The mean period is 2.5 days, with a one-sigma spread of 1.4 days.

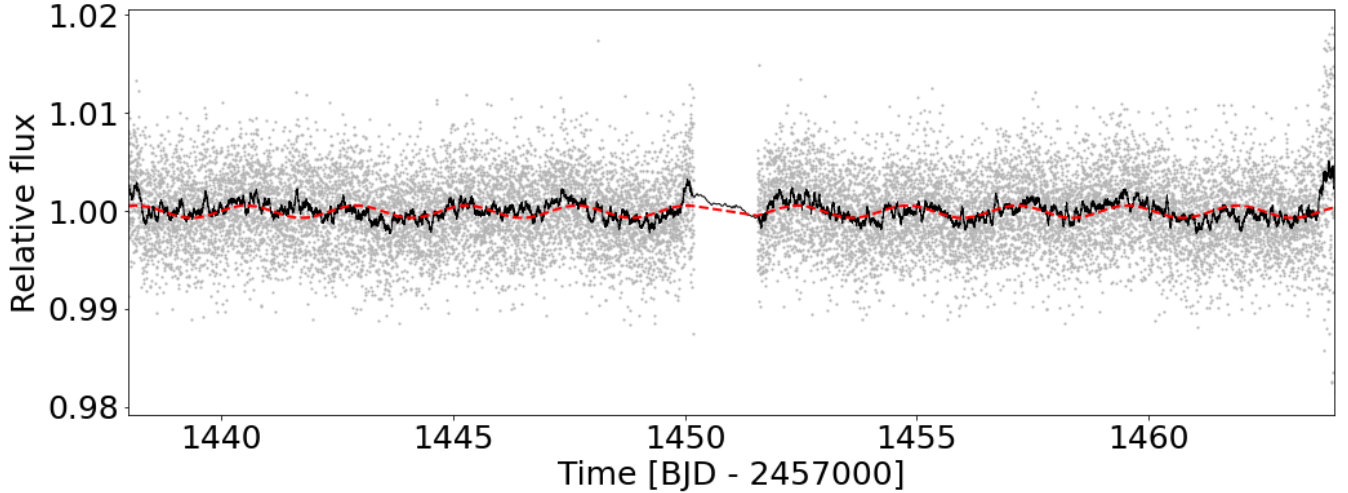


Fig. 4. TIC 13069774, a variable star showing a number of crossings more than twice the predicted value for sinusoidal variation.

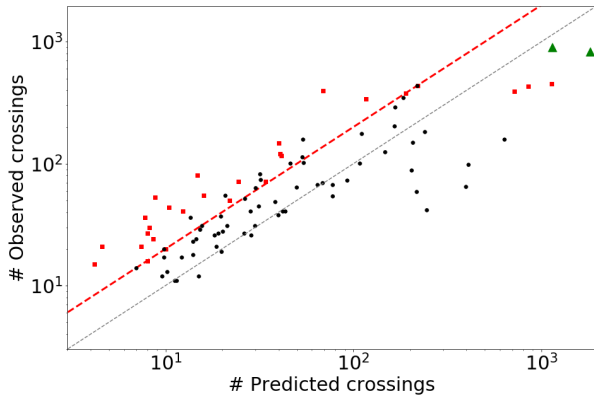


Fig. 5. Observed number of zero crossings as a function of the predicted number of crossings for all 90 variables. The two g -mode hot subdwarf pulsators are shown as green triangles. The two dashed lines represent equality (bottom, in grey) and observed number of crossings equal to twice the number of predicted crossings (top, in red). Objects not included as rotational variables are shown as red squares. Objects with a high number of predicted crossings due to showing short periods often show less observed crossings because TESS data is not continuous, presenting a gap every ≈ 13 days when data was being transmitted to Earth.

To obtain a comparison with field main sequence stars with no hot subdwarf companions, we have used the data from Reinhold & Gizon (2015), who determined the rotational periods for more than 18 500 stars observed by the *Kepler* mission. To account for the temperature distribution of our sample, which excludes cool companions that cannot be detected in composite binaries, we selected for each object in our sample the stars in Reinhold & Gizon (2015) with same effective temperature (within 5%).

The temperature for the main sequence stars in the systems in our sample was determined with a multi-component fit to the spectral energy distribution (SED), taking into account both the contribution of the hot subdwarf and of the companion. The SED fitting procedure uses literature photometry from APASS (Henden et al. 2015), 2MASS (Skrutskie et al. 2006), WISE (Cutri et al. 2012), and *Gaia* (Gaia Collaboration 2018; Riello et al. 2018; Evans et al. 2018), and is constrained by the reddening obtained from the dust maps of Lallement et al.

(2019) and the *Gaia* parallax. To model the SED, Tübingen NLTE Model-Atmosphere package models (Werner et al. 2003) and Kurucz atmosphere models (Kurucz 1979) are used for respectively the hot subdwarf star and the cool companion. A more detailed description of the SED fitting procedure is given in Vos et al. (2017, 2018b).

Next, given a sample of stars with consistent temperature for each of our objects, we accounted for the fact that there is an upper limit to detectable periods by randomly selecting the period of one of the stars in the comparison sample considering only periods within our detectable range (we assumed that periods shorter than the maximum period in our sample, of ≈ 7.5 days, could be detected). We repeated this a hundred times, obtaining thus one period histogram for each realisation. We then calculated the mean histogram, as well as an uncertainty given by the standard deviation. This histogram is shown in blue in Fig. 6.

The period distribution for main sequence companions to hot subdwarfs is clearly different from the distribution of field main sequence stars. This is confirmed by a two-sample Anderson-Darling test, which suggests that the null hypothesis that these two distributions are sampled from the same population can be safely rejected (p -value < 0.001).

Performing a similar comparison for the amplitude of the observed photometric variability results in Fig. 7. To avoid differences due to variable precision in different magnitude ranges, in this case we have also constrained the comparison sample to have a similar magnitude distribution to our observed sample, by drawing comparison objects with magnitudes within 5% of the value for each of our systems (or within 10% when no pair was found). Albeit more subtle for the amplitude distribution compared to the period distribution, a two-sample Anderson-Darling test confirms that the behaviour of the companion stars also does not follow the trend of canonical main sequence stars (p -value < 0.001).

Figures 6 and 7 suggest that main sequence stars with a subdwarf companion show, in average, shorter rotation periods and lower photometric variability amplitudes than the bulk of main sequence stars. The analysed main sequence stars should be as old as their hot subdwarf companions, which likely descend from F stars that have already evolved beyond the RGB, suggesting ages of at least a few billion years. The fact that their rotation is systematically faster than field main sequence stars,

Table 1. 61 variables in our sample whose variability was attributed to rotation of the main sequence companion, identified by their TESS Input Catalogue (TIC) numbers.

TIC	G	CROWDSAP	P (days)	Amplitude (%)	FAP	$T_{\text{eff}}^{\text{MS}}$ (K)	R^{MS} (R_{\odot})
3990402	11.08	0.98	3.5805(23)	0.3169(23)	0.00e+00	5794(78)	1.14(6)
12528447	12.50	1.00	0.67138(9)	0.3340(46)	0.00e+00	6720(163)	1.61(6)
16876025	12.86	1.00	2.326(7)	0.205(8)	0.00e+00	6172(73)	1.27(7)
30019744	12.12	0.71	2.113(11)	0.163(7)	0.00e+00	5758(25)	1.57(6)
32556882	13.82	0.80	5.35(5)	0.454(28)	0.00e+00	5328(20)	1.221(50)
33526769	12.24	0.99	2.2285(41)	0.1467(36)	0.00e+00	5531(42)	0.986(40)
64112207	15.32	0.99	7.26(16)	0.252(40)	5.39e-06	5772(75)	2.10(26)
65263746	13.40	0.78	4.498(28)	0.171(10)	6.49e-72	6146(117)	0.82(7)
68942649	10.04	0.98	2.8383(8)	0.1954(10)	0.00e+00	6400(400)	1.10(5)
69841801	12.25	1.00	1.251(17)	0.88(14)	0.00e+00	5896(41)	1.398(48)
70451188	14.22	0.99	2.836(14)	0.305(19)	0.00e+00	5965(24)	1.28(6)
71248239	12.83	0.89	0.9728(18)	0.173(9)	0.00e+00	6050(36)	1.304(34)
71716888	12.97	0.99	1.0491(23)	0.066(29)	3.75e-24	6992(39)	1.62(8)
92865531	13.12	0.96	1.40297(17)	1.888(7)	0.00e+00	5004(14)	1.432(37)
116416387	14.65	0.84	3.819(38)	0.402(43)	0.00e+00	5515(46)	0.99(6)
118269334	13.82	0.97	3.073(7)	0.717(19)	0.00e+00	5479(74)	0.970(45)
143058705	14.40	0.98	5.027(30)	0.540(28)	0.00e+00	5449(42)	1.00(6)
146323153	12.15	0.96	0.219040(20)	0.1987(34)	0.00e+00	6793(44)	1.663(41)
149767908	13.00	0.99	0.4557(6)	0.229(10)	0.00e+00	7300(56)	1.67(12)
151641733	12.65	0.96	0.5592(8)	0.028(5)	2.03e-10	6540(41)	1.48(5)
157323544	12.69	0.99	4.462(43)	0.080(7)	0.00e+00	6250(291)	2.41(10)
158335560	13.08	0.92	2.0007(41)	0.244(13)	0.00e+00	6063(71)	1.45(8)
159805154	14.80	0.90	2.686(9)	0.29(34)	5.95e-32	5642(50)	1.50(23)
160583519	14.43	0.98	1.9731(7)	0.175(11)	0.00e+00	5994(52)	1.292(48)
164754858	14.70	0.80	2.679(24)	0.228(26)	1.66e-11	5864(53)	1.87(26)
165650748	11.38	1.00	2.11600(19)	0.0768(18)	0.00e+00	6626(123)	1.401(26)
198240464	13.52	0.89	2.35724(7)	0.816(6)	0.00e+00	5646(53)	1.195(23)
202466623	13.81	0.97	3.3207(7)	0.237(11)	0.00e+00	6009(60)	1.155(30)
202507151	12.69	0.99	1.98289(36)	0.135(5)	0.00e+00	6356(69)	1.032(27)
206688085	13.77	0.99	1.91975(28)	2.337(9)	0.00e+00	4936(47)	2.43(7)
207208668	13.33	0.98	2.5671(6)	0.36(36)	0.00e+00	6111(52)	1.166(37)
209397773	12.73	0.83	3.58(9)	0.08(5)	1.05e-69	5460(34)	1.230(40)
212320065	11.64	0.98	1.8627(7)	1.416(8)	0.00e+00	5097(14)	2.4992(9)
219988867	13.03	0.96	1.9209(19)	0.1007(39)	0.00e+00	6093(57)	1.446(38)
228508601	14.40	0.99	5.58(6)	0.346(24)	0.00e+00	5400(41)	1.97(33)
231845752	13.72	0.96	2.0923(35)	0.088(8)	1.51e-31	5864(62)	1.69(5)
247017534	12.15	0.92	1.8154(46)	0.09(10)	0.00e+00	5945(28)	1.355(49)
263014094	15.03	0.88	2.91052(14)	1.531(25)	0.00e+00	5000(9)	1.64(8)
277892210	13.91	0.95	1.807791(24)	1.658(28)	0.00e+00	5460(49)	1.234(32)
293463617	15.13	0.87	1.74504(12)	1.337(40)	0.00e+00	4612(39)	0.802(39)
298093039	11.62	1.00	5.5610(6)	0.1620(25)	0.00e+00	5877(127)	0.897(18)
304103779	12.96	0.99	1.12766(11)	0.0599(47)	9.54e-37	5968(29)	1.542(36)
317129309	13.44	0.98	3.86(12)	1.5(2.6)	6.53e-24	6501(35)	1.83(14)
320529836	14.65	0.88	0.8353(8)	1.84(13)	0.00e+00	5251(44)	0.969(45)
320965274	12.66	0.99	1.759(6)	0.0442(48)	8.53e-22	5286(28)	1.80(11)
325566833	13.35	0.98	1.0628(15)	0.069(7)	9.39e-23	5291(22)	1.283(19)
335682563	13.55	0.99	4.4173(21)	0.112(7)	0.00e+00	5987(68)	0.942(28)
346597868	11.52	0.97	1.782(6)	0.0320(34)	5.51e-28	6438(97)	2.29(7)
349367583	13.05	0.99	2.302(14)	0.23(24)	0.00e+00	5919(53)	1.465(49)
365771053	13.37	0.85	1.3515(6)	1.089(14)	0.00e+00	5981(27)	1.139(20)
369371996	15.91	0.98	2.606(9)	0.150(10)	2.14e-40	5802(163)	2.34(14)

Notes. G is the magnitude in the *Gaia* DR2 catalogue, and the value of CROWDSAP is the one calculated by the SPOC pipeline. For objects with data from more than one sector, this is the averaged value. Period and amplitude uncertainties were determined with a hundred Monte-Carlo runs of the multi-component fit to the light curve, re-drawing the fluxes from a normal distribution taking the quoted uncertainties into account. The FAP was calculated using the `astropy LombScargle` function. T_{eff} and radius for the main sequence companion were obtained from a SED fit, as described in the text. Uncertainties are given on the last significant digits, e.g. $3.5805(23) = 3.5805 \pm 0.0023$, $1.5(2.6) = 1.5 \pm 2.6$, $6400(400) = 6400 \pm 400$.

Table 1. continued.

TIC	G	CROWDSAP	P (days)	Amplitude (%)	FAP	$T_{\text{eff}}^{\text{MS}}$ (K)	R^{MS} (R_{\odot})
382518318	14.01	0.29	4.33102(40)	1.402(25)	0.00e+00	5206(25)	1.274(36)
389752750	15.24	0.82	0.67638(22)	0.889(40)	0.00e+00	4807(84)	1.34(30)
393941149	14.73	0.86	3.873(29)	0.364(25)	0.00e+00	5119(45)	1.04(11)
398940155	13.08	0.47	0.5039(7)	0.62(12)	0.00e+00	6976(65)	2.10(14)
405471275	15.19	0.33	3.510(40)	0.42(6)	2.66e-12	5915(56)	1.29(29)
406239686	13.45	0.98	1.633(5)	0.12(13)	1.16e-41	5499(32)	1.395(46)
420049852	12.13	0.81	1.666(7)	0.0538(46)	6.95e-35	6313(58)	1.361(42)
437237493	15.36	0.72	1.2648(39)	0.84(42)	0.00e+00	6186(60)	1.41(19)
441401311	13.74	0.99	2.915(6)	0.275(12)	0.00e+00	5741(21)	1.46(7)
461156754	14.96	0.74	1.610(6)	0.321(42)	2.32e-20	5730(59)	1.57(17)

Table 2. 29 objects whose cause for variability is undetermined.

TIC	G	CROWDSAP	P (days)	Amplitude (%)	FAP	$T_{\text{eff}}^{\text{MS}}$ (K)	R^{MS} (R_{\odot})
13069774	12.29	0.97	2.380(11)	0.058(28)	0.00e+00	5969(23)	1.288(21)
31636688	16.01	0.78	2.806(15)	0.39(6)	2.88e-07	6974(36)	1.62(37)
71133157	14.06	0.98	2.156(16)	0.121(15)	3.17e-10	6751(74)	1.31(7)
80057233	15.79	0.62	6.53(12)	2.98(43)	1.49e-14	5986(73)	1.78(38)
89529774	14.31	0.96	4.38(6)	0.106(13)	4.73e-08	5549(31)	2.41(9)
141628019	14.34	0.95	10.42(5)	0.060(9)	2.75e-38	5518(28)	2.32(18)
147115112	14.27	0.60	1.643(13)	0.098(17)	2.25e-04	6458(77)	1.60(12)
152374958	13.08	0.73	4.86(6)	0.093(11)	2.04e-28	6015(23)	2.36(9)
159669717	13.81	0.72	7.57(31)	0.071(49)	2.00e-07	6174(81)	1.64(11)
181820016	12.82	0.99	10.26(44)	0.055(8)	4.67e-18	6518(129)	1.48(8)
197693940	14.40	0.90	6.40(13)	0.249(40)	5.11e-12	4974(47)	0.530(40)
220026025	15.67	0.87	9.85(7)	18(10)	2.26e-23	5346(63)	1.8(7)
220472655	14.48	0.96	3.1301(46)	0.078(10)	6.23e-18	6734(93)	1.35(6)
246881770	15.39	0.89	7.13(9)	0.379(45)	6.31e-07	5681(76)	1.27(18)
253932935	16.00	0.89	13.4(1.8)	0.29(47)	3.86e-17	6159(110)	1.88(40)
257024892	13.05	0.99	2.2077(16)	0.0222(46)	2.91e-07	6197(35)	2.20(7)
259963278	10.61	1.00	0.83783(7)	0.0089(8)	1.15e-24	6495(20)	1.460(24)
266347283	12.55	0.99	0.9011(11)	0.0334(47)	4.07e-15	6523(140)	1.420(40)
274035031	13.96	0.46	2.825(13)	0.090(16)	2.41e-07	6055(22)	1.666(49)
289737935	14.97	0.90	3.030(37)	0.182(32)	1.09e-04	5769(93)	1.46(22)
313303167	12.46	0.88	0.4270633(17)	0.7749(47)	0.00e+00	7136(129)	1.369(37)
320176500	15.79	0.46	6.39(38)	0.65(26)	6.34e-10	6158(48)	1.88(38)
389520459	14.03	0.99	1.350(6)	0.092(13)	6.41e-06	5800(51)	2.18(16)
410135274	15.41	0.25	6.96(8)	0.86(6)	7.30e-44	5497(22)	2.04(25)
410390905	13.39	0.99	0.99130(10)	0.061(5)	2.77e-33	5900(45)	1.576(26)
424941595	14.49	0.34	6.88(19)	0.226(39)	2.12e-15	5454(37)	2.4991(12)
453366788	13.94	0.23	5.065(38)	0.285(29)	1.12e-33	6250(50)	1.19(8)

Notes. Columns are the same as in Table 1.

which show a large spread in age and thus rotation rates, can only be explained by accretion. As the hot subdwarf progenitor reaches the red giant phase and fills its Roche-lobe, the companion will accrete mass and be spun up to near the critical velocity, when the centrifugal acceleration exactly balances gravity. At this point, accretion can no longer cause the companion star to spin up, and it will start to spin down (Popham & Narayan 1991; Paczynski 1991; Deschamps et al. 2013). The short rotation periods can therefore be interpreted as evidence for previous interaction in these wide binaries. In fact, the shape of the observed period distribution as well as the observed range of periods resembles what is found for young open clusters (e.g. Rebull et al. 2016, 2018), in which stars are still rotating somewhat close to their critical velocities. A similar effect has

also been observed for post-mass-transfer blue straggler stars (Leiner et al. 2018).

The amplitudes are lower likely due to a combination of factors. On one hand, stellar activity is found to decrease with age (e.g. Davenport et al. 2019), therefore this difference in amplitude suggests that the composite companions are older than the main sequence stars in the comparison sample. However, metallicity also plays a role in the level of activity, and hence the lower amplitudes can also be suggesting that the companions have lower metallicities. There is no comprehensive study of the metallicity of main sequence stars in composite systems with hot subdwarfs, although a preliminary analysis of a few systems indicates that they seem to be slightly subsolar (Molina et al., in prep.).

Table 3. Systems for which no periodic variability has been detected.

TIC	<i>G</i>	CROWDSAP	Detection limit (%)	$T_{\text{eff}}^{\text{MS}}$ (K)	R^{MS} (R_{\odot})
9102069	15.04	0.88	0.17	6011(163)	1.72(23)
13090700	14.73	0.99	0.13	6689(57)	1.85(17)
25245570	15.12	0.69	0.28	5950(82)	1.88(34)
32661254	11.29	0.97	0.013	6425(53)	1.74(7)
56648314	14.13	0.99	0.09	5771(26)	1.84(28)
71150825	14.61	0.66	0.13	5382(17)	1.35(8)
71410075	15.87	0.75	0.30	6324(150)	1.04(13)
98871628	14.34	0.93	0.11	5697(24)	1.13(7)
117626475	12.60	1.00	0.035	6161(112)	1.05(9)
121550523	14.32	0.92	0.11	6128(69)	1.49(7)
141602548	12.10	0.98	0.014	6706(171)	1.700(36)
146437397	13.47	0.97	0.047	5797(59)	1.63(5)
151892844	14.98	0.98	0.22	5047(69)	0.57(8)
179278778	15.07	0.86	0.31	5855(96)	2.04(24)
220370211	14.84	0.37	0.34	5782(70)	1.26(10)
248949857	12.23	1.00	0.025	6507(28)	1.82(14)
260839766	15.39	0.85	0.31	6065(213)	1.89(25)
261427146	12.07	0.95	0.021	6070(121)	1.7(7)
261679852	16.22	0.90	0.45	5095(64)	1.47(34)
281851153	14.96	0.72	0.19	6501(35)	1.83(14)
283866221	15.58	0.69	0.38	8117(218)	1.38(42)
301405970	12.57	1.00	0.031	6606(87)	2.03(10)
339525222	13.80	0.98	0.06	6017(26)	1.87(8)
362105045	15.39	0.97	0.14	6400(79)	1.05(10)
370282569	14.60	0.97	0.11	5845(54)	2.22(15)
377053047	14.82	0.45	0.15	6550(50)	1.46(15)
392703299	15.81	0.70	0.32	5431(109)	2.13(23)
394631720	14.39	0.76	0.11	5311(58)	1.29(7)
413300076	15.77	0.37	0.42	5117(74)	1.7(6)
421951567	13.90	0.88	0.08	6216(46)	2.08(21)
422149668	14.48	0.98	0.14	5608(62)	1.71(13)
436639479	14.41	0.86	0.15	6297(83)	0.773(49)
441399312	13.28	0.57	0.06	5499(124)	1.89(10)

Notes. TIC, *G*, CROWDSAP, T_{eff} , and radius are the same as in Table 1. The detection limit has been calculated as five times the average amplitude in a Fourier transform of the light curve.

3. *Gaia* DR2 search for common proper motion companions

One of the many applications of the unprecedented *Gaia* DR2 is the search for common proper motion pairs (e.g. El-Badry & Rix 2018; Fouesneau et al. 2019). Whereas close binaries (separations $\lesssim 20$ mas) are not resolved by *Gaia*, wider binaries can be identified as co-moving pairs thanks to the precise *Gaia* astrometry. For hot subdwarfs, radial velocity variability has been used as the main indicator for binarity, which limits the detection to objects with periods of a few tens of years at best (the discovery of hot subdwarfs dates back to Humason & Zwicky 1947, although their evolutionary origin was only understood much later). This is equivalent to separations smaller than ≈ 20 au, or ≈ 20 mas at a distance of 1 kpc, coinciding with objects unresolved by *Gaia*.

Gaia therefore opens a new window to study hot subdwarf binarity by allowing us, for the first time, to seek binary companions beyond 20 au. We have performed a search for common proper motion companions to spectroscopically confirmed hot subdwarfs in the catalogue of Geier (2020). We followed the approach of Fouesneau et al. (2019), and searched for co-moving sources with proper motions consistent with those of the

hot subdwarfs within 3σ according to:

$$\frac{((\mu_{\alpha})_{\text{SD}} - (\mu_{\alpha})_{\text{Gaia}})^2}{(\sigma_{\mu,\alpha})_{\text{SD}}^2 + (\sigma_{\mu,\alpha})_{\text{Gaia}}^2} + \frac{((\mu_{\delta})_{\text{SD}} - (\mu_{\delta})_{\text{Gaia}})^2}{(\sigma_{\mu,\delta})_{\text{SD}}^2 + (\sigma_{\mu,\delta})_{\text{Gaia}}^2} \leq (3 \text{ mas yr}^{-1})^2, \quad (1)$$

where μ_{α} is the proper motion in right ascension (α), μ_{δ} is the proper motion in declination (δ), $\sigma_{\mu,\alpha}$ is the uncertainty in μ_{α} , and $\sigma_{\mu,\delta}$ is the uncertainty in μ_{δ} . The subscripts “SD” and “*Gaia*” refer to the queried hot subdwarfs, and to objects in the *Gaia* catalogue other than the hot subdwarf. Similarly, we have also restricted the parallax (ϖ) difference between the two sources to 3 sigma:

$$\frac{(\varpi_{\text{SD}} - \varpi_{\text{Gaia}})^2}{(\sigma_{\varpi})_{\text{SD}}^2 + (\sigma_{\varpi})_{\text{Gaia}}^2} \leq (3 \text{ mas})^2. \quad (2)$$

Finally, we have only considered *Gaia* sources whose projected separation was smaller than 20 000 AU (~ 0.1 pc), because pairs with larger separations are likely to be eventually disrupted by external gravitational perturbations (Retterer & King 1982; Weinberg et al. 1987). This also helps limiting the contamination by chance alignments, which grows rapidly at large

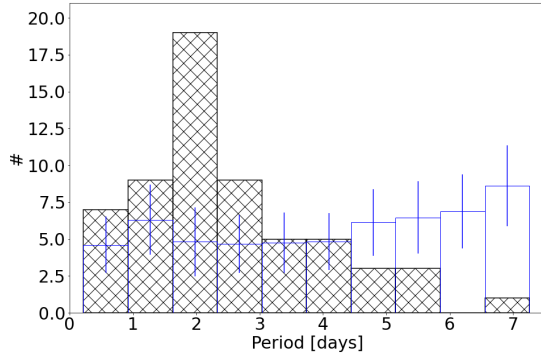


Fig. 6. Number histogram of the obtained rotational periods for the hot subdwarf companions (black, hatched). As a comparison, we show a number histogram obtained from drawing a sample of objects from Reinhold & Gizon (2015) with the same temperature distribution as our sample and periods within the detectable range (in blue). This was repeated a hundred times; the height of the histogram is the average over all realisations, whereas the error bar is the standard deviation.

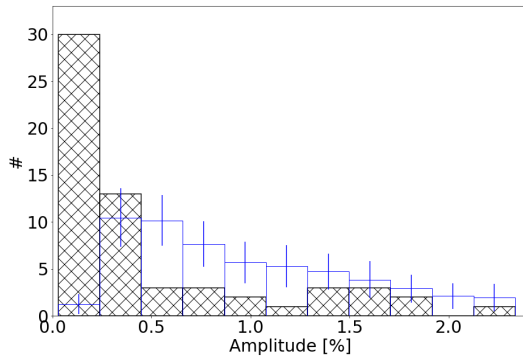


Fig. 7. Same as Fig. 6, but for the detected amplitude of variability.

separations (Andrews et al. 2017). The ADQL query applying these conditions can be found in Appendix B.

The query returned 299 matches for 237 stars. We next applied quality filters to the astrometry of both hot subdwarf and candidate companion, by selecting only objects with parallax uncertainties smaller than 20%, and applying the quality filters of Lindegren et al. (2018), that is

$$1.0 + 0.015 (G_{BP} - G_{RP})^2 < E < 1.3 + 0.06 (G_{BP} - G_{RP})^2, \quad (3)$$

where E is the `phot_bp_rp_excess_noise`, the photometric excess factor obtained by comparing fluxes in the G_{BP} and G_{RP} passbands to the total G flux (see e.g. Evans et al. 2018), and

$$u < 1.2 \max(1, \exp(-0.2(G - 19.5))), \quad (4)$$

where $u = \sqrt{\frac{\text{astrometric_chi2_al}}{(\text{astrometric_n_good_obs_al}-5)}}$, with `astrometric_chi2_al` being the value of the chi-square statistic of the astrometric solution, and `astrometric_n_good_obs_al` being the number of good observations; both are given in the *Gaia* DR2 table.

This results on 16 common proper motion candidates, listed in Table 4. The comparison between *Gaia* measurements for the pairs is shown in Fig. 8. Figure 9 illustrates the position of both the hot subdwarfs and their candidate companions in a colour-magnitude diagram. We provide more details of each of these hot subdwarfs in Appendix C.

Given the number of hot subdwarfs with good astrometry (Eqs. (3) and (4)), even if all our identifications are confirmed as

hot subdwarfs with a common proper motion pair, this implies a fraction of only $\approx 0.5\%$. We note that this fraction refers to the inhomogeneous sample of spectroscopically classified hot subdwarfs, and cannot be generalised given that no selection effects are taken into account. Yet, this very small incidence of common proper motion pairs among confirmed hot subdwarfs suggests that such systems are much less common than for their progenitors.

4. Discussion

We find that a large fraction of composite hot subdwarf binaries present evidence of interaction in the form of accretion, with at least 61 of the 123 analysed systems showing variability consistent with rotation of the companion. The rotation periods shown by the main sequence companions are significantly smaller than those shown by a comparison sample of main sequence stars.

The observed periods can be well described by a log-normal distribution with mean $\log P[\text{days}] = 0.35$ and standard deviation $\log P[\text{days}] = 0.27$. The period distribution for main sequence stars in Reinhold & Gizon (2015) within the temperature range of the our sample can be described by a log-normal distribution with mean $\log P[\text{days}] = 1.19$ and standard deviation $\log P[\text{days}] = 0.26$. The distributions show therefore the same width, but the mean is shifted towards much lower values for the hot subdwarf companions. The longest period in our sample has about 10% chance of coming from the distribution with larger mean, with all other periods showing probabilities lower than 5%. However, we see no evidence for bi-modality in our sample, and a Shapiro-Wilk test cannot reject the null hypothesis that the logarithms of the observed periods follow a normal distribution (assuming a confidence level of 99%), therefore we interpret all observed periods to come from the same distribution.

The observed amplitudes of the photometric variability are also found to be significantly lower than for the comparison sample. This reflects the fact that the hot subdwarf companions are an older, lower-metallicity population than the stars in the comparison sample. Although the observed stars are rejuvenated by accretion, which explains their short orbital periods, the accretion would not affect their interiors significantly (given that accretion rates are fairly small, Toonen et al. 2012; Vos et al. 2020), hence their level of activity is unaffected and the amplitudes remain low. In other words, these stars appear young if their rotational periods are considered, but the amplitudes reveal them to be old.

For a further 29 stars, variability is detected, but the periods are less significant, or the light curve is not obviously periodic. These objects seem to be an unremarkable subsample of the complete sample of 123 composite systems, with G magnitude, CROWDSAP, number of observed sectors, and effective temperature of the companion all similarly distributed to the entire sample, as shown in Fig. 10. This is also indicated by two-sample KS tests, in which the null hypothesis that the parameters for these 29 stars are drawn from the same population as the parameters for the whole sample of 123 objects cannot be rejected. In order to compile a sample of clear rotators, we therefore remove these objects whose period or cause for variability is uncertain from our sample, with the exception of two systems for which only the pulsation of the subdwarf is detected, but no rotation of the companion even after pre-whitening is performed. This effectively reduces our sample to 96 systems, out of which 35 show no observed variability due to rotation, and 61 show variability consistent with rotation spun-up by accretion. Considering

Table 4. Identified common proper motion candidates.

Hot subdwarf					Candidate companion					Pair properties			
source_id	G (mag)	ϖ (mas)	μ_α (mas yr ⁻¹)	μ_δ (mas yr ⁻¹)	source_id	G (mag)	ϖ (mas)	μ_α (mas yr ⁻¹)	μ_δ (mas yr ⁻¹)	θ (")	a (AU)	$\Delta\varpi$	$\Delta\mu$
312628749626419328*	13.1	1.73	-8.80	-11.27	312628745331966976	18.7	1.47	-9.74	-12.16	6.8	3920	1.1	2.8
601188910547673728	14.6	0.69	-5.02	-0.80	601188910547673600	15.4	0.58	-5.15	-0.75	2.7	3856	1.6	1.3
992534888766785024*	12.0	2.93	-25.48	-25.16	992534888766784640	13.8	3.03	-25.57	-25.01	7.0	2384	1.3	1.3
1332156747638095488	15.9	0.46	-5.22	-27.03	1332156747638095360	16.7	0.65	-5.41	-27.29	4.1	8996	1.7	1.7
1659750327258228352	16.2	0.53	-1.74	-0.70	1659750327258228224	17.9	0.62	-2.02	-0.65	1.9	3595	0.7	1.3
1660055029417965952	13.4	2.18	-18.82	3.51	1660055098137442944	17.5	2.10	-18.82	3.95	39.8	18291	0.7	2.7
1883850072814402048	13.0	0.98	-1.80	-13.31	1883850072814402432	17.4	0.96	-1.59	-13.57	11.5	11655	0.2	1.9
1891098500140100352	12.8	2.11	11.43	-1.30	1891098500140101120	12.9	2.05	11.41	-1.17	26.0	12349	0.9	1.5
2002880555945732992	14.4	1.46	4.72	1.57	2002880555945731968	17.0	1.42	4.97	1.70	3.4	2346	0.4	2.2
2103959862471941632*	14.1	1.55	-0.64	-8.95	2103959858173621760	18.8	1.50	-0.74	-8.72	15.9	10253	0.2	0.6
3381286602335612416	14.0	0.60	-3.11	-7.56	3381286636695992448	17.9	1.08	-2.70	-7.16	8.5	14220	2.9	2.0
3484319745326973824*	11.3	1.95	-7.66	-23.66	3484320501241217792	16.1	1.92	-8.10	-23.65	6.4	3307	0.2	2.4
3868418219635118080*	14.2	1.08	-21.76	13.79	3868418219635275520	16.0	1.41	-21.81	13.87	8.6	8019	1.9	0.2
4491274930955326080	15.6	0.61	0.08	-10.03	4491274930955325440	16.8	0.49	0.27	-10.06	4.9	8014	1.3	1.3
4877263019073081600*	12.3	1.72	7.03	20.44	4877263023370516096	17.3	1.59	7.36	20.51	20.9	12144	1.6	2.5
1429755412672689536	13.7	1.30	-6.44	-4.82	1429755374017588608	12.6	1.43	-6.50	-4.50	3.6	2764	2.4	2.9

Notes. The four columns to the left refer to the hot subdwarf, whereas the next four refer to the candidate common proper motion companion. All values come directly from the *Gaia* DR2 catalogue. The last four columns contain pair properties, namely the angular separation θ , the projected orbital separation a , assuming the distance of the hot subdwarf, and the differences in parallax and proper motion in units of standard deviation, $\Delta\varpi$ and $\Delta\mu$. The six objects marked with asterisks have identified close companions, being therefore candidate triple systems (see Appendix C).

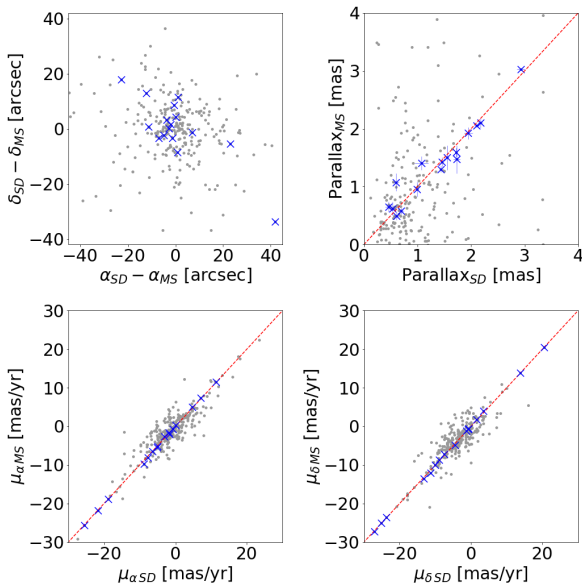


Fig. 8. Comparison between parameters for all matches (grey) and only those with good astrometry (blue). *Top left panel:* difference between coordinates of the hot subdwarf and the candidate companion. The *top right panel* compares the parallax of the two objects, whereas the *bottom panels* compare each component of the proper motion. The dashed lines represent equality.

this sample, the fraction of composite systems with evidence for accretion is $63.5^{+4.6}_{-5.1}\%$, where the uncertainties were calculated assuming a binomial distribution given the low-number statistics (see e.g. Burgasser et al. 2003) and indicate the 68% confidence level interval.

However, it is important to notice that the probability of detection of variability is not homogeneous throughout the sample. The NOV systems are, on average, fainter than the systems for which rotational variability has been detected (median

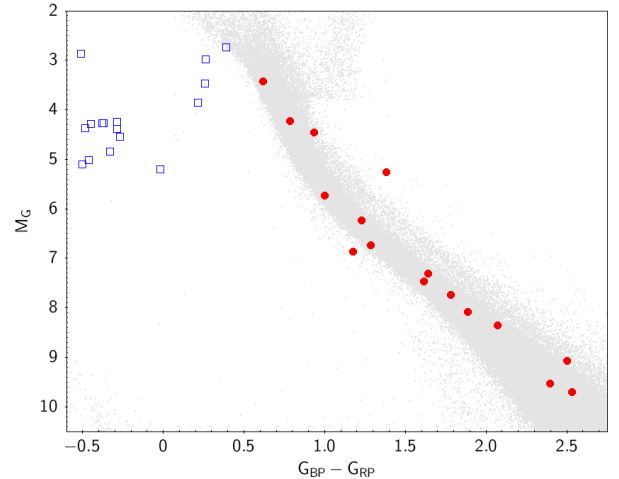


Fig. 9. Colour-magnitude diagram showing the position of all hot subdwarfs that have a common proper motion pair candidate. The hot subdwarfs are shown as open blue squares, and the candidate companions are shown as filled red circles. Light grey is the same as in Fig. 1.

$G = 13.4$ for rotational variables, compared to $G = 14.6$ for NOV systems). They are also in fields showing larger crowding, with the median of CROWDSAP being equal to 0.97 for rotational variables, but 0.89 for NOV systems. Furthermore, most of the NOV systems have data in only one sector (29 out of 33, 88%), while almost 30% of the rotational variables have data in more than one sector. This implies that the detection power is smaller for the systems in which no variability has been detected, compared to those with observed variability.

To minimise these factors, we estimate the fraction of composite stars with evidence for interaction considering only objects brighter than $G = 13.5$ and with CROWDSAP ≥ 0.97 . In this case there are 26 systems, out of 21 are consistent with rotational variables. This yields a fraction of $77.8^{+5.9}_{-9.8}\%$. For a confidence interval of 99.7% (3σ), the fraction is as high as 93%

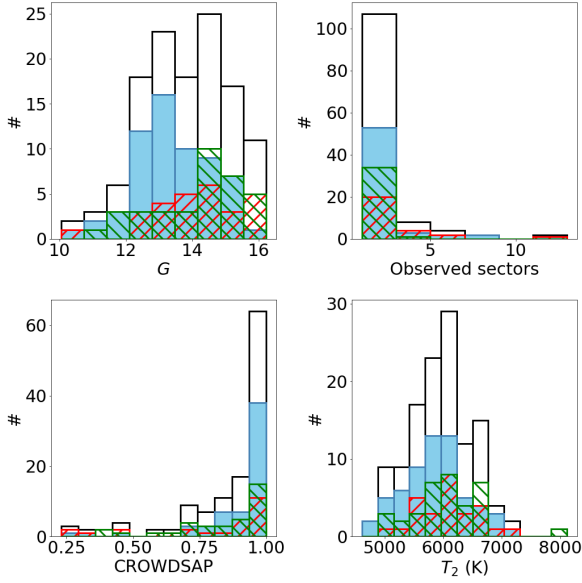


Fig. 10. Number histograms comparing the distribution of *Gaia* G magnitude (*top left*), TESS observed number of sectors (*top right*) and CROWDSAP parameter (*bottom left*), and companion effective temperature (*bottom right*) between the whole sample of 123 composites (unfilled, black), 61 rotational variables (filled, blue), 33 NOV systems (//, green), and 29 other variable systems (//, red). As these 29 systems seem to follow the distribution of the entire sample, they are excluded from our statistical analysis.

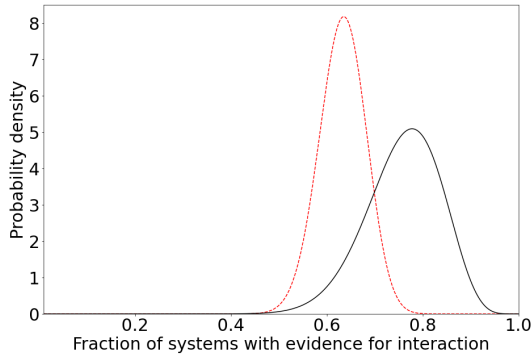


Fig. 11. Probability density for the fraction of composite systems showing evidence for interaction. The black solid line assumes the reduced sample, excluding stars that are faint and/or in crowded regions. The red dashed line assumes the whole sample.

(see Fig. 11). For the six systems brighter than $G = 12.0$, the fraction of rotational variables is 100%.

Our search for common proper motion companions has resulted in 16 candidates, with projected orbital distances ranging from 2350 to 18300 AU. Considering that 2938 stars in our sample have passed the good astrometry criteria, this suggests that only an extremely small fraction of hot subdwarfs are in very wide binaries. Among the progenitors, the fraction of wide binaries is around 15% (Zapatero Osorio & Martín 2004; Raghavan et al. 2010; Moe & Di Stefano 2017; Moe et al. 2019). As the fraction is much smaller for hot subdwarfs, this suggests that they cannot easily be formed in these non-interacting systems, and therefore they would also not be expected to form from single stars.

We note also that for six objects there is evidence of an inner binary companion (see Appendix C), suggesting that these systems are rather hierarchical triples. For the progeni-

tors, El-Badry & Rix (2018) have found that, for 36% of common proper motion pairs in the main sequence, at least one of the components is a close binary. Combining this with a wide binary fraction of 15% would suggest a rate of 5.4% hierarchical triples for progenitor systems. According to Moe & Di Stefano (2017), the fraction of triple and quadruple systems for solar-type stars is $10 \pm 2\%$. The real fraction of triple or multiple systems is unknown for our systems, because no comprehensive search for close companions has been performed for most of them, but the high fraction among the progenitors suggests that the few detected common proper motion pairs could be the progeny of triples, where the inner binary gave origin to the hot subdwarf through one of the canonical binary interaction channels. In fact, Igoshev et al. (2020), who have also found a smaller fraction of wide companions to hot subdwarfs than for their progenitors, suggest that the low fraction of wide companions could be explained by the third member of some systems becoming unbound when the inner binary, which gives origin to the hot subdwarf, goes through a common envelope phase.

5. Conclusion

We find that (i) the fraction of hot subdwarfs in composite binaries in which there is evidence for past interaction is higher than 60%, and can approach 100% when detection limits are taken into account, and (ii) only an extremely small number of hot subdwarfs (16 out of 2938) could be part of a common proper motion pair. We interpret this as a strong evidence against the formation of hot subdwarf stars in single systems, and conclude that binary interaction is in fact always required.

Binary evolution scenarios must, therefore, also explain currently single objects. The merger of two He white dwarfs is one possible channel, although the agreement between observation and model predictions is still poor. The scenario proposed by de Marchi & Paresce (1996), in which envelope stripping is caused by dynamical processes, would disrupt wide binaries and thus, in principle, also produce single hot subdwarfs with no common proper motion companions. However, the scenario has been proposed for dense globular clusters and would not work for field stars. A promising alternative is offered by the scenario proposed by Clausen & Wade (2011), in which single hot subdwarfs form from the merger of a He white dwarf with a hydrogen-burning star. This scenario seems to be able to better explain the observed rotation rates and mass distribution.

It must be noted, however, that the observed mass distribution of hot subdwarfs is still a work-in-progress, as they have historically been assumed to have masses equal to the canonical He-core flash value of around $0.5 M_{\odot}$ (Heber 1986; Saffer et al. 1994). Moreover, the apparent lack of companions could be explained by other factors, such as low-mass companions, which can be difficult to detect (Nelemans 2010). The possible shortage of progenitors is also not established, since surveys for He-core white dwarfs are still ongoing and the population is growing (Pelisoli & Vos 2019; Brown et al. 2020; Kosakowski et al. 2020). Moreover, alternative non-single formation scenarios must be considered as well, such as supernova stripping (Justham et al. 2009), the merger of cataclysmic variables and AM CVn systems (Nelemans et al. 2005; Zorotovic & Schreiber 2017), or interaction with sub-stellar companions (Soker 1998). Upcoming large spectroscopic surveys that will allow precise radial velocity measurements for hot subdwarfs (e.g. 4MOST, de Jong et al. 2014) will provide a better insight onto the true fraction of currently single hot subdwarfs, as well as onto the observed density of possible progenitors, and further constrain the possible formation scenarios of hot subdwarfs.

Acknowledgements. We are grateful to Sydney Barnes for an enlightening discussion on stellar rotation that helped motivate this work. We thank Sydney Barnes and Valerie Van Grootel for providing comments on an earlier version of this manuscript. IP was partially funded by the Deutsche Forschungsgemeinschaft under grant GE2506/12-1. This work was supported by a fellowship for postdoctoral researchers from the Alexander von Humboldt Foundation awarded to JV. ASB gratefully acknowledges financial support from the Polish National Science Center under projects No. UMO-2017/26/E/ST9/00703 and UMO-2017/25/B/ST9/02218. This research made use of Astropy, <http://www.astropy.org> a community-developed core Python package for Astronomy (Astropy Collaboration 2013, 2018), and of TOPCAT (Taylor et al. 2005). This paper includes data collected by the TESS mission. Funding for the TESS mission is provided by the NASA Explorer Program. This work has made use of data from the European Space Agency (ESA) mission *Gaia* (<https://www.cosmos.esa.int/gaia>), processed by the *Gaia* Data Processing and Analysis Consortium (DPAC, <https://www.cosmos.esa.int/web/gaia/dpac/consortium>). Funding for the DPAC has been provided by national institutions, in particular the institutions participating in the *Gaia* Multilateral Agreement.

References

- Andrews, J. J., Chanamé, J., & Agüeros, M. A. 2017, *MNRAS*, 472, 675
- Astropy Collaboration (Robitaille, T. P., et al.) 2013, *A&A*, 558, A33
- Astropy Collaboration (Price-Whelan, A. M., et al.) 2018, *AJ*, 156, 123
- Baran, A., Oreiro, R., Pigulski, A., et al. 2009, *MNRAS*, 392, 1092
- Baran, A. S., Reed, M. D., Stello, D., et al. 2012, *MNRAS*, 424, 2686
- Barlow, B. N., Wade, R. A., Liss, S. E., Østensen, R. H., & Van Winckel, H. 2012, *ApJ*, 758, 58
- Barlow, B. N., Liss, S. E., Wade, R. A., & Green, E. M. 2013, *ApJ*, 771, 23
- Basri, G., & Nguyen, H. T. 2018, *ApJ*, 863, 190
- Brown, W. R., Kilic, M., Kosakowski, A., et al. 2020, *ApJ*, 889, 49
- Burgasser, A. J., Kirkpatrick, J. D., Reid, I. N., et al. 2003, *ApJ*, 586, 512
- Charpinet, S., Brassard, P., Fontaine, G., et al. 2009, *Am. Inst. Phys. Conf. Ser.*, 1170, 585
- Chen, X., Han, Z., Deca, J., & Podsiadlowski, P. 2013, *MNRAS*, 434, 186
- Clausen, D., & Wade, R. A. 2011, *ApJ*, 733, L42
- Copperwheat, C. M., Morales-Rueda, L., Marsh, T. R., Maxted, P. F. L., & Heber, U. 2011, *MNRAS*, 415, 1381
- Cutri, R. M., Skrutskie, M. F., van Dyk, S., et al. 2012, *VizieR Online Data Catalog*: II/311
- Davenport, J. R. A., Covey, K. R., Clarke, R. W., et al. 2019, *ApJ*, 871, 241
- D’Cruz, N. L., Dorman, B., Rood, R. T., & O’Connell, R. W. 1996, *ApJ*, 466, 359
- de Jong, R. S., Barden, S., Bellido-Tirado, O., et al. 2014, *Proc. SPIE*, 9147, 91470M
- de Marchi, G., & Paresce, F. 1996, *ApJ*, 467, 658
- De Rosa, R. J., Patience, J., Wilson, P. A., et al. 2014, *MNRAS*, 437, 1216
- Deca, J., Marsh, T. R., Østensen, R. H., et al. 2012, *MNRAS*, 421, 2798
- Deschamps, R., Siess, L., Davis, P. J., & Jorissen, A. 2013, *A&A*, 557, A40
- Drilling, J. S., Jeffery, C. S., Heber, U., Moehler, S., & Napiwotzki, R. 2013, *A&A*, 551, A31
- Duchêne, G., & Kraus, A. 2013, *ARA&A*, 51, 269
- El-Badry, K., & Rix, H.-W. 2018, *MNRAS*, 480, 4884
- El-Badry, K., & Rix, H.-W. 2019, *MNRAS*, 482, L139
- Evans, D. W., Riello, M., De Angeli, F., et al. 2018, *A&A*, 616, A4
- Fouesneau, M., Rix, H.-W., von Hippel, T., Hogg, D. W., & Tian, H. 2019, *ApJ*, 870, 9
- Gaia Collaboration (Brown, A. G. A., et al.) 2018, *A&A*, 616, A1
- Geier, S. 2020, *A&A*, 635, A193
- Geier, S., & Heber, U. 2012, *A&A*, 543, A149
- Geier, S., Hirsch, H., Tillich, A., et al. 2011a, *A&A*, 530, A28
- Geier, S., Classen, L., & Heber, U. 2011b, *ApJ*, 733, L13
- Geier, S., Heber, U., Heuser, C., et al. 2013, *A&A*, 551, L4
- Geier, S., Fürst, F., Ziegerer, E., et al. 2015, *Science*, 347, 1126
- Geier, S., Østensen, R. H., Németh, P., et al. 2017, *A&A*, 600, A50
- Geier, S., Raddi, R., Gentile Fusillo, N. P., & Marsh, T. R. 2019, *A&A*, 621, A38
- Green, E. M., Fontaine, G., Reed, M. D., et al. 2003, *ApJ*, 583, L31
- Han, Z., Podsiadlowski, P., Maxted, P. F. L., Marsh, T. R., & Ivanova, N. 2002, *MNRAS*, 336, 449
- Han, Z., Podsiadlowski, P., Maxted, P. F. L., & Marsh, T. R. 2003, *MNRAS*, 341, 669
- Heber, U. 1986, *A&A*, 155, 33
- Heber, U. 2016, *PASP*, 128, 082001
- Heber, U., Moehler, S., Napiwotzki, R., Thejll, P., & Green, E. M. 2002, *A&A*, 383, 938
- Henden, A. A., Levine, S., Terrell, D., & Welch, D. L. 2015, *Am. Astron. Soc. Meeting Abstracts*, 225, 336.16
- Howell, S. B., Sobek, C., Haas, M., et al. 2014, *PASP*, 126, 398
- Humason, M. L., & Zwicky, F. 1947, *Contributions from the Mount Wilson Observatory / Carnegie Institution of Washington*, 724, 1
- Igoshev, A. P., Perets, H. B., & Michaely, E. 2020, *MNRAS*, 494, 1448
- Justham, S., Wolf, C., Podsiadlowski, P., & Han, Z. 2009, *A&A*, 493, 1081
- Kilkenny, D., O’Donoghue, D., Koen, C., Stobie, R. S., & Chen, A. 1997, *MNRAS*, 287, 867
- Kippenhahn, R., & Meyer-Hofmeister, E. 1977, *A&A*, 54, 539
- Kosakowski, A., Kilic, M., Brown, W. R., & Gianninas, A. 2020, *ApJ*, 894, 53
- Kupfer, T., Korol, V., Shah, S., et al. 2018, *MNRAS*, 480, 302
- Kurucz, R. L. 1979, *ApJS*, 40, 1
- Lallement, R., Babusiaux, C., Vergely, J. L., et al. 2019, *A&A*, 625, A135
- Latour, M., Randall, S. K., Calamida, A., Geier, S., & Moehler, S. 2018, *A&A*, 618, A15
- Leiner, E., Mathieu, R. D., Gosnell, N. M., & Sills, A. 2018, *ApJ*, 869, L29
- Lindgren, L., Hernández, J., Bombrun, A., et al. 2018, *A&A*, 616, A2
- Lomb, N. R. 1976, *Ap&SS*, 39, 447
- Maxted, P. F. L., Marsh, T. R., & North, R. C. 2000, *MNRAS*, 317, L41
- Maxted, P. F. L., Heber, U., Marsh, T. R., & North, R. C. 2001, *MNRAS*, 326, 1391
- McNamara, B. J., Jackiewicz, J., & McKeever, J. 2012, *AJ*, 143, 101
- Moe, M., & Di Stefano, R. 2017, *ApJS*, 230, 15
- Moe, M., Kratter, K. M., & Badenes, C. 2019, *ApJ*, 875, 61
- Morales-Rueda, L., Maxted, P. F. L., Marsh, T. R., North, R. C., & Heber, U. 2003, *MNRAS*, 338, 752
- Nelemans, G. 2005, *ASP Conf. Ser.*, 330, 27
- Nelemans, G. 2010, *Ap&SS*, 329, 25
- Németh, P., Kawka, A., & Vennes, S. 2012, *MNRAS*, 427, 2180
- O’Connell, R. W. 1999, *ARA&A*, 37, 603
- Østensen, R. H., Silvotti, R., Charpinet, S., et al. 2010, *MNRAS*, 409, 1470
- Pablo, H., Kawaler, S. D., Reed, M. D., et al. 2012, *MNRAS*, 422, 1343
- Paczynski, B. 1991, *ApJ*, 370, 597
- Pelisoli, I., & Vos, J. 2019, *MNRAS*, 488, 2892
- Popham, R., & Narayan, R. 1991, *ApJ*, 370, 604
- Raghavan, D., McAlister, H. A., Henry, T. J., et al. 2010, *ApJS*, 190, 1
- Rebull, L. M., Stauffer, J. R., Bouvier, J., et al. 2016, *AJ*, 152, 113
- Rebull, L. M., Stauffer, J. R., Cody, A. M., et al. 2018, *AJ*, 155, 196
- Reed, M. D., Foster, H., Telting, J. H., et al. 2014, *MNRAS*, 440, 3809
- Reinhold, T., & Gizon, L. 2015, *A&A*, 583, A65
- Reinhold, T., & Hekker, S. 2020, *A&A*, 635, A43
- Reinhold, T., & Reiners, A. 2013, *A&A*, 557, A11
- Retterer, J. M., & King, I. R. 1982, *ApJ*, 254, 214
- Ricker, G. R., Winn, J. N., Vanderspek, R., et al. 2015, *J. Astron. Telescopes Instr. Syst.*, 1, 014003
- Riello, M., De Angeli, F., Evans, D. W., et al. 2018, *A&A*, 616, A3
- Saffer, R. A., Bergeron, P., Koester, D., & Liebert, J. 1994, *ApJ*, 432, 351
- Saffer, R. A., Livio, M., & Yungelson, L. R. 1998, *ApJ*, 502, 394
- Scargle, J. D. 1982, *ApJ*, 263, 835
- Schneider, D., Heber, U., Geier, S., Latour, M., & Irrgang, A. 2019, *Fundamental Parameters of Hot Subdwarf Stars from Gaia Astrometry*
- Silvotti, R., Solheim, J. E., Gonzalez Perez, J. M., et al. 2000, *A&A*, 359, 1068
- Skrutskie, M. F., Cutri, R. M., Stiening, R., et al. 2006, *AJ*, 131, 1163
- Soker, N. 1998, *AJ*, 116, 1308
- Stark, M. A., & Wade, R. A. 2003, *AJ*, 126, 1455
- Sweigart, A. V. 1997, *ApJ*, 474, L23
- Taylor, M. B. 2005, *ASP Conf. Ser.*, 347, 29
- Tillich, A., Heber, U., Geier, S., et al. 2011, *A&A*, 527, A137
- Toonen, S., Nelemans, G., & Portegies Zwart, S. 2012, *A&A*, 546, A70
- Vos, J., Østensen, R. H., Degroote, P., et al. 2012, *A&A*, 548, A6
- Vos, J., Østensen, R. H., Németh, P., et al. 2013, *A&A*, 559, A54
- Vos, J., Østensen, R. H., Vučković, M., & Van Winckel, H. 2017, *A&A*, 605, A109
- Vos, J., Németh, P., Vučković, M., Østensen, R., & Parsons, S. 2018a, *MNRAS*, 473, 693
- Vos, J., Zorotovic, M., Vučković, M., Schreiber, M. R., & Østensen, R. 2018b, *MNRAS*, 477, L40
- Vos, J., Bobrick, A., & Vuckovic, M. 2020, *A&A*, 641, A163
- Wang, L., Gies, D. R., & Peters, G. J. 2018, *ApJ*, 853, 156
- Weinberg, M. D., Shapiro, S. L., & Wasserman, I. 1987, *ApJ*, 312, 367
- Werner, K., Deetjen, J. L., Dreizler, S., et al. 2003, *ASPCs*, 288, 31
- Zapatero Osorio, M. R., & Martín, E. L. 2004, *A&A*, 419, 167
- Zhang, X., Chen, X., & Han, Z. 2009, *A&A*, 504, L13
- Zhao, G., Zhao, Y., Chu, Y., Jing, Y., & Deng, L. 2012, *ArXiv e-prints* [arXiv:1206.3569]
- Zorotovic, M., & Schreiber, M. R. 2017, *MNRAS*, 466, L63

Appendix A: Two new g -mode pulsators

The amplitude spectrum of TIC 071013467 shows four significant frequencies with one just below our adopted threshold ($S/N = 4.5$). Other sdBVs observed from space often show an asymptotic period spacing, which can be used for modal degree identification. Unluckily, the amplitude spectrum is too patchy and finding a complete sequence of consecutive overtones is very difficult. The period spacing between f_4 and f_5 is close to the expected 250 s, suggestive of dipole modes, however the spacings between the remaining frequencies do not indicate either single or multiples of around 250 s. They are also too large to identify quadrupole modes. We found no multiplet pattern, either.

In the amplitude spectrum of TIC 382518318 we detected two dominant frequencies in the g -mode region, and one low amplitude frequency, too short to be considered a g -mode. All these frequencies meet our $S/N = 4.5$ criterion, where $N = 0.035$ ppt, though suggestive frequencies below this threshold are also considered. In addition, we detected one frequency, f_3 with $S/N = 4.1$ close to f_2 , along with two other frequencies, between f_2 and f_3 , but with even smaller amplitudes falling way below our threshold. All these four frequencies suggest a quintuplet with one component missing, and an average frequency splitting around $1.45 \mu\text{Hz}$, which translates to a rotation period of 4 days. This would be the shortest period in sdB stars detected thus far. On the other hand, if a smaller amplitude frequency shows rotational splitting, we could expect the higher amplitude frequency would show such a signature even clearer, since

Table A.1. Solutions for the two newly identified pulsators.

TIC 071013467 ($G = 13.4$)				
Mode	Frequency		Amplitude (ppt)	S/N
	(μHz)	(s)		
f_1	250.105(38)	3998.3(6)	0.50(8)	5.3
f_2	320.392(38)	3121.17(37)	0.50(8)	5.3
f_3	328.782(44)	3041.53(41)	0.43(8)	4.6
f_4	400.954(25)	2494.05(16)	0.76(8)	8.1
f_5	443.929(45)	2252.61(23)	0.42(8)	4.4
TIC 158235404 ($G = 11.6$)				
Mode	Frequency		Amplitude (ppt)	S/N
	(μHz)	(s)		
f_1	17.801(36)	56178(112)	0.188(30)	5.3
f_2	184.484(17)	5420.52(49)	0.397(30)	11.2
f_3	190.132(45)	5259.5(1.3)	0.147(30)	4.1
f_4	232.006(6)	4310.23(11)	1.126(30)	31.8

g -modes cannot be $l=0$. The highest amplitude frequency shows no multiplet splitting. We can always invoke that the split components are not driven but this interpretation is less likely. The low frequency f_1 can be interpreted by either a binary signature or a contamination by neighbouring stars. The latter can easily be excluded by no presence of bright stars that could contaminate the target flux in large TESS pixels (21 arc sec on side). We therefore conclude that f_1 is likely the signature of a binarity.

Appendix B: ADQL query for co-moving sources within 20 000 AU

```

SELECT sd.NAME, sd.source_id, sd.ra, sd.dec, sd.parallax, sd.parallax_error,
       sd.pmra, sd.pmdec, sd.pmra_error, sd.pmdec_error,
       g.source_id, g.ra, g.dec, g.parallax, g.parallax_error,
       g.pmra, g.pmra_error, g.pmdec, g.pmdec_error,
       g.phot_g_mean_mag, g.bp_rp, g.phot_bp_rp_excess_factor,
       g.astrometric_chi2_al, g.astrometric_n_good_obs_al,
       DISTANCE(POINT('ICRS', sd.ra, sd.dec), POINT('ICRS', g.ra, g.dec)) AS dist
FROM [INPUT TABLE] AS sd
JOIN gaiadr2.gaia_source AS g
ON 1=CONTAINS(POINT('ICRS', sd.ra, sd.dec), CIRCLE('ICRS', g.ra, g.dec, 20.0*sd.parallax/3600.))
WHERE (sd.source_id != g.source_id)
AND ( ( (sd.pmra - g.pmra)*(sd.pmra - g.pmra)/
(sd.pmra_error*sd.pmra_error + g.pmra_error*g.pmra_error) +
(sd.pmdec - g.pmdec)*(sd.pmdec - g.pmdec)/
(sd.pmdec_error*sd.pmdec_error + g.pmdec_error*g.pmdec_error) ) <= 9.0 )
AND ( (sd.parallax - g.parallax)*(sd.parallax - g.parallax)/
(sd.parallax_error*sd.parallax_error + g.parallax_error*g.parallax_error) <= 9.0 )

```


Appendix C: Hot subdwarfs with candidate common proper motion companions

The 16 objects in the hot subdwarf catalogue of Geier (2020) with identified possible common proper motion companions are described in more detail below. We refer to the objects using the *Gaia* DR2 source id, but also include their identification as in Geier (2020) for readability.

312628749626419328 (GALEX J01012+3125). It is classified as sdB+MS in Geier (2020). The available LAMOST spectra show instead a single sdB, and the *Gaia* $G_{BP} - G_{RP}$ colour of -0.37 also suggests there is no composite companion. The classification might rely on photometry that could have been contaminated by the common proper motion companion, which is $6.8''$ away. There is, on the other hand, a shift of $37 \pm 2 \text{ km s}^{-1}$ between LAMOST spectra taken 678 days apart, which cannot be explained by the common proper motion companion, suggesting that there is an inner binary and that this could be a triple system.

601188910547673728 (LAMOST J082517.99+113106.3). Also classified as sdB+MS (Geier 2020), but in this case the classification would seem to be confirmed at first glance by the available LAMOST spectrum. However, the size of the LAMOST fibres of $3.3''$ means that the common proper motion companion, which is only $2.7''$ away and has similar brightness, contaminates the spectrum.

992534888766785024 (GALEX J063952.00+515658.00). It is classified as a single sdB (Geier 2020), but Németh et al. (2012) suggest it could be a close binary because of the large radial velocity ($>100 \text{ km s}^{-1}$) with respect to the kinematic local standard of rest (LSR). This is thus another candidate to a triple system.

1332156747638095488 (PG 1623+386). Classified as sdOB (Geier 2020), it has been flagged as a visual double by Saffer et al. (1998). This is likely because of the common proper motion pair at a distance of $4.1''$.

1883850072814402048 (GALEX J22484+2714). The literature on this object is scarce; it has only been included in the catalogues of Geier et al. (2019) and Geier (2020) as sdB+MS. The brightness ($G = 13.4$) and relative red colour ($G_{BP} - G_{RP} = 0.26$) suggest it might be instead a misclassified blue horizontal branch (BHB) star. We note that the companion is almost $40''$ away, and therefore should not contaminate the *Gaia* colour.

2103959862471941632 (Kepler J19028+4134). This star has been observed by the *Kepler* mission. Whereas Østensen et al. (2010) reported no pulsations compatible with a hot subdwarf, McNamara et al. (2012) identified a

peak at 0.21 cycles/day with an amplitude of 0.0194%, and classified the object as a possible slowly rotating B star. However, *Gaia* places this object within the hot subdwarf cloud ($M_G = 9.7, G_{BP} - G_{RP} = -0.46$), which suggests that the variability has instead another origin, likely related to a binary companion other than the common proper motion pair, since such period is not expected to be observed in a single hot subdwarf or due to a distant ($\theta = 16''$) companion, making this system another possible triple.

3484319745326973824 (EC 11429-2701). This object has also been observed by TESS (TIC 32661254) and was included in our analysis of Sect. 2. It was observed and classified as part of the Edinburgh-Cape Blue Object Survey (EC Survey, Kilkenny et al. 1997), and our SED fit indicates the presence of a composite companion with $T_{\text{eff}} \approx 6400 \text{ K}$. The common proper motion companion is $6.44''$ away, is five magnitudes fainter than the hot subdwarf, and has its own photometry measurements in VizieR, therefore it should not have affected our SED fit. This is thus likely a triple system, with an inner unresolved binary.

3868418219635118080 (GALEX J11009+1055). It has been classified as a composite hot subdwarf by Németh et al. (2012), with a F6V type companion showing $T_{\text{eff}} \approx 6430 \text{ K}$. Given that the common proper motion companion is resolved and more than $8.5''$ away, it is rather unlikely that it contaminated the spectrum. Moreover, the *Gaia* DR2 archive suggests a $T_{\text{eff}} = 4750^{+245}_{-128} \text{ K}$ and $R = 0.578^{+0.032}_{-0.027} R_{\odot}$ for the common proper motion companion, which is more compatible with a late-G or early-K main sequence star. Therefore this is possibly a hierarchical triple system.

4877263019073081600 (EC 05015-2831). It is a known composite system that has also been included in the analysis of Sect. 2 (TIC 13069774, shown in Fig. 4). The common proper motion companion is at almost $21''$ away, having no contribution to the SED. This is another triple candidate.

1429755412672689536 (PG 1618+562). Although it is classified as sdBV+F3 in Geier (2020), Drilling et al. (2013) include this object as a single sdB reference star. The colour-excess which lead to the composite classification is actually due to the common proper motion companion at $3.6''$, which was previously identified by Silvotti et al. (2000).

For the remaining systems (1659750327258228352 = PG 1411+590; 1660055029417965952 = GALEX J14085+5940; 1891098500140100352 = FBS 2253+335; 2002880555945732992 = KPD 2254+5444; 3381286602335612416 = LAMOST J065446.63+244926.8; 4491274930955326080 = SDSS J172125.76+090311.2), the literature refers mostly to their inclusion in hot subdwarf catalogues. There is no study on their binarity to the best of our knowledge.

Formation of sdB-stars via common envelope ejection by substellar companions

M. Kramer¹, F. R. N. Schneider^{2,1}, S. T. Ohlmann³, S. Geier⁴, V. Schaffenroth⁴, R. Pakmor⁵, and F. K. Röpke^{1,6}

¹ Heidelberger Institut für Theoretische Studien, Schloss-Wolfsbrunnenweg 35, 69118 Heidelberg, Germany
e-mail: friedrich.roepke@h-its.org

² Astronomisches Rechen-Institut, Zentrum für Astronomie der Universität Heidelberg, Mönchhofstr. 12-14, 69120 Heidelberg, Germany

³ Max Planck Computing and Data Facility, Gießenbachstr. 2, 85748 Garching, Germany

⁴ Institut für Physik und Astronomie, Universität Potsdam, Haus 28, Karl-Liebknecht-Str. 24/25, 14476 Potsdam-Golm, Germany

⁵ Max-Planck-Institut für Astrophysik, Karl-Schwarzschild-Str. 1, 85748 Garching, Germany

⁶ Institut für Theoretische Astrophysik, Zentrum für Astronomie der Universität Heidelberg, Philosophenweg 12, 69120 Heidelberg, Germany

Received 19 June 2020 / Accepted 10 August 2020

ABSTRACT

Common envelope (CE) phases in binary systems where the primary star reaches the tip of the red giant branch are discussed as a formation scenario for hot subluminescent B-type (sdB) stars. For some of these objects, observations point to very low-mass companions. In hydrodynamical CE simulations with the moving-mesh code AREPO, we test whether low-mass objects can successfully unbind the envelope. The success of envelope removal in our simulations critically depends on whether or not the ionization energy released by recombination processes in the expanding material is taken into account. If this energy is thermalized locally, envelope ejection eventually leading to the formation of an sdB star is possible with companion masses down to the brown dwarf range. For even lower companion masses approaching the regime of giant planets, however, envelope removal becomes increasingly difficult or impossible to achieve. Our results are consistent with current observational constraints on companion masses of sdB stars. Based on a semi-analytic model, we suggest a new criterion for the lowest companion mass that is capable of triggering a dynamical response of the primary star thus potentially facilitating the ejection of a CE. This gives an estimate consistent with the findings of our hydrodynamical simulations.

Key words. hydrodynamics – binaries : close – subdwarfs – brown dwarfs

1. Introduction

Hot subluminescent B-type (sdB) stars are helium-core-burning stars that contain almost no hydrogen. They reach hot surface temperatures of about 2×10^4 K to 4×10^4 K, which places them on the blue end of the horizontal branch (Heber 1986). To form sdB stars, almost all of the hydrogen envelope of the progenitor must be removed by the time the helium ignition is triggered in the core. When this process commences, it thus has most likely evolved to the tip of the red giant branch (RGB).

A natural mechanism for removing the hydrogen envelope is the interaction with a binary companion. About 50% of sun-like stars evolve alongside a companion and this fraction is even higher for more massive stars (Duchêne & Kraus 2013; Moe & Di Stefano 2017). When one star in a close binary system reaches the RGB, it expands rapidly, thus overflowing its Roche lobe (RL), and can trigger unstable mass transfer. If the receiving companion cannot accrete all of this material, it will be engulfed and a common envelope (CE) is formed (Paczynski 1976) around the two compact stellar cores. These cores spiral inward and transfer angular momentum and energy to the envelope material. As a result, the envelope expands and might be partially or even completely ejected from the system (Ivanova et al. 2013). The separation between the cores is greatly reduced and a close binary forms.

Observations have indeed shown that 40% to 70% of single-lined sdB stars exist in close binary systems with periods ranging from 0.03 d to 10 d (Maxted et al. 2001). This strongly suggests a previous CE phase, in which the orbital separation is reduced and the red giant (RG) progenitor loses most of his hydrogen-rich envelope material in the interaction with its companion (Han et al. 2002, 2003). Surprisingly, several sdB binaries with companions in the brown dwarf (BD) regime have been found in recent surveys (Geier et al. 2011; Schaffenroth et al. 2014, 2015). This raises the question of whether a CE interaction with such low-mass companions can indeed trigger successful envelope ejection. Based on estimates assuming a one-dimensional (1D) static structure of the primary, Soker (1998) and Nelemans & Tauris (1998) argue that companions with masses lower than about $10^{-2} M_{\odot}$ evaporate or lose their mass in RL overflow before completely ejecting the envelope material.

Such estimates bear large uncertainties because they do not follow the hydrodynamic evolution and call for a closer investigation. The dynamics of common envelope evolution (CEE) can only be captured self-consistently in three-dimensional (3D) hydrodynamical simulations. With the wide range of spatial scales involved and the need to follow the system over many orbits, such simulations pose substantial challenges to numerical approaches. Smoothed-particle hydrodynamics (SPH) offers a way to account for the “Lagrangian nature” of the problem, but

it usually lacks spatial resolution in the dilute stellar envelopes. Moving mesh techniques, that combine the efficiency of (nearly) Lagrangian methods with the accuracy of grid-based hydrodynamics solvers, are an improvement (Ohlmann et al. 2016a,b; Prust & Chang 2019; Sand et al. 2020). Despite recent progress in numerical techniques and available computational resources, a fundamental question of CEE remains unanswered: How is the envelope ejected? If driven by the release of orbital energy only, the ejection remains incomplete in all published CE simulations (for instance Ricker & Taam 2012; Passy et al. 2012; Ohlmann et al. 2016a; Reichardt et al. 2020; Sand et al. 2020). Additional physics seems to be required for a successful envelope removal. The ionization energy stored in the envelope will be released by recombination processes provided that the material expands sufficiently. If thermalized locally, this energy leads to further unbinding of material (Nandez et al. 2015; Nandez & Ivanova 2016; Prust & Chang 2019; Reichardt et al. 2020) and a complete envelope ejection seems possible.

No hydrodynamic CE simulations have previously been carried out in the context of the formation of sdB stars. We present such simulations aiming to determine if substellar companions are sufficient to trigger a significant unbinding of the envelope material in cases where the primary star is at the tip of its RGB. In the subsequent sections, we explain the methods and the setup of our simulations (Sect. 2) and present their results (Sect. 3). Based on these results, we develop a semi-analytic model for the inspiral of the stellar cores (Sect. 3.5), discuss the fate of the companion, and compare our results to observations (Sect. 4) before concluding (Sect. 5).

2. Methods

Following the work of Ohlmann et al. (2016a,b, 2017), we employed the moving-mesh magnetohydrodynamics code AREPO (Springel 2010; Pakmor et al. 2011; Pakmor & Springel 2013) to simulate the CE phase in a system composed of a primary star at the tip of its RGB and a compact low-mass companion. This code is particularly well-suited for this task because of its shock capturing abilities and the excellent conservation of angular momentum and energy. It allows for arbitrary refinement criteria to achieve higher resolution in specific areas. For most of our simulations, we used the OPAL equation of state (EoS; Rogers et al. 1996; Rogers & Nayfonov 2002). It accounts for ionization effects and allows us to track the release of recombination energy. This energy is, in our current implementation, assumed to be thermalized locally. For comparison, one simulation was carried out with an ideal gas EoS as detailed by Ohlmann et al. (2016a,b).

2.1. Red giant star model

With the stellar evolution code MESA (Paxton et al. 2013, 2015) in version 6208, we created a suitable RG progenitor model as the primary star (denoted with subscript 1 in the following) for the subsequent binary simulations. A $1 M_{\odot}$ zero-age main sequence star was evolved until the tip of the RGB. The metallicity was set to $Z = 0.02$, a mixing length parameter of $\alpha_{\text{MLT}} = 2$ was applied, and the Reimers prescription with $\eta = 0.5$ was used for RG winds. Due to mass loss via winds, we reach a stellar model that has a total mass of $M_1 = M_{\text{RG}} = 0.77 M_{\odot}$, a radius of $R_1 = R_{\text{RG}} = 173 R_{\odot}$, a core mass of $M_{\text{core}} = 0.47 M_{\odot}$, and an envelope mass of $M_{\text{env}} = 0.30 M_{\odot}$.

The 1D MESA profile was then mapped onto a 3D grid following the procedure described in Ohlmann et al. (2017). We cut

out the core at five percent of the radius of the MESA model and replaced it with a point mass that only interacts gravitationally, henceforth called “core particle”. When combining a grid-based representation of matter with point particles, the gravitational potential has to be softened (Springel 2010). This is the case in our simulations and we set the initial softening length to $h = 3.1 R_{\odot}$.

To obtain a stellar model in hydrostatic equilibrium (HSE) where

$$\rho \mathbf{g} = \nabla P, \quad (1)$$

a modified Lane-Emden equation was solved to create a profile with a smooth transition between the core and the envelope (Ohlmann et al. 2017).

2.2. Relaxation

The spatial resolution is coarser in our 3D setup than in the 1D stellar evolution model, resulting in discretization errors. As a consequence, spurious motions arise in the mapped stellar structure. To restore HSE, we carried out a relaxation run of the mapped stellar model for ten dynamical timescales t_{dyn} , which corresponds to 930 d. Velocities were damped by a constant factor during the first $2 t_{\text{dyn}}$ and then constantly reduced until we reached $t = 5 t_{\text{dyn}}$. For the remaining $5 t_{\text{dyn}}$, the damping was completely shut off which allowed us to check if the star stays stable in the relaxed configuration.

In the top panel of Fig. 1, the Mach number, the ratio between the absolute value of the local fluid velocity v and the speed of sound c_s , $Ma \equiv v/c_s$, in the mapped stellar model is plotted over the radius at different times. The inner part of the star stays subsonic with $Ma \sim 0.1$. This shows that spurious velocities were damped successfully and the star’s envelope settles into a stable state. For technical reasons, the grid outside the star cannot be empty but has to be filled with low-density material. We chose a uniform background density of $\rho_{\text{bg}} = 10^{-16} \text{ g cm}^{-3}$, and the material is not in HSE. Consequently, in these regions, Mach numbers above 0.5 occur, but because these flows contain only $6.3 \times 10^{-4} M_{\odot}$, they are irrelevant for the dynamics of the stellar envelope.

The middle panel of Fig. 1 shows that the density profile does not change over time after we stopped the damping. We observe some expansion of surface material. This is caused by the steep initial pressure gradient, that cannot be fully resolved, which makes it impossible to fulfill the condition of HSE (1) for the original profile. Therefore, the relaxed profile settles into a new equilibrium with shallower surface gradients. Still, no mass is lost from the system and the original profile of the MESA output is well represented in the inner parts of the star, where most of the mass is concentrated.

In the bottom panel of Fig. 1, the relative difference between both sides of the HSE Eq. (1),

$$\Delta_{\text{HSE}} \equiv \frac{|\rho \mathbf{g} - \nabla P|}{\max(|\rho \mathbf{g}|, |\nabla P|)}, \quad (2)$$

is shown. Throughout most of the envelope, deviations from HSE stay at low values of $\Delta_{\text{HSE}} \approx 0.02$. Near the center, close to the core particle, the error increases due to the slight decrease in density, as well as close to the surface due to the expansion. We computed a sphere centered on the core particle that contains 99.9% of the mass of the initial RG to define a final radius of $R_1 = R_{\text{RG}} = 118 R_{\odot}$ at the end of the relaxation.

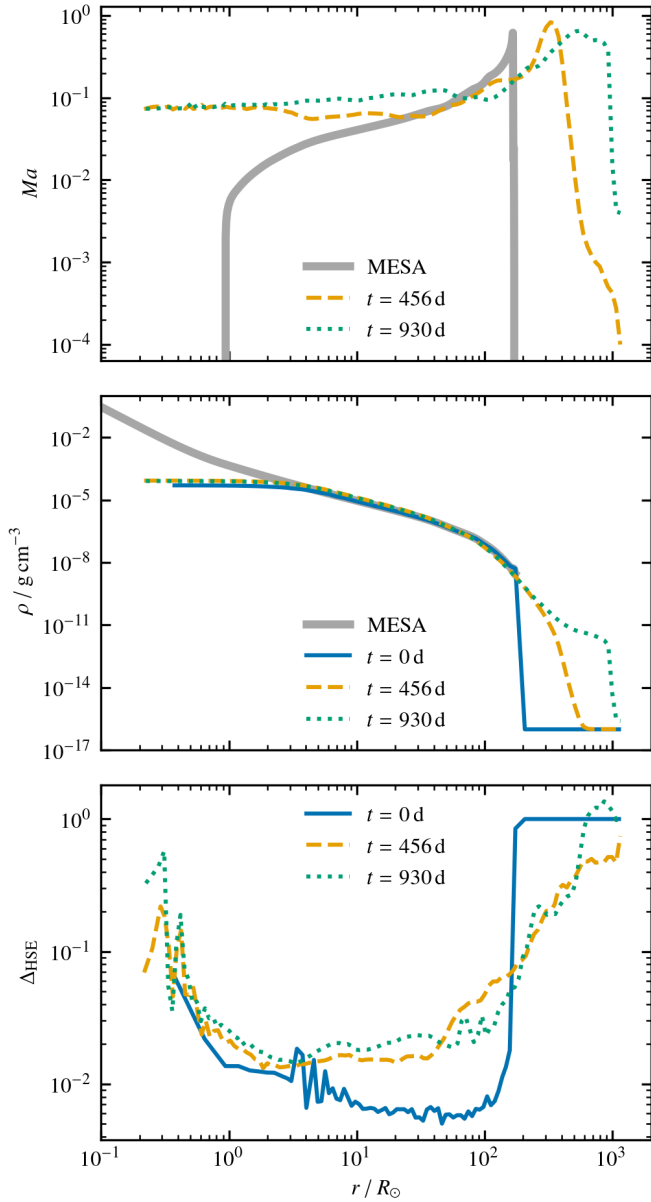


Fig. 1. Mach number Ma , density ρ , and relative deviation from HSE Δ_{HSE} according to Eq. (2) over radius of the relaxed giant at the tip of the RGB. The quantities are binned over the radius and averaged in shells.

This shows that the relaxed model represents a star at the tip of the RGB. It stays stable over sufficiently many dynamical timescales to simulate the subsequent CE phase in a binary system.

2.3. Binary simulations

To setup our binary simulations, we placed a compact companion – denoted with subscript 2 in the following and technically realized as a second core particle of mass M_2 – at an orbital separation a that corresponds to 80% of the RL radius. The binary components were placed on a Kepler orbit at a frequency of

$$\Omega = \sqrt{\frac{G(M_1 + M_2)}{a^3}}, \quad (3)$$

where G is the gravitational constant. To facilitate the inspiral, we imposed a corotation factor of $\chi = 0.95$, so that initial

velocity of the envelope is given by:

$$\mathbf{v}_{\text{env}} = \chi (\boldsymbol{\Omega} \times [\mathbf{r} - \mathbf{r}_{\text{core}}]). \quad (4)$$

Here, \mathbf{r}_{core} is the position of the RG core and $\boldsymbol{\Omega}$ points into the z -direction.

We note that an earlier start of the simulations, close to the onset of Roche-lobe overflow, would be desirable, but it is prevented by the slow initial evolution of the considered system. Until plunge-in of the companion into the primary star, many orbits would have to be covered. The excellent angular momentum conservation of the moving-mesh code AREPO allows us to follow this evolution in principle, but the computational expense is prohibitive. The error in orbital energy introduced by placing the companion at 80% RL radius is on the order of one percent and therefore acceptable. Moreover, even in the chosen initial setup, it takes several orbits before the separation of the cores shrinks significantly. This leaves enough time for the stellar envelope to adjust to the modified effective potential after adding the companion.

In our simulations, we solved for full magnetohydrodynamics. Following Ohlmann et al. (2016b), the magnetic field of the RG star was initialized as dipole along the z -axis with 10^{-6} G at the pole. In our current treatise, however, we focus on the hydrodynamical evolution. The magnetic fields in our simulations are dynamically irrelevant and will be discussed in a forthcoming publication.

3. Results

In this section, we present the results of our 3D hydrodynamical CE simulations. All are based on the same initial MESA model for the RG primary star. Some general features of the dynamics are described in Sect. 3.1 based on a “reference simulation” with a companion mass of $M_2 = 0.08 M_{\odot}$. We then vary model parameters of the reference run independently: the spatial resolution around the core particles (Sect. 3.2) to test numerical convergence of the simulation and the EoS (Sect. 3.3) to investigate the effect of recombination energy release on envelope ejection. Based on the results of these runs, we carry out simulations, which explore the effect of the most important physical parameter of the systems under consideration – the mass of the companion – in a setup otherwise identical to the reference run (Sect. 3.4). Finally, we present a semi-analytic model that yields a new criterion for determining the lowest companion mass that is still capable of triggering envelope ejection (Sect. 3.5).

3.1. Reference simulation

For the reference run we choose a companion mass of $M_2 = 0.08 M_{\odot}$, implying a mass ratio of the companion to the primary star of $q \equiv M_2/M_1 = 0.01$. The companion is placed at a distance of $a_i = 164 R_{\odot}$ to the center of the RG (the initial period at the start of our simulation is $P_i = 329d$) and the OPAL EoS is applied. The companion spirals in, thereby ejecting a large fraction of the envelope. We follow this process in our simulation until $t = 955d$. At this point, we terminate the simulation because the time steps become prohibitively small to follow the further evolution. The reason for the decreasing time step is that we reduce the softening length around the core particles when they approach each other to avoid overlap. The number of grid cells per softening length is kept constant and, due to the CFL criterion (Courant et al. 1928), the time step must be reduced. During the complete run, the relative error amounts to 0.6% in the total energy and to 1.3% in angular momentum.

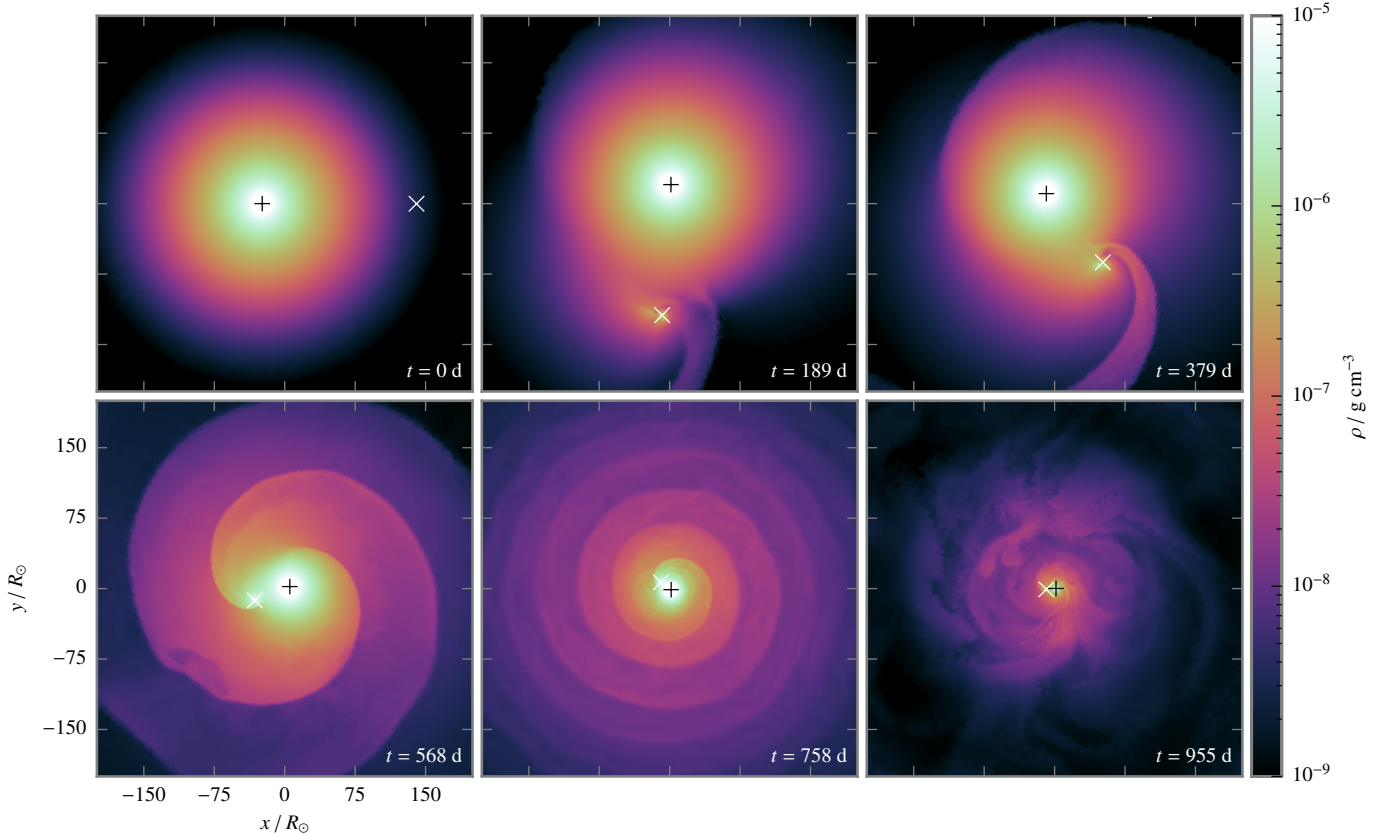


Fig. 2. Time series of density snapshots in the orbital plane at different times. The positions of the cores of the RG primary and the $0.08 M_{\odot}$ companion are marked by an \times and $+$ respectively. Each frame is centered on the center of mass of the binary system.

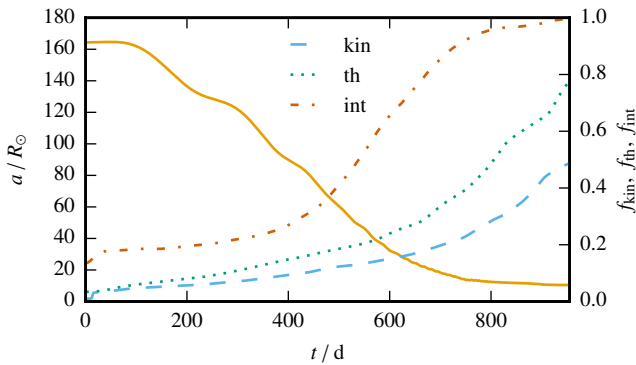


Fig. 3. Orbital separation a between companion and core of the RG over time t for a companion mass of $0.08 M_{\odot}$ (solid, left axis) and ejected mass fractions f according to the three criteria based on the kinetic (“kin”), thermal (“th”), and internal (“int”) energy as defined in the text (dashed, right axis).

In Fig. 2, density slices through the orbital plane at different times are shown. During the first orbit, the structure of the RG remains almost unperturbed. Between $t = 0$ d and $t \sim 189$ d, the companion accumulates mass in its wake and forms a tidal arm in the envelope material. The inspiral enters a faster phase and shear instabilities emerge at the edge of the tidal arm. From $t \sim 600$ d to $t \sim 750$ d, a layered structure emerges with shear instabilities between the adjacent layers. At the end of the simulation at $t = 955$ d, the initial structure of the RG is completely disrupted and a large fraction of the initial envelope has been removed.

In Fig. 3, we show the evolution of the orbital separation a . At $t = 161$ d, the rate of orbital decay \dot{a}/a surpasses 0.1 and thus initializes the phase of rapid inspiral, that stops at $t = 695$ d at an orbital separation of $a \approx 20 R_{\odot}$. The separation decreases at a slower rate until it reaches $a = 10.4 R_{\odot}$ at the end of the simulation.

The fraction of unbound mass is plotted as a function of time in Fig. 3. We apply three different criteria to determine if mass is unbound, all based on the energy budget of the envelope material: The “kinetic energy criterion” counts mass as unbound if $e_{\text{kin}} + e_{\text{pot}} > 0$, the “thermal energy criterion” if $e_{\text{kin}} + e_{\text{pot}} + e_{\text{th}} > 0$, and the “internal energy criterion” if $e_{\text{kin}} + e_{\text{pot}} + e_{\text{int}} > 0$, where e_{kin} , e_{pot} , e_{th} , and e_{int} denote the kinetic, the potential gravitational, the thermal, and the internal energy of the gas, respectively. The internal energy includes both the thermal and the ionization energy of the gas. These criteria provide different estimates of the unbound mass. We refer to the ratio of unbound mass to the initial envelope mass M_{env} under the respective criterion as f_{kin} , f_{th} , and f_{int} .

The kinetic energy criterion regards material as unbound only if its kinetic energy has overcome the gravitational binding energy. The other energy components, however, may ultimately be converted into kinetic energy and thus contribute to mass ejection, although this has not happened yet at the instant of measurement. The unbound mass fractions are still rising at the end of our simulation for both the kinetic and the thermal energy criteria. The orbital shrinkage has flattened out and thus orbital energy release ceases its contribution to envelope ejection. This shows that the conversion of thermal and ionization energy is still ongoing. Therefore, the kinetic energy criterion certainly underestimates the amount of material that can be

Table 1. Overview of the results of the resolution runs.

n_c	a_f/R_\odot	P_f/d	ΔE_{rel}	ΔJ_{rel}	f_{kin}	f_{th}	f_{int}	$N_f/10^6$
40	10.4	5.3	0.6%	1.1%	48.8%	77.8%	99.7%	2.95
30	10.7	5.4	0.5%	0.9%	49.8%	78.2%	99.2%	2.65
20	53.7	50.4	2.2%	0.8%	49.3%	71.2%	95.3%	2.32
10	110.5	174.5	2.9%	0.2%	71.2%	90.5%	99.8%	2.14

unbound and provides a conservative lower limit. The ionization energy criterion assumes that all energy released in recombination processes can be used for envelope ejection. It provides an optimistic upper limit for mass ejection, because some of the energy may be transported away by radiation and/or convection (Grichener et al. 2018; Sabach et al. 2017; Wilson & Nordhaus 2019, 2020). The unbound mass according to the thermal energy criterion is a compromise between these two limiting cases and we will use it as a fiducial value. The final verdict on unbound mass requires us to follow the evolution until envelope ejection stalls for the kinetic energy criterion when also including radiation and convection effects.

We attribute the initial small offset in Fig. 3 in the unbound mass for both the thermal and the internal energy criterion to a readjustment of the energy contributions when placing the core particle representing the companion onto the grid containing the relaxed progenitor star. During the inspiral, the unbound masses determined with the kinetic and the thermal energy criterion both increase at a low rate, that grows after the orbit is stabilized. This is expected, because the ionization energy of the gas is only converted into thermal and kinetic energy when the envelope has significantly expanded and cooled. Assuming that all of the ionization energy will be used eventually, we obtain a fraction of unbound mass of $f_{\text{int}} = 99.7\%$. The thermal energy criterion yields $f_{\text{th}} = 77.8\%$ of unbound gas and is still increasing steeply at the end of the run, because ionization energy is still being converted into thermal energy. This strongly suggests that further mass unbinding will take place. Consequently, even low-mass companions appear to suffice to completely unbind the envelope of the RG and form sdB systems.

3.2. Resolution study

For the CE dynamics, the transfer of orbital energy and angular momentum from the cores to envelope gas is critical. This proceeds around the cores. It is therefore necessary to sufficiently resolve the regions around the core particles in our simulations. As a test, we conduct a number of simulations with varying spatial resolution. The initial total number of cells in our simulation domain is approximately 2.4×10^6 . These parameters are applied to all simulations presented in this work. Using a special refinement criterion of AREPO, we vary the number of cells per softening length n_c around the core particles between 10 and 40 and compare the evolution of the system. Except for n_c , we use setups identical to the reference simulation of Sect. 3.1. We summarize the convergence test runs in Table 1. Because the refinement criterion produces additional grid cells around the core particles, the final total number of cells N_f in the simulation domain is larger by 37% for the highest-resolved run compared to that with the lowest resolution (see Table 1). This implies a growth in computational cost and for this reason the run with $n_c = 40$ terminates at $t = 955 d$, while the other three extend to $t = 1000 d$.

In the lower panel of Fig. 4, the orbital separation between the core particles is plotted over time. The final separations a_f

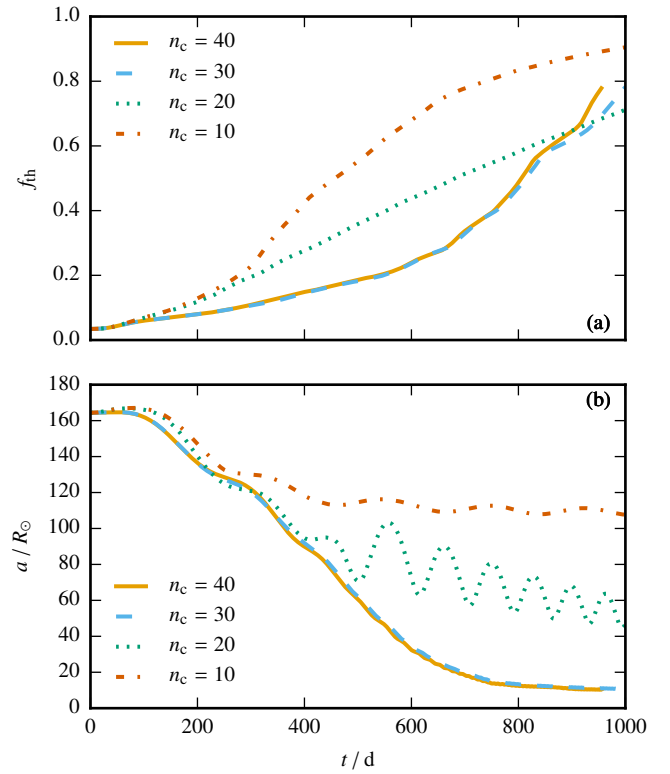


Fig. 4. Upper panel: fraction of unbound mass f_{th} under the thermal energy criterion over time. The legend denotes the imposed number of cells n_c per softening length. Lower panel: separation between the core particles is shown.

and periods P_f are given in Table 1. The results of the simulations with $n_c = 40$ and $n_c = 30$ and the two simulations with $n_c = 20$ and $n_c = 10$ are qualitatively and quantitatively different. Overall, the two highest-resolved simulations are similar in their orbital evolution. The values of the final unbound mass fractions according to the thermal energy criterion and also the final orbital parameters are very close. This indicates that they are numerically converged. Both 10 and 20 cells per softening length are insufficient to capture the orbital energy and angular momentum transfer between the companion and the surrounding cells, which results in incomplete inspirals. More mass is unbound earlier in the simulations with low resolution, probably due to under-resolved gravitational interaction of the core particles. This can lead to spurious velocities that inject kinetic energy. It is interesting to note that the lowest-resolved simulation shows the largest mass ejection. This emphasizes the danger of wrong conclusions drawn from under-resolved CE simulations and underlines the necessity of thorough convergence studies.

All simulations conserve angular momentum and total energy relatively well, which is a necessary prerequisite for

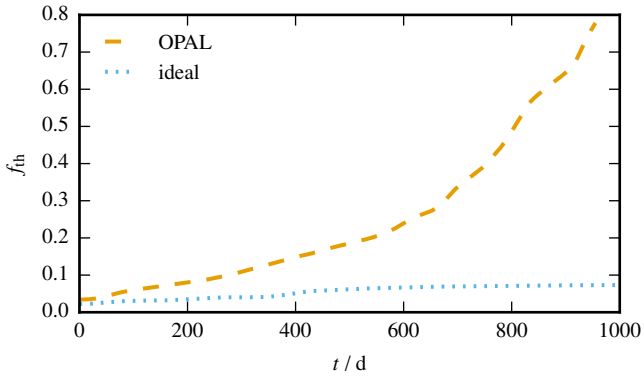


Fig. 5. Evolution of the fraction of the unbound mass f_{th} assuming the thermal energy criterion for simulations with different EoS.

meaningful physical results, but, as demonstrated here, not a guarantee for numerical convergence. Table 1 summarizes the relative energy errors $\Delta E_{\text{rel}} = \frac{1}{E_0}|E_0 - E_f|$, with E_0 and E_f denoting the initial and final values of total energy in our simulation domain, and the analogously defined relative errors in total angular momentum $\Delta J_{\text{rel}} = \frac{1}{J_0}|J_0 - J_f|$.

From our test simulations, it is clear that the gravitational softening length has to be resolved with at least 30 cells. To be on the safe side, we opt for the highest resolution with $n_c = 40$ in all simulations presented below. This ensures numerically converged results with favorable angular momentum and energy conservation.

3.3. The influence of ionization energy

To analyze the influence of recombination energy release on mass ejection, we repeat our reference run discussed in Sect. 3.1 with an ideal gas EoS thus ignoring ionization effects. We compare the results with our reference run, that employs the OPAL EoS and assumes local thermalization of recombination energy without cooling losses. Starting out from the same MESA model, the relaxation procedure outlined in Sect. 2.2 is repeated, but this time employing an ideal gas EoS. With the thus obtained RG star model, a binary system is set up adopting the same companion mass of $M_2 = 0.08 M_\odot$ and the same initial orbital parameters as in our reference simulation.

Figure 5 compares the evolution of unbound mass fraction according to the thermal energy criterion for both simulations. We reach a final value of $f_{\text{th}} = 77.8\%$ in the reference run accounting for ionization effects, and the value is still increasing at the end of the simulation. In contrast, very little mass is ejected when applying the ideal gas EoS. Here, only $f_{\text{th}} = 7.3\%$ are unbound at the end of the simulation and this fraction is hardly increasing any longer.

This clearly emphasizes the importance of ionization energy and recombination processes for the ejection of the envelope for the considered case with $M_2 = 0.08 M_\odot$. Companions of even lower masses can certainly not eject the envelope when only tapping the orbital energy reservoir. As mentioned above, recombination energy is released when the gas of the envelope has sufficiently expanded and cooled to allow for electron captures. This is reflected in the fact that the unbinding only starts when the inspiral is already well underway. Since the envelope of the progenitor RG is only weakly bound, even small perturbations by low-mass companions cause a significant release of ionization energy that can ultimately lead to a nearly complete unbinding.

Figure 6 illustrates the final state of the two simulations. Its Panel b shows a density slice through the orbital plane at the end of the simulation with the OPAL EoS where ionization energy is included. Comparing with the initial RG primary in panel a shows that outer envelope is largely lost and the low density of the remaining material exhibits an irregular pattern. In contrast, the envelope material of the RG for the run without ionization effects in panel c is notably less disrupted and smoother. The envelope has expanded (cf. panel a), but since ionization energy is not taken into account, no recombination energy can be released and only a small amount of mass is unbound.

3.4. Varying companion masses

To study the influence of the companion's mass on the envelope ejection, we conduct further simulations with identical setups as for the reference run in Sect. 3.1, but with lower M_2 (see Table 2). With its $0.08 M_\odot$, companion of the reference simulation marks the limit above which hydrogen burning ignites and the objects become true stars. With our parameter study, we map out the mass range of BDs down to the most massive giant planets with $M \lesssim 0.01 M_\odot$. Table 2 summarizes parameters of our simulations. For comparison, we also include our simulation with the ideal gas EoS. In all runs, relative error in energy stays below 1% and in angular momentum under 2%. We list the initial separations between the core particles a_i and the initial orbital periods P_i , as well as the corresponding values at the end of the respective simulations (a_f and P_f).

The top panel of Fig. 7 shows the evolution of the fraction of unbound mass f_{th} according to the thermal energy criterion. Higher companion masses cause stronger perturbation of the envelope and lead to increased mass ejection. However, for masses as low as $M_2 = 0.05 M_\odot$ ($q = 0.06$), 52.1% of the envelope become unbound under the thermal energy criterion until the end of our simulation. It is also clear that material is still being ejected from the system at this point. If we apply the internal energy criterion which also accounts for ionization energy, the fraction increases to $f_{\text{int}} = 98.1\%$ (see Table 2). The simulation with the lowest companion mass, however, shows a different picture (see upper panel of Fig. 7): the unbound mass according to the thermal energy criterion quickly reaches about 10% and then stagnates. Only 16.6% of the envelope mass is unbound at the end of the simulation. When employing the internal energy criterion, we find $f_{\text{int}} = 0.46$, implying that even if all available ionization energy is used, less than half of the envelope will eventually become unbound.

In the bottom panel of Fig. 7, the orbital separation between the core particles over time is plotted. While for the runs with the companion masses of $0.08 M_\odot$ and $0.05 M_\odot$ the separation between the core particles shows a qualitatively similar evolution, we see a distinct behavior for the companion with the lowest mass of $0.01 M_\odot$, where the orbital separation slowly but steadily decreases. These results indicate that around $M_2 = 0.03 M_\odot$ there is a companion mass threshold below which the dynamic interaction with the envelope is not strong enough to trigger significant envelope ejection (we discuss this further in Sect. 3.5).

This qualitatively different behavior can also be seen when comparing the density slices through the orbital plane at the end of the different simulations in Fig. 6. In panel a, the final state of the RG at the end of the relaxation run is given before placing the companion. As discussed above, a direct comparison of the relaxed model and the final state after the binary interaction

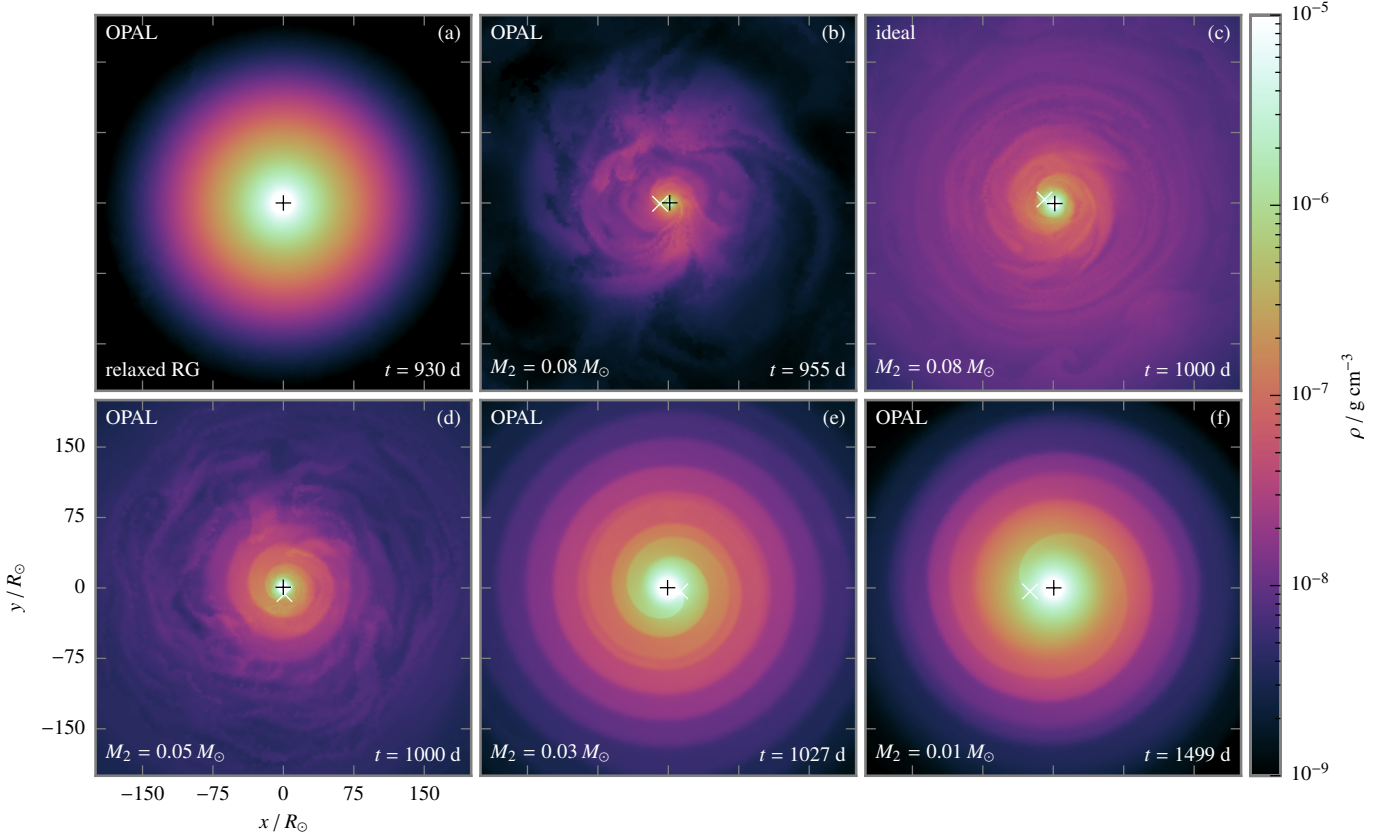


Fig. 6. Density snapshots in the orbital plane for different systems. *Panel a*: initial state of the primary RG star before a companion is added. Here, the time indicates that of the relaxation run. For the binary simulations in (*panels b–f*), the mass of the companion is given on the *bottom left* side of each panel, the time after adding the companion at the *bottom right* and the equation of state at the *top left*. The positions of the cores of the RG primary star and the companion are marked by an \times and $+$ respectively. Each frame is centered on the center of mass of the binary system.

Table 2. Overview of the simulation runs with different companion masses.

M_2/M_\odot	q	t_f/d	a_i/R_\odot	a_f/R_\odot	P_i/d	P_f/d	e_f	ΔE_{rel}	ΔJ_{rel}	f_{kin}	f_{th}	f_{int}	EoS
0.08	0.10	955.1	164.3	10.4	329.4	5.3	0.042	0.6%	1.1%	48.8%	77.8%	99.7%	OPAL
0.05	0.06	1000.0	154.7	7.5	309.3	3.2	0.033	0.2%	1.4%	28.6%	52.1%	98.1%	OPAL
0.03	0.04	1027.0	146.2	14.2	289.9	8.6	0.062	0.3%	1.5%	13.4%	21.8%	71.8%	OPAL
0.01	0.01	1500.0	133.4	12.4	257.9	7.4	0.032	0.6%	0.8%	13.5%	16.6%	46.3%	OPAL
0.08	0.10	1000.0	163.9	11.6	328.1	6.3	0.026	0.2%	1.7%	4.2%	7.3%	7.3%	ideal

with the $M_2 = 0.08 M_\odot$ ($q = 0.10$) companion makes the degree of perturbation of the envelope material apparent. Large scale instabilities have emerged and the smooth envelope is notably disrupted. The same can be observed for a companion mass of $M_2 = 0.05 M_\odot$ ($q = 0.06$), which is shown in panel d. However, the disruption in the inner part is not as strong and more material remains in the outer regions. This is not surprising considering the slower mass ejection in this case (see top panel of Fig. 7). As the unbound mass fraction f_{th} is still increasing and $f_{\text{int}} \approx 1$, this marks only a snapshot in an evolution that ultimately will lead to almost complete envelope removal. This is different for the two lower companion masses. Their density slices in panels e and f of Fig. 6 display a less perturbed envelope. While layered spiral structures have emerged, no large scale perturbations occur. For the companion mass of $M_2 = 0.03 M_\odot$ ($q = 0.04$), the radius of the star appears to have slightly expanded, but for $M_2 = 0.01 M_\odot$ ($q = 0.01$) the expansion is marginal if present at all (see Sect. 3.5).

3.5. Minimum mass for envelope ejection

We have seen from our simulations that lower-mass companions eject less mass (Table 2 and Fig. 7). Even more so, the runs with companion masses of $0.03 M_\odot$ and $0.01 M_\odot$ have envelope ejection fractions of $f_{\text{th}} \lesssim 20\%$ over the course of our computations. This suggests that there exist a minimum companion mass below which the envelope of the RGB star is not perturbed strongly enough to cause significant envelope ejection. To further illuminate this lower mass threshold qualitatively, we consider a companion of mass M_2 orbiting in the unperturbed envelope of our RGB star under the influence of a drag force (see also MacLeod & Ramirez-Ruiz 2015; MacLeod et al. 2017; Chamandy et al. 2019),

$$F_{\text{drag}} = \dot{M} v_{\text{rel}} = \pi R_a^2 \rho (v_{\text{rel}}^2 + c_s^2)^{1/2} v_{\text{rel}}. \quad (5)$$

In this equation, v_{rel} is the relative velocity of the companion with respect to the bulk rotational velocity of the RGB star's

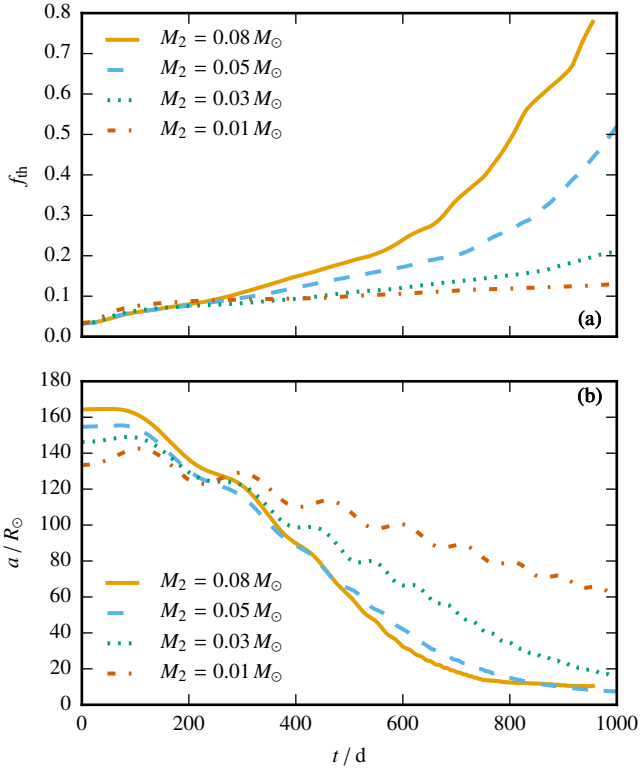


Fig. 7. Fraction of unbound mass f_{th} according to the thermal energy criterion and orbital separation a between the core particles over time for simulations with the indicated companion masses M_2 .

envelope, ρ and c_s are the local density and sound speed in the unperturbed RGB star, respectively, and R_a a mass-accretion radius that we approximate by Bondi–Hoyle–Littleton theory (Bondi & Hoyle 1944; Bondi 1952),

$$R_a = \frac{2GM_2}{v_{\text{rel}}^2 + c_s^2}. \quad (6)$$

We further multiply the drag force by a drag coefficient C_d such that we finally have

$$F_{\text{drag}} = C_d \frac{4\pi G^2 M_2^2 \rho v_{\text{rel}}}{(v_{\text{rel}}^2 + c_s^2)^{3/2}}. \quad (7)$$

We initially place the companion as in the AREPO runs (that is, at the same initial orbital separation with an initial velocity according to a Keplerian orbit) and assume that the RGB star’s envelope rotates as a solid body that is in 95% co-rotation with the companion’s initial orbit. We use the unperturbed envelope structure from the MESA model of the RGB star and then solve the equation of motion of the companion under the influence of the drag force in Eq. (7) with a fourth-order Runge–Kutta method. In this simplified model, the dynamical response of the envelope to the deposition of released orbital energy is neglected. The drag coefficient C_d is adjusted by hand such that the temporal evolution of the orbital separation is close to that found in the AREPO simulations (Fig. 8a).

The instantaneous energy injection into the RGB star’s envelope within this simplified model is $\dot{E}_{\text{drag}} = F_{\text{drag}} v_{\text{rel}}$. With this energy injection rate, we define a local inspiral time,

$$t_{\text{inspiral}} = \frac{\Delta E_{\text{orb}}}{\dot{E}_{\text{drag}}}, \quad (8)$$

where $\Delta E_{\text{orb}} = GM_1 M_2 / 2 (1/a_t - 1/a_i)$ is the absolute change of the orbital energy from the beginning to the current time (with a_t the current and a_i the initial orbital separation). In the following, we compare this inspiral time to the convective turn-over time,

$$t_{\text{conv}} = \frac{\alpha_{\text{mlt}} H_P}{v_{\text{conv}}}, \quad (9)$$

where $H_P = P/(g\rho)$ is the local pressure scale height with pressure P , density ρ , and gravitational acceleration g , v_{conv} is the velocity of convective eddies and α_{mlt} relates to the convective mixing efficiency within mixing-length theory ($\alpha_{\text{mlt}} = 2.0$ in our model). This is the relevant timescale in our problem, because convection dominates the energy transport in the envelope of the RGB star (photon diffusion only plays a role in the outermost envelope and the inspiral time is always faster than the photon diffusion time for separations $a \lesssim 140 R_\odot$).

This is of course only true if convection is still established despite a companion star perturbing the envelope by its inspiral. In the presence of rotational fluid motions, the Solberg–Høiland criterion can be used to assess convective stability (see, for instance, Kippenhahn et al. 2012). Ohlmann et al. (2016a) find in their CE simulation that convection is partly suppressed in the stirred-up envelope. Also in outflowing envelope material that is unbound and hence no longer in hydrostatic equilibrium, convection cannot occur. The following discussion is therefore only true if convection can still contribute to the energy transport in the perturbed RGB star’s envelope (see also Wilson & Nordhaus 2020).

We further define a local dynamic response number in the RGB star’s envelope,

$$R_d = \frac{\dot{E}_{\text{drag}} t_{\text{conv}}}{E_{\text{int}}}, \quad (10)$$

that compares the local energy injection over a convective turn-over time to the local internal energy of the gas in the envelope. The so defined dynamic response number is a measure to judge whether the envelope is expected to react dynamically, potentially leading to mass ejection. Energy, which is injected locally in the envelope, may be transported to the stellar surface by convection, where it can be radiated away. To trigger a dynamic response of the convective envelope, one has to

- inject energy faster than can be transported to the surface by convection and
- inject more energy than the local binding or equivalently internal energy of the gas (the unperturbed envelope is in virial equilibrium).

For $R_d \gg 1$, the energy injection into the RGB star’s envelope over a convective convective turn-over time because of the drag force acting on the companion is much larger than the local internal energy of the gas. Therefore, a dynamical response of the envelope is expected and this will likely lead to significant mass ejection. Conversely, for $R_d \lesssim 1$, the injected energy may simply be transported to the stellar surface by convection where it is lost by radiation. In this case, the envelope will not dynamically respond to orbital energy release and little or no envelope ejection is expected.

In Fig. 8b, we plot the dynamic response number and the ratio of the inspiral and convective turn-over timescale for companion masses of $0.05 M_\odot$, $0.03 M_\odot$, and $0.01 M_\odot$. The inspiral time is longer than the convective turn-over time in all cases, implying that convective energy transport is indeed relevant. Because $F_{\text{drag}} \propto M_2^2$, the inspiral time is longer for less massive companions and convection becomes more important in transporting away the locally injected energy. Moreover, the total

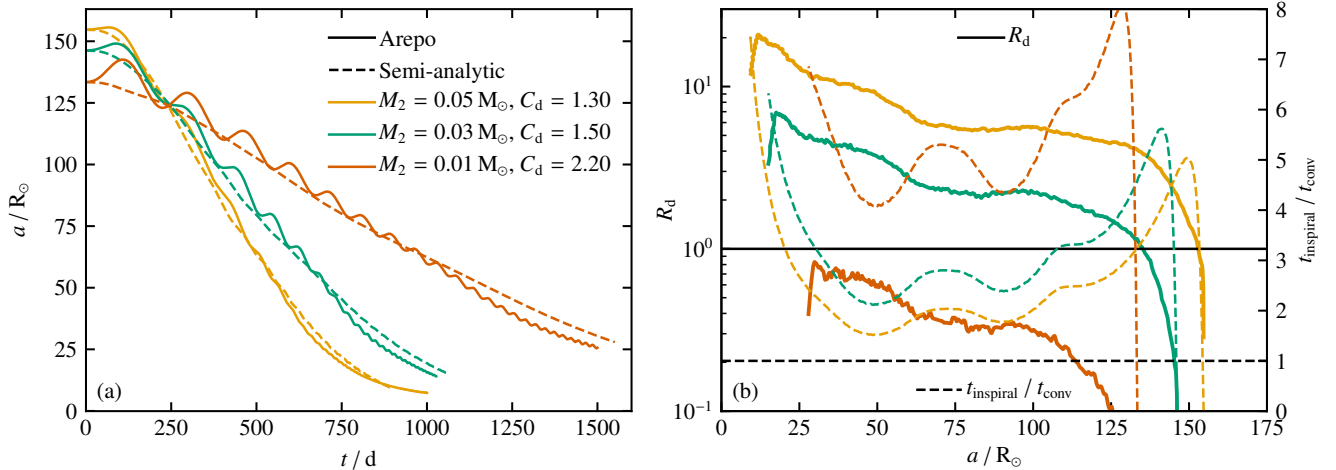


Fig. 8. Comparison of the evolution of the orbital separation of the various AREPO runs with the simplified drag model (*left panel a*), and the dynamic response number R_d and the local ratios of inspiral and convective turn-over time (*right panel b*). The evolution of the orbital separation of a $0.08 M_\odot$ companion is similar to that of the $0.05 M_\odot$ companion (Fig. 7) and therefore not shown here for clarity.

Table 3. Drag coefficient C_d , tidal & evaporation radii (r_{tid} , r_{eva}), and corresponding mass coordinates (m_{tid} , m_{eva}) from the semi-analytic models for the different companion masses M_2 .

M_2/M_\odot	C_d	r_{tid}/R_\odot	m_{tid}/M_\odot	r_{eva}/R_\odot	m_{eva}/M_\odot
0.08	0.95	0.04	0.4616	0.11	0.4622
0.05	1.30	0.05	0.4617	0.17	0.4625
0.03	1.50	0.05	0.4617	0.31	0.4628
0.01	2.20	0.06	0.4619	1.27	0.4638

injected energy, that is essentially the available orbital energy $E_{\text{orb}} \propto M_2$, is also smaller for less massive companions. These two aspects are reflected in the dynamic response number R_d in Fig. 8b: R_d is of order 5–10 for the $0.05 M_\odot$ companion, but only on the order of a few for $0.03 M_\odot$ and lower than 1 for $0.01 M_\odot$. This implies that a dynamic response and hence significant envelope ejection is expected for our $>0.05 M_\odot$ companions, while this is no longer the case for a $0.01 M_\odot$ companion. Our $0.03 M_\odot$ companion setup marks a marginal case.

During the CE phase, the inspiralling companion may be tidally disrupted and could evaporate. We compute the tidal disruption radius as $r_{\text{tid}} = R_2(\rho/\rho_2)^{1/3}$, where $R_2 = 0.1 R_\odot$ is the characteristic radius (Chabrier & Baraffe 2000) and ρ_2 is the average density of an inspiralling BD companion. The evaporation radius r_{eva} is defined as that radius where the sound speed of the ambient RGB star’s envelope equals the escape velocity from the inspiralling companion (for instance, Livio & Soker 1984; Soker 1998; Nelemans & Tauris 1998, but see also Jia & Spruit 2018 for an alternative criterion). The tidal disruption radius is always smaller than the radius at which evaporation is expected to become important (Table 3). The evaporation radius is larger in lower-mass companions and it is $1.3 R_\odot$ for $M_2 = 0.01 M_\odot$. In case there is no envelope ejection, we expect the companion to start evaporating before it may finally be tidally disrupted. Both, tidal disruption and evaporation would take place near the very bottom of the convective envelope at mass coordinates of 0.462 to $0.464 M_\odot$ such that the companion’s material is likely mixed throughout the convective envelope of the RGB star.

In summary, we find that for a number of arguments there is a lower mass threshold below which CE ejection becomes

impossible. Contrary to the estimates of Soker (1998) and Nelemans & Tauris (1998), however, this threshold is not determined by the evaporation of the companion, although this may also be its fate in our models (see Sect. 4.1). It is rather set by the ability of the companion to trigger a dynamical response of the envelope. In two different approaches – 3D hydrodynamic simulations and 1D semi-analytical modeling – we have explored the value of the threshold. It is important to note that both treatments capture somewhat different parts of the relevant physical processes: While our 3D hydrodynamical simulations account for the expansion of the envelope material because of the release of orbital energy, which is neglected in the semi-analytical treatment, they most likely do not fully resolve convection in the envelope. Both effects, however, are essential to determine the mass threshold, because for a successful envelope ejection, the above discussed conditions (i) and (ii) have to be met. On the one hand, our 3D hydrodynamic simulations determine the correct energy needed locally for mass unbinding, but it remains unclear whether released energy leads to a dynamic envelope expansion and mass ejection rather than being transported away by convection. The spiral structure seen in the simulations (see Figs. 2 and 6), however, question the persistence of initial global convective motions in this phase. On the other hand, our semi-analytic models fail to correctly determine the local binding energy of envelope material because it should have expanded in the inspiralling process – at least in the cases of more massive companions. We argue that in the case of low-mass companion, expansion will be inefficient and therefore our model (although not correctly describing CEE high companion masses) still provides a meaningful estimate of the mass threshold for envelope unbinding. The fact that both models predict the threshold to be somewhere around $0.03 M_\odot$ is reassuring and consequently this value marks our current best estimate for the mass threshold above which one can expect envelope ejection in a CE phase with our RGB star.

4. Discussion

4.1. Final fate

For companions of $M_2 \gtrsim 0.03 M_\odot$, the inspiral results in a strong dynamical response of the RGB star and we expect

mass ejection. For $M_2 \gtrsim 0.05 M_\odot$, almost the whole envelope (98.1%, Table 2) may be ejected if all of the available ionization energy at the end of the run can be employed in unbinding the envelope. For $M_2 \approx 0.03\text{--}0.05 M_\odot$, it seems that not the whole envelope can be ejected (for instance, we find $f_{\text{int}} = 71.8\%$ for $M_2 = 0.03 M_\odot$). The envelope ejection fractions are still increasing at the end of our simulations (Fig. 7), so the above companion mass ranges for which full and partial envelope ejection are expected will likely be shifted to lower values.

In case of full envelope ejection ($M_2 \gtrsim 0.05 M_\odot$), our final orbital separations appear to have converged. However, this is not to say that the orbit will not change anymore. For example, there is still matter inside the binary orbit at the end of our simulation that may affect the final orbital configuration. When this mass is lost from the inner binary, the orbit may widen or harden, depending on the specific angular momentum taken away by it. For example, if almost no specific angular momentum is removed (for instance in case of an outflow along the z -direction from the center of mass), the binary orbit may widen, because the mass loss reduces the gravitational attraction. If mass is lost with high specific angular momentum (perhaps via mass loss from the outer Lagrangian points), the orbit would shrink. Furthermore, if some high specific-angular-momentum material of the former envelope remains bound to the binary system, a circumbinary disk may form that could exert a torque on the inner binary and thereby lead to further orbital shrinkage and possibly eccentricity pumping (Artymowicz et al. 1991; Artymowicz & Lubow 1994; Kashi & Soker 2011; Dermine et al. 2013; Reichardt et al. 2019). If such a disk is massive enough and long lived, there could even be planet formation as has been suggested in the literature in other and similar situations (for instance, Podsiadlowski 1993; Perets et al. 2010; Beuermann et al. 2010; Völschow et al. 2014).

For partial envelope ejection ($M_2 \approx 0.03\text{--}0.05 M_\odot$), the RGB star will retain parts of its original envelope and other, high specific-angular-momentum parts may settle into a circumstellar disk. Retaining only a few percent of the original envelope mass is usually enough to maintain giant-star-like radii. As can be seen in our simulations, the dynamical drag on the companion is small at the end of our computations such that the orbital separation has settled to a final value (Fig. 7). From here on, the spiral-in slows down and we anticipate that the system enters a self-regulated phase where the released orbital energy may be transported to the stellar surface by turbulent convection and radiated away (see also Meyer & Meyer-Hofmeister 1979; Podsiadlowski 2001). The companion will then likely dissolve inside the envelope by evaporation rather than being tidally disrupted (Table 3). During the self-regulated CE phase, energy is continuously injected into the envelope of the RGB star, which can trigger pulsations and thereby help to eject the further envelope material (Clayton et al. 2017). Ultimately, this may lead to the full ejection of the envelope.

In case of no ($M_2 \lesssim 0.03 M_\odot$) and partial envelope ejection, the further evolution of the RGB star may be affected in various ways as studied by several authors and groups (see, for instance, Soker 1998; Siess & Livio 1999; Israelian et al. 2001; Stephan et al. 2020, and references therein):

- Orbital energy is injected into the RGB star and this additional energy will subsequently be radiated away during a phase in which the star regains thermal equilibrium. Such a transient will roughly last for a thermal timescale of that part of the envelope in which energy has been injected.

- Some fraction of the initial orbital angular momentum has been ingested into the RGB star such that it may rotate rapidly.
- In case of partial envelope ejection, the resulting star has an unusual core-envelope structure for its evolutionary stage. During core-helium burning as a horizontal-branch star, this peculiar structure may introduce features to the horizontal-branch morphology of stellar populations (see also D’Cruz et al. 1996).
- As discussed in Sect. 3.5, the companion likely evaporates inside the convective envelope such that its chemical constituents are mixed up to the surface of the RGB star. Moreover, the dissolution of BDs and planets may activate hot-bottom burning during which lithium can be produced and subsequently mixed to the stellar surface. Altogether, planet-eating stars may show unusual surface abundances.
- The rapid rotation of the convective envelope may boost a magnetic dynamo such that the star obtains a strong magnetic field and might show enhanced magnetic activity. Furthermore, during the CEE as well as main-sequence mergers, the magneto-rotational instability is found to amplify an initially weak seed magnetic field and thereby highly magnetizes the stellar envelope (Ohlmann et al. 2016b; Schneider et al. 2019). A dynamo operating in this convective envelope could then lead to an even stronger magnetic field than what may be expected otherwise from a convective dynamo in a rapidly rotating envelope (for instance Featherstone et al. 2009; Braithwaite & Spruit 2017). As mentioned above, our 3D magnetohydrodynamic simulations allow us to follow such effects and we will discuss them in a forthcoming publication.

4.2. Comparison to observations of sdB stars

Originally, our study is motivated by the strong evidence for low-mass companions of sdB stars found in observations. More specifically, the analysis of HW Vir systems shows that a significant fraction of sdBs are orbited by close companions in the mass regime of BDs (Schaffenroth et al. 2018). Geier et al. (2011) determine the companion mass of SDSS J082053.53+000843.4 to be between 0.045 and $0.068 M_\odot$. Moreover, SDSS J162256.66+473051.1 and V2008–1753 likely harbour BD companions with masses of $0.064 M_\odot$ and $0.069 M_\odot$, respectively (Schaffenroth et al. 2014, 2015). The mass of the close companion to AADor ($0.079 M_\odot$) is very close to the hydrogen-burning limit and it might therefore also be a massive BD (Vučković et al. 2016). Furthermore, Schaffenroth et al. (2014) report the discovery of two non-eclipsing sdB binaries with very small minimum masses for the companions. Both the cool companions of PHL 457 ($>0.027 M_\odot$) and CPD–64° 481 ($>0.048 M_\odot$) might be BDs. SdBs with BDs will eventually evolve to detached white dwarf systems with BD companions. Of such systems nine are known, seven of them with white dwarfs very close to the masses expected for sdB stars. Their companion masses fall into the range of 0.05 to $0.07 M_\odot$ (Casewell et al. 2018, and references therein). These systems might therefore have formed from the scenario we study in this work.

Our simulations show successful envelope ejection for systems with BD companions as indicated by the observations. Also, the lower mass limit determined here is supported by observations: Despite considerable effort no giant planet has so far been identified in close orbit around a hot sdB star yet (Schaffenroth et al. 2019; Casewell et al. 2018). However, there may be a bias because the lowest-mass companions are

expected at longer periods of about 0.3 d. Otherwise, the companion would exceed its Roche lobe leading to mass transfer onto the primary (see Fig. 14 of Schaffenroth et al. 2019). Such long-period systems are harder to follow up and only few of them have been investigated until now.

Despite the success of our simulations to reproduce the formation scenario inferred from observations, the resulting systems do not match the observed orbital separations of about $0.4 R_{\odot}$ to $1.3 R_{\odot}$ (see Casewell et al. 2018, and references therein; Schaffenroth et al. 2018). Our simulations yield final orbital separations between the cores that are larger by a factor of ~ 10 . This points to physical processes impacting the final separations that are not accounted for in our simulations, such as energy loss by convection (Wilson & Nordhaus 2020) or mass loss of the companion by continuous evaporation during the inspiral. It is also possible that the resulting systems form a circumbinary disk on timescales longer than those followed in our simulations, that interacts with the inner binary changing its orbital parameters. Another possibility is that higher-mass RG primaries lead to a deeper spiral-in of the companion. Whether this can account for the observed difference has to be tested in simulations.

5. Conclusion

In numerical and semi-analytical approaches, we address the question under which conditions sdB stars can form from stars at the tip of the RGB when interacting with low-mass companions. Observations of eclipsing close binary systems consisting of sdB and cool low-mass companions (HW Vir type systems, see Schaffenroth et al. 2019, and references therein) indicate that such a formation channel is indeed realized in nature.

Based on 3D hydrodynamic simulations of CEE, we show that envelope ejection in such systems is possible even with companions in the mass range of BD – provided that the ionization energy released when the envelope expands is thermalized locally and supports gravitational unbinding of the material. This limit is tested in our simulations as well as a model where no ionization energy is used, in which case little envelope material is expelled. The question of whether recombination energy can significantly increase mass ejection compared to cases where mass loss is powered by the release of orbital energy only has been discussed controversially by Grichener et al. (2018), but see Ivanova (2018). They, however, refer to systems that differ from those under consideration here. Recent 3D hydrodynamic simulations of CEE with asymptotic-giant branch primary stars (Sand et al. 2020) suggest that in this case the majority of recombination energy is indeed released in optically thick regions and contributes to envelope removal. Although this ultimately has to be confirmed in simulations accounting for radiative transport, the situation is even more favorable for the systems considered here: Low-mass companions lead to less efficient expansion of the envelope so that if the necessary conditions are reached for recombination, it will be in rather dense and optically thick regions. This strongly suggests that trapping of released ionization energy is a realistic assumption.

Determining the lowest companion mass admissible for successful envelope ejection is a fundamental problem of CEE modeling. A safe upper limit is that sufficient orbital energy is deposited in the envelope to overcome its binding energy. Hydrodynamical simulations show that this is usually prevented by envelope expansion inhibiting energy transfer by tidal drag before significant amounts of material are expelled. We confirm this for our specific setup. The envelope expansion,

however, leads to the release of ionization energy that can further unbind envelope material. Therefore, we suggest as a lower limit for successful envelope ejection a companion mass that triggers a dynamical response of the stellar envelope. Combining the findings of our 3D hydrodynamic CE simulations with a semi-analytic model, we conclude that in our setup this is the case for companions with more than about $0.03 M_{\odot}$. This suggests that for giant planets as companions the formation of sdB stars in CE episodes with stars at the tip of the RGB is difficult to achieve. Our result is consistent with currently available observations of sdB stars with low-mass companions. A failure to eject the envelope may lead to recurrent CE episodes eventually removing the envelope, the formation of a circumbinary disk, or an evaporation of the companion inside the envelope with several implications for observables of the remaining RGB star.

The exact threshold, however, is likely to also depend on the mass of the primary star: for higher primary masses, more envelope material needs to be lifted, which may require a larger companion mass. This has to be explored in future simulations. Another effect that has not been accounted for in our models but may alter the threshold is a potential mass gain or loss of the companion due to accretion or ablation when spiralling into the envelope. Although we find that complete evaporation is not the key to determine the lowest companion mass for successful envelope ejection, it may be a continuous process that changes the companion mass in the evolution.

The final orbital separation remains an open question. Compared with observations, our simulations predict values that are larger by a factor of about 10. This may imply that the observed systems had more massive RG primaries than assumed in our simulation. It could, however, also imply that physical processes are important for determining the orbital parameters of the resulting system which our current simulations do not account for.


Acknowledgements. The work of MK, FS, and FKR is supported by the Klaus Tschira Foundation. SG and VS are partly supported by the Deutsche Forschungsgemeinschaft (DFG) through grant GE 2506/9-1. We thank Orsola De Marco, Noam Soker and our referee for their helpful comments.

References

- Artymowicz, P., & Lubow, S. H. 1994, *ApJ*, **421**, 651
- Artymowicz, P., Clarke, C. J., Lubow, S. H., & Pringle, J. E. 1991, *ApJ*, **370**, L35
- Beuermann, K., Hessman, F. V., Dreizler, S., et al. 2010, *A&A*, **521**, L60
- Bondi, H. 1952, *MNRAS*, **112**, 195
- Bondi, H., & Hoyle, F. 1944, *MNRAS*, **104**, 273
- Braithwaite, J., & Spruit, H. C. 2017, *R. Soc. Open Sci.*, **4**, 160271
- Casewell, S. L., Braker, I. P., Parsons, S. G., et al. 2018, *MNRAS*, **476**, 1405
- Chabrier, G., & Baraffe, I. 2000, *ARA&A*, **38**, 337
- Chamandy, L., Blackman, E. G., Frank, A., et al. 2019, *MNRAS*, **490**, 3727
- Clayton, M., Podsiadlowski, P., Ivanova, N., & Justham, S. 2017, *MNRAS*, **470**, 1788
- Courant, R., Friedrichs, K. O., & Lewy, H. 1928, *Math. Ann.*, **100**, 32
- D’Cruz, N. L., Dorman, B., Rood, R. T., & O’Connell, R. W. 1996, *ApJ*, **466**, 359
- Dermine, T., Izzard, R. G., Jorissen, A., & Van Winckel, H. 2013, *A&A*, **551**, A50
- Duchêne, G., & Kraus, A. 2013, *ARA&A*, **51**, 269
- Featherstone, N. A., Browning, M. K., Brun, A. S., & Toomre, J. 2009, *ApJ*, **705**, 1000
- Geier, S., Classen, L., & Heber, U. 2011, *ApJ*, **733**, L13
- Grichener, A., Sabach, E., & Soker, N. 2018, *MNRAS*, **478**, 1818
- Han, Z., Podsiadlowski, P., Maxted, P. F. L., Marsh, T. R., & Ivanova, N. 2002, *MNRAS*, **336**, 449
- Han, Z., Podsiadlowski, P., Maxted, P. F. L., & Marsh, T. R. 2003, *MNRAS*, **341**, 669
- Heber, U. 1986, *A&A*, **155**, 33
- Israelian, G., Santos, N. C., Mayor, M., & Rebolo, R. 2001, *Nature*, **411**, 163

- Ivanova, N. 2018, [ApJ](#), **858**, L24
- Ivanova, N., Justham, S., Chen, X., et al. 2013, [A&ARv](#), **21**, 59
- Jia, S., & Spruit, H. C. 2018, [ApJ](#), **864**, 169
- Kashi, A., & Soker, N. 2011, [MNRAS](#), **417**, 1466
- Kippenhahn, R., Weigert, A., & Weiss, A. 2012, [Stellar Structure and Evolution](#) (Berlin Heidelberg: Springer-Verlag)
- Livio, M., & Soker, N. 1984, [MNRAS](#), **208**, 763
- MacLeod, M., & Ramirez-Ruiz, E. 2015, [ApJ](#), **803**, 41
- MacLeod, M., Antoni, A., Murguía-Berthier, A., Macías, P., & Ramirez-Ruiz, E. 2017, [ApJ](#), **838**, 56
- Maxted, P. F. L., Heber, U., Marsh, T. R., & North, R. C. 2001, [MNRAS](#), **326**, 1391
- Meyer, F., & Meyer-Hofmeister, E. 1979, [A&A](#), **78**, 167
- Moe, M., & Di Stefano, R. 2017, [ApJS](#), **230**, 15
- Nandez, J. L. A., & Ivanova, N. 2016, [MNRAS](#), **460**, 3992
- Nandez, J. L. A., Ivanova, N., & Lombardi, J. C. 2015, [MNRAS](#), **450**, L39
- Nelemans, G., & Tauris, T. M. 1998, [A&A](#), **335**, L85
- Ohlmann, S. T., Röpke, F. K., Pakmor, R., & Springel, V. 2016a, [ApJ](#), **816**, L9
- Ohlmann, S. T., Röpke, F. K., Pakmor, R., Springel, V., & Müller, E. 2016b, [MNRAS](#), **462**, L121
- Ohlmann, S. T., Röpke, F. K., Pakmor, R., & Springel, V. 2017, [A&A](#), **599**, A5
- Paczyński, B. 1976, in *Structure and Evolution of Close Binary Systems*, eds. P. Eggleton, S. Mitton, & J. Whelan, [IAU Symp.](#), **73**, 75
- Pakmor, R., & Springel, V. 2013, [MNRAS](#), **432**, 176
- Pakmor, R., Bauer, A., & Springel, V. 2011, [MNRAS](#), **418**, 1392
- Passy, J.-C., De Marco, O., Fryer, C. L., et al. 2012, [ApJ](#), **744**, 52
- Paxton, B., Cantiello, M., Arras, P., et al. 2013, [ApJS](#), **208**, 4
- Paxton, B., Marchant, P., Schwab, J., et al. 2015, [ApJS](#), **220**, 15
- Perets, H. B., Gal-Yam, A., Mazzali, P. A., et al. 2010, [Nature](#), **465**, 322
- Podsiadlowski, P. 1993, in *Planets Around Pulsars*, eds. J. A. Phillips, S. E. Thorsett, & S. R. Kulkarni, [ASP Conf. Ser.](#), **36**, 149
- Podsiadlowski, P. 2001, in *Evolution of Binary and Multiple Star Systems*, eds. P. Podsiadlowski, S. Rappaport, A. R. King, F. D'Antona, & L. Burderi, [ASP Conf. Ser.](#), **229**, 239
- Prust, L. J., & Chang, P. 2019, [MNRAS](#), **486**, 5809
- Reichardt, T. A., De Marco, O., Iaconi, R., Tout, C. A., & Price, D. J. 2019, [MNRAS](#), **484**, 631
- Reichardt, T. A., De Marco, O., Iaconi, R., Chamandy, L., & Price, D. J. 2020, [MNRAS](#), **494**, 5333
- Ricker, P. M., & Taam, R. E. 2012, [ApJ](#), **746**, 74
- Rogers, F. J., & Nayfonov, A. 2002, [ApJ](#), **576**, 1064
- Rogers, F. J., Swenson, F. J., & Iglesias, C. A. 1996, [ApJ](#), **456**, 902
- Sabach, E., Hillel, S., Schreier, R., & Soker, N. 2017, [MNRAS](#), **472**, 4361
- Sand, C., Ohlmann, S. T., Schneider, F. R. N., Pakmor, R., & Roepke, F. K. 2020, [ApJ](#), submitted [arXiv:2007.11000]
- Schaffenroth, V., Classen, L., Nagel, K., et al. 2014, [A&A](#), **570**, A70
- Schaffenroth, V., Barlow, B. N., Drechsel, H., & Dunlap, B. H. 2015, [A&A](#), **576**, A123
- Schaffenroth, V., Geier, S., Heber, U., et al. 2018, [A&A](#), **614**, A77
- Schaffenroth, V., Barlow, B. N., Geier, S., et al. 2019, [A&A](#), **630**, A80
- Schneider, F. R. N., Ohlmann, S. T., Podsiadlowski, P., et al. 2019, [Nature](#), **574**, 211
- Siess, L., & Livio, M. 1999, [MNRAS](#), **308**, 1133
- Soker, N. 1998, [AJ](#), **116**, 1308
- Springel, V. 2010, [MNRAS](#), **401**, 791
- Stephan, A. P., Naoz, S., Gaudi, B. S., & Salas, J. M. 2020, [ApJ](#), **889**, 45
- Völschow, M., Banerjee, R., & Hessman, F. V. 2014, [A&A](#), **562**, A19
- Vučković, M., Østensen, R. H., Németh, P., Bloemen, S., & Pápics, P. I. 2016, [A&A](#), **586**, A146
- Wilson, E. C., & Nordhaus, J. 2019, [MNRAS](#), **485**, 4492
- Wilson, E. C., & Nordhaus, J. 2020, [MNRAS](#), **497**, 1895

A quantitative in-depth analysis of the prototype sdB+BD system SDSS J08205+0008 revisited in the *Gaia* era

V. Schaffenroth,¹★ S. L. Casewell,² D. Schneider,³ D. Kilkeny,⁴ S. Geier,¹ U. Heber,³ A. Irrgang,³ N. Przybilla,⁵ T. R. Marsh,⁶ S. P. Littlefair⁷ and V. S. Dhillon⁸ 

¹*Institute for Physics and Astronomy, University of Potsdam, Karl-Liebknecht-Str. 24/25, D-14476 Potsdam, Germany*

²*Department of Physics and Astronomy, University of Leicester, University Road, Leicester LE1 7RH, UK*

³*Dr. Karl Remeis-Observatory and ECAP, Astronomical Institute, Friedrich-Alexander-University Erlangen-Nuremberg, Sternwartstr. 7, D-96049 Bamberg, Germany*

⁴*Department of Physics and Astronomy, University of the Western Cape, Private Bag X17, Bellville 7535, South Africa*

⁵*Institut für Astro- und Teilchenphysik, Universität Innsbruck, Technikerstrasse 25, 6020, Innsbruck, Austria*

⁶*Department of Physics, University of Warwick, Gibbet Hill Road, Coventry CV4 7AL, UK*

⁷*Department of Physics and Astronomy, University of Sheffield, Sheffield S3 7RH, UK*

⁸*Instituto de Astrofísica de Canarias (IAC), E-38200 La Laguna, Tenerife, Spain*

Accepted 2020 November 19. Received 2020 November 19; in original form 2020 August 4

ABSTRACT

Subdwarf B stars are core-helium-burning stars located on the extreme horizontal branch (EHB). Extensive mass loss on the red giant branch is necessary to form them. It has been proposed that substellar companions could lead to the required mass loss when they are engulfed in the envelope of the red giant star. J08205+0008 was the first example of a hot subdwarf star with a close, substellar companion candidate to be found. Here, we perform an in-depth re-analysis of this important system with much higher quality data allowing additional analysis methods. From the higher resolution spectra obtained with ESO-VLT/XSHOOTER, we derive the chemical abundances of the hot subdwarf as well as its rotational velocity. Using the *Gaia* parallax and a fit to the spectral energy distribution in the secondary eclipse, tight constraints to the radius of the hot subdwarf are derived. From a long-term photometric campaign, we detected a significant period decrease of $-3.2(8) \times 10^{-12} \text{ dd}^{-1}$. This can be explained by the non-synchronized hot subdwarf star being spun up by tidal interactions forcing it to become synchronized. From the rate of period decrease we could derive the synchronization time-scale to be 4 Myr, much smaller than the lifetime on EHB. By combining all different methods, we could constrain the hot subdwarf to a mass of $0.39\text{--}0.50 M_{\odot}$ and a radius of $R_{\text{sdb}} = 0.194 \pm 0.008 R_{\odot}$, and the companion to $0.061\text{--}0.071 M_{\odot}$ with a radius of $R_{\text{comp}} = 0.092 \pm 0.005 R_{\odot}$, below the hydrogen-burning limit. We therefore confirm that the companion is most likely a massive brown dwarf.

Key words: stars: abundances – stars: atmospheres – stars: fundamental parameters – stars: horizontal branch – stars: low-mass – subdwarfs .

1 INTRODUCTION

Subluminous B stars (subdwarf B stars or sdBs) are stars with thin hydrogen envelopes, currently undergoing helium-core burning, which are found on the extreme horizontal branch (EHB). Their masses were determined to be around $0.47 M_{\odot}$ (Heber 2009, 2016). About half of the known single-lined sdB stars are found to be members of short-period binaries ($P \lesssim 30$ d, most even with $P \lesssim 10$ d, Maxted et al. 2001; Napiwotzki et al. 2004a; Kupfer et al. 2015). A large mass loss on the red giant branch (RGB) is required to form these stars, which can be caused by mass transfer to the companion, either via stable Roche lobe overflow or the formation and eventual ejection of a common envelope (Han et al. 2002, 2003). For the existence of apparently single sdB stars binary evolution might play an important role as well, as such stars could

be remnants of helium white dwarf (WD) mergers (Webbink 1984; Iben & Tutukov 1984) or from engulfing a substellar object, which might get destroyed in the process (Soker 1998; Nelemans & Tauris 1998).

Eclipsing sdB+dM binaries (HW Vir systems) having short orbital periods (0.05–1 d) and low companion masses between 0.06 and $0.2 M_{\odot}$ (see Schaffenroth et al. 2018, 2019, for a summary of all known HW Vir systems) have been known for decades (Menzies & Marang 1986) and illustrate that objects close to the nuclear-burning limit of $\sim 0.070\text{--}0.076 M_{\odot}$ for an object of solar metallicity and up to $0.09 M_{\odot}$ for metal-poor objects (see Dieterich et al. 2014, for a review) can eject a common envelope and lead to the formation of an sdB. The light traveltime technique was used to detect substellar companion candidates to sdB stars (e.g. Beuermann et al. 2012; Kilkeny & Koen 2012, and references therein). However, in these systems the substellar companions have wide orbits and therefore cannot have influenced the evolution of the host star.

* E-mail: schaffenroth@astro.physik.uni-potsdam.de

The short-period eclipsing HW Vir type binary SDSS J082053.53+000843.4, hereafter J08205+0008, was discovered as part of the MUCHFUSS project (Geier et al. 2011a, b). Geier et al. (2011c) derived an orbital solution based on time-resolved medium resolution spectra from Sloan Digital Sky Survey (SDSS) (Abazajian et al. 2009) and ESO-NTT/EFOSC2. The best-fitting orbital period was $P_{\text{orb}} = P = 0.096 \pm 0.001$ d and the radial velocity (RV) semi-amplitude $K = 47.4 \pm 1.9$ km s⁻¹ of the sdB. An analysis of a light curve taken with Merope on the Mercator telescope allowed them to constrain the inclination of the system to $85.8^\circ \pm 0.16$.

The analysis resulted in two different possible solutions for the fundamental parameters of the sdB and the companion. As the sdB sits on the EHB the most likely solution is a core-He-burning object with a mass close to the canonical mass for the He flash of $0.47 M_\odot$. Population synthesis models (Han et al. 2002, 2003) predict a mass range of $M_{\text{sdB}} = 0.37\text{--}0.48 M_\odot$, which is confirmed by asteroseismological measurements (Fontaine et al. 2012). A more massive ($2\text{--}3 M_\odot$) progenitor star would ignite the He core under non-degenerate conditions and lower masses down to $0.3 M_\odot$ are possible. Due to the shorter lifetime of the progenitors such lower mass hot subdwarfs would also be younger. Higher masses for the sdB were ruled out as contemporary theory did not predict that. By a combined analysis of the spectrum and the light curve, the companion was derived to have a mass of $0.068 \pm 0.003 M_\odot$. However, the derived companion radius for this solution was significantly larger than predicted by theory.

The second solution that was consistent with the atmospheric parameters was a post-RGB star with an even lower mass of only $0.25 M_\odot$. Such an object can be formed whenever the evolution of the star on the RGB is interrupted due to the ejection of a common envelope before the stellar core mass reaches the mass, which is required for helium ignition. Those post-RGB stars, also called prehelium WDs, cross the EHB and evolve directly to WDs. In this case, the companion was determined to have a mass of $0.045 \pm 0.003 M_\odot$ and the radius was perfectly consistent with theoretical predictions.

The discovery of J08205+0008 was followed by the discovery of two more eclipsing systems with brown dwarf (BD) companions, J162256+473051 (Schaffenroth et al. 2014a) and V2008–1753 (Schaffenroth et al. 2015), both with periods of less than 2 h. Two non-eclipsing systems were also discovered by Schaffenroth et al. (2014b), and a subsequent analysis of a larger population of 26 candidate binary systems by Schaffenroth et al. (2018) suggests that the fraction of sdB stars with close substellar companions is as high as 3 per cent, much higher than the 0.5 ± 0.3 per cent that is estimated for BD companions to WDs (e.g. Steele et al. 2011). Seven of the nine known WD–BD systems have primary masses within the mass range for an He-core-burning hot subdwarf and might therefore have evolved through this phase before.

In this paper, we present new phase-resolved spectra of J08205+0008 obtained with ESO-VLT/UVES and XSHOOTER and high cadence light curves with ESO-NTT/ULTRACAM (ULTRAFast CAMera). Combining these data sets, we have refined the RV solution and light-curve fit. We performed an in-depth analysis of the sdB atmosphere and a fit of the spectral energy distribution (SED) using the ULTRACAM secondary eclipse measurements to better constrain the radius and mass of the sdB primary and the companion. We also present our photometric campaign using the South African Astronomical Observatory (SAAO)/1-m telescope and Bonn University Simultaneous CAMera (BUSCA) mounted at the Calar Alto/2.2m telescope which has been underway for more than 10 yr now, and which has allowed us to derive variations of the orbital period.

2 SPECTROSCOPIC AND PHOTOMETRIC DATA

2.1 UVES spectroscopy

We obtained time-resolved, high-resolution ($R \simeq 40\,000$) spectroscopy of J08205+0008 with ESO-VLT/UVES (Dekker et al. 2000) on the night of 2011 April 05 as part of program 087.D-0185(A). In total 33 single spectra with exposure times of 300 s were taken consecutively to cover the whole orbit of the binary. We used the 1 arcsec slit in seeing of ~ 1 arcsec and airmass ranging from 1.1 to 1.5. The spectra were taken using cross dispersers CD nos 2 and 3 on the blue and red chips, respectively, to cover a wavelength range from 3300 to 6600 Å with two small gaps ($\simeq 100$ Å) at 4600 and 5600 Å.

The data reduction was done with the UVES reduction pipeline in the MIDAS package (Banse et al. 1983). In order to ensure an accurate normalization of the spectra, two spectra of the DQ-type white dwarf WD 0806–661 were also taken (Subasavage et al. 2009). Since the optical spectrum of this carbon-rich WD is featureless, we divided our data by the co-added and smoothed spectrum of this star.

The individual spectra of J08205+0008 were then RV corrected using the derived RV of the individual spectra as described in Section 3.6 and co-added for the atmospheric analysis. In this way, we increased the signal-to-noise ratio to $S/N \sim 90$, which was essential for the subsequent quantitative analysis.

2.2 XSHOOTER spectroscopy

We obtained time resolved spectra of J08205+0008 with ESO-VLT/XSHOOTER (Vernet et al. 2011) as part of programme 098.C-0754(A). The data were observed on the night of 2017 February 17 with 300 s exposure times in nod mode and in seeing of 0.5–0.8 arcsec. We obtained 24 spectra covering the whole orbital phase (see Fig. B1) in each of the UVB ($R \sim 5400$), VIS ($R \sim 8900$), and NIR ($R \sim 5600$) arms with the 0.9–1.0 arcsec slits. The spectra were reduced using the ESO REFLEX package (Freudling et al. 2013) and the specific XSHOOTER routines in nod mode for the NIR arm, and in stare mode for the UVB and VIS arms.

To correct the astronomical observations for atmospheric absorption features in the VIS and NIR arms, we did not require any observations of telluric standard stars, as we used the MOLECFIT software, which is based on fitting synthetic transmission spectra calculated by a radiative transfer code to the astronomical data (Smette et al. 2015; Kausch et al. 2015). The parameter set-up (fitted molecules, relative molecular column densities, degree of polynomial for the continuum fit, etc.) for the telluric absorption correction evaluation of the NIR-arm spectra were used according to table 3 of Kausch et al. (2015). Unfortunately, the NIR arm spectra could not be used after the telluric corrections since the S/N ratio and the fluxes are too low. Fig. A1 shows an example comparison between the original and the telluric absorption corrected XSHOOTER VIS arm spectra. The quality of the telluric correction is sufficient to allow us to make use of the hydrogen Paschen series for the quantitative spectral analysis.

Accurate RV measurements for the single XSHOOTER spectra were performed within the analysis program SPAS (Spectral Analysis Software) (Hirsch 2009), whereby selected sharp metal lines listed in Table D1 were used. We used a combination of Lorentzian, Gaussian, and straight line (in order to model the slope of the continuum) function to fit the line profiles of the selected absorption lines. After having corrected all single spectra by the averaged RVs, a co-added spectrum was created in order to achieve $S/N \sim 460/260$ in the UVB and VIS channels, respectively.

The co-added spectrum then was normalized also within SPAS. Numerous anchor points were set where the stellar continuum to be normalized was assumed. In this way, the continuum was approximated by a spline function. To obtain the normalized spectrum, the original spectrum was divided by the spline.

2.3 ULTRACAM photometry

Light curves in the SDSS $u'g'r'$ filters were obtained simultaneously using the ULTRACAM instrument (Dhillon et al. 2007) on the 3.5-m-ESO-NTT at La Silla. The photometry was taken on the night of 2017 March 19 with airmass 1.15–1.28 as part of programme 098.D-679 (PI: Schaffenroth). The data were taken in full frame mode with 1×1 binning and the slow readout speed with exposure times of 5.75 s resulting in 1755 frames obtained over the full orbit of the system. The dead-time between each exposure was only 25 ms. We reduced the data using the HiperCam pipeline (<http://deneb.astro.warwick.ac.uk/phsaap/hipercam/docs/html>). The flux of the sources was determined using aperture photometry with an aperture scaled variably according to the full width at half-maximum. The flux relative to a comparison star within the field of view (08:20:51.941 +00:08:21.64) was determined to account for any variations in observing conditions. This reference star has SDSS magnitudes of $u' = 15.014 \pm 0.004$, $g' = 13.868 \pm 0.003$, and $r' = 13.552 \pm 0.003$ which were used to provide an absolute calibration for the light curve.

2.4 SAAO photometry

All the photometry was obtained on the 1-m (Elizabeth) telescope at the Sutherland site of the SAAO. Nearly all observations were made with the STE3 CCD, except for the last two (Table G1), which were made with the STE4 camera. The two cameras are very similar with the only difference being the pixel size as the STE3 is 512×512 pixels in size and the STE4 is 1024×1024 . We used a 2×2 pre-binned mode for each CCD resulting in a read-out time of around 5 and 20 s, respectively, so that with typical exposure times around 10–12s, the time resolution of STE4 is only about half as good as STE3. Data reduction and eclipse analysis were carried out as outlined in Kilkeny (2011); in the case of J08205+008, there are several useful comparison stars, even in the STE3 field, and – given that efforts were made to observe eclipses near the meridian – usually there were no obvious ‘drifts’ caused by differential extinction effects. In the few cases where such trends were seen, these were removed with a linear fit to the data from just before ingress and just after egress. The stability of the procedures (and the SAAO time system over a long time base) is demonstrated by the constant-period system AA Dor (fig. 1 of Kilkeny 2014) and by the intercomparisons in fig. 8 of Baran et al. (2018), for example.

2.5 BUSCA photometry

Photometric follow-up data were also taken with the BUSCA (see Reif et al. 1999), which is mounted to the 2.2-m telescope located at the Calar Alto Observatory in Spain. This instrument observes in four bands simultaneously giving a very accurate eclipse measurement and good estimate of the errors. The four different bands we used in our observation are given solely by the intrinsic transmission curve given by the beam splitters (UB, BB, RB, IB, <http://www.caha.es/CAHA/Instruments/BUSCA/bands.txt>) and the efficiency of the CCDs, as no filters were used to ensure that all the visible light is used most efficiently.

The data were taken during one run on 2011 February 25 and March 1. We used an exposure time of 30 s. Small windows were defined around the target and four comparison stars to decrease the read-out time from 2 min to 15 s. As comparison stars we used stars with similar magnitudes ($\Delta m < 2$ mag) in all SDSS bands from u to z , which have been pre-selected using the SDSS DR 9 skyserver (<http://skyserver.sdss.org/dr9/en/>). The data were reduced using IRAF;¹ a standard CCD reduction was performed using the IRAF tools for bias- and flat-field corrections. Then, the light curves of the target and the comparison stars were extracted using the aperture photometry package of DAOPHOT. The final light was constructed by dividing the light curve of the target by the light curves of the comparison stars.

3 ANALYSIS

3.1 The hybrid LTE/NLTE approach and spectroscopic analysis

Both the co-added UVES and XSHOOTER (UVB and VIS arm) spectra were analysed using the same hybrid local thermodynamic equilibrium (LTE)/non-LTE (NLTE) model atmospheric approach. This approach has been successfully used to analyse B-type stars (see, for instance, Przybilla, Nieva & Edelmann 2006a; Przybilla et al. 2006b; Nieva & Przybilla 2007, 2008; Przybilla, Nieva & Butler 2011) and is based on the three generic codes ATLAS12 (Kurucz 1996), DETAIL, and SURFACE (Giddings 1981; Butler & Giddings 1985, extended and updated).

Based on the mean metallicity for hot subdwarf B stars according to Naslim et al. (2013), metal-rich and line-blanketed, plane-parallel and chemically homogeneous model atmospheres in hydrostatic and radiative equilibrium were computed in LTE within ATLAS12. Occupation number densities in NLTE for hydrogen, helium, and for selected metals (see Table B1) were computed with DETAIL by solving the coupled radiative transfer and statistical equilibrium equations. The emergent flux spectrum was synthesized afterwards within SURFACE, making use of realistic line-broadening data. Recent improvements to all three codes (see Irrgang et al. 2018, for details) with regard to NLTE effects on the atmospheric structure as well as the implementation of the occupation probability formalism (Hubeny, Hummer & Lanz 1994) for H I and He II and new Stark broadening tables for H (Tremblay & Bergeron 2009) and He I (Beauchamp, Wesemael & Bergeron 1997) are considered as well. For applications of these models to sdB stars, see Schneider et al. (2018).

We included spectral lines of H and He I, and in addition, various metals in order to precisely measure the projected rotational velocity ($v \sin i$), RV (v_{rad}), and chemical abundances of J08205+0008. The calculation of the individual model spectra is presented in detail in Irrgang et al. (2014). In Table B2, the covered effective temperatures, surface gravities, helium, and metal abundances for the hybrid LTE/NLTE model grid used are listed.

The quantitative spectral analysis followed the methodology outlined in Irrgang et al. (2014), that is, the entire useful spectrum and all 15 free parameters (T_{eff} , $\log g$, v_{rad} , $v \sin i$, $\log n(\text{He}) := \log \left[\frac{N(\text{He})}{N(\text{all elements})} \right]$, plus abundances of all metals listed in Table B1) were simultaneously fitted using standard χ^2 minimization techniques. Macroturbulence ζ and microturbulence ξ were fixed

¹<http://iraf.noao.edu/>

to zero because there is no indication for additional line-broadening due to these effects in sdB stars (see, for instance, Geier & Heber 2012; Schneider et al. 2018).

3.2 Effective temperature, surface gravity, helium content, and metal abundances

The excellent match of the global best-fitting model spectrum to the observed one is demonstrated in Fig. 1 for selected spectral ranges in the co-added XSHOOTER spectrum of J08205+0008 (UVB + VIS arm).

The wide spectral range covered by the XSHOOTER spectra allowed, besides the typical hydrogen Balmer series and prominent He I lines in the optical, Paschen lines to be included in the fit, which provides additional information that previously could not be used in sdB spectral analysis, but provides important consistency checks.

In the framework of our spectral analysis, we also tested for variations of the atmospheric parameters over the orbital phase as seen in other reflection effect systems (e.g. Heber et al. 2004; Schaffenroth et al. 2013). As expected, due to the relatively weak reflection effect of less than 5 per cent, the variations were within the total uncertainties given in the following and can therefore be neglected (see also Fig. B1 for details).

The resulting effective temperatures, surface gravities, and helium abundances derived from XSHOOTER and UVES are listed in Table 3. The results include 1σ statistical errors and systematic uncertainties according to the detailed study of Lisker et al. (2005), which has been conducted in the framework of the ESO Supernova Ia Progenitor Survey. For stars with two exposures or more, Lisker et al. (2005) determined a systematic uncertainty of ± 374 K for T_{eff} , ± 0.049 dex for $\log(g)$, and ± 0.044 dex for $\log n(\text{He})$ (see table 2 in Lisker et al. 2005 for details).

Fig. 2 shows the $T_{\text{eff}}-\log(g)$ diagram, where we compare the UVES and XSHOOTER results to predictions of evolutionary models for the horizontal branch for a canonical mass sdB with different envelope masses from Dorman et al. (1993), as well as evolutionary tracks assuming solar metallicity and masses of 0.50 and $0.55 M_{\odot}$ (Han et al. 2002). With $T_{\text{eff}} = 26\,000 \pm 400$ K and $\log(g) = 5.54 \pm 0.05$ (XSHOOTER, statistical and systematic errors) and $T_{\text{eff}} = 25\,600 \pm 400$ K and $\log(g) = 5.51 \pm 0.05$ (UVES, statistical and systematic errors), J08205+0008 lies within the EHB, as expected. Our final result ($T_{\text{eff}} = 25\,800 \pm 290$ K, $\log(g) = 5.52 \pm 0.04$), the weighted average of the XSHOOTER and UVES parameters, is also in good agreement with the LTE results of Geier et al. (2011c), which are $T_{\text{eff}} = 26\,700 \pm 1000$ K and $\log(g) = 5.48 \pm 0.10$, respectively.

The determined helium content of J08205+0008 is $\log n(\text{He}) = -2.06 \pm 0.05$ (XSHOOTER, statistical and systematic errors) and $\log n(\text{He}) = -2.07 \pm 0.05$ (UVES, statistical and systematic errors), hence clearly subsolar (see Asplund et al. 2009 for details). The final helium abundance ($\log n(\text{He}) = -2.07 \pm 0.04$), the weighted average of XSHOOTER and UVES, therefore is comparable with Geier et al. (2011c), who measured $\log n(\text{He}) = -2.00 \pm 0.07$, and with the mean helium abundance for sdB stars from Naslim et al. (2013), which is $\log n(\text{He}) = -2.34$ (see also Fig. 3).

Moreover, it was possible to identify metals of various different ionization stages within the spectra (see Table D1 and Fig. 4) and to measure their abundances. Elements found in more than one ionization stage are oxygen (O I/II), silicon (Si II/III), and sulfur (S II/III), whereas carbon (C II), nitrogen (N II), magnesium (Mg II), aluminum (Al III), argon (Ar II), and iron (Fe III) are only detected in

a single stage. We used the model grid in Table B2 to measure the individual metal abundances in both the co-added XSHOOTER and the UVES spectrum. We were able to fit the metal lines belonging to different ionization stages of the same elements similarly well (see Fig. 4). The corresponding ionization equilibria additionally constrained the effective temperature.

All metal abundances together with their total uncertainties are listed in Table 1. Systematic uncertainties were derived according to the methodology presented in detail in Irrgang et al. (2014) and cover the systematic uncertainties in effective temperature and surface gravity as described earlier.

The results of XSHOOTER and UVES are in good agreement, except for the abundances of oxygen, sulfur, and argon, where differences of 0.15, 0.19, and 0.22 dex, respectively, are measured. However, on average these metals also have the largest uncertainties, in particular argon, such that the abundances nearly overlap if the corresponding uncertainties are taken into account. According to Fig. 3, J08205+0008 is underabundant in carbon and oxygen, but overabundant in nitrogen compared to solar (Asplund et al. 2009), showing the prominent CNO signature as a remnant of the star's hydrogen core-burning through the CNO cycle. Aluminum and the alpha elements (neon, magnesium, silicon, and sulfur) are underabundant compared to solar. With the exception of neon, which is not present, the chemical abundance pattern of J08205+0008 generally follows the metallicity trend of hot subdwarf B stars (Naslim et al. 2013), even leading to a slight enrichment in argon and iron compared to solar. The latter may be explained by radiative levitation, which occurs in the context of atomic transport, that is, diffusion processes in the stellar atmosphere of hot subdwarf stars (Greenstein 1967; see Michaud, Alecian & Richer 2015 for a detailed review).

Due to the high resolution of the UVES (and XSHOOTER) spectra, we were also able to measure the projected rotational velocity of J08205+0008 from the broadening of the spectral lines, in particular from the sharp metal lines, to $v \sin i = 66.0 \pm 0.1 \text{ km s}^{-1}$ (UVES, 1σ statistical errors only) and $v \sin i = 65.8 \pm 0.1 \text{ km s}^{-1}$ (XSHOOTER, 1σ statistical errors only).

3.3 Search for chemical signatures of the companion

Although HW Vir type systems are known to be single-lined, traces of the irradiated and heated hemisphere of the cool companion have been found in some cases. Wood & Saffer (1999) discovered the H α absorption component of the companion in the prototype system HW Vir (see also Edelmann 2008).

Metal lines in emission were found in the spectra of the hot sdOB star AA Dor by Vučković et al. (2016) moving in antiphase to the spectrum of the hot sdOB star indicating an origin near the surface of the companion. After the removal of the contribution of the hot subdwarf primary, which is dominating the spectrum, the residual spectra showed more than 100 shallow emission lines originating from the heated side of the secondary, which show their maximum intensity close to the phases around the secondary eclipse. They analysed the residual spectrum in order to model the irradiation of the low-mass companion by the hot subdwarf star. The emission lines of the heated side of the secondary star allowed them to determine the RV semi-amplitude of the centre of light. After the correction to the centre of mass of the secondary they could derive accurate masses of both components of the AA Dor system, which is consistent with a canonical sdB mass of $0.46 M_{\odot}$ and a companion of $0.079 \pm 0.002 M_{\odot}$ very close to the hydrogen-burning limit. They also computed a first generation

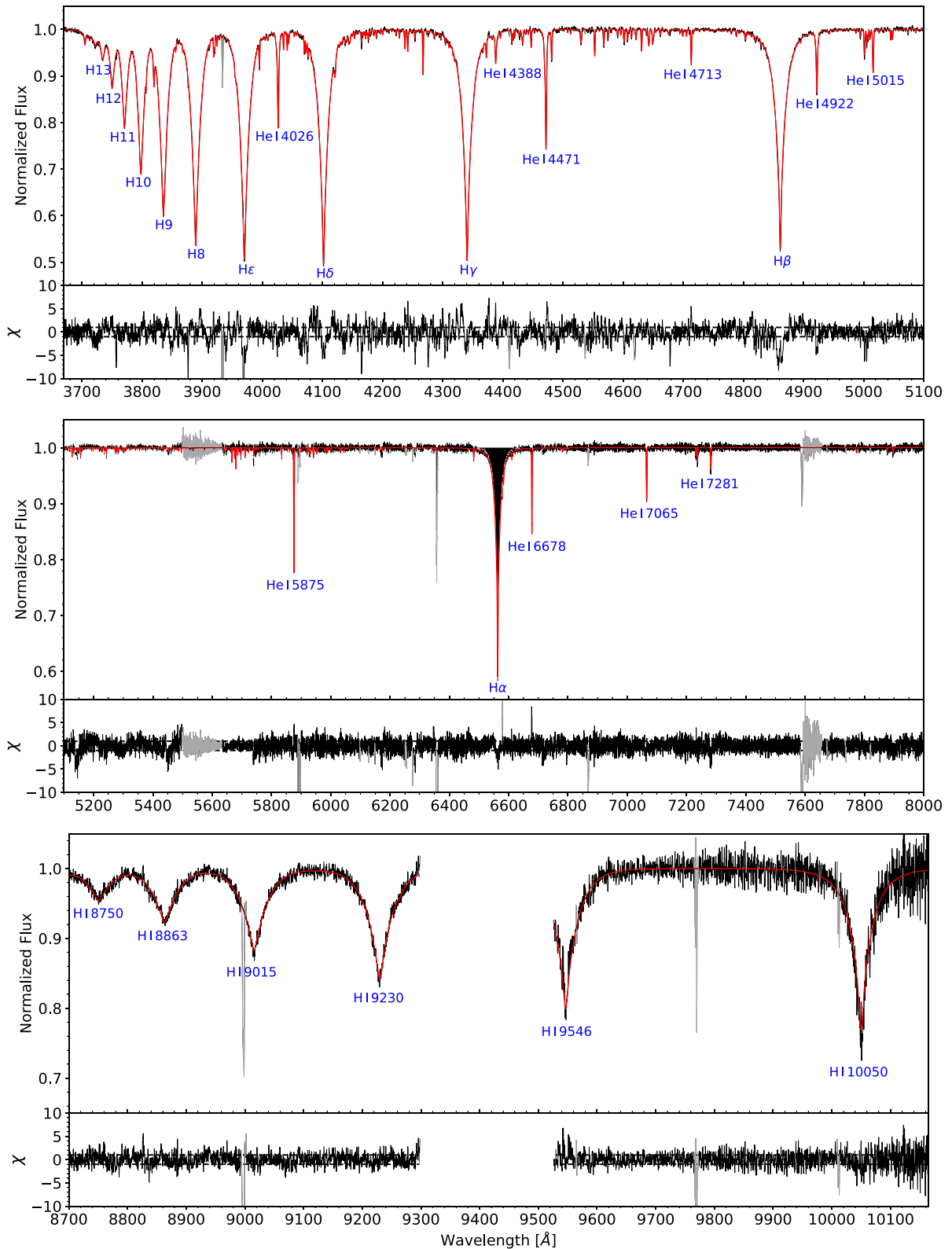


Figure 1. Comparison between observation (solid black line) and global best fit (solid red line) for selected spectral ranges in the co-added XSHOOTER spectrum of J08205+0008. Prominent hydrogen and He I lines are marked by blue labels and the residuals for each spectral range are shown in the bottom panels, whereby the dashed horizontal lines mark deviations in terms of $\pm 1\sigma$, that is, values of $\chi = \pm 1$ (0.2 per cent in UVB and 0.4 per cent in VIS, respectively). Additional absorption lines are caused by metals (see Fig. 4). Spectral regions, which have been excluded from the fit, are marked in grey (observation) and dark red (model), respectively. Since the range between H I 9230 Å and H I 9546 Å strongly suffers from telluric lines (even after the telluric correction with MOLECFIT), it is excluded from the figure.

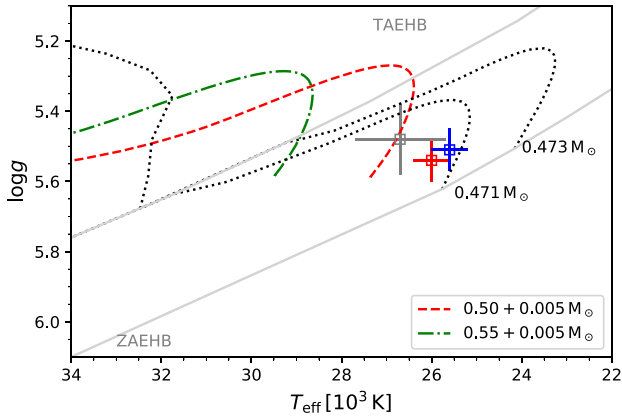


Figure 2. $T_{\text{eff}}\text{-}\log(g)$ diagram for J08205+0008. While the blue square represents the UVES solution, the red square results from XSHOOTER. The grey square marks the LTE solution of Geier et al. (2011c). The ZAEHB and terminal-age horizontal branch (TAEHB) for a canonical mass sdB are shown in grey as well as evolutionary tracks for a canonical mass sdB with different envelope masses from Dorman, Rood & O’Connell (1993) with black dotted lines. Additionally, we show evolutionary tracks with solar metallicity for different sdB masses with hydrogen layers of $0.005 M_{\odot}$, according to Han et al. (2002) to show the mass dependence of the EHB. The error bars include 1σ statistical and systematic uncertainties as presented in the text (see Section 3.2 for details).

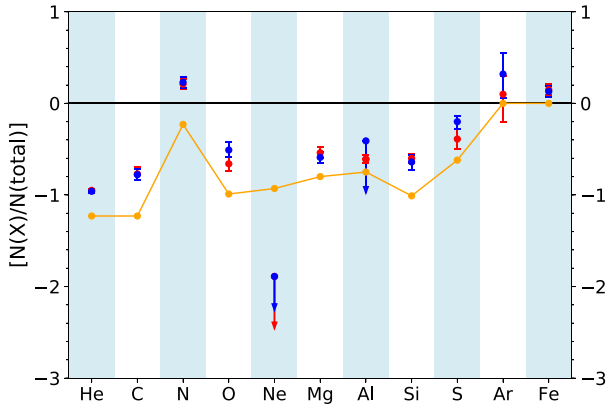


Figure 3. The chemical abundance pattern of J08205+0008 (red: XSHOOTER and blue: UVES) relative to solar abundances of Asplund et al. (2009), represented by the black horizontal line. The orange solid line represents the mean abundances for hot subdwarf B stars according to Naslim et al. (2013) used as the metallicity for our quantitative spectral analysis. Upper limits are marked with downward arrows and $\left[\frac{N(X)}{N(\text{total})}\right] := \log_{10} \left\{ \frac{N(X)}{N(\text{total})} \right\} - \log_{10} \left\{ \frac{N(X(\text{solar}))}{N(\text{total})} \right\}$.

atmosphere model of the low mass secondary including irradiation effects.

J08205+0008 is significantly fainter and cooler than AA Dor but with a much shorter period. We searched the XSHOOTER spectra for signs of the low-mass companion of J08205+0008. This was done by subtracting the spectrum in the secondary minimum where the companion is eclipsed from the spectra before and after the secondary eclipse where most of the heated atmosphere of the companion is visible. However, no emission or absorption lines from the companion were detected (see Figs E1 and E2). Also, in the XSHOOTER NIR arm spectra, no emission lines could be found.

3.4 Photometry: angular diameter and interstellar reddening

The angular diameter of a star is an important quantity, because it allows the stellar radius to be determined, if the distance is known, for example, from trigonometric parallax. The angular diameter can be determined by comparing observed photometric magnitudes to those calculated from model atmospheres for the stellar surface. Because of contamination by the reflection effect the apparent magnitudes of the hot subdwarf can be measured only during the secondary eclipse, where the companion is completely eclipsed by the larger subdwarf. We performed a least-squares fit to the flat bottom of the secondary eclipse in the ULTRACAM light curves to determine the apparent magnitudes and derived $u' = 14.926 \pm 0.009$ mag, $g' = 15.025 \pm 0.004$ mag, and $r' = 15.450 \pm 0.011$ mag (1σ statistical errors).

Because the star lies at low Galactic latitude ($b = 19^\circ$) interstellar reddening is expected to be significant. Therefore, both the angular diameter and the interstellar colour excess have to be determined simultaneously. We used the reddening law of Fitzpatrick et al. (2019) and matched a synthetic flux distribution calculated from the same grid of model atmospheres that were also used in the quantitative spectral analysis (see Section 3.1) to the observed magnitudes as described in Heber, Irrgang & Schaffenroth (2018). The χ^2 based fitting routine uses two free parameters: the angular diameter θ , which shifts the fluxes up and down according to $f(\lambda) = \theta^2 F(\lambda)/4$, where $f(\lambda)$ is the observed flux at the detector position and $F(\lambda)$ is the synthetic model flux at the stellar surface, and the colour excess.² The final atmospheric parameters and their respective uncertainties derived from the quantitative spectral analysis (see Section 3.2) result in an angular diameter of $\theta = 6.22 (\pm 0.15) \times 10^{-12}$ rad and an interstellar reddening of $E(B - V) = 0.041 \pm 0.013$ mag. The latter is consistent with values from reddening maps of Schlegel, Finkbeiner & Davis (1998) and Schlafly & Finkbeiner (2011): 0.039 and 0.034 mag, respectively.

In addition, ample photometric measurements of J08205+0008 are available in different filter systems, covering the spectral range all the way from the ultraviolet (GALEX) through the optical (e.g. SDSS) to the infrared (2MASS, UKIDSS, and WISE, see Fig. 5). However, those measurements are mostly averages of observations taken at multiple epochs or single epoch measurements at unknown orbital phase. Therefore, those measurements do not allow us to determine the angular diameter of the sdB because of the contamination by light from the heated hemisphere of the companion. However, an average SED of the system can be derived. This allows us to redetermine the interstellar reddening and to search for an infrared excess caused by light from the cool companion.

The same fitting technique is used in the analysis of the SED as described above for the analysis of the ULTRACAM magnitudes. Besides the sdB grid, a grid of synthetic spectra of cool stars ($2300 \text{ K} \leq T_{\text{eff}} \leq 15000 \text{ K}$, Husser et al. 2013) is used. In addition to the angular diameter and reddening parameter, the temperature of the cool companion as well as the surface ratio are free parameters in the fit. The fit results in $E(B - V) = 0.040 \pm 0.010$ mag, which is fully consistent with the one derived from the ULTRACAM photometry as well as with the reddening map. The apparent angular diameter is larger than that from ULTRACAM photometry by 2.8 per cent, which is caused by the contamination by light from the companion’s

²Fitzpatrick et al. (2019) use $E(44 - 55)$, the monochromatic equivalent of the usual $E(B - V)$ in the Johnson system, using the wavelengths $\lambda = 4400$ and 5000 \AA , respectively. In fact, $E(44 - 55)$ is identical to $E(B - V)$ for high effective temperatures as determined for J08205+0008.

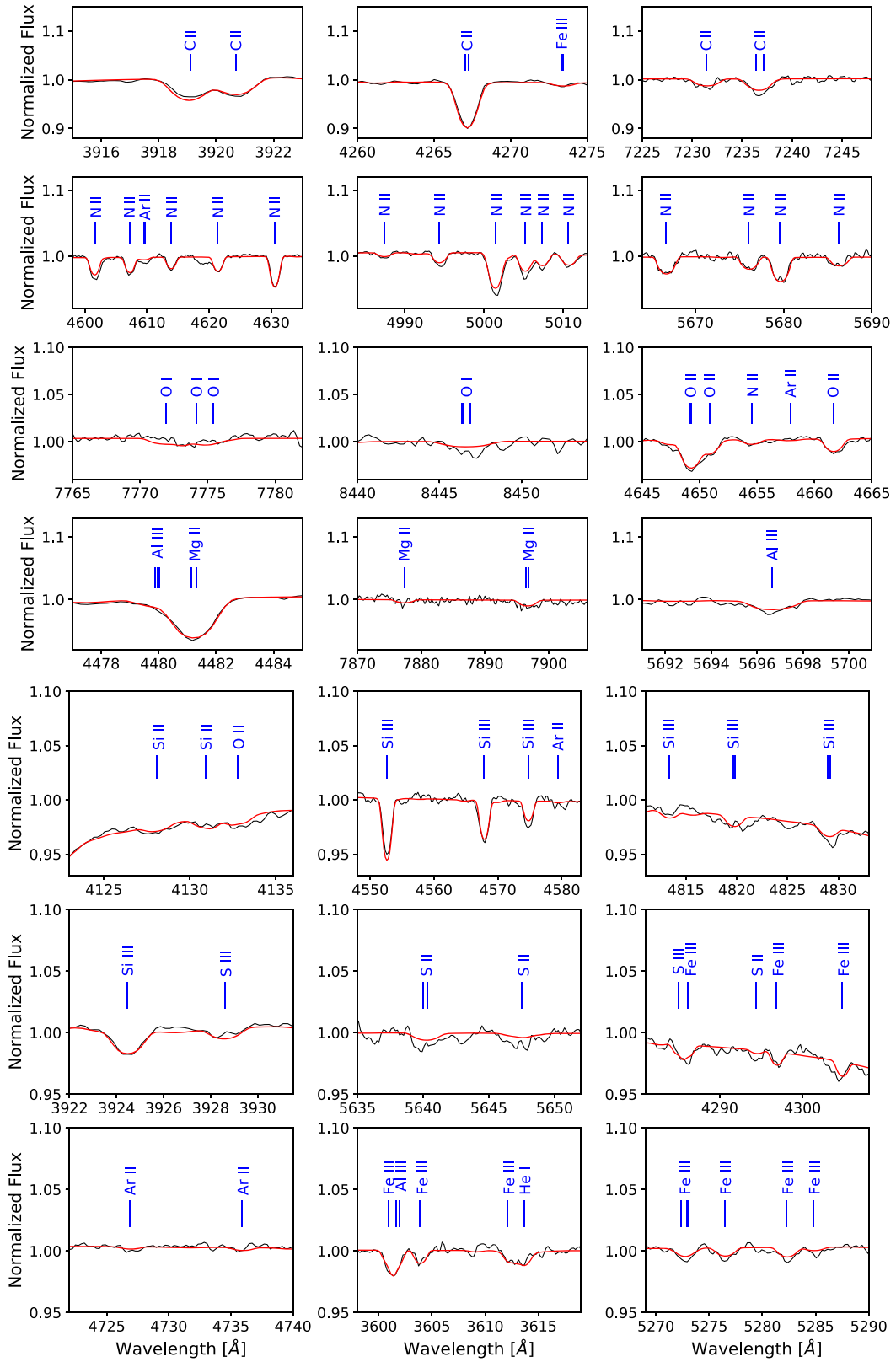


Figure 4. Selected metal lines in the co-added XSHOOTER spectrum of J08205+0008. The observed spectrum (solid black line) and the best fit (solid red line) are shown. Solid blue vertical lines mark the central wavelength positions and the ionization stages of the individual metal lines according to Table D1.

Downloaded from https://academic.oup.com/mnras/article/501/3/3847/6006282 by Universitaetsbibliothek Potsdam user on 08 December 2022

Table 1. Metal abundances of J08205+0008 derived from XSHOOTER and UVES.[†]

Parameter	XSHOOTER	UVES
$\log n(\text{C})$	-4.38 ± 0.05	$-4.39^{+0.04}_{-0.03}$
$\log n(\text{N})$	$-4.00^{+0.03}_{-0.02}$	-3.98 ± 0.03
$\log n(\text{O})$	$-4.01^{+0.05}_{-0.06}$	$-3.86^{+0.07}_{-0.06}$
$\log n(\text{Ne})$	≤ -6.00	≤ -6.00
$\log n(\text{Mg})$	$-4.98^{+0.05}_{-0.04}$	-5.03 ± 0.05
$\log n(\text{Al})$	-6.20 ± 0.03	≤ -6.00
$\log n(\text{Si})$	-5.13 ± 0.04	$-5.17^{+0.07}_{-0.08}$
$\log n(\text{S})$	$-5.31^{+0.11}_{-0.10}$	$-5.12^{+0.06}_{-0.08}$
$\log n(\text{Ar})$	$-5.54^{+0.15}_{-0.27}$	$-5.32^{+0.19}_{-0.23}$
$\log n(\text{Fe})$	-4.39 ± 0.04	$-4.41^{+0.04}_{-0.05}$

Notes: [†]Including 1σ statistical and systematic errors.

$$\log n(X) := \log \left[\frac{N(X)}{N(\text{all elements})} \right]$$

heated hemisphere. The effective temperature of the companion is unconstrained and the best match is achieved for the surface ratio of zero, which means there is no signature from the cool companion. In a final step we allow the effective temperature of the sdB to vary and determine it along with the angular diameter and the interstellar reddening, which results in $T_{\text{eff}} = 26900^{+1400}_{-1500}$ K in agreement with the spectroscopic result (see Fig. 5 for the comparison of synthetic and observed photometry).

3.5 Stellar radius, mass, and luminosity

Since *Gaia* data release 2 (DR2; Gaia Collaboration 2018), trigonometric parallaxes are available for a large sample of hot subdwarf stars, including J08205+0008 for which 10 per cent precision has been reached. We corrected for the *Gaia* DR2 parallax zero-point offset of -0.029 mas (Lindgren et al. 2018).

Combining the parallax measurement with the results from our quantitative spectral analysis ($\log g$ and T_{eff}) and with the angular diameter θ derived from ULTRACAM photometry, allows for the determination of the mass of the sdB primary in J08205+0008 via:

$$M = \frac{g\theta^2}{4G\varpi^2} \quad (1)$$

The respective uncertainties of the stellar parameters are derived by Monte Carlo error propagation. The uncertainties are dominated by the error of the parallax measurement. Results are summarized in Table 3. Using the gravity and effective temperature derived by the spectroscopic analysis, the mass for the sdB is $M = 0.48^{+0.12}_{-0.09} M_{\odot}$ and its luminosity is $L = 16^{+3.6}_{-2.8} L_{\odot}$ in agreement with canonical models for EHB stars (see fig. 13 of Dorman et al. 1993). The radius of the sdB is calculated by the angular diameter and the parallax to $R = 0.200^{+0.021}_{-0.018} R_{\odot}$.

3.6 Radial velocity curve and orbital parameters

The RVs of the individual XSHOOTER spectra were measured by fitting all spectral features simultaneously to synthetic models as described in Section 3.1.

Due to lower S/N of the individual UVES spectra, which were observed in poor conditions, only the most prominent features in the spectra are suitable for measuring the Doppler shifts. After excluding very poor quality spectra, RVs of the remaining 28 spectra were

measured using the FITSB2 routine (Napiwotzki et al. 2004b) by fitting a set of different mathematical functions to the hydrogen Balmer lines as well as He I lines. The continuum is fitted by a polynomial, and the line wings and line core by a Lorentzian and a Gaussian function, respectively. The barycentrically corrected RVs together with formal 1σ errors are summarized in Table F1.

The orbital parameters T_0 , period P , system velocity γ , and RV semi-amplitude K as well as their uncertainties were derived with the same method described in Geier et al. (2011a). To estimate the contribution of systematic effects to the total error budget additional to the statistic errors determined by the FITSB2 routine, we normalized the χ^2 of the most probable solution by adding systematic errors to each data point e_{norm} until the reduced χ^2 reached $\simeq 1.0$.

Combining the UVES and XSHOOTER RVs, we derived $T_0 = 57801.54954 \pm 0.00024$ d, $P = 0.096241 \pm 0.000003$ d, $K = 47.9 \pm 0.4$ km s⁻¹, and the system velocity $\gamma = 26.5 \pm 0.4$ km s⁻¹. No significant systematic shift was detected between the two data sets and the systematic error added in quadrature was therefore very small $e_{\text{norm}} = 2.0$ km s⁻¹. The gravitational redshift is significant at $1.6^{+0.02}_{-0.05}$ km s⁻¹ and might be important if the orbit of the companion could be measured by future high-resolution measurements (see e.g. Vos et al. 2013).

To improve the accuracy of the orbital parameters even more we then tried to combine them with the RV data set from Geier et al. (2011c), medium-resolution spectra taken with ESO-NIT/EFOSC2 and SDSS. A significant, but constant systematic shift of $+17.4$ km s⁻¹ was detected between the UVES+XSHOOTER and the SDSS+EFOSC2 data sets. Such zero-point shifts are common between low- or medium-resolution spectrographs. It is quite remarkable that both medium-resolution data sets behave in the same way. However, since the shift is of the same order as the statistical uncertainties of the EFOSC2 and SDSS individual RVs we refrain from interpreting it as real.

Adopting a systematic correction of $+17.4$ km s⁻¹ to the SDSS+EFOSC2 data set, we combined it with the UVES+XSHOOTER data set and derived $T_0(\text{BJD}_{\text{TDB}}) = 2457801.59769 \pm 0.00023$ d, $P = 0.09624077 \pm 0.00000001$ d, which is in perfect agreement with the photometric ephemeris, $K = 47.8 \pm 0.4$ km s⁻¹ and $\gamma = 26.6 \pm 0.4$ km s⁻¹. This orbital solution is consistent with the solution from the XSHOOTER+UVES data sets alone. Due to the larger uncertainties of the SDSS+EFOSC2 RVs, the uncertainties of γ and K did not become smaller. The uncertainty of the orbital period on the other hand improved by two orders of magnitude due to the long timebase of 11 yr between the individual epochs. Although this is still two orders of magnitude larger than the uncertainty derived from the light curve (see Section 3.7), the consistency with the light-curve solution is remarkable. The RV curve for the combined solution phased to the orbital period is given in Fig. 6. Around phase 0, the Rossiter–McLaughlin effect (Rossiter 1924; McLaughlin 1924) is visible. This effect is an RV deviation that occurs as parts of a rotating star are blocked out during the transit of the companion. The effect depends on the radius ratio and the rotational velocity of the primary. We can derive both parameters much more precisely with the spectroscopic and photometric analyses, but we plotted a model of this effect using our system parameters on the residuals of the RV curve to show that is consistent.

Except for the corrected system velocity, the revised orbital parameters of J08205+0008 are consistent with those determined by Geier et al. (2011c) ($P = 0.096 \pm 0.001$ d, $K = 47.4 \pm 1.9$ km s⁻¹), but much more precise.

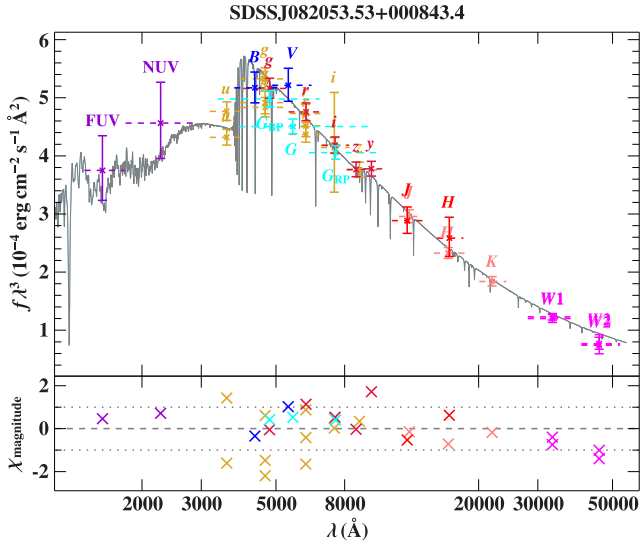


Figure 5. Comparison of synthetic and observed photometry: top panel: SED: filter-averaged fluxes converted from observed magnitudes are shown in different colours. The respective full width at tenth maximum are shown as dashed horizontal lines. The best-fitting model, degraded to a spectral resolution of 6 Å is plotted in grey. In order to reduce the steep SED slope the flux is multiplied by the wavelength cubed. Bottom panel: difference between synthetic and observed magnitudes divided by the corresponding uncertainties (residual χ). The following colour code is used for the different photometric systems: GALEX (violet, Bianchi, Shiao & Thilker 2017), SDSS (golden, Alam et al. 2015), Pan-STARRS1 (dark red, Flewelling et al. 2020), Johnson (blue, Henden et al. 2015), *Gaia* (cyan, Evans et al. 2018, with corrections and calibrations from Maíz Apellániz & Weiler 2018), 2MASS (red, Cutri et al. 2003), UKIDSS (pink, Lawrence et al. 2007), and WISE (magenta, Cutri et al. 2014; Schlafly, Meisner & Green 2019).

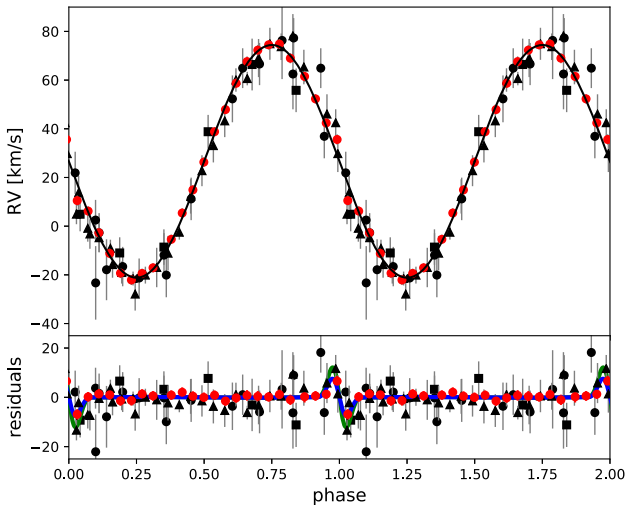


Figure 6. RV of J08205+0008 folded on the orbital period. The residuals are shown together with a prediction of the Rossiter–McLaughlin effect using the parameters derived in this paper in blue and a model with a higher rotational velocity assuming bound rotation in green. The RVs were determined from spectra obtained with XSHOOTER (red circles), UVES (black triangles), EFOSC2 (black circles), and SDSS (black rectangles). The EFOSC2 and SDSS RVs have been corrected by a systematic shift (see the text for details).

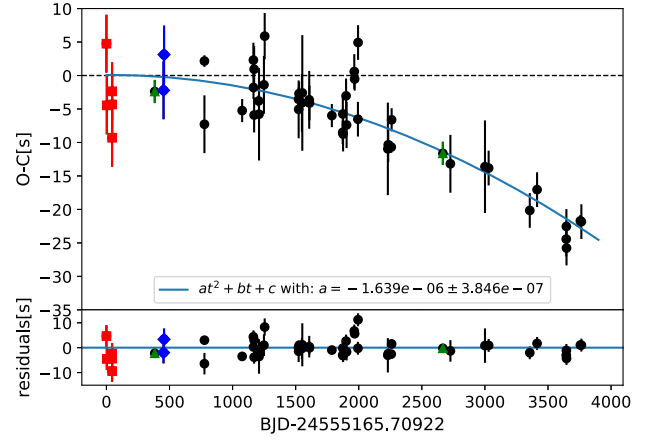


Figure 7. (O–C) diagram for J08205+0008 using eclipse times observed with Merope (red squares), BUSCA (blue diamonds), ULTRACAM (green triangles), and the SAAO-1-m/1.9-m telescope (black circles). The solid line represents a fit of a parabola to account for the period change of the orbital period. The derived quadratic term is given in the legend. The parameters of the fit are provided in the legend. In the lower panel, the residuals between the observations and the best fit are shown.

3.7 Eclipse timing

Since the discovery that J08205+00008 is an eclipsing binary in 2009 November, we have monitored the system regularly using BUSCA mounted at the 2.2-m telescope in Calar Alto, Spain, ULTRACAM and the 1 m in Sutherland Observatory (SAAO), South Africa. Such studies have been performed for several post-common envelope systems with sdB or WD primaries and M dwarf companions (see Lohr et al. 2014, for a summary). In many of those systems period changes have been found.

The most convenient way to reveal period changes is to construct an observed minus calculated (O–C) diagram. Thereby we compare the observed mid-eclipse times (O) with the expected mid-eclipse times (C) assuming a fixed orbital period P_0 and using the mid-eclipse time for the first epoch T_0 . Following Kepler et al. (1991), if we expand the observed mid-eclipse of the *Eth* eclipse (T_E with $E = t/P$) in a Taylor series, we get the (O–C) equation:

$$O - C = \Delta T_0 + \frac{\Delta P_0}{P_0} t + \frac{1}{2} \frac{\dot{P}}{P_0} t^2 + \dots \quad (2)$$

This means that with a quadratic fit to the O–C data we can derive the ephemeris T_0 , P , and \dot{P} in BJD_{TDB} .

Together with the discovery data observed with Merope at the Mercator telescope on La Palma (Geier et al. 2011c), it was possible to determine timings of the primary eclipse over more than 10 yr, as described in Sections 2.4 and 2.5. All measured mid-eclipse times can be found in Table G1.

We used all eclipse timings to construct an O–C diagram, which is shown in Fig. 7. We used the ephemeris given in Geier et al. (2011c) as a starting value to find the eclipse numbers of each measured eclipse time and detrended the O–C diagram by varying the orbital period until no linear trend was visible to improve the determination of the orbital period. During the first 7–8 yr of observations, the ephemeris appeared to be linear. This was also found by Pulley et al. (2018). As their data show a large scatter, we do not use it in our analysis. However, in the last two years a strong quadratic effect was revealed. The most plausible explanation is a decrease in the orbital period of the

system. This enabled us to derive an improved ephemeris for J08205+0008:

$$\begin{aligned} T_0 &= 2455165.709211(1) \\ P &= 0.09624073885(5) \text{ d} \\ \dot{P} &= -3.2(8) \times 10^{-12} \text{ dd}^{-1} \end{aligned}$$

3.8 Light-curve modelling

With the new very high-quality ULTRACAM $u'g'r'$ light curves, we repeated the light-curve analysis of (Geier et al. 2011c) obtaining a solution with much smaller errors. For the modelling of the light curve we used LCURVE, a code written to model detached and accreting binaries containing a WD (for details, see Copperwheat et al. 2010). It has been used to analyse several detached WD–M dwarf binaries (e.g. Parsons et al. 2010). Those systems show very similar light curves with very deep, narrow eclipses and a prominent reflection effect, if the primary is a hot WD. Therefore, LCURVE is ideally suited for our purpose.

The code calculates monochromatic light curves by subdividing each star into small elements with a geometry fixed by its radius as measured along the line from the centre of one star towards the centre of the companion. The flux of the visible elements is always summed up to get the flux at a certain phase. A number of different effects that are observed in compact and normal stars are considered, for example, Roche distortions observed when a star is distorted from the tidal influence of a massive, close companion, as well as limb-darkening and gravitational darkening. Moreover, lensing and Doppler beaming, which are important for very compact objects with close companions, can be included. The Roemer delay, which is a light traveltime effect leading to a shift between primary and secondary eclipse times due to stars of different mass orbiting each other and changing their distance to us, and asynchronous orbits can be considered. The latter effects are not visible in our light curves and can hence be neglected in our case.

As we have a prominent reflection effect it is very important to model this effect as accurately as possible. The reflection effect, better called the irradiation effect, results from the huge difference in temperature between the two stars, together with their small separation. The (most likely) tidally locked companion is heated up on the side facing the hot subdwarf because of the strong irradiation by the hot primary. Therefore, the contribution of the companion to the total flux of the system varies with phase and increases as more of the heated side is visible to the observer. We use a quite simple model, which calculates the fluxes from the temperatures of both companions using a blackbody approximation. The irradiation is approximated by assigning a new temperature to the heated side of the companion

$$\sigma T_{\text{sec}}'^4 = \sigma T_{\text{sec}}^4 + F_{\text{irr}} = \sigma T_{\text{sec}}^4 \left[1 + \alpha \left(\frac{T_{\text{prim}}}{T_{\text{sec}}} \right)^4 \left(\frac{R_{\text{prim}}}{a} \right)^2 \right], \quad (3)$$

with α being the albedo of the companion and F_{irr} the irradiating flux, accounting for the angle of incidence and distance from the hot subdwarf. The irradiated side is heated up to a temperature of 13 000–15 000 K similar to HW Vir (Kiss et al. 2000), which is slightly hotter but has a longer period. Hence, the amplitude of the effect is increasing from blue to red as can be seen in Fig. 8, as the sdB is getting fainter compared to the companion in the red. If the irradiation effect is very strong, the description given above might not be sufficient, as the back of the irradiated star is completely unaffected in this description, but heat transport could heat it up,

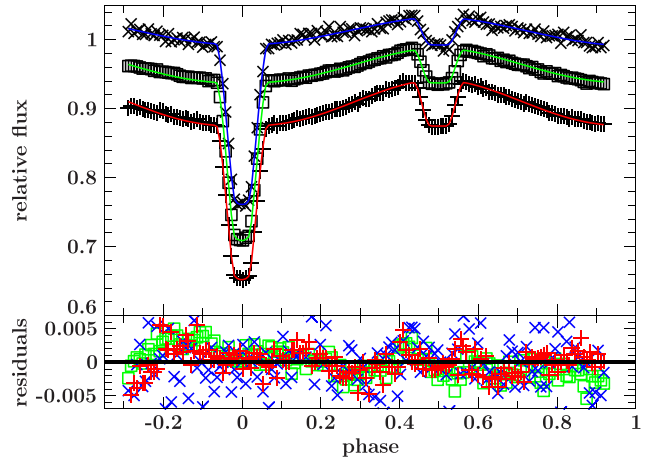


Figure 8. ULTRACAM $u'g'r'$ light curves of J08205+0008 together with the best fit of the most consistent solution. The light curves in the different filters have been shifted for better visualization. The lower panel shows the residuals. The deviation of the light curves from the best fit is probably due to the fact that the comparison stars cannot completely correct for atmospheric effects due to the different colour and the crude reflection effect model used in the analysis is insufficient to correctly describe the shape of the reflection effect.

Table 2. Parameters of the light-curve fit of the ULTRACAM $u'g'r'$ band light curves.

Band	u'	g'	r'
Fixed parameters			
q		0.147	
P		0.09624073885	
$T_{\text{eff, sdB}}$		25800	
$x_{1,1}$	0.1305	0.1004	0.0788
$x_{1,2}$	0.2608	0.2734	0.2281
g_1		0.25	
g_2		0.08	
Fitted parameters			
i	85.3 ± 0.6	85.6 ± 0.2	85.4 ± 0.3
r_1/a	0.2772 ± 0.0029	0.2734 ± 0.0010	0.2748 ± 0.0014
r_2/a	0.1322 ± 0.0018	0.1297 ± 0.0006	0.1304 ± 0.0008
$T_{\text{eff, comp}}$	3000 ± 500	2900 ± 500	3200 ± 560
Absorb	1.54 ± 0.08	1.58 ± 0.03	2.08 ± 0.05
x_2	0.70	0.78	0.84
T_0 (MJD)	57832.0355	57832.0354	57832.0354
slope	-0.000968	-0.002377	0.00013417
$\frac{L_1}{L_1+L_2}$	0.992578	0.98735	0.97592

increasing the luminosity of unirradiated parts as well. This is not considered in our simple model.

As the light-curve model contains many parameters, not all of them independent, we fixed as many parameters as possible (see Table 2). The temperature of the sdB was fixed to the temperature determined from the spectroscopic fit. We used the values determined by the co-added XSHOOTER spectra, as they have higher S/N. The gravitational limb-darkening coefficients were fixed to the values expected for a radiative atmosphere for the primary (von Zeipel 1924) and a convective atmosphere for the secondary (Lucy 1967) using a blackbody approximation to calculate the resulting intensities. For the limb darkening of the primary we adopted a quadratic limb-darkening law using the tables by Claret & Bloemen (2011). As the tables include only surface gravities up to $\log g = 5$ we used

the values closest to the parameters derived by the spectroscopic analysis.

As it is a well-separated binary, the two stars are approximately spherical, which means the light curve is not sensitive to the mass ratio. Therefore, we computed solutions with different, fixed mass ratios. To localize the best set of parameters, we used a SIMPLEX algorithm (Press et al. 1992) varying the inclination, the radii, the temperature of the companion, the albedo of the companion (absorb), the limb darkening of the companion, and the time of the primary eclipse to derive additional mid-eclipse times. Moreover, we also allowed for corrections of a linear trend, which is often seen in the observations of hot stars, as the comparison stars are often redder and so the correction for the airmass is often insufficient. This is given by the parameter ‘slope’. The model of the best fit is shown in Fig. 8 together with the observations and the residuals.

To get an idea about the degeneracy of parameters used in the light-curve solutions, as well as an estimation of the errors of the parameters we performed Markov Chain Monte Carlo (MCMC) computations with EMCEE (Foreman-Mackey et al. 2013) using the best solution we obtained with the SIMPLEX algorithm as a starting value varying the radii, the inclination, the temperature of the companion as well as the albedo of the companion. As a prior we constrained the temperature of the cool side of the companion to 3000 ± 500 K. Due to the large luminosity difference between the stars the temperature of the companion is not significantly constrained by the light curve. The computations were done for all three light curves separately.

For the visualization, we used the PYTHON package CORNER (see Fig. 9 Foreman-Mackey 2016). The results of the MCMC computations of the light curves of all three filters agree within the error (see Table 2). A clear correlation between both radii and the inclination is visible as well as a weak correlation of the albedo of the companion (absorb) and the inclination. This results from the fact that the companion is only visible in the combined flux due to the reflection effect and the eclipses and the amplitude of the reflection effect depends on the inclination, the radii, the separation, the albedo, and the temperatures. Looking at the χ^2 of the temperature of the companion we see that all temperatures give equally good solutions showing that the temperature can indeed not be derived from the light-curve fit. The albedo we derived has, moreover, a value > 1 , which has been found in other HW Vir systems as well and is due to the simplistic modelling of the reflection effect. The reason for the different distribution in the inclination is not clear to us. However, it is not seen in the other bands. It might be related to the insufficient correction of atmospheric effects by the comparison stars.

3.9 Absolute parameters of J08205+00008

As explained before, we calculated solutions for different mass ratios ($q = 0.11$ – 0.20). We obtain equally good χ^2 for all solutions, showing that the mass ratio cannot be constrained by the light-curve fit as expected. Hence, the mass ratio needs to be constrained differently. However, the separation, which can be calculated from the mass ratio, period, semi-amplitude of the RV curve and the inclination, is different for each mass ratio. The masses of both companions can then be calculated from the mass function. From the relative radii derived from the light-curve fit together with the separation, the absolute radii can be calculated. This results in different radii and masses for each mass ratio.

As stated before, the previous analysis of Geier et al. (2011c) resulted in two possible solutions: A post-RGB star with a mass of $0.25 M_{\odot}$ and a core helium-burning star on the EHB with a mass of

$0.47 M_{\odot}$. From the analysis of the photometry together with the *Gaia* magnitudes (see Section 3.5), we get an additional good constraint on the radius of the sdB. Moreover, the surface gravity was derived from the fit to the spectrum. This can be compared to the mass and radius of the sdB (and a photometric $\log g$: $g = GM/R^2$) derived in the combined analysis of RV and light curves. This is shown in Fig. 10. We obtain a good agreement for of all three methods (spectroscopic, photometric, and parallax-based) for an sdB mass between 0.39 and $0.60 M_{\odot}$. This means that we can exclude the post-RGB solution. The position of J0820 in the $T_{\text{eff}}-\log g$ diagram, which is shown in Fig. 2, gives us another constraint on the sdB mass. By comparing the atmospheric parameters of J08205+0008 to theoretical evolutionary tracks calculated by Han et al. (2002), it is evident that the position is not consistent with sdB masses larger than $\sim 0.50 M_{\odot}$, which we, therefore, assume as the maximum possible mass for the sdB.

Accordingly, we conclude that the solution that is most consistent with all different analysis methods is an sdB mass close to the canonical mass (0.39 – $0.50 M_{\odot}$). For this solution, we have an excellent agreement of the parallax radius with the photometric radius only, if the parallax offset of -0.029 mas suggested by Lindegren et al. (2018) is used. Otherwise the parallax-based radius is too large. The companion has a mass of 0.061 – $0.71 M_{\odot}$, which is just below the limit for hydrogen-burning. Our final results can be found in Table 3. The mass of the companion is below the hydrogen-burning limit and the companion is hence most likely a massive BD.

We also investigated the mass and radius of the companion and compared it to theoretical calculations by Baraffe et al. (2003) and Chabrier & Baraffe (1997) as shown in Fig. 11. It is usually assumed that the progenitor of the sdB was a star with about 1 – $2 M_{\odot}$ (Heber 2009, 2016). Therefore, we expect that the system is already quite old (5 – 10 Gyr). For the solutions in our allowed mass range the measured radius of the companion is about 20 per cent larger than expected from theoretical calculations. Such an effect, called inflation, has been observed in different binaries and also planetary systems with very close Jupiter-like planets. A detailed discussion will be given later. This effect has already been observed in other hot subdwarf close binary systems (e.g. Schaffenroth et al. 2015).

However, if the system would still be quite young with an age of about 1 Gyr, the companion would not be inflated. We performed a kinematic analysis to determine the Galactic population of J08205+0008. As seen in Fig. 12, the sdB binary belongs to the thin disc where star formation is still ongoing and could therefore indeed be as young as 1 Gyr, if the progenitor was a $2 M_{\odot}$ star. About half of the sdO/Bs at larger distances from the Galactic plane (0.5 kpc) are found in the thin disc (Martin et al. 2017). However, it is unclear whether a BD companion can eject the envelope from such a massive $2 M_{\odot}$ star. Hydrodynamical simulations performed by Kramer et al. (2020) indicate that a BD companion of ~ 0.05 – $0.08 M_{\odot}$ might just be able to eject the CE of a lower mass ($1 M_{\odot}$) red giant.

4 DISCUSSION

4.1 Tidal synchronization of sdB+dM binaries

In close binaries, the rotation of the components is often assumed to be synchronized to their orbital motion. In this case, the projected rotational velocity can be used to put tighter constraints on the companion mass. Geier et al. (2010) found that assuming tidal synchronization of the subdwarf primaries in sdB binaries with orbital periods of less than $\simeq 1.2$ d leads to consistent results in most cases. In particular, all the HW Vir type systems analysed in the Geier et al. (2010) study turned out to be synchronized.

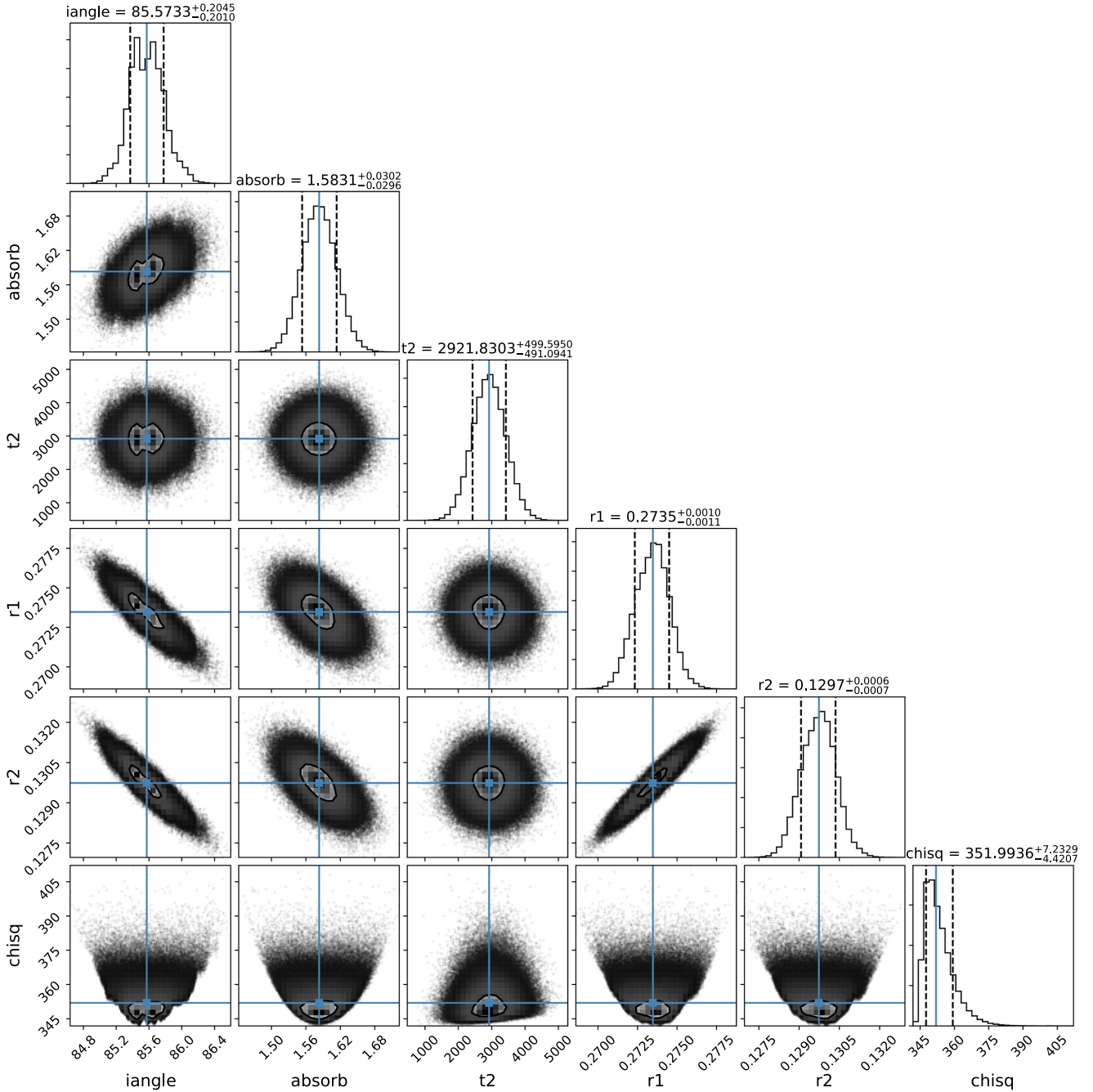


Figure 9. MCMC calculations showing the distributions of the parameter of the analysis of the ULTRACAM g' -band light curve.

In contrast to this, the projected rotational velocity of J08205+0008 is much smaller than is required for tidal synchronization. We can calculate the expected rotational velocity (v_{rot}) using the inclination (i), rotational period (P_{rot}), and the radius of the primary (R_1) from the light-curve analysis if we assume the system is synchronized:

$$P_{\text{rot},1} = \frac{2\pi R_1}{v_{\text{rot}}} \equiv P_{\text{orb}} \rightarrow v_{\text{synchro}} \sin i = \frac{2\pi R_1 \sin i}{P_{\text{orb}}}. \quad (4)$$

Due to the short period of this binary, the sdB should spin with $v_{\text{synchro}} \simeq 102 \text{ km s}^{-1}$ similar to the other known systems (see Geier et al. 2010, and references therein).

Other observational results in recent years also indicate that tidal synchronization of the sdB primary in close sdB+dM binaries is not always established in contrast to the assumption made by Geier et al. (2010). New theoretical models for tidal synchronization (Preece, Tout & Jeffery 2018, 2019) even predict that none of the hot subdwarfs in close binaries should rotate synchronously with the orbital period.

From the observational point of view, the situation appears to be rather complicated. Geier et al. (2010) found the projected rotational velocities of the two short-period ($P = 0.1\text{--}0.12 \text{ d}$) HW Vir systems HS 0705+6700 and the prototype HW Vir to be consistent with synchronization. Charpinet et al. (2008) used the splitting of the

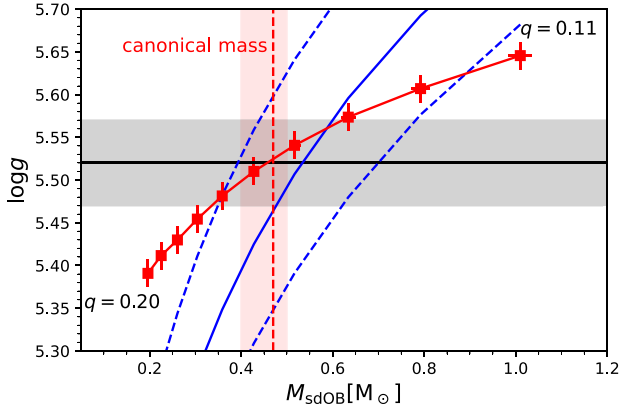


Figure 10. Mass of the sdB versus the photometric $\log g$ for J08205+0008 for different mass ratios from 0.11 to 0.20 in steps of 0.01 (red solid line). The parameters were derived by combining the results from the analysis of the light and RV curves. The grey area marks the spectroscopic $\log g$ that was derived from the spectroscopic analysis. The blue dashed lines indicate the $\log g$ derived by the radius from the SED fitting and the *Gaia* distance for different sdB masses. The red area marks the mass range for which we get a consistent solution by combining all different methods. The red vertical line represents the solution for a canonical mass sdB.

Table 3. Parameters of J08205+0008.

Spectroscopic parameters		
γ	(km s^{-1})	26.5 ± 0.4
K_1	(km s^{-1})	47.8 ± 0.4
$f(M)$	(M_\odot)	0.0011 ± 0.0001
$T_{\text{eff, sdB}}$	(K)	$25800 \pm 290^*$
$\log g, \text{sdB}$		$5.52 \pm 0.04^*$
$\log n(\text{He})$		$-2.07 \pm 0.04^*$
$v \sin i$	(km s^{-1})	$65.9 \pm 0.1^\dagger$
a	(R_\odot)	0.71 ± 0.02
M_1	(M_\odot)	$0.39\text{--}0.50$
M_2	(M_\odot)	$0.061\text{--}0.071$
Photometric parameters		
T_0	(BJD _{TDB})	2455165.709211(1)
P	(d)	0.09624073885(5)
\dot{P}	(d d^{-1})	$-3.2(8) \times 10^{-12}$
i	($^\circ$)	85.6 ± 0.3
R_1	(R_\odot)	0.194 ± 0.008
R_2	(R_\odot)	0.092 ± 0.005
$\log g$		5.52 ± 0.03
SED fitting		
ϖ_{Gaia}	(mas)	$0.6899 \pm 0.0632^\dagger$
$E(B - V)$	(mag)	$0.040 \pm 0.010^\dagger$
θ	(10^{-12} rad)	$6.22 \pm 0.15^*$
R_{Gaia}	(R_\odot)	$0.200^{+0.021*}_{-0.018}$
M_{Gaia}	(M_\odot)	$0.48^{+0.12*}_{-0.09}$
$\log(L_{\text{Gaia}}/L_\odot)$		$16^{+3.6*}_{-2.8}$

Notes: *Gaia*: based on measured *Gaia* parallax, but applying a zero-point offset of -0.029 mas (see Section 3.5 for details).

† 1σ statistical errors only.

*Listed uncertainties result from statistical and systematic errors (see Sections 3.2 and 3.4 for details).

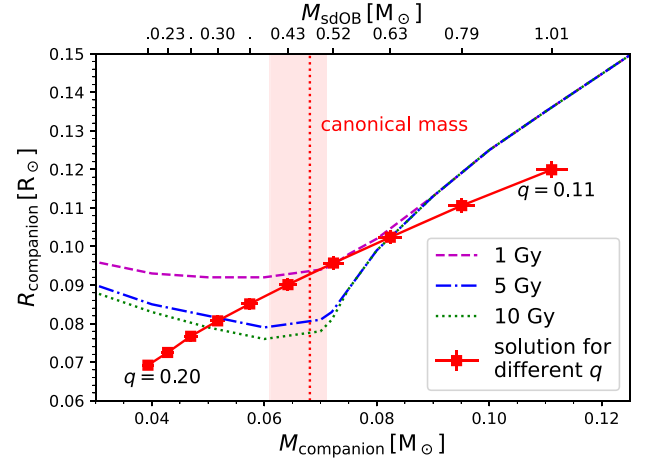


Figure 11. Comparison of theoretical mass–radius relations of low-mass stars (Baraffe et al. 2003; Chabrier & Baraffe 1997) to results from the light-curve analysis of J08205+0008. We used tracks for different ages of 1 Gy (dashed), 5 Gy (dotted–dashed), and 10 Gy (dotted). Each red square together with the errors represents a solution from the light-curve analysis for a different mass ratio ($q = 0.11\text{--}0.20$ in steps of 0.01). The red vertical line represents the solution for a canonical mass sdB. The red area marks the mass range of the companion corresponding to the mass range we derived for the sdB.

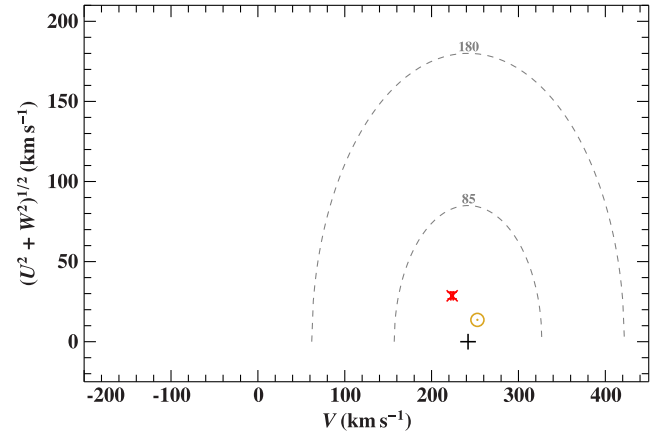


Figure 12. Toomre diagram of J08205+0008: the quantity V is the velocity in direction of Galactic rotation, U towards the Galactic centre, and W perpendicular to the Galactic plane. The two dashed ellipses mark boundaries for the thin (85 km s^{-1}) and thick disc (180 km s^{-1}) following Fuhrmann (2004). The red cross marks J08205+0008, the yellow circled dot the Sun, and the black plus the local standard of rest. The location of J08205+0008 in this diagram clearly hints at a thin disc membership.

pulsation modes to derive the rotation period of the pulsating sdB in the HW Vir-type binary PG 1336–018 and found it to be consistent with synchronized rotation. This was later confirmed by the measurement of the rotational broadening (Geier et al. 2010).

However, the other two sdBs with BD companions J162256+473051 and V2008–1753 (Schaffenroth et al. 2014a, 2015) have even shorter periods of only 0.07 d and both show subsynchronous rotation with 0.6 and 0.75 of the orbital period, respectively, just like J0820+0008. AA Dor on the other hand, which has a companion very close to the hydrogen-burning limit and a longer period of 0.25 d, seems to be synchronized (Vučković et al.

2016, and references therein), but it has already evolved beyond the EHB and is therefore older and has had more time to synchronize.

Pablo, Kawaler & Green (2011) and Pablo et al. (2012) studied three pulsating sdBs in reflection effect sdB+dM binaries with longer periods and again used the splitting of the pulsation modes to derive their rotation periods ($P \simeq 0.39\text{--}0.44$ d). All three sdBs rotate much slower than synchronized. But also in this period range the situation is not clear, since a full asteroseismic analysis of the sdB+dM binary Feige 48 ($P \simeq 0.38$ d) is consistent with synchronized rotation.

Since synchronization time-scales of any kind (Geier et al. 2010) scale dominantly with the orbital period of the close binary, these results seem puzzling. Especially since the other relevant parameters such as mass and structure of the primary or companion mass are all very similar in sdB+dM binaries. They all consist of core-helium-burning stars with masses of $\sim 0.5 M_{\odot}$ and low-mass companions with masses of $\sim 0.1 M_{\odot}$. And yet five of the analysed systems appear to be synchronized, while six rotate slower than synchronized without any significant dependence on companion mass or orbital period. This fraction, which is of course biased by complicated selection effects, might be an observational indication that the synchronization time-scales of such binaries are of the same order as the evolutionary time-scales.

It has to be pointed out that although evolutionary tracks of EHB stars exist, the accuracy of the derived observational parameters (usually T_{eff} and $\log g$) is not high enough to determine their evolutionary age on the EHB by comparison with those tracks as accurate as it can be done for other types of stars (see Fig. 2). As shown in Fig. 2, the position of the EHB is also dependent on the core and envelope mass and so it is not possible to find a unique track to a certain position in the $T_{\text{eff}}\text{--}\log g$ diagram and in most sdB systems the mass of the sdB is not constrained accurately enough.

Lisker et al. (2005) showed that sdB stars move at linear speed over the EHB and so the distance from the zero-age EHB (ZAEHB) represents how much time the star already spent on the EHB. If we look at the position of the non-synchronized against the position of the synchronized systems in the $T_{\text{eff}}\text{--}\log g$ diagram (Fig. 13), it is obvious that all the systems, which are known to be synchronized, appear to be older. There also seems to be a trend that systems with a higher ratio of rotational to orbital velocity are further away from the ZAEHB. This means that the fraction of rotational to orbital period might even allow an age estimate of the sdB.

The fact that the only post-EHB HW Vir system with a candidate substellar companion in our small sample (AA Dor) appears to be synchronized, while all the other HW Vir stars with very low-mass companions and shorter periods are not, fits quite well in this scenario. This could be a hint to the fact that for sdB+dM systems the synchronization time-scales are comparable to or even smaller than the lifetime on the EHB. Hot subdwarfs spend ~ 100 Myr on the EHB before they evolve to the post-EHB stage lasting ~ 10 Myr. So we would expect typical synchronization time-scales to be of the order of a few tens of millions of years, as we see both synchronized and unsynchronized systems.

4.2 A new explanation for the period decrease

There are different mechanisms of angular momentum loss in close binaries leading to a period decrease: gravitational waves, mass transfer (which can be excluded in a detached binary), or magnetic braking (see Qian et al. 2008). Here, we propose that tidal synchronization can also be an additional mechanism to decrease the orbital period of a binary.

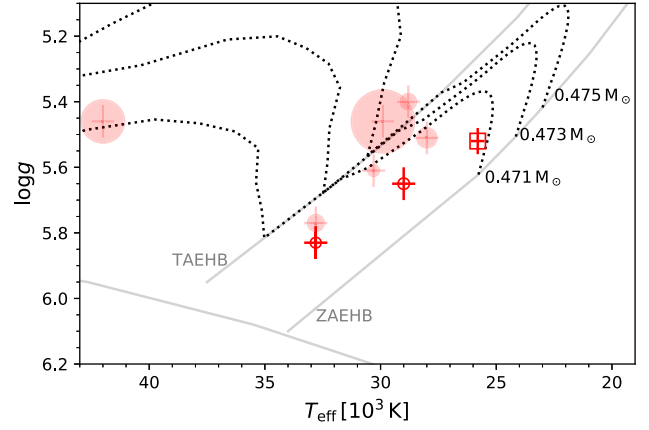


Figure 13. $T_{\text{eff}}\text{--}\log(g)$ diagram for the sdB+dM systems with known rotational periods mentioned in Section 4.1. The filled symbols represent synchronized systems, the open symbols, systems which are known to be non-synchronized. The square marks the position of J08205+0008. The sizes of the symbols scale with the orbital period, with longer periods having larger symbols. Plotted error bars are the estimated parameter variations due to the reflection effect, as found, for example, in Schaffenroth et al. (2013). The ZAEHB and TAEHB for a canonical mass sdB as well as evolutionary tracks for a canonical mass sdB with different envelope masses from Dorman et al. (1993) are also shown.

From the rotational broadening of the stellar lines (see Section 4.1), we derived the rotational velocity of the subdwarf to be about half of what would be expected from the sdB being synchronized to the orbital period of the system. This means that the sdB is currently spun up by tidal forces until synchronization is reached causing an increase in the rotational velocity. As the mass of the companion is much smaller than the mass of the sdB, we assume synchronization for the companion.

The total angular momentum of the binary system is given by the orbital angular momentum J_{orb} and the sum of the rotational angular momentum of the primary and secondary star $I_{\text{spin},1/2}$, with ω being the orbital angular velocity and Ω_i the rotational, angular velocity:

$$J_{\text{tot}} = J_{\text{orb}} + \sum_{i=1}^2 I_{\text{spin},i} \quad (5)$$

$$J_{\text{orb}} = (m_1 a_1^2 + m_2 a_2^2) \omega = \frac{m_1 m_2}{m_1 + m_2} a^2 \omega \quad (6)$$

$$a^2 = \left(\frac{G(m_1 + m_2)}{\omega^2} \right)^{2/3} \quad (7)$$

$$I_{\text{spin},i} = k_r^2 M_i R_i^2 \Omega_i \quad (8)$$

with k_r^2 the radius of gyration of the star. It refers to the distribution of the components of an object around its rotational axis. It is defined as $k_r^2 = I/MR^2$, where I is the moment of inertia of the star. Geier et al. (2010) used a value of 0.04 derived from sdB models, which we adopt.

For now we neglect angular momentum loss due to gravitational waves and magnetic braking. If we assume that the companion is already synchronized and its rotational velocity stays constant ($\frac{d\Omega_2}{dt} = 0$) and that the masses and radii do not change, as we do not expect any mass transfer after the common envelope phase, we obtain

$$\frac{dJ_{\text{tot}}}{dt} = p_1 \frac{d\omega^{-1/3}}{dt} + p_2 \frac{d\Omega_1}{dt} = -p_1 \frac{\dot{\omega}}{3\omega^{4/3}} + p_2 \dot{\Omega} = 0 \quad (9)$$

with

$$p_1 = \frac{m_1 m_2 G^{2/3}}{(m_1 + m_2)^{1/3}} \quad (10)$$

and

$$p_2 = k_r^2 m_1 R_1^2 \quad (11)$$

This shows that from an increase in the rotational velocity of the primary, which is expected from tidal synchronization, we expect an increase of the orbital velocity, which we observe in the case of J08205+0008. We can now calculate the current change of orbital velocity:

$$\dot{\Omega}_1 = \frac{p_1}{3p_2} \frac{\dot{\omega}}{\omega^{4/3}} = \frac{m_2 G^{2/3}}{3k_r^2 R_1^2 (m_1 + m_2)^{1/3}} \frac{\dot{\omega}}{\omega^{4/3}} \quad (12)$$

From this equation, we can clearly see that rotational velocity change depends on the masses of both stars, the radius of the primary, the orbital velocity change, and the current orbital velocity. An increasing rotational velocity causes an increasing orbital velocity and hence a period decrease.

4.3 Synchronization time-scale

If we assume that the observed period decrease is only due to the rotational velocity change, we can calculate the rate of the rotational velocity change and the time-scale until synchronization is reached. According to Preece et al. (2018), the change of rotational angular velocity is given by

$$\frac{d\Omega}{dt} = \frac{\omega}{\tau_{\text{tide}}} \left(1 - \frac{\Omega}{\omega}\right) \frac{M_2}{M_1 + M_2} \frac{a^2}{R^2 k_r^2} \propto \left(1 - \frac{\Omega}{\omega}\right) \quad (13)$$

where τ_{tide} is the tidal time-scale depending on the density, radius and mass of the star, and the viscous time-scale of the convective region. The current position of J08205+0008 on the $T_{\text{eff}}-\log g$ diagram and the mass we derived from our analysis suggest that the sdB is currently in the evolutionary phase of helium-burning. The lifetime of this phase is approximately 100 Myr. So we do not expect the structure of the star to change significantly in the next few Myr. Because the moment of inertia of an sdB star is small compared to that of the binary orbit, the change in separation and angular velocity can be neglected.

Therefore, we can calculate the time-scale until synchronization is reached using the equation given in Zahn (1989):

$$\frac{1}{T_{\text{sync}}} = -\frac{1}{\Omega_1 - \omega} \frac{d\Omega_1}{dt} \quad (14)$$

Using our equation (13) and calculating and substituting the angular velocities by the periods we derive an expression for the synchronization time-scale:

$$T_{\text{sync}} = \left(1 - \frac{2\pi R_1 \sin i}{P_{\text{orb}} v \sin i}\right) \frac{P_{\text{orb}}^{2/3} v \sin i}{\dot{P}_{\text{orb}} \sin i} \frac{3(2\pi)^{1/3} k_r^2 R_1 (m_1 + m_2)^{1/3}}{m_2 G^{2/3}} \quad (15)$$

Using the orbital period, the masses, radii, and inclination from our analysis, we calculate a synchronization time T_{sync} of 2.1 ± 0.1 Myr, well within the lifetime of a helium-burning object on the EHB. The orbital period will change by about 200 s (3.5 per cent) in this 2 Myr, which means a change in the separation of only $0.01 R_{\odot}$, which shows that our assumption of a negligible change in separation is valid. If we assume that the rotation after the common envelope phase was close to zero, the total time-scale until the system reaches synchronization is about 4 Myr. This assumption is plausible as most

red giant progenitors rotate slowly and the common envelope phase is very short-lived and so no change of the rotation is expected.

This means that this effect could significantly add to the observed period decrease. The fact that the synchronized systems appear to be older than the non-synchronized ones confirms that the synchronization time-scale is of the expected order of magnitude and it is possible that we might indeed measure the synchronization time-scale.

As mentioned before, Preece et al. (2018) predict that the synchronization time-scales are much longer than the lifetime on the EHB and that none of the HW Vir systems should be synchronized. Preece et al. (2019) investigated also the special case of NY Vir, which was determined to be synchronized from spectroscopy and asteroseismology, and came to the conclusion that they cannot explain, why it is synchronized. They proposed that maybe the outer layers of the sdB were synchronized during the common envelope phase. However, observations show that synchronized sdB+dM systems are not rare, but that synchronization occurs most likely during the phase of helium-burning, which shows that synchronization theory is not yet able to predict accurate synchronization time-scales.

4.4 Orbital period variations in HW Vir systems

As mentioned before, there are several mechanisms that can explain period changes in HW Vir systems. The period change due to gravitational waves is usually very small in HW Vir systems and would only be observable after observations for many decades (e.g. Kilkeny 2014). Using the equation given in Kupfer et al. (2020) with the system parameters derived in this paper, we predict an orbital period decay due to gravitational waves of $\dot{P} = -4.5e-14 \text{ ss}^{-1}$. The observed change in orbital period is hence about 100 times higher than expected by an orbital decay due to gravitational waves.

HW Vir and NY Vir have also been observed to show a period decrease of the same order of magnitude (Qian et al. 2008; Kilkeny 2014) but have been found to rotate (nearly) synchronously. Both also show additionally to the period decrease a long-period sinusoidal signal (Lee et al. 2009, 2014). These additional variations in the O-C diagram have been interpreted as caused by circumbinary planets in both cases, however the solutions were not confirmed with observations of longer baselines. Observations of more than one orbital period of the planet would be necessary to confirm it. The period decrease was explained to be caused by angular momentum loss due to magnetic stellar wind braking.

Following the approach of Qian et al. (2007), we calculated the relation between the mass-loss rate and the Alfvén radius that would be required to account for the period decrease in J08205+0008 due to magnetic braking. This is shown in Fig. 14. Using the tidally enhanced mass-loss rate of Tout & Eggleton (1988) we derive that an Alfvén radius of $75 R_{\odot}$ would be required to cause the period decrease we measure, much larger than the Alfvén radius of the Sun. This shows that, as expected, the effect of magnetic braking in a late M dwarf or massive BD is very small at best and cannot explain the period decrease we derive.

Bours et al. (2016) made a study of close WD binaries and observed that the amplitude of eclipse arrival time variations in K dwarf and early M dwarf companions is much larger than in late M dwarf, BD or WD companions, which do not show significant orbital period variations. They concluded that these findings are in agreement with the so-called Applegate mechanism, which proposes that variability in the binary orbits can be driven by magnetic cycles in the secondary stars. In all published HW Vir systems with a longer observational baseline of several years quite large period variations on the order of

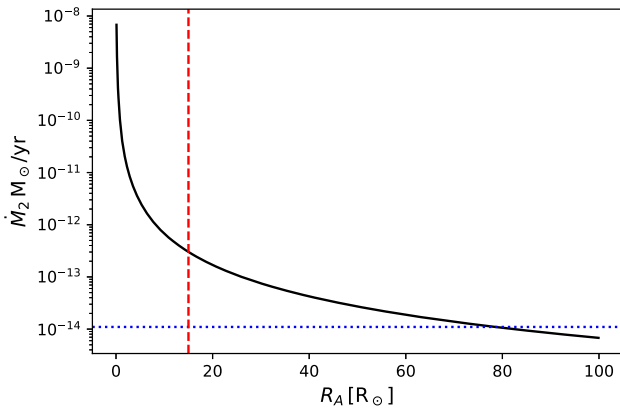


Figure 14. Correlation between the Alfvén radius and the mass-loss rate for the companion of J08205+0008. The red dashed line marks the Alfvén radius for the Sun, the blue dotted line indicates the tidally enhanced mass-loss rate determined using the parameters of the sdB using the formula of Tout & Eggleton (1988).

minutes have been detected (see Zorotovic & Schreiber 2013; Pulley et al. 2018, for an overview), with the exception of AA Dor (Kilkenny 2014), which still shows no sign of period variations after a baseline of about 40 yr. Also the orbital period decrease in J08205+0008 is on the order of seconds and has only been found after 10 yr of observation and no additional sinusoidal signals have been found as seen in many of the other systems. This confirms that the findings of Bours et al. (2016) apply to close hot subdwarf binaries with cool companions. The fact that the synchronized HW Vir system AA Dor does not show any period variations also confirms our theory that the period variations in HW Vir systems with companions close to the hydrogen-burning limit might be caused by tidal synchronization. In higher mass M dwarf companions, the larger period variations are likely caused by the Applegate mechanism and the period decrease can be caused dominantly by magnetic braking and additionally tidal synchronization.

It seems that orbital period changes in HW Vir systems are still poorly understood and have also not been studied observationally to the full extent. More observations over long time spans of synchronized and non-synchronized short-period sdB binaries with companions of different masses will be necessary to understand synchronization and orbital period changes of hot subdwarf binaries. Most likely it cannot be explained with just one effect and is likely an interplay of different effects.

4.5 Inflation of brown dwarfs and low-mass M dwarfs in eclipsing WD or sdB binaries

Close BD companions that eclipse main-sequence stars are rare, with only 23 known to date (Carmichael et al. 2020). Consequently, BD companions to the evolved form of these systems are much rarer with only three (including J08205+0008) known to eclipse hot subdwarfs, and three known to eclipse WDs. These evolved systems are old (> 1 Gyr), and the BDs are massive, and hence not expected to be inflated (Thorngren & Fortney 2018).

Surprisingly, of the three hot subdwarfs with BD companions, J08205+0008 is the one that receives the least irradiation – almost half that received by V2008–1753 and SDSSJ162256.66+473051.1, both of which have hotter primaries (32000 K, 29000 K) and shorter periods (~ 1.6 h) than J08205+0008. This suggests that more irradiation, and more irradiation at shorter wavelengths does not

equate to a higher level of inflation of a BD. Indeed this finding is consistent with that for BDs irradiated by WDs, where the most irradiated object with a measured radius is SDSS J1205-0242B, in a 71.2 min orbit around a 23681 K WD and yet the BD is not inflated (Parsons et al. 2017). The BD in this system only receives a hundredth of the irradiation that J08205+0008 does. However, WD1032+011, an old WD ($T_{\text{eff}} \sim 10000$ K) with a high-mass BD companion ($0.0665 M_{\odot}$) does appear to be inflated (Casewell et al. 2020). As can be seen from Fig. 15, the majority of the low-mass BDs ($M < 35 M_{\text{Jup}}$) are inflated, irrelevant of how much irradiation they receive. For the few old (5–10 Gyr), higher mass inflated BDs, the mechanism leading to the observed inflation is not yet understood.

4.6 Previous and future evolution of the system

As stated before, stars with a cool, low-mass companion sitting on the EHB are thought to have formed by a common-envelope phase from a progenitor of up to two solar mass on the RGB. Due to the large mass ratio only unstable mass transfer is possible. If the mass transfer happened at the tip of the RGB, a core-helium-burning object with about $0.5 M_{\odot}$ will be formed. If the mass transfer happened earlier then the core of the progenitor has not enough mass to start He-core-burning and the pre-He WD will move to the WD cooling track crossing the EHB. Our analysis of J08205+0008 showed that a low-mass solution ($0.25 M_{\odot}$, as discussed previously) can be excluded and that the primary star is indeed currently a core He-burning object.

Kupfer et al. (2015) calculated the evolution of J08205+0008 and considering only angular momentum loss due to gravitational waves and found that the companion will fill its Roche lobe in about 2.2 Gyr and mass transfer is expected to start forming a cataclysmic variable. We detected a significantly higher orbital period decrease in this system than expected from gravitational waves. Up to now, we could not detect any change in the rate of this period decrease. If we assume that the orbital period change is due to rotational period change until synchronization is reached and afterwards the period decrease will be solely due to gravitational waves, we can calculate when the companion will fill its Roche lobe and accretion to the primary will start. To calculate the Roche radius, the equation derived in Eggleton (1983) was used:

$$R_L = \frac{0.49q^{2/3}}{0.6q^{2/3} + \ln(1 + q^{1/3})} a \quad (16)$$

Using the values derived in our analysis, we calculate that the Roche lobe of the companion will be filled at a system separation of $0.410 R_{\odot}$, 56 per cent of the current separation, which is reached at a period of 3525 s. From this, we calculate a time scale of 1.8 Gyr until the Roche lobe will be filled.

Systems with a mass ratio $q = M_2/M_1 < 2/3$, with M_1 being the mass of the accretor, are assumed to be able to undergo stable mass transfer. Our system has a mass ratio of $0.147 \ll 2/3$. The subdwarf will already have evolved to a WD and a cataclysmic variable will be formed. It is expected that the period of an accreting binary with a hydrogen-rich donor star will decrease until a minimum period of $\simeq 70$ min is reached at a companion mass around $0.06 M_{\odot}$ and the period will increase again afterwards (Nelson et al. 2018). Such systems are called period bouncers. Our system comes into contact already close to the minimum period and should hence increase the period when the mass transfer starts.

The future of the system depends completely on the period evolution. A longer baseline of observations of this system is necessary to confirm that the period decrease is indeed stable and caused by the tidal synchronization.

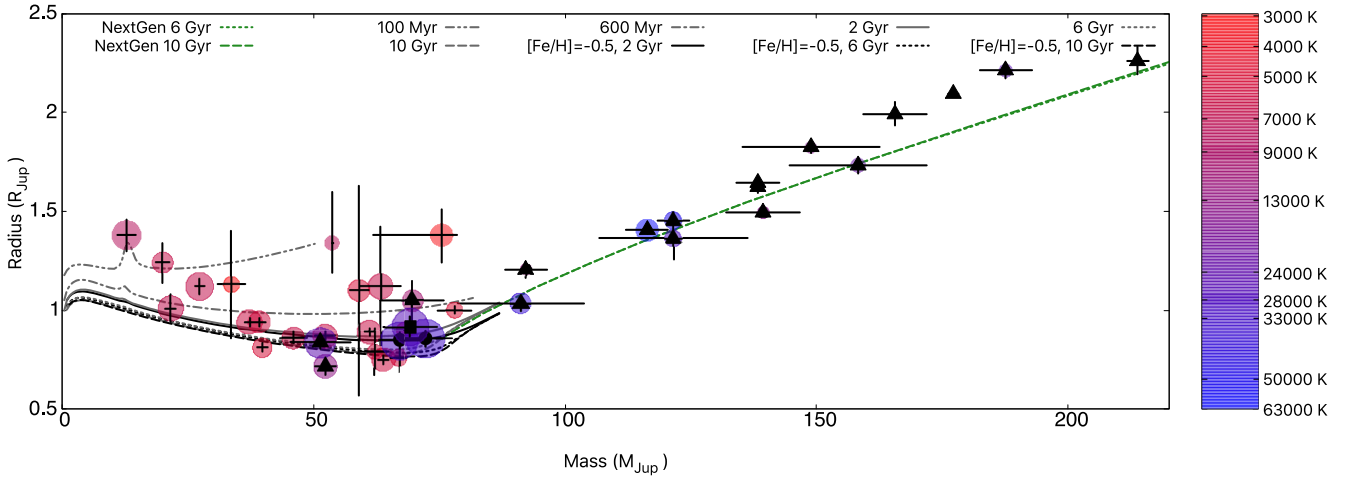


Figure 15. All known eclipsing binary WDs with detached BD (triangles: Parsons et al. 2017; Littlefair et al. 2014) and late M dwarf companions (triangles) from Parsons et al. (2018), hot subdwarfs with eclipsing BD companions (circles: Schaffenroth et al. 2014b, 2015), and all known eclipsing BD companions to main-sequence stars (+: Carmichael et al. 2020). J08205+0008 is plotted as the filled square. The colour is proportional to the effective temperature of the primary in each system and the coloured circle size is proportional to the amount of total incident radiation the secondary receives. Also shown are the Sonora Bobcat BD evolutionary models³ of Marley et al. (in preparation) for solar and subsolar metallicity and the NextGen models (Baraffe et al. 1997).

5 CONCLUSION AND SUMMARY

The analysis of J08205+0008 with higher quality data from ESO-VLT/XSHOOTER, ESO-VLT/UVES, and ESO-NTT/ULTRACAM allowed us to constrain the masses of the sdB and the companion much better by combining the analysis of the RV and the light curves. We determine an sdB mass of 0.39–0.50 M_{\odot} consistent with the canonical mass and a companion mass of 0.061 – 0.071 M_{\odot} close to the hydrogen-burning limit. Therefore, we confirm that the companion is likely be a massive BD.

The atmospheric parameters and abundances show that J08205+0008 is a typical sdB and comparison with stellar evolution tracks suggest that the mass has to be less than 0.50 M_{\odot} consistent with our solution and also the mass derived by a spectrophotometric method using *Gaia* parallaxes and the SED derived in the secondary eclipse, where the companion is not visible.

If the sdB evolved from a 1 M_{\odot} star, the age of the system is expected to be around 10 Gyr. In this case, the radius of the BD companion is about 20 per cent inflated compared to theoretical calculations. Such an inflation is observed in several sdB/WD+dM/BD systems but not understood yet. However, the inflation seems not to be caused by the strong irradiation. The sdB binary belongs to the thin disc, as do about half of the sdB at this distance from the Galactic plane. This means that they also could be young, if they have evolved from a more massive progenitor. Then, we get a consistent solution without requiring inflation of the companion. However, a BD companion might not be able to remove the envelope of a more massive progenitor.

We detected a significant period decrease in J0820+0008. This can be explained by the spin-up of the sdB due to tidal synchronization. We calculated the synchronization time-scale to 4 Myr well within the lifetime on the EHB. The investigation of the parameters of all known Vir systems with rotational periods (see Section 4.1) shows that the synchronized systems tend to be older, showing that the synchronization time-scale seems to be comparable but smaller than the lifetime on the EHB in contrast to current synchronization theories.

By investigating the known orbital period variations in HW Vir systems, we can confirm the findings by Bours et al. (2016) that

period variations in systems with higher mass M dwarf companions seem to be larger. Hence, we conclude that the large period variations in those systems are likely caused by the Applegate mechanism and the observed period decreases dominantly by magnetic braking. In lower mass companions close to the hydrogen-burning limit, on the other hand, tidal synchronization spinning up the sdB could be responsible for the period decrease, allowing us to derive a synchronization time-scale.

The results of our analysis are limited by the precision of the available trigonometric parallax. As the *Gaia* mission proceeds, the precision and accuracy of the trigonometric parallax will improve, which will narrow down the uncertainties of the stellar parameters. A very important goal is to detect spectral signatures from the companion and to measure the RV curve of the companion. We failed to do so, because the infrared spectra at hand are of insufficient quality. The future IR instrumentation on larger telescopes, such as the ESO-ELT, will be needed. A high precision measurement of the RV curves of both components will then allow us to derive an additional constraint on mass and radius from the difference of the stars’ gravitational redshifts (Vos et al. 2013). Such measurements will give an independent determination of the nature of the companion and will help to test evolutionary models for low mass star near the hydrogen-burning limit via the mass–radius relation.

The combination of many different methods allowed us to constrain the masses of both components much better without having to assume a canonical mass for the sdB. This is only the fourth HW Vir system for which this is possible.

ACKNOWLEDGEMENTS

DS is supported by the Deutsche Forschungsgemeinschaft (DFG) under grant HE 1356/70-1 and IR190/1-1. VS is supported by the Deutsche Forschungsgemeinschaft, DFG through grant GE 2506/9-1. SLC is supported by an STFC (Science and Technology Facilities Council) Ernest Rutherford Fellowship ST/R003726/1. DK thanks the SAAO for generous allocations of telescope time and the National

³<https://zenodo.org/record/1309035>

Research Foundation of South Africa and the University of the Western Cape for financial support. VSD, SPL, and ULTRACAM are supported by the STFC. We thank J. E. Davis for the development of the `slxfig` module, which has been used to prepare figures in this work. MATPLOTLIB (Hunter 2007) and NUMPY (van der Walt, Colbert & Varoquaux 2011) were used in order to prepare figures in this work. This work has made use of data from the European Space Agency (ESA) mission *Gaia* (<https://www.cosmos.esa.int/gaia>), processed by the *Gaia* Data Processing and Analysis Consortium (DPAC, <https://www.cosmos.esa.int/web/gaia/dpac/consortium>). Funding for the DPAC has been provided by national institutions, in particular the institutions participating in the *Gaia* Multilateral Agreement. Based on observations at the Cerro Paranal Observatory of the European Southern Observatory (ESO) in Chile under the program IDs 087.D-0185(A), and 098.C-0754(A). Based on observations at the La Silla Observatory of the ESO in Chile under the program IDs 082.D-0649(A), 084.D-0348(A), and 098.D-679. This paper uses observations made at the South African Astronomical Observatory. We made extensive use of NASAs Astrophysics Data System Abstract Service (ADS) and the SIMBAD and VizieR database, operated at CDS, Strasbourg, France.

DATA AVAILABILITY STATEMENT

Most data are incorporated into the article and its appendix. All other data (light curves and spectra) are available on request.

REFERENCES

- Abazajian K. N. et al., 2009, *ApJS*, 182, 543
 Alam S. et al., 2015, *ApJS*, 219, 12
 Asplund M., Grevesse N., Sauval A. J., Scott P., 2009, *ARA&A*, 47, 481
 Banse K., Crane P., Grosbol P., Middleburg F., Ounnas C., Ponz D., Waldthausen H., 1983, *The Messenger*, 31, 26
 Baraffe I., Chabrier G., Allard F., Hauschildt P. H., 1997, *A&A*, 327, 1054
 Baraffe I., Chabrier G., Barman T. S., Allard F., Hauschildt P. H., 2003, *A&A*, 402, 701
 Baran A. S. et al., 2018, *MNRAS*, 481, 2721
 Beauchamp A., Wesemael F., Bergeron P., 1997, *ApJS*, 108, 559
 Becker S. R., 1998, in Howarth I., ed., *ASP Conf. Ser. Vol. 131, Properties of Hot Luminous Stars*. Astron. Soc. Pac., San Francisco, p. 137
 Becker S. R., Butler K., 1988, *A&A*, 201, 232
 Beuermann K. et al., 2012, *A&A*, 540, A8
 Bianchi L., Shiao B., Thilker D., 2017, *ApJS*, 230, 24
 Bours M. C. P. et al., 2016, *MNRAS*, 460, 3873
 Butler K., Giddings J. R., 1985, *Newsletter of Analysis of Astronomical Spectra*, No. 9. Univ. London, London
 Carmichael T. W. et al., 2020, *AJ*, 160, 53
 Casewell S. L. et al., 2020, *MNRAS*, 497, 3571
 Chabrier G., Baraffe I., 1997, *A&A*, 327, 1039
 Charpinet S., Van Grootel V., Reese D., Fontaine G., Green E. M., Brassard P., Chayer P., 2008, *A&A*, 489, 377
 Claret A., Bloemen S., 2011, *A&A*, 529, A75
 Copperwheat C. M., Marsh T. R., Dhillon V. S., Littlefair S. P., Hickman R., Gänsicke B. T., Southworth J., 2010, *MNRAS*, 402, 1824
 Cutri R. M. et al., 2003, *2MASS All Sky Catalog of Point Sources*, available at <http://irsa.ipac.caltech.edu/applications/Gator/>
 Cutri R. M. et al., 2014, *VizieR Online Data Catalog*, II/328
 Dekker H., D'Odorico S., Kaufer A., Delabre B., Kotzlowski H., 2000, in Iye M., Moorwood A. F., eds, *Proc. SPIE Conf. Ser. Vol. 4008, Optical and IR Telescope Instrumentation and Detectors*. SPIE, Bellingham, p. 534
 Dhillon V. S. et al., 2007, *MNRAS*, 378, 825
 Dieterich S. B., Henry T. J., Jao W.-C., Winters J. G., Hosey A. D., Riedel A. R., Subasavage J. P., 2014, *AJ*, 147, 94
 Dorman B., Rood R. T., O'Connell R. W., 1993, *ApJ*, 419, 596
 Edelman H., 2008, in Heber U., Jeffery C. S., Napiwotzki R., eds, *ASP Conf. Ser. Vol. 392, Hot Subdwarf Stars and Related Objects*. Astron. Soc. Pac., San Francisco, p. 187
 Eggleton P. P., 1983, *ApJ*, 268, 368
 Evans D. W. et al., 2018, *A&A*, 616, A4
 Fitzpatrick E. L., Massa D., Gordon K. D., Bohlin R., Clayton G. C., 2019, *ApJ*, 886, 108
 Flewelling H. A. et al., 2020, *ApJS*, 251, 7
 Fontaine G., Brassard P., Charpinet S., Green E. M., Randall S. K., Van Grootel V., 2012, *A&A*, 539, A12
 Foreman-Mackey D., 2016, *J. Open Source Softw.*, 1, 24
 Foreman-Mackey D., Hogg D. W., Lang D., Goodman J., 2013, *PASP*, 125, 306
 Freudling W., Romaniello M., Bramich D. M., Ballester P., Forchi V., García-Dabó C. E., Moehler S., Neeser M. J., 2013, *A&A*, 559, A96
 Gaia Collaboration, 2018, *A&A*, 616, A1
 Geier S., Heber U., 2012, *A&A*, 543, A149
 Geier S., Heber U., Podsiadlowski P., Edelman H., Napiwotzki R., Kupfer T., Müller S., 2010, *A&A*, 519, A25
 Geier S. et al., 2011a, *A&A*, 526, A39
 Geier S. et al., 2011b, *A&A*, 530, A28
 Geier S. et al., 2011c, *ApJ*, 731, L22
 Giddings J. R., 1981, PhD thesis, Univ. London
 Greenstein G. S., 1967, *Nature*, 213, 871
 Han Z., Podsiadlowski P., Maxted P. F. L., Marsh T. R., Ivanova N., 2002, *MNRAS*, 336, 449
 Han Z., Podsiadlowski P., Maxted P. F. L., Marsh T. R., 2003, *MNRAS*, 341, 669
 Heber U., 2009, *ARA&A*, 47, 211
 Heber U., 2016, *PASP*, 128, 082001
 Heber U. et al., 2004, *A&A*, 420, 251
 Heber U., Irrgang A., Schaffenroth J., 2018, *Open Astron.*, 27, 35
 Henden A. A., Levine S., Terrell D., Welch D. L., 2015, in *American Astronomical Society Meeting Abstracts #225*. p. 336.16
 Hirsch H. A., 2009, PhD thesis, Friedrich-Alexander University Erlangen-Nürnberg
 Hubeny I., Hummer D. G., Lanz T., 1994, *A&A*, 282, 151
 Hunter J. D., 2007, *Comput. Sci. Eng.*, 9, 90
 Husser T. O., Wende-von Berg S., Dreizler S., Homeier D., Reiners A., Barman T., Hauschildt P. H., 2013, *A&A*, 553, A6
 Iben I. J., Tutukov A. V., 1984, *ApJS*, 54, 335
 Irrgang A., Przybilla N., Heber U., Böck M., Hanke M., Nieva M. F., Butler K., 2014, *A&A*, 565, A63
 Irrgang A., Kreuzer S., Heber U., Brown W., 2018, *A&A*, 615, L5
 Kausch W. et al., 2015, *A&A*, 576, A78
 Kepler S. O. et al., 1991, *ApJ*, 378, L45
 Kilkeny D., 2011, *MNRAS*, 412, 487
 Kilkeny D., 2014, *MNRAS*, 445, 4247
 Kilkeny D., Koen C., 2012, *MNRAS*, 421, 3238
 Kiss L. L., Csák B., Szatmáry K., Furész G., Sziládi K., 2000, *A&A*, 364, 199
 Kramer M., Schneider F. R. N., Ohlmann S. T., Geier S., Schaffenroth V., Pakmor R., Roepke F. K., 2020, *A&A*, 642, A97
 Kupfer T. et al., 2015, *A&A*, 576, A44
 Kupfer T. et al., 2020, *ApJ*, 891, 45
 Kurucz R. L., 1996, in Adelman S. J., Kupka F., Weiss W. W., eds, *ASP Conf. Ser. Vol. 108, M.A.S.S., Model Atmospheres and Spectrum Synthesis*. Astron. Soc. Pac., San Francisco, p. 160
 Lawrence A. et al., 2007, *MNRAS*, 379, 1599
 Lee J. W., Kim S.-L., Kim C.-H., Koch R. H., Lee C.-U., Kim H.-I., Park J.-H., 2009, *AJ*, 137, 3181
 Lee J. W., Hinse T. C., Youn J.-H., Han W., 2014, *MNRAS*, 445, 2331
 Lindegren L. et al., 2018, *A&A*, 616, A2
 Lisker T., Heber U., Napiwotzki R., Christlieb N., Han Z., Homeier D., Reimers D., 2005, *A&A*, 430, 223
 Littlefair S. P. et al., 2014, *MNRAS*, 445, 2106
 Lohr M. E. et al., 2014, *A&A*, 566, A128
 Lucy L. B., 1967, *ZAp*, 65, 89

Maíz Apellániz J., Weiler M., 2018, *A&A*, 619, A180
 Martin P., Jeffery C. S., Naslim N., Woolf V. M., 2017, *MNRAS*, 467, 68
 Maxted P. F. L., Heber U., Marsh T. R., North R. C., 2001, *MNRAS*, 326, 1391
 McLaughlin D. B., 1924, *ApJ*, 60, 22
 Menzies J. W., Marang F., 1986, in Hearnshaw J. B., Cottrell P. L., eds, IAU Symp. Vol. 118, Instrumentation and Research Programmes for Small Telescopes, D. Reidel Publishing Company, Dordrecht, Holland. p. 305
 Michaud G., Alecian G., Richer J., 2015, *Atomic Diffusion in Stars*. Springer International Publ., Switzerland
 Morel T., Butler K., 2008, *A&A*, 487, 307
 Morel T., Butler K., Aerts C., Neiner C., Briquet M., 2006, *A&A*, 457, 651
 Napiwotzki R., Karl C. A., Lisker T., Heber U., Christlieb N., Reimers D., Nelemans G., Homeier D., 2004a, *Ap&SS*, 291, 321
 Napiwotzki R. et al., 2004b, in Hilditch R. W., Hensberge H., Pavlovski K., eds, ASP Conf. Ser. Vol. 318, Spectroscopically and Spatially Resolving the Components of the Close Binary Stars. Astron. Soc. Pac., San Francisco, p. 402
 Naslim N., Jeffery C. S., Hibbert A., Behara N. T., 2013, *MNRAS*, 434, 1920
 Nelemans G., Tauris T. M., 1998, *A&A*, 335, L85
 Nelson L., Schwab J., Ristic M., Rappaport S., 2018, *ApJ*, 866, 88
 Nieva M. F., Przybilla N., 2006, *ApJ*, 639, L39
 Nieva M. F., Przybilla N., 2007, *A&A*, 467, 295
 Nieva M. F., Przybilla N., 2008, *A&A*, 481, 199
 Nieva M. F., Przybilla N., 2012, *A&A*, 539, A143
 Pablo H., Kawaler S. D., Green E. M., 2011, *ApJ*, 740, L47
 Pablo H. et al., 2012, *MNRAS*, 422, 1343
 Parsons S. G., Marsh T. R., Copperwheat C. M., Dhillon V. S., Littlefair S. P., Gänsicke B. T., Hickman R., 2010, *MNRAS*, 402, 2591
 Parsons S. G. et al., 2017, *MNRAS*, 471, 976
 Parsons S. G. et al., 2018, *MNRAS*, 481, 1083
 Preece H. P., Tout C. A., Jeffery C. S., 2018, *MNRAS*, 481, 715
 Preece H. P., Tout C. A., Jeffery C. S., 2019, *MNRAS*, 485, 2889
 Press W. H., Teukolsky S. A., Vetterling W. T., Flannery B. P., 1992, Numerical Recipes in FORTRAN. The Art of Scientific Computing, 2nd edn. Cambridge Univ. Press, Cambridge
 Przybilla N., 2005, *A&A*, 443, 293
 Przybilla N., Butler K., 2001, *A&A*, 379, 955
 Przybilla N., Butler K., 2004, *ApJ*, 609, 1181
 Przybilla N., Butler K., Becker S. R., Kudritzki R. P., Venn K. A., 2000, *A&A*, 359, 1085
 Przybilla N., Butler K., Becker S. R., Kudritzki R. P., 2001, *A&A*, 369, 1009
 Przybilla N., Nieva M. F., Edelmann H., 2006a, *Balt. Astron.*, 15, 107
 Przybilla N., Butler K., Becker S. R., Kudritzki R. P., 2006b, *A&A*, 445, 1099
 Przybilla N., Nieva M.-F., Butler K., 2011, *J. Phys. Conf. Ser.*, 328, 012015
 Pulley D., Faillace G., Smith D., Watkins A., von Harrach S., 2018, *A&A*, 611, A48
 Qian S. B., Dai Z. B., He J. J., Yuan J. Z., Xiang F. Y., Zejda M., 2007, *A&A*, 466, 589

Qian S. B., Dai Z. B., Zhu L. Y., Liu L., He J. J., Liao W. P., Li L. J., 2008, *ApJ*, 689, L49
 Reif K. et al., 1999, in Blouke M. M., Williams G. M., eds, *Proc. SPIE Conf. Ser. Vol. 3649, Sensors, Cameras, and Systems for Scientific/Industrial Applications*. SPIE, Bellingham, p. 109
 Rossiter R. A., 1924, *ApJ*, 60, 15
 Schaffenroth V., Geier S., Drechsel H., Heber U., Wils P., Østensen R. H., Maxted P. F. L., di Scala G., 2013, *A&A*, 553, A18
 Schaffenroth V., Geier S., Heber U., Kupfer T., Ziegerer E., Heuser C., Classen L., Cordes O., 2014a, *A&A*, 564, A98
 Schaffenroth V., Classen L., Nagel K., Geier S., Koen C., Heber U., Edelmann H., 2014b, *A&A*, 570, A70
 Schaffenroth V., Barlow B. N., Drechsel H., Dunlap B. H., 2015, *A&A*, 576, A123
 Schaffenroth V., Geier S., Heber U., Gerber R., Schneider D., Ziegerer E., Cordes O., 2018, *A&A*, 614, A77
 Schaffenroth V. et al., 2019, *A&A*, 630, A80
 Schlafly E. F., Finkbeiner D. P., 2011, *ApJ*, 737, 103
 Schlafly E. F., Meisner A. M., Green G. M., 2019, *ApJS*, 240, 30
 Schlegel D. J., Finkbeiner D. P., Davis M., 1998, *ApJ*, 500, 525
 Schneider D., Irrgang A., Heber U., Nieva M. F., Przybilla N., 2018, *A&A*, 618, A86
 Smette A. et al., 2015, *A&A*, 576, A77
 Soker N., 1998, *AJ*, 116, 1308
 Steele P. R., Burleigh M. R., Dobbie P. D., Jameson R. F., Barstow M. A., Satterthwaite R. P., 2011, *MNRAS*, 416, 2768
 Subasavage J. P., Jao W.-C., Henry T. J., Bergeron P., Dufour P., Ianna P. A., Costa E., Méndez R. A., 2009, *AJ*, 137, 4547
 Thorngren D. P., Fortney J. J., 2018, *AJ*, 155, 214
 Tout C. A., Eggleton P. P., 1988, *MNRAS*, 231, 823
 Tremblay P. E., Bergeron P., 2009, *ApJ*, 696, 1755
 van der Walt S., Colbert S. C., Varoquaux G., 2011, *Comput. Sci. Eng.*, 13, 22
 Vernet J. et al., 2011, *A&A*, 536, A105
 von Zeipel H., 1924, *MNRAS*, 84, 665
 Vos J., Østensen R. H., Németh P., Green E. M., Heber U., Van Winckel H., 2013, *A&A*, 559, A54
 Vrancken M., Butler K., Becker S. R., 1996, *A&A*, 311, 661
 Vučković M., Østensen R. H., Németh P., Bloemen S., Pápics P. I., 2016, *A&A*, 586, A146
 Webbink R. F., 1984, *ApJ*, 277, 355
 Wood J. H., Saffer R., 1999, *MNRAS*, 305, 820
 Zahn J. P., 1989, *A&A*, 220, 112
 Zorotovic M., Schreiber M. R., 2013, *A&A*, 549, A95

APPENDIX A: TELLURIC CORRECTION

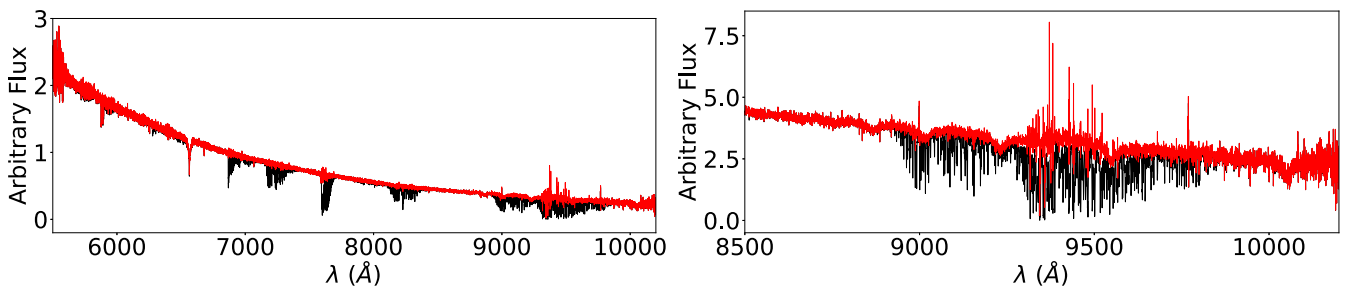


Figure A1. Left-hand panel: quality of telluric absorption correction for a full example spectrum of J08205+0008 taken with the VIS arm of the XSHOOTER spectrograph. The telluric absorption corrected spectrum (red) is shown in comparison with the original spectrum (black). Note that fluxes were scaled for illustrative purposes. Right-hand panel: same as left-hand panel, but for the spectral range of the hydrogen Paschen series.

APPENDIX B: ATMOSPHERIC MODEL PARAMETERS**Table B1.** Model atoms for NLTE calculations used for the hybrid LTE/NLTE approach.

Ion	Model atom
H I	Przybilla & Butler (2004)
He I	Przybilla (2005)
C II	Nieva & Przybilla (2006), Nieva & Przybilla (2008)
N II	Przybilla & Butler (2001) [†]
O I/II	Przybilla et al. (2000), Becker & Butler (1988) [†]
Ne I/II	Morel & Butler (2008) [†]
Mg II	Przybilla et al. (2001)
Al III	Przybilla (in prep.)
Si II/III/IV	Przybilla & Butler (in prep.)
S II/III	Vrancken, Butler & Becker (1996) [†]
Ar II	Butler (in prep.)
Fe II/III	Becker (1998), Morel et al. (2006) [†]

Note: [†]Updated and corrected as described by Nieva & Przybilla (2012).

Table B2. Hybrid LTE/NLTE model grid used for the quantitative spectral analysis of J08205+0008.

Parameter	Grid size	Step size
	25 000 to 30 000 K	1000 K
$\log(g)$	5.2 to 5.8	0.2
$\log n(\text{He})$	-2.2 to -1.6	0.2
$\log n(\text{C})$	-4.6 to -4.0	0.2
$\log n(\text{N})$	-4.2 to -3.6	0.2
$\log n(\text{O})$	-4.4 to -3.8	0.2
$\log n(\text{Ne})$	-7.0 to -6.0	0.2
$\log n(\text{Mg})$	-5.4 to -4.4	0.2
$\log n(\text{Al})$	-7.0 to -6.0	0.2
$\log n(\text{Si})$	-5.4 to -5.0	0.2
$\log n(\text{S})$	-6.0 to -5.2	0.2
$\log n(\text{Ar})$	-5.8 to -5.4	0.2
$\log n(\text{Fe})$	-4.8 to -4.2	0.2

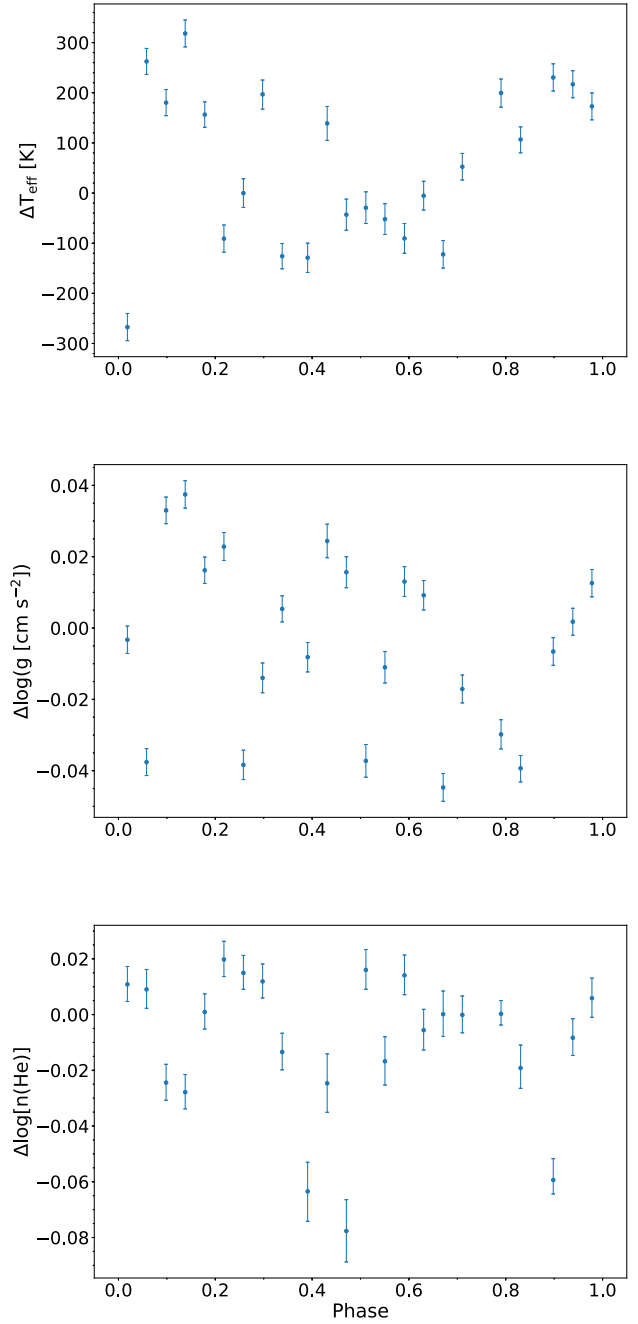


Figure B1. Change of the atmospheric parameters determined from the single XSHOOTER spectra plotted against the orbital phase. While the differences plotted on the y axes result from the subtraction of the best-fitting parameters derived from the co-added XSHOOTER spectrum from the determined parameters for the single spectra, the orbital phase was calculated based on the photometric solutions of T_0 and P (see Table 3 for details). Due to the relatively weak reflection effect of less than 5 per cent, the variations measured for effective temperature (upper panel), surface gravity (middle panel), and helium abundance (lower panel) are of the order of the total uncertainties listed in Table 3 and therefore are not significant.

APPENDIX C: LINE FITS

APPENDIX D: LIST OF METAL LINES

Table D1. List of selected metal lines in the co-added XSHOOTER and UVES spectra of J08205+0008.

El. + ion. stage	λ (Å)	El. + ion. stage	λ (Å)	El. + ion. stage	λ (Å)	El. + ion. stage	λ (Å)
C II	3918.97	N II	5686.21	Al III	4512.565	Fe III	3600.943
C II	3920.68	N II	5710.77	Al III	5696.604	Fe III	3603.890
C II	4267.00	N II	5927.81	Al III	5722.730	Fe III	3611.736
C II	4267.26	N II	5931.78	Si II	3856.018	Fe III	3999.325
C II	5132.95	N II	5940.24	Si II	3862.595	Fe III	4000.518
C II	5133.28	N II	5941.65	Si II	4128.067	Fe III	4005.573
C II	5145.16	N II	5952.39	Si II	4130.893	Fe III	4137.130
C II	6151.265	N II	5954.28	Si II	6347.103	Fe III	4139.350
C II	6151.534	N II	6150.75	Si II	6371.359	Fe III	4140.482
C II	6461.95	N II	6482.05	Si III	3590.465	Fe III	4164.916
C II	6578.05	N II	6610.56	Si III	3806.526	Fe III	4194.051
C II	6582.88	O I	7771.94	Si III	3806.7	Fe III	4210.674
C II	6779.94	O I	7774.17	Si III	3806.779	Fe III	4222.271
C II	6780.59	O I	7775.39	Si III	3924.468	Fe III	4248.773
C II	6783.91	O I	8446.25	Si III	4552.622	Fe III	4261.391
C II	6791.47	O I	8446.36	Si III	4567.84	Fe III	4273.372
C II	6800.69	O I	8446.76	Si III	4574.757	Fe III	4273.409
C II	7231.33	O II	3390.21	Si III	4716.654	Fe III	4286.091
C II	7236.42	O II	3712.74	Si III	4813.333	Fe III	4286.128
C II	7237.17	O II	3727.32	Si III	4819.631	Fe III	4286.164
N II	3328.72	O II	3911.96	Si III	4819.712	Fe III	4296.814
N II	3329.70	O II	3912.12	Si III	4819.814	Fe III	4296.851
N II	3330.32	O II	4069.62	Si III	4828.95	Fe III	4304.748
N II	3331.31	O II	4069.88	Si III	4829.03	Fe III	4304.767
N II	3437.14	O II	4072.16	Si III	4829.111	Fe III	4310.355
N II	3995.00	O II	4075.86	Si III	4829.214	Fe III	4419.596
N II	4035.08	O II	4132.80	Si III	5696.49	Fe III	4649.271
N II	4041.31	O II	4185.44	Si III	5739.73	Fe III	5063.421
N II	4043.53	O II	4189.58	S II	3613.03	Fe III	5073.903
N II	4176.16	O II	4189.79	S II	5201.027	Fe III	5086.701
N II	4199.98	O II	4366.89	S II	5201.379	Fe III	5194.160
N II	4227.74	O II	4395.93	S II	5212.267	Fe III	5272.369
N II	4237.05	O II	4414.46	S II	5212.62	Fe III	5272.900
N II	4241.76	O II	4414.90	S II	5345.712	Fe III	5272.975
N II	4432.74	O II	4452.38	S II	5346.084	Fe III	5276.476
N II	4433.48	O II	4590.97	S II	5428.655	Fe III	5282.297
N II	4447.03	O II	4595.96	S II	5432.797	Fe III	5284.827
N II	4601.48	O II	4596.18	S II	5639.977	Fe III	5288.887
N II	4601.69	O II	4638.86	S II	5640.346	Fe III	5289.304
N II	4607.15	O II	4649.13	S II	5647.02	Fe III	5290.071
N II	4613.87	O II	4650.84	S III	3632.024	Fe III	5293.780
N II	4621.39	O II	4661.63	S III	3662.008	Fe III	5295.027
N II	4630.54	O II	4676.23	S III	3717.771	Fe III	5298.114
N II	4643.09	O II	4698.44	S III	3928.595	Fe III	5299.926
N II	4654.53	O II	4699.01	S III	4253.589	Fe III	5302.602
N II	4779.72	O II	4699.22	S III	4284.979	Fe III	5306.757
N II	4780.44	O II	4941.07	S III	4294.402	Fe III	5310.337
N II	4781.19	O II	4943.01	Ar II	3603.904	Fe III	5340.535
N II	4788.14	Mg II	4481.126	Ar II	4013.856	Fe III	5363.764
N II	4803.29	Mg II	4481.15	Ar II	4072.004	Fe III	5375.566
N II	4987.38	Mg II	4481.325	Ar II	4072.325	Fe III	5535.475
N II	4994.36	Mg II	7877.054	Ar II	4072.384	Fe III	5573.424
N II	5001.13	Mg II	7896.04	Ar II	4372.095	Fe III	5813.302
N II	5001.47	Mg II	7896.366	Ar II	4372.490	Fe III	5833.938
N II	5005.15	Al III	3601.630	Ar II	4545.052	Fe III	5848.744
N II	5007.33	Al III	3601.927	Ar II	4579.349	Fe III	5920.394
N II	5010.62	Al III	3612.355	Ar II	4609.567	Fe III	6032.673
N II	5045.10	Al III	4149.913	Ar II	4657.901	Fe III	7320.230
N II	5073.59	Al III	4149.968	Ar II	4726.868	Fe III	7920.559
N II	5495.65	Al III	4150.173	Ar II	4735.905	Fe III	7920.872

Table D1 – continued

El. + ion. stage	λ (Å)	El. + ion. stage	λ (Å)	El. + ion. stage	λ (Å)	El. + ion. stage	λ (Å)
N II	5666.63	Al III	4479.885	Ar II	4806.020	Fe III	7921.186
N II	5676.02	Al III	4479.971	Ar II	4965.079	Fe III	7921.500
N II	5679.56	Al III	4480.000	Ar II	6643.697	Fe III	7921.814

APPENDIX E: COMPARISON OF THE SPECTRA WITH AND WITHOUT COMPANION VISIBLE

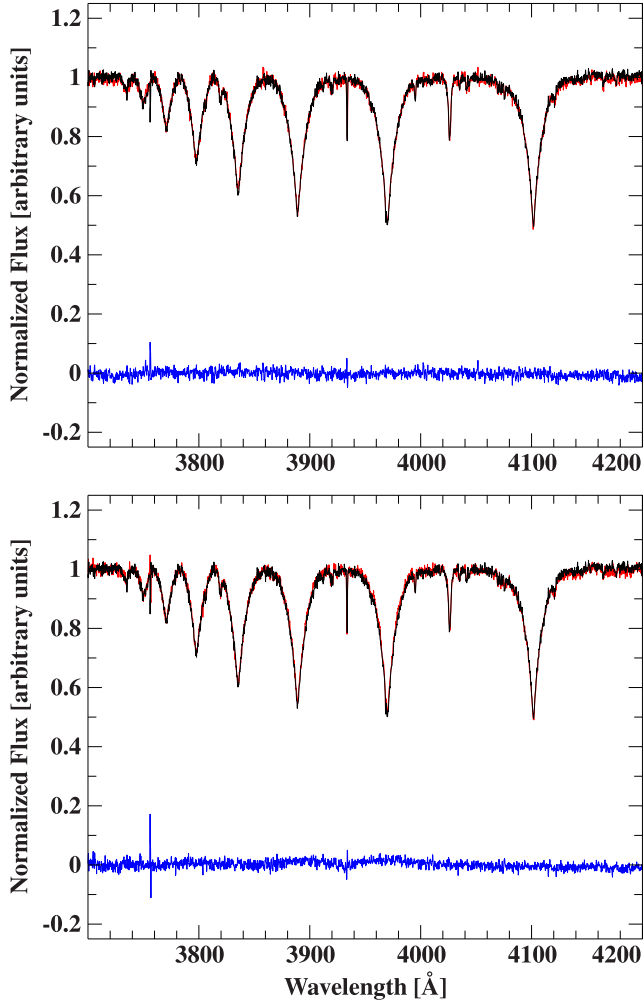


Figure E1. Subtraction of the XSHOOTER UVB spectrum in the secondary eclipse (black, orbital phase: 0.018) from the spectra before and after the secondary eclipse (red, orbital phases: 0.978 and 0.058). The residuals are given in blue.

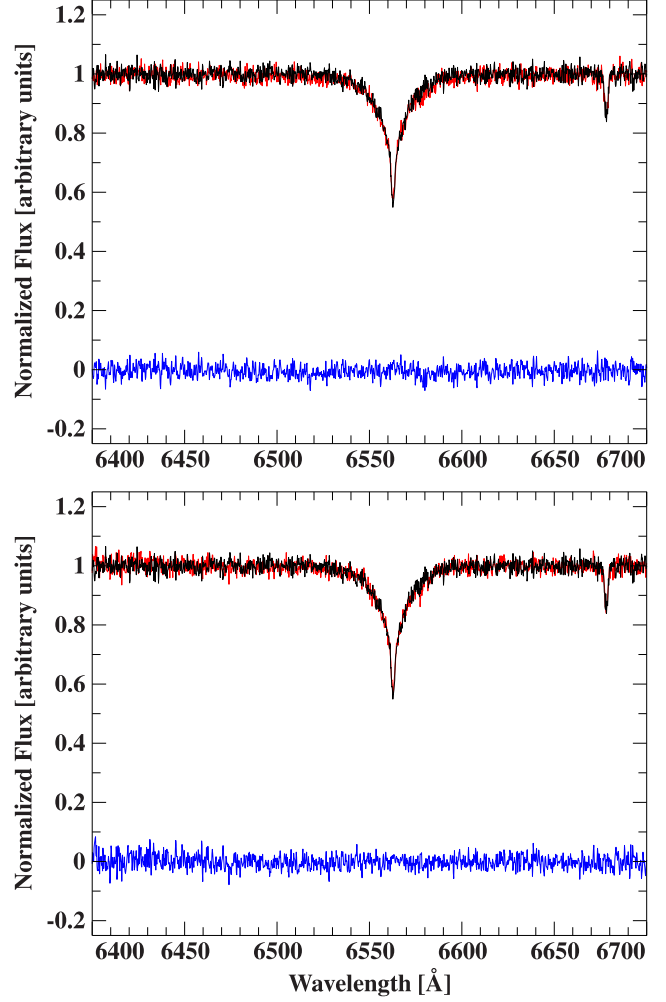


Figure E2. Same figure as Fig. E1, but for the VIS arm around $H\alpha$.

APPENDIX F: RADIAL VELOCITIES

Table F1. Radial velocities.

mid-BJD _{TDB} -2 450 000	RV (km s ⁻¹)	Instrument
3816.608090	-12.5 ± 6.8	SDSS [†]
3816.622170	-28.4 ± 6.2	
3816.637894	-26.0 ± 7.1	
3816.653623	21.4 ± 6.7	
3816.669271	49.0 ± 10.5	
3816.684919	38.4 ± 8.8	
4755.79740	58.9 ± 15.8	EFOSC2 [†]
4755.80127	45.1 ± 14.4	
4757.84839	-40.7 ± 15.0	
4757.85225	-35.4 ± 12.4	
5146.80965	47.5 ± 8.0	
5146.82778	59.9 ± 8.0	
5146.83743	47.5 ± 8.0	
5147.80109	19.5 ± 8.9	
5147.81597	-14.9 ± 8.1	
5147.82562	-34.0 ± 7.9	
5147.84031	-29.3 ± 8.9	
5147.84997	-6.2 ± 8.6	
5147.86465	34.9 ± 9.5	
5147.87430	49.2 ± 8.5	
5148.77113	4.5 ± 8.5	
5148.77964	-20.1 ± 7.9	
5148.79388	-38.7 ± 7.8	
5148.80354	-37.5 ± 9.0	
5657.49252374	42.5 ± 5.3	UVES
5657.49654962	4.9 ± 3.7	
5657.50057560	-0.9 ± 5.2	
5657.50461775	-4.8 ± 5.6	
5657.50866197	-9.1 ± 3.1	
5657.51270167	-19.0 ± 4.2	
5657.51674196	-21.5 ± 2.3	
5657.52107057	-20.1 ± 3.0	
5657.52509622	-17.0 ± 7.9	
5657.52912257	-11.1 ± 6.9	
5657.53316028	-2.5 ± 2.5	
5657.53720219	12.2 ± 6.8	
5657.54124410	22.8 ± 6.1	
5657.54528808	33.1 ± 6.7	
5657.54932975	43.2 ± 6.5	
5657.55337328	60.0 ± 4.5	
5657.55741668	60.6 ± 2.2	
5657.56145535	69.1 ± 7.6	
5657.56549517	74.9 ± 6.4	
5657.56953256	73.7 ± 5.2	
5657.57357041	78.2 ± 8.8	
5657.57760966	65.4 ± 6.9	
5657.58569149	46.0 ± 8.0	
5657.58973698	29.8 ± 7.4	
5657.59377830	13.7 ± 6.7	
5657.59782484	-3.2 ± 5.8	
5657.60590841	-15.8 ± 5.1	
5657.61398712	-27.9 ± 6.5	
7801.53891733	61.5 ± 1.6	XSHOOTER
7801.54280358	52.3 ± 1.0	
7801.54661453	42.4 ± 0.9	
7801.55049162	35.6 ± 1.3	
7801.55428555	10.5 ± 1.2	
7801.55816729	6.2 ± 1.0	
7801.56197835	-2.7 ± 1.1	
7801.56585983	-11.2 ± 1.0	
7801.56967460	-19.3 ± 1.1	
7801.57356027	-22.1 ± 1.2	
7801.57736624	-19.4 ± 0.9	

Table F1 – *continued*

mid-BJD _{TDB} -2 450 000	RV (km s ⁻¹)	Instrument
7801.58125282	-17.1 ± 0.9	
7801.58774688	-5.4 ± 0.9	
7801.59163370	5.4 ± 1.0	
7801.59543481	14.9 ± 1.0	
7801.59932441	26.3 ± 1.0	
7801.60313072	38.8 ± 0.8	
7801.60701615	47.9 ± 1.0	
7801.61081599	58.7 ± 1.0	
7801.61851422	72.3 ± 1.3	
7801.62238622	74.5 ± 0.9	
7801.62620191	74.8 ± 1.1	
7801.63009857	69.0 ± 1.2	

Note: [†]Geier et al. (2011c).

APPENDIX G: TIMES OF PRIMARY ECLIPSES

Table G1. Times of the primary eclipse of J08205+0008.

Eclipse number	Time of primary eclipse [BJD _{TDB}]	Source
0	2455165.709266 ± 0.000050	Merope [†]
31	2455168.692622 ± 0.000050	Merope [†]
465	2455210.461047 ± 0.000050	Merope [†]
466	2455210.557368 ± 0.000050	Merope [†]
467	2455210.653586 ± 0.000050	Merope [†]
3980	2455548.747324 ± 0.000020	ULTRACAM
4704	2455618.425621 ± 0.000050	BUSCA
4745	2455622.371553 ± 0.000050	BUSCA
8071	2455942.468130 ± 0.000050	SAAO
8072	2455942.564480 ± 0.000010	SAAO
11179	2456241.584370 ± 0.000020	SAAO
12103	2456330.510900 ± 0.000030	SAAO
12113	2456331.473260 ± 0.000020	SAAO
12164	2456336.381490 ± 0.000030	SAAO
12165	2456336.477810 ± 0.000040	SAAO
12537	2456372.279310 ± 0.000010	SAAO
12568	2456375.262750 ± 0.000080	SAAO
12973	2456414.240300 ± 0.000050	SAAO
13035	2456420.207310 ± 0.000040	SAAO
15822	2456688.430140 ± 0.000020	SAAO
15832	2456689.392530 ± 0.000050	SAAO
15863	2456692.376020 ± 0.000020	SAAO
16101	2456715.281300 ± 0.000050	SAAO
16132	2456718.264780 ± 0.000100	SAAO
16703	2456773.218230 ± 0.000050	SAAO
16724	2456775.239280 ± 0.000030	SAAO
18567	2456952.610940 ± 0.000020	SAAO
19459	2457038.457650 ± 0.000020	SAAO
19470	2457039.516330 ± 0.000030	SAAO
19490	2457041.441110 ± 0.000030	SAAO
19739	2457065.405120 ± 0.000030	SAAO
19780	2457069.350940 ± 0.000040	SAAO
20413	2457130.271420 ± 0.000030	SAAO
20444	2457133.254870 ± 0.000020	SAAO
20714	2457159.239800 ± 0.000030	SAAO
20724	2457160.202340 ± 0.000030	SAAO
23179	2457396.473170 ± 0.000080	SAAO
23210	2457399.456640 ± 0.000030	SAAO
23459	2457423.420580 ± 0.000010	SAAO
23490	2457426.404090 ± 0.000020	SAAO

Table G1 – *continued*

Eclipse number	Time of primary eclipse [BJD _{TDB}]	Source
27710	2457832.53995 ± 0.000020	ULTRACAM
28330	2457892.209190 ± 0.000050	SAAO
31179	2458166.399050 ± 0.000080	SAAO
31480	2458195.367510 ± 0.000030	SAAO
34868	2458521.431060 ± 0.000030	SAAO
35469	2458579.271780 ± 0.000030	SAAO
37872	2458810.538190 ± 0.000030	SAAO
37883	2458811.596860 ± 0.000030	SAAO
37893	2458812.559230 ± 0.000030	SAAO
39034	2458922.369960 ± 0.000010	SAAO
39117	2458930.357940 ± 0.000030	SAAO

Note: †Geier et al. (2011c).

This paper has been typeset from a $\text{\TeX}/\text{\LaTeX}$ file prepared by the author.



Multifilter Time-series Observations of Eleven Blue Short-period ATLAS Variable Stars

C. Koen¹, V. Schaffenroth², and A. Kniazev^{3,4,5}

¹ Department of Statistics, University of the Western Cape, Private Bag X17, Bellville, 7535 Cape, South Africa

² Institut für Physik und Astronomie, Universität Potsdam, Karl-Liebknecht-Strasse 24/25, Germany

³ South African Astronomical Observatory, P.O. Box 9, Observatory, 7935 Cape, South Africa

⁴ Southern African Large Telescope, P.O. Box 9, Observatory, 7935 Cape, South Africa

⁵ Special Astrophysical Observatory, Niznij Arkhyz, Karachai-Circassia, 369167, Russia

Received 2022 December 30; revised 2023 February 2; accepted 2023 February 2; published 2023 March 2

Abstract

Eleven periodic variable stars were observed photometrically through two to four filters from the set $UBVR_CI_C$. Phase-folded data for each star cover full cycles of variation. Spectral energy distributions, based on absolute photometry extracted from the literature, are used to inform models of the stars. The stars include four eclipsing systems with hot subdwarfs of spectral type O or B (sdO/B). Periods are in the range 1.8–2.2 hr. Four reflection-effect binaries, with amplitudes as large as 0.5 mag in the R_C filter were observed; periods range from 1.6 to 2.4 hr. In two of these latter systems, the primary stars are also sdB stars, while two have white-dwarf components. In all eight of these binaries the companion stars are probably M dwarfs. The remaining three stars are pulsators: one large-amplitude δ Scuti star previously misclassified as an eclipsing system; one field SX Phe star near the Galactic plane; and one multiperiodic high-luminosity star of unknown type. The amplitude is usually a strong function of the wavelength in pulsating stars, but this is not the case for the high-luminosity variable. One possible explanation is that the luminous star has a pulsating companion. The SX Phe and high-luminosity star are both heavily reddened ($A_V > 5$ mag).

Unified Astronomy Thesaurus concepts: [Subdwarf stars \(2054\)](#); [Close binary stars \(254\)](#); [Variable stars \(1761\)](#)

Supporting material: figure sets

1. Introduction

As pointed out by Koen (2019), the Asteroid Terrestrial-impact Last Alert System (ATLAS) variable star catalog (Heinze et al. 2018) is an important resource in the search for binary stars with very short periods (here meaning $P < 0.2$ days). In particular, because of the large number ($>300,000$) of stars in the ATLAS catalog, it is not difficult to find candidates with color indices characteristic of either very high or very low temperatures. Arguments were presented in Koen (2019) as to why very hot and very cool short-period binaries are of special interest—in short, ascertaining the physical properties of such systems helps to understand the binary evolution of stars with extreme temperatures. The point is discussed at some length by Schaffenroth et al. (2018) for the case of hot subdwarf stars in short-period binary systems. These systems are thought to be the products of common envelope evolution during which the subdwarf star loses considerable mass while passing through a red-giant phase. In this context, the nature of the companion star is of interest in order to test the statistics of binary population models (e.g., Han et al. 2002, 2003).

Here we present photometry of 11 stars from an ongoing observational program devoted to further study of ATLAS binaries. The target stars (see Table 1) were all selected on the basis of their $g-i$ and $r-z$ color indices, and their accessibility from the observing site at 34° South. Eight of the stars are sufficiently blue ($g-i < -0.4$, $r-z < -0.4$) for them to have entries in either a catalog of hot subdwarf candidates (Geier et al. 2019) and/or a catalog of white-dwarf

candidates (Gentile Fusillo et al. 2019). The exceptions are, first, ATL 1843+0226 and ATL 1853+0339, which were actually selected for their short periods and extremely red colors ($g-i > 2.2$, $r-z > 1.5$) as candidate ultrashort-period ($P < 0.2$ days) late-type binary stars. Analysis however revealed that these two objects are heavily reddened blue stars. The other exception is ATL 0843-1159, which is not quite as blue as the hot subdwarf and white-dwarf candidates, though evidently still quite hot ($g-i = -0.25$, $r-z = -0.32$). The star is classified as a contact binary with a period of 0.115 day (2.8 hr) by Heinze et al. (2018); the combination of this variability type and color is unusual.

Table 1 summarizes some basic information about the target stars. The abbreviated names in the second column will be used in the rest of the paper. None of these objects have received individual attention in the literature, i.e., all published information about them is part of large studies of many stars. The periods of the stars in Table 1 are not all given to the same accuracy. This is because some periods were determined from Catalina Sky Survey (CSS; Drake et al. 2014) photometry: the time baseline of the CSS is longer, and hence period determinations from those data are potentially more accurate. Note that for ATL 0843-1159 and ATL 1843+0226 the correct periods are half the ATLAS catalog values. In the case of ATL 1544-1816, the periodogram maxima occur at 14.2397, 16.2447, and 15.2423 day^{-1} for the ATLAS c , ATLAS o , and CSS data, respectively, while the ATLAS catalog period is 0.140453 d, corresponding to a frequency of $14.2396/2 \text{ day}^{-1}$. The new observations discussed in this paper confirm that the period derived from the CSS data is the correct alias.

The ATLAS survey uses two filters— c (“cyan”) and o (“orange”), with respective ranges of 420–650 and 560–820 nm. Each star was observed ~ 100 times through



Original content from this work may be used under the terms of the [Creative Commons Attribution 4.0 licence](#). Any further distribution of this work must maintain attribution to the author(s) and the title of the work, journal citation and DOI.

Table 1
Summary of Some Properties of the Stars Discussed in this Paper

Catalog name	Short Name	Period (day)	g (mag)	$g - i$ (mag)	$r - z$ (mag)	$p(\sigma_p)$ (mas)	Type
ATO J079.5290-23.1459	ATL 0518-2308	0.0911720	15.704	-0.707	-0.615	0.4162(0.0372)	sdB
ATO J084.4719-00.8240	ATL 0537-0049	0.0755278	15.118	-0.422	-0.451	0.8031(0.0322)	sdB
ATO J109.7403+07.6537	ATL 0718+0739	0.084461	15.100	-0.785	-0.532	0.5247(0.0476)	sdO/B
ATO J129.0543-08.0399	ATL 0836-0802	0.0888684	15.143	-0.751	-0.605	0.5070(0.0495)	sdB
ATO J130.7753-11.9973	ATL 0843-1159	0.0575772h	14.302	-0.250	-0.323	0.4512(0.0187)	A-F
ATO J236.1079-18.2809	ATL 1544-1816	0.0656070h	17.428	-0.565	-0.546	0.9952(0.1121)	WD
ATO J267.1557+09.1634	ATL 1748+0909	0.096456	16.579	-0.515	-0.538	0.4825(0.0571)	sdB
ATO J280.9765+02.4482	ATL 1843+0226	0.039549h	19.374	2.998	1.788	0.5773(0.0699)	A-F
ATO J283.3857+03.6586	ATL 1853+0339	0.118055	18.759	3.696	2.373	0.3624(0.0456)	B-A
ATO J300.8707+08.6464	ATL 2003+0838	0.098602	14.388	-0.922	-0.658	2.5890(0.0421)	WD
ATO J307.2199+06.1675	ATL 2028+0610	0.094216	14.711	-0.538	-0.495	0.8981(0.0340)	sdO/B

Note. Periods from Catalina Sky Survey observations are quoted when these are available; otherwise periods are from the ATLAS catalog. Periods marked with an “h” are half the ATLAS period. The magnitudes and colors are from the “Panoramic Survey Telescope and Rapid Response System” (Pan-STARRS) survey. The penultimate column gives the Gaia Early Data Release 3 parallax (Gaia Collaboration 2021) and its error. For the eight bluest stars, the last column indicates whether the star is in the Geier et al. (2019) catalog of hot subdwarf stars and/or the Gentile Fusillo et al. (2019) catalog of white-dwarf (WD) candidates. For the remaining three stars, crudely estimated spectral types were obtained by fitting spectral energy distributions to published photometry—see Section 6 for details.

each filter, with measurements spread over time periods of 1.5–1.9 yr. The phase-folded ATLAS light curves are presented in the Appendix A figure set. Phased CSS light curves are included for stars observed by that survey.

The acquisition of new time-series photometry of the stars is described in the next section of the paper. The subsequent three sections deal with our binary modeling approach and its application to eclipsing and noneclipsing systems. Section 6 is devoted to the properties of three pulsating stars, followed by a brief concluding section.

2. SAAO Photometry

All observations were made with the 1 m telescope of the South African Astronomical Observatory (SAAO) situated near Sutherland, South Africa. Two CCD cameras were used—STE4 (5.28×5.28 arcmin² field of view; cryogenically cooled) and SHOC (2.85×2.85 arcmin² field of view; thermoelectrically cooled to -50°C). Both camera chips have 1024×1024 pixels and were operated in the 2×2 prebinning mode. The readout time for the STE4 camera is ~ 20 s, but SHOC is operated in frame-transfer mode, giving essentially instantaneous readout. Typically, various combinations of the Johnson UBV and Cousins $R_C I_C$ filters were used contemporaneously. (Below, the subscripts on R_C and I_C will be dropped for convenience). The exposure times were tailored to the specific stars and atmospheric conditions.

A slightly modified version of the DOPHOT CCD reduction program (Schechter et al. 1993) was used. Photometry from fitting point-spread functions is used throughout, as the noise properties were found to be better than results from aperture photometry. All photometry was differentially corrected with respect to nonvariable stars (light curves scatter typically 3–7 mmag) in the field of view. The number of suitable comparison stars depended on the number of the stars in the field of view with brightnesses greater than or similar to that of the target star, and varied from 2 to 9, with typical numbers being 4–5.

Table 2 is a log of the observations. The observing runs covered ~ 145 hrs, during which more than 8400 measurements were made.

3. Binary Modeling

The aims here are to make multicolor photometry of reasonable quality available, to provide preliminary models, and to supply enough information so interesting objects can be selected for follow-up work. Definitive values of the mass ratios will require radial velocity measurements (e.g., Terrell & Wilson 2005).

The light curves of the eight sdO/B or WD candidates show prominent reflection effects, characteristic of very close binaries with large temperature differences between components and equal or larger radii of companions compared to the hot primary stars. This is often observed in systems with hot compact primary stars, and late dwarf (dM) or even brown dwarf (BD) secondaries; some central stars of planetary nebula also show similar light curves (e.g., Jones & Boffin 2017). To constrain the nature of the primary star, the absolute Gaia magnitude M_G (Gaia Collaboration 2021) was used: this could be compared with the distribution of the known sdO/B+dM/BD system values. Three of the stars (ATL 0718+0739, ATL 0537-0049, and ATL 1748+0606) have absolute magnitudes typical of sdO/B+dM/BD systems ($M_G = 3.5$ – 5.5 mag; see Schaffenroth et al. 2019). However, ATL 2003+0838 has an absolute magnitude between those of sdB and WD stars (6.5 mag) and is probably a hot WD. A least-squares method was used to fit theoretical spectral energy distributions (SEDs) to literature values of photometry of the stars. Details of the calculation of the synthetic spectra and the fitting methodology can be found in Schaffenroth et al. (2021, 2022). Of course, the intrinsic variability of the stars adds to the uncertainties on the published photometry. This point was explored by Schaffenroth et al. (2022), who compared their SED fitting results to spectroscopically determined parameters, and found good agreement.

In this way we could constrain the temperature of the primary stars as well as the angular diameter and any color excess. Combining these results with the Gaia parallaxes, we additionally could derive the radii of the primary stars. Plots of the SED fits can be found in the figure set in Appendix B.

Light-curve modeling was performed with LCURVE, a code developed specifically for detached and accreting binaries containing a WD (for details see Copperwheat et al. 2010). This software has been used to analyze several detached WD+dM binaries (e.g., Parsons et al. 2010). The LCURVE code has

Table 2
Photometric Observing Log

Starting Time (HJD 2450000+)	Filters	Run Length (h)	<i>N</i>
ATL 0518			
9210.3036	<i>BVR</i>	3.6	120–122
9211.2864	<i>B</i>	4.3	402
9212.2921	<i>VR</i>	5.1	354–395
9602.3107	<i>V</i>	2.3	216
9603.2884	<i>R</i>	2.6	198
9605.2883	<i>B</i>	2.9	210
9606.2774	<i>I</i>	2.3	190
ATL 0537–0049			
8893.3570	<i>R</i>	2.2	532
8894.2842	<i>BR</i>	2.9	257–274
ATL 0718+0739			
8893.4604	<i>R</i>	1.8	448
8894.4135	<i>B</i>	2.1	518
ATL 0836–0802			
9301.2481	<i>VR</i>	3.7	75–95
9303.2325	<i>V</i>	2.9	137
9303.3660	<i>I</i>	1.9	84
9304.2295	<i>B</i>	1.6	38
9602.4260	<i>R</i>	2.3	187
9602.5219	<i>I</i>	2.2	180
9605.4342	<i>B</i>	1.3	73
9606.3862	<i>B</i>	2.1	140
ATL 0843–1159			
9200.5578	<i>VRI</i>	1.4	31
9201.5104	<i>VRI</i>	2.4	17–60
9210.4613	<i>VR</i>	3.3	97–108
9212.5186	<i>B</i>	2.2	45
ATL 1544–1816			
9292.5015	<i>VR</i>	3.6	34–40
9296.4925	<i>VR</i>	4.3	38–63
9438.2754	<i>I</i>	1.0	34
9440.2087	<i>I</i>	2.4	40
ATL 1748+0909			
9007.4114	<i>BVR</i>	3.4	32–43
9097.2185	<i>VR</i>	3.4	64–64
9099.2136	<i>BR</i>	3.1	45–55
9100.2127	<i>BVR</i>	4.1	47–50
ATL 1843+0226			
9008.4276	<i>RI</i>	5.4	80–81
9009.5167	<i>RI</i>	3.1	41–42
9010.5079	<i>VI</i>	3.4	39–42
9013.4339	<i>V</i>	4.6	76
9014.4327	<i>R</i>	3.1	74
ATL 1853+0339			
9014.5816	<i>RI</i>	2.1	57
9015.4324	<i>VRI</i>	3.5	39–41
9017.4102	<i>VRI</i>	5.4	61–64
9101.2289	<i>VRI</i>	2.0	21–23
9102.2149	<i>VRI</i>	3.9	41–45
9449.2580	<i>RI</i>	4.3	86–87
ATL 2003+0838			
9004.5059	<i>UBVR</i>	4.2	58–65
9005.4920	<i>UBVR</i>	4.3	40–69
9016.4652	<i>UBVR</i>	5.1	52–55
ATL 2028+0610			
9006.5626	<i>BVR</i>	2.7	51
9103.2622	<i>VR</i>	3.3	60–62

Note. The numbers of measurements across filters are in the last column.

also been successful in modeling sdB+WD or double WD systems showing ellipsoidal deformation (e.g., Kupfer et al. 2017). Therefore, LCURVE is ideally suited for systems containing hot blue objects.

The code calculates monochromatic light curves by subdividing the surface of each star into small elements with a geometry fixed by its radius as measured along the line from the center of one star toward the center of the companion. The flux of all visible elements is summed to obtain the observed flux at a given phase. A number of different effects that are observed in compact and normal stars are taken into account, such as Roche distortions due to the tidal influence of a massive, close companion, as well as limb darkening and gravitational darkening (e.g., Kallrath & Milone 2009).

As the light-curve model is based on many parameters, not all of them independent, as many parameters as possible were kept fixed when iterating toward a solution. The temperature derived by the fit to the SED or typical values for an sdB star were used. As the luminosity ratio of the components is very large, the temperature of the companion cannot be derived. We fixed the temperature of the companion to 3000 K, which is typical for a dM. Varying the temperature of the companion has no influence on the light-curve solutions. It was not possible to constrain the mass ratios of the systems, as the light curve is not sensitive to changes in the mass ratio; hence we assumed a canonical sdB mass ($0.47 M_{\odot}$; Heber 2016) and a mass corresponding to the radius of the companion (taken from Pecaute & Mamajek 2013). For the WDs, we assume $M = 0.5 M_{\odot}$ (Schaffenroth et al. 2018); the results are very similar for values in the range 0.4–0.6 M_{\odot} . The quadratic limb darkening coefficients were taken from Claret & Bloemen (2011).

We used a simplex algorithm (e.g., Press et al. 1992), varying the starting guesses for parameters over a large range of values to find the best-fitting light-curve model, and varying the inclination and the relative radii of the components. The light curves in the different bands were either fitted separately or the fit from the highest S/N light curve was used and the other bands were used as a consistency check. More details on the light-curve fitting methodology can be found in Schaffenroth et al. (2021).

The results are summarized in Table 3 and are discussed in the next two sections of the paper. The model fits to the observations are illustrated in Figures 1–8; these are evidently excellent. The standard deviation of the scatter varies from 0.6% to 2.7%, with the mean being 1.5%.

4. The Eclipsing Binaries

4.1. ATL 0518-2308

Also known as HE 0516-2311 and EC 05160-2311, the star has been classified as a B-type hot subdwarf (sdB) based on spectroscopy (Edelmann 2003; O’Donoghue et al. 2013). Edelmann (2003) determined $T_{\text{eff}} = 31,000 \pm 300$ K and $\log g = 5.5 \pm 0.1$ by spectral model fitting. It was found as an eclipsing sdO/B candidate with a dM/BD companion (HW Vir system) by Schaffenroth et al. (2019). The star has been observed by the Transiting Exoplanet Survey Satellite (TESS; Ricker et al. 2015); the light curve can be seen in Baran et al. (2021).

Table 3
Summary of the Models Fitted to the Binary Stars

Name	q	r_1	r_2	T_1 (K)	T_2 (K)	i (deg)
Eclipsing systems						
ATL 0518–2308	0.34	0.235	0.227	31000	3000	71.9
ATL 0537–0049	0.42	0.311	0.255	28300	3000	66.8
ATL 0718+0739	0.34	0.282	0.257	40000	3000	82.7
ATL 0836–0802	0.34	0.275	0.210	26200	3000	69.3
Reflection-effect binaries						
ATL 1544–1816	0.16	0.022	0.199	38000	3000	35
ATL 1748+0909	0.32	0.215	0.283	34000	3000	62
ATL 2003+0838	0.15	0.068	0.313	50000	3000	36
ATL 2028+0610	0.26	0.297	0.278	27300	3000	44

Note. Subscripts 1 and 2, respectively, refer to the primary (hot, compact) and secondary (cool companion) stars. The temperatures of the primary stars were determined by SED fitting, with absolute radii following from absolute magnitudes. The temperatures of the secondary stars cannot be determined from the photometry and were fixed at 3000 K. The radii are given as fractions of the separation between the stars. The masses of primary stars were set at $\sim 0.5M_\odot$, while the masses of the secondary stars were deduced from tabled mass–radius data (Pecaut et al. 2012, Pecaut & Mamajek 2013).

Using the atmospheric parameters we could derive the radius and the mass of the sdB star by combining the fit of the SED with the Gaia parallax (see Schaffenroth et al. 2021 for more details on the method). We obtain a mass of $0.47_{-0.12}^{+0.17} M_\odot$, which is typical for a sdB, and a radius of $0.208_{-0.018}^{+0.021} R_\odot$. With the relative radii determined by the light-curve analysis (see Table 3), we can derive a separation of $0.89 \pm 0.08 R_\odot$ and a radius of the companion of $0.20 \pm 0.02 R_\odot$. This radius would imply a secondary star of spectral type about M5 and a mass of about $0.16 M_\odot$ —see e.g., Pecaut et al. (2012) and Pecaut & Mamajek (2013).⁶

The phased observational and theoretical light curves are plotted in Figure 1.

4.2. ATL 0537-0049

The star is in the candidate hot subdwarf catalog of Geier et al. (2019). It was also found to be a probable HW Vir system by Schaffenroth et al. (2019). The fit of the SED together with the Gaia parallax resulted in a temperature of $28,300_{-1600}^{+2100}$ K and a radius of $0.200 \pm 0.012 R_\odot$ giving a gravity $\log g$ of 5.51 ± 0.06 , when assuming a canonical sdB mass of $0.47 M_\odot$. Such atmospheric parameters are typical for a sdB. Combining this with the relative radii from the light-curve analysis, we can derive a system separation of $0.83 \pm 0.05 R_\odot$ and a companion radius of $0.26 \pm 0.02 R_\odot$, which would imply a spectral type of M4 and a mass of about $0.2 M_\odot$ (Pecaut et al. 2012; Pecaut & Mamajek 2013).⁷ The observed and model light curves are plotted in Figure 2.

4.3. ATL 0718+0739

ATL 0718+0739 is also a candidate hot subdwarf (Geier et al. 2019) and was considered a HW Vir system candidate by Schaffenroth et al. (2019). With an absolute magnitude

$M_G = 3.48 \pm 0.31$ mag the primary is at the bright end of the distribution of sdB luminosities suggesting it might have a higher temperature than the 26,000–31,000 K typical for sdBs (Schaffenroth et al. 2022). Unfortunately not enough good-quality photometric data are available for a definitive SED fit, so we will need spectroscopic data for a better characterization of the system. The light curve and a fit of the light curve assuming a temperature of 40,000 K are shown in Figure 3; the model results in Table 3 should only be considered plausible.

4.4. ATL 0836-0802

This star appears in the Geier et al. (2019) catalog of hot subdwarf candidates and the Schaffenroth et al. (2019) catalog of candidate HW Vir stars. The SED and the absolute magnitude obtained from the Gaia parallax confirm that the star is an HW Vir system with an sdB primary. Proceeding as for ATL 0537-0049, the properties of the sdB are $T = 26,200_{-2200}^{+2500}$ K, $R = 0.242_{-0.026}^{+0.031} R_\odot$, $\log g = 5.35 \pm 0.07$ with the assumption of a canonical $0.47 M_\odot$ sdB mass. Using relative radii from the model fitting (Table 3) gives a binary separation of $0.89 R_\odot$ and a radius of the secondary star of $0.184 \pm 0.024 R_\odot$. The implied mass and spectral type of the secondary star are $M_2 = 0.162 M_\odot$ and M5 (Pecaut et al. 2012; Pecaut & Mamajek 2013).⁸

The phase-folded observations together with model fits are plotted in Figure 4.

5. Reflection-effect Binaries

The four stars discussed in this section all show increases in the amplitude with increasing wavelength (Figures 5–8): in the least obvious case (ATL 2028+0610; Figure 8), the amplitudes are $6.9\% \pm 0.3\%$, $7.9\% \pm 0.2\%$, and $8.8\% \pm 0.2\%$ in B , V , and R , respectively. This demonstrates that the principal source of the variability is the changing aspect of reflection off a cool secondary star, rather than ellipsoidal deformation (e.g., Hilditch et al. 1996). For the noneclipsing reflection-effect systems, it is not possible to constrain the inclination, as there is a degeneracy with the radius of the companion (e.g., Hilditch et al. 1996). However, it is possible to distinguish between higher and lower inclinations using the shape of the reflection effect (e.g., Østensen et al. 2013; Schaffenroth et al. 2014), and the change in amplitude from filter to filter contains information about the temperature of the primary. Hence we searched for consistent solutions that fit the light curves in all different bands, assuming an inclination. This will not be a unique solution but can be used to estimate the nature of the companion under this assumption.

5.1. ATL 1544–1816

Gentile Fusillo et al. (2019) found a 0.76 probability that this star is a WD. This is also in accordance with the low luminosity ($M_G = 7.51 \pm 0.24$). The amplitude of the reflection effect varies from 20% in V to 35% in I . The large amplitude and the increase in amplitude with the wavelength of about 75% shows that the primary has to be a very compact hot star. The SED is not sensitive to the temperature in the likely temperature range, but it can be constrained by the wavelength dependence of the amplitude. The change in the amplitude

⁶ http://www.pas.rochester.edu/~emamajek/EEM_dwarf_UBVIJHK_colors_Teff.txt

⁷ http://www.pas.rochester.edu/~emamajek/EEM_dwarf_UBVIJHK_colors_Teff.txt

⁸ http://www.pas.rochester.edu/~emamajek/EEM_dwarf_UBVIJHK_colors_Teff.txt

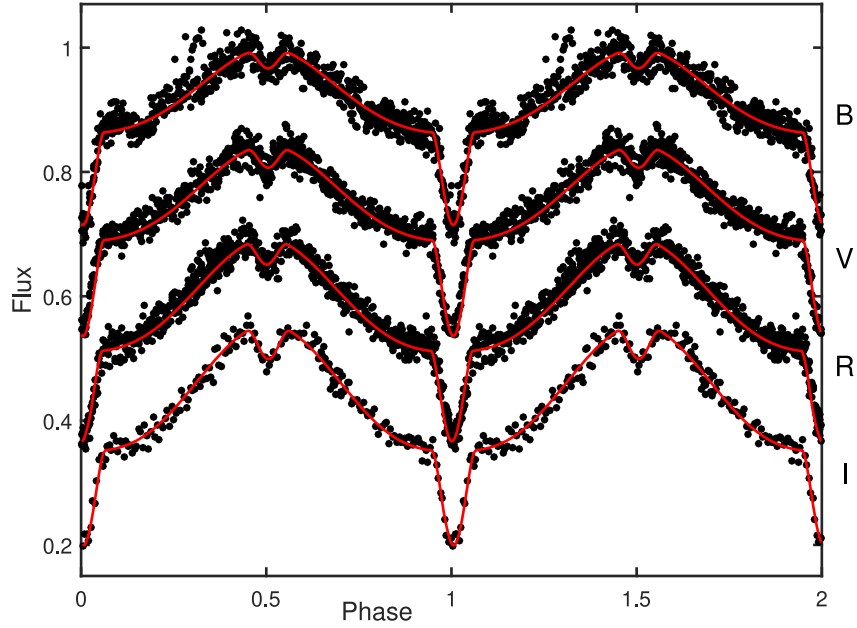


Figure 1. Phase-folded *BVRI* SAAO photometry of ATL 0518–2308 (dots) with model fits (lines). The fluxes have been normalized but have arbitrary zero-points.

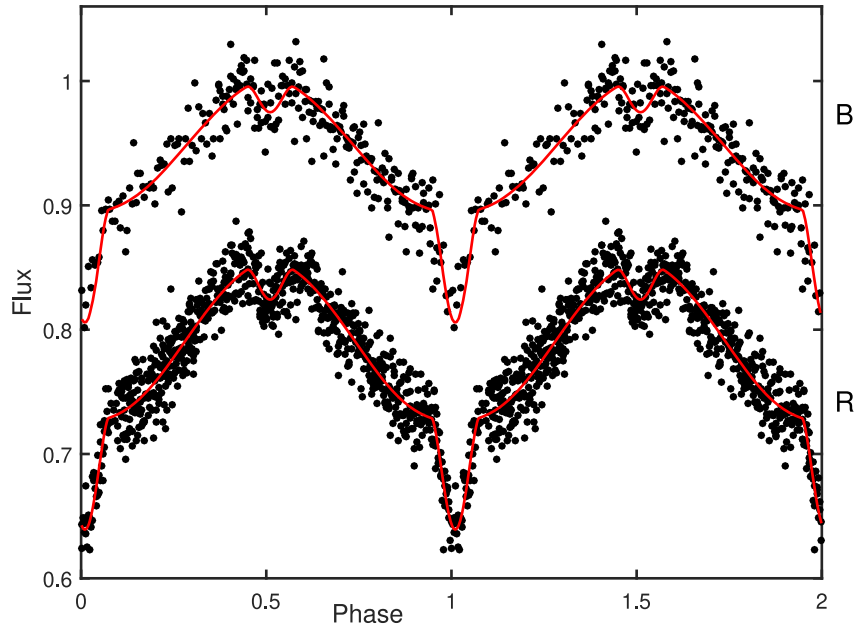


Figure 2. Phase-folded *BR* SAAO photometry of ATL 0537–0049 (dots) with model fits (lines). The fluxes have been normalized but have arbitrary zero-points.

from filter to filter is mostly dependent on the ratio of the flux of the primary star and the hot side of the companion. For a primary temperature of 38,000 K, we found a solution fitting the light curves in all three filters well. There is a degeneracy between the inclination and radius of the primary and secondary. However, the nearly sinusoidal shape of the reflection effect suggests that the inclination cannot be too high. So we assumed an inclination of $\sim 35^\circ$. (Taking $i = 60^\circ$ gives notably worse model fits). With the derived temperature and the assumed inclination given in Table 3 as well as the distance to the system from the Gaia parallax the radius of the primary can be constrained to about $0.04R_\odot$, which is typical for a WD. Using the relative radii determined by the light-curve

analysis, we obtain a radius of $0.11R_\odot$ for the companion, which suggests an M8 spectral type, close to the hydrogen burning limit. The determination of the radius of the primary star however depends on the temperature used, and so this has to be confirmed with spectroscopy. A higher assumed inclination will result in a smaller radius of the companion and vice versa. A higher S/N light curve will be necessary to better constrain the inclination.

Figure 5 shows the observed and model light curves.

5.2. ATL 1748+0909

Although ATL 1748+0909 appears in the WD candidate catalog of Gentile Fusillo et al. (2019), the authors assign a

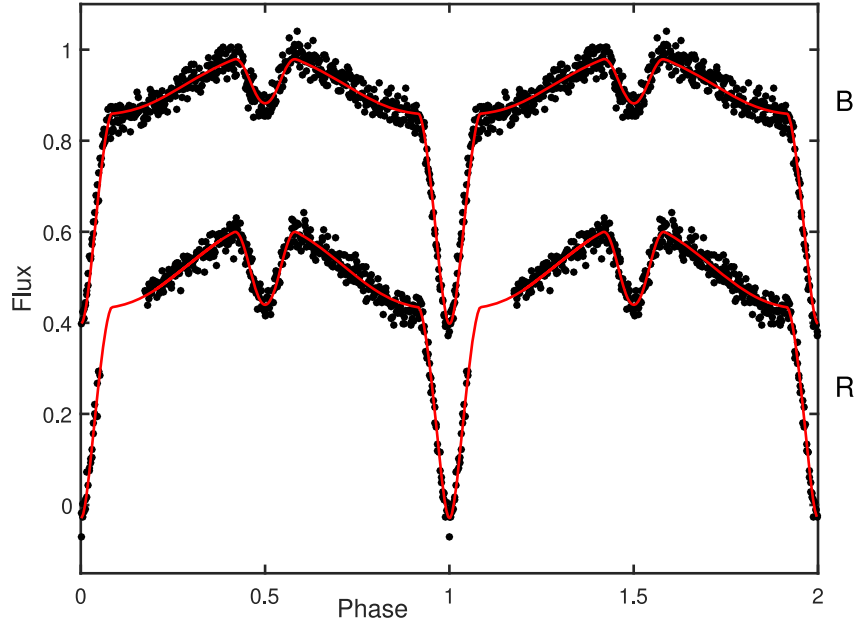


Figure 3. Phase-folded *BR* SAAO photometry of ATL 0718+0739 (dots) with model fits (lines). The fluxes have been normalized but have arbitrary zero-points.

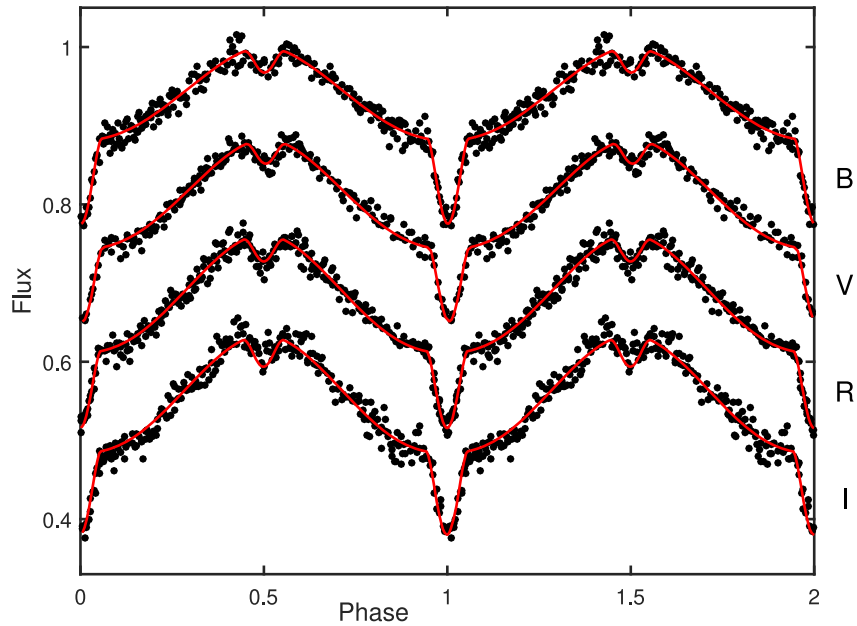


Figure 4. Phase-folded *BVRI* SAAO photometry of ATL 0836-0802 (dots) with model fits (lines). The fluxes have been normalized but have arbitrary zero-points.

negligible (0.005) probability that this star with $M_G = 5.10 \pm 0.26$ mag is indeed a WD. The model results in Table 3 suggest that its classification as a sdB by Geier et al. (2019) is correct. The *R*-filter amplitude is 0.28 mag, which is quite large for a sdO/B+dM system. This suggests that the sdB is hotter and/or smaller than a typical sdB. This is confirmed by the SED fit, which results in a temperature of $34,000^{+7000}_{-4000}$ K and a radius of $0.134^{+0.022}_{-0.019} R_\odot$. Assuming a mass of $0.47 M_\odot$ we get a surface gravity of $\log g = 5.86 \pm 0.12$. The flat bottom of the reflection effect suggests a higher inclination; we assumed $i = 62^\circ$ ($i = 40^\circ$ gave a poorer fit). We can then derive the separation of the system as $a = 0.62 \pm 0.10 R_\odot$ and a companion radius of

$0.176 \pm 0.032 R_\odot$. This implies an M5 companion with a mass of about $0.15 M_\odot$.

The phased data and the model fits are plotted in Figure 6.

5.3. ATL 2003+0838

According to Gentile Fusillo et al. (2019) the probability that ATL 2003+0838 is a WD is 0.28. Although the star also has an entry in the Geier et al. (2019) hot subdwarf candidate catalog, the physical properties ($M_G = 6.54 \pm 0.035$ mag) and very large reflection-effect amplitude change of 25% in *U* and 55% in *R* suggest that the primary star is a very hot WD. For a temperature of about 50,000 K we could obtain a good model fit of the light curve in all filters. Using this temperature we get

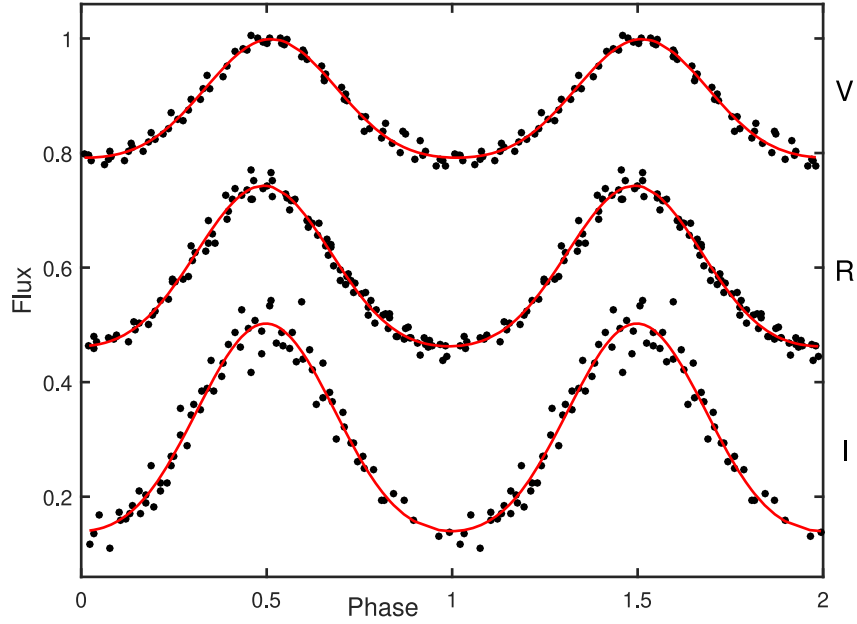


Figure 5. Phase-folded *VRI* SAAO photometry of ATL 1544–1816 (dots) with model fits (lines). The fluxes have been normalized but have arbitrary zero-points.

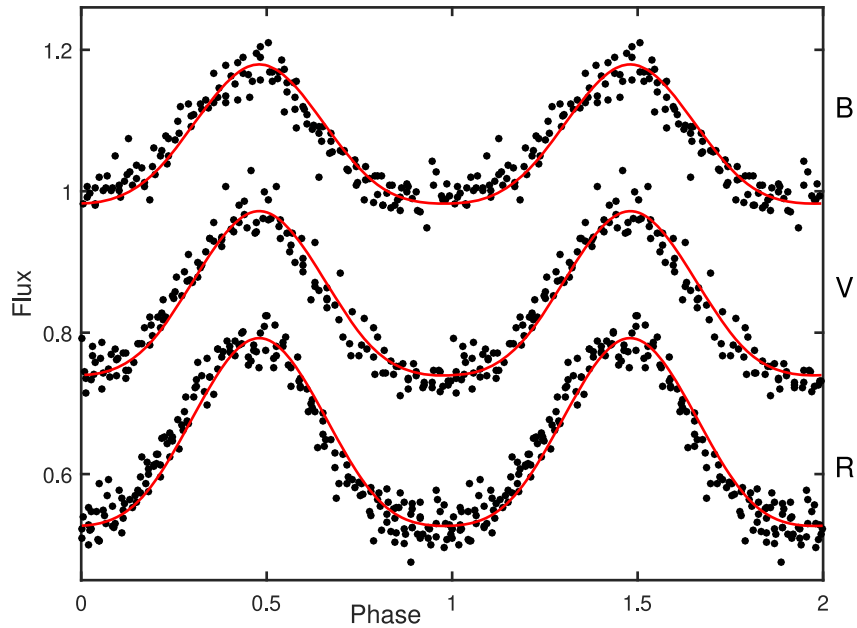


Figure 6. Phase-folded *BVR* SAAO photometry of ATL 1748+0909 (dots) with model fits (lines). The fluxes have been normalized but have arbitrary zero-points.

a radius of $0.059 \pm 0.003 R_{\odot}$ for the WD and a companion radius of $0.27 R_{\odot}$. However, this depends on the assumed WD temperature; hence spectroscopy is necessary to better constrain the companion properties. Moreover, as no eclipses are visible, the inclination is also difficult to determine by the light-curve fit. This is especially true at lower inclinations, as the light-curve shape due to the reflection effect is sinusoidal and a different inclination will also result in a different radius for the companion. We note that no physical models could be fitted assuming $i = 20^{\circ}$, while $i = 60^{\circ}$ led to poor light-curve fits.

Observed and theoretical light curves can be seen in Figure 7.

5.4. ATL 2028+0610

This star is a hot subdwarf candidate (Geier et al. 2019). With the model parameters in Table 3, $M_G = 4.57 \pm 0.082$ mag, and a modest *R*-filter amplitude of 0.10 mag, it seems to be a typical sdB+dM system. This is confirmed by the SED fit assuming a canonical-mass sdB ($T_{\text{eff}} = 27,300^{+1900}_{-1600}$ K, $R_{\text{sdB}} = 0.195 \pm 0.012 R_{\odot}$, $\log g = 5.53 \pm 0.05$). Using the relative radii derived from the light-curve fit and assuming an inclination of 44° this would suggest an M5 companion with a radius of $0.18 \pm 0.1 R_{\odot}$ and a mass of $0.15 \pm 0.1 M_{\odot}$. Taking $i = 60^{\circ}$ leads to a model of similar quality, while an inclination as low as 20° can be ruled out, as the required secondary star radius would be unphysically large. Time-resolved

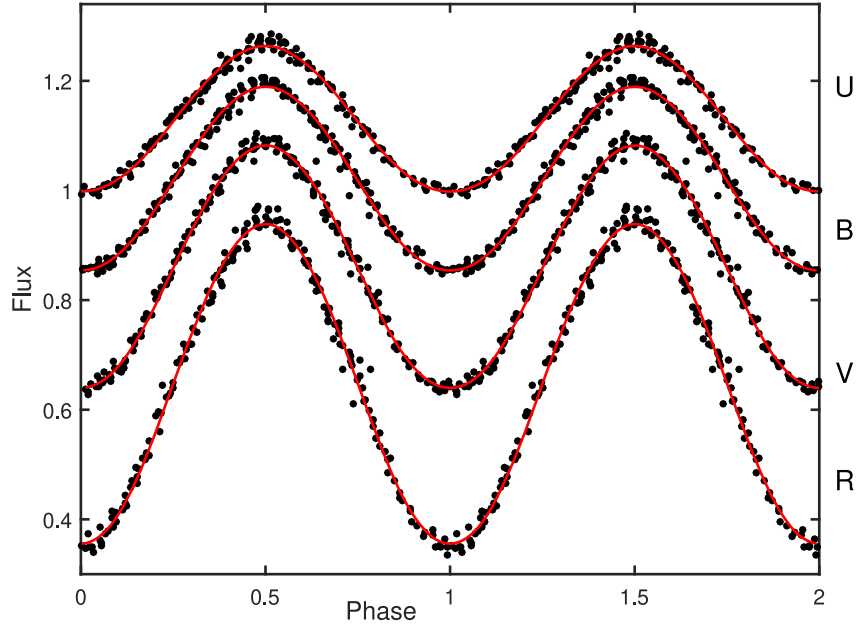


Figure 7. Phase-folded *UBVR* SAAO photometry of ATL 2003+0838 (dots) with model fits (lines). The fluxes have been normalized but have arbitrary zero-points.

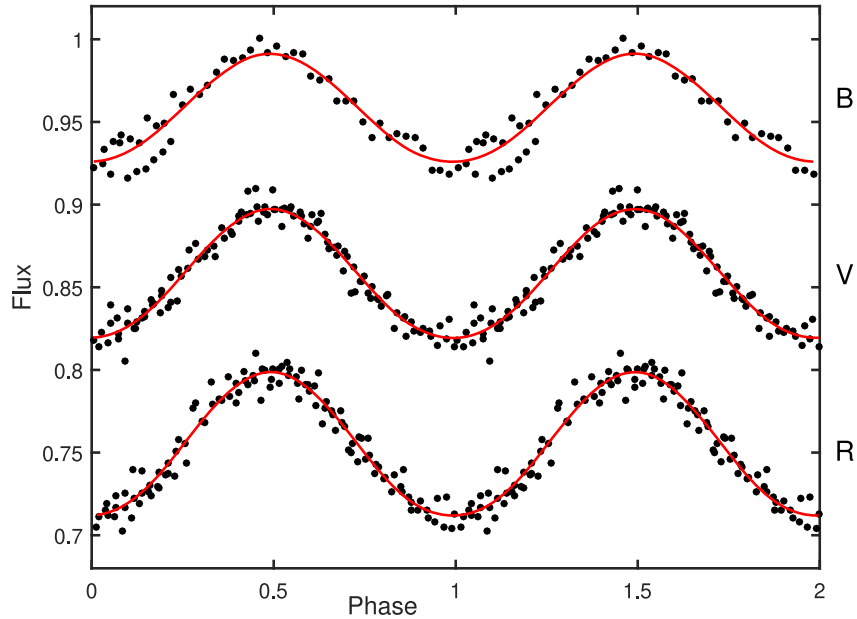


Figure 8. Phase-folded *BVR* SAAO photometry of ATL 2028+0610 (dots) with model fits (lines). The fluxes have been normalized but have arbitrary zero-points.

spectroscopy to determine the radial velocity curve and a higher S/N light curve are necessary to confirm the model. See Figure 8 for the observational and model light curves.

6. Three Pulsating Stars

ATL 1843+0226 and ATL 1853+0339 were originally selected from the ATLAS variable star catalog on the basis of their very red colors (see Table 1) as candidate late-type binary stars. ATL 0843–1159, on the other hand, is classified by Heinze et al. (2018) as a close binary system. Closer scrutiny of their light curves and other properties suggest that all three are likely δ Scuti pulsators (e.g., Guzik 2021, and numerous references therein).

Table 4 contains the physical properties and reddening of the three stars derived from photometry covering the visible and near-infrared parts of the spectrum, extracted from the Vizier database.⁹ Original sources of measurements include the AAVSO Photometric All-Sky Survey (APASS; Henden et al. 2015), Gaia (Gaia Collaboration 2021), the Panoramic Survey Telescope and Rapid Response System (Pan-STARRS; Chambers et al. 2016), the SkyMapper Southern Survey (Wolf et al. 2018; Onken et al. 2019), the Two Micron All-Sky Survey (2MASS; Skrutskie et al. 2006), the Wide-field Infrared Survey Explorer (WISE; Wright et al. 2010), and the Galaxy Evolution Explorer (GALEX; Bianchi et al. 2011). Use was

⁹ <https://vizier.u-strasbg.fr/viz-bin/VizieR>

Table 4
Physical Properties, Derived from Absolute Photometry, of the Three Stars Discussed in Section 6

Star	A_V (mag)	T_{eff} (K)	$\log g$ (dex)	M_{bol} (mag)	$\sigma_M(p)$ (mag)	SpT	SpM	n
ATL 0843–1159	0.10	7640(150)	4.0(0.6)	2.5(0.1)	0.09	A7	F0	23
	0.30(0.11)	7940(245)	3.7(1.0)	2.3(0.2)		A6	A9	
	0.10	7550(99)	4.5(0.5)	2.5(0.1)		A8	F0	21
ATL 1843+0226	0.32(0.06)	7830(116)	4.3(0.3)	2.34(0.1)	0.26	A7	A9	12
	5.36	7680(194)	5.1(1.2)	1.6(0.3)		A7	A3	
ATL 1853+0339	5.42(0.27)	7810(649)	5.1(1.1)	1.6(0.4)	0.27	A7	A3	13
	6.36	7250(186)	5.9(0.6)	−1.4(0.3)		F0	B7	
	7.20(0.29)	9540(1550)	5.8(0.5)	−2.3(0.6)		A0	B5	

Note. For each star, the first line in the Table assumes extinction fixed at the value extracted from Green et al. (2018), while the second line reports results with A_V as a free parameter. The contribution of the parallax uncertainty to the error on the bolometric magnitude is denoted by $\sigma_M(p)$. SpT and SpM are spectral types deduced, respectively, from the temperature and bolometric magnitude estimates. The last column gives the number of photometric measurements taken into account. Bolometric corrections for ATL 0843–1159 and ATL 1853+0339 assumed solar metallicity, while $[\text{Fe}/\text{H}] = -0.75$ for ATL 1843+0226, in accordance with its spectroscopic metallicity determination (see Table 5).

also made of parallaxes from Gaia Collaboration (2021), the extinction law $f_\lambda = A_\lambda/A_V$ from Schafly et al. (2016), the cumulative reddening map of Green et al. (2018)¹⁰, and bolometric corrections from the Modules for Experiments in Stellar Astrophysics (MESA) Isochrones and Stellar Tracks website.¹¹ Online availability of these sources is gratefully acknowledged.

Photometry was used to estimate the luminosity, temperature, and reddening of each star. This is conveniently done by minimizing the differences between the bolometric magnitudes estimated from the individual photometric measurements and the objective function being the sum of squared residuals

$$\begin{aligned}
 \text{SS} &= \sum_{\lambda}^{N_\lambda} [M_{\text{bol}} - \widehat{M}_{\text{bol},\lambda}]^2 \\
 &= \sum_{\lambda}^{N_\lambda} \{M_{\text{bol}} - [(m_\lambda + 5 + 5 \log_{10} p) - A_V f_\lambda + BC_\lambda]\}^2
 \end{aligned}
 \tag{1}$$

where λ is wavelength; m_λ are the photometric measurements; A_V and f_λ , respectively, are the V -filter absorption and the extinction law; M_{bol} and BC_λ the bolometric magnitude and bolometric correction, respectively; and p is the parallax. The notation $\widehat{M}_{\text{bol},\lambda}$ indicates the bolometric magnitude estimated from the measurement through the filter with an effective wavelength λ .

The uncertainties were estimated using a bootstrapping procedure—see Koen (2022) for details. The spectral types corresponding to, respectively, the temperature and bolometric magnitude were taken from Pecaut et al. (2012) and Pecaut & Mamajek (2013);¹² these are designated “SpT” and “SpM” in Table 4.

A discussion of the results for the individual stars follows.

6.1. ATL 0843–1159

Two of the photometric measurements (APASS g' and r') give outlying (by ~ 0.2 mag) estimates of M_{bol} . If these are excluded, the second set of solutions in Table 4 is obtained.

¹⁰ <http://argonaut.skymaps.info/>

¹¹ http://waps.cfa.harvard.edu/MIST/model_grids.html#bolometric

¹² http://www.pas.rochester.edu/~emamajek/BEM_dwarf_UBVJHK_colors_Teff.txt

The derived temperatures and luminosities suggest that the star is of late A/early F spectral type. The line-of-sight absorption is 0.1–0.3 mag.

The light curves of ATL 0843–1159 (Figure 9) resemble those of RR Lyrae stars. However, the short period (~ 1.4 hr) and value of the absolute magnitude are consistent with the star being a high-amplitude δ Scuti (HADS) pulsator. The APASS observation $V = 14.2$ can be corrected for absorption to $A_V \approx 14.0$ mag, and $M_V = 2.3$ mag follows from the Gaia parallax. Furthermore, using the recent period–luminosity relation for δ Scuti stars

$$M_V = -2.94 \log_{10} P - 1.34$$

(Ziaali et al. 2019), the predicted absolute magnitude of the star is $M_V = 2.3$ mag. Examination of Figure 5 in Ziaali et al. (2019) suggests that evolutionarily it is close to the main sequence.

6.2. ATL 1843+0226

The apparent brightness of the star increases monotonically with increasing wavelength, from Pan-STARRS g to WISE $W3$, except for the $W2$ measurement, which is anomalously faint. This measurement also leads to a bolometric magnitude estimate ~ 0.5 mag fainter than that associated with the rest of the photometry. It was therefore excluded in calculating the results in Table 4. ATL 1843+0226 is of similar spectral type to ATL 0843–1159, but the reddening is substantial.

Two successive exposures of 15 minutes each on the star were also obtained with the Robert S. Stobie (RSS) spectrograph of the 10 m Southern African Large Telescope, covering 3400–6400 Å. The spectra were co-added, and standard reduction techniques were applied, including calibration using a spectrophotometric standard. The total reduced spectrum of ATL 1843+0226 was analyzed with use of the Fitting Binary Stars (FBS; Kniazev et al. 2020) package. This software was developed to determine the parameters of individual components of binary systems such as the effective temperature T_{eff} , surface gravity $\log g$, projected rotational velocity $v \sin i$, metallicity $[\text{Fe}/\text{H}]$, and heliocentric radial velocity V_{hel} , as well as the color excess $E(B - V)$ of the system. The software simultaneously approximates the observed spectrum by a model, which is obtained by interpolating over the grid of theoretically calculated high-

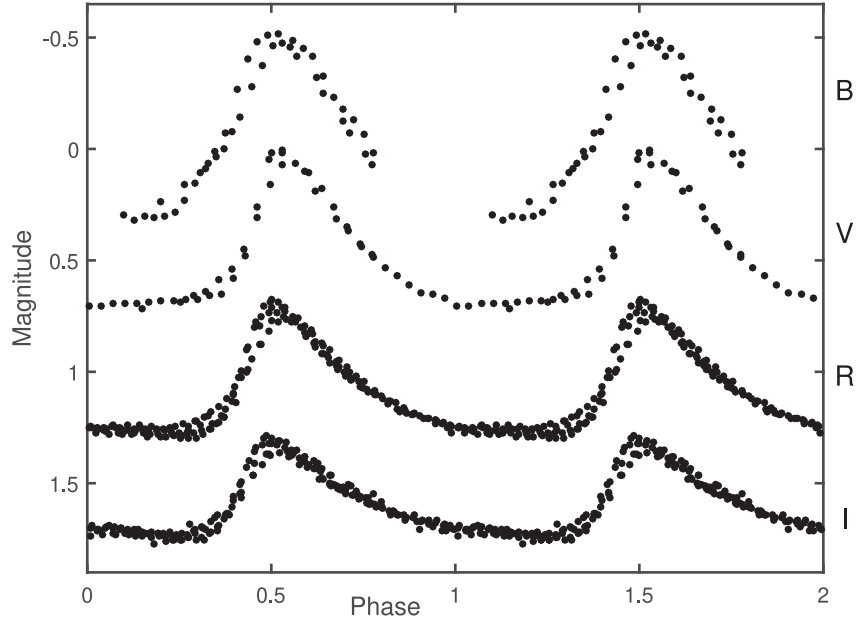


Figure 9. Phase-folded *BVRI* SAAO photometry of ATL 0843–1159. The zero-points of the light curves are arbitrary.

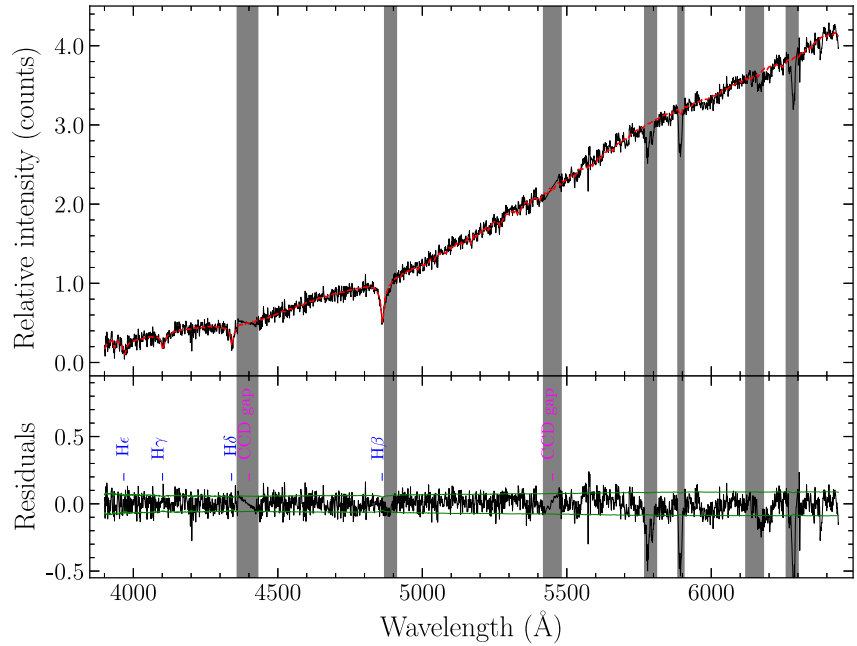


Figure 10. Results of modeling of the fully reduced spectrum of ATL 1843+0226. Upper panel: comparison of the observed spectrum (solid black line) with the best-fitting model (red dashed line) obtained with the FBS software. The gray vertical areas show spectral regions excluded from the spectral fit because of their contamination by most prominent diffuse interstellar bands. Bottom panel: difference between the observed and model spectra (black noisy line). The green solid lines indicate 1σ errors in the observed spectrum. The positions of identified Balmer lines and CCD gaps are indicated.

Table 5
Results of Fitting Main-sequence Models to the Spectroscopic Observations of ATL 1843+0226

Spectral Type	T_{eff} (K)	$\log g$ (dex)	[Fe/H]	v_r (km s^{-1})	$E(B - V)$ (mag)	A_V (mag)
A9-F0V	7300 (500)	4.2 (0.25)	-0.70 (0.15)	43 (7)	1.75 (0.05)	5.4

Note. Uncertainties are given in brackets.

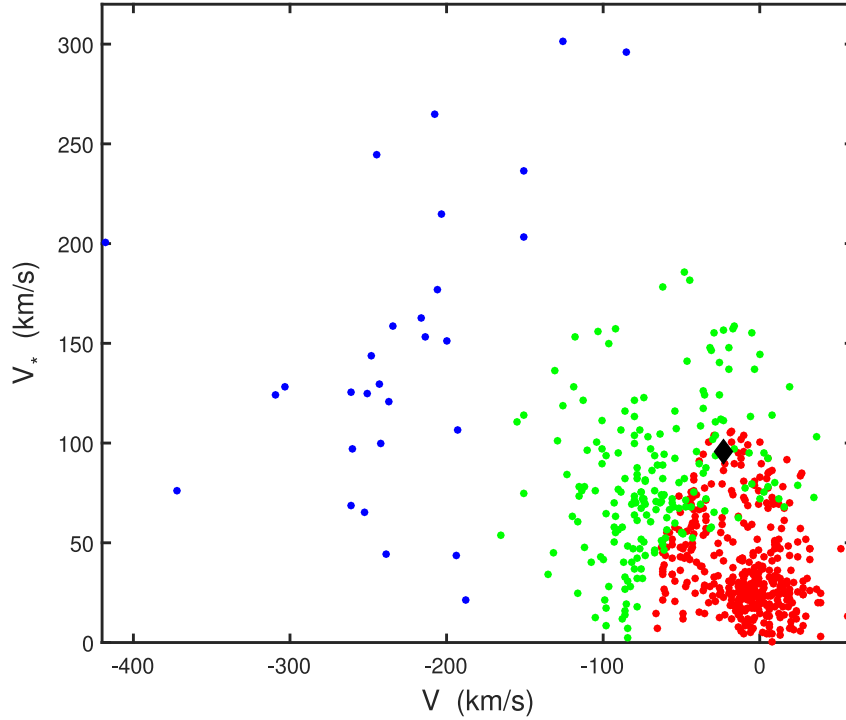


Figure 11. Toomre diagram, showing the positions of 706 field stars from Bensby et al. (2014). Red, green, and blue dots, respectively, indicate stars in the thin disk, thick disk, and halo. The velocity components of ATL 1843+0226 are shown by the black diamond.

resolution stellar spectra, and convolves it with a function that takes the broadening and wavelength shift into account. In case of a single star the fitting routine uses one model spectrum for the single star. In our case the set of PHOENIX models (Husser et al. 2013) was used, previously convolved to match the RSS instrumental resolution. As shown in Muhie et al. (2021), FBS modeling of RSS spectra performs well in the total range of metallicities from $-3 \leq [\text{Fe}/\text{H}] \leq 0$ with 1σ error ~ 0.20 dex.

The model spectrum fitting results are shown in Figure 10 and Table 5. Assuming

$$R_V = A_V / E(B - V) = 3.1$$

(e.g., Fitzpatrick 1999), $A_V = 5.43$, in very good agreement with the photometrically derived results and the value from the cumulative absorption map. The temperature-based spectral type of A7 is also close to the A9–F0 classification.

Given the information above, it is concluded that the star is either an HADS or an SX Phoenicis pulsator (e.g., McNamara 1995). The low metallicity is evidence in favor of the latter; we turn to kinematics to further discriminate between the two possibilities.

The Galactic coordinates of ATL 1843+0226 are $\ell = 34.2542$, $b = 2.7911$, i.e., the star is close to the Galactic plane. In fact, given the 1.73 ± 0.21 kpc distance from the Sun (from the parallax in Table 1), its distance above the plane is only 84 ± 10 pc, which would place it in the thin disk. The Gaia parallax and proper motions of the star can be used to calculate space velocities $U = 88.2$, $V = -23.3$, $W = -37.0$ km s^{-1} (using the formulation of Johnson & Soderblom 1987, with corrections for the solar motion taken from Coşkunoğlu et al. 2011). Also of interest is the total velocity $V_t = \sqrt{U^2 + V^2 + W^2} = 98.5$ km s^{-1} .

Toomre diagrams are plots of $V_* = \sqrt{U^2 + W^2}$ (95.7 km s^{-1} , in the case of ATL 1843+0226) versus V . Figure 11 is a recreation of Figure 9 in Kovalev et al. (2019), to which the (V, V_*) position of ATL 1843+0226 has been added. Shown are the positions of the thin disk, thick disk, and halo stars. Data were taken from Bensby et al. (2014), and the classification criteria of Kovalev et al. (2019; their Appendix C) were applied. Given the large value of V_t , together with the low metallicity, it may be concluded that ATL 1843+0226 is an SX Phe star near the thin disk/thick disk boundary.

Some insight into the nature of the pulsation can be gained from the pulsation constant Q given by

$$\log Q = -6.454 + \log P + 0.5 \log g + 0.1 M_{\text{bol}} + \log T_{\text{eff}}$$

where P is the pulsation period in days (e.g., Breger & Bregman 1975). Substituting with the parameter values from Table 5, $Q \approx 0.034$, which implies pulsation in the fundamental radial mode (Fitch 1981). This is consistent with the asymmetry in the light curve and the large amplitude (e.g., McNamara 1995).

There is a slight bump visible in the light curves in Figure 12, near light maximum on the descending branch. This phenomenon is well known in Cepheid and RR Lyrae pulsators (see, e.g., the summaries in Paxton et al. 2019). We could find only one instance of an SX Phe variable—XX Cyg—for which (transient) light-curve bumps have been reported (e.g., Sadun & Ressler 1986; Blake et al. 2003).

Most SX Phe stars have been found in globular clusters, in the form of blue stragglers; examples in the field being relatively rare (e.g., Jeon et al. 2010).

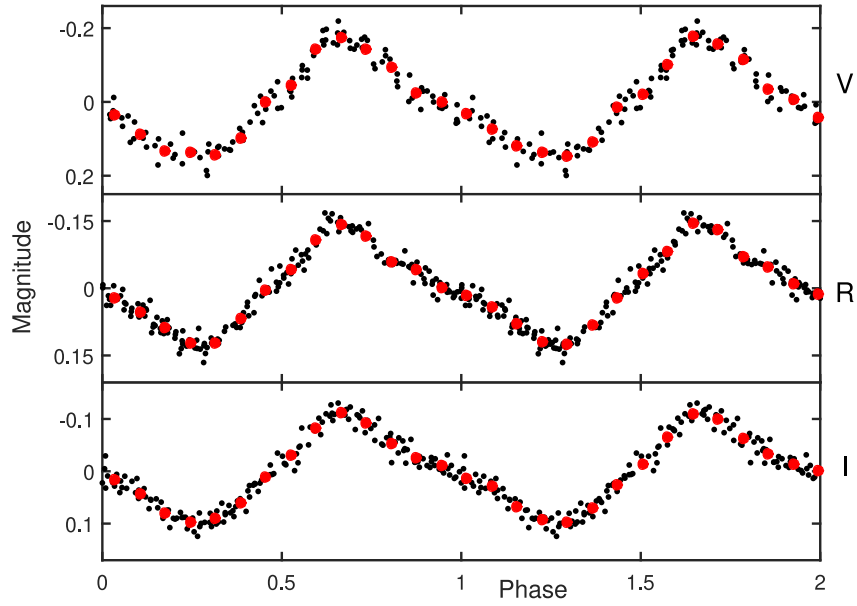


Figure 12. Phase-folded SAAO light curves of ATL 1843+0226. Small (black) dots are raw observations, and large (red) dots are the averages of phase bins with width 0.07. Note that the vertical scales on the panels are different the better to show the nonsinusoidal nature of each light curve—the panel heights are 0.51, 0.42, and 0.34 mag from top to bottom. The zero-points are arbitrary.

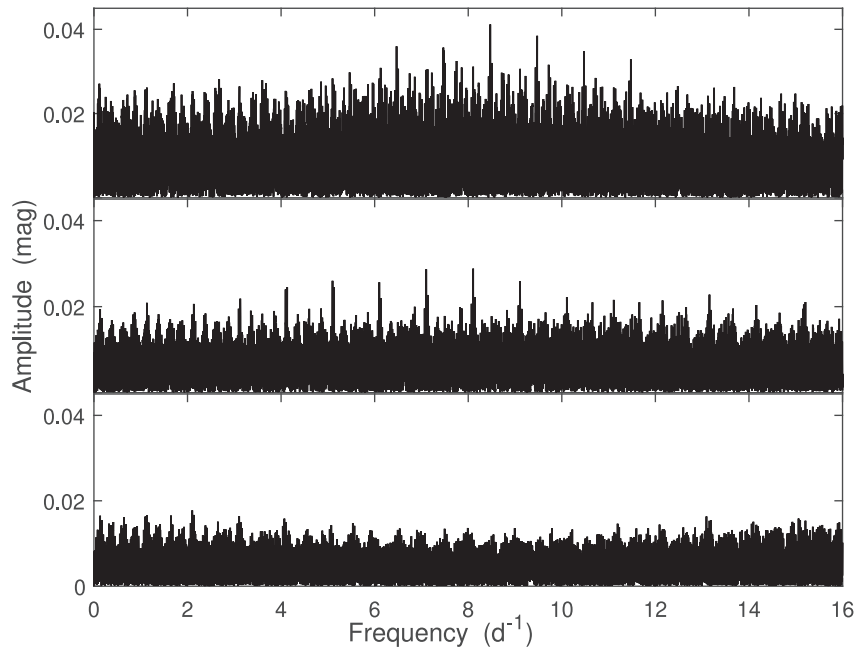


Figure 13. Top panel: amplitude spectrum of the o filter ATLAS photometry of ATL 1853+0339. Middle panel: amplitude spectrum of the residuals after prewhitening by the most prominent frequency (8.47068 day^{-1}) in the top panel. Bottom panel: amplitude spectrum after prewhitening the photometry by frequencies 8.47068 and 8.1052 day^{-1} .

6.3. ATL 1853+0339

This star is even more heavily reddened than ATL 1843+0226; dust absorption estimates in Table 4 differ by $\sim 10\%$ and are in the range 6.4–7.2 mag. The Galactic latitude is only $1^\circ 20'$, and at a distance of $2.76 \pm 0.35 \text{ kpc}$ (from the parallax in Table 1), the distance above the plane is a mere $58 \pm 7 \text{ pc}$.

The estimated luminosity of the star is much larger than that of a main-sequence star of the estimated temperature. Invoking a companion of comparable brightness does not come close to resolving the problem. A possible explanation is that the star is

evolved. It is noted that ATL 1853+0339 is in a catalog of luminous OBA candidates selected on the basis of photometry, parallaxes, and kinematics (Zari et al. 2021).

The tallest peak in the periodogram of the somewhat noisy and sparse ($N = 70$) ATLAS c filter observations of the star is at 9.47 day^{-1} , which is an alias of the catalog value $f = 1/0.118055 = 8.4706 \text{ day}^{-1}$. Prewhitening by this frequency leads to an essentially featureless spectrum. Figure 13 (top panel) shows an amplitude spectrum of the ATLAS o filter photometry; the largest peak is indeed at 8.4708 day^{-1} . Interestingly, prewhitening by this frequency reveals the

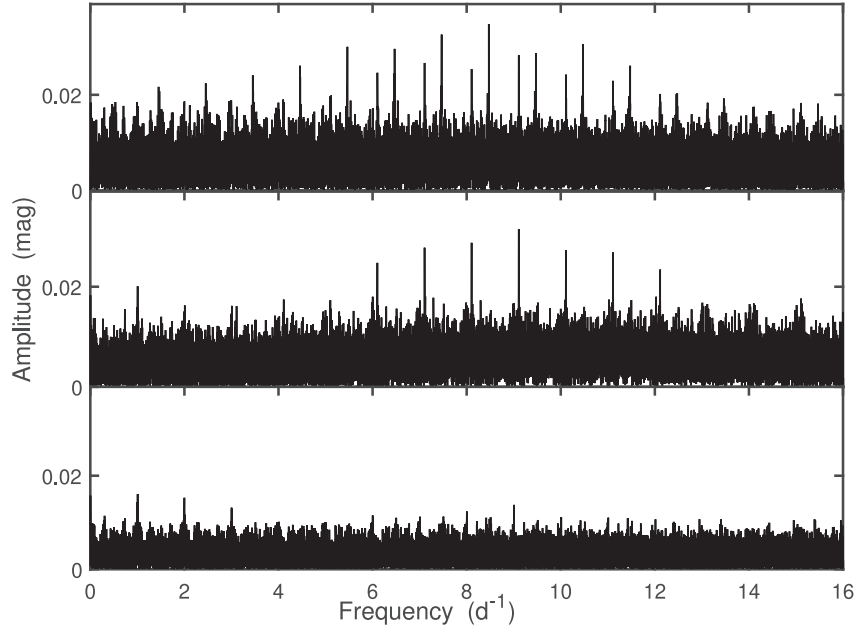


Figure 14. Top panel: amplitude spectrum of the r -filter ZTF photometry of ATL 1853+0339. Middle panel: amplitude spectrum of the residuals after prewhitening by the most prominent frequency (8.47069 day^{-1}) in the top panel. Bottom panel: amplitude spectrum after prewhitening the photometry by frequencies 8.47069 and 9.10779 day^{-1} .

presence of a second periodicity. The largest peak in the residual spectrum (middle panel of Figure 13) is at a frequency of 8.1052 day^{-1} , though this is by no means secure due to aliasing. Note that prewhitening by both frequencies leaves an essentially flat spectrum characteristic of white noise (bottom panel of Figure 13).

Additional insight can be gained by studying the Zwicky Transient Facility (ZTF; Bellm et al. 2019) observations of ATL 1853+0339. The star is included in the ZTF catalog of periodic variable stars (Chen et al. 2020) with $P = 0.2361$ days (i.e., a frequency of 4.236 day^{-1}). There are 629 ZTF r -filter measurements of the star. These cover a time baseline of 3.2 yr and are generally “dense,” in the sense that the time interval between successive observations is mostly less than a day (419 out of 628). An amplitude spectrum of the ZTF photometry is plotted in the top panel of Figure 14. It is evident from the complicated pattern of peaks in the interval $4 < f < 12 \text{ day}^{-1}$ that there is more than one periodicity in the data. The largest peak is at a frequency of 8.47069 day^{-1} , which is in excellent agreement with $f = 8.47063 \text{ day}^{-1}$ in the ATLAS variable star catalog. The spectrum of the residuals after prewhitening by the former frequency is in the middle panel of the figure; most of the peaks in the top panel have disappeared, confirming that they were at aliases of the 8.47069 day^{-1} periodicity. The largest peak in the middle panel is at 9.10788 day^{-1} , i.e., a 1 day^{-1} alias of the second frequency found in the ATLAS o data. If $f = 9.10788 \text{ day}^{-1}$ is also prewhitened from the g -filter data the spectrum in the bottom panel of Figure 14 results. The most prominent peaks in this final spectrum are at 1 day^{-1} and its aliases, suggesting slight zero-point differences for different nights.

It should be noted that the level of the residual (i.e., noise) spectrum in the bottom panel of Figure 14 is $\sim 30\%$ lower than that in the bottom panel of Figure 13. This is primarily due to the larger number of data in the ZTF photometry.

Analysis of the SAAO data—which are dense within individual nights—confirms that the aliases identified in the ZTF data are the correct ones. Using these two frequencies as starting values, the model

$$m(t) = a_0 + a_1 \cos(2\pi f_1 t + \phi_1) + a_2 \cos(2\pi f_2 t + \phi_2) + \text{error}$$

was fitted to the r photometry. The results were $f_1 = 8.47069(3) \text{ day}^{-1}$, $f_2 = 9.10779(4) \text{ day}^{-1}$, $a_1 = 0.041 \pm 0.002 \text{ mag}$, and $a_2 = 0.033 \pm 0.002 \text{ mag}$. The amplitude of the largest peak in the residual spectrum is 0.014 mag , and prewhitening by its frequency (1 day^{-1}) leaves a featureless spectrum with a mean level of 3.3 mmag .

Given that the star is much brighter in the red, it is no surprise that the ZTF g -filter photometry is less informative: aside from the largest peak (0.047 mag) at $f = 8.47067 \text{ day}^{-1}$, the spectrum is noise-dominated.

The two frequencies extracted from the ZTF photometry can now be fitted to the SAAO observations (see Figure 15 for an example); this gives more detailed information about the dependence of the amplitudes on the wavelength. Interestingly, spectra of the residuals (Figure 16) show two broad humps of excess power, centered roughly on 6 day^{-1} and 13 day^{-1} . The highest peaks are at 7.23 and 13.18 day^{-1} (I), 6.18 and 13.19 day^{-1} (R), 5.71 and 13.21 day^{-1} (V). Obviously aliasing prohibits more definitive results, but it seems clear that there are two additional periodicities in the data, one with a probable frequency $\sim 13.2 \text{ day}^{-1}$, and the other at a lower frequency in the approximate range $5.5\text{--}7.5 \text{ day}^{-1}$.

The amplitudes associated with all four periodicities are listed in Table 6. For three of the four frequencies, the amplitude does not vary much over the effective wavelength range $\sim 5500\text{--}7900 \text{ \AA}$ covered by the VRI filters. The exception is $f = 9.11 \text{ day}^{-1}$, for which the amplitude increases with decreasing wavelength. The reader’s attention is also drawn to the anomalously large g -filter amplitude of the 8.47 day^{-1} mode.

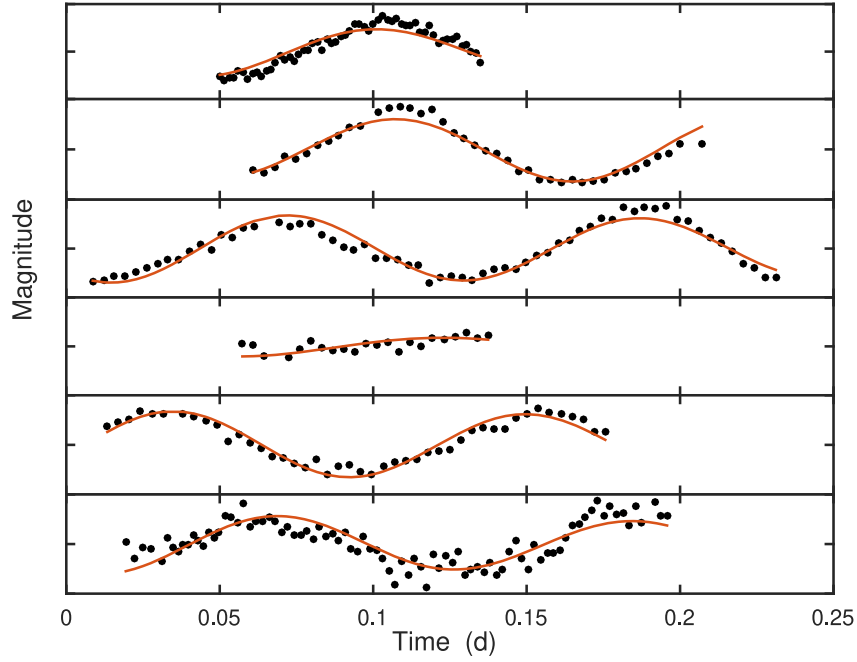


Figure 15. Two-frequency fit (red lines) to the six sets of SAAO *R*-filter observations of ATL 1853+0339 (dots). The vertical width of each panel is 0.2 mag. Both the magnitude and time zero-points for each panel are arbitrary.

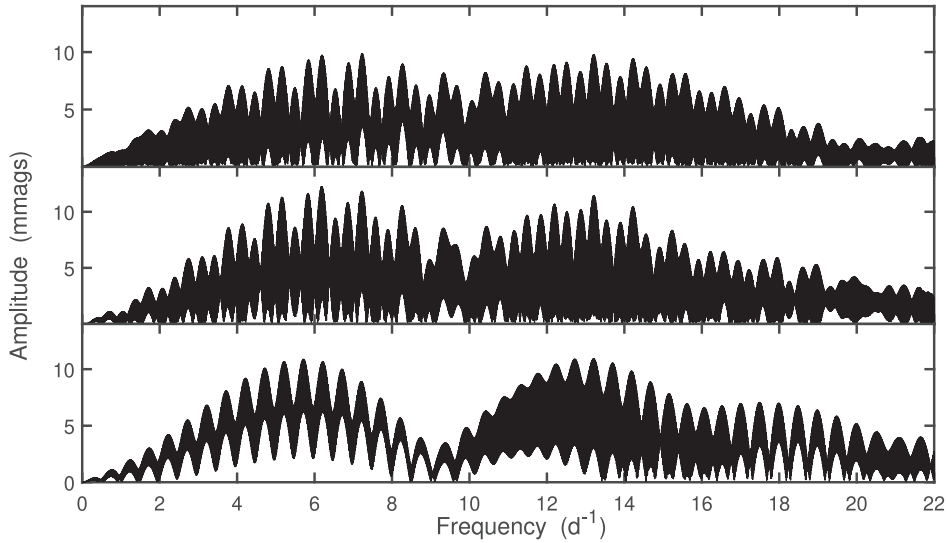


Figure 16. Amplitude spectra of the residuals left after prewhitening the SAAO photometry of ATL 1853+0339 by frequencies 8.47069 and 9.10779 day^{-1} . From top to bottom: *I*-, *R*-, and *V*-filter observations.

Table 6

Amplitudes (in Millimagnitudes) of the Periodicities in the Photometry of ATL 1853+0339

Frequency (day^{-1})	Filter						
	<i>g</i>	<i>c</i>	<i>V</i>	<i>r</i>	<i>R</i>	<i>o</i>	<i>I</i>
8.47069	47	61	45(2)	41(2)	44(2)	40(4)	41(1)
9.10779	35(2)	33(2)	26(2)	24(4)	25(1)
13.2	11	...	9	...	9
5.7–7.2	10	...	12	...	10

Note. The uncertainty in the last digit is given in brackets, for those amplitudes determined by model fitting; other amplitudes are the spectral peak heights.

Given the relatively short period (2.8 hr) and high temperature, two candidate classes of pulsating stars come to mind: β Cephei and δ Scuti. The former can probably be ruled out by the fact that β Cephei stars are of early B spectral types (B0–B2.5; see, e.g., Stankov & Handler 2005), i.e., most likely considerably hotter than ATL1853+0339. δ Scuti stars, on the other hand, also appear unlikely as the luminosity of the star is $\log(L/L_{\odot}) = 2.4\text{--}2.8$, which, for example, exceeds that of all stars in the well-populated $\log L\text{--}T_{\text{eff}}$ diagram of Ziaali et al. (2019; see their Figure 5). However, Balona (2018) calculated the luminosities of δ Scuti stars in the Kepler field and found a scattering of these pulsators with $\log(L/L_{\odot}) > 2$.

The rate of increase in the amplitudes with decreasing wavelength (Table 6) is unusually slow for a δ Scuti star—compare with, for example, Figure 7 in Rodríguez et al. (2007) and Figure 3 in Ulusoý et al. (2013). One possibility is that the star is in fact a binary, consisting of a δ Scuti pulsator with a luminous blue companion. The excess short-wavelength radiation contributed by the companion would then dilute the amplitude of the pulsations in the blue. However, this does not readily explain the difference between the wavelength dependence of the two primary modes.

7. Conclusions

Six of the binary stars modeled in this paper, four eclipsing systems and two reflection-effect binaries, consist of subdwarf B stars with cool secondaries. Periods lie in the range 1.8–2.3 hr. The two reflection-effect systems are among the shortest-period systems known in this class (Schaffenroth et al. 2019, 2022). Two further binaries consist of hot WD primaries with cool companions. From the light-curve fits together with fits of the SEDs and the Gaia parallaxes we tried to constrain the companions, which seem to be M dwarfs in all cases.

The remaining three stars are pulsators, two of which are very highly reddened. ATL 1843+0226 is a highly obscured ($A_V > 5$ mag) SX Phoenicis star. It is unusual for that type of object in that it is a field star, residing near the Galactic thin disk. Furthermore, it shows an unusual bump on the descending branch of its light curve. The nature of ATL 1853+0339 is unknown: the light variations are dominated by 0.110 and 0.118 day periodicities, but there is evidence of at least two further periodicities. Only one of the periodicities show the amplitude increase with decreasing wavelength, which is expected for a pulsating star.

Nine of the eleven stars lack spectroscopy; this is required to improve the modeling of these objects. Spectra could be used for more accurate SED fitting, and, in the case of binary systems, for the determination of mass ratios from radial velocity measurements. In the case of ATL 1853+0339, spectroscopy promises to be particularly interesting. First, it could be used to check the suspected high luminosity and

reddening of the star. Second, it might reveal whether ATL 1853+0339 is a binary, either through a composite spectrum, or, if a close system, through large radial velocity changes. Third, high-dispersion time-series spectroscopy could provide additional information about pulsation modes, either through small radial velocity shifts, or through line profile variations.

Allocation of telescope time by the South African Astronomical Observatory, and the smooth operation of the equipment, are acknowledged. The authors are particularly grateful for Director’s Discretionary Time awarded in order to obtain SALT spectra of ATL 1843+0226. This research has made use of the VizieR catalog access tool and the Simbad Astronomical Database at CDS, Strasbourg, France; bolometric corrections from the MESA Isochrones and Stellar Tracks; the cumulative reddening maps of Green et al. (2018);¹³ and the results of various large photometric surveys referred to in Section 6 of the paper. A.K. acknowledges support from the National Research Foundation (NRF) of South Africa and from the Ministry of Science and Higher Education of the Russian Federation grant 075-15-2022-262 (13.MNPMU.21.0003). Helpful comments from the referee led to improvements in the paper.

Data Availability

ATLAS and CSS photometry are respectively available from the Mikulski Archive for Space Telescopes at DOI:[10.17909/t9-2p3r-7651](https://doi.org/10.17909/t9-2p3r-7651) and from the Catalina Surveys Data Release 2 site.¹⁴ SAAO photometry is available from the first author.

Appendix A Phased ATLAS and CSS Light Curves

Phase-folded light curves of the ATLAS and (where available) CSS photometry of the stars (Figure A1).

¹³ <http://argonaut.skymaps.info/>

¹⁴ <http://nesssi.cacr.caltech.edu/DataRelease/>

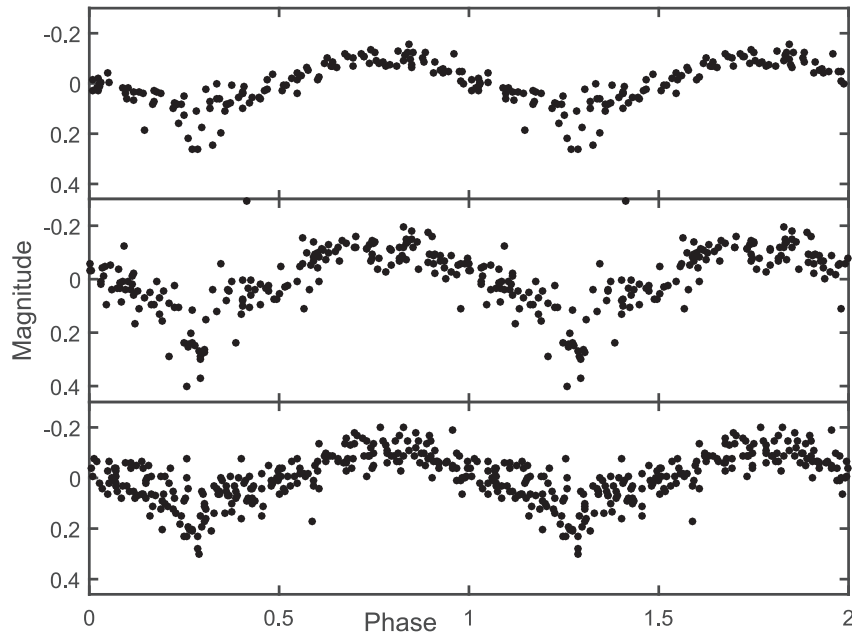


Figure A1. From top to bottom: ATLAS *c*, ATLAS *o*, and CSS photometry. The complete figure set (11 images) is available in the online journal. (The complete figure set (11 images) is available.)

Appendix B ED Fits

Plots of the SED fits for the binary stars (Figure B1).

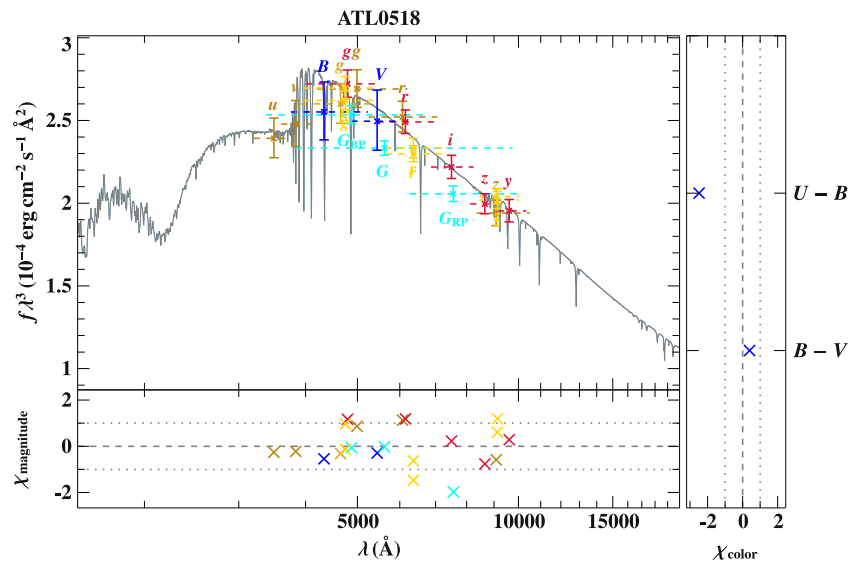


Figure B1. The color coding of the sources of the photometry is GALEX (dark violet), TDI (dark violet), FAUST (dark violet), Johnson (blue), Geneva (crimson), Stroemgren (green), SDSS (golden), VST (golden), SkyMapper (dark golden), PS1 (crimson), Hipparcos (cyan), Tycho (brown), Gaia (cyan), BATC (gold), JPLUS (steel blue), SPLUS (steel blue), DECam (gold), DENIS (orange), 2MASS (red), UKIDSS (pink4), VISTA (red4), INT (maroon), SMASH (gold), HST (black), WISE (magenta), Spitzer (purple), SWIFT (deep pink), XMM (deep pink), and NSFCam (red4). The complete figure set (8 images) is available in the online journal. (The complete figure set (8 images) is available.)

ORCID iDs

C. Koen  <https://orcid.org/0000-0003-2291-2660>A. Kniazev  <https://orcid.org/0000-0001-8646-0419>

References

- Balona, L. A. 2018, *MNRAS*, **479**, 183
- Baran, A. S., Østensen, R. H., Heber, U., et al. 2021, *MNRAS*, **503**, 2157
- Bellm, E. C., Kulkarni, S. R., Barlow, T., et al. 2019, *PASP*, **131**, 8002
- Bensby, T., Fletzing, S., & Oey, M. S. 2014, *A&A*, **562**, A71
- Bianchi, L., Herald, J., Efremova, B., et al. 2011, *Ap&SS*, **335**, 161
- Blake, R. M., Delaney, P., Khosravani, H., Tome, J., & Lightman, M. 2003, *PASP*, **115**, 212
- Breger, M., & Bregman, J. N. 1975, *ApJ*, **200**, 343
- Chambers, K. C., Magnier, E. A., Metcalfe, N., et al. 2016, arXiv:1612.05560
- Chen, X., Wang, S., Deng, L., et al. 2020, *ApJS*, **249**, 18
- Claret, A., & Bloemen, S. 2011, *A&A*, **529**, A75
- Coşkunoğlu, B., Ak, S., Bilir, S., et al. 2011, *MNRAS*, **412**, 1237
- Copperwheat, C. M., Marsh, T. R., Dhillon, V. S., et al. 2010, *MNRAS*, **402**, 1824
- Drake, A. J., Graham, M. J., Djorgovski, S. G., et al. 2014, *ApJS*, **213**, 9
- Edelmann, H. 2003, PhD, Friedrich-Alexander-University, Erlangen-Nürnberg
- Fitch, W. S. 1981, *ApJ*, **249**, 218
- Fitzpatrick, E. L. 1999, *PASP*, **111**, 63
- Gaia Collaboration 2021, *A&A*, **649**, A1
- Geier, S., Raddi, R., Gentile Fusillo, N. P., & Marsh, T. R. 2019, *A&A*, **621**, A38
- Gentile Fusillo, N. P., Tremblay, P.-E., Gansicke, B. T., et al. 2019, *MNRAS*, **482**, 4570
- Green, G. M., Schlafly, E. F., Finkbeiner, D., et al. 2018, *MNRAS*, **478**, 651
- Guzik, J. A. 2021, *FrASS*, **8**, 55
- Han, Z., Podsiadlowski, P., Maxted, P. F. L., & Marsh, T. R. 2003, *MNRAS*, **341**, 669
- Han, Z., Podsiadlowski, P., Maxted, P. F. L., Marsh, T. R., & Ivanova, N. 2002, *MNRAS*, **336**, 449
- Heber, U. 2016, *PASP*, **28**, 082001
- Heinze, A. N., Tonry, J. L., Denneau, L., et al. 2018, *AJ*, **156**, 241
- Henden, A. A., Levine, S., Terrell, D., & Welch, D. L. 2015, AAS Meeting, **225**, 336.16
- Hilditch, R. W., Harries, T. J., & Hill, G. 1996, *MNRAS*, **279**, 1380
- Husser, T.-O., Wende-von Berg, S., Dreizler, S., et al. 2013, *A&A*, **553**, A6
- Jeon, Y.-B., Kim, S.-L., & Nemeč, J. M. 2010, *PASP*, **122**, 17
- Johnson, D. R. H., & Soderblom, D. R. 1987, *AJ*, **93**, 864
- Jones, D., & Boffin, H. M. J. 2017, *NatAs*, **1**, 0117
- Kallrath, J., & Milone, E. F. 2009, *Eclipsing Binary Stars: Modeling and Analysis* (2nd ed.; New York: Springer)
- Kniazev, A. Y., Malkov, O. Y., Katkov, I. Y., & Berdnikov, L. N. 2020, *RAA*, **20**, 119
- Koen, C. 2019, *MNRAS*, **490**, 1283
- Koen, C. 2022, *MNRAS*, **510**, 1857
- Kovalev, M., Bergemann, M., Ting, Y.-S., & Rix, H.-W. 2019, *A&A*, **628**, A54
- Kupfer, T., Ramsay, G., Roestel, J. v., et al. 2017, *ApJ*, **851**, 28
- McNamara, D. H. 1995, *AJ*, **109**, 1751
- Muhie, T. D., Dambis, A. K., Berdnikov, L. N., Kniazev, A. Y., & Grebel, E. K. 2021, *MNRAS*, **502**, 4074
- O'Donoghue, D., Kilkeny, D., Koen, C., et al. 2013, *MNRAS*, **431**, 240
- Onken, C. A., Wolf, C., Bessell, M. S., et al. 2019, *PASA*, **36**, 33
- Østensen, R. H., Geier, S., Schaffenroth, V., et al. 2013, *A&A*, **559**, A35
- Parsons, S. G., Marsh, T. R., Copperwheat, C. M., et al. 2010, *MNRAS*, **402**, 2591
- Paxton, B., Smolec, R., Schwab, J., et al. 2019, *ApJS*, **243**, 10
- Pecaut, M. J., & Mamajek, E. E. 2013, *ApJS*, **208**, 9
- Pecaut, M. J., Mamajek, E. E., & Bubar, E. J. 2012, *ApJ*, **756**, 154
- Press, W. H., Teukolsky, S. A., Vetterling, W. T., & Flannery, B. P. 1992, *The Art of Scientific Computing* (2nd ed.; Cambridge: Cambridge Univ. Press)
- Ricker, G. R., Winn, J. N., Vanderspek, R., et al. 2015, *JATIS*, **1**, 014003
- Rodríguez, E., Fauvaud, S., Farrell, J. A., et al. 2007, *A&A*, **471**, 255
- Sadun, A. C., & Ressler, M. 1986, *PASP*, **98**, 504
- Schaffenroth, V., Casewell, S. L., Schneider, D., et al. 2021, *MNRAS*, **501**, 3847
- Schaffenroth, V., Classen, L., Nagel, K., et al. 2014, *A&A*, **570**, A70
- Schaffenroth, V., Geier, S., Heber, U., et al. 2018, *A&A*, **614**, A77
- Schaffenroth, V., Barlow, B. N., Geier, S., et al. 2019, *A&A*, **630**, A80
- Schaffenroth, V., Pelisoli, I., Barlow, B. N., et al. 2022, *A&A*, **666**, A182
- Schafly, E. F., Meisner, A. M., Stutz, A. M., et al. 2016, *ApJ*, **821**, 78
- Schechter, P. L., Mateo, M., & Saha, A. 1993, *PASP*, **105**, 1342
- Skrutskie, M. F., Cutri, R. M., Stiening, R., et al. 2006, *AJ*, **131**, 1163
- Stankov, A., & Handler, G. 2005, *ApJS*, **158**, 193
- Terrell, D., & Wilson, R. E. 2005, *Ap&SS*, **296**, 221
- Ulusoy, C., Gulmez, T., Stateva, I., et al. 2013, *MNRAS*, **428**, 3551
- Wolf, C., Onken, C. A., Luvaul, L. C., et al. 2018, *PASA*, **35**, E010
- Wright, E. L., Eisenhardt, P. R. M., Mainzer, A. K., et al. 2010, *AJ*, **140**, 1868
- Zari, E., Rix, H.-W., Frankel, N., et al. 2021, *A&A*, **650**, A112
- Ziaali, E., Bedding, T. R., Murphy, S. J., Van Reeth, T., & Hey, D. R. 2019, *MNRAS*, **486**, 4348



Eclipsing Binaries Found by the EREBOS Project: Gaia DR2 6097540197980557440—a Deeply Eclipsing sdB+dM System

Kyle A. Corcoran¹, Brad N. Barlow², Veronika Schaffenroth³, Uli Heber⁴, Stephen Walser⁵, and Andreas Irgang⁴

¹University of Virginia, Department of Astronomy, 530 McCormick Rd., Charlottesville, VA 22904, USA; kac8aj@virginia.edu

²High Point University, Department of Physics, One University Parkway, High Point, NC 27268, USA

³Universität Potsdam, Institut für Physik und Astronomie, Haus 28, Karl-Liebknecht-Str. 24/25, D-14476, Potsdam-Golm, Germany

⁴Dr. Karl Remeis-Observatory & ECAP, Astronomical Institute, Friedrich-Alexander University Erlangen-Nuremberg (FAU), Sternwartstr. 7, D-96049 Bamberg, Germany

⁵Virginia Tech, Department of Physics, 850 West Campus Drive, Blacksburg, VA 24061, USA

Received 2021 January 18; revised 2021 June 10; accepted 2021 June 11; published 2021 September 1

Abstract

We present time-series spectroscopy and photometry of Gaia DR2 6097540197980557440, a new deeply eclipsing hot subdwarf B (sdB) + M dwarf (dM) binary. We discovered this object during the course of the Eclipsing Reflection Effect Binaries from Optical Surveys (EREBOS) project, which aims to find new eclipsing sdB+dM binaries (HW Vir systems) and increase the small sample of studied systems. In addition to the primary eclipse, which is in excess of ~ 5 mag in the optical, the light curve also shows features typical for other HW Vir binaries such as a secondary eclipse and strong reflection effect from the irradiated, cool companion. The orbital period is 0.127037 days (~ 3 hr), falling right at the peak of the orbital period distribution of known HW Vir systems. Analysis of our time-series spectroscopy yields a radial velocity semi-amplitude of $K_{\text{sdB}} = 100.0 \pm 2.0 \text{ km s}^{-1}$, which is among the fastest line-of-sight velocities found to date for an HW Vir binary. State-of-the-art atmospheric models that account for deviations from local thermodynamic equilibrium are used to determine the atmospheric parameters of the sdB. Although we cannot claim a unique light-curve modeling solution, the best-fitting model has an sdB mass of $M_{\text{sdB}} = 0.47 \pm 0.03 M_{\odot}$ and a companion mass of $M_{\text{dM}} = 0.18 \pm 0.01 M_{\odot}$. The radius of the companion appears to be inflated relative to theoretical mass–radius relationships, consistent with other known HW Vir binaries. Additionally, the M dwarf is one of the most massive found to date among this type of binary.

Unified Astronomy Thesaurus concepts: [Eclipsing binary stars \(444\)](#); [Fundamental parameters of stars \(555\)](#); [B subdwarf stars \(129\)](#)

1. Introduction

Most hot subdwarfs are core He-burning extreme horizontal branch stars that formed from red giant progenitors that experienced mass loss near the tip of the giant branch, due to binary interactions (see Heber 2016, for a detailed review). With temperatures from 20,000 to 45,000 K and spectra dominated by broad H Balmer lines, they are classified as either sdB stars or sDOB stars if they display the He II 4686 Å line. They show a tight mass distribution peaking near $0.47 M_{\odot}$ (the “canonical” mass) and have radii around $0.2 R_{\odot}$. Theoretical models such as those in Han et al. (2002, 2003) describe sdB formation scenarios that account for the mass loss in these systems, with three possible formation channels depending on the initial configuration and mass ratio of the binary. One formation channel produces an sdB via Roche lobe overflow to a main-sequence companion of K type and earlier. The binaries that form in this way are typically wide binaries ($P = 10\text{--}1500$ days). These systems are often called “composite” binaries, as both stars are seen in the spectrum and account for 30%–40% of all sdBs (for an overview see Vos et al. 2019). The rest of the sdBs do not show any signs of a companion in their spectra. Maxted et al. (2001) showed that a high fraction of those sdBs do exist in short-period binaries, leading to radial velocity (RV) variations. Those can be formed by common envelope (CE) evolution, which produces close binaries with periods as short as ~ 1.5 hr with a hot subdwarf primary and a cool, low-mass companion. In this scenario, an evolving red giant and a companion object enter a CE, and the angular momentum resonant in the orbit of the binary is

deposited into the envelope, ejecting it from the system. Typically, this companion is stellar in nature; however, Soker (1998) proposed that substellar and even planetary-mass companions could be sufficient to provide the orbital angular momentum necessary to eject the envelope (e.g., Schaffenroth et al. 2015). The remaining sdBs do not show any RV variations and hence appear single. Such single sdBs could be formed by the merger of two He white dwarfs (WDs). Another possibility is that a substellar companion was responsible for the mass loss, which was destroyed during the CE phase.

The main challenge in studying close sdB binaries and their properties comes from the single-lined nature of these systems, allowing only for mass limits inferred based on the proposed inclination; however, some systems benefit from the presence of an eclipse, which helps to constrain the inclination and allows for more precise mass measurements. These so-called HW Vir systems also show photometric variation due to the reflection effect and have orbital periods of $P < 1$ day, making them vital tools for sdB studies owing to the relative ease in identifying them. The prototypical HW Vir is an sdB and M dwarf (dM) binary. A few systems containing a brown dwarf (BD) have also been discovered (e.g., Schaffenroth et al. 2014a).

The Eclipsing Reflection Effect Binaries from Optical Surveys (EREBOS) project (Schaffenroth et al. 2019) is an effort to increase the sample of known HW Vir systems and to measure orbital, atmospheric, and fundamental parameters of those binaries. It is especially interested in finding the lower-mass limit of an object able to remove the envelope in a CE

phase and survive this phase in order to investigate the effect that substellar companions have on the late stages of stellar evolution. Moreover, this project aims at studying post-CE systems spanning the entire range of periods and companion masses for these systems. For a better understanding of the poorly understood CE phase, see Ivanova et al. (2013). Until recently, the number of HW Vir binaries with known fundamental parameters was relatively small at 18 total systems. The EREBOS project dramatically increased this number by inspecting light curves from the Optical Gravitational Lensing Experiment (OGLE; Pietrukowicz et al. 2013; Soszyński 2015) and Asteroid Terrestrial-impact Last Alert System (ATLAS; Tonry et al. 2018) surveys, finding over 150 new HW Vir candidates (Schaffenroth et al. 2019). With an extensive spectroscopic and photometric follow-up campaign we will dramatically increase the number of systems with robust solutions.

Despite this unprecedented increase, HW Vir systems still represent only a small fraction of the sdB population. Given the typical radii of both components, these systems have to be relatively edge-on to show any eclipse. For example, the smallest grazing eclipses occur in systems such ASAS 102322–3737 (Schaffenroth et al. 2013), an sdB+dM, at $i = 65^\circ 9'$; however, inclinations do range up to perfectly edge-on systems such as AA Dor (Kilkenny et al. 1978), an sdOB+dM/BD. One HW Vir system, Konkoly J064029.1+385652.2 (Derekas et al. 2015), is an sdO+dM binary that even shows a total eclipse owing to a relatively small ($R = 0.096 R_\odot$) sdO being in a nearly edge-on ($i = 87.11$) orbit with an inflated dM. Total eclipses are sometimes seen in WD+dM binaries such as NN Ser (Parsons et al. 2010), where a high inclination angle allows the dM to completely block the smaller WD along our line of sight. Due to the similarity in size between typical sdBs and dMs, even edge-on systems struggle to achieve geometries sufficient to produce a total eclipse.

Here we present system parameters for the first deeply eclipsing sdB+dM system Gaia DR2 6097540197980557440, which exhibits an eclipse in excess of ~ 5 mag in the optical. We discovered Gaia DR2 6097540197980557440 in the course of the EREBOS project while obtaining follow-up observations of known HW Vir systems using the Goodman spectrograph (Clemens et al. 2004) on the 4.1 m Southern Astrophysical Research (SOAR). In Section 2 we describe the initial observations leading to its discovery. In Section 3 we present time-series spectroscopic observations, as well as the radial velocities and atmospheric parameters derived from them. In Section 4 we present multicolor, time-series photometric observations and the details of our light-curve modeling solution. Section 5 presents system parameters derived from the best-fitting light-curve modeling solution. In Section 6 we discuss how the system compares to the EREBOS sample, as well as potential follow-up studies. Finally, we summarize our work in Section 7.

2. Discovery Run

During a small amount of downtime between SOAR/Goodman observations of EREBOS targets on 2019 June 9, we discovered Gaia DR2 6097540197980557440 with approximately 45 minutes of time-series photometry using a Johnson *V* filter. We had previously identified Gaia DR2 6097540197980557440 as a strong candidate variable hot subdwarf from its anomalously high Gaia DR2 photometric uncertainty and its inclusion in the Geier et al. (2019) catalog of candidate hot subdwarf stars (for details see Barlow et al., in preparation; Guidry et al. 2021). We unwittingly

began observing just before primary eclipse and, upon noticing the star disappear from the raw image frames⁶ (shown in Figure 1), continued observing long enough to safely capture egress. Using the processes described in Section 4.1, we constructed a light curve and determined that the primary eclipse lasted approximately 25 minutes. The shape of the eclipse stuck out to us immediately as being different than in other HW Vir binaries. Whereas the ingress and egress segments of most primary eclipses have *positive* second time derivatives (i.e., concave up), Gaia DR2 6097540197980557440's second derivatives are *negative* during ingress and egress (i.e., concave down). This can only be explained by the geometry of a nearly perfectly edge-on eclipse, so we were eager to obtain photometry and spectroscopy over the full orbit to solve for all system parameters.

Unfortunately, we were unable to determine a precise orbital period for the system using our exploratory time-series photometry. However, Gaia DR2 6097540197980557440 was also observed by TESS in Sector 11 through full-frame image (FFI), 30-minute-cadence observations. The data⁷ were downloaded from the Mikulski Archive for Space Telescopes (MAST) web portal, and the `lightkurve` (Lightkurve Collaboration et al. 2018) Python package was used to extract time-series photometry from the FFIs. A Lomb–Scargle periodogram (Scargle 1982) was computed and yielded an initial estimate of the system's orbital period of $P = 3.0614$ hr. This estimate helped guide subsequent observations.

3. Time-series Spectroscopy

3.1. Observations and Reductions

We obtained 53 spectra using SOAR/Goodman on 2019 July 25 and 46 spectra on 2020 February 17, both in an uninterrupted series of back-to-back exposures. Each of these data sets covered roughly 75% of the ~ 3 hr orbital period. We used the 0''8-long slit, 2×2 binning, and the 930 mm^{-1} volume phase holographic grating (0.84 Å per binned pixel dispersion), giving us average spectral resolutions of 2.38 and 2.04 Å over the wavelength range 3600–5300 Å for the 2019 and 2020 data, respectively. We note that the spectral resolutions are different despite using the same instrumental configuration owing to the camera–collimator focus values not being set to their optimal values during the 2019 observations. On both observing nights, we aligned the slit axis to a position angle of $278^\circ 3'$ E of N in order to place a bright star⁸ $23''.5$ away on the slit and monitor any drifts in the wavelength solution due to instrumental flexure. Individual spectra in each series were integrated for 120 s, yielding an average signal-to-noise ratio (S/N) of ~ 30 per resolution element. We also obtained spectra of FeAr lamps immediately following each series for wavelength calibration purposes.

Reduction of the frames was carried out using the `ccdproc` task in IRAF (Tody 1986, 1993). After bias-subtracting and flat-fielding all spectral images, we ran the `apall` task to extract a one-dimensional spectrum for each frame and remove a fit to the sky background. For the 2020 data, a wavelength solution was generated from the FeAr lamp spectra and applied to all individual spectra. We note that slow drifts in the

⁶ At this moment, Stephen Walser, who was monitoring the frames as they came in, apologetically informed us he had “lost our star.”

⁷ Using the same data, Sahoo et al. (2020) concurrently found this object to be an eclipsing binary.

⁸ Gaia DR2 6097528446950034944.

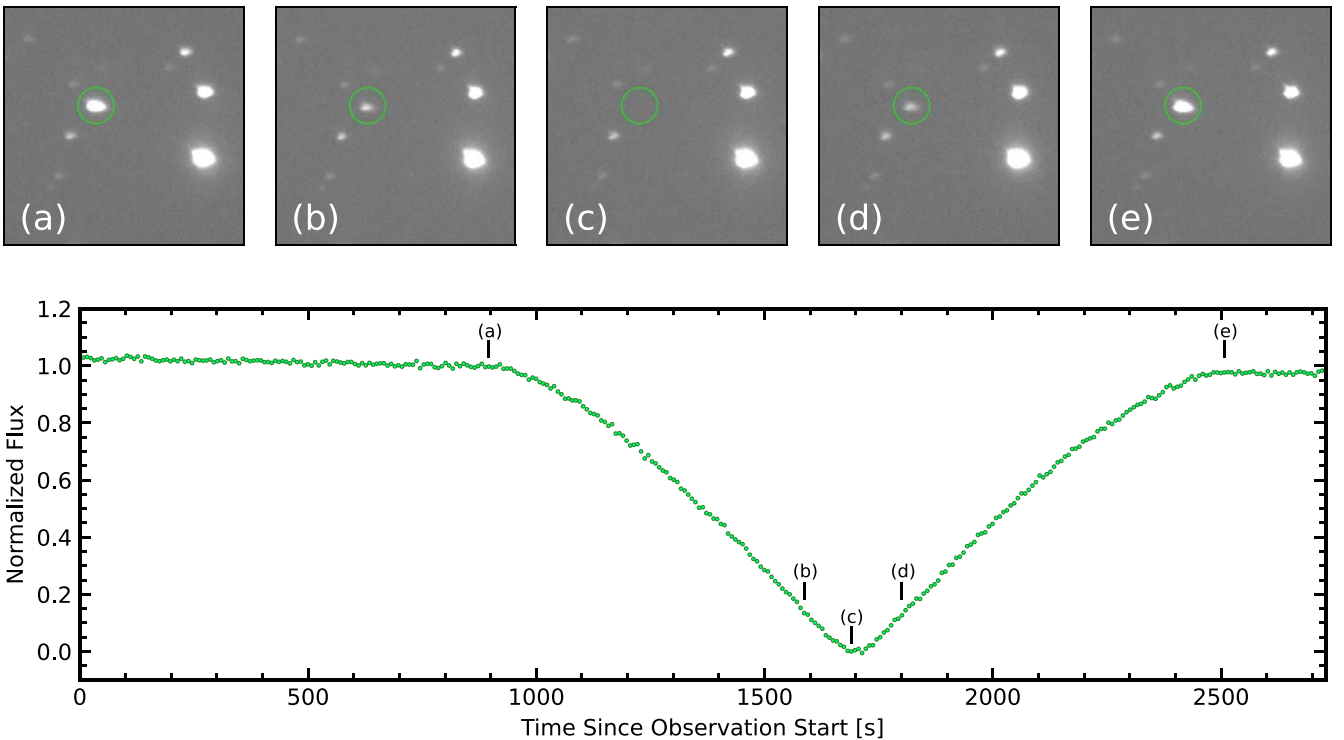


Figure 1. Discovery data for Gaia DR2 6097540197980557440 from SOAR/Goodman. Top: raw Johnson V filter frames from the discovery data set obtained on 2019 June 9. We highlight five select frames corresponding to the marked locations on the light curve in the bottom panel. These frames represent phases (a) just prior to ingress, (b) shortly before the systems drops below detection limits, (c) during primary eclipse totality, (d) shortly after the system returns above detection limits, and (e) just after egress. Bottom: the corresponding light curve of Gaia DR2 6097540197980557440 in the Johnson V filter.

wavelength solution over the course of the series are expected owing to instrumental flexure, and thus the FeAr wavelength solution does not provide an accurate zero-point—only an accurate dispersion solution. For the 2019 data, an intermittent issue with the FeAr lamp prevented us from obtaining an accurate dispersion solution with it. Instead, we created a self-template from the combined 2019 spectra and used the Balmer and He I lines to determine the wavelength solution. Once again, this only provides a dispersion solution and not an absolute RV zero-point. Consequently, we are unable to report on the binary’s systemic velocity. The spectrum of Gaia DR2 6097540197980557440, shown in Figure 3, is dominated by strong H Balmer absorption features and weaker He I lines (4026, 4471, 4921, 5015 Å). The absence of the He II 4686 Å line rules out an sdOB classification.

3.2. Radial Velocity Curve

RV shifts were determined from nonlinear, least-squares fits of Gaussian profiles to the sdB H Balmer lines, which were carried out using the `curve_fit` function in the Python package `scipy` (Virtanen et al. 2020). The He I profiles were too noisy in individual spectra for this purpose. In order to correct for drifts in the wavelength solution (and thus drifts in the RVs) due to instrumental flexure during the observations, we also measured the relative velocity shifts of the absorption features of the second star on the slit. This object displayed spectral features consistent with a G/K-type star, and so we used the `crosscorrRV` function in the `PyAstronomy` library (Czesla et al. 2019) to measure velocity shifts via cross-correlation. The second star’s RV curves revealed gradual,

nearly linear shifts on the order of $\sim 75 \text{ km s}^{-1}$ over $\sim 2 \text{ hr}$, in both the 2019 and 2020 data sets. The magnitude and pattern of these shifts—slightly different on the two nights—were consistent with expectations given the target’s R.A., decl., average hour angle during each run, and associated Nasmyth cage rotations. We are confident that they are due to instrumental flexure and not intrinsic RV variations of the second star on the slit. To remove this flexure drift from the target RV curves, we fitted low-order polynomials to the comparison star’s RV curves and subtracted this fit from the raw target star RV curves. The resulting RV curves are shown in Figure 2.

In order to determine the RV semiamplitude of the sdB (K_{sdB}), we fitted sine waves to each of the data sets separately, with the orbital period and phase fixed to the values described in Section 4.2. From the 2019 July 25 data, we find $K_{\text{sdB}} = 97.9 \pm 2.6 \text{ km s}^{-1}$, and from the 2020 February 17 data, we derive $K_{\text{sdB}} = 102.1 \pm 3.0 \text{ km s}^{-1}$. These results agree within their 1σ uncertainties, and we adopt as our final RV semiamplitude their weighted average: $K_{\text{sdB}} = 100.0 \pm 2.0 \text{ km s}^{-1}$. The residuals in the bottom panels of Figure 2 are consistent with random noise and show that the data are consistent with a circular orbit, as expected for post-CE HW Vir binaries.

3.3. Atmospheric Parameters

For use in the spectroscopic analysis, model spectra are computed following the so-called hybrid approach (Przybilla et al. 2006a, 2006b; Nieva & Przybilla 2008). In this approach, deviations from local thermodynamic equilibrium (LTE) can be treated very efficiently using a combination of updated versions

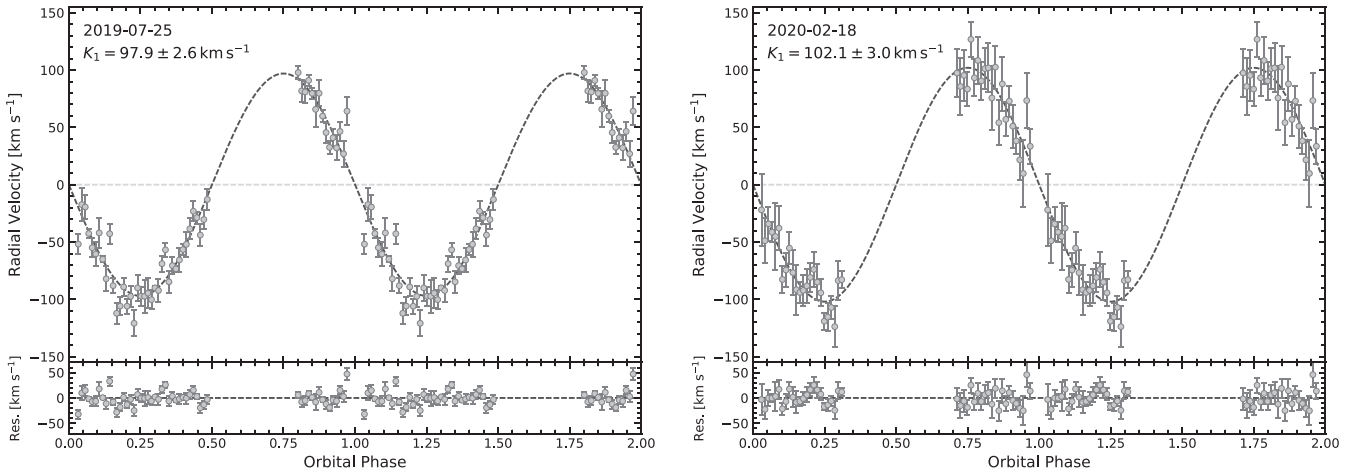


Figure 2. RV curves constructed from spectra obtained with SOAR/Goodman, plotted twice for better visualization. Left: best-fitting model for the data taken in 2019. Right: best-fitting model for the data taken in 2020. Both of these solutions agree within the error bars with the weighted average $K_{\text{sdb}} = 100.0 \pm 2.0 \text{ km s}^{-1}$.

of the ATLAS12 (Kurucz 1996), DETAIL (Giddings 1981; Butler & Giddings 1985), and SURFACE (Giddings 1981; Butler & Giddings 1985) codes. The ATLAS12 code, for which the mean metallicity for hot sdB according to Naslim et al. (2013) is used here, is initially used to compute the temperature/density structure of a line-blanketed, plane-parallel, and chemically homogeneous atmosphere in hydrostatic and radiative equilibrium. This LTE atmosphere is then used as input for the DETAIL code, which solves the coupled radiative transfer and statistical equilibrium equations to obtain occupation numbers in non-LTE (NLTE) for hydrogen and helium. Finally, the SURFACE code is used to compute the final synthetic spectrum using the atmosphere from ATLAS12 and the occupation numbers from DETAIL, as well as more sophisticated line-broadening data. Also taken into consideration are the recent improvements to all three codes (Irrgang et al. 2018) concerning NLTE effects on the atmospheric structure, the implementation of the occupation probability formalism (Hubeny et al. 1994) for hydrogen and neutral helium, and new Stark broadening tables for hydrogen (Tremblay & Bergeron 2009) and neutral helium (Beauchamp et al. 1997). The application of these models to sdBs is also shown in Schaffenroth et al. (2021).

The observed spectra are matched to the model grid by χ^2 minimization as described by Saffer et al. (1994) as implemented by Napiwotzki et al. (1999). We use six H Balmer lines and four He I lines. H ϵ is excluded because of contamination by interstellar Ca II. Since the binary orbit is so tight, tidal forces probably have spun up the sdB star, which causes extra line broadening. However, the resolution of the spectra is insufficient to measure the projected rotational velocity $v \sin i$. We assume that the rotation of the sdB is tidally locked to the binary orbit and convolve the model spectrum with a rotational broadening profile with a corresponding $v \sin i = 87 \text{ km s}^{-1}$ in the fitting procedure.

Previous studies have shown that some sdBs with reflection effects have atmospheric parameters that can vary with phase when analyzing spectra of sufficiently high S/N taken at different phases of the orbit (e.g., Schaffenroth et al. 2013, 2014b). These variations can be explained by the companion’s phase-variable contributions to the spectrum from only the reflection effect, causing apparent variations of order 1000–1500 K and 0.1 dex in the sdB temperature and surface gravity, respectively.

To account for any of these variations, we derived the atmospheric parameters from the single-RV-corrected spectra. Exemplary fits are shown for individual spectra from the 2019 and 2020 observing runs for similar orbital phases in Figure 3. Results from both observing runs are consistent. The variations of the atmospheric parameters, which are consistent with previous determinations, can be seen in Figure 4. The effective temperature appears to increase slightly near the secondary eclipse. Any variations in the surface gravity or helium abundance remain below detection limits. In order to determine the atmospheric parameters of the sdB, we averaged the parameters near the primary eclipse, where only the dark side of the companion is visible: $T_{\text{eff}} = 26100 \pm 400 \text{ K}$, $\log(g) = 5.50 \pm 0.07$, and $\log(y) = -2.32 \pm 0.10$.

4. Time-series Photometry

4.1. Observations and Reductions

Follow-up time-series photometry was obtained on 2020 February 18 using SOAR/Goodman in imaging mode. In an effort to obtain multicolor photometry for more precise modeling, the filter wheel was manually switched between the Johnson *B* and *R* filters every few minutes when not in primary or secondary eclipse, and every 30 s during eclipses. The integration time was fixed to 5 s for both filters in order to minimize dead time and errors associated with changing this value back and forth every few minutes. We used 2×2 binning and read out only a 350×175 binned pixel subset of the image to minimize the readout time between exposures. This relatively small field still provided several nearby comparison stars through which to track sky transparency variations. We achieved a duty cycle of roughly 54% over the course of our observations, which covered a little more than one full orbital period. A more efficient duty cycle would have required either decreasing the subframe region further and sacrificing comparison stars or increasing the exposure time and risk saturating the target and comparison stars.

Reduction of the SOAR frames was once again carried out using the `ccdproc` procedure in IRAF. Each raw image frame was first bias-subtracted and flat-fielded. We then extracted aperture photometry using a range of aperture sizes with a

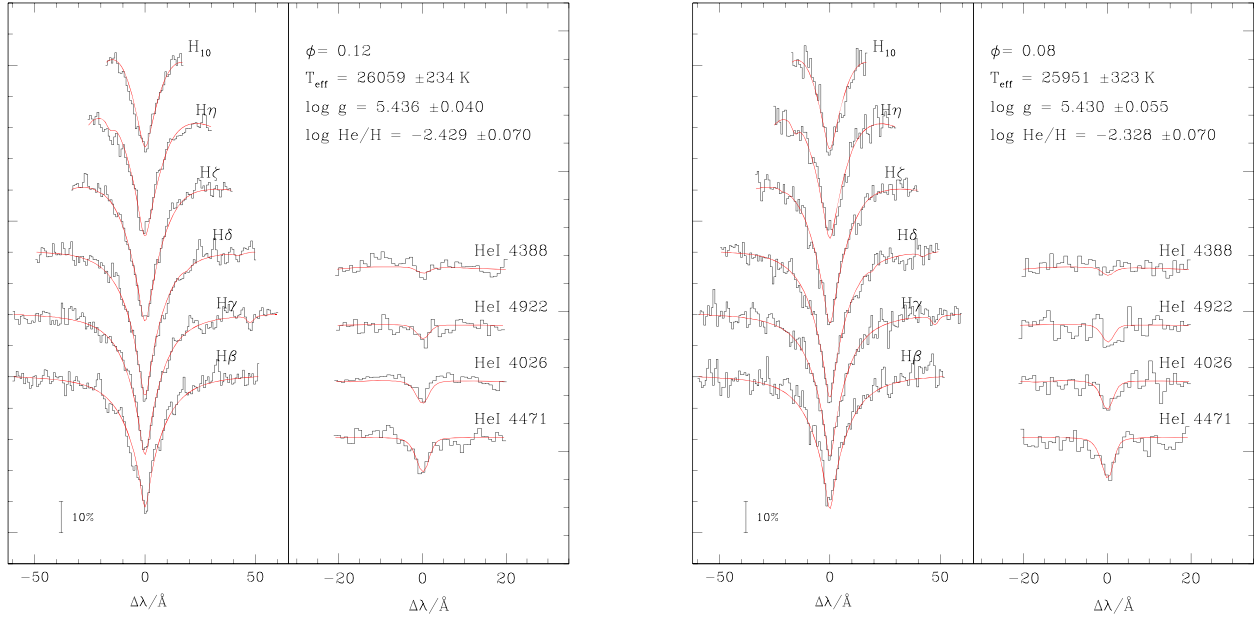


Figure 3. Line fits to the hydrogen Balmer and neutral helium lines in individual SOAR/Goodman spectra from 2019 (left panel) and 2020 (right panel). Listed in the upper right corner of each panel is the orbital phase and the resulting set of best-fitting atmospheric parameters.

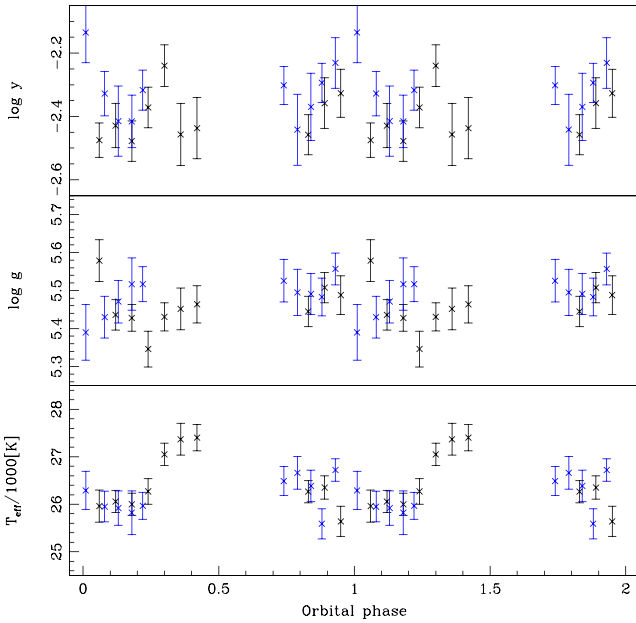


Figure 4. Apparent T_{eff} (bottom), $\log g$ (middle), and $\log y$ (top) variations with 1σ error bars as a function of the orbital phase. Results from spectra taken in 2019 are shown in black, while those from 2020 are shown in blue.

custom code utilizing the `photutils` (Bradley et al. 2019) Python package. Sky counts were removed using sky annuli drawn around the apertures. Apertures were chosen to maximize the S/N in each light curve. This process was repeated on multiple nearby, bright comparison stars to remove sky transparency variations and flux-normalize the light curves. Multiple cycles of observing are typically needed to remove air-mass-related changes in the flux; therefore, any of these slight flux variations were not removed during the reduction process. The resulting differential light curves are shown in Figure 5 and used for modeling the binary.

4.2. Binary Light-curve Modeling

The Gaia DR2 6097540197980557440 light curve exhibits all the typical HW Vir features. The amplitude of the reflection effect is noticeably stronger in the R filter ($\sim 30\%$) than in the B filter ($\sim 20\%$), and it is quite strong in general compared to other reflection effect systems. Initially, this led us to believe that either the sdB was slightly hotter than in typical HW Vir systems or the companion was slightly larger than usual. The deep primary eclipse, implying a nearly edge-on inclination, lent credence to the latter explanation. The shape of the eclipse itself sticks out among other HW Vir binaries. As mentioned in Section 2, the ingress and egress segments of the primary eclipse have negative second derivatives (more V shaped) instead of the more frequently observed positive second derivatives (more U shaped). This implies that the eclipse geometry is nearly perfectly edge-on and that the companion might be slightly larger than the primary. Secondary eclipses are also present in the light curve, during which the sdB is blocking irradiated light from the cool companion. Notably, the flux at the center of the secondary eclipse returns to its exact value immediately preceding and following ingress and egress, respectively, further implying that the inclination must be nearly edge-on.

To model the light curves, we use the code `LCURVE` (for details, see Appendix A in Copperwheat et al. 2010). In addition to recreating deep eclipses, `LCURVE` was designed for binaries with WDs and has been used to fit WD+dM systems exhibiting the reflection effect (e.g., Parsons et al. 2010); therefore, HW Vir binaries are naturally suited to be modeled in a similar fashion (see Schaffenroth et al. 2021, for an example and further details). To form full solutions for these systems, there are many parameters that are not all independent, so we can greatly improve our ability to constrain each solution by fixing as many parameters as possible. We fixed the sdB temperature to the value determined in our spectroscopic fit (described in Section 3.3). We also fix the gravitational limb-darkening coefficients to values expected of a primary with a

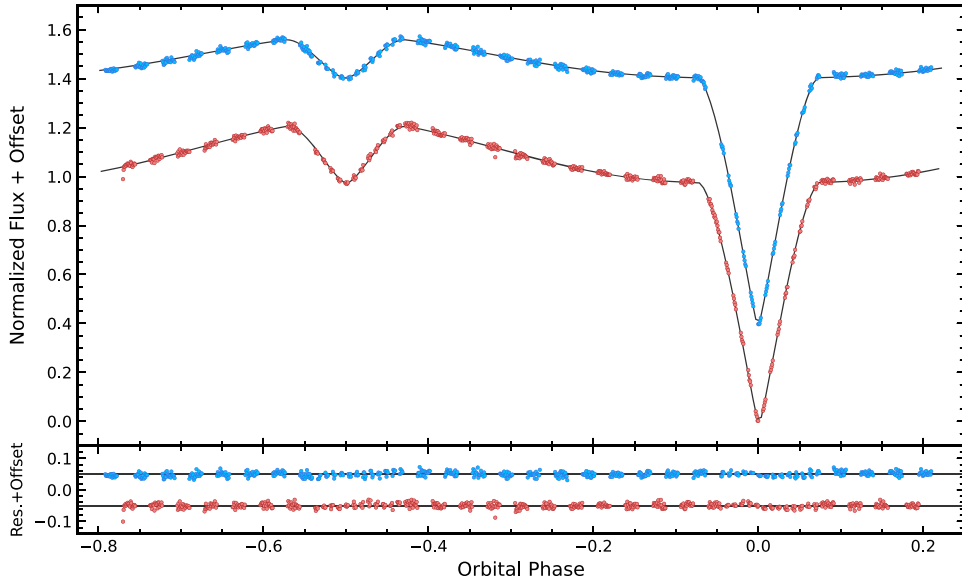


Figure 5. SOAR/Goodman light curves of Gaia DR2 6097540197980557440 in both the Johnson *B* (blue points) and *R* (red points) filters, along with their respective best-fitting models from Section 4.2. The *B*-filter light curve is offset by 0.4 for better visualization. Residuals are shown in the bottom panel with offsets of 0.05 and -0.05 for the *B* and *R* curves, respectively.

radiative atmosphere (von Zeipel 1924) and a companion with a convective atmosphere (Lucy 1967) by calculating the resulting intensities using a blackbody approximation. Then, we adopted a quadratic limb-darkening law for the primary using the values in Claret & Bloemen (2011) closest to the parameters derived in our spectroscopic fits.

It is important to note that there is a large degeneracy in the light-curve solutions of HW Vir binaries, even when fixing all of the above parameters. The orbit is certainly almost circular, so each model is not sensitive to the mass ratio (q) of the system. For this reason we calculated different solutions over a range of various, fixed mass ratios. We then use a SIMPLEX algorithm (Press et al. 1992) to vary parameters such as the inclination, both radii, the companion’s temperature, albedo, and limb darkening, and even the period and primary eclipse time to help localize the solutions. Additionally, we allow for linear trends due to air-mass-related changes in flux over the course of the observations.

Next, we tested the degeneracy of each light-curve solution and determined the parameter errors by performing Markov Chain Monte Carlo computations using `emcee` (Foreman-Mackey et al. 2013). We used the best-fit solution from our SIMPLEX algorithm for initial values, and then we again varied the inclination angle, both radii, the limb-darkening coefficient assuming a linear limb-darkening law for the companion, and the companion’s temperature and albedo for the mass ratio of our most probable solution (see Section 5). In all cases, the temperature of the companion is not well constrained, as its fractional luminosity contribution to the system—outside of the reflection effect—is negligible. We therefore constrained the companion’s temperature to the range 2500–3500 K (the expected range for the low-mass companion). The results and errors from our `emcee` run (shown in Table 1) then form the basis for our most probable solution.

4.3. Orbital Ephemeris

To aid in future observations of Gaia DR2 6097540197980557440, we have listed its orbital ephemeris (T_0 , P) in Table 2. We adopt the orbital period from our best-fit `emcee` solution in Section 4.2. To construct an initial eclipse time (T_0), we fit inverted Gaussian profiles to both the *B* and *R* time-series data using `curve_fit`. We then adopt the weighted average of the central times from both filter series as our T_0 value.

5. System Parameters

In Figure 6, we plot the surface gravity and sdB mass for each of the potential solutions, and we compare the photometric surface gravities to our spectroscopically derived surface gravity.

Based on the spectroscopic surface gravity, we get a consistent solution for an sdB mass of $0.3\text{--}0.64 M_\odot$. All possible solutions fit the light-curve data nearly equally well; thus, we cannot claim a unique solution without additional data (e.g., velocity measurements from the dM). The most probable solution is the one with an sdB mass consistent with the canonical mass of $0.47 M_\odot$. The adopted best-fitting light-curve solution and all relevant parameters are given in Table 1, and both of these best-fit models are shown together with their respective observations and residuals in Figure 5. All possible solutions are given in Table 3 of the Appendix.

We compute the binary mass function for Gaia DR2 6097540197980557440 using the expression

$$f = \frac{K_{\text{sdb}}^3 P}{2\pi G} = \frac{M_{\text{sdb}} q^3 \sin^3 i}{(1 + q)^2}, \quad (1)$$

finding $f = 0.0132 \pm 0.0008 M_\odot$ using the period and sdB velocity semi-amplitude. Combining this with the adopted mass ratio derived before, we find the sdB and dM masses to be $M_{\text{sdb}} = 0.47 \pm 0.03 M_\odot$ and $M_{\text{dM}} = 0.18 \pm 0.01 M_\odot$, respectively.

Table 1
Parameters Used to Model the Light Curve for Both the SOAR/Goodman *B* and *R* Data

Parameter	SOAR/Goodman— <i>B</i>	SOAR/Goodman— <i>R</i>	Unit	Description
Fixed Parameters				
q ($M_{\text{dM}}/M_{\text{sdB}}$)	0.375	0.375		Mass ratio
P	0.127037	0.127037	days	Orbital period
T_{sdB}	26100	26100	K	Primary temperature from spectroscopy
g_1	0.25	0.25		Gravitational darkening exponent
g_2	0.08	0.08		Gravitational darkening exponent
$x_{1,a}$	0.097	0.070		Primary linear limb-darkening coefficient
$x_{1,b}$	0.285	0.222		Primary quadratic limb-darkening coefficient
Adjusted Parameters				
i	$90^{+0.0}_{-0.3}$	$90^{+0.0}_{-0.4}$	deg	Inclination angle
$x_{2,a}$	0.2992	0.2734		Companion linear limb-darkening coefficient
R_{sdB}/a	0.2180 ± 0.0007	0.2174 ± 0.0007		Primary radius
R_{dM}/a	0.2402 ± 0.0006	0.2407 ± 0.0006		Companion radius
T_{dM}	2800 ± 500	3100 ± 500	K	Companion temperature
A_2	1.14 ± 0.01	1.4 ± 0.01		Companion albedo (absorb)
m	0.00026 ± 0.00001	0.00026 ± 0.00001		Slope

Table 2

Overview of Derived Parameters for Gaia DR2 6097540197980557440 That Represent the Most Probable Solution from the Set of Potential Solutions

Parameter	Value	Unit
Basic Information		
$\alpha^{a,b}$	213.577775581303	deg
$\delta^{a,b}$	-43.552249057309	deg
G^a	16.358994	mag
$G_{\text{bp}} - G_{\text{rp}}^a$	-0.27529526	mag
System Properties		
T_0	$2,458,898.85724 \pm 0.00003$	BJD
P	0.127037 ± 0.000001	days
i	$90^{+0.0}_{-0.3}$	deg
q	0.375 ± 0.003	
a	0.921 ± 0.018	R_{\odot}
sdB Properties		
M_{sdB}	0.47 ± 0.03	M_{\odot}
R_{sdB}	0.199 ± 0.004	R_{\odot}
T_{eff}	$26,100 \pm 400$	K
$\log(g)$	5.50 ± 0.07	
$\log(y)$	-2.32 ± 0.10	
K_{sdB}	100.0 ± 2.0	km s^{-1}
dM Properties		
M_{dM}	0.177 ± 0.010	M_{\odot}
R_{dM}	0.222 ± 0.004	R_{\odot}
T_{eff}	3000 ± 500	K

Notes.

^a From Gaia DR2 (Gaia Collaboration et al. 2018).

^b Epoch J2015.5.

Using Kepler’s third law, we then find the orbital separation to be $a = 0.921 \pm 0.018 R_{\odot}$. We also find $R_{\text{sdB}} = 0.199 \pm 0.004 R_{\odot}$ and $R_{\text{dM}} = 0.222 \pm 0.004 R_{\odot}$. Table 2 gives an overview of the adopted parameters for Gaia DR2 6097540197980557440.

In Figure 7, we show each set of parameters for the companion and the theoretical mass–radius relations for low-mass

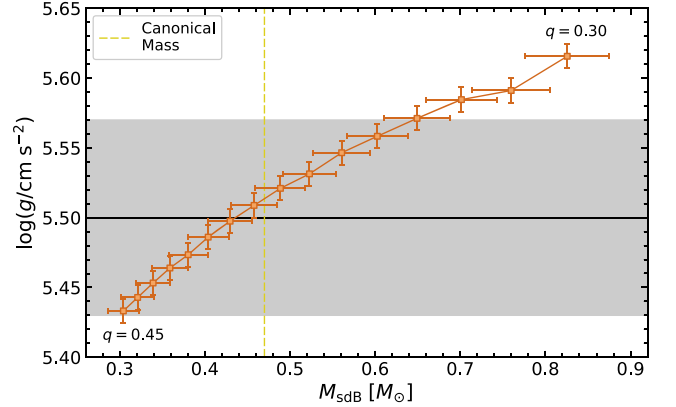


Figure 6. Photometric surface gravities plotted against their respective sdB masses for different mass ratio solutions ranging from $q = 0.3$ to 0.45 , in 0.01 increments. The solid horizontal line (black) and shaded area represent the spectroscopically derived $\log(g)$ and associated 1σ error, respectively. The vertical dashed line (yellow) represents the canonical sdB mass of $0.47 M_{\odot}$. The intersection of these two lines shows that our most probable solution is the one with an sdB mass just below the canonical mass.

main-sequence stars from Baraffe et al. (2015) as an additional check. It is clear that each solution yields a companion radius that is inflated relative to what is predicted by theory, which is a trend commonly seen in close binaries with M dwarf components (Parsons et al. 2018). For our most probable solution we get a companion inflation of about $\sim 13\%$.

6. Discussion

Our analysis of Gaia DR2 6097540197980557440 represents the first EREBOS case study following the Schaffenroth et al. (2019) report of newly discovered sdB+dM systems. With each additional system that is solved, EREBOS comes one step closer to achieving one of its goals to make statistical statements about a homogeneously selected population of close sdB systems. While one new system by itself might not push the boundaries of key parameters in these studies, each system provides self-consistent feedback about the methodology used

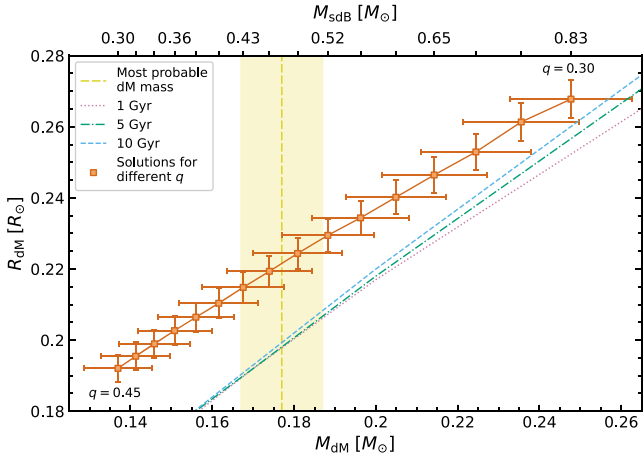


Figure 7. Mass–radius diagram for the dM companion illustrating the degeneracy in model solutions (orange squares). Theoretical mass–radius relations of low-mass stars (Baraffe et al. 2015) for 1 Gyr (dashed blue line), 5 Gyr (dashed–dotted green line), and 10 Gyr (dotted pink line) are also included. The vertical yellow line and shaded region represent the most probable dM mass and 1σ error, respectively, associated with the adopted $0.47 M_{\odot}$ sdB solution.

to study the overall population. It is only through these self-consistent measures that EREBOS can eventually make statements regarding the effects stellar and substellar companions have on the late stages of stellar evolution.

Our light-curve and atmospheric modeling solutions imply that Gaia DR2 6097540197980557440 is a fairly typical sdB+dM system, aside from the chance alignment of its orbital plane nearly perfectly along our line of sight. The peak of the EREBOS orbital period distribution for both new and previously published systems from Schaffenroth et al. (2019) is at $P = 0.1$ days, meaning that Gaia DR2 6097540197980557440 falls at the typical period for HW Vir systems. The most probable solution is an sdB with a mass of the canonical mass $M_{\text{sdb}} = 0.47 \pm 0.03 M_{\odot}$. Additionally, our derived $\log(g)$ and $\log(y)$ values are also fairly typical of sDBs in HW Vir systems, but it is worth noting that our T_{eff} value is slightly lower than is typically found (for comparison, see Figure 6 in Schaffenroth et al. 2019).

There are also noteworthy aspects of the system that are somewhat atypical among HW Vir systems, namely, the derived companion mass and sdB velocity semiamplitude. The companion mass is tied for the most massive in an HW Vir binary, along with that of Konkoly J064029.1+385652.2—also a deeply eclipsing HW Vir–type (sdO+dM) binary. Gaia DR2 6097540197980557440 has an orbital period that is ~ 1.5 hr shorter than Konkoly J064029.1+385652.2 and will one day evolve into a more rapid analog of Konkoly J064029.1+385652.2 when the sdB evolves into an sdO after the He in the core is exhausted and then, inevitably, into a WD. The sdB semiamplitude we derive from the two sets of RV data makes Gaia DR2 6097540197980557440 the fastest line-of-sight sdB velocity semiamplitude reported to date for an HW Vir binary.

The most striking aspect of Gaia DR2 6097540197980557440 is the total eclipse of the sdB by its companion. Due to this system being relatively bright ($G \sim 16.4$ mag), a large eclipse depth means future eclipse timing ($O - C$) analyses to search for changes in the orbital period (\dot{P}), and even Rømer delay studies should be possible using telescopes with a variety of

aperture sizes (e.g., Barlow et al. 2012). Additionally, Gaia DR2 6097540197980557440 will be observed at 2-minute cadence in Sector 38 of TESS Cycle 3 through the Guest Investigator program (proposal #G03221), providing space-quality data spanning 27 days of observations. This is a unique opportunity to explore a relatively novel parameter space with one of the most accurate astrophysical clocks known (e.g., Kilkenny 2014).

7. Summary

We have presented photometric and spectroscopic observations of Gaia DR2 6097540197980557440, the first deeply eclipsing sdB+dM binary. Other than the remarkably striking nature of the eclipse, the system is a rather typical sdB+dM system. We find an orbital period of $P = 0.127037$ days and an sdB velocity semiamplitude of $K_{\text{sdb}} = 100.0 \text{ km s}^{-1}$, which, combined with the most probable light-curve solution, yields masses of $M_{\text{sdb}} = 0.47 M_{\odot}$ and $M_{\text{dM}} = 0.18 M_{\odot}$, respectively. This gives a radius of $R_{\text{dM}} = 0.222 R_{\odot}$ for the companion, which is slightly inflated relative to theoretical mass–radius relationships of low-mass main-sequence stars. Gaia DR2 6097540197980557440 represents the first HW Vir solved as part of the EREBOS project. Eventual solutions for the more than 100 new HW Vir binaries uncovered by EREBOS will help improve our understanding of the CE channel leading to sDBs and help determine the effects nearby low-mass stellar and substellar objects can have on stars climbing the giant branch.

K.A.C., B.N.B., and S.W. acknowledge the support of the National Science Foundation under grant AST-1812874. B.B. also acknowledges partial support of this work by NASA through the TESS Guest Investigator program, under grant 80NSSC19K1720. V.S. is supported by the Deutsche Forschungsgemeinschaft (DFG) through grant GE 2506/9-1. A.I. acknowledges funding by the DFG through grant HE1356/70-1.

This research draws on data provided by NOIRLab 2019A-0255 and 2020A-0268; PI B. Barlow as distributed by the NOIRLab Astro Data Archive. NOIRLab is managed by the Association of Universities for Research in Astronomy (AURA) under a cooperative agreement with the National Science Foundation.

Based on observations obtained at the Southern Astrophysical Research (SOAR) telescope, which is a joint project of the Ministério da Ciência, Tecnologia, Inovações e Comunicações (MCTIC) do Brasil, the U.S. National Optical Astronomy Observatory (NOAO), the University of North Carolina at Chapel Hill (UNC), and Michigan State University (MSU).

This paper includes data collected with the TESS mission, obtained from the MAST data archive at the Space Telescope Science Institute (STScI). Funding for the TESS mission is provided by the NASA Explorer Program. STScI is operated by the Association of Universities for Research in Astronomy, Inc., under NASA contract NAS 5-26555.

This research made use of Lightkurve, a Python package for Kepler and TESS data analysis (Lightkurve Collaboration et al. 2018). This research made use of Photutils, an Astropy package for detection and photometry of astronomical sources (Bradley et al. 2019).

Appendix

Shown in Figures 8 and 9 are the corner plots for the SOAR/Goodman *B* and *R* light-curve solutions, respectively, using the Python package `corner` (Foreman-Mackey 2016) for visualization. Also, we give the full set of possible solutions from the light-curve modeling in Table 3.

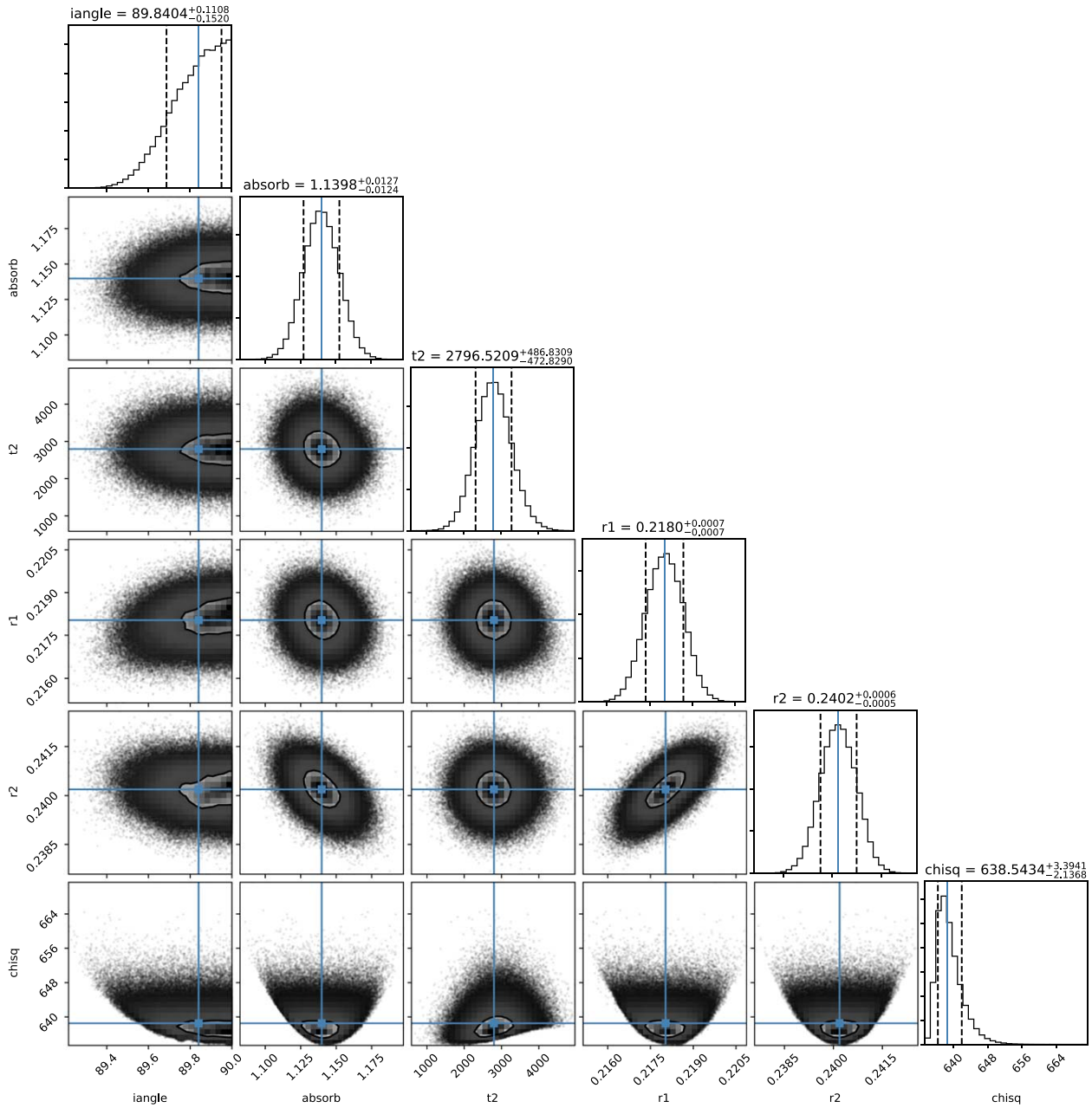


Figure 8. Corner plot of the most probable light-curve solution for the SOAR/Goodman—*B* data.

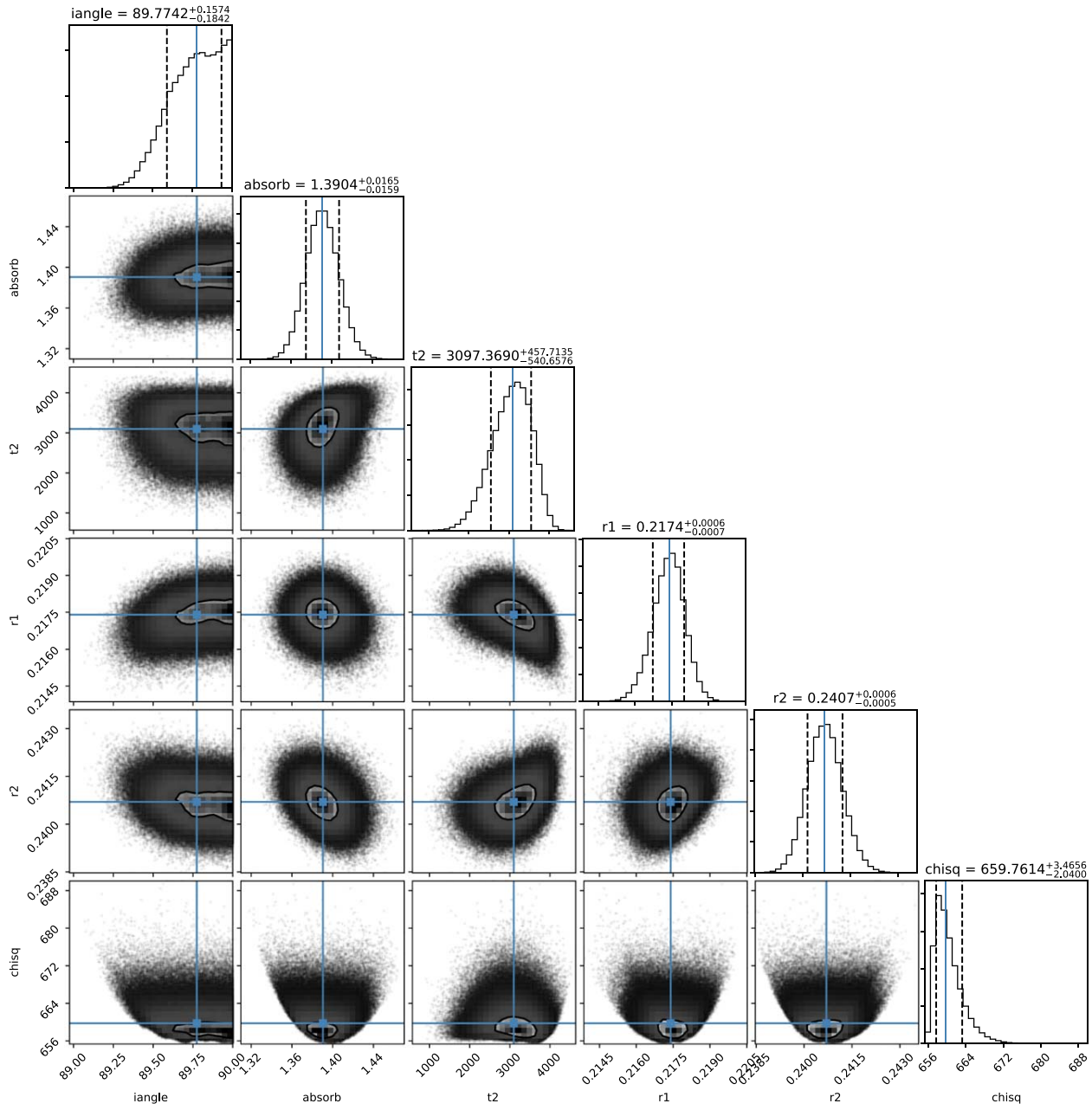


Figure 9. Corner plot of the most probable light-curve solution for the SOAR/Goodman-R data.

Table 3
All of the Possible Light-curve Solutions Output by LCURVE

q	a (R_{\odot})	M_{sdB} (M_{\odot})	M_{dM} (M_{\odot})	R_{sdB} (R_{\odot})	R_{dM} (R_{\odot})	$\log(g)$
0.30	1.090 ± 0.022	0.826 ± 0.050	0.248 ± 0.015	0.234 ± 0.005	0.268 ± 0.005	5.616 ± 0.009
0.31	1.063 ± 0.021	0.760 ± 0.046	0.236 ± 0.014	0.231 ± 0.005	0.261 ± 0.005	5.591 ± 0.009
0.32	1.038 ± 0.021	0.701 ± 0.042	0.224 ± 0.013	0.224 ± 0.004	0.253 ± 0.005	5.585 ± 0.009
0.33	1.014 ± 0.020	0.649 ± 0.039	0.214 ± 0.013	0.219 ± 0.004	0.246 ± 0.005	5.571 ± 0.009
0.34	0.992 ± 0.020	0.603 ± 0.036	0.205 ± 0.012	0.214 ± 0.004	0.240 ± 0.005	5.558 ± 0.009
0.35	0.971 ± 0.019	0.561 ± 0.034	0.196 ± 0.012	0.209 ± 0.004	0.234 ± 0.005	5.547 ± 0.009
0.36	0.951 ± 0.019	0.523 ± 0.031	0.188 ± 0.011	0.205 ± 0.004	0.229 ± 0.005	5.531 ± 0.009
0.37	0.932 ± 0.019	0.489 ± 0.029	0.181 ± 0.011	0.201 ± 0.004	0.224 ± 0.004	5.521 ± 0.009
0.38 ^a	0.914 ± 0.018	0.458 ± 0.027	0.174 ± 0.010	0.197 ± 0.004	0.219 ± 0.004	5.509 ± 0.009
0.39	0.897 ± 0.018	0.430 ± 0.026	0.168 ± 0.010	0.194 ± 0.004	0.215 ± 0.004	5.497 ± 0.009
0.40	0.881 ± 0.018	0.404 ± 0.024	0.162 ± 0.010	0.190 ± 0.004	0.210 ± 0.004	5.486 ± 0.009
0.41	0.865 ± 0.017	0.380 ± 0.023	0.156 ± 0.009	0.187 ± 0.004	0.206 ± 0.004	5.473 ± 0.009
0.42	0.851 ± 0.017	0.359 ± 0.022	0.151 ± 0.009	0.184 ± 0.004	0.203 ± 0.004	5.464 ± 0.009
0.43	0.837 ± 0.017	0.339 ± 0.020	0.146 ± 0.009	0.181 ± 0.004	0.199 ± 0.004	5.453 ± 0.009
0.44	0.824 ± 0.016	0.321 ± 0.019	0.141 ± 0.008	0.178 ± 0.004	0.195 ± 0.004	5.443 ± 0.009
0.45	0.811 ± 0.016	0.304 ± 0.018	0.137 ± 0.008	0.175 ± 0.004	0.192 ± 0.004	5.433 ± 0.009

Note.

^a Most probable solution as outlined in the text.


ORCID iDs

Kyle A. Corcoran  <https://orcid.org/0000-0002-2764-7248>

Brad N. Barlow  <https://orcid.org/0000-0002-8558-4353>

Veronika Schaffenroth  <https://orcid.org/0000-0001-6339-6768>

Uli Heber  <https://orcid.org/0000-0001-7798-6769>

Stephen Walser  <https://orcid.org/0000-0001-8444-2305>

Andreas Irgang  <https://orcid.org/0000-0002-0465-3725>

References

- Baraffe, I., Homeier, D., Allard, F., & Chabrier, G. 2015, *A&A*, **577**, A42
- Barlow, B. N., Wade, R. A., & Liss, S. E. 2012, *ApJ*, **753**, 101
- Beauchamp, A., Wesemael, F., & Bergeron, P. 1997, *ApJS*, **108**, 559
- Bradley, L., Sipőcz, B., Robitaille, T., et al. 2019, *astropy/photutils*: v0.6, Zenodo, doi:[10.5281/zenodo.2533376](https://doi.org/10.5281/zenodo.2533376)
- Butler, K., & Giddings, J. R. 1985, *Newsletter of Analysis of Astronomical Spectra*, No. 9 (London: Univ. College London)
- Claret, A., & Bloemen, S. 2011, *A&A*, **529**, A75
- Clemens, J. C., Crain, J. A., & Anderson, R. 2004, *Proc. SPIE*, **5492**, 331
- Copperwheat, C. M., Marsh, T. R., Dhillon, V. S., et al. 2010, *MNRAS*, **402**, 1824
- Czesla, S., Schröter, S., Schneider, C. P., et al. 2019, *PyA: Python astronomy-related packages*, *Astrophysics Source Code Library*, ascl:[1906.010](https://ascl.net/1906.010)
- Derekas, A., Németh, P., Southworth, J., et al. 2015, *ApJ*, **808**, 179
- Foreman-Mackey, D. 2016, *JOSS*, **1**, 24
- Foreman-Mackey, D., Hogg, D. W., Lang, D., & Goodman, J. 2013, *PASP*, **125**, 306
- Gaia Collaboration, Brown, A. G. A., Vallenari, A., et al. 2018, *A&A*, **616**, A1
- Geier, S., Raddi, R., Gentile Fusillo, N. P., & Marsh, T. R. 2019, *A&A*, **621**, A38
- Giddings, J. R. 1981, PhD thesis, Univ. London
- Guidry, J. A., Vanderbosch, Z. P., Hermes, J. J., et al. 2021, *ApJ*, **912**, 125
- Han, Z., Podsiadlowski, P., Maxted, P. F. L., & Marsh, T. R. 2003, *MNRAS*, **341**, 669
- Han, Z., Podsiadlowski, P., Maxted, P. F. L., Marsh, T. R., & Ivanova, N. 2002, *MNRAS*, **336**, 449
- Heber, U. 2016, *PASP*, **128**, 082001
- Hubeny, I., Hummer, D. G., & Lanz, T. 1994, *A&A*, **282**, 151
- Irgang, A., Kreuzer, S., Heber, U., & Brown, W. 2018, *A&A*, **615**, L5
- Ivanova, N., Justham, S., Chen, X., et al. 2013, *A&ARv*, **21**, 59
- Kilkenny, D. 2014, *MNRAS*, **445**, 4247
- Kilkenny, D., Hilditch, R. W., & Penfold, J. E. 1978, *MNRAS*, **183**, 523
- Kurucz, R. L. 1996, in *Model Atmospheres and Spectrum Synthesis*, ed. S. J. Adelman, F. Kupka, & W. W. Weiss (San Francisco: ASP), 160
- Lightkurve Collaboration, Cardoso, J. V. d. M., Hedges, C., et al. 2018, *Lightkurve: Kepler and TESS time series analysis in Python*, *Astrophysics Source Code Library*, ascl:[1812.013](https://ascl.net/1812.013)
- Lucy, L. B. 1967, *ZAp*, **65**, 89
- Maxted, P. F. L., Heber, U., Marsh, T. R., & North, R. C. 2001, *MNRAS*, **326**, 1391
- Napiwotzki, R., Green, P. J., & Saffer, R. A. 1999, *ApJ*, **517**, 399
- Naslim, N., Jeffery, C. S., Hibbert, A., & Behara, N. T. 2013, *MNRAS*, **434**, 1920
- Nieva, M. F., & Przybilla, N. 2008, *A&A*, **481**, 199
- Parsons, S. G., Gänsicke, B. T., Marsh, T. R., et al. 2018, *MNRAS*, **481**, 1083
- Parsons, S. G., Marsh, T. R., Copperwheat, C. M., et al. 2010, *MNRAS*, **402**, 2591
- Pietrukowicz, P., Mróz, P., Soszyński, I., et al. 2013, *AcA*, **63**, 115
- Press, W. H., Teukolsky, S. A., Vetterling, W. T., & Flannery, B. P. 1992, *Numerical recipes in FORTRAN. The art of scientific computing* (2nd edn.; Cambridge: Cambridge Univ. Press)
- Przybilla, N., Butler, K., Becker, S. R., & Kudritzki, R. P. 2006a, *A&A*, **445**, 1099
- Przybilla, N., Nieva, M. F., & Edelman, H. 2006b, *BaltA*, **15**, 107
- Saffer, R. A., Bergeron, P., Koester, D., & Liebert, J. 1994, *ApJ*, **432**, 351
- Sahoo, S. K., Baran, A. S., Sanjayana, S., & Ostrowski, J. 2020, *MNRAS*, **499**, 5508
- Scargle, J. D. 1982, *ApJ*, **263**, 835
- Schaffenroth, V., Barlow, B. N., Drechsel, H., & Dunlap, B. H. 2015, *A&A*, **576**, A123
- Schaffenroth, V., Barlow, B. N., Geier, S., et al. 2019, *A&A*, **630**, A80
- Schaffenroth, V., Casewell, S. L., Schneider, D., et al. 2021, *MNRAS*, **501**, 3847
- Schaffenroth, V., Classen, L., Nagel, K., et al. 2014a, *A&A*, **570**, A70
- Schaffenroth, V., Geier, S., Drechsel, H., et al. 2013, *A&A*, **553**, A18
- Schaffenroth, V., Geier, S., Heber, U., et al. 2014b, *A&A*, **564**, A98
- Soker, N. 1998, *AJ*, **116**, 1308
- Soszyński, I., Stępień, K., Pilecki, B., et al. 2015, *AcA*, **65**, 39
- Tody, D. 1986, *Proc. SPIE*, **627**, 733
- Tody, D. 1993, in *ASP Conf. Ser. 52, Astronomical Data Analysis Software and Systems II*, ed. R. J. Hanisch, R. J. V. Brissenden, & J. Barnes (San Francisco, CA: ASP), 173
- Tonry, J. L., Denneau, L., Heinze, A. N., et al. 2018, *PASP*, **130**, 064505
- Tremblay, P. E., & Bergeron, P. 2009, *ApJ*, **696**, 1755
- Virtanen, P., Gommers, R., Oliphant, T. E., et al. 2020, *NatMe*, **17**, 261
- von Zeipel, H. 1924, *MNRAS*, **84**, 665
- Vos, J., Vučković, M., Chen, X., et al. 2019, *MNRAS*, **482**, 4592

EPIC 216747137: a new HW Vir eclipsing binary with a massive sdOB primary and a low-mass M-dwarf companion

R. Silvotti¹,¹★ V. Schaffenroth,² U. Heber,³ R. H. Østensen,⁴ J. H. Telting,⁵ J. Vos,² D. Kilkeny,⁶ L. Mancini¹,^{1,7,8} S. Ciceri,⁹ A. Irrgang³ and H. Drechsel³

¹INAF – Osservatorio Astrofisico di Torino, Strada dell’Osservatorio 20, I-10025 Pino Torinese, Italy

²Institute of Physics and Astronomy, University of Potsdam, Karl-Liebknecht-Str. 24-25, D-14476 Potsdam, Germany

³Dr. Remeis-Sternwarte and ECAP, Astronomical Institute, University of Erlangen-Nürnberg, Sternwartstr. 7, D-96049 Bamberg, Germany

⁴Department of Physics, Astronomy and Materials Science, Missouri State University, 901 S. National, Springfield, MO 65897, USA

⁵Nordic Optical Telescope, Rambla José Ana Fernández Pérez 7, E-38711 Breña Baja, Spain

⁶Department of Physics and Astronomy, University of the Western Cape, Private Bag X17, Bellville 7535, South Africa

⁷Department of Physics, University of Rome ‘Tor Vergata’, Via della Ricerca Scientifica 1, I-00133 Roma, Italy

⁸Max Planck Institute for Astronomy, Königstuhl 17, D-69117 Heidelberg, Germany

⁹Department of Astronomy, Stockholm University, SE-106 91 Stockholm, Sweden

Accepted 2020 October 18. Received 2020 October 16; in original form 2020 October 1

ABSTRACT

EPIC 216747137 is a new HW Virginis system discovered by the *Kepler* spacecraft during its K2 ‘second life’. Like the other HW Vir systems, EPIC 216747137 is a post-common-envelope eclipsing binary consisting of a hot subluminescent star and a cool low-mass companion. The short orbital period of 3.87 h produces a strong reflection effect from the secondary (~ 9 per cent in the *R* band). Together with AA Dor and V1828 Aql, EPIC 216747137 belongs to a small subgroup of HW Vir systems with a hot evolved sdOB primary. We find the following atmospheric parameters for the hot component: $T_{\text{eff}} = 40400 \pm 1000$ K, $\log g = 5.56 \pm 0.06$, and $\log(N(\text{He})/N(\text{H})) = -2.59 \pm 0.05$. The sdOB rotational velocity $v \sin i = 51 \pm 10$ km s⁻¹ implies that the stellar rotation is slower than the orbital revolution and the system is not synchronized. When we combine photometric and spectroscopic results with the *Gaia* parallax, the best solution for the system corresponds to a primary with a mass of about $0.62 M_{\odot}$ close to, and likely beyond, the central helium exhaustion, while the cool M-dwarf companion has a mass of about $0.11 M_{\odot}$.

Key words: binaries: eclipsing – stars: horizontal branch – stars: individual: EPIC 216747137.

1 INTRODUCTION

Post-common-envelope binaries (PCEBs) are crucial to study the poorly understood and short-lived common-envelope (CE) phase of stellar evolution.

Among PCEBs, HW Virginis stars are a specific class of eclipsing binaries consisting of a hot subdwarf primary with an M-dwarf companion (see Heber 2016 for a recent review on hot subdwarf stars). There are two subgroups of HW Vir stars: those similar to the prototype, with a core-helium-burning sdB (subdwarf B) primary, located in the extreme horizontal branch (EHB) part of the H-R diagram. And those like AA Dor, with a hotter and more evolved primary of sdOB spectral class, beyond the central helium exhaustion.

The possibility of measuring accurate dynamical masses in HW Virginis systems is important to shed light on the formation mechanism of hot subdwarfs. These stars are characterized by very thin hydrogen envelopes and masses close to the canonical mass of $0.47 M_{\odot}$.

To form such an object, the hydrogen envelope of the red giant progenitor must be removed almost completely. Han et al. (2002, 2003, see also Clausen et al. 2012) describe three main binary evolution scenarios to form an sdB star: (i) CE ejection, (ii) stable Roche lobe overflow (RLOF), and (iii) the merger of two He white dwarfs (WD). The latter scenario may contribute only for a very small fraction of sdBs given that the high masses and high rotation rates foreseen are not supported by the observations (Fontaine et al. 2012; Charpinet et al. 2018; Reed et al. 2018). Since ~ 50 per cent of the non-composite-spectrum hot subdwarfs are members of short-period binaries with orbital periods between 0.027 and ~ 30 d (Maxted et al. 2001; Napiwotzki et al. 2004; Kupfer et al. 2015, 2020), mostly with a WD or an M-type main-sequence (MS) companion, CE ejection triggered by a close companion is generally regarded as the main formation channel. As far as the RLOF scenario is concerned, an important recent work by Pelisoli et al. (2020) shows that almost all the wide binaries with K- to F-type MS companions that they analysed show evidence of previous interaction, confirming that the RLOF is another efficient way to form ~ 30 – 40 per cent of hot subdwarfs, and suggesting that binary interaction may *always* be required to form a hot subdwarf star. Indeed, Stark & Wade (2003) found that ~ 40 per cent of hot subdwarfs have colours consistent with

* E-mail: roberto.silvotti@inaf.it

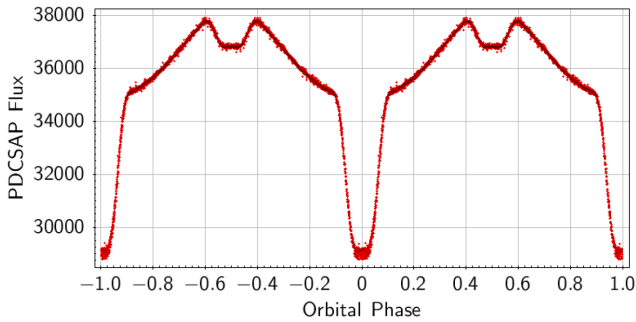


Figure 1. K2 light curve.

the presence of an unresolved late-type companion in a magnitude-limited sample (or ~ 30 per cent in a volume-limited sample). Putting these numbers together, we can estimate that ~ 35 per cent of hot subdwarfs are in close binaries with M-dwarf or WD companions, while ~ 30 per cent are in wide binaries with F/G/K companions.

However, the remaining fraction of ~ 35 per cent consists of apparently single hot subdwarfs. For them, different formation mechanisms have been invoked, including the merger of a He WD with a low-mass hydrogen-burning star (Clausen & Wade 2011). The presence of a substellar companion, difficult to detect, orbiting the sdB progenitor is another possibility (Soker 1998; Han et al. 2012), only partially supported by the observations.

On the one hand, no planets transiting hot subdwarfs were found in a large survey with the Evryscope, capable of detecting planets with radii slightly smaller than Jupiter (Ratzloff et al. 2020). Neither were planetary transits of hot subdwarfs found up to now by the *Kepler/K2* or the *TESS* space missions. Moreover, no significant radial velocity (RV) variations were found from high-accuracy Harps-N measurements of a small sample of eight bright apparently single sdB stars (Silvotti, Østensen & Telting 2020), excluding the presence of close substellar companions down to a few Jupiter masses and, for half of these stars, excluding also the presence of higher mass companions in wide orbits. These null results do not exclude that the planets were completely destroyed during the CE phase or that their envelope was removed leaving a very small and dense planetary core, difficult to detect (see e.g. the controversial cases of KIC 5807616 and KIC 10001893, Charpinet et al. 2011; Silvotti et al. 2014).

On the other hand, there are at least three known HW-Vir systems with brown dwarf (BD) companions having masses between 0.04 and $0.07 M_{\odot}$ (Geier et al. 2011; Schaffenroth et al. 2014, 2015), plus two more with masses close to the hydrogen-burning limit (Schaffenroth et al. 2019, figs 14 and 15). And there are a few controversial cases of planet detections through the eclipse or pulsation timing method (see e.g. Baran, Bachulski & Curyło 2016, and references therein).

Thanks to the high number of new HW-Vir systems discovered recently from the light curves of the OGLE and ATLAS projects (Schaffenroth et al. 2019), and the new ones that are being discovered by the *TESS* mission, the number of HW-Vir systems with substellar companions is likely to grow significantly in the short term. With enough statistics, it should be possible to determine the minimum mass for a substellar companion to eject the red giant envelope and survive engulfment. According to theory, it was thought that this limit could be near $10 M_{\text{Jup}}$ (Soker 1998; Han et al. 2012), but a recent article suggests that this mass limit could be higher, around $30\text{--}50 M_{\text{Jup}}$ (Kramer et al. 2020).

The system described in this paper, EPIC 216747137 (alias UCAC2 23234937), is a new HW-Vir binary relatively bright (*Gaia* DR2 magnitude $G = 13.767 \pm 0.004$), located about 880 pc from

us (*Gaia* DR2 parallax of 1.14 ± 0.06 mas). The eclipsing system was independently discovered by Mariusz Bajer on 2019 February 8 and the discovery was published in the Variable Star Index data base under the name BMAM-V272. In the next sections, we present the results of an analysis of both photometric and spectroscopic data of EPIC 216747137, that allow us to infer the orbital parameters of the system and the main characteristics of the primary and secondary components. The eclipsing system was independently discovered by Mariusz Bajer on February 8, 2019 and the discovery was published in the Variable Star Index database under the name BMAM-V272.¹

2 TIME-SERIES PHOTOMETRY

2.1 K2 discovery

EPIC 216747137 was observed by the *Kepler* space telescope during cycle 7 of its *K2* secondary mission in long-cadence mode, with a sampling time of 29.42 min. We downloaded the data from the ‘Barbara A. Mikulski Archive for Space Telescopes’ (MAST)² and we used the PDCSAP fluxes (PDC=Presearch Data Conditioning, SAP=Simple Aperture Photometry, see *K2* documentation for more details). After having removed some bad data point (those with SAP_QUALITY flag different from zero or 2048 plus two outliers), the data set we used, as shown in Fig. 1, consists of 81.3 d from BJD_{TDB} 2457301.48620 to 2457382.80453 (corresponding to 2015 October 05–December 26).

2.2 SAAO BVR data

EPIC 216747137 was re-observed at the Sutherland site of the South African Astronomical Observatory (SAAO) using the 1-m Elizabeth telescope with the STE3 CCD photometer which has a readout time of about 6 s (pre-binned 2×2), small compared to the exposure times for filters *B* (60 s), *V* (30 s), and *R* (30 s). Observations were made using each filter on a separate night (2017 May 18, 17, and 19, respectively) to maximize the resolution of the light curve. Reduction of the CCD frames, magnitude extraction by profile-fitting, and differential correction using several field stars were performed using software written by Darragh O’Donoghue and partly based on the DoPHOT program described by Schechter, Mateo & Saha (1993).

The *BVR* light curves are shown in Fig. 2. Comparing Fig. 1 with Fig. 2, we immediately note the different shape and depth of the primary and secondary eclipses, due to the smearing caused by the poor sampling rate of the *K2* long-cadence data. In Fig. 1, the primary and secondary eclipses have a depth of ~ 17 per cent and less than 3 per cent respectively, while they are much deeper in the SAAO data (~ 39 per cent and ~ 8 per cent in the *R* band). For this reason, the *K2* data were used only to improve the ephemeris, while the analysis of the light curve was performed using the ground-based photometry.

3 RADIAL VELOCITIES

EPIC 216747137 was observed spectroscopically with various instruments. As a first step, in order to measure the RVs of the primary, nine high-resolution spectra were obtained at different orbital phases in 2016 July and September using FEROS with the 2.2-m MPG/ESO telescope at La Silla Observatory in Chile,

¹<http://www.aavso.org/vsx/index.php?view=detail.top&oid=684233>

²archive.stsci.edu

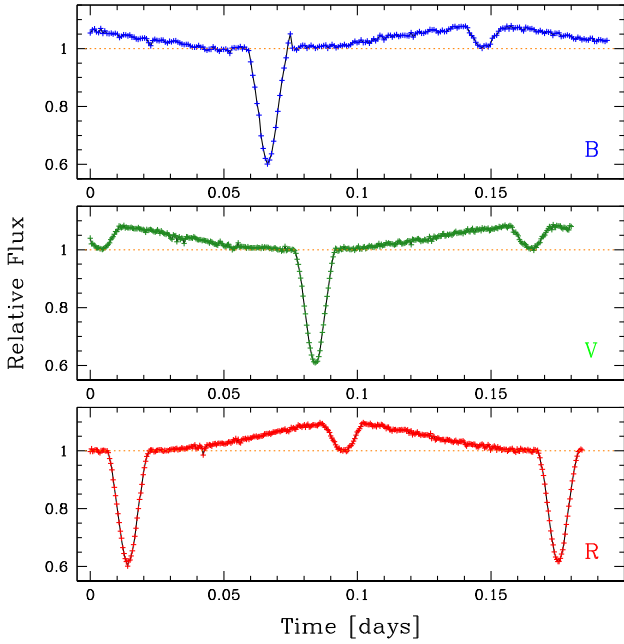


Figure 2. SAAO BVR light curves. The flux is normalized to the level just before and just after the primary eclipse.

with exposure times of 1800 s.³ The FEROS spectra were reduced using CERES, a pipeline written for échelle spectrographs described in Brahm, Jordán & Espinoza (2017). The raw spectra were first corrected with calibration frames obtained in the afternoon or during twilight, and then calibrated in wavelength using a Th–Ar spectrum. The RVs of the sdOB star were measured from the He II line at 4686 Å, while the Balmer lines were not used because they give more noisy results. However, the results were quite poor due to the low signal-to-noise ratio of the FEROS spectra.

For this reason, new observations were carried out as part of our K2 sdBV follow-up spectroscopic survey (Telting et al. 2014). We obtained 32 low-resolution spectra ($R \sim 2000$, or 2.2 Å) in two runs (22 spectra in 2017 July, 10 spectra 2018 between March and August) at the 2.56-m Nordic Optical Telescope (NOT, La Palma) using ALFOSC, 600 s exposure times, grism no. 18, 0.5 arcsec slit, and CCD no. 14, giving an approximate wavelength range 345–535 nm. The spectra were homogeneously reduced and analysed. Standard reduction steps within IRAF include bias subtraction, removal of pixel-to-pixel sensitivity variations, optimal spectral extraction, and wavelength calibration based on helium arc-lamp spectra. The peak signal-to-noise ratio of the individual spectra ranges from 50 to 125. The RVs were measured using the lines H β , H γ , H δ , H8, and H9 through a cross-correlation analysis in which we used as a template a synthetic fit to an orbit-corrected average (all spectra shifted to zero velocity before averaging).

Finally, 32 medium-resolution spectra were obtained with MagE@Magellan I at Las Campanas Observatory in Chile in 3.5 h on 2017 September 17, with 300 s exposure times, 1 arcsec slit, $R \sim 4100$ and a useful wavelength range of 3500–8100 Å. The typical signal-to-noise ratios were between 80 and 110. The spectra were reduced using the MagE pipeline (Kelson et al. 2000; Kelson 2003). The RVs were measured using Balmer lines and two He I lines at 4471 and 5875 Å.

³For the first two spectra we used 1000 and 1500 s.

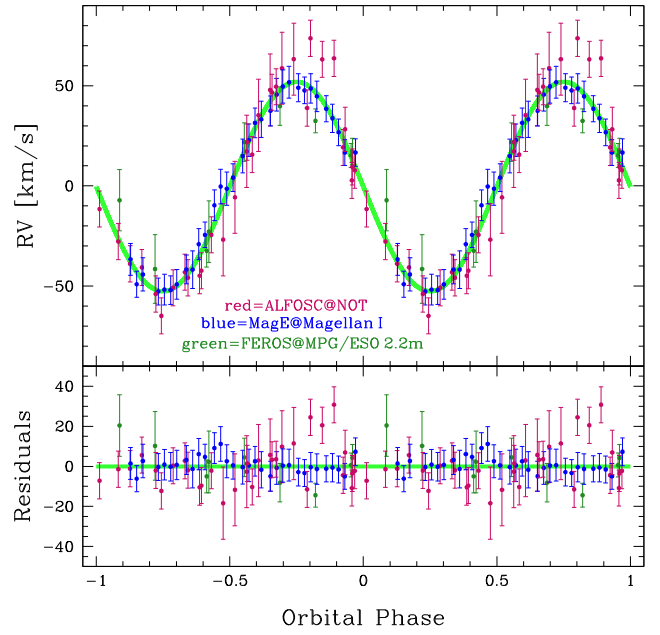


Figure 3. Radial velocities.

The RV measurements obtained from the MagE spectra are the most accurate due to the best compromise between high SN ratio, relatively high resolution and short exposure times, which means lower smearing. However, the ALFOSC and FEROS RVs were also used using appropriate weights (Fig. 3). From the best RV fit, we obtain a circular orbit with an RV amplitude $K = 52.3 \pm 1.3 \text{ km s}^{-1}$, and a system velocity $v_0 = -6.4 \pm 1.2 \text{ km s}^{-1}$. Smearing is not considered as it is negligible for MagE and ALFOSC spectra (0.08 per cent and 0.3 per cent, respectively) and has little importance only for FEROS spectra (3 per cent). By fitting all the 73 RVs listed in Table 1 with an eccentric solution, we can constrain the eccentricity to a value smaller than 0.091.⁴

Both the ALFOSC and MagE spectra were used not only to measure the RVs, but also to derive accurate atmospheric parameters and the rotational velocity of the sdOB star and to measure their variations as a function of the orbital phase, as described in the next section.

4 ATMOSPHERIC PARAMETERS AND ROTATIONAL VELOCITY OF THE PRIMARY

The reflection effect adds additional light to the sdOB spectrum, which varies with phase. Because we cannot model this contribution, each individual spectrum is matched separately to a grid of synthetic models to derive the effective temperature, gravity, and helium abundance. If the contribution to the spectrum of the primary is significant, the resulting atmospheric parameters should show trends with orbital phase as a consequence of the varying light pollution. Indeed, such apparent variations of atmospheric parameters have been found in other reflection binaries such as HW Vir (Wood & Saffer 1999), HS 0705+6700 (Drechsel et al. 2001), and most distinctively in HS 2333+3937 (Heber et al. 2004). The best estimate of the atmospheric parameters comes from data taken during secondary

⁴We obtain an eccentricity of 0.019 ± 0.024 , which translates into a 3σ upper limit of 0.091.

Table 1. RV measurements.

BJD _{TDB} -2450000.	RV (km s ⁻¹)	Error (km s ⁻¹)	Instr.	UT date
7590.682242	11.14	6.64	FEROS	2016-07-21
7590.755434	-38.47	8.18	FEROS	2016-07-21
7645.521343	-28.90	15.42	FEROS	2016-09-14
7645.542780	15.74	9.59	FEROS	2016-09-14
7645.564206	33.73	9.60	FEROS	2016-09-14
7645.585628	26.38	6.00	FEROS	2016-09-14
7645.607066	9.17	6.00	FEROS	2016-09-14
7645.628503	-13.21	15.33	FEROS	2016-09-14
7645.649944	-47.56	17.09	FEROS	2016-09-14
7958.472032	-51.96	9.00	ALFOSC	2017-07-23
7958.479132	-50.91	9.00	ALFOSC	2017-07-23
7958.486222	-30.49	9.00	ALFOSC	2017-07-23
7958.493322	-32.92	18.00	ALFOSC	2017-07-23
7958.500422	-11.79	18.00	ALFOSC	2017-07-24
7958.507522	11.19	18.00	ALFOSC	2017-07-24
7958.514612	29.18	18.00	ALFOSC	2017-07-24
7958.521712	41.84	18.00	ALFOSC	2017-07-24
7958.528812	52.66	18.00	ALFOSC	2017-07-24
7958.535902	57.18	18.00	ALFOSC	2017-07-24
7958.565612	13.15	9.00	ALFOSC	2017-07-24
7958.572712	1.74	9.00	ALFOSC	2017-07-24
7958.579812	-17.64	9.00	ALFOSC	2017-07-24
7958.591172	-33.85	9.00	ALFOSC	2017-07-24
7958.598262	-44.95	9.00	ALFOSC	2017-07-24
7958.605362	-46.79	9.00	ALFOSC	2017-07-24
7960.478821	67.59	9.00	ALFOSC	2017-07-25
7960.485921	57.11	9.00	ALFOSC	2017-07-25
7960.493021	57.61	9.00	ALFOSC	2017-07-25
7960.549991	-70.95	9.00	ALFOSC	2017-07-26
7960.557091	-56.91	9.00	ALFOSC	2017-07-26
7960.564181	-49.15	9.00	ALFOSC	2017-07-26
8014.490569	-42.73	7.92	MagE	2017-09-17
8014.494309	-55.17	6.49	MagE	2017-09-17
8014.498039	-50.28	8.30	MagE	2017-09-17
8014.507289	-58.76	6.72	MagE	2017-09-18
8014.511029	-57.84	7.66	MagE	2017-09-18
8014.514759	-58.11	7.13	MagE	2017-09-18
8014.518489	-55.26	7.36	MagE	2017-09-18
8014.524279	-47.81	7.19	MagE	2017-09-18
8014.528019	-47.87	9.37	MagE	2017-09-18
8014.531749	-35.15	7.80	MagE	2017-09-18
8014.535489	-30.53	6.37	MagE	2017-09-18
8014.541189	-15.77	7.71	MagE	2017-09-18
8014.544929	-6.39	8.64	MagE	2017-09-18
8014.548659	-7.49	8.26	MagE	2017-09-18
8014.552399	-1.96	6.91	MagE	2017-09-18
8014.558219	8.82	8.43	MagE	2017-09-18
8014.561949	16.75	8.10	MagE	2017-09-18
8014.565679	25.39	7.44	MagE	2017-09-18
8014.569419	27.14	9.01	MagE	2017-09-18
8014.574989	31.38	7.49	MagE	2017-09-18
8014.578729	39.47	8.14	MagE	2017-09-18
8014.582469	43.56	8.29	MagE	2017-09-18
8014.586199	45.64	7.96	MagE	2017-09-18
8014.591779	42.95	6.97	MagE	2017-09-18
8014.595519	41.63	6.68	MagE	2017-09-18
8014.599249	42.56	7.36	MagE	2017-09-18
8014.602999	38.63	7.62	MagE	2017-09-18
8014.608619	32.41	6.52	MagE	2017-09-18
8014.612359	27.67	7.08	MagE	2017-09-18
8014.616089	20.70	6.67	MagE	2017-09-18
8014.619829	10.60	6.42	MagE	2017-09-18

Table 1 – *continued*

BJD _{TDB} -2450000.	RV (km s ⁻¹)	Error (km s ⁻¹)	Instr.	UT date
8014.626199	10.55	6.89	MagE	2017-09-18
8201.763003	32.78	9.00	ALFOSC	2018-03-24
8211.685742	-48.44	9.00	ALFOSC	2018-04-03
8268.635281	3.39	9.00	ALFOSC	2018-05-30
8269.702361	9.53	9.00	ALFOSC	2018-05-31
8304.505900	40.62	9.00	ALFOSC	2018-07-05
8304.596910	-60.01	9.00	ALFOSC	2018-07-05
8307.568760	43.45	9.00	ALFOSC	2018-07-08
8312.607699	-3.29	9.00	ALFOSC	2018-07-13
8338.477179	15.78	9.00	ALFOSC	2018-08-07
8338.536299	22.17	11.10	ALFOSC	2018-08-08

eclipse and just before and after primary eclipse, when the light pollution should be lowest.

We closely follow the analysis strategy outlined by Heber et al. (2004). The Balmer and helium lines in the ALFOSC and MagE spectra are used to determine effective temperature, gravity and helium abundance, and the projected rotation velocity $v \sin i$. Because the spectral resolution of the ALFOSC spectra is insufficient for $v \sin i$ to be determined, the latter is derived from the MagE spectra. The ALFOSC spectra show the entire Balmer series with a well defined continuum and can, therefore, be used to determine T_{eff} , $\log g$, and $\log y = \log(N(\text{He})/N(\text{H}))$. For the MagE spectra, their wavy run of the continuum prohibits the Balmer lines to be used. However, they are very useful to derive the projected rotation velocity and allow us to investigate the helium ionization equilibrium including lines not covered by the ALFOSC spectral range, from which an independent estimate of the effective temperature can be obtained. Since the helium lines are quite insensitive to gravity, the gravity had to be fixed in the analysis of the MagE spectra to $\log g = 5.56$ derived from the ALFOSC spectra. We match the Balmer ($H\beta$ to $H 11$) and He I (4471 and 4026 Å), as well as He II 4686 and 4542 Å line profiles in the ALFOSC spectra, and He I (4471 and 5875 Å) and He II (4686 and 5411 Å) lines in the MagE spectra with a grid of synthetic spectra.

The models are computed using three codes. First, the ATLAS12 code (Kurucz 1996) is used to compute the atmospheric structure (temperature/density stratification) in LTE (local thermodynamic equilibrium). Non-LTE population numbers are then calculated with the DETAIL code (Giddings 1981) and the coupled equations of radiative transfer and statistical equilibrium are solved numerically. In the final step, the SURFACE code (Giddings 1981) computes the emergent spectrum based on the non-LTE occupation numbers provided by DETAIL. In this step detailed line-broadening tables are incorporated. All three codes have been updated recently (see Irrgang et al. 2018). The impact of departures from LTE for hydrogen and helium on the atmospheric structure is modelled by feeding back population numbers calculated by DETAIL to ATLAS12 and iterate. In addition, the occupation probability formalism (Hubeny, Hummer & Lanz 1994) for hydrogen has been implemented and line broadening tables have been updated. Stark broadening tables for hydrogen and neutral helium are taken from Tremblay & Bergeron (2009) and Beauchamp, Wesemael & Bergeron (1997), respectively. The broadening of the lines of ionized helium was treated as described by Auer & Mihalas (1972).

The observed spectra are matched to the model grid by χ^2 minimization as described by Saffer et al. (1994) using implementations

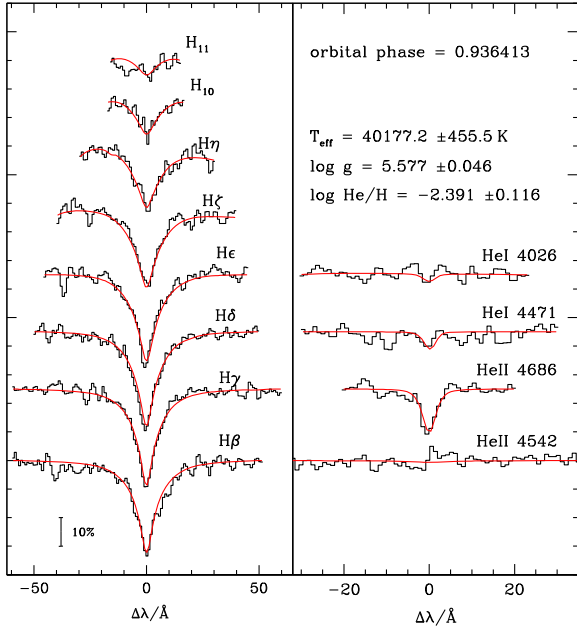


Figure 4. Fit of one of the ALFOSC spectra corresponding to orbital phase 0.9364, close to the primary eclipse, for which the contribution of the secondary is minimum.

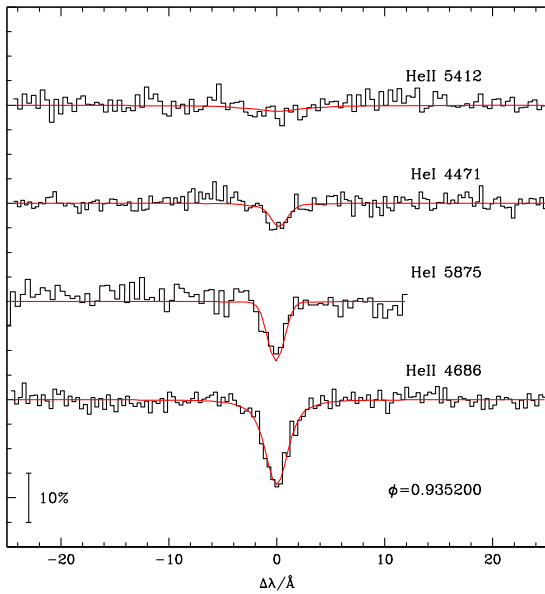


Figure 5. Same as Fig. 4, but for one of the MagE spectra corresponding to orbital phase 0.9352.

by Napiwotzki, Green & Saffer (1999) and Hirsch (2009). Exemplary fits to an ALFOSC and a MagE spectrum are shown in Figs 4 and 5.

The results of the quantitative spectral analysis of all ALFOSC and MagE spectra are summarized in Fig. 6. In the left-hand panels (ALFOSC), the apparent variations of the effective temperature with phase and an amplitude of ~ 2500 K are obvious. The lowest temperatures (~ 40 kK) occur near primary eclipse and in the secondary eclipse, where the contribution by extra light should be minimal. Hence, the increase during other orbital phases is caused by reflected light and, therefore, not real. Similarly, variations of the helium abundance are observed. The apparent variations of the surface

gravity, however, are small. The mean values adopted for T_{eff} , $\log g$, and $\log y$, summarized in Table 2, are obtained by selecting six spectra close to the primary eclipse with phase between -0.1 and $+0.1$ and adding one spectrum at phase 0.52. The analysis of the MagE spectra also results in effective temperatures and helium abundances that seem to vary with orbital phase (cf. Fig. 6, right-hand panels), but with amplitudes less pronounced than those from the ALFOSC spectra. For this reason, we use all the MagE spectra to compute mean values and standard deviations of T_{eff} and $\log y$ (cf. Table 2).

The effective temperature and surface gravity of EPIC 216747137 ($T_{\text{eff}} = 40400$ K and $\log g = 5.56$) are very similar to the hot HW Vir systems AA Dor (Klepp & Rauch 2011) and V1828 Aql (= NSVS 14256825, Almeida et al. 2012). EPIC 216747137 also shares an underabundance of helium ($\log y = -2.59$) with the two others.

The projected rotational velocity, as derived from the individual MagE spectra (central right panel of Fig. 6), results in a mean $v \sin i = 51 \pm 10$ km s $^{-1}$, significantly less than ~ 70 km s $^{-1}$ expected for tidally locked rotation. Mean rotational velocity of 51 km s $^{-1}$ and standard deviation of 10 km s $^{-1}$ are obtained excluding only a single outlier close to phase 0 (see central right panel of Fig. 6).

5 STELLAR PARAMETERS: RADIUS, MASS, AND LUMINOSITY

The second data release of *Gaia* provided a precise (5 per cent) parallax measurement which allows the stellar parameters (radius, mass, and luminosity) to be derived from the atmospheric parameters, if the angular diameter were known. The latter can be derived from the spectral energy distribution (SED).

5.1 Angular diameter and interstellar reddening

The angular diameter Θ is derived from the observed flux $f(\lambda)$ and the synthetic stellar surface flux via the relation $f(\lambda) = \Theta^2 F(\lambda)/4$, which means that Θ is just a scaling factor which shifts fluxes up and down. Strictly speaking, the apparent magnitudes of the sdOB can be measured during secondary eclipses only, when the companion is completely eclipsed by the larger subdwarf, because of the contamination by light from the companion's heated hemisphere. Such data are not available. Nevertheless, many photometric measurements are available in different filter systems, covering the spectral range in the optical and infrared. However, those measurements are mostly averages of observations taken at multiple epochs and, therefore, may be subject to light pollution from the companion.

The low Galactic latitude ($b = -9.9^\circ$) implies that interstellar reddening may be large. Therefore the angular diameter has to be determined along with the interstellar colour excess. The reddening law of Fitzpatrick et al. (2019) and a synthetic flux distribution from the grid of model atmospheres described in Section 4 is matched to the observed magnitudes employing a χ^2 -based fitting routine (see Heber, Irrgang & Schaffenroth 2018 for details). The final atmospheric parameters and their respective uncertainties derived from the quantitative spectral analysis (see Section 4) are used. Indeed, interstellar reddening is significant with $E(B - V) = 0.213^{+0.010}_{-0.016}$ mag (see Table 3). The latter is consistent with values from reddening maps of Schlegel, Finkbeiner & Davis (1998) and Schlafly & Finkbeiner (2011): 0.253 mag and 0.217 mag, respectively.

Because of light pollution from the companion's heated hemisphere, the resulting angular diameter will be somewhat overestimated, as that is not accounted for in the synthetic SED. Red and infrared magnitudes are expected to be more affected than the blue

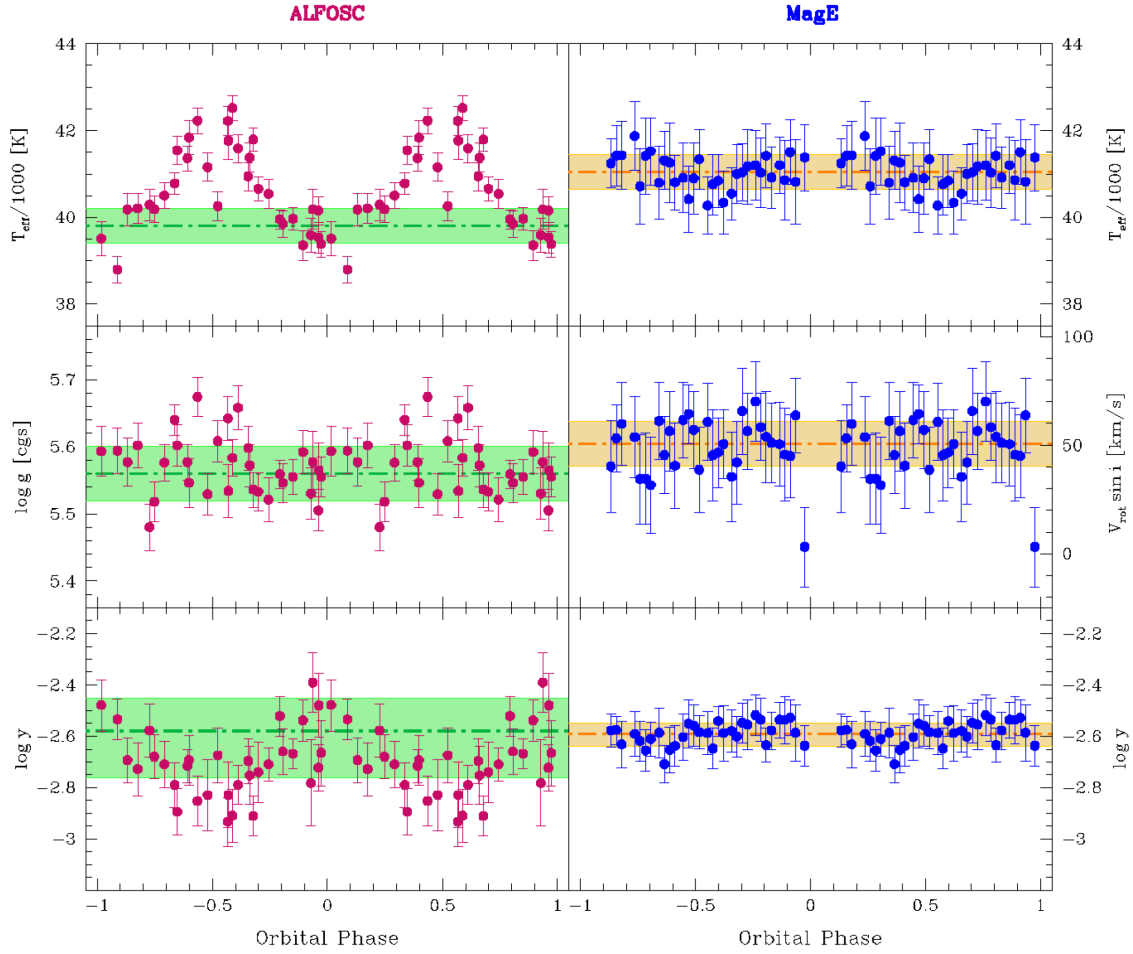


Figure 6. T_{eff} , $\log g$, $\log y$, and $v_{\text{rot}} \sin i$ variations as a function of the orbital phase. Left-hand panels: ALFOSC. The green dotted–dashed horizontal lines mark the adopted T_{eff} , $\log g$, and $\log y$ and the associated errors (cf. Table 2 and text). Note the two points with low T_{eff} near phase 0.5 (secondary eclipse), when the contribution of the secondary is strongly reduced. Right-hand panels: MagE. The orange dotted–dashed horizontal lines mark the average values and associated errors of T_{eff} , $v_{\text{rot}} \sin i$, and He abundance. In the central panel, note the outlier near phase zero (primary eclipse).

Table 2. SdOB atmospheric parameters and rotational velocity.

	ALFOSC	MagE	Adopted
T_{eff} (K)	39800 ± 400	41000 ± 400	40400 ± 1000
$\log g$ (cgs)	5.56 ± 0.04		5.56 ± 0.06
$\log y$	$-2.58^{+0.13}_{-0.18}$	$-2.59^{+0.04}_{-0.05}$	-2.59 ± 0.05
$v \sin i$ (km s^{-1})		51 ± 10	51 ± 10

ones. To account for the additional light, we added a blackbody spectrum to the fit, allowing its temperature as well as the relative emission area to vary. The final fit is shown in Fig. 7 and results summarized in Table 3.

5.2 Stellar radius, mass, and luminosity

The *Gaia* DR2 parallax is corrected for a zero-point offset of -0.029 mas as recommended by Lindegren et al. (2018) and applied by Bailer-Jones et al. (2018) to derive distances. By combining it with the atmospheric parameters ($\log g$ and T_{eff}) and the angular diameter, we can determine the star’s radius R , mass M , and luminosity L . The respective uncertainties of the stellar parameters are derived by Monte Carlo error propagation. Results are summarized in Table 3. Once the radius ($R = 0.206 \pm 0.012 R_{\odot}$)

Table 3. SED + *Gaia* DR2 results.

Atmospheric parameters from spectral analysis	
Effective temperature T_{eff}	$40400 \pm 1000 \text{ K}$
Surface gravity $\log(g(\text{cm s}^{-2}))$	5.56 ± 0.06
Helium abundance $\log y$	-2.59 ± 0.05
Parameters from SED fit and <i>Gaia</i> DR2 parallax	
Colour excess $E(B - V)$	$0.213^{+0.010}_{-0.016} \text{ mag}$
Metallicity z (fixed)	0 dex
Angular diameter $\log(\Theta(\text{rad}))$	$-10.975^{+0.009}_{-0.015}$
Blackbody temperature T_{bb}	$2900^{+2600}_{-1300} \text{ K}$
Blackbody surface ratio $A_{\text{eff, bb}}/A_{\text{eff}}$	$2.5^{+4.3}_{-1.4}$
Generic excess noise δ_{excess} (fixed)	0.033 mag
Parallax ϖ (RUWE=1.04, offset=0.029 mas)*	$1.14 \pm 0.06 \text{ mas}$
$R = \Theta/(2\varpi)$	$0.206 \pm 0.012 R_{\odot}$
$M = gR^2/G$	$0.56^{+0.11}_{-0.10} M_{\odot}$
$L/L_{\odot} = (R/R_{\odot})^2(T_{\text{eff}}/T_{\text{eff}, \odot})^4$	100^{+16}_{-15}

Notes: * We use the RUWE parameter as a quality indicator, best is 1, <1.4 is acceptable, 1.04 is good.

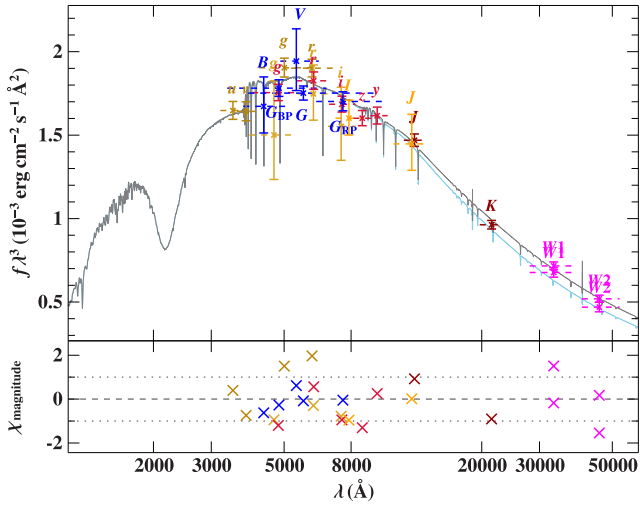


Figure 7. Comparison of synthetic and observed photometry (flux times wavelength to the power of 3): top panel: SED, filter-averaged fluxes converted from observed magnitudes. Dashed horizontal lines depict the approximate width of the respective filters (widths at tenth maximum). The best-fitting model, smoothed to a spectral resolution of 6 \AA , is shown in grey. Bottom panel: residual χ , difference between synthetic and observed magnitudes divided by the corresponding uncertainties. The different photometric systems are assigned the following colours: SDSS (APASS, golden; Alam et al. 2015), SkyMapper (golden; Wolf et al. 2018; Onken et al. 2019), PAN-STARRS (red; Chambers & et al. 2017), Johnson (APASS, blue; Henden et al. 2015), *Gaia* (blue; Evans et al. 2018 with corrections and calibrations from Maíz Apellániz & Weiler 2018), DENIS (yellow; Fouqué et al. 2000), VHS-DR6 (brown; Lawrence et al. 2007), and *WISE* (magenta; Wright et al. 2010; Schlafly, Meisner & Green 2019).

has been derived from angular diameter and parallax, the mass ($0.56_{-0.10}^{+0.11} M_{\odot}$) follows from gravity and the luminosity ($100_{-15}^{+16} L_{\odot}$) from radius and effective temperature.

A comparison with evolutionary models for EHB stars by Han et al. (2002) is shown in Fig. 8 and demonstrates that the hot subdwarf has likely just evolved beyond the core-helium-burning phase, similar to AA Dor (Klepp & Rauch 2011) and V1828 Aql (Almeida et al. 2012), or is at the very end of helium burning, depending on the hot subdwarf mass and envelope mass.

6 EPHEMERIS

First we computed independent ephemerides from photometric and RV data, obtaining a good agreement on the orbital period. The orbital period derived from the RVs has a higher precision thanks to the longer baseline (2.0 versus 1.6 yr) and also because of the poor time resolution of the *K2* data. Then, considering both spectroscopic and photometric data together, we were able to remove the degeneracy due to the spectral windows and obtain a better determination of the orbital period thanks to the longer baseline (2.8 yr). In practice, taking as reference the center of the primary eclipse, we verified that the time difference between the last primary eclipse of our data set (determined from RVs) and the first one (determined from photometry) was very close to an integer multiple of the orbital period determined from the RVs. Then, imposing that such time difference is *exactly* a multiple of the orbital period, we obtain the best determination of the orbital period and the following best ephemeris:

$$\text{BJD}_{\text{TDB}} = (2457301.56346 \pm 0.00041) \\ + (0.16107224 \pm 0.0000017) E$$

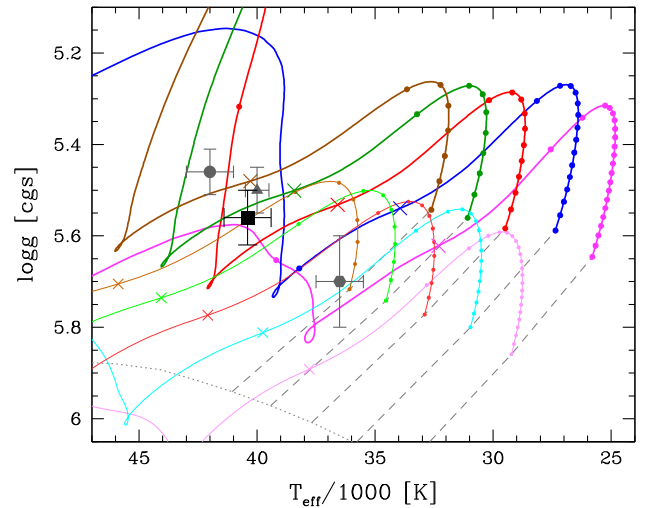


Figure 8. $T_{\text{eff}}\text{-log } g$ diagram with the position of EPIC 216747137 (square symbol) compared with the evolutionary tracks by Han et al. (2002) for different stellar masses: from right to left $0.45, 0.50, 0.55, 0.60,$ and $0.65 M_{\odot}$, (magenta, blue, red, green, and brown respectively in the online version). The envelope mass is $0.005 M_{\odot}$ (thick lines) or 0.001 (thin lines and light colours). Along the evolutionary tracks, the age differences between adjacent dots are 10^7 yr. The crosses mark the point of central helium exhaustion. Helium MS and zero-age EHB (ZAEHB) are shown as dotted and dashed lines respectively. The positions of the evolved HW Vir systems AA Dor (circle, Klepp & Rauch 2011) and V1828 Aql (triangle, Almeida et al. 2012) and of the evolved reflection-effect sdB+dM binary HS 2333+3927 (pentagon, Heber et al. 2004) are also reported. Note that AA Dor and V1828 Aql have masses of 0.47 and $0.42 M_{\odot}$ respectively, and therefore should definitely be post-EHB [compare with the $0.45 M_{\odot}$ (magenta) and $0.50 M_{\odot}$ (blue) tracks].

where BJD_{TDB} is the barycentric Julian date of the centre of each primary eclipse using barycentric dynamical time (see e.g. Eastman, Siverd & Gaudi 2010).

7 MODELLING OF THE LIGHT CURVE

The SAAO *BRV* light curves show relatively deep eclipses together with a reflection effect with increasing amplitude from *B* to *R*, and a secondary eclipse only visible due to the reflection effect. Such a light curve is characteristic for sdO/B systems with close, cool, low-mass companions. For the modelling of the light curve we used *LCURVE*, a code written to model detached but also accreting binaries containing a WD (for details, see Copperwheat et al. 2010). It has been used to analyse several detached WD-M dwarf binaries (e.g. Parsons et al. 2010), which show very similar light curves with deep eclipses and a prominent reflection effect, if the primary is a hot WD. Recently, *LCURVE* was used also for an sdB+BD system (submitted Schaffenroth et al. 2020). The code subdivides each star into small elements with a geometry fixed by its radius as measured along the direction towards the other star. Roche distortions and irradiation are also included, as well as limb-darkening, gravitational darkening, lensing, Doppler beaming, Rømer delay, and asynchronous orbits. The latter three effects, lensing, Doppler beaming and Rømer delay, are not detectable in our light curves. The irradiation is approximated by assigning a new temperature to the heated side of the companion:

$$\sigma T_{\text{sec}}^{/4} = \sigma T_{\text{sec}}^4 + F_{\text{irr}} = \sigma T_{\text{sec}}^4 \left[1 + \alpha \left(\frac{T_{\text{prim}}}{T_{\text{sec}}} \right)^4 \left(\frac{R_{\text{prim}}}{a} \right)^2 \right]$$

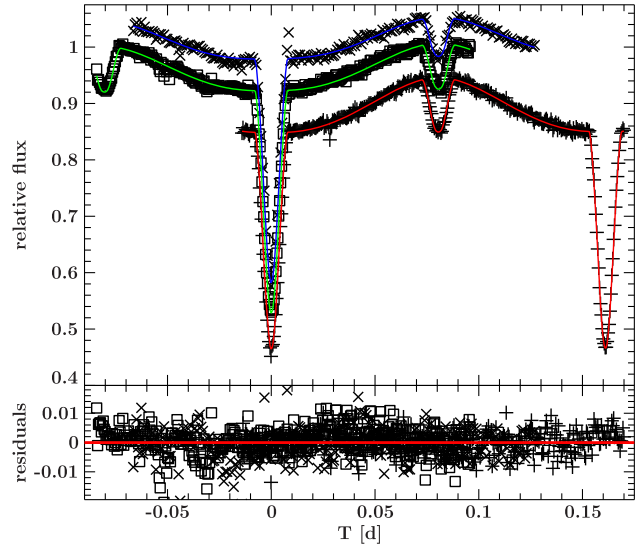
Table 4. Parameters of the light-curve fit of the SAAO *BVR*-band light curves for the best model.

Band	<i>B</i>	<i>V</i>	<i>R</i>
Fixed parameters			
<i>q</i>		0.175	
<i>P</i>		0.1610732	
$T_{\text{eff, sdB}}$		40400	
$x_{1,1}$	0.0469	0.0434	0.0379
$x_{1,2}$	0.2668	0.2346	0.2082
g_1		0.25	
g_2		0.08	
Fitted parameters			
<i>i</i>	85.04 ± 0.40	85.62 ± 0.19	85.51 ± 0.14
r_1/a	0.1887 ± 0.0016	0.1890 ± 0.0008	0.1887 ± 0.0005
r_2/a	0.1251 ± 0.0028	0.1216 ± 0.0012	0.1222 ± 0.0009
$T_{\text{eff, comp}}$	3000 ± 500	2965 ± 482	3042 ± 503
A_2	0.95 ± 0.08	1.01 ± 0.04	1.25 ± 0.04
x_2	0.33	0.27	0.28
T_0	2457892.53884	2457891.57235	2457893.66629
slope	0.004729	0.003015	0.00088
$\frac{L_1}{L_1+L_2}$	0.98028	0.972691	0.94864

with α being the Bond albedo of the companion and F_{irr} the irradiating flux, accounting for the angle of incidence and distance from the hot subdwarf. If the irradiation effect is very strong, the description given above might not be sufficient. The backside of the irradiated star is completely unaffected in this description, but heat transport could heat it up, increasing the luminosity of unirradiated parts as well.

Since the model contains many parameters, not all of them independent, we fixed as many parameters as possible (see Table 4). The sdOB temperature was fixed to the temperature determined from the spectroscopic fit. The gravitational darkening coefficients were fixed to the values expected for a radiative atmosphere for the primary (von Zeipel 1924) and a convective atmosphere for the secondary (Lucy 1967), using a blackbody approximation to calculate the resulting intensities. More sophisticated models such as those proposed by Espinosa Lara & Rieutord (2011) or Claret & Bloemen (2011, see also Claret et al. 2020) were not used because the deformations from a spherical shape are very small and in fact gravity darkening has almost no impact. For the limb darkening of the primary, we adopted a quadratic limb-darkening law using the tables by Claret & Bloemen (2011). As the tables include only surface gravities up to $\log g = 5$, we used the values closest to the parameters derived by the spectroscopic analysis. As the two stars are almost spherical (we do not see significant ellipsoidal deformations), the light curve is not sensitive to the mass ratio and therefore we computed solutions with different, fixed mass ratios. To localize the best set of parameters, we used a SIMPLEX algorithm (Press et al. 1992) varying the inclination, the radii, the temperature of the companion, the geometric albedo of the companion (A_2), the limb darkening of the companion, the period and the time of the primary eclipse. Moreover, we also allowed for corrections of a linear trend, which is often absorbed in observing hot stars, as the comparison stars are often redder and so the correction for the airmass is often insufficient (slope). The model of the best fit is shown in Fig. 9, together with the observations and the residuals.

To get an idea about the degeneracy of the light-curve solutions, as well as the errors of the parameters, we performed also Markov Chain Monte Carlo (MCMC) computations using the best solution obtained with the SIMPLEX algorithm as a starting value and varying the radii, the inclination, the temperature of the companion, as well as the

**Figure 9.** Normalized SAAO *B*(\times), *V*(\square), and *R*($+$)-band light curves together with the best fit. For better visualization, the *V*- and *R*-band light curves have been shifted. The lower panel shows the residuals.

albedo of the companion (Figs A1–A3). A clear correlation between the radius of the companion, the inclination, and the geometric albedo of the companion (A_2) can be seen, which results from the fact that the companion is only visible in the light curve due to the reflection effect and the amplitude depends on the inclination, the radius of the companion and the albedo, as well as the separation and temperature and radius of the primary, which is given by the spectroscopic analysis.

8 NATURE OF THE COMPANION

As stated before, it is not possible to derive the mass ratio from the light-curve analysis. Since we have only a single-lined system, it is necessary to look for other possibilities to constrain the mass ratio of the system. Taking into account the sdOB atmospheric parameters obtained from our spectroscopic analysis, the sdOB star is likely an evolved post-EHB star or just at the end of helium burning, depending on the hot subdwarf mass and envelope mass.

When we combine the analysis of the RV and the light curves, we get different masses and radii of both components, as well as a different separation for each solution with a different mass ratio. From the spectroscopic analysis we derived the surface gravity of the hot subdwarf, which can be compared to a photometric surface gravity calculated from the mass and radius derived from the light-curve analysis and the mass function. Moreover, from the radius determined by the *Gaia* parallax and the SED fit, we can calculate a *Gaia* surface gravity. The comparison of the photometric, spectroscopic, and *Gaia* surface gravity is shown in Fig. 10. An agreement is seen for a mass between ~ 0.47 and $\sim 0.67 M_{\odot}$. This means a post-EHB hot subdwarf with a canonical mass of $0.47 M_{\odot}$ cannot be excluded.

Another possibility to constrain the masses further is to consider the mass–radius relation of the companion (Fig. 11), and compare it to theoretical predictions (Baraffe et al. 2003; Chabrier & Baraffe 1997). Using the mass–radius relation for the cool companion, the best agreement is found for an sdOB mass of $\sim 0.62 M_{\odot}$. This is hence the most consistent solution, that implies a ~ 2 per cent inflation of

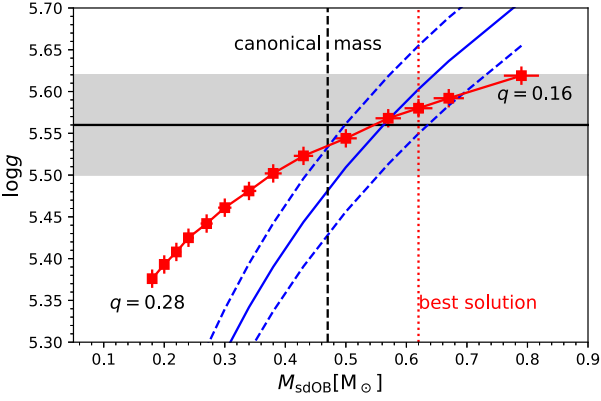


Figure 10. Mass of the sdOB versus the photometric $\log g$ for different mass ratios from 0.16 to 0.28 in steps of 0.1 (adding 0.175 for the best solution). They were derived from combining the results from the analysis of the light curve and RV curve. The grey area marks the spectroscopic $\log g$ that was derived by the spectroscopic analysis. The blue lines mark the surface gravity derived from the radius determined by the *Gaia* parallax and the SED fit. The vertical lines represent the two solutions which are given in Table 5.

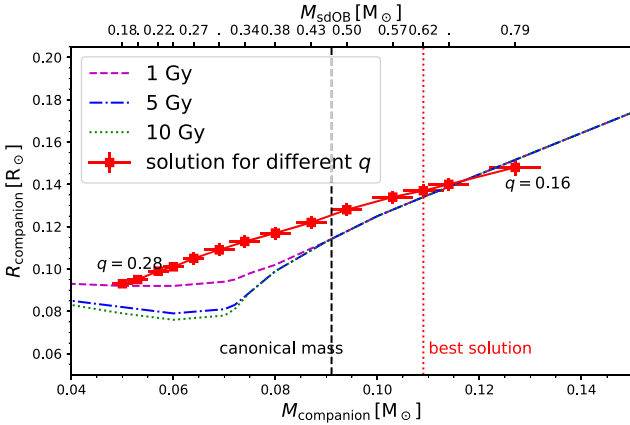


Figure 11. Comparison of theoretical mass–radius relations of BDs by Baraffe et al. (2003) and low-mass M dwarfs by Chabrier & Baraffe (1997) for an age of 1 Gyr (dashed), 5 Gyr (dotted–dashed), and 10 Gyr (dotted) to results from the light-curve analysis. Each error cross represents a solution from the light-curve analysis for a different mass ratio ($q = 0.16$ – 0.28 in steps of 0.1 and adding 0.175 for the best solution). The vertical lines represent the two solutions of Table 5.

the M-dwarf radius. A lower mass would imply a more inflated radius for the M dwarf.

In Table 5, we consider two solutions (absolute system parameters) of the light-curve analysis resulting from two different assumptions on the mass ratio q . A massive one at $q = 0.175$, corresponding to an sdOB mass of $0.62 M_{\odot}$, which we prefer because it avoids strong inflation of the companion, and a second solution at $q = 0.194$, which corresponds to the canonical mass ($M = 0.47 M_{\odot}$). For the preferred solution of a high-mass post-EHB star, we obtain a companion mass of $0.109 \pm 0.004 M_{\odot}$, corresponding to a low-mass M dwarf. For a canonical mass sdOB, the mass of the M star would be even less ($0.091 \pm 0.003 M_{\odot}$), only slightly above the stellar mass limit.

9 SUMMARY AND DISCUSSION

EPIC 216747137 is a new HW Vir system that belongs to the small subgroup of eclipsing hot subdwarf binaries in which the primary is a hot, evolved, sdOB star. The other two members of this

Table 5. Absolute parameters of the system.

	Best solution	Post-EHB canonical
q	0.175	0.194
$a (R_{\odot})$	1.121 ± 0.028	1.028 ± 0.025
$M_{\text{sdOB}} (M_{\odot})$	0.620 ± 0.023	0.470 ± 0.017
$M_{\text{comp}} (M_{\odot})$	0.109 ± 0.004	0.091 ± 0.003
$R_{\text{sdOB}} (R_{\odot})$	0.212 ± 0.005	0.194 ± 0.005
$R_{\text{comp}} (R_{\odot})$	0.137 ± 0.003	0.125 ± 0.003
$\log g_{\text{phot}} (\text{cgs})$	5.58 ± 0.01	5.54 ± 0.01

group, AA Dor and V1828 Aql, with a mass of 0.47 and $0.42 M_{\odot}$ respectively (Klepp & Rauch 2011; Almeida et al. 2012), should definitely be post-EHB stars (and this is particularly true for AA Dor that has been intensively studied by various teams). While for EPIC 216747137, due to its larger mass of ~ 0.62 , we can just say that it is close, and likely beyond, central helium exhaustion.

Among the 20 published HW Vir systems, only AA Dor, V1828 Aql, and EPIC 216747137 have effective temperatures near 40 kK , while all the others have T_{eff} between 25 and 35 kK , compatible with He-core burning (Wolz et al. 2018). Moreover, these three hotter HW Vir systems seem to follow a different relation in the $T_{\text{eff}}\text{--}\log y$ plane (Edelmann et al. 2003) respect to all the other HW Vir stars. The position of all the published HW Vir in a $T_{\text{eff}}\text{--}\log y$ plane can be seen in Wolz et al. (2018, fig. 5). Since the number of new HW Vir systems is rapidly increasing, with 25 new systems already spectroscopically confirmed and many more to come (Schaffenroth et al. 2019), the larger statistics will allow us to confirm or not that HW Vir stars follow two different sequences in the $T_{\text{eff}}\text{--}\log y$ plane.

The orbital period of EPIC 216747137, $\sim 0.161 \text{ d}$, and the mass of its dM companion, $\sim 0.11 M_{\odot}$, fit well with the period distribution and the companion mass distribution of the hot subdwarf binaries with a dM companion (Figs 7 and 8, Kupfer et al. 2015). However, in the preferred light-curve solution, the sdOB mass is unusually high ($0.62 M_{\odot}$). Such a high mass could result from post-AGB evolution, but this possibility is ruled out because it would imply a luminosity 10 times higher than observed. When we consider constraints from spectroscopy, light-curve solution and parallax, the mass must be between 0.47 and $0.67 M_{\odot}$. Hence a mass as low as $0.47 M_{\odot}$ cannot be ruled out, but it implies that the cool companion is significantly inflated. Although inflation in M dwarfs is not a well understood phenomenon (see e.g. Parsons et al. 2018), a strong inflation appears quite unlikely, and this is why we prefer the high-mass option.

A mass as high as $\sim 0.62 M_{\odot}$ provides a challenge for the hot subdwarf formation theories since the CE ejection channel struggles to form stars with a mass higher than ~ 0.47 , while the RLOF channel does not work for orbital periods shorter than $\sim 1 \text{ d}$ (see e.g. figs 10 and 12, respectively, Han et al. 2003).

Another interesting aspect of our results is that EPIC 216747137 is not synchronized. Among the other nine systems with published rotational velocities, only three of them are not synchronized (submitted, and references therein Schaffenroth et al. 2020), all of them being relatively young and not evolved (and with a BD candidate companion, but this might be related to a selection effect considering that it is easier to obtain high-resolution data when the companion is a BD), while the other six more evolved systems are all synchronized. The growing number of synchronized systems seems in contradiction with the prediction by Preece, Tout & Jeffery (2018) that synchronization time-scales are longer than the sdB lifetime.

Hot subdwarf stars are found in all stellar populations (Martin et al. 2017; Luo, Németh & Li 2020). EPIC 216747137 lies just 155 pc below the Galactic plane. This hints at thin disc membership.

In order to check this assumption, we carried out a kinematical investigation calculating Galactic trajectories in a Galactic potential (for details, see Appendix B). The Galactic orbit is almost perfectly circular and the binary orbits within (though close to) the solar circle (Fig. B1). Hence, we conclude that the binary belongs to the thin disc population, which is also confirmed by its position in the Toomre diagram (Fig. B2).

ACKNOWLEDGEMENTS

The K2 data presented in this paper was obtained from the Mikulski Archive for Space Telescopes (MAST). Space Telescope Science Institute is operated by the Association of Universities for Research in Astronomy, Inc., under NASA contract NAS5-26555. This paper uses observations made at the SAAO. The spectroscopic results are based on observations collected at the MPG/ESO 2.2-m telescope; at the 2.6-m NOT, operated jointly by Denmark, Finland, Iceland, Norway, and Sweden; and at the 6.5-m Magellan I telescope. RS acknowledges financial support from the INAF project on ‘Stellar evolution and asteroseismology in the context of the PLATO space mission’ (PI: S. Cassisi). VS is supported by the Deutsche Forschungsgemeinschaft, DFG through grant GE 2506/9-1. DK thanks the University of the Western Cape and the National Research Foundation of South Africa for financial support. We thank Jantje Freudenthal for support at the SAAO 1-m Elizabeth telescope, Michel Rieutord and an anonymous referee for useful comments. RS wishes to remember and thank Nicolò D’Amico, President of INAF, who suddenly passed away a few days before the submission of this article.

DATA AVAILABILITY

The data underlying this article will be shared on reasonable request to the corresponding author.

REFERENCES

- Alam S. et al., 2015, *ApJS*, 219, 12
 Allen C., Santillan A., 1991, *Rev. Mex. Astron. Astrofis.*, 22, 255
 Almeida L. A., Jablonski F., Tello J., Rodrigues C. V., 2012, *MNRAS*, 423, 478
 Auer L. H., Mihalas D., 1972, *ApJS*, 24, 193
 Bailer-Jones C. A. L., Rybizki J., Fousneau M., Mantelet G., Andrae R., 2018, *AJ*, 156, 58
 Baraffe I., Chabrier G., Barman T. S., Allard F., Hauschildt P. H., 2003, *A&A*, 402, 701
 Baran A. S., Bachulski S., Curylo M., 2016, *IAU Focus Meeting*, 29B, 497
 Beauchamp A., Wesemael F., Bergeron P., 1997, *ApJS*, 108, 559
 Brahm R., Jordán A., Espinoza N., 2017, *PASP*, 129, 034002
 Chabrier G., Baraffe I., 1997, *A&A*, 327, 1039
 Chambers K. C., et al., 2017, The Pan-STARRS release 1 (PS1) Survey - DR1 : II/349, available at <https://cdsarc.unistra.fr/viz-bin/cat/II/349>,
 Charpinet S. et al., 2011, *Nature*, 480, 496
 Charpinet S., Giammichele N., Zong W., Van Grootel V., Brassard P., Fontaine G., 2018, *Open Astron.*, 27, 112
 Claret A., Bloemen S., 2011, *A&A*, 529, A75
 Claret A., Cukanovaite E., Burdge K., Tremblay P. E., Parsons S., Marsh T. R., 2020, *A&A*, 634, A93
 Clausen D., Wade R. A., 2011, *ApJ*, 733, L42
 Clausen D., Wade R. A., Kopparapu R. K., O’Shaughnessy R., 2012, *ApJ*, 746, 186
 Copperwheat C. M., Marsh T. R., Dhillon V. S., Littlefair S. P., Hickman R., Gänsicke B. T., Southworth J., 2010, *MNRAS*, 402, 1824
 Wright E. L., et al., 2010, *AJ*, 140, 1868
 Drechsel H. et al., 2001, *A&A*, 379, 893
 Eastman J., Siverd R., Gaudi B. S., 2010, *PASP*, 122, 935
 Edelmann H., Heber U., Hagen H. J., Lemke M., Dreizler S., Napiwotzki R., Engels D., 2003, *A&A*, 400, 939
 Espinosa Lara F., Rieutord M., 2011, *A&A*, 533, A43
 Evans D. W. et al., 2018, *A&A*, 616, A4
 Fitzpatrick E. L., Massa D., Gordon K. D., Bohlin R., Clayton G. C., 2019, *ApJ*, 886, 108
 Fontaine G., Brassard P., Charpinet S., Green E. M., Randall S. K., Van Grootel V., 2012, *A&A*, 539, A12
 Fouqué P. et al., 2000, *A&AS*, 141, 313
 Fuhrmann K., 2004, *Astron. Nachr.*, 325, 3
 Geier S. et al., 2011, *ApJ*, 731, L22
 Giddings J. R., 1981, PhD thesis Univ. London
 Han Z., Podsiadlowski P., Maxted P. F. L., Marsh T. R., Ivanova N., 2002, *MNRAS*, 336, 449
 Han Z., Podsiadlowski P., Maxted P. F. L., Marsh T. R., 2003, *MNRAS*, 341, 669
 Han Z., Chen X., Lei Z., Podsiadlowski P., 2012, in Kilkeny D., Jeffery C. S., Koen C., eds, *ASP Conf. Ser. Vol. 452, Fifth Meeting on Hot Subdwarf Stars and Related Objects*. Astron. Soc. Pac., San Francisco, p. 3
 Heber U., 2016, *PASP*, 128, 966
 Heber U. et al., 2004, *A&A*, 420, 251
 Heber U., Irrgang A., Schaffenroth J., 2018, *Open Astron.*, 27, 35
 Henden A. A., Levine S., Terrell D., Welch D. L., 2015, in *American Astronomical Society Meeting Abstracts #225*. p. 336.16
 Hirsch H. A., 2009, PhD thesis, Friedrich-Alexander University Erlangen-Nürnberg
 Hubeny I., Hummer D. G., Lanz T., 1994, *A&A*, 282, 151
 Irrgang A., Wilcox B., Tucker E., Schiefelbein L., 2013, *A&A*, 549, A137
 Irrgang A., Kreuzer S., Heber U., Brown W., 2018, *A&A*, 615, L5
 Kelson D. D., 2003, *PASP*, 115, 688
 Kelson D. D., Illingworth G. D., van Dokkum P. G., Franx M., 2000, *ApJ*, 531, 159
 Klepp S., Rauch T., 2011, *A&A*, 531, L7
 Kramer M., Schneider F. R. N., Ohlmann S. T., Geier S., Schaffenroth V., Pakmor R., Roepke F. K., 2020, *A&A*, 642, A97
 Kupfer T. et al., 2015, *A&A*, 576, A44
 Kupfer T. et al., 2020, *ApJ*, 891, 45
 Kurucz R. L., 1996, in Adelman S. J., Kupka F., Weiss W. W., eds, *ASP Conf. Ser. Vol. 108, Model Atmospheres and Spectrum Synthesis*. Astron. Soc. Pac., San Francisco, p. 160
 Lawrence A. et al., 2007, *MNRAS*, 379, 1599
 Lindegren L. et al., 2018, *A&A*, 616, A2
 Lucy L. B., 1967, *Z. Astrophys.*, 65, 89
 Luo Y., Németh P., Li Q., 2020, *ApJ*, 898, 64
 Maíz Apellániz J., Weiler M., 2018, *A&A*, 619, A180
 Martin P., Jeffery C. S., Naslim N., Woolf V. M., 2017, *MNRAS*, 467, 68
 Maxted P. F. L., Heber U., Marsh T. R., North R. C., 2001, *MNRAS*, 326, 1391
 Napiwotzki R., Green P. J., Saffer R. A., 1999, *ApJ*, 517, 399
 Napiwotzki R., Karl C. A., Lisker T., Heber U., Christlieb N., Reimers D., Nelemans G., Homeier D., 2004, *Ap&SS*, 291, 321
 Onken C. A. et al., 2019, *PASA*, 36, e033
 Parsons S. G., Marsh T. R., Copperwheat C. M., Dhillon V. S., Littlefair S. P., Gänsicke B. T., Hickman R., 2010, *MNRAS*, 402, 2591
 Parsons S. G. et al., 2018, *MNRAS*, 481, 1083
 Pauli E. M., Napiwotzki R., Heber U., Altmann M., Odenkirchen M., 2006, *A&A*, 447, 173
 Pelisoli I., Vos J., Geier S., Schaffenroth V., Baran A. S., 2020, *A&A*, 642, A180
 Preece H. P., Tout C. A., Jeffery C. S., 2018, *MNRAS*, 481, 715
 Press W. H., Teukolsky S. A., Vetterling W. T., Flannery B. P., 1992, *Numerical Recipes in FORTRAN. The Art of Scientific Computing*, 2nd edn. Cambridge Univ. Press, Cambridge
 Ratzloff J. K. et al., 2020, *ApJ*, 890, 126
 Reed M. D. et al., 2018, *Open Astron.*, 27, 157
 Saffer R. A., Bergeron P., Koester D., Liebert J., 1994, *ApJ*, 432, 351
 Schaffenroth V., Geier S., Heber U., Kupfer T., Ziegerer E., Heuser C., Classen L., Cordes O., 2014, *A&A*, 564, A98

Schaffenroth V., Barlow B. N., Drechsel H., Dunlap B. H., 2015, *A&A*, 576, A123
 Schaffenroth V. et al., 2019, *A&A*, 630, A80
 Schaffenroth V. et al., 2020, *MNRAS*, preprint (arXiv:2011.10013)
 Schechter P. L., Mateo M., Saha A., 1993, *PASP*, 105, 1342
 Schlafly E. F., Finkbeiner D. P., 2011, *ApJ*, 737, 103
 Schlafly E. F., Meisner A. M., Green G. M., 2019, *ApJS*, 240, 30
 Schlegel D. J., Finkbeiner D. P., Davis M., 1998, *ApJ*, 500, 525
 Silvotti R. et al., 2014, *A&A*, 570, A130
 Silvotti R., Østensen R. H., Teltng J. H., 2020, preprint (arXiv:2002.04545)
 Soker N., 1998, *AJ*, 116, 1308
 Stark M. A., Wade R. A., 2003, *AJ*, 126, 1455

Teltng J., Østensen R., Reed M., Kjaerød F., Farris L., Baran A., Oreiro R., O'Toole S., 2014, in van Grootel V., Green E., Fontaine G., Charpinet S., eds, *ASP Conf. Ser. Vol. 481, 6th Meeting on Hot Subdwarf Stars and Related objects*. Astron. Soc. Pac., San Francisco, p. 287
 Tremblay P. E., Bergeron P., 2009, *ApJ*, 696, 1755
 von Zeipel H., 1924, *MNRAS*, 84, 665
 Wolf C. et al., 2018, *PASA*, 35, e010
 Wolz M. et al., 2018, *Open Astron.*, 27, 80
 Wood J. H., Saffer R., 1999, *MNRAS*, 305, 820

APPENDIX A: MCMC FITS OF THE SAAO BVR LIGHT CURVES

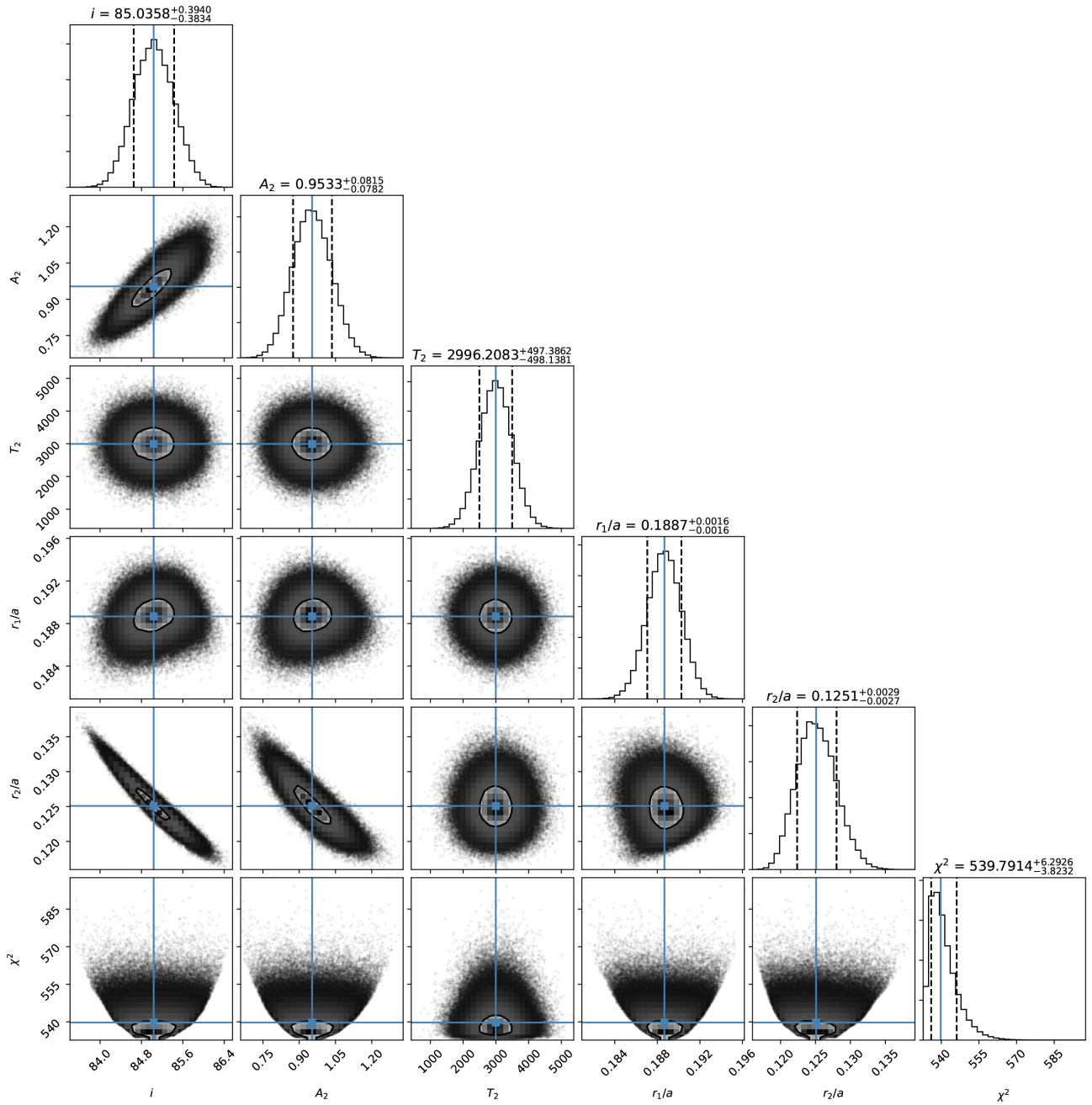


Figure A1. MCMC computations showing the degeneracy and the parameter errors of the *B*-band light-curve solutions.

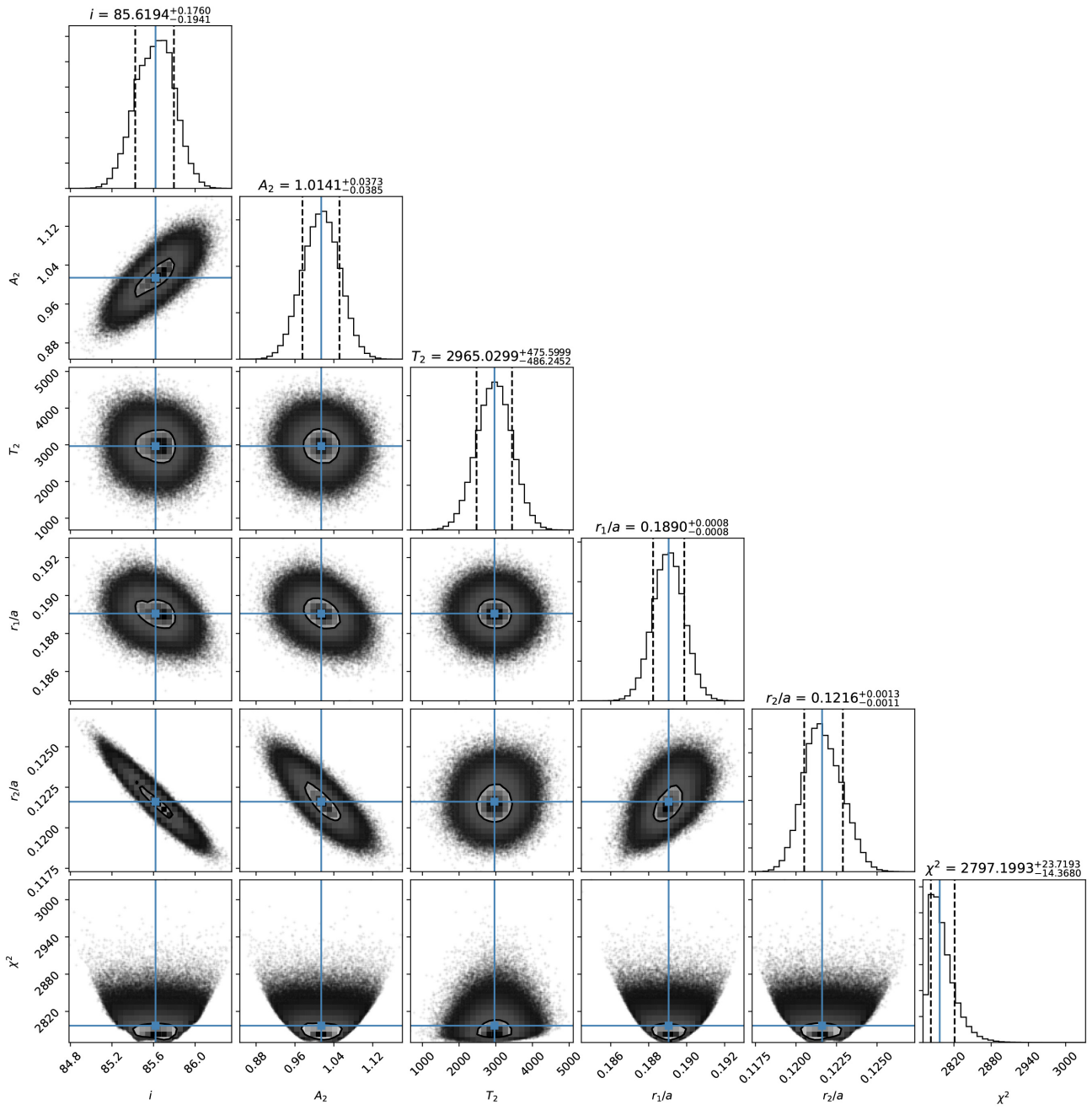


Figure A2. Same as Fig. A1, but for the V-band light curve.

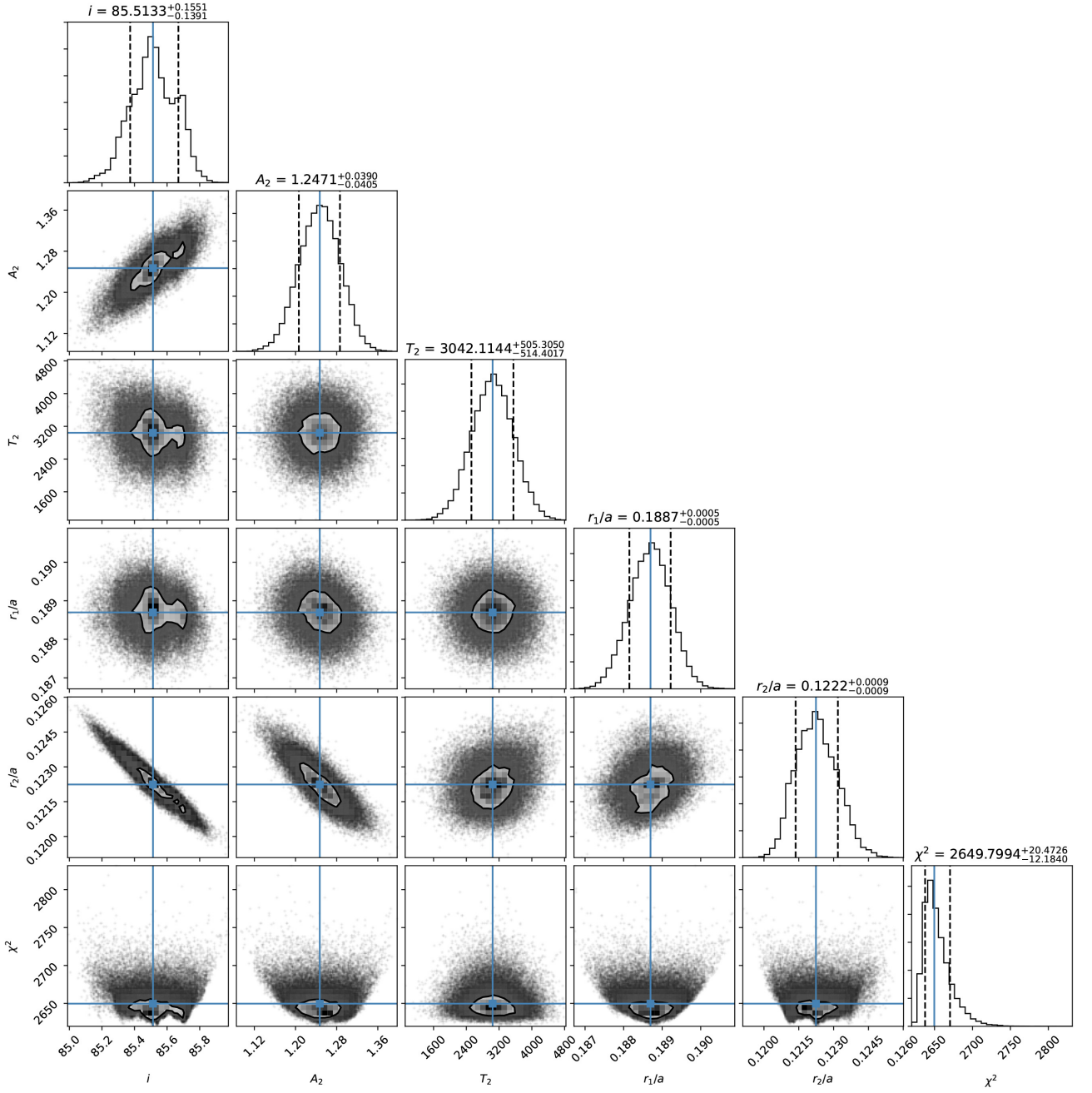


Figure A3. Same as Fig. A1, but for the R-band light curve.

APPENDIX B: KINEMATICS OF EPIC 216747137

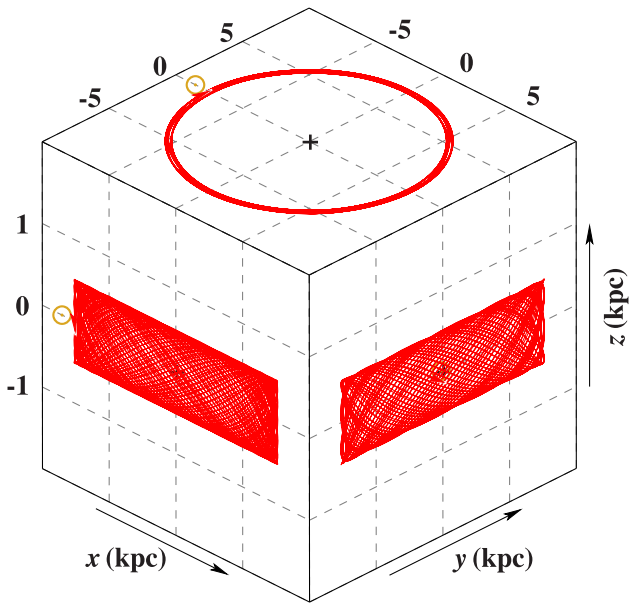


Figure B1. EPIC 216747137's 3D orbit in a Cartesian Galactic coordinate system. The centre of the Galaxy lies at the origin, the Sun (yellow circled dot) on the negative x -axis. The z -axis points to the Galactic north pole. Trajectories were computed back in time for 10 Gyr using a standard, axisymmetric model for the Galactic gravitational potential (an updated version of that of Allen & Santillan 1991, see Irrgang et al. 2013, for details). The shape of the orbit is almost circular, with vertical oscillations of a few hundred pc amplitude, typical for a thin-disc star (see e.g. Pauli et al. 2006).

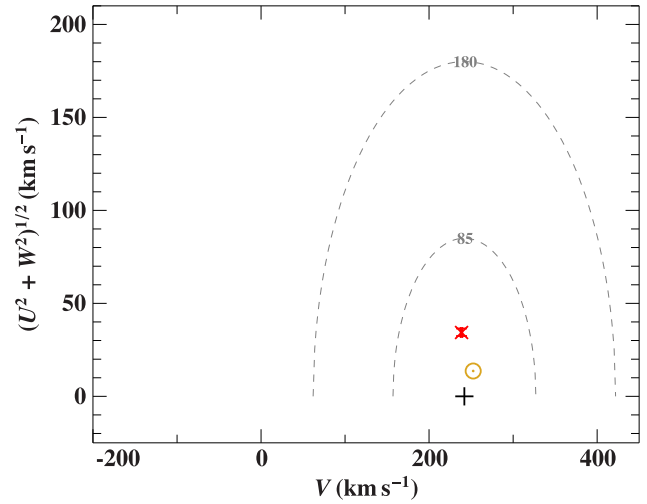


Figure B2. The position of EPIC 216747137 (red cross with 1σ error bars) in the Toomre diagram. The velocity component V is measured in the direction of the rotation of the Galaxy, U towards the Galactic centre, and W perpendicular to the plane. The yellow circled dot marks the position of the Sun. The local standard of rest (LSR) is marked by a plus sign. According to Fuhrmann (2004), the boundaries for thin and thick discs are located at 85 and 180 km s^{-1} , respectively (dashed circles centred around the LSR).

This paper has been typeset from a $\text{\TeX}/\text{\LaTeX}$ file prepared by the author.



Pulse Timing Discovery of a Three-day Companion to the Hot Subdwarf BPM 36430

Bryce A. Smith¹ , Brad N. Barlow¹ , Benjamin Rosenthal^{2,3} , J. J. Hermes³ , and Veronika Schaffenroth⁴ ¹Department of Physics and Astronomy, High Point University, High Point, NC 27268, USA; bsmith6@highpoint.edu²Friends Seminary, 222 E16th Street, New York, NY 10003, USA³Department of Astronomy, Boston University, 725 Commonwealth Avenue, Boston, MA 02215, USA⁴Institute for Physics and Astronomy, University of Potsdam, Karl-Liebknecht-Str. 24/25, D-14476 Potsdam, Germany

Received 2022 August 9; revised 2022 September 19; accepted 2022 September 19; published 2022 November 2

Abstract

Hot subdwarf B stars are core-helium-burning objects that have undergone envelope stripping, likely by a binary companion. Using high-speed photometry from the Transiting Exoplanet Survey Satellite, we have discovered the hot subdwarf BPM 36430 is a hybrid sdBV_{rs} pulsator exhibiting several low-amplitude *g*-modes and a strong *p*-mode pulsation. The latter shows a clear, periodic variation in its pulse arrival times. Fits to this phase oscillation imply BPM 36430 orbits a barycenter approximately 10 light-seconds away once every 3.1 days. Using the CHIRON echelle spectrograph on the CTIO 1.5 m telescope, we confirm the reflex motion by detecting a radial-velocity variation with semiamplitude, period, and phase in agreement with the pulse timings. We conclude that a white dwarf companion with minimum mass of $\approx 0.42 M_{\odot}$ orbits BPM 36430. Our study represents only the second time a companion orbiting a pulsating hot subdwarf or white dwarf has been detected from pulse timings and confirmed with radial velocities.

Unified Astronomy Thesaurus concepts: [Binary stars \(154\)](#); [Stellar pulsations \(1625\)](#)

1. Introduction

Hot subdwarf B (sdB) stars are evolved, low-mass objects believed to have helium-burning cores and thin hydrogen atmospheres. Their properties place them on the far blue end of the horizontal branch, known as the extreme horizontal branch. Most sdB stars have masses around $0.47 M_{\odot}$ (Fontaine et al. 2012). Their effective temperatures range from $T_{\text{eff}} = 20,000\text{--}40,000$ K, and their surface gravities range from $\log g = 4.5\text{--}6.5$ (Heber 2016).

The red giant progenitors of hot subdwarfs experienced significant mass loss near the tip of the red giant branch. The majority of their hydrogen envelope was expelled, leaving behind only the helium-burning core and a thin hydrogen envelope. This hydrogen layer is too thin to sustain nuclear burning, and so hot subdwarfs will directly enter the white dwarf cooling sequence upon core-helium exhaustion. Han et al. (2002, 2003) proposed several Roche-lobe-overflow (RLOF) and common-envelope (CE) evolution channels that can produce hot subdwarfs through binary interactions. Pelisoli et al. (2020) recently presented strong observational evidence that *all* hot subdwarf B stars must have been formed in binary systems. In most cases, the companions survive the RLOF and CE interactions, and studying their properties can give us important insight into the formation channels of these unique systems and help tune model parameters like envelope-binding energy, common-envelope-ejection efficiency, and angular momentum transfer (e.g., Schaffenroth et al. 2022). Hot subdwarf binaries are most commonly found from radial-velocity variations or flux changes in their light curves caused by eclipses, the reflection effect, ellipsoidal modulations, and/or Doppler beaming (e.g., Barlow et al. 2022).

Some hot subdwarf B stars exhibit pulsations, and they can be classified into three basic groups: slow gravity-mode

(*g*-mode) pulsators (sdBV_s stars), rapid pressure-mode (*p*-mode) pulsators (sdBV_r stars), and hybrid pulsators (sdBV_{rs} stars). Lynas-Gray (2021) presented an overview of their properties and efforts to analyze them with asteroseismology.

Some sdBV pulsations are strong and stable enough to be used as precise ticks of a clock. Measuring their arrival times and comparing them to an ephemeris of predicted times allows one to constrain secular evolution rates of the star or look for signs of orbital reflex motion due to a nearby companion (Hermes 2018). In the case of orbital reflex motion, pulses will be delayed when the sdBV is on the far side of its orbit, and they will be advanced when the sdBV is on the near side. The orbital period, radial-velocity semiamplitude, and minimum mass of the companion can be determined through precise measurements of these timing variations. Barlow et al. (2011) and Otani et al. (2018) used this method to find previously unknown companions to sdBV_r stars. The former was the first and only time that pulse timing results were confirmed using radial-velocity measurements for a compact star.

BPM 36430 (Gaia EDR3 5371215147518355328; $G = 12.8$ mag; TIC 273218137) is a newly discovered sdBV_{rs} star displaying weak *g*-mode pulsations and a strong, radial-mode pulsation that is well suited for pulse timing studies (Krzyszinski & Balona 2022). Using Transiting Exoplanet Survey Satellite (TESS) photometry, we measured precise pulse arrival times of the dominant 342 s pulsation period. We also monitored the radial velocities of BPM 36430 with the CHIRON echelle spectrograph. Here, we present both sets of observations and show that BPM 36430 displays orbital reflex motion every 3.1 days due to a nearby companion.

2. Time-series Photometry

2.1. TESS Observations

The TESS provides extended time-series photometry for millions of objects across the entire sky (Ricker et al. 2014). BPM 36430 was observed by TESS in sector 10 (at 2 minutes



Original content from this work may be used under the terms of the [Creative Commons Attribution 4.0 licence](#). Any further distribution of this work must maintain attribution to the author(s) and the title of the work, journal citation and DOI.

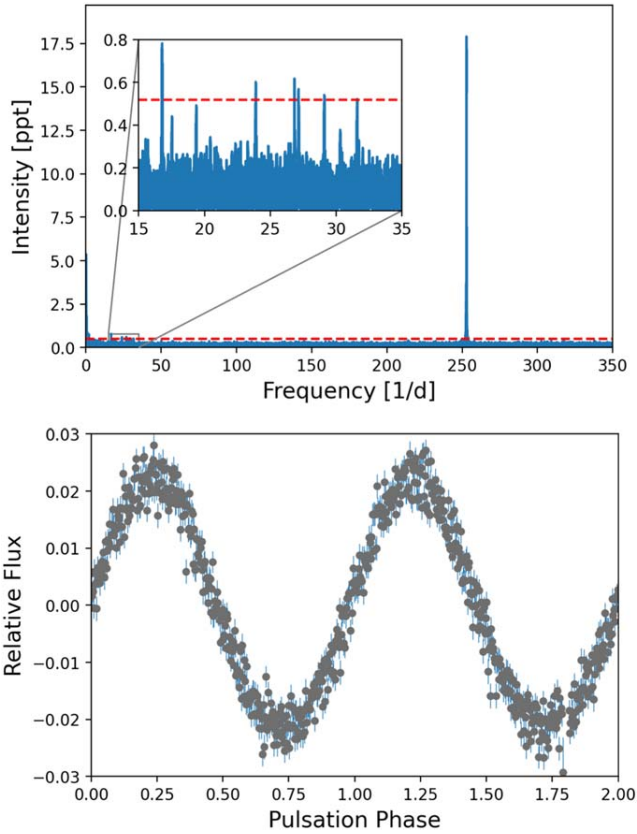


Figure 1. Lomb–Scargle periodogram of the full, 2 minutes cadence TESS light curve of BPM 36430 showing a strong radial-mode pulsation and an inset of g -mode pulsations (top). A dashed red line denotes the 5.1σ level, which corresponds to a false alarm probability of 0.1%. Also shown is the 20 s cadence light curve phase-folded on the dominant pulsation mode at 341.6734767 s (bottom).

cadence) and sector 37 (at 20 s cadence) through guest investigator programs G011113 and G03221, respectively. The sector 37 data are also available in their stacked 2 minutes cadence form. We used the Mikulski Archive for Space Telescopes⁵ (MAST) to download the calibrated light curves, which were automatically reduced and corrected for instrumental systematics using the TESS data processing pipeline⁶ (Jenkins et al. 2016). For the flux we used the `PDCSAP_FLUX` values, which are simple aperture photometry (`SAP_FLUX`) values corrected for systematic trends common to all stars on that chip. The sector 10 and 37 light curves of BPM 36430 have `CROWSAP` values of 0.33 and 0.31, respectively, and are moderately contaminated with light from other stars in the extraction aperture. Consequently, the measured amplitudes of any pulsations are diluted by background light. This dilution should not affect the results of this study, which relies on frequency and phase measurements.

We calculated the Lomb–Scargle periodogram of both the 20 s and 2 minutes cadence light curves using the SciPy library (Virtanen et al. 2020). As shown in the top panel of Figure 1, BPM 36430 is a hybrid sdBV_{ts} star showing both g - and p -mode pulsations. We used an iterative prewhitening process to locate and measure all pulsation peaks. Table 1 presents the results of this analysis using the combined 2 minutes cadence light curve.

⁵ <https://archive.stsci.edu/missions-and-data/tess>

⁶ <https://heasarc.gsfc.nasa.gov/docs/tess/pipeline.html>

Table 1
Pulsation Frequencies from 2 Minutes Cadence Data

Frequency (day^{-1})	Amplitude		Comments
	(ppt)	(σ)	
16.791015(60)	0.75(11)	6.9	g -mode
17.535(28)	0.46(12)	4.2	g -mode
19.378(33)	0.53(13)	4.9	g -mode
23.8973(21)	0.66(12)	6.0	g -mode
26.8361(37)	0.60(14)	5.6	g -mode
29.098(28)	0.65(11)	6.0	g -mode
31.596(76)	0.53(12)	4.9	g -mode
252.8730086(26)	18.61(13)	171.0	p -mode, likely radial

We find four peaks consistent with g -mode pulsations that have amplitudes above the 5.1σ threshold, which corresponds to a false alarm probability of 0.1% (Baran & Koen 2021). Additionally, we find three other g -modes that are below this threshold but appear above 4σ in each of the sector 10 and sector 37 light-curve periodograms, when analyzed individually. Altogether, we report seven independent frequencies consistent with g -mode pulsations, all of which have amplitudes between roughly 0.45–0.75 ppt.

The overall variability of BPM 36430 is dominated by a single, 342 s oscillation mode with amplitude around 2.2%.⁷ Although we cannot provide definitive classification of the pulsation mode, we note that its period and large amplitude are quite similar to known radial p -modes in other sdBV pulsators like CS 1246 (Barlow et al. 2010) and Balloon 090100001 (Baran et al. 2008).

2.2. $O-C$ Diagram

BPM 36430 is well suited for pulse timing analysis due to its simple frequency spectrum being dominated by a single pulsation. In order to quantify the stability of the main pulsation mode, we divided the 20 s TESS light curve into subsets using a K-means clustering algorithm⁸ and targeted each epoch to be roughly 0.2 days long. Data subsets were generated so that none spanned the large download gap in the middle of the sector. We did not include the 2 minutes cadence light curve in this analysis given its slower sampling rate, which would lead to less reliable timing due to phase smearing. We used linear least-squares regressions to measure the pulsation phase within each subset of the 20 s cadence light curve. We plot relative phase shifts in an observed-minus-calculated ($O-C$) diagram, shown in Figure 2.

The pulse timings of BPM 36430 exhibit a strong, sinusoidal phase oscillation once every 3.1 days, with a semi-amplitude of around 10 s. Although some sdBV stars do show intrinsic amplitude and even phase modulation in their pulsations (Kilkenny 2010; Zong et al. 2018), the simplest explanation for the observed phase oscillation is reflex motion of the sdB due to a nearby companion in a circular orbit. In this case, the $O-C$ diagram reveals light-travel-time variations in the pulsations as the sdBV orbits the barycenter of the binary. When the sdBV is on the side of its orbit closest to Earth, we detect its pulses 10 s earlier than we do on average, and similarly we detect a 10 s delay when it is on the far side of its orbit.

⁷ Due to phase smearing, the amplitude of the 342 s pulsation appears lower in the 2 minutes cadence TESS light curve.

⁸ <https://github.com/dstein64/kmeans1d>

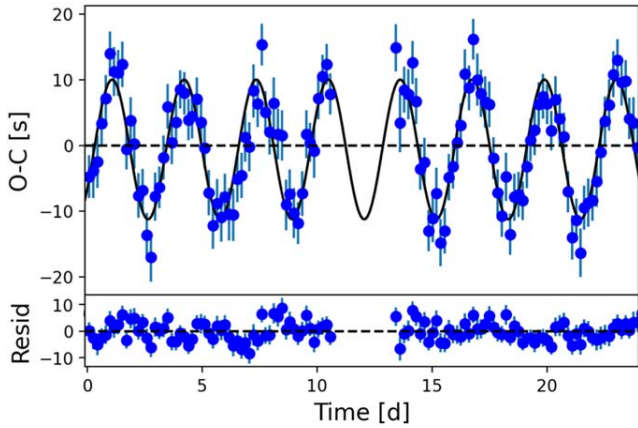


Figure 2. $O - C$ diagram (top) constructed from pulse timing measurements of roughly 0.2 day subsets of the 342 s pulsation period, along with residuals after subtracting the best-fitting sinusoid from the data (bottom).

2.3. Pulse Timing Analysis

Since the TESS light curve is essentially continuous with a simple window function, we can model the entire light curve simultaneously with a phase-dependent sinusoidal function, instead of dividing the data into chunks to analyze the pulsation phases and generate an $O - C$ diagram. As previously discussed, the Lomb–Scargle periodogram of the TESS light curve shows a strong pulsation at 342 s (top panel, Figure 3). The phase oscillations found in the $O - C$ analysis should be encoded in the periodogram as a splitting of the main pulsation peak.

To look for and quantify this feature, we subtracted from the full light curve the best-fitting sinusoid with constant amplitude, period, and phase. Subtracting the main pulsation peak revealed two smaller peaks equidistant from the original pulsation signal (middle panel, Figure 3). While such peaks could be indicative of rotational splitting, the $O - C$ diagram already gives us reason to believe there is a phase oscillation inherent in the pulsation. Therefore, we assume that the equidistant splittings encode this phase oscillation. We fitted a phase-modulated sinusoid to the data to determine the pulsational and orbital parameters of the potential binary system simultaneously using the expression:

$$f(t) = A_p \sin\left(\frac{2\pi t}{P_p} + \phi(t)\right), \quad (1)$$

where $\phi(t)$, the new time-variable phase due to the orbital reflex motion, is given by

$$\phi(t) = \phi_p + 2\pi \left(\frac{A_b}{P_b}\right) \sin\left(\frac{2\pi t}{P_b} + \phi_b\right), \quad (2)$$

where A_b is the light travel time across the radius of the orbit of BPM 36430, P_b is the period of the orbit, and ϕ_p and ϕ_b are phases for the pulsation and binary orbit, respectively. When this phase-modulated form of the sinusoid was subtracted from the full light curve, only noise remained (bottom panel, Figure 3). We carried out the above analysis on both the 20 s cadence light curve (sector 37) and the 2 minutes cadence light curve (sectors 10 + 37).

We ran Markov Chain Monte Carlo (MCMC) iterations to determine parameter uncertainties using `emcee`, an implementation of an MCMC sampler that uses a number of parallel chains

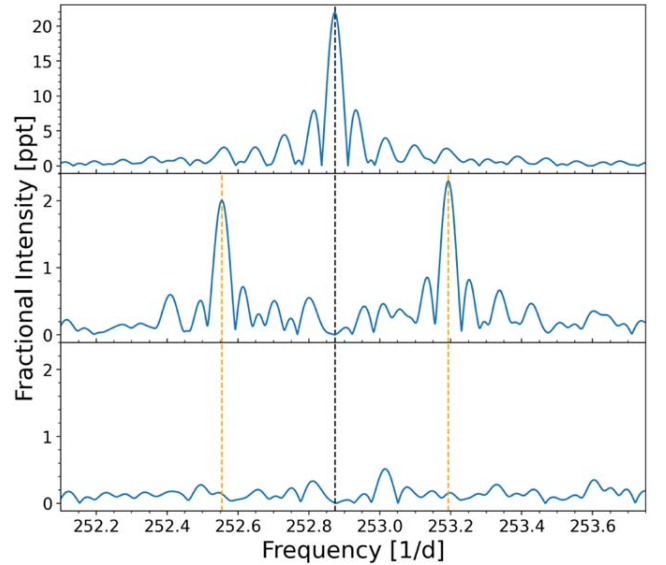


Figure 3. Lomb–Scargle periodogram of the 20 s cadence TESS light curve of BPM 36430, zoomed in on the dominant pulsation mode (top). Also shown are the periodograms after subtracting a fixed sinusoid (middle) and a phase-modulated sinusoid from the data (bottom). The dashed vertical lines mark position of the pulsation mode (black) and the two equidistant splittings (orange) arising from the orbital frequency of 0.32 cycles per day.

to explore the solution space. Our MCMC sampling used 100,000 steps with 99 walkers (Foreman-Mackey et al. 2019). Once the distribution was sampled, the best-fitting parameters and their uncertainties were determined. Our MCMC corner plots all have normally distributed posterior distributions, indicating that we did not have significant covariances in our fit.

As shown in Table 2, the results from fitting the 20 s and 2 minutes cadence light curves agree with one another within the uncertainties. The only exception is the pulsation amplitude, which, due to phase smearing, is reduced by 19.1% and 0.6% in the 2 minutes and 20 s light curves, respectively. After inflating these amplitudes by factors of 1.24 and 1.006 to correct for smearing (Baldry 1999), we derive consistent amplitudes of $A_p = 2.33\% \pm 0.12\%$ and $A_p = 2.226\% \pm 0.013\%$ for the 2 minutes and 2 s light curves, respectively.

If the variation in the arrival times of the pulses is interpreted as circular reflex motion, the phase oscillation period and strength give us the orbital parameters. Adopting the more precise values from the 2 minutes light-curve analysis, we measure the period and radius of the sdB orbit to be 3.12465 ± 0.00018 days and 9.7 ± 0.4 light-seconds, respectively. It is possible that the star could exhibit internal variations leading to oscillatory pulse timing variations without the need for an orbiting companion (e.g., Dalessio et al. 2013; Zong et al. 2016). To confirm binarity, radial-velocity monitoring is required. Under the assumption of orbital reflex motion, our pulse timing results predict that the hot subdwarf should show a $K_{\text{sdB}} = 67.7 \pm 2.9$ km s⁻¹ radial-velocity variation with a 3.1 days period.

3. Time-resolved Spectroscopy

3.1. CHIRON Observations

In order to confirm orbital reflex motion as the cause of the pulse-arrival-time variations, we obtained 25 high-resolution spectra ($R = 28,000$) of BPM 36430 in 2021 and 2022 using

Table 2
Best-fitting Parameters to Equation (1) from Photometry

Parameter	Value from 20 s Data	Value from 2 Minutes Data	Unit	Comments
A_p	2.213 ± 0.013	1.88 ± 0.10	%	Pulsation semi-amplitude ^a
P_p	341.673 ± 0.002	341.673475 ± 0.000003	s	Pulsation period
ϕ_p	5.126 ± 0.006	5.114 ± 0.008	radians	Pulsation phase ^b
A_b	10.7 ± 0.5	9.7 ± 0.4	s	Phase oscillation semi-amplitude
P_b	3.132 ± 0.009	3.12465 ± 0.00018	days	Phase oscillation period
ϕ_b	1.52 ± 0.04	1.58 ± 0.06	radians	Phase oscillation phase ^b

Notes.

^a Pulsation amplitude in 2 minutes cadence data suffers phase smearing.

^b Phase at $\text{BJD}_{\text{TDB}} = 2459320.485462$.

the fiber-fed CHIRON echelle spectrograph on the 1.5 m SMARTS telescope at the Cerro Tololo Inter-American Observatory (Tokovinin et al. 2013). All spectra covered the wavelength range 4500–8360 Å and were exposed for exactly 1367 s, or four cycles of the 342 s pulsation. This specific integration time was chosen to insure that the physical expansion and contraction of the star during each pulse did not influence our radial-velocity measurements. Data were reduced using a customized reduction pipeline described in Tokovinin et al. (2013), which is run by members of the RECONS team⁹ at Georgia State University.

3.2. Radial Velocity Curve

The He I absorption line at 5875 Å was the only spectral feature with high enough signal-to-noise to use for measuring radial velocities. While H α and H β were also visible, their profiles each spanned multiple echelle orders, and so they did not produce reliable results. We wrote a custom Python code that used SciPy’s `curve_fit` routine (Virtanen et al. 2020) to fit inverse Gaussians to the absorption profiles. Individual radial velocities were calculated using the Doppler shift from the accepted NIST¹⁰ value. The RV semi-amplitude of the sdB was determined by using the same `curve_fit` function to fit a sine wave to the velocities. The RV curve demonstrated clear orbital reflex motion with a period $P_b = 3.12458 \pm 0.00012$ day and semi-amplitude of $K_{\text{sdB}} = 69.6 \pm 0.6 \text{ km s}^{-1}$. These values agree with the results of our light-curve analysis within their 1σ uncertainties. Figure 4 presents the RV curve phase-folded over the orbital period, and Table 3 shows the best-fitting parameters.

4. Nature of the Hidden Companion

In order to determine the nature of the companion in BPM 36430, we must first confirm the status of the primary star as a hot subdwarf and constrain its mass. Unfortunately, we do not possess an identification spectrum to model with synthetic spectra, which is the easiest way to derive the effective temperature and surface gravity. However, we can still measure these parameters, along with the radius R and luminosity L , by fitting the spectral energy distribution (SED) of the target with model spectra and combining the results of this fit with the distance constrained by its Gaia parallax. Full details of our SED fitting method are presented by Heber et al. (2018) and Irrgang et al. (2021). An analysis of several well-studied sdB binaries

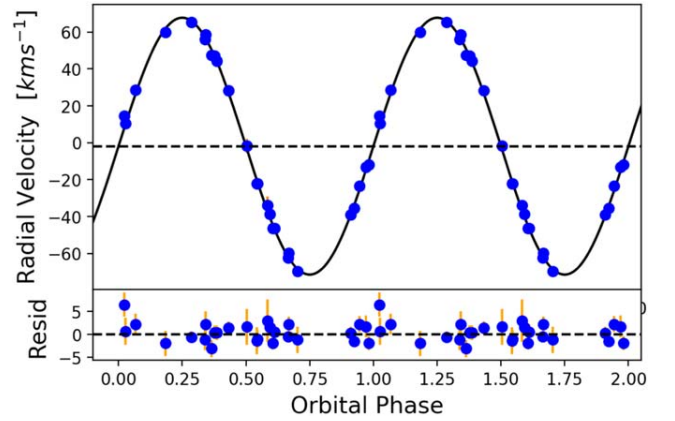


Figure 4. Radial-velocity curve of the sdBV primary in BPM 36430 (top). Residuals after subtracting the best-fitting sinusoid are also shown (bottom).

Table 3
Best-fitting Binary Parameters from Spectroscopy

Parameter	Value Uncertainty	Unit	Comments
P_b	3.12458 ± 0.00012	Days	Orbital period
K_{sdB}	69.6 ± 0.6	km s^{-1}	sdB RV semi-amplitude
γ	-1.9 ± 0.4	km s^{-1}	Systemic velocity
f	0.109 ± 0.003	M_{\odot}	Binary mass function

with white dwarf and low-mass main-sequence companions by Schaffenroth et al. (2022) shows that the SED determines effective temperature quite reliably for hot subdwarfs with $T_{\text{eff}} < 32,000 \text{ K}$.

Figure 5 and Table 4 present the results of our SED fitting, which confirm that the primary star in BPM 36430 is likely an sdB. We find a surface temperature $T_{\text{eff}} \approx 29,400 \text{ K}$, radius of $R \approx 0.2 R_{\odot}$, and luminosity of $L \approx 26 L_{\odot}$. We are unable to calculate masses from these values since we lack a measured $\log g$ from spectroscopy. However, we note that there are several sdBV stars that are dominated by a single pulsation mode quite similar in period and strength to that of BPM 36430, and they all cluster tightly in the $\log g - T_{\text{eff}}$ plane, near $T_{\text{eff}} \approx 29,000 \text{ K}$ and $\log g \approx 5.45$. Such stars include CS 1246 (Barlow et al. 2010), Balloon 090100001 (Oreiro et al. 2004), RAT0455+1305 (Baran & Fox-Machado 2010), J08069+1527 (Baran et al. 2011), and five other unpublished sdBVs (Bradshaw et al., 2022, private communication). If we assume a typical surface gravity for these similar pulsating hot subdwarfs ($\log g = 5.45$), we derive an sdB mass near $0.40 M_{\odot}$. This mass, combined with the orbital period P_b and sdB RV semi-amplitude K_{sdB} , results in a companion mass

⁹ <http://recons.org/>

¹⁰ <http://physics.nist.gov>

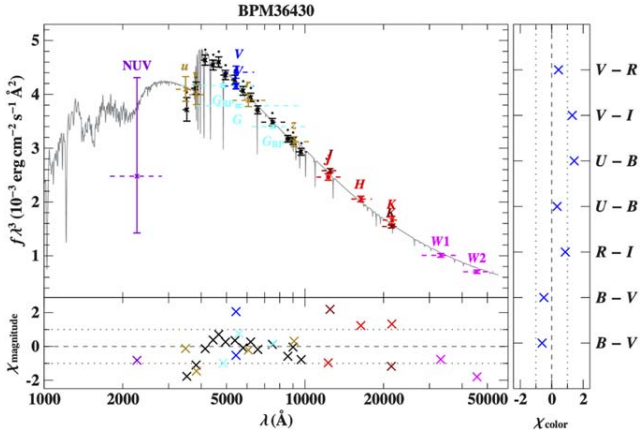


Figure 5. Spectral energy distribution of BPM 36430 and our model fit, which shows that a $\approx 29,000$ K sdB star dominates the light from the system.

Table 4
Best-fitting Parameters from the SED Modeling

Parameter	68% Conf. Interval
Color excess $E(44-55)$	$0.057^{+0.008}_{-0.008}$ mag
Angular diameter $\log(\Theta)$ (rad)	$-10.775^{+0.010}_{-0.011}$
Parallax ϖ (Gaia, RUWE = 0.80)	1.88 ± 0.04 mas
Effective temperature T_{eff}	29400^{+1100}_{-900} K
Surface gravity $\log(g)$ (cm s^{-2}); fixed	5.45
Radius $R = \Theta/(2\varpi)$	$0.198^{+0.007}_{-0.006}$ R_{\odot}
Mass $M = gR^2/G$	0.40 ± 0.03 M_{\odot}
Luminosity = L/L_{\odot}	26^{+5}_{-4}
Gravitational redshift $v_{\text{grav}} = GM/(Rc)$	$1.29^{+0.05}_{-0.05}$ km s^{-1}

of $m \sin i \approx 0.42 M_{\odot}$ orbiting at a separation distance of $a \sin i \approx 8.4 R_{\odot}$. Without eclipses, we do not know the orbital inclination angle and are limited to only computing minimum values for the separation distance and companion mass.

There are several reasons that we believe the companion is a white dwarf. First, the period and companion mass are much more consistent with those of known sdB+WD systems. Schaffenroth et al. (2022) shows that our sdB and companion masses fall directly in the middle of the observed distributions for sdB+WD binaries, and that our 3.1 days orbital period is much longer than those observed in sdB+dM/BD binaries. Second, if the companion were a main-sequence star with a mass of $0.42 M_{\odot}$ or greater, we would expect to see an infrared excess. Our SED shows no such excess and is consistent with a single sdB star (Figure 5). Finally, if the companion star were a late-type main-sequence star, we would expect to see a reflection effect as a signal in the periodogram, with peaks at both the orbital frequency and possibly its first harmonic. The amplitude at the orbital frequency would be $\approx 1\%$, several times above our detection limit (see Figure 15 from Schaffenroth et al. 2022). We see neither of these signals in the 2 minutes cadence or 20 s cadence light-curve periodograms.

With such a short period and separation distance, BPM 36430 likely formed through the stable RLOF+CE channel presented by Han et al. (2002, 2003), if it is truly a sdB+WD binary. In this scenario, two main-sequence stars existed in a binary. The more massive star evolved to the red giant stage first. It filled its Roche lobe, transferred mass, and then became the white dwarf. Then, the less-massive main-sequence star (the progenitor to the sdB we

see today) evolved to become a red giant. It began unstable RLOF mass transfer to the white dwarf star. A common envelope formed, which brought the stars closer together. Once the common envelope was ejected, this left behind an sdB star with a white dwarf companion in a tight orbit. This model predicts that the sdB and companion would have similar masses, which is the case for a $0.40 M_{\odot}$ sdB orbited every 3.1 days by a $>0.42 M_{\odot}$ companion (Han et al. 2002, 2003).

5. Summary

Using 2 minutes and 20 s cadence data from TESS, we have discovered hybrid g - and p -mode pulsations in the sdB star BPM 36430. Its photometric variations are dominated by a single pulsation mode with a period of 342 s and amplitude around 2%. From a pulse timing analysis, we find a clear, 3.1 days periodic variation in the arrival times of this signal. We interpreted the cause of this variation to be orbital reflex motion. To confirm this we obtained spectroscopic observations with the CHIRON echelle spectrograph and performed a radial-velocity analysis. The orbital period and RV semiamplitude derived from the photometric phase delay via an $O-C$ analysis and our spectroscopic RV analysis are consistent within 1σ , confirming that the variation in the pulsation arrival timing is due to orbital reflex motion. Given the period of the system and lack of infrared excess, the companion is most likely a white dwarf.

Our results provide additional evidence of the practicality of using pulse timing measurements to uncover companions to hot subdwarfs. It marks only the second time for which a hot subdwarf binary found via pulse timings has been confirmed using RV measurements. Uncovering additional similar systems with pulse timing and other methods will help further constrain the binary population synthesis models producing these enigmatic objects. The sensitivity of the pulse timing method to low-mass companions brings the exciting opportunity to find substellar and even planetary companions to hot subdwarfs, although follow-up RV measurements are a necessity for confirming any such discoveries.

B.B. and B.S. acknowledge financial support from NASA grant 80NSSC21K0364. J.J.H. acknowledges financial support from TESS Guest Investigator Programs 80NSSC20K0592 and 80NSSC22K0737. J.J.H. would also like to thank the Maria Mitchell Observatory, as well as coordination from the 2021 RISE program at Boston University. V.S. was funded by the Deutsche Forschungsgemeinschaft under grant GE2506/9-1. B.B. and B.S. also acknowledge Berggasthof Eckbauer for providing good space to have discussions about this manuscript. B.S. would like to personally acknowledge Bean Foster's Cafe in Golden, CO, for providing a good space to work on this manuscript.

This research made use of `Lightkurve`, a Python package for Kepler and TESS data analysis (Lightkurve Collaboration et al. 2018). This paper includes data collected by the TESS mission, which are publicly available from the Mikulski Archive for Space Telescopes (MAST). Funding for the TESS mission is provided by NASA's Science Mission directorate.

ORCID iDs

Bryce A. Smith <https://orcid.org/0000-0002-5717-2538>
 Brad N. Barlow <https://orcid.org/0000-0002-8558-4353>
 Benjamin Rosenthal <https://orcid.org/0000-0001-9526-4436>
 J. J. Hermes <https://orcid.org/0000-0001-5941-2286>
 Veronika Schaffenroth <https://orcid.org/0000-0001-6339-6768>

References

- Baldry, I. K. 1999, PhD thesis, Univ. Sydney, Australia
- Baran, A., & Fox-Machado, L. 2010, *Ap&SS*, 329, 193
- Baran, A., Pigulski, A., & O’Toole, S. J. 2008, *MNRAS*, 385, 255
- Baran, A. S., Gilker, J. T., Reed, M. D., et al. 2011, *MNRAS*, 413, 2838
- Baran, A. S., & Koen, C. 2021, *AcA*, 71, 113
- Barlow, B. N., Corcoran, K. A., Parker, I. M., et al. 2022, *ApJ*, 928, 20
- Barlow, B. N., Dunlap, B. H., Clemens, J. C., et al. 2010, *MNRAS*, 403, 324
- Barlow, B. N., Dunlap, B. H., & Clemens, J. C. 2011, *ApJL*, 737, L2
- Dalessio, J., Sullivan, D. J., Provencal, J. L., et al. 2013, *ApJ*, 765, 5
- Fontaine, G., Brassard, P., Charpinet, S., et al. 2012, *A&A*, 539, A12
- Foreman-Mackey, D., Farr, W., Sinha, M., et al. 2019, *JOSS*, 4, 1864
- Han, Z., Podsiadlowski, P., Maxted, P. F. L., & Marsh, T. R. 2003, *MNRAS*, 341, 669
- Han, Z., Podsiadlowski, P., Maxted, P. F. L., Marsh, T. R., & Ivanova, N. 2002, *MNRAS*, 336, 449
- Heber, U. 2016, *PASP*, 128, 082001
- Heber, U., Irrgang, A., & Schaffenroth, J. 2018, *OAsT*, 27, 35
- Hermes, J. J. 2018, in *Handbook of Exoplanets*, ed. H. J. Deeg & J. A. Belmonte (New York: Springer International), 6
- Irrgang, A., Geier, S., Heber, U., et al. 2021, *A&A*, 650, A102
- Jenkins, J. M., Twicken, J. D., McCauliff, S., et al. 2016, *Proc. SPIE*, 9913, 99133E
- Kilkenny, D. 2010, *Ap&SS*, 329, 175
- Krziesinski, J., & Balona, L. A. 2022, *A&A*, 663, A45
- Lightkurve Collaboration, Cardoso, J. V. d. M., Hedges, C., et al. 2018, *Lightkurve: Kepler and TESS time series analysis in Python*, Astrophysics Source Code Library, ascl:1812.013
- Lynas-Gray, A. E. 2021, *FrASS*, 8, 19
- Oreiro, R., Ulla, A., Pérez Hernández, F., et al. 2004, *A&A*, 418, 243
- Otani, T., Oswald, T. D., Lynas-Gray, A. E., et al. 2018, *ApJ*, 859, 145
- Pelisoli, I., Vos, J., Geier, S., Schaffenroth, V., & Baran, A. S. 2020, *A&A*, 642, A180
- Ricker, G. R., Winn, J. N., Vanderspek, R., et al. 2014, *JATIS*, 1, 014003
- Schaffenroth, V., Pelisoli, I., Barlow, B. N., Geier, S., & Kupfer, T. 2022, arXiv:2207.02001
- Tokovinin, A., Fischer, D. A., Bonati, M., et al. 2013, *PASP*, 125, 1336
- Virtanen, P., Gommers, R., Oliphant, T. E., et al. 2020, *NatMe*, 17, 261
- Zong, W., Charpinet, S., Fu, J.-N., et al. 2018, *ApJ*, 853, 98
- Zong, W., Charpinet, S., Vauclair, G., Giammichele, N., & Van Grootel, V. 2016, *A&A*, 585, A22



A hot subdwarf–white dwarf super-Chandrasekhar candidate supernova Ia progenitor

Ingrid Pelisoli^{1,2}✉, P. Neunteufel³, S. Geier¹, T. Kupfer^{4,5}, U. Heber⁶, A. Irrgang⁶, D. Schneider⁶, A. Bastian¹, J. van Roestel⁷, V. Schaffenroth¹ and B. N. Barlow⁸

Supernovae Ia are bright explosive events that can be used to estimate cosmological distances, allowing us to study the expansion of the Universe. They are understood to result from a thermonuclear detonation in a white dwarf that formed from the exhausted core of a star more massive than the Sun. However, the possible progenitor channels leading to an explosion are a long-standing debate, limiting the precision and accuracy of supernovae Ia as distance indicators. Here we present HD 265435, a binary system with an orbital period of less than a hundred minutes that consists of a white dwarf and a hot subdwarf, which is a stripped core-helium-burning star. The total mass of the system is 1.65 ± 0.25 solar masses, exceeding the Chandrasekhar limit (the maximum mass of a stable white dwarf). The system will merge owing to gravitational wave emission in 70 million years, likely triggering a supernova Ia event. We use this detection to place constraints on the contribution of hot subdwarf–white dwarf binaries to supernova Ia progenitors.

Type Ia supernovae (SNe Ia) represent one of the crucial rungs on the cosmic distance ladder. As bright standard candles, they contribute to obtaining measurements of the Hubble constant H_0 , which describes how fast the Universe is expanding at different distances^{1–3}. An accurate determination of the systematic uncertainties involved in these cosmological measurements requires a reliable identification of the progenitor channels that contribute to the observed SN Ia population. Current measurements of H_0 in the local Universe that rely on SNe Ia⁴ are inconsistent with estimates using the cosmic microwave background radiation observed by the Planck experiment⁵. To establish whether this H_0 tension⁶ is evidence for new physics or rather a consequence of poor determination of systematic uncertainties, it is imperative to understand possible SN Ia channels and their relative contributions.

Although the origin of SNe Ia has long been understood as a thermonuclear detonation in a white dwarf⁷, triggered when a critical mass near the Chandrasekhar limit of $1.4 M_\odot$ is reached, the mechanism for the explosion itself remains under debate⁸. Possible channels for achieving critical mass can be generally grouped as either double-degenerate or single-degenerate. In the double-degenerate channel, the white dwarf has another compact star as a companion, and the detonation is triggered by the merger of the two objects^{9–11}. In the single-degenerate channel, the white dwarf accretes mass from a companion to a point at which thermonuclear explosion is triggered^{9,12}. Confirmed progenitors are extremely scarce for both channels¹³, making it challenging to explain observed rates¹⁴. The once promising Henize 2-428 system¹⁵ has recently been shown to have a total mass significantly lower than previously derived, and can no longer be considered as an SN Ia progenitor¹⁶. Even in the dedicated European Southern Observatory (ESO) Supernovae Type Ia Progenitor Survey (SPY), only two systems (WD2020-425 and HE2209-1444) have been identified as possible progenitors,

both with sub-Chandrasekhar total masses¹⁷. The only known super-Chandrasekhar candidate progenitor is KPD 1930+2752 (ref. ¹⁸), a hot subdwarf with a close white dwarf companion. Another similar albeit less massive binary, CD-30°11223 (refs. ^{19,20}), also qualifies as SN Ia progenitor. These merging massive systems can also be of interest as gravitational wave sources, in particular as verification sources for the upcoming Laser Interferometer Space Antenna (LISA).

Here we report the discovery that HD 265435 is a candidate supernova progenitor and LISA verification binary composed of a hot subdwarf with a massive white dwarf companion. This binary system, with an apparent visual magnitude $V = 11.78$, is at a distance of less than 500 pc from the Sun, making it the closest super-Chandrasekhar candidate supernova progenitor. We analysed the light curve obtained by the Transiting Exoplanet Survey Satellite (TESS)²¹ together with time-series spectroscopy to characterize the system and determine the component masses. The properties of this binary make it a candidate for both the single-degenerate and double-degenerate SN Ia channels.

Results

HD 265435 (TIC 68495594) was observed by TESS in Sector 20. The data revealed strong ellipsoidal variation, suggesting that the visible component of the system is tidally deformed by a compact object. The light curve also reveals pulsation frequencies showing rotational splitting. Following this discovery, we obtained time-series spectroscopy at the Palomar 200-inch telescope with the Double-Beam Spectrograph (DBSP)²² covering one orbital cycle, with the aim of obtaining the radial velocity curve of the visible star. We also obtained high-resolution spectra with the Echelle Spectrograph and Imager (ESI) at the Keck II telescope to determine the line-of-sight rotational velocity, $v \sin i$. Combining the

¹Institut für Physik und Astronomie, Universität Potsdam, Potsdam-Golm, Germany. ²Department of Physics, University of Warwick, Coventry, UK.

³Max Planck Institut für Astrophysik, Garching bei München, Germany. ⁴Kavli Institute for Theoretical Physics, University of California, Santa Barbara, CA, USA. ⁵Department of Physics & Astronomy, Texas Tech University, Lubbock, TX, USA. ⁶Dr. Karl Remeis Observatory, Erlangen Center for Astroparticle Physics, Astronomical Institute, Friedrich-Alexander University Erlangen-Nuremberg, Bamberg, Germany. ⁷Division of Physics, Mathematics and Astronomy, California Institute of Technology, Pasadena, CA, USA. ⁸Department of Physics and Astronomy, High Point University, High Point, NC, USA.

✉e-mail: ingrid.pelisoli@warwick.ac.uk

Table 1 | Astrometric, stellar and orbital parameters for HD 265435

Parameter	Spectroscopic solution	Light curve solution	Adopted value
RA (J2000)	-	-	06:53:24.30
dec. (J2000)	-	-	+33:03:34.2
ϖ (mas)	-	-	2.216 ± 0.055
μ_α (mas yr ⁻¹)	-	-	-4.83 ± 0.06
μ_δ (mas yr ⁻¹)	-	-	-4.583 ± 0.0492
$T_{\text{eff, sd}}$ (K)	$34,300 \pm 400$	Fixed	$34,300 \pm 400$
$\log g_{\text{sd}}$ [cgs]	5.62 ± 0.10	5.52 ± 0.04	$5.55^{+0.12}_{-0.06}$
$\log y_{\text{sd}}$	-1.46 ± 0.10	-	-
$M_{\text{sd}} (M_\odot)$	$0.62^{+0.17}_{-0.13}$	$0.64^{+0.10}_{-0.09}$	$0.63^{+0.13}_{-0.12}$
$R_{\text{sd}} (R_\odot)$	0.203 ± 0.006	0.230 ± 0.012	$0.213^{+0.025}_{-0.013}$
$L_{\text{sd}} (L_\odot)$	51 ± 4	67^{+8}_{-7}	57^{+14}_{-8}
$M_{\text{WD}} (M_\odot)$	$0.91^{+0.11}_{-0.10}$	1.10 ± 0.11	1.01 ± 0.15
T_0 (BJD)	fixed	24571909.6899552(26)	-
P (days)	fixed	0.0688184888(32)	-
K_{sd} (km s ⁻¹)	343.1 ± 1.2	Gaussian prior	343.1 ± 1.2
V_0 (km s ⁻¹)	8.2 ± 0.8	-	-
q	$1.46^{+0.22}_{-0.18}$	$1.70^{+0.11}_{-0.09}$	$1.63^{+0.15}_{-0.26}$
i (degrees)	76 ± 6	60 ± 2	64^{+14}_{-5}
a (R_\odot)	$0.805^{+0.048}_{-0.042}$	0.851 ± 0.034	$0.831^{+0.043}_{-0.050}$
τ (Myr)	76^{+25}_{-19}	63^{+15}_{-11}	70^{+26}_{-16}
\mathcal{A} (10^{-22})	$3.1^{+1.1}_{-0.8}$	$3.7^{+0.8}_{-0.7}$	$3.5^{+1.0}_{-0.9}$

Astrometric parameters are from Gaia EDR3²³, with a zero-point correction applied to the parallax²⁴. For stellar and orbital parameters, we show the values obtained from both spectroscopic analyses and the light curve fit, if derived independently, as well as the adopted values that result from combining the two solutions by concatenating the distributions obtained for each parameter. Quoted values are the median, and uncertainties give the 68% confidence interval. Where a χ^2 fit was employed, the systematic uncertainty was quadratically added to the statistical fit uncertainty. Quantities shown are the right ascension RA; declination dec.; parallax ϖ ; proper motions in the right ascension, μ_α , and declination, μ_δ , directions; hot subdwarf effective temperature $T_{\text{eff, sd}}$; surface gravity $\log g_{\text{sd}}$; helium abundance $\log y_{\text{sd}}$; mass M_{sd} ; radius R_{sd} ; luminosity L_{sd} ; white dwarf mass M_{WD} ; zero point of the ephemeris T_0 ; orbital period P ; radial velocity semi-amplitude of the hot subdwarf K_{sd} ; systemic velocity of the binary V_0 ; mass ratio q ; orbital inclination i ; orbital distance a ; merging time owing to gravitational waves τ ; and gravitational wave amplitude \mathcal{A} .

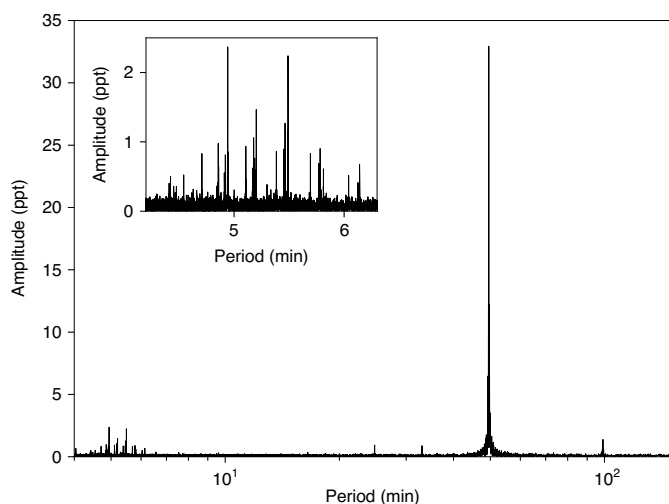


Fig. 1 | Periodogram of the TESS light curve. In the full periodogram, a dominant peak can be seen at 49.54959(15) min, corresponding to half of the orbital period. Multiple low-period peaks can also be identified in the range of 4–6 min, as detailed in the inset.

spectra with the radius estimate from fitting the spectral energy distribution (SED) using the Gaia Early Data Release 3 (EDR3)²³ parallax, we completely characterized the visible component, a hot

subdwarf of spectral type OB (sdOB). The orbital inclination i of the system was obtained from the estimated $v \sin i$, given the evidence that the hot subdwarf is tidally locked, and that in turn allowed us to constrain the mass of the unseen companion, which is likely a white dwarf with a carbon–oxygen (CO) core. We also fitted the TESS light curve without relying on any stellar parameters derived from the spectroscopy, obtaining a consistent solution (within 2σ) that confirms the nature of the companion. The obtained stellar and binary parameters for HD 265435 are provided in Table 1.

Period determination. A Lomb–Scargle periodogram of the TESS light curve showed a dominant peak at 49.54959(15) min (Fig. 1). Phase-folding of the light curve to twice this dominant peak revealed the occurrence of Doppler boosting²⁴, which caused a height difference of $\sim 0.3\%$ between consecutive maxima, indicating that the real orbital period is $P = 99.09918(29)$ min. A smaller amplitude peak can be seen at this period, as well as harmonics at $P/3$ and $P/4$. The periodogram also shows a wealth of short-period peaks, which are in the correct range for p -mode pulsations of the hot subdwarf^{25,26}. We identified a total of 33 frequencies above a detection level of five times the average amplitude of the Fourier transform (Supplementary Table 1). Many of these frequencies are part of rotational multiplets, which result from the spherical symmetry being broken by rotation²⁷. The separation is expected to be proportional to the rotation period and close to equal to it for p -mode oscillations²⁸. We find the separation between peaks to be equal to the orbital period (Supplementary Fig. 1), suggesting thus that the

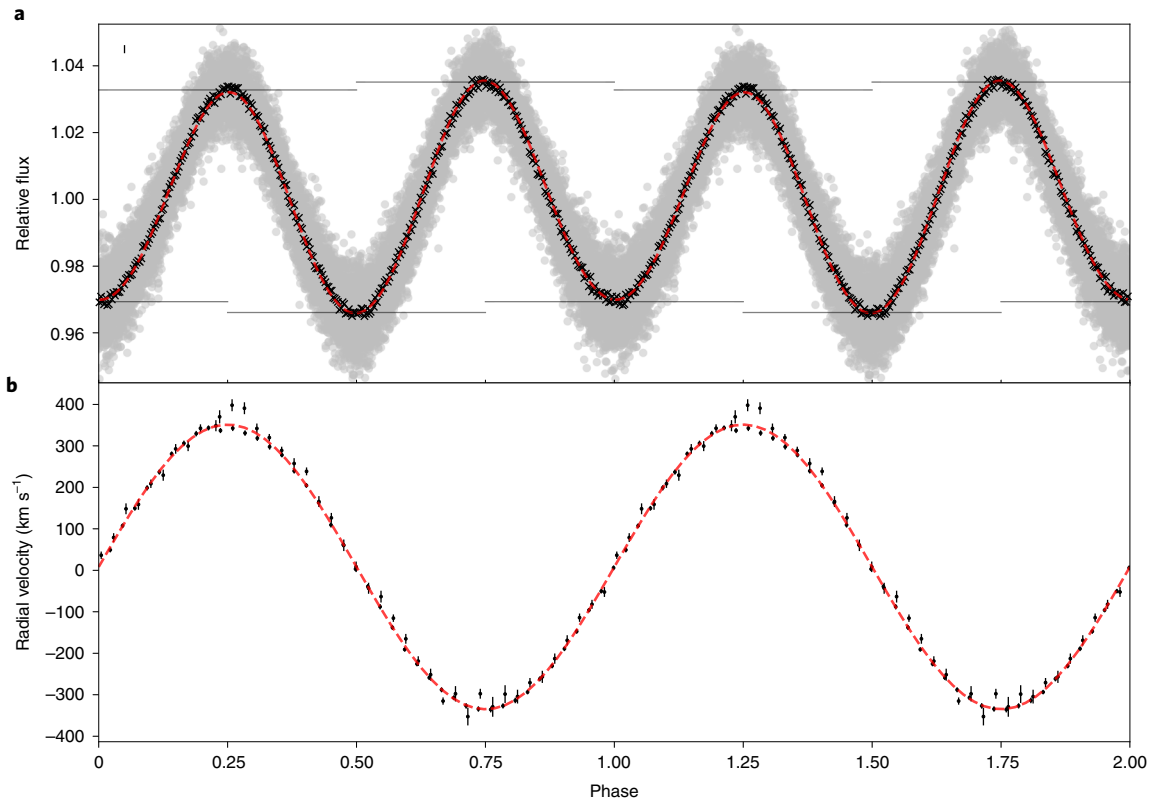


Fig. 2 | Phased data for HD 265435. a,b, Light curve data (**a**) and radial velocity data (**b**), all phase-folded to the obtained ephemeris. In **a**, the original TESS data are shown as grey dots. The phased data were binned every 50 points for the light curve fit, as shown by the black crosses. The median 1σ uncertainty for the binned data is shown as a bar at the top left. In **b**, the individual radial velocity estimates are shown in black with their 1σ uncertainties. The best-fit model is shown as red dashed lines in both panels. The dominant effect in the light curve is an ellipsoidal variation caused by the tidal deformation of the visible component. The tidal deformation also leads to gravity darkening, causing the two minima to show different depths. The less prominent effect of Doppler boosting, which causes maxima to show different heights, is in turn caused by the orbital motion of the visible companion. We trace the location of each minimum and maximum with solid horizontal lines, to make the effect of these phenomena more noticeable.

rotation period of the subdwarf is equal to the orbital period, that is, the system is synchronized, as is often observationally inferred for hot subdwarf binaries with orbital periods of less than half a day²⁹.

The TESS two-minute cadence is not adequate for correctly sampling such short periods, and therefore we attempted no asteroseismological analysis. These periods were identified so that their effect could be subtracted from the light curve before modelling the effect of the binary companion; otherwise, they would have led to systematic errors on the final fit parameters. This was done recursively: we first calculated a preliminary model for the variability due to binarity (Methods), which we then subtracted from the original light curve to determine the short periods. Next, we performed a global fit using all 33 identified peaks and subtracted the obtained model from the original light curve. The preliminary model was also used to fit the full light curve to refine the period and determine the zero point of the ephemeris (adopted here as the superior conjunction of the unseen companion). We obtained a period of $P = 0.0688184888(32)$ days and a zero point with Barycentric Julian Date of $\text{BJD}_0 = 24571909.6899552(26)$ days. The light curve and radial velocity data folded using this ephemeris is shown in Fig. 2.

Radial velocity curve of the hot subdwarf. We determined the radial velocities by cross-correlating each spectrum obtained with DBSP with a best-fit spectral template (see Methods for a full description of the procedure). We analysed spectra from the blue and red arms separately, as they are not obtained simultaneously, and obtained consistent radial velocities. We fitted the radial velocities assuming

a circular orbit with the period fixed to the photometric period, as the time span of our radial velocity curve would not allow a precise independent determination of the period. We allowed the zero point of the ephemeris to vary by $P/2$ to account for possible phase shifts between the photometric and spectroscopic data, obtaining a value consistent with the photometry within four decimal places. The best-fit model is shown in Fig. 2b. The obtained radial velocities revealed a large radial semi-amplitude of $K_{\text{sd}} = 343.1 \pm 1.2 \text{ km s}^{-1}$, implying a mass function for the unseen companion of

$$f_{\text{comp}} = \frac{M_{\text{comp}}^3 \sin^3(i)}{(M_{\text{sd}} + M_{\text{comp}})^2} = \frac{P K_{\text{sd}}^3}{2\pi G} = 0.288 \pm 0.003 M_{\odot}. \quad (1)$$

By combining the obtained systemic velocity with the Gaia astrometric information, we found the system to show dynamics consistent with the thin disk of the Galaxy (Methods).

Characterizing the system and the nature of the companion. The obtained spectra revealed the visible component to be an sdOB, as already suggested based on its Gaia DR2 parameters³⁰. We performed spectral fits of the Doppler-corrected DBSP spectra (Methods), obtaining an effective temperature of $T_{\text{eff}} = 34,300 \pm 400 \text{ K}$ and surface gravity with $\log g = 5.62 \pm 0.10$. With T_{eff} and $\log g$ fixed, we obtained $v \sin i$ and helium-to-hydrogen ratio (by number) $\log y$ by fitting each of the high-resolution ESI spectra separately, to avoid additional broadening introduced by co-adding the spectra. This resulted in $\log y = -1.46 \pm 0.04$ and $v \sin i = 152 \pm 6 \text{ km s}^{-1}$.

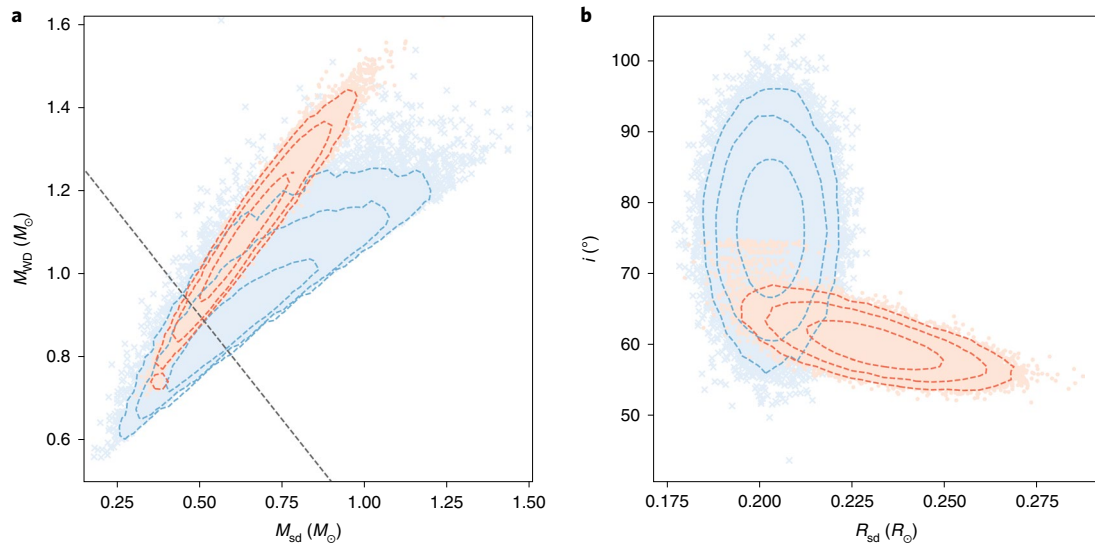


Fig. 3 | Comparison between photometric and spectroscopic solutions. a, b. Component masses (a) and hot subdwarf radius and inclination of the system (b). The blue crosses show values derived by spectroscopic analyses, whereas the orange dots result from the light curve solution. The dashed contours show confidence intervals corresponding to 68%, 95% and 99%. Mass combinations above the dashed grey line in **a** are above the Chandrasekhar limit.

By performing a fit to the SED (Methods), we found the photometry to be consistent with a single hot subdwarf, finding no contribution from the unseen companion. Using the Gaia EDR3 parallax, our SED fit provided a radius estimate of $R_{sd} = 0.203 \pm 0.006 R_{\odot}$, implying a hot subdwarf mass of $0.62^{+0.17}_{-0.13} M_{\odot}$ from the obtained $\log g$. Based on the indication that the rotational period of the hot subdwarf is synchronized with the orbital period, the orbital inclination can also be obtained from the radius and from $v \sin i$, which give $76 \pm 6^{\circ}$. Finally, equation (1) can be solved to obtain the mass of the unseen companion, which is found to be $0.91^{+0.11}_{-0.10} M_{\odot}$; this corroborates its nature as a compact object, as no contribution from an early-type companion is observed.

Alternatively, the multiple effects observed in the light curve of HD 265435 can be used to constrain some stellar parameters of the system independently from the spectroscopy. The ellipsoidal variation, gravity darkening and Doppler boosting effects depend mainly on the radius of the hot subdwarf and on the masses of both components. The temperature and radius of the unseen companion, by contrast, can still not be constrained, as its contribution to the light curve is negligible and no eclipses are observed.

We fitted the light curve using LCURVE (v.1.3)³¹, a code that uses an inhomogeneous grid of points, which was optimized to reproduce the stellar surface area, to model the brightness of two orbiting stars with shapes set by a Roche potential. We left as free parameters the mass ratio q , the inclination angle i , the scaled equatorial radius of the hot subdwarf $r_{sd} = R_{sd}/a$, where a is the orbital distance, and the velocity scale $V_{scale} = (K_{sd} + K_{comp})/\sin i$, where K_{comp} is the semi-amplitude of the companion. The value of K_{sd} was required to be consistent with the determination from the radial velocity observations, but no other priors were applied (see Methods for details on the procedure).

We obtained $q = 1.70^{+0.11}_{-0.09}$, $i = 60 \pm 2^{\circ}$, $r_{sd} = 0.289 \pm 0.009$ and $V_{scale} = 625 \pm 25 \text{ km s}^{-1}$. These parameters imply masses of $M_{sd} = 0.64^{+0.10}_{-0.09} M_{\odot}$ and $M_{comp} = 1.10 \pm 0.11 M_{\odot}$ and a hot subdwarf radius of $R_{sd} = 0.232 \pm 0.012 R_{\odot}$, which are consistent with the parameters derived from spectroscopic fitting within their 95% confidence intervals, as illustrated in Fig. 3.

By combining the two consistent solutions by concatenating the distributions obtained for each parameter, we found the stellar and orbital parameters given in the third column of Table 1. The mass of the companion is found to be $M_{comp} = 1.01 \pm 0.15 M_{\odot}$. This implies

that the companion is likely a white dwarf with a CO core, although an O–Ne(–Mg) composition is possible if the mass is above $1.088 M_{\odot}$ (ref. ³²). The total mass of the system is found to be $1.65 \pm 0.25 M_{\odot}$.

Future evolution of HD 265435. The evolution of a binary is primarily determined by the total mass of the system, the initial orbital separation and the evolutionary status of the hot subdwarf at the time of Roche-lobe overflow (RLOF). The obtained radius hints at a hydrogen envelope with a current mass around $1.5 \times 10^{-4} M_{\odot}$, which is typical for hot subdwarf stars³³.

We carried out numerical simulations of the evolution of the system to determine its possible outcomes. Assuming solar metallicity, a helium star with a total mass of $0.63 M_{\odot}$ and a remaining H-envelope of $10^{-4} M_{\odot}$ about halfway through its expected core-helium-burning lifetime yields physical parameters consistent with the observed values (Fig. 4a). The model was placed in a binary with a carbon–oxygen-core white dwarf approximated by a point mass. We included the effects of rotation, assuming tidal locking and angular momentum loss through gravitational radiation. Our benchmark model assumes no wind mass loss, which is the standard assumption in modelling of hot subdwarfs. However, as our results are partially sensitive to the occurrence of winds, which are, in the case of hot subdwarf stars, still a matter of debate, we also included a weak wind³⁴ in an alternative model. We note that inclusion of wind suggests an initial mass of the hydrogen envelope of $3 \times 10^{-4} M_{\odot}$, half of which has been ejected by the time of observation. Further details of the simulation are given in the Methods section.

We found that RLOF is precipitated by the end of the hot subdwarf’s core-helium-burning phase after ~ 29.6 million years (Fig. 4b,c). In our benchmark model, subsequent expansion then leads to RLOF. The transferred material will be hydrogen-enriched for the first ~ 3.0 million years of RLOF, and will subsequently become helium-enriched as the remaining hydrogen envelope is stripped. The He-enriched phase is expected to last for ~ 1 million years, resulting in $\sim 0.015 M_{\odot}$ of He-rich material being transferred. Mass transfer rates are expected to lie in the range of $10^{-11} - 10^{-9} M_{\odot} \text{ yr}^{-1}$, enough to indicate a phase of classical nova eruptions^{35,36}, and will not exceed $2.5 \times 10^{-8} M_{\odot} \text{ yr}^{-1}$ during the He-rich phase, which indicates that helium will be accumulated quiescently, without igniting^{37,38}, on the white dwarf.

The introduction of a weak wind has the effect of delaying the RLOF phase, which then happens after ~ 37 million years (Fig. 4b,d).

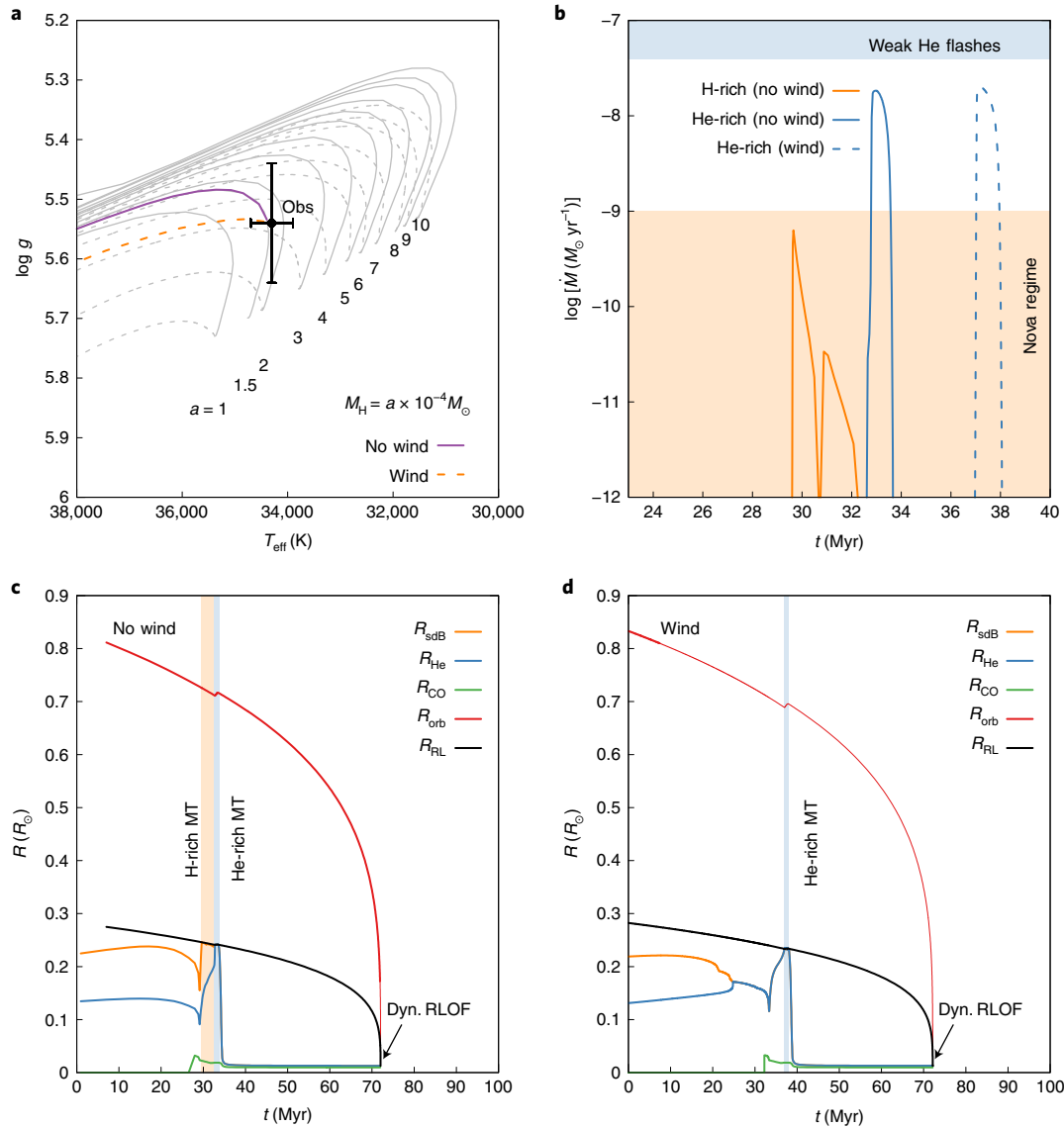


Fig. 4 | Model and prediction of the future evolution of HD 265435. **a**, Predicted evolutionary tracks in $T_{\text{eff}}\text{-}\log g$ for hot subdwarfs of mass $0.63 M_{\odot}$ and H envelopes between $10^{-4} M_{\odot}$ and $10^{-3} M_{\odot}$. The solid purple line represents the favoured models with $-1.5 \times 10^{-4} M_{\odot}$ (no wind) starting from the beginning of the binary run. The weak wind model with an initial hydrogen envelope of $-1.5 \times 10^{-4} M_{\odot}$ is represented by the dashed orange line. The observed position of the hot subdwarf in the diagram is as indicated, with error bars representing the systematic uncertainty of the obtained spectral parameters. **b**, Evolution of the system's mass transfer rate under the assumption of either no wind (solid lines) or a weak wind (dashed). Colour indicates whether the transferred mass is H-enriched or He-enriched. Shaded areas indicate where H-accretion-induced novae or He-accretion-induced flashes are expected. **c**, Orbital evolution of the benchmark model system without wind. R_{sdB} is the total radius of the hot subdwarf, including hydrogen envelope; R_{He} is the radius of the He-rich shell; R_{CO} is the radius of the inert CO core; and R_{RL} is the radius of the Roche lobe of the hot subdwarf. The shaded areas indicate expected mass transfer (MT) phases and dominant composition of the transferred material. Dyn. RLOF marks the occurrence of dynamically unstable Roche Lobe Overflow. **d**, Graph equivalent to **c** but for the weak wind model.

This discrepancy in the onset of RLOF is explained first by the benchmark model requiring ~ 5 million years longer to acquire the observed properties and, second, by the presence of a H-enriched envelope, which is removed by winds in the alternative scenario. This envelope expands faster than the H-depleted parts of the envelope as the star moves into He-shell burning. The expansion of the helium envelope preceding the end of core-helium burning in the alternative model is a result of the removal of the H-rich envelope by the weak wind, to which the helium envelope, in preserving the star's boundary conditions and smooth pressure gradient, reacts by expanding. We note that our qualitative and quantitative predictions for the future evolution of this system are otherwise unaffected by the presence of a wind.

This mass transfer rate is sufficient to stabilize the binary against further inspiral due to gravitational wave radiation for the duration of the mass transfer phase, leading to an increase of the merger time (71.8 Myr according to our simulation)^{39,40}. Quiescent accumulation is a prerequisite for ignition of a thermonuclear SN according to the double-detonation mechanism (Methods); however, the amount of transferred material is too small. The end of this mass transfer phase is precipitated by the remaining helium envelope of the hot subdwarf losing sufficient mass, owing to both nuclear burning and mass transfer to the companion, for further helium burning to become unsustainable. At this point the hot subdwarf will contract thermally to become a CO white dwarf with a remnant He envelope of $\sim 0.03 M_{\odot}$, that is, a hybrid He-CO white dwarf.

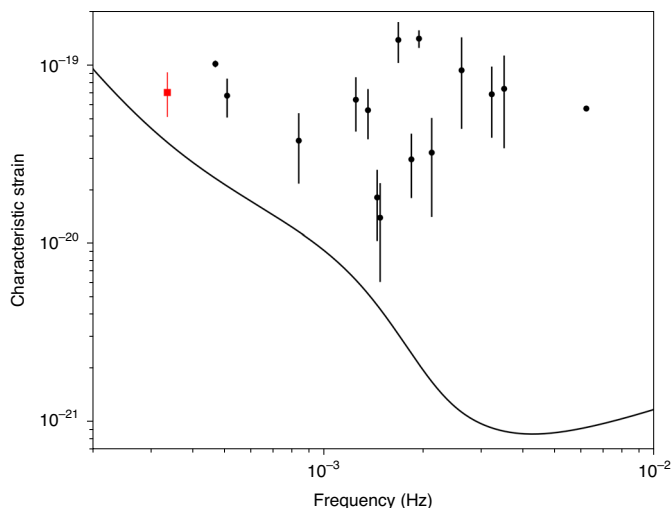


Fig. 5 | Gravitational wave frequency and strain of HD 265435. The black line shows the LISA sensitivity curve for a four-year mission¹⁰⁷. The red square shows the median strain and frequency of HD 265435, with the error bar representing the 68% confidence interval. Black data points are previously known verification binaries¹⁰⁸.

Following this mass transfer phase, the system will continue to lose angular momentum because of gravitational wave radiation. The former hot subdwarf will then fill its Roche lobe once again. With a mass ratio of $q \approx 1.64$, this episode will likely lead to dynamically unstable RLOF, in the course of which the former hot subdwarf is disrupted and merges with the heavier companion. This would result in one of three possible channels for the thermonuclear detonation: a prompt detonation⁴¹ of the more massive white dwarf, a violent merger of the two white dwarfs⁴², or unstable ignition of helium on the more massive white dwarf travelling along the accretion stream and leading to the double detonation of the white dwarf donating mass⁴³. However, we emphasize the presence of a non-negligible amount of unburnt helium on the accretor. The derived masses allow us to constrain the merger time because of gravitational wave emission⁴⁴, which is found to be 70^{+26}_{-16} Myr, consistent with our numerical simulation. The characteristic strain^{45,46} of the system places it above the detection limit of LISA (Fig. 5).

We note that, given our obtained mass intervals, there is a $\sim 16\%$ probability that the total mass of the system is below the Chandrasekhar mass. In this case, the system would not lead to a supernova through any standard double-degenerate or single-degenerate channel. The likely scenario is recurrent novae starting some 20 Myr from the time of observation, followed by a double-degenerate dynamical merger. There remains a possibility for prompt detonation, which depends on the presence of helium on the former hot subdwarf^{41,47}.

Discussion

The newly discovered system HD 265435 brings the number of hot subdwarf with white dwarf companions that qualify as supernova progenitors to three, making this the class of binaries with the most observed progenitor candidates. These supernovae may ultimately not show typical SN Ia spectra, but may appear subluminal and/or peculiar depending on their mass ratio⁴². HD 265435 has very similar properties to KPD 1930+2752: both harbour a relatively hot subdwarf star ($T_{\text{eff}} > 30,000$ K) and a massive white dwarf with a CO core as companion, bringing the total mass of the system above the Chandrasekhar limit. In addition, the hot subdwarfs in both HD 265435 and KPD 1930+2752 have been observed to show peaks in the range of p -mode pulsations. CD-30°11223, by contrast,

has lower-mass components and total mass slightly below the Chandrasekhar limit. However, KPD 1930+2752 will likely evolve through the core-helium-burning phase without filling its Roche lobe and transferring mass to the companion³⁸, whereas mass transfer is predicted to happen to both HD 265435 and CD-30°11223. Therefore, in terms of its evolutionary fate, HD 265435 is more similar to CD-30°11223. A class of Roche-lobe-filling hot subdwarf binaries has recently been discovered⁴⁸, providing observational evidence for the existence of systems undergoing mass transfer before the hot subdwarf evolves into a white dwarf.

Perhaps the most remarkable common property of these candidate supernova progenitors is the fact that they are all found within 1 kpc of the Sun and seem to be members of the thin disk, showing relatively low Galactic latitudes, b . Given their Gaia EDR3 zero-point-corrected parallaxes, CD-30°11223 is at 349 ± 6 pc and $b = 28.9^\circ$, HD 265435 is at 451 ± 11 pc and $b = 14.8^\circ$ and KPD 1930+2752 is at 825^{+27}_{-24} pc and $b = 4.3^\circ$. With the assumption that these three objects constitute the entire sample of hot subdwarf–white dwarf binaries that qualify as supernova progenitors within 1 kpc and taking into account a Poissonic uncertainty, that would imply a space density of 0.22 ± 0.13 kpc⁻³ for this type of system, considering the effective volume given by the thin-disk density⁴⁹. We can also roughly estimate the rate of SNe Ia that can be attributed to such systems. There are $\sim 3,000$ hot subdwarf candidates within 1 kpc (ref. ³⁰). Accounting for an estimated contamination level of 10% (ref. ³⁰), this would suggest that 3 of the 2,700 hot subdwarfs within 1 kpc are possible SN Ia progenitors. Given the birth rate of such stars of 0.014–0.063 yr⁻¹ (ref. ³⁰), this implies that the SN Ia rate that can be attributed to hot subdwarf–white dwarf binaries is $1.5\text{--}7 \times 10^{-5}$ yr⁻¹. Population synthesis simulations suggest a larger value of $\sim 3 \times 10^{-4}$ yr⁻¹ for the contribution of helium star–white dwarf binaries to the SN Ia rate⁵¹, but this estimate includes also helium stars more massive than hot subdwarfs. Our estimate is comparable to the estimated contribution from double-degenerate white dwarf binaries, which is $2.1 \pm 1.0 \times 10^{-5}$ yr⁻¹ (ref. ¹³). The Galactic SN Ia rate is in turn estimated to be $7.2 \pm 2.3 \times 10^{-3}$ yr⁻¹ (refs. ^{52,53}). Therefore, our estimate suggests that hot subdwarf–white dwarf binaries cannot bring the Galactic SN Ia rate into agreement with observed progenitor rates, despite being the most numerous observed class of progenitors. Our estimate should, however, be regarded as a lower limit, as we have assumed that there are no other SN Ia progenitors consisting of hot subdwarf–white dwarf binaries within 1 kpc. The TESS extended mission, as well as future missions such as the Legacy Survey of Space and Time, will put this assumption to test.

Methods

Observations and data reduction. HD 265435 (TIC 68495594) was observed by TESS in Sector 20, yielding two-minute cadence data over a baseline of 26.3 days, with a three-day gap after 12.3 days during which the data were being downloaded to Earth. We retrieved the light curve derived by the TESS Science Processing Operations Center (SPOC) and used the PDCSAP flux, which corrects the simple aperture photometry (SAP) to remove instrumental trends and contributions to the aperture that are expected from neighbouring stars identified in a pre-search data conditioning (PDC). The pipeline also provides an estimate of the contribution of the target to the flux in the aperture, called CROWDSAP, which takes into account possible contamination by neighbouring targets. The CROWDSAP value for HD 265435 is 0.65. The contamination is likely due to a star with Gaia G magnitude of 12.3 that is $28''$ away, given the TESS pixel size of $21''$. This much redder star ($G_{\text{BP}} - G_{\text{RP}} = 0.786$, compared to $G_{\text{BP}} - G_{\text{RP}} = -0.469$ for HD 265435) is likely a main sequence F star given the stellar parameters in the Gaia DR2 ($T_{\text{eff}} = 5,860$ K and $R = 1.50 R_{\odot}$ (ref. ⁵⁴)). We identified no variability that could be attributed to this contaminating source, and therefore we assumed it to be constant and assumed that the light curve amplitude has been corrected appropriately by the SPOC pipeline.

Optical spectra were obtained at the Palomar 200-inch telescope with DBSP using a low-resolution mode ($R \approx 1,200$). We obtained 40 exposures of 120 s covering 1.65 h on 2 March 2020. An average bias and normalized flat-field frame was made out of 10 individual bias and 10 individual lamp flat fields. To account for telescope flexure, an arc lamp was taken at the position of the target after each observing sequence. For the blue arm, FeAr arc exposures were taken, and HeNeAr for the red arm. Both arms of the spectrograph were reduced using a custom PyRAF-based pipeline⁵⁵. The pipeline

performs standard image processing and spectral reduction procedures, including bias subtraction, flat-field correction, wavelength calibration, optimal spectral extraction and flux calibration. The trailed spectra (Supplementary Fig. 2) clearly show periodical changes of the line centres. Finally, we obtained ten 60-s exposures with ESI at the Keck II telescope on 10 September 2020, which were combined into an $R \approx 6,000$, high signal-to-noise ratio ($S/N \approx 170$) spectrum. ThAr arc exposures were taken at the end of the night. The spectra were reduced using the MAKEE pipeline following the standard procedure, which consists of bias subtraction, flat fielding, sky subtraction, order extraction and wavelength calibration.

Spectral fit of the hot subdwarf. The observed spectra were matched to a model grid by χ^2 minimization⁵⁶. The quantitative spectral analysis is based on a new grid of model atmospheres and synthetic hydrogen and helium spectra that account for deviations from local thermodynamic equilibrium (LTE). We start from an LTE temperature/density stratification calculated with the ATLAS12 code⁵⁷. Non-LTE population numbers of hydrogen and helium levels are then calculated with the DETAIL code^{58,59} and handed back to ATLAS12 to correct the atmospheric structure for non-LTE effects in an iterative process⁵⁰. After convergence, DETAIL is used again to numerically solve the coupled equations of radiative transfer and statistical equilibrium. Finally, the SURFACE code^{58,59} is used to calculate the emergent spectrum using the non-LTE occupation numbers and detailed line-broadening tables. This hybrid approach has been shown to reproduce observations of B-type stars⁶¹ and has since been applied to the entire T_{eff} and $\log g$ range of sdB and sdOB stars, from the coolest ($\sim 23,000$ K)^{62,63} to the very hottest ($\sim 40,000$ K)⁶⁴. Recent updates to all three codes⁶⁰, such as the implementation of the occupation probability formalism⁶⁵ for hydrogen and Stark broadening tables for hydrogen and neutral helium^{66,67}, are considered. We first fitted the individual DBSP spectra, which have better normalization and cover the Balmer jump, to determine T_{eff} and $\log g$; $v \sin i$ was also left as a free parameter. We found $T_{\text{eff}} = 34,300 \pm 400$ K and $\log g = 5.62 \pm 0.10$. Our $\log g$ estimate differs from previous literature results⁶⁸ because of orbital smearing of their spectra, which were exposed for $\sim 1/3$ of the orbital period. Next, we fitted each of the higher-resolution ESI spectra to determine $v \sin i$ and $\log y$, fixing the values of T_{eff} and $\log g$ to those determined from the DBSP spectra. We fitted only the helium lines, which are more sensitive than the Balmer lines, obtaining $\log y = -1.46 \pm 0.10$ and $v \sin i = 152 \pm 7$ km s⁻¹. Exemplary spectroscopic fits are shown in Supplementary Fig. 3.

Spectral energy distribution fitting method. The observed magnitudes were matched to a synthetic flux distribution employing a χ^2 -based fitting routine⁶⁹. The synthetic flux distribution is interpolated from a grid of model SEDs calculated with ATLAS12, as described in the previous section, for the spectroscopically inferred atmospheric parameters. With the SED fit, we derive the angular diameter $\Theta = 2R/d$ (with the stellar radius R and distance d), a scaling factor derived from the observed flux $f(\lambda)$ and the synthetic stellar surface flux $F(\lambda)$ by making use of the geometric flux dilution, that is, $f(\lambda) = \Theta^2 F(\lambda)/4$. The radius can then be determined from $R = \Theta/(2\varpi)$ using the trigonometric parallax measurement ϖ provided by the Gaia EDR3, which has high-precision and quality indicators within specifications, in particular the re-normalized unit weight error⁷⁰.

As HD 265435 is located at low Galactic latitude ($b = +14.8^\circ$), interstellar reddening must be taken into account by fitting the interstellar colour excess along with the angular diameter. To model interstellar absorption we used the reddening law of Fitzpatrick et al.⁷¹. We found interstellar reddening to be relatively small, with $E(B-V) = 0.044 \pm 0.011$, compared to values from reddening maps^{72,73}, implying that most of the line-of-sight reddening occurs beyond HD 265435. We derived the stellar radius from the angular diameter Θ and the parallax ϖ by accounting for a Gaia EDR3 zero-point offset of -0.049 mas, calculated for HD 265435 (ref. 74), and found $R = 0.203 \pm 0.06 R_\odot$. Our fit is shown in Supplementary Fig. 4.

Radial velocity fitting method. Radial velocities were determined using the IRAF package RVS AO 2.7.8 (ref. 75) by performing cross-correlation with the task xcsao. Barycentric corrections were calculated and applied within this same task. We initially used a spectral template for a pure-hydrogen atmosphere with $T_{\text{eff}} = 30,000$ K and $\log g = 5.5$. Each spectrum was then Doppler-corrected and all spectra from the same arm were co-added. The co-added spectrum was used as input for a spectral fit. A template calculated using the best parameters from this spectroscopic fit was then used to re-calculate the radial velocities with xcsao. The values obtained (Supplementary Tables 2 and 3) were consistent with the initial values using the pure-hydrogen template, but uncertainties were lower by a factor of two. We performed a fit to the radial velocity curve using the Markov chain Monte Carlo (MCMC) method implemented with the emcee package⁷⁶. We assumed a circular orbit and thus fitted the radial velocities by using

$$RV(t) = V_0 + K_{\text{sd}} \sin[2\pi(t - t_0)/P], \quad (2)$$

where V_0 is the systemic velocity, K_{sd} is the radial velocity semi-amplitude of the hot subdwarf, t_0 is the zero point of the ephemeris and P is the orbital period. The period was fixed to the photometric period, whereas t_0 was allowed to vary by $P/2$. The velocities V_0 and K_{sd} were left to vary freely within physical limits, but we used values from χ^2 minimization as the initial guess. We note that, given

that the spectral lines of hot subdwarfs are inherently broad, the effect of orbital smearing for our integration time of 2% of the orbital period is of the same order of magnitude as the radial velocity uncertainties, which were taken into account in our MCMC fit. We obtained $V_0 = 8.2 \pm 0.8$ km s⁻¹ and $K_{\text{sd}} = 343.1 \pm 1.2$ km s⁻¹.

Galactic orbit of HD 265435. We calculated the Galactic orbit of HD 265435 using the galpy package (v. 1.4.0)⁷⁷. The Galactic potential was modelled with three components (bulge, disk and halo) plus a central black hole of mass $4 \times 10^6 M_\odot$ (refs. 77,78). The Sun was placed at a distance of $R_0 = 8.27 \pm 0.29$ kpc from the Galactic centre with peculiar motion in the Local Standard of Rest of $(U_\odot, V_\odot, W_\odot) = (11.1, 12.24, 7.25)$ km s⁻¹, and the Milky Way rotation speed at the Solar circle was set to $V_c = 238 \pm 9$ km s⁻¹ (refs. 79,80). The system shows dynamics consistent with the thin disk of the Galaxy (Supplementary Fig. 5). Other indicators, namely the Galactic velocity components ($U = 11 \pm 2$ km s⁻¹, $V = 232 \pm 4$ km s⁻¹, $W = -14 \pm 2$ km s⁻¹) and angular momentum and eccentricity ($J_z = 2130 \pm 3$ kpc km⁻¹ s⁻¹ and $e = 0.227 \pm 0.001$) also point to thin-disk membership⁸¹.

Light-curve fitting method. We used LCURVE³¹ to carry out the light curve analysis. This code uses a grid of points to model the two stars, with shapes set by a Roche potential. The flux emitted by each grid point is calculated from a blackbody with a given estimated temperature at the bandpass wavelength, taking into account corrections for the effects of limb darkening, gravity darkening, Doppler beaming and reflection.

We assumed that the orbit is circular, as we did for the radial velocity fit. The temperature of the hot subdwarf was fixed at the value determined from the spectroscopy. The lack of blue excess in the SED fit implies a maximum temperature for the companion of $T_{\text{comp}} \approx 90,000$ K. Assuming the minimum mass obtained from the spectroscopy and the mass–radius relationship for a carbon–oxygen white dwarf (which will give the maximum radius, and therefore maximum luminosity, for the unseen companion), we obtained that the companion contribution to the light is no more than 0.5%. Test runs of an MCMC fit to the light curve showed that the companion temperature and radius indeed cannot be constrained given the lack of contribution to the observed flux. Therefore, we kept the companion temperature and radius fixed to arbitrary values of $T_{\text{comp}} = 30,000$ K and $R_{\text{comp}}/a = 0.0125$, which are consistent with values for a white dwarf and result in a contribution of $\sim 0.15\%$.

For the hot subdwarf, limb-darkening and gravity-darkening coefficients and the Doppler boosting factor were interpolated from Tables 4 and y of Claret et al.⁸². We used the values for a pure-hydrogen composition ($\log[\text{He}/\text{H}] = -10.0$), because coefficients are unavailable at our derived values of T_{eff} and $\log g$ for models with intermediate helium abundance. Test runs indicate that this choice does not affect our solution significantly, and leaving these parameters as free results in values consistent with the tabulated values that were used. These coefficients were all set to zero for the secondary, as it has no measurable contribution. This left as free parameters in our light curve fit the mass ratio q , the inclination angle i , the scaled radius of the primary $r_{\text{sd}} = R_{\text{sd}}/a$, where a is the orbital distance, and the velocity scale $V_{\text{scale}} = (K_{\text{sd}} + K_{\text{comp}}) / \sin i$.

We first computed a preliminary fit of the light curve phased to the period determined from the Lomb–Scargle periodogram using the Levenberg–Marquardt algorithm for χ^2 minimization. For this initial fit our goal was not to obtain the best physical solution, but to calculate a model describing the light curve well enough to allow a more precise determination of the ephemeris, and to subtract the binary contribution from the light curve to determine the contribution of pulsations. The pulsation analysis was carried out with Period04 1.2.0 (ref. 83). We found 33 frequencies above a detection level of five times the average amplitude of the Fourier transform. We performed a global fit in Period04 using all 33 identified frequencies, and subtracted the obtained model from the original light curve.

Next, we performed an MCMC fit to the pulsations-subtracted light curve phase-folded to the determined period. The starting point was the set of parameters obtained from spectroscopic analyses. Initially we let all free parameters vary freely by imposing no priors on their values. This resulted in a solution with a velocity scale that was inconsistent with the observed radial velocity semi-amplitude of the hot subdwarf. We then performed a new fit, applying a Gaussian prior to the radial velocity semi-amplitude of the hot subdwarf, to guarantee its consistency with the value estimated from spectroscopic observations. Our best-fit model is shown in Fig. 2a, and the corner plot for our MCMC run is shown in Supplementary Fig. 6. We note that the quoted $\log g$ for the light curve solution was computed using a flux-weighted radius, not the equatorial radius.

Evolution of the system. We conducted a numerical analysis of this system using the Modules for Experiments in Stellar Astrophysics (MESA) release 12778 (refs. 84–88). We note that the radius of the hot subdwarf component radius is about 1.7 times that of a pure-helium hot subdwarf of the same mass³³; this hints at the presence of a thin ($\leq 10^{-3} M_\odot$) remnant H-rich envelope, which is typical of observed hot subdwarf stars. We found that the observational parameters best fit an evolved helium star with a remnant hydrogen envelope of $1.5 \times 10^{-4} M_\odot$ and solar metallicity. This model was created by initializing a H-depleted pre-main sequence model with solar metallicity and allowing it to contract, with nuclear

burning disabled, to hydrostatic equilibrium. A H-rich envelope of appropriate mass and metallicity was then accreted onto this model and the model again relaxed to hydrostatic equilibrium. Following this, the model was evolved until it matched the observational properties of the observed hot subdwarf star. To preserve consistency, this was repeated for an alternative model with the inclusion of a weak wind (see below). We found that, with a wind, an initial hydrogen envelope of $3.0 \times 10^{-4} M_{\odot}$ was required. At the point at which the alternative model matched the observations, about half of this envelope had been removed by winds. However, to evolve from its initial position in the Hertzsprung–Russell diagram, the benchmark model took ~ 31.2 Myr, whereas the alternative model required only ~ 26.2 Myr. The initial model was then placed in a binary system with an orbital period of $P_{\text{orb}} = 101$ min and with a $1.02 M_{\odot}$ white dwarf, which was approximated as a point mass.

To model the evolution of the hot subdwarf star, we used the predictive mixing scheme included in MESA with the same parameter setting as Ostrowski et al. (Appendix B in ref. ⁸⁹) and a semi-convection parameter of $\alpha = 0.1$. (Note that inclusion of semi-convection tends to induce so-called ‘breathing pulses’ in the models, which are deemed non-physical numerical artefacts. We chose a semi-convection parameter in our study that would avoid this issue.) We note that this scheme tends to underestimate the growth of the hot subdwarf’s convective core, leading to an underestimation of the hot subdwarf’s remaining He-burning lifetime. This does not substantially impact the reliability of our predictions, which are in agreement with those of previous studies. As hot subdwarf winds are currently a matter of debate, we present our analysis under two different assumptions, namely no winds (the standard assumption) or a nominal wind following a prescription by de Jager et al.⁹⁰. The latter prescription yields wind mass loss rates on the order of $10^{-11} M_{\odot} \text{yr}^{-1}$, which agrees well with theoretical predictions³⁴ but falls short of the $10^{-9} M_{\odot} \text{yr}^{-1}$ claimed by more recent studies⁹¹. We included the effects of rotation, assuming tidal locking and angular momentum loss through gravitational radiation, and RLOF-driven mass transfer was assumed to be conservative. Preceding any interaction, the system is expected to lose angular momentum through the emission of gravitational radiation, leading to RLOF after ~ 29.6 Myr (no wind). For the following ~ 3.0 Myr of this RLOF phase, the transferred material will be H-enriched with mass transfer rates well below $10^{-9} M_{\odot} \text{yr}^{-1}$. This may be sufficient to lead to a series of classical nova outbursts by the accreting white dwarf^{35,36}. In the alternative scenario with a weak wind, RLOF is expected to occur after ~ 37 Myr. In either case, the phase of He-enriched mass transfer is expected to last ~ 1.0 Myr, at the end of which the envelope of the hot subdwarf will have lost sufficient amounts of He owing to ongoing nuclear burning and mass transfer for continued He fusion to become unsustainable. At the end of the He burning in the hot subdwarf star and its subsequent contraction to a CO white dwarf, a considerable amount of unburnt helium ($\sim 0.03 M_{\odot}$) will remain on its surface, sufficient to classify it as a hybrid He–CO white dwarf. We note that our simulations and predictions of the amount of remaining and transferred helium independently corroborate previous studies of systems of this type^{38,92}. This He-rich material will be accumulated at rates not exceeding $2.5 \times 10^{-8} M_{\odot} \text{yr}^{-1}$, sufficiently low to allow for the material to be accumulated without ignition (that is, quiescently). Quiescent accumulation allows for build-up of a substantial layer of unburnt helium on the white dwarf. When this pristine helium ignites explosively, ignition of the underlying carbon–oxygen core may follow, leading to an SN^{93–95} (double-detonation mechanism); however, the amount of material transferred is too small by $\geq 0.04 M_{\odot}$. With nuclear burning thus quenched, the hot subdwarf will contract to become a white dwarf. The close double-degenerate binary thus formed will then merge ~ 71.8 Myr from the current epoch. Although the mass ratio remains below that previously predicted^{42,96–99} for likely progenitor systems of typical SN Ia, namely ~ 1.11 , a thermonuclear supernova is the most likely outcome given the high total mass of the system. However, the observed spectrum may not resemble a typical SN Ia, but instead an SN Iax or an otherwise subluminal or spectrally peculiar SN Ia^{37,42,100–102}.

A number of viable channels for the production of a binaries like HD 265435 have been proposed in the past³³. A hot subdwarf star of this mass is expected to form via unstable RLOF at the end of its progenitor’s first giant branch, leading to common-envelope evolution^{50,103}. Assuming this formation channel and using once more the MESA framework, we evolved a number of likely hot subdwarf progenitors until the end of their respective first giant branch. In broad agreement with Han et al.^{50,103} we found that the likely progenitor of the hot subdwarf is a main sequence star in the mass range of ~ 4.3 – $4.4 M_{\odot}$, which, with a white dwarf progenitor of $\sim 6 M_{\odot}$ (ref. ¹⁰⁴), will determine the evolutionary timescale of the system. Note that Han et al.^{50,103} do not provide delay times, leading to our retreat of their analysis. Discrepancies are due to the overshooting prescription used. Under these conditions, the lifetime of the progenitor binary is ~ 140 Myr. The system requires an additional ~ 31.2 Myr (benchmark) or ~ 26.2 Myr (alternative) for the hot subdwarf to evolve to its currently observed physical properties. Accordingly, the timescale from zero-age main sequence to merger would be on the order of ~ 238 – 243 Myr.

Data availability

The TESS data used in this work are publicly available and can be accessed via the Barbara A. Mikulski Archive for Space Telescopes (<https://mast.stsci.edu/>).

Obtained follow-up spectra, evolutionary models and MESA inlists are available on Zenodo (<https://doi.org/10.5281/zenodo.4792304>).

Code availability

This research made extensive use of Astropy (<http://www.astropy.org>), a community-developed core Python package for Astronomy^{105,106}. The PyRAF-based pipeline for DBSP spectra reduction is available at <https://github.com/ebellm/pyraf-dbsp>, and the MAKEE pipeline for ESI spectra can be found at http://www.astro.caltech.edu/~tb/ipac_staff/tab/makee/. The radial velocity determination code RVSAO is available from <http://tdc-www.harvard.edu/iraf/rvsao/>. The package galpy can be installed following <https://docs.galpy.org/en/v1.6.0/>. The SED and spectral fitting routines are publicly documented as described above, but not publicly available. The Period04 software employed for pre-whitening the light curve can be obtained from <https://www.univie.ac.at/tops/Period04/>. L CURVE is available at <https://github.com/trmrsh/cpp-lcurve>. The stellar evolution code MESA can be downloaded from <http://mesa.sourceforge.net/>.

Received: 2 February 2021; Accepted: 28 May 2021;

Published online: 12 July 2021

References

- Schmidt, B. P. et al. The high-Z supernova search: measuring cosmic deceleration and global curvature of the universe using Type Ia supernovae. *Astrophys. J.* **507**, 46–63 (1998).
- Riess, A. G. et al. Observational evidence from supernovae for an accelerating universe and a cosmological constant. *Astron. J.* **116**, 1009–1038 (1998).
- Perlmutter, S. et al. Measurements of Ω and Λ from 42 high-redshift supernovae. *Astrophys. J.* **517**, 565–586 (1999).
- Riess, A. G., Casertano, S., Yuan, W., Macri, L. M. & Scolnic, D. Large Magellanic Cloud Cepheid standards provide a 1% foundation for the determination of the Hubble constant and stronger evidence for physics beyond Λ CDM. *Astrophys. J.* **876**, 85 (2019).
- Aghanim, N. et al. Planck 2018 results. VI. Cosmological parameters. *Astron. Astrophys.* **641**, A6 (2020).
- Bernal, J. L., Verde, L. & Riess, A. G. The trouble with H_0 . *J. Cosmol. Astropart. Phys.* **2016**, 019 (2016).
- Hoyle, F. & Fowler, W. A. Nucleosynthesis in supernovae. *Astrophys. J.* **132**, 565–590 (1960).
- Hillebrandt, W., Kromer, M., Röpke, F. K. & Ruiter, A. J. Towards an understanding of Type Ia supernovae from a synthesis of theory and observations. *Front. Phys.* **8**, 116–143 (2013).
- Whelan, J. & Iben, I. Jr. Binaries and supernovae of Type I. *Astrophys. J.* **186**, 1007–1014 (1973).
- Iben, I. Jr. & Tutukov, A. V. Supernovae of Type I as end products of the evolution of binaries with components of moderate initial mass. *Astrophys. J. Suppl. Ser.* **54**, 335–372 (1984).
- Liu, D., Wang, B. & Han, Z. The double-degenerate model for the progenitors of Type Ia supernovae. *Mon. Not. R. Astron. Soc.* **473**, 5352–5361 (2018).
- Han, Z. & Podsiadlowski, Ph. The single-degenerate channel for the progenitors of Type Ia supernovae. *Mon. Not. R. Astron. Soc.* **350**, 1301–1309 (2004).
- Rebassa-Mansergas, A., Toonen, S., Korol, V. & Torres, S. Where are the double-degenerate progenitors of Type Ia supernovae? *Mon. Not. R. Astron. Soc.* **482**, 3656–3668 (2019).
- Maoz, D. & Mannucci, F. Type-Ia supernova rates and the progenitor problem: a review. *Publ. Astron. Soc. Austral.* **29**, 447–465 (2012).
- Santander-García, M. et al. The double-degenerate, super-Chandrasekhar nucleus of the planetary nebula Henize 2-428. *Nature* **519**, 63–65 (2015).
- Reindl, N. et al. An in-depth reanalysis of the alleged type Ia supernova progenitor Henize 2-428. *Astron. Astrophys.* **638**, A93 (2020).
- Napiwotzki, R. et al. The ESO supernovae type Ia progenitor survey (SPY). The radial velocities of 643 DA white dwarfs. *Astron. Astrophys.* **638**, A131 (2020).
- Maxted, P. F. L., Marsh, T. R. & North, R. C. KPD 1930+2752: a candidate Type Ia supernova progenitor. *Mon. Not. R. Astron. Soc.* **317**, L41–L44 (2000).
- Vennes, S., Kawka, A., O’Toole, S. J., Németh, P. & Burton, D. The shortest period sdB plus white dwarf binary CD-30 11223 (GALEX J1411-3053). *Astrophys. J. Lett.* **759**, L25 (2012).
- Geier, S. et al. A progenitor binary and an ejected mass donor remnant of faint type Ia supernovae. *Astron. Astrophys.* **554**, A54 (2013).
- Ricker, G. R. et al. Transiting Exoplanet Survey Satellite (TESS). *J. Astron. Telesc. Instrum. Syst.* **1**, 014003 (2015).
- Oke, J. B. & Gunn, J. E. An efficient low- and moderate-resolution spectrograph for the Hale telescope. *Publ. Astron. Soc. Pac.* **94**, 586–594 (1982).

23. Brown, A. G. A. et al. Gaia Early Data Release 3. Summary of the contents and survey properties. *Astron. Astrophys.* **649**, A1 (2021).
24. Shakura, N. I. & Postnov, K. A. Doppler-effect modulation of the observed radiation flux from ultracompact binary stars. *Astron. Astrophys.* **183**, L21–L22 (1987).
25. Charpinet, S., Fontaine, G., Brassard, P. & Dorman, B. The potential of asteroseismology for hot, subdwarf B stars: a new class of pulsating stars? *Astrophys. J.* **471**, L103 (1996).
26. Kilkenny, D., Koen, C., O'Donoghue, D. & Stobie, R. S. A new class of rapidly pulsating star — I. EC 14026-2647, the class prototype. *Mon. Not. R. Astron. Soc.* **285**, 640–644 (1997).
27. Kawaler, S. D. & Hostler, S. R. Internal rotation of subdwarf B stars: limiting cases and asteroseismological consequences. *Astrophys. J.* **621**, 432–444 (2005).
28. Reed, M. D. et al. Analysis of the rich frequency spectrum of KIC 10670103 revealing the most slowly rotating subdwarf B star in the *Kepler* field. *Mon. Not. R. Astron. Soc.* **440**, 3809–3824 (2014).
29. Geier, S., Karl, C., Edelmann, H., Heber, U. & Napiwotzki, R. in *Hot Subdwarf Stars and Related Objects* Vol. 392 (eds Heber, U., Jeffery, C. S. et al.) 207–214 (ASP Conference Series, 2008).
30. Geier, S., Raddi, R., Gentile Fusillo, N. P. & Marsh, T. R. The population of hot subdwarf stars studied with Gaia. II. The Gaia DR2 catalogue of hot subluminescent stars. *Astron. Astrophys.* **621**, A38 (2019).
31. Copperwheat, C. M. et al. Physical properties of IP Pegasi: an eclipsing dwarf nova with an unusually cool white dwarf. *Mon. Not. R. Astron. Soc.* **402**, 1824–1840 (2010).
32. Lauffer, G. R., Romero, A. D. & Kepler, S. O. New full evolutionary sequences of H- and He-atmosphere massive white dwarf stars using MESA. *Mon. Not. R. Astron. Soc.* **480**, 1547–1562 (2018).
33. Heber, U. Hot subluminescent stars. *Publ. Astron. Soc. Pac.* **128**, 082001 (2016).
34. Unglaub, K. Mass-loss and diffusion in subdwarf B stars and hot white dwarfs: do weak winds exist? *Astron. Astrophys.* **486**, 923–940 (2008).
35. Iben, I. Jr, Fujimoto, M. Y. & MacDonald, J. On mass-transfer rates in classical nova precursors. *Astrophys. J.* **384**, 580–586 (1992).
36. Shara, M. M., Prialnik, D., Hillman, Y. & Kovetz, A. The masses and accretion rates of white dwarfs in classical and recurrent novae. *Astrophys. J.* **860**, 110 (2018).
37. Woosley, S. E. & Kasen, D. Sub-Chandrasekhar mass models for supernovae. *Astrophys. J.* **734**, 38 (2011).
38. Neunteufel, P., Yoon, S.-C. & Langer, N. Models for the evolution of close binaries with He-star and white dwarf components towards Type Ia supernova explosions. *Astron. Astrophys.* **589**, A43 (2016).
39. Tutukov, A. V. & Yungelson, L. R. On the influence of emission of gravitational waves on the evolution of low-mass close binary stars. *Acta Astron.* **29**, 665–680 (1979).
40. Neunteufel, P. Exploring velocity limits in the thermonuclear supernova ejection scenario for hypervelocity stars and the origin of US 708. *Astron. Astrophys.* **641**, A52 (2020).
41. Kromer, M. et al. Double-detonation sub-Chandrasekhar supernovae: synthetic observables for minimum helium shell mass models. *Astrophys. J.* **719**, 1067–1082 (2010).
42. Pakmor, R. et al. Sub-luminous type Ia supernovae from the mergers of equal-mass white dwarfs with mass $\sim 0.9M_{\odot}$. *Nature* **463**, 61–64 (2010).
43. Pakmor, R., Zenati, Y., Perets, H. B. & Toonen, S. Thermonuclear explosion of a massive hybrid HeCO white dwarf triggered by a He detonation on a companion. *Mon. Not. R. Astron. Soc.* **503**, 4734–4747 (2021).
44. Kraft, R. P., Mathews, J. & Greenstein, J. L. Binary stars among cataclysmic variables. II. Nova WZ Sagittae: a possible radiator of gravitational waves. *Astrophys. J.* **136**, 312–315 (1962).
45. Shah, S., van der Sluys, M. & Nelemans, G. Using electromagnetic observations to aid gravitational-wave parameter estimation of compact binaries observed with LISA. *Astron. Astrophys.* **544**, A153 (2012).
46. Moore, C. J., Cole, R. H. & Berry, C. P. L. Gravitational-wave sensitivity curves. *Class. Quantum Gravity* **32**, 015014 (2015).
47. Gronow, S. et al. SNe Ia from double detonations: impact of core-shell mixing on the carbon ignition mechanism. *Astron. Astrophys.* **635**, A169 (2020).
48. Kupfer, T. et al. A new class of Roche lobe-filling hot subdwarf binaries. *Astrophys. J. Lett.* **898**, L25 (2020).
49. Jurić, M. et al. The Milky Way tomography with SDSS. I. Stellar number density distribution. *Astrophys. J.* **673**, 864–914 (2008).
50. Han, Z., Podsiadlowski, P., Maxted, P. F. L. & Marsh, T. R. The origin of subdwarf B stars – II. *Mon. Not. R. Astron. Soc.* **341**, 669–691 (2003).
51. Wang, B. et al. Birthrates and delay times of Type Ia supernovae. *Sci. China Phys. Mech. Astron.* **53**, 586–590 (2010).
52. Li, W. et al. Nearby supernova rates from the Lick Observatory Supernova Search – III. The rate-size relation, and the rates as a function of galaxy Hubble type and colour. *Mon. Not. R. Astron. Soc.* **412**, 1473–1507 (2011).
53. Maoz, D., Mannucci, F. & Nelemans, G. Observational clues to the progenitors of Type Ia supernovae. *Annu. Rev. Astron. Astrophys.* **52**, 107–170 (2014).
54. Andrae, R. et al. Gaia Data Release 2. First stellar parameters from Apsis. *Astron. Astrophys.* **616**, A8 (2018).
55. Bellm, E. C. & Sesar, B. pyraf-dbsp: reduction pipeline for the Palomar Double Beam Spectrograph. Record No. 1602.002 (Astrophysics Source Code Library, 2016).
56. Irrgang, A. et al. A new method for an objective, χ^2 -based spectroscopic analysis of early-type stars. First results from its application to single and binary B- and late O-type stars. *Astron. Astrophys.* **565**, A63 (2014).
57. Kurucz, R. L. in *M.A.S.S., Model Atmospheres and Spectrum Synthesis* Vol. 108 (eds Adelman, S. J., Kupka, F. et al.) 160 (ASP Conference Series, 1996).
58. Giddings, J. R. *Hydrogen and Helium Line Formation in OB Dwarfs and Giants. A Hybrid Non-LTE Approach*. PhD thesis, Univ. London (1981).
59. Butler, K. & Giddings, J. R. *Newsletter on Analysis of Astronomical Spectra* No. 9, 723 (Univ. London, 1985).
60. Irrgang, A., Kreuzer, S., Heber, U. & Brown, W. A quantitative spectral analysis of 14 hypervelocity stars from the MMT survey. *Astron. Astrophys.* **615**, L5 (2018).
61. Przybilla, N., Nieva, M.-F. & Butler, K. Testing common classical LTE and NLTE model atmosphere and line-formation codes for quantitative spectroscopy of early-type stars. *J. Phys. Conf. Ser.* **328**, 012015 (2011).
62. Silvotti, R. et al. High-degree gravity modes in the single sdB star HD 4539. *Mon. Not. R. Astron. Soc.* **489**, 4791–4801 (2019).
63. Sahoo, S. K. et al. Mode identification in three pulsating hot subdwarfs observed with TESS satellite. *Mon. Not. R. Astron. Soc.* **495**, 2844–2857 (2020).
64. Silvotti, R. et al. EPIC 216747137: a new HW Vir eclipsing binary with a massive sdOB primary and a low-mass M-dwarf companion. *Mon. Not. R. Astron. Soc.* **500**, 2461–2474 (2021).
65. Hubeny, I., Hummer, D. G. & Lanz, T. NLTE model stellar atmospheres with line blanketing near the series limits. *Astron. Astrophys.* **282**, 151–167 (1994).
66. Tremblay, P.-E. & Bergeron, P. Spectroscopic analysis of DA white dwarfs: stark broadening of hydrogen lines including nonideal effects. *Astrophys. J.* **696**, 1755–1770 (2009).
67. Beauchamp, A., Wesemael, F. & Bergeron, P. Spectroscopic studies of DB white dwarfs: improved stark profiles for optical transitions of neutral helium. *Astrophys. J. Suppl. Ser.* **108**, 559–573 (1997).
68. Lei, Z., Zhao, J., Németh, P. & Zhao, G. New hot subdwarf stars identified in Gaia DR2 with LAMOST DR5 spectra. *Astrophys. J.* **868**, 70 (2018).
69. Heber, U., Irrgang, A. & Schaffenroth, J. Spectral energy distributions and colours of hot subluminescent stars. *Open Astron.* **27**, 35–43 (2018).
70. Lindegren, L. Re-normalising the astrometric chi-square in Gaia DR2. Technical note GAIA-C3-TN-LU-LL-124-01 (European Space Agency, 2018); <https://www.cosmos.esa.int/web/gaia/public-dpac-documents>
71. Fitzpatrick, E. L., Massa, D., Gordon, K. D., Bohlin, R. & Clayton, G. C. An analysis of the shapes of interstellar extinction curves. VII. Milky Way spectrophotometric optical-through-ultraviolet extinction and its R-dependence. *Astrophys. J.* **886**, 108 (2019).
72. Schlegel, D. J., Finkbeiner, D. P. & Davis, M. Maps of dust infrared emission for use in estimation of reddening and cosmic microwave background radiation foregrounds. *Astrophys. J.* **500**, 525–553 (1998).
73. Schlafly, E. F. & Finkbeiner, D. P. Measuring reddening with Sloan Digital Sky Survey stellar spectra and recalibrating SFD. *Astrophys. J.* **737**, 103 (2011).
74. Lindegren, L. et al. Gaia Early Data Release 3. Parallax bias versus magnitude, colour, and position. *Astron. Astrophys.* **649**, A4 (2021).
75. Kurtz, M. J. & Mink, D. J. RVSAO 2.0: digital redshifts and radial velocities. *Publ. Astron. Soc. Pac.* **110**, 934–977 (1998).
76. Foreman-Mackey, D., Hogg, D. W., Lang, D. & Goodman, J. emcee: the MCMC hammer. *Publ. Astron. Soc. Pac.* **125**, 306 (2013).
77. Bovy, J. galpy: a python library for galactic dynamics. *Astrophys. J. Suppl. Ser.* **216**, 29 (2015).
78. Bovy, J. & Rix, H.-W. A direct dynamical measurement of the Milky Way's disk surface density profile, disk scale length, and dark matter profile at $4\text{ kpc} \lesssim R \lesssim 9\text{ kpc}$. *Astrophys. J.* **779**, 115 (2013).
79. Schönrich, R., Binney, J. & Dehnen, W. Local kinematics and the local standard of rest. *Mon. Not. R. Astron. Soc.* **403**, 1829–1833 (2010).
80. Schönrich, R. Galactic rotation and solar motion from stellar kinematics. *Mon. Not. R. Astron. Soc.* **427**, 274–287 (2012).
81. Pauli, E.-M., Napiwotzki, R., Heber, U., Altmann, M. & Odenkirchen, M. 3D kinematics of white dwarfs from the SPY project. II. *Astron. Astrophys.* **447**, 173–184 (2006).
82. Claret, A. et al. Gravity and limb-darkening coefficients for compact stars: DA, DB, and DBA eclipsing white dwarfs. *Astron. Astrophys.* **634**, A93 (2020).
83. Lenz, P. & Breger, M. Period04: statistical analysis of large astronomical time series. Record No. 1407.009 (Astrophysics Source Code Library, 2014).

84. Paxton, B. et al. Modules for Experiments in Stellar Astrophysics (MESA). *Astrophys. J. Suppl. Ser.* **192**, 3 (2011).
85. Paxton, B. et al. Modules for Experiments in Stellar Astrophysics (MESA): planets, oscillations, rotation, and massive stars. *Astrophys. J. Suppl. Ser.* **208**, 4 (2013).
86. Paxton, B. et al. Modules for Experiments in Stellar Astrophysics (MESA): binaries, pulsations, and explosions. *Astrophys. J. Suppl. Ser.* **220**, 15 (2015).
87. Paxton, B. et al. Modules for Experiments in Stellar Astrophysics (MESA): convective boundaries, element diffusion, and massive star explosions. *Astrophys. J. Suppl. Ser.* **234**, 34 (2018).
88. Paxton, B. et al. Modules for Experiments in Stellar Astrophysics (MESA): pulsating variable stars, rotation, convective boundaries, and energy conservation. *Astrophys. J. Suppl. Ser.* **243**, 10 (2019).
89. Ostrowski, J., Baran, A. S., Sanjayan, S. & Sahoo, S. K. Evolutionary modelling of subdwarf B stars using MESA with the predictive mixing and convective pre-mixing schemes. *Mon. Not. R. Astron. Soc.* **503**, 4646–4661 (2021).
90. de Jager, C., Nieuwenhuijzen, H. & van der Hucht, K. A. Mass loss rates in the Hertzsprung-Russell diagram. *Astron. Astrophys. Suppl. Ser.* **72**, 259–289 (1988).
91. Krtićka, J. et al. Hot subdwarf wind models with accurate abundances. I. Hydrogen dominated stars HD 49798 and BD+18° 2647. *Astron. Astrophys.* **631**, A75 (2019).
92. Zenati, Y., Toonen, S. & Perets, H. B. Formation and evolution of hybrid He–CO white dwarfs and their properties. *Mon. Not. R. Astron. Soc.* **482**, 1135–1142 (2019).
93. Nomoto, K. Supernova explosions in accreting white dwarfs and Type I supernovae. In *Proc. Texas Workshop on Type I Supernovae* (ed. Wheeler, J. C.) 164–181 (Univ. Texas at Austin, 1980).
94. Livne, E. Successive detonations in accreting white dwarfs as an alternative mechanism for type I supernovae. *Astrophys. J. Lett.* **354**, L53 (1990).
95. Shen, K. J. & Bildsten, L. The ignition of carbon detonations via converging shock waves in white dwarfs. *Astrophys. J.* **785**, 61 (2014).
96. Pakmor, R., Hachinger, S., Röpke, F. K. & Hillebrandt, W. Violent mergers of nearly equal-mass white dwarf as progenitors of subluminous Type Ia supernovae. *Astron. Astrophys.* **528**, A117 (2011).
97. Pakmor, R. et al. Normal Type Ia supernovae from violent mergers of white dwarf binaries. *Astrophys. J. Lett.* **747**, L10 (2012).
98. Röpke, F. K. et al. Constraining Type Ia supernova models: SN 2011fe as a test case. *Astrophys. J. Lett.* **750**, L19 (2012).
99. Sato, Y. et al. The critical mass ratio of double white dwarf binaries for violent merger-induced type Ia supernova explosions. *Astrophys. J.* **821**, 67 (2016).
100. Li, W. et al. SN 2002cx: the most peculiar known Type Ia supernova. *Publ. Astron. Soc. Pac.* **115**, 453–473 (2003).
101. Foley, R. J. et al. Type Iax supernovae: a new class of stellar explosion. *Astrophys. J.* **767**, 57 (2013).
102. Wang, B., Justham, S. & Han, Z. Producing Type Iax supernovae from a specific class of helium-ignited WD explosions. *Astron. Astrophys.* **559**, A94 (2013).
103. Han, Z., Podsiadlowski, P., Maxted, P. F. L., Marsh, T. R. & Ivanova, N. The origin of subdwarf B stars – I. The formation channels. *Mon. Not. R. Astron. Soc.* **336**, 449–466 (2002).
104. Weidemann, V. Revision of the initial-to-final mass relation. *Astron. Astrophys.* **363**, 647–656 (2000).
105. Robitaille, T. P. et al. Astropy: a community Python package for astronomy. *Astron. Astrophys.* **558**, A33 (2013).
106. Price-Whelan, A. M. et al. The Astropy Project: building an open-science project and status of the v2.0 core package. *Astron. J.* **156**, 123 (2018).
107. Robson, T., Cornish, N. J. & Liu, C. The construction and use of LISA sensitivity curves. *Class. Quantum Gravity* **36**, 105011 (2019).
108. Kupfer, T. et al. LISA verification binaries with updated distances from Gaia Data Release 2. *Mon. Not. R. Astron. Soc.* **480**, 302–309 (2018).

Acknowledgements

I.P. and V.S. were partially funded by the Deutsche Forschungsgemeinschaft (DFG) under grant no. GE2506/12-1. I.P. also acknowledges funding by the United Kingdom's Science and Technology Facilities Council, grant no. ST/T000406/1. P.N. gratefully acknowledges funding provided by the Max Planck Society. A.I. acknowledges funding by the DFG through grant no. HE1356/71-1. D.S. was supported by the DFG under grant nos. HE1356/70-1 and IR190/1-1. B.B. acknowledges support from the National Aeronautics and Space Administration (NASA) under the TESS Guest Investigator program, grant no. 80NSSC19K1720. T.K. acknowledges support by the United States National Science Foundation through grant no. NSF PHY-1748958. We thank T. R. Marsh for enlightening discussions and for providing an MCMC wrapper to be used with LCURVE. We are grateful to A. S. Baran and D. Jones for providing helpful comments to an earlier version of this manuscript. This article includes data collected by the TESS mission; funding for this mission is provided by the NASA Explorer Program. This work has also made use of data from the European Space Agency mission Gaia (<https://www.cosmos.esa.int/gaia>), processed by the Gaia Data Processing and Analysis Consortium (<https://www.cosmos.esa.int/web/gaia/dpac/consortium>); funding for this consortium has been provided by national institutions, in particular the institutions participating in the Gaia Multilateral Agreement. Finally, some of the data presented here were obtained at the W. M. Keck Observatory, which is operated as a scientific partnership among the California Institute of Technology, the University of California and NASA. The Observatory was made possible by the generous financial support of the W. M. Keck Foundation. We wish to recognize and acknowledge the very important cultural role that the summit of Mauna Kea has always had within the indigenous Hawaiian community and the reverence that the community has for it. We are most fortunate to have the opportunity to conduct observations from this mountain.

Author contributions

I.P. carried out the radial velocity estimates and fitting and the light curve fitting, and led the writing of the manuscript. P.N. calculated the evolution of the system. S.G. and U.H. performed the spectral fitting. T.K. did the spectroscopic reduction and cross-checked the light curve fitting. D.S. and U.H. performed the SED fitting. A.I. wrote the SED fitting tool and calculated the spectral models used for SED and spectral fitting. A.B. calculated the Galactic orbit of the system. J.v.R. performed the spectroscopic observations and contributed to the light curve fit. V.S. and B.N.B. contributed to the analysis of the light curve. All authors reviewed the manuscript.

Competing interests

The authors declare no competing interests.

Additional information

Supplementary information The online version contains supplementary material available at <https://doi.org/10.1038/s41550-021-01413-0>.

Correspondence and requests for materials should be addressed to I.P.

Peer review information *Nature Astronomy* thanks Zhanwen Han and the other, anonymous, reviewer(s) for their contribution to the peer review of this work.

Reprints and permissions information is available at www.nature.com/reprints.

Publisher's note Springer Nature remains neutral with regard to jurisdictional claims in published maps and institutional affiliations.

© The Author(s), under exclusive licence to Springer Nature Limited 2021

New X-ray observations of the hot subdwarf binary HD 49798/RX J0648.0–4418

S. Mereghetti¹,¹★ F. Pintore²,²★ T. Rauch,³ N. La Palombara¹,¹ P. Esposito,⁴ S. Geier,⁵ I. Pelisoli⁵,^{5,6}
M. Rigoselli¹,¹ V. Schaffenroth⁵ and A. Tiengo⁴

¹INAF – IASF Milano, Via A. Corti 12, I-20133 Milano, Italy

²INAF – IASF Palermo, Via U. La Malfa 153, I-90146 Palermo, Italy

³Institute for Astronomy and Astrophysics, Kepler Center for Astro and Particle Physics, Eberhard Karls University, Sand 1, D-72076 Tübingen, Germany

⁴Scuola Universitaria Superiore IUSS Pavia, Piazza della Vittoria 15, I-27100 Pavia, Italy

⁵Institut für Physik und Astronomie, Universität Potsdam, Haus 28, Karl-Liebknecht-Str 24/25, D-14476 Potsdam-Golm, Germany

⁶Department of Physics, University of Warwick, Coventry, CV4 7AL, UK

Accepted 2021 April 7. Received 2021 April 7; in original form 2021 February 23

ABSTRACT

HD 49798/RX J0648.0–4418 is the only confirmed X-ray binary in which the mass donor is a hot subdwarf star of O spectral type and, most likely, it contains a massive white dwarf ($1.28 \pm 0.05 M_{\odot}$) with a very fast spin period of 13.2 s. Here, we report the results of new *XMM-Newton* pointings of this peculiar binary, carried out in 2018 and in 2020, together with a reanalysis of all the previous observations. The new data indicate that the compact object is still spinning-up at a steady rate of $(-2.17 \pm 0.01) \times 10^{-15} \text{ s s}^{-1}$, consistent with its interpretation in terms of a young contracting white dwarf. Comparison of observations obtained at similar orbital phases, far from the eclipse, shows evidence for long-term variability of the hard ($>0.5 \text{ keV}$) spectral component at a level of $\sim(70 \pm 20)$ per cent, suggesting the presence of time-dependent inhomogeneities in the weak stellar wind of the HD 49798 subdwarf. To investigate better the soft spectral component that dominates the X-ray flux from this system, we computed a theoretical model for the thermal emission expected from an atmosphere with element abundances and surface gravity appropriate for this massive white dwarf. This model gives a best fit with effective temperature of $T_{\text{eff}} = 2.25 \times 10^5 \text{ K}$ and an emitting area with a radius of $\sim 1600 \text{ km}$, larger than that found with blackbody fits. This model also predicts a contribution of the pulsed emission from the white dwarf in the optical band significantly larger than previously thought and possibly relevant for optical variability studies of this system.

Key words: subdwarfs – white dwarfs – X-rays: binaries.

1 INTRODUCTION

HD 49798/RX J0648.0–4418 is the only known accreting X-ray binary in which the mass donor belongs to the class of hot subdwarf stars (Heber 2016). This binary, likely the outcome of a common envelope stage, is relevant in the context of evolutionary models of intermediate-mass stars, possibly leading to the formation of millisecond pulsars or Type Ia supernovae (Wang & Han 2010; Brooks, Kupfer & Bildsten 2017; Wu & Wang 2019). It is also interesting because, through the study of its X-ray emission, it offers the possibility to obtain some information on the weak stellar wind of the hot subdwarf (Mereghetti & La Palombara 2016; Krtićka et al. 2019).

HD 49798/RX J0648.0–4418 is composed of a compact object spinning at $P = 13.2 \text{ s}$ and a subdwarf star of O spectral type (Kudritzki & Simon 1978; Israel et al. 1997; Mereghetti et al. 2011). The orbital period, determined through optical spectroscopy since early observations of HD 49798, is 1.55 d (Thackeray 1970). The masses of the two stars are well constrained by the measurement of the optical and X-ray mass functions, the system inclination being derived from the duration of the X-ray eclipse: the compact object

has a mass of $1.28 \pm 0.05 M_{\odot}$ and is most likely a white dwarf, while the mass of HD 49798 is $1.50 \pm 0.05 M_{\odot}$ (Mereghetti et al. 2009). The most recent parallax obtained with *Gaia* EDR3 corresponds to a distance of $521 \pm 14 \text{ pc}$ (Brown et al. 2020).

Contrary to the majority of X-ray binaries, which are transient or highly variable, RX J0648.0–4418 is a persistent X-ray source: a luminosity of $\sim 10^{32} \text{ erg s}^{-1}$ was seen in all observations, that now span almost 30 yr. With a radius of $\sim 1 R_{\odot}$, HD 49798 underfills its Roche lobe, but it is one of the few hot subdwarfs with strong evidence for a stellar wind (Hamann et al. 1981; Hamann 2010). The most recent estimate, obtained through the modeling of high-resolution UV/optical spectra, yields a mass-loss rate of $2.1 \times 10^{-9} M_{\odot} \text{ yr}^{-1}$ and a wind terminal velocity of 1570 km s^{-1} (Krtićka et al. 2019). With these stellar wind parameters, the observed X-ray luminosity is consistent with that expected from accretion on to a massive white dwarf (Mereghetti et al. 2009, 2011).

Besides the low X-ray luminosity, much smaller than that expected if the accreting object were a neutron star, there are other arguments that support the presence of a white dwarf in this system. Most of the X-ray flux is emitted in a very soft and strongly pulsed thermal component, well fitted by a blackbody with temperature of $kT \sim 30 \text{ eV}$ and an emitting radius of $\sim 30 \text{ km}$ (Mereghetti et al. 2016). These dimensions are consistent with those of a hotspot on the surface of a

* E-mail: sandro.mereghetti@inaf.it (SM); fabio.pintore@inaf.it (FP)

Table 1. Log of the *XMM-Newton* observations of HD 49798.

Date	Obs. ID	Start (MJD)	Stop (MJD)	Exposure pn/MOS (ks)	Orbital phase
2002 May 3	0112450301	52397.46	52397.55	4.5/7.2	0.45–0.48
2002 May 4	0112450401	52397.98	52398.06	1.4/5.4	0.78–0.81
2002 May 4	0112450501	52398.56	52398.59	0.6/2.5	0.17–0.16
2002 Sep 17	0112450601	52534.58	52534.72	6.9/11.9	0.06–0.11
2008 May 10	0555460201	54596.90	54597.38	36.7/43.0	0.56–0.87
2011 May 2	0671240901	55683.55	55683.76	17.0/18.3	0.70–0.82
2011 Aug 18	0671241001	55791.88	55792.07	15.0/16.4	0.69–0.80
2011 Aug 20	0671241101	55793.46	55793.62	11.8/14.1	0.72–0.80
2011 Aug 25	0671241201	55798.04	55798.27	18.0/19.2	0.67–0.81
2011 Sep 3	0671241301	55807.35	55807.54	15.0/16.4	0.69–0.80
2011 Sep 8	0671241401	55811.10	55812.19	15.0/16.4	0.70–0.80
2013 Nov 10	0721050101	56605.80	56606.25	37.9/39.1	0.60–0.86
2014 Oct 18	0740280101	56948.37	56948.71	27.1/29.1	0.95–0.15
2018 Nov 8	0820220101	58430.46	58430.92	34.3/40.9	0.56–0.85
2020 Feb 27	0841270101	58906.31	58906.81	37.3/45.4	0.03–0.35

white dwarf, but are too large for a neutron star. This emitting radius could be reconciled with a neutron star only if the X-ray emission comes from the whole (or a large part of the) star surface, but this is at variance with the very high pulsed fraction of the soft X-ray pulse profile (~ 65 per cent).

The steady long-term spin-up of RX J0648.0–4418, at a rate of $\dot{P} = -2.15 \times 10^{-15} \text{ s s}^{-1}$, is difficult to explain by accretion torques (Mereghetti et al. 2016). On the other hand, Popov et al. (2018) showed that it is consistent with that caused by the radial contraction of a young white dwarf with age of a few millions years. Such a small age is in agreement with the evolutionary models that account for the properties of this binary. Finally, we note that population synthesis simulations of hot subdwarf binaries predict that those hosting white dwarfs greatly outnumber those with a neutron star (Yungelson & Tutukov 2005; Wu et al. 2018).

To continue our long-term monitoring of this unique X-ray binary, we observed it with *XMM-Newton* in 2018 and 2020. Here, we present the results of these new observations, complemented by a reanalysis of all the previous data, including the first spectral fits with a white dwarf atmosphere model applied to this system.

2 DATA ANALYSIS AND RESULTS

XMM-Newton observed RX J0648.0–4418 for ~ 34 ks on 2018 November 8 and for ~ 37 ks on 2020 February 27. We use the data obtained with the EPIC instrument, which consists of one pn and two MOS cameras (Strüder et al. 2001; Turner et al. 2001). As in all the previous observations, the pn and MOS cameras were operated in full-frame mode, giving time resolutions of 73 ms and 2.6 s, respectively.

To compare properly the new observations with the previous ones, we processed all the available *XMM-Newton* data using SAS v.16.1 and the most recent calibration files. We filtered out time intervals with high background and selected single- and double-pixels events for the pn ($\text{PATTERN} \leq 4$), and single- and multiple-pixels events for the MOS ($\text{PATTERN} \leq 12$). The resulting exposure times are given in Table 1. Source and background events were extracted from circular regions with radii of 30 and 60 arcsec, respectively.

For the timing analysis, we used also the *ROSAT* data obtained on 1992 November 11. We selected the counts obtained with the PSPC instrument in the energy range 0.1–0.5 keV, from a source region with radius of 1 arcmin.

Table 2. Phase-coherent timing solution valid in the 48937.75–58761.81 MJD range.

Parameter	Value	Units
Right ascension	$6^{\text{h}} 48^{\text{m}} 4^{\text{s}}.7$	J2000
Declination	$-44^{\circ} 18' 58''.4$	J2000
Orbital period	1.547666	d
$A_X \sin i$	9.78646	light-s
T^*	43962.017 ^a	MJD
ν_0	0.075848091873(12)	Hz
$\dot{\nu}$	$1.250(7) \times 10^{-17}$	Hz s^{-1}
P_0	13.184247295(2)	s
\dot{P}	$-2.17(1) \times 10^{-15}$	s s^{-1}
T_0	55793.4827567	MJD

Note. ^a Due to a typo, this parameter was incorrectly reported in table 2 of Mereghetti et al. (2016). With this definition of T^* the eclipse occurs at orbital phase 0.75.

For all data sets, the times of arrival of the events were corrected to the Solar system barycentre using the source coordinates given in Table 2.

2.1 Timing analysis results

The source pulsations at 13.2 s are clearly visible in the 2018 and 2020 data. The spin periods measured in these new observations are consistent with those predicted by the ephemeris reported in Mereghetti et al. (2016), which were derived from a phase-coherent timing of all the data obtained before 2015. Therefore, we included the new data in the phase-coherent analysis. Briefly, this consists in deriving the time of arrivals of a fiducial phase of the pulse profile measured in the different observations and, after correcting for the effect of orbital motion, fitting them with a quadratic function $\phi(t) = \phi_0(t) + \nu_0(t - T_0) + 0.5\dot{\nu}(t - T_0)^2$. The phases were determined by fitting a sinusoidal function to the 0.15–0.5 keV pulse profiles measured in time intervals of 2000 s. This procedure was done iteratively, starting from the most closely spaced observations, and progressively including the other ones, as the improved timing parameters allow to maintain phase coherence. The orbital parameters were kept fixed at the values of Table 2.

Our final solution provided a good fit ($\chi^2_{\nu} = 1.21$ for 44 degrees of freedom) and a highly significant quadratic term with the parameters

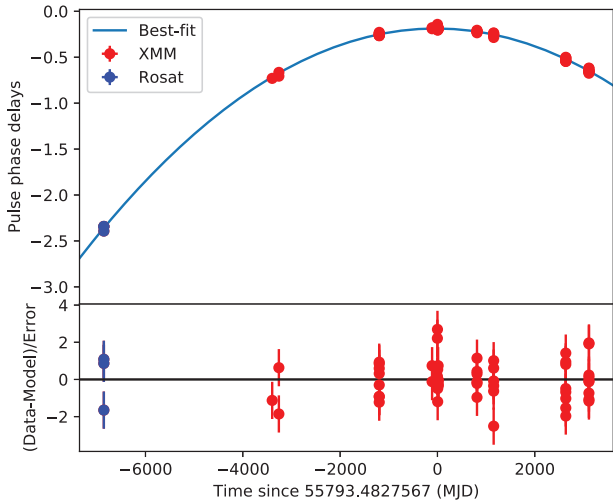


Figure 1. Timing solution (in units of phase, the solid blue line) for ~ 28 yr of observations of HD 49798/RX J0648.0–4418. The residuals of the best-fitting model are presented in the bottom panel.

given in Table 2. The best fit and its residuals are shown in Fig. 1. This timing solution is consistent with that of Mereghetti et al. (2016), but, because of the longer baseline, it has smaller uncertainties on the best-fitting parameters.

To search for long-term variability, disentangling the effects related to the orbital phase, we produced background-subtracted light curves folded at the orbital period (Fig. 2). They refer to the soft (0.2–0.5 keV) and hard (0.5–10 keV) energy bands. It can be seen that there is some evidence that the hard X-ray flux in 2020 was slightly lower than in previous observations that covered similar orbital phases. This is indeed confirmed by the spectral analysis described below. The 2020 hard X-ray light curve shows also evidence for some variability on time-scales of few hundreds seconds. In fact a fit with a constant of the data binned at 400 s yields $\chi^2_\nu = 1.66$ for 108 degrees of freedom.

2.2 X-ray emission during the eclipse

The 2018 observation covered the orbital phases around the eclipse of the X-ray pulsar and confirms the presence of significant X-ray emission also when the compact object is occulted by its subdwarf companion, as it was seen in previous eight observations (Mereghetti et al. 2009, 2013). To investigate possible long-term variability of the emission during the eclipse, we extracted EPIC-pn images (in the 0.3–4.5 keV range) in a time interval of 4300 s (the eclipse duration measured in Mereghetti et al. 2013) centred at phase 0.75 and carried out source detections using the SAS task *edetect.chain*. HD 49798 was detected in all the nine images, with count rates consistent with a constant value of 0.048 ± 0.002 counts s^{-1} ($\chi^2_\nu = 1.44$ for 8 degrees of freedom).

We then produced a pn and an MOS spectrum of the eclipse emission by stacking all the source spectra of the individual observations, extracted from the above orbital phase interval. These two spectra were fit simultaneously using the sum of three thermal plasma emission models (*vapex* in XSPEC) with abundances fixed to the most recent values found for HD 49798 (see table 2 of Krtićka et al. 2019). The resulting temperatures of 0.15, 0.9, and 6 keV, and the corresponding model normalizations, were consistent with those found by Mereghetti & La Palombara (2016). Under the assumption that the X-ray flux seen during the eclipse is due to intrinsic emission

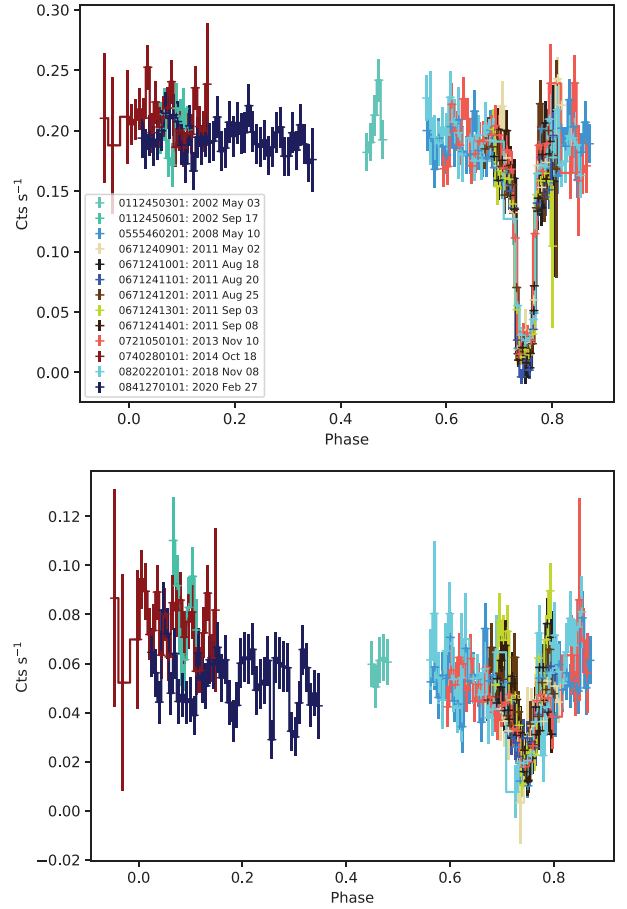


Figure 2. Light curves folded at the orbital period in the soft (0.2–0.5 keV, top) and hard (0.5–10 keV, bottom) energy ranges. The eclipse occurs at phase 0.75. The time bin is 1000 s.

from HD 49798, and thus present at all orbital phases, we included this best-fitting eclipse model as a fixed component in all the subsequent spectral fits discussed below.

2.3 Variability in the hard X-ray component

The 2020 observation provided the first data set with a long exposure time at orbital phases far from the eclipse, which were covered only marginally by previous *XMM-Newton* pointings. For a first analysis of these data and to facilitate the comparison with previous results, we adopted a blackbody plus power-law model and we concentrated on a comparison with the 2014 observation, which covered similar orbital phases.

Separate fits to the 2014 and 2020 spectra, in the 0.3–10 keV range, gave consistent values for the blackbody component, but different best-fitting parameters for the power law, indicating a lower flux in 2020. Therefore, we fitted the 2014 and 2020 pn spectra simultaneously, imposing common values for all the parameters except for the power-law normalization. This resulted in a good fit ($\chi^2_\nu = 1.15$ for 167 degrees of freedom) with 0.3–10 keV fluxes of the power law component of $(1.7 \pm 0.2) \times 10^{-13}$ erg $cm^{-2} s^{-1}$ in 2014 and $(1.0 \pm 0.1) \times 10^{-13}$ erg $cm^{-2} s^{-1}$ in 2020. These flux values confirm the evidence for the variability seen in the hard X-ray light curves of Fig. 2. All the other spectral parameters were consistent with those obtained from the sum of all the data taken before 2015

(Mereghetti et al. 2016), although they had larger uncertainties due to their lower counting statistics.

2.4 The soft thermal component

Since with the new observations we found no evidence for long-term variability in the soft thermal component, we performed a spectral analysis using the spectra obtained by stacking all the available observations. In the following, we present the results obtained with the EPIC-pn spectra,¹ corresponding to a total exposure time of 170 ks. In addition to fits with the usual blackbody plus power law model, we also explored a more physically motivated scenario, replacing the blackbody component with a white dwarf atmosphere model that we computed specifically for this source.

The effects of an atmosphere on the emerging thermal radiation depend on many parameters, including elemental composition and surface gravity, but it is impossible to constrain all of them with the limited spectral resolution and narrow bandwidth of the current data. Therefore, we explored only a single model that we computed assuming a surface gravity of $\log g = 9$ (appropriate for this massive white dwarf) and a composition based on the abundances measured for HD 49798 (Krtićka et al. 2019). This choice for the abundances is based on the hypothesis that the white dwarf surface, or at least the regions where matter accretes and that are responsible for the X-ray emission, are covered by matter coming from the companion star.

To model stellar spectra in the relevant T_{eff} and $\log g$ ranges, non-local thermodynamic equilibrium (NLTE) model atmospheres are mandatory. Thus, we employed the Tübingen NLTE Model-Atmosphere Package² (Werner et al. 2003; Werner, Dreizler & Rauch 2012) to calculate plane-parallel and chemically homogeneous atmospheres in hydrostatic and radiative equilibrium. We considered opacities of H, He, C, N, O, Fe, and Ni. The atomic data were taken from the Tübingen Model-Atom Database (TMAD) and, for Fe and Ni, calculated with our Iron Opacity and Interface program (IrOnIc), which uses a statistical approach with so-called super levels and super lines (Rauch & Deetjen 2003) based on Kurucz’s line lists³ (Kurucz 2009, 2011) and Opacity Project data⁴ (Seaton et al. 1994). We adopted the abundances given by the following normalized mass fractions: H (8.045×10^{-2}), He (9.134×10^{-1}), C (2.337×10^{-4}), N (3.431×10^{-3}), O (1.239×10^{-4}), Fe (2.168×10^{-3}), and Ni (1.817×10^{-4}). Some examples of the model for different values of the effective temperature are shown in Fig. 3. Due to the presence of many absorption lines and edges, they deviate significantly from blackbody spectra, especially at the shortest wavelengths. This is also illustrated in Fig. 4, which presents an enlarged view of the energy range covered by our X-ray data. In this figure, the theoretical model has been convolved with the instrumental response of the EPIC pn detector, which results in a smearing of the sharp spectral features.

By fitting the pn spectrum with the atmosphere model plus a power law, we could not obtain a unique best-fitting solution. In fact, exploring the whole range of temperatures covered by our model,⁵ we found similarly good results with effective temperatures of about 2.2 or 2.9×10^5 K ($\chi^2_{\nu} = 1.26$ and 1.28 , respectively). These fits imply emitting regions more than one hundred times larger than that

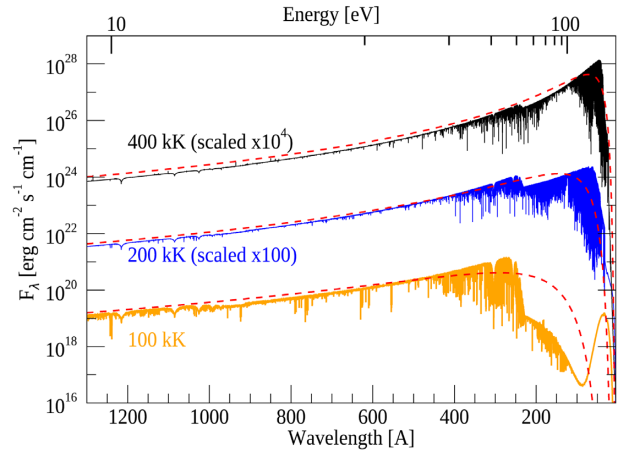


Figure 3. Examples of our white dwarf atmosphere model for effective temperatures of 10^5 , 2×10^5 , and 4×10^5 K. Note that the two latter have been rescaled by two and four decades for clarity. The red-dashed lines indicate for comparison blackbody models with the corresponding temperatures.

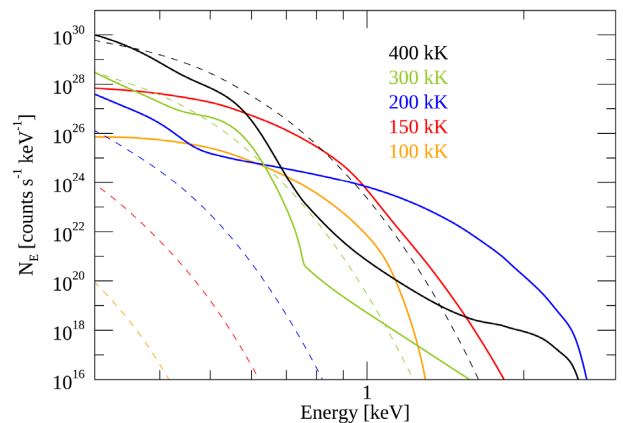


Figure 4. Examples of our white dwarf atmosphere model in the 0.3–3 keV energy range folded through the EPIC pn response. The dashed lines represent blackbody models with the corresponding temperatures.

derived with the blackbody model (see Table 3). Another reasonably good fit, with only a slightly worse $\chi^2_{\nu} = 1.39$, was found for $T_{\text{eff}} = 3.7 \times 10^5$ K.

The reason for these multiple solutions can be qualitatively understood by examining Fig. 4: in the ~ 0.3 – 0.6 keV range, where the thermal emission dominates over the power-law component, the atmosphere model has an average spectral slope that varies with temperature in a non-monotonic way. The slope observed in the X-ray data, and well described by a blackbody of $\sim 3.7 \times 10^5$ K, can be well approximated by atmosphere models with different values of T_{eff} , also considering the effect of changes in N_{H} and in the power-law parameters (see best-fitting values in Table 3).

The best-fitting to the pn spectrum with an atmosphere of $T_{\text{eff}} = 2.25 \times 10^5$ K is shown in Fig. 5. The residuals in the fits, which lead to a χ^2_{ν} value slightly higher than that obtained with a blackbody, could be reduced by changing the atmosphere metal abundances and/or surface gravity (as well as by allowing some small variations in the eclipse model used to describe the contribution from HD 49798). However, besides increasing the number of free parameters, this would not lead to a unique solution and we believe

¹We checked that similar results were obtained with the MOS.

²<http://astro.uni-tuebingen.de/~TMAP>

³<http://kurucz.harvard.edu/atoms.html>

⁴<http://cdsweb.u-strasbg.fr/topbase/topbase.html>

⁵We imposed values of $N_{\text{H}} > 10^{20} \text{ cm}^{-2}$ to avoid convergence of the fits to unreasonable values.

Table 3. Spectral results (errors at 90% c.l.).

Model	N_{H} 10^{20} cm^{-2}	T_{eff} 10^5 K	R^a (km)	Photon index	F_{PL}^b $10^{-13} \text{ erg cm}^{-2} \text{ s}^{-1}$	χ^2_{ν} /degrees of freedom
BB + PL	1 (fixed)	3.65 ± 0.18	41^{+13}_{-10}	1.80 ± 0.06	1.18 ± 0.05	1.16/116
Atm + PL	14.3 ± 1.5	$2.25^{+0.02}_{-0.04}$	1604^{+207}_{-212}	1.75 ± 0.09	1.23 ± 0.06	1.26/116
Atm + PL	8.5 ± 0.8	2.94 ± 0.01	397 ± 32	1.66 ± 0.09	1.20 ± 0.06	1.28/116
Atm + PL	6.3 ± 1.5	$3.73^{+0.04}_{-0.19}$	66^{+26}_{-9}	1.92 ± 0.06	1.22 ± 0.05	1.39/116

Notes. ^aEmission radius for $d = 521 \text{ pc}$.

^bUnabsorbed flux of power law component in the 0.3–10 keV energy range.

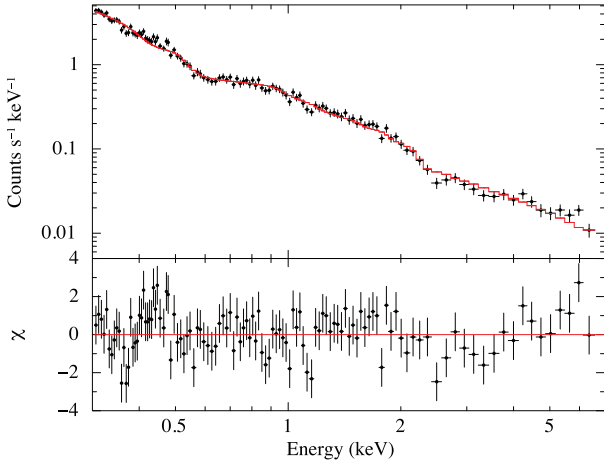


Figure 5. Best fit (top) and residuals (bottom) of the total pn spectrum with a power law plus atmosphere model with $T_{\text{eff}} = 2.25 \times 10^5 \text{ K}$.

that such more refined analysis should wait for the availability of future data with better spectral resolution and statistics.

3 DISCUSSION AND CONCLUSIONS

Evidence for small (~ 30 percent) variability in the hard X-ray component of HD 49798 was first reported by Mereghetti et al. (2011), based on the observations of 2002 September and 2008 May. Since those data were obtained at very different orbital phases, it was not clear if such variation was related to the source position in the orbit or to real long-term changes in the properties of the system. The latter possibility seems favoured by our new results, which show a ~ 70 percent flux variation between two observations spaced by six years, but taken at similar orbital phases. This suggests that the stellar wind from the hot subdwarf HD 49798, despite being much weaker than those of normal early-type stars, might be subject to time variable inhomogeneities leading to changes in the mass accretion rate, similar to those seen in high-mass X-ray binaries. The resulting luminosity variations are more prominently appearing in the harder spectral component, likely originating in shocks occurring within the accretion stream.

The new *XMM-Newton* data reported here show that the pulsar in HD 49798/RX J0648.0–4418 has continued also after 2014 its regular spin-up at the same rate of $\dot{P} = -2.17 \times 10^{-15} \text{ s s}^{-1}$. As discussed in Mereghetti et al. (2016), the mass accretion rate in this system is insufficient to cause this rapid spin-up if the compact object is a white dwarf. On the other hand, such a remarkably steady spin-up rate is difficult to explain for a neutron star subject to wind accretion: changes in the torque, resulting from variations in the stellar wind gravitationally captured by the compact object, should affect its spin

period. However, no changes in \dot{P} were seen, despite the observed long-term variability. These results support the interpretation of the spin-up in terms of the secular contraction of a white dwarf of few Myr age, as proposed by Popov et al. (2018).

Most of the X-ray luminosity of RX J0648.0–4418 is emitted in a soft thermal component, probably originating on the white dwarf surface. The large size of the emitting area, inferred from blackbody fits, has been one of the arguments used to disfavour a neutron star interpretation. Here, we presented the first attempt to describe this soft component with a more physical model, accounting for the presence of an atmosphere and assuming that the white dwarf is covered by helium-rich material accreted from its companion star. Fitting with this model plus a power law, we obtained reasonably good results, although the temperature could not be uniquely constrained. Remarkably, these fits result in significantly larger emission radii than those derived with the blackbody model, implying that the thermal component originates from a large fraction, or even from the totality, of the star surface.

Another relevant implication of these fits is that the contribution of the thermal emission in the UV/optical bands is much larger than that expected by the extrapolation of the best-fitting blackbody model. For example, the best atmosphere fit with $T_{\text{eff}} = 2.25 \times 10^5 \text{ K}$ gives an optical flux about three orders of magnitude larger than that of the blackbody. We cannot exclude that models with slightly different compositions could give an even larger flux at long wavelengths, when fitted to the X-ray data. This emission might produce detectable pulsations in the optical band, if it is modulated as strongly as in the soft X-ray band. Previous searches for optical pulsations at the spin period of 13.2 s provided an upper limit of $6 \times 10^{-4} \text{ photons cm}^{-2} \text{ s}^{-1} \text{ \AA}^{-1}$ at 3600 \AA (Mereghetti et al. 2011). The extrapolation of the best-fitting atmosphere model is only about one order of magnitude below this upper limit, suggesting that more sensitive searches could lead to the detection of optical pulsations or to useful constraints in case of null results.

4 SUMMARY

Because of new *XMM-Newton* observations of HD 49798/RX J0648.0–4418 carried out in 2018 and 2020, we could extend its phase-connected timing solution, now spanning a time interval of almost 30 yr, without finding any evidence of variations in the spin-up rate, despite the long-term variability in the flux of the hard X-ray component reported here for the first time.

We computed a specific white dwarf atmosphere model for this system, adopting appropriate composition and surface gravity values, and used it to describe the soft X-ray component, which was traditionally fitted with a blackbody. Our analysis showed that, in order to fully exploit the potential diagnostics of physical models of this type, data with higher spectral resolution are needed, as can be provided by future experiments such as XRISM (XRISM Science

Team 2020) and Athena/XIFU (Barret, Lam Trong & den Herder 2018). On the other hand, this first attempt indicates that atmosphere models lead to lower temperatures and much larger emission regions compared to blackbody fits. Interestingly, our best-fitting results imply that the pulsed thermal component emitted from the compact object gives a contribution in the optical/UV bands much larger than predicted by the blackbody. This opens promising prospects for future searches of optical pulsations and, more in general, for the investigation of variability in the optical band, where the contribution from the bright and hot HD 49798 is dominant.

ACKNOWLEDGEMENTS

We acknowledge financial support from INAF, through grant DP n.43/18 (Main-streams), and from the Italian Ministry for University and Research, through grant 2017LJ39LM (UNIAM). The TMAD service (<http://astro-uni-tuebingen.de/~TMAD>) used for this paper was constructed as part of the activities of the German Astrophysical Virtual Observatory. IP and VS were partially funded by the Deutsche Forschungsgemeinschaft (DFG) under grants GE2506/12-1 and GE2506/9-1, respectively. This work is based on data from observations with *XMM-Newton*, an ESA science mission with instruments and contributions directly funded by ESA Member States and the USA (NASA).

DATA AVAILABILITY

The data underlying this article will be shared on reasonable request to the corresponding author.

REFERENCES

- Barret D., Lam Trong T., den Herder et al., 2018, in den Herder J.-W. A., Nikzad S., Nakazawa K., eds, Society of Photo-Optical Instrumentation Engineers (SPIE) Conference Series Vol. 10699, Space Telescopes and Instrumentation 2018: Ultraviolet to Gamma Ray. p. 106991G, preprint ([arXiv:1807.06092](https://arxiv.org/abs/1807.06092))
- Brooks J., Kupfer T., Bildsten L., 2017, *ApJ*, 847, 78
- Brown A. G. A. Gaia Collaboration, et al., Gaia Collaboration, 2020, *A&A*, in press
- Hamann W., Gruschinske J., Kudritzki R. P., Simon K. P., 1981, *A&A*, 104, 249
- Hamann W.-R., 2010, *Ap&SS*, 329, 151
- Heber U., 2016, *PASP*, 128, 082001
- Israel G. L., Stella L., Angelini L., White N. E., Kallman T. R., Giommi P., Treves A., 1997, *ApJ*, 474, L53
- Krtićka J., Janík J., Krtićková I., Mereghetti S., Pintore F., Németh P., Kubát J., Vučković M., 2019, *A&A*, 631, A75
- Kudritzki R. P., Simon K. P., 1978, *A&A*, 70, 653
- Kurucz R. L., 2009, in Hubeny I., Stone J. M., MacGregor K., Werner K., eds, AIP Conf. Ser. Vol. 1171, Recent Directions in Astrophysical Quantitative Spectroscopy and Radiation Hydrodynamics. Am. Inst. Phys., New York, p. 43
- Kurucz R. L., 2011, *Canadian J. Phys.*, 89, 417
- Mereghetti S., La Palombara N., 2016, *Adv. Space Res.*, 58, 809
- Mereghetti S., Tiengo A., Esposito P., La Palombara N., Israel G. L., Stella L., 2009, *Science*, 325, 1222
- Mereghetti S., La Palombara N., Tiengo A., Pizzolato F., Esposito P., Woudt P. A., Israel G. L., Stella L., 2011, *ApJ*, 737, 51
- Mereghetti S., La Palombara N., Tiengo A., Sartore N., Esposito P., Israel G. L., Stella L., 2013, *A&A*, 553, A46
- Mereghetti S., Pintore F., Esposito P., La Palombara N., Tiengo A., Israel G. L., Stella L., 2016, *MNRAS*, 458, 3523
- Popov S. B., Mereghetti S., Blinnikov S. I., Kuranov A. G., Yungelson L. R., 2018, *MNRAS*, 474, 2750
- Rauch T., Deetjen J. L., 2003, in Hubeny I., Mihalas D., Werner K., eds, ASP Conf. Ser. Vol. 288, Stellar Atmosphere Modeling. Astron. Soc. Pac., San Francisco, p. 103
- Seaton M. J., Yan Y., Mihalas D., Pradhan A. K., 1994, *MNRAS*, 266, 805
- Strüder L., Briel U., Dennerl K., et al., 2001, *A&A*, 365, L18
- Thackeray A. D., 1970, *MNRAS*, 150, 215
- Turner M. J. L., Abbey A., Arnaud M., et al., 2001, *A&A*, 365, L27
- Wang B., Han Z.-W., 2010, *Res. Astron. Astrophys.*, 10, 681
- Werner K., Deetjen J. L., Dreizler S., Nagel T., Rauch T., Schuh S. L., 2003, in Hubeny I., Mihalas D., Werner K., eds, ASP Conf. Ser. Vol. 288, Stellar Atmosphere Modeling. Astron. Soc. Pac., San Francisco, p. 31
- Werner K., Dreizler S., Rauch T., 2012, Astrophysics Source Code Library, record ascl:1212.015
- Wu C., Wang B., 2019, *MNRAS*, 486, 2977
- Wu Y., Chen X., Li Z., Han Z., 2018, *A&A*, 618, A14
- XRISM Science Team, 2020, preprint ([arXiv:2003.04962](https://arxiv.org/abs/2003.04962))
- Yungelson L. R., Tutukov A. V., 2005, *Astron. Rep.*, 49, 871

This paper has been typeset from a $\text{\TeX}/\text{\LaTeX}$ file prepared by the author.

Mysterious, variable, and extremely hot: White dwarfs showing ultra-high excitation lines

I. Photometric variability

Nicole Reindl¹, Veronika Schaffenroth¹, Semih Filiz¹, Stephan Geier¹, Ingrid Pelisoli^{1,2}, and Souza Oliveira Kepler³

¹ Institute for Physics and Astronomy, University of Potsdam, Karl-Liebknecht-Str. 24/25, 14476 Potsdam, Germany
e-mail: nreindl885@gmail.com

² Department of Physics, University of Warwick, Coventry CV4 7AL, UK

³ Instituto de Física, Universidade Federal do Rio Grande do Sul, 91501-900 Porto-Alegre, RS, Brazil

Received 6 January 2021 / Accepted 3 February 2021

ABSTRACT

Context. About 10% of all stars exhibit absorption lines of ultra-highly excited (UHE) metals (e.g., O VIII) in their optical spectra when entering the white dwarf cooling sequence. This is something that has never been observed in any other astrophysical object, and poses a decades-long mystery in our understanding of the late stages of stellar evolution. The recent discovery of a UHE white dwarf that is both spectroscopically and photometrically variable led to the speculation that the UHE lines might be created in a shock-heated circumstellar magnetosphere.

Aims. We aim to gain a better understanding of these mysterious objects by studying the photometric variability of the whole population of UHE white dwarfs, and white dwarfs showing only the He II line problem, as both phenomena are believed to be connected.

Methods. We investigate (multi-band) light curves from several ground- and space-based surveys of all 16 currently known UHE white dwarfs (including one newly discovered) and eight white dwarfs that show only the He II line problem.

Results. We find that $75^{+8}_{-13}\%$ of the UHE white dwarfs, and $75^{+9}_{-19}\%$ of the He II line problem white dwarfs are significantly photometrically variable, with periods ranging from 0.22 d to 2.93 d and amplitudes from a few tenths to a few hundredths of a magnitude. The high variability rate is in stark contrast to the variability rate amongst normal hot white dwarfs (we find $9^{+4}_{-2}\%$), marking UHE and He II line problem white dwarfs as a new class of variable stars. The period distribution of our sample agrees with both the orbital period distribution of post-common-envelope binaries and the rotational period distribution of magnetic white dwarfs if we assume that the objects in our sample will spin-up as a consequence of further contraction.

Conclusions. We find further evidence that UHE and He II line problem white dwarfs are indeed related, as concluded from their overlap in the *Gaia* HRD, similar photometric variability rates, light-curve shapes and amplitudes, and period distributions. The lack of increasing photometric amplitudes towards longer wavelengths, as well as the nondetection of optical emission lines arising from the highly irradiated face of a hypothetical secondary in the optical spectra of our stars, makes it seem unlikely that an irradiated late-type companion is the origin of the photometric variability. Instead, we believe that spots on the surfaces of these stars and/or geometrical effects of circumstellar material might be responsible.

Key words. white dwarfs – stars: variables: general – starspots – binaries: close

1. Introduction

White dwarfs are the end products of the vast majority of all stars, with about 20% of them being H-deficient. They are observed over a huge temperature interval, ranging from 250 000 K (Werner & Rauch 2015) down to 2710 K (Gianninas et al. 2015). The early stages of white dwarf cooling occur very rapidly. When a star enters the white dwarf cooling sequence, it cools down to 65 000 K within less than a million years, while the cooling phase down to 3000 K takes several billion years (Althaus et al. 2009; Renedo et al. 2010). Thus, although about 37 000 white dwarfs have been spectroscopically confirmed (Kepler et al. 2019), only a tiny fraction (<1%) have effective temperatures (T_{eff}) above 65 000 K.

These extremely hot white dwarfs cover a large but sparsely populated region in the Hertzsprung-Russell Diagram (HRD) and represent an important link in stellar evolution between the (post-)asymptotic giant branch (AGB) stars, and the bulk of the

white dwarfs on the cooling sequence. Several intriguing physical processes take place during the early stages of white dwarf cooling that mark those stars as important astronomical tools even beyond stellar evolution studies. The intense extreme ultraviolet (UV) radiation from a very hot white dwarf can evaporate giant planets. A fraction of the evaporated volatiles may then be accreted, polluting the atmosphere of the white dwarf (Gänsicke et al. 2019; Schreiber et al. 2019). Therefore, detailed abundance analyses of hot white dwarfs can provide information on the potential of these objects to reconstruct the composition of exosolar gaseous planets. Some white dwarfs in the T_{eff} interval 58 000–85 000 K were found to display high abundances of trans-iron group elements (atomic number $Z > 29$), which is thought to be caused by efficient radiative levitation of those elements (Chayer et al. 2005; Hoyer et al. 2017, 2018; Löbbling et al. 2020). These stars serve as important stellar laboratories to derive atomic data for highly ionized species of trans-iron elements (Rauch et al. 2012, 2014a,b, 2015a,b, 2016, 2017a,b).

Hot white dwarfs have also proven to be powerful tools for Galactic archaeology and cosmology. They are employed to check a dependency of fundamental constants, for example the fine structure constant α , with gravity (Berengut et al. 2013; Bainbridge et al. 2017; Hu et al. 2021), to derive the age of the Galactic halo (Kalirai 2012; Kilic et al. 2019) or to derive the properties of weakly interacting particles via the hot white dwarf luminosity function (Isern et al. 2008; Miller Bertolami 2014; Miller Bertolami et al. 2014).

A particularly baffling phenomenon that takes place at the beginning of the white dwarf cooling sequence is the presence of (partly very strong) absorption lines of ultra-highly excited (UHE) metals (e.g., N VII, O VIII) in the optical spectra of the hottest white dwarfs. The occurrence of these obscure features requires a dense environment with temperatures of the order 10^6 K, by far exceeding the stellar effective temperature. A photospheric origin can therefore be ruled out. As some of the UHE lines often exhibit an asymmetric profile shape, it was first suggested that those lines might form in a hot, optically thick stellar wind (Werner et al. 1995). Another peculiarity of these objects is that all of them show the Balmer or He II line problem, meaning that their Balmer/He II lines are unusually deep and broad and cannot be fitted with any model. There are also white dwarfs showing only the Balmer/He II line problem, but no UHE lines. Regarding the H-rich (DA-type) white dwarfs, it was found that the Balmer line problem is to some extent due to the neglect of metal opacities in the models (Werner 1996). But there are also cases in which the Balmer line problem persists, even when sophisticated models are used (Gianninas et al. 2011; Werner et al. 2018a, 2019). However, for the He-dominated (DO-type) white dwarfs showing the He II line problem, even the addition of metal opacities to the models does not help to overcome this problem. As the He II line problem is observed in every UHE white dwarf – without exception –, a link between these two phenomena seems very likely (Werner et al. 2004). It is thought that the “He II line problem” objects are related to the UHE white dwarfs and that the same process is operating in these stars but is failing to generate the UHE features (Werner et al. 2014).

The Balmer/He II line problem also makes it difficult – if not impossible – to derive accurate temperatures, gravities, and spectroscopic masses. Some objects show weak He I lines that allow to constrain their T_{eff} to some degree. High-resolution UV spectroscopy is available only for three UHE white dwarfs, which were analyzed by Werner et al. (2018b). These latter authors found that the T_{eff} derived by exploiting several ionization balances of UV metal lines agree with what can be estimated from the He I/He II ionization equilibrium in the optical. In addition, the study revealed that light metals (C, N, O, Si, P, and S) are found in these objects at generally subsolar abundances and heavy elements from the iron group (Cr, Mn, Fe, Co, Ni) with solar or supersolar abundances. This is not different from other hot white dwarfs and can be understood as a result of gravitational settling and radiative levitation of elements. Werner et al. (2018b) discussed the possibility that the UHE lines might form in a multicomponent radiatively driven wind that is frictionally heated. Such winds are expected to occur in a narrow strip in the $T_{\text{eff}} - \log g$ -diagram (Fig. 4 in Krtićka & Kubát 2005), which indeed overlaps with the region in which the UHE white dwarfs are observed (see Fig. 3 in Reindl et al. 2014).

While this strip could explain why the occurrence of UHE features is restricted to white dwarfs hotter than $\approx 65\,000$ K, the model does not explain why not all hot white dwarfs located in this region show this phenomenon. In addition, the frictionally heated wind model, which assumes a spherically symmetric wind, fails to explain the photometric and spectroscopic variability of the UHE white dwarf J01463+3236 discovered by Reindl

et al. (2019). These latter authors reported for the first time rapid changes of the equivalent widths (EWs) of the UHE features in the spectra of J01463+3236, which were found to be correlated to the photometric period of the star (≈ 0.24 d). Interpreting this period as the rotational period of the star, they argue that the UHE features are rotationally modulated and stem from a co-rotating, shock-heated, circumstellar magnetosphere. Furthermore, they suggested that the cooler parts of the magnetosphere likely constitute an additional line-forming region of the overly broad and overly deep He II lines (or Balmer lines in the case of DAs). White dwarfs that lack the UHE lines and only show the Balmer/He II line problem could then be explained by having cooler magnetospheres with temperatures not high enough to produce UHE lines. As this model requires the white dwarfs to be at least weakly magnetic (meaning that they should have magnetic field strengths above a few hundred to a thousand Gauss), it could also explain why only a fraction of the hottest white dwarfs show UHE lines.

The UHE phenomenon affects about 10% of all stars in the universe when entering the white dwarf cooling sequence, and therefore a better understanding of these objects is highly desirable. Here, we aim to study the properties of the UHE white dwarfs, as well as their relatives – white dwarfs showing only the He II line problem – as a whole. In particular, we want to find out whether or not the photometric and spectroscopic variability observed in J0146+3236 is something that affects all UHE white dwarfs, and possibly also the He II line problem white dwarfs. This article is the first in a series of papers and introduces the sample of UHE and He II line problem white dwarfs and investigates their photometric variability. In Sect. 2 we first present the sample and discuss the location of these stars in the *Gaia* HRD. We then present our search for photometric variability using light curves from various ground- and space-based surveys (Sect. 3). The overall results of this study are presented in Sect. 4. Finally, we discuss our findings (Sect. 5) and provide an outlook on how more progress can be made (Sect. 6).

2. The sample of UHE and He II line problem white dwarfs

The first two UHE white dwarfs, the DO-type white dwarfs HS 0713+3958 and HE 0504–2408, were discovered by Werner et al. (1995). Soon afterwards, Dreizler et al. (1995) announced a further three DO-type UHE white dwarfs (HS 0158+2335, HS 0727+6003, and HS 2027+0651) as well as the first H-rich UHE white dwarf (HS 2115+1148), which they found in the Hamburg-Schmidt (HS) survey (Hagen et al. 1995). The number of UHE white dwarfs increased even further with the Sloan Digital Sky Survey (SDSS). Hügelmeier et al. (2006) reported two DO-type UHE white dwarfs and one DOZ (PG 1159) UHE white dwarf from the SDSS DR4. Within the SDSS DR10, two more DO-type UHE white dwarfs were found (Werner et al. 2014; Reindl et al. 2014), and Kepler et al. (2019) announced the discovery of two more DA-type UHE white dwarfs as well as one (or possibly two) more DO-type UHE white dwarf within the SDSS DR14. One more DO-type UHE white dwarf was discovered by Reindl et al. (2019) based on spectroscopic follow-up of UV-bright sources. Finally, we announce the discovery of a sixteenth member of the UHE white dwarfs, the DOZ-type WD 0101–182. In archival UVES spectra of this star ($R \approx 18\,500$, ProgID 167.D-0407(A), PI: R. Napiwotzki), we detect for the first time UHE lines around 3872, 4330, 4655, 4785, 5243, 5280, 6060, 6477 Å (Fig. B.1). Using non-local thermodynamic equilibrium (NLTE) models for DO-type white dwarfs (Reindl et al. 2014, 2018) that were calculated with the Tübingen NLTE Model-Atmosphere Package (TMAP,

Table 1. Names, spectral types, J2000 coordinates, observed *Gaia* eDR3 *G* band magnitudes, distances, *Gaia* extinction coefficients, dereddened *Gaia* color indexes, and the absolute dereddened *G* band magnitudes of all known UHE white dwarfs and white dwarfs showing only the He II line problem.

Name	Spectral type	RA J2000	Dec J2000	<i>G</i> [mag]	<i>d</i> [pc]	A_G [mag]	$(BP - RP)_0$ [mag]	M_{G_0} [mag]
UHE white dwarfs								
SDSS J003213.14+160434.8 ^(a)	DOZ*V UHE	8.05472	16.07633	15.75	413 ⁺⁹ ₋₉	0.13	-0.63	7.55
WD 0101-182 ^(b)	DOZ*V UHE	16.06273	-18.02916	15.74	398 ⁺¹⁰ ₋₉	0.04	-0.61	7.71
SDSS J014636.73+323614.3 ^(c)	DO*V UHE	26.65308	32.60403	15.54	331 ⁺⁷ ₋₆	0.13	-0.67	7.82
HS 0158+2335 ^{(d),(e)}	DO*V UHE	30.36338	23.83134	16.97	476 ⁺¹⁷ ₋₁₆	0.22	-0.54	8.39
SDSS J025403.75+005854.5 ^(f)	DO*V UHE	43.51563	0.98173	17.41	764 ⁺⁷⁶ ₋₆₃	0.18	-0.59	7.87
HE 0504-2408 ^{(g),(h)}	DO UHE	76.57540	-24.06685	15.69	468 ⁺¹¹ ₋₁₁	0.03	-0.61	7.31
HS 0713+3958 ^{(e),(g),(h)}	DO*V UHE	109.26134	39.88989	16.56	654 ⁺³⁵ ₋₃₂	0.12	-0.56	7.40
HS 0727+6003 ^{(d),(h)}	DO*V UHE	112.83912	59.96028	16.09	426 ⁺¹¹ ₋₁₁	0.13	-0.62	7.83
HS 0742+6520 ^(e)	DO UHE	116.85481	65.21699	15.73	332 ⁺⁵ ₋₅	0.07	-0.63	8.07
SDSS J090023.89+234353.2 ^(a)	DA UHE	135.09954	23.73146	18.74	2133 ⁺²⁶⁷⁵ ₋₇₆₃	0.06	-0.62	7.29
SDSS J105956.00+404332.4 ⁽ⁱ⁾	DOZ*V UHE	164.98336	40.72568	18.31	2499 ⁺²³⁹¹ ₋₈₂₁	0.03	-0.67	6.63
SDSS J121523.08+120300.7 ^(f)	DOZ*V UHE	183.84619	12.05022	18.14	1402 ⁺³⁴⁹ ₋₂₃₃	0.06	-0.71	7.51
SDSS J125724.04+422054.2 ^(a)	DA*V UHE	194.35026	42.34845	17.44	889 ⁺⁹⁶ ₋₇₉	0.04	-0.42	7.75
SDSS J151026.48+610656.9 ^(f)	DO*V UHE	227.61031	61.11581	17.26	786 ⁺⁴⁰ ₋₃₆	0.02	-0.59	7.84
HS 2027+0651 ^(d)	DO*V UHE	307.38544	7.01881	16.62	524 ⁺¹⁹ ₋₁₈	0.18	-0.52	7.87
HS 2115+1148 ^{(d),(i),(h)}	DAO*V UHE	319.57804	12.02558	16.44	523 ⁺¹⁹ ₋₁₈	0.13	-0.60	7.74
White dwarfs showing only the He II line problem								
SDSS J082134.59+173919.4 ⁽ⁱ⁾	DOZ*V UHE:	125.39562	17.65539	19.01	1173 ⁺⁵¹⁷ ₋₂₇₅	0.08	-0.47	8.72
SDSS J082724.44+585851.7 ⁽ⁱ⁾	DO UHE:	126.85192	58.98104	17.47	579 ⁺²⁹ ₋₂₇	0.32	-0.37	8.36
SDSS J094722.49+101523.6 ⁽ⁱ⁾	DOZ UHE:	146.84374	10.25657	18.00	898 ⁺¹⁴³ ₋₁₀₈	0.05	-0.59	8.29
SDSS J102907.31+254008.3 ^(a)	DO*V UHE:	157.28044	25.66901	17.05	583 ⁺³⁰ ₋₂₇	0.04	-0.59	8.24
HE 1314+0018 ^(j)	DOZ*V	199.35303	0.04380	16.01	321 ⁺⁸ ₋₈	0.06	-0.60	8.42
SDSS J151215.72+065156.3 ⁽ⁱ⁾	DOZ*V	228.06540	6.86566	17.22	1019 ⁺¹²² ₋₉₈	0.07	-0.55	7.21
HS 1517+7403 ^(k)	DOZ*V	229.19388	73.86848	16.63	774 ⁺³⁹ ₋₃₅	0.06	-0.61	7.19
SDSS J155356.81+483228.6 ^(f)	DO*V	238.48667	48.54126	18.61	1138 ⁺¹⁸³ ₋₁₃₈	0.04	-0.55	8.43

References. ^(a)Kepler et al. (2019); ^(b)this work; ^(c)Reindl et al. (2019); ^(d)Dreizler et al. (1995); ^(e)Reindl et al. (2014); ^(f)Hügelmeier et al. (2006); ^(g)Werner et al. (1995); ^(h)Werner et al. (2018b); ⁽ⁱ⁾Werner et al. (2014); ^(j)Werner et al. (2004); ^(k)Dreizler & Heber (1998).

Werner et al. 2003, 2012), we find that the weak He I $\lambda 5876 \text{ \AA}$ line and the C IV $\lambda 5803, 5814 \text{ \AA}$ doublet are best reproduced with $T_{\text{eff}} = 90\,000 \text{ K}$ and $C = 0.003$ (mass fraction).

In addition to these 16 UHE white dwarfs, our sample includes eight more objects that show only the He II line problem but no clear sign of UHE lines. The prototype of this class of stars is HE 1314+0018, which was discovered by Werner et al. (2004). The high-resolution and high-signal-to-noise spectrum of HE 1314+0018 lacks any UHE absorption lines. The other seven objects are from the samples of Dreizler & Heber (1998), Werner et al. (2014), and Kepler et al. (2019). Four of them possibly show the UHE feature around 5430–5480 \AA , which is also one of the strongest UHE features observed in the UHE white dwarfs.

In Figs. B.1 and B.2 we show the optical spectra of all UHE white dwarfs and spectra of all white dwarfs showing only the He II line problem, respectively. For HS 2027+0651, HST/STIS spectra are shown that were observed with the G430L and G750L gratings ($R \approx 700$). We downloaded these observations from the Mikulski Archive for Space Telescopes (MAST, proposal IDs: 8422, 7809, PIs: H. Ferguson and C. Leitherer, respectively). For WD 0101-182, the UVES spectrum (see above), and for HE 0504-2408 an EFOSC 1 spectrum obtained at the ESO 3.6 m telescope

($R \approx 1500$, Werner et al. 1995) are shown. The spectra of J0146+3236, HS 0158+2335, HS 0713+3958, HS 0727+6003, HS 0742+6520, and HE 1314+0018 were obtained by us in October and November 2014 at the Calar Alto 3.5 m telescope (ProgID H14-3.5-022, see also Reindl et al. 2019). We used the TWIN spectrograph and a slit width of 1.2 arcsec. For the blue channel grating No. T08, and for the red channel grating No. T04 were used. The spectra have a resolution of 1.8 \AA . After each spectrum, we required ThAr wavelength calibration. Data were reduced using IRAF. We did not flux-calibrate our data. For HS 1517+7403 and HS 2115+1148, TWIN spectra are shown that were obtained by Dreizler et al. (1995) and Dreizler & Heber (1998) and have a resolution of 3.5 \AA . For the remaining objects, SDSS spectra ($R \approx 1800$) are shown. Overplotted in red are TMAP models with atmospheric parameters determined within this work (WD 0101-182) or with parameters reported by previous works (see footnote of Table 1).

Table 1 lists all UHE and He II line problem white dwarfs along with their spectral types, J2000 coordinates, observed *Gaia* early DR3 *G* band magnitudes (Gaia Collaboration 2016, 2018), distances, d , *Gaia* extinction coefficients, A_G , the dereddened *Gaia* color indexes, $(BP - RP)_0$, and the absolute dereddened *G* band magnitudes. A spectral type DOZ UHE indicates a He-rich white dwarf that shows photospheric metal lines in the

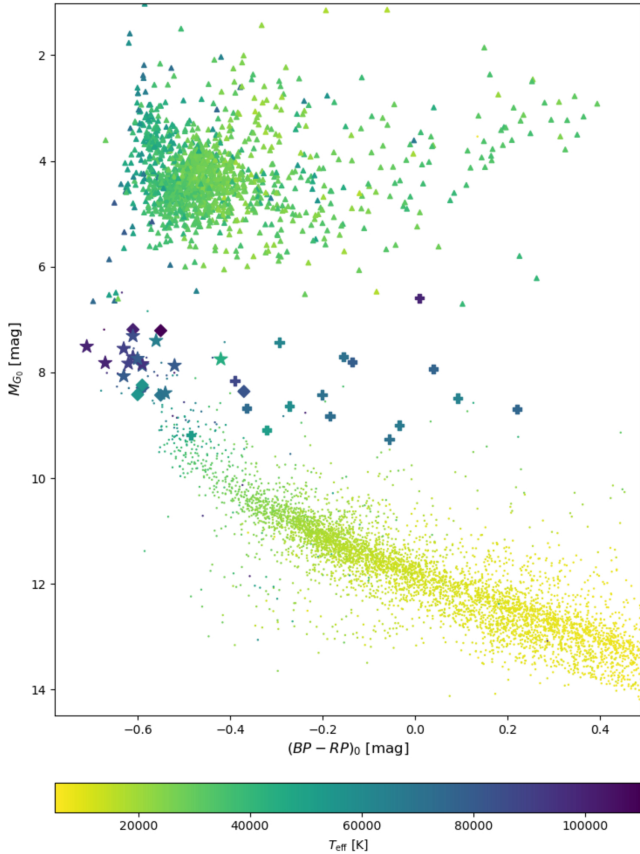


Fig. 1. Locations of the UHE white dwarfs (star symbols) and white dwarfs showing only the He II line problem (diamonds) in the *Gaia* HRD. Hot subdwarfs (triangles), SDSS white dwarfs (dots), and white dwarf–main sequence binaries (plus symbols) containing a very hot ($T_{\text{eff}} \geq 50\,000$ K) white dwarf are also shown. The color coding indicates the effective temperatures of the stars.

optical as well as UHE lines. A spectral subtype ‘UHE’: indicates an object with an uncertain identification of UHE lines. We calculated distances from the parallaxes (via $1000/\pi$), which we corrected for the zeropoint bias using the Python code provided by [Lindegren et al. \(2021\)](#)¹. Following [Gentile Fusillo et al. \(2019\)](#), we assume that the extinction coefficient A_G in the *Gaia* G passband scales as $0.835 \times A_V$ based on the nominal wavelengths of the respective filters and the reddening versus wavelength dependence employed by [Schlafly & Finkbeiner \(2011\)](#). Values for A_V were obtained from the 3D dust map of [Lallement et al. \(2018\)](#) using the distance calculated from the *Gaia* parallax of each object. Nine of our stars are located outside of the [Lallement et al. \(2018\)](#) 3D dust map (that is stars with a distance from the Galactic plane of $|z| \gtrsim 500$ pc). For those, we obtained A_V from the 2D dust map of [Schlafly & Finkbeiner \(2011\)](#) and assumed that A_G scales with a factor of $1 - \exp(-|z|/200 \text{ pc})$, as most of the absorbing material along the line of sight is concentrated along the plane of the Galactic disk. We note that the difference in reddening obtained from the two methods varies by a factor of 0.65 to 2.24 for stars located within the 3D dust map ($-500 \text{ pc} < z < 500 \text{ pc}$). This demonstrates that an accurate determination is not easy. The color indices, $(BP - RP)_0$, were calculated using Eqs. (18) and (19) in [Gentile Fusillo et al. \(2019\)](#). The absolute *Gaia* magnitude in the G band was calculated via $M_{G_0} = G - A_G + 5 + 5 \times \log(\pi/1000)$, where π is the

zero-point-corrected parallax in milliarcseconds from the *Gaia* early DR3.

Figure 1 shows the locations of the UHE white dwarfs (star symbols) and white dwarfs showing only the He II line problem (diamonds) that have parallaxes better than 20% in the *Gaia* HRD. Also shown are the locations of white dwarfs from the SDSS (dots) with *Gaia* parallaxes better than 5% and a reddening smaller than $E_{B-V} < 0.015$ ([Gaia Collaboration 2018](#)), as well as hot subdwarfs (triangles) from [Geier \(2020\)](#) with *Gaia* parallaxes better than 20%. The latter were dereddened following the approach of [Gentile Fusillo et al. \(2019\)](#). Finally, we also show the locations of white dwarf–main sequence binaries (bold plus signs) from the sample of [Rebassa-Mansergas et al. \(2010\)](#) that contain a very hot ($T_{\text{eff}} \geq 50\,000$ K) white dwarf primary and have parallaxes better than 30%.

It can be seen that the UHE white dwarfs and white dwarfs showing only the He II line problem overlap in a narrow region ($-0.71 \text{ mag} \leq (BP - RP)_0 \leq -0.37 \text{ mag}$, and $7.19 \text{ mag} \leq M_G \leq 8.43 \text{ mag}$). Both are located well below the hot subdwarf cloud and are just on top of the white dwarf banana². It also becomes clear that the stars in our sample are amongst the bluest objects. Most of the hot white dwarfs with an M-type companion are found at similar absolute magnitudes, but redder colors. This is a consequence of the flux of the low-mass companion that significantly contributes to the flux in the optical wavelength range. The only object from the sample of [Rebassa-Mansergas et al. \(2010\)](#) that lies directly on the white dwarf banana is SDSS J033622.01–000146.7. For this object, the late-type companion is not noticeable in the continuum flux (no increased flux at longer wavelengths) and also shows no absorption lines from the secondary. Only the emission lines in the core of the Balmer series are seen, which originate from the close and highly irradiated side of the cool companion. Two of our stars, the DA-type UHE white dwarf J1257+4220 and J0827+5858, which shows only the He II line problem, are found at noticeably redder colors (-0.42 mag and -0.37 mag , respectively) than the rest of our sample. While J0827+5858 is located at a region with a particularly high reddening $A_g = 0.32 \text{ mag}$, which might be underestimated by the 3D dust map, this is unlikely the case for J1257+4220 ($A_G = 0.04 \text{ mag}$). Looking at the *Gaia* eDR3 Renormalized Unit Weight Error (RUWE) values of our stars, we find they all have a value close to one (indicating that the single-star model provides a good fit to the astrometric observations), except for J1257+4220. Here we find a RUWE value much larger than one, namely 1.3387. This might suggest that J1257+4220 is a (wide) binary or it was otherwise problematic for the astrometric solution.

The mean dereddened color index of our sample is $\overline{BP - RP_0} = -0.58 \text{ mag}$ (standard deviation $\sigma = -0.08 \text{ mag}$), with the UHE white dwarfs being slightly bluer ($\overline{BP - RP_0} = -0.60 \text{ mag}$, $\sigma = -0.07 \text{ mag}$) than white dwarfs showing only the He II line problem ($\overline{BP - RP_0} = -0.54 \text{ mag}$, $\sigma = -0.08 \text{ mag}$). We also find that the mean dereddened absolute G band magnitude of the UHE white dwarfs with parallaxes better than 20% ($\overline{M_G} = 7.76 \text{ mag}$, $\sigma = -0.27 \text{ mag}$) is slightly brighter than that of white dwarfs showing only the He II line problem ($\overline{M_G} = 8.02 \text{ mag}$, $\sigma = -0.56 \text{ mag}$).

We note that 18 out of the 24 stars in our sample have a probability of being a white dwarf (PWD) of greater than 90% as defined by [Gentile Fusillo et al. \(2019\)](#). For the remaining objects, we find PWDs between 72% and 89%. The only object that is not included in the catalog of [Gentile Fusillo et al. \(2019\)](#) is J0900+2343, which is also the only object in our sample that has a negative parallax in the *Gaia* DR2. For comparison, the

¹ https://gitlab.com/icc-ub/public/gaiadr3_zeropoint

² The term ‘white dwarf banana’ was coined by [Girven et al. \(2011\)](#).

catalog of hot subdwarf candidates from the *Gaia* DR2 by Geier et al. (2019) contains only three of our stars. This is because for objects with parallaxes better than 20%, Geier et al. (2019) included only objects with absolute magnitudes in the range $-1.0 \text{ mag} \leq M_G \leq 7.0 \text{ mag}$.

3. Light-curve analysis

The discovery of photometric variability in the UHE white dwarf J01463+3236 raises the question of whether photometric variability is a common feature of UHE white dwarfs, and possibly also of the He II line problem white dwarfs. Here we want to investigate this possibility by searching for periodic signals in the light curves of these objects.

For the analyses of the light curves, we used the VAR-TOOLS program (Hartman & Bakos 2016) to perform a generalized Lomb-Scargle (LS) search (Zechmeister & Kürster 2009; Press et al. 1992) for periodic sinusoidal signals. We classify objects that show a periodic signal with a false alarm probability (FAP) of $\log(\text{FAP}) \leq -4$ as significantly variable, objects with $-3 \leq \log(\text{FAP}) < -4$ as possibly variable, and objects that only show a periodic signal with $\log(\text{FAP}) > -3$ as not variable. In cases where we found more than one significant period, we whitened the light curve by removing the strongest periodic signal (including its harmonics and subharmonics) from the light curve. The periodogram was then recomputed to check whether or not the FAP of the next strongest signal still remains above our variability threshold ($\log(\text{FAP}) \leq -4$). This whitening procedure was repeated until no more significant periodic signals could be found.

Using the `-killharm` command we fitted a harmonic series of the form

$$m(t) = A \times \sin\left(\frac{2\pi(t - t_0)}{P}\right) - B \times \cos\left(\frac{2\pi(t - t_0)}{P}\right) + m_0 \quad (1)$$

to each light curve. We use this to determine the peak-to-peak amplitude of the light curve, which we define as the difference between the maximum and minimum of the fit. The same function was also used to estimate the uncertainties on the derived periods by running a Differential Evolution Markov chain Monte Carlo (DEMCMC) routine (Ter Braak 2006) employing the `-nonlinfit` command. The number of accepted links was set to 10 000. As initial guesses we used the period obtained from the LS search, and for the remaining parameters the values from the `killharm` fit.

In Tables A.1 and A.2, we summarize the light curves used in our analysis, the data points of each light curve, the mean magnitude in each band, the median value of each period and its uncertainty as calculated in the DEMCMC simulation, and amplitudes for the UHE white dwarfs and white dwarfs showing only the He II line problem, respectively. In the following, we provide an overview of the data sets used in our work (Sect. 3.1) and then provide notes on individual objects (Sect. 3.2).

3.1. Data sets

Light curves were obtained from various surveys as well as our own observing campaign.

TESS. The Transiting Exoplanet Survey Satellite (TESS) scans the sky with 26 segments and with a 27.4 day observing period per segment. TESS uses a red-optical bandpass covering the wavelength range from about 6000 to 10 000 Å centered on 7865 Å, as in the traditional Cousins *I*-band. We downloaded the target pixel files (TPF) of each object from MAST as FITS

format. The FITS files are already processed based on the Pre-Search Data Conditioning Pipeline (Jenkins et al. 2016) from which we extracted the barycentric corrected dynamical Julian days (“BJD – 2457000”, a time system that is corrected by leap seconds; see Eastman et al. 2010) and the pre-search Data Conditioning Simple Aperture Photometry flux (“PDCSAP FLUX”) for which long-term trends have been removed using the co-trending basis vectors. In this work, we used the PDC light curves and converted the fluxes to fractional variations from the mean (i.e., differential intensity). As TESS has a poor spatial resolution (one detector pixel corresponds to 21 arcsec on the sky) and our targets are faint, we carefully checked for blends with close-by stars using the `tpfplotter` code (Aller et al. 2020). In Fig. 2 we show the TPF plots for the UHE and He II line problem white dwarfs. The red circles represent *Gaia* sources, which are scaled by magnitude contrast against the target source. Also shown is the aperture mask used by the pipeline to extract the photometry. In total, ten UHE, and two He II problem white dwarfs were observed by TESS in the two-minute cadence mode.

K2. In a series of sequential observing campaigns, 20 fields, which were distributed around the ecliptic plane, were observed by the K2 mission (campaign duration ≈ 80 d, Howell et al. 2014). Throughout the mission, K2 observed in two cadence modes: long cadence (≈ 30 min data-point cadence) and short cadence (≈ 1 min data-point cadence). The latter was only provided for selected targets, and the long cadence was used as the default observing mode. Two of the stars in our sample, J0821+1739 and J0900+2343, were observed in long-cadence mode. K2 data contain larger systematic errors than the original *Kepler* mission. This is because of the reduction in pointing precision as a result of the spacecraft drift during the mission. Thus, several pipelines have been developed to process K2 light curves. Here, we are using the light curves produced by the K2 Self Flat Fielding (K2SFF, Vanderburg & Johnson 2014) and the EPIC Variability Extraction and Removal for Exoplanet Science Targets (EVEREST, Luger et al. 2016, 2018) pipelines. The data were obtained from the MAST archive.

ATLAS. Since 2015, the Asteroid Terrestrial-impact Last Alert System (ATLAS, Tonry et al. 2018) has been surveying approximately $13\,000 \text{ deg}^2$ at least four times per night using two independent and fully robotic 0.5 m telescopes located at Haleakala and Mauna Loa in Hawaii. It provides *c*- and *o*-band light curves (effective wavelengths $0.53 \mu\text{m}$ and $0.68 \mu\text{m}$, respectively) which are taken with an exposure time of 30 s. Eight stars in our sample have ATLAS light curves.

Catalina Sky Survey. The Catalina Sky Survey uses three 1 m class telescopes to cover the sky in the declination range $-75^\circ < \delta < +65^\circ$, but avoids the crowded Galactic plane region by $10\text{--}15^\circ$ due to reduced source recovery. It consists of the Catalina Schmidt Survey (CSS), the Mount Lemmon Survey (MLS) in Tucson, Arizona, and the Siding Spring Survey (SSS) in Siding Spring, Australia. The second data release contains *V*-band photometry for about 500 million objects with *V* magnitudes between 11.5 and 21.5 from an area of $33\,000 \text{ sq. deg.}$ (Drake et al. 2009, 2014). Most of the stars in our sample are covered by this survey, though we find that at least 200–300 data points are needed to find a periodic signal. This is likely because of the larger uncertainties on the photometric measurements compared to other surveys employed in this work.

SDSS stripe 82. The SDSS Stripe 82 covers an area of 300 deg^2 on the celestial equator, and has been repeatedly scanned in the *u*-, *g*-, *r*-, *i*-, and *z*-bands by the SDSS imaging

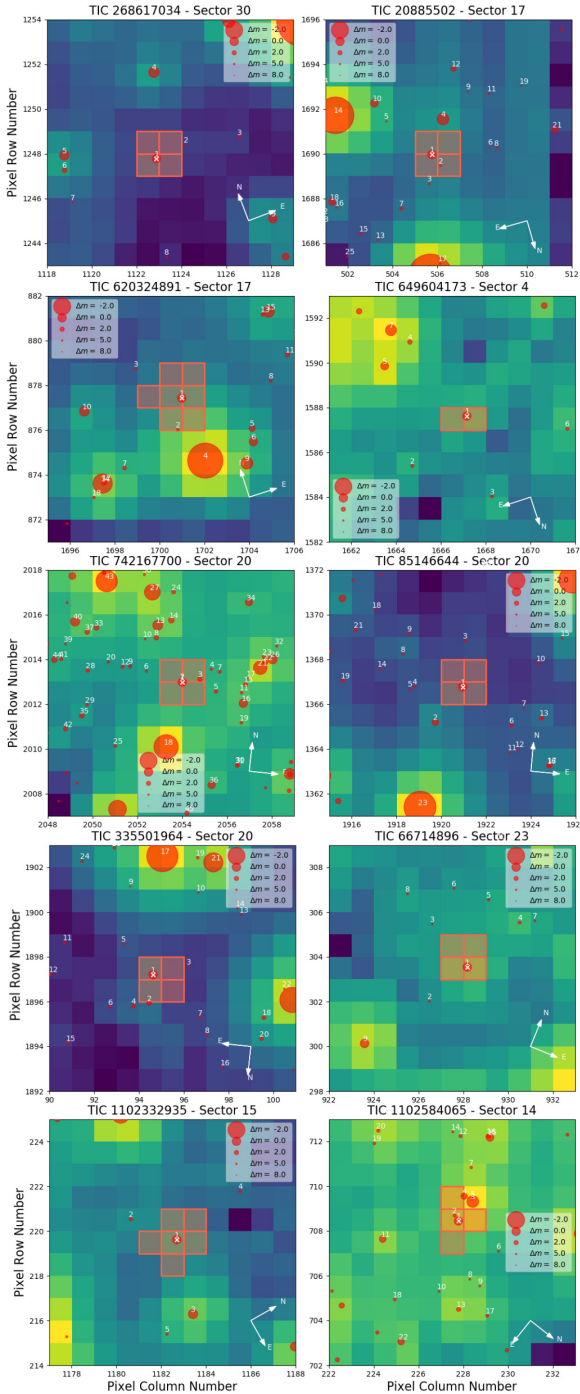


Fig. 2. From left to right and top to bottom: target pixel files (TPFs) of WD 0101–182, J0146+3236, HS 0158+2335, J0254+0058, HS 0713+3958, HS 0727+6003, HS 0742+6520, HE 1314+0018, J1510+6106, and HS 1517+7403. The red circles are the sources of the *Gaia* catalog in the field with scaled magnitudes (see legend). Number 1 indicates the location of the targets. The aperture mask used by the pipeline to extract the photometry is also marked.

survey (Abazajian et al. 2009). For J0254+0058, the only object in our sample that is included in the SDSS stripe 82, we acquired the u -, g -, r -, i -, and z -band light curves (about 70 data points each) from Ivezić et al. (2007).

ZTF. The Zwicky Transient Facility (ZTF, Bellm et al. 2019; Masci et al. 2019) survey uses a 48-inch Schmidt telescope with

a 47 deg^2 field of view, which ensures that the ZTF can scan the entire northern sky every night. We obtained data from the DR4 which were acquired between March 2018 and September 2020, covering a time-span of around 470 days. The photometry is provided in the g and r bands, and also in the i -band but with less frequency, with a uniform exposure time of 30 s per observation. Most objects in our sample are covered by this survey, with 21 having at least 50 data points in at least one band.

BUSCA. For HS 0727+6003 we obtained photometry using the Bonn University Simultaneous Camera (BUSCA, Reif et al. 1999) at the 2.2 m telescope at the Calar Alto Observatory. The star was observed during two consecutive nights on 21 and 22 December 2018. The beam splitters of BUSCA allow visible light to be collected simultaneously in four different bands, namely U_B , B_B , R_B , and I_B . However, due to technical problems with BUSCA, we were not able to obtain data in I_B band. Instead of filters, we used the intrinsic transmission curve given by the beam splitters to avoid light loss. We used the IRAF aperture photometry package to reduce the data.

3.2. Notes on individual objects

3.2.1. UHE white dwarfs

J0032+1604. This object is a DO-type UHE white dwarf with the strongest UHE features seen in any of the objects discussed here. It was observed within CSS and ATLAS. The periodograms of all light curves show the strongest signal around 0.91 d. Heinze et al. (2018) reported twice the period ($P = 1.81619 \text{ d}$). The amplitude of the light curve variations ranges from 0.05 mag to 0.07 mag, but is not found to differ significantly. In the first two rows on the left side of Fig. 3, we show the periodogram and phase-folded light curve from the ATLAS c -band, which predicts lowest FAP. The original periodogram is shown in gray and the whitened periodogram is shown in light blue. No other significant signal is left after whitening the light curve for the 0.91 d periodicity. The black line on top of the phase-folded light curve (red) is a fit of a harmonic series used to predict the peak-to-peak amplitude.

WD0101–182. This bright ($G = 15.74 \text{ mag}$) DOZ-type UHE white dwarf was observed with TESS, CSS, and ATLAS. The periodogram of the TESS light curve shows the strongest peak around 2.32 d. This period is also confirmed by the CSS V band and ATLAS c band light curves, respectively. The periodogram of the ATLAS o -band light curve predicts the strongest peak at 1.747674 d, but another significant peak occurs at 2.31 d, close to what is found in the ATLAS c , CSS V , and TESS band. We also note that the 2.32 d periodicity is already clearly visible in the unfolded TESS light curve and is also reported by Heinze et al. (2018). The amplitudes of the ATLAS and CSS phase-folded light curves are consistent.

J0146+3236. This is the only object for which rapid changes in the EW of the UHE features have been observed. Drake et al. (2014) and Heinze et al. (2018) reported photometric variability of $P = 0.484074 \text{ d}$ (based on CSS data) and $P = 0.48408 \text{ d}$ (based on ATLAS data), respectively, while Reindl et al. (2019) reported half of that value. We can confirm the period found by Reindl et al. (2019) based on ATLAS, ZTF, and TESS data. The periodogram of the TESS light curve shows the strongest signal at $P = 0.242037 \text{ d}$. All other significant peaks turned out to be (sub-)harmonics of this period (Fig. 3). The shape of the phase-folded light curves is roughly sinusoidal, with extended flat minima.

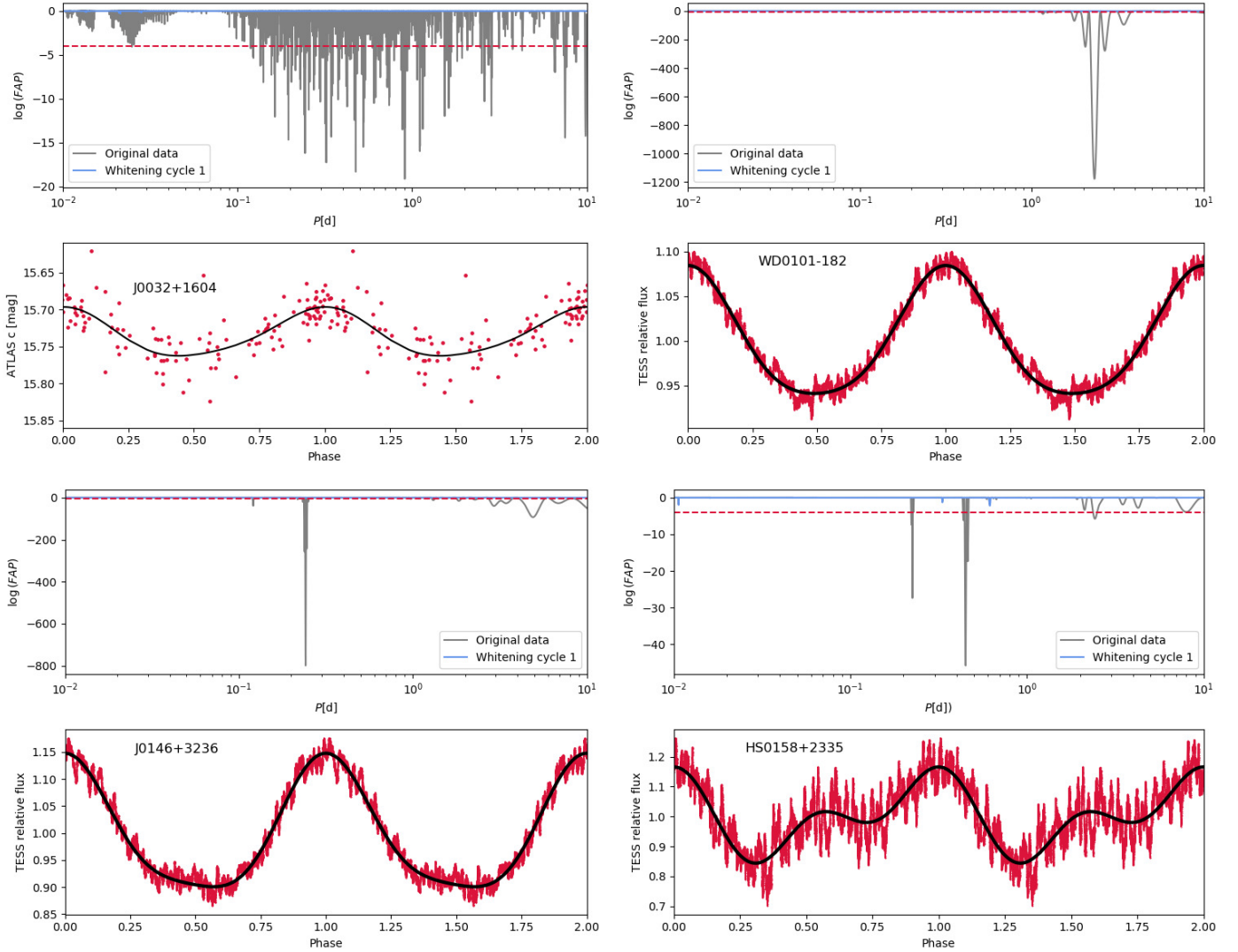


Fig. 3. Periodograms and phase-folded light curves of the UHE white dwarfs J0032+1604, WD 0101–182, J0146+3236, and HS 0158+2335. The red solid lines are phase-averaged light curves, while the dotted light curve represents the actual data. The black line is a fit of a harmonic series used to predict the peak-to-peak amplitude.

HS 0158+2335. This object was observed with CSS, ATLAS, ZTF, and TESS. In the TESS light curve, we detect the strongest signal around 0.45 d. No other significant period is left after the first whitening cycle. In the periodograms calculated for the ATLAS *o*-band (96 data points) and ZTF *g*-band (43 data points) no significant periodic signal can be detected. In all other light curves we also find a significant period at $P \approx 0.45$ d. The period found by us is confirmed by Drake et al. (2014) who reported $P = 0.449772$ d based on CSS DR 1 data. Heinze et al. (2018), on the other hand, reported twice the period ($P = 0.899571$ d) found by us. The shape of the phase-folded light curves clearly shows two maxima, with the first one being at phase 0.0, and the second at approximately phase 0.6, and the minimum is located around phase 0.3.

J0254+0058. This object was observed within CSS, ATLAS, ZTF, and TESS, and is the only object in our sample included in the SDSS stripe 82 survey. Becker et al. (2011), Drake et al. (2014), and Heinze et al. (2018) report a period of about 2.17 d for this object based on SDSS stripe 82 (*u*, *g*, and *r* band), CSS *V* band, and ATLAS *o*- and *c*-band light curves, respectively. The periodograms of the light curves of

all surveys mentioned above predict the strongest periodic signal at around 1.09 d. The amplitudes of the phase-folded light curves are always around 0.3 mag and do not differ significantly amongst the different bands. The shapes of the phase-folded light curves are, as in J0146+3236, roughly sinusoidal, with broad and flat minima (top row left in Fig. 4). After whitening the TESS light curve for the 1.09 d periodic signal and its (sub-)harmonics, we find one more significant peak around 1.3 d (marked with an “x” in Fig. 4) just above our variability threshold ($\log(\text{FAP}) = -4.4 < -4$). After the second whitening cycle, no other significant peak is left in the periodogram.

HE 0504–2408 is one of the objects showing the strongest UHE features, and one of the brightest ($G = 15.77$ mag) stars in our sample. It was observed in the course of the CSS (69 data points) and the SSS (182 data points). The SSS light curve indicates that the star underwent a brightening of 0.4 mag from MJD = 53599 to MJD = 53755 and remained at $V \approx 15.65$ mag. Using only data obtained after MJD = 53755 we find a period of 0.684304 d with an associated $\log(\text{FAP}) = -3.4$. The amplitude of the phase-folded light curve is 0.08 mag, and its shape is sinusoidal. We classify this star as possibly variable.

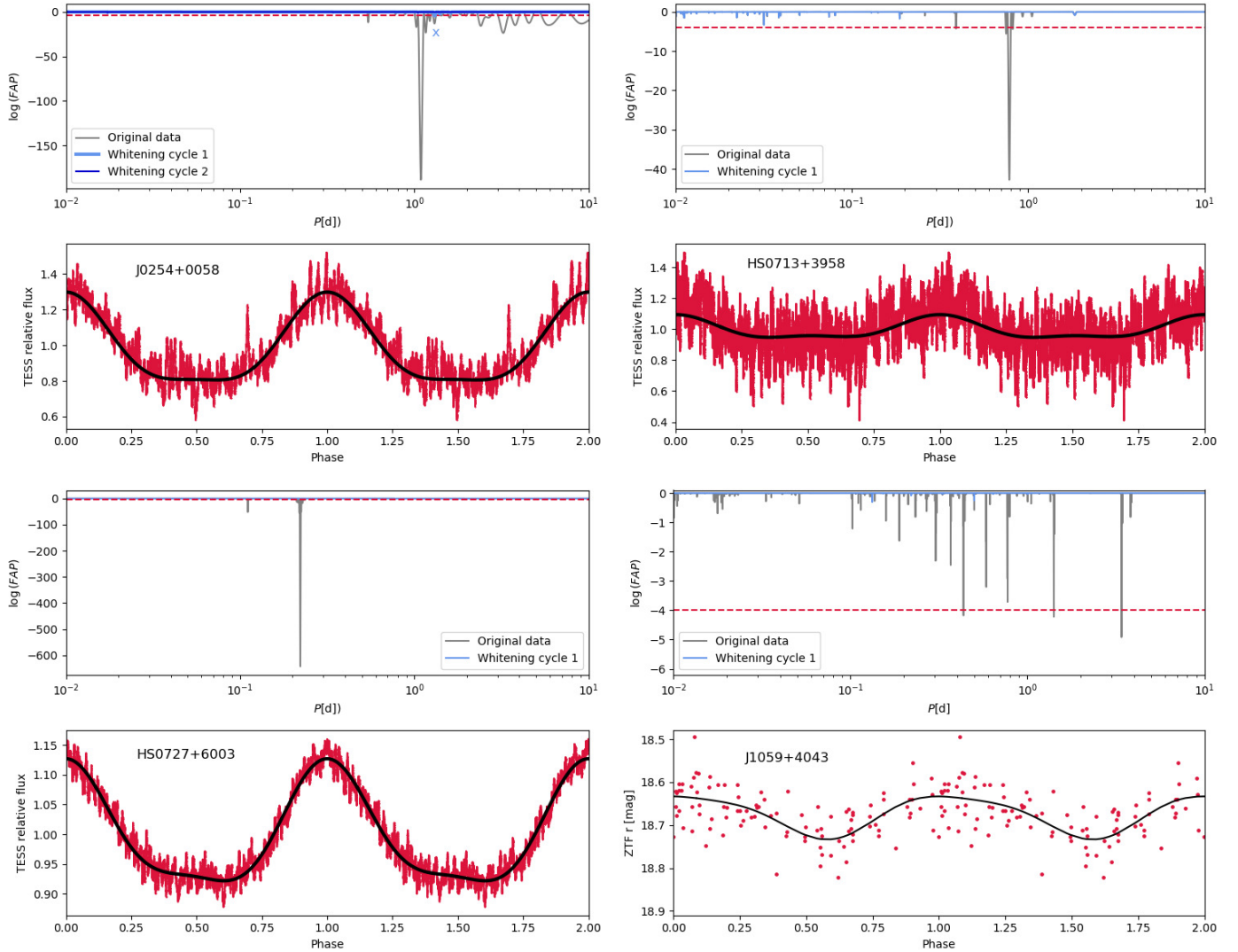


Fig. 4. As in Fig. 3 for the UHE white dwarfs J0254+0058, HS 0713+3958, HS 0727+6003, and J1059+4043.

HS 0713+3958. This object is yet another example where the phase-folded light curve shows extended, flat minima (second row right in Fig. 4). The periodogram of the TESS light curve shows the strongest periodic signal around $P = 0.78$ d (first row right in Fig. 4). No other significant signal is left in the periodogram after whitening the light curve for this periodicity. The strongest periodic signals in the CSS and ZTF g - and r -band light curves are also detected around 0.78 d. In the ATLAS c - and o -band light curve, the strongest periodic signals are found at 1.379916 d and 0.304796 d, respectively. However, we also find periodic signals around 0.78 d above our FAP threshold in both periodograms. [Heinze et al. \(2018\)](#) report a period of $P = 0.609618$ d, which is twice what we found as the strongest signal in the ATLAS o -band. We adopt the 0.781646 d period from the TESS light curve.

Ground-based infrared photometry by [Napiwotzki \(1997\)](#) revealed a nearby star to HS 0713+3958. [Werner et al. \(2018a\)](#), who recorded an optical spectrum with the *Hubble Space Telescope* (HST) of this late-type star, determined a spectral type of M5V and found that the spectroscopic distances of both stars agree within the error limits. Comparing the fluxes of the HST spectrum of the M5V star with the SDSS spectrum, we find that the flux of the cool star only dominates beyond 10 000 Å, which

is beyond the TESS filter pass band. This implies that the periodicity found in our light curve analysis most likely originates from the hot white dwarf and not from the cool star. Another interesting fact is that companions of spectral type M5 or later may easily be hidden in the optical due to the still high luminosity of the white dwarf. We also note that *Gaia* clearly resolved the white dwarf and the M5 star (we calculate a separation of 1.0396 ± 0.0005 arcsec), and therefore it is not possible that the two stars form a close binary.

HS 0727+6003. The periodogram of the TESS light curve for this object shows the strongest periodic signal around $P = 0.22$ d (penultimate row right in Fig. 4). No other significant period is found after the first whitening cycle. The ≈ 0.22 d period is also found in the CSS, ATLAS c - and o -band, and ZTF g - and r -band light curves. Again, the minima of the phase-folded light curves are broad and flat. The amplitudes are all around 0.13 mag and do not differ significantly amongst the different bands. [Drake et al. \(2014\)](#) gives a period of $P = 0.28437$ d, higher than what we find. [Heinze et al. \(2018\)](#) reports twice our period ($P = 0.442823$ d). With BUSCA we were able to record almost two phases, and find that the amplitudes of the U_B , B_B , and R_B band light curves (0.128 ± 0.014 mag, 0.131 ± 0.008 mag,

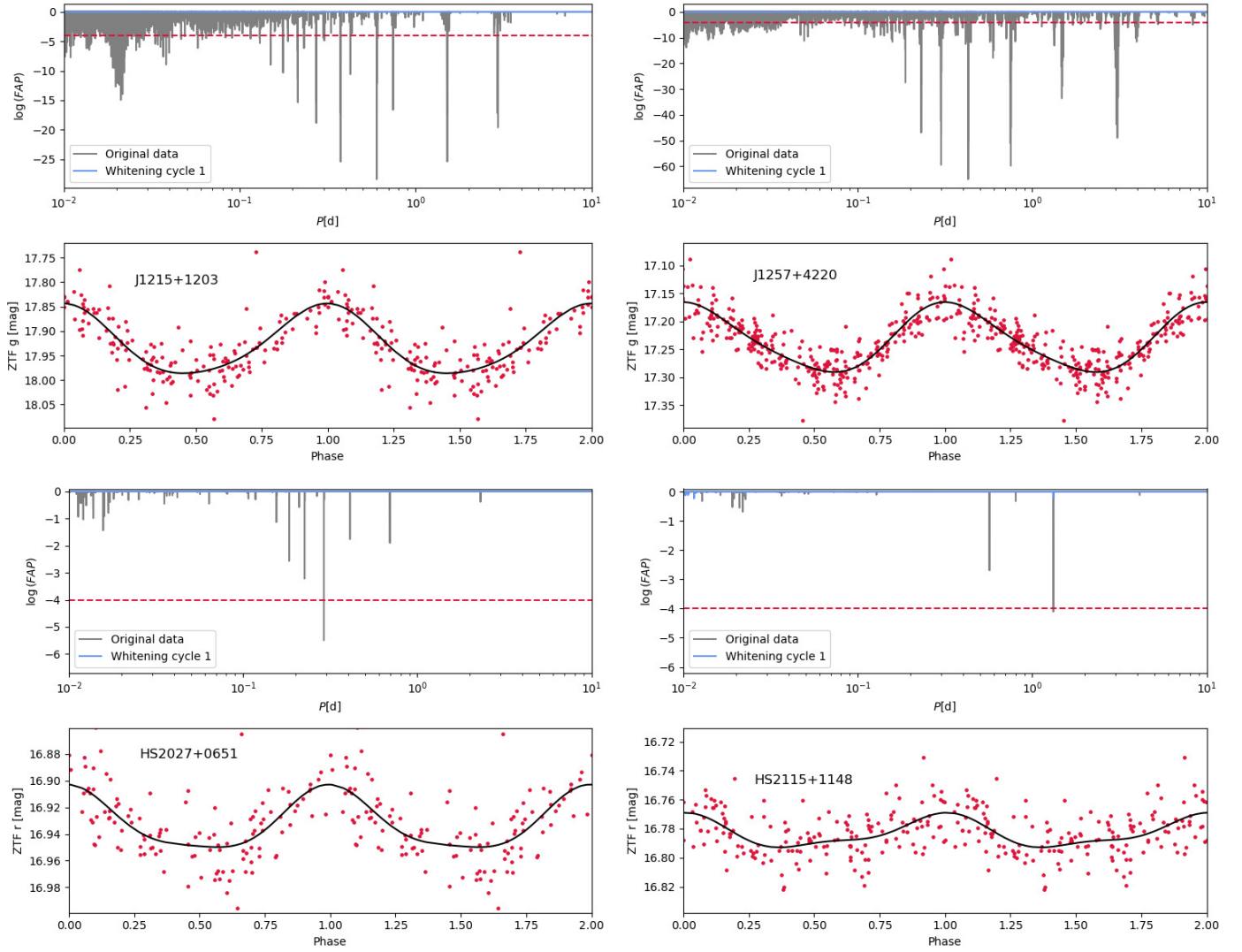


Fig. 5. As in Fig. 3 but for the UHE white dwarfs J1215+1203, J1257+4220, HS 2027+0651, and HS 2115–1148.

and 0.128 ± 0.011 mag, respectively) agree with each other as well as with the amplitudes from the light curves from the other surveys.

HS 0742+6520. Like HE 0504–2408, this object shows some of the strongest UHE features and is found to be not significantly variable. It was observed only 121 times in the course of the CSS. The TESS light curve predicts the strongest peak at 0.281989 d with an associated $\log(\text{FAP}) = -1.7$. The phase-folded light curve has an amplitude of 0.01 mag only. Thus, this star is likely not variable.

J0900+2343. This object is a faint ($G = 18.79$ mag) DA-type UHE white dwarf. Visual inspection of the K2 light curves processed by the EVEREST and K2SSF pipeline indicates that the data still suffer from systematic errors. Thus, we discard the K2 data for this object from our analysis. The star was also observed within the CSS (469 data points) and ZTF (only 44 data points in both the g - and r -band), but no significant periodic signal can be detected in those light curves. The nondetection of variability in this object may be the consequence of the faintness of the star.

J1059+4043. This object is half a magnitude brighter ($G = 18.34$ mag) than J0900+2343. In the periodogram of the ZTF

g and r band light curves (about 230 data points each) we detect the strongest periods around $P = 1.41$ d. The phase-folded light curves have an amplitude of 0.08 mag and their shapes are roughly sinusoidal (bottom row right in Fig. 4 for the ZTF g band data). No significant period can be found in the periodogram of the CSS V -band light curve (315 data points).

J1215+1203. This faint ($G = 18.17$ mag) DO-type UHE white dwarf was observed in the course of the CSS, and ZTF. The periodograms of all these light curves show the strongest periodic signal at $P \approx 0.60$ d. The shape of the phase-folded light curve is roughly sinusoidal (top row, left in Fig. 5).

J1257+4220. This object is a DA-type UHE white dwarf and was observed in the course of the CSS, ZTF, and ATLAS. While in the CSS V -band and ATLAS o -band no significant periodic signal can be detected, the ZTF light curves and ATLAS c -band light curves indicate the strongest periodic signal at $P \approx 0.43$ d. Heinze et al. (2018) classified J1257+4220 as a sinusoidal variable with significant residual noise and, again, reports twice the period ($P = 0.857925$ d) found by us.

J1510+6106 is a DO UHE white dwarf and two minute cadence light curves are available from four TESS sectors. There are no blends with other stars in the TESS aperture or a

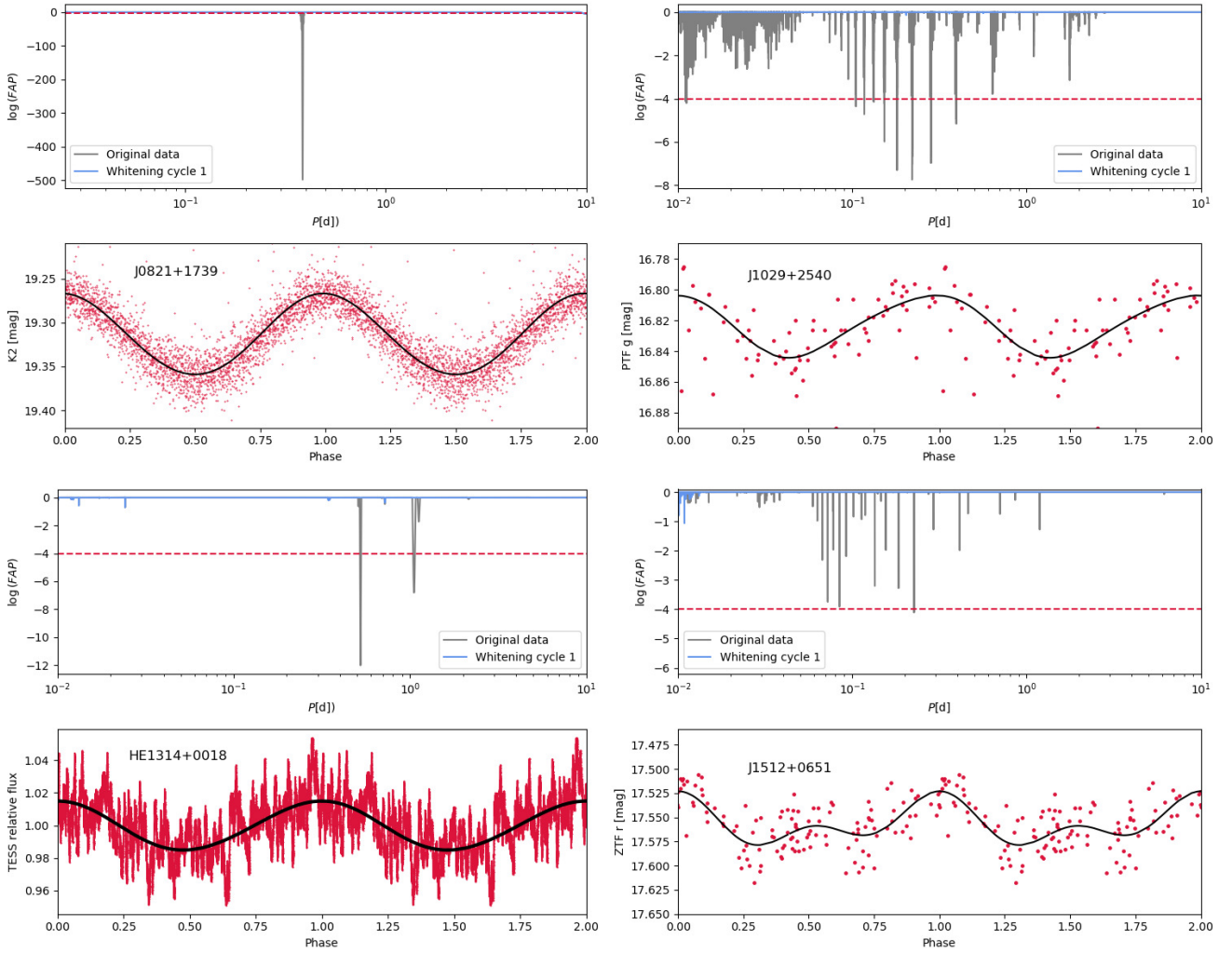


Fig. 6. As in Fig. 3 but for the He II line problem white dwarfs J0821+1739 and J1029+2540, HE 1314+0018, and J1512+0651.

contamination by nearby bright stars (Fig. 2). In the periodogram of the combined TESS light curve, we find one significant peak at 5.187747 d ($\log(\text{FAP}) = -5.1$), however this signal is not found in any individual sector light curve. This white dwarf was also observed more than 500 times in both the ZTF g - and r -band. No significant periodic signals can be found in those light curves. Thus, we remain skeptical about the five-day period from the combined TESS light curve, and classify this star only as a possibly variable.

HS2027+0651. This object is a DO UHE white dwarf that was observed within the ZTF. The periodogram of the ZTF g -band light curve indicates $P \approx 0.29$ d. The amplitude of the phase-folded light curve is 0.06 mag, and its minimum is again broad and flat (bottom left panel in Fig. 5).

HS2115–1148. This object is a DAO-type UHE white dwarf with very weak UHE lines. The periodogram of the ZTF r -band (Fig. 6) predicts the strongest signal around 1.32 d. The amplitude of the phase-folded light curve is 0.04 mag.

3.2.2. White dwarfs showing only the He II line problem

J0821+1739. This is the faintest object in our sample ($G = 19.07$ mag). In the periodogram (top row left in Fig. 6) of the K2 light curve processed by the EVEREST pipeline only one

strong signal can be found at $P = 0.384875$ d. This variability is already clearly visible in the (unfolded) light curve. We note that both the amplitude and shape of the phase-folded K2 light curve must not be regarded as reliable due to the long exposure time (5% of the period). The ≈ 0.38 d period is also confirmed by the K2 light curve processed by the K2SFF pipeline, although we obtain a higher FAP for the variability. Even though the target is quite faint, we also find the ≈ 0.38 d period in the CSS and ZTF g -band light curves. However, this period is not significant ($\log(\text{FAP}) = -3.0 < 4$) in the latter. The amplitude of the phase-folded CSS light curve is 0.13 mag.

J0827+5858. This object was observed 332 times in the course of the CSS ($V = 17.46$ mag), and about 200 times in both the ZTF g - and r -bands. We do not find a significant periodic variability in any of those light curves.

J0947+1015. This source was observed 447 times in the course of the CSS ($V \approx 18.07$ mag), and 64 and 81 times in the ZTF g - and r -bands, respectively. The periodogram of the CSS light curve indicates a period of 0.257938 d with an associated $\log(\text{FAP}) = -3.6$. The amplitude of the phase-folded light curve is 0.10 mag. We classify this star as a possibly variable.

J1029+2540. In the periodogram of the ZTF g -band light curve for this object we find the strongest periodic signal in the

ZTF g -band around $P = 0.28$ d (first row right in Fig. 6). This period is confirmed by the CSS V -band and ZTF r -band data.

HE 1314+0018. We find a significant period around 0.52 d in the TESS data of this fairly bright ($G = 16.05$ mag) star. The amplitude of the phase folded light curve is only 0.03%. After the first whitening cycle no other significant peak remains in the periodogram (penultimate row left of Fig. 6). The star was also observed 368 times within the CSS, but no significant periodic signal can be found in this data set.

J1512+0651. This source has been observed 103 and 119 times in the ZTF g - and r -band, and 365 times in the CSS V -band. We find the strongest signal at 0.226 d in the periodogram of the ZTF r band. We also find the 0.226 d period in the ZTF g and CSS V band, albeit at FAPs below our threshold. The amplitude of the phase-folded ZTF r band light curve is 0.06 mag.

HS 1517+7403. In the periodograms of the ZTF g - and r -band light curves we find the strongest signals around 1.09 d, respectively. After the first whitening cycle, no other significant signal remains. The star was also observed with TESS. The periodogram of the TESS light curve predicts the strongest peak around 8.78 d, but another strong signal is detected at 1.09 d confirming what is found from the ZTF light curves. Because we do not see a significant peak at around 8.78 d in the ZTF periodograms, we adopt 1.09 d as the photometric period of the star. After whitening the TESS light curve for the 1.09 d period (including it harmonics and subharmonics), the signal at 8.78 d disappears, but other significant signals around 7 d and 2 d remain. As these latter signals are not detected in the ZTF periodograms, we conclude that they most likely originate from the other star(s) inside the aperture mask, or the two-orders-of-magnitude-brighter star right next to it (bottom row, right of Fig. 2).

J1553+4832. This faint ($G = 18.65$ mag) object was observed about 1200 times in the course of the ZTF. In both the periodograms of the ZTF g and r band, we find the strongest signals around 2.93 d. The amplitudes of the phase-folded light curves in both bands is about 0.05 mag. We note that there are also aliases at lower periods (e.g., at 1.52 d and 0.74 d), which have a similar FAP (all of them are removed after the first whitening cycle). Thus, it may be possible that the real photometric period is shorter. The star was also observed 171 times within the CSS, but no significant periodic signal can be found in this light curve.

4. Overall results

4.1. Variability rates

We find that 12 out of the 16 UHE white dwarfs are significantly photometrically variable, meaning their light curves exhibit periodic signals with a $\log(\text{FAP}) \leq -4$. This leads to a variability rate of $75^{+8}_{-13}\%$. Given the low-number statistics, the uncertainties were calculated assuming a binomial distribution and indicate the 68% confidence-level interval (see e.g., Burgasser et al. 2003). For two objects, HE 0504–2408 and HS 0742+6520, we find periodic signals with associated $\log(\text{FAPs}) \approx -3$. For J1510+6106 we do not trust the signal around 5.19 d discovered in the combined TESS light curve, because it can neither be found in the ZTF g or r band light curve (about 500 data points each), nor in the four individual TESS light curves. Those latter three objects we consider as possibly variable. For the DA-type UHE white dwarf J0900+2343, no hint of variability could be

found, which might nevertheless be a consequence of the faintness of the star ($G = 18.79$ mag). For the white dwarfs that show only the He II line problem, we find a similar variability rate of $75^{+9}_{-19}\%$, meaning that six out of the eight He II line problem white dwarfs are significantly photometrically variable. For J0827+5858 we cannot find a significant periodic signal, and J0947+1015 we classify as possibly variable. The high photometric variability rate amongst these stars suggests that the UHE and He II line problem phenomena are linked to variability.

However, it is not yet clear whether the photometric variability is indeed an intrinsic characteristic of these stars alone, or is rather something that is observed amongst all very hot white dwarfs. In order to clarify this matter, we obtained ZTF DR4 light curves of a comparison sample and searched for photometric variability in those light curves as well. Our comparison sample consists of several very hot ($T_{\text{eff}} \geq 65\,000$ K) DO-type (55 in total, including 28 PG 1159-type stars) white dwarfs from Dreizler & Werner (1996), Dreizler & Heber (1998), Hügelmeyer et al. (2005, 2006), Werner & Herwig (2006), Werner et al. (2014), and Reindl et al. (2014, 2018), as well as very hot ($T_{\text{eff}} \geq 65\,000$ K) DA-type (90 in total) white dwarfs from the samples of Gianninas et al. (2011) and Tremblay et al. (2019). We considered only ZTF light curves that have at least 50 data points (this was found from our previous analysis to be the approximate number of points needed to detect periodic signals in the ZTF data). We find that amongst the H-deficient white dwarfs, only one of the 41 objects with sufficient data points in the ZTF is significantly variable (variability rate: $2^{+5}_{-1}\%$)³. For the H-rich white dwarfs, we find a higher variability rate of $14^{+6}_{-3}\%$ (59 stars had at least 50 data points and eight turned out to be significantly variable). In Table A.3, we list all of the normal white dwarfs which we found to be variable based on the ZTF data, including the mean magnitudes, derived periods, and amplitudes. The variability rate of all normal white dwarfs together is then $9^{+4}_{-2}\%$, in stark contrast to the combined variability rate of $67^{+8}_{-11}\%$ based on ZTF data for the UHE and He II line problem white dwarfs⁴. Thus, we conclude that periodic photometric variability is indeed a characteristic of UHE and He II line problem white dwarfs.

4.2. Light-curve shapes

The shapes of the light curves are quite diverse. Some objects show near perfect sinusoidal variations (e.g., HE 1314+0018, J1029+2540), while the light curves of seven objects in our sample (about one-third amongst the variable ones) show extended, flat minima (J0254+0058, J0146+3236, HS 0713+3958, HS 0727+6003, HS 2027+0651, J1553+4832, and HS 1517+7403). Particularly interesting are the light curves of HS 0158+2335, that show two uneven maxima. This might also be the case for J1512+0651 (shows only the He II line problem), though higher S/N light curves would be needed to confirm this.

4.3. Amplitudes

The amplitudes of the light-curve variations range from a few hundredths of a magnitude to a few tenths of a magnitude. For

³ We note that the ZTF data are not suitable to detect pulsations. Otherwise a higher variability rate could be expected for very hot H-deficient white dwarfs, as many of them are GW Vir pulsators.

⁴ Amongst the UHE and He II line problem white dwarfs 21 objects have at least 50 data points in at least one ZTF band, and 14 of them turned out to be variable based on the ZTF data.

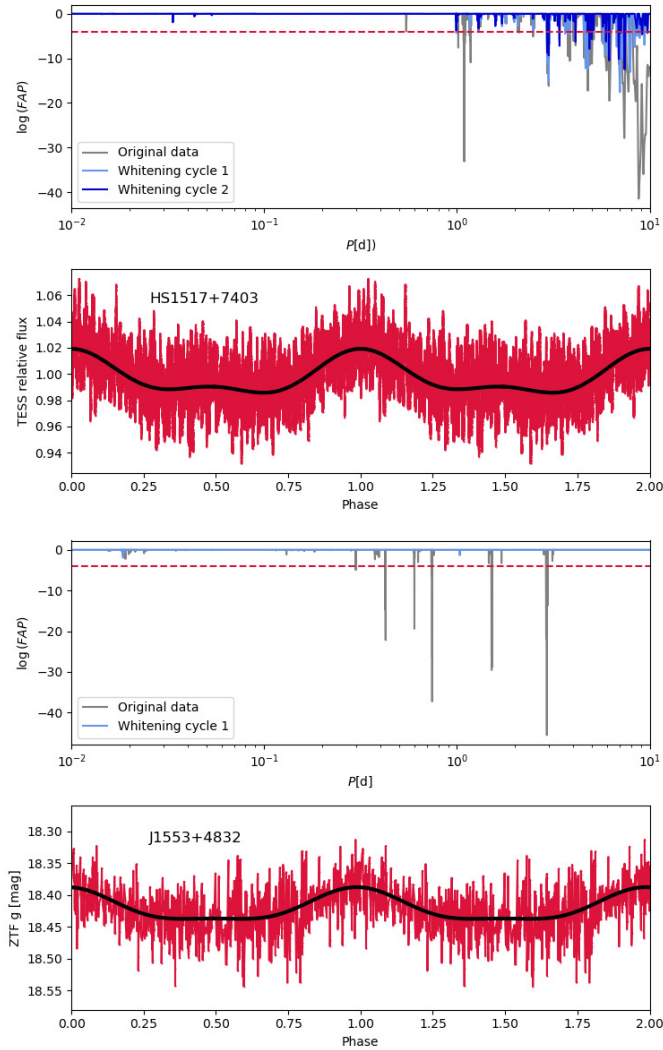


Fig. 7. As in Fig. 3 but for the He II line problem white dwarfs HS 1517+7403 and J1553+4832.

a given object, the amplitudes in the different bands do not vary significantly. This means that we find that the difference in the amplitudes as measured in the different bands is smaller than or equal to the standard deviation of the difference between the observations and our mathematical fit (black lines in Figs. 3–7). In particular, the SDSS stripe 82 light curves of J0254+0058 (the only object in our sample with u to z band data) do not indicate an increase in the amplitudes towards shorter or longer wavelengths. Also, in the BUSCA light curves of HS 0727+6003 (only other object with U -band light curve) we found no hint of a difference in the amplitudes.

We note that we do not trust the amplitudes of the TESS light curves. This is because the TESS mission was designed for stars brighter than 15 mag, and all our targets are fainter than this. Further, the large pixel size implies that an accurate background subtraction is very complicated, in particular in crowded fields. The majority of the TESS light curves predict amplitudes that are larger than what is observed in the other bands. For example, the amplitude of the phase-folded TESS light curve of J0254+0058 is 0.54 mag, which almost twice that observed in the other bands (≈ 0.3 mag). If this large TESS amplitude were real, we would expect to see similarly large amplitudes in the SDSS i - and z -band as well, but this is not the case. The faintness of our tar-

gets and the large TESS pixel size of 21 arcsec – which often leads to contamination from neighboring stars – also result in a large scatter in the TESS light curves. This in combination with the shorter duration of the TESS light curves compared to those obtained from ground-based surveys like ZTF (about one month compared to more than two years) explains the larger uncertainties on the periods obtained from the TESS data.

4.4. Periods

The photometric periods of the UHE white dwarfs range from 0.22 to 2.32 d, with a median of 0.69 d and a standard deviation of 0.59 d. For the six photometrically variable white dwarfs showing only the He II line problem, we find a very similar period range from 0.22 to 2.93 d, with a median of 0.45 d and a standard deviation of 0.95 d. Considering both classes together we find a median of 0.56 d with a standard deviation of 0.73 d.

The observed periods are consistent with typical white dwarf rotational rates (Kawaler 2004; Hermes et al. 2017a), but could also indicate post-common envelope (PCE) binaries (Nebot Gómez-Morán et al. 2011). It is therefore worth comparing the period distribution of those objects to the period distribution of our sample in detail.

Figure 8 shows the combined period distribution of the UHE white dwarfs and white dwarfs showing only the He II line problem. The left panel shows a comparison of their period distribution to the orbital period distribution of confirmed post-common envelope (PCE) binary central stars of planetary nebulae (CSPNe; light green, Jones & Boffin 2017; Boffin & Jones 2019)⁵ and PCE white dwarf and main sequence binaries (light yellow) from the sample of Nebot Gómez-Morán et al. (2011). The right panel shows a comparison with the rotational periods of pulsating white dwarfs (light green with dashed contours; values taken from Kawaler 2004; Hermes et al. 2017a) and apparently single magnetic white dwarfs (bold yellow lines, values taken from Ferrario et al. 2015). We note that there are also a few longer period magnetic white dwarfs (Putney & Jordan 1995; Bergeron et al. 1997; Schmidt et al. 1999; Kawka & Vennes 2012) and PCE binary central stars (Miszalski et al. 2018a,b; Brown et al. 2019) that we omit from Fig. 8 for better visualization. From this figure it already seems that the period distribution of our sample more closely resembles the period distribution of PCE binaries than the rotational period distribution of white dwarfs. The median rotational period of nonmagnetic white dwarfs is 1.20 d, while the median period of our sample is half of that. The observed rotational periods of magnetic white dwarfs as determined from polarimetry and photometry range from a few minutes, through hours and days, to over decades and centuries. The short-spin-period white dwarfs show their peak near 0.1 d, a period much shorter than what we observe for the UHE white dwarfs and white dwarfs showing the He II line problem.

In order to test the statistical significance of this impression we performed two-sample Kolmogorov–Smirnov tests. This test allows us to compare two samples and to check the equality of their one-dimensional probability distributions without making specific distributional assumptions. The statistical analysis is based on a D -value that represents the maximum distance between the empirical cumulative distribution function of the sample and the cumulative distribution function of the reference distribution. Based on the D -value, we then calculate the p -value, which is used to evaluate whether or not the outcomes

⁵ <http://www.drdjones.net/bcspn/>

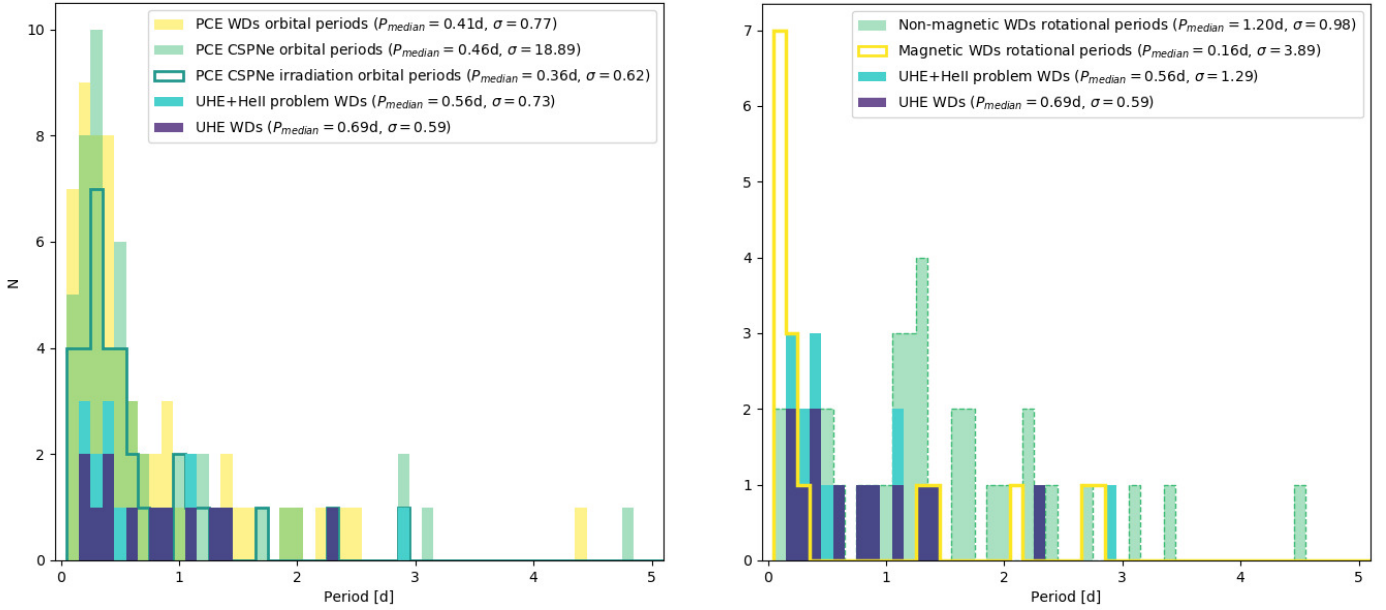


Fig. 8. Distribution of the photometric periods of the variable UHE and He II line problem white dwarfs (blue), and the period distribution of only the UHE white dwarfs (purple). On the left their period distribution is compared to the orbital period distribution of PCE CSPNe (light green; the bold teal line indicates the period distribution of binary CSPNe that show a reflection effect) and white dwarfs plus main sequence binaries (light yellow). *Left panel:* a comparison with the rotational periods of normal white dwarfs (light green with dashed contours) and magnetic white dwarfs (bold yellow lines). The median period and standard deviation of each sample is indicated.

differ significantly; this latter is a measure of the probability of obtaining test results at least as extreme as the results actually observed, assuming that the null hypothesis is correct. In our case, the null hypothesis is that the two samples compared follow the same distribution. A p -value of one indicates perfect agreement with the null hypothesis, while a p -value approaching zero rejects the null hypothesis. We performed these tests for the various samples mentioned above. First, we find that the period distributions of both UHE white dwarfs, and white dwarfs showing only the He II line problem agree with each other ($p = 1.00$). We also find that the period distribution of our sample agrees with that of PCE white dwarfs plus main sequence binaries ($p = 0.42$) and PCE CSPNe ($p = 0.60$ for all binary CSPNe and $p = 0.25$ for only the binary CSPNe showing a reflection effect). No agreement is found with the rotational period distribution of magnetic ($p = 0.007$), and nonmagnetic white dwarfs ($p = 0.04$).

However, we should keep in mind that the stars in our sample are in earlier evolutionary stages compared to the white dwarfs with measured rotational periods. According to Althaus et al. (2009), the radius of a DO white dwarf with typical mass of $0.6 M_{\odot}$ decreases from $0.017 R_{\odot}$ to $0.013 R_{\odot}$ while the star cools down from 80 000 K (typical T_{eff} for a UHE white dwarf) to 20 000 K (the majority of magnetic white dwarfs from Ferrario et al. 2015 are reported to have temperatures below this value, as are all of the nonmagnetic white dwarfs from Kawaler 2004; Hermes et al. 2017a). If we assume conservation of angular momentum then the rotational period should decrease approximately by a factor of 0.5. Therefore, we repeated the statistical tests under the simplified assumption that all of the objects in our sample will halve their periods as they cool down. We find that there is no agreement with the rotational period distribution of nonmagnetic white dwarfs ($p = 0.0001$), but that there is a statistically meaningful agreement with the rotational period distribution of magnetic white dwarfs ($p = 0.11$).

5. Discussion

We find that both UHE and He II line problem white dwarfs overlap in a narrow region in the *Gaia* HRD. As expected, they lie on top of the white dwarf banana and are well separated from the hot subdwarf stars, and are much bluer than similarly hot white dwarfs with M dwarf companions. On average, UHE white dwarfs are found to be slightly bluer and have slightly brighter absolute G -band magnitudes than the white dwarfs showing only the He II line problem. This might suggest that white dwarfs with UHE lines could evolve into objects that show only the He II line problem. However, better constraints on the temperatures of these stars as well as a larger sample would be needed to investigate this possibility further.

Our light curve studies reveal that the majority of both the UHE white dwarfs ($75^{+8}_{-13}\%$) and He II line problem white dwarfs ($75^{+9}_{-19}\%$) are photometrically variable. The fact that their photometric period distributions agree with each other, and that their light curves exhibit similar amplitudes and shapes, reinforces the hypothesis that both classes are indeed related. What remains to be discussed is the cause of the photometric variability and how it is linked to the occurrence of the UHE features and He II line problem.

The photometric periods of all stars in our sample are well above the theoretical upper limit of 10^4 s predicted for nonradial g -mode pulsations that are frequently observed amongst PG 1159 stars (most of them having periods below 3000 s; Quirion et al. 2007; Córscico et al. 2019, 2021). Thus, we see two possible scenarios that could instead account for the photometric variability in our stars; one is linked to close binaries, and the other one related to magnetic fields.

5.1. Binaries

Because of the very good agreement of the period distribution of our stars with that of PCE systems, an obvious assumption is that

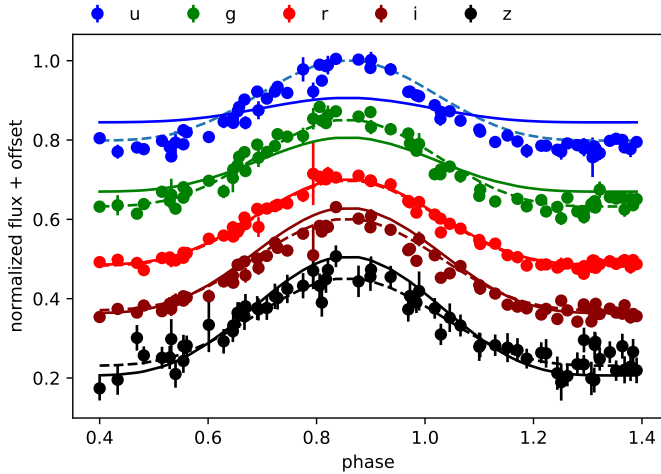


Fig. 9. SDSS-*ugriz* light curves of J0254+0058. The solid line shows the light curve models using the parameters derived by fitting the SDSS-*r* light curve and a fixed albedo of $A = 1$ in all bands. The dashed lines give the light curve model fit that allows for unphysical variations in the albedo of the companion.

our stars are close binaries. If so, a variety of physical processes could lead to the observed periodic variability. We rule out that the objects in our sample are (over-)contact binaries, because the light curves of such systems have extended maxima and narrow (sometimes V-shaped) photometric minima and also often two uneven minima (e.g., Miszalski et al. 2009; Drake et al. 2014). Also, ellipsoidal deformation, which occurs in a detached system where one star is distorted due to the gravity of its companion, can be ruled out as the main source for the photometric variability. This is because the amplitudes of the light-curve variations caused by ellipsoidal deformation in systems that contain a hot and compact white dwarf and an extended companion are always much smaller than that from the so-called irradiation effect.

An irradiation or reflection effect caused by the heated face (day-side) of a cooler companion whose rotational period is synchronized to the orbital period appears to be a likely scenario. Irradiation binaries display sinusoidal light-curve variations, but when the system is seen under a high inclination angle, the light curves have extended and flat photometric minima, which is precisely what we find for seven objects in our sample (Sect. 4.2). Well-studied examples that exhibit this latter kind of light curve are the hot subdwarf plus M-dwarf binary HS 2333+3927 (Heber et al. 2004), and the hot white dwarf plus M-dwarf binaries HS 1857+5144 (Aungwerojwit et al. 2007) and NN Ser (which also shows eclipses, Brinkworth et al. 2006). The observed amplitudes can be as low as 0.01 mag and reach up to about 1 mag (Shimansky et al. 2006; Brinkworth et al. 2006), covering the observed amplitude range of our objects. However, we see serious problems with the irradiation effect system scenario. First, we would expect to find – at least for some objects – noticeable differences in the amplitudes observed in the different bands. For example, in the very hot ($T_{\text{eff}} \geq 49\,500$ K) white dwarf plus low-mass main sequence star irradiation systems SDSS J212531.92–010745.9, and the central stars of Abell 63, V477 Lyr, ESO330–9, and PN HaTr 7, the ratio of the *R*-band to *V*-band amplitude ranges from 1.13 to 1.38 (Shimansky et al. 2015; Afşar & Ibanoglu 2008; Hillwig et al. 2017). WD1136+667 and NN Ser even display *r*-band to *g*-band amplitude ratios of 1.44 and 1.67, respectively (shown by the present study, and Brinkworth et al. 2006). An even larger difference in

the amplitudes – by a factor of almost two – is expected when *u*-band photometry is also available (De Marco et al. 2008). This should be easily noticeable in the light curves of J0254+0058 and HS 0727+6003.

In order to test this we calculated reflection-effect models for the SDSS-*ugriz* light curves of J0254+0058. We used the code LCURVE (for details, see Appendix A of Copperwheat et al. 2010), which was developed for white dwarfs plus M-dwarf systems and has been used to fit detached or accreting white dwarfs plus M-dwarf and hot subdwarf plus M-dwarf systems showing a significant reflection effect (see Parsons et al. 2010; Schaffenroth et al. 2021, for more details). For that we assumed $T_{\text{eff}} = 80\,000$ K for the white dwarf (Hügelmeier et al. 2006) and typical values for the masses and radii of white dwarfs plus M-dwarf systems ($q = 0.21$, $R_1 = 0.02 R_{\odot}$, $R_2 = 0.15 R_{\odot}$, Parsons et al. 2010). To find a first good model we fitted the SDSS-*r* light curve by letting the inclination i , the temperature of the companion T_2 , and the albedo of the companion vary. We found a perfectly fitting model for an inclination of $i = 86.8^{\circ}$ and a temperature of the companion of $T_2 = 4500$ K. To see if this is also consistent in the other bands, we fixed the stellar parameters of both stars and derived light curve models for the other bands. We were only able to fit the light curve if the albedo of the companion was varied significantly ($A = 0.6$ in SDSS-*z* to $A = 3.5$ in SDSS-*u*, dashed line in Fig. 9). Such a large change in the albedo is unphysical, as the albedo gives the percentage of the flux from the white dwarf that is used to heat up the irradiated side of the companion. If we assume an albedo of $A = 1$, the amplitude of the light curve varies significantly from smaller in the blue to larger in the red, as shown in Fig. 9.

As explained before, this increase in the amplitude of the reflection effect from blue to red is expected. The amplitude of the reflection effect is calculated as the difference in the flux between phase 0, where the white dwarf and the maximum projected area of the cool side of the companion is visible, and phase 0.5, where the white dwarf and the maximum projected area of the heated side of the companion is visible. Depending on the temperature of the white dwarf and the orbital separation of the system, the companion is heated up to around 10 000–20 000 K. As the white dwarf has maximum flux in the UV, the contribution of the companion increases from blue to red.

To simulate this, we used the parameters that we derived in the light curve fit and used a black body approximation to calculate the amplitude of the reflection effect as a function of the temperature of the heated side of the companion. As the period of the putative binary system is relatively long, we calculated amplitudes up to 8000 K for the heated side of the companion. This is shown in Fig. 10. A significant increase in the amplitude from SDSS-*u* (5%) to SDSS-*z* (40%) is predicted, which is not observed. From Fig. 10 it also becomes clear that the amplitude in the *r* band should be about twice that in the *g* band. However, none of the ten other objects, which show significant periodic variations in both ZTF bands, show an increased amplitude in the *r* band compared to the *g* band.

The second drawback of the reflection effect scenario is that none of our stars exhibit spectral features of a cool secondary (Figs. B.1 and B.2). As mentioned before, a late-type M dwarf or a brown dwarf may easily be outshined by the still luminous white dwarf, and therefore the nondetection of an increased continuum flux in the optical or lack of (molecular) absorption features from the companion cannot be taken as irrefutable evidence. However, to the very best of our knowledge, without exception all PCE systems containing a very hot ($T_{\text{eff}} \geq 60\,000$ K) white dwarf primary (and even those who

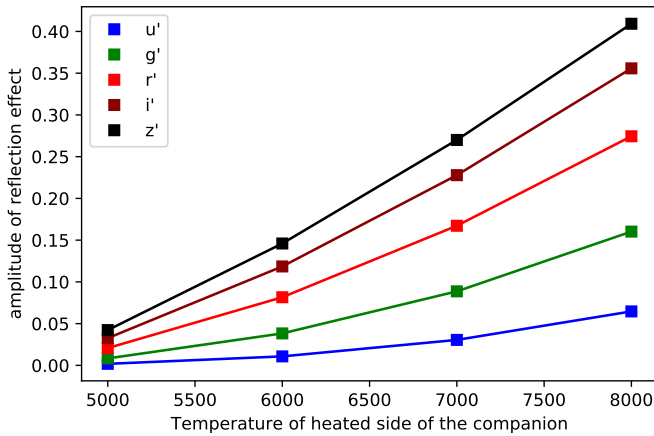


Fig. 10. Expected amplitude for J0254+0058 of the reflection effect as a function of the temperature of the heated side of the companion. The amplitude was calculated as the difference in flux of a white dwarf and a M-dwarf companion with the parameters derived in the light curve fit in phase 0 and phase 0.5 using a black-body approximation.

outshine their cool companions in the optical) exhibit emission lines (e.g., the Balmer series or the CNO complex around 4650 Å) arising from the highly irradiated hemisphere of a secondary. These emission lines are typically quite strong and can therefore also be detected in low-resolution (e.g., SDSS) spectra (Nagel et al. 2006; Nebot Gómez-Morán et al. 2011). It is also well known that the emission lines appear and disappear over the orbital cycle, reaching maximum strength at photometric maximum. Thus, it may be possible that the emission lines are not detectable when the systems are observed close to the photometric minimum. However, it is very unlikely that all spectra of the stars in our sample were taken at that same phase.

For a reflection effect, the amplitudes of the light-curve variations are expected to be correlated with the temperature of the day-side of the irradiated companion. If we assume that all hypothetical close companions to our stars have the same temperature, then the amplitudes should correlate with $L/P^{2/3}$, where L is the luminosity of the white dwarf and P the orbital (photometric) period. This means that more luminous primaries at shorter orbital periods are expected to cause a larger reflection effect than less luminous primaries at longer periods. However, using M_{G_0} as a proxy for L , no correlation between $M_{G_0}/P^{2/3}$ and the mean amplitudes is found (Pearson correlation coefficient: $r = -0.01$)^{6,7}. This serves as a third argument against our stars being reflection-effect binaries.

Finally, we would like to note that, if the variability in all our objects were found to indeed be caused by close companions, this would imply an exceptionally high compact binary fraction amongst H-deficient stars of 30%⁸. Of the immediate precursors of DO-type white dwarfs, only one O(He) star and one

luminous PG 1159 star⁹ are known to be radial-velocity variable (Reindl et al. 2016). Another O(He)-type star, the central star of Pa 5, shows photometric variability of 1.12 d, which nevertheless might also be attributed to spots on its surface (De Marco et al. 2015). Although no systematic search for close binaries has yet been conducted for PG 1159 and O(He) stars, this would lead us to an estimated close binary fraction in the H-deficient pre-white dwarfs of 11.5%, which is a factor of 2.6 below what would be needed to explain the variability in our stars via close binaries.

5.2. Magnetic fields

The fraction of the hottest white dwarfs that show UHE lines or the He II line problem (about 10%) matches the fraction of magnetic white dwarfs (2–20% are reported, Liebert et al. 2003; Giannichele et al. 2012; Sion et al. 2014; Kepler et al. 2013, 2015). In addition, we find that the period distribution of our stars agrees with that of magnetic white dwarfs if we assume that they will spin up as a consequence of further contraction. Proposing that UHE white dwarfs are magnetic, Reindl et al. (2019) suggested that optically bright spots on the magnetic poles and/or geometrical effects of a circumstellar magnetosphere could be responsible for the photometric variability in J0146+3236.

Spots on hot white dwarfs are expected to be caused by the accumulation of metals around the magnetic poles (Hermes et al. 2017b). This is also the case for chemically peculiar stars, where the magnetic field produces large-scale chemical abundance inhomogeneities causing periodic modulations of spectral line profiles and light curves (Oksala et al. 2015; Prvák et al. 2015, 2020; Krtićka et al. 2018, 2020a; Momany et al. 2020). This is understood as a result from the interaction of the magnetic field with photospheric atoms diffusing under the competitive effects of gravity and radiative levitation (Alecian & Stift 2017). If the radiative and gravitational forces are of similar orders of magnitude, these structures are able to form and subsist (Wade & Neiner 2018). In fact, it was found by Reindl et al. (2014) that the DO-type UHE and He II line problem white dwarfs are located at this very region in the $T_{\text{eff}} - \log g$ diagram, where also the wind limit as predicted by Unglaub & Bues (2000) occurs. This further supports the hypothesis that effects of gravitational settling and radiation-driven mass loss are about the same in our stars, and that long-lived spots can therefore be expected.

Reindl et al. (2019) showed that the light curve of J0146+3236 can be modeled assuming two uneven spots whose brightness is slightly over 125% relative to the rest of the stellar surface. In order to get an idea of the metal enhancement needed to achieve such an increase in brightness, we calculated test models with TMAP. In the model atmosphere calculations, we assumed $T_{\text{eff}} = 80\,000$ K, $\log g = 8.0$, and included opacities of He and the iron-group elements (Ca, Sc, Ti, V, Cr, Mn, Fe, Co, and Ni), of which Fe was found to be the most abundant trace element in UHE white dwarfs (Werner et al. 2018b). Iron-group elements were combined in a generic model atom, using a statistical approach, employing seven superlevels per ion linked by superlines, together with an opacity-sampling method (Anderson 1989; Rauch & Deetjen 2003). Ionization stages IV–VII augmented by a single ground-level stage VIII were considered and we assumed solar abundance ratios. The models were calculated for metallicities of 10^{-3} , 10^{-2} , and 10^{-1}

⁶ We only used objects with a relative uncertainty for the parallax smaller than 20% to check for this correlation.

⁷ The inclination angle of the system also has an impact on the amplitudes, which would cause an additional scatter. However, it is unlikely that the inclinations are distributed in such a way that the correlation between the amplitude and $M_{G_0}/P^{2/3}$ simply vanishes.

⁸ 30% of all DO-type white dwarfs hotter than 65 000 K show UHE lines or only the He II line problem. If we exclude those that are classified as PG 1159 stars ($C/He > 0.02$, number fraction) from the group of normal DO-type white dwarfs, we obtain a value of 47%.

⁹ Only ten O(He) stars and 16 PG 1159 pre-white dwarfs ($\log g < 7.0$) are known.

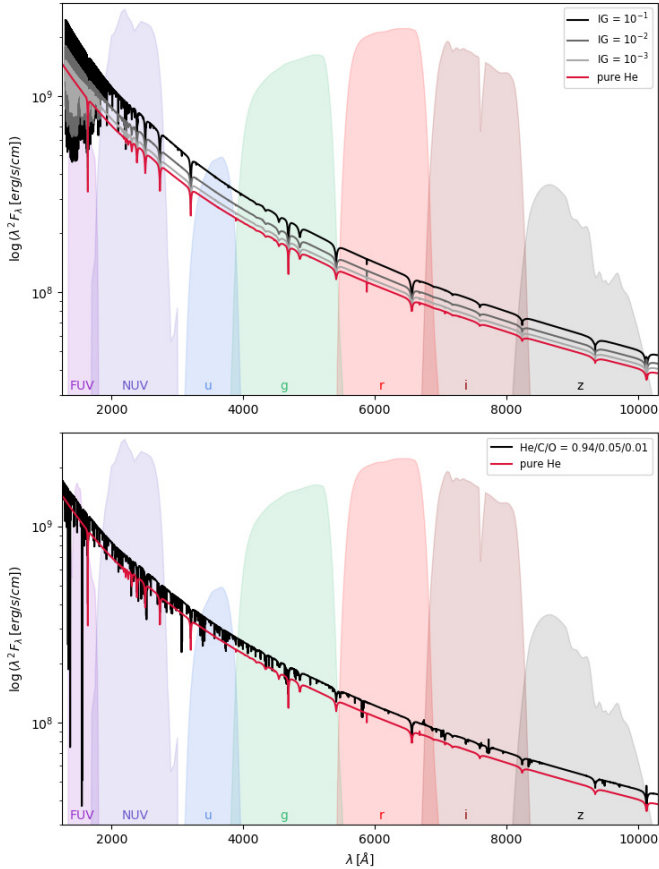


Fig. 11. Differences in the flux of models with different metal contents and a model containing only He (red). *Upper panel:* fluxes for different abundances of the iron-group elements, and *lower panel:* a model that contains opacities of He, C, and O. The filter response functions of the Galex FUV, NUV, and SDSS *u*, *g*, *r*, *i*, and *z* bands are indicated.

(mass fractions). In addition, we calculated a model including, in addition to He, opacities of C, and O at typical abundance values of low-luminosity PG 1159 stars (mass fractions of 5×10^{-2} , and 1×10^{-2} , respectively). For the calculations, we considered ionization stages III–V and III–VII for C and O, respectively, and a total of 404 NLTE levels. Finally, a pure He model was also computed. After that, the model fluxes were convolved with filter response functions of the Galex FUV, NUV, and the SDSS *u*, *g*, *r*, *i*, and *z* bands in order to calculate synthetic magnitudes.

Figure 11 shows the various synthetic spectra, and the filter response functions are indicated. The differences in the resulting magnitudes relative to our pure He model are listed in Table 2. We find that with an increasing abundance of the iron-group elements, the continuum flux becomes steeper towards the UV. Most of the bound-bound transitions are located at FUV wavelengths at this effective temperature, which in turn causes a flattening of total flux in the FUV band (upper panel in Fig. 11). Comparing our pure He model to our model that also contains C and O, we find that the continuum flux also increases from the near-infrared (NIR) to the far-UV, and therefore also produces optically bright spots. However, because many strong bound-bound transitions of C and O are located in the optical (especially in the SDSS *g* band; lower panel in Fig. 11), the behavior of the amplitude differences varies significantly from our models with iron-group elements. This has been shown for a Cen by Krtićka et al. (2020b), where for example an enhancement in He,

Table 2. Predicted differences in the resulting magnitudes from synthetic spectra containing metals relative to a model containing only He.

Model	IG 10^{-3}	IG 10^{-2}	IG 10^{-1}	C, O 5×10^{-2} 1×10^{-2}
Band	Δm [mag]	Δm [mag]	Δm [mag]	Δm [mag]
FUV	0.096	0.234	0.462	0.148
NUV	0.239	0.381	0.624	0.182
<i>u</i>	0.223	0.339	0.535	0.176
<i>g</i>	0.037	0.133	0.296	0.089
<i>r</i>	0.062	0.146	0.289	0.160
<i>i</i>	0.040	0.117	0.247	0.103
<i>z</i>	0.061	0.133	0.249	0.168

Notes. The different photometric bands and metal abundances adopted in the calculations are listed.

Si, or Fe not only predicts a different amplitude, respectively, but also the maxima of the light curve variations are found to occur at different phases.

We also note that because spots cover only a part of the stellar surface, the amplitudes listed in Table 2 can be seen merely as an upper limit of what could be expected observationally from the metal enhancement in the spot. Nevertheless, this demonstrates that chemical spots could indeed explain the relatively large amplitude variations we see in our stars. The only drawback is that, for all the metals considered here, the predicted amplitude in the *u* band is always significantly larger than in the redder bands. This is not observed for the two stars in our sample for which we have *u* band light curves. However, only time-resolved UV spectroscopy combined with detailed light curve modeling will be able to shed light on which enhancement of elements is responsible for the observed light curve variability and whether or not chemical spots are indeed the source of the variability.

Besides a chemically inhomogeneous photosphere, stellar magnetism can create another source of photometric variability. Munoz et al. (2020) recently hypothesized that the photometric variability observed in magnetic O-type stars is a consequence of electron scattering in the obliquely rotating magnetosphere, which periodically occults the stellar disk. These latter authors presented theoretical light curves for various inclinations, *i*, and magnetic obliquity angles, β , mass-feeding rates, magnetic field strengths, terminal wind velocities, and smoothing lengths. Increasing the latter four parameters, they find that the amplitude of the light-curve variations should increase. For low inclination and obliquity angles, they find roughly sinusoidal light-curve variations. When $i + \beta > 90^\circ$, the magnetic equator crosses the observer’s line-of-sight twice per rotation cycle and a second maximum in the light curve shows up. Interestingly, for intermediate inclination and obliquity angles (e.g., $i = \beta = 50^\circ$), their models predict a relatively long, and almost flat photometric minimum, which is precisely what we observe for seven of our stars. One of these stars is J0146+3236 for which Reindl et al. (2019) already suggested $i \approx \beta \approx 45^\circ$. Also, the models of Munoz et al. (2020) predict that the photometric minimum should occur when the circumstellar magnetosphere is seen edge-on, that is, when the column density of the magnetospheric material occulting the stellar disk is highest. The magnetospheric occultation model might even be able to explain the extraordinary light curve of HS 0158+2335, which exhibits two uneven

maxima. Its light curve resembles that of LMCe136–1, which could be reproduced by Munoz et al. (2020) assuming a dipolar offset model.

6. Conclusions

Our work reveals exceptionally high photometric variability rates amongst both UHE white dwarfs and white dwarfs that show only the He II line problem, marking them a new class of variable stars. We find further evidence that both classes are indeed related, as concluded from their overlap in the *Gaia* HRD, similar photometric variability rates, light curve shapes and amplitudes, and period distributions. While an irradiation effect could explain their observed period distribution, and the shapes of their light curves, we believe that this scenario is unlikely. This is because we do not detect increasing amplitudes towards longer wavelengths in any object, nor do we see emission lines arising from the strongly irradiated side of a hypothetical close binary. Instead, we hold on to the suggestion of Reindl et al. (2019) that the variability is caused by magnetic spots and/or the co-rotating, circumstellar material.

Further investigations are needed for a profound understanding of these special objects. A systematic search for radial-velocity variations, as well as an IR excess in combination with detailed light-curve modeling, will help to clarify whether or not the close binary scenario can really be ruled out. On the other hand, the spots/magnetosphere scenario can be verified with spectro-polarimetric observations and time-resolved UV (where photospheric metals can be detected) spectroscopy, which in turn could reveal the magnetic field strengths and chemical spots, respectively. Last but not least, the discovery that the majority of the UHE and He II line problem white dwarfs are photometrically variable provides an important observational constraint that can be used to detect more of these systems.

Acknowledgements. We thank Jiri Krtička, Thomas Kupfer, and JJ Hermes for helpful comments. We thank Stefan Dreizler for providing us with the TWIN spectrum of HS1517+7403. VS is supported by the Deutsche Forschungsgemeinschaft, DFG through grant GE 2506/9-1. IP acknowledges support from the UK's Science and Technology Facilities Council (STFC), grant ST/T000406/1. IP was partially supported by the Deutsche Forschungsgemeinschaft, DFG through grant GE2506/12-1. The BUSCA observing run was made possible with support from STFC grant ST/T001380/1. Some of the data presented in this paper were obtained from the Mikulski Archive for Space Telescopes (MAST). This research has made use of NASA's Astrophysics Data System and the SIMBAD database, operated at CDS, Strasbourg, France. Based on observations collected at the German-Spanish Astronomical Center, Calar Alto, jointly operated by the Max-Planck-Institut für Astronomie Heidelberg and the Instituto de Astrofísica de Andalucía (CSIC). Based on data obtained from the ESO Science Archive Facility under request number nreindl/584030. The TMAD (<http://astro.uni-tuebingen.de/~TMAD>) and TIRO tool (<http://astro.uni-tuebingen.de/~TIRO>) used for this paper was constructed as part of the activities of the German Astrophysical Virtual Observatory. This work has made use of data from the European Space Agency (ESA) mission *Gaia* (<https://www.cosmos.esa.int/gaia>), processed by the *Gaia* Data Processing and Analysis Consortium (DPAC, <https://www.cosmos.esa.int/web/gaia/dpac/consortium>). Funding for the DPAC has been provided by national institutions, in particular the institutions participating in the *Gaia* Multilateral Agreement. The CSS survey is funded by the National Aeronautics and Space Administration under Grant No. NNG05GF22G issued through the Science Mission Directorate Near-Earth Objects Observations Program. The CRTS survey is supported by the U.S. National Science Foundation under grants AST-0909182 and AST-1313422. Based on observations obtained with the Samuel Oschin 48-inch Telescope at the Palomar Observatory as part of the Zwicky Transient Facility project. ZTF is supported by the National Science Foundation under Grant No. AST-1440341 and a collaboration including Caltech, IPAC, the Weizmann Institute for Science, the Oskar Klein Center at Stockholm University, the University of Maryland, the University of Washington, Deutsches Elektronen-Synchrotron and Humboldt University, Los Alamos National Laboratories, the TANGO Consortium of Taiwan, the University of Wisconsin at

Milwaukee, and Lawrence Berkeley National Laboratories. Operations are conducted by COO, IPAC, and UW. This work includes data from the Asteroid Terrestrial-impact Last Alert System (ATLAS) project. ATLAS is primarily funded to search for near earth asteroids through NASA grants NN12AR55G, 80NSSC18K0284, and 80NSSC18K1575; byproducts of the NEO search include images and catalogs from the survey area. The ATLAS science products have been made possible through the contributions of the University of Hawaii Institute for Astronomy, the Queen's University Belfast, the Space Telescope Science Institute, and the South African Astronomical Observatory. This paper includes data collected by the TESS mission. Funding for the TESS mission is provided by the NASA Explorer Program. This work made use of *tpfplotter* by J. Lillo-Box (publicly available in www.github.com/jlillo/tpfplotter), which also made use of the python packages *astropy*, *lightkurve*, *matplotlib*, and *numpy*. IRAF is distributed by the National Optical Astronomy Observatory, which is operated by the Association of Universities for Research in Astronomy (AURA) under a cooperative agreement with the National Science Foundation. Funding for the Sloan Digital Sky Survey IV has been provided by the Alfred P. Sloan Foundation, the US Department of Energy Office of Science, and the Participating Institutions. SDSS-IV acknowledges support and resources from the Center for High Performance Computing at the University of Utah. The SDSS website is www.sdss.org. SDSS-IV is managed by the Astrophysical Research Consortium for the Participating Institutions of the SDSS Collaboration including the Brazilian Participation Group, the Carnegie Institution for Science, Carnegie Mellon University, Center for Astrophysics, Harvard & Smithsonian, the Chilean Participation Group, the French Participation Group, Instituto de Astrofísica de Canarias, The Johns Hopkins University, Kavli Institute for the Physics and Mathematics of the Universe (IPMU)/University of Tokyo, the Korean Participation Group, Lawrence Berkeley National Laboratory, Leibniz Institut für Astrophysik Potsdam (AIP), Max-Planck-Institut für Astronomie (MPIA Heidelberg), Max-Planck-Institut für Astrophysik (MPA Garching), Max-Planck-Institut für Extraterrestrische Physik (MPE), National Astronomical Observatories of China, New Mexico State University, New York University, University of Notre Dame, Observatório Nacional/MCTI, The Ohio State University, Pennsylvania State University, Shanghai Astronomical Observatory, United Kingdom Participation Group, Universidad Nacional Autónoma de México, University of Arizona, University of Colorado Boulder, University of Oxford, University of Portsmouth, University of Utah, University of Virginia, University of Washington, University of Wisconsin, Vanderbilt University, and Yale University.

References

- Abazajian, K. N., Adelman-McCarthy, J. K., Agüeros, M. A., et al. 2009, *ApJS*, **182**, 543
- Afşar, M., & Ibañoğlu, C. 2008, *MNRAS*, **391**, 802
- Alecian, G., & Stiff, M. J. 2017, *MNRAS*, **468**, 1023
- Aller, A., Lillo-Box, J., Jones, D., Miranda, L. F., & Barceló Forteza, S. 2020, *A&A*, **635**, A128
- Althaus, L. G., Panei, J. A., Miller Bertolami, M. M., et al. 2009, *ApJ*, **704**, 1605
- Anderson, L. S. 1989, *ApJ*, **339**, 558
- Aungwerojwit, A., Gänsicke, B. T., Rodríguez-Gil, P., et al. 2007, *A&A*, **469**, 297
- Bainbridge, M., Barstow, M., Reindl, N., et al. 2017, *Universe*, **3**, 32
- Becker, A. C., Bochanski, J. J., Hawley, S. L., et al. 2011, *ApJ*, **731**, 17
- Bellm, E. C., Kulkarni, S. R., Graham, M. J., et al. 2019, *PASP*, **131**
- Berengut, J. C., Flambaum, V. V., Ong, A., et al. 2013, *Phys. Rev. Lett.*, **111**
- Bergeron, P., Ruiz, M. T., & Leggett, S. K. 1997, *ApJS*, **108**, 339
- Boffin, H. M. J., & Jones, D. 2019, *The Importance of Binaries in the Formation and Evolution of Planetary Nebulae* (Berlin, New York: Springer-Verlag)
- Brinkworth, C. S., Marsh, T. R., Dhillon, V. S., & Knigge, C. 2006, *MNRAS*, **365**, 287
- Brown, A. J., Jones, D., Boffin, H. M. J., & Van Winckel, H. 2019, *MNRAS*, **482**, 4951
- Burgasser, A. J., Kirkpatrick, J. D., Reid, I. N., et al. 2003, *ApJ*, **586**, 512
- Chayer, P., Vennes, S., Dupuis, J., & Kruk, J. W. 2005, *ApJ*, **630**, L169
- Copperwheat, C. M., Marsh, T. R., Dhillon, V. S., et al. 2010, *MNRAS*, **402**, 1824
- Córsico, A. H., Althaus, L. G., Miller Bertolami, M. M., & Kepler, S. O. 2019, *A&ARv*, **27**, 7
- Córsico, A. H., Uzundag, M., Kepler, S. O., et al. 2021, *A&A*, **645**, A117
- De Marco, O., Hillwig, T. C., & Smith, A. J. 2008, *AJ*, **136**, 323
- De Marco, O., Long, J., Jacoby, G. H., et al. 2015, *MNRAS*, **448**, 3587
- Drake, A. J., Djorgovski, S. G., Mahabal, A., et al. 2009, *ApJ*, **696**, 870
- Drake, A. J., Graham, M. J., Djorgovski, S. G., et al. 2014, *ApJS*, **213**, 9
- Dreizler, S., & Heber, U. 1998, *A&A*, **334**, 618
- Dreizler, S., & Werner, K. 1996, *A&A*, **314**, 217
- Dreizler, S., Heber, U., Napiwotzki, R., & Hagen, H. J. 1995, *A&A*, **303**, L53

- Eastman, J., Siverd, R., & Gaudi, B. S. 2010, *PASP*, **122**, 935
- Ferrario, L., de Martino, D., & Gänsicke, B. T. 2015, *Space Sci. Rev.*, **191**, 111
- Gaia Collaboration (Prusti, T., et al.) 2016, *A&A*, **595**, A1
- Gaia Collaboration (Babusiaux, C., et al.) 2018, *A&A*, **616**, A10
- Gänsicke, B. T., Schreiber, M. R., Toloza, O., et al. 2019, *Nature*, **576**, 61
- Geier, S. 2020, *A&A*, **635**, A193
- Geier, S., Raddi, R., Gentile Fusillo, N. P., & Marsh, T. R. 2019, *A&A*, **621**, A38
- Gentile Fusillo, N. P., Tremblay, P.-E., Gänsicke, B. T., et al. 2019, *MNRAS*, **482**, 4570
- Giammichele, N., Bergeron, P., & Dufour, P. 2012, *ApJS*, **199**, 29
- Gianninas, A., Bergeron, P., & Ruiz, M. T. 2011, *ApJ*, **743**, 138
- Gianninas, A., Curd, B., Thorstensen, J. R., et al. 2015, *MNRAS*, **449**, 3966
- Girven, J., Gänsicke, B. T., Steeghs, D., & Koester, D. 2011, *MNRAS*, **417**, 1210
- Hagen, H.-J., Groote, D., Engels, D., & Reimers, D. 1995, *A&AS*, **111**, 195
- Hartman, J. D., & Bakos, G. Á. 2016, *Astron. Comput.*, **17**, 1
- Heber, U., Drechsel, H., Østensen, R., et al. 2004, *A&A*, **420**, 251
- Heinze, A. N., Tonry, J. L., Denneau, L., et al. 2018, *AJ*, **156**, 241
- Hermes, J. J., Gänsicke, B. T., Kawaler, S. D., et al. 2017a, *ApJS*, **232**, 23
- Hermes, J. J., Kawaler, S. D., Bischoff-Kim, A., et al. 2017b, *ApJ*, **835**, 277
- Hillwig, T. C., Frew, D. J., Reindl, N., et al. 2017, *AJ*, **153**, 24
- Howell, S. B., Sobek, C., Haas, M., et al. 2014, *PASP*, **126**, 398
- Hoyer, D., Rauch, T., Werner, K., Kruk, J. W., & Quinet, P. 2017, *A&A*, **598**, A135
- Hoyer, D., Rauch, T., Werner, K., & Kruk, J. W. 2018, *A&A*, **612**, A62
- Hu, J., Webb, J. K., Ayres, T. R., et al. 2021, *MNRAS*, **500**, 1466
- Hügelmeier, S. D., Dreizler, S., Werner, K., et al. 2005, *A&A*, **442**, 309
- Hügelmeier, S. D., Dreizler, S., Homeier, D., et al. 2006, *A&A*, **454**, 617
- Isern, J., García-Berro, E., Torres, S., & Catalán, S. 2008, *ApJ*, **682**, L109
- Ivezić, Ž., Smith, J. A., Miknaitis, G., et al. 2007, *AJ*, **134**, 973
- Jenkins, J. M., Twicken, J. D., McCauliff, S., et al. 2016, in *Software and Cyberinfrastructure for Astronomy IV*, eds. G. Chiozzi, & J. C. Guzman, *SPIE Conf. Ser.*, **9913**, 99133E
- Jones, D., & Boffin, H. M. J. 2017, *Nat. Astron.*, **1**, 0117
- Kalirai, J. S. 2012, *Nature*, **486**, 90
- Kawaler, S. D. 2004, in *Stellar Rotation*, eds. A. Maeder, & P. Eenens, *IAU Symp.*, **215**, 561
- Kawka, A., & Vennes, S. 2012, *MNRAS*, **425**, 1394
- Kepler, S. O., Pelisoli, I., Jordan, S., et al. 2013, *MNRAS*, **429**, 2934
- Kepler, S. O., Pelisoli, I., Koester, D., et al. 2015, *MNRAS*, **446**, 4078
- Kepler, S. O., Pelisoli, I., Koester, D., et al. 2019, *MNRAS*, **486**, 2169
- Kilic, M., Bergeron, P., Dame, K., et al. 2019, *MNRAS*, **482**, 965
- Krtićka, J., & Kubát, J. 2005, in *14th European Workshop on White Dwarfs*, eds. D. Koester, & S. Moehler, *ASP Conf. Ser.*, **334**, 337
- Krtićka, J., Huang, L., Jagelka, M., et al. 2018, *Contrib. Astron. Obs. Skaln. Pleso*, **48**, 170
- Krtićka, J., Kawka, A., Mikulášek, Z., et al. 2020a, *A&A*, **639**, A8
- Krtićka, J., Mikulášek, Z., Prvák, M., et al. 2020b, *MNRAS*, **493**, 2140
- Lallement, R., Capitanio, L., Ruiz-Dern, L., et al. 2018, *A&A*, **616**, A132
- Liebert, J., Bergeron, P., & Holberg, J. B. 2003, *AJ*, **125**, 348
- Lindgren, L., Bastian, U., Biermann, M., et al. 2021, *A&A*, in press, <https://doi.org/10.1051/0004-6361/202039653>
- Löbbling, L., Maney, M. A., Rauch, T., et al. 2020, *MNRAS*, **492**, 528
- Luger, R., Agol, E., Kruse, E., et al. 2016, *AJ*, **152**, 100
- Luger, R., Kruse, E., Foreman-Mackey, D., Agol, E., & Saunders, N. 2018, *AJ*, **156**, 99
- Masci, F. J., Laher, R. R., Rusholme, B., et al. 2019, *PASP*, **131**
- Miller Bertolami, M. M. 2014, *A&A*, **562**, A123
- Miller Bertolami, M. M., Melendez, B. E., Althaus, L. G., & Isern, J. 2014, *JCAP*, **10**, 069
- Miszalski, B., Acker, A., Moffat, A. F. J., Parker, Q. A., & Udalski, A. 2009, *A&A*, **496**, 813
- Miszalski, B., Manick, R., Mikołajewska, J., et al. 2018a, *MNRAS*, **473**, 2275
- Miszalski, B., Manick, R., Mikołajewska, J., Van Winckel, H., & Iłkiewicz, K. 2018b, *PASA*, **35**, e027
- Momany, Y., Zaggia, S., Montalto, M., et al. 2020, *Nat. Astron.*, **4**, 1092
- Munoz, M. S., Wade, G. A., Nazé, Y., et al. 2020, *MNRAS*, **492**, 1199
- Nagel, T., Schuh, S., Kusterer, D.-J., et al. 2006, *A&A*, **448**, L25
- Napiwotzki, R. 1997, in *The Third Conference on Faint Blue Stars*, eds. A. G. D. Philip, J. Liebert, R. Saffer, & D. S. Hayes, 207
- Nebot Gómez-Morán, A., Gänsicke, B. T., Schreiber, M. R., et al. 2011, *A&A*, **536**, A43
- Oksala, M. E., Kochukhov, O., Krtićka, J., et al. 2015, *MNRAS*, **451**, 2015
- Parsons, S. G., Marsh, T. R., Copperwheat, C. M., et al. 2010, *MNRAS*, **402**, 2591
- Press, W. H., Teukolsky, S. A., Vetterling, W. T., & Flannery, B. P. 1992, *Numerical Recipes in C. The Art of Scientific Computing* (New York: Cambridge University Press)
- Prvák, M., Liška, J., Krtićka, J., Mikulášek, Z., & Lüftinger, T. 2015, *A&A*, **584**, A17
- Prvák, M., Krtićka, J., & Korhonen, H. 2020, *MNRAS*, **492**, 1834
- Putney, A., & Jordan, S. 1995, *ApJ*, **449**, 863
- Quirion, P. O., Fontaine, G., & Brassard, P. 2007, *ApJS*, **171**, 219
- Rauch, T., & Deetjen, J. L. 2003, in *Stellar Atmosphere Modeling*, eds. I. Hubeny, D. Mihalas, & K. Werner, *ASP Conf. Ser.*, **288**, 103
- Rauch, T., Werner, K., Biémont, É., Quinet, P., & Kruk, J. W. 2012, *A&A*, **546**, A55
- Rauch, T., Werner, K., Quinet, P., & Kruk, J. W. 2014a, *A&A*, **566**, A10
- Rauch, T., Werner, K., Quinet, P., & Kruk, J. W. 2014b, *A&A*, **564**, A41
- Rauch, T., Werner, K., Quinet, P., & Kruk, J. W. 2015a, *A&A*, **577**, A6
- Rauch, T., Hoyer, D., Quinet, P., Gallardo, M., & Raineri, M. 2015b, *A&A*, **577**, A88
- Rauch, T., Quinet, P., Hoyer, D., et al. 2016, *A&A*, **587**, A39
- Rauch, T., Gamrath, S., Quinet, P., et al. 2017a, *A&A*, **599**, A142
- Rauch, T., Quinet, P., Knörzner, M., et al. 2017b, *A&A*, **606**, A105
- Rebassa-Mansergas, A., Gänsicke, B. T., Schreiber, M. R., Koester, D., & Rodríguez-Gil, P. 2010, *MNRAS*, **402**, 620
- Reif, K., Bagschik, K., de Boer, K. S., et al. 1999, in *Sensors, Cameras, and Systems for Scientific/Industrial Applications*, eds. M. M. Blouke, & G. M. Williams, *SPIE Conf. Ser.*, **3649**, 109
- Reindl, N., Rauch, T., Werner, K., et al. 2014, *A&A*, **572**, A117
- Reindl, N., Geier, S., Kupfer, T., et al. 2016, *A&A*, **587**, A101
- Reindl, N., Geier, S., & Østensen, R. H. 2018, *MNRAS*, **480**, 1211
- Reindl, N., Bainbridge, M., Przybilla, N., et al. 2019, *MNRAS*, **482**, L93
- Renedo, I., Althaus, L. G., Miller Bertolami, M. M., et al. 2010, *ApJ*, **717**, 183
- Schafferoth, V., Casewell, S. L., Schneider, D., et al. 2021, *MNRAS*, **501**, 3847
- Schlafly, E. F., & Finkbeiner, D. P. 2011, *ApJ*, **737**, 103
- Schmidt, G. D., Liebert, J., Harris, H. C., Dahn, C. C., & Leggett, S. K. 1999, *ApJ*, **512**, 916
- Schreiber, M. R., Gänsicke, B. T., Toloza, O., Hernandez, M.-S., & Lagos, F. 2019, *ApJ*, **887**, L4
- Shimansky, V., Sakhbullin, N. A., Bikmaev, I., et al. 2006, *A&A*, **456**, 1069
- Shimansky, V. V., Borisov, N. V., Nurdinova, D. N., et al. 2015, *Astron. Rep.*, **59**, 199
- Sion, E. M., Holberg, J. B., Oswalt, T. D., et al. 2014, *AJ*, **147**, 129
- Ter Braak, C. J. F. 2006, *Stat. Comput.*, **16**, 239
- Tonry, J. L., Denneau, L., Heinze, A. N., et al. 2018, *PASP*, **130**
- Tremblay, P. E., Cukanovaite, E., Gentile Fusillo, N. P., Cunningham, T., & Hollands, M. A. 2019, *MNRAS*, **482**, 5222
- Unglaub, K., & Bues, I. 2000, *A&A*, **359**, 1042
- Vanderburg, A., & Johnson, J. A. 2014, *PASP*, **126**, 948
- Wade, G. A., & Neiner, C. 2018, *Contrib. Astron. Obs. Skaln. Pleso*, **48**, 106
- Werner, K. 1996, *ApJ*, **457**, L39
- Werner, K., & Herwig, F. 2006, *PASP*, **118**, 183
- Werner, K., & Rauch, T. 2015, *A&A*, **584**, A19
- Werner, K., Dreizler, S., Heber, U., et al. 1995, *A&A*, **293**, L75
- Werner, K., Deetjen, J. L., Dreizler, S., et al. 2003, in *Stellar Atmosphere Modeling*, eds. I. Hubeny, D. Mihalas, & K. Werner, *ASP Conf. Ser.*, **288**, 31
- Werner, K., Rauch, T., Napiwotzki, R., et al. 2004, *A&A*, **424**, 657
- Werner, K., Dreizler, S., & Rauch, T. 2012, *Astrophys. Source Code Libr. [record ascl:1212.015]*
- Werner, K., Rauch, T., & Kepler, S. O. 2014, *A&A*, **564**, A53
- Werner, K., Rauch, T., & Kruk, J. W. 2018a, *A&A*, **616**, A73
- Werner, K., Rauch, T., & Kruk, J. W. 2018b, *A&A*, **609**, A107
- Werner, K., Rauch, T., & Reindl, N. 2019, *MNRAS*, **483**, 5291
- Zechmeister, M., & Kürster, M. 2009, *A&A*, **496**, 577

Appendix A: Additional tables

Table A.1. Periods, mean magnitudes, and amplitudes as derived from various light curves for all periodically variable UHE white dwarfs.

Name	Band	Data points	Magnitude [mag]	P [d]	Amplitude [mag]	Comment
J0032+1604	CSS	335	15.71	0.907846 ± 0.000090	0.05	DOZ UHE
	ATLAS- <i>c</i>	119	15.73	0.907871 ± 0.000080	0.07	
WD 0101–182	CSS	154	15.83	2.323148 ± 0.000107	0.18	DOZ UHE
	ATLAS- <i>c</i>	166	15.72	2.323235 ± 0.000140	0.19	
J0146+3236	ATLAS- <i>o</i>	170	16.17	2.323285 ± 0.000219	0.19	DO UHE
	TESS	15985		2.322138 ± 0.001939		
	CSS	333	15.59	0.242037 ± 0.000002	0.18	
	ATLAS- <i>c</i>	123	15.54	0.242035 ± 0.000003	0.17	
	ATLAS- <i>o</i>	124	16.01	0.242036 ± 0.000003	0.16	
	ZTF- <i>g</i>	222	15.37	0.242038 ± 0.000001	0.18	
	ZTF- <i>r</i>	279	15.91	0.242037 ± 0.000001	0.16	
HS 0158+2335	ZTF- <i>i</i>	22	16.37	0.242057 ± 0.000029	0.17	DO UHE
	TESS	12936		0.242037 ± 0.000010		
	CSS	332	16.83	0.449773 ± 0.000005	0.17	
	ATLAS- <i>c</i>	105	16.91	0.449817 ± 0.000035	0.22	
	ZTF- <i>g</i>	206	16.79	0.449776 ± 0.000004	0.24	
	ZTF- <i>r</i>	236	17.23	0.449783 ± 0.000005	0.21	
J0254+0058	TESS	12891		0.449767 ± 0.000471		DO UHE
	CSS	336	17.39	1.087163 ± 0.000021	0.26	
	ATLAS- <i>c</i>	114	17.39	1.087221 ± 0.000074	0.28	
	ZTF- <i>g</i>	250	17.25	1.087160 ± 0.000015	0.30	
	ZTF- <i>r</i>	263	17.73	1.087168 ± 0.000027	0.30	
	SDSS- <i>u</i>	72	16.73	1.087148 ± 0.000006	0.26	
	SDSS- <i>g</i>	72	17.15	1.087145 ± 0.000002	0.27	
	SDSS- <i>r</i>	73	17.67	1.087153 ± 0.000007	0.26	
	SDSS- <i>i</i>	72	18.03	1.087147 ± 0.000005	0.29	
	SDSS- <i>z</i>	70	18.35	1.087169 ± 0.000021	0.28	
HS 0713+3958	TESS	15746		1.089108 ± 0.001332		DO UHE
	CSS	434	16.61	0.782390 ± 0.000017	0.09	
	ATLAS- <i>c</i>	188	16.52	0.782404 ± 0.000070	0.08	
	ATLAS- <i>o</i>	199	16.93	0.782537 ± 0.000447	0.08	
	ZTF- <i>g</i>	173	16.34	0.782351 ± 0.000023	0.11	
	ZTF- <i>r</i>	193	16.89	0.782370 ± 0.000023	0.09	
HS 0727+6003	TESS	33045		0.782594 ± 0.001509		DO UHE
	CSS	184	16.15	0.221410 ± 0.000002	0.13	
	ATLAS- <i>c</i>	121	16.08	0.221410 ± 0.000003	0.13	
	ATLAS- <i>o</i>	135	16.51	0.221411 ± 0.000060	0.14	
	ZTF- <i>g</i>	202	15.90	0.221412 ± 0.000002	0.13	
	ZTF- <i>r</i>	231	16.42	0.221409 ± 0.000001	0.13	
	BUSCA- <i>U</i>	399		0.221399 ± 0.000003	0.128	
	BUSCA- <i>B</i>	495		0.221396 ± 0.000010	0.131	
	BUSCA- <i>R</i>	493		0.221438 ± 0.000015	0.128	
J1059+4043	TESS	17632		0.221453 ± 0.000039		DOZ UHE
	ZTF- <i>g</i>	238	18.09	1.410591 ± 0.000151	0.08	
J1215+1203	ZTF- <i>r</i>	229	18.68	1.410589 ± 0.000154	0.07	DOZ UHE
	CSS	441	18.20	0.601307 ± 0.000011	0.14	
J1257+4220	ZTF- <i>g</i>	158	17.93	0.601319 ± 0.000014	0.14	DA UHE
	ZTF- <i>r</i>	173	18.51	0.601296 ± 0.000035	0.10	
	ATLAS- <i>c</i>	123	17.40	0.428993 ± 0.000016	0.18	
HS 2027+0651	ZTF- <i>g</i>	287	17.24	0.428996 ± 0.000006	0.13	DO UHE
	ZTF- <i>r</i>	307	17.78	0.428993 ± 0.000009	0.11	
	ZTF- <i>g</i>	84	16.48	0.290784 ± 0.000005	0.06	
HS 2115+1148	ZTF- <i>r</i>	119	16.93	0.290782 ± 0.000007	0.05	DAO UHE
	ZTF- <i>r</i>	157	16.78	1.319665 ± 0.000263	0.02	

Table A.2. Periods, mean magnitudes, and amplitudes as derived from various light curves for all periodically variable white dwarfs showing only the He II line problem.

Name	Band	Data points	Magnitude [mag]	P [d]	Amplitude [mag]	Comment
J0821+1739	CSS	275	19.14	0.384835 ± 0.000084	0.13	DOZ UHE:
	K2	2478	19.32	0.384878 ± 0.000006		
J1029+2540	CSS	470	17.11	0.282933 ± 0.000016	0.04	DO UHE:
	ZTF- <i>g</i>	130	16.85	0.282932 ± 0.000007	0.05	
	ZTF- <i>r</i>	144	17.39	0.282926 ± 0.000011	0.04	
HE 1314+0018	TESS	13449		0.524170 ± 0.001505		DOZ
J1512+0651	ZTF- <i>r</i>	119	17.56	0.226022 ± 0.000010	0.06	
HS 1517+7403	ZTF- <i>g</i>	259	16.42	1.091158 ± 0.000057	0.05	DOZ
	ZTF- <i>r</i>	237	16.97	1.091142 ± 0.000011	0.04	DO
	TESS	94063		1.091338 ± 0.000278		DOZ
J1553+4832	ZTF- <i>g</i>	1203	18.42	2.928482 ± 0.000462	0.05	DO
	ZTF- <i>r</i>	1261	18.97	2.928408 ± 0.000990	0.04	

Table A.3. Periods, mean magnitudes, and amplitudes as derived from ZTF DR4 light curves for all periodically variable normal hot white dwarfs.

Name	Band	Data points	Magnitude [mag]	P [d]	Amplitude [mag]	Comment
KUV 07523+4017	ZTF- <i>g</i>	294	17.62	0.866092 ± 0.000087	0.05	DOZ (PG 1159)
KUV 07523+4017	ZTF- <i>r</i>	443	18.12	0.866169 ± 0.000098	0.06	
WD J012828.99+385436.63	ZTF- <i>g</i>	154	15.75	5.008217 ± 0.001885	0.06	DA
WD J012828.99+385436.63	ZTF- <i>r</i>	192	16.24	5.006654 ± 0.002163	0.05	
WD J031858.29+002325.66	ZTF- <i>g</i>	106	18.44	3.527273 ± 0.001443	0.10	DA
WD J055924.87+104140.41	ZTF- <i>r</i>	244	17.49	0.570768 ± 0.000058	0.06	DA (PN WeDe 1)
WD J095125.94+530930.72	ZTF- <i>g</i>	222	15.03	3.452674 ± 0.000244	0.20	DA
WD J095125.94+530930.72	ZTF- <i>r</i>	450	15.58	3.452675 ± 0.000155	0.20	
WD J112954.78+510000.26	ZTF- <i>g</i>	242	17.52	2.895375 ± 0.000366	0.10	DA
WD J112954.78+510000.26	ZTF- <i>r</i>	240	18.04	2.895613 ± 0.000691	0.09	
WD J113905.98+663018.30	ZTF- <i>g</i>	330	13.64	0.835974 ± 0.000008	0.18	DAO+K7V
WD J113905.98+663018.30	ZTF- <i>r</i>	290	13.59	0.835952 ± 0.000005	0.26	
WD J161613.10+252012.68	ZTF- <i>g</i>	138	17.87	0.389031 ± 0.000009	0.09	DA
WD J161613.10+252012.68	ZTF- <i>r</i>	154	18.32	0.279841 ± 0.000009	0.07	
WD J162449.00+321702.00	ZTF- <i>r</i>	559	16.26	1.095514 ± 0.000069	0.03	DA+dM

Appendix B: Additional figures

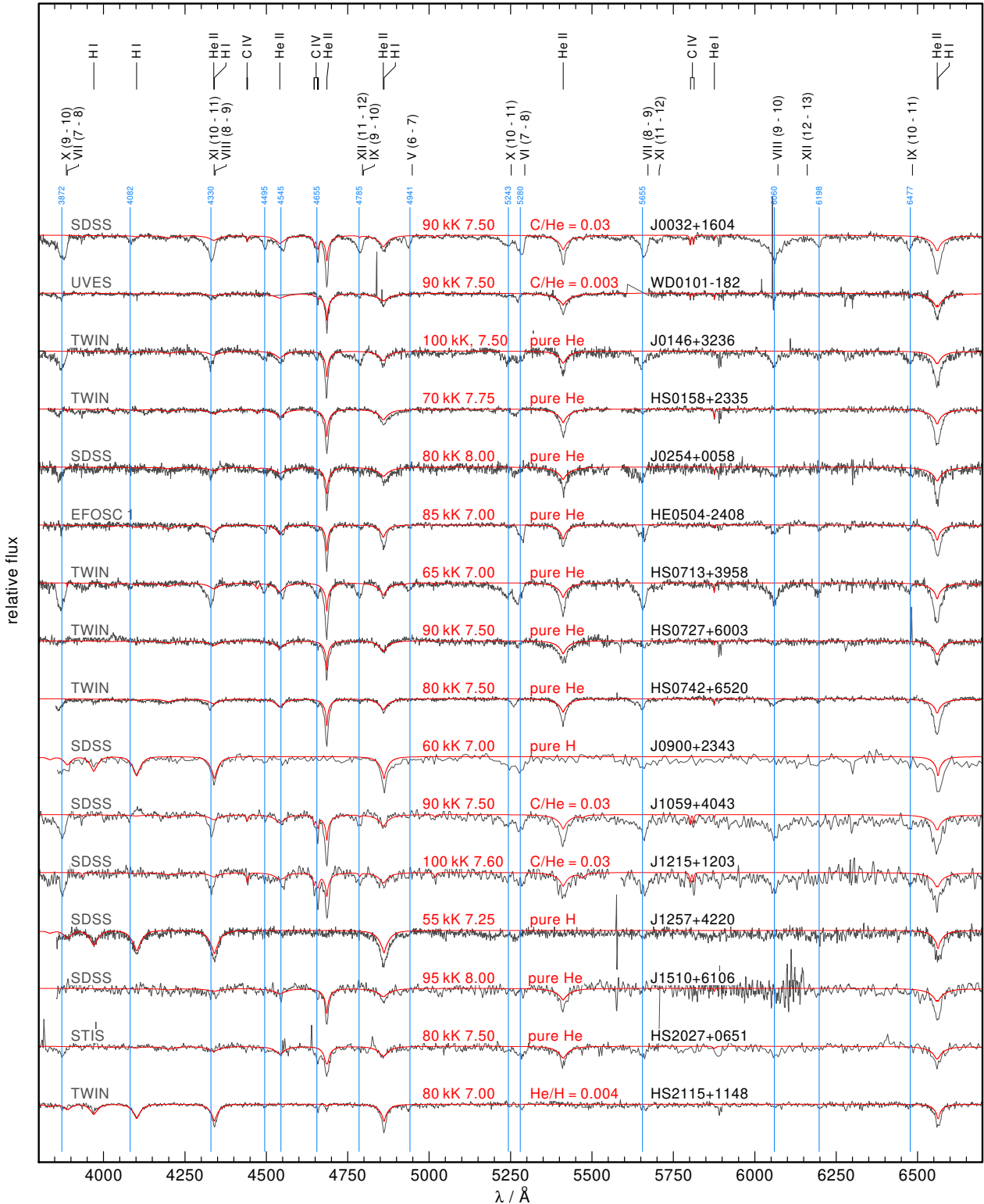


Fig. B.1. Spectra of all known UHE white dwarfs. The positions of photospheric lines (H I, He I, He II and C IV), α and β transitions between Rydberg states ($n - n'$) of the ionization stages V–X, and approximate line positions of the UHE features (blue) are marked. Overplotted in red are TMAP models and the effective temperatures, surface gravities, and chemical compositions (in mass fractions) as determined in previous works (see footnote of Table 1) or in the present study. The spectrograph used for the observation is indicated in gray.

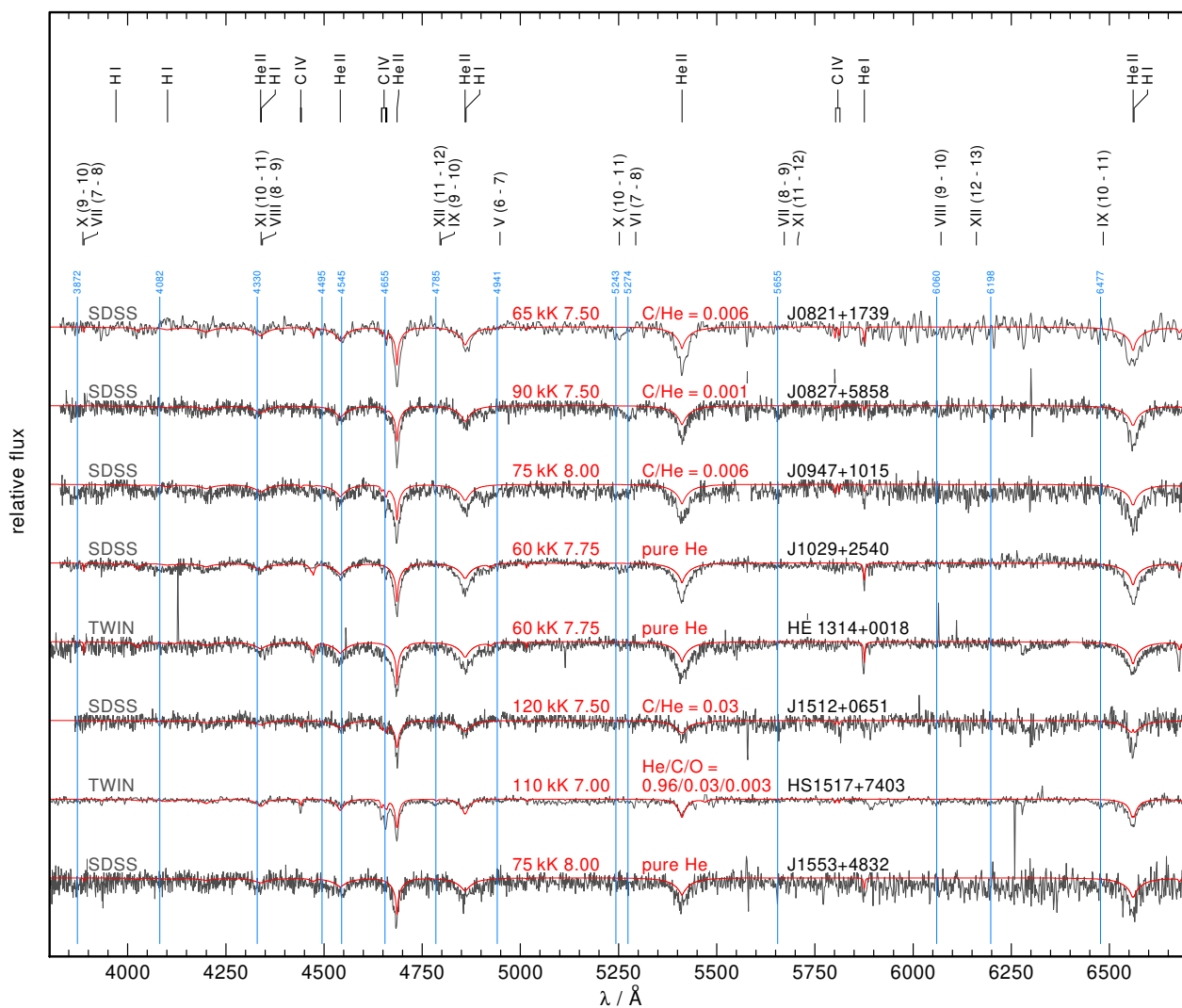


Fig. B.2. As in Fig. B.1 but for all known white dwarfs showing only the He II line problem but no UHE lines.

An in-depth reanalysis of the alleged type Ia supernova progenitor Henize 2–428

N. Reindl¹, V. Schaffenroth¹, M. M. Miller Bertolami^{2,3}, S. Geier¹, N. L. Finch⁴, M. A. Barstow⁴,
S. L. Casewell⁴, and S. Taubenberger⁵

¹ Institute for Physics and Astronomy, University of Potsdam, Karl-Liebknecht-Str. 24/25, 14476 Potsdam, Germany
e-mail: nreindl1885@gmail.com

² Instituto de Astrofísica de La Plata, UNLP-CONICET, La Plata 1900, Buenos Aires, Argentina

³ Facultad de Ciencias Astronómicas y Geofísicas, UNLP, Buenos Aires, Argentina Paseo del Bosque s/n, FWA, 1900 La Plata, Buenos Aires, Argentina

⁴ Department of Physics and Astronomy, University of Leicester, University Road, Leicester LE1 7RH, UK

⁵ Max Planck Institut für Astrophysik, Karl-Schwarzschild-Straße 1, 85748 Garching, Germany

Received 7 April 2020 / Accepted 14 May 2020

ABSTRACT

Context. The nucleus of the planetary nebula Hen 2–428 is a short orbital-period (4.2 h), double-lined spectroscopic binary, whose status as a potential supernova type Ia progenitor has raised some controversy in the literature.

Aims. With the aim of resolving this debate, we carried out an in-depth reanalysis of the system.

Methods. Our approach combines a refined wavelength calibration, thorough line-identifications, improved radial-velocity measurements, non-LTE spectral modeling, as well as multi-band light-curve fitting. Our results are then discussed in view of state-of-the-art stellar evolutionary models.

Results. Besides systematic zero-point shifts in the wavelength calibration of the OSIRIS spectra which were also used in the previous analysis of the system, we found that the spectra are contaminated with diffuse interstellar bands. Our Voigt-profile radial velocity fitting method, which considers the additional absorption of these diffuse interstellar bands, reveals significantly lower masses ($M_1 = 0.66 \pm 0.11 M_\odot$ and $M_2 = 0.42 \pm 0.07 M_\odot$) than previously reported and a mass ratio that is clearly below unity. Our spectral and light curve analyses lead to consistent results, however, we find higher effective temperatures and smaller radii than previously reported. Moreover, we find that the red-excess that was reported before to prove to be a mere artifact of an outdated reddening law that was applied.

Conclusions. Our work shows that blends of He II $\lambda 5412 \text{ \AA}$ with diffuse interstellar bands have led to an overestimation of the previously reported dynamical masses of Hen 2–428. The merging event of Hen 2–428 will not be recognised as a supernova type Ia, but most likely leads to the formation of a H-deficient star. We suggest that the system was formed via a first stable mass transfer episode, followed by common envelope evolution, and it is now composed of a post-early asymptotic giant branch star and a reheated He-core white dwarf.

Key words. stars: individual: Hen 2–428 – binaries: spectroscopic – binaries: close – ISM: lines and bands

1. Introduction

The detection and analysis of compact binary systems is fundamental to various areas of astrophysics (Jones 2020). Binary interactions are thought to play a key role in the shaping of planetary nebulae (PNe, De Marco et al. 2009; Jones 2019) and are needed to explain the formation of diverse objects, such as hot sub-dwarf stars, extremely low mass white dwarfs (Paczynski 1976; Webbink 1984; Iben & Tutukov 1986), or post-red giant branch (RGB) central stars of planetary nebulae (CSPNe, Hall et al. 2013; Hillwig et al. 2017). Compact binaries are crucial to understand common envelope (CE) evolution and they serve as important tests for general relativity as very close binary systems (periods of less than a few hours) emit considerable amounts of gravitational radiation (Weisberg & Taylor 2005; Burdge et al. 2019).

The emission of gravitational waves in very close white dwarf binary systems leads to a shrinkage of their orbits resulting in mass transfer between the white dwarfs or even the merger of the white dwarfs. The ultimate fate of these systems depends on their total mass as well as the mass ratio, $q = M_2/M_1$,

and whether mass transfer remains dynamically stable or not (Shen 2015). The outcomes of such interaction have been proposed to lead to the formation of exotic objects showing He-dominated atmospheres such as R Coronae Borealis stars (RCB), extreme helium (EHe) stars, He-rich hot subdwarf O (He-sdO) stars, or O(He) stars (Webbink 1984; Iben & Tutukov 1984; Saio & Jeffery 2002; Justham et al. 2011; Zhang & Jeffery 2012a,b; Zhang et al. 2014; Reindl et al. 2014a). Also stars with C/O-dominated atmospheres such as the very hot white dwarfs H1504+65 and RXJ0439.8–6809 (Werner & Rauch 2015), WO-type central stars (Gvaramadze et al. 2019), or hot DQ white dwarfs (Kawka et al. 2020) have been proposed to be the outcome of such mergers.

For sufficiently high mass progenitors the merger of the two white dwarfs can also lead to Type Ia supernovae (SN Ia) or faint thermonuclear supernovae (SN.Ia), which reach only one-tenth of the brightness of a SN Ia. This may occur via the so-called double-degenerate channel in which the resulting merger has a mass near the Chandrasekhar limit (Iben & Tutukov 1984; Webbink 1984), but various other evolutionary pathways for the double degenerate SN Ia channel have

been proposed for which the progenitor systems may also have sub-Chandrasekhar masses. These include the double-detonation mechanism (Woosley & Weaver 1994; Fink et al. 2007, 2010; Liu et al. 2018; Shen et al. 2018), the violent merger model (Pakmor et al. 2011, 2013; Liu et al. 2016), or the core degenerate channel (Sparks & Stecher 1974; Kashi & Soker 2011).

The detection of progenitor systems for the double-degenerate SN Ia model is extremely challenging as recently demonstrated by Rebassa-Mansergas et al. (2019), who predict an observational probability only of the order 10^{-5} for finding double white dwarf SN Ia progenitors in our Galaxy with current telescopes. Large observational efforts to search for double-degenerate SN Ia progenitor systems amongst double white dwarfs or white dwarf and pre-white dwarf (hot subdwarf) systems (Napiwotzki et al. 2001, 2020; Geier et al. 2011; Breedt et al. 2017) have revealed some progenitor candidates (Maoz et al. 2014), but none of them has been confirmed unambiguously and robustly. The only exception might be the binary system residing in the planetary nebula Hen 2–428, which is subject of this paper.

Hen 2–428 was discovered by Henize (1976) and a first hint of the binarity of its nucleus was suggested by Rodríguez et al. (2001) based on the discovery of a red-excess emission. The non-ambiguous evidence that Hen 2–428 hosts a binary central star, was only delivered by Santander-García et al. (2015, hereafter SG+15). They made the stunning discovery that the system is a double-lined spectroscopic binary system composed of two hot pre-white dwarfs. Fitting Gaussian profiles to the double lined and time variable He II $\lambda 5412 \text{ \AA}$ line they found the radial velocity (RV) semi-amplitudes of both stars to be the same ($206 \pm 8 \text{ km s}^{-1}$ and $206 \pm 12 \text{ km s}^{-1}$). In addition, they derived a photometric period of 4.2 h and showed that the light curves can be reproduced assuming an over-contact system seen at an inclination angle of $i = 64.7 \pm 1.4^\circ$. From this they derived dynamical masses of $0.88 \pm 0.13 M_\odot$ for both stars, and concluded that the system is composed of two hot pre-white dwarfs with a combined mass higher than the Chandrasekhar limit which will merge within 700 million years triggering a SN Ia.

This scenario has since been challenged by García-Berro et al. (2016), who criticized the strong mismatch between the luminosities and radii of both pre-white dwarf components as derived by SG+15 with the predictions from single-star stellar evolution models (Bloeker & Schoenberner 1991; Bloeker 1993; Renedo et al. 2010). In addition, García-Berro et al. (2016) suggested that the variable He II $\lambda 5412 \text{ \AA}$ line might instead be a superposition of an absorption line plus an emission line, possibly arising from the nebula, the irradiated photosphere of a close companion, or a stellar wind. Since this would question the dynamical masses derived by SG+15, García-Berro et al. (2016) repeated the light curve fitting and showed that the light curves of Hen 2–428 may also be fitted well by assuming an over-contact binary system that consists of two lower mass (i.e., masses of $0.47 M_\odot$ and $0.48 M_\odot$) stars. Thus, they concluded that the claim that Hen 2–428 provides observational evidence for the double degenerate scenario for SN Ia is premature.

Given the potential importance of Hen 2–428 as a unique laboratory to study the double degenerate merger scenario, it is highly desirable to resolve this debate. This is the goal of this work. The paper is organized as follows. In Sect. 2, we give an overview of the available observations, and provide a detailed description of continuum and line contributions to the spectra (Sect. 2.2). In Sect. 3, we examine the wavelength calibration accuracy and perform an improved RV analysis. After

that we carry out a non-LTE spectral analysis to derive atmospheric parameters (Sect. 4) and perform multi-band light-curve fits (Sect. 5). The dynamical masses are presented in Sect. 6 along with a discussion of the evolutionary status of the system. We summarize and present our conclusions in Sect. 7.

2. Observations

2.1. Photometry

SG+15 obtained time-resolved *i*-band (effective wavelength $0.44 \mu\text{m}$) photometry with the MERcator Optical Photometric ImagEr (MEROPE, Davignon et al. 2004) on the Mercator telescope on La Palma on 28 and 30 August 2009, and on 2 September 2009. Another *i*-band time-series was obtained by them on 2 August 2013 with the Wide Field Camera at the 2.5m Isaac Newton Telescope (INT) as well as a Johnson *B*-band (effective wavelength $0.78 \mu\text{m}$) time-series with the South African Astronomical Observatory (SAAO) 1 m telescope on 11 July 2013. In addition, we acquired Asteroid Terrestrial-impact Last Alert System (ATLAS, Tonry et al. 2018) *c*- and *o*-band light curves (effective wavelengths $0.53 \mu\text{m}$ and $0.68 \mu\text{m}$, respectively) of Hen 2–428.

2.2. Spectroscopy

Low-resolution spectroscopy of Hen 2–428 was obtained by Rodríguez et al. (2001) using the Intermediate Dispersion Spectrograph (IDS) at the INT. These observations have a spectral resolution of $\approx 8 \text{ \AA}$ and cover the wavelength range of 3500–9000 \AA .

SG+15 obtained four observations with the FOCal Reducer/low dispersion Spectrograph 2 (FORs2) mounted on the Unit Telescope 1 (UT1) of the ESO Very Large Telescope (VLT) array (ProgIDs: 085.D-0629(A), 089.D-0453(A)). The observations were obtained in 2010 and 2012 using the 1200G grism (spectral resolution of $\approx 3 \text{ \AA}$, resolving power $R = 1605$). We downloaded these observations from the ESO archive and reduced them using standard IRAF procedures.

The most useful set of observations (15 exposures in total, Table 1) was obtained at the Gran Telescopio Canarias (GTC) using the Optical System for Imaging and low Resolution Integrated Spectroscopy (OSIRIS) with the R2000B grating (ProgID: GTC41-13A). The spectra ($R = 2165$) with a mean exposure time of 868 s cover the full orbital period of the system and were used by SG+15 to derive the RV curves of the system. The signal-to-noise ratio (S/N) of these observations is similar to the ones of the FORs2 observations (≈ 70 at 4600 \AA), but they have a higher resolution (2 \AA instead of 3 \AA). We downloaded the OSIRIS observations that were reduced by SG+15 from the GTC Public Archive.

Additionally, we obtained observations using the UV-Visual high-resolution Echelle Spectrograph (UVES) mounted at the 8.2 m Kueyen (UT2) telescope (ProgID: 295.D-5032(A)). The poor signal to noise ($S/N \approx 5$) of these spectra, however, does not allow the identification of photospheric lines, thus we discarded these observations from our analysis of the central stars.

The spectra of Hen 2–428 are a complex superposition of nebular, photospheric, interstellar, and circumstellar contributions. The continuum flux is noticeably affected by interstellar and circumstellar reddening and – as claimed by Rodríguez et al. (2001) – possibly by a late type companion that causes a red-excess. For the further analysis it is crucial to first disentangle and check these various contributions.

Table 1. OSIRIS observations of Hen 2–428.

Nr.	ID	HJD _{middle}	t_{exp} [s]	H δ [km s ⁻¹]	H γ [km s ⁻¹]	H β [km s ⁻¹]	H δ, γ, β [km s ⁻¹]
#1	0000411146	2456516.44874	868	65 ± 3	65 ± 1	69 ± 1	66 ± 1
#2	0000411147	2456516.45964	868	67 ± 5	67 ± 2	69 ± 2	68 ± 6
#3	0000411148	2456516.47053	868	62 ± 6	62 ± 2	65 ± 1	63 ± 2
#4	0000411149	2456516.48142	868	56 ± 2	55 ± 2	59 ± 2	56 ± 4
#5	0000411150	2456516.49231	868	53 ± 3	54 ± 1	58 ± 2	55 ± 5
#6	0000411152	2456516.52202	650	34 ± 2	35 ± 1	42 ± 2	37 ± 5
#7	0000411161	2456516.55371	868	30 ± 3	33 ± 1	39 ± 4	34 ± 4
#8	0000411162	2456516.56460	868	28 ± 2	28 ± 2	35 ± 2	30 ± 2
#9	0000411163	2456516.57549	868	29 ± 3	28 ± 3	36 ± 2	31 ± 5
#10	0000411164	2456516.58638	868	17 ± 2	17 ± 3	23 ± 2	19 ± 6
#11	0000411165	2456516.59728	868	14 ± 3	14 ± 3	20 ± 2	16 ± 5
#12	0000411166	2456516.60817	868	12 ± 3	11 ± 4	20 ± 4	14 ± 6
#13	0000411167	2456516.61906	868	20 ± 2	17 ± 3	21 ± 2	19 ± 4
#14	0000411168	2456516.62995	868	20 ± 3	16 ± 2	20 ± 1	19 ± 5
#15	0000411169	2456516.64084	868	24 ± 3	20 ± 2	22 ± 3	22 ± 5

Notes. The Heliocentric Julian Day at middle of the exposure, exposure times, and RVs as measured from the different Balmer lines (indicating the drift of the zero-point in course of the observing run) are listed.

2.2.1. Nebular contributions

The nebula only contributes a negligible fraction to the continuum flux, for instance [Rodríguez et al. \(2001\)](#) estimated that the strongest source of nebular continuum (the recombination continuum of H I) may only account for a few percent to the total flux in the optical. Much more prominent are the nebular emission lines, which are labeled in black in Fig. 1 where we show the coadded OSIRIS spectrum.

For the nebular line identifications we made use of the nebular line list for Hen 2–428 provided in [Rodríguez et al. \(2001\)](#), published line lists of other PNe ([Zhang et al. 2012](#); [Corradi et al. 2015](#)), as well as The Atomic Line List v2.05b21¹ ([van Hoof 2018](#)). Thanks to the higher resolution of the OSIRIS spectra compared to the IDS spectra used in the nebular analysis by [Rodríguez et al. \(2001\)](#), we found in addition also collisionally excited lines of [Cl III], [Ar I], [Ar IV], [Fe I], [Fe II], and [Fe III] as well as optical recombination lines of N III and O II. The latter could be blended with photospheric lines, but since they do not vary over the orbital period, we conclude that these lines mainly originate from the nebula.

With regard to the concept of [García-Berro et al. \(2016\)](#), that the small reversals in the cores of the He II lines might originate from nebular emission lines, we note that in this case the nebular line flux of He II $\lambda 4686 \text{ \AA}$ should be about one order of magnitude higher than that of the remaining He II lines (e.g., [Zhang et al. 2012](#)). In addition, it was already reported by [Tylenda et al. \(1994\)](#) and SG+15 that Hen 2–428 does not show the He II $\lambda 4686 \text{ \AA}$ nebular line. Therefore, the presence of the He II $\lambda \lambda 4200, 4542, 5412 \text{ \AA}$ nebular lines, which are much weaker, can be excluded as well. We also note that no He II emission lines can be detected in the UVES observations.

2.2.2. Photospheric contributions

The spectra show photospheric absorption lines of H I $\lambda \lambda 4102, 4340, 4861 \text{ \AA}$ which are blended with photospheric absorption lines of He II $\lambda \lambda 4100, 4339, 4859 \text{ \AA}$, as well as He I $\lambda \lambda 4026, 4388, 4472, 4922 \text{ \AA}$ (marked in red in Fig. 1,

¹ <https://www.pa.uky.edu/~peter/newpage/>

He I $\lambda \lambda 4026 \text{ \AA}$ is blended with the weaker He II $\lambda \lambda 4026 \text{ \AA}$). All of these lines are blended with nebular lines, i.e. they show photospheric absorption wings, while the line cores exhibit either H I or He I nebular emission lines. The only photospheric lines, which are not blended with nebular lines are He II $\lambda \lambda 4200, 4542, 4686, 5412 \text{ \AA}$ (marked in magenta in Fig. 1).

We also would like to comment here on the idea of [García-Berro et al. \(2016\)](#) that the He II $\lambda 5412 \text{ \AA}$ line might be a superposition of a single absorption line plus an emission line. Compared to synthetic spectra for hot (pre-)white dwarfs, all He II lines in the spectra of Hen 2–428 are at the same time unusually broad and deep. This could, in principle, be explained by a pure He atmosphere of a very fast rotating star. However, then the observed absorption wings of the Balmer lines should be much weaker. Thus, we conclude that the He II lines are indeed double-lined and stem from the photospheres of the two hot stars as reported by SG+15. This is also perfectly supported by the RV analysis (Sect. 3).

The fluxes of the two hot stars constitute the dominant contribution to the continuum flux, whose shape is, however, altered by reddening which we will discuss in the next section.

2.2.3. Interstellar and circumstellar contributions

The determination of the reddening of the observations is important to investigate the nature of the claimed red-excess by [Rodríguez et al. \(2001\)](#), which could have a noticeable impact on the RV, light curve, and spectral analysis. This is because a cool companion might leave behind spectral features contaminating the spectrum and add an additional continuum light to both the spectroscopic and photometric observations. Furthermore, the knowledge of the reddening is also essential for the distance determination.

We determined the reddening by de-reddening the IDS and OSIRIS observations for different values of E_{B-V} with the reddening law of [Fitzpatrick \(1999\)](#) until a good agreement with our best fit model spectrum (see Sect. 4) was found. In Fig. 2, our best fit model is shown in red, the de-reddened OSIRIS spectrum #2 in gray, and the de-reddened IDS spectrum in black. For the IDS spectrum we find $E_{B-V} = 1.15 \pm 0.05 \text{ mag}$

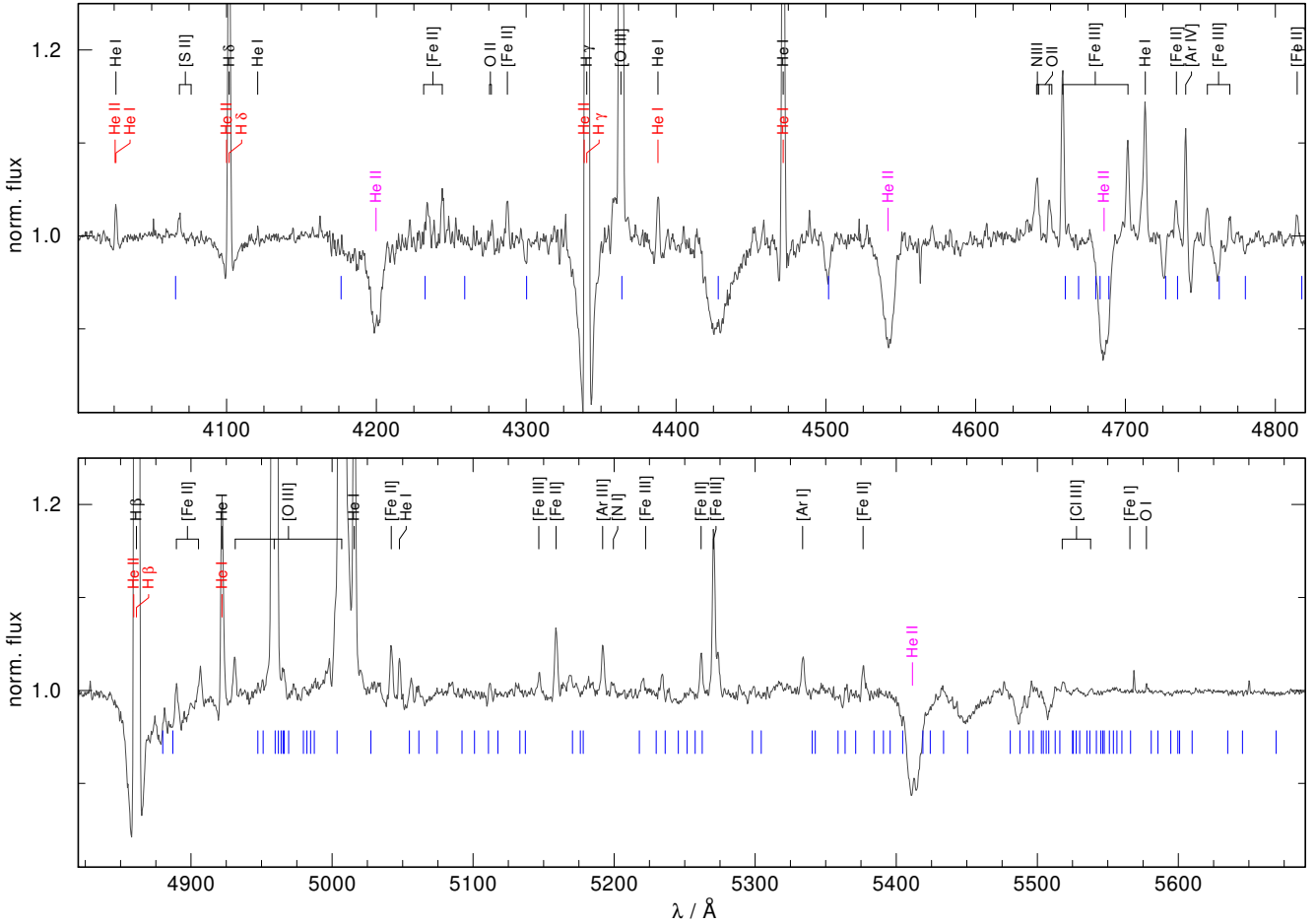


Fig. 1. Co-added and normalized OSIRIS spectrum. The locations of known diffuse interstellar bands (blue), nebular (black), and photospheric lines (red) are marked. Photospheric lines used in for the RV analysis are marked in magenta.

corresponding to $A_V = 3.57 \pm 0.16$ mag (assuming $R_V = 3.1$), while the OSIRS observations suggest a slightly higher value of $E_{B-V} = 1.20 \pm 0.05$ mag. Using the nebula line ratio of $H\alpha/H\beta$ and the reddening law of Cardelli et al. (1989), Rodríguez et al. (2001) found $A_V = 2.96 \pm 0.34$ mag, which is about 20% smaller than the values derived by us².

In Fig. 2 we also show in blue the IDS spectrum de-reddened with the reddening law of Cardelli et al. (1989) instead of the Fitzpatrick (1999) law. This causes a clearly visible depression of the observed flux from 4400 to 5400 Å, which reaches its maximum deviation from the model spectrum around 4900 Å. The Cardelli reddening law is considered as outdated, i.e. based on fits to the location of the blue tip of the stellar locus in various SDSS fields, Schlafly et al. (2010) report that the Fitzpatrick reddening law is clearly favored over Cardelli. We therefore conclude that the red excess claimed by Rodríguez et al. (2001) is merely a consequence of the reddening law used, which makes it appear as if there is an increased continuum emission red-wards of about 5000 Å. This also implies that Hen 2–428 has likely no late-type companion, at least none that is noticeable in the optical wavelength range.

Hen 2–428 is located at a low galactic latitude ($b = 2.48^\circ$) and embedded in the galactic disk, therefore the relatively high extinction towards this source is not surprising. The 3D

Reddening Map of interstellar dust by Lallement et al. (2018)³ extends to 2.63 kpc in the direction of Hen 2–428 (which is close to the distance given by Frew et al. (2016), who derived 2.72 ± 0.86 kpc using the $H\alpha$ surface brightness–radius relation) and predicts $E_{B-V} = 0.81 \pm 0.05$. Thus, about one third of the reddening towards Hen 2–428 might be circumstellar and caused by the compact nebula.

Interstellar and circumstellar contributions, however, do not only leave a noticeable impact the continuum flux. The spectra of Hen 2–428 also exhibit numerous additional absorption lines, which we all identify as absorptions caused by diffuse interstellar bands (DIBs). These absorption features, often seen in highly reddened stars, originate in the interstellar medium (ISM) and are typically broader than expected from the Doppler broadening of turbulent gas motions in the ISM (Jenniskens & Desert 1994). DIBs are widely assumed to be caused by large molecules (e.g., C_{60}^+ Campbell et al. 2015), however, not all DIBs have yet been conclusively identified. In the wavelength range from 4000 to 10 000 Å, there are several classes of molecules considered to be possible DIB absorbers and which may produce a few strong bands along with a much larger array of weaker bands (Hobbs et al. 2008, and references therein).

The blue bars in Fig. 1 mark the locations of DIBs identified in the high-resolution, high S/N spectrum of HD 204827 by Hobbs et al. (2008). We note that due to the lower resolution and lower S/N of the OSIRIS observations, only

² We note that differences up to 50% in E_{B-V} as derived from different spectra or nebula lines have also been noticed in the CSPN SAO 245567 (Arhipova et al. 2013; Reindl et al. 2014b).

³ <https://stilism.obspm.fr/>

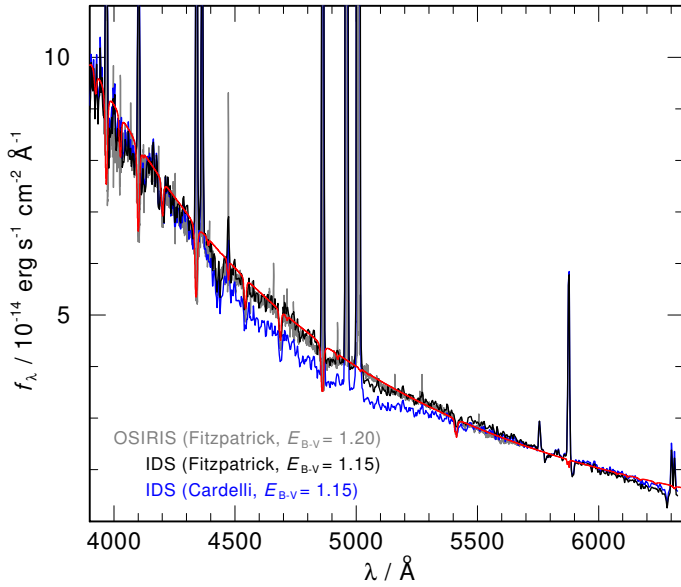


Fig. 2. Determination of the reddening. The OSIRIS spectrum #2 de-redded with the Fitzpatrick reddening law (gray) and the IDS spectrum de-redded once with the Fitzpatrick reddening law (black) and once with the Cardelli reddening law (blue) are compared to our best fit TMAP model (red).

relatively strong DIBs are visible. The strength of the most prominent DIB at 4430 Å resembles the strengths of the photospheric He II lines, but other strong DIBs at 4501.79, 4726.83, 4762.61, 5450.62, 5487.69, 5525.48 Å are clearly visible as well. HD 204827 has a very similar reddening ($E_{B-V} = 1.11$, Hobbs et al. 2008) compared to Hen 2–428 ($E_{B-V} = 1.15$, see above). Since the equivalent width of DIBs is correlated to the value of E_{B-V} (e.g., Kos & Zwitter 2013; Królowski et al. 2019), one can expect that the DIBs in Hen 2–428 are of similar strengths to what is observed in HD 204827. A quite crucial point that now becomes obvious when looking at Fig. 1 is that three of the four He II lines are blended with DIBs. He II $\lambda 4686$ Å and He II $\lambda 5412$ Å are blended with three and four weaker DIBs, respectively. Bluewards (at about 4176 Å) of He II $\lambda 4200$ Å a relatively broad and strong DIB is located, which was first noted by Jenniskens & Desert (1994) in the spectra of HD 30614, HD 21389, HD 190603, and HD 183143. This leaves only the He II $\lambda 4542$ Å line unaffected by DIB absorption.

3. Radial velocity analysis

3.1. Wavelength calibration accuracy of the OSIRIS spectra

The accuracy of the wavelength calibration is a crucial point when determining the RVs of a binary system. We used the nebular lines to check the wavelength calibration of the OSIRIS spectra, as the RVs of these lines should not change over the orbital period and correspond to the system velocity. For that we first measured the RVs of the Balmer emission lines by fitting them with a set of mathematical functions (Gaussians, Lorentzians, and polynomials) using SPAS (Spectrum Plotting and Analysing Suite, Hirsch 2009). The error determination is done by using the bootstrapping method. We find that the line to line variations are small within a single exposure, suggesting an accuracy of the wavelength calibration of 5 km s^{-1} in the wavelength range 4101–4681 Å. However, the RVs of the Balmer lines from the

different exposures show large variations, indicating zero-point shifts of the wavelength calibration up to 54 km s^{-1} (Table 1). Consequently, we corrected each observation for the RV measured by fitting all three Balmer emission lines simultaneously, which leaves us with an artificial system velocity of 0 km s^{-1} .

It is worth mentioning that wavelength calibration exposures for the OSIRIS spectra were taken only in the beginning of the observing run. Therefore, the velocity measured simultaneously from H δ , H γ , and H β from observation #1 ($66 \pm 1 \text{ km s}^{-1}$) should reflect the true system velocity. This value also agrees with the system velocity of $70 \pm 8 \text{ km s}^{-1}$ reported by Rodríguez et al. (2001).

To check the wavelength calibration in the red part of the spectra (i.e., around He II $\lambda 5412$ Å, used by SG+15 to determine the masses), we measured the RVs of the Fe II $\lambda 5376$ Å nebular line (closest nebular line to He II $\lambda 5412$ Å) in the zero-point corrected observations. We found variations up to 68 km s^{-1} in the different spectra. Since those lines are relatively weak, we could not detect them in three of the fifteen observations and we also note that the average uncertainty on the measured RVs of Fe II $\lambda 5376$ Å are 20 km s^{-1} . Therefore, we refrain from applying additional corrections to the spectra and merely state that the wavelength calibration accuracy seems to get worse than 5 km s^{-1} in the red part of the spectrum.

3.2. Radial velocity amplitudes

Since Gaussian line profiles as used by SG+15 only provide a good fit to the line cores of the He II lines but not to their wings, we used Voigt profiles to measure the RVs for both components. Using Python, Voigt profiles were calculated via the Faddeeva function and fitted to the zero-point corrected OSIRIS spectra using the non-linear least squares method of Levenberg-Marquardt (Jones et al. 2001). The semi-amplitudes of the RV curves (K_1 , K_2) were then obtained by sinusoidal fitting of the individual RV measurements obtained for both components of the binary system. The system velocity, γ , the orbital period, P , and the zero point of the RV curve (the latter two within the uncertainties determined from the light curves by SG+15) were allowed to vary, but required to be the same for both stars.

Examples of the Voigt profile fits to the four observed He II lines (gray lines) are shown in Fig. 3, along with the resulting RV curves for each line. The red and blue lines correspond to the absorption lines and RV curves of the primary and secondary, respectively. The purple line indicates the combined fit. The black, dashed line in the RV curve plots indicates the system velocity (remember we applied an artificial system velocity of 0 km s^{-1} based on the HI nebular emission lines, see Sect. 3.1).

First, the RV fitting was performed assuming only two Voigt profiles for each He II feature corresponding to the absorption lines of the two stars. In case of He II $\lambda 4686$ Å and He II $\lambda 5412$ Å we next included additional, fixed Voigt profiles in order to simulate the DIBs (light blue, dashed lines in Fig. 3). The equivalent widths and full widths at half maximum of these DIBs were required to be the same as reported by Hobbs et al. (2008) for HD 204827. The DIB blue-ward of He II $\lambda 4200$ Å, which also blends with this line, is clearly visible in the co-added OSIRIS spectrum (Fig. 3). Therefore, we obtained the Voigt profile for this DIB directly from the co-added OSIRIS spectrum, and used this line profile in each subsequent RV fit.

Neglecting DIBs, we find for He II $\lambda 5412$ Å similar RV amplitudes of $K_1 = 178 \pm 17 \text{ km s}^{-1}$ and $K_2 = 209 \pm 18 \text{ km s}^{-1}$, which is close to the values derived by SG+15 by Gaussian

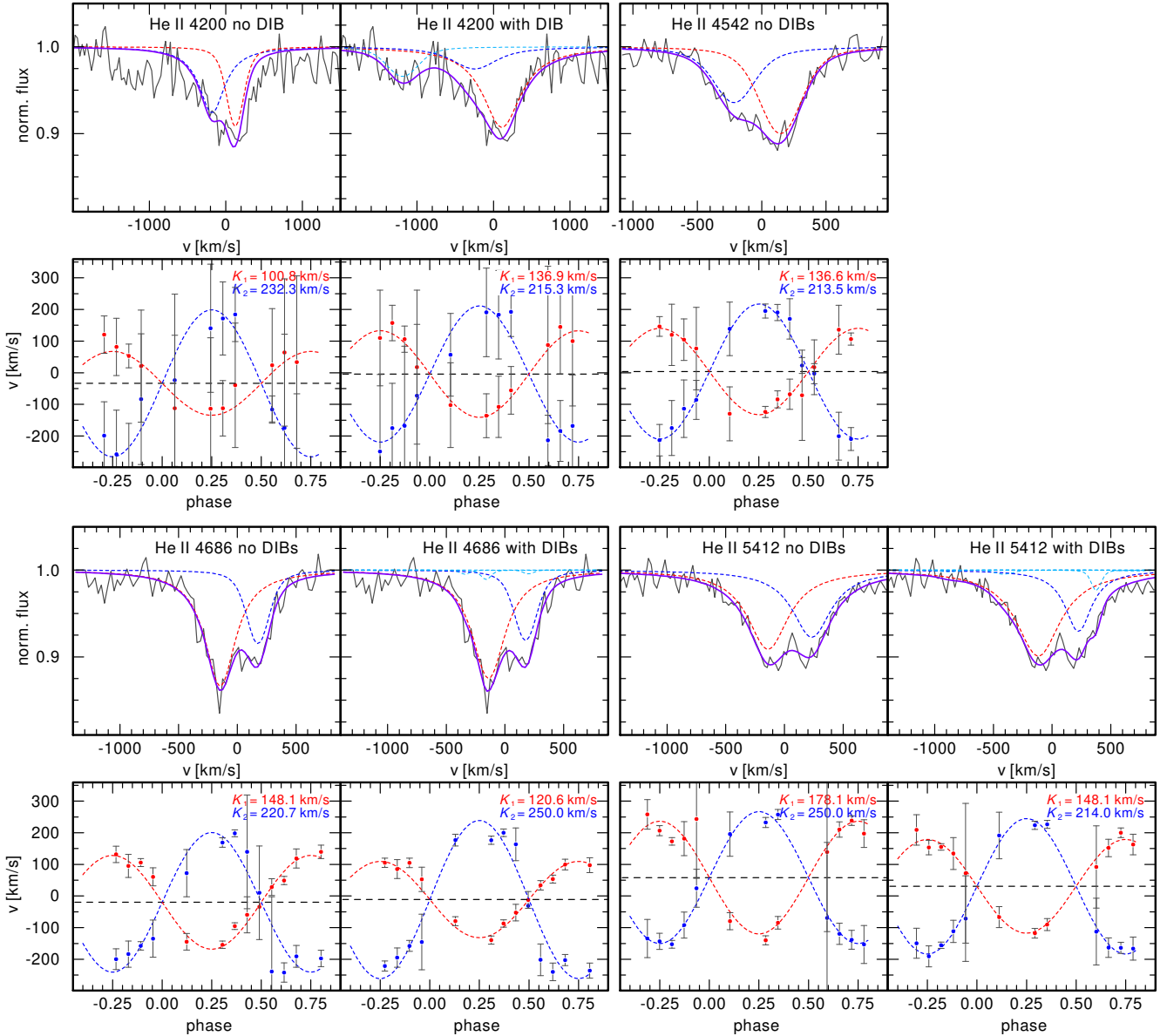


Fig. 3. Examples of Voigt profile fits (blue: secondary, red: primary, light blue: DIBs, purple: combined fit) to the four observed He II lines (gray). *Top panels:* observation #2 taken around phase -0.25 , *bottom panels:* observation #7 taken around phase 0.28 . RV curves (blue: secondary, red: primary) obtained for the respective He II lines with the RV amplitudes are shown below. The black, dashed line in RV curve plots indicates the system velocity.

fitting of the He II $\lambda 5412 \text{ \AA}$ absorption lines ($K_1 = 206 \pm 8 \text{ km s}^{-1}$ and $K_2 = 206 \pm 12 \text{ km s}^{-1}$). We note that we obtain a system velocity much larger than zero ($\gamma = 58 \pm 9 \text{ km s}^{-1}$), indicating already a problematic result. The picture, however, changes noticeably if additional DIB absorption lines are included in the RV fitting process. We then obtain very distinct RV amplitudes of $K_1 = 148 \pm 9 \text{ km s}^{-1}$ and $K_2 = 214 \pm 10 \text{ km s}^{-1}$, i.e. we find that the RV amplitude of the primary star could be 30 km s^{-1} smaller. The value for the system velocity ($\gamma = 31 \pm 5 \text{ km s}^{-1}$) improves, but is still clearly larger than zero. This likely indicates that DIBs in Hen 2–428 are different to HD 204827 and/or that the wavelength calibration in the red part of the spectrum becomes slightly worse (see Sect. 3.1).

For He II $\lambda 4686 \text{ \AA}$ we find two different RV amplitudes ($K_1 = 148 \pm 22 \text{ km s}^{-1}$ and $K_2 = 221 \pm 24 \text{ km s}^{-1}$) even if we neglect the DIBs. Including DIBs in the fitting, the differences become even more noticeable ($K_1 = 121 \pm 18 \text{ km s}^{-1}$

and $K_2 = 250 \pm 21 \text{ km s}^{-1}$). Also in this case, the RV curve fitting suggests system velocities which are smaller than zero ($\gamma = -20 \pm 10 \text{ km s}^{-1}$, when no DIBs are considered, and $\gamma = -11 \pm 9 \text{ km s}^{-1}$, when the DIBs are included). However, the deviation from zero is not as drastic as in the case of He II $\lambda 5412 \text{ \AA}$.

An interesting point to notice is that the line profiles of He II $\lambda 5412 \text{ \AA}$ of both the primary and secondary are very similar if DIBs are neglected. Including DIBs in the fits, the line of the secondary becomes much weaker (see the right hand panel in the second to last row of Fig. 3). For He II $\lambda 4686 \text{ \AA}$ (which is blended with weaker DIBs than He II $\lambda 5412 \text{ \AA}$) and He II $\lambda 4542 \text{ \AA}$ (not blended with any DIB) it is already evident from the observed line profiles, that the line of the secondary must be weaker than the line of the primary.

The RV amplitudes of He II $\lambda 4542 \text{ \AA}$ are of greatest interest as it is the only line not blended with any DIB. For this line we obtain again very different RV amplitudes of

$K_1 = 137 \pm 12 \text{ km s}^{-1}$ for the primary and $K_2 = 214 \pm 14 \text{ km s}^{-1}$ for the secondary. This supports the results from the RV fits of He II $\lambda 4686 \text{ \AA}$ and He II $\lambda 5412 \text{ \AA}$ if DIBs are included. We also stress that in the case of He II $\lambda 4542 \text{ \AA}$, we obtain a system velocity of only $4 \pm 6 \text{ km s}^{-1}$, consistent with zero.

The blue parts of the OSIRIS spectra covering He II $\lambda 4200 \text{ \AA}$ have a lower S/N, resulting in larger uncertainties of the individual RV measurements. If we neglect the absorption of the broad DIB blue-ward of He II $\lambda 4200 \text{ \AA}$, we obtain RV amplitudes of $K_1 = 101 \pm 25 \text{ km s}^{-1}$ and $K_2 = 232 \pm 34 \text{ km s}^{-1}$, and $\gamma = -34 \pm 10 \text{ km s}^{-1}$. If we, however, include our DIB model which we obtained directly from the co-added spectrum (see above), we end up with RV amplitudes of $K_1 = 137 \pm 18 \text{ km s}^{-1}$ and $K_2 = 215 \pm 21 \text{ km s}^{-1}$, confirming the results from He II $\lambda 4542 \text{ \AA}$ surprisingly well. Also in this case we find that the system velocity is very small ($-4 \pm 9 \text{ km s}^{-1}$) and consistent with zero.

In summary, if DIBs are not included in the RV fitting, we end up with conflicting RV semi-amplitudes for the four He II lines. However, when including the DIBs we obtain consistent results. Since our DIB models for He II $\lambda 4686 \text{ \AA}$ and He II $\lambda 5412 \text{ \AA}$ may not be perfect assumptions (as indicated from the non-zero system velocities), the RV amplitudes derived from He II $\lambda 4200 \text{ \AA}$ and He II $\lambda 4542 \text{ \AA}$ should be the ones to rely on. For these lines very distinct RV amplitudes are found as opposed to the findings of SG+15.

4. Atmospheric analysis

For the spectral analysis we restricted ourselves to the OSIRIS observation #2. This is because this observation was taken closest to maximum RV separation and, hence, smearing of the lines due to the orbital motion (i.e., the change of the RV over the duration of the exposure) is only a few km s^{-1} (close to phase 0 and 0.5 the orbital smearing reaches about 78 km s^{-1}). Also in observations #2 none of the four He II lines are contaminated with emission lines. The spectrum was decomposed by subtracting the line profiles obtained from the RV fitting (Sect. 3) for the DIBs and the other star from the observation.

For the model calculations we employed the Tübingen non-LTE model-atmosphere package (TMAP⁴, Werner et al. 2003, 2012; Rauch & Deetjen 2003) which allows plane-parallel, non-LTE, fully metal-line blanketed model atmospheres in radiative and hydrostatic equilibrium to be computed. Model atoms were taken from the Tübingen model atom database TMAD⁵. Metal-free model grids were calculated for six different He abundances ($\log \text{He}/\text{H} = +2, +1, 0, -1, -2,$ and -3 , logarithmic number ratios). Each grid spans from $T_{\text{eff}} = 30\,000\text{--}70\,000 \text{ K}$ (step size 2500 K) and from $\log g = 3.75\text{--}6.0$ (step size 0.25 dex). Models above the Eddington limit (i.e., $T_{\text{eff}} > 60\,000 \text{ K}$ for $\log g = 4.25$, $T_{\text{eff}} > 50\,000 \text{ K}$ for $\log g = 4.00$, and $T_{\text{eff}} > 47\,500 \text{ K}$ for $\log g = 3.75$) were not calculated. To calculate synthetic line profiles, we used Stark line-broadening tables provided by Barnard et al. (1969) for He I $\lambda\lambda 4026, 4388, 4471, 4921 \text{ \AA}$, Barnard et al. (1974) for He I $\lambda 4471 \text{ \AA}$, and Griem (1974) for all other He I lines. For He II, we used the tables provided by Schöning & Butler (1989), and for H I tables provided by Tremblay & Bergeron (2009). For He II 20 levels were considered in non-LTE, for He I 29 levels, and for H I 15 levels.

To derive effective temperatures, surface gravities, and He abundances we fitted simultaneously all four decomposed He II lines of each star. The parameter fit was performed by means of

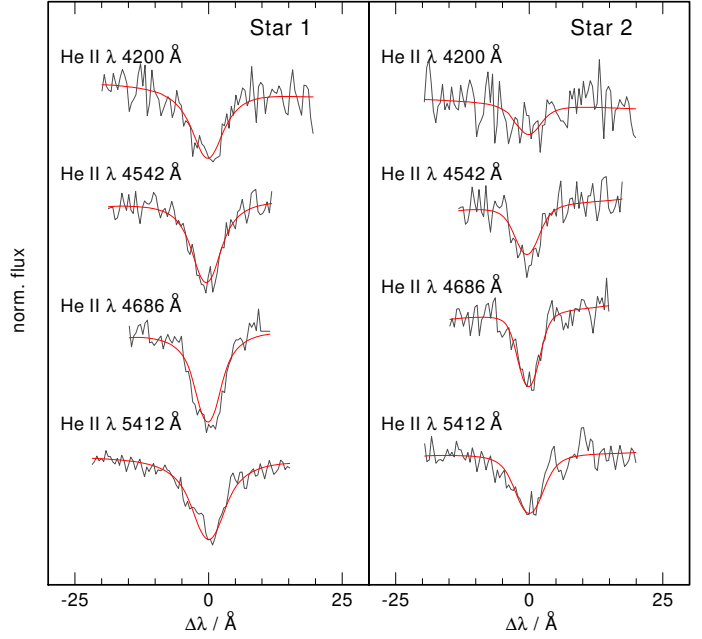


Fig. 4. He II lines of the decomposed OSIRIS spectrum #2 (gray) shown along with the best fit TMAP models (red).

a χ^2 minimization technique with SPAS (Spectrum Plotting and Analysing Suite, Hirsch 2009), which is based on the FITSB2 routine (Napiwotzki 1999). Although we do not expect the system to be fully synchronized shortly after a common envelope event, both stars have likely high rotational velocities. Therefore, we considered the projected rotational velocity $v \sin i$ as a fourth parameter in our fit.

Our initial fit assumes a flux ratio of one, and the effective temperatures, surface gravities, He abundances, and rotational velocities were considered as free parameters. Based on these results we performed light curve fits (Sect. 5) and used the updated flux ratios and rotational velocities (assuming a synchronized system) to repeat the spectral fits. This iterative process was repeated until a good agreement between the results from the light curve fitting and the spectral analysis was obtained. In our final spectroscopic fit we assume a flux ratio of 1.4 and projected rotational velocities of $v \sin i = 156 \text{ km s}^{-1}$ for the primary and $v \sin i = 133 \text{ km s}^{-1}$ for the secondary.

Our best fits to spectrum #2 are shown in Fig. 4 and the results of our analysis are summarized in Table 2. We note that our best fit also reproduces very well the wings of the Balmer and He I lines (Fig. A.1). The effective temperatures ($T_{\text{eff}} = 39\,555 \text{ K}$ and $T_{\text{eff}} = 40\,858 \text{ K}$, for the primary and secondary, respectively) and surface gravities ($\log g = 4.50$ and $\log g = 4.62$) obtained for both stars are found to be very similar and agree well within the error limits with the results from the light curve fitting (see Sect. 5 and Table 2). The He abundance of the primary ($X_{\text{He}} = -0.16 \pm 0.10$, logarithmic mass fraction), which has the stronger lines, is found to be super solar ($X_{\text{He}_\odot} = -0.60$, Asplund et al. 2009), while the secondary has a slightly sub-solar He abundance ($X_{\text{He}} = -1.01 \pm 0.20$).

Our effective temperatures are larger than the ones reported by SG+15, who derived the effective temperatures from light curve fitting. The narrow temperature range (30–40 kK) adopted by SG+15, however, is not valid as already pointed out by García-Berro et al. (2016). SG+15 established the upper limit of 40 kK based on the absence of He II emission lines, but there are many CSPNe with even higher T_{eff} and which also lack

⁴ <http://astro.uni-tuebingen.de/~TMAP>

⁵ <http://astro.uni-tuebingen.de/~TMAD>

Table 2. Orbital and stellar parameters of Hen 2–428. He abundances are given in logarithmic mass fractions.

	Primary	Secondary
P [days] ^(a)	0.1758 ± 0.0005	
γ [km s ⁻¹]	66 ± 1	
$q \equiv M_2/M_1$	$0.64^{+0.25}_{-0.18}$	
i [°]	63.59 ± 0.54	
a [R_\odot]	1.35 ± 0.07	
T_{eff} [K] (Spec.)	39555 ± 3000	40858 ± 4500
T_{eff} [K] (LC)	40179 ± 370	40356 ± 175
$\log g$ (Spec.)	4.50 ± 0.30	4.62 ± 0.30
$\log g$ (LC)	4.69 ± 0.03	4.64 ± 0.04
X_{He}	-0.16 ± 0.10	-1.01 ± 0.20
v_{rot} [km s ⁻¹] ^(b)	174	148
K_{4542} [km s ⁻¹]	136.6 ± 12.0	213.5 ± 13.7
M_{4542} [M_\odot]	0.66 ± 0.11	0.42 ± 0.07
R [mean, R_\odot]	0.603 ± 0.038	0.514 ± 0.033
L [L_\odot]	803 ± 264	665 ± 305

Notes. ^(a)Taken from SG+15. ^(b)Assuming a synchronized system.

He II nebular lines. The difference to our previously reported values for the atmospheric parameters (Finch et al. 2018, 2019; Reindl et al. 2018) is a consequence of the rotational velocity which was neglected in our previous fits, as well as the extended model grid, the avoidance of observations which are noticeably affected by smearing of the lines due to the orbital motion of the system, the updated flux ratio of the system revealed by the light curve analysis, and the consideration of the DIB absorptions.

We emphasize that an accurate spectral analysis of the system is very challenging. This is because we lack the knowledge of the exact rotational velocities (the intrinsically broad He II lines are not a good approach to determine the rotational velocity, especially if only medium-resolution spectra are available), neglect the special geometry of the system, the incoming radiation of the other star, as well as metal opacities in our model atmosphere calculations. Finally the exact equivalent widths of the DIBs blending with He II λ 4686 Å and He II λ 5412 Å are not known, adding another uncertainty. The errors given in Table 2 therefore not only include the formal fitting errors, but also estimates on the systematic uncertainties mentioned above.

5. Light curve modelling

The analysis of the light curves was carried out simultaneously in the Johnson B -band, Sloan i -band, and ATLAS c -band filters. Because of its poor S/N, the ATLAS o -band light curve was omitted from our analysis. First fits of the light curves showed that the mass ratio is not constrained by the shape of the light curves. This is due to the significant degeneracies of the many dependent parameters used in the light curve analysis, which permits in many cases the determination of the mass ratio by light curve analysis (e.g., Schaffenroth et al. 2014). Only when ellipsoidal deformation is visible can the mass ratio be constrained (e.g., Kupfer et al. 2017). Therefore, we fixed the mass ratio of the system to the one which was derived by the RV analysis of He II λ 4542 Å and used the effective temperatures derived by the spectral analysis as starting values.

For the analysis we used MORO (Modified Roche Program, see Drechsel et al. 1995). It is based on the Wilson-Devinney

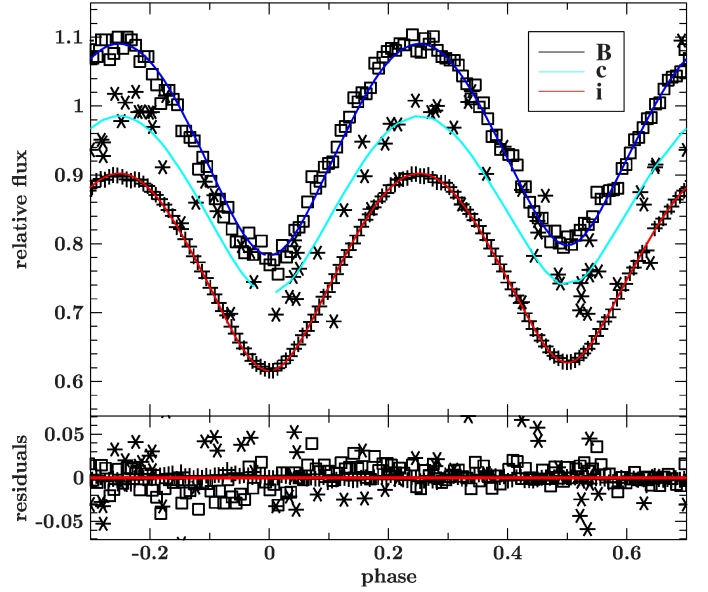


Fig. 5. Relative fluxes of the Johnson B -band (squares), ATLAS c -band (asterisks), and Sloan i -band (crosses) light curves compared to our best fit MORO models (blue, light-blue, and red, respectively). The light curves are shifted vertically for clarity. Residuals are shown at the bottom.

mode 3 code, that is used for overcontact systems (see Kallrath & Milone 2009) using a modified Roche model considering the influence of the radiation pressure on the shape of the stars. The program assumes equal Roche potentials, limb darkening and gravitational darkening coefficients for both stars. The optimization of parameters is achieved by the simplex algorithm. The gravitational darkening parameters were fixed at 1.0 as predicted for radiative envelopes (von Zeipel 1924). The limb darkening coefficients were taken from Claret & Bloemen (2011) using the value closest to the parameters determined by the spectroscopic analysis for the different filters respectively. As both stars have comparable temperatures we also fixed the albedo to 1.0. We also considered a third light source, accounting for the nebular continuum and line emission. By varying the radiation pressure parameter, inclination, temperatures, Roche potentials, luminosity ratio of both stars, and the third light contribution, the curves are reproduced nicely. We note that our fit reproduces the light curves better than the one of García-Berro et al. (2016), and also slightly better than the model of SG+15.

Our best fits to the light curves are shown in Fig. 5 and the results of our analysis are summarized in Table 2 (see also Table B.1 for all parameters of the best light curve fit). We find a relative luminosity $\frac{L_1}{L_1+L_2}$ of 58.37% in the B -band, similar effective temperatures for both stars ($T_{\text{eff}} \approx 40$ kK), and that the mean radius of the secondary is 15% smaller than the radius of the primary. We derived an additional constant flux component of 0.8% in B , 2.8% in i , and 20.5% in the ATLAS c -band⁶. Combining it

⁶ We note, that for compact nebulae, the flux contribution of the nebular lines can be significant when broad band filters are used (Shaw & Kaler 1985; Gathier & Pottasch 1988). For example the V -band magnitude of the CSPN of the Stingray Nebula measured with the *Hubble* Space Telescope and, thus, resolving the CSPN, is four orders of magnitude smaller than what is measured from the ground (Bobrowsky et al. 1998; Schaefer & Edwards 2015). Therefore, the high additional flux contributions in the ATLAS c -band, which covers numerous nebular lines (e.g., [O III] λ 5007 Å), is not surprising.

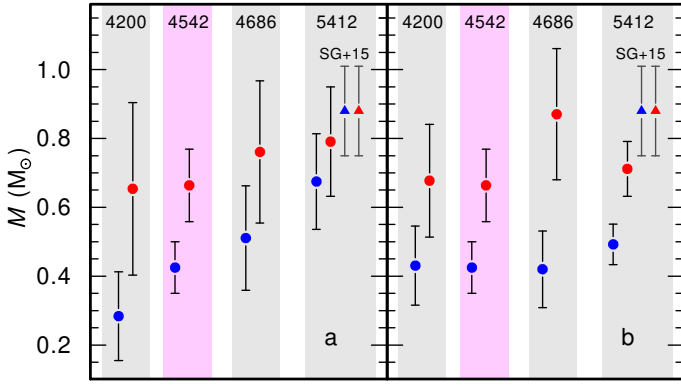


Fig. 6. Dynamical masses of the primary (red dots) and the secondary (blue dots) as determined with the inclination angle from our light curve analysis and our RV fitting of the four He II lines excluding (*panel a*) and including DIBs (*panel b*). Masses obtained from He II lines that blend with DIBs are highlighted in grey, He II $\lambda 4542$ Å which is not blended with any DIB is highlighted in pink. The blue and red triangles are the masses reported by SG+15.

with the results from the RV curves the absolute parameters M , R could be derived (Table 2, see also Sect. 6). The errors were determined by a bootstrapping method (see Schaffenroth et al. 2014) and represent only the statistical error resulting from the noise in the light curves and do not consider the degeneracies in the light curve.

6. Dynamical masses and evolutionary status

Since the inclination of the system ($i = 63.59 \pm 0.54^\circ$) can be constrained well from the light curve fitting, the dynamical masses of the two stars can be calculated via the binary mass function

$$f(M_1, M_2) = \frac{K_1^3 P}{2\pi G} = \frac{M_2 \sin^3 i}{\left(1 + \frac{M_1}{M_2}\right)^2}.$$

Our results are shown in Fig. 6. In panel a, we show the dynamical masses as obtained using our Voigt profile fitting routine and neglecting DIBs. It can be seen, that our masses obtained from He II $\lambda 5412$ Å with the Voigt profile RV fitting and after applying the zero point correction ($M_1 = 0.79 \pm 0.16 M_\odot$ and $M_2 = 0.67 \pm 0.14 M_\odot$) agree within the error limits with the results of SG+15, who find $0.88 \pm 0.13 M_\odot$ for both stars. However, for all other lines contradictory results are found.

When DIBs are included in the RV fitting significantly different results are obtained for the masses of the two CSPNe (e.g., $M_1 = 0.71 \pm 0.08 M_\odot$ and $M_2 = 0.49 \pm 0.06 M_\odot$ for He II $\lambda 5412$ Å, panel b in Fig. 6). In this case we find that the masses from the different He II lines agree with each other, but no longer with the results from SG+15. This is a consequence of the zeropoint corrections, using Voigt profiles instead of Gaussians in the RV fitting, and most importantly the inclusion of DIBs when determining the RVs.

We stress that masses obtained from He II $\lambda\lambda 4200, 4542$ Å are the ones to be trusted. This is because only He II $\lambda 4542$ Å is not blended with any DIB and for He II $\lambda 4200$ Å a good fit to the DIB which blends with this line can be found, though the S/N in this part of the spectrum is rather poor. For He II $\lambda 4686$ Å and He II $\lambda 5412$ Å we can only assume the DIBs are of about the same strength as in HD 204827 based on the similar reddening. However, the equivalent widths of the DIBs blending with these

lines might be different, for example because of a different chemical composition of the interstellar or circumstellar medium.

The masses obtained for He II $\lambda 4542$ Å are $M_1 = 0.66 \pm 0.11 M_\odot$ and $M_2 = 0.42 \pm 0.07 M_\odot$, and agree very well with the masses obtained from He II $\lambda 4200$ Å ($M_1 = 0.68 \pm 0.16 M_\odot$ and $M_2 = 0.43 \pm 0.11 M_\odot$). This is a striking result, as with the masses derived from He II $\lambda 4542$ Å the total mass of the system ($M = 1.08 \pm 0.18$), no longer exceeds the Chandrasekhar mass limit.

The total mass of the system is still high enough that a merger of the system will occur within a Hubble time. However, with the combined dynamical mass of the system no longer exceeding the Chandrasekhar mass limit, the merger will not produce a SN Ia via the traditional double-degenerate channel (Han & Podsiadlowski 2004). The individual masses of the two CSPNe are also too small for a reasonable production of ^{56}Ni (which determines the explosion brightness) in case of a dynamical explosion during the merger process (Pakmor et al. 2013; Shen et al. 2018). Thus, the merging event of Hen 2–428 will not be identified as a SN Ia.

Most likely, the merger of Hen 2–428 will then lead to the formation of a (He-rich) RCB star \rightarrow EHe star \rightarrow massive O(He) star \rightarrow CO white dwarf (Schwab 2019; Shen 2015; Zhang et al. 2014). If both stars should have CO-cores at the time of the merger, the formation of a star with a C/O-dominated atmosphere could be possible. This would make Hen 2–428 a promising progenitor for the CO-dominated hot white dwarf stars H1504+65 and RXJ0439.8–6809 (Werner & Rauch 2015), and for the C-dominated hot DQ white dwarfs (Kawka et al. 2020). The formation of an AM CVn type system via the double white dwarf channel (Paczyński 1967), that will end up in a faint thermonuclear supernova, however, seems very unlikely due to the high mass ratio of the system (Nelemans et al. 2001; Marsh et al. 2004).

In Fig. 7, we show the locations of the two CSPNe in the Hertzsprung Russell diagram (HRD), as derived with the effective temperatures from our spectroscopic analysis and the radii from the light curve analysis (primary is shown in red, the secondary in blue). It can be seen, that the luminosities and radii of the two stars are too low for what is expected for normal post-asymptotic giant branch (AGB) stars (black lines indicate H-shell burning post-AGB tracks from Miller Bertolami 2016). The dynamical mass and location in the HRD of the secondary agrees with predications for post-RGB stars (light-blue lines, Hall et al. 2013), while the dynamical mass of the primary is too high for this scenario. The secondary could also be a post-extreme horizontal branch (post-EHB) star (pink lines in Fig. 7 are post-EHB tracks from Dorman et al. 1993), while the mass of the primary is again too high for this scenario. It is worthwhile mentioning that the mass of the remaining H layer ($\leq 0.001 M_\odot$) of EHB stars is much too low to produce a nebula at the end of the He-core burning stage. Thus, it is not possible for both stars to be post-EHB stars.

The solid purple lines in Fig. 7 correspond to evolutionary tracks for stars stripped through Roche-lobe overflow and were calculated by Göteborg et al. (2018). The stars had initial masses of 3.65, 2.99, and 2.44 M_\odot and the tracks show the evolution from central H-burning, the mass transfer phase, consequent blue-ward evolution, until He-core burning is reached. The mass of the secondary is too small in order to descend from such a star, while the primary could be a candidate for being a stripped He-star, shortly before the central He-core burning phase. The surface He abundances predicted by Göteborg et al. (2018) for this evolutionary stage ($X_{\text{He}} \approx -0.15$) matches surprisingly well

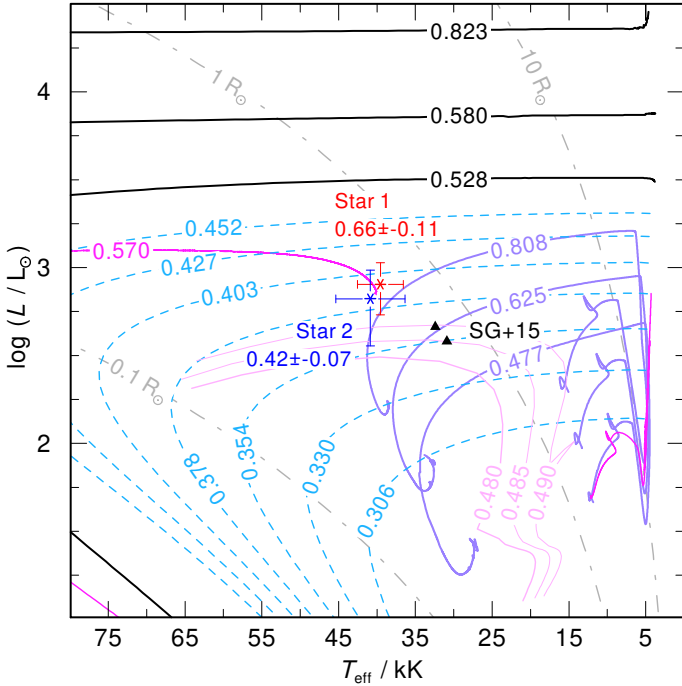


Fig. 7. Locations of the two CSPNe and their dynamical masses (primary is shown in red, the secondary in blue) in the HRD compared to stellar evolutionary tracks. Black lines indicate H-shell burning post-AGB tracks from Miller Bertolami (2016), dashed, light-blue lines post-AGB tracks from Hall et al. (2013), purple lines stripped star evolutionary tracks from Göteborg et al. (2018), and in pink post-EHB evolutionary tracks from Dorman et al. (1993). The magenta line indicates an evolutionary track of a He-shell burning stripped post-early AGB star. The gray dashed-dotted lines indicate radii of 0.1, 1, and $10 R_{\odot}$.

with what we find in our spectroscopic analysis of the primary ($X_{\text{He}} = -0.16$).

We stress that the comparison with these evolutionary tracks should be treated with caution, as obviously none of these models can account for the real evolution of Hen 2–428. Stable Roche-lobe overflow, for example, cannot account for the short orbital period and over-contact nature of the system, meaning the latest mass-transfer phase must have ended in a common envelope ejection. In addition it is not clear to what extent the evolutionary tracks (and the mass-radius relationship) are altered for over-contact systems. Short orbital period ($P < 1$ d) low-mass main sequence stars, for example, show an inflation by 10% (Kraus et al. 2011), thus it could be possible that the radii and luminosities of two CSPNe of Hen 2–428 are also too large compared to single-star evolutionary tracks. For the massive over-contact system VFTS 352 (temperature-wise very similar to Hen 2–428), it was found that single-star models predict effective temperatures which are 6% lower than what would be expected from the dynamical masses (Almeida et al. 2015).

With all caveats in mind we can still make an educated guess of what the evolution of the system might have been. In light of the actual close configuration of the system and the presence of surrounding material we know that the last mass transfer episode was unstable and led to the formation and ejection of a common envelope. In addition, the derived dynamical masses ($M_1 = 0.66 \pm 0.11 M_{\odot}$ and $M_2 = 0.42 \pm 0.07 M_{\odot}$), temperatures and luminosities (and radii), together with a comparison with stellar evolution models suggests that the secondary (in the following Star 2) has a post-AGB like structure, meaning it has

a degenerate He-core surrounded by a H-burning shell and a thin envelope on top. The nature of the more massive component (in the following Star 1) is less certain. The actual mass of the object, however, indicates that before the last mass transfer episode Star 1 was not a low-mass RGB star and its mass before the last mass transfer episode was beyond that needed for non-degenerate He ignition. As Star 2 is already a low-mass evolved star we can safely conclude that Star 1 was originally the less massive component and increased its mass during a previous (first) mass transfer episode. This implies that the total initial mass of the system was necessarily $M_1^i + M_2^i \lesssim 3.6 M_{\odot}$ (Bressan et al. 2012), and $M_2 \lesssim 3.2 M_{\odot}$ before the common envelope episode.

As mentioned above, the inferred surface properties and mass of Star 1 are in good agreement with the predicted evolution of an intermediate mass star that was stripped of in its post-main sequence evolution before the ignition of He-core burning. A serious shortcoming of this scenario is that, for this to happen, Star 1 needs to fill its Roche lobe before He-ignition, but intermediate-mass stars with $M_2 \approx 3.2 M_{\odot}$ reach at most $R_2 \sim 45 R_{\odot}$ before He-ignition. With a q -value of $q \approx 3.2 M_{\odot} / 0.4 M_{\odot} = 8$ that means that the Roche lobe of the $0.4 M_{\odot}$ companion should have been $R_1 \lesssim 18 R_{\odot}$ at the end of the first (stable) mass transfer episode. Due to the tight core mass-radius relation of RGB stars, and the fact that during Roche lobe overflow $R_{\star} \approx R_{\text{Roche}}$ (Han et al. 2000), Star 2 would have probably been peeled off well before the mass of the degenerate He-core reached $\approx 0.3 M_{\odot}$. Given that $M_2 = 0.42 \pm 0.07 M_{\odot}$, this scenario seems unlikely.

Interestingly, stars with masses in the range $2.5\text{--}3 M_{\odot}$ expand in the early-AGB phase⁷ to very large radii of $R_{\star} > 100 R_{\odot}$. Moreover, during the early AGB, a star in this mass range shuts down its H-burning shell, making the stripping of the H-rich material easier, which in the light of the high He enrichment found in the primary of the system makes this scenario more compelling. The magenta line in Fig. 7 shows the evolution of a $0.57 M_{\odot}$ post-early AGB model constructed by artificially stripping the envelope of a $2.5 M_{\odot}$ star once it reached the luminosity of Star 1. The surface He mass fraction of the model is $X_{\text{He}} \approx -0.28$.

Figure 8 shows a toy model for such scenario. Lets assume that we start the evolution with a pair of low-mass stars in a relatively close orbit (panel A in Fig. 8, $M_2^i = 1.55 M_{\odot}$, $M_1^i = 1.3 M_{\odot}$, $a \approx 33 R_{\odot}$). As soon as the more massive star ends its main sequence evolution it will evolve into the RGB and when it reaches $R_1 \approx 13 R_{\odot}$ it will start to transfer mass to its companion (panel B in Fig. 8). Due to the low mass ratio of the system at that point ($q \lesssim 1.19$) mass transfer will be stable, and as soon as $M_1 < M_2$ it will evolve on a nuclear timescale (Podsiadlowski 2014), and stable mass transfer continues as Star 2 evolves on the RGB. If the envelope of Star 2 is removed once its He-degenerate core reaches $0.35 M_{\odot}$ the star will contract and form a $M_2^f \approx 0.35 M_{\odot}$ He-core white dwarf. Under the simplifying assumption that mass loss is conservative (Postnov & Yungelson 2014) our system would be composed of a $0.35 M_{\odot}$ He-core white dwarf, and a rejuvenated $M_1^{\text{rj}} = 2.5 M_{\odot}$ main-sequence companion, separated by $a \approx 174 R_{\odot}$. The Roche lobe of Star 1 under such situation would be of $R_{\text{Roche}}^1 \approx 95 R_{\odot}$.

⁷ This is, after the end of core-helium burning and before the development of thermal pulses.

⁸ We note however that this is just a toy model, as the sequence in Fig. 7 was stripped on the AGB at $R \approx 50 R_{\odot}$ in order to match the luminosity of the primary component.

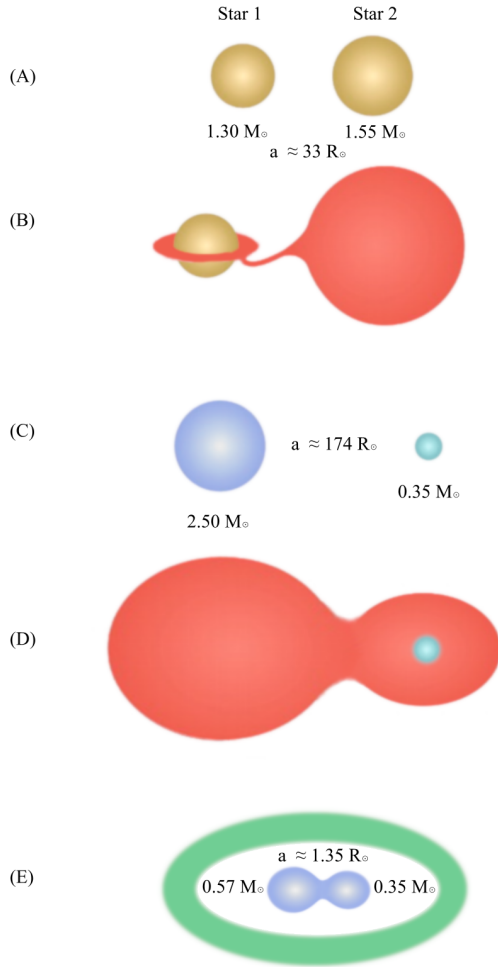


Fig. 8. Sketch of a possible evolutionary scenario for Hen 2–428.

Star 1 will then end its main sequence phase, and go to the He-core burning phase without interacting with its companion. But once He-core burning is finished, the star will evolve to the early AGB. In isolation a $2.5 M_{\odot}$ star would expand to about $R^1 \approx 170 R_{\odot}$ before developing thermal pulses, but due to the presence of its companion as soon as Star 1 fills its Roche lobe at $R_{\text{Roche}}^1 \approx 95 R_{\odot}$ it will start transferring mass. Given the extreme mass ratio of the system ($q = M_1^i/M_2^f \approx 7.14$) mass transfer will be highly unstable, leading to the formation of a common envelope (panel D in Fig. 8), the shrinking of the orbits and the final ejection of the common envelope. The current state of the system would be an overcontact close binary system composed of the post-early AGB core of $M_1^f \approx 0.57 M_{\odot}$, a post-RGB core of $M_2^f \approx 0.35 M_{\odot}$ with its envelope reheated by the last mass transfer episode, and a surrounding PN composed of the ejected material (panel E in Fig. 8).

7. Summary and conclusion

We performed a detailed reanalysis of the alleged type Ia supernova progenitor Hen 2–428. Our study reveals that the red-excess reported by Rodríguez et al. (2001) is merely a consequence of the Cardelli et al. (1989) reddening law used in their work. Fitting the IDS spectrum with our best fit model and using the Fitzpatrick (1999) reddening law we find

$A_V = 3.57 \pm 0.16$ mag, which is slightly higher than the value ($A_V = 2.96 \pm 0.34$ mag) reported by Rodríguez et al. (2001).

Furthermore, we discovered zeropoint shifts in the wavelengths calibration of the OSIRIS spectra up to 54 km s^{-1} (Table 1). Correcting for these and using Voigt profiles instead of Gaussian profiles in the RV fitting, our results for He II $\lambda 5412 \text{ \AA}$ agree with the values reported by SG+15, but for all other He II lines we end up with conflicting RV amplitudes.

This issue was resolved by the realization that the spectra, and most notably three of the four double-lined He II lines, are contaminated by DIBs. Including the DIBs in the RV fitting, we obtain consistent results for all four He II lines and importantly, very distinct RV amplitudes of $K_1 = 137 \pm 12 \text{ km s}^{-1}$ for the primary and $K_2 = 214 \pm 14 \text{ km s}^{-1}$ for the secondary (using He II $\lambda 4542 \text{ \AA}$, the only line not blended with any DIB). These values no longer agree with the results of SG+15.

We then performed spectroscopic fits to the He II lines using metal-free non-LTE models. Using the results from the RV and spectral analysis, we carried out light curve fits to the *B*-band, Sloan *i*-band, and ATLAS *c*-band filters, to derive the geometry of the system. We find the effective temperatures of both stars are about the same ($T_{\text{eff}} \approx 40 \text{ kK}$), but higher than reported by SG+15. The radii of the two stars ($0.603 R_{\odot}$ for the primary and $0.514 R_{\odot}$ for the secondary) are also found to differ from the results of SG+15, who found $R = 0.68 R_{\odot}$ for both stars. The inclination angle found by us ($i = 63.59 \pm 0.54^{\circ}$) agrees within the error limits with what is reported by SG+15 ($i = 64.7 \pm 1.4^{\circ}$).

The most striking result of our analysis is that the mass ratio of the system no longer equals one and that the dynamical masses of both stars ($M_1 = 0.66 \pm 0.11 M_{\odot}$ and $M_2 = 0.42 \pm 0.07 M_{\odot}$) are significantly smaller compared to the results of SG+15 ($M_1 = M_2 = 0.88 \pm 0.13 M_{\odot}$). The total mass of the system ($M = 1.08 \pm 0.18$) no longer exceeds the Chandrasekhar mass limit, which again, is mainly a result of blends of He II $\lambda 5412 \text{ \AA}$ with DIBs, which have led to an overestimation of the dynamical masses of Hen 2–428 by SG+15. With these new findings, the merging event of Hen 2–428 will not be recognised as SN Ia, but most likely lead to the formation of a H-deficient star.

Based on the dynamical masses and atmospheric parameters revealed by our work, we propose that the primary is a He-shell burning post-early AGB star, and the secondary is the reheated core of a post-RGB star. The formation of the system could be explained by a first stable mass transfer episode in which Star 2 (now secondary) transferred most of its mass to Star 1 (now primary) before it ignited He-core burning. As Star 1 evolved up the early AGB, a common envelope was formed, and later ejected, with the ejected material being now visible as the PN.

Even though the system can no longer be considered as a SN Ia progenitor, this does not diminish the importance of Hen 2–428 for studying common envelope evolution, the formation of H-deficient stars via the double white dwarf merger channel, and the creation of (asymmetrical) PNe via non-canonical (i.e., non-post-AGB) evolutionary path ways. Hen 2–428 is the only double-degenerate CSPN observed in an over-contact configuration, thus, it might provide insights on the common envelope ejection efficiency. Future spectroscopic observations offering a better S/N especially in the blue part of the spectrum could improve the dynamical masses and help to better constrain the evolutionary status of this interesting system. A nebular abundance analysis will help to determine the metallicity of the system. Finally, detailed evolutionary calculations that are able to reproduce the history and future evolution of the system are highly encouraged.

Acknowledgements. We thank Mónica Rodríguez for providing us with the INT/IDS spectra. We appreciate useful discussions with David Jones and Tom Marsh during the CWDB meeting. V.S. is supported by the Deutsche Forschungsgemeinschaft, DFG through grant GE 2506/9-1. Part of this work was supported by a MinCyT-DAAD bilateral cooperation program through grant DA/16/07. Based on data from the GTC PublicArchive at CAB (INTA-CSIC). Based on observations collected at the European Organisation for Astronomical Research in the Southern Hemisphere under ESO programme 295.D-5032(A). IRAF is distributed by the National Optical Astronomy Observatory, which is operated by the Association of Universities for Research in Astronomy (AURA) under a cooperative agreement with the National Science Foundation. This work includes data from the Asteroid Terrestrial-impact Last Alert System (ATLAS) project. ATLAS is primarily funded to search for near earth asteroids through NASA grants NN12AR55G, 80NSSC18K0284, and 80NSSC18K1575; by products of the NEO search include images and catalogs from the survey area. The ATLAS science products have been made possible through the contributions of the University of Hawaii Institute for Astronomy, the Queen's University Belfast, the Space Telescope Science Institute, and the South African Astronomical Observatory.

References

- Almeida, L. A., Sana, H., de Mink, S. E., et al. 2015, *ApJ*, **812**, 102
- Arkhipova, V. P., Ikonnikova, N. P., Kniazev, A. Y., & Rajoelimanana, A. 2013, *Astron. Lett.*, **39**, 201
- Asplund, M., Grevesse, N., Sauval, A. J., & Scott, P. 2009, *ARA&A*, **47**, 481
- Barnard, A. J., Cooper, J., & Shamey, L. J. 1969, *A&A*, **1**, 28
- Barnard, A. J., Cooper, J., & Smith, E. W. 1974, *J. Quant. Spectr. Radiat. Transf.*, **14**, 1025
- Bloecker, T. 1993, *Acta Astron.*, **43**, 305
- Bloecker, T., & Schoenberner, D. 1991, *A&A*, **244**, L43
- Bobrowsky, M., Sahu, K. C., Parthasarathy, M., & García-Lario, P. 1998, *Nature*, **392**, 469
- Breedt, E., Steeghs, D., Marsh, T. R., et al. 2017, *MNRAS*, **468**, 2910
- Bressan, A., Marigo, P., Girardi, L., et al. 2012, *MNRAS*, **427**, 127
- Burdge, K. B., Coughlin, M. W., Fuller, J., et al. 2019, *Nature*, **571**, 528
- Campbell, E. K., Holz, M., Gerlich, D., & Maier, J. P. 2015, *Nature*, **523**, 322
- Cardelli, J. A., Clayton, G. C., & Mathis, J. S. 1989, *ApJ*, **345**, 245
- Claret, A., & Bloemen, S. 2011, *A&A*, **529**, A75
- Corradi, R. L. M., García-Rojas, J., Jones, D., & Rodríguez-Gil, P. 2015, *ApJ*, **803**, 99
- Davignon, G., Blecha, A., Burki, G., et al. 2004, in *CCD Camera and Automatic Data Reduction Pipeline for the Mercator Telescope on La Palma*, eds. A. F. M. Moorwood, & M. Iye, *SPIE Conf. Ser.*, **5492**, 871
- De Marco, O., Farihi, J., & Nordhaus, J. 2009, *J. Phys. Conf. Ser.*, **172**, 012031
- Dorman, B., Rood, R. T., & O'Connell, R. W. 1993, *ApJ*, **419**, 596
- Drechsel, H., Haas, S., Lorenz, R., & Gayler, S. 1995, *A&A*, **294**, 723
- Fink, M., Hillebrandt, W., & Röpke, F. K. 2007, *A&A*, **476**, 1133
- Fink, M., Röpke, F. K., Hillebrandt, W., et al. 2010, *A&A*, **514**, A53
- Finch, N. L., Reindl, N., Barstow, M. A., et al. 2018, *Open Astron.*, **27**, 57
- Finch, N. L., Braker, I. P., Reindl, N., et al. 2019, in *Spectral Analysis of Binary Pre-white Dwarf Systems*, eds. K. Werner, C. Stehle, T. Rauch, & T. Lanz, *ASP Conf. Ser.*, **519**, 231
- Fitzpatrick, E. L. 1999, *PASP*, **111**, 63
- Frew, D. J., Parker, Q. A., & Bojičić, I. S. 2016, *MNRAS*, **455**, 1459
- García-Berro, E., Soker, N., Althaus, L. G., Ribas, I., & Morales, J. C. 2016, *New Astron.*, **45**, 7
- Gathier, R., & Pottasch, S. R. 1988, *A&A*, **197**, 266
- Geier, S., Hirsch, H., Tillich, A., et al. 2011, *A&A*, **530**, A28
- Götberg, Y., de Mink, S. E., Groh, J. H., et al. 2018, *A&A*, **615**, A78
- Griem, H. R. 1974, in *Spectral Line Broadening by Plasmas* (New York: Academic Press, Inc.), *Pure Appl. Phys.*, **39**, 421
- Gvaramadze, V. V., Gräfener, G., Langer, N., et al. 2019, *Nature*, **569**, 684
- Hall, P. D., Tout, C. A., Izzard, R. G., & Keller, D. 2013, *MNRAS*, **435**, 2048
- Han, Z., & Podsiadlowski, P. 2004, *MNRAS*, **350**, 1301
- Han, Z., Tout, C. A., & Eggleton, P. P. 2000, *MNRAS*, **319**, 215
- Henize, K. G. 1976, *ApJS*, **30**, 491
- Hillwig, T. C., Frew, D. J., Reindl, N., et al. 2017, *AJ*, **153**, 24
- Hirsch, H. A. 2009, PhD Thesis, University Erlangen-Nürnberg, Germany
- Hobbs, L. M., York, D. G., Snow, T. P., et al. 2008, *ApJ*, **680**, 1256
- Iben, I., Jr., & Tutukov, A. V. 1984, *ApJS*, **54**, 335
- Iben, I., Jr., & Tutukov, A. V. 1986, *ApJ*, **311**, 742
- Jenniskens, P., & Desert, F.-X. 1994, *A&AS*, **106**, 39
- Jones, D. 2019, in *Highlights on Spanish Astrophysics X*, eds. B. Montesinos, A. Asensio Ramos, F. Buitrago, et al., 340
- Jones, D. 2020, ArXiv e-prints [arXiv:2001.03337]
- Jones, E., Oliphant, T., Peterson, P., et al. 2001, *SciPy: Open Source Scientific Tools for Python*
- Justham, S., Podsiadlowski, P., & Han, Z. 2011, *MNRAS*, **410**, 984
- Kallrath, J., & Milone, E. F. 2009, *Eclipsing Binary Stars: Modeling and Analysis* (New York: Springer-Verlag)
- Kashi, A., & Soker, N. 2011, *MNRAS*, **417**, 1466
- Kawka, A., Vennes, S., & Ferrario, L. 2020, *MNRAS*, **491**, L40
- Kos, J., & Zwitter, T. 2013, *ApJ*, **774**, 72
- Kraus, A. L., Tucker, R. A., Thompson, M. I., Craine, E. R., & Hillenbrand, L. A. 2011, *ApJ*, **728**, 48
- Krelowski, J., Galazutdinov, G., Godunova, V., & Bondar, A. 2019, *Acta Astron.*, **69**, 159
- Kupfer, T., van Roestel, J., Brooks, J., et al. 2017, *ApJ*, **835**, 131
- Lallement, R., Capitanio, L., Ruiz-Dern, L., et al. 2018, *A&A*, **616**, A132
- Liu, D. D., Wang, B., Podsiadlowski, P., & Han, Z. 2016, *MNRAS*, **461**, 3653
- Liu, D., Wang, B., & Han, Z. 2018, *MNRAS*, **473**, 5352
- Maos, D., Mannucci, F., & Nelemans, G. 2014, *ARA&A*, **52**, 107
- Marsh, T. R., Nelemans, G., & Steeghs, D. 2004, *MNRAS*, **350**, 113
- Miller Bertolami, M. M. 2016, *A&A*, **588**, A25
- Napiwotzki, R. 1999, *A&A*, **350**, 101
- Napiwotzki, R., Christlieb, N., Drechsel, H., et al. 2001, *Astron. Nachr.*, **322**, 411
- Napiwotzki, R., Karl, C. A., Lisker, T., et al. 2020, *A&A*, in press, <https://doi.org/10.1051/0004-6361/201629648>
- Nelemans, G., Portegies Zwart, S. F., Verbunt, F., & Yungelson, L. R. 2001, *A&A*, **368**, 939
- Paczynski, B. 1967, *Acta Astron.*, **17**, 287
- Paczynski, B. 1976, in *Structure and Evolution of Close Binary Systems*, eds. P. Eggleton, S. Mitton, & J. Whelan, *IAU Symp.*, **73**, 75
- Pakmor, R., Hachinger, S., Röpke, F. K., & Hillebrandt, W. 2011, *A&A*, **528**, A117
- Pakmor, R., Kromer, M., Taubenberger, S., & Springel, V. 2013, *ApJ*, **770**, L8
- Podsiadlowski, P. 2014, *Binary Systems, their Evolution and Environments*, 13
- Postnov, K. A., & Yungelson, L. R. 2014, *Liv. Rev. Relativ.*, **17**, 3
- Rauch, T., & Deetjen, J. L. 2003, in *Stellar Atmosphere Modeling*, eds. I. Hubeny, D. Mihalas, & K. Werner, *ASP Conf. Ser.*, **288**, 103
- Rebassa-Mansergas, A., Toonen, S., Korol, V., & Torres, S. 2019, *MNRAS*, **482**, 3656
- Reindl, N., Rauch, T., Werner, K., Kruk, J. W., & Todt, H. 2014a, *A&A*, **566**, A116
- Reindl, N., Rauch, T., Parthasarathy, M., et al. 2014b, *A&A*, **565**, A40
- Reindl, N., Finch, N., Schaffenroth, V., et al. 2018, *Galaxies*, **6**, 88
- Renedo, I., Althaus, L. G., Miller Bertolami, M. M., et al. 2010, *ApJ*, **717**, 183
- Rodríguez, M., Corradi, R. L. M., & Mampaso, A. 2001, *A&A*, **377**, 1042
- Saio, H., & Jeffery, C. S. 2002, *MNRAS*, **333**, 121
- Santander-García, M., Rodríguez-Gil, P., Corradi, R. L. M., et al. 2015, *Nature*, **519**, 63
- Schaefer, B. E., & Edwards, Z. I. 2015, *ApJ*, **812**, 133
- Schaffenroth, V., Geier, S., Heber, U., et al. 2014, *A&A*, **564**, A98
- Schlafly, E. F., Finkbeiner, D. P., Schlegel, D. J., et al. 2010, *ApJ*, **725**, 1175
- Schöning, T., & Butler, K. 1989, *A&AS*, **78**, 51
- Schwab, J. 2019, *ApJ*, **885**, 27
- Shaw, R. A., & Kaler, J. B. 1985, *ApJ*, **295**, 537
- Shen, K. J. 2015, *ApJ*, **805**, L6
- Shen, K. J., Kasen, D., Miles, B. J., & Townsley, D. M. 2018, *ApJ*, **854**, 52
- Sparks, W. M., & Stecher, T. P. 1974, *ApJ*, **188**, 149
- Tonry, J. L., Denneau, L., Heinze, A. N., et al. 2018, *PASP*, **130**, 064505
- Tremblay, P.-E., & Bergeron, P. 2009, *ApJ*, **696**, 1755
- Tylenda, R., Stasińska, G., Acker, A., & Stenholm, B. 1994, *A&AS*, **106**, 559
- van Hoof, P. A. M. 2018, *Galaxies*, **6**, 63
- von Zeipel, H. 1924, *MNRAS*, **84**, 665
- Webbink, R. F. 1984, *ApJ*, **277**, 355
- Weisberg, J. M., & Taylor, J. H. 2005, in *The Relativistic Binary Pulsar B1913+16: Thirty Years of Observations and Analysis*, eds. F. A. Rasio, & I. H. Stairs, *ASP Conf. Ser.*, **328**, 25
- Werner, K., & Rauch, T. 2015, *A&A*, **584**, A19
- Werner, K., Deetjen, J. L., Dreizler, S., et al. 2003, in *Stellar Atmosphere Modeling*, eds. I. Hubeny, D. Mihalas, & K. Werner, *ASP Conf. Ser.*, **288**, 31
- Werner, K., Dreizler, S., & Rauch, T. 2012, *Astrophysics Source Code Library* [record ascl:1212.015]
- Woosley, S. E., & Weaver, T. A. 1994, *ApJ*, **423**, 371
- Zhang, X., & Jeffery, C. S. 2012a, *MNRAS*, **419**, 452
- Zhang, X., & Jeffery, C. S. 2012b, *MNRAS*, **426**, L81
- Zhang, Y., Fang, X., Chau, W., et al. 2012, *ApJ*, **754**, 28
- Zhang, X., Jeffery, C. S., Chen, X., & Han, Z. 2014, *MNRAS*, **445**, 660

Appendix B: Additional table

Table B.1. Best light curve solution of Hen 2–428.

Fixed parameters:		
$q (=M_2/M_1)$		0.64
A_1 ^(a)		1.0
A_2 ^(a)		1.0
g_1 ^(b)		1.0
g_2 ^(b)		1.0
$x_1(B)$ ^(c)		0.25
$x_1(i)$ ^(c)		0.17
$x_1(c)$ ^(c)		0.20
$x_2(B)$ ^(c)		0.25
$x_2(i)$ ^(c)		0.17
$x_2(c)$ ^(c)		0.20
Adjusted parameters:		
i	[°]	63.59 ± 0.54
$T_{\text{eff}}(1)$	[K]	40179 ± 370
$T_{\text{eff}}(2)$	[K]	40356 ± 175
δ_1 ^(d)		0.02174 ± 0.0052
δ_2 ^(d)		0.0033 ± 0.0021
$\frac{L_1}{L_1+L_2}(B)$ ^(e)		0.5837 ± 0.0068
$\frac{L_1}{L_1+L_2}(i)$ ^(e)		0.5842 ± 0.0068
$\frac{L_1}{L_1+L_2}(c)$ ^(e)		0.5939 ± 0.0168
Ω_1 ^(f)		2.965 ± 0.017
Ω_2 ^(f)		2.965 ± 0.017
$l_3(B)$ ^(g)		0.0079 ± 0.0043
$l_3(i)$ ^(g)		0.0279 ± 0.0066
$l_3(c)$ ^(g)		0.2046 ± 0.0312
Roche radii ^(h) :		
$r_1(\text{mean})$	[a]	0.4472 ± 0.0041
$r_1(\text{pole})$	[a]	0.4121 ± 0.0030
$r_1(\text{point})$	[a]	-1.0000
$r_1(\text{side})$	[a]	0.4407 ± 0.0039
$r_1(\text{back})$	[a]	0.4806 ± 0.0056
$r_2(\text{mean})$	[a]	0.3809 ± 0.0042
$r_2(\text{pole})$	[a]	0.3465 ± 0.0028
$r_2(\text{point})$	[a]	-1.0000
$r_2(\text{side})$	[a]	0.3676 ± 0.0036
$r_2(\text{back})$	[a]	0.4212 ± 0.0067

Notes. ^(a)Bolometric albedo. ^(b)Gravitational darkening exponent. ^(c)Linear limb darkening coefficient; taken from [Claret & Bloemen \(2011\)](#). ^(d)Radiation pressure parameter, see [Drechsel et al. \(1995\)](#). ^(e)Relative luminosity; L_2 is not independently adjusted, but recomputed from r_2 and $T_{\text{eff}}(2)$. ^(f)Roche potentials. ^(g)Fraction of third light at maximum. ^(h)Fractional Roche radii in units of separation of mass centers.

An extremely hot white dwarf with a rapidly rotating K-type subgiant companion: UCAC2 46706450

Klaus Werner¹, Nicole Reindl², Lisa Löbbling¹, Ingrid Pelisoli², Veronika Schaffenroth²,
Alberto Rebassa-Mansergas^{3,4}, Puji Irawati⁵, and Juanjuan Ren⁶

¹ Institut für Astronomie und Astrophysik, Kepler Center for Astro and Particle Physics, Eberhard Karls Universität, Sand 1, 72076 Tübingen, Germany

e-mail: werner@astro.uni-tuebingen.de

² Institut für Physik und Astronomie, Universität Potsdam, Karl-Liebknecht-Straße 24/25, Germany

³ Departament de Física, Universitat Politècnica de Catalunya, c/Esteve Terrades 5, 08860 Castelldefels, Spain

⁴ Institut d'Estudis Espacials de Catalunya, Ed. Nexus-201, c/Gran Capità 2-4, 08034 Barcelona, Spain

⁵ National Astronomical Research Institute of Thailand, Sirindhorn AstroPark, Donkaew, Mae Rim, Chiang Mai 50180, Thailand

⁶ Key Laboratory of Space Astronomy and Technology, National Astronomical Observatories, Chinese Academy of Sciences, Beijing 100101, PR China

Received 3 June 2020 / Accepted 5 September 2020

ABSTRACT

The subgiant UCAC2 46706450 is a late-type star with an ultraviolet (UV) excess. It was considered as a candidate to establish a sample of stars of spectral type F, G, and K with white dwarf (WD) companions that could be used to test binary evolution models. To verify the WD nature of the companion, UV spectroscopy has previously been performed by other authors. Via a detailed model-atmosphere analysis, we show that the UV source is an extremely hot WD with an effective temperature of $T_{\text{eff}} = 105\,000 \pm 5000$ K, mass of $M/M_{\odot} = 0.54 \pm 0.02$, radius of $R/R_{\odot} = 0.040^{+0.005}_{-0.004}$, and luminosity of $L/L_{\odot} = 176^{+55}_{-49}$, meaning that the compact object is just about to enter the WD cooling sequence. Investigating spectra of the cool star ($T_{\text{eff}} = 4945 \pm 250$ K), we found that it is a K-type subgiant with $M/M_{\odot} = 0.8\text{--}2.4$, $R/R_{\odot} = 5.9^{+0.7}_{-0.5}$, and $L/L_{\odot} = 19^{+5}_{-5}$ that is rapidly rotating with $v \sin(i) = 81$ km s⁻¹. Optical light curves reveal a period of two days and an *o*-band peak-to-peak amplitude of 0.06 mag. We suggest that it is caused by stellar rotation in connection with star spots. With the radius, we infer an extremely high rotational velocity of $v_{\text{rot}} = 151^{+18}_{-13}$ km s⁻¹, thus marking the star as one of the most rapidly rotating subgiants known. This explains chromospheric activity observed by H α emission and emission-line cores in Ca II H and K as well as NUV flux excess. From equal and constant radial velocities of the WD and the K subgiant as well as from a fit to the spectral energy distribution, we infer that they form a physical, wide (though unresolved) binary system. Both components exhibit similar metal abundances and show iron-group elements with slightly oversolar (up to 0.6 dex) abundance, meaning that atomic diffusion in the WD atmosphere is not yet active due to a residual, weak radiation-driven wind. Kinematically and from its height above the Galactic plane, the system belongs to the Galactic thick disk, indicating that it is an old system and that the initial masses of both stars were close to $1 M_{\odot}$.

Key words. stars: individual: UCAC2 46706450 – stars: atmospheres – stars: abundances – stars: AGB and post-AGB – white dwarfs – starspots

1. Introduction

Stellar multiplicity is an omnipresent outcome of the star-formation process. About every other solar-type (mass $M \approx 0.7\text{--}1.3 M_{\odot}$) star is found in the binary system (see Duchêne & Kraus 2013 for a review). At solar metallicity, about one quarter of these stars is found in close binaries (orbital period $P < 10^4$ d, separation $a < 10$ AU), and the close-binary fraction is found to increase strongly with decreasing metallicity and may be as high as 53% at a metallicity of $[\text{Fe}/\text{H}] = -3$ dex (Moe et al. 2019). When the more massive member of the binary evolves off the main sequence, such close systems will eventually interact with each other by exchanging mass and angular momentum (Willems & Kolb 2004). This in turn influences their evolution and can lead to a broad range of astrophysical phenomena that are absent for the life of single stars. Systems that will undergo a common-envelope event will end up as very close binaries with final orbital periods typically between 0.1 and 10 d (Nebot Gómez-Morán et al. 2011), or even merge (Han et al. 2002).

Systems that transferred mass via stable Roche-lobe overflow or wind accretion can be found at longer final periods of a few $10^2\text{--}10^3$ d (Pastetter & Ritter 1989; Han et al. 2002; Nie et al. 2012; Chen et al. 2013). Evolved systems with periods longer than about 3000 d are thought to always remain detached (Van der Swaelmen et al. 2017).

Detailed studies of evolved binaries are fundamental for various reasons. The mass and period distribution of very short orbital period binaries provides important observational constraints on the poorly understood common-envelope phase (Ritter 1986; Schreiber et al. 2010; Davis et al. 2010; Zorotovic et al. 2011). In addition, these binaries can be employed to search for and study supernovae type Ia progenitor candidates (Napiwotzki et al. 2001; Geier et al. 2013; Santander-García et al. 2015; Rebassa-Mansergas et al. 2019; Reindl et al. 2020) or help us to understand how binary interactions alter the intrinsic properties of the stars (such as their atmospheric composition, rotational rates, pulsations, mass loss, dust formation, and circumstellar-envelope morphology; Van Winckel 2018). Last

but not least, binaries that avoided mass exchange can be used to investigate the initial-final mass relation, which is a key constraint on stellar evolution theory and important to understanding the chemical enrichment and the efficiency of star formation in galaxies (Silvestri et al. 2005; Catalán et al. 2008; Zhao et al. 2012b; Baxter et al. 2014; Andrews et al. 2015).

Aiming to provide a large sample to test binary evolution models and type Ia supernovae formation channels, Parsons et al. (2016) established a group of 934 main-sequence FGK stars from the Large Sky Area Multi-Object Fiber Spectroscopic Telescope (LAMOST, Zhao et al. 2012a) survey and the Radial Velocity Experiment survey (Kordopatis et al. 2013), which show excess flux at ultraviolet (UV) wavelengths, and hence likely have a white dwarf (WD) companion. Such systems are still very rarely known in comparison to thousands of M stars with WD companions (Holberg et al. 2013; Rebassa-Mansergas et al. 2016). For nine objects in their sample, Parsons et al. (2016) obtained follow-up spectroscopy with the *Hubble* Space Telescope (HST).

One of these nine systems, UCAC2 46706450, is the subject of this work. A spectroscopic analysis of the late-type star was performed by various authors revealing, for example, an effective temperature of $T_{\text{eff}} = 4905 \pm 16$ K and a surface gravity of $\log g = 2.90 \pm 0.04$ (Ho et al. 2017), indicating that the star is an early K subgiant. Assuming that the observed Ly α line in the HST spectrum is of photospheric origin, a model-atmosphere fit by Parsons et al. (2016) to the Ly α profile yielded $T_{\text{eff}} = 24\,000$ K and a low surface gravity of $\log g \approx 5.0$, indicating that the hot component is a pre-WD object like a hot subdwarf.

In the present paper, we analyze in detail the UV spectrum of the compact companion and show that its temperature was strongly underestimated, and that it is among the hottest known WDs (Sect. 2). We then reassess the spectroscopic observations to characterize the K-type star (Sect. 3), search for radial velocity (RV) variations (Sect. 4), and investigate its Galactic population membership (Sect. 5). We derive stellar parameters of both components (Sect. 6) and examine the optical photometric variability (Sect. 7). We conclude in Sect. 8.

In the following, we refer to the spectroscopic binary components as UCAC2 46706450–A and UCAC2 46706450–B for the K subgiant and the hot WD, respectively.

2. Analysis of UV spectroscopy of the hot white dwarf

The star UCAC2 46706450 was observed on Oct. 30, 2014, with the Cosmic Origins Spectrograph (COS) aboard HST, using the G130M grating centered on 1291 Å for a 2109 s exposure (dataset LCKY08010, PI: S. Parsons). The spectrum was retrieved from the MAST archive. The approximate useful wavelength coverage is 1138–1278 Å and 1296–1426 Å. The spectral resolution is about 0.1 Å. For our analysis, we smoothed the spectra with a 0.1 Å-wide boxcar to increase the signal-to-noise ratio (SNR). For comparison with observations, model spectra were convolved with a Gaussian ($FWHM = 0.14$ Å). The spectrum and our model fit are shown in Fig. 1. We identified lines from highly ionized light metals, namely, C IV, N IV–V, O IV–V, Si IV–V, S VI as well as from iron-group elements, namely, Cr VI, Mn VI, Fe VI–VIII, and Ni VI. Evidently the spectrum is that of a very hot WD. Concerning the ionization stages observed in the UV, it appears similar to other hot objects, for example, the DA PG 0948+534 with $T_{\text{eff}} = 105\,000$ K (Werner et al. 2019) and the DAO central stars of Sh 2-216 and EGB 6 with $T_{\text{eff}} = 95\,000$ K

and 105 000 K, respectively (Rauch et al. 2007; Werner et al. 2018b).

The broad Ly α profile is dominated by interstellar hydrogen, and the COS spectrum does not cover any helium line. Thus, the H/He ratio is unknown, and in principle the object could be either a He-rich (DO or DOA) WD or a H-rich (DA or DAO) WD. Nevertheless, we show that the effective temperature and metal abundance measurements are rather independent of this.

The photospheric lines are blueshifted by -10 km s $^{-1}$. Accordingly, the observed spectrum is shifted to rest wavelengths in all figures presented here. Some of the most prominent interstellar lines were modeled. They are blueshifted between -15 and -35 km s $^{-1}$. From Ly α , we derived a neutral H column density of $\log n_H = 20.4 \pm 0.04$ toward the WD. Comparing the continuum shape of our final model and observation, we found a reddening of $E_{B-V} = 0.03 \pm 0.01$. The models presented here are attenuated by this reddening value. We note the reddening derived by us also agrees with values reported in the 2D dust maps of Schlegel et al. (1998) and Schlafly & Finkbeiner (2011), as well as with the lower limit provided by the 3D dust map of Lallement et al. (2018).

We used the Tübingen Model-Atmosphere Package (TMAP¹) to compute non-LTE, plane-parallel, line-blanketed atmosphere models in radiative and hydrostatic equilibrium (Werner & Dreizler 1999; Werner et al. 2003, 2012). The models include H, He, C, N, O, Si, P, S, Cr, Mn, Fe, Co, and Ni. The employed model atoms are described in detail by Werner et al. (2018a). In addition, we performed line formation iterations (i.e., keeping the atmospheric structure fixed) for fluorine using the model atom presented in Werner et al. (2015).

2.1. Effective temperature, surface gravity, and H/He ratio

We started our analysis by fixing the value of the surface gravity to $\log g = 7.4$. At $T_{\text{eff}} \approx 100\,000$ K, this corresponds to a WD with a mass of $\approx 0.54 M_{\odot}$. We also fixed the H/He ratio to the solar value. We then varied T_{eff} and the metal abundances to obtain a good fit to the line features. We found $T_{\text{eff}} = 105\,000 \pm 5000$ K and the abundances listed in Table 1. The abundance measurements are described in detail below (Sect. 2.2). Finally, we looked how $\log g$ can be constrained and how the H/He ratio affects the derived atmospheric parameters.

The relatively small error in T_{eff} follows from the fact that we can exploit several ionization balances, first of all, iron. We do not see Fe V, imposing a strict lower limit of 100 000 K. The relative strengths of Fe VI to Fe VII lines then yield the value of 105 000 K (Fig. 2). In addition, at temperatures above 110 000 K, the only observed Fe VIII line (at 1148.2 Å) becomes too strong (a problem with a blending Ni VI line is discussed in Sect. 2.2). Another sensitive indicator for T_{eff} is oxygen. With increasing temperature, the O IV multiplets (Fig. 2) and O V 1371 Å become weaker, whereas the highly excited O V multiplet at 1420 Å becomes stronger. The detection of N IV lines (around 1190 and 1271 Å) rules out a T_{eff} value well over 105 000 K. The absence of the C III multiplet at 1175 Å, on the other hand, requires T_{eff} above 100 000 K.

Next, we looked at how the surface gravity affects the model spectrum. Reducing $\log g$ from the fiducial value 7.4 to 7.1 results in unobserved sharp line cores of the C IV doublet at 1352 Å. An increase to $\log g = 7.7$ results in too broad wings of the C IV lines

¹ <http://astro.uni-tuebingen.de/~TMAP>

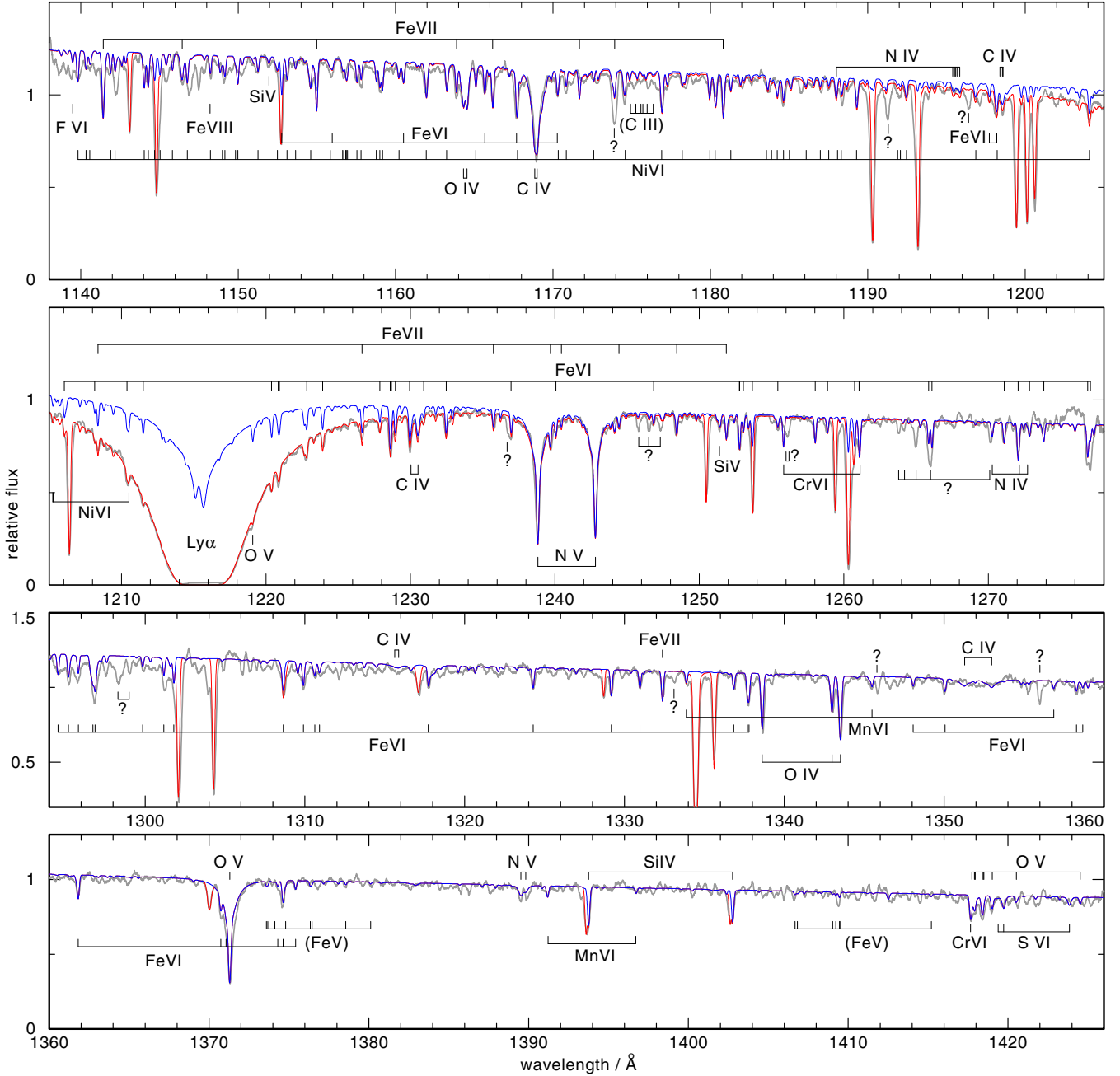


Fig. 1. HST/COS spectrum of the white dwarf in UCAC2 46706450 (gray) compared to a photospheric model spectrum (blue graph: $T_{\text{eff}} = 105\,000\text{ K}$, $\log g = 7.4$) with the measured metal abundances (Table 1) and assuming solar H and He abundances. The same model attenuated by interstellar lines is plotted in red. Prominent photospheric lines are identified. Identifications in brackets denote uncertain detections. Question marks indicate unidentified photospheric lines.

observed at 1178 and 1198 Å. We adopt $\log g = 7.4 \pm 0.5$, with a conservative error estimate.

We then explored how the metal lines depend on different values of the H/He ratio, which remains undetermined at the moment. The reduction of helium from the assumed solar value down to 1.3×10^{-5} (mass fraction) is affecting the UV metal line strengths only marginally. The increase of helium to 98 % is slightly shifting the ionization balance of metals to lower stages such that an increase of T_{eff} by about 5000 K would be necessary to match the observed line strengths. Therefore, within error ranges, the measured metal abundances do not depend on the assumed H/He ratio and hold irrespective of whether the star is a DA or a DO white dwarf.

2.2. Metal abundances

We present in detail how elemental abundances were inferred. The employed lines are identified in Fig. 1. The resulting abundance values are listed in Table 1.

2.2.1. CNO

Three C IV multiplets are detectable and were fit, namely 3d–4f, 3d–4p, and 3p–4s, at 1169, 1198, and 1230 Å, respectively. It is worthwhile to note that two other, more highly excited, C IV multiplets are not detectable: 4p–7d at 1316 Å and the blend of 4d–7f and 4f–7g at 1351 and 1353 Å. They serve to constrain the

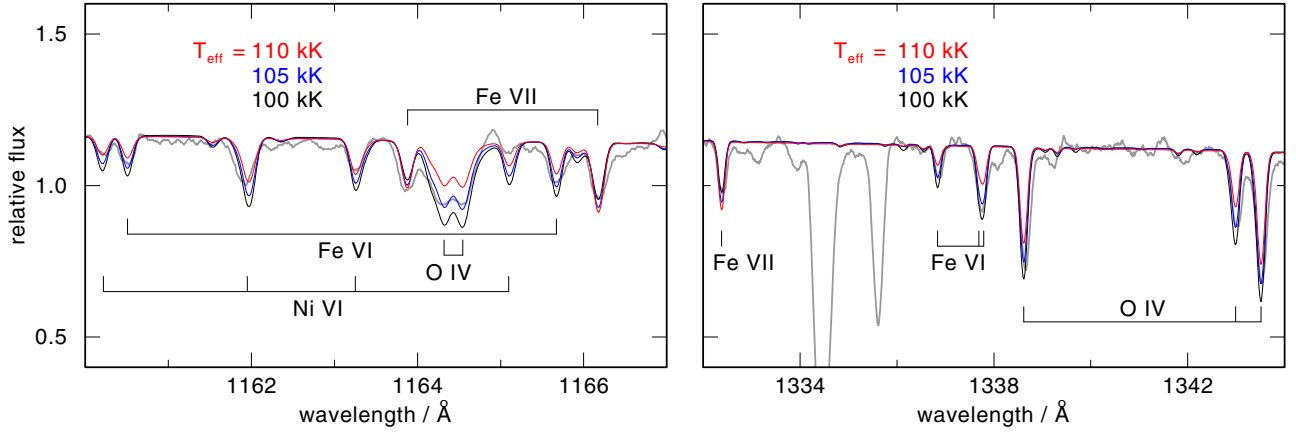


Fig. 2. Details of observed WD spectrum compared with three models with different temperatures ($T_{\text{eff}} = 105\,000 \pm 5000$ K) representing the error range in determination of T_{eff} . *Left:* O IV multiplet gets weaker with increasing T_{eff} , as well as lines from Fe VI and Ni VI, while Fe VII lines get stronger. *Right:* same behavior of oxygen and iron lines in another wavelength range.

Table 1. Atmospheric parameters of the WD in UCAC2 46706450.

T_{eff} (K)	105 000 \pm 5000	
$\log(g)$ (cm s^{-2})	7.4 \pm 0.5	
Abundance	X_i	$[X_i]$
C	2.0×10^{-3}	-0.07
N	2.0×10^{-3}	0.46
O	5.0×10^{-3}	-0.06
F	$< 5.0 \times 10^{-7}$	< 0.16
Si	8.0×10^{-4}	0.08
S	3.1×10^{-4}	0.00
Cr	8.0×10^{-5}	0.70
Mn	3.0×10^{-5}	0.45
Fe	3.5×10^{-3}	0.46
Co	$< 3.0 \times 10^{-5}$	< 0.91
Ni	3.0×10^{-4}	0.64

Notes. Abundances given in mass fractions (Col. 2) and logarithmic abundances relative to solar value (Col. 3; solar abundances from [Asplund et al. 2009](#)). Error limits for the abundances are ± 0.5 dex.

upper limit on the C abundance and the lower limit on surface gravity (see Sect. 2.1).

Besides the strong N V resonance doublet, we observe a weak and highly excited N V multiplet (4s–5p) at 1390 Å, and several N IV lines. There is a singlet at 1188 Å ($^1S-^1P^o$), which, however, is blended by a Ni VI line and a multiplet at 1196 Å ($^3D-^3P^o$). A triplet appears at 1271 Å ($^3P^o-^3D$), but two components are blended by Fe VI lines.

Two prominent O IV multiplets are detected, namely a blend of components at 1164 Å ($^2D-^2F^o$) and the three components of the $^2P-^2D^o$ transition at 1338.6 Å, 1343.0 Å, and 1343.5 Å. We also detect several O V lines: the prominent O V 1371 Å, the $^1D-^1D^o$ singlet at 1219 Å, and an accumulation of weak lines in the region 1418–1426 Å, which stem from the transitions $^3P^o-^3D$ and $^3D-^3F^o$.

2.2.2. Light metals: F, Si, and S

We detect a very weak feature at the position of the F VI 1139.5 Å line, which is often observed in hot WDs (e.g., EGB 6, [Werner](#)

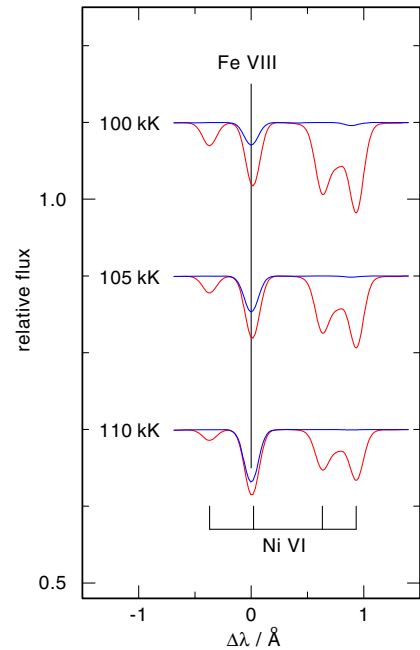


Fig. 3. Effect of increasing temperature on the Ni VI/Fe VIII line blend at 1148.2 Å ($T_{\text{eff}} = 100, 105,$ and 110 kK, from top to bottom). Blue graphs show spectra computed without Ni lines, that is to say, we only see the Fe VIII line profile. The nickel lines become weaker and the iron line becomes stronger. As a result, the line Fe+Ni blend stays almost constant. The models have abundances of $\text{Fe} = 3.5 \times 10^{-3}$ and $\text{Ni} = 3.0 \times 10^{-4}$ by mass.

[et al. 2018b](#)). It can be fit with a solar fluorine abundance, however, this result is regarded as uncertain given the poor SNR at the blue edge of the COS spectrum. We therefore adopted the solar abundance as an upper limit.

Besides the Si IV resonance doublet at 1394/1402 Å, we detect two weak Si V lines at 1152.0 and 1251.4 Å, which are components of the $^3P^o-^3P$ and $^3P^o-^3D$ transitions, respectively. The Si IV doublet is blended by an ISM component that is blueshifted by -25 km s^{-1} relative to the photospheric one. A weak S VI line at 1419.7 Å is identified, which is the strongest of three components of the 4d–5p transition, allowing for a sulfur abundance measurement.

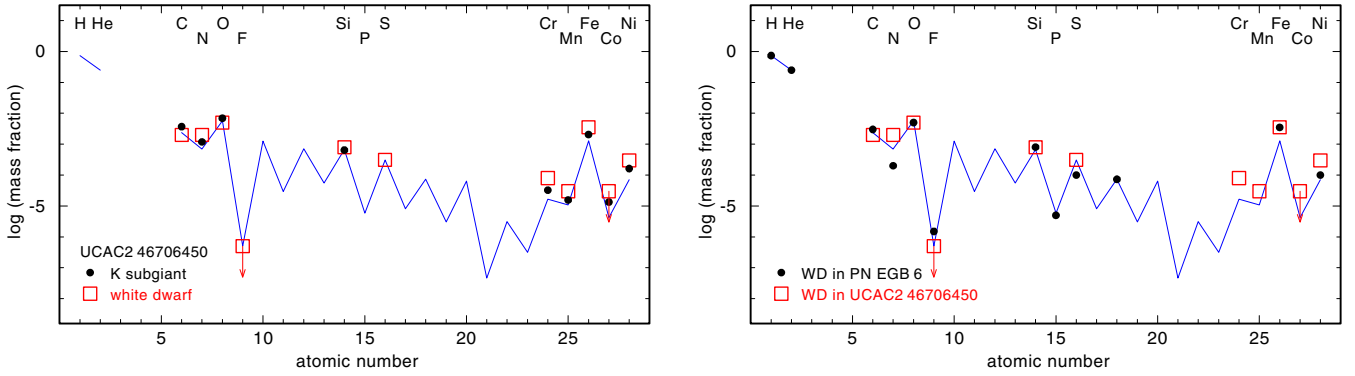


Fig. 4. *Left:* element abundances measured in the WD (red squares) and in the K subgiant (black dots) of the binary UCAC2 46706450. *Right:* abundances in the WD of UCAC2 46706450 (red squares), compared to the DAO WD in EGB 6 (black dots). The blue line indicates solar abundances.

2.2.3. Iron group elements: Cr, Mn, Fe, Co, and Ni

A line of Cr VI is visible at 1417.7 Å. Another one, at 1261.1 Å, is a blend with an Fe VI line. A third one is seen at 1255.8 Å, but this is blended with a broad, unidentified feature. Five weak Mn VI lines are detected at 1333.9, 1345.5, 1356.9, 1391.2, and 1396.7 Å.

As mentioned previously, we identified iron lines from Fe VI–VIII. Care must be taken when using the only Fe VIII line (at 1148.2 Å) as a temperature indicator (Fig. 3). Its strength increases with T_{eff} , but there is a blending Ni VI line whose strength decreases with T_{eff} . In effect, the line blend stays constant in the temperature regime discussed here. We do not see lines of Fe V. Some of the Fe V lines that we see in models at slightly lower temperature in the wavelength region of 1373–1414 Å are indicated in Fig. 1.

Our models predict many Co VI lines, mainly in the short-wavelength range of the COS spectrum, provided the cobalt abundance is high enough. We do not detect any such line and derive an upper abundance limit.

Many Ni VI lines are found, mainly in the short wavelength region up to about 1210 Å. Similarly to iron, Ni V lines are absent due to the high effective temperature.

2.2.4. Unidentified lines

A number of photospheric lines remain unidentified. The strongest appear at these wavelengths: 1173.6, 1191.0, 1195.7, 1236.4, 1246.2, 1256.3, 1266.9, 1298.3, 1332.8, 1345.5, and 1355.7 Å. These are indicated in Fig. 1 with a question mark. We also found these lines in other hot WDs or central stars of planetary nebulae (PNe) and suspect that some of them could be unknown Fe VII lines.

2.2.5. Summary of abundance analysis of the WD

Within error limits, the abundances of light metals are solar (Table 1, Fig. 4). For the iron-group elements a slight enhancement (0.45–0.70 dex oversolar) is found. This overabundance might point to radiative acceleration acting in the atmosphere, but we report below that the K subgiant also exhibits an overabundance of these elements (left panel of Fig. 4). Hence, the element abundance pattern probably reflects the initial metallicity of both stars. In the right panel of Fig. 4, we compare the abundances found for UCAC2 46706450–B with those of the WD central star of the PN EGB 6, which has the same T_{eff} and

$\log g$ (Werner et al. 2018b). Apart from nitrogen, the abundance patterns are rather similar.

3. Optical and IR spectroscopy of the K star

Subgiant UCAC2 46706450–A dominates the flux in the optical and infrared (IR) wavelength range. Optical spectroscopy ($\lambda \approx 3700$ – 9000 Å) of the system was obtained in course of the LAMOST survey (resolving power $R \approx 1800$). Furthermore, moderately high-resolution ($R \approx 22\,500$) IR ($\lambda \approx 15\,100$ – $17\,000$ Å) spectroscopy was obtained with the Apache Point Observatory Galactic Evolution Experiment (APOGEE; Majewski et al. 2017). In the course of the *Gaia* mission, a medium-resolution ($R \approx 11\,700$) spectrum over the wavelength range 8450–8720 Å (around the Ca II triplet) was collected with the Radial Velocity Spectrometer.

Additional follow-up spectroscopy were obtained at the 5.1-m Palomar Hale telescope in California, USA, and the Thai National Telescope (TNT) at the National Observatory in Thailand. One spectrum was obtained at the Palomar Hale Telescope during the night of the Jan. 20, 2014. We used the double spectrograph together with the 1200 lines/mm grating in the red and the 600 lines/mm grating in the blue. The observations were carried out using the long slit with 1'' width. This configuration resulted in a wavelength coverage of ≈ 7600 – 9300 Å in the red and ≈ 3500 – 6500 Å in the blue at $R = 6400$ and $R = 1400$, respectively. The spectrum was reduced and calibrated using the pamela (Marsh 1989) and molly² softwares, respectively. Thirteen additional spectra were obtained during the 2015–2017 period at the TNT using the Middle Resolution fiber-fed Echelle Spectrograph (MRES). The spectra covered the ≈ 4300 – 8800 Å wavelength range at $R = 15\,000$. The spectra were reduced and calibrated using the DECH software package.

The two LAMOST spectra from data release 2 (DR2) were analyzed by Luo et al. (2016), who derived T_{eff} , $\log g$, $[\text{Fe}/\text{H}]$, as well as the RV values from the individual observations. These spectra were also analyzed by Ho et al. (2017), who provide results for T_{eff} , $\log g$, $[\text{Fe}/\text{H}]$, as well as the α -enhancement $[\alpha/\text{M}]$. Two additional LAMOST spectra were obtained within the DR5 that were analyzed (along with the previous spectra) by Luo et al. (2019). Abundances of several elements (C, Cl, N, O, Mg, Al, Si, P, K, Ca, Ti, V, Cr, Mn, Fe, Co, Ni, and Rb), T_{eff} ,

² Tom Marsh’s molly package is available at <http://deneb.astro.warwick.ac.uk/phsaap/software>

Table 2. Atmospheric parameters, masses as obtained from evolutionary calculations, and radii and luminosities of the subgiant UCAC2 46706450–A and the white dwarf UCAC2 46706450–B.

	UCAC2 46706450–A	UCAC2 46706450–B
T_{eff} (K)	4945 ± 250	$105\,000 \pm 5000$
$\log g$ (cm s^{-2})	3.04 ± 0.25	7.4 ± 0.5
M / M_{\odot}	0.8–2.4	0.54 ± 0.02
R / R_{\odot}	$5.9^{+0.7}_{-0.5}$	$0.040^{+0.005}_{-0.004}$
L / L_{\odot}	19^{+5}_{-5}	176^{+55}_{-49}

$\log g$, and RV from the APOGEE spectrum are provided by the APOGEE Stellar Parameter and Chemical Abundances Pipeline (ASPCAP, García Pérez et al. 2016). Some of these element abundances relevant for the comparison with the WD companion are depicted in the left panel of Fig. 4. The iron-group elements are slightly enhanced, by 0.2–0.5 dex. An interesting point to notice is that ASPCAP predicts an unusually high rotational velocity of $v \sin(i) = 80.76 \text{ km s}^{-1}$. Atmospheric parameters from the APOGEE spectrum were also derived with the data driven method called the Cannon (Ness et al. 2015; Casey et al. 2016). However, the χ^2 of the Cannon fit is quite large, indicating that the parameters and abundances are not reliable, and thus we did not consider these values further. Finally, the *Gaia* DR2 also provides values for T_{eff} and RV.

In Table 2, we provide the average of the T_{eff} and $\log g$ values derived by the various analyses and give an estimate of the error, which also includes the systematic error (estimated from the scatter of the results from the individual analyses). We note that the fits to the optical spectrum do not consider the contribution of the flux of the WD to the blue part of the spectrum. On the other hand, values from the fit to the LAMOST spectrum do not differ too much from what is obtained from the APOGEE and *Gaia* spectra.

A closer inspection of the LAMOST spectra reveals that the line cores of the Ca II H and K doublet (Fig. 5) appear in emission. The double-peaked H α emission (also seen in the TNT spectra, Fig. 6), can be explained by the superposition of a very broad emission line plus a photospheric absorption line. The strength of these emission lines is found to be time variable. Emissions in these lines are typical for chromospherically active stars (Wilson 1963, 1968; Gray & Corbally 2009).

4. Radial velocity variability

The scatter of the RV values from the three individual APOGEE spectra (which were all obtained within one month) is smaller than 1 km s^{-1} , which already indicates that the system is very likely not a close binary. We also searched for RV variations using the values we measured from the LAMOST, Palomar, and TNT spectra, as well as those provided in the catalogs for the APOGEE and *Gaia* spectra (total time coverage is about four years, see Table 3). In order to check if the RV variations are significant or are merely produced by random fluctuations, we followed the approach as outlined in Maxted et al. (2001) and Geier et al. (2015). For this, we calculated the inverse-variance weighted mean velocity from all RV measurements. Assuming this mean velocity to be constant, we calculated the χ^2 . Comparing this value with the χ^2 distribution for the appropriate number of degrees of freedom, the probability p of obtaining

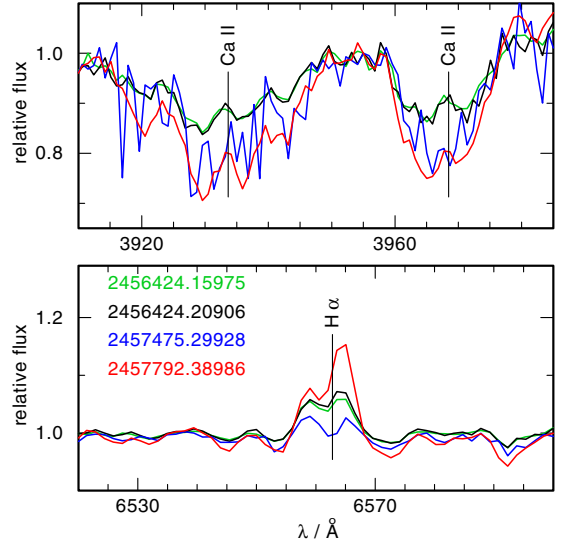


Fig. 5. Time-variable emission line cores in the Ca II H and K doublet and H α emission observed in the LAMOST spectra indicate that UCAC2 46706450–A is chromospherically active. The HJD of the observations is provided.

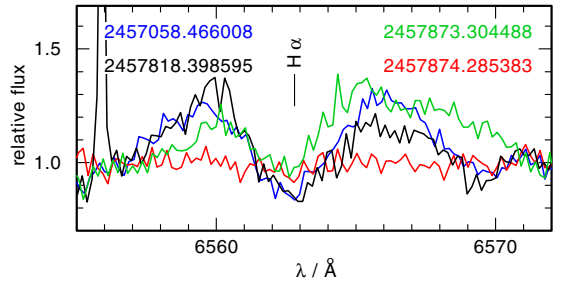


Fig. 6. Time-variable H α emission observed in TNT spectra indicate that UCAC2 46706450–A is chromospherically active. The HJD of the observations is provided.

Table 3. HJD and radial velocities of UCAC2 46706450–A as measured from the different spectra.

HJD	v_{rad} (km s^{-1})	survey
2 456 424.148720	-22.0 ± 10.6	LAMOST
2 456 424.160200	-23.7 ± 10.6	LAMOST
2 456 424.171710	-21.6 ± 10.6	LAMOST
2 456 424.190910	-22.9 ± 10.5	LAMOST
2 456 424.210070	-20.3 ± 10.5	LAMOST
2 456 424.228520	-18.6 ± 10.6	LAMOST
2 456 678.061937	-21.9 ± 6.0	Palomar
2 456 709.957320	-18.81318 ± 0.15	APOGEE
2 456 717.996280	-17.94056 ± 0.12	APOGEE
2 456 735.937290	-19.22651 ± 0.17	APOGEE
2 457 058.466008	-27.2 ± 3.4	TNT
2 457 475.290870	-26.0 ± 10.4	LAMOST
2 457 475.300180	-26.0 ± 10.4	LAMOST
2 457 475.309490	-21.5 ± 10.5	LAMOST
2 457 792.389120	-31.5 ± 13.2	LAMOST
2 457 817.394727	-33.1 ± 3.4	TNT
2 457 818.398595	-21.0 ± 3.4	TNT
2 457 819.380124	-18.1 ± 4.1	TNT
2 457 819.400669	-30.3 ± 7.3	TNT

the observed value of χ^2 or higher from random fluctuations around a constant value can be calculated. We obtain a value of $\log p = -1.8$, and hence conclude that UCAC2 46706450–A is not significantly RV variable and very likely not a close binary.³

It is worth mentioning that [Rebassa-Mansergas et al. \(2017\)](#) claimed UCAC2 46706450–A to be RV variable. They obtained the RV values by fitting the Na I absorption doublet at around 5900 Å. However, revising these fits, we realized that some of the RVs they used were affected by embedded emission (likely resulting from the night sky) and are hence not reliable. By excluding these RV values, UCAC2 46706450–A does not show RV variation, in agreement with the results obtained here.

The WD spectrum is blueshifted by $-10 \pm 8 \text{ km s}^{-1}$. Considering the gravitational redshift of $v_{\text{grav}} = 8.6 \pm 1.3 \text{ km s}^{-1}$ gives a RV value for the WD of $v_{\text{rad}} = -18.6 \pm 8.1 \text{ km s}^{-1}$ (calculated using the mass and radius from Sect. 6). This agrees very well with the most precisely measured RV value of the K star ($v_{\text{rad}} = -18.35 \pm 0.07 \text{ km s}^{-1}$ from ASPCAP) and can be seen as a first hint that the system is indeed a physically connected binary and that the velocities of both stars represent the system velocity.

We stress, however, that with the current set of RV measurements we are only able to detect RV amplitudes larger than $\approx 15 \text{ km s}^{-1}$, and that in case of a low inclination angle or a long orbital period, the amplitude can be much smaller than this.

5. Distance and Galactic population membership

The distance of UCAC2 46706450–A (the dominant source in the optical) based on the *Gaia* DR2 parallax is provided in the [Bailer-Jones et al. \(2018\)](#) catalog and amounts to $d = 1417_{-43}^{+45} \text{ pc}$. From this we calculate a height above the Galactic plane of $z = 1154_{-35}^{+36} \text{ pc}$, that is to say we find that it lies in a region where the thick disk dominates.

The Galactic population membership of UCAC2 46706450 can be further constrained by looking at the chemistry of UCAC2 46706450–A, as well as the kinematics of the system. Both thick disk and thin disk stars are observed over a wide metallicity range ([Fe/H] between -0.8 and 0.2 dex, [Kordopatis et al. 2015](#)), but thick disk stars are found to be more α -rich at a given metallicity compared to thin disk stars (e.g., [Fuhrmann 1998](#); [Recio-Blanco et al. 2014](#)). At metallicities above [Fe/H] = 0.1 dex, the separation of the two populations is, however, unclear (e.g., [Hayden et al. 2017](#)). At the average values [Fe/H] = 0.09 dex (standard deviation 0.10 dex) and [α /M] = 0.02 dex (standard deviation 0.07 dex) reported for UCAC2 46706450–A in the LAMOST and ASPCAP catalogs, the star appears just on the borderline between the two populations (see, e.g., Fig. 1 in [Hayden et al. 2017](#)). Therefore, it is worth also looking at the kinematics of the system. Since LAMOST, APOGEE, TNT, Palomar, *Gaia*, and HST/COS spectra do not indicate significant RV variations, we adopt the mean RV (-21.95 ± 4.55 , where the error represents the standard deviation of the individual measurements) as system velocity. With this and the proper motion and parallax from the *Gaia* DR2, we calculate space velocities of $U = 46.4 \pm 1.0 \text{ km s}^{-1}$, $V = -21.8 \pm 2.5 \text{ km s}^{-1}$, and $W = -23.6 \pm 3.7 \text{ km s}^{-1}$ ⁴. The kinematic Galactic population membership can then be derived on the basis of the Mahalanobis distance, which is the

³ [Geier et al. \(2015\)](#) considered objects with $\log p > 4.0$ as significantly variable, and objects with $-1.3 > \log p > -4.0$ as possibly variable.

⁴ Cardinal directions, with U being positive toward the Galactic center. Values have been adjusted for the Solar motion using the numbers of [Tian et al. \(2015\)](#).

number of standard deviations between the space velocities of UCAC2 46706450 and the velocity ellipsoids of the thin disk, thick disk, and the halo ([Gianninas et al. 2015](#)). Using the velocity ellipsoid values from [Kordopatis et al. \(2011\)](#), we find that the kinematics of UCAC2 46706450 clearly point to membership of the thick disk. A final, and probably most decisive, criterion that can be used to determine the Galactic population membership is the age of the system, and this is discussed further in the next section.

6. Radii, luminosities, masses, and ages

In order to determine the radii of the two stellar components, we performed a fit to the spectral energy distribution (SED), by varying their solid angles $\pi(R/d)^2$ (which relates the astrophysical flux on the surface of the stars to what is received on Earth) until a good agreement of the combined synthetic flux and the observations was found. We assumed a reddening of $E_{B-V} = 0.03$ (see Sect. 2) and the distance provided by [Bailer-Jones et al. \(2018\)](#) based on the *Gaia* parallax. For UCAC2 46706450–B, we used our best fit model from Sect. 2. For UCAC2 46706450–A, we used a NextGen model ([Allard et al. 2012](#)) with $T_{\text{eff}} = 4950 \text{ K}$, $\log g = 3.0$, and a metallicity of [Fe/H] = 0 dex, which is close to the average values of the derived parameters from various analyses. The errors on the radii were determined taking into account the uncertainties of the effective temperatures and the distance given by [Bailer-Jones et al. \(2018\)](#).

Our best fit is shown in Fig. 7. The black dots indicate filter-averaged fluxes that were converted from observed magnitudes. GALEX *FUV* and *NUV* magnitudes were taken from [Bianchi et al. \(2014\)](#) and converted to fluxes as outlined in [Reindl et al. \(2016\)](#). *B*, *V*, *g*, *r*, and *i* magnitudes were taken from [Henden et al. \(2015\)](#), 2MASS *J*, *H*, and *K* magnitudes from [Cutri et al. \(2003\)](#). To convert these magnitudes into fluxes, we used the zero-points provided in [Holberg & Bergeron \(2006\)](#). Wide-field Infrared Survey Explorer (WISE) *W1*, *W2*, *W3*, and *W4* magnitudes were taken from [Cutri et al. \(2003\)](#) and converted to fluxes using the zero-points and the flux corrections for a K2V star provided in [Wright et al. \(2010\)](#). The light blue, green, and red lines in Fig. 7 indicate the SEDs of UCAC2 46706450–B, UCAC2 46706450–A, and the combined best fit model, respectively. All model fluxes are corrected for interstellar reddening, using the reddening law of [Fitzpatrick \(1999\)](#) with $E_{B-V} = 0.03$. The gray lines in Fig. 7 correspond to the HST/COS, co-added LAMOST, and APOGEE spectra. Overall, the combined model flux reproduces the observed SED well. Only the observed *NUV* flux exceeds the predicted flux by about 0.1 dex. We attribute this to the chromospheric flux of the K-type star, as chromospheric fluxes are known to exceed the photospheric flux by several orders of magnitude in chromospherically active stars ([Stelzer et al. 2013, 2016](#); [Dixon et al. 2020](#)). Based on the *NUV* excess of 0.1 dex, we estimate that chromospheric flux of the K-type star exceeds its photospheric flux by about two orders of magnitude and which is also what is found for other such rapidly rotating and chromospherically active giants ([Dixon et al. 2020](#)). The WISE *W3* and *W4* fluxes also indicate a slight excess, but these bands are in particular sensitive to the flux corrections (gray open circles in Fig. 7 indicate WISE fluxes for which the flux correction was not taken into account). Thus, we regard the far-IR excess as uncertain.

For UCAC2 46706450–A, we derive a radius of $R_A = 5.9_{-0.5}^{+0.7} R_{\odot}$, and for the hot WD, $R_B = 0.040_{-0.004}^{+0.005} R_{\odot}$. Using $L = 4\pi\sigma R_{\text{eff}}^2 T_{\text{eff}}^4$, where σ is the Stefan-Boltzmann constant, we

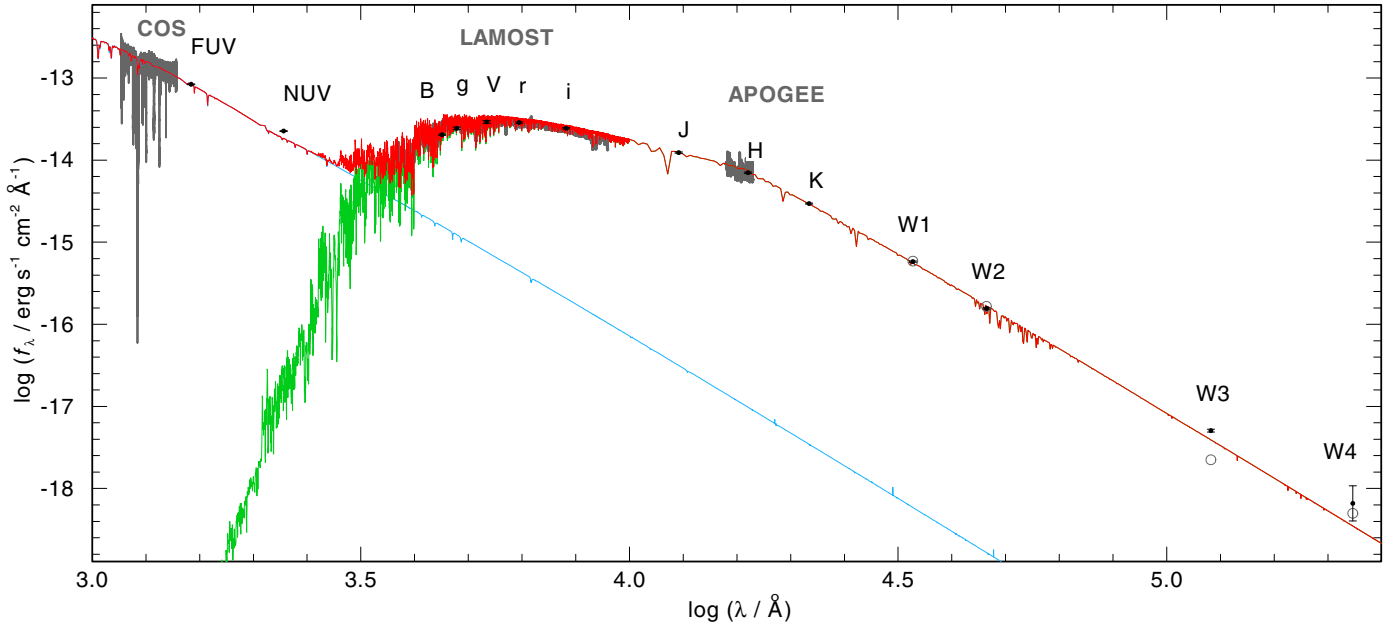


Fig. 7. Fit to the SED of UCAC2 46706450. HST/COS, LAMOST (normalized to r -band magnitude), and APOGEE spectra are shown in gray. The model fluxes from the hot WD and the K-type subgiant are shown in light blue and green, respectively. The combined model flux is shown in red. The black dots indicate filter-averaged fluxes that were converted from observed magnitudes. Gray open circles indicate WISE fluxes for which the flux correction was not taken into account.

calculate luminosities of $L_A = 19^{+5}_{-5} L_\odot$ and $L_B = 176^{+55}_{-49} L_\odot$ for UCAC2 46706450–A and UCAC2 46706450–B, respectively. These values are what is expected for a subgiant star and a hot WD that is just about to enter the WD cooling sequence. Hence, we conclude that the system is indeed a physical binary.

With the spectroscopically determined surface gravities (average value for the K star from Table 2) and using $M = gR^2/G$, where G is the gravitational constant, we calculate masses of $M_A = 1.4^{+1.2}_{-0.7} M_\odot$ and $M_B = 1.5^{+4.4}_{-1.1} M_\odot$ for the K-type subgiant and the hot WD, respectively. We note that the large errors on the masses are mainly a consequence of large uncertainties of the surface gravities of both stars. The masses can be constrained more precisely when we compare their locations in the Hertzsprung Russell diagram (HRD) with predictions from stellar evolutionary calculations. But this mass determination also has its limitations, as is outlined in the following. In the upper panel of Fig. 8, we show the location of UCAC2 46706450–A in the HRD compared to stellar evolutionary tracks of Pietrinferni et al. (2004). The tracks are calculated for $Z = 0.01$ ($[Fe/H] = 0-0.25$ dex) and a helium mass fraction of 0.259 (upper panel in Fig. 8) and suggest a mass of $M_A = 1.2^{+0.7}_{-0.4} M_\odot$. In the lower panel of Fig. 8, we show the evolutionary tracks of Pietrinferni et al. (2004), which were calculated for a slightly higher metallicity of $Z = 0.03$ ($[Fe/H] = 0.26$ dex) and a helium mass fraction of 0.288. These tracks are shifted toward higher effective temperatures, and thus suggest a higher mass of $M_A = 1.9^{+0.5}_{-0.9} M_\odot$. This shows that the mass of the K-type subgiant obtained from the HRD depends significantly on the chemistry used in the evolutionary calculations. We therefore infer a possible mass range of $M_A = 0.8-2.4 M_\odot$ based on these evolutionary models.

In Fig. 9, we show the location of UCAC2 46706450–B in the HRD compared to evolutionary calculations of H-shell burning post-asymptotic giant branch (AGB) stars from Miller Bertolami (2016). This suggests a mass of $M_B = 0.54 \pm 0.02 M_\odot$ and that the surface gravity of the WD might be rather at

the lower boundary of the error margin ($\log g = 7.0 \pm 0.1$) determined spectroscopically. In gray, a He-shell burning very late thermal pulse (VLTP) evolutionary track is shown. This track extends toward higher T_{eff} at the luminosity found for UCAC2 46706450–B, which supports the assumption that the WD is indeed H-rich (higher envelope mass; much lower mass not possible due to the limited age of the disk/Milky Way). In Fig. 9, we also indicate the initial masses assumed for the computation of the evolutionary tracks. This suggests that if the initial-to-final mass relation (IFMR) assumed in these calculations are accurate and the system has not interacted in previous evolutionary phases, the initial mass of the hot WD was about $1 M_\odot$, or only slightly higher. A low mass of the WD is also supported by the absence of a PN. The tracks of Miller Bertolami (2016) calculated for $Z = 0.01$ predict a post-AGB age of about 72 kyrs for the $0.52 M_\odot$ model and only about 10 kyrs for the $0.56 M_\odot$ ($Z = 0.01$) model. This means that if UCAC2 46706450–B should have ejected a PN on the AGB, and we assume that a PN is typically visible for 30 kyrs, then, in the case of a low mass post-AGB star, the PN should have faded away already, while for higher masses, the PN should still be visible. Radii, luminosities, and masses of UCAC2 46706450–A and UCAC2 46706450–B are summarized in Table 2.

If we assume again that the system has not undergone mass transfer in its past and the initial mass of the WD was between 1.0 and $1.25 M_\odot$, this would imply that the initial mass of UCAC2 46706450–A is only slightly lower than this. The total lifetime of stars in that mass range at solar metallicity stated by Miller Bertolami (2016) lies between 5.3 and 12.5 Gyrs. Thus, it is entirely possible that the system indeed belongs to the thick disk, which is generally found to be exclusively old, meaning older than nine Gyrs (Feltzing & Bensby 2009; Kilic et al. 2017; Hayden et al. 2017). We also note that in the course of their study of main-sequence turnoff and subgiant stars from the AMBRE:HARPS survey, Hayden et al. (2017) find stars at the metallicity of UCAC2 46706450–A that have ages between

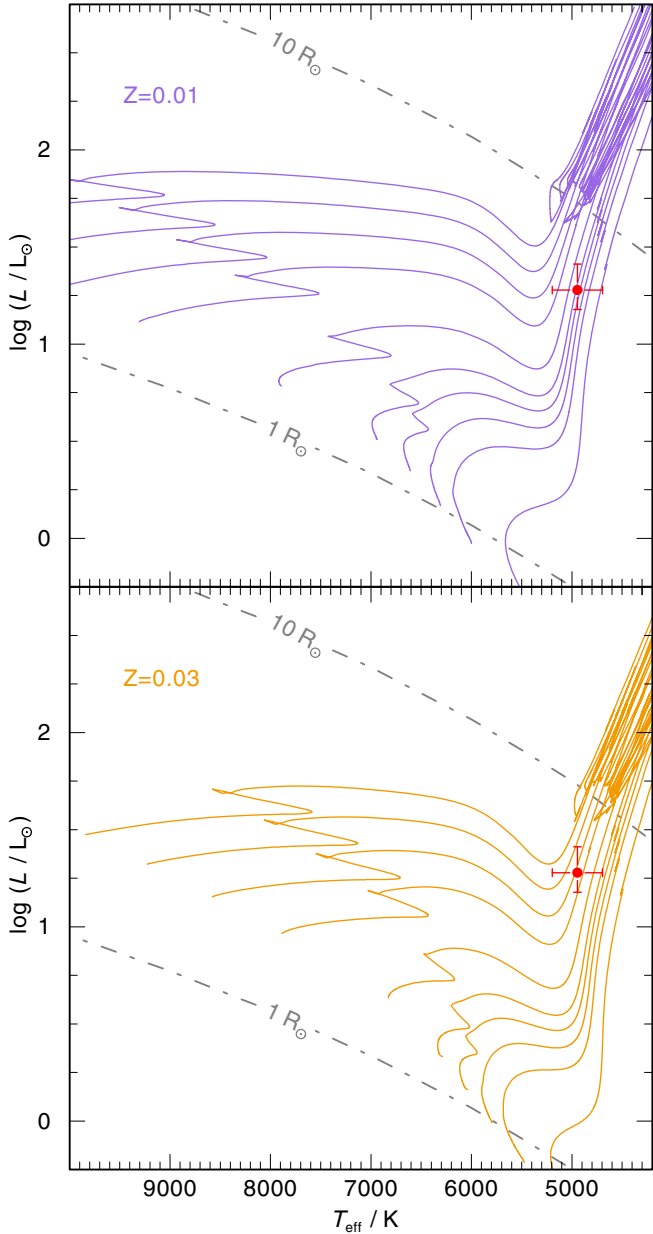


Fig. 8. Location of UCAC2 46706450–A (red) in the HRD compared to stellar evolutionary tracks of Pietrinferni et al. (2004) for initial masses of 0.8, 1.0, 1.1, 1.2, 1.3, 1.5, 1.8, 2.0, 2.2, and $2.4 M_{\odot}$. *Upper panel:* evolutionary tracks calculated for $Z=0.01$ ($[\text{Fe}/\text{H}]=0.25$ dex) and a He mass fraction of 0.259. *Lower panel:* tracks calculated for $Z=0.03$ ($[\text{Fe}/\text{H}]=0.26$ dex) and a He mass fraction of 0.288. The gray dashed-dotted lines indicate radii of 1 and $10 R_{\odot}$.

8 and 10 Gyrs. However, since the IFMR is poorly constrained at the low-mass end, and mass loss on the RGB is not well understood, it is not possible to give a more precise estimate of the system’s age.

7. Light curve variability

We obtained the Catalina Sky Survey (CSS, Drake et al. 2009) DR2 V -band light curve of UCAC2 46706450 as well as c - and o -band light curves (effective wavelengths 0.53 and $0.68 \mu\text{m}$, respectively) from the Asteroid Terrestrial-impact Last Alert System (ATLAS, Tonry et al. 2018) DR1 (Fig. 10).

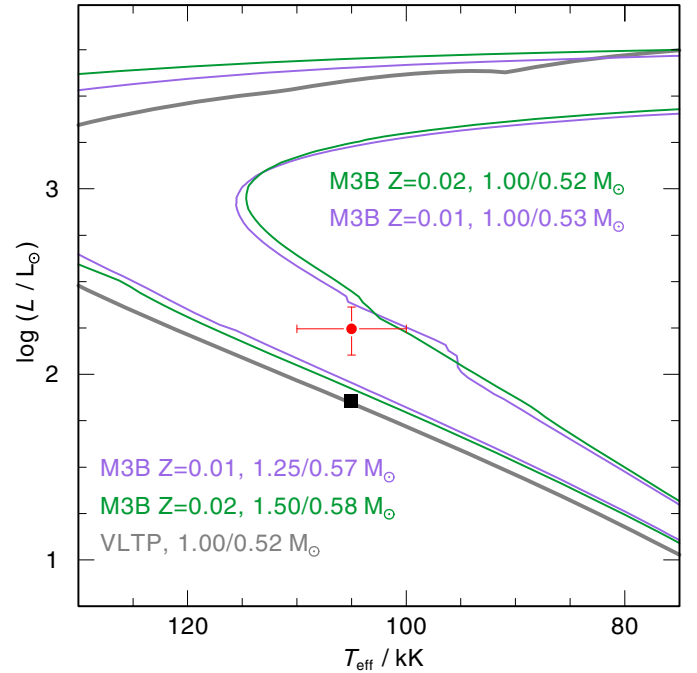


Fig. 9. Location of UCAC2 46706450–B (red) in the HRD compared to stellar evolutionary tracks of Miller Bertolami (2016) calculated for $Z=0.01$ (purple) and $Z=0.02$ (green). Initial and final masses of the tracks are indicated. Shown in gray is a VLTP evolutionary track. The black square indicates the position of EGB 6.

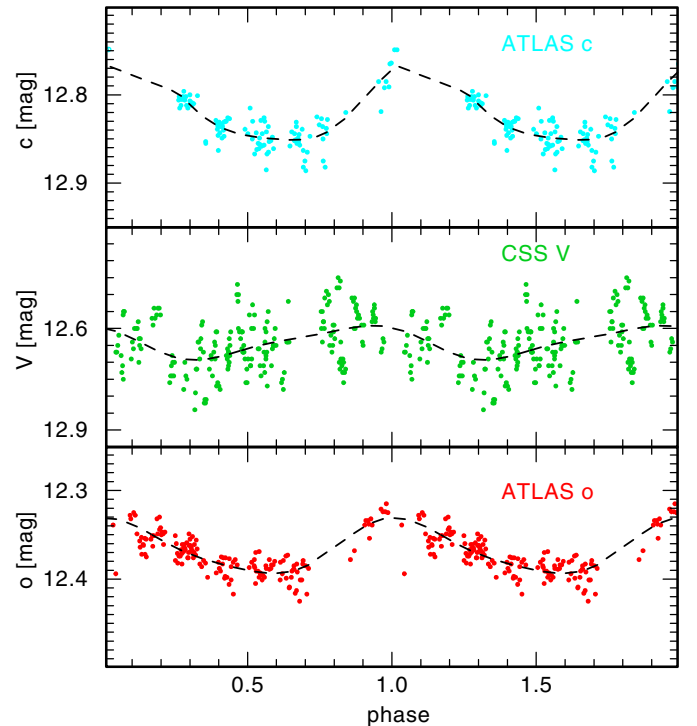


Fig. 10. ATLAS c -band, CSS V -band, and ATLAS o -band phase-folded light curves. The CSS light curve is folded with the 1.97861678 d period.

We also observed the light curve of UCAC2 46706450 in the V -band using the Tübingen 80 cm $f/8$ telescope on April 14, 15, and 16 (Fig. 11). The images were taken with an integration time of 120 s using a SBIG STL-1001 CCD camera and a binning of 2×2 pixels. Almost every night, data could be obtained

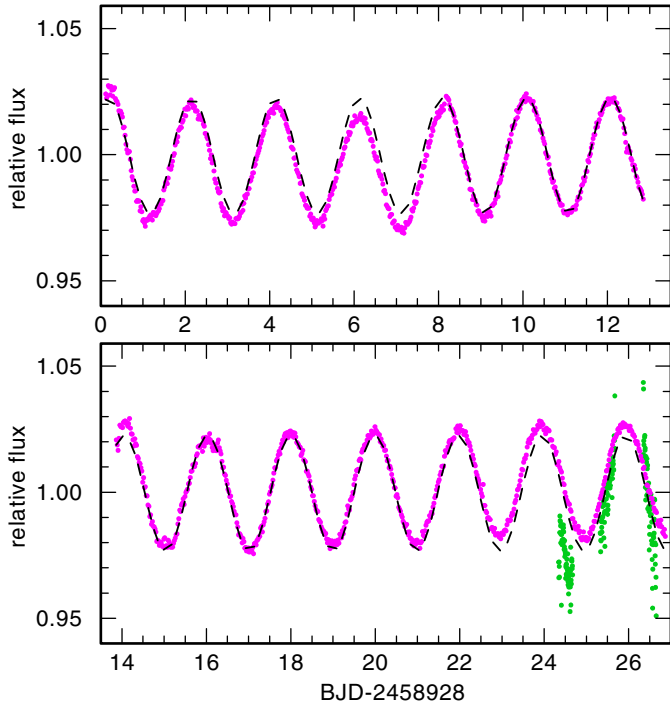


Fig. 11. TESS (magenta) and Tübingen 80 cm telescope V-band (green) light curves. The V-band light curve has been shifted by one period.

over seven hours. The sky was clear during the first two nights, whereas thin cirrus was passing throughout the third night. All images were background and flatfield corrected using the IDL software Time Resolved Imaging Photometry Package (TRIPP, Schuh et al. 2003), which was also used to perform aperture photometry. The flux error was minimized by testing different aperture radii with respect to comparison star variances. We note that the data were obtained under non-photometric conditions, with the weather conditions being worst in the third night. As there is only one equally bright star in the field of view, we used only one comparison star for the first and third nights. During the second night, the observing conditions were best, so a second comparison star could be used.

In addition, we used Transiting Exoplanet Survey Satellite (TESS) observations of UCAC246706450 (Fig. 11). The star was in the TESS field of view during Sector 23 observations. As there is no 2-min cadence light curve available, we performed photometry using the 30-min cadence full-frame images (FFIs) using LIGHTKURVE (Lightkurve Collaboration 2018). We used a relatively small 4×4 pixel aperture to minimize contamination from two nearby stars, and subtracted a background estimated using the same aperture on a nearby region with no sources.

For the analyses of the light curves, we used the VARTOOLS program (Hartman & Bakos 2016) to perform a generalized Lomb-Scargle search (Zechmeister & Kürster 2009; Press et al. 1992) for periodic sinusoidal signals. For the ATLAS *c*- and *o*-bands, we find the strongest signal at $P = 1.97913923$ d and $P = 1.97899913$ d, with associated false alarm probabilities (FAPs) of 10^{-37} and 10^{-28} , respectively. The derived period from the *o*-band equals exactly half the period given in Heinze et al. (2018), who classified the light curve of UCAC246706450 as an irregular variable. This class serves in their catalog as a “catch-all” bin for objects that do not seem to fit into any of their more specific categories. We also performed a generalized Lomb-Scargle search on the CSS light curve, and find

the strongest signal at $P = 0.21064926$ d, which, however, has a much higher FAP of 10^{-13} . A possible explanation could be that UCAC246706450 is indeed an irregular variable and that its photometric period and amplitude change over time. Thus, in the much longer CSS light curve (time coverage ≈ 8 yr) no clean signal can be detected. Another point to notice for the CSS light curve is that during MJD = 53 550 and MJD = 53 901, UCAC246706450 underwent a brightness variation of 0.7 mag. Using only CSS data obtained after MJD = 54 000, we repeated the generalized Lomb-Scargle search by looking only for periods between 1.9 and 2.1 d. By that, we find a significant peak at $P = 1.97861678$ (FAP = 10^{-6}), close to the value found for the ATLAS light curves. In Fig. 10, we show the phase-folded ATLAS *c*- and *o*-band and CSS light curves. The black dashed lines are fits of a harmonic series to the phase-folded light curves (see Eq. (49) in Hartman & Bakos 2016) and predict peak-to-peak amplitudes of 0.08, 0.10, and 0.06 mag in the *V*-, *c*- and *o*-bands, respectively. We note, however, that due to the photometric uncertainties (0.05 mag for CSS, and 0.01 mag for the ATLAS light curves), the differences in the amplitudes might not be real.

For the TESS light curve, we derive a period of 1.98063847 d (FAP = 10^{-755}). The light curve is shown in Fig. 11 along with the V-band light curve obtained with the Tübingen 80 cm telescope, which is shifted for one period. We find that the phases of both light curves match nicely, though the amplitudes differ. We note, however, that the amplitudes of both should be treated with caution. As mentioned above, the Tübingen 80 cm telescope light curve was obtained under non-photometric conditions, and due to the large pixel-size of TESS two neighboring nearby stars may add additional continuum flux, which in turn may reduce the amplitude of the TESS light curve. What can also be seen in Fig. 11 is that the shape of the TESS light curve changes slightly, which is typical for star spot evolution (Kóvári et al. 2019).

If we assume the observed period of the light curve variation corresponds to an orbital period, and a mass of $0.54 M_{\odot}$ for the WD and $1.0 M_{\odot}$ of the K-type subgiant (Sect. 6), then we calculate via the third Kepler law, a separation of the two stars of $a = 7.7 R_{\odot}$. In that case, a strong reflection effect should be noticeable. In such systems, a tidally-locked cool companion is strongly irradiated by the hot primary, also causing sinusoidal light curve variations at the orbital period of the system. Then, however, the amplitudes of the light curve variations should be increasing toward longer wavelengths, which is not observed. In addition, we would expect to see all Balmer lines, the CNO line complex around 4560 \AA , and possibly also some other lines in emission. These two observational properties are seen in BEUMa, which also has a $T_{\text{eff}} = 105\,000$ K hot primary, an orbital period of 2.29 d, and a distance $a = 8.6 R_{\odot}$ from its cool companion (Ferguson & James 1994) and in many other reflection effect systems containing a very hot primary (e.g., Sing et al. 2004; Exter et al. 2005; Nagel et al. 2006; Shimansky et al. 2015; Mitrofanova et al. 2016).

Thus, we conclude that the variations are caused by spots on the surface of the star and that the photometric period corresponds to the rotational period of UCAC246706450–A. With a radius of $5.9_{-0.5}^{+0.7} R_{\odot}$ and rotation period of 1.98 d, we calculate a rotational velocity of $v_{\text{rot}} = 151_{-13}^{+18} \text{ km s}^{-1}$. If we assume that the mass is close to $1 M_{\odot}$ (Sect. 6), this value is close to the breakup velocity⁵. With $v \sin(i) = 80.76 \text{ km s}^{-1}$ as suggested

⁵ The breakup velocity $v_{\text{breakup}} = \sqrt{GM/R}$ of a $1.0/2.0 M_{\odot}$ star with a radius of $5.9 R_{\odot}$ is $180/254 \text{ km s}^{-1}$, respectively.

by the ASPCAP fit of the APOGEE spectrum, one can estimate that the inclination of rotational axis is $i = 32^\circ$.

If we assume a bound rotation (as seen in many RS CVn stars), that the inclination angle of the rotational axis is perpendicular to the orbital plane, and the masses given in Table 2, then RV semi-amplitudes of $58\text{--}105\text{ km s}^{-1}$ and $23\text{--}41\text{ km s}^{-1}$ would be expected for the WD and subgiant, respectively. The latter is much larger than the standard deviation of the individual RV measurements of UCAC2 46706450–A (4.55 km s^{-1} , see Sect. 5) and, thus, again speaks against a close binary system.

8. Conclusions

From the SED fit, the fact that we do not find significant RV variability, that the RVs of UCAC2 46706450–A and UCAC2 46706450–B agree, and that no reflection effect is noticeable in the light curves and spectra, we conclude the system is most likely a wide, physically connected binary system. UCAC2 46706450–A is a subgiant just about to climb up the RGB, while UCAC2 46706450–B is an extremely hot WD just about to enter the WD cooling sequence.

Kinematically, and from its height above the Galactic plane, the system belongs to the Galactic thick disk. This can also explain the low mass of the WD without the need for binary interactions, as the thick disk is generally found to contain exclusively old, and by that low-mass stars.

8.1. The white dwarf

We determined the atmospheric parameters of the hot WD in the binary UCAC2 46706450. Within error limits, the light metal (C, N, O, F, Si, S) abundances are solar, whereas iron-group elements (Cr, Mn, Fe, Ni) are slightly enhanced (0.45–0.70 dex oversolar). The H/He ratio cannot be determined from the available spectra. However, by comparison with another WD we can conclude that it is likely a DAO white dwarf. The effective temperature ($T_{\text{eff}} = 105\,000\text{ K}$) is the same as that of EGB 6, a DAO central star of a PN (Werner et al. 2018b). The metal abundance pattern of EGB 6 is very similar, and its H/He ratio is solar (Fig. 4, right panel). It was concluded that EGB 6 is at the wind limit of its cooling track, shortly before gravitational settling and radiative acceleration of elements begin to affect the photospheric abundance pattern. Before the wind limit, a radiation-driven wind prevents atomic diffusion (e.g., Unglaub & Bues 2000). Thus, UCAC2 46706450–B is probably a DAO white dwarf. The He abundance could be subsolar since the slightly oversolar heavy-metal abundances indicate that diffusion began to act. On the other hand, heavy-metal abundances in the K-type subgiant are also oversolar (Fig. 4, left panel), thus, the element abundance pattern probably reflects the initial metallicity of both stars. UCAC2 46706450–B could be just crossing the wind-limit. Observational evidence testifies that the wind limit for H-rich WDs is indeed located at $T_{\text{eff}} \approx 105\,000\text{ K}$ (Werner et al. 2018b, 2019) and recent theoretical work confirms this result (Krtićka et al. 2020).

We emphasize, however, that we cannot rule out that the WD is a helium-rich DO white dwarf. Before the wind limit, DOs can also exhibit a near-solar metal abundance pattern (Werner et al. 2017). To make a conclusive decision, an observation covering the position of He II 1640 Å is needed. We can exclude that the WD belongs to the non-DA PG1159 class whose members have very abundant C and O (Werner & Herwig 2006).

EGB 6 is slightly more massive ($M = 0.58^{+0.12}_{-0.04} M_{\odot}$, Fig. 9) than UCAC2 46706450–B ($M = 0.54 \pm 0.02 M_{\odot}$), and thus

EGB 6 evolved from the AGB to its current position more rapidly (post-AGB time is about $\log(t_{\text{evol}} \text{ yr}^{-1}) = 3.60^{+1.26}_{-0.09}$) than UCAC2 46706450–B ($\log(t_{\text{evol}} \text{ yr}^{-1}) \approx 4.86$). This might explain why for EGB 6 the PN is still visible, while for UCAC2 46706450–A no PN can be detected.

8.2. The K subgiant

We reported the discovery of a time-variable emission of H α as well as emission line cores in the Ca II H and K doublet, which is a strong hint to chromospheric activity. Further evidence for chromospheric activity can be seen from the NUV excess. Furthermore, we found that the object is photometrically variable with a period of $\approx 2\text{ d}$ only. The TESS light curve shows small variations in the shape of light curve. Hence, we conclude that the variations are caused by (evolving) spots on the surface of UCAC2 46706450–A. With the radius from the SED fit, we find that the star is rotating extremely fast with $v_{\text{rot}} = 151^{+18}_{-13} \text{ km s}^{-1}$. This marks UCAC2 46706450–A as one of the most rapidly rotating subgiants known.

The chromospheric activity, NUV excess flux, star spots, and very rapid rotation is what is also seen in FK Comae Berenices (FK Com) stars, a small group (only a handful of objects known) of single, rapidly rotating, and very active GK-type subgiants, which are believed to be the product of a recent merger (Eggen & Iben 1989). The prototype FK Com is the undisputed “king of spin” amongst these single red giants with an equatorial spin velocity of $v_{\text{eq}} = 179\text{ km s}^{-1}$, followed by HD 199178, the so called “spin vice king” amongst giant stars (Costa et al. 2015), with $v_{\text{eq}} = 93\text{ km s}^{-1}$ (Strassmeier 2009). A related class is that of the more frequently known RS Canum Venaticorum (RS CVn) variable stars, which are close binary systems consisting of a chromospherically active subgiant component, which exhibits brightness variations caused by large cool spots (Hall 1972), and which is also known to be fast rotating (Strassmeier 2009). There are also two other hot (pre-) WDs known, which are in a binary system with chromospherically active and rapidly rotating cool companions: LW Hya and LoTr 5. The latter is a wide binary in a highly eccentric orbit ($e \approx 0.3$, $P = 2700\text{ d}$, Jones et al. 2017) consisting of a hot pre-WD or WD, and the cool component, IN Com, is a rapidly rotating ($v_{\text{eq}} = 95\text{ km s}^{-1}$, Strassmeier 2009) and magnetically active G5 III giant that also shows H α line-profile variations (Kóvári et al. 2019). LW Hya is a resolved binary system composed of a hot DAO WD (the ionizing star of A 35, Ziegler et al. 2012; Löbbling et al. 2019) and a magnetically active G8 III-IV-type companion ($v_{\text{eq}} = 127\text{ km s}^{-1}$, Strassmeier 2009). For LW Hya, it is, however, not clear if the system is really a physical binary, due to the mismatch of the spectroscopic distance of the WD and the optical parallax.

The driving mechanism for the chromospheric activity and the reason for the rapid rotation observed in UCAC2 46706450–A remains to be explored. In main sequence stars of spectral type F, G, K, and early M, a self-sustaining magnetic dynamo driven by rotation and convection is believed to be the source of chromospheric activity. Since due to magnetic braking, the rotational velocity of the star is expected to decrease with age, the chromospheric activity is thought to decrease as well. However, if angular momentum is sustained, by tidal interaction as in the case of short-period binaries (this holds for the RS CVn stars), or maintained by convection, chromospheric activity can be preserved (Zhao et al. 2011).

Besides a recent stellar merger, sudden dredge-up of angular momentum from the stellar interior (Simon & Drake 1989), and accretion of a substellar companion (Peterson et al. 1983;

Carlberg et al. 2012) are considered as possible explanations for the abnormally high rotation rates of FK Com stars. As mentioned before, the lack of significant RV variations makes the close-binary scenario for UCAC2 46706450 very unlikely. One may therefore speculate that the system used to be a hierarchical triple system, and that UCAC2 46706450–A was produced by the merger of the inner binary, as was suggested for IN Com (Jasniewicz et al. 1987; Malasan et al. 1991).

8.3. Has UCAC2 46706450 an ultra-wide companion?

Recently, Tian et al. (2020) reported that based on common *Gaia* parallaxes and proper motions, UCAC2 46706450 is in an ultra-wide binary system with *Gaia* DR2 1391040916768689280 (alias SDSS J152844.16+430417.1), separated by 75.48951'' (111 634 AU). This fainter star has an absolute *Gaia* *G*-band magnitude of $M_G = 6.76$ mag and a color index of $G_{BP} - G_{RP} = 1.26$ (Tian et al. 2020), thus it is likely a K-type main-sequence star. That implies a low mass ($M \leq 0.8 M_\odot$) of the possible ultra-wide companion, which would also be in line with the lower limit of the (initial) masses of UCAC2 46706450–A and UCAC2 46706450–B, meaning that they indeed could have formed at the same time.

8.4. Prospects

A future detailed spectral analysis of UCAC2 46706450–A, which considers all spectral observations at once and also considers the flux contribution of the hot WD in the blue, would be highly desirable. This would help to better constrain the chemical composition and the mass of the star, as well as the age of the system. Near-UV spectroscopy could help to determine the helium abundance of the WD and to investigate the nature of the NUV excess flux. Long-term, high-resolution monitoring, that allows RVs to be measured with an accuracy of a few hundred m s^{-1} , will help to constrain the orbital period of the system and in turn makes it possible to conclude if the system underwent any mass transfer or wind accretion in its past, and to check if the merger scenario could be possible. Spectroscopic follow-up of SDSS J152844.16+430417.1 would allow us to verify if it is an ultra-wide companion by testing if its RV and chemical composition agree with UCAC2 46706450–A.

Acknowledgements. We thank the referee, Uli Heber, for his constructive report. We appreciate useful discussions with M3B and Stephan Geier. We thank Matti Dorsch and Boris Gänsicke for pointing out this system to us and useful discussions. A.R.M. acknowledges support from the MINECO under the Ramón y Cajal programme (RYC-2016-20254) and the AYA2017-86274-P grant, and the AGAUR grant SGR-661/2017. The TMAD tool (<http://astro.uni-tuebingen.de/~TMAD>) used for this paper was constructed as part of the activities of the German Astrophysical Virtual Observatory. This work has made use of data obtained at the Thai National Observatory on Doi Inthanon, operated by NARIT. Some of the data presented in this paper were obtained from the Mikulski Archive for Space Telescopes (MAST). This research has made use of NASA's Astrophysics Data System and the SIMBAD database, operated at CDS, Strasbourg, France. This research made use of Lightkurve, a Python package for Kepler and TESS data analysis (Lightkurve Collaboration 2018). This work has made use of data from the European Space Agency (ESA) mission *Gaia* (<https://www.cosmos.esa.int/gaia>), processed by the *Gaia* Data Processing and Analysis Consortium (DPAC, <https://www.cosmos.esa.int/web/gaia/dpac/consortium>). Funding for the DPAC has been provided by national institutions, in particular the institutions participating in the *Gaia* Multilateral Agreement. This work has made use of BaSTI web tools. This work includes data from the Asteroid Terrestrial-impact Last Alert System (ATLAS) project. ATLAS is primarily funded to search for near Earth asteroids through NASA grants NN12AR55G, 80NSSC18K0284, and 80NSSC18K1575; byproducts of the NEO search include images and catalogs from the survey area. The ATLAS science products have been made possible through the contributions of the University of Hawaii Institute for Astronomy, the Queen's University

Belfast, the Space Telescope Science Institute, and the South African Astronomical Observatory. Guoshoujing Telescope (the Large Sky Area Multi-Object Fiber Spectroscopic Telescope LAMOST) is a National Major Scientific Project built by the Chinese Academy of Sciences. Funding for the project has been provided by the National Development and Reform Commission. LAMOST is operated and managed by the National Astronomical Observatories, Chinese Academy of Sciences. Funding for the Sloan Digital Sky Survey IV has been provided by the Alfred P. Sloan Foundation, the U.S. Department of Energy Office of Science, and the Participating Institutions. SDSS-IV acknowledges support and resources from the Center for High-Performance Computing at the University of Utah. The SDSS web site is www.sdss.org. SDSS-IV is managed by the Astrophysical Research Consortium for the Participating Institutions of the SDSS Collaboration including the Brazilian Participation Group, the Carnegie Institution for Science, Carnegie Mellon University, the Chilean Participation Group, the French Participation Group, Harvard-Smithsonian Center for Astrophysics, Instituto de Astrofísica de Canarias, The Johns Hopkins University, Kavli Institute for the Physics and Mathematics of the Universe (IPMU) / University of Tokyo, the Korean Participation Group, Lawrence Berkeley National Laboratory, Leibniz Institut für Astrophysik Potsdam (AIP), Max-Planck-Institut für Astronomie (MPIA Heidelberg), Max-Planck-Institut für Astrophysik (MPA Garching), Max-Planck-Institut für Extraterrestrische Physik (MPE), National Astronomical Observatories of China, New Mexico State University, New York University, University of Notre Dame, Observatório Nacional / MCTI, The Ohio State University, Pennsylvania State University, Shanghai Astronomical Observatory, United Kingdom Participation Group, Universidad Nacional Autónoma de México, University of Arizona, University of Colorado Boulder, University of Oxford, University of Portsmouth, University of Utah, University of Virginia, University of Washington, University of Wisconsin, Vanderbilt University, and Yale University.

References

- Allard, F., Homeier, D., & Freytag, B. 2012, *Phil. Trans. R. Soc. London Ser. A*, **370**, 2765
- Andrews, J. J., Agüeros, M. A., Gianninas, A., et al. 2015, *ApJ*, **815**, 63
- Asplund, M., Grevesse, N., Sauval, A. J., & Scott, P. 2009, *ARA&A*, **47**, 481
- Bailer-Jones, C. A. L., Rybizki, J., Fouesneau, M., Mantelet, G., & Andrae, R. 2018, *AJ*, **156**, 58
- Baxter, R. B., Dobbie, P. D., Parker, Q. A., et al. 2014, *MNRAS*, **440**, 3184
- Bianchi, L., Conti, A., & Shiao, B. 2014, *VizieR Online Data Catalog: II/335*
- Carlberg, J. K., Cunha, K., Smith, V. V., & Majewski, S. R. 2012, *ApJ*, **757**, 109
- Casey, A. R., Hogg, D. W., Ness, M., et al. 2016, *ArXiv e-prints* [[arXiv:1603.03040](https://arxiv.org/abs/1603.03040)]
- Catalán, S., Isern, J., García-Berro, E., et al. 2008, *A&A*, **477**, 213
- Chen, X., Han, Z., Deca, J., & Podsiadlowski, P. 2013, *MNRAS*, **434**, 186
- Costa, A. D., Canto Martins, B. L., Bravo, J. P., et al. 2015, *ApJ*, **807**, L21
- Cutri, R. M., Skrutskie, M. F., van Dyk, S., et al. 2003, *VizieR Online Data Catalog: II/246*
- Davis, P. J., Kolb, U., & Willems, B. 2010, *MNRAS*, **403**, 179
- Dixon, D., Tayar, J., & Stassun, K. G. 2020, *AJ*, **160**, 12
- Drake, A. J., Djorgovski, S. G., Mahabal, A., et al. 2009, *ApJ*, **696**, 870
- Duchêne, G., & Kraus, A. 2013, *ARA&A*, **51**, 269
- Eggen, O. J., & Iben, I., Jr. 1989, *AJ*, **97**, 431
- Exter, K. M., Pollacco, D. L., Maxted, P. F. L., Napiwotzki, R., & Bell, S. A. 2005, *MNRAS*, **359**, 315
- Feltzing, S., & Bensby, T. 2009, *IAU Symp.*, **258**, 23
- Ferguson, D. H., & James, T. A. 1994, *ApJS*, **94**, 723
- Fitzpatrick, E. L. 1999, *PASP*, **111**, 63
- Fuhrmann, K. 1998, *A&A*, **338**, 161
- García Pérez, A. E., Allende Prieto, C., Holtzman, J. A., et al. 2016, *AJ*, **151**, 144
- Geier, S., Marsh, T. R., Wang, B., et al. 2013, *A&A*, **554**, A54
- Geier, S., Kupfer, T., Heber, U., et al. 2015, *A&A*, **577**, A26
- Gianninas, A., Kilic, M., Brown, W. R., Canton, P., & Kenyon, S. J. 2015, *ApJ*, **812**, 167
- Gray, R. O., & Corbally, C., Jr. 2009, *Stellar Spectral Classification* (Princeton: Princeton University Press)
- Hall, D. S. 1972, *PASP*, **84**, 323
- Han, Z., Podsiadlowski, P., Maxted, P. F. L., Marsh, T. R., & Ivanova, N. 2002, *MNRAS*, **336**, 449
- Hartman, J. D., & Bakos, G. Á. 2016, *Astron. Comput.*, **17**, 1
- Hayden, M. R., Recio-Blanco, A., de Laverny, P., Mikolaitis, S., & Worley, C. C. 2017, *A&A*, **608**, L1
- Heinze, A. N., Tonry, J. L., Denneau, L., et al. 2018, *AJ*, **156**, 241
- Henden, A. A., Levine, S., Terrell, D., & Welch, D. L. 2015, *AAS Meeting Abstracts*, **225**, 336.16
- Ho, A. Y. Q., Ness, M. K., Hogg, D. W., et al. 2017, *ApJ*, **836**, 5
- Holberg, J. B., & Bergeron, P. 2006, *AJ*, **132**, 1221

- Holberg, J. B., Oswalt, T. D., Sion, E. M., Barstow, M. A., & Burleigh, M. R. 2013, *MNRAS*, **435**, 2077
- Jasniewicz, G., Duquennoy, A., & Acker, A. 1987, *A&A*, **180**, 145
- Jones, D., Van Winckel, H., Aller, A., Exter, K., & De Marco, O. 2017, *A&A*, **600**, L9
- Kővári, Z., Strassmeier, K. G., Oláh, K., et al. 2019, *A&A*, **624**, A83
- Kilic, M., Munn, J. A., Harris, H. C., et al. 2017, *ApJ*, **837**, 162
- Kordopatis, G., Recio-Blanco, A., de Laverny, P., et al. 2011, *A&A*, **535**, A107
- Kordopatis, G., Gilmore, G., Steinmetz, M., et al. 2013, *AJ*, **146**, 134
- Kordopatis, G., Wyse, R. F. G., Gilmore, G., et al. 2015, *A&A*, **582**, A122
- Krtićka, J., Kubát, J., & Krtićková, I. 2020, *A&A*, **635**, A173
- Lallement, R., Capitanio, L., Ruiz-Dern, L., et al. 2018, *A&A*, **616**, A132
- Lightkurve Collaboration (Cardoso, J. V. d. M. a., et al.) 2018, *Lightkurve: Kepler and TESS time series analysis in Python*
- Löbbling, L., Maney, M. A., Rauch, T., et al. 2019, *MNRAS*, **441**, 2831
- Luo, A. L., Zhao, Y. H., Zhao, G., et al. 2016, *VizieR Online Data Catalog: V/149*
- Luo, A. L., Zhao, Y. H., Zhao, G., et al. 2019, *VizieR Online Data Catalog: V/164*
- Majewski, S. R., Schiavon, R. P., Frinchaboy, P. M., et al. 2017, *AJ*, **154**, 94
- Malasan, H. L., Yamasaki, A., & Kondo, M. 1991, *AJ*, **101**, 2131
- Marsh, T. R. 1989, *PASP*, **101**, 1032
- Maxted, P. F. L., Heber, U., Marsh, T. R., & North, R. C. 2001, *MNRAS*, **326**, 1391
- Miller Bertolami, M. M. 2016, *A&A*, **588**, A25
- Mitrofanova, A. A., Shimansky, V. V., Borisov, N. V., Spiridonova, O. I., & Gabdeev, M. M. 2016, *Astron. Rep.*, **60**, 252
- Moe, M., Kratter, K. M., & Badenes, C. 2019, *ApJ*, **875**, 61
- Nagel, T., Schuh, S., Kusterer, D. J., et al. 2006, *A&A*, **448**, L25
- Napiwotzki, R., Christlieb, N., Drechsel, H., et al. 2001, *Astron. Nachr.*, **322**, 411
- Nebot Gómez-Morán, A., Gänsicke, B. T., Schreiber, M. R., et al. 2011, *A&A*, **536**, A43
- Ness, M., Hogg, D. W., Rix, H. W., Ho, A. Y. Q., & Zasowski, G. 2015, *ApJ*, **808**, 16
- Nie, J. D., Wood, P. R., & Nicholls, C. P. 2012, *MNRAS*, **423**, 2764
- Parsons, S. G., Rebassa-Mansergas, A., Schreiber, M. R., et al. 2016, *MNRAS*, **463**, 2125
- Pastetter, L., & Ritter, H. 1989, *A&A*, **214**, 186
- Peterson, R. C., Tarbell, T. D., & Carney, B. W. 1983, *ApJ*, **265**, 972
- Pietrinferni, A., Cassisi, S., Salaris, M., & Castelli, F. 2004, *ApJ*, **612**, 168
- Press, W. H., Teukolsky, S. A., Vetterling, W. T., & Flannery, B. P. 1992, *Numerical Recipes in C. The Art of Scientific Computing* (Cambridge: Cambridge University Press)
- Rauch, T., Ziegler, M., Werner, K., et al. 2007, *A&A*, **470**, 317
- Rebassa-Mansergas, A., Ren, J. J., Parsons, S. G., et al. 2016, *MNRAS*, **458**, 3808
- Rebassa-Mansergas, A., Ren, J. J., Irawati, P., et al. 2017, *MNRAS*, **472**, 4193
- Rebassa-Mansergas, A., Toonen, S., Korol, V., & Torres, S. 2019, *MNRAS*, **482**, 3656
- Recio-Blanco, A., de Laverny, P., Kordopatis, G., et al. 2014, *A&A*, **567**, A5
- Reindl, N., Geier, S., Kupfer, T., et al. 2016, *A&A*, **587**, A101
- Reindl, N., Schaffenroth, V., Miller Bertolami, M. M., et al. 2020, *A&A*, **638**, A93
- Ritter, H. 1986, *A&A*, **168**, 105
- Santander-García, M., Rodríguez-Gil, P., Corradi, R. L. M., et al. 2015, *Nature*, **519**, 63
- Schlafly, E. F., & Finkbeiner, D. P. 2011, *ApJ*, **737**, 103
- Schlegel, D. J., Finkbeiner, D. P., & Davis, M. 1998, *ApJ*, **500**, 525
- Schreiber, M. R., Gänsicke, B. T., Rebassa-Mansergas, A., et al. 2010, *A&A*, **513**, L7
- Schuh, S. L., Dreizler, S., Deetjen, J. L., & Göhler, E. 2003, *Balt. Astron.*, **12**, 167
- Shimansky, V. V., Borisov, N. V., Nurtdinova, D. N., et al. 2015, *Astron. Rep.*, **59**, 199
- Silvestri, N. M., Hawley, S. L., & Oswalt, T. D. 2005, *AJ*, **129**, 2428
- Simon, T., & Drake, S. A. 1989, *ApJ*, **346**, 303
- Sing, D. K., Holberg, J. B., Burleigh, M. R., et al. 2004, *AJ*, **127**, 2936
- Stelzer, B., Marino, A., Micela, G., López-Santiago, J., & Liefke, C. 2013, *MNRAS*, **431**, 2063
- Stelzer, B., Damasso, M., Scholz, A., & Matt, S. P. 2016, *MNRAS*, **463**, 1844
- Strassmeier, K. G. 2009, *A&ARv*, **17**, 251
- Tian, H.-J., Liu, C., Carlin, J. L., et al. 2015, *ApJ*, **809**, 145
- Tian, H.-J., El-Badry, K., Rix, H.-W., & Gould, A. 2020, *ApJS*, **246**, 4
- Tonry, J. L., Denneau, L., Heinze, A. N., et al. 2018, *PASP*, **130**, 064505
- Unglaub, K., & Bues, I. 2000, *A&A*, **359**, 1042
- Van der Swaelmen, M., Boffin, H. M. J., Jorissen, A., & Van Eck, S. 2017, *A&A*, **597**, A68
- Van Winckel, H. 2018, ArXiv e-prints, [arXiv:1809.00871]
- Werner, K., & Dreizler, S. 1999, *J. Comput. Appl. Math.*, **109**, 65
- Werner, K., & Herwig, F. 2006, *PASP*, **118**, 183
- Werner, K., Deetjen, J. L., Dreizler, S., et al. 2003, *ASP Conf. Ser.*, **288**, 31
- Werner, K., Dreizler, S., & Rauch, T. 2012, *Astrophysics Source Code Library* [record ascl:1212.015]
- Werner, K., Rauch, T., & Kruk, J. W. 2015, *A&A*, **582**, A94
- Werner, K., Rauch, T., & Kruk, J. W. 2017, *A&A*, **601**, A8
- Werner, K., Rauch, T., & Kruk, J. W. 2018a, *A&A*, **609**, A107
- Werner, K., Rauch, T., & Kruk, J. W. 2018b, *A&A*, **616**, A73
- Werner, K., Rauch, T., & Reindl, N. 2019, *MNRAS*, **483**, 5291
- Willems, B., & Kolb, U. 2004, *A&A*, **419**, 1057
- Wilson, O. C. 1963, *ApJ*, **138**, 832
- Wilson, O. C. 1968, *ApJ*, **153**, 221
- Wright, E. L., Eisenhardt, P. R. M., Mainzer, A. K., et al. 2010, *AJ*, **140**, 1868
- Zechmeister, M., & Kürster, M. 2009, *A&A*, **496**, 577
- Zhao, J. K., Oswalt, T. D., Rudkin, M., Zhao, G., & Chen, Y. Q. 2011, *AJ*, **141**, 107
- Zhao, G., Zhao, Y.-H., Chu, Y.-Q., Jing, Y.-P., & Deng, L.-C. 2012a, *Res. A&A*, **12**, 723
- Zhao, J. K., Oswalt, T. D., Willson, L. A., Wang, Q., & Zhao, G. 2012b, *ApJ*, **746**, 144
- Ziegler, M., Rauch, T., Werner, K., Köppen, J., & Kruk, J. W. 2012, *A&A*, **548**, A109
- Zorotovic, M., Schreiber, M. R., Gänsicke, B. T., et al. 2011, *A&A*, **536**, L3

Quantitative spectral analysis of the sdB star HD 188112: A helium-core white dwarf progenitor

M. Latour¹, U. Heber¹, A. Irrgang¹, V. Schaffenroth^{1,2}, S. Geier^{1,3}, W. Hillebrandt⁴, F. K. Röpkke^{5,6},
S. Taubenberger^{3,4}, M. Kromer⁷, and M. Fink⁸

¹ Dr. Karl Remeis-Observatory & ECAP, Astronomical Institute, Friedrich-Alexander University Erlangen-Nuremberg, Sternwartstr. 7, 96049 Bamberg, Germany
e-mail: marilyn.latour@fau.de

² Institute for Astro- and Particle Physics, University of Innsbruck, Technikerstr. 25/8, 6020 Innsbruck, Austria

³ ESO, Karl-Schwarzschild-Str. 2, 85748 Garching bei München, Germany

⁴ Max-Planck-Institut für Astrophysik, Karl-Schwarzschild-Str. 1, 85741 Garching bei München, Germany

⁵ Heidelberger Institut für Theoretische Studien, Schloss-Wolfsbrunnenweg 35, 69118 Heidelberg, Germany

⁶ Zentrum für Astronomie der Universität Heidelberg, Institut für Theoretische Astrophysik, Philosophenweg 12, 69120 Heidelberg, Germany

⁷ The Oskar Klein Centre & Department of Astronomy, Stockholm University, AlbaNova, 106 91 Stockholm, Sweden

⁸ Institut für Theoretische Physik und Astrophysik, Universität Würzburg, Emil-Fischer-Str. 31, 97074 Würzburg, Germany

Received 24 September 2015 / Accepted 8 November 2015

ABSTRACT

Context. HD 188112 is a bright ($V = 10.2$ mag) hot subdwarf B (sdB) star with a mass too low to ignite core helium burning and is therefore considered a pre-extremely low-mass (ELM) white dwarf (WD). ELM WDs ($M \lesssim 0.3 M_{\odot}$) are He-core objects produced by the evolution of compact binary systems.

Aims. We present in this paper a detailed abundance analysis of HD 188112 based on high-resolution *Hubble* Space Telescope (HST) near- and far-ultraviolet spectroscopy. We also constrain the mass of the star's companion.

Methods. We use hybrid non-LTE model atmospheres to fit the observed spectral lines, and to derive the abundances of more than a dozen elements and the rotational broadening of metallic lines.

Results. We confirm the previous binary system parameters by combining radial velocities measured in our UV spectra with the previously published values. The system has a period of 0.60658584 days and a WD companion with $M \geq 0.70 M_{\odot}$. By assuming a tidally locked rotation combined with the projected rotational velocity ($v \sin i = 7.9 \pm 0.3 \text{ km s}^{-1}$), we constrain the companion mass to be between 0.9 and 1.3 M_{\odot} . We further discuss the future evolution of the system as a potential progenitor of an underluminous type Ia supernova. We measure abundances for Mg, Al, Si, P, S, Ca, Ti, Cr, Mn, Fe, Ni, and Zn, and for the trans-iron elements Ga, Sn, and Pb. In addition, we derive upper limits for the C, N, O elements and find HD 188112 to be strongly depleted in carbon. We find evidence of non-LTE effects on the line strength of some ionic species such as Si and Ni. The metallic abundances indicate that the star is metal-poor, with an abundance pattern most likely produced by diffusion effects.

Key words. stars: abundances – stars: atmospheres – stars: individual: HD 188112 – subdwarfs – white dwarfs – binaries: general

1. Introduction

HD 188112 is one of the brightest known ($V = 10.2$ mag) hot subdwarf B (sdB) stars, and it is a peculiar one. Subdwarf B stars are low-mass ($\sim 0.5 M_{\odot}$) helium-core burning objects with a hydrogen envelope that is not massive enough to sustain significant hydrogen shell burning. These stars form the extreme horizontal branch (EHB), which is a hot extension ($T_{\text{eff}} \gtrsim 21\,000$ K) of the horizontal branch. The majority of sdB stars are thus found between the zero-age EHB and the terminal-age EHB, which corresponds to the central helium burning phase (Heber 2009). The subsequent, more rapid evolution during helium shell burning brings the star above the EHB.

Given its fundamental parameters ($T_{\text{eff}} = 21\,500$ K, $\log g = 5.66$), HD 188112 was classified as an sdB; however, it lies at an odd position in the $\log g - T_{\text{eff}}$ diagram, i.e., significantly below the zero-age EHB (Heber et al. 2003). This is an indication that the star has too little mass to be He-core burning. The

low-mass nature of HD 188112 was confirmed in Heber et al. (2003) by comparing the trigonometric distance of the star (from the H parallax) with the spectroscopic distance; a mass of $\sim 0.24 M_{\odot}$ is required for both values to match. Comparing the fundamental parameters of HD 188112 with models for post red giant branch evolution (Driebe et al. 1998) led to a similar mass of $\sim 0.23 M_{\odot}$ (see Figure 4 in Heber et al. 2003). Such a star is likely to be formed via unstable mass transfer during its red giant phase, which leads to the formation of a common envelope. The subsequent spiralling-in of both components, and the eventual ejection of the envelope will leave behind a short-period binary system. If the envelope is removed before the core helium burning begins, the star evolves with an inert helium core and becomes a helium core white dwarf (WD; Han et al. 2002, 2003). Such low-mass evolved stars need to be formed via close binary evolution because the universe is not old enough to produce such a star through single-star evolution (Marsh et al. 1995). It is thus no surprise that HD 188112 was

found to be radial velocity (RV) variable with an orbital period $P = 0.606585$ d, a semi-amplitude $K_1 = 188.3$ km s⁻¹, a systemic velocity $\gamma_0 = 26.6$ km s⁻¹, and a minimum companion mass of $0.73 M_\odot$ (Heber et al. 2003). This indicates that the companion is a rather massive WD, as a main-sequence (MS) star of such a mass would be detectable in the spectral energy distribution of HD 188112, which does not show any deviation from that of a single star.

At the time of the discovery of HD 188112, very few low-mass He-core objects were known. The first was discovered as the companion of a neutron star in a millisecond pulsar (van Kerkwijk et al. 1996); another serendipitous discovery followed a few years later, among the first data release of the Sloan Digital Sky Survey (SDSS; Liebert et al. 2004). No more than a handful of such objects had been spectroscopically confirmed (Eisenstein et al. 2006; Kawka et al. 2006; Kilic et al. 2007) when a dedicated search for what are now called extremely low-mass (ELM) WDs was undertaken in the SDSS data base (Gianninas et al. 2015; Brown et al. 2013, and references therein). Because these stars are the product of close binary evolution, they are monitored for radial velocity variations, and the majority of them have indeed been found to have an orbital period shorter than a day. By determining the mass of the star and the orbital parameters of the system, it is possible to derive a minimum mass for the companion, which allows to study the future outcome of these systems. Some of them will merge within a Hubble time, and some might be progenitors of type Ia supernovae (SNe Ia). Systems with very short periods (≤ 0.2 d) are expected to merge within a Hubble time. To date, 38 of these systems have been found (Gianninas et al. 2015; Brown et al. 2013, and references therein). Their fate depends on the mass of both components. If the mass of the companion is high enough, then it might be a SN Ia progenitor. Once a He-WD has filled its Roche lobe, a typical scenario involves a C/O core WD companion that starts accreting He-rich material from the He-WD. Once a sufficiently large shell of He has been accreted, a detonation can be triggered in the He-shell resulting in underluminous type Ia SNe (Bildsten et al. 2007). However, some simulations have shown that the explosion of the He-shell almost inevitably triggers a subsequent detonation in the C/O core. Depending on the mass of the C/O core, this might produce SNe Ia explosions (Livne & Glasner 1990; Fink et al. 2007, 2010; Pakmor et al. 2013). This double-detonation scenario happens at a sub-Chandrasekhar mass and a C/O WD accretor of $\sim 1.0 M_\odot$ is a good candidate for producing a normal SN Ia (Sim et al. 2010). If the mass of the companion is much lower than $1 M_\odot$ then extreme-helium stars, R Coronae Borealis (RCrB) stars, single hot subdwarfs, or single WDs can ultimately be formed, depending on the mass ratio of the components. This is why, in order to constrain the future product of the binary systems hosting these ELM WDs, the masses of both components need to be determined accurately.

The mass of the ELM WD is usually determined by comparing the atmospheric parameters (effective temperature, T_{eff} , and surface gravity, $\log g$) of the star with theoretical evolutionary tracks for different masses (Driebe et al. 1998; Panei et al. 2007; Kilic et al. 2010; Althaus et al. 2013). However, the precision of such mass determination is limited and also depends on the evolutionary track used. In addition, the mass of the companion depends on the inclination of the system, which remains unknown unless eclipses are seen (Steinfadt et al. 2010; Brown et al. 2011; Vennes et al. 2011; Parsons et al. 2011; Kilic et al. 2014; Hallakoun et al. 2015) or distortion effects (such as ellipsoidal variations) in the light curve allow the system's

parameters to be constrained (Kilic et al. 2011b; Hermes et al. 2014a). However, these are very rare cases, and for the vast majority of systems only a minimum companion mass can be determined or, using the mean inclination angle for a random sample, a most likely companion mass can be estimated.

Given all of these new ELM systems found (more than 70), HD 188112 might look like a common system among others, but this is not the case. First, when compared to the majority of ELM systems, its combination of hot temperature and low surface gravity makes it stand out on the $\log g$ - T_{eff} plane (see, e.g., Fig. 1 in Brown et al. 2013). This indicates that HD 188112 is at a rather early stage of its cooling process, which is why it is also classified as a low-mass sdB. Such “young” objects are sometimes referred to as pre-ELM WDs. In terms of fundamental parameters, only four systems so far are roughly similar to HD 188112: KIC 6614501 (Silvotti et al. 2012), SDSS J1625+3632 (Kilic et al. 2011a), SDSS J0815+2309 (Brown et al. 2013), and GALEX J0805-1058 (Kawka et al. 2015). Second, it is by far the brightest of the known ELM systems; it has a parallax measured by H α , and we can expect a *Gaia* measurement soon. The parallax allows a mass to be derived for the star that is independent of evolutionary models. Additionally, its brightness allows high-resolution, high signal-to-noise spectroscopy.

As an alternative to finding eclipses or modeling light-curves of distorted stars, if one assumes the system to be tidally locked, then its inclination can be measured via the rotational broadening ($v_{\text{rot}} \sin i$) of metallic lines (Geier et al. 2010). The surface rotation velocity of the star (v_{rot}) is estimated from the orbital period (=rotation period) and then, by measuring the rotational broadening, the inclination can be derived. Given the fact that the optical spectrum of the star is devoid of metallic lines, except for a magnesium feature too weak for such a measurement, we turned to the UV range instead where at least some magnesium lines are expected to be observed. The UV spectra of HD 188112 turned out to be much richer in metallic lines than anticipated, allowing an in-depth chemical composition analysis of the star. In our preliminary analysis we presented abundances for Mg, Si, and Fe (Latour et al. 2015); in this paper, we extend the measured abundances to a dozen additional elements. This is of great interest since detailed abundance analyses of ELM WD are still scarce (Hermes et al. 2014b; Gianninas et al. 2014b; Kaplan et al. 2013). We present the UV observations in Sect. 2 and review some of the binary parameters of the system in Sect. 3. Section 4 is dedicated to the spectroscopic analysis, it includes a description of the models, the determination of the rotational broadening, and the abundances of all metallic species seen in the spectra. Finally, a discussion follows in Sect. 5.

2. Observations

Ultraviolet spectra of HD 188112 were obtained with the Space Telescope Imaging Spectrograph (STIS) installed on the *Hubble* Space Telescope (HST) during cycle 20 (program ID 12865) on April 27, 2013.

First there is a set of 22 exposures of 120 s each taken with the E140H grating ($R = 114\,000$) covering the wavelength range 1242–1440 Å. Because of the radial velocity variations of the star and the high resolution of the observations, a series of short exposures was necessary in order to avoid orbital smearing of the metallic lines¹. This exposure time leads to ~ 3 km s⁻¹

¹ Time-tag mode, as used for the NUV spectrum, would have been preferable, but the star is too bright in the far-UV.

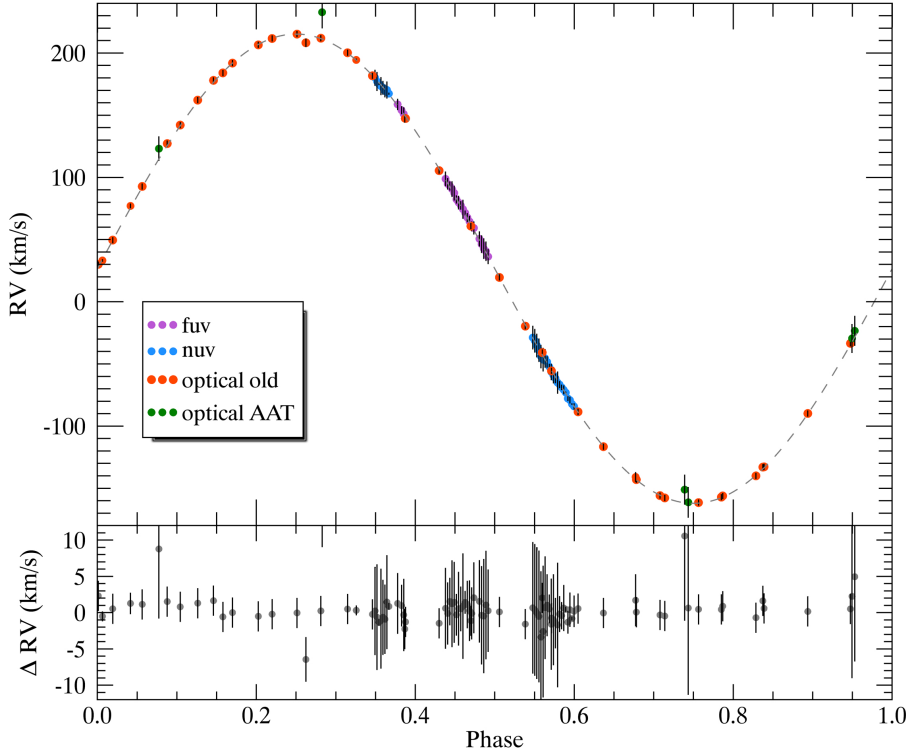


Fig. 1. Radial velocity curve, with measurements from different sources are indicated with different colors (see Sect. 3). The “optical old” refers to values published in Heber et al. (2003) and Edelmann et al. (2005).

differences between subsequent spectra. The data retrieved from the HST Archive were reduced and processed with the CALSTIS pipeline. Radial velocities were measured for each exposure and the spectra were shifted to rest wavelength (information on the radial velocity measurements is presented in the following section). The 22 “shifted” spectra were then coadded into a single spectrum suitable for spectroscopic analysis.

Additionally, two near-UV observations were taken with the E230H grating (also $R = 114\,000$) in Time-Tag mode. The wavelength range covered by these spectra is 2666–2932 Å. There is a short (1040.2 s, hereafter called NUV1) and a long (2860.2 s, hereafter called NUV2) exposure, taken at different orbital phases. Again, to avoid orbital smearing of the spectral lines, the retrieved data were processed following the STIS Time-Tag Analysis Guide² in order to create subexposures that were then reduced using CALSTIS. This way, we created 8 spectra of 130 s for the NUV1 observation, and 21 spectra of 136.2 s for the NUV2. Radial velocities were measured for each spectrum that was then shifted to rest wavelength. The main spectral features of the near-UV spectra are a series of four Mg lines around 2797 Å, among which the two resonance lines also have interstellar (IS) components. The NUV1 observation was taken far away from the conjunction phase, so the IS components are distinct from the stellar lines. This is not the case though for the NUV2 observation; the first spectra of the series show blending of the stellar and IS resonance lines. For this reason, when we coadded the subexposures of NUV2, we included only the 11 spectra where the lines are not blended. As for NUV1, the 8 subexposures were combined together.

3. Binary system parameters

The HST spectra were obtained for spectroscopic analysis, but the radial velocities measured for the individual exposures are

² <http://www.stsci.edu/hst/stis/documents/isrs/200002.pdf>

also useful to put new constraints on the orbital parameters determined in Heber et al. (2003) and Edelmann et al. (2005), or at least to confirm them. By combining our new values with the previous measurements taken between 2000 and 2004, we extended the temporal coverage to 13 years.

Radial velocities were measured in the UV spectra using strong unblended lines: the Si resonance lines (1393.7 and 1402.8 Å), Si 1296.7 Å, and Fe 1273.8 Å. For the NUV spectra, the three strongest Mg lines were used, except for six subexposures of NUV2 where the resonance lines were strongly blended with the IS lines. In this case, only the 2798.8 Å line was used. The mean values of individual measurements were used, which gave maximum standard deviations of 2.5 km s⁻¹, but typically of ~1.5 km s⁻¹. In addition to the previously published optical RVs, we also added five values kindly provided by J. Norris, from low-resolution spectra taken at the Anglo-Australian Telescope (AAT) in 2003.

A periodogram analysis was performed, including the 98 RV measurements and our resulting folded RV curve is shown in Fig. 1. The orbital parameters we obtained are in very good agreement with those stated in Heber et al. (2003); we have $P = 0.60658584 (\pm 5e-8)$ d, $K_1 = 188.7 \pm 0.2$ km s⁻¹, and $\gamma_0 = 26.6 \pm 0.2$ km s⁻¹. This leads to a mass function

$$f(m) = \frac{M_{\text{comp}}^3 \sin^3 i}{(M_{\text{comp}} + M)^2} = \frac{PK^3}{2\pi G} \quad (1)$$

of $f(m) = 0.4221 M_{\odot}$. By allowing for an eccentric orbit during the fitting procedure, we derive an upper limit of $e \leq 0.00006$. This low eccentricity value is consistent with a circular orbit.

The parallax of HD 188112 from the new reduction of the H catalogue is 13.6 ± 1.7 mas (van Leeuwen 2007). We then used the V (10.22) and B (10.01) magnitudes from the TYCHO 2 catalogue (Høg et al. 2000) combined with the synthetic flux from a model atmosphere appropriate for HD 188112 in order to derive the stellar radius. We did not consider any

reddening due to the proximity of the star. Both magnitudes could be satisfactorily reproduced without extinction. This allowed us to derive a spectroscopic mass of $0.245^{+0.075}_{-0.055} M_{\odot}$ and a radius of $0.12^{+0.02}_{-0.01} R_{\odot}$. The main uncertainty results from the parallax measurement. The spectroscopic mass indicates a $M_{\text{comp}} \geq 0.73 M_{\odot}$ and a most likely mass $M_{\text{comp}(52^{\circ})} = 1.21 M_{\odot}$ (Gray 2008).

The latest development in terms of evolutionary sequences for ELM WDs is due to Althaus et al. (2013). Their models predict that for masses in the range $0.18\text{--}0.4 M_{\odot}$, the star is expected to undergo H-shell flashes (in CNO burning) during the early cooling phase. This can happen multiple times while the star is “trying” to contract and cool down, each time following tracks in a slightly different region of the $\log g\text{--}T_{\text{eff}}$ diagram (see Figs. 3 and 4 of Althaus et al. 2013). This makes the determination of the mass a bit more complicated since it is not known if the star is on its final or an intermediate cooling sequence. Moreover, the different cooling tracks of stars from different masses are found in similar places on the HR diagram. The approach of Althaus et al. (2013) is a statistical one, weighting the time spent by models of different masses in each region of the $\log g\text{--}T_{\text{eff}}$ plane. This way, they determine a mass of $0.211 \pm 0.0175 M_{\odot}$ for HD 188112 as well as a cooling age of 329 ± 207 Myr. This mass is a bit lower than that determined by the parallax, but it nevertheless fits well within the spectroscopic mass uncertainty. Assuming $0.21 M_{\odot}$ for HD 188112 leads to $M_{\text{comp}} \geq 0.70 M_{\odot}$ and a most probable mass $M_{\text{comp}(52^{\circ})} = 1.17 M_{\odot}$. As mentioned before, the absence of NIR excess in the observed flux of the star excludes the possibility of a main-sequence companion, thus implying that it has to be a rather massive WD.

4. Spectroscopic analysis

4.1. Model atmospheres and synthetic spectra

The model atmospheres used for our analysis are computed following the hybrid non-local thermodynamical equilibrium (NLTE) approach discussed in Przybilla et al. (2006a) and Nieva & Przybilla (2007, 2008); it is a combination of three codes: Atlas, Detail, and Surface (hereafter ADS). The structure of the atmosphere, such as the temperature stratification and density, is based on line-blanketed, plane-parallel, homogeneous, and hydrostatic LTE-model atmospheres computed with the Atlas12 code (Kurucz 1996). The NLTE effects are accounted for in the computation of the atomic population numbers via updated versions of the Detail and Surface codes (Giddings 1981). Using the Atlas12 LTE atmospheric structure as input, Detail solves the coupled radiative transfer and statistical equilibrium equations to obtain population numbers in non-LTE. This is then used by Surface, which produces the final synthetic spectrum using more detailed line-broadening data. The ADS approach is successfully used to study some types of hot stars (e.g., OB-type stars and BA-type supergiants; Nieva & Przybilla 2012). It has also been tested in the sdB regime (Przybilla et al. 2006a). Compared to the fully NLTE approach, the hybrid approach is much less time-consuming in terms of computation. Given the atmospheric parameters of HD 188112, no strong NLTE effects are expected on the temperature–density stratification of the atmosphere and the ADS models are appropriate. It must be kept in mind that an NLTE computation of atomic populations requires specific model atoms. Such model atoms are available only for a limited number of atomic species (see Sect. 4.3). When no such

models exist, the populations are computed assuming the LTE approximation.

Given the very low metallicity expected for the star, a metallicity of 3% (by numbers) solar was used in the computation of the Atlas12 LTE model atmospheres. Afterward, small grids of different abundances were computed for all the atomic species seen in our spectra. It should also be mentioned that the He abundance was kept fixed at the value of $\log N(\text{He})/N(\text{H}) = -5.0$ derived in Heber et al. (2003). In order to generate spectra including the lines of all visible elements, normalized synthetic spectra computed for the various elements were multiplied following the technique described in Irrgang et al. (2014). This approach is appropriate when blending of lines originating from different species is sparse, as is the case for HD 188112. The metallic lines are then fitted using a standard χ^2 minimization technique.

4.2. Rotational velocity measurement

As a first step, we measured the rotational velocity ($v_{\text{rot}} \sin i$) using the Mg lines in the NUV spectra, as well as the Fe lines in the FUV spectra. At the same time, we also fitted the microturbulent velocity as it can contribute to line broadening, even though it is not expected to be very important for hot subdwarf stars because of their stable and radiative atmospheres. Microturbulence has to be taken into account during the model atmosphere computation, as opposed to the rotational broadening that is applied afterward to the synthetic spectra. So we computed models with microturbulence between 0 and 8 km s^{-1} only for Mg and Fe. Microturbulence affects the strong and weak lines in different ways, so the choice of Mg and Fe allowed lines of various strength to be fit in the NUV and FUV spectra. The rotational broadening, microturbulence, magnesium, and iron abundances were thus fitted simultaneously. The microturbulence could be constrained to $v_{\text{micro}} \lesssim 2 \text{ km s}^{-1}$; its effect below this value is rather small and did not influence the resulting χ^2 much. We measured a rotational broadening of $v_{\text{rot}} \sin i = 7.9 \pm 0.3 \text{ km s}^{-1}$. The resulting fit for the Mg lines in the NUV1 spectrum and the residual of the fit are shown in Fig. 2. The IS lines are plotted in grey and were excluded from the fitting procedure.

If it is assumed that the system is in synchronous rotation, then the star’s rotation period is the same as the orbital period. Using the mass of the star to determine the radius, the equatorial rotation velocity can be derived:

$$v_{\text{rot}} = \frac{2\pi R}{P}. \quad (2)$$

Combined with the measured $v \sin i$, it yields the inclination angle. For a mass of $0.21 M_{\odot}$, as predicted by theoretical models, we find $i = 57^{\circ} \pm 4^{\circ}$ and a companion mass of $1.0^{+0.10}_{-0.08} M_{\odot}$.

If we use the slightly higher sdB mass resulting from the H parallax ($0.245 M_{\odot}$), we find $i = 52^{\circ} \pm 3^{\circ}$ and a companion mass of $1.2^{+0.13}_{-0.09} M_{\odot}$.

4.3. Metal abundance determinations

Our FUV spectrum reveals a number of lines from various elements, namely Si, Al, P, S, Ti, Cr, Mn, Fe, Ni, Zn, Ga, Sn, and Pb. The NUV spectrum is rather poor in metallic lines: besides the strong Mg lines, only a handful of weak Fe lines are visible. Our model atmospheres were computed using the parameters derived by Heber et al. (2003): $T_{\text{eff}} = 21\,500 \pm 500 \text{ K}$,

³ Only the uncertainty on i is considered in these estimates of the companion mass.

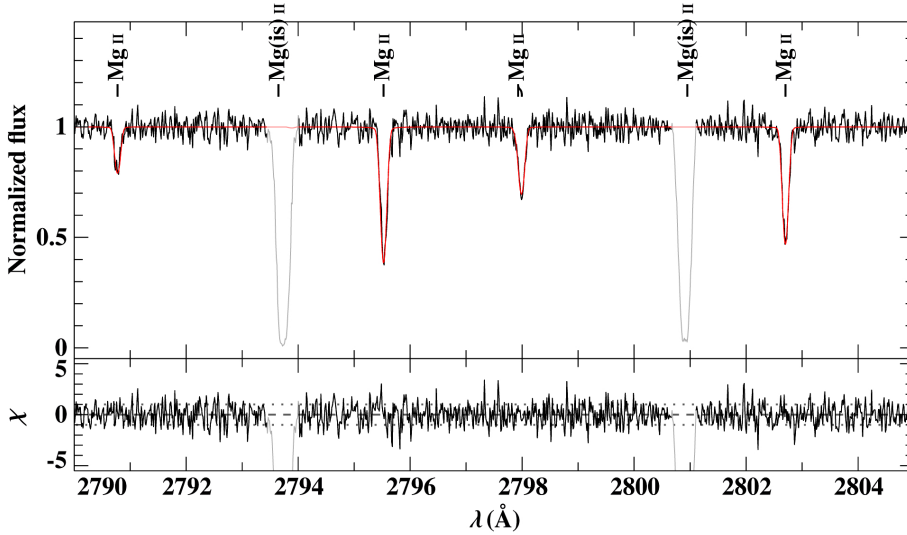


Fig. 2. Fit of the Mg II lines in the NUV1 spectrum for $v_{\text{rot}} \sin i = 7.9 \text{ km s}^{-1}$ and $v_{\text{micro}} = 1.1 \text{ km s}^{-1}$. The IS Mg lines are shown in grey and were not included in the fit.

$\log g = 5.66 \pm 0.06$, and $\log N(\text{He})/N(\text{H}) = -5.0$. Our grid also included the extreme parameters resulting from the uncertainties on T_{eff} and $\log g$, which were used to check the effects of changing those parameters on the metallic abundances. Microturbulence was kept to zero in our metal grids and $v \sin i = 7.9 \text{ km s}^{-1}$ was used during the fitting procedures.

As mentioned earlier, in order to compute NLTE population numbers, detailed model atoms are needed. To date, the model atoms available for Detail cover C, N, O, Mg, Al, Si, S, and Fe, so these elements were treated in NLTE in Detail, while all others were computed using the LTE approximation. We note that the LTE approximation is expected to be adequate given the atmospheric parameters of the star (Przybilla et al. 2006b) and it is the usual approach for abundance analysis of white dwarfs and hot subdwarfs having similar or higher T_{eff} . Nevertheless, we also computed LTE models for Mg, Al, Si, S, and Fe in order to compare abundances derived with both types of models. This is discussed in more detail in Sect. 5.1. Our resulting abundances are listed in Table 1 where the results obtained with NLTE and LTE models are indicated in two separate columns. The comparison between our final synthetic spectrum and the entire UV spectrum can be found in Fig. A.1.

4.3.1. Upper limits for C, N, and O

No lines of the C, N, O elements are visible in the UV spectra. This is not very surprising in the cases of nitrogen and oxygen as no strong lines are predicted in our UV ranges.

For oxygen, the strongest predicted features are three O lines at 1302, 1304, and 1305 Å. They were used to put an upper limit of $\log N(\text{O})/N(\text{H}) = -6.3$. For nitrogen nothing useful is predicted in the UV range, so we turned toward the optical instead, where we used the high-resolution FEROS spectra of HD 188112 obtained by Edelmann et al. (2005). The N lines at 3995 and 4630 Å were used to put an upper limit of $\log N(\text{N})/N(\text{H}) = -5.0$, which is, however, only slightly below the solar value.

The situation is different for carbon. Three strong lines are predicted in the UV range, including C resonance lines at 1334.5 and 1335.7 Å. The absence of these lines in our spectrum results in an extremely low upper limit of $\log N(\text{C})/N(\text{H}) = -9.6$. This is six orders of magnitude below the solar value. Carbon has essentially vanished from the surface of the star.

Table 1. Abundances of metals detected in the spectra of HD 188112.

Element Z	Abundance $\log N(\text{Z})/N(\text{H})$	
	NLTE	LTE
C	<-9.6	–
N ^a	<-5.0	–
O	<-6.3	–
Mg	-6.40 ± 0.07	-6.20 ± 0.07
Al	-7.37 ± 0.05	-7.39 ± 0.05
Si - -	-7.3 ± 0.1	-7.6 ± 0.1
P	–	-9.2 ± 0.1
S	-8.0 ± 0.1	-8.4 ± 0.1
Ca ^a	-7.3 ± 0.2	–
Ti	–	-8.30 ± 0.05
Cr	–	-7.55 ± 0.05
Mn	–	-8.00 ± 0.05
Fe -	-5.75 ± 0.15	-6.1 ± 0.1
Ni	-6.6 ± 0.1	-6.7 ± 0.1
Zn	–	-7.72 ± 0.07
Ga -	–	-9.6 ± 0.1
Sn	–	$-10.6^{+0.6}_{-0.1}$
Pb	–	-10.0 ± 0.2

Notes. ^(a) Upper limit or abundance determined with optical spectra.

4.3.2. Mg, Al, Si, P, and S

Only four Mg lines are visible in the NUV spectra. Their abundances were fitted during the determination of the projected rotational velocity (see Fig. 2). We also fitted them in the NUV2 spectra, shown in the last panel of Fig. A.1. The fits with both spectra lead to very similar results, with an abundance of 1/100 solar. This is essentially the same abundance as was first estimated by Heber et al. (2003) based on the Mg $\lambda 4481$ line visible in the optical spectrum.

The FUV spectrum shows the Al doublet at 1379, 1384 Å that matches an abundance of $\log N(\text{Al})/N(\text{H}) = -7.37$.

Only two very weak sulphur lines are visible at the blue end of the FUV spectra, but they were nevertheless used to constrain the abundance of this element to $\log N(\text{S})/N(\text{H}) = -8.0$.

One phosphorus line was used to fit: P $\lambda 1344.32$. Because of the lack of a line list for this ion in Surface, we used the public

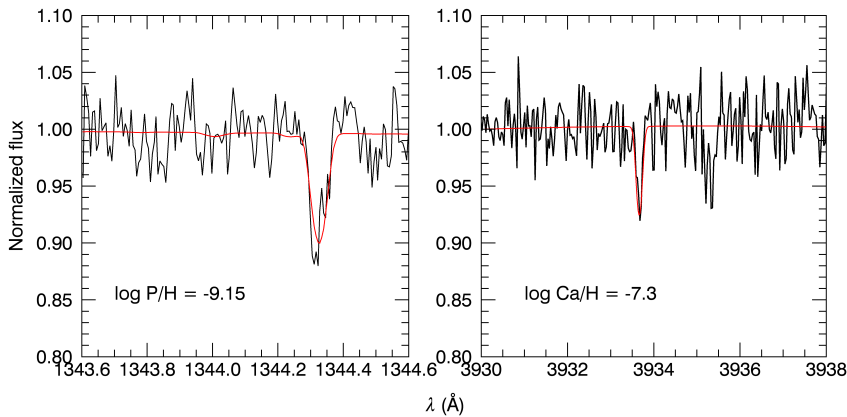


Fig. 3. Best fits for the P IV line in the FUV spectrum as well as for the Ca II line in an optical FEROS spectrum.

codes TLUSTY and SYNSPEC⁴ to perform an independent fit of the line. TLUSTY allows the computation of NLTE stellar atmospheres, assuming plane-parallel geometry and hydrostatic and thermal equilibrium; SYNSPEC is then used to compute synthetic spectra, given an atmospheric structure (Lanz & Hubeny 2007). An NLTE model atmosphere was computed including hydrogen and helium only and as no model atom is available for P IV, we included it in an LTE way through Synspec. The resulting fit can be seen in Fig. 3.

Silicon is an interesting element since it shows strong lines originating from three different ionization stages. Lines originating from all three of them are well reproduced with an abundance of $\log N(\text{Si})/N(\text{H}) = -7.3$. This is a good sign that the ionization equilibrium for this element is correct given the hybrid NLTE approach and the effective temperature of the star. Interstellar components to Si II $\lambda\lambda 1301, 1303$ are present, but are not blended with the photospheric lines due to the relatively high radial velocity of the star during the FUV exposures. The IS features seen in our spectra are broadened by the radial velocity correction applied to the individual exposures, which explains their unusual shape in Fig. A.1.

4.3.3. Ca

Calcium is an important element because it has been claimed that all ELM WDs with $\log g \lesssim 5.9$ show Ca in their optical spectra (Hermes et al. 2014b; Gianninas et al. 2014a). This was first illustrated by Kaplan et al. (2013) who combined results from different studies of ELM WDs in their Fig. 6. However, they erroneously indicated that HD 188112 showed Ca II in its optical spectra, confusing it with the Mg II feature mentioned in Heber et al. (2003). Nevertheless, since the tendency is true for all other ELM WDs analyzed so far, we went back to the optical spectra of HD 188112 to look for this expected Ca II K line. After correcting a few spectra for their radial velocity, and scrupulously comparing them, we indeed found weak calcium features: one stable line at the predicted wavelength, thus of photospheric origin, and one moving around, being a very small IS component. As can be seen in Fig. 3, this line is very weak indeed, but present in the different spectra, thus real. It is understandable why it was first overlooked in Heber et al. (2003). It must also be kept in mind that most of the ELM WDs in which Ca has been measured have $T_{\text{eff}} < 16\,000$ K. At high temperatures, the strength of these lines rapidly decreases as Ca becomes ionized. Nevertheless, the tiny line we found in HD 188112 indicates an abundance of

$\log N(\text{Ca})/N(\text{H}) = -7.3$. Calcium was also measured in another ELM WD (SDSS J0815+2309) having essentially the same temperature as HD 188112 but a slightly higher surface gravity (Gianninas et al. 2014a). Compared to HD 188112, the Ca abundance derived for J0815+2309 is a hundred times higher ($\log N(\text{Ca})/N(\text{H}) = -5.27$). As for other ELM WDs, the Ca abundance of HD 188112 is similar to the lowest abundances measured in the sample of Gianninas et al. (2014a).

4.3.4. The iron-group elements

Titanium, chromium, iron, and nickel show many strong lines from their main ionization stage (I) that could be reproduced well by our synthetic spectra. Two well-defined lines of Mn II are seen at 1283 and 1287 Å, and two lines of Zn II are also visible at 1318 and 1328 Å. The resulting abundances are listed in Table 1.

Iron and nickel are the only iron-group elements that also show lines from their singly ionized stage. There is a small discrepancy in the abundances measured with the Fe II lines in the FUV and the Fe III lines mainly found in the NUV. Compared with the abundance of $\log N(\text{Fe II})/N(\text{H}) = -5.87 \pm 0.07$, the Fe III lines need a slightly *higher* abundance of -5.6 ± 0.1 to be reproduced. Another investigation of UV iron lines in B-type stars using ADS models found a scatter of ~ 0.25 dex for FUV lines when abundances measured from different lines are compared (Schaffenroth 2015). The reason for this, possibly related to the ADS models, will be explored further in a future publication (Schaffenroth et al., in prep.). In any case, this scatter is similar to the discrepancy we found between the FUV and NUV lines of HD 188112. We thus adopt a mean abundance of -5.75 ± 0.15 for iron, as indicated in Table 1.

We also encountered a discrepancy between lines originating from both ionization stages of nickel, but this time with a significant difference. In the case of nickel, fitting the Ni II lines results in an abundance of $\log N(\text{Ni II})/N(\text{H}) = -7.25$, which is 0.55 dex *below* what is predicted by the main ionization stage ($\log N(\text{Ni I})/N(\text{H}) = -6.7$ when using the ADS models). In other words, at the abundance derived from the Ni II lines, the Ni I lines are much too strong, as can be seen in Fig. A.1. Something to keep in mind is that, unlike iron, nickel is treated using the LTE approximation in ADS. As nickel model atoms are available for TLUSTY (but only for Ni II to Ni III), we built a small grid of NLTE models with various Ni abundances in

⁵ We use the nomenclature Fe II here and below to indicate the abundance derived by using lines from a specific ion.

⁴ <http://nova.astro.umd.edu/>

order to fit the Ni lines. We obtained an abundance of $\log N(\text{Ni})/N(\text{H}) = -6.6 \pm 0.1$ dex, essentially the same as derived with ADS. This is not surprising since Ni is the main ionization stage. It is also reassuring in the sense that we can expect the LTE abundances derived for the other iron-group elements via their main ionization stage to be reliable. However, owing to the lack of a Ni model atom for TLUSTY, this ion was treated in LTE and an abundance discrepancy similar to the one seen with the ADS models was observed.

4.3.5. Trans-iron elements: Ga, Sn, and Pb

We found lines originating from three trans-iron elements, gallium, tin, and lead, in the spectra of HD 188112. Such heavy elements are also seen in hot subdwarfs (O'Toole 2004; O'Toole & Heber 2006) as well as hot DA and DO WDs (Vennes et al. 2005; Werner et al. 2012; Rauch et al. 2013). However, they have not been detected yet in colder WDs, with the exception of the heavily polluted WD GD 362, in which a strontium line has been detected (Zuckerman et al. 2007). The metallic elements in this cool star are accreted from a debris disk surrounding the star. With its temperature of 21 500 K, HD 188112 is among the coolest WD/sdB stars for which trans-iron elements have been detected.

The Ga abundance of $\log N(\text{Ga})/N(\text{H}) = -9.55$ was determined using the $\lambda 1414.4$ resonance line of Ga as well as two weak Ga lines at 1267 Å and 1293 Å. All of them are reproduced well with this abundance.

A sole line of lead is present in our spectra, the 1313 Å resonance line of Pb, which indicates an abundance of $\log N(\text{Pb})/N(\text{H}) = -10.0$, slightly above the solar value.

We see the resonance line of Sn at 1251.39 Å, as well as the resonance doublet of Sn $\lambda\lambda$ 1314, 1437. The fit of the Sn line gives an abundance of $N(\text{Sn})/N(\text{H}) = -10.6$. However, at this abundance, the Sn lines are barely visible in our synthetic spectra. In order to reproduce them, we need an abundance of -8.4 , which is more than 2 dex higher than what is indicated by the Sn line. This is reminiscent of the problem encountered with nickel, but much more dramatic. Given the fact that these three transitions are resonances, their oscillator strengths, taken from Morton (2000) are considered to be reliable. The Sn line is blended with a Cr line (1251.417 Å), which is however predicted to be rather weak at the Cr abundance determined. Indeed, a fit of the Sn line without the contribution of the Cr feature leads to an abundance only slightly higher, -10.5 dex, still far from the -8.4 dex needed to reproduce the Sn lines. As we did for nickel, we turned toward NLTE models in an attempt to solve the tin abundance discrepancy. An NLTE fit of the Sn lines was performed using this time the Tübingen NLTE model-atmosphere package (TMAP; Rauch & Deetjen 2003) because a simple NLTE Sn model atom for this code was built in the course of the spectral analysis of the hot DA white dwarf G191-B2B (Rauch et al. 2013; T. Rauch, private comm.). With NLTE models, the Sn line leads to an abundance of -10.0 , and the Sn lines indicate -8.2 (1314.5 Å) and -8.5 (1437.5 Å). According to these results, NLTE effects apparently cannot solve the “tin problem”. However, because the model atom for tin is rather simple (3 and 6 NLTE levels for Sn and, respectively) and resonance lines can be very sensitive to NLTE effects, it would be premature to exclude these effects as the cause of the discrepancy and to blame it on the atomic data. Because Sn has the same ionization energy as Fe and Cr, it is expected to be the main ionization stage, as for the iron-group elements, so

we adopt an abundance of $\log N(\text{Sn})/N(\text{H}) = -10.6^{+0.6}_{-0.1}$. This is based on our ADS results, but the upper limit includes the value indicated by TMAP.

5. Discussion

5.1. Non-LTE effects

The discrepancies found between the ionization stages of Ni and Sn show the same trend: the lowest ionization stage visible indicates a lower abundance. This is sometimes seen in much hotter stars and is a signature of NLTE effects when analyses are made using the LTE approximation. As stated in Dreizler & Werner (1993), in a consistent NLTE model, ionization equilibrium is shifted to higher stages. In our case, this could explain why the Ni lines are too strong in our models, while the Sn lines are too weak. However, these effects are not really expected to appear in an sdB at 21 500 K, although some line-by-line differences between LTE and NLTE treatment were found in HD 205805, an sdB star at 25 000 K and $\log g = 5.0$ (Przybilla et al. 2006b). This is why we decided to compute additional LTE models for Mg, Al, Si, S, and Fe and to redo the fitting procedure in order to derive LTE abundances for these elements⁶. The resulting abundances are indicated in Table 1. For magnesium and aluminium, the LTE and NLTE abundances are similar, while there is a difference of 0.4 dex for the sulfur abundance. Most interesting is silicon; a simultaneous fit of all the Si lines leads to an abundance of $\log N(\text{Si})/N(\text{H}) = -7.56$ dex, but the quality of the fit is poor and it shows conspicuous hints of an incorrect ionization equilibrium. Instead, the lines originating from the different ions had to be fitted separately in order to be correctly reproduced, thus leading to discrepant abundances:

$$\log N(\text{Si})/N(\text{H}) = -7.8 \pm 0.1;$$

$$\log N(\text{Si})/N(\text{H}) = -7.33 \pm 0.05;$$

$$\text{and } \log N(\text{Si})/N(\text{H}) = -7.1 \pm 0.1.$$

The abundance of the main ionization stage (Si) remains the same as derived in NLTE, but the Si abundance is 0.5 dex lower. The Fe lines in the NUV spectrum also lead to an LTE abundance 0.5 dex lower than the value derived with NLTE models. To illustrate this effect on the spectral lines, we select four spectral ranges featuring Si lines and show the corresponding LTE spectrum in Fig. 4. The spectrum includes the abundances determined with the NLTE models. The Si lines (as well as few Fe lines and one S line) appear too strong, as can be seen with the Ni lines (Fig A.1).

It thus becomes clear that NLTE effects are present in HD 188112 and influence the line strengths, especially those of the non-dominant ionic species. For Si, S, and Fe the differences in strength of the modeled lines between LTE and NLTE lead to a ~ 0.5 dex shift in abundances. However, the LTE abundances derived for the main ionization stage (in this case doubly ionized) are consistent with the NLTE values. This result confirms that the abundances derived for the elements that could not be treated in NLTE can be regarded as reliable since the main ionization stage was used. The only exception is lead, for which only one Pb line was visible. In this case the derived abundance might be overestimated. The strongest gallium line is from Ga, but the LTE models simultaneously reproduced this line and the two weak Ga features. However, some mystery still remains about the Sn lines: it is not clear what is causing the

⁶ We remind the reader that the hybrid approach of ADS only includes NLTE effects in the computation of the population numbers; in all cases (NLTE and LTE) the atmospheric structure is computed assuming the LTE approximation.

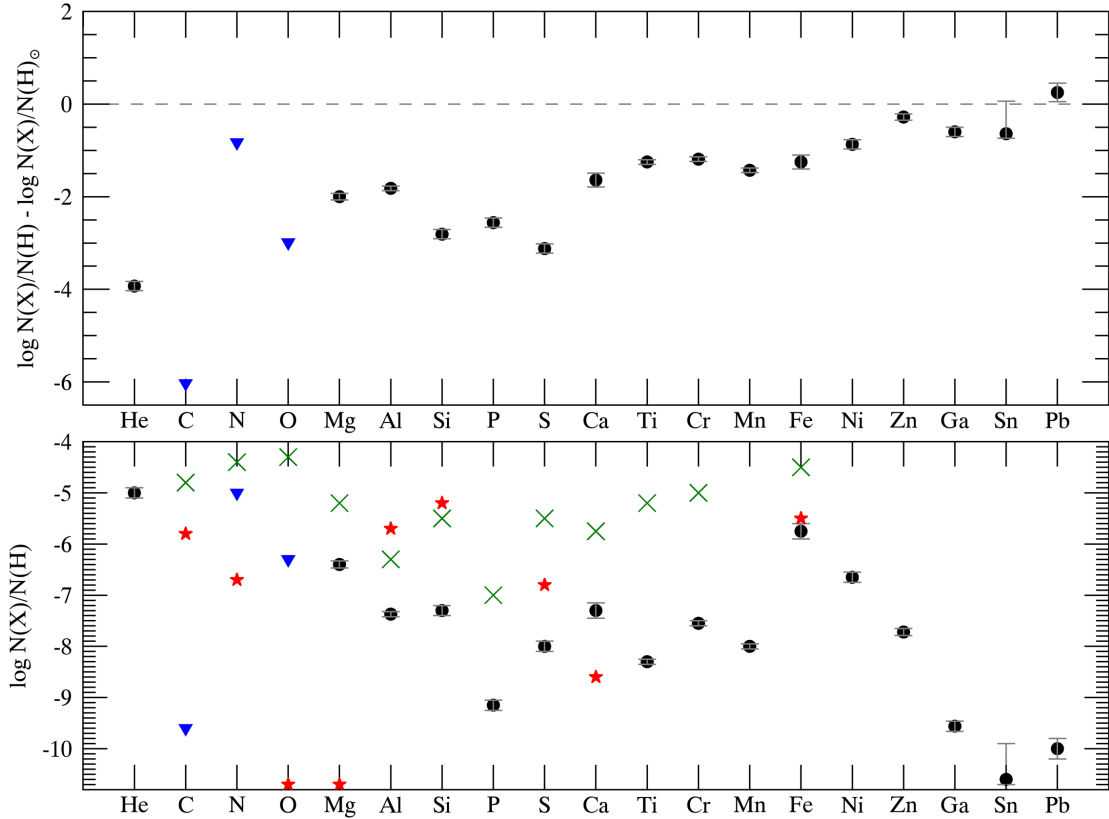


Fig. 5. Summary of the determined chemical composition of HD 188112. The *top panel* shows the abundances relative to the solar ones (Asplund et al. 2009) and the *bottom panel* the absolute values. Down-pointing triangles indicate upper limits determined for C, N, and O. The stars in the bottom panel indicate abundances predicted by radiative levitation (P. Chayer, priv. comm.). No support is expected for oxygen and magnesium, thus the stars are at the bottom of the plot. The green crosses indicate the average abundances for sdB stars.

elements (Ti and heavier) being the most abundant relative to solar (see top panel of Fig. 5). Lead is, however, slightly above the solar value. This abundance pattern suggests that diffusion mechanisms counteract gravitational settling in order to keep a relatively considerable amount of heavy elements in the photosphere.

5.2.1. Comparison with diffusion models

The bottom panel of Fig. 5 also features abundances predicted by radiative levitation (red stars) for the atomic species included in TOPbase⁷. These abundances were computed for a model with $T_{\text{eff}} = 21\,000$ K and $\log g = 5.6$ according to the method described in Chayer et al. (1995) (P. Chayer, priv. comm.). In most cases (C, Al, Si, S, Fe) we measured abundances below the value predicted by radiative support, though the Fe abundance is quite close to the prediction. The two exceptions are Mg and Ca. Calcium is 1.5 dex higher than the predicted abundance while no support at all is expected for magnesium.

5.2.2. Comparison with ELM WDs

A UV spectrum has been analyzed for only one other ELM WD so far, namely that of GALEX J1717+6757 (Hermes et al. 2014b). This star has $\log g = 5.67$, essentially identical to that of HD 188112, and $T_{\text{eff}} = 14\,900$ K, which gives a mass of $\sim 0.19 M_{\odot}$. Hermes et al. (2014b) detected lines from nine metals, and for all of them they derived an abundance higher (by

roughly 0.5 to 2.0 dex) than that measured for HD 188112. In their discussion, Hermes et al. (2014b) point out that radiative levitation for N, O, Si, P, and Fe gives predictions that are in line with the abundance pattern seen in the star. One noteworthy exception is carbon for which strong radiative support was predicted, but the element is extremely underabundant (by a factor of 1000 with respect to the sun) in the atmosphere of J1717. Interestingly, this is reminiscent of the situation for HD 188112, where important radiative support is also predicted for carbon at 21 000 K, but the element is strongly depleted in the stellar atmosphere. Hermes et al. (2014b) argue that a possible explanation for carbon depletion might be a history of repeated CNO flashes, as predicted by evolutionary models with $M \gtrsim 0.18 M_{\odot}$. This might also apply to HD 188112, although we do not see the metal enrichment that might be associated with CNO-flash surface convection. Calcium is another element that defies radiative levitation predictions in J1717: more Ca is observed than predicted, just as it is for HD 188112. According to Fig. 5 in Hermes et al. (2014b) the abundance pattern of J1717 is not very different from those of WDs with ongoing accretion from debris discs, except for Mg and O. However, the authors conclude that debris-disk accretion is unlikely in the case of J1717 because of the discrepancy in oxygen abundance, and because accretion from a circumbinary disk is dynamically difficult to explain.

Two ELM WDs are known to be metal rich: PSR J1816+4510 ($T_{\text{eff}} = 16\,000$ K, $\log g = 4.9$), the companion of a massive millisecond pulsar (Kaplan et al. 2013), and SDSS J0745+1949 ($T_{\text{eff}} = 8,380$ K, $\log g = 6.2$), a tidally distorted star (Gianninas et al. 2014b). The analyses of their optical spectra allowed for the abundance determination of a few elements. The

⁷ <http://cdsweb.u-strasbg.fr/topbase/topbase.html>

abundances of Mg, Ca, Ti, Cr, and Fe turned out to be close to solar in the case of J0745 while He, Mg, Ca, Si, and Fe are about 10 times solar in J1816. The origin of the metals in these two stars is not fully understood. A recent shell flash is a possible explanation for the high metallicity of J1816, but the rather low mass inferred for J0745 ($M = 0.16 M_{\odot}$) does not suggest the star could have gone through such shell flash episodes. On the other hand, accretion of metals from a debris disk was discussed as a possibility for J0745, while the pulsar companion of J1816 prevents such an accretion.

Even though detailed abundances are known for only three other ELM-WDs, [Gianninas et al. \(2014a\)](#) measured abundances of He, Ca, and Mg in their sample of 61 stars (though such elements were visible only in a minority of stars). As mentioned previously, they noticed the presence of Ca lines in basically all of their stars having $\log g \lesssim 6.0$. HD 188112, which has low gravity, now also falls into this category thanks to the tiny line we identified in its optical spectra. The abundance we derived ($\log N(\text{Ca})/N(\text{H}) = -7.3$), though below the [Gianninas et al. \(2014a\)](#) detection threshold, is comparable to the lowest abundances measured in their cooler ELM WDs (we note here that the Ca lines get stronger at lower temperature). The same observation holds for Mg, where the abundance of HD 188112 is similar to the lowest values detected in the [Gianninas et al. \(2014a\)](#) sample.

5.2.3. Comparison with sdB stars

Given its fundamental parameters, HD 188112 is considered an sdB star, so it might be worth comparing its abundances with those of sdBs. To this end we also included in Fig. 5 the “upper averages” (including determinations and upper limits) of the [Geier \(2013\)](#) sample, consisting of a hundred sdBs. It thus appears that HD 188112 is a particularly metal-poor sdB, but also an especially cool one. PG1627+017 is a cool pulsating sdB ($T_{\text{eff}} \sim 21\text{--}24$ kK) that can be compared to HD 188112 in terms of effective temperature, but the lower $\log g$ of PG1627+017 places it onto the EHB, meaning that the star is likely to be more massive than HD 188112. Indeed, a mass of $\sim 0.45 M_{\odot}$ was suggested by its seismic properties ([Randall et al. 2006](#)). The UV spectrum of PG1627+017 has allowed a detailed abundance determination, and the star is clearly more metal-rich than HD 188112 (see Fig. 6 in [Blanchette et al. 2008](#)). Carbon is the most extremely depleted element in HD 188112. Past studies of sdBs have shown a large star-to-star variation in atmospheric carbon. Very low carbon upper limits ($\log N(\text{C})/N(\text{C}_{\odot}) = -5.7$ and -5.3) were determined for CD $-24^{\circ}731$ and PG 1219+534, respectively ([O’Toole & Heber 2006](#)). The sdOB star Feige 110 is another example of a carbon poor star ([Rauch et al. 2014](#); [Heber et al. 1984](#)). Lead is the most enriched element in HD 188112, and it has been identified in 22 out of the 27 hot subdwarf UV spectra examined by [O’Toole \(2004\)](#). Further abundance analysis of sdBs showed that lead enrichment varies from 10 to 1000 times solar ([O’Toole & Heber 2006](#); [Blanchette et al. 2008](#)). These two studies also showed that trans-iron elements tend to be overabundant in the atmosphere of sdB stars. In this respect, the abundance pattern of HD 188112 is similar to other sdBs.

5.3. Binary system

In addition to the spectroscopic analysis, we attempted a better characterization of the HD 188112 binary system. By combining

our new UV radial velocity measurement with the already published values, we refined the parameters of the binary system: period (0.60658584(5) d), amplitude (188.7 ± 0.2 km s $^{-1}$), and systemic velocity (26.6 ± 0.2 km s $^{-1}$). Access to a H parallax for a star provides an independent mass measurement, i.e., independent of stellar evolution models. In our case, the spectroscopic mass of $0.245^{+0.075}_{-0.055} M_{\odot}$ derived with the parallax distance agrees quite well with that indicated by evolutionary models of low-mass He-core WDs, which predict $0.211 \pm 0.0175 M_{\odot}$ ([Althaus et al. 2013](#)). However, the uncertainty on the spectroscopic mass is rather large (due to the uncertainty on the parallax itself) and allows for a mass up to $0.32 M_{\odot}$. Such a mass is at the lower limit of He-core burning for an sdB star ([Han et al. 2002](#); [Hu et al. 2007](#)). Low-mass sdB stars are created when a massive progenitor ($2\text{--}2.5 M_{\odot}$) ignites helium under non-degenerate conditions. According to binary synthesis models, the second common envelope ejection channel can produce sdBs with masses down to $0.33 M_{\odot}$ in close binaries with a WD companion ([Han et al. 2003](#)). The position of HD 188112 in the $\log g - T_{\text{eff}}$ diagram would fit within the $0.33 M_{\odot}$ EHB band (see Fig. 7 from [Silvotti et al. 2012](#)). Although there is a possibility that HD 188112 is a He-core burning object, one must keep in mind that these low-mass sdBs occur much less frequently than the canonical ($\sim 0.47 M_{\odot}$) sdBs and that the extreme upper limit of our spectroscopic mass coincides with the extreme lower limit of the He-core burning. Given the current parallax value, we thus consider it unlikely that HD 188112 is such an object. For the lower mass limit on HD 188112, both the parallax and evolutionary models give a value of $\sim 0.19 M_{\odot}$. In this case, the star is certainly a pre-ELM WD.

In our attempt to constrain the mass of the WD companion, we considered both the 0.21 and $0.245 M_{\odot}$ solutions indicated respectively by evolutionary models and the parallax. We derived a minimum mass of $0.7 M_{\odot}$ for the companion⁸. It is interesting to compare this minimum mass with the minimum mass distributions of sdB binaries with WD companions and of ELM WD binaries illustrated in Fig. 14 in [Kupfer et al. \(2015\)](#). When considering the distribution for sdB binaries, it appears that a $0.7 M_{\odot}$ companion is quite massive; only two known sdBs have a more massive WD companion⁹. After a survey was dedicated to finding massive companions to sdBs ([Geier et al. 2011](#)), it now seems that such systems are quite rare. On the other hand, when looking at the observed minimum mass distribution of ELM systems (data from [Gianninas et al. 2014a](#)), the companion masses are evenly distributed between 0.1 and $0.9 M_{\odot}$ with a few more massive outliers. In this context, the companion of HD 188112 would be on the massive side, but not outstandingly so.

We measured the rotational broadening of metallic lines in our UV spectra and derived $v_{\text{rot}} \sin i = 7.9 \pm 0.3$ km s $^{-1}$. In order to constrain the inclination of the system, we assumed it to be tidally locked, which led to inclination values between 49° and 61° . This range nicely overlaps with the most likely inclinations for a random sample. Our inclination range indicates companion masses between 0.92 and $1.33 M_{\odot}$. The synchronization assumption thus seems reasonable, or at least does not lead to improbable results. Recent statistical investigations on the mass distribution of companions to ELM WDs found a mean mass of $\sim 0.75 M_{\odot}$, with $\sigma \sim 0.25 M_{\odot}$ ([Andrews et al. 2014](#); [Boffin 2015](#)). Both studies found very similar results when assuming a

⁸ If we consider $0.19 M_{\odot}$ for HD 188112 the minimum mass of the companion decreases only slightly to $0.68 M_{\odot}$.

⁹ HD 188112 was not included in the [Kupfer et al. \(2015\)](#) sample because of its low mass.

Gaussian distribution to model the companion's mass population and comparing it with the observed ELM WD systems of Brown et al. (2013) and Gianninas et al. (2014a). If the HD 188112 system is indeed synchronized, the companion would thus be on the massive side of these mass distributions. The possibility of a neutron star companion should not be discarded, as it would require an inclination angle only slightly below 49° , and would imply the star is rotating faster than synchronized. This last assumption is plausible considering the fact that evolutionary models predict that the rotation of the star should increase after the ejection of the common envelope, as the star is contracting toward the white dwarf regime. Given the orbital parameters of the HD 188112 system, the rotation period of the star can hardly be less than half the orbital period, in which case the inclination would be less than 25° and the companion mass above $6 M_\odot$. A search for possible X-ray emission from the companion of HD 188112 might help to constrain its nature (Kilic et al. 2014).

It might be interesting to look at the possible future of the system. As the star contracts toward the cooling track it is likely to experience hydrogen shell flashes during which the star will expand and fill its Roche lobe (Istrate et al. 2014). Brief episodes of mass transfer might lead to mass loss of a few times $10^{-4} M_\odot$ during a shell flash (see Fig. 12 in Nelson et al. 2004). Because the hydrogen fuel is diminished both by burning and mass loss, the evolution of the star will speed up. In the long run, gravitational wave radiation will lead to a decay of the orbit resulting finally in a merger of the components after a few Hubble times. By the time of merging, the system has evolved into a degenerate He-core white dwarf and a massive companion, most likely a white dwarf of 0.7 to $1.3 M_\odot$.

The outcome of the merger depends strongly on the mass of the white dwarf companion and its composition. If the mass is as low as $0.7 M_\odot$, the white dwarf is of C/O composition and the merger most likely produces a RCrB star (Webbink 1984; Clayton et al. 2007). Mergers of He-core white dwarfs with more massive C/O white dwarfs may lead to SNe Ia (Pakmor et al. 2013; Dan et al. 2015). Some simulations showed that the He-shell ignition induced by the accretion of material onto a sub-Chandrasekhar C/O WD is very likely to trigger a detonation in the core, leading to a SN Ia explosion (double-detonation scenario, Fink et al. 2007, 2010; Moll & Woosley 2013). If the core fails to ignite¹⁰, then the helium explosion alone can produce a fainter type Ia SN (Bildsten et al. 2007). At the high end of the companion mass range ($>1.1 M_\odot$), the system would have a low mass ratio ($q \lesssim 0.20$) and thus evolve via stable mass transfer into an AM Canum Venaticorum (AM CVn; Marsh et al. 2004; Dan et al. 2011), which is a potential SN Ia progenitor (Shen & Bildsten 2014). However, it is usually assumed that white dwarfs more massive than about $1.1 M_\odot$ have O/Ne/Mg cores and these objects, when accreting matter, are not likely to explode, but would rather collapse into a neutron star via electron capture (Nomoto & Kondo 1991; Shen & Bildsten 2014). On the other hand, recent investigations showed that near-Chandrasekhar mass (~ 1.1 – $1.3 M_\odot$) white dwarfs may have a hybrid composition of C/O/Ne and could be prone to explode, leading to faint SNe of the observed type Iax (Chen et al. 2014; Kromer et al. 2015). In either case, the outcome of the system depends on the stability of the mass transfer, which in turn depends on the mass ratio of the components (Marsh et al. 2004). For mass ratio q in the range ~ 0.25 – 0.70 the mass transfer can

be either stable or unstable (see Fig. 1 in Dan et al. 2011). For the HD 188112 system, q can be up to ~ 0.32 if the companion mass is close to the minimum value.

6. Conclusion

We began our analysis of the UV spectra of HD 188112 with the main goal of determining the projected rotational velocity, in order to put tighter constraints on the mass of the companion. However, the high-resolution spectra showed a large number of metallic lines that allowed us to perform a comprehensive abundance analysis of this pre-ELM WD. This is extremely interesting since the chemical compositions of only a few ELM WDs have been determined to date. Additionally, because it is a pre-ELM WD, HD 188112 represents an earlier evolutionary stage and comparing its metallic content with those of cooler, more compact, and thus older (in terms of cooling age) ELM WDs might help to determine the origin of their metals.

The spectral analysis was performed using hybrid NLTE model atmospheres, in which the NLTE effects are taken into account in the computation of the population numbers while the atmospheric structure is computed in LTE. The computation of NLTE populations was only possible for a limited number of species (C, N, O, Mg, Al, Si, S, Ca, and Fe); otherwise, the LTE approximation had to be used. By comparing both LTE and NLTE spectra for a few metallic species, we concluded that the spectral lines originating from the main ionization stages of an element were not affected, or were only marginally affected, by NLTE effects. Thus, they can be used reliably to derive abundances with LTE models. However, we clearly saw in our model spectra that NLTE effects affect lines of non-dominant ionic species. Fits of these lines led to discrepant abundances, by up to ~ 0.5 dex. As these effects are seen in HD 188112, they are likely to also be present in stars having a temperature higher than $\sim 21\,000$ K. This is why we emphasize that it is more accurate to consider only lines originating from the dominant ionic species when using LTE models in order to derive appropriate abundances.

Based on our abundance determination and comparisons with other ELM WDs and hot subdwarf stars, HD 188112 appears to be an especially metal-poor object. Its abundance pattern suggests diffusion effects where gravitational settling is probably counteracted by radiative levitation. In contrast to other more metal-rich ELM WDs, HD 188112 does not require any “metal enrichment” mechanism to explain the presence of metals in its atmosphere. It is also unlikely that its metallicity will increase as it ultimately cools down and becomes more compact; radiative levitation should become weaker as T_{eff} decreases and gravitational settling stronger as $\log q$ increases. However, given its mass, HD 188112 is likely to experience an H-shell flash that would temporarily increase the surface abundance of metals, especially He and N, although gravitational settling is expected to act quickly as the star contracts again. Considering the four detailed abundance analyses currently available for ELM/pre-ELM WDs, it seems that they show a rather wide variety of metallicities, from metal-rich to metal-poor, as is also observed for sdB stars.

Despite our efforts to constrain the mass of the HD 188112 companion, we are limited by the unknown inclination of the system and by the uncertainty on the mass of HD 188112 itself. By assuming tidally locked rotation, we could constrain the inclination to be between 49° and 61° . Unfortunately, we cannot currently test or verify whether the system is indeed tidally locked. Nevertheless, this assumption leads to inclinations close

¹⁰ In the case of a very low-mass (and low-density) C/O WD companion or a high-mass WD companion with O/Ne composition, a secondary detonation may be less likely (Shen & Bildsten 2014).

to the most likely ones for a random sample, so it does not appear to be inappropriate. This inclination range indicates a companion mass between 0.92 and 1.33 M_{\odot} , i.e., a rather massive WD, while the minimum mass is 0.7 M_{\odot} . For the mass of HD 188112, a value up to 0.32 M_{\odot} is possible according to the H distance, in which case the star would be at the limit of the He-burning mass range. *Gaia* should provide us with a more precise distance.

Acknowledgements. This work was supported by the Deutsches Zentrum für Luft- und Raumfahrt (grant 50 OR 1315). Based on observations made with the NASA/ESA *Hubble* Space Telescope, obtained at the Space Telescope Science Institute, which is operated by the Association of Universities for Research in Astronomy, Inc., under NASA contract NAS 5-26555. These observations are associated with program no. 12865, cycle 20. We are most grateful to P. Chayer for sharing the results of his radiative levitation computation and T. Rauch for fitting the tin lines with TMAP model atmospheres. We also thank A. Istrate and H. Dreschel for interesting discussions. The work of F.K.R. is supported by the ARCHES prize of the German Ministry of Education and Research (BMBF) and by the DAAD/Go8 German-Australian exchange programme for travel support. WH and ST acknowledge support by project TRR 33 'The Dark Universe' of the German Research Foundation (DFG) This research has made use of ISIS functions provided by ECAP/Remeis observatory and MIT (<http://www.sternwarte.uni-erlangen.de/isis/>). We thank John E. Davis for the development of the module used to prepare some of the figures in this paper.

References

- Althaus, L. G., Miller Bertolami, M. M., & Córscico, A. H. 2013, *A&A*, 557, A19
- Andrews, J. J., Price-Whelan, A. M., & Agüeros, M. A. 2014, *ApJ*, 797, L32
- Asplund, M., Grevesse, N., Sauval, A. J., & Scott, P. 2009, *ARA&A*, 47, 481
- Bildsten, L., Shen, K. J., Weinberg, N. N., & Nelemans, G. 2007, *ApJ*, 662, L95
- Blanchette, J.-P., Chayer, P., Wesemael, F., et al. 2008, *ApJ*, 678, 1329
- Boffin, H. M. J. 2015, *A&A*, 575, L13
- Brown, W. R., Kilic, M., Hermes, J. J., et al. 2011, *ApJ*, 737, L23
- Brown, W. R., Kilic, M., Allende Prieto, C., Gianninas, A., & Kenyon, S. J. 2013, *ApJ*, 769, 66
- Chayer, P., Fontaine, G., & Wesemael, F. 1995, *ApJS*, 99, 189
- Chen, M. C., Herwig, F., Denissenkov, P. A., & Paxton, B. 2014, *MNRAS*, 440, 1274
- Clayton, G. C., Geballe, T. R., Herwig, F., Fryer, C., & Asplund, M. 2007, *ApJ*, 662, 1220
- Dan, M., Rosswog, S., Guillochon, J., & Ramirez-Ruiz, E. 2011, *ApJ*, 737, 89
- Dan, M., Guillochon, J., Brügggen, M., Ramirez-Ruiz, E., & Rosswog, S. 2015, *MNRAS*, 454, 4411
- Dreizler, S., & Werner, K. 1993, *A&A*, 278, 199
- Driebe, T., Schoenberner, D., Bloeker, T., & Herwig, F. 1998, *A&A*, 339, 123
- Edelmann, H., Heber, U., Altmann, M., Karl, C., & Lisker, T. 2005, *A&A*, 442, 1023
- Eisenstein, D. J., Liebert, J., Harris, H. C., et al. 2006, *ApJS*, 167, 40
- Fink, M., Hillebrandt, W., & Röpke, F. K. 2007, *A&A*, 476, 1133
- Fink, M., Röpke, F. K., Hillebrandt, W., et al. 2010, *A&A*, 514, A53
- Geier, S. 2013, *A&A*, 549, A110
- Geier, S., Heber, U., Podsiadlowski, P., et al. 2010, *A&A*, 519, A25
- Geier, S., Hirsch, H., Tillich, A., et al. 2011, *A&A*, 530, A28
- Gianninas, A., Dufour, P., Kilic, M., et al. 2014a, *ApJ*, 794, 35
- Gianninas, A., Hermes, J. J., Brown, W. R., et al. 2014b, *ApJ*, 781, 104
- Gianninas, A., Kilic, M., Brown, W. R., Canton, P., & Kenyon, S. J. 2015, *ApJ*, 812, 167
- Giddings, J. R. 1981, Ph.D. Thesis, University of London
- Gray, F. D. 2008, *The Observation and Analysis of Stellar Photospheres* (Cambridge University Press)
- Hallakoun, N., Maoz, D., Kilic, M., et al. 2015, ArXiv e-prints [[arXiv:1507.06311](https://arxiv.org/abs/1507.06311)]
- Han, Z., Podsiadlowski, P., Maxted, P. F. L., Marsh, T. R., & Ivanova, N. 2002, *MNRAS*, 336, 449
- Han, Z., Podsiadlowski, P., Maxted, P. F. L., & Marsh, T. R. 2003, *MNRAS*, 341, 669
- Heber, U. 2009, *ARA&A*, 47, 211
- Heber, U., Hamann, W.-R., Hunger, K., et al. 1984, *A&A*, 136, 331
- Heber, U., Edelmann, H., Lisker, T., & Napiwotzki, R. 2003, *A&A*, 411, L477
- Hermes, J. J., Brown, W. R., Kilic, M., et al. 2014a, *ApJ*, 792, 39
- Hermes, J. J., Gänsicke, B. T., Koester, D., et al. 2014b, *MNRAS*, 444, 1674
- Høg, E., Fabricius, C., Makarov, V. V., et al. 2000, *A&A*, 355, L27
- Hu, H., Nelemans, G., Østensen, R., et al. 2007, *A&A*, 473, 569
- Irrgang, A., Przybilla, N., Heber, U., et al. 2014, *A&A*, 565, A63
- Istrate, A. G., Tauris, T. M., Langer, N., & Antoniadis, J. 2014, *A&A*, 571, L3
- Kaplan, D. L., Bhalariao, V. B., van Kerkwijk, M. H., et al. 2013, *ApJ*, 765, 158
- Kawka, A., Vennes, S., Oswalt, T. D., Smith, J. A., & Silvestri, N. M. 2006, *ApJ*, 643, L123
- Kawka, A., Vennes, S., O'Toole, S., et al. 2015, *MNRAS*, 450, 3514
- Kilic, M., Allende Prieto, C., Brown, W. R., & Koester, D. 2007, *ApJ*, 660, 1451
- Kilic, M., Brown, W. R., Allende Prieto, C., Kenyon, S. J., & Panei, J. A. 2010, *ApJ*, 716, 122
- Kilic, M., Brown, W. R., Allende Prieto, C., et al. 2011a, *ApJ*, 727, 3
- Kilic, M., Brown, W. R., Kenyon, S. J., et al. 2011b, *MNRAS*, 413, L101
- Kilic, M., Hermes, J. J., Gianninas, A., et al. 2014, *MNRAS*, 438, L26
- Kromer, M., Ohlmann, S. T., Pakmor, R., et al. 2015, *MNRAS*, 450, 3045
- Kupfer, T., Geier, S., Heber, U., et al. 2015, *A&A*, 576, A44
- Kurucz, R. L. 1996, in M.A.S.S., *Model Atmospheres and Spectrum Synthesis*, eds. S. J. Adelman, F. Kupka, & W. W. Weiss, ASP Conf. Ser., 108, 160
- Lanz, T., & Hubeny, I. 2007, *ApJS*, 169, 83
- Latour, M., Irrgang, A., Heber, U., & Schaffenroth, V. 2015, in 19th European Workshop on White Dwarfs, eds. P. Dufour, P. Bergeron, & G. Fontaine, ASP Conf. Ser., 493, 9
- Liebert, J., Bergeron, P., Eisenstein, D., et al. 2004, *ApJ*, 606, L147
- Livne, E., & Glasner, A. S. 1990, *ApJ*, 361, 244
- Marsh, T. R., Dhillon, V. S., & Duck, S. R. 1995, *MNRAS*, 275, 828
- Marsh, T. R., Nelemans, G., & Steeghs, D. 2004, *MNRAS*, 350, 113
- Moll, R., & Woosley, S. E. 2013, *ApJ*, 774, 137
- Morton, D. C. 2000, *ApJS*, 130, 403
- Nelson, L. A., Dubeau, E., & MacCannell, K. A. 2004, *ApJ*, 616, 1124
- Nieva, M. F., & Przybilla, N. 2007, *A&A*, 467, 295
- Nieva, M. F., & Przybilla, N. 2008, *A&A*, 481, 199
- Nieva, M.-F., & Przybilla, N. 2012, *A&A*, 539, A143
- Nomoto, K., & Kondo, Y. 1991, *ApJ*, 367, L19
- O'Toole, S. J. 2004, *A&A*, 423, L25
- O'Toole, S. J., & Heber, U. 2006, *A&A*, 452, 579
- Pakmor, R., Kromer, M., Taubenberger, S., & Springel, V. 2013, *ApJ*, 770, L8
- Panei, J. A., Althaus, L. G., Chen, X., & Han, Z. 2007, *MNRAS*, 382, 779
- Parsons, S. G., Marsh, T. R., Gänsicke, B. T., Drake, A. J., & Koester, D. 2011, *ApJ*, 735, L30
- Przybilla, N., Butler, K., Becker, S. R., & Kudritzki, R. P. 2006a, *A&A*, 445, 1099
- Przybilla, N., Nieva, M. F., & Edelmann, H. 2006b, *Balt. Astron.*, 15, 107
- Randall, S. K., Fontaine, G., Green, E. M., et al. 2006, *ApJ*, 643, 1198
- Rauch, T., & Deetjen, J. L. 2003, in *Stellar Atmosphere Modeling*, eds. I. Hubeny, D. Mihalas, & K. Werner, ASP Conf. Ser., 288, 103
- Rauch, T., Werner, K., Bohlin, R., & Kruk, J. W. 2013, *A&A*, 560, A106
- Rauch, T., Rudkowski, A., Kampka, D., et al. 2014, *A&A*, 566, A3
- Schaffenroth, V. 2015, Ph.D. Thesis, Friedrich-Alexander-Universität Erlangen-Nürnberg
- Shen, K. J., & Bildsten, L. 2014, *ApJ*, 785, 61
- Silvotti, R., Østensen, R. H., Bloemen, S., et al. 2012, *MNRAS*, 424, 1752
- Sim, S. A., Röpke, F. K., Hillebrandt, W., et al. 2010, *ApJ*, 714, L52
- Steinfadt, J. D. R., Kaplan, D. L., Shporer, A., Bildsten, L., & Howell, S. B. 2010, *ApJ*, 716, L146
- van Kerkwijk, M. H., Bergeron, P., & Kulkarni, S. R. 1996, *ApJ*, 467, L89
- van Leeuwen, F. 2007, *A&A*, 474, 653
- Vennes, S., Chayer, P., & Dupuis, J. 2005, *ApJ*, 622, L121
- Vennes, S., Thorstensen, J. R., Kawka, A., et al. 2011, *ApJ*, 737, L16
- Webbink, R. F. 1984, *ApJ*, 277, 355
- Werner, K., Rauch, T., Ringat, E., & Kruk, J. W. 2012, *ApJ*, 753, L7
- Zuckerman, B., Koester, D., Melis, C., Hansen, B. M., & Jura, M. 2007, *ApJ*, 671, 872

Appendix A: Additional material

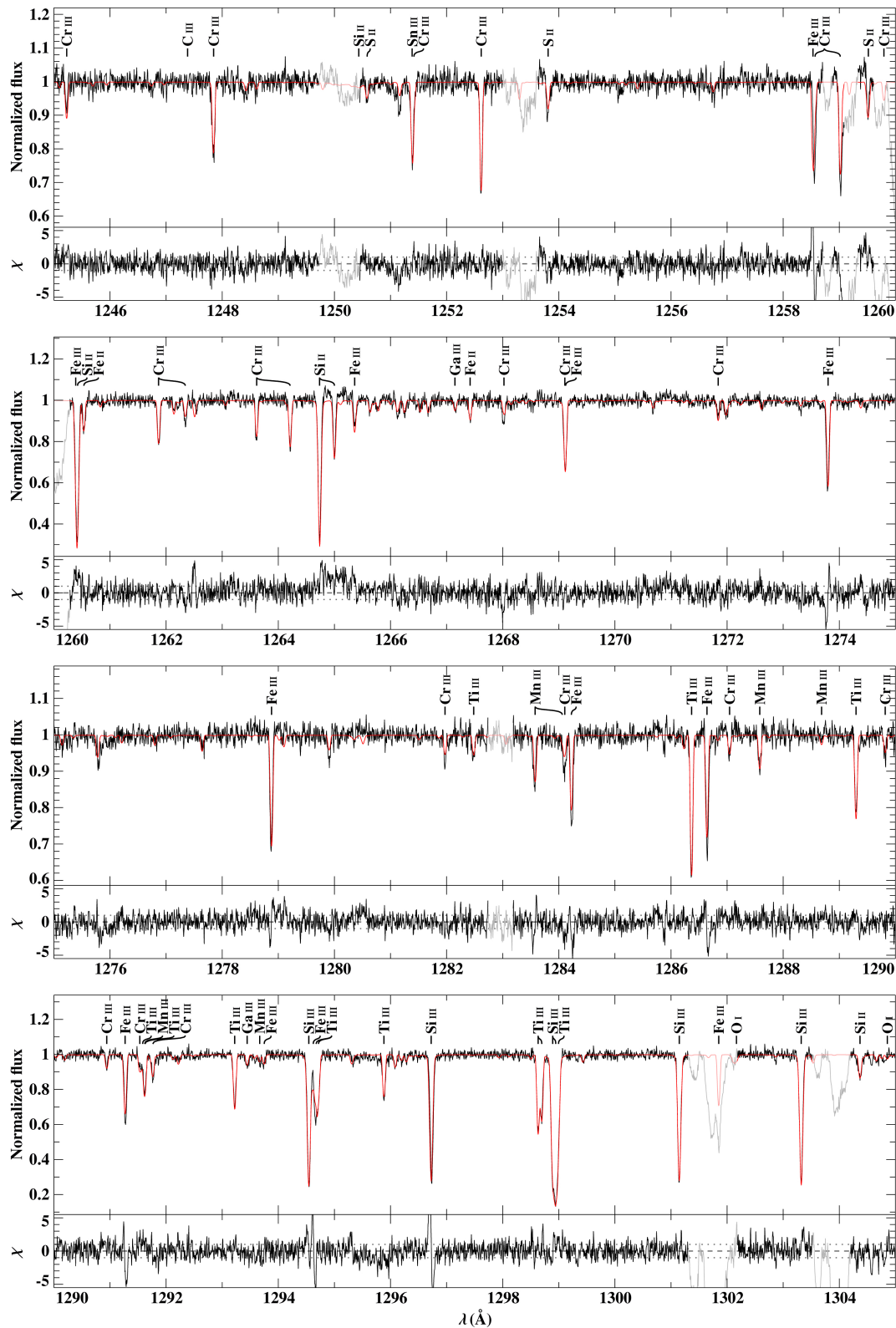


Fig. A.1. Entirety of our UV spectra of HD 188112, compared with our best fitting model. The *bottom* of each panel features the difference between the observation and the model divided by the noise as χ . The *bottom* of each panel features the difference between the observation and the model divided by the noise as χ . The portions of the spectrum plotted in grey are regions excluded from the fits. Most of them feature blueshifted IS lines. The IS lines are artificially broadened by the RV correction applied to the individual spectra and show two components due to a time gap in the series of FUV spectra. For this panel, the abundance of Sn was set to the value matching the Sn line.

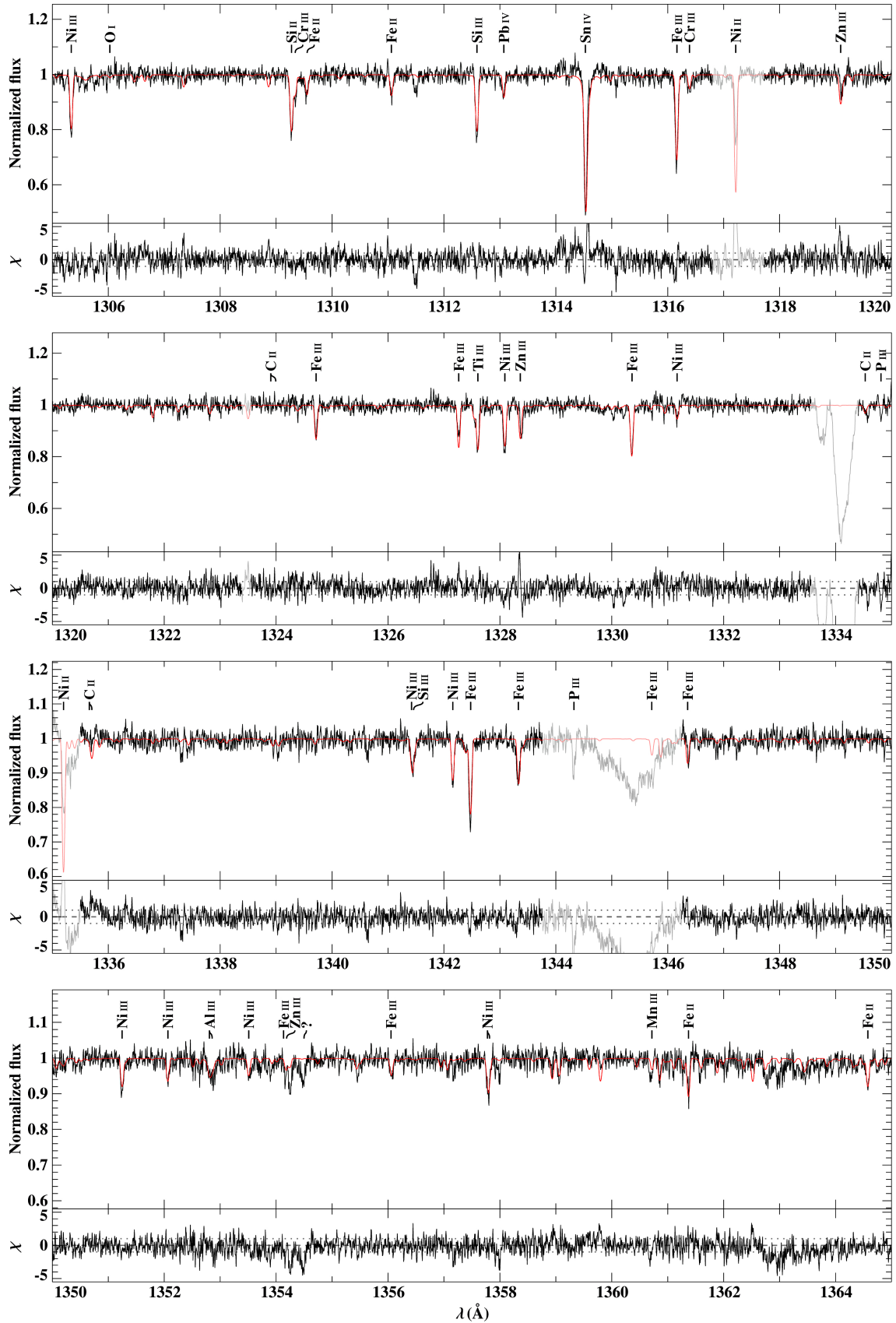


Fig. A.1. continued. Here and in the following panels, the Sn abundance is set to the value matching the Sn lines. Nickel was included at the abundance determined by the Ni lines, thus the Ni lines appear too strong and were excluded from the fits (see Sect. 4.3.4). The broad feature at around 1345 \AA is an artifact (blemish) from the STIS detector.

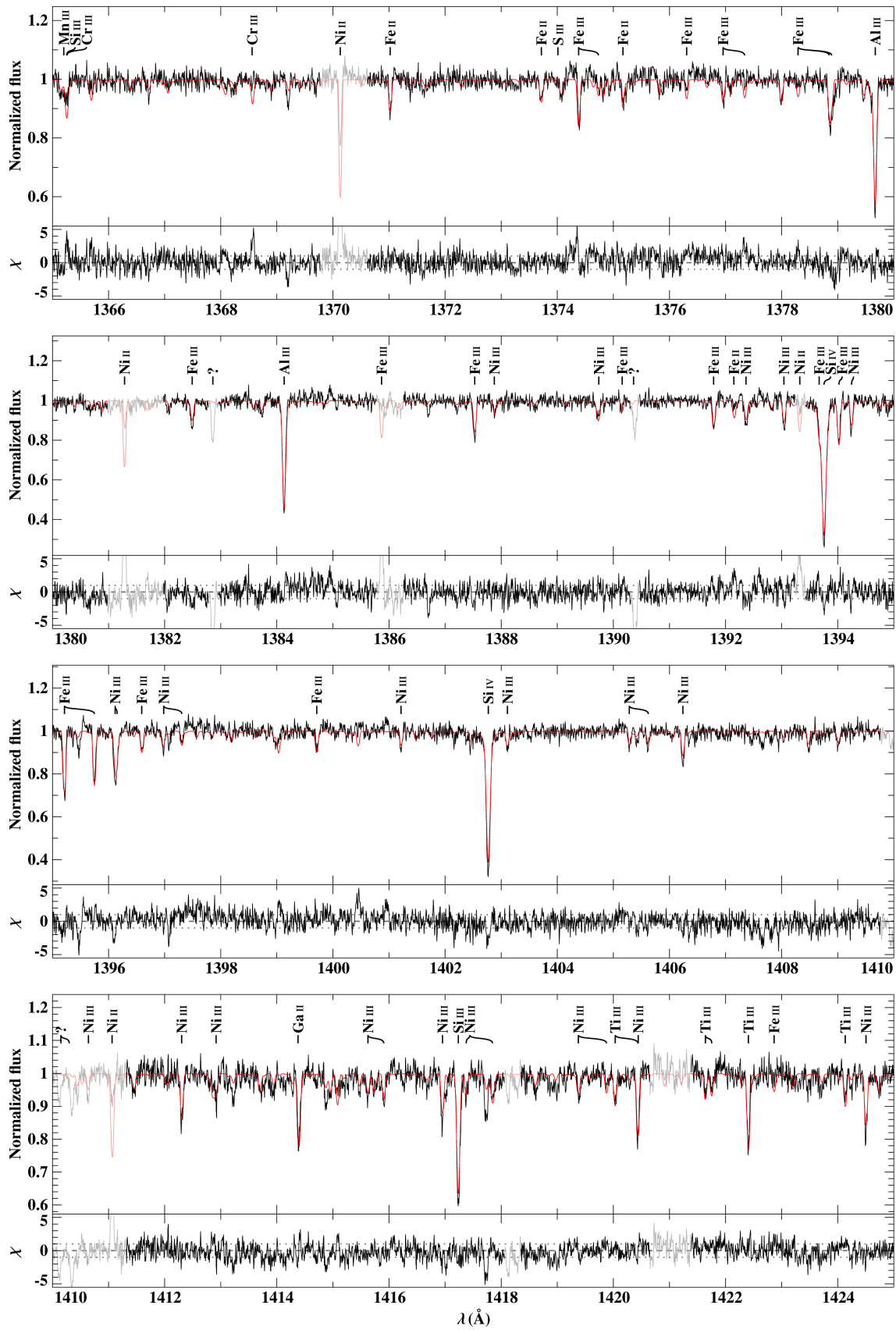


Fig. A.1. continued.

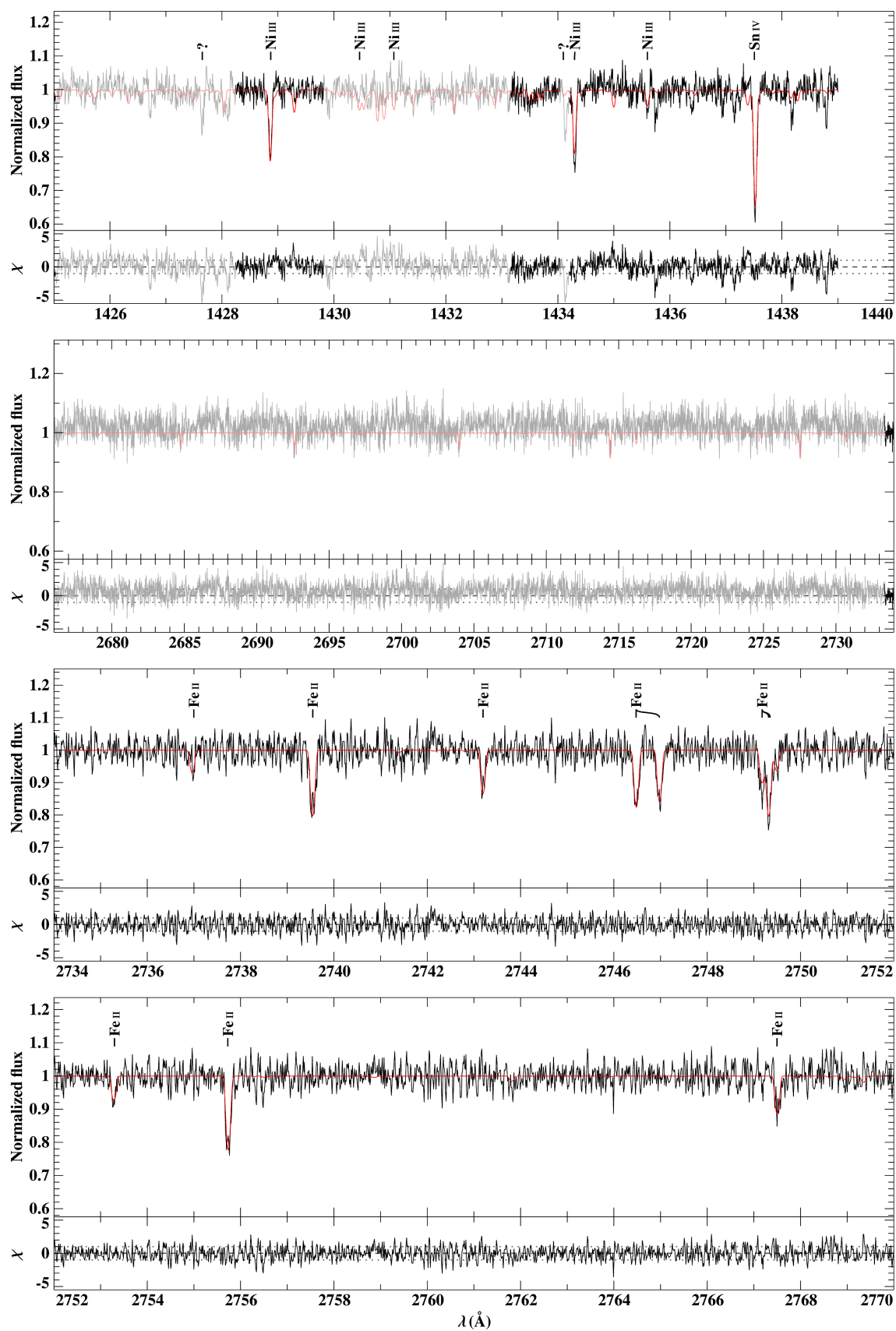


Fig. A.1. continued. Here starts the NUV2 spectrum. The scaling of the wavelength varies to include the spectral intervals devoid of fitted lines in unique panels. The iron abundance was set to the value derived with the Fe II lines.

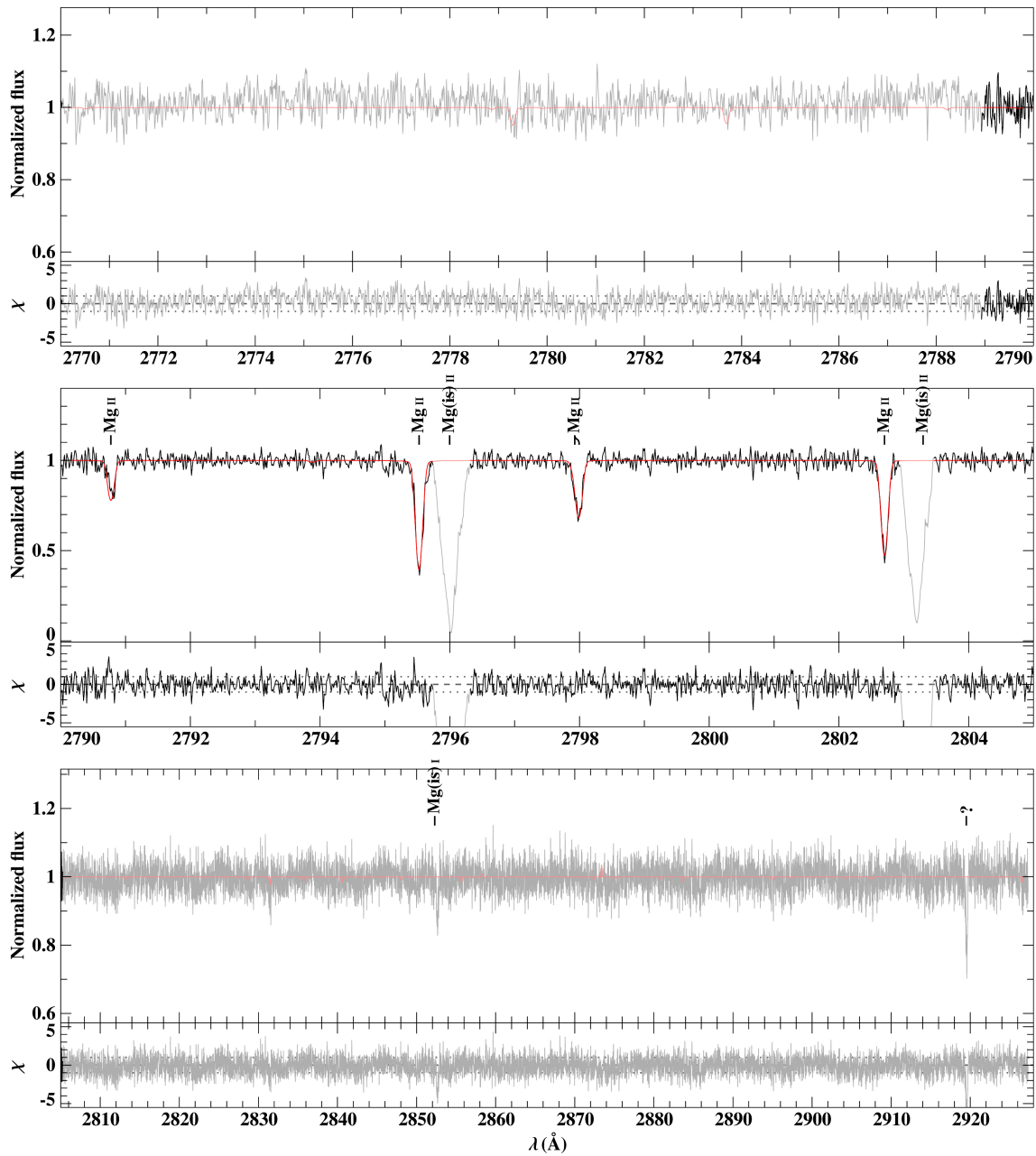


Fig. A.1. continued.

Bibliography

- Applegate, J. H. 1992, *ApJ*, 385, 621
- Bédard, A., Bergeron, P., Brassard, P., & Fontaine, G. 2020, *ApJ*, 901, 93
- Bennett, J. O. 2018, *The essential cosmic perspective*, 8th Edition
- Boffin, H. M. J. & Jones, D. 2019, *The Importance of Binaries in the Formation and Evolution of Planetary Nebulae*
- Bolmont, E., Gallet, F., Mathis, S., et al. 2017, *A&A*, 604, A113
- Bours, M. C. P., Marsh, T. R., Parsons, S. G., et al. 2016, *MNRAS*, 460, 3873
- Butler, K. & Giddings, J. R. 1985, in , *Newsletter of Analysis of Astronomical Spectra*, No. 9 (Univ. London)
- Chen, J., Ferraro, F. R., Cadelano, M., et al. 2021, *Nature Astronomy*, 5, 1170
- Chen, X., Han, Z., Deca, J., & Podsiadlowski, P. 2013, *MNRAS*, 434, 186
- Copperwheat, C. M., Marsh, T. R., Dhillon, V. S., et al. 2010, *MNRAS*, 402, 1824
- Culpan, R., Geier, S., Reindl, N., et al. 2022, *A&A*, 662, A40
- Decin, L., Montargès, M., Richards, A. M. S., et al. 2020, *Science*, 369, 1497
- Drechsel, H., Haas, S., Lorenz, R., & Gayler, S. 1995, *A&A*, 294, 723
- Eggleton, P. 2006, *Evolutionary Processes in Binary and Multiple Stars*
- Eggleton, P. P. 1983, *ApJ*, 268, 368
- Fontaine, G., Brassard, P., Charpinet, S., et al. 2012, *A&A*, 539, A12
- Ge, H., Tout, C. A., Chen, X., et al. 2022, *ApJ*, 933, 137
- Geier, S., Napiwotzki, R., Heber, U., & Nelemans, G. 2011a, *A&A*, 528, L16
- Geier, S., Raddi, R., Gentile Fusillo, N. P., & Marsh, T. R. 2019, *A&A*, 621, A38
- Geier, S., Schaffenroth, V., Drechsel, H., et al. 2011b, *APJ*, 731, L22+
- Giddings, J. R. 1981, *Phd thesis*, University of London
- Han, Z., Podsiadlowski, P., Maxted, P. F. L., & Marsh, T. R. 2003, *MNRAS*, 341, 669
- Han, Z., Podsiadlowski, P., Maxted, P. F. L., Marsh, T. R., & Ivanova, N. 2002, *MNRAS*, 336, 449

- Heber, U. 2009, *ARA&A*, 47, 211
- Heber, U. 2016, *PASP*, 128, 082001
- Heber, U., Irrgang, A., & Schaffenroth, J. 2018, *Open Astronomy*, 27, 35
- Heinze, A. N., Tonry, J. L., Denneau, L., et al. 2018, *AJ*, 156, 241
- Hilditch, R. W. 2001, *An Introduction to Close Binary Stars*
- Ivanova, N., Justham, S., Chen, X., et al. 2013, *A&A Rev.*, 21, 59
- Ivanova, N., Justham, S., & Ricker, P. 2020, *Common Envelope Evolution*
- Jackson, B. K., Lewis, N. K., Barnes, J. W., et al. 2012, *ApJ*, 751, 112
- Jones, D. 2020, *Galaxies*, 8, 28
- Kippenhahn, R., Weigert, A., & Weiss, A. 2013, *Stellar Structure and Evolution*
- Kiss, L. L., Csák, B., Szatmáry, K., Furész, G., & Sziládi, K. 2000, *A&A*, 364, 199
- Kruckow, M. U., Neunteufel, P. G., Di Stefano, R., Gao, Y., & Kobayashi, C. 2021, *ApJ*, 920, 86
- Kupfer, T., Geier, S., Heber, U., et al. 2015, *A&A*, 576, A44
- Kurucz, R. L. 1996, in *Astronomical Society of the Pacific Conference Series*, Vol. 108, M.A.S.S., *Model Atmospheres and Spectrum Synthesis*, ed. S. J. Adelman, F. Kupka, & W. W. Weiss, 160
- Lutz, R. 2011, PhD thesis, Georg August University of Göttingen, Germany
- Naslim, N., Jeffery, C. S., Hibbert, A., & Behara, N. T. 2013, *MNRAS*, 434, 1920
- Nieva, M. F. & Przybilla, N. 2007, *A&A*, 467, 295
- Offner, S. S. R., Moe, M., Kratter, K. M., et al. 2022, arXiv e-prints, arXiv:2203.10066
- Ohlmann, S. T., Röpke, F. K., Pakmor, R., & Springel, V. 2016, *ApJ*, 816, L9
- Palacios, A. 2013, in *EAS Publications Series*, Vol. 62, *EAS Publications Series*, ed. P. Hennebelle & C. Charbonnel, 227–287
- Parsons, S. G., Hernandez, M. S., Toloza, O., et al. 2023, *MNRAS*, 518, 4579
- Pols, O. R. 2011, *Lecture Notes on Stellar Structure and Evolution*, https://www.astro.ru.nl/~onnop/education/stev_utrecht_notes/
- Preece, H. P., Tout, C. A., & Jeffery, C. S. 2018, *MNRAS*, 481, 715
- Ricker, G. R., Winn, J. N., Vanderspek, R., et al. 2015, *Journal of Astronomical Telescopes, Instruments, and Systems*, 1, 014003
- Schaffenroth, J. 2016, Master's thesis, Universität Erlangen-Nürnberg
- Schaffenroth, V., Barlow, B. N., Drechsel, H., & Dunlap, B. H. 2015, *A&A*, 576, A123

- Schaffenroth, V., Geier, S., Heber, U., et al. 2014, *A&A*, 564, A98
- Schreiber, M. R., Gänsicke, B. T., Rebassa-Mansergas, A., et al. 2010, *A&A*, 513, L7
- Sion, E. M. 2011, in *White Dwarf Atmospheres and Circumstellar Environments*, ed. D. W. Hoard, 1–24
- Soker, N., Grichener, A., & Sabach, E. 2018, *ApJ*, 863, L14
- Springel, V. 2010, *MNRAS*, 401, 791
- Tassoul, M. & Tassoul, J.-L. 1992, *ApJ*, 395, 604
- Tonry, J. L., Denneau, L., Heinze, A. N., et al. 2018, *PASP*, 130, 064505
- Udalski, A., Szymański, M. K., & Szymański, G. 2015, *Acta Astron.*, 65, 1
- VanderPlas, J. T. 2018, *ApJS*, 236, 16
- Vos, J., Vučković, M., Chen, X., et al. 2019, *MNRAS*, 482, 4592
- Vučković, M., Østensen, R. H., Németh, P., Bloemen, S., & Pápics, P. I. 2016, *A&A*, 586, A146
- Wang, L., Gies, D. R., Peters, G. J., et al. 2021, *AJ*, 161, 248
- Zahn, J.-P. 1977, *A&A*, 57, 383
- Zorotovic, M. & Schreiber, M. 2022, *MNRAS*, 513, 3587
- Zorotovic, M., Schreiber, M. R., Gänsicke, B. T., & Nebot Gómez-Morán, A. 2010, *A&A*, 520, A86

Acknowledgement

I want to thank Stephan Geier, who supervised me from my first project on and supported my work since then. He encouraged me and gave me the opportunity to do the work presented in this thesis by employing me first in Tübingen and later in Potsdam and always supported its progress with discussions and good ideas. Special thanks goes to my PhD supervisor Uli Heber, who always handed out advice and first introduced me to this topic already in my diploma thesis. I also want to thank my second PhD supervisor, Norbert Przybilla, who gave me the opportunity to start the EREBOS project, which is the basis of this thesis. I am deeply grateful to my collaborators, especially Brad Barlow, Ingrid Pelisoli, Dave Kilkenny and Marek Wolf, who supported this work and the EREBOS project greatly.

I want to thank my colleagues in Potsdam, who made my time there always interesting and exciting. I also want to thank the University of Potsdam for giving me the opportunity to gain a lot of experience by allowing me to give my own lectures and to supervise students so that I could easily fulfill the requirements for the habilitation.

I am thankful to my new colleagues in Tautenburg and my new boss Markus Roth for giving me the possibility to finish this thesis.

My deepest thanks goes to my family and especially my husband Richard, who always supports me, especially in stressful times and moved with me from one working place to the next.